

AD-A248 270



AGARD-AR-270

①

AGARD-AR-270

# AGARD

ADVISORY GROUP FOR AEROSPACE RESEARCH & DEVELOPMENT  
7 RUE ANCELLE 92200 NEUILLY SUR SEINE FRANCE

AGARD ADVISORY REPORT 270  
Fluid Dynamics Panel Working Group 13

## Air Intakes for High Speed Vehicles

(Prises d'Air pour Véhicules à Grande Vitesse)

DTIC  
ELECTE  
MAR 18 1992  
S B D

DISTRIBUTION STATEMENT A

Approved for public release;  
Distribution Unlimited

*This Advisory Report was prepared at the request of the  
Fluid Dynamics Panel of AGARD.*

92-06897



NORTH ATLANTIC TREATY ORGANIZATION

92 3 17 019

Published September 1991

Distribution and Availability on Back Cover

**Best  
Available  
Copy**

# AGARD

ADVISORY GROUP FOR AEROSPACE RESEARCH & DEVELOPMENT

7 RUE ANCELLE 92200 NEUILLY SUR SEINE FRANCE

---

AGARD ADVISORY REPORT 270

Fluid Dynamics Panel Working Group 13

## Air Intakes for High Speed Vehicles

(Prises d'Air pour Véhicules à Grande Vitesse)

This Advisory Report was prepared at the request of the  
Fluid Dynamics Panel of AGARD.



North Atlantic Treaty Organization  
*Organisation du Traité de l'Atlantique Nord*

---

# The Mission of AGARD

According to its Charter, the mission of AGARD is to bring together the leading personalities of the NATO nations in the fields of science and technology relating to aerospace for the following purposes:

- Recommending effective ways for the member nations to use their research and development capabilities for the common benefit of the NATO community;
- Providing scientific and technical advice and assistance to the Military Committee in the field of aerospace research and development (with particular regard to its military application);
- Continuously stimulating advances in the aerospace sciences relevant to strengthening the common defence posture;
- Improving the co-operation among member nations in aerospace research and development;
- Exchange of scientific and technical information;
- Providing assistance to member nations for the purpose of increasing their scientific and technical potential;
- Rendering scientific and technical assistance, as requested, to other NATO bodies and to member nations in connection with research and development problems in the aerospace field.

The highest authority within AGARD is the National Delegates Board consisting of officially appointed senior representatives from each member nation. The mission of AGARD is carried out through the Panels which are composed of experts appointed by the National Delegates, the Consultant and Exchange Programme and the Aerospace Applications Studies Programme. The results of AGARD work are reported to the member nations and the NATO Authorities through the AGARD series of publications of which this is one.

Participation in AGARD activities is by invitation only and is normally limited to citizens of the NATO nations.

The content of this publication has been reproduced directly from material supplied by AGARD or the authors.

Published September 1991

Copyright © AGARD 1991  
All Rights Reserved

ISBN 92-835-0637-5



Printed by Specialised Printing Services Limited  
40 Chigwell Lane, Loughton, Essex IG10 3TZ



## Recent Publications of the Fluid Dynamics Panel

### AGARDOGRAPHS (AG)

**Experimental Techniques in the Field of Low Density Aerodynamics**  
AGARD AG-318 (E), April 1991

**Techniques Expérimentales Liées à l'Aérodynamique à Basse Densité**  
AGARD AG-318 (FR), April 1990

**A Survey of Measurements and Measuring Techniques in Rapidly Distorted Compressible Turbulent Boundary Layers**  
AGARD AG-315, May 1989

**Reynolds Number Effects in Transonic Flows**  
AGARD AG-303, December 1988

**Three Dimensional Grid Generation for Complex Configurations — Recent Progress**  
AGARD AG-309, March 1988

### REPORTS (R)

**Aircraft Dynamics at High Angles of Attack: Experiments and Modelling**  
AGARD R-776, Special Course Notes, March 1991

**Inverse Method: in Airfoil Design for Aeronautical and Turbomachinery Applications**  
AGARD R-780, Special Course Notes, November 1990

**Aerodynamics of Rotorcraft**  
AGARD R-781, Special Course Notes, November 1990

**Three-Dimensional Supersonic/Hypersonic Flows Including Separation**  
AGARD R-764, Special Course Notes, January 1990

**Advances in Cryogenic Wind Tunnel Technology**  
AGARD R-774 Special Course Notes, November 1989

### ADVISORY REPORTS (AR)

**Appraisal of the Suitability of Turbulence Models in Flow Calculations**  
AGARD AR-291, Technical Status Review, July 1991

**Rotary-Balance Testing for Aircraft Dynamics**  
AGARD AR-265, Report of WG 11, December 1990

**Calculation of 3D Separated Turbulent Flows in Boundary Layer Limit**  
AGARD AR-255, Report of WG10, May 1990

**Adaptive Wind Tunnel Walls: Technology and Applications**  
AGARD AR-269, Report of WG12, April 1990

**Drag Prediction and Analysis from Computational Fluid Dynamics: State of the Art**  
AGARD AR-256, Technical Status Review, June 1989

### CONFERENCE PROCEEDINGS (CP)

**Vortex Flow Aerodynamics**  
AGARD CP-494, July 1991

**Missile Aerodynamics**  
AGARD CP-493, October 1990

**Aerodynamics of Combat Aircraft Controls and of Ground Effects**  
AGARD CP-465, April 1990

**Computational Methods for Aerodynamic Design (Inverse) and Optimization**  
AGARD CP-463, March 1990

**Applications of Mesh Generation to Complex 3-D Configurations**  
AGARD CP-464, March 1990

Accession For	
NTIS GFA&I	<input checked="" type="checkbox"/>
DTIC TAB	<input type="checkbox"/>
Unannounced	<input type="checkbox"/>
Justification	
By	
Distribution/	
Availability Codes	
Dist	Avail and/or Special
A-1	

**Fluid Dynamics of Three-Dimensional Turbulent Shear Flows and Transition**  
AGARD CP-438, April 1989

**Validation of Computational Fluid Dynamics**  
AGARD CP-437, December 1988

**Aerodynamic Data Accuracy and Quality: Requirements and Capabilities in Wind Tunnel Testing**  
AGARD CP-429, July 1988

**Aerodynamics of Hypersonic Lifting Vehicles**  
AGARD CP-428, November 1987

**Aerodynamic and Related Hydrodynamic Studies Using Water Facilities**  
AGARD CP-413, June 1987

**Applications of Computational Fluid Dynamics in Aeronautics**  
AGARD CP-412, November 1986

**Store Airframe Aerodynamics**  
AGARD CP-389, August 1986

**Unsteady Aerodynamics — Fundamentals and Applications to Aircraft Dynamics**  
AGARD CP-386, November 1985

**Aerodynamics and Acoustics of Propellers**  
AGARD CP-366, February 1985

**Improvement of Aerodynamic Performance through Boundary Layer Control and High Lift Systems**  
AGARD CP-365, August 1984

**Wind Tunnels and Testing Techniques**  
AGARD CP-348, February 1984

**Aerodynamics of Vortical Type Flows in Three Dimensions**  
AGARD CP-342, July 1983

**Missile Aerodynamics**  
AGARD CP-336, February 1983

**Prediction of Aerodynamic Loads on Rotorcraft**  
AGARD CP-334, September 1982

**Wall Interference in Wind Tunnels**  
AGARD CP-335, September 1982

**Fluid Dynamics of Jets with Applications to V/STOL**  
AGARD CP-308, January 1982

**Aerodynamics of Power Plant Installation**  
AGARD CP-301, September 1981

**Computation of Viscous-Inviscid Interactions**  
AGARD CP-291, February 1981

**Subsonic/Transonic Configuration Aerodynamics**  
AGARD CP-285, September 1980

**Turbulent Boundary Layers Experiments, Theory and Modelling**  
AGARD CP-271, January 1980

**Aerodynamic Characteristics of Controls**  
AGARD CP-262, September 1979

**High Angle of Attack Aerodynamics**  
AGARD CP-247, January 1979

**Dynamic Stability Parameters**  
AGARD CP-235, November 1978

**Unsteady Aerodynamics**  
AGARD CP-227, February 1978

**Laminar-Turbulent Transition**  
AGARD CP-224, October 1977

## Preface

Future fighter concepts require air intakes with not only good performance characteristics over an even wider operating range, but also require inlet designs constrained by low signature requirements. For the engineers who have to deal with the problems of intake design, there exists the need to evaluate design tools and experimental capabilities for providing the innovative design concepts needed to meet the ever demanding challenges for engine inlets of advanced air vehicle configurations.

In recognition of this the AGARD Fluid Dynamics Panel established Working Group 13 to report on the state-of-the-art in the field and compare different computational tools on the basis of available test cases. The test case results can be used for further comparisons and are meant as a first step to improve computational tools. A comparison has been made of testing techniques used in different wind tunnels for the measurement of intake dynamic distortion using one common intake model. Design guidelines and rules have been reviewed and summarized.

The report presents the results of the Working Group study and its conclusions and recommendations.

## Préface

Les spécifications de conception des futurs avions de combat exigent des prises d'air qui soient à la fois de faible signature et performantes sur une grande plage d'utilisation. Pour les ingénieurs d'études qui sont confrontés aux problèmes de la conception des prises d'air, il y a lieu d'évaluer les outils de conception et les installations expérimentales afin d'apprécier leur capacité à fournir les concepts d'étude innovateurs nécessaires pour répondre aux spécifications de plus en plus rigoureuses des prises d'air adaptées aux configurations avancées des véhicules aériens.

En conséquence, le Panel AGARD de la Dynamique des Fluides a créé le groupe de travail No. 13 pour rendre compte de l'état de l'art dans ce domaine et pour comparer les différents outils de calcul à partir des cas d'essai disponibles. Les résultats des cas d'essais peuvent servir pour des comparaisons ultérieures et doivent être considérés comme un premier pas pour l'amélioration des outils de calcul. Les techniques d'essai employées dans différentes souffleries pour la mesure de la distorsion dynamique à l'aide d'un seul modèle de prise d'air ont déjà été comparées. Des directives et des règles de conception ont été examinées et résumées.

Ce rapport présente les résultats obtenus par le groupe de travail No. 13, ainsi que ses recommandations et ses conclusions.

Wolfgang Schmidt  
Chairman, WG13

Richard G. Bradley  
Deputy Chairman, WG13

## **Abstract**

This report presents the results of a study by Working Group 13 of the AGARD Fluid Dynamics Panel which was formed to investigate the state-of-the-art of methodologies for aerodynamic design of engine intakes for high speed vehicles. The scope of the investigation included intake aerodynamics, intake/engine compatibility, and intake/airframe integration for both aircraft and missiles.

The present capability of Computational Fluid Dynamics (CFD) methods was assessed through a comparative analysis of both CFD predictions and experimental data. This analysis was conducted for eight different flow field test cases designed to produce critical features of air-intake flow fields. Flow field results and comparisons are presented both in the report and in a microfiche appendix.

Air-inlet wind tunnel testing techniques and limitations were also investigated and reported. Results from measurements of inlet performance from three European wind tunnels using a common axisymmetric pitot intake are also presented.

The participants in Working Group 13 represented Belgium, France, Germany, Italy, the United Kingdom, and the United States.

# Contents

	Page
RECENT PUBLICATIONS OF THE FLUID DYNAMICS PANEL	iii
PREFACE	v
ABSTRACT	vi
1 OBJECTIVES AND SCOPE OF THE WORKING GROUP 13	1
2 INTAKE DESIGN AND PERFORMANCE	4
2.1 Introduction	5
2.2 Definition of Intake Performance Parameters & Description of Intake Flows	7
2.2.1 Internal Flow	7
2.2.1.1 Efficiency of Ram Compression	7
2.2.1.2 Flow Distortion at the Engine Face	8
2.2.1.2.1 Steady State Flow Distortion	8
2.2.1.2.2 Dynamic Distortion	10
2.2.1.3 Flow Angularity	11
2.2.1.4 Flow Stability	11
2.2.1.4.1 Buzz	11
2.2.1.4.2 Multi-intake Stability	12
2.2.1.5 Flow Quantity	12
2.2.1.6 Matching of Intake and Engine Airflow	14
2.2.2 External Flow	14
2.2.2.1 Pre-entry and Cowl Forces for a Pitot Intake	14
2.2.2.2 Pre-entry and cowl forces for an intake with a compression surface	16
2.2.2.3 Spillage Drag	17
References	18
2.3 The Initial Design Process	19
2.3.1 Introduction	19
2.3.2 Generalized Inlet Model & Calculation Procedures	20
2.3.3 Specific Experience with the Level II Inlet Installation Program (IIP)	20
2.3.4 Conclusions & Recommendations	22
References	22
2.4 Intake Design & Performance for Supersonic Cruise/Hypersonic Operation	23
2.4.1 Finding a Mission for High Speed	23
2.4.2 Intakes for Mach Number 2 to 3+ Cruise	24
2.4.2.1 Characteristics of Intake Design	24
2.4.2.2 Intake Technology in Current Mach 2-3+ Aircraft	24
2.4.3 Mach Number 4-6 Intakes	27
2.4.3.1 Requisite Technologies	27
2.4.3.2 Specific Applications	28
2.4.4 Mach Number 6+ to 8 Air Intakes for First Stage Accelerators	29
2.4.5 Air Intakes for Scramjet Propulsion Mach Number 8 to 25+	30
References	31
2.5 Intake Design & Performance for Agile Tactical Fighters	33
2.5.1 Introduction	33
2.5.2 Isolated Intakes	34
2.5.2.1 Internal Flow	34
(a) Flow in the Subsonic Diffuser	34
(b) Combination of Intake and Subsonic Diffusers	36
2.5.2.2 External Flow	38
2.5.2.3 Intakes with Compression Surfaces at Subsonic and Supersonic Speeds	39
2.5.2.3.1 At Subsonic Speeds	39
2.5.2.3.2 At Supersonic Speeds	40
2.5.3 Intake-Airframe Integration	43
2.5.3.1 Fuselage Flow Fields for Side Mounted Inlets	44
2.5.3.2 Performance of a Rectangular Compression Surface Intake on the side of a Fuselage	45
2.5.3.3 Performance of Axisymmetric Half Cone Intakes on the Side of a Fuselage	46
2.5.3.4 Performance of a Pitot Intake on the Side of a Fuselage	47
2.5.3.5 Fuselage/Wing Flow Fields for Shielded Intake Installations	48
2.5.3.6 Performance of Shielded Compression Surface Intakes	49
(a) Rectangular Intakes	49
(b) Half Axisymmetric Intakes	50

	Page
2.5.3.7 Comparison of Performance of Shielded and Unshielded Rectangular and Half Axisymmetric Inlets	50
2.5.3.8 Performance of Shielded Pitot Intakes	51
2.5.4 Technology Implementation in Current Aircraft	52
2.5.5 Concluding Remarks	56
References	56
2.6 VSTOL Aircraft Intakes, Design & Performance	57
2.6.1 Introduction	57
2.6.2 General Concepts, Specific Examples of Flight Tested Vehicles and Future Possibilities	57
2.6.2.1 Fixed, Direct Lift Engine Intakes	57
2.6.2.2 Rotating Engine Intakes	57
2.6.2.2.1 State-of-the-Art Experience	57
2.6.2.2.2 Future Possibilities	57
2.6.2.3 Fixed Horizontal Engine with Flow Diverters	58
2.6.2.3.1 State-of-the-Art Experience	58
2.6.2.3.2 Future Possibilities	58
2.6.3 Performance of VSTOL Intakes in Static and Transient Conditions	59
2.6.3.1 The Vertical Axis Inlet	59
2.6.3.1.1 Inlet Physics	59
2.6.3.1.2 The Lift Engines Intakes of the Do 31 VSTOL Transport Aircraft	59
2.6.3.2 The Fixed Horizontal Axis Intake - Harrier Type	60
2.6.3.2.1 Design Problems	60
2.6.3.2.2 Total pressure Recovery	61
2.6.3.2.3 Spillage Drag	61
2.6.3.2.4 Velocity Distribution	62
2.6.3.2.5 Low-Drag Cowl Section	62
2.6.3.3 The Rotating Axis Intake - VJ-101	62
References	63
2.7 Intake Design and Performance for Missiles with Airbreathing Propulsion	65
2.7.1 Introduction	65
2.7.1.1 The relevance of Air Breathing Engines for Missiles	65
2.7.1.2 Types of Air Breathing Propulsion	65
2.7.1.3 Specific Problems of Missile Intakes	66
2.7.2 Configuration Evolution and Constraints	66
2.7.2.1 Early Configurations	66
2.7.2.2 Operational Constraints	67
2.7.2.3 More recent Developments	67
2.7.3 Isolated Intakes	68
2.7.3.1 Intakes for Subsonic or Low Supersonic Speed Missiles	68
2.7.3.1.1 Pitot Intakes	68
2.7.3.1.2 Flush Intakes	68
2.7.3.2 Supersonic Intakes	68
2.7.3.2.1 Axisymmetric and Derived Intakes	69
2.7.3.2.2 Rectangular and Derived Intakes	70
2.7.3.2.3 Design Mach Number	71
2.7.3.2.4 Intake Size	71
2.7.3.2.5 Three Dimensional Intakes	72
2.7.4 Fuselage Flow Field	73
2.7.4.1 Fuselage with Circular Cross Sections	73
2.7.4.1.1 Zero Incidence	73
2.7.4.1.2 Non Zero Incidence	74
2.7.5 Missile Configurations	75
2.7.5.1 Electromagnetic Detection	75
2.7.5.2 Types of Steering	75
2.7.5.2.1 Skid to Turn Steering	75
2.7.5.2.2 Bank to Turn Steering	76
2.7.5.3 Possible Configurations with Circular Fuselages	76
2.7.5.3.1 One Intake	76
2.7.5.3.2 Single Intake at Subsonic Speeds	77
2.7.5.3.3 Twin Intakes	78
2.7.5.3.4 Three Intakes	79
2.7.5.3.5 Four Intakes	79
2.7.5.3.6 More than four Intakes	83
2.7.5.4 Fuselages with Wings or Strakes	83
2.7.5.4.1 Wings	83
2.7.5.4.2 Strakes	84
2.7.5.5 Fuselages with Non Circular Cross Sections	85
2.7.6 Performance Prediction	86
2.7.6.1 Isolated Intakes	86
2.7.6.2 Flow field around the Fuselage	86

	Page
2.7.6.3 Mounted intakes	87
2.7.6.3.1 One Intake	87
2.7.6.3.2 Several Intakes	87
2.7.7 Air Breathing Missile Design	87
2.7.8 Conclusions	88
References	88
3 NUMERICAL SIMULATION OF AIR INTAKES	91
3.1 Introduction	91
3.2 CFD methods for inlets	92
3.2.1 Introduction	92
3.2.2 Grid Generation	92
3.2.2.1 Surface Grids	92
3.2.2.2 Field Grids	93
3.2.3 Flow Solvers	94
3.2.3.1 Flow Equations	94
3.2.3.2 Solutions Algorithms	96
3.2.3.3 Turbulence Models	96
3.2.3.4 Current Status	97
3.2.4 Processing and Post-processing	98
3.2.5 References	99
3.3 Analysis of test cases	101
3.3.1 Test case 1 - Transonic normal shock/turbulent boundary layer interactions	101
3.3.1.1 Introduction	101
3.3.1.2 Problem description	101
3.3.1.3 CFD techniques	101
3.3.1.4 Results	101
3.3.1.4.1 Test case 1.1	101
3.3.1.4.2 Test case 1.2	102
3.3.1.4.3 Test case 1.3	103
3.3.1.5 Conclusions	104
3.3.1.6 References	104
Appendix 3.3.1: Supplementary figures for test case 1	117
Microfiche 3.3.1: Contributions to test case 1	
3.3.2 Test case 2 - Glancing shock/boundary layer interaction	128
3.3.2.1 Introduction	128
3.3.2.2 Problem description	128
3.3.2.3 CFD techniques	129
3.3.2.4 Results	129
3.3.2.5 Conclusions	132
3.3.2.6 References	133
Appendix 3.3.2: Full comparison of CFD and Experiment	134
Microfiche 3.3.2: Contributions to test case 2	
3.3.3 Test case 3 - Subsonic/transonic circular intake	139
3.3.3.1 Introduction	139
3.3.3.2 Problem description	139
3.3.3.3 CFD techniques	139
3.3.3.4 Results	140
3.3.3.4.1 Test case 3.1	140
3.3.3.4.2 Test case 3.2	142
3.3.3.5 Conclusions	142
Appendix 3.3.3: Supplementary figures for test case 3	156
Microfiche 3.3.3/3.3.4: Contributions to test case 3 and 4	
3.3.4 Test case 4 - Subsonic/transonic semi-circular intake	163
3.3.4.1 Introduction	163
3.3.4.2 Problem description	163
3.3.4.3 CFD techniques	163
3.3.4.4 Results	163
3.3.4.4.1 Test case 4.1	163
3.3.4.4.2 Test case 4.2	164
3.3.4.5 Conclusions	164
Appendix 3.3.4: Supplementary figures for test case 4	167
Microfiche 3.3.3/3.3.4: Contributions to test case 3 and 4	
3.3.5 Test case 5 - Supersonic circular pitot intake	171
3.3.5.1 Introduction	171
3.3.5.2 Problem description	171
3.3.5.3 CFD techniques	171
3.3.5.4 Results	171
3.3.5.4.1 Test case 5.1	172
3.3.5.4.2 Test case 5.2	172

	Page
3.3.5.4.3 Test case 5.3	172
3.3.5.4.4 Intake Pressure Recovery	173
3.3.5.5 Conclusions	173
Microfiche 3.3.5: Contributions to test case 5	
3.3.6 Test case 6 - 2D hypersonic intake	183
3.3.6.1 Introduction	183
3.3.6.2 Problem description	183
3.3.6.3 CFD techniques	184
3.3.6.4 Results	184
3.3.6.5 Conclusions	189
3.3.6.6 References	190
Appendix 3.3.6: Full comparison of CFD and Experiment	192
Microfiche 3.3.6: Contributions to test case 6	
3.3.7 Test case 7 - Axisymmetric mixed compression inlet	202
3.3.7.1 Introduction	202
3.3.7.2 Problem description	202
3.3.7.3 CFD techniques	202
3.3.7.4 Results	203
3.3.7.5 Conclusions	205
3.3.7.6 References	206
Appendix 3.3.7: Full comparison of CFD and Experiment	207
Microfiche 3.3.7: Contributions to test case 7	
3.3.8 Test case 8 - Intake/airframe integration	212
3.3.8.1 Introduction	212
3.3.8.2 Problem description	212
3.3.8.3 CFD techniques	212
3.3.8.4 Results	212
3.3.8.5 Conclusions/Recommendations	215
3.3.8.6 References	215
Microfiche 3.3.8: Contribution to Test Case 8	216
3.4 CONCLUSIONS AND RECOMMENDATIONS	
4 AIR INTAKE TESTING	217
4.1 Scope and Purpose of Air Intake Tests	217
4.1.1 Validation of Air Intake Test Runs without and Engine	217
4.1.2 Test of the Air Intakes with Engine	217
4.1.3 Air Intake Interaction with the Aircraft	217
4.1.4 Similitude Parameters	218
4.2 Tests of Subsonic Transport Aircraft Intakes	218
4.2.1 General Aspects	218
4.2.2 Test of Air Intakes in High Subsonic Flow	218
4.2.2.1 Principle of the Test Setup	218
4.2.2.2 Engine Face Equipment and Measurement of Pressure Recovery $P_R$	219
4.2.2.3 Flow Rate Measurement	219
4.2.2.4 Drag Measurement with External Probes	220
4.2.2.5 Other Drag Measurement Methods	220
4.2.3 Low Velocity Air Intake Tests	221
4.2.3.1 General Conditions	221
4.2.3.2 Test Setups	221
4.2.3.3 Engine Face Instrumentation and Measurement of the Distortion	222
4.2.3.4 Flow Rate Measurement	222
4.2.3.5 Drag Measurement	222
4.2.3.6 Effect of the Aircraft Aerodynamic Field	222
4.2.4 Nacelle Installation Test Using Turbine Power Simulator (T.P.S)	223
4.3 Supersonic Air Intake Tests	224
4.3.1 General aspects	224
4.3.2 Study of the Internal Flow	224
4.3.2.1 Test Setups	224
4.3.2.2 Engine Face Instrumentation	225
4.3.2.3 Flow Rate Measurement	226
4.3.3 Drag, Lift and Moment Measurements	227
4.4 Transonic and Subsonic Tests of Fighter Plane Air Intakes	228



	Page
4.5 Special Test Devices	229
4.5.1 Unsteady Flow Distortion Acquisition System	229
4.5.1.1 Complete Measurement	229
4.5.1.2 RMS Analysis	230
4.5.2 Intake Flow Dynamic Study	231
4.5.3 Complete Internal Flow Probing	232
4.6 Measurements in Three European Wind Tunnels at Subsonic and Supersonic Speeds of Dynamic Distortion and Steady State Performance of an Axisymmetric Pitot Intake	232
4.6.1 Introduction	233
4.6.2 Model Geometries	233
4.6.3 Instrumentation	234
RAE	235
ONERA	235
MBB/DLR	235
4.6.4 Test Programmes and Test Conditions	235
RAE	236
ONERA	236
DLR	236
4.6.5 Data Reduction and Presentation	236
4.6.6 Comparison of Measurements	236
4.6.6.1 At Subsonic Speeds	236
(a) Effect of Incidence Variation	236
(b) Effect of Variation of Free Stream Mach Number ( $\alpha = 15^\circ$ only) (Fig.48)	236
(c) Effect of Reynolds number	238
4.6.6.2 At Supersonic Speeds	239
(a) Effect of Incidence Variation (Fig.50(a)-(d))	239
4.6.7 Results Unique to ONERA and DLR Tests	240
4.6.8 Repeatability Study at RAE	242
4.7 CONCLUSIONS AND RECOMMENDATIONS	242
References	243
5 CONCLUDING REMARKS	245

## Microfiche Appendix

The Microfiche Appendix which accompanies this Publication contains 'Contributions to Test Cases' relating to Section 3.3 'Analysis of Test Cases' as shown below and in the main contents listing.

Sub-Section		Page No.	Fiche No.
3.3.1	Contributions to Test Case 1 — Transonic normal shock/turbulent	A1	1
3.3.2	Contributions to Test Case 2 — Glancing shock/boundary layer interaction	A33	1
3.3.3/3.3.4	Contributions to Test Case 3 and 4 — Case 3 Subsonic/transonic circular intake — Case 4 Subsonic/transonic semi-circular intake	A103	2
3.3.5	Contributions to Test Case 5 — Supersonic circular pitot intake	A184	2
3.3.6	Contributions to Test Case 5 — 2D hypersonic intake	A209	3
3.3.7	Contributions to Test Case 7 — Axisymmetric mixed compression inlet	A339	4
3.3.8	Contributions to Test Case 8 — Intake/airframe integration	A446	4

Note: Fiche No.5 contains the four reproductions referred to throughout Fiche No's 1 to 4.

## CHAPTER 1

### OBJECTIVES AND SCOPE OF THE WORKING GROUP 13

Intakes for air breathing engines represent a major and very important component of high speed air vehicles. Intake efficiency contributes significantly to the performance and handling characteristics of modern aircraft. Intake design and integration exhibit significant interactions with the air vehicle configuration. Flow field structures are essentially very complex.

Over the last two decades there has been a continuous evolution and improvement of airframe-intake integration and intake design, mainly based on a wide set of wind tunnel tests. Problems which were detected in a number of cases only after prototype flying, i.e. damage of the intake structure during engine surges, distortion-induced intake/engine incompatibility etc. required modifications at a very late stage of an aircraft program. Problems that arose with highly integrated intake positions and complex supersonic intake solutions led to a comprehensive experimental intake/airframe integration study in the USA (project Tailor Mate) in the late 1960's. An AGARD lecture series (LS53) was held in 1972 to review the state-of-the-art of airframe/engine integration at that time.

Since then computational methods as well as windtunnel testing techniques have improved and deeper physical understanding has led to innovations such as the intake-airframe integration on the Rafale aircraft and to the intake design on the European Fighter Aircraft.

More recent achievements in Euler and Navier-Stokes methods along with new mesh generation capabilities are providing tools for detailed flow field analysis and intake optimization. For unsteady phenomena such as buzz have been analysed analytically.

A large amount of experimental data has been collected at the various airframe- and engine companies and development centres in the USA and in Europe. Besides collecting data for the assessment of intake performance, increasing effort was placed on the subject of intake/engine compatibility. This effort has progressed from simple measurement of steady state total pressure distortion to the measuring of instantaneous distortion with digital, analog and hybrid data screening and the measurement of flow swirl at the engine face.

Efforts have also been made during the last few years with some success to reduce the amount of complex and expensive dynamic intake flow measurements by synthesizing dynamic distortion parameters based on a limited number of turbulence measurements. One problem however is that a universally applicable distortion parameter is not available. More effort is required to achieve a better understanding of the complex interaction of intake- and engine compressor flow.

Current goals in the intake design field include improved design concepts and rules, development and application of computational methods in the whole speed regime (subsonic to hypersonic), prediction of intake duct flow, understanding of the interaction of the intake- and engine compressor flow, development of techniques to reduce the complexity of intake distortion measurement and improvement of intake test techniques.

Future air vehicle concepts require air intakes with not only good performance characteristics over an even wider operating range, but also require inlet designs with low observable characteristics. The thrust of this AGARD study is to evaluate existing design tools and experimental capabilities for providing the innovative design concepts that meet the ever demanding challenges for engine inlets of advanced vehicle configurations.

The present Working Group 13 was formed to investigate the subjects of intake aerodynamics, intake/engine compatibility and intake/airframe integration using results from both experimental and computational techniques. Prediction of intake performance (pressure recovery, distortion and swirl) and care free handling of engines are of utmost importance to future military and civil aircraft projects.

After conducting a review of the state-of-the-art on intake design and performance for both aircraft and missiles (with air breathing engines) the group has compared critically results from the presently available methods for computing both external and internal intake flow fields. The experimental methods used to measure intake internal performance, drag and compatibility testing have also been critically compared and proposals for their improvement have been made.

Emphasis has been placed on the testing techniques for the assessment of intake flow distortion, the evaluation of relevant distortion parameters including swirl and the interaction of the intake flow with the engine compressor. Due to the high degree of this interaction, cooperation between the FDP and the PEP was considered essential and a group with PEP representation was formed.

The Working Group was composed of the following members.

FDP PANEL MEMBERS

Dr. W. Schmidt (Chairman)  
Messerschmitt-Bölkow-Blohm GmbH, UF  
Postfach 80 11 60  
D-8000 München 80 - Germany

Dr. R.C. Bradley (Deputy Chairman)  
General Dynamics  
GD/FW-MZ 2888  
P. O. Box 748  
Fort Worth, TX 76101 - USA

Mr. J. Leynaert  
Direction Grands Moyens d'Essais  
ONERA  
B.P. 72  
92322 Chatillon - France

NON-PANEL MEMBERS

Mr. T.J. Benson  
NASA Lewis Research Center  
Internal Fluid Mechanics Division  
Mail Stop 5-7  
Cleveland, OH 44135 - USA

Mr. G. Laruelle  
ONERA  
B.P. 72  
92322 Chatillon - France

Dr. N.C. Bissinger  
Messerschmitt-Bölkow-Blohm, UF  
Postfach 80 11 60  
D-8000 München 80 - Germany

Dr. F.A. Mackrodt  
DLR HA-WK  
Bunsenstr. 10  
3400 Göttingen - Germany

Mr. E. Farinazzo  
Internal Aerodynamics - Propulsion  
AERITALIA-GRUPPO VELIVOLI DA COMBATTIMENTO  
C. MARCHE  
TURIN - ITALY

Mr. L.E. Surber  
Airframe Propulsion Integration  
Flight Dynamics Laboratory  
AFWAL/FIMM  
Wright-Patterson AFB, OH 45433 - USA

Mr. E.L. Goldsmith  
ARA  
Manton Lane  
Bedford MK41 7PF - GB

Mr. D. Welte  
Dornier Luftfahrt GmbH  
Postfach 1420  
7990 Friedrichshafen - Germany

PEP PANEL MEMBER

Prof. Ch. Hirsch  
Vrije Universiteit Brussel  
Dienst Stromingsmechanica  
Plainlaan 2  
1050 Brussel - Belgique

The term of the Working Group was three years, Sept. 1987 until Sept. 1990. Much of the preparatory effort was however organized and carried out between the formal meetings by the following three subcommittees for consideration and approval by the Working Group at large:

Committee A (Chairman: E.L. Goldsmith)  
Intake Design and Performance

Committee B (Chairman: N.C. Bissinger)  
Numerical Simulation of Air Intakes

Committee C (Chairman: J. Leynaert)  
Air Intakes Testing Methods

The chapters were written by the authors noted in parenthesis and reflect the consensus of the Working Group:

CHAPTER 2 - INTAKE DESIGN AND PERFORMANCE  
(E.L. Goldsmith, L.E. Surber, D. Welte, G. Laruelle)

CHAPTER 3 - NUMERICAL SIMULATION OF INTAKES  
(T.J. Benson, N.C. Bissinger, R.G. Bradley)

CHAPTER 4 - AIR INTAKE TESTING  
(J. Leynaert, E.L. Goldsmith)

The Working Group is grateful to all individual contributors and their organizations for contributing and supporting the Working Group and this report.

Finally we would like to thank NASA Langley, RAE Bedford, ONERA Modane and DLR Göttingen for hosting Working Group meetings and presenting their test facilities.

## INTAKE DESIGN & PERFORMANCE

## LIST OF SYMBOLS

$\hat{A}$	cross sectional area	$\alpha$	angle of incidence
$C_D$	drag coefficient $\left[ \frac{D}{q_0 A_{ref}} \right]$	$\beta$	" " sideslip/yaw
$C_N$	normal force coefficient $\left[ - \frac{N}{q_0 A_{ref}} \right]$	$\gamma$	ratio of specific heats
$C_T$	thrust coefficient $\left[ - \frac{T}{q_0 A_{ref}} \right]$	$\delta_n$	compression surface angles
$C_k$	intake lip contraction ratio	$\delta$	boundary layer thickness
$D$	drag	$\epsilon$	mass flow ratio $A_0/A_c$
$D, d$	diameter	$\eta_i, \eta_e$	cowl internal & external angles
$P_t$	total pressure distortion	$\eta$	compression efficiency
$H$	height	$\lambda$	intake total pressure loss factor
$h$	height of diverter		
$I_A$ & $DC60$	specific distortion indexes	<u>Surfaces</u>	
$\frac{K}{K_{lim}}$	proportion of maximum allowable engine face distortion	$b$	bleed
$L, l$	length	BL	boundary layer
$L$	lift	c, cap.	capture plane
$M$	Mach number	$D$	design or SOL
$P$	pressure	ex	exit plane
$PR, P_R$	pressure recovery $(= P_t/P_{t_0})$	$F$	centre of pressure
$R, r$	radius	$f, f_2$	engine face
$R$	gas constant	$I$	intake entry plane
$Re$	Reynolds number	$j$	jet
$S$	surface area	$L$	local
$T$	temperature	$N$	exit nozzle
$T$	thrust	$n$	behind normal shock wave
$V$	velocity	$o$	free stream
$w$	width	$o$	at datum or reference condition
$W, \dot{m}$	mass flow	$s$	surface
$x, X$	axes	SOL	shock-on-lip
$y, Y$	& associated lengths	sw	sidewall
$z, Z$		spill	at spillage
		th, l	throat plane
		$w$	behind oblique shock wave
		*	at sonic conditions

## 2.1 INTRODUCTION

The importance of the intake and the exhaust nozzle on the performance of the total propulsion unit for any type of aircraft has been emphasised on several occasions. Examples of this importance for two vastly different aircraft operating at either end of the speed range  $M_0=0.2-2.0$  are shown in Figs. 1.1 and 1.2. The first illustrates the distribution of thrust forces throughout the nacelle of the Concorde aircraft and the second shows the importance of high intake efficiency at static conditions for the Harrier aircraft when taking off vertically or hovering.

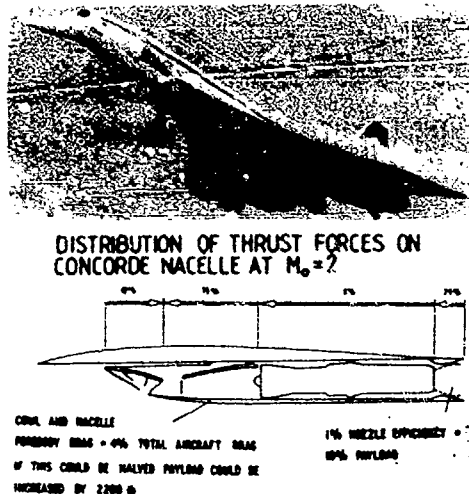


FIG 1.1 SOME ASPECTS OF THE IMPORTANCE OF THE POWERPLANT NACELLE ON CONCORDE CRUISE FLIGHT EFFICIENCY

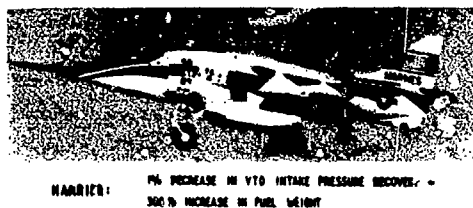


FIG 1.2 SENSITIVITY OF HARRIER INTAKE EFFICIENCY UNDER STATIC CONDITIONS

Perhaps even more important than performance aspects are those of intake and engine compatibility. If a wrong choice is made in the geometry of the intake (e.g. choice of lip bluntness, auxiliary intake area, or perhaps subsonic diffuser shape) then the aircraft's engine may surge even before taxiing to the end of the runway for take off. For a ramjet powered missile, for similar reasons of poor flow distribution at the entry to the engine, ramjet operation may never occur and flight will be terminated at burn-out of the rocket boost motor.

It is appropriate at this time to review experience of intake design and performance gathered since the last major AGARD publications that attempted anything similar - Airframe and Engine Integration (AGARD LS53 May 1972) and Inlets and nozzles for Aerospace Engines (AGARD CP91 Sept. 1971). Since that time some aspects of intake operation and performance have been included in:-

Aerodynamic Interference (AGARD CP 71-1 Sept. 1976)  
Airplane/Propulsion Interference (AGARD CP-150 Sept. 1974)  
Distortion Induced Engine Instability (AGARD LS 72 Nov. 1974)  
Advanced Control Systems for Aircraft powerplants (AGARD CP.274 Oct. 1979)  
Aerodynamics of Power Plant Installation (AGARD CP 301 May 1981)  
Improvement of Aerodynamic performance through Boundary Layer Control and High lift Systems (AGARD CP365 May 1984)  
Ramjets and Rocket Propulsion Systems for Missiles (AGARD LS136 Sept. 1984)  
Engine Response to Distorted Inflow Conditions (AGARD LS136 Sept. 1986)  
Special course in Missile Aerodynamics (AGARD R754 May 1987)

In addition over this time period one specialist lecture series on intakes has been held at VKI Brussels (Intake Aerodynamic, Feb. 1988).

After three general Sections this review divides broadly into Sections based on classes of vehicle i.e. long range (supersonic) cruise aircraft, tactical fighter aircraft, VSTOL aircraft and missiles with airbreathing propulsion. The most obvious omissions are subsonic cruise transport aircraft and helicopters. The former has been omitted because nearly all the propulsion aerodynamics interest is centred on the problems of external interference between nacelle/pylon/wing/body and is therefore almost wholly a complete airframe subject. The latter primarily because of the limited range of the subject and the scarcity of available data.

Again because of the quantity of data available (which reflects the scale of the activity over the last fifteen or so years) the most substantial sections are numbers 5 & 7. It was decided not to re-review the intense activity devoted to the intakes of the B.70, Concorde and the Boeing SST and other SST designs of the 1960's. Thus Section 4 deals with the rather more general aspects of design studies for a future SST, that have appeared more recently and whatever data is available for the SR-71 aircraft. However interest in this class of vehicle together with the associated area of air breathing propulsion for hypersonic vehicles is beginning to grow rapidly at this time.

In this area we return to the theme of importance of the propulsion unit. For the high supersonic and hypersonic speed range the whole layout of the airframe is dominated by the geometry of the intake and the exhaust nozzle as evidenced clearly in Fig. 1.3.

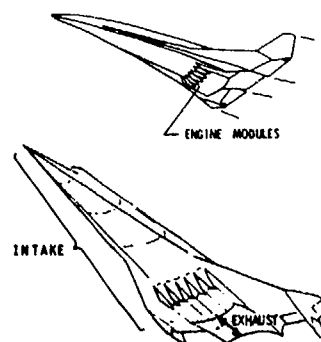


FIG 1.3 AIRFRAME INTEGRATED SUPERSONIC COMBUSTION RAMJETS

Fig 1.4 illustrates in more detail the possible geometries that emerge for a scramjet as a result of integration of the intake and the supersonic combustor combined with need wherever possible to keep all leading edges swept.

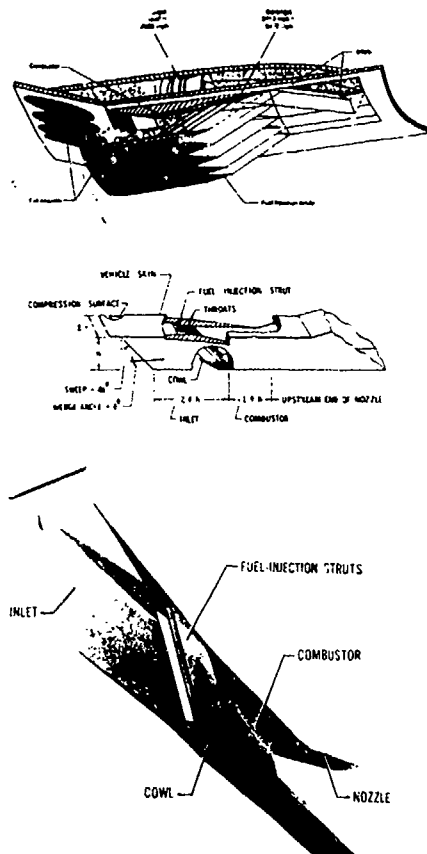
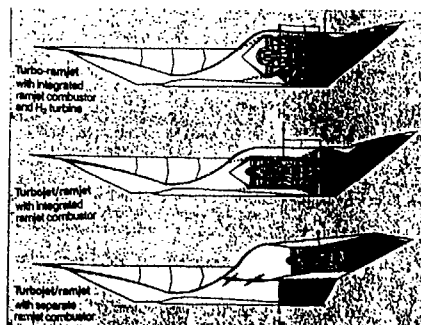
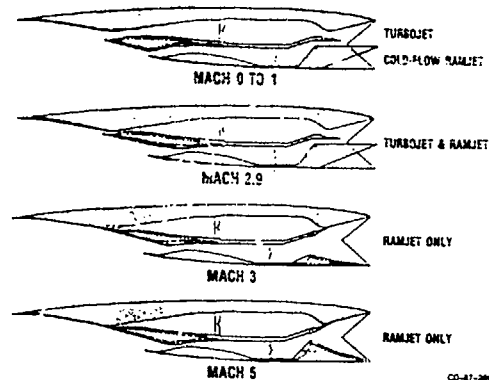


FIG 1.4 SCRAMJET INTAKES

However for many applications flight from Mach number zero to hypersonic speeds is necessary and dual mode powerplants (usually a combination of turbojet and ramjet) are needed. Fig.1.5 shows some possible combination powerplants that show the size and particularly the inevitable complication of variable geometry intakes and ducts.



#### OVER-UNDER TURBOJET/RAMJET



#### THE MTU HYPERCRISP COMBINATION TURBOFAN & RAMJET

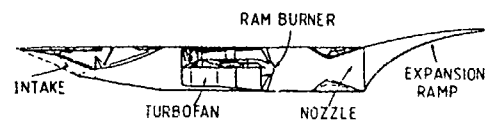


FIG 1.5 POSSIBLE COMBINATION POWERPLANTS

Thus whatever form the powerplant takes - and the choice is wide - ramjet, turbo-ramjet, vurborocket, ramrocket, variable cycle turbojet, scramjet and combinations of these - the intake will always be a vital element of the propulsion unit. Research and development of intakes must therefore proceed, as in the past, at all speeds from zero to hypersonic velocities.

## 2.2. DEFINITION OF INTAKE PERFORMANCE PARAMETERS & DESCRIPTION OF INTAKE FLOWS

### CONTENTS

- 2.2.1 INTERNAL FLOW
  - 2.2.1.1 Efficiency of ram compression
    - 2.2.1.2 Flow distortion at the engine face
      - 2.2.1.2.1 Steady state flow distortion
      - 2.2.1.2.2 Dynamic distortion
    - 2.2.1.3 Flow angularity
    - 2.2.1.4 Flow stability
      - 2.2.1.4.1 Buzz
      - 2.2.1.4.2 Multi-intake stability
    - 2.2.1.5 Flow quantity
    - 2.2.1.6 Matching of intake and engine airflows
  - 2.2.2 EXTERNAL FLOW
    - 2.2.2.1 Pre-entry and cowl forces for a pitot intake
    - 2.2.2.2 Pre-entry and cowl forces for an intake with a compression surface
    - 2.2.2.3 Spillage drag

### REFERENCES

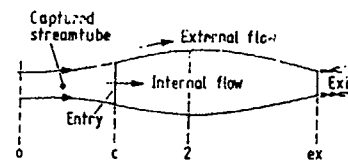


FIG. 2.1 NACELLE FLOW STATIONS

This equation can be made independent of the engine face Mach number  $M_2$  by assuming that further compression to zero velocity is achieved isentropically so that  $M_2 = 0$  and  $P_2 = P_{t2}$  and thus:-

$$\eta_\sigma = \frac{\left[ \left( \frac{P_{t2}}{P_o} \right)^{\frac{\gamma-1}{\gamma}} - 1 \right]}{\frac{\gamma-1}{2} M_o^2}$$

which for incompressible flow reduces to:-

$$\eta_{o1} = \eta_{ram} = \frac{P_{t2} - P_o}{q_o}$$

This quantity has been used extensively to define performance of subsonic intakes at low forward speeds. However the definition cannot be used at zero forward speed.

In this condition, it is usual to use a loss coefficient defined as:-

$$\lambda = \frac{P_{t0} - P_{t2}}{q_2}$$

At high free stream speeds and particularly for supersonic flow a more convenient measure of efficiency than  $\eta_\sigma$  is the simple ratio of mean total pressure at the engine face to free stream total pressure  $P_{t2}/P_{t0}$  which is widely known

as pressure recovery. This is sometimes designated as  $\eta$  or  $\eta_p$  but will be presented in this report as the above total pressure ratio or as PR.

It is impractical (and many times impossible) to take measurements at the compressor face when the engine is installed and operating. Consequently, the engine and intake designers agree upon an Aerodynamic Interface Plane (AIP) (which is forward of the compressor face but sufficiently close to the compressor face to have a similar flow field) for the definition of  $P_{t2}$ .

The various merits of weighting individual pitot pressure measurements made at this position to form a mean value have been discussed exhaustively in ref.2.1. Area mean, mass flow mean, mass derived and constant momentum derived, and entropy flux mean are all options. Although pressure recovery is usually measured by means of a pitot rake, it can also be deduced from measurements of mass flow and static pressure. Air intakes for missile engines sometimes have to be operated in conditions when large areas of separation can occur at the engine entry. Fig.2.2 shows some curves of pressure recovery

## 2.2. DEFINITION OF INTAKE PERFORMANCE PARAMETERS AND DESCRIPTION OF INTAKE FLOWS

### 2.2.1 INTERNAL FLOW

There are six properties of the internal flow that are usually measured by the intake aerodynamicist and are of concern to the engine manufacturer whose engine has to operate in the flow delivered by the combination of intake and following duct. These six quantities are efficiency of ram compression, static and dynamic distortion and flow angularity, stability and quantity.

#### 2.2.1.1 Efficiency of Ram Compression

The most natural definition of efficiency of the ram compression process is:-

$$\eta_\sigma = \frac{\text{Work done in compression}}{\text{Kinetic energy available}}$$

which for compressible flow is:-

$$\eta_\sigma = \frac{\left[ \left( \frac{P_2}{P_o} \right)^{\frac{\gamma-1}{\gamma}} - 1 \right]}{\frac{\gamma-1}{2} [M_o^2 - M_2^2]}$$

where station '0' is in the free stream and station '2' is at the engine face (Fig. 2.1).



for such a condition calculated by conserving:-

1. mass flow - entropy
2. mass flow - momentum
3. static pressure - momentum
4. static pressure - mass flow

and confirming the pressure recovery so calculated with a mean obtained from a pitot rake.

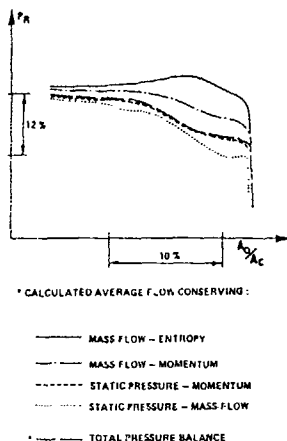


FIG 2.2 PRESSURE RECOVERY DEFINITION

If the flow does not contain large areas of separation, and this is usually the case for acceptable performance from turbojet and turbofan engines then all the methods of weighting give values which do not greatly differ from each other. Area weighting is the simplest and it is the one most commonly used.

#### 2.2.1.2 Flow Distortion at the Engine Face

Sources of total pressure distortion can be inherent in both the geometric and aerodynamic design - intake shock and boundary layer interaction on an adjacent aircraft surface or on an intake compression surface can result in separation behind the terminal shock (Fig.2.3a); separation in a duct can result because of choice of a too high rate of diffusion and/or the presence of sharp bends (Fig.2.3b); the absence of auxiliary intakes combined with thin intake lips can cause separation at take off (static) conditions (Fig.2.3c).

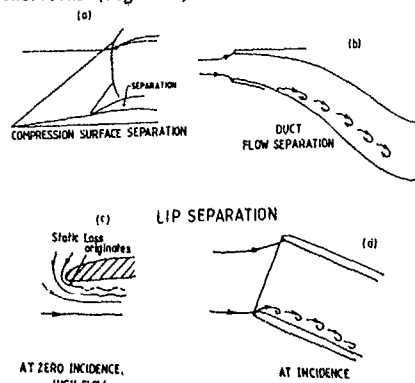


FIG 2.3(a)-(d) SOURCES OF FLOW SEPARATION

Total pressure distortion can also appear in an otherwise distortion free geometry at design conditions due to aircraft attitude which leads to lip separation (Fig.2.3d) at incidence or yaw (again related to lip thickness) or to mismatching between engine and intake airflows which results in subcritical (Fig 2.3e) or supercritical (Fig.2.3f) operation.

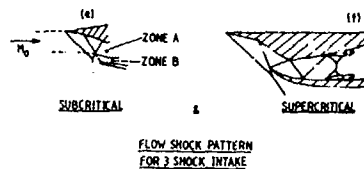


FIG 2.3(e)-(f) SOURCES OF FLOW SEPARATION

Flow velocity, Mach number and Reynolds number are required at the compressor entry to determine relative angle of incidence. Mach number and Reynolds number of the flow on to the compressor blades. If both static temperature and pressure can be assumed constant and steady across the compressor face then both velocity and Mach number can be considered as a function only of total pressure and the distribution of this quantity is the only measurement that needs to be made.

In order to obtain this type of flow distortion information, total pressure measurements are taken at the A.I.P. Total pressure probes are mounted in a series of equally spaced radial rakes such that they form a series of concentric rings (Fig.2.4).

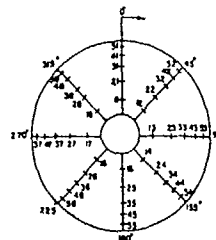


FIG 2.4 PROBE ORIENTATION - VIEW LOOKING FORWARD

Increased accuracy and convenience of data reduction can be obtained if the radius of each ring is set such that all probes are at the centroids of equal compressor face areas. This means that probe radial spacing decreases from the innermost ring to the outermost ring.

#### 2.2.1.2.1 Steady State Flow Distortion

Probably the most widespread quantitative distortion parameter available in the literature because of its use in the earliest measurements on intakes in the 1950s is the simple:-

$$D_t = \frac{\Delta P_t}{P_t} = \frac{P_{t2 \max} - P_{t2 \min}}{P_{t2 \text{mean}}}$$

and this is always a useful quantity to measure for comparison purposes and to describe the general 'health' of an intake flow irrespective of the type of powerplant (turbojet, turbofan, liquid or solid fuelled ramjet or ramrocket) that may be used.

More advanced methods introduced in the late 1960s and 1970s take into account the  $\Delta P_t/P_t$  distortion for each ring of total pressure measurements (with  $\Delta P_t$  now being between ring average and minimum total pressures). These ring distortions are weighted by circumferential extent factors  $\theta$ , (the sector angle of the ring for which recovery is below face average). Other improvements include factors to quantify the relative influence of the circumferential and radial distortions.

The effect of a circumferential distortion on compressor surge margin is displayed in Fig.2.5. Here, the 180° profile essentially drops the maximum pressure ratio of a constant corrected speed line.

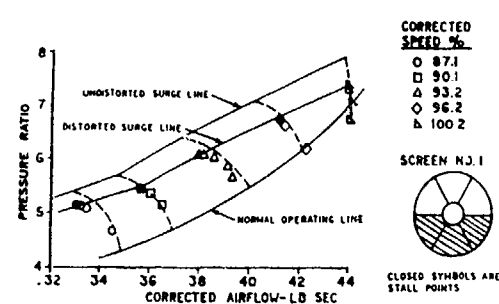


FIG 2.5 Effect of Circumferential Distortion

The effect of a hub radial distortion on compressor performance is displayed in Fig.2.6. In this case the constant corrected speed lines move to the left. That is, a given rotor speed pumps less air flow so that surge is encountered again at a lower pressure ratio.

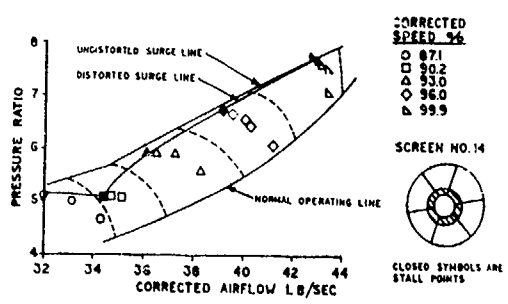


FIG 2.6 Effect of Radial Distortion

Critical circumferential distortion extent angles ( $\theta$ ) are determined in current methods since it has been demonstrated that the blades do not have time to react to narrow dips in the circumferential pressure profile. Above this critical angle, extent factors are calculated to determine the effect of the low pressure region on surge margin loss; however, Fig.2.7 illustrates the fact that the bulk of surge margin loss occurs with a 60° to 90° extent angle.

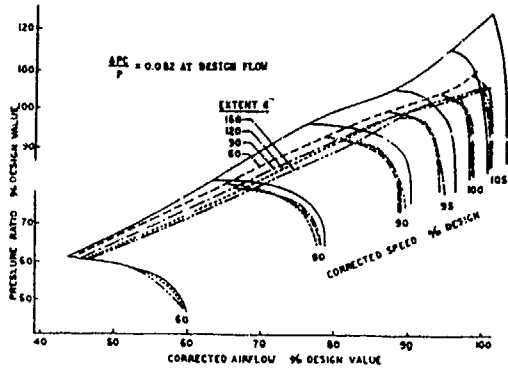


FIG 2.7 EFFECT OF EXTENT ANGLE

One of the simplest quoted indices of distortion from Rolls Royce (Fig.2.8)

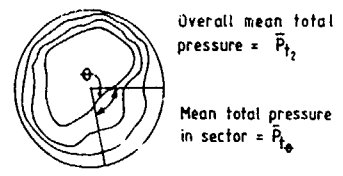


FIG 2.8 DEFINITION OF  $DC_\theta$

which relates specifically to engine compressor surge margins is:-

$$DC_\theta = \frac{\bar{P}_{t2} - \bar{P}_{t\theta}}{q_2}$$

where  $\bar{P}_{t\theta}$  is the mean total pressure in the 'worst' section of extent  $\theta$  and

$\bar{P}_{t2}$  and  $q_2$  are the mean total and dynamic pressures respectively at the

agreed engine interface plane. Significant  $\theta$  values can vary with the engine design and commonly are 60°, 90° and 120°. For a bypass engine  $DC_{\theta CG}$  where CG indicates that the index is taken over the area of the gas generator can be more significant than taking the whole engine face in relating to surge margin.

American engine manufacturers use more complex descriptors of the flow which have been evolved to take account of both radial and circumferential distortion. One relatively simple radially weighted circumferential index is:-

$$K_{D1} \text{ or } K_{D2} = 100 \frac{\sum_{n=1}^n \left[ \frac{(\Delta P_{tn} \cdot \theta)}{\bar{P}_{tn}} \right]_{\max} \cdot \frac{r_2}{r_n}}{\sum_{n=1}^n \frac{r_2}{r_n}}$$

where  $\Delta P_{tn} = (\bar{P}_t - P_{tmin})_n$  and  $\bar{P}_t, P_{tmin}$  are respectively the mean and lowest pressure in a ring ( $n$  is often 5 or 6) and  $\theta$  is an extent factor.

A multiple per revolution factor may also be used to determine the effect of more than one low pressure region in a circumferential distribution.

Other distortion indices and comparisons between them are given in refs. 2.2 and 2.3.

Using this type of parameter, the loss in surge margin can be calculated directly with the distortion value based on both the intake flow field and the engine design (Fig.2.9).

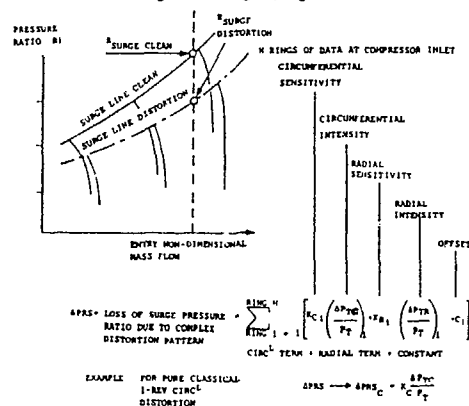


FIG 2.9 CORRELATION OF COMPLEX DISTORTIONS/ GENERAL FORMULATION

Correlations between predicted and calculated loss in surge margin for each type of distortion are displayed in Fig.2.10 for a turbo fan compressor and a F-100 fan. These plots show good prediction accuracy of these parameters for a wide variety of flow conditions and engine components. An error band of plus and minus two percent is indicated and the majority of the data falls well inside the two percent band (Ref.2.4).

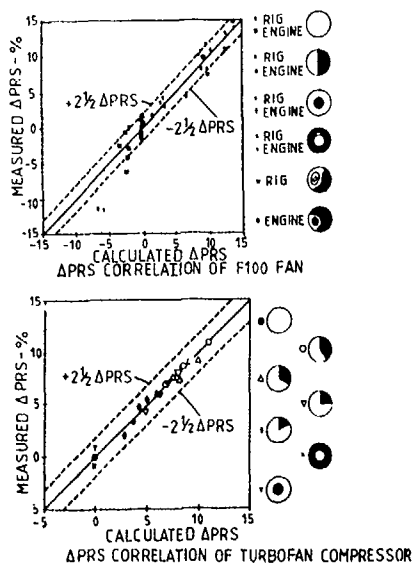


FIG 2.10 PREDICTION/MEASUREMENT CORRELATION- FANS, COMPRESSORS, CORES

### 2.2.1.2.2 Dynamic Distortion

After initial suspicions in the early 1960's that time variant distortion could be responsible for compressor surge it was shown in the late 1960's that although compressor blades need a minimum extent of circumferential distortion to react to, compressor blades do also react if exposed to this critical extent for a sufficient time. Thus surge would follow if the critical steady state distortion index was exceeded for a time period of the order of that for one engine revolution, typically about 5 milliseconds.

For example, during prototype flight tests of the F-111A, it became apparent that the desired flight envelope was restricted. Maneuvers of the aircraft at high subsonic and supersonic speeds resulted in engine compressor stalls at steady-state distortion levels which engine tests (using upstream screens to create these distortions) had shown to be acceptable. This inlet-engine incompatibility gave rise to comprehensive flight test and wind tunnel investigations to identify and correct the causes of the unexplained compressor stalls.

Flight tests of the F-111A were used to determine how the dynamic nature of intake pressure fluctuations related to engine operational stability. Steady state values of the flow distortion were compared with values taken at 400 sps (samples per second). A typical comparison is shown in Fig.2.11 for a Mach 1.6 case. This data clearly shows that while the low response data would not indicate the potential for stall, the high response parameter measurements yield a substantial peak approximately 15 milliseconds prior to surge.

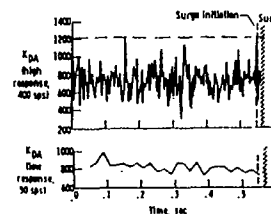


FIG 2.11 High and Low Response  $K_{DA}$  Comparison for F-111A Flight Test; Mach 1.6

For a preliminary assessment of dynamic distortion in a given intake, a rough rule of thumb can be applied, based on turbulence of the flow expressed as values of root-mean-square of the fluctuations in static pressure. If  $(\Delta p)_{\text{rms}}/P_t$  is not greater than one per cent, the problem of dynamic distortion can confidently be excluded: if the same factor is as high as four or five per cent, then detailed distortion measurements are advisable.

The determination of dynamic distortion, requires, much additional instrumentation and both experiment and analysis take on a different order of complexity.

Unsteady pressures have to be measured at a large number of points at the engine-face position, for representative free-stream conditions in a wind tunnel. The number of points necessary in a development test has been variously recommended as between 36 and 60. These pressures are recorded on miniature high-response differential-pressure transducers.

Details of the means of measuring and collecting the very large amount data required and the subsequent editing and analysis to produce values of dynamic distortion are given in Chapter 4.

### 2.2.1.3 Flow Angularity

Angularity of the duct flow will either increase or decrease incidence on to the compressor blades and is therefore obviously an important measurement for compatibility of intake engine airflows. If an engine is equipped with inlet guide vanes that straighten the flow before the first compressor stage then this importance may be somewhat diminished.

Flow angularity or swirl develops after a duct bend and is the result of an interaction between the centrifugal pressure gradient and a low energy region such as a boundary layer or a region of separation. The centrifugal pressure gradient is proportional to  $\frac{\rho V^2}{R}$  where  $V$  is mainstream velocity and  $R$  is the bend radius and results in pressure at the outside of the bend being greater than on the inside. If there is a boundary layer on the bottom of the duct with reduced velocity  $V'$  the local centrifugal gradient  $\frac{\rho V'^2}{R}$  is insufficient to balance the

pressure difference between the walls so that the flow in this region is directed towards the inside wall. If there is a similar boundary layer on the top wall, flow is also directed inwards in this region. Both top and bottom inward flows return to the outside wall in the region of the centre of the duct and the result is two cells of swirling flow (Fig. 2.12a).

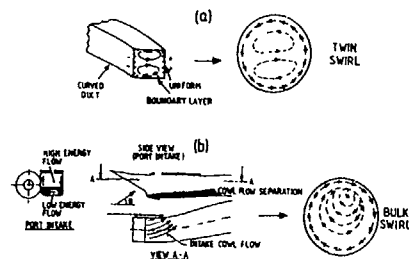


FIG 2.12 GENERATION OF TWIN & BULK SWIRLS

If a large low energy region such as a separation occurs on either the top or bottom wall of the duct upstream of the bend then a single directed or bulk swirl results as shown typically in Fig. 2.12b. The resulting swirl measured at the engine face is a combination of the bulk swirl and twin swirl patterns (Fig. 2.13).

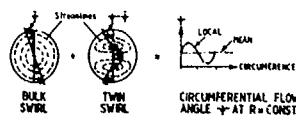


FIG 2.13 SUPERIMPOSING OF BULK & TWIN SWIRLS

### 2.2.1.4 Flow Stability

One form of unstable flow, compressor surge has already been referred to, but this is a phenomenon resulting from engine malfunction. However when two intakes are closely coupled, the possibility exists that a surge of one engine causes the surge of the second engine. This is due to disturbances that the hammer shock overpressure originated by the surge of the first engine induces on the adjacent intake, and occurs primarily at supersonic speeds, when the adjacent intake shock system is affected.

If it is not possible to completely separate the intakes, the problem can be avoided or attenuated by means of a suitable splitter plate dividing the intakes, and/or cutback endplates to the supersonic compression surfaces which will attenuate the overpressure. There are in addition two forms of flow instability emanating solely from the intake. The first is confined to supersonic speeds and is caused by oscillation of the intake shock system (known colloquially as 'buzz'). The second occurs when two or more intakes supply flow to a single duct and is usually known as twin (or multi) intake instability.

#### 2.2.1.4.1 Buzz

External and mixed compression intakes operating subcritically are subject to an unsteady flow oscillation called "buzz". Unless the supersonic freestream Mach number is very low all supersonic intakes with external compression surfaces appear to exhibit this instability of the flow at some point in the subcritical flow regime. The intake flow states of supercritical, critical and subcritical and the probable occurrence and form of shock oscillations in these flow states are described in ref. 2.5 and shown in Fig. 2.14.

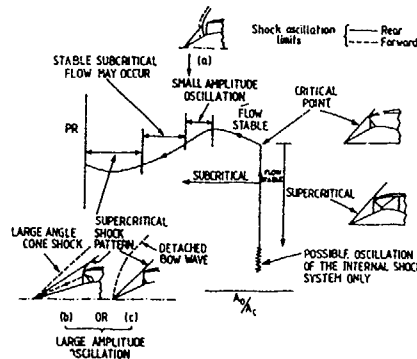


FIG 2.14 SHOCK OSCILLATION & THE INTAKE PRESSURE RECOVERY vs. FLOW CHARACTERISTIC

The phenomenon normally occurs at mass flow ratios below design and serves to limit the operating range of the intake-engine combination. Buzz can be responsible for structural damage to the intake, compressor surge or ramjet flame out. Buzz begins when the intake becomes choked because of massive flow separation. The cause of the separation may be associated with shock wave boundary layer interaction, diffuser flow separation, or shock wave interference ahead of the inlet. Fig. 2.15 illustrates two suggested mechanisms of buzz triggering resulting from massive separation in the diffuser. In any event; the normal shock is pushed far out on the compression surfaces to spill the unpassed flow. The flow situation which caused the separation is altered dramatically, reestablishing attached flow with a greatly reduced static pressure created by the starving engine. The normal shock is consequently sucked into the subsonic diffuser. As the system stabilizes, the flow structure which caused the initial separation reappears such that the cycle repeats itself.

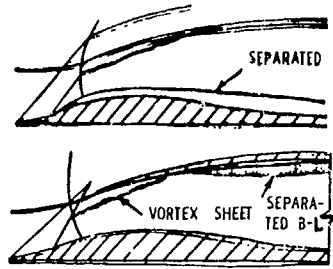


FIG 2.15 Buzz Triggering Mechanisms

Fig.2.16 shows the shock cycle and corresponding diffuser pressure. Buzz is characterized by low frequency and high amplitude. Sustained buzz can result in an engine compressor stall.

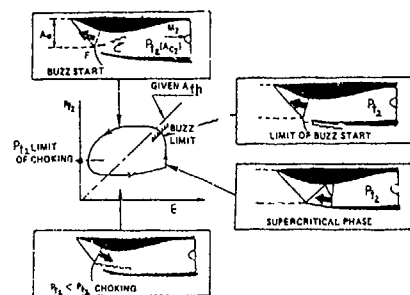


FIG 2.16 'BUZZ' CYCLE

The condition called "hammer-shock" already mentioned may also result from sustained buzz and/or compressor stall. Transient overpressures generated by a sudden engine surge can reach values well above theoretical maximum steady-state  $P_2$ . Such a transient fractured the North American F-107 intake ramps during flight test.

Normal shock oscillations can also occur at high mass flow ratios and supercritical operation (Fig. 2.14). In this condition the normal shock may oscillate in the subsonic diffuser due to the basic instability of the strong shock wave boundary layer interaction. These oscillations are of higher frequency and lower amplitude than buzz, but can still generate high turbulence and distortion at the compressor face, possibly surging the engine.

What usually matters to the intake designer and the engine manufacturer is the definition of the point on the subcritical characteristic of an intake at which 'buzz' is initiated i.e. the stable flow range. The match point between engine and intake flows can then always be made to fall within this range. Stable flow range or margin is usually characterised either

$$\text{as } \left( \frac{A_0}{A_C} \right)_{\min \text{ stable}} \quad \text{or as} \quad \frac{\left( \frac{A_0}{A_C} \right)_{\max} - \left( \frac{A_0}{A_C} \right)_{\min \text{ stable}}}{\left( \frac{A_0}{A_C} \right)_{\max}}$$

The possible 'triggering' mechanisms that could cause the onset of 'buzz' have already been mentioned and are discussed in more detail in ref.23, together with measures that can be taken in intake design to maximise the stable subcritical flow region.

#### 2.2.1.4.2 Multi-Intake Stability

For aircraft this phenomenon is usually associated with twin intakes situated on either side of a fuselage feeding air to a single engine. When intake flow is reduced by control of the exit of the common duct a critical point is reached below which unequal flows develop in the two intakes. On one side the flow increases again while on the other it falls rapidly to zero and can become negative. The net result on the flow reaching the engine is that total pressure recovery falls suddenly and total pressure distribution deteriorates as this critical point is passed. The critical point occurs when the slope of the static pressure recovery versus flow curve in the single duct changes from negative to positive so that it is possible then to have two flows, a high one and a low one that have the same static pressure (Fig.2.17).

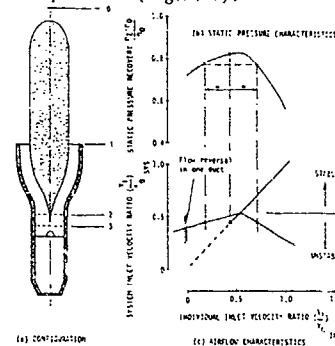


FIG 2.17 TWIN DUCT INSTABILITY

Sometimes the unequal distribution of flow between the two intakes is time dependent. Again as with intake buzz the concern is to measure the flow at which the phenomenon occurs so that it can be avoided. If the dividing wall between the two ducts is taken to the compressor entry the pressure equalising process can be transferred to the compressor exit and the instability may be prevented from developing.

The more complex multi-intake interactions typical of missile installations feeding a single ramjet combustion chamber are discussed in Section 7.

#### 2.2.1.5 Flow Quantity

All important internal flow phenomena and the external drag are quite critically dependent on the relative amount of flow through the intake. At subsonic and low supersonic speeds the flow quantity determines the severity of the pre-entry pressure rise and hence whether or not the boundary layer on the aircraft surface approaching the intake will be attached or separated (Fig.2.18).

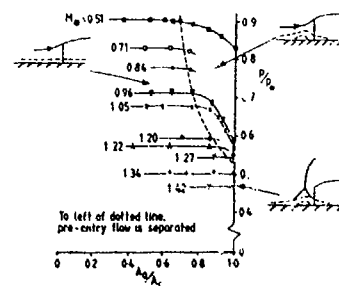


FIG 2.18 VARIATION OF STATIC PRESSURE IN ENTRY PLANE FOR INTAKE WITH FORWARD WETTED SURFACE

At supersonic speeds for an external compression intake the flow determines the extent to which the designed for shock pattern is deformed by the upstream movement of the final normal shock (Fig. 2.19).

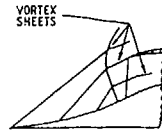


FIG 2.19 DISTORTION OF SHOCK WAVE PATTERN DUE TO SUBCRITICAL OPERATION

For an intake with internal compression it determines whether or not the intake shock system remains in its efficient 'started' configuration (Fig. 2.20).

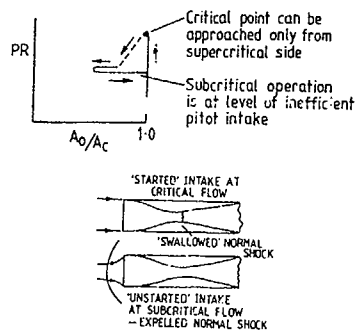


FIG 2.20 FLOW STATES FOR INTERNALLY CONTRACTING INTAKE

As has been seen in the foregoing sections either the value of the performance parameter being measured (such as pressure recovery or total pressure distortion) is primarily a function of flow or it is vital to define the flow at which an undesirable flow phenomenon such as 'buzz' occurs so that it can be avoided. In addition the accurate measurement of flow enables other quantities such as supersonic side spill that are difficult to measure directly to be deduced and it enables one dimensional Mach number to be evaluated at any duct station which is a useful parameter for correlating subsonic diffuser performance.

Flow measurement in a wind tunnel is usually done either at the engine face, or in a venturi section just aft of the engine face or if the control valve that varies flow is choked, just upstream of this choked exit.

The mass flow or more accurately the mass flow rate (Kg/sec) is:-

$$W = \rho VA$$

$$= \frac{\rho_0 A_0}{\sqrt{\gamma}} \sqrt{\frac{\gamma}{RT_0}}$$

or alternatively

$$= \frac{\rho_0 A_0}{\sqrt{\gamma}} \sqrt{\frac{\gamma}{RT_0}} \left[ \frac{1+\gamma-1}{2} M^2 \right]^{\frac{\gamma+1}{2(\gamma-1)}}$$

From the formula for sonic area ratio:-

$$\frac{A}{A^*} = \frac{1}{M} \left[ \frac{2}{\gamma+1} \left( 1 + \frac{\gamma-1}{2} M^2 \right) \right]^{\frac{\gamma+1}{2(\gamma-1)}}$$

$$W = \frac{\sqrt{\gamma}}{RT_0} \left[ \frac{2}{\gamma+1} \right]^{\frac{\gamma+1}{2(\gamma-1)}} \cdot \frac{A^*}{A} \cdot P_0 \cdot A$$

or the non dimensional mass flow function

$$\frac{W/\sqrt{T_0}}{AP} = \text{Constant} \times \frac{A^*}{A}$$

In intake work it is usual to express measured mass flow as a ratio of flow being ingested to the flow that would be ingested at datum conditions.

Thus the mass flow at the engine face:-

$$P_2 V_2 A_2 = P_0 V_0 A_0$$

and the flow ratio or capture area ratio is:-

$$\frac{P_0 V_0 A_0}{P_2 V_2 A_2} = \frac{A_0}{A_2}$$

It is evaluated at the engine face or at a venturi section 'v' just downstream of the engine face where static pressure only is measured:-

$$\frac{A_0}{A_c} = \frac{P_{t2}}{P_{t0}} \cdot \left[ \frac{A^*}{A} \right]_2 \cdot \frac{A_2}{A_c} \cdot \left[ \frac{A}{A^*} \right]_0$$

Each measurement of total pressure at the engine face is associated with an adjacent static pressure (or a mean of a small number of wall statics) so that local Mach number (from  $P_2/P_{t2}$ ) is determined and hence the local value of

$\left[ \frac{A}{A^*} \right]_2$  Thus for n total pressure points:-

$$\frac{A_0}{A_c} = \left[ \frac{P_{t2}}{P_{t0}} \cdot \left[ \frac{A^*}{A} \right]_2 \cdot \frac{\Delta A_2}{A_c} \cdot \left[ \frac{A}{A^*} \right]_0 \right]$$

where  $\Delta A_2$  is the engine face area associated with each total pressure tube.

For the venturi section,  $\left[ \frac{A^*}{A} \right]_v$  can be evaluated

from  $P_v/P_{t2}$  & values of  $P_{t2}/P_{t0}$  and  $A_v/A_c$  are used

in the above equation.

If there is a choked exit:-

$$\frac{A_0}{A_c} = \frac{P_{t2}}{P_{t0}} \cdot \frac{A_{ex}}{A_c} \cdot \left[ \frac{A}{A^*} \right]_0$$

For both equations it is necessary to add a calibration factor that is determined in a separate test where flows that are known to a higher accuracy than is required from the intake mass flow evaluation, are measured, by the engine face or choked exit instrumentation.

$$\text{Thus } \frac{A_0}{A_c} = \left[ \frac{P_{t2}}{P_{t0}} \cdot \left[ \frac{A^*}{A} \right]_2 \cdot \frac{\Delta A_2}{A_c} \cdot \left[ \frac{A}{A^*} \right]_0 \right] K_2$$

$$\text{and } \frac{A_0}{A_c} = \frac{P_{t2}}{P_{t0}} \cdot \frac{A_{ex}}{A_c} \cdot \left[ \frac{A}{A^*} \right]_0 C_d$$

where:  $K_2$  is an engine face calibration factor and

$C_d$  (an exit discharge coefficient)  $\frac{A_{ex} \text{ effective}}{A_{ex} \text{ geometric}}$

### 2.2.1.6 Matching of Intake and Engine Airflows

Before considering definitions of external drag it is appropriate to consider the matching between intake and engine airflows.

For a given flight condition and ramjet or gas turbine throttle setting, the intake airflow supply will satisfy the engine airflow demand at one unique point on the intake pressure recovery versus flow characteristic. The demand characteristics of both ramjet and gas turbine engines can be simulated by the characteristics of a choked hole of variable area. This area is a function of the fuel burnt in the engine. By writing the equations for mass flow conservation between entry and choked hole exit, the engine demand appears on the intake characteristic as a straight line passing through the origin. The slope of this line will vary with intake entry area and engine throttle setting. An optimum intake entry area can be chosen to ensure 'matched' operation at a desired location on the intake characteristic. The most desirable location will give a maximum thrust minus drag and will be at or very close to the critical operating point of the intake.

Fig. 2.21 shows the consequences of mismatching engine and intake airflows due to wrong choice of intake size and the effect of engine throttle setting on the match point.

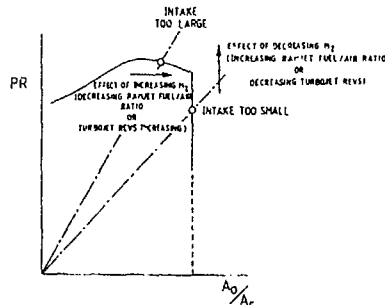


FIG 2.21 EFFECT OF INTAKE SIZE & ENGINE THROTTLE SETTING ON INTAKE/ENGINE MATCH POINT

Fig. 2.22 similarly, shows the effect on the match point of altering stagnation temperature (which can occur due to change of day temperature or altitude) or of free stream Mach number) both for a ramjet and (oppositely) for a turbojet engine.

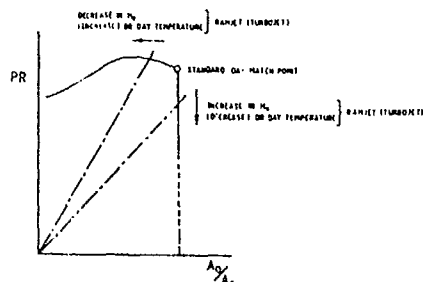


FIG 2.22 EFFECT OF CHANGE OF STAGNATION TEMPERATURE ON ENGINE INTAKE MATCH POINT

The position of the match point is further complicated in practice by the change in the shape of intake characteristics and maximum values of ingested flow (particularly for intakes with compression surfaces) as shown typically when free stream Mach number (Fig 2.23) and intake attitude (Fig 2.24) are varied.

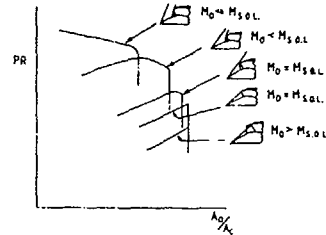


FIG 2.23 CHANGE OF TYPICAL CHARACTERISTIC WITH FREE STREAM MACH NO.

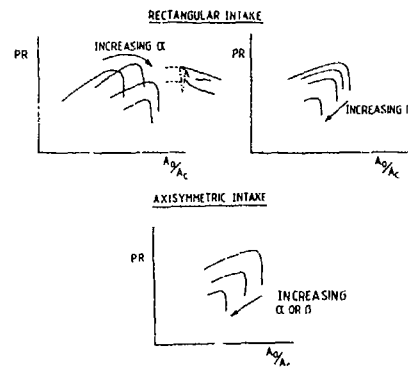


FIG 2.24 CHANGE OF TYPICAL INTAKE CHARACTERISTICS WITH INTAKE ATTITUDE

## 2.2.2 EXTERNAL FLOW

All the external forces on an engine nacelle except drag at cruise incidence are usually measured and calculated as part of the complete aircraft and are therefore outside the scope of this review. External drag however is dependent on the flow through the intake, the strength and disposition of compression surface shock waves and the shape of the intake in the immediate vicinity of the cowl lip and is therefore an important aspect of intake design and performance. External drag is usually only a significant part of zero lift or cruise attitude drag of the whole vehicle and therefore measurements on intakes are normally made at zero or small positive incidence.

### 2.2.2.1 Pre-entry and Cowl Forces for a Pitot Intake

A practical thrust definition acceptable to both airframe and engine manufacturer is known as net standard thrust and is the difference between pressure and momentum forces at the physical exit to the engine and the incoming streamtube to the intake at free stream conditions (Fig.2.1) i.e.

$$T_N = [(P_{ex} - P_0) + \rho_{ex} V_{ex}^2] A_{ex} - P_0 V_0^2 A_0 \quad (1)$$

The use of the free stream value of the entering momentum in the streamtube approaching the intake in this equation, implies the existence of a pre-entry thrust force in the above equation, where:-

$$T_{PRE} = [(P_0 - P_0) + \rho_0 V_0^2] A_c - P_0 V_0^2 A_0 \quad (2)$$

acts on the boundary of the pre-entry streamtube (Fig.2.25). Because the flow boundary is a streamline the pressure  $P_{int}$  acting on the internal surface must be balanced by pressures  $P_{ext}$  acting on the external surface and these external pressures give rise to an equal and opposite force to  $T_{PRE}$  in the drag direction, known as the pre-entry or in the USA, additive drag ( $D_{PRE}$  or  $D_{ADD}$ ).

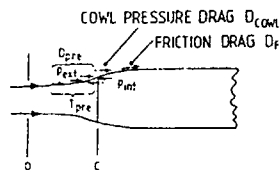


FIG.2.25 PRE-ENTRY & COWL PRESSURE FORCES FOR PITOT INTAKE

When the flow ratio  $A_0$  is unity the pre-entry

streamtube is undeflected upstream of the capture area,  $P_c = P_n$  and  $\rho_c V_c^2 A_c = \rho_o V_o^2 A_o$  so that  $T_{PRE}$  ( $=D_{PRE}$ ) is zero. This can be regarded as a

datum condition from which changes (either  $A_0 >$  or  $< A_c$ ) can be studied. From the datum condition, the curved pre-entry flow induces changes in the cowl pressure distribution from the stagnation line position on the cowl lip which divides external and internal flows. For  $A_0 < 1.0$  these changes in pressure distribution on

$A_c$  the cowl constitute a thrust force which in subsonic potential flow will be equal and opposite to the pre-entry force. In a viscous subsonic flow this cowl thrust is reduced below the potential flow value by (a) the presence of the boundary layer on the cowl and (b) the appearance of shock waves on the forward facing surfaces of the cowl if the flow over the cowl becomes supercritical.

At the datum flow condition when the external flow is free of shocks the cowl drag is the summation of friction and pressure drag. This is known as profile drag and is often for convenience presented as a form factor  $\lambda$  in which the drag coefficient is normalised by the mean skin friction drag coefficient of a flat plate with the same Reynolds number based on total length of the cowl.

At supersonic speeds the pre-entry thrust and drag forces are still equal and opposite but a net drag force is now associated with an increase in wave drag as the attached cowl lip shock changes to a detached wave ahead of the intake capture plane when  $A_0 < A_c$ . As at subsonic speeds, cowl pressure distribution changes from the datum condition in a favourable sense but the cowl thrust developed is now much smaller and does not nearly offset the pre-entry drag (as it does at subsonic speeds when  $A_0$  initially decreases just below  $A_c$  and viscous effects are small). Cowl drag in the datum condition is again the summation of skin friction and pressure drag. Pressure drag is now the result of the shock wave emanating from the cowl lip and can be calculated by linear theory or by the use of the method of characteristics (ref 13 summarises and correlates some results from these methods) or by solving the Euler equations for the combined external and internal flow.

For a pitot intake  $T_{PRE}$  ( $=D_{PRE}$ ) can be calculated from equation (2) or more conveniently can be expressed in coefficient form in terms of tabulated flow functions as:-

$$C_{T_{PRE}} = \frac{T_{PRE}}{q_o A_c} = \left[ \left( \frac{P_c}{P_{t_o}} \cdot \frac{P_{t_c}}{P_{t_o}} \cdot \frac{P_{t_o}}{q_o} - \frac{P_o}{q_o} \right) + \frac{2q_o}{P_{t_o}} \cdot \frac{P_{t_c}}{P_{t_o}} \cdot \frac{P_{t_o}}{q_o} \right] - 2 \frac{A_o}{A_c}$$

where at subsonic speeds  $\frac{P_{t_c}}{P_{t_o}} = 1$

and at supersonic speeds  $\frac{P_{t_c}}{P_{t_o}} = \frac{P_{t_n}}{P_{t_o}}$  the

stagnation pressure change across a normal shock;

or in terms of Mach numbers as:-

$$C_{T_{PRE}} = \frac{2}{\gamma M_o^2} \left[ \frac{\left( \frac{1+\gamma M_c^2}{2} \right)^{\frac{\gamma}{\gamma-1}}}{\left( \frac{1+\gamma M_o^2}{2} \right)^{\frac{\gamma}{\gamma-1}}} (1+\gamma M_o^2) - 1 \right] - 2 \frac{A_o}{A_c}$$

In such calculations the assumption is made that the stagnation line is at the cowl highlight (capture area) position and that the flow is one dimensional. For a sharp lipped cowl errors due to both these assumptions are probably reasonably small until  $A_0 \ll A_c$ . For a thick lipped cowl this situation should be examined more carefully (especially when correlating values for drag obtained from experimental measurements and those from computational methods) and is discussed under the heading of spillage drag.

The calculation of  $C_{T_{PRE}}$  or  $C_{D_{PRE}}$  from

computational methods using full potential flow at subsonic speeds or the Euler equations at subsonic and supersonic speeds can be done directly by integrating surface pressures along the stagnation streamline. However it is often more convenient to use a similar approach to the one dimensional calculation but now using a station downstream of the capture plane for the downstream momentum plane, where the flow can be regarded as truly uniform and axial.

With the pressure and exit momentum terms now based on station '2' (Fig.2.1) the cowl internal pressure force from the stagnation line to station '2' has to be evaluated to obtain  $C_{T_{PRE}}$ .

The internal thrust from upstream infinity 'o' to station '2' is:-

$$T_2 = \rho_o V_o A_o V_2 + (P_2 - P_o) A_2 - \rho_o V_o^2 A_o$$

$$\text{and } C_{T_2} = \frac{T_2}{q_o A_c} = \frac{2A_o}{A_c} \left[ \frac{V_2}{V_o} - 1 \right] + (P_2 - P_o) \frac{A_2}{q_o A_c}$$

$$\text{where } \frac{V}{\sqrt{\gamma RT}} = M \left[ \frac{1+\gamma-1}{2} M^2 \right]^{-\frac{1}{2}}$$

and  $M_2$  is derived from:-



$$\frac{A_2^*}{A_2} = \frac{\frac{A_0}{A_c} \cdot \frac{A_0^*}{A_0} \cdot \frac{A_c}{A_2}}{P_{t2}/P_{t0}}$$

$$C_{T2} = C_{Tint} + C_{TPRE}$$

$$\text{and as } C_{TPRE} = C_{DPRE}$$

$$C_{DPRE} = C_{T2} - C_{Tint}$$

where  $C_{Tint}$  is the duct internal pressure force coefficient integrated from the stagnation point to station '2'. The stagnation point can be found accurately by locating the point at which the surface velocity changes sign,  $\frac{A_0}{A_c} = 1$  &  $C_D = 0$

is a limiting condition at supersonic speeds.

At subsonic speeds it can be regarded as a convenient datum condition but it is not a limiting condition. This is obtained when the intake flow is choked either at its capture plane or at some throat plane 'th' downstream of the capture plane where  $A_{th} < A_c$ . Thus at low subsonic speeds if the lip is not thin the flow can increase beyond  $\frac{A_0}{A_c} = 1.0$  up to the choking

flow  $\frac{A_0}{A_c}$  or  $\frac{A_0}{A_{th}} \triangleq \frac{A_0}{A_0^*}$  and the one dimensional  $C_D$

will increase again from zero. At high subsonic and low supersonic speeds internal contraction to  $A_{th}$  will create a choking condition ( $M_{th} = 1.0$ ) at a flow ratio  $\frac{A_0}{A_c} < 1.0$

which then precludes the datum condition ever being reached. It then has to be accepted that the intake operates in a spilling condition  $\frac{A_0}{A_c}$

< 1.0 even at full flow and  $C_{DPRE}$  will never attain a zero value.

#### 2.2.2.2 Pre-entry and cowl forces for an intake with a compression surface

At supersonic speeds due to the presence of a compression surface the datum condition of  $\frac{A_0}{A_c} = 1.0$  is only obtained at Mach numbers above

which the compression surface shock (or shocks) impinge on or go within the cowl lip ( $M_0 > M_{SOL}$ , Fig. 2.26).

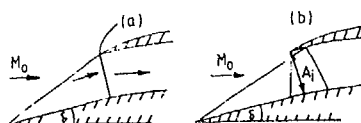


FIG 2.26 WEDGE INTAKE AT (a)  $M_0 = M_{SOL}$   
(b)  $M_0 > M_{SOL}$ ;  $D_{PRE0} = 0$  FOR (a) & (b)

Below  $M_0 = M_w$  the datum condition is determined by the position of the compression surface shocks in front of the cowl lip and the maximum flow ratio  $(A_0/A_c)_{max}$  is always less than unity. This maximum flow ratio is associated with a pre-entry drag and thrust corresponding to the fore spillage of  $1 - \left(\frac{A_0}{A_c}\right)_{max}$  and this again is a

denoted by the suffix 'o'.

At both subsonic and supersonic speeds  $T_{PRE}$  ( $= D_{PRE}$ ) can be obtained from application of the momentum equation to the internal flow in a manner similar to the pitot intake evaluation of  $T_{PRE}$ . For a single wedge intake of angle  $\delta$  (Fig. 2.27) this is

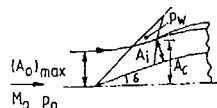


FIG 2.27 WEDGE INTAKE AT  $M_0 < M_{SOL}$ ,  $D_{PRE0} \neq 0$

$$T_{PRE0} = \rho_i V_i^2 A_i \cos \delta + (p_i - p_0) A_i \cos \delta$$

$$+ (p_w - p_0) A_w - \rho_0 V_0^2 A_0$$

where  $A_w$  is the projected area of the wedge

$p_w$  at supersonic speeds is the constant wedge surface pressure;

$p_w$  at subsonic speeds is either taken as  $\frac{p_0 + p_i}{2}$  or is obtained from

a correlation of pressures measured on wedges in isolation (ref 2.6).

At supersonic speeds it is often easier to evaluate  $D_{PRE0}$  directly by summing the pressures on the external limiting streamline. For a single wedge this is very simply:-

$$D_{PRE0} = (p_w - p_0)(A_c - A_{0max})$$

The expression for the two wedge compression surface is lengthier and is given in ref. 2.5. For the single cone compression surface  $p_w$  is not constant but can be integrated numerically along the limiting conical flow streamline. The second shock on a double cone is curved and the flow field can be evaluated by the method of characteristics.

At subsonic speeds the choice of a datum condition is more arbitrary than for the cases considered hitherto. At low subsonic speeds the value of  $A_i$  due to the presence of the compression surface may not be sufficient to cause throat choking before the condition  $\frac{A_0}{A_c} = 1$

is reached. In this case because of the presence of the compression surface the entering streamline will not be undeflected and parallel to the free stream direction and thus  $T_{PRE}$  will not necessarily be zero.

At moderate and high subsonic speeds and at supersonic speeds when the wedge shock is detached the throat (or capture plane) choking flow could be considered as an appropriate datum condition and this will now be associated with values of  $A_0$  that are less than unity. One other

datum condition is the flow such that the throat velocity  $V_t$  or  $V_{th}$  is equal to the free stream velocity  $V_0$ .

Cowl pressures for the maximum flow condition at supersonic speeds should be calculated using the flow direction and Mach number at the cowl lip that result from the compression surface flow at that position. In practice two dimensional calculations of cowl drag show that the values obtained by this procedure differ very little from those obtained ignoring the compression surface flowfield and assuming free stream Mach number and direction at the cowl lip.

In the absence of more comprehensive data similarly it is often assumed that the decrease in cowl drag when the intake operates subcritically is the same as for a pitot intake with the same geometry cowl.

### 2.2.2.3 Spillage Drag

As already indicated, a reduction of flow ratio below the datum or maximum flow value results in an increase in pre-entry drag force and a corresponding increase in cowl forebody thrust force (which are equal and opposite in subsonic potential flow) and therefore results in no net axial force. In viscous subsonic flow if the flow over the cowl remains subcritical the change in cowl pressure gradients result in a thickening of the cowl boundary layer and ultimately, as flow ratio decreases further, to separation of the flow from the cowl lip. Under these circumstances cowl thrust is decreased from the potential flow value and a rapid rise in drag from the datum or maximum flow value is measured that is called spillage drag.

When the flow over the cowl is supercritical this spillage drag will occur as a result of both boundary layer thickening and shock wave formation. The wave drag component will probably increase initially as flow ratio decreases or free stream Mach number increases and then be succeeded by a flow separation at the foot of a reduced strength lambda shock and finally by a complete collapse of the supercritical flow as separation moves forward to the cowl lip.

At supersonic speeds because of the increased strength of the head shock, directly flow is reduced below the datum level there is an increase in pre-entry drag. This is not balanced by a corresponding increase in cowl thrust so that spillage drag is positive when subsonic foreshallage occurs. Cowl drag is reduced as spillage increases and initially cowl flow remains attached. However at greater spillages, flow can detach from the cowl lip and form a small bubble separation followed by a weak reattachment shock (Fig.2.28). The size of the bubble and the strength of the reattachment shock grow as flow ratio decreases further.

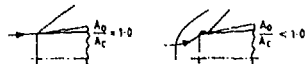


FIG 2.28 FLOW PATTERNS AROUND PITOT INTAKE AT SUPERSONIC SPEEDS

Spillage drag  $C_{D\text{SPILL}}$  is calculated from:-

$$C_{D\text{SPILL}} = C_{D\text{EXT}} - C_{D\text{EXT}_0}$$

where  $C_{D\text{EXT}} = C_{D\text{PRE}}(\text{or } C_{D\text{ADD}}) + C_{D\text{COWL}}$

and  $C_{D\text{EXT}_0} = C_{D\text{PRE}_0} + C_{D\text{COWL}_0}$

where again the suffix 'o' denotes a datum condition.

For spilling flows the stagnation line is on the internal surface of the lip and not at the capture plane position. Thus if the one dimensional value of  $C_{D\text{PRE}}$  based on the capture plane area  $C_{D\text{PRE}_C}$  is used this should be added to cowl drag  $C_{D\text{COWL}_C}$  that is the summation of the axial cowl pressure force components downstream from the capture plane. If the true external cowl drag  $C_{D\text{COWL}_t}$  is used i.e. the summation of the axial cowl pressure force components from the stagnation line position forward to the capture plane and then back externally to the maximum diameter position then this should be added to a pre-entry drag  $C_{D\text{PRE}_t}$  which can be one dimensionally using the

stagnation line area and not the capture plane area.

$$\text{i.e. either } C_{D\text{EXT}} = C_{D\text{PRE}_C} + C_{D\text{COWL}_C}$$

$$\text{or } C_{D\text{EXT}} = C_{D\text{PRE}_t} + C_{D\text{COWL}_t}$$

Unlike the evaluation of  $C_{D\text{PRE}_C}$  the calculation

of  $C_{D\text{PRE}_t}$  is not simple in that the position of

the stagnation line has to be found experimentally by pressure plotting the lip in fine detail or from potential flow theory or by solving the Euler equations.

The variation of drag with flow ratio at supersonic speeds for a pitot intake is shown in Fig.2.29a and the more complex situation for a wedge or cone compression surface intake in Fig.2.29b.

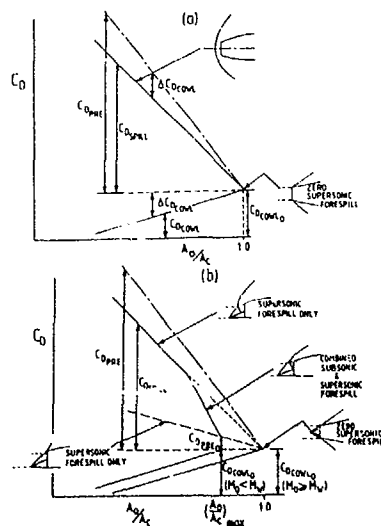


FIG.2.29 FLOW STATES & DRAG DEFINITIONS AT SUPERSONIC SPEEDS FOR (a) PITOT & (b) COMPRESSION SURFACE INTAKES

This latter figure illustrates the potential advantages of variable geometry (by translating or varying the compression surface angle) available to the compression surface intake but not the pitot intake. Flow can be spilled by supersonic forespill at a much lower rate of drag increase with flow reduction than is obtained by subsonic forespill only or by combined supersonic and subsonic forespill.

#### REFERENCES

- 2.1 Livesey, J.L. (1982) 'Flow property averaging methods for compressible internal flows'. AIAA, 82-0135.
- 2.2 Martin, R.J. and Melick, H.C. 'A Feasibility Study for definition of Inlet Flow Quality and Development criteria'. AIAA 72-1098, December, 1972.
- 2.3 Hercock, R.G. and Williams, D.D. (1974) 'Distortion-induced engine instability. Aerodynamic response'. AGARD, LS72-Paper No.3.
- 2.4 Society of Automatic Engineers 'Aerospace Recommended Practice ARP 1420 Engine Inlet Flow distortion guidelines. March 1978
- 2.5 Seddon, J. and Goldsmith, E.L. 'Intake Aerodynamics'. Collins, London, 1985
- 2.6 Bryson, A.E. 'An experimental investigation of transonic flow past two dimensional wedge and circular arc sections using a Mach-Zehnder interferometer NACA TN 2560

## 2.3 THE INITIAL DESIGN PROCESS

### CONTENTS

- 2.3.1 INTRODUCTION
- 2.3.2 GENERALIZED INLET MODEL & CALCULATION PROCEDURES
- 2.3.3 SPECIFIC EXPERIENCE WITH THE LEVEL II INLET INSTALLATION PROGRAM (IIP)
- 2.3.4 CONCLUSIONS & RECOMMENDATIONS
- REFERENCES

### 2.3.1 INTRODUCTION

Supersonic aircraft design has evolved to the point where even the earliest phases of design can benefit many times from consideration of air intake integration, component design and performance analysis. Figure 3.1a (from Ref 3.1) offers some insight into the rationale behind this statement. In this Figure a trend can be seen toward reduced range factor in fighter aircraft which is associated with an increasing ratio of intake capture area to aircraft wetted area ( $A_C/A_S$ ). Increased relative intake size in advanced fighters is required to accommodate the higher maximum mass flows associated with increased thrust/weight ratio, but it also generally means a wider range of airflows, leading to greater values of intake flow spillage at cruise conditions and more sophisticated intake variable geometry. The Figure suggests that the combination of increased propulsion stream size and propulsion installation complexity make integration more difficult. Also, it suggests that the levels of intake and nozzle performance decrements are significant in the determination of performance. Therefore, in order to discriminate adequately among competing supersonic aircraft concepts, it is useful in preliminary design to show the relative impact of different intake integrations and/or the effect of significant perturbations in an air intake design. Any such analysis needs to be simple and quick, but give a reasonably accurate intake performance.

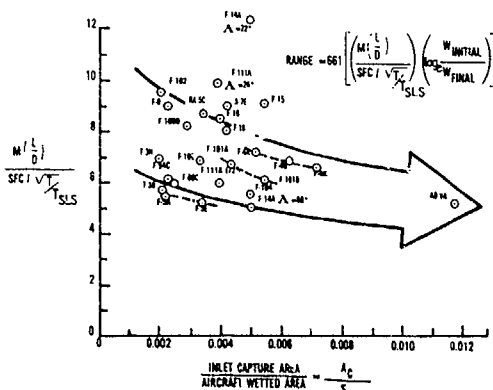


FIG 3.1a SUBSONIC CRUISE PERFORMANCE (REF 3.1)

A number of different intake installation prediction programs exist in industry but tend to be guarded rather closely. The Level II Inlet Installation Program (IIP) analysis summarized here and described more at length in Ref. 3.2 is similar in concept to other methods but is not tied to any particular organization's proprietary data. It was developed for the USAF by Grumman Aerospace Corporation primarily to predict the performance of well-defined existing intakes and

assess the relative performance of inlets and their subsystems for studies of airframe-propulsion integration. The program was intended to be accurate and comprehensive, with improvement of the method as new data became available.

Another object of IIP was rapid calculation and convenient use for inexperienced users. The IIP operates interactively, using a blend of theoretical analysis and empirical correlations to model the flowfields about installed air induction systems. No extensive flowfield solvers or boundary layer codes are employed. A complete on-design analysis starting from an interactive input session can be completed in approximately twenty minutes.

IIP is capable of analysing a broad range of inlets and approach flowfield conditions. The program consists of six major software modules capable of analysing both two-dimensional and axisymmetric supersonic compression types including pitot (normal shock), all external or mixed external-internal. Inlet subsystems including boundary layer bleed, bypass, and auxiliary inlets can also be analysed. The flight conditions may range from static operation up to Mach 3.5 at any altitude. The user can also specify non-atmospheric freestream conditions, such as wind tunnel test conditions. Angle-of-incidence effects can be analysed for horizontal ramp two-dimensional inlets only (no attempt was made at estimating the 3-D flowfields of axisymmetric spikes or vertical 2-D ramps at angle-of-incidence).

Performance output from IIP consists of internal flow thermodynamic losses and external aerodynamic drag. Total pressure recovery losses are followed through the induction process (oblique shock losses, normal shock loss, cowl lip losses, and subsonic diffuser losses). A complete drag component breakdown is given with absolute values of drag components as well as  $C_D$  changes relative to a specified reference condition. Flow characteristics such as onset of buzz, oblique shock ingestion, and inlet 'unstart' are displayed. Also included are massflow ratios for all of the inlet subsystems.

Although IIP is mainly for analysing existing geometries, limited design assistance is also available. On-design values of compression surface angles and lengths for maximum recovery and specified mass flow ratio is available. Also, bleed and bypass sizing for maximum recovery can be determined. Auxiliary inlets can be sized for a specified recovery (trading auxiliary inlet mass flow ratio for reduced cowl lip losses). At off-design conditions, variable geometry ramp schedules or translating spike positions can be determined for a desired mass flow ratio and an assumed throat Mach number of 0.7. This is done by varying compression ramp angles for 2-D inlets or translating the spike for axisymmetric inlets while checking for undesirable shock-shock intersections and/or detached oblique shocks.

IIP is capable of using scheduled or variable geometry and engine mass flow as functions of Mach number and angle-of-incidence. This option is used for continuous calculation of inlet performance throughout a vehicle flight envelope.

### 2.3.2 GENERALIZED INLET MODEL AND CALCULATION PROCEDURES

IIP models six basic elements of any inlet: 1) compression system, 2) cowl lip, 3) subsonic duct, 4) boundary layer removal systems, 5) bypass system, and 6) auxiliary inlet system. Figure 3.1b shows these basic elements in terms of parametric influence.

The procedure for estimating inlet performance involves first calculating all portions of the supersonic flowfield up to the normal shock. The flowfield results are then output since the supersonic flow is not affected by engine operating conditions. The procedure then calculates an independent engine operating parameter, for pitot and external compression inlets, the throat Mach number is treated as the independent parameter and governs all subsonic

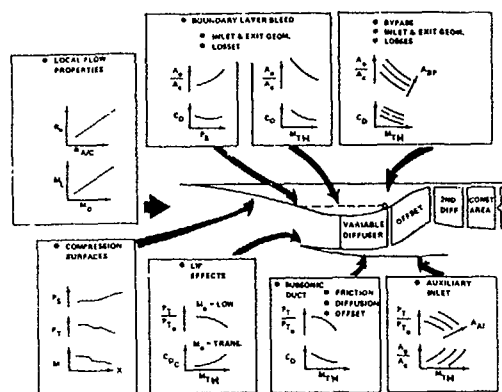


FIG 3.1b IIP BASIC ELEMENTS (REF 3.2)

portions of the flowfield. Geometry is defined such that throat Mach number may start at a choked condition (Mach 1) and be incrementally decreased, with intake performance calculated and printed out at each increment. As throat Mach number is reduced below 1.0, the resulting normal shock moves upstream from the cowl lip onto the compression surface(s) until a slipline ingestion (and onset of buzz, see Section 2 of Chapter 1) is detected. At this point the calculation terminates. For mixed compression intakes, normal shock position is the independent parameter since the throat is still supersonic and does not change with engine operation. All downstream subsonic flowfields are dependent on this position. The normal shock is initially positioned at one third of the diffuser length or at the downstream end of a diffuser bleed section if there is one. It is then moved incrementally toward the throat until the verge of 'unstart', at which point the calculation proceeds as for external compression intakes. In this way, total pressure recovery and drag are predicted for a range of engine operating conditions.

Specific prediction methods are described below. For subsonic operation, 1-D isentropic flow is assumed up to the cowl lip with a linear variation of static pressure on the external compression surfaces. For 2-D supersonic flow, oblique shock theory is used. For axisymmetric supersonic flow, an approximate empirical analysis involving equivalent conical wedges is used. Internal supersonic flow is calculated using an equivalent 2-D converging passage. Mass flows for bleed and bypass subsystems are determined by the difference in local surface pressure and ambient back pressure with assumed internal loss factors. Supersonic surface bleed is unaffected by the independent parameter, but

subsonic surface bleed or bypass mass flow does change with engine mass flow. Bleed and bypass drag is determined using momentum conservation (taking loss factors into account) plus a component for pressure drag on exit doors protruding into the freestream. Cowl lip losses are based on empirical correlations that depend on a fairly detailed description of the lip geometry. Subsonic duct friction losses are based on an average friction factor and the throat dynamic head. Duct divergence and offset losses are determined from empirical correlations. Spillage drag, which is the sum of pre-entry drag and cowl lip drag, is based on the previously mentioned reference condition. This reference condition is specified as an engine mass flow ratio. The pre-entry drag is calculated by a simple pressure-area integration of the spilled streamtube. Cowl lip drag effects are calculated using the same empirical data for cowl lip losses in conjunction with transonic similarity theory.

Figure 3.2 shows a schematic of these calculation procedures.

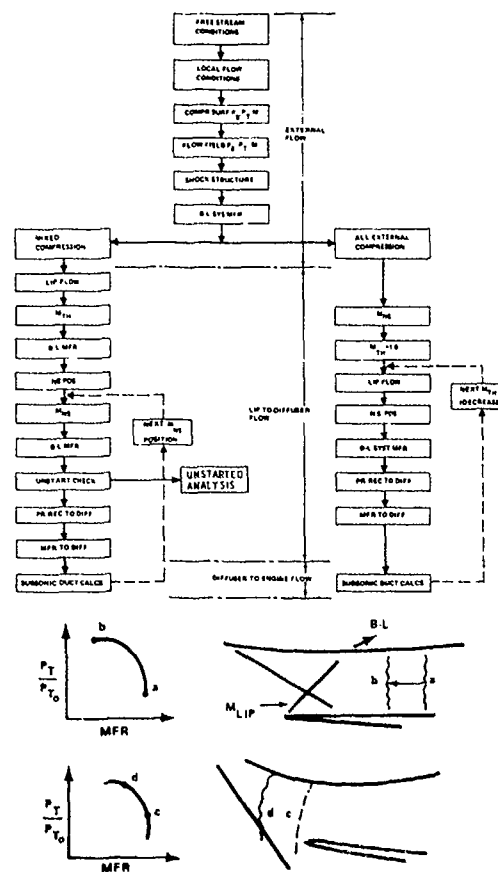


FIG 3.2 COMPUTATIONAL FLOW DIAGRAM (REF 3.2)

### 2.3.3 SPECIFIC EXPERIENCE WITH THE LEVEL II INLET INSTALLATION PROGRAM (IIP)

The IIP Program is used by a number of USAF organizations to analyze potential or existing intake configurations. Three examples are given here to provide an indication of its accuracy and show its use in evaluation.

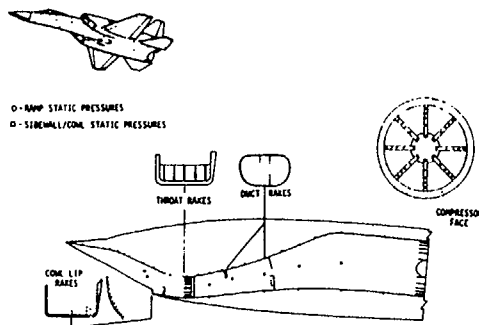


FIG 3.3a SIDE-MOUNTED INLET CONFIGURATION AND INSTRUMENTATION (REF 3.4)

The first example, intake data from project Tailor-Mate (Ref 3.3) were used to evaluate the method's ability to predict total pressure recovery over a range of Mach numbers and pitch angles. The Tailor-Mate A-1 intake (Fig 3.3a Ref 3.4) is a two-dimensional external compression, side-mounted, overhead ramp configuration designed for a Mach 2.5 fighter. The intake has three variable compression ramps, porous ramp bleed, throat slot bleed/bypass, and a subsonic diffuser with both vertical and horizontal offset. The intake was tested from Mach 0.9 to 2.5 and angles-of-incidence between -5 and 20 degrees. Test data included engine face total pressure recovery and all subsystem mass flow ratios. Unfortunately, no drag data were taken to compare with IIP output. Several problems were encountered in modelling the A-1 geometry.

First, sideplate porous bleed was incorporated in the A-1 test model but no provisions for sideplate bleed are available in IIP. Second, IIP assumes duct geometry as shown in Figure 3.3b.

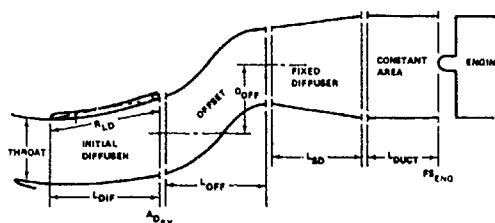


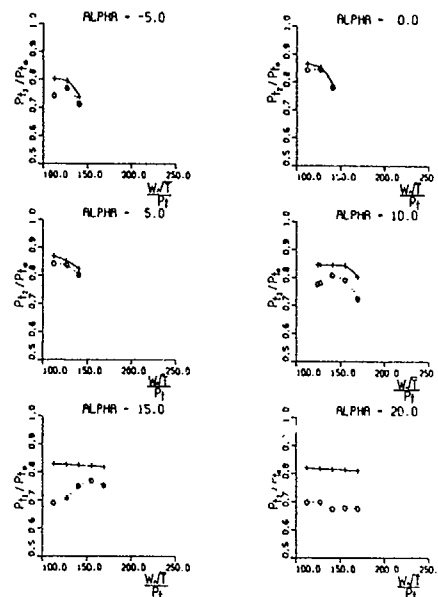
FIG 3.3b IIP DUCT GEOMETRY (REF 3.2)

Offset can be input for one direction only for a constant area duct section. All diffusion is assumed to take place in straight sections upstream and downstream of the offset section. The A-1 duct, however, has offset in two directions and has continuously varying area (which is typical of advanced fighter configurations). The approach taken was to input a similar offset to length ratio into IIP using the total diagonal offset distance of the A-1 diffuser. Third, the throat area as calculated by IIP (not a direct input) was always smaller than the A-1 data indicated. The predicted throat Mach numbers for a given engine mass flow were generally higher than A-1 measured throat Mach numbers. Several sample data comparisons are shown in Figure 3.4. Recovery was predicted reasonably well at moderate angles-of-incidence despite the geometric discrepancies, but accuracy

fell off at higher angles. Transonic comparisons were excellent, except at -5 degrees where IIP probably underestimated the severity of separation at the intake sideplate leading edges.

MACH = 2.5

LEGEND  
+ - LEVEL II  
o - TAILOR-MATE



MACH = 0.9

LEGEND  
+ - LEVEL II  
o - TAILOR-MATE

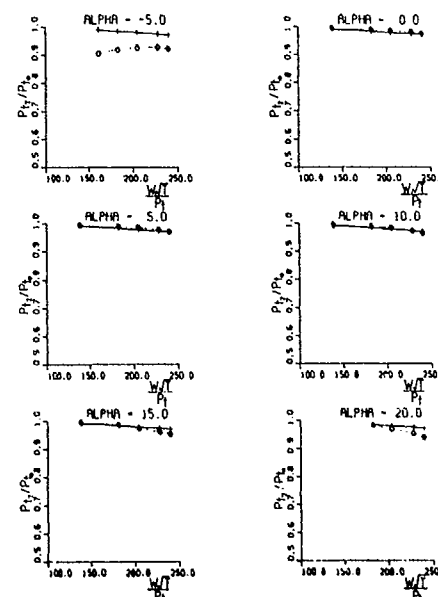


FIG 3.4 SAMPLE IIP COMPARISONS (REF 3.3)

Next, several advanced short-take-off/vertical-landing (ASTOVL) configurations were analysed in support of an international project (Ref 3.5). The intakes for all four configurations were designed for Mach 1.8 cruise: two employed a single fixed compression ramp, and two were simple pitot intakes. All of the configurations involved some degree of shaping for reduced radar signature, such that the intake apertures were three-dimensional. Since IIP cannot model such feature differences, the approach taken was to maintain the correct intake capture area, throat area, and compression ramp angles for an equivalent 2-D intake. Recovery comparisons were generally very good for all the configurations, giving a reasonable degree of confidence in the contractors' quoted performance. Spillage drag comparisons were not as promising, however. Trends with Mach number compared well, but absolute drag levels were different by as much as fifty percent. USAF experience with IIP suggests that its cowl lip drag predictions are particularly sensitive to the input lip geometry, requiring a high degree of detail. However, engineering sketches rarely give the level of detail required to discern this geometry and it must therefore be approximated. Also, the intake drag is highly dependent on the degree of intake-airframe integration. This effect also cannot be modelled by IIP since it assumes an isolated intake. The combined effect of these limitations is to reduce confidence in predicted drag levels.

Finally, IIP was employed recently to help analyse an advanced supercruise fighter forebody/intake test model. The IIP analysis indicated possible problems with oblique shock detachment and the boundary layer removal system, which after further detailed analysis resulted in test model modifications.

#### 2.3.4 CONCLUSIONS AND RECOMMENDATIONS

The LEVEL II Inlet Installation Program (IIP) has been developed for fast, accurate analysis of intake designs. It is also capable of limited design and optimisation options, particularly for off-design operation. It has been used by a number of USAF agencies and is similar in concept and methods to US industry programs developed for preliminary intake design. The IIP total pressure recovery prediction accuracy is considered relatively good. The drag prediction accuracy must be taken with caution, however, because of the sensitivity to input data and the integration aspects. The format of the output information is considered excellent. An entire intake performance envelope can be obtained in a matter of hours. The interactive input sessions

can however become tedious due to the number of responses required and if the information asked for is not available, the process must be prematurely terminated.

Several enhancements would make a program like IIP more usable as a design tool. The unfamiliar user would be helped by 'menu' driven input sessions. Graphical aids would be invaluable in defining parameters so that referral to a printer manual is not required. Also, graphical display of the output would help the user interpret the results of change of his design parameters.

Improvements of the method would be necessary to increase the application to more advanced designs. The ability to determine the effects of 3-D apertures (to first order at least) and highly offset subsonic diffusers on recovery and flow capture is desired. Sufficient data exists to develop empirical correlations for these concepts. Their inclusion would make IIP applicable to highly survivable aircraft designs. The current maximum Mach number limit of IIP limits the use of the mixed compression programs, but extending the empirical correlations up to Mach No. 4 or 6 would allow application to many evolving high speed aircraft.

#### References:

- 3.1. Surber, L.E. & Robinson, C.P. Survey of Inlet Development for Supersonic Tactical Aircraft AIAA 83-1164 June 1983
- 3.2. Tindell, R., and Tamplin, G., "An Inlet System Installed Performance Prediction Program Using Simplified Modelling", AIAA 83-0567, June 1983.
- 3.3. Numbers, K., "LEVEL II Inlet Installation Program Validation Results", AFWAL/FIMM Memo, September 1986.
- 3.4. Surber, Lewis E., "Effect of Forebody Shape and Shielding Technique on 2-D Supersonic Inlet Performance", AIAA Paper No 75-1183.
- 3.5. Bowers, D., Hart, B., and Numbers, K., "Propulsion Integration Normalisation Team Report", AFWAL/FIMM Memo, May 1989.

#### 2.4 INTAKE DESIGN & PERFORMANCE FOR SUPERSONIC CRUISE/HYPersonic OPERATION

##### CONTENTS

- 2.4.1 FINDING A MISSION FOR HIGH SPEED
- 2.4.2 INTAKES FOR MACH NUMBER 2 TO 3+ CRUISE
  - 2.4.2.1 Characteristics of intake design
  - 2.4.2.2 Intake technology in current Mach 2-3+ aircraft
- 2.4.3 MACH NUMBER 4-6 INTAKES
  - 2.4.3.1 Requisite technologies
  - 2.4.3.2 Specific applications
- 2.4.4 MACH NUMBER 6+ TO 8 AIR INTAKES FOR FIRST STAGE ACCELERATORS
- 2.4.5 AIR INTAKES FOR SCRAMJET PROPULSION MACH NUMBER 8 TO 25+

##### 2.4.1 FINDING A MISSION FOR HIGH SPEED

There was, for many years, a natural trend toward higher speed for almost all types of aircraft, but there seems to have been a more or less natural Mach number ceiling for particular functions/missions. In fighter aircraft this Mach number cut off point appears to be in the 2.0 to 2.5 range. Supersonic strike/bomber concepts have been explored for many years, but subsonic sea level flight remains the preferred mode of penetration. Intercept/reconnaissance missions have consistently excited interest in high speed and in fact have provided the motivation for the Mig-25 (interceptor) and SR-71 (reconnaissance) aircraft, the best examples of high speed (Mach 3+) air intake technology available. Most commercial aircraft operate in the high subsonic regime, but the Anglo-French Concorde and Soviet TU144 have demonstrated the general technology necessary to cruise at Mach 2.

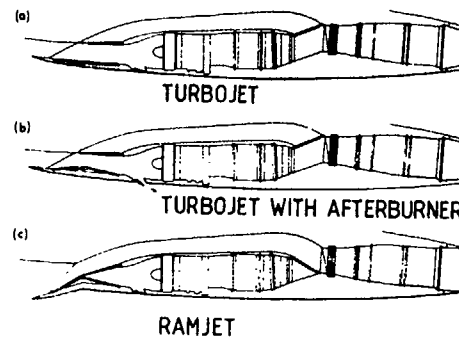
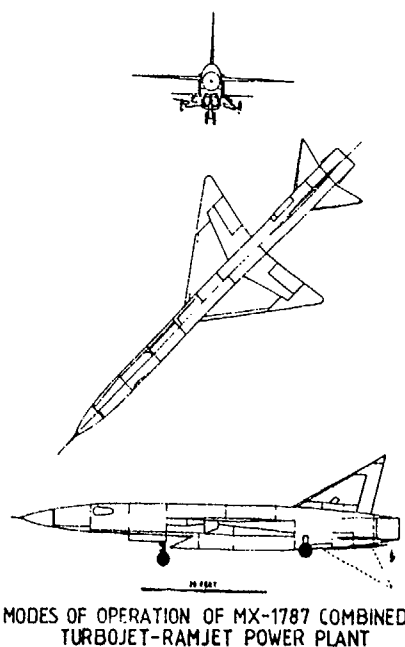


FIG 4.1 REPUBLIC XF-103 & POWERPLANT

In the US, other forerunners of high Mach number technology can be seen in the B-70 and in two Century series interceptor designs, the F-103 (Fig 4.1) and F-108 (Fig 4.2). All these concepts employed efficient two-dimensional mixed compression intakes; but whereas the B-70 and F-108 were turbojet powered, the F-103 was designed for a dual mode turbojet/ramjet propulsion system. Engineers and scientists involved in research and development in the 1960s continued beyond Mach 3 to investigate ramjet propulsion integration into the high supersonic and hypersonic regimes. The air intake was seen to be a key factor in this development; therefore considerable attention was given to efficient diffusion of propulsion streams over a wide range of speeds.

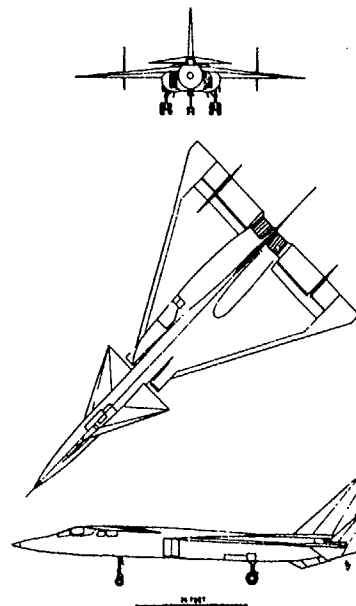


FIG 4.2 NORTH AMERICAN XF 108

The earliest work above Mach 3 concentrated on air intakes for subsonic combustion ramjets, but when exploration of ever higher speeds reached about Mach 8, the potential for ramjet effective specific impulse was dropping rapidly (Fig 4.3). This observation brought consideration of supersonic combustion to the forefront and originated the idea in the US for an aerospace plane. A number of different concepts for such a



vehicle were explored in the early 1960's, all making use of scramjet propulsion above about Mach 6-8. Unfortunately, the magnitude of propulsion technology barriers, resistance from the rocket community and the more immediate needs for propulsion integration at lower speeds pulled attention away from hypersonics. There was a strong tendency to concentrate resources on transonic/supersonic intakes as opposed to very high speed flight. Any high altitude supersonic system that could be conceived was perceived as vulnerable to projected defenses.

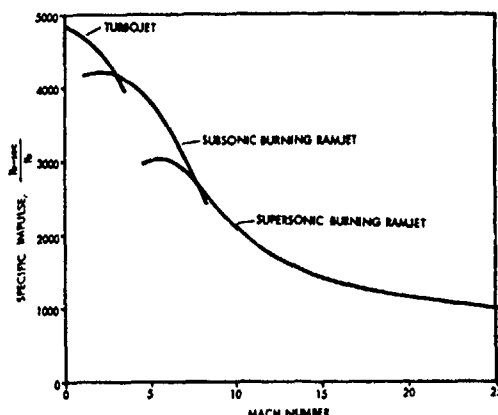


FIG 4.3  
SPECIFIC IMPULSE OF HYDROGEN-FUELLED  
ENGINES

When mission analysts began to look beyond Mach 3 significant levels of interest in high speed flight reemerged. In the US interest in high speed flight came about in the resurrection of the single-stage-to-orbit airbreathing aircraft concept. The National Aero-Space Plane (NASP), makes use of a dual-mode ramjet/scramjet engine to achieve near orbital velocities. A related mission would be the so-called "orient express," a hypersonic passenger aircraft which would provide quick trans-Pacific transport. The work on NASP, then, led naturally to examination of other intermediate speed applications, both as new missions and as alternatives to NASP. Starting from the lower end of this Mach 4 to 25 regime, mission analysts were able to see utility for systems operating from Mach 4 to 6 for intercept, reconnaissance or interdiction purposes. Beyond that, in the Mach 6-8 range, potential for a ramjet or ramjet-powered first stage of a two-stage-to-orbit vehicle has been examined in a number of places, e.g., the German Sänger vehicle. Also, suborbital Mach 8-12 missions have been postulated which hold considerable promise in terms of both reaction time and survivability (Ref 4.1 & 2).

Thus, the possibility of high speed flight has been revived, and with it, the need for high speed air intakes. Several distinct areas of interest can be identified:

Max Mach number	Potential Applications
a. 2-3+	High speed civil transport (HSCT)
b. 4-6	Transport L'Avion à Grande Vitesse (AGV), Intercept, Reconnaissance & Interdiction aircraft
c. 6-8	First stage of two-stage-to-orbit vehicle (Sänger) or part of a ramjet/rocket single-stage-to-orbit (British Noto) concept

d. 8-25

- o 8-12 Reconnaissance, fast-response global interdiction aircraft
- o 12-25 Air breathing single-stage-to-orbit (SSTO) vehicle

It should be noted that the value of these possible flight vehicles does not hinge on the anticipation of a future major power conflict. Some of them, however, suggest the need for continuing allied power vigilance and the recognition that there will continue to be global "hot spots" which could require high speed intervention (Ref 4.1). Inherent in these technologies is the potential for civilian application. Interest has been revived in high speed atmospheric flight, and the challenges for high-speed air intakes are substantial, increasing in difficulty as Mach number increases. While there are many overlapping requirements for intake technology across these regions, several key factors can be considered. The balance of this section will deal with progress in technology and requirements for future solutions.

#### 2.4.2 INTAKES FOR MACH 2 to 3+ CRUISE

##### 2.4.2.1 Characteristics of Intake Design

Air intakes designed for supersonic cruise have different priorities to those designed for supersonic dash flight. In regard to dash aircraft, intake designs such as those used on F-15 and Tornado provide relatively high pressure recovery and low flow distortion, even during combat manoeuvres. They place relatively less emphasis on low drag. Supersonic cruise aircraft on the other hand, spend the major portion of their time at or near a supersonic design point; consequently their intakes require reduced cowl lip thickness, more efficient boundary layer bleed and relatively sophisticated bypass systems to provide a precise mass flow match between intake and engine and stable operation. Intake bleed flow in particular must be exhausted efficiently to minimize potential drag contributions. As supersonic cruise takes place at higher and higher Mach numbers, the importance grows of reducing contributions to bleed, bypass and spillage drag and the need to reduce cowl drag leads to the use of mixed compression. The technology currently available to accomplish these tasks can best be illustrated by their implementation on current aircraft and in the design of advanced supersonic cruise aircraft.

##### 2.4.2.2 Intake Technology in Current Mach 2-3+ Aircraft

The Concorde, operating at Mach 2.0, represents a unique intake employed at the lower edge of the supercruise range (Ref 4.3). The Concorde designers were able to employ a low drag external compression design (Fig 4.4). This intake, as can

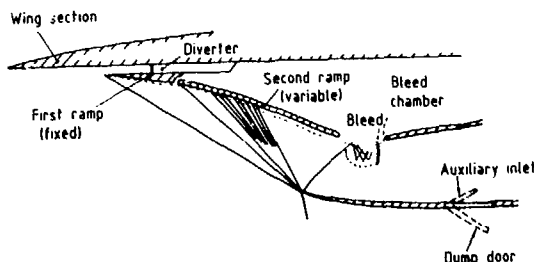


FIG 4.4  
AERODYNAMIC FEATURES OF CONCORDE INTAKE

be seen from the Figure, is basically a three-shock design, but adds some isentropic compression on the second ramp and operates between a complex field of expansions/shocks internally near the ramp bleed gap, and the standard normal shock at intake entry. By allowing a small amount of duct contraction aft of the entry plane the external cowl angle is kept to a minimum consistent with shock attachment at the lip and a self starting intake. The wide bleed slot behind the compression ramp allows a free shear layer to accommodate changes in mass flow. It automatically adjusts the bleed slot streamline and the amount of flow removal required for flow matching. From a purely mechanical point of view, the Concorde intake is a model of simplicity. It uses a variable second compression ramp and an auxiliary intake (for takeoff) combined with a dump door for over-board bypass. Transient controls activate the dump door which is made easier due to the fact that the inlet operates stably from supercritical to subcritical conditions. Its advantage is seen in the combination of simplicity and reliability with performance adequate for Mach 2.0 operation. With this type of design (ie without mixed internal/external compression) at higher Mach numbers it would be difficult to maintain high total pressure without unacceptable increases in drag and bleed flow quantity.

Although in the US a prototype supersonic transport was never built, its air intake was one of the more fully developed designs in the history of US research and development. Variations on its axisymmetric mixed compression design continued in NASA for several years after abandonment of the SST itself, exploring mixed compression ranging from 40% to 60% internal contraction, developing highly efficient boundary layer control and refining means of achieving inlet stability. Tjonneland outlined some of the chief design characteristics of the Boeing SST intake design in Ref.4.4 as it applied to the Mach 2.7 commercial cruise vehicle (Fig.4.5a). This reference points out that in the development of the intake design, a number of improvements in intake design were required, especially in the areas of boundary layer prediction and control, intake stability and intake/engine airflow matching. It noted that, even with optimistic pressure recovery and bleed estimates, an SST with a 3500 mile range would experience cruise range loss in excess of 12% due to total pressure losses and bleed drags alone. As a consequence, it was necessary to set very high performance and stability objectives for the intake. For example, the 'started' intake at Mach 2.65 operated at a pressure recovery of 91% and was designed to accept a step reduction of 5% in engine corrected airflow without controller action and remain 'started'. Similarly, operating on-design, the inlet was not to 'unstart' when experiencing a Mach number reduction up to 0.05. The overall system was matched so that no overboard bypass was required for matching during normal climb and cruise operation. The complex Boeing design incorporated:

- A translating spike for matching and bleed optimization
- Four throat doors to obtain flow area variation needed from take-off to transonic conditions.
- Four overboard bypass doors (which in turn incorporated suck-in doors) to spill excess airflow during descent or other conditions involving an inoperative engine.

- Distributed centerbody spike and cowl bleed plus a spike shoulder scoop bleed for boundary layer and shock wave boundary layer interaction control (Fig 4.5b). An intricate control system blended these variable geometry features and an automatic vortex valve (Fig 4.5c) to solve problems with:

- Takeoff/landing performance
- Takeoff noise abatement

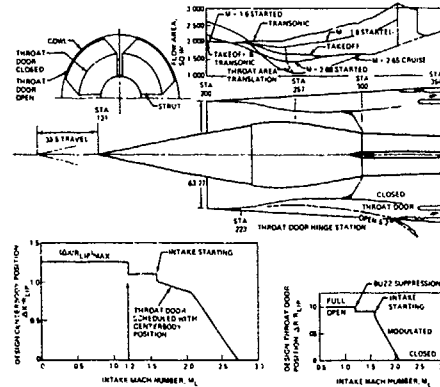


FIG 4.5a INTAKE GEOMETRY

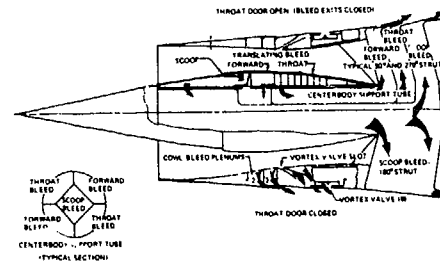


FIG 4.5b BOUNDARY LAYER BLEED SYSTEM

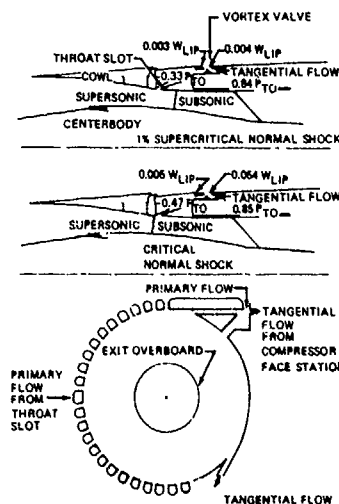


FIG 4.5c VORTEX VALVE SCHEMATIC

FIG 4.5 BOEING SST INTAKE

- o Stable supersonic "started" operation
- o Intake buzz suppression
- o Optimizing supersonic diffuser/bleed system operation
- o Minimization of bleed drag
- o Normal shock system stability

Even recent reports on NASA's investigation of an advanced SST (Ref 4.5) feature a similar intake design, but operating with advanced higher temperature variable cycle engines. The intake could employ an expanding centerbody compression surface for noise reduction features such as intake choking during landing or takeoff to block noise from propagating outside the intake (Ref 4.6). Similarly, updated versions of the Concorde (Ref 4.7) have been suggested (Fig 4.6). The ATSF (Avion De Transport Supersonique du Futur) would operate in the Mach 2.4 to 2.5 regime, possibly with a variable cycle engine which would operate as a turbofan at take off and as a turbojet for supersonic cruise, the "flow multiplier" fan being driven by a secondary turbine for takeoff and subsonic cruise (Fig 4.7). With such a flight vehicle, crucial needs include a "smart" control system, a high efficiency intake and careful integration of all aspects of engine and airframe design from the outset of development.

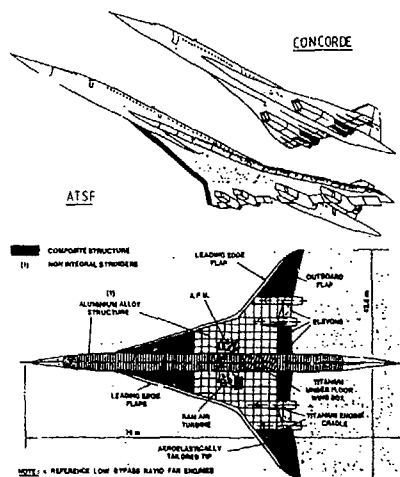


FIG 4.6 COMPARISON OF L'AVION DE TRANSPORT SUPERSONIQUE DU FUTUR & CONCORDE

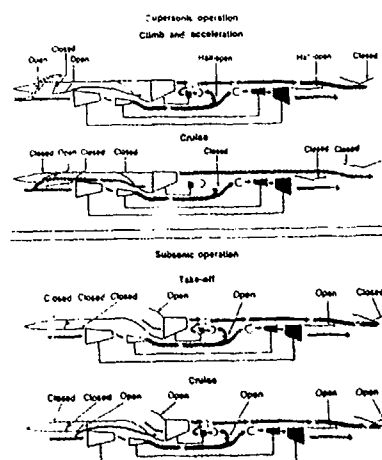


FIG 4.7 SNECMA VARIABLE CYCLE ENGINE

It would have seemed incredible 25 years ago to predict that the YF-12/SR-71 would persist as the state-of-the-art for Mach 3+ manned cruise flight, but even as it retired, it was the reigning example of high supersonic cruise. A number of reports on this aircraft's intakes (e.g., Ref 4.8-13) offer insight to the flying Mach 3+ cruise state-of-the-art for induction systems. This Mach 3+ axisymmetric mixed compression intake operates essentially as an isolated intake, only a slight downward cant and toe-in being provided to align the intake with the forebody flow field (Fig 4.8). The

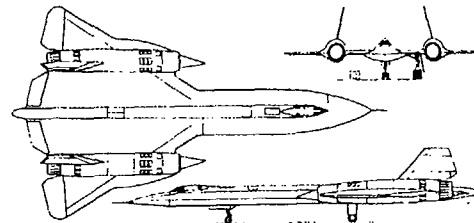


FIG 4.8 LOCKHEED SR-71A

compression spike translates for off-design spillage operation and to provide inlet 'restart' capability. Its bleed regions for boundary layer control and shock stability are located on both the spike and cowl. Spike bleed is by means of a series of surface slots. Cowl bleed uses a combination of flush slots and a ram scoop referred to as the shock trap (Fig 4.9). The

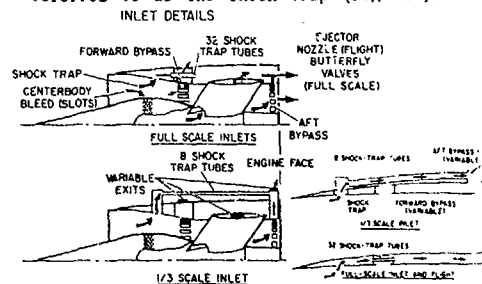


FIG 4.9 DETAILS OF THE SR-71A FULL SCALE AND 1/3 SCALE INLET SYSTEM

YF-12/SR-71 intake system has two bypass systems, using the forward bypass to position the normal shock and to dump large amounts of flow during a 'restart' cycle. The aft system provides for some engine cooling, but is also used for engine matching below Mach 3.0 (Fig. 4.10). A digital inlet control developed later was able to attenuate disturbance induced shock excursions for frequencies of about 1 hertz and below.

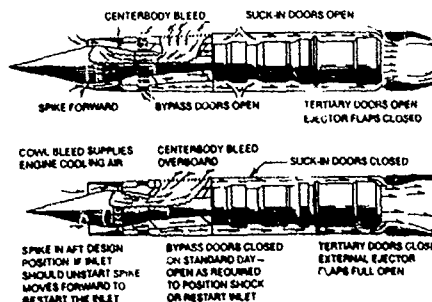


FIG 4.10 AIR FLOW PATTERNS-STATIC AIRCRAFT (TOP)  
-HIGH SPEED (BOTTOM)

Development of the SR-71 inlet during its lifetime has dealt largely with terminal shock stability problems. Solutions working with existing flight vehicle actuation hardware met with some success, but other systems which would require more drastic inlet modification showed excellent promise. In one case (Ref 4.10) a YF-12 aircraft inlet modified to provide a porous cowl-bleed region just upstream of the intake's shock trap and bleed flow was controlled by relief-type mechanical valves (Fig 4.11), designed for high Mach number (Mach 3+) flight.

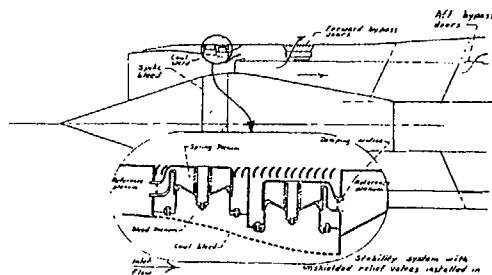


FIG 4.11 YF-12 INLET WITH STABILITY SYSTEM

The valves provided their own reference pressure and, hence, did not respond to the slow response perturbations handled by the inlet's control system. Such a system was shown to be able to absorb diffuser-exit airflow disturbances that are too fast for the inlet's production control system. If the SR-71 were being developed today, it appears that the level of technology would be adequate to facilitate synthesis of a more stable intake.

#### 2.4.3 MACH 4 - 6 INTAKES

##### 2.4.3.1 Requisite Technologies

For the most part, the difficulties of designing intake at Mach 3 continue into the Mach 4 to 6 regime, but with revised priorities. Major changes in emphasis stem from the off-design flow matching problem and from the utilization of a combined cycle turbo-ramjet engine (Fig 4.12).

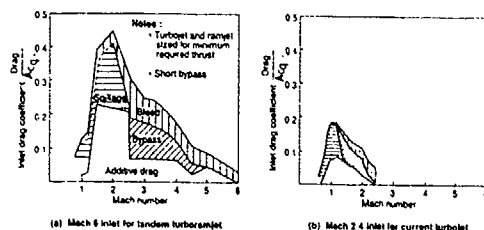


FIG 4.12 COMPARISON OF INLET DRAG COMPONENTS

Maximum Mach number propulsion flow requirements produce a large intake capture area relative to other aircraft dimensions (Fig 4.13). This

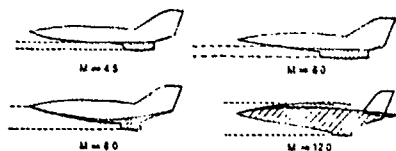


FIG 4.13 SIZE OF CAPTURE AREA & INFLUENCE OF PROPULSION SYSTEM GROWTH WITH SPEED

situation creates an acceleration problem because the inlet sized for maximum Mach number is unable to pass the capture area streamtube at transonic and low supersonic flight conditions. Coupling this situation with reduced engine demand at the lower Mach numbers requires spillage bypass of up to 90% of the approaching capture area streamtube (Fig 4.14). Getting rid of the excess air, in turn produces high spillage and bypass drags. Consequently a critical need is identified for Mach 4 to 6 intakes which exhibit low off-design drag. On the other hand, the requirement to maximize total pressure recovery (as with a Mach 3 turbojet) is relaxed in a high Mach number environment where a ramjet is either included with the turbojet or takes over completely.

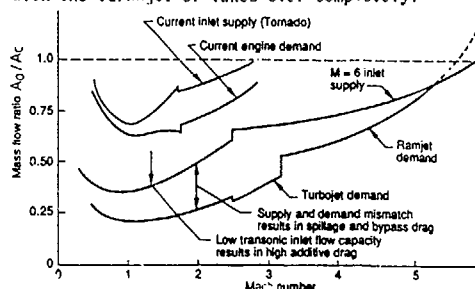


FIG 4.14 COMPARISON OF INLET SUPPLY & ENGINE DEMAND  $M=6$  vs CURRENT PROPULSION SYSTEM

A number of design issues can be identified for air intakes operating in the Mach 4 to 6 range. In the supersonic diffuser the compression ramps are designed not only as to number and length of ramps, but also whether to use hinged ramps exclusively or include flexible ramp(s) to approximate isentropic compression. Variable geometry also helps to provide efficient transonic spillage. An efficient boundary layer control system for compression ramp(s) and sidewalls is designed not only to maximize pressure recovery, but also to maximize total system performance with absolute reliability. Intake throat design for these applications considers the effect of throat Mach number on performance and stability and it provides for normal shock position control, whether by bleed, shock trap mechanism or other device. Design of the flight vehicle itself also considers the forebody boundary layer - whether to divert, bleed or ingest some or all of it. Because of the high pressures and temperatures in the intake, mechanical design takes on increased importance for accurately controlled actuation, for sealing of ramps against leakage and for providing adequate thermal protection for subsystems. Even the subsonic diffuser design is critical. Care must be taken to maintain attached flow with the high area ratios associated with maximum Mach number, (a) to provide for smooth transition from turbojet to ramjet operation, (b) to use the ramjet duct appropriately for bypass in low speed (transonic) flight and (c) to assure adequate diffuser wall cooling.

The foregoing deals with air intake design as a component, but in this Mach 4 to 6 regime the integration of air intake with the airframe takes on increased importance. As mentioned previously, the intake size at higher Mach numbers increases with respect to the rest of the aircraft. This forces the vehicle designer to consider utilizing part of the airframe as inlet compression surface, thereby effectively reducing airframe wave drag and, potentially, wetted area.

airframe wave drag and, potentially, wetted area. Air intake design - as well as the entire propulsion system - must be accomplished integrally with the flight vehicle from the outset of preliminary design.

#### 2.4.3.2 Specific Applications

Intakes may not vary greatly in general appearance, but still provide dramatically different engine flow conditions. Reference 4.14 indicates that the fuselage forebody boundary layer will be turbulent, and could be ingested at least partially by the intake in an integrated configuration. It notes the potential for improved aircraft performance from forebody precompression and offers experimental data from four different compression surfaces at Mach 6.0 to show potential differences in boundary layer progression (Fig 4.15). The four developed

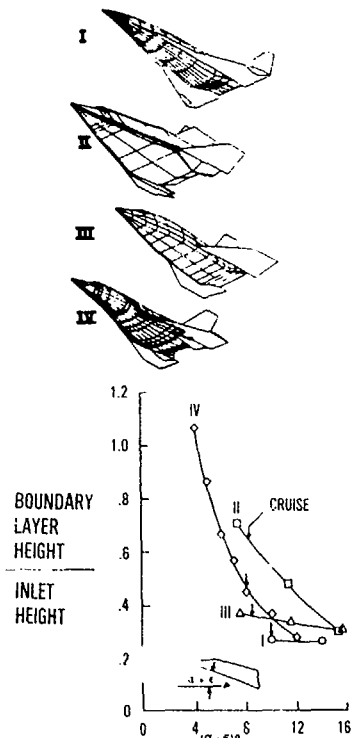


FIG 4.15 SCRAMJET INLET VISCOUS EFFECTS

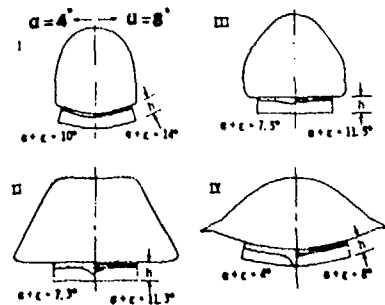
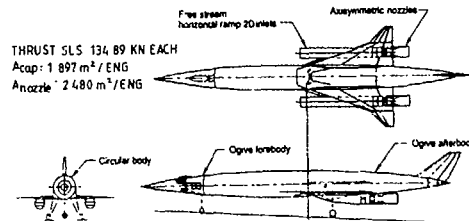


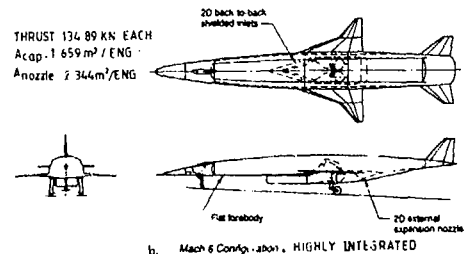
FIG 4.16 BOUNDARY-LAYER SHAPES FOR TWO ANGLES OF INCIDENCE & FOUR FUSELAGE SHAPES. SCRAMJET ENGINE OF HEIGHT  $h$  AT THE ENGINE INLET STATION

boundary layers are quite different in height and shape and can fill a significant portion of the intake (Fig 4.16). The differences were seen to be determined by parameters such as forebody transverse curvature, transverse static pressure gradient and the degree of isolation of the forebody compression from crossflow influence.

With this potential influence of forebody boundary layer development in mind, a specific study of Mach 4 to 6 airframe - propulsion system integration is considered (Ref 4.15). This investigation found intakes with low boundary layer bleed requirements and good angle-of-incidence characteristics to be highly desirable. Such attributes were found to permit efficient engine operation including manoeuvre at hypersonic speeds. If, as in many applications, a hypersonic manoeuvring requirement sizes the intake capture area, this study showed it possible to achieve a 20% to 50% reduction in intake capture area by using horizontal ramp intakes or shielded intakes (Fig 4.17). In this case, airframe integration of the intake has been used effectively to reduce flow spillage requirements. Also, if done properly integration can lead to reduced vehicle weight, fuselage wave and viscous drags (Fig 4.18). On the other hand,



a. Mach 6 Baseline, ISOLATED INTAKES



b. Mach 6 Configuration, HIGHLY INTEGRATED

FIG 4.17 MACH 6 RECONNAISSANCE AIRCRAFT

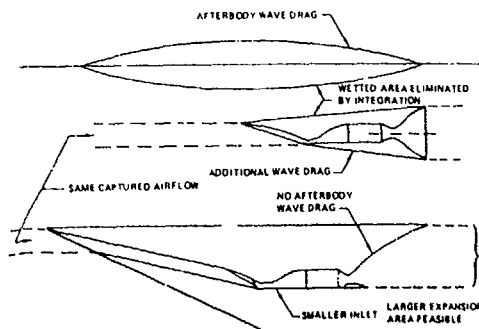


FIG 4.18 PERFORMANCE BENEFITS DUE TO INTEGRATION

the study warns that non-optimum structural designs can actually increase weight in integrated concepts and that high drag boundary layer diverters may be required. In this design task special effort was extended to produce a compact mixed compression intake design which employed isentropic compression in both ramp and cowl, and internal shock cancellation in the

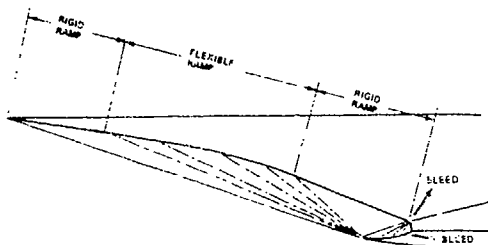


FIG 4.19  
MACH 4.5 INLET DESIGN SHOCK STRUCTURE

throat region (Fig 4.19). Bleed on both ramp and cowl sides of this shock cancellation corner is used to prevent separation due to shock - boundary layer interaction. This bleed also provides a measure of stability by increasing sharply with forward movement of the shock. It is estimated that this type of inlet would require only about 5% total bleed, including 1% on each of the sidewalls. The idea behind this is that any range decrement due to loss in total pressure recovery would more than be made up by the reduction in bleed drag. Experience with the conventional mixed compression NASA LERC Mach 5.0 inlet test demonstrates that high Mach number inlets can demand huge amounts of bleed flow to produce stable, high performance operation. The focused compression concept of the Ref 4.15 study is inherently high in risk, but offers sizing and bleed drag reductions worthy of further exploration.

Aerospatiale, as well as US concerns, have been examining commercial applications of Mach 4 to 6 flight. The French version, L'Avion à Grande Vitesse (AGV), would cruise at Mach 5.4 (Fig 4.20).

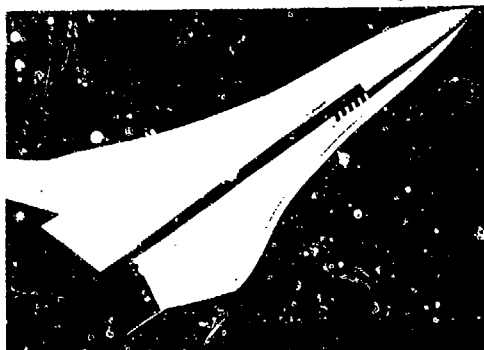


FIG 4.20 AEROSPATIALE HYPERSONIC AIRCRAFT CONCEPT, AGV

Its designers were quoted (Reference 4.16) as being confident that they possess the necessary theoretical and experimental bases required to initiate the design of such an aircraft. They cite experience with ram-propulsion engines (ramjet and ramrocket) in missile work and capability to deal with supersonic flight on a large aircraft from Concorde experience. This would presumably include the ability to deal with air intake problems, but based on recent US experience there is a considerable leap in complexity of intakes from Mach 2.0 to Mach 5.0.

Judging from the results of investigations and developments over the past thirty years since Mach 4 to 6 propulsion integration work began in earnest, there appears to be little doubt that the foundation technology for manned Mach 4 to 6 air breathing flight exists. The question, rather, is whether there is sufficient military support or civilian potential to pay for the development and flight test of such a system.

#### 2.4.4 MACH 6+ TO 8 AIR INTAKES FOR FIRST STAGE ACCELERATORS

This application is represented most notably by Germany's Sänger Vehicle, but numerous versions of this alternative to the NASP-type single-stage-to-orbit have been generated. It offers lower risk in terms of propulsion system development in general and, consequently, air intake technology. In the case of the Sänger, the large first stage launch platform accelerates to about Mach 6.8 powered by turbojet-ramjet engines (Fig 4.21). At this point it separates

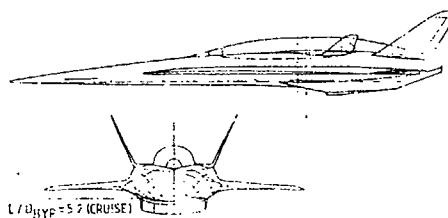


FIG 4.21 SÄNGER BLENDED BODY/WING CONFIGURATION

from the smaller, top-mounted "Horus" second stage which goes into orbit via a rocket (Ref 4.17). Another proposed system is Hotol, an orbital vehicle conceived by British Aerospace and Rolls Royce (Fig 4.22). While Hotol is not

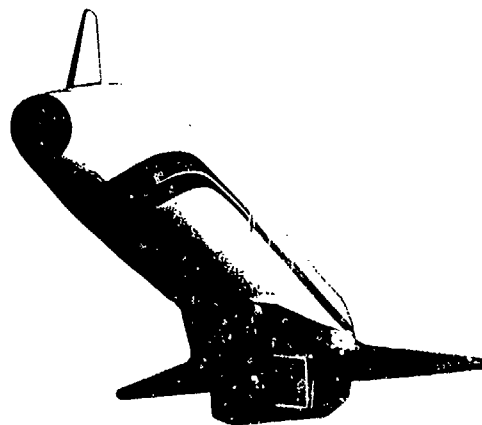


FIG 4.22 HOTOL CONFIGURATION

per se a staged vehicle, the air breathing propulsion system operates only to about Mach 5.0, at which point ascent continues on rocket power. Thus many of the air intake requirements are the same as for the Sänger, the primary difference coming, apparently, from the secondary use of the Hotol inlet during ascent to gather air for production of liquid oxygen used in its rocket phase (Ref 4.18). Air intakes for this type of vehicle would vary from those of the previous section in that, as accelerator-dedicated components, they would not be so heavily concerned with bleed drag nor design point performance. They might therefore

provide applications for the so-called oversped intake, (Fig 4.23) somewhat undersized for the maximum Mach number condition in order to reduce spillage drag at the transonic condition. Mach 8 is given as the upper limit for this application with the assumption that it would be feasible to

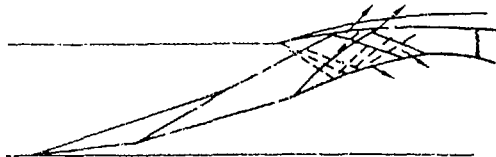


FIG 4.23 OVERSPED MIXED COMPRESSION UNIT

consider using subsonic combustion ramjets at this speed. In any case, avoiding the jump in technology requirement associated with scramjet operation would have a strong influence on the maximum Mach number of staging or shifting to rocket propulsion.

Some valuable measurements on research type axisymmetric intakes or perturbations on axisymmetric intakes in this Mach number range (5 to 8.5) were done by NASA Langley in the 1970s (Refs 4.19-21).

#### 2.4.5 AIR INTAKES FOR SCRAMJET PROPULSION, MACH 8 TO 25+

As indicated previously there are some mission differences associated with various levels of maximum scramjet powered flight Mach number.

Suborbital missions have been defined for the Mach 8 to 12 regime, but the greatest attention by far recently has been given to the development of a single-stage-to-orbit flight vehicle using dual mode (ramjet-scramjet) propulsion. In general the technology challenges are similar across this regime, but obviously escalate with increasing Mach number.

Some of the primary challenges of high Mach number vehicles were well defined in 1986 (Ref 4.22).

It was pointed out that in ramjet/scramjet-powered vehicles, intakes and exhaust nozzles would comprise the major part of the entire vehicle so that intake performance would be directly related to forebody precompression. At the same time this inlet precompression creates a significant portion of the vehicle's lift and pitching moment. Also, intake, airframe, combustor and exhaust nozzle must be structurally integrated. While the airframe and propulsion system are thus inextricably linked, the aerodynamic interface varies with engine operating mode, complicating the responsibility for the design weight and performance. Ref 4.23 (1987) asserted that there was sufficient knowledge to design and build rocket-boosted scramjet-powered missiles for Mach 3 to 7 operation, but that extension to orbital speeds or integration with a vehicle that operates from take-off would require "additional development." This reference also mentioned the role of CFD (computational fluid dynamics), saying that it was still in a formative stage and lacked fundamental process data to validate a number of the physical and chemical models being used. Intake development, in particular, would be affected by the need to understand turbulence, especially at supersonic and hypersonic flight speeds, and to be able to predict its effect on wall shear and heat transfer, boundary layer separation/reattachment, fuel injection and mixing as well as chemical kinetics. Reference 4.24 (also in 1987) echoed these basic thoughts, pointing out that, in the area of boundary layer

transition and development, factors that had been insignificant at lower speeds would assume major roles at hypersonic speeds. For instance, rapid growth of high speed boundary layers effectively changes surface shape and "entropy swallowing" pulls energy from the stream that would otherwise energize downstream boundary layers. Wind tunnel verification testing would be compromised by the fact that wall noise interferes with transition. Inlet development and analysis is further complicated by the significance of real gas effects above about Mach 10.

With this background, it is appropriate to review some recent intake technology developments and notice the advancement of capability in the relatively short period of time from 1987 to 1989. First, Ref 4.25 reports development on intake boundary layer control at the lower Mach numbers. This work presents Navier-Stokes solutions for strong shock interactions, incident oblique shocks, compression corners and shock expansions associated with high speed air intakes (Fig 4.24). Also, it presents results of

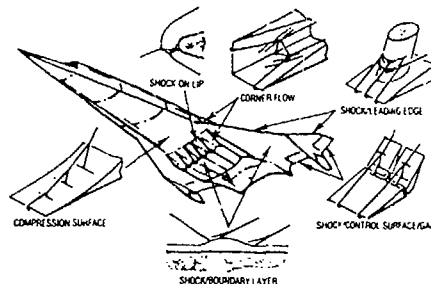


FIG 4.24 SHOCK INTERACTION FLOW FIELDS

tangential air injection to control shockwave-boundary layer interaction in the Mach 3 to 5 region, showing the importance of proper injector location in order to effect flow control. Another source (Ref 4.26) discusses the application of a 3-D Navier Stokes code to the analysis of an intake module where flow is compressed by swept, wedge-shaped sidewalls. The combination of sidewall sweep and aft cowl placement in this fixed geometry design facilitates efficient spillage and good inlet characteristics over a range of operating Mach numbers. Three wedge-shaped fuel injection struts double as additional compression surfaces to complete the diffusion process (Fig 4.25).

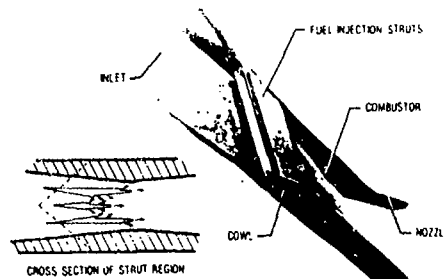


FIG 4.25 SCRAMJET ENGINE MODULE AND ITS CROSS SECTION

Obviously, the throat flow is highly complex, experiencing side wall interaction with strut shocks and expansion waves, cowl shocks, and effect expansion waves and separation induced shockwaves. The author points to good agreement of this complex analysis with experimental data in order to claim good ability to simulate the

complex flow fields associated with sophisticated hypersonic vehicle air intakes. The utility of such analysis capability is particularly evident from the observation in Ref 4.27 of very significant differences in NASP intake concepts. The propulsion modules associated with the two concepts described will be tested over the Mach 0 to 8 range. Accurate intake computational simulation will be crucial not only in the intake designs, but also in assessing the influence of different combustor approach flow conditions and extrapolation of propulsive performance to cover the full range of scramjet operation (Fig 4.26).

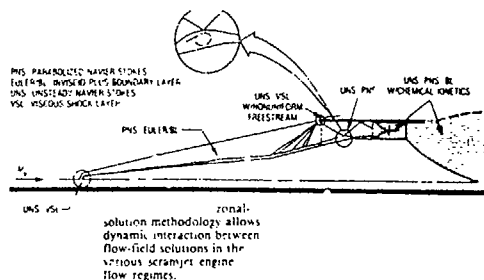


FIG 4.26 POSSIBLE CFD METHODS FOR INTAKE ANALYSIS

Even the most optimistic plans for high speed test facility investment (Refs 4.28 and 4.29) will provide only spot checks of intake flow development and intake flow effects on propulsion system performance. Thus for a single-stage-to-orbit scramjet vehicle, much of the intake development must be accomplished by computational means and verified insofar as possible by experimental test.

There are some areas of interdisciplinary intake development which as yet do not lend themselves to any kind of exclusively computational analysis. Actively cooled leading edges applicable to intake cowl lips are an example of such developmental work. The designs must be analysed, fabricated and tested in a hot gas facility. Analysis techniques at this point are only fair, but are still a useful adjunct to continuing experimental development.

While there are many hurdles yet to clear, the advances in knowledge pertaining to hypersonic air-breathing flight have been impressive. Propulsion and propulsion integration have always been regarded as key areas, but progress has been made on a number of fronts, including intake development. Rapid advances in areas such as turbulence modelling, transition prediction, leading edge cooling and combustion analysis are helping researchers to define realistic intake and ramjet and intake - ram/scramjet designs for future hypersonic flight vehicles. As in many cases, increased knowledge brings increased understanding of the cost involved. In the relatively near term the cost of development and ownership of hypersonic flight vehicles will be sufficiently clear to determine where limited resources should be concentrated.

#### REFERENCES

- 4.1. Williams, Robert M., "National Aero-Space Plane: Technology for America's Future," *Aerospace America*, Nov 1986, pp 18-22.
- 4.2. Coleman, Herbert J., "NASA, Defense Dept Award Contracts for Aerospace Plane," *AW&ST*, 14 Apr 1986, pp 24,25.
- 4.3. Seddon & Goldsmith, *Intake Aerodynamics*, Ch 12 - "Matching & Control" - The Concorde Intake, pp 329-333 - AIAA Education Series.
- 4.4. Tjonneland, E., "The Design, Development and Testing of a Supersonic Transport Inlet System," ACARD CP 91-71, Sep 1971.
- 4.5. Driver, Cornelius "How Different a Modern SST Would Be," *Aerospace America*, Nov 1986.
- 4.6. Kandebo, Stanley W., "HSCT Propulsion Studies Focus on Reducing Emissions, Noise" *AW&ST*, 10 Jul 89.
- 4.7. "Birch, Stuart, "Advancing Technologies," International Viewpoints Section, *Aerospace Engineering*, Oct 89.
- 4.8. Johnson, Clarence L., "Development of the Lockheed SR-71 Blackbird," *Lockheed Horizons*, Winter 1981/1982.
- 4.9. Smeltzer, Donald B.; Smith, Ronald H.; and Cubbison, Robert W., "Wind Tunnel and Flight Performance of the YF-12 Inlet System," *Journal of Aircraft*, Vol 12, No 3, Mar 1975, pp 182-187.
- 4.10. Cole, Gary L.; Dustin, Miles O.; and Neiner, George H., "Wind Tunnel Performance of a Throat Bypass Stability System for the YF-12 Inlet," NASA Conf Pub 2054, *YF-12 Experiments Symposium*, Vol 1, Sep 1978.
- 4.11. Reukauf, Paul; Olinger, Frank V.; Ehernberger, L.J.; and Yanagidate, Craig, "Flight-Measured Transients Related to Inlet Performance on the YF-12 Airplane," NASA Conf Pub 2054, *YF-12 Experiments Symposium*, Vol 1, Sep 1978.
- 4.12. Cole, Gary; Neiner, Geo.; and Dustin, Miles, "Wind Tunnel Evaluation of YF-12 Inlet Response to Internal Airflow Disturbances With and Without Control," NASA Conference Pub 2054, *YF-12 Experiments Symposium*, Vol 1, Sep 1978.
- 4.13. Wilson, J.R. and Wright, V.A., "Use of Engine speed Trim to Automate the Supersonic Engine/Inlet Match in the AR-71," 29 Jun - 2 Jul 1987.
- 4.14. Lawing, Peirce L. and Johnson, Charles B., "Inlet B.L. Shapes on Four A/C Forebodies at Mach 6," *Journal of Aircraft Engineering Notes*, Vol 15, No 1 Jan 1978.
- 4.15. Salemann, Victor and Andrews, Mark, "Propulsion System Integration for Mach 4 to 6 Vehicles," AIAA Paper, 1988.
- 4.16. Birch, Stuart, "Hermes Update," *Aerospace Engineering*, Feb 1989.
- 4.17. Covalt, Craig, "Sanger Aero-Space Plane Gains Increased Support In Europe," *AW&ST*, 10 Jul 89.
- 4.18. Burns, ERA, "Horizontal Takeoffs for Future Launch Vehicles," *Aerospace Engineering*, Aug 87.
- 4.19. M G Torrence, "Experimental Investigation of a Mach 6 fixed geometry inlet featuring a swept external-internal compression field" NASA TN D-7998 Oct. 1975.



- 4.20 E.H. Andrews, J.W. Russell, E.A. Mackey & A.L. Simmonds, 'An inlet analysis for the NASA hypersonic research engine aerothermodynamic integration model' NASA TM X-3038 Nov. 1974.
- 4.21 E.H. Andrews, A.M. Agnone & S.Z. Pinckney, 'Experimental & analytical study of an inlet forebody for an airframe integrated scramjet concept.' NASA TM X-3158 Jan. 1975.
- 4.22 Coons, L.L., "Propulsion Challenges of Hypersonic Flight," AIAA-86-2620, Oct 86.
- 4.23 Waltrup, P.J., "Hypersonic Airbreathing Propulsion: Evolution & Opportunities," AGARD CP No 428, Aerodynamics of Hypersonic Lifting Vehicles," Paper #12, 1987.
- 4.24 Johnston, Whitehead and Chapman, "Fitting Aerodynamics and Propulsion into the Puzzle," Aerospace America, Sep 87 pp 32ff.
- 4.25 White, M.E.; Thompson, M.W.; Carpenter A.; Lee, R.E.; Yante, W.L., "Tangential Mass Addition for the Control of Shock Wave/Boundary Layer Interactions in Scramjets Inlets," IX ISOABE, Sep 89, Athens, Greece.
- 4.26 Kumar, Ajav, "Numerical Simulation of Flow Through a Two-Strut Scramjet Inlet," AIAA J. of Propulsion, Vol 5, No 3 May-Jun 1989.
- 4.27 Kandebo, S.W., "NASP Program Office Retains Two Propulsion Contractors," AW&ST, May 8, 1989.
- 4.28 Anon, "Aerojet Tech Systems Facility to Test Hypersonic Engines Designed for NASP," AW&ST, 12 Jun 89.
- 4.29 Harvey, David, "NASP Program on Track," Defense Science, May 1989, pp16-21.

## 2.5 INTAKE DESIGN & PERFORMANCE FOR AGILE TACTICAL FIGHTERS

### CONTENTS

- 2.5.1 INTRODUCTION
- 2.5.2 ISOLATED INTAKES
  - 2.5.2.1 Internal flow
    - (a) Flow in the subsonic diffuser
    - (b) Combination of intake and subsonic diffusers
  - 2.5.2.2 External flow
  - 2.5.2.3 Intakes with compression surfaces at subsonic and supersonic speeds
- 2.5.3 INTAKE-AIRFRAME INTEGRATION
  - 2.5.3.1 Fuselage flow fields for side mounted inlets
  - 2.5.3.2 Performance of a rectangular compression surface intake on the side of a fuselage
  - 2.5.3.3 Performance of half cone intakes on the side of a fuselage
  - 2.5.3.4 Performance of a pitot intake on the side of a fuselage
  - 2.5.3.5 Fuselage and wing flow fields for shielded intake installations
  - 2.5.3.6 Performance of shielded compression surface intakes
    - (a) Rectangular intakes
    - (b) Half axisymmetric intakes
  - 2.5.3.7 Comparison of performance of shielded and unshielded rectangular and half axisymmetric inlets
  - 2.5.3.8 Performance of shielded pitot intakes
- 2.5.4 TECHNOLOGY IMPLEMENTATION IN CURRENT AIRCRAFT
- 2.5.5 CONCLUDING REMARKS

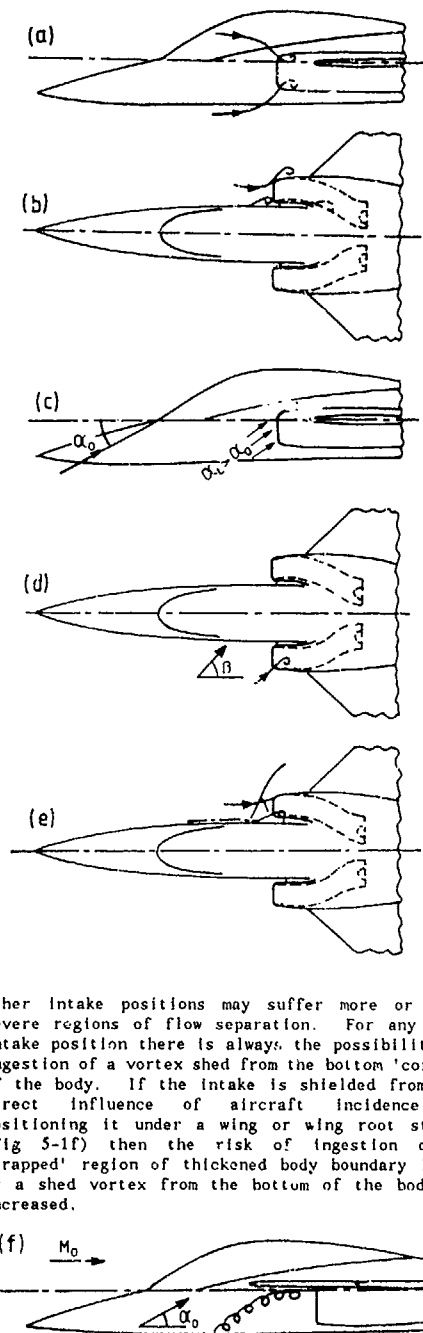
### 2.5.1 INTRODUCTION

The design of intakes for high performance over the range of conditions experienced by an agile strike-fighter aircraft is not simple. The difficulty in intake design is trying to achieve good efficiency, low drag, and high margins of stability at all operating conditions together with low weight and cost. Compromises in all four characteristics are usually made to maintain acceptable performance levels at various flight Mach numbers, angles of incidence, sideslip and power setting. The limits of speed and attitude can be highly variable depending on requirements which become increasingly severe with the passage of time, and, in particular, whether or not post stall manoeuvring is regarded as being necessary. Typically, a Mach number range from zero to 2.0 or 3.0, a range of incidence (without post stall manoeuvring capability) from  $-10^\circ$  to  $+40^\circ$ , a sideslip variation of  $\pm 10^\circ$  to  $20^\circ$  and a range of engine airflows from maximum to flight idling may be required. Under these conditions, separated flow and complex shock and boundary layer interactions at or downstream of the intake entry plane will be present over an appreciable part of the flight envelope.

The major features of flow patterns around and inside an air intake installed on the side of a body are shown in Figs 5-1a-h. At zero and small incidence, internal lip separation can occur at high engine airflows and low forward speed (Fig 5-1a). At high forward speed with an ingested streamtube size smaller than the intake at all engine flows, separation can occur externally over the cowl and in the pre-entry boundary layer on the approach surface to the intake (Fig 5-1b). Separation may occur internally also, particularly at high intake throat Mach number, if the duct shape bends and/or diffuses too rapidly. At high incidence separation occurs at the lower lip internally. Upwash around the body will often lower the threshold of incidence at which this will occur (Fig 5-1c).

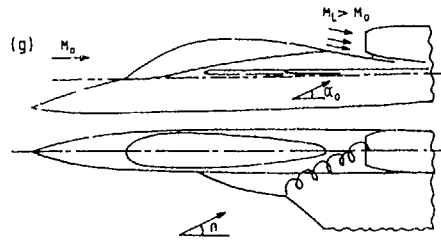
A similar situation occurs at yaw as depicted in the port intake of Fig 5-1d. At supersonic speeds the well known lambda shock formation (Fig 5-1e,

starboard intake) occurs as the intake normal shock intersects the body boundary layer and the resulting separated flow may be ingested into the intake.



Other intake positions may suffer more or less severe regions of flow separation. For any side intake position there is always the possibility of ingestion of a vortex shed from the bottom 'corner' of the body. If the intake is shielded from the direct influence of aircraft incidence by positioning it under a wing or wing root strake (Fig 5-1f) then the risk of ingestion of a 'trapped' region of thickened body boundary layer or a shed vortex from the bottom of the body is increased.

A dorsal position for the intake behind the cockpit canopy may have the advantage of lower aircraft radar signature (from ground based radar) and reduced hot gas ingestion for a VSTOL aircraft. However, it has the disadvantage of possible ingestion of the canopy wake or a vortex from the wing root or strake at sideslip and at supersonic speeds local Mach number in front of the intake will be in excess of the free stream value (Fig 5-1g).



The underbody position has undoubted advantages at incidence at both subsonic and supersonic speeds (Fig 5-1h). The onset of lip separation will be considerably delayed at subsonic speeds if the intake is well shielded by the body and at supersonic speeds the reduced local Mach number will increase pressure recovery as incidence is increased.

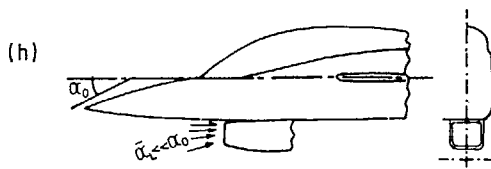


FIG 5.1(a)-(h) FLOW PATTERNS FOR BODY MOUNTED INTAKES

To understand and predict the performance of an intake installed on an agile tactical fighter, it is necessary to build up the performance from simpler component parts. In the next section, first the characteristics of isolated pitot intakes and then those with a compression surface are examined. For isolated intakes, the build up is illustrated from the duct alone, the duct plus the intake at zero incidence and finally, the combination at incidence. This is then followed in section 5.3 by illustrations of how the characteristics of an isolated intake and duct are altered by their integration with the flow fields around a body or body and wing combination.

## 2.5.2 ISOLATED INTAKES

### 2.5.2.1 Internal flow

#### (a) Flow in the subsonic diffusers

Fig 5-2 illustrates the basic duct loss due to skin friction on duct walls as measured in a duct with a bellmouth intake that is sucked to give a range of throat Mach number. The small duct total pressure loss of Fig 5-2 increases as (a) duct length is increased, (b) the duct becomes curved and changes cross sectional shape.

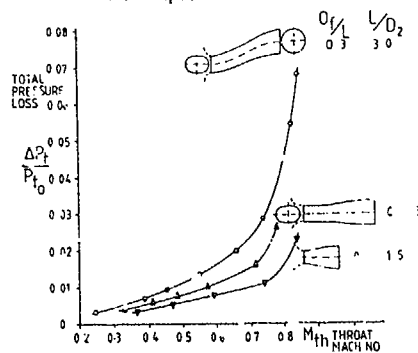
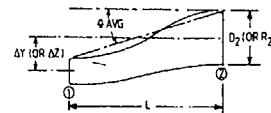


FIG 5.2 BASIC DUCT LOSS

Fox & Kline (Ref 5-1) have defined boundaries of flow states in two dimensional ducts. The lowest boundary of 'first stall' defines an area in which the flow is always attached except perhaps for small separated flow areas near to the final area  $A_2$ . The next boundary of 'appreciable stall' defines an area in which the flow experiences transitory separation and the flow is no longer steady at the engine face. Tindell in Ref 5-2 uses an average wall slope and diffuser area ratio  $A_2/A_1$  to relate more general diffuser shapes to Fox & Kline's boundaries (Fig 5-3). Tindell also uses the Himat and Grumman configurations as a basis for the calculation (by a finite difference and by a panel method) of the onset of duct separation as the basic geometry of these ducts is systematically altered to vary area ratio and average slope of the inboard wall.



	$\frac{A_2}{A_1}$	$\frac{L}{D_2 \text{ OR } R_2}$	$\phi \text{ AVG}$	$\frac{A_2}{A_1}$
A&D	1.35	4.07	19.8°	1.13
HIMAT	0.45	3.18	11.5°	1.50
GRUMMAN	1.05	2.20	30.0°	1.89

\* USE  $R_2$  FOR A&D

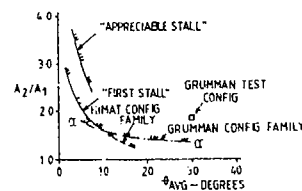
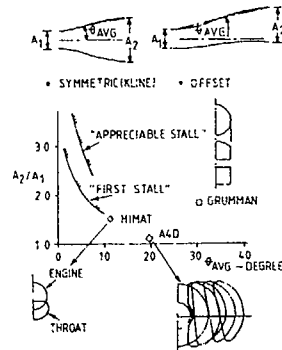


FIG 5.3

COMPARISON OF THEORETICALLY DERIVED FAMILIES OF VERGE-OF-SEPARATION CHARACTERISTICS WITH TRANSFORMED CORRELATION OF KLINE

With the advent of more advanced fighter designs, tighter integration of the engine into the airframe sometimes requires highly offset diffusers (Fig 5-4). New methods of avoiding or controlling boundary layer separation are needed to achieve adequate performance. One of the most fundamental approaches is to provide a favourable area distribution and centreline offset shape. Ref 5-2 shows a study of these parameters. Three centreline shapes were chosen consisting of: 1) modest turning, 2) rapid turning at the exit, and 3) rapid turning at the entrance (Fig 5-5). These centreline shapes were analysed in conjunction with

three area distributions: 1) modest diffusion, 2) high diffusion at the exit, and 3) high diffusion at the entrance. The 3 x 3 matrix was analysed using flow computation methods; results are shown in Fig 5-6. Obviously, slow turning with high diffusion at the entrance is more favourable in terms of low boundary layer blockage and high total pressure recovery.

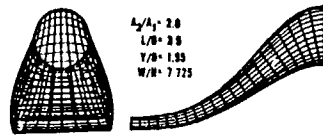


FIG 5.4 ADVANCED COMPACT DIFFUSER

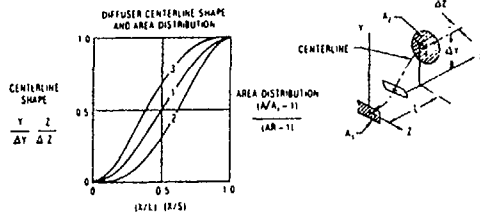


FIG 5.5 DIFFUSER CENTRELINE/ AREA DISTRIBUTION

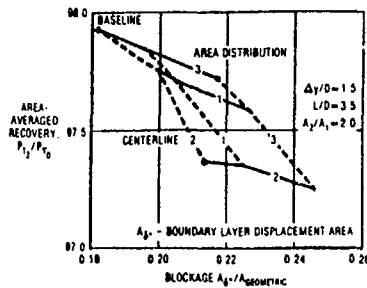


FIG 5.6 EFFECT OF CENTRELINE/ AREA DISTRIBUTION ON DIFFUSER RECOVERY

The S duct flow may include some areas of separated flow followed by reattachment and certainly by the movement of the boundary layer from the outside wall of the first bend towards the inside and the generation of some swirl at the engine face. If the rate of diffusion combined with the sharpness of the bends becomes too high, massive separation will occur downstream of the first bend with consequent unacceptably high total pressure loss and flow distortion at the engine face. The series of ducts shown in Fig 5-7 have constant length, a constant radius final bend, and a common area distribution. As the first bend is usually the primary source of engine face total pressure loss and distortion, the series of ducts successively decreases the extent of the first bend by decreasing its radius and canting the entry plane with the consequent reductions in total pressure loss that are shown.

For highly offset diffusers with separation in the turns, Gerlach area shaping (Fig 5-8, Ref 5-3) has been shown to minimise the extent of the separation. In turning ducts, a pressure gradient normally exists between the inner and outer walls due to centrifugal forces. High pressures at the outer walls often are the cause of large separated regions. When the duct cross-section is shaped such that the velocity is increased at the outer wall and decreased at the inner wall, the pressure

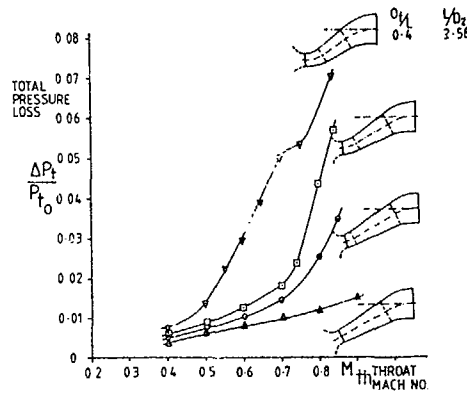


FIG 5.7 BASIC DUCT LOSS FOR S BEND DUCT DUE TO CHANGES IN FIRST BEND SHAPE

gradient between the walls can be reduced. Thus, the extent of separation can also be reduced without changing the average flow velocity.

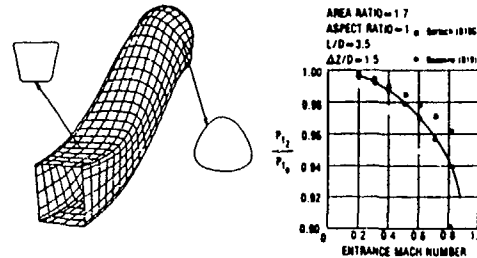


FIG 5.8 GERLACH AREA SHAPING

Small airfoil shaped vortex generators in the diffuser upstream of a known separation point are still one of the better ways to minimise separation as shown in Fig 5-9. The diffuser separation characteristics must be known a priori, however, because the vortex generators are most effective when placed just ahead of the separated regions. Therefore, adequate diffuser analysis methods must be available to determine the location of separated regions before the vortex generators can be installed.

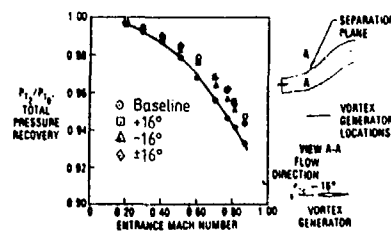
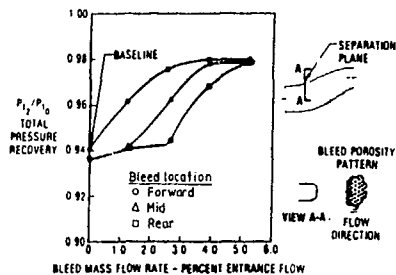


FIG 5.9 VORTEX GENERATOR DIFFUSER PERFORMANCE ENHANCEMENT

Active boundary layer control in the form of bleeding and blowing is often more effective than passive control. However, the cost may be higher in intake bleed drag or increased compressor workload. The amount and distribution of bleed in the diffuser is critical. Too little bleed flow does not control the separation while too much is

not economical. The performance enhancement is seen to be most beneficial in Ref 5-3 when bleed is located upstream of the separation (Fig 5-10).



5.10 BOUNDARY LAYER BLEED

Computational methods are now coming into routine use which can calculate the flow through S ducts. Fig 5-11 shows a comparison between engine face total pressure contours as calculated by a NASA (Lewis) parabolised Navier Stokes program and measurements at high throat Mach number for an S bend duct with constant circular sections (Ref 5-4). Regions of separated flow occur upstream of the engine face. Nevertheless, the general pattern of total pressure loss at the engine face is reasonably well predicted.

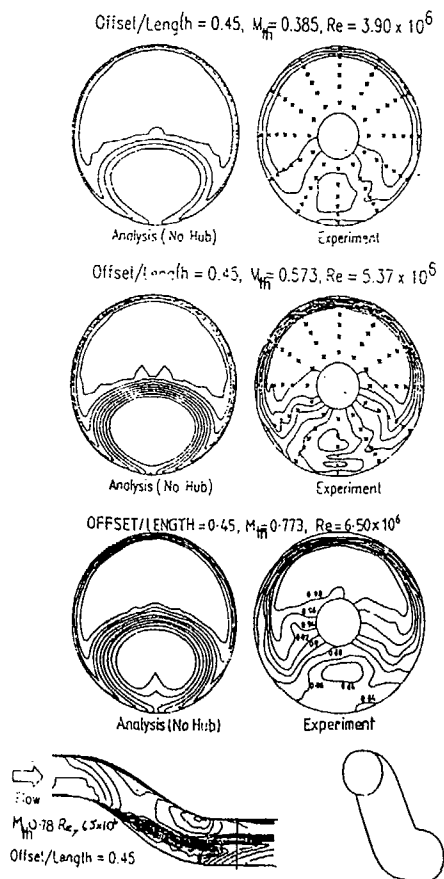


FIG 5.11 COMPARISON OF CALCULATED (NASA LEWIS) & MEASURED (RAE 2129 S DUCT) ENGINE FACE RECOVERY CONTOURS FOR CIRCULAR SECTION S DUCT

#### (b) Combination of intake and subsonic diffusers

The next element to consider is the effect of forward speed and replacement of the bellmouth by a representative intake lip. The magnitude of total pressure loss (other than skin friction) over the full forward speed range from zero to transonic is determined by the occurrence and resulting size of the separation at the lip and the magnitude of throat Mach number. In general at zero and low forward speed (except at very low throat Mach numbers) the ingested stream tube will be larger than the intake capture area ( $A_0/A_c > 1.0$ ) and separation will occur on the inside of the lip if the lip is sharp (Fig 5-1a). The magnitude of the loss due to mixing following separation rises rapidly with increase in throat Mach number. As forward speed increases, the streamtube rapidly decreases in size for a given throat Mach number and when it becomes less than the capture area, ( $A_0/A_c < 1.0$ ), lip separation has disappeared and losses rapidly return to the skin friction level of the basic duct loss. In Fig 5-12 total pressure loss is shown plotted as a function of  $M_{th}$  and of inverse capture ratio  $A_c/A_0$  rather than capture ratio so that the important static case of  $A_0/A_c = \infty$  ( $A_c/A_0 = 0$ ) can be included.

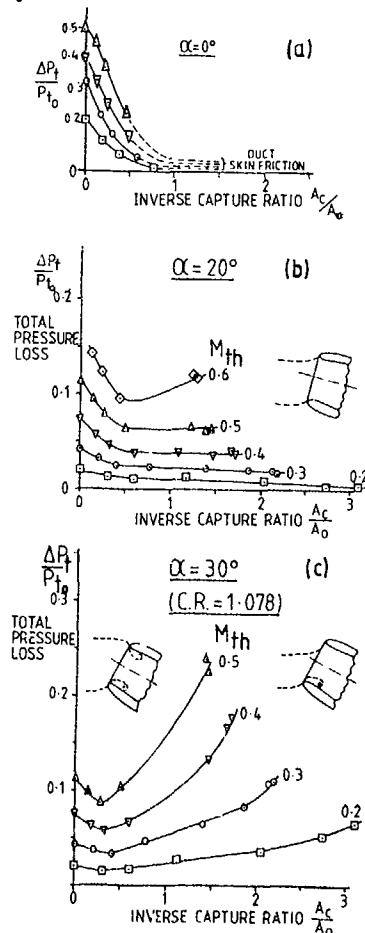


FIG 5.12 STRAIGHT DUCTS: VARIATION OF LOSS WITH THROAT MACH NO, INVERSE CAPTURE RATIO & INCIDENCE

At incidence, lip separation can occur at all values of  $A_c/A_0$  and not just at low values of  $A_c/A_0$  as at zero incidence. Fig 5-12 shows a progressive change in loss pattern as incidence increases from  $0^\circ$  to  $20^\circ$  and  $30^\circ$ . At  $20^\circ$  the pattern of losses is similar to that at zero incidence but the thickened boundary layer downstream of the windward lip results in higher losses that are still however invariant with  $A_c/A_0$  at  $A_c/A_0 > 0.7$ . For this particular lip shape at the highest value of  $M_{th}$  the effect of a small area of lip separation is just evident as the losses no longer remain constant at  $A_c/A_0 > 0.7$ . At an incidence of  $30^\circ$  lip (Fig 5-12c) separation occurs at all values of  $M_{th}$  and this pattern of increasing loss is typical at all values of  $A_c/A_0$  above about 0.3.

There are two geometric parameters that can markedly affect the magnitude of total pressure loss due to lip separation. The first is lip contraction ratio CR ( $= A_c/A_{th}$ ) and Fig 5-13a illustrates the effect of changing CR from 1.078 to 1.25 at  $20^\circ$  incidence and low forward speed conditions. In this case, the differences in performance between the contraction ratios are principally the result of whether or not separation has occurred. In the second illustration (Fig 5-13b) the streamtube size is smaller than the capture area and separation will have occurred for all contraction ratios; the differences in loss are due to the decreasing size of the separation region as contraction ratio decreases.

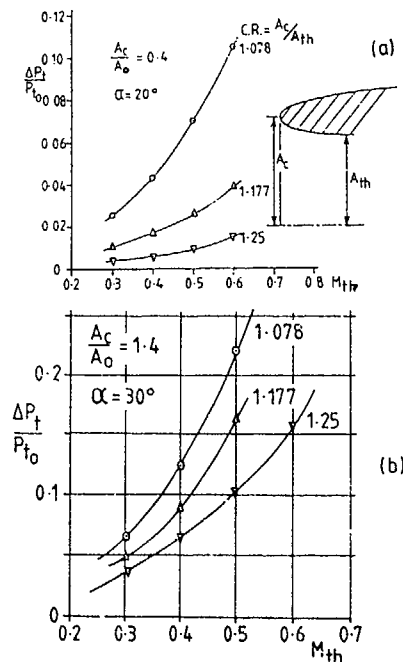


FIG 5.13  
EFFECT OF LIP CONTRACTION RATIO ON  
TOTAL PRESSURE LOSS AT SUBSONIC SPEEDS

The second, which has an even larger effect on loss due to lip separation, is the effect of intake scarring or lip stagger. The upper lip turns the flow from the free stream incidence so that the lower lip is shielded and if the stagger angle is high enough, lower lip separation is delayed probably until incidences of  $50^\circ$  -  $60^\circ$  are reached. Fig 5-14 shows the variation of loss with inverse capture ratio and throat Mach number for a  $50^\circ$  stagger angle at  $30^\circ$  incidence. Losses fall continuously with increase in  $A_c/A_0$  in contrast to

the loss variation of the unstaggered intake (Fig 5-12c).

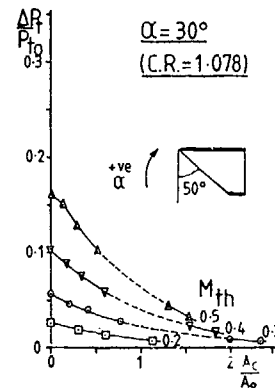


FIG 5.14  
VARIATION OF TOTAL PRESSURE LOSS WITH  
INVERSE CAPTURE RATIO & THROAT MACH NO.  
FOR INTAKE WITH  $50^\circ$  LIP STAGGER

At low forward speeds with  $A_c/A_0 < 1.0$  for a staggered intake, more flow is sucked over the lower lip than the upper one so the unstaggered intake with its symmetrical separation region suffers less loss as shown in the comparison of Fig 5-15. However, as forward speed increases from about  $M_0$  0.1 to 0.2-0.3 (inverse capture ratios of 0.3-0.6 approximately depending on throat Mach number), a cross-over point occurs and at higher increase capture ratios the favourable effect of lip stagger increases rapidly.

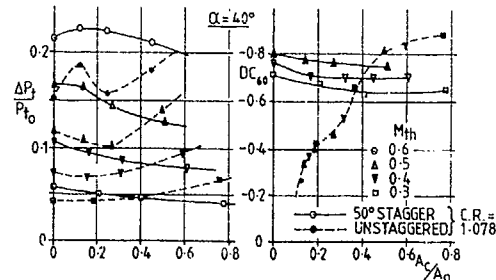


FIG 5.15 EFFECT OF LIP STAGGER AT LOW  
FORWARD SPEEDS

Thus, in practice, the staggered intake would require slightly larger or more efficient auxiliary intakes to restore take off and low forward speed performance to the level of the performance of the unstaggered intake.

The influence of other geometry variables that have smaller effects on performance and the effect of active geometric variation that can result in large changes in performance are dealt with in section 5.4.

At supersonic speeds, as incidence increases from zero, the entry plane of a pitot intake increasingly inclines away from the vertical but the intake normal shock remains approximately normal to the free stream direction. As flow ratio is reduced from unity, the shock becomes detached from the leeward lip and moves upstream across the inclined capture plane. At the windward lip the flow remains unaffected until, with increasing spillage, the normal shock finally becomes completely detached from the entry plane. When the shock is in this position (low values of  $M_{th}$ ) the variation of total pressure loss is then a function

of capture ratio and throat Mach number as at zero incidence. When however the normal shock is impinging on the internal windward surface, the increase in loss is at a higher rate than at subsonic speeds. In these circumstances, the total pressure loss is now not only a function of capture area ratio and throat Mach number but also free stream Mach number because this determines the strength of the adverse shock and boundary layer interaction on the inside of the windward lip. Thus, total pressure loss and engine face distortion is correlated over the full Mach number range from 0 to 2.0 by the use of the parameters  $M_{th}$  and  $M_0/M_{th}$  as shown in Fig 5-16 rather than the parameters  $M_{th}$  and  $A_c/A_0$ .

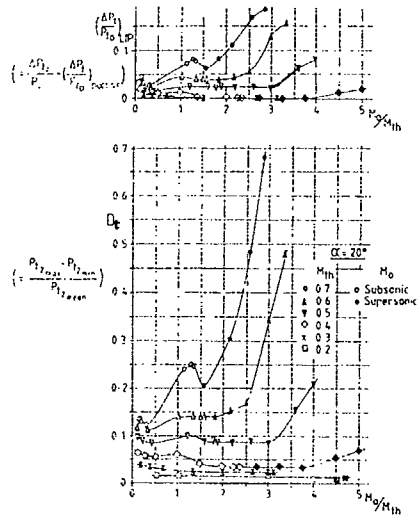


FIG 5.16 VARIATION OF LIP LOSS & ENGINE FACE DISTORTION FOR AXISYMMETRIC PITOT INTAKE AT  $\alpha = 20^\circ$  FOR A MACH NUMBER RANGE FROM 0 TO 2.0 (REF 5.5)

#### 2.5.2.2 External flow

The basic definitions of components of intake drag have been outlined in Section II - Definition of intake performance parameters and description of intake flows - for both pitot and compression surface intakes. Evaluation of forces on pitot intake cowls, from full flow down to the flow at which separation from the cowl lip is initiated, (Fig 5-1b), is particularly amenable to calculation by full potential flow or by Euler methods. Full potential flow methods are very adequate to calculate drag (or thrust) due to supercritical flow development over the external surface of the cowl up to local Mach numbers of 1.3 - 1.4 (despite being isentropic in concept) at subsonic free stream Mach numbers and Euler (non isentropic) methods are equally valid at both subsonic and supersonic free stream speeds. Fig 5-17 shows comparisons between forces measured and calculated on axisymmetric cowls by these two methods over the Mach number range 0.4 to 1.8. The departure of measured and calculated curves clearly indicates the onset of cowl leading edge separation which is confirmed by examination of cowl pressure distributions.

Pre-entry drag can also be evaluated by full potential flow or Euler methods and agrees well with measured values (Fig 5-18). If the intake lip is sharp then the classic one dimensional momentum evaluation of pre-entry drag (also shown on Fig 5-18) is sufficiently accurate for most purposes.

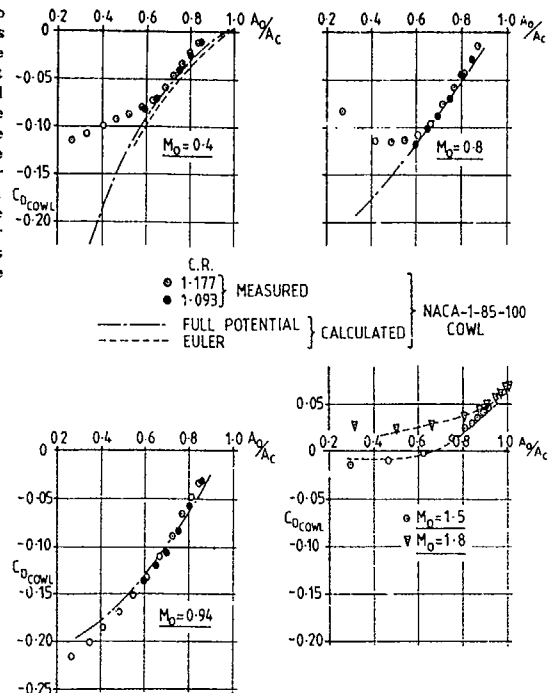


FIG 5.17 COMPARISON OF MEASURED & CALCULATED AXISYMMETRIC COWL PRESSURE FORCE AT SUB & SUPERSONIC SPEEDS (REF 5.6)

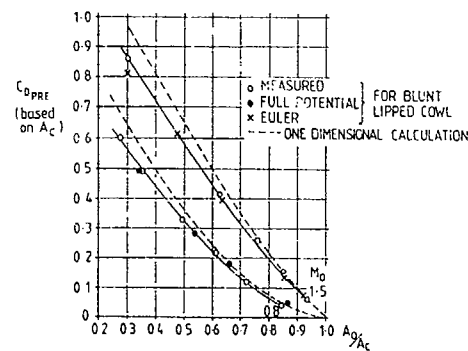


FIG 5.18 COMPARISON OF MEASURED & CALCULATED PRE-ENTRY DRAG FOR AXISYMMETRIC PITOT INTAKES AT SUBSONIC & SUPERSONIC SPEEDS (REF 5.6)

Cowl wave drag at supersonic speeds can be calculated using the Euler equations or by the method of characteristics. A useful digest of axisymmetric cowl wave drag based on characteristics calculations and measurements is shown in Fig 5-19.

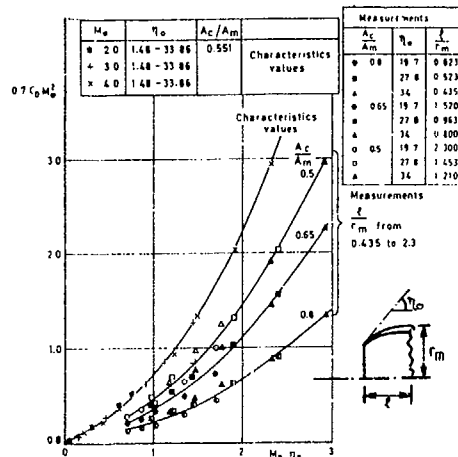


FIG 5.19 DRAG OF AXISYMMETRIC COWLS (REF 57)

### 2.3 Intakes with Compression Surfaces at Subsonic & Supersonic Speeds

The design and performance of intakes for long range supersonic cruise aircraft, whose compression surfaces only operate over a small range of incidence and sideslip, is considered in Section IV of this review. This focusses on both external and combined compression intakes with complex variable geometry and multi-bleed systems. However, for tactical fighter aircraft, the emphasis is on simpler designs having only one or two boundary layer bleeds, external compression only and the variation of probably only one hinged or translating surface. Greater emphasis is placed on compromising the supersonic design to obtain good performance over the full Mach number range from zero upwards.

One of the more fundamental problems in supersonic intake design is matching the intake and engine flow rates at off-design conditions. Aside from the engine demand, the intake may have to provide air for an environmental control system (ECS), bypass system, bleed systems, etc. Fig 5-20 shows a typical flow rate breakdown as a function of Mach number. Notice that the most spillage occurs at transonic flight speeds. This transonic flow mismatch is one of the primary factors which complicate supersonic intake design.

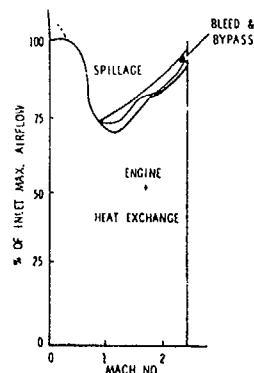


FIG. 5.20 INLET/ENGINE AIRFLOW MATCHING

The range of manoeuvre, together with the extreme range of hot and cold day operation required by combat aircraft, often leads to the need for matching inlet and engine airflows other than solely by variation of the geometry of the compression surface. Thus, aft spill from the subsonic diffuser, either direct to the free stream or by bypassing air around the engine to a base area or ejector nozzle, is required and adds further complication of operation and control of moving surfaces (Fig 5-21).

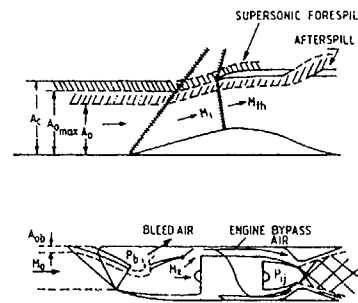


FIG. 5.21 AFT SPILL & ENGINE BYPASS

#### 2.5.2.3.1 At subsonic speeds

One of the purposes of variable compression surface geometry is to provide the enlarged throat area required at subsonic speeds to pass the engine flow without throat choking. Ideally, this entails the complete collapse of the wedge or axisymmetric centrebody. In practice, this is most conveniently approximated when employing a rectangular intake by reducing the second wedge surface to the free stream direction or slightly below this if the actuating mechanism beneath this surface will allow it (Fig 5-22). Although the data shown in 5.2.1 is strictly for pitot intakes, the flow states discussed there will in general apply to intakes with 'collapsed' compression surfaces. The inward camber and sharper lips of a compression surface intake will however increase losses and engine face flow distortion at zero and low forward speeds and there will often be a need for large auxiliary intakes to obtain the required engine flow at high intake efficiency for take off and low speed operation (Fig 5-23).

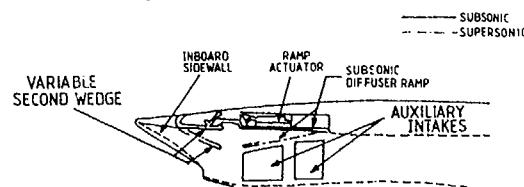


FIG. 5.22 TORNADO INTAKE RAMPS IN SUBSONIC & SUPERNONIC SPEED POSITIONS

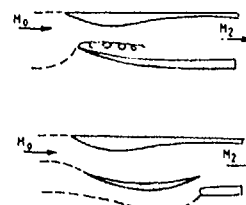


FIG 5.23 AUXILIARY INLET OPERATION



Numbers of auxiliary door arrangements for the BAe Tornado intake are shown in Fig 5-24 without intrusive doors in Configurations A & D and with internally intrusive doors in the other configurations. Their performance under static conditions is summarised in the bar charts and engine face distributions of Fig 5-24.

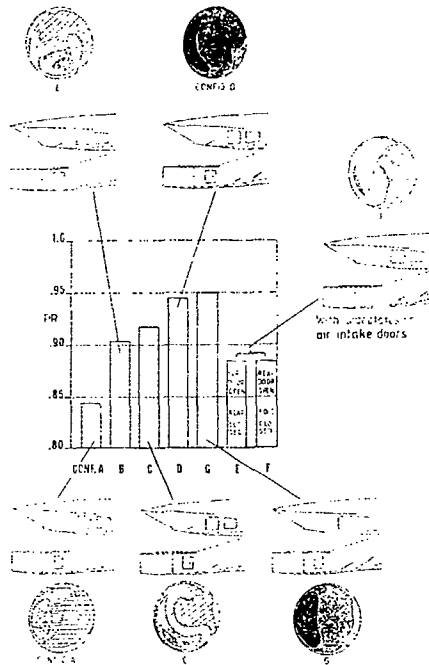


FIG 5.24 EFFECT OF VARIOUS AUXILIARY INTAKE GEOMETRIES ON PERFORMANCE OF A COMPRESSION SURFACE INTAKE AT STATIC CONDITIONS

The form of the rectangular intake, with a collapsed second ramp and endwalls to the compression surface that are swept from the front ramp tip to the cowl lip, is then very akin to the staggered pitot intakes discussed in Section 5.2.1. Thus, if the intake lip is not sharp, performance of the wedge compression surface supersonic intake, (when suitably orientated with the first wedge leading edge horizontal) at high incidence at subsonic speeds, should be adequate.

No such happy coincidence occurs when using axisymmetric centrebody intakes. These pose larger problems for obtaining adequate throat area by centrebody translation. Indeed, on the F111 aircraft (Fig 5-25), the second cone angle consists

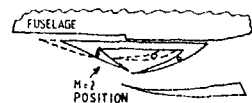


FIG 5.25 1/4 AXISYMMETRIC (F111) INTAKE WITH TRANSLATING & COLLAPSING CENTREBODY

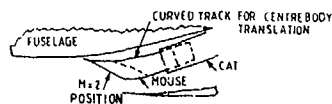


FIG 5.26 1/2 AXISYMMETRIC (MIRAGE) INTAKE WITH TRANSLATING CENTREBODY ON CURVED TRACK

of interleaving elements that allow the centrebody to collapse (it also translates) to obtain adequate throat area. This would however be very difficult if not impossible if the intake was an isolated full axisymmetric nacelle. Another solution to this problem, only possible with the installed half axisymmetric centrebody intake, is to translate the half conical centrebody on a circular track to obtain a larger throat area, as exemplified by the well known 'mouse' in the intake of the Mirage series of aircraft (Fig 5-26).

### 2.5.2.3.2 At supersonic speeds

As flight Mach number increases, multiple compression surfaces and variable geometry may be employed to improve performance, but the increase in complexity also increases weight and cost. The aircraft designer must look at the effect of intake design on total aircraft performance before selecting an intake type. In some cases, the designer may make a sacrifice in recovery performance in order to get the lower weight and cost of a simpler design.

A family of curves depicting the maximum pressure recovery attainable through a series of oblique or conical shocks and a terminal normal shock is shown in Fig 5-27 and reflects the ideal performance potential of axisymmetric supersonic intakes. Increasing the number of shock waves yields higher pressure recovery values. Thus, an isentropic compression surface generating an infinite number of Mach waves yields the maximum recovery.

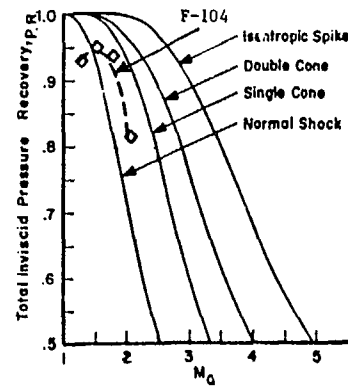


FIG 5.27 CONICAL SHOCK RECOVERY

Fig 5-27 also shows the performance of the Lockheed F-104 intake which has a single fixed geometry cone designed for Mach 1.8. The recovery drops off rapidly at off-design flight conditions.

### FIGHTER AIRCRAFT INLET TOTAL PRESSURE RECOVERY

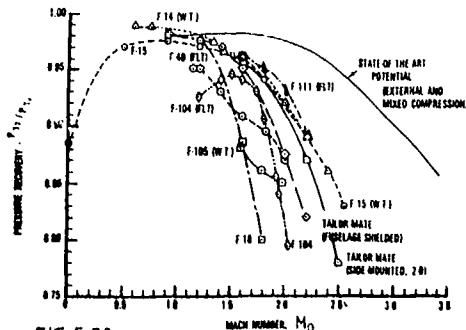


FIG 5.28 VARIABLE GEOMETRY INLET DEVELOPMENT (REF 5.8)

An interesting trend in US variable geometry development is illustrated in Fig 5-28. Attempts at improving performance over the fixed geometry F-104 were made in the F-105 and F-4. Acceptable performance was obtained over a wider range of Mach number, but the full benefit of variable ramps was not realised until the advent of the F-111, F-14 and F-15 aircraft.

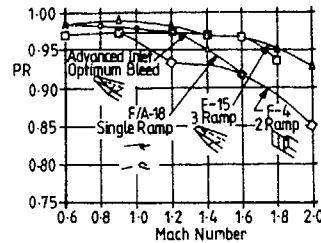


FIG 5.29 COMPARISON OF ADVANCED 2-D INLET PERFORMANCE WITH CURRENT INLETS, MATCHED AIRFLOW  $\alpha = 0^\circ$ ,  $\beta = 0^\circ$

Some of the recent progression in intake design efficiencies are illustrated in Fig 5-29. Although these are for installed intakes, at  $\alpha = \beta = 0$ , the results should be very close to that of isolated intakes.

A successful bleed design is one that gives large increases in pressure recovery for relatively small bleed flows. When this is achieved, pressure recovery values that differ from the theoretical shock recovery by only the duct skin friction loss are obtained (Fig 5-30) for bleed flows in the region 4-6%.

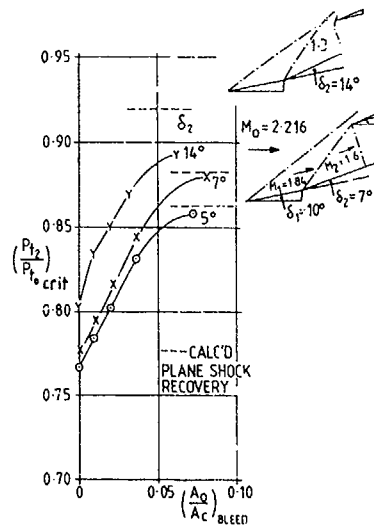


FIG 5.30 EFFECT OF VARIATION OF BLEED FLOW ON PERFORMANCE OF A DOUBLE RAMP SUPERSONIC INTAKE

The drawbacks inherent in using large amounts of external compression at supersonic speeds are well known. It results in high external drag due to large flow turning from the free stream direction and the development of long boundary layers on the compression surface that are subject to high adverse pressure gradients which cause them to thicken and/or separate, particularly at multi-compression surface intersection points (Fig 5-31).

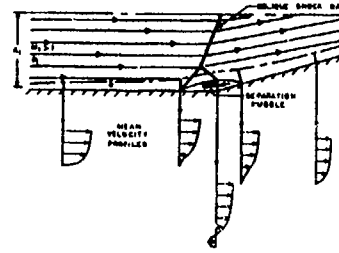


FIG 5.31 OBLIQUE SHOCK-BOUNDARY LAYER INTERACTION

Cowl drag associated with a given amount of external compression can be determined at an early stage in the design process from the requirement of oblique shock attachment on the inside surface of the cowl lip. The consequences of selecting an internal cowl angle (and hence external cowl angle and thus external drag) to just give an attached undersurface shock on maximum shock pressure recovery that can possibly be attained (using an idealised isentropic compression surface) is shown in Fig 5-32. Thus, at Mach number 3, a cylindrical undersurface that would be associated with a very low cowl drag is limited to a shock recovery of 0.72, whereas a moderate cowl drag with an undersurface angle of  $12^\circ$  would have an upper limit to shock recovery of 0.83.

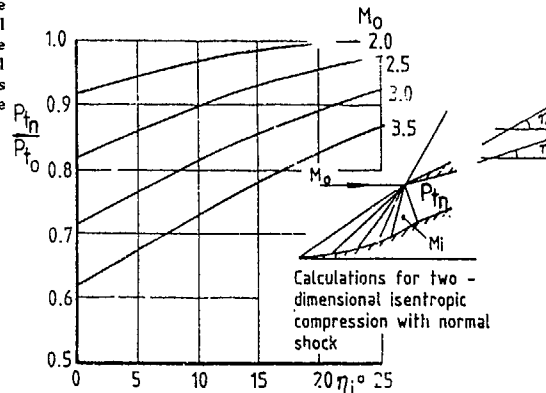


FIG 5.32 MAXIMUM SHOCK PRESSURE RECOVERY FOR EXTERNAL COMPRESSION WITH A GIVEN COWL EXTERNAL ANGLE (REF.5.7)

The increase in surface wetted area in front of the capture plane can be linked to the increasing number of supersonic ramps or cones and hence increasing shock pressure recovery (Fig 5-33).

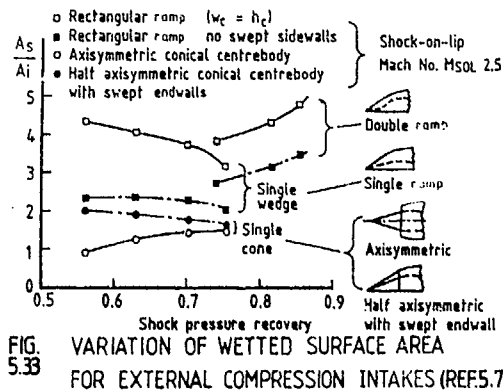


FIG 5.33 VARIATION OF WETTED SURFACE AREA FOR EXTERNAL COMPRESSION INTAKES (REF.5.7)

This diagram also emphasises the large differences in approach surface area between square and axisymmetric intakes and the increase due to enclosing the shock system of the square intake between swept endwalls. It is no surprise that rectangular intakes invariably feature boundary layer control on the compression surfaces whereas single or even double cone centrebodies often do not.

The realisation that cowl internal angles do not need to be at the same inclination as the final ramp of the compression surface, together with close integration of the design of the bleed on the compression surface just downstream of the entry plane, with the shocks from the low angle cowl under surface, has led to development of optimum low drag external compression intakes. The resulting wide slot bleed unchoked at its entry also has the advantage that matching initially occurs by spillage through the bleed (Fig 5-34) and does not involve conventional subsonic foreshallage over the cowl (Fig 5-35) with its attendant high drag and possible shock instability.

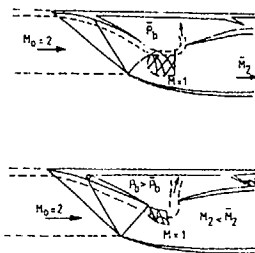


FIG 5-34 WIDE THROAT BLEED OPERATION

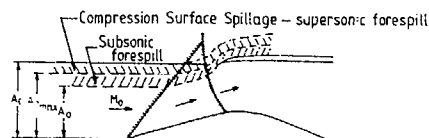


FIG 5-35 SUPERSONIC &amp; SUBSONIC FORESPILL

At incidence, if the ramp compression surface is horizontal, then the variation of shock loss can be calculated until the ramp shock(s) become detached. Fig 5-36 shows a comparison between calculated and measured pressure recovery for a two ramp intake with a wide slot throat bleed.

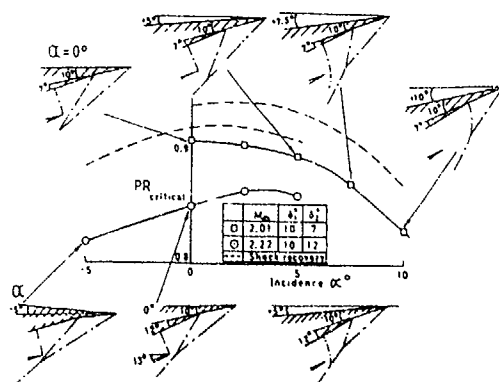


FIG 5-36 EFFECT OF INCIDENCE ON PRESSURE RECOVERY &amp; SHOCK WAVE PATTERNS FOR A HORIZONTAL DOUBLE-RAMP INTAKE (REF 5-7)

Other purely measured values of pressure recovery referenced to pressure recovery at zero incidence for a wider range of conditions are shown in Fig 5-37.

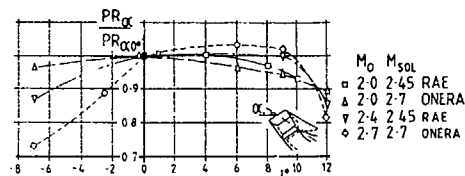


FIG 5-37 VARIATION OF PRESSURE RECOVERY WITH INCIDENCE FOR TWO-RAMP INTAKE

If the intake is yawed, the variation of shock recovery is no longer readily predictable and again Fig 5-38 shows measured variation of pressure recovery.

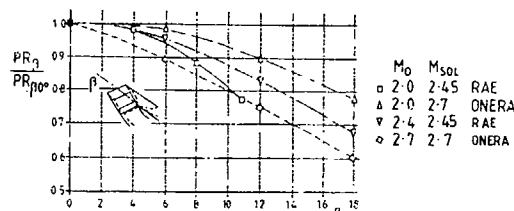


FIG 5-38 VARIATION OF PRESSURE RECOVERY WITH SIDESLIP ANGLE FOR TWO-RAMP INTAKE

In this case, performance is sensitive to changes in endwall shape and quite small changes in configuration can result in relatively large changes in pressure recovery (Fig 5-39).

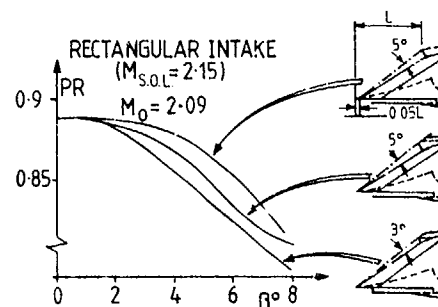


FIG 5-39 EFFECT OF SMALL CHANGES IN ENDWALL SHAPE ON PERFORMANCE OF YAWED RECTANGULAR INTAKE

With axisymmetric external compression intakes, the flow in detail at incidence is complex but the basic pattern of shock angle variation is akin to that of a pitot intake. The conical forebody can be regarded as pivoting about its apex with shock angles changing much less than cone surface angles relative to free stream direction. As incidence increases, the cone shock moves into the windward lip and the leeward lip moves away from it. When this happens an increasing proportion of the flow is compressed through a normal shock only and the result is a sharp fall off in pressure recovery. Thus, the change in pressure recovery with incidence is largely influenced by whether or not the cone shock at zero incidence is on or well outside the cowl lip, as illustrated in Fig 5-40.

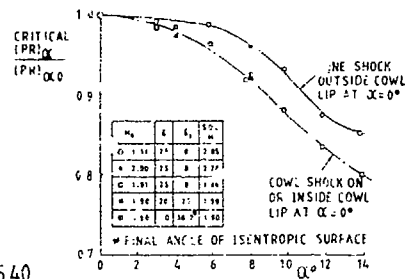


FIG 5.40  
EFFECT OF INCIDENCE ON PRESSURE RECOVERY OF  
AXISYMMETRIC FOREBODY INTAKES (REF 5.7)

A second influence on pressure recovery comes from the tendency for the boundary layer on the centrebody to be swept up to the leeward side. Thus, a long centrebody with a high shock on lip Mach number  $M_{SOL}$  will have a worse performance than one with a low  $M_{SOL}$  (Fig 5.41). This trend in principle is of course in the opposite sense to that of Fig 5.40.

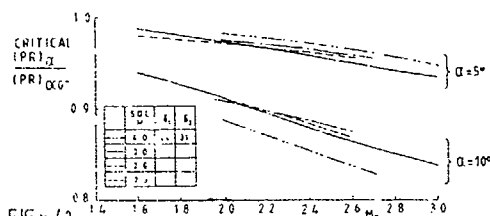


FIG 5.41  
INFLUENCE OF FOREBODY LENGTH ON PRESSURE  
RECOVERY AT INCIDENCE OF DOUBLE-CONE  
INTAKES (REF 5.7)

There is no simple way of predicting maximum flow ratio for axisymmetric intakes at incidence. Fig 5.42 shows some measured values referred to the zero incidence value for single cone, double cone and isentropic centrebody intakes at  $M_0 1.9$ .

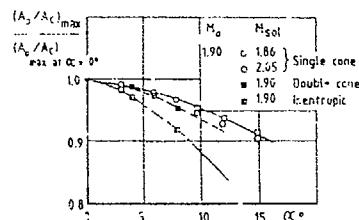


FIG 5.42  
EFFECT OF INCIDENCE ON MAXIMUM FLOW OF  
AXISYMMETRIC FOREBODY INTAKES (REF 5.7)

### 2.5.3 Intake-airframe integration

It was discovered early in jet aircraft design that allowing the forebody boundary layer to be ingested into the intake imposed a serious loss of recovery at the compressor. The nub of the problem, as has been seen (Fig 2-7 Section 2) is the interaction of the boundary layer with the pre-entry pressure rise which is incurred in the process of producing a relative retardation of airspeed from the flight velocity towards that required at inlet to the engine. Broadly speaking, the severity of the problem is greater the higher the flight speed and the presence of shock waves at supersonic speeds adds a special dimension to it. If the boundary

layer separates or comes close to separation, the effects are particularly adverse and generally not restricted to a lowering of mean pressure recovery: other adverse features include total-pressure distortion and flow instability (Section 2).

Removing the boundary layer at some stage from the intake provides an escape from, or easement of, the difficulties. This is done by means of bleeds or diverters. The term 'bleed' denotes a separate duct which leads away the boundary layer. The term 'diverter' implies that the intake stands off from a particular surface, allowing the boundary layer on that surface to escape down the intermediate channel. In either case the boundary layer removed from the intake usually becomes a part of the aircraft system, that is to say it represents an additional item in the aircraft drag but the effect of the increased pressure recovery invariably outweighs the drag penalty.

Common forms of bleed and diverter are illustrated in Fig 5.43. Diverters may be of the step type (a) or channel type (b), (c). A step diverter is a useful form in the wing root of a subsonic aircraft, because the forward extension allows a good wing-root profile to be preserved. Step diverters are not generally recommended for supersonic aircraft, however, because fresh boundary layer initiated on the surface of the diverter may itself produce most of the interaction loss of the original longer boundary layer. Channel diverters are suitable for both subsonic and supersonic application, provided that a reasonably aerodynamic 'prow' shape can be obtained between the intake and the boundary-layer surface. The recommended width for step diverters is about one and a half times the thickness of the boundary layer, when this is undisturbed by the presence of the intake, and for channel diverters about one such boundary layer thickness.

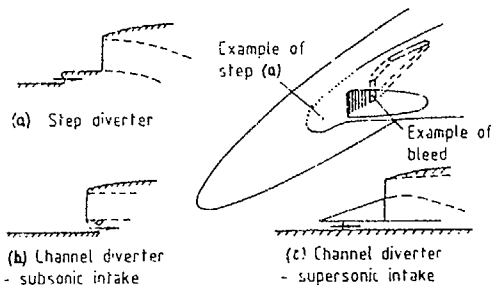


FIG 5.43 EXAMPLES OF STEP & CHANNEL DIVERTERS

Boundary layer bleed systems can become more complex at supersonic speeds as on the F-111 aircraft (Fig 5.44) and need more careful design to ensure their successful operation over all engine flow rates and aircraft attitudes that will be encountered

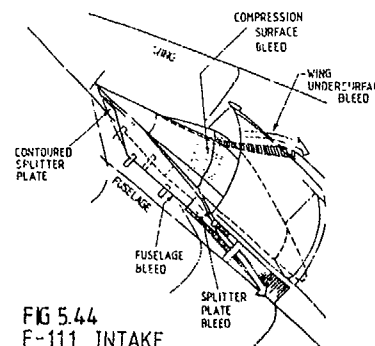


FIG 5.44  
F-111 INTAKE

Tactical aircraft are required to be maneuverable at subsonic, transonic and supersonic conditions without giving up good subsonic cruise efficiency. Consequently, proper integration of the engine intake with the airframe is of paramount interest. The range of incidence and sideslip, although reduced at supersonic speeds from the values outlined in the Introduction, still remains wide compared with those required by the high altitude supersonic cruise vehicle. Within these reduced ranges, at supersonic speeds for the installed intake, not only Mach number and flow direction will vary in the approach flow field to the intake but also total pressure due to the presence of an upstream curved and in some cases detached shock from the body nose.

Design for optimum airframe-inlet integration has the following specific goals:

1. Minimise approach flow angularity with respect to inlet leading edges
2. Deliver uniform, high pressure recovery flow to the inlet entrance at velocities equal to or below free stream conditions
3. Prevent boundary layer ingestion by the inlet
4. Reduce the probability of foreign object or hot gas ingestion to acceptable levels
5. Minimise the potential for flow field interference from weapon carriage/firing, landing gear deployment, fuel tanks, pods, pressure probes etc.

Similarly, the airframe-intake design should minimise any deleterious effect on the design/operation of lifting surfaces, landing gear and avionics and how they integrate with aircraft structures.

Because of the many factors which influence airframe flow fields, it is expedient to discuss a set of coordinated data so that the effect of isolated parameters may be illustrated. To this end, the series of fighter configurations shown in Fig 5-45 (Tailor-Mate Program, Ref 5-10 to 5-14) will be used to isolate some of the primary effects of fuselage shaping inlet location and how the inlet configuration interacts with location in sections 5.3.1-5.3.5.

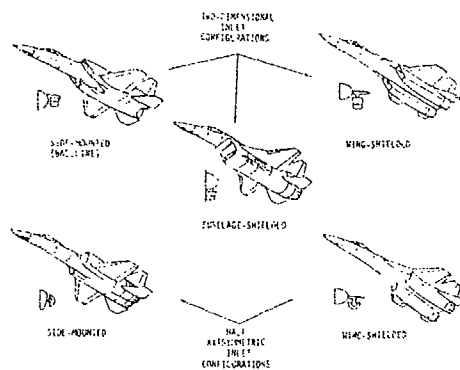


FIG 5-45 TAILOR-MATE AIR FRAME INLET CONFIGURATIONS (REF 5-10-5-14)

### 5.3.3.1 Fuselage flow fields for side mounted intakes

Wind tunnel tests under the Tailor-Mate program were conducted in the Arnold Engineering Development Center (AEDC) Propulsion Wind Tunnel 16 foot test sections.

Fig 5-46 depicts the forebody cross-section shapes investigated for side-mounted intakes and shows the

location of boundary layer and none probes used to define flow fields approaching the intakes.

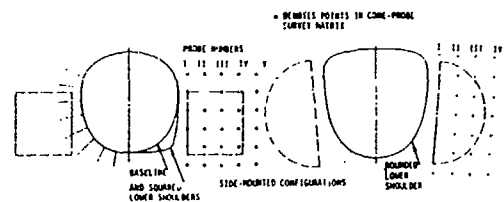


FIG 5-46 FOREBODY FLOW FIELD MODEL INSTRUMENTATION

Flow fields are characterised by vector plots or by lines of constant local angle-of-incidence,  $\alpha_L$ , or local angle-of-sideslip,  $\beta_L$ . The vector plots give an overall impression of flow angularity whereas the  $\alpha_L$  and  $\beta_L$  contours provide more precise definitions. Flow field variations for relatively high manoeuvre conditions at Mach 2.2 are examined to aid understanding of the limits of performance.

Fig 5-47 shows a vector plot depicting combined  $\alpha_L$  and  $\beta_L$  vectors around the BASELINE body shape at  $M_0 = 2.2$ ,  $\alpha_0 = 15^\circ$ . Flow angularity is highest near the body and there is a significant sideslip flow condition in the region of the inlet inboard surface.

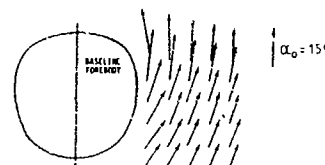


FIG 5-47 BASELINE FOREBODY VECTOR FLOW FIELD;  $M_0 = 2.2$ ,  $\alpha_0 = 15^\circ$ ,  $\beta_0 = 0^\circ$

A more careful examination (Figs 5-48 and 5-49) shows lines of constant  $\alpha_L$  and  $\beta_L$  for the BASELINE shape and the SQUARED shape. There is little difference in  $\alpha_L$  distributions, but the flow in the region of the lower inboard sideplate at sideslip conditions varies measurably between the shapes. The maximum  $\beta_L$  value in the region of the intake inboard sideplate is least for the BASELINE shape ( $\beta_L = 8.6^\circ$ ) and greatest for the SQUARED shape ( $\beta_L = 9.2^\circ$ ).

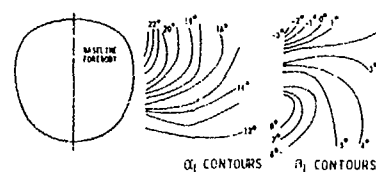


FIG 5-48 BASELINE FOREBODY FLOW FIELD ANGULARITY MAPS;  $M_0 = 2.2$ ,  $\alpha_0 = 15^\circ$ ,  $\beta_0 = 0^\circ$

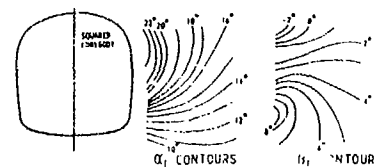


FIG 5-49 SQUARED FOREBODY FLOW FIELD ANGULARITY MAPS;  $M_0 = 2.2$ ,  $\alpha_0 = 15^\circ$ ,  $\beta_0 = 0^\circ$

Figs 5-50 and 5-51 show  $\beta_L$  contours associated with a combination of aircraft pitch and yaw for baseline and square bottom fuselages at  $M_0 = 2.2$ ,  $\alpha_0 = 15^\circ$ ,  $\beta = 4^\circ$ . The leeward (right) side  $\beta_L$  plots for both fuselage shapes at  $\beta_0 = 4^\circ$  are similar in appearance to the  $\beta_0 = 0^\circ$  plots but with approximately  $2^\circ$  to  $4^\circ$   $\beta_L$  added to each measurement point. The flowfield differences may appear to be minor but inlet data will show a significant effect on performance.

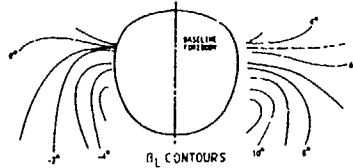


FIG 5.50 BASELINE FOREBODY FLOW FIELD IN SIDESLIP;  $M_0 = 2.2$ ,  $\alpha_0 = 15^\circ$ ,  $\beta_0 = 4^\circ$

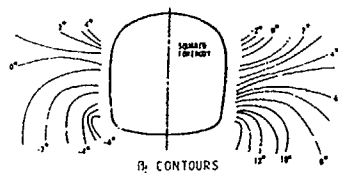


FIG 5.51 SQUARED FOREBODY FLOW FIELD IN SIDESLIP;  $M_0 = 2.2$ ,  $\alpha_0 = 15^\circ$ ,  $\beta_0 = 4^\circ$

#### 2.5.3.2 Performance of a rectangular compression surface intake on the side of a fuselage

The variable geometry rectangular intake shown in Fig 5-52 was tested with both the baseline and squared forebody shapes. It featured a variable first ramp as well as variable second and third ramps for efficient compression at supersonic conditions.

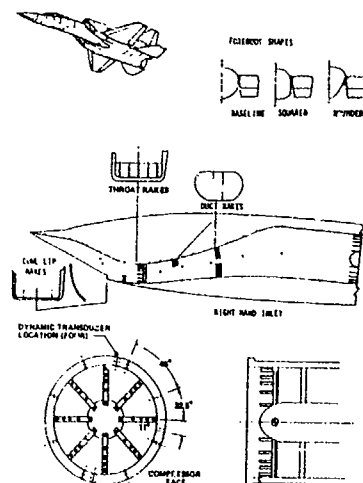


FIG 5.52 SIDE-MOUNTED INLET CONFIGURATION AND INSTRUMENTATION

It had a long subsonic duct ( $L/D = 5.23$ ) with a low diffusion rate. Boundary layer control on the ramps was provided by perforated bleed on the compression ramps and on the side plates. The variable gap offset between the third ramp and aft ramp allowed a combination of flow bypass and boundary layer control at the throat region. Throat bleed flow was measured with flow metering

systems and bleed on the perforated side plates was estimated from plenum and exit static pressure measurements.

Intake instrumentation was provided at the left-hand compressor face to measure total pressure recovery and both steady state and dynamic inlet flow distortion by use of 40 combination steady-state and high response total pressure probes. Additional instrumentation on the opposite (right-hand) side of the double intake system, consisted of total pressure rakes and static pressure measurements through the duct as noted in the figure. In the following discussion, "positive sideslip" is defined as that condition where the inlet under consideration is on the leeward side of the fuselage.

Figure 5-53a,b takes two intake data points for the BASELINE forebody at  $M_0 = 2.2$  ( $\alpha_0 = 0^\circ, 20^\circ$ ) and depicts the progression of flow through the intake in order to shed some light on the variation in levels of performance experienced with increasing  $\alpha_0$ . At  $\alpha_0 = 0^\circ$  total pressures are all high at the inlet cowl lip and intake throat or aft ramp station. Pressures farther down the duct indicate that some low energy flow exists in the upper part of the duct, but this situation shifts rapidly, with the low energy flow showing up only in the lower portion of the compressor face. Since no low energy flow is in evidence in the lower part of the duct at the first three data stations, it must be supposed that the flow defect originated in the region of the aft ramp leading edge (behind the throat slot) and that static pressure gradients in the duct were sufficient to move this region to the lower portion of the compressor face.

At  $\alpha_0 = 20^\circ$ , flow at the inlet lip is relatively uniform, but with a lower total pressure than in the previous case. In the upper thrust region, low pressures are measured, suggesting a greater flow interference of the flow with the aft ramp leading edge. More low energy flow and flow separation in the upper part of the duct are in evidence midway in the duct. In this case, rotation of the low energy flow through the duct to the inboard and lower part of the compressor face appears to be quite evident.

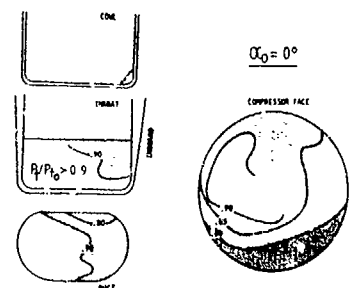


FIG 5.53a BASELINE INLET TOTAL PRESSURE MAPS;  $M_0 = 2.2$ ,  $\alpha_0 = 0^\circ$ ,  $\beta_0 = 0^\circ$

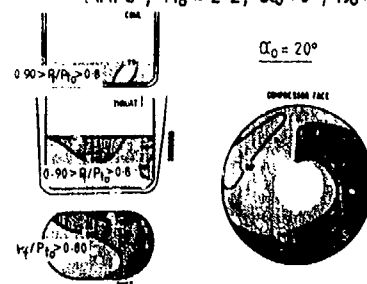


FIG 5.53b BASELINE INLET TOTAL PRESSURE MAPS;  $M_0 = 2.2$ ,  $\alpha_0 = 20^\circ$ ,  $\beta_0 = 0^\circ$

The next Figure (Fig 5-54) shows an example of the effect of sideslip at  $\alpha_0 = 15^\circ$  on progression of flow through a right-hand intake integrated with the baseline forebody. At  $\beta_0 = 0^\circ$ , there is evidence from the lip wakes of inboard sideplate leading edge flow interference. This defect is still in evidence at the inlet throat, and further on down the duct the low energy flow region extends over an extensive portion of the inboard side of the duct. Once again, at the compressor face, the low energy air appears to have emigrated downwards, but flow conditions are relatively uniform. With the intake experiencing  $4^\circ$  leeward sideslip, there is now extensive flow separation on the inboard sideplate at the cow lip. The separation and its effects spread significantly at the throat, and continue to spread in the duct. As before, the region of lowest energy air rotates downward so that, at the compressor face, the very lowest pressures have moved to the bottom and the only remnant of the high pressure flow from the lower throat region now exists in the upper region of the compressor face.

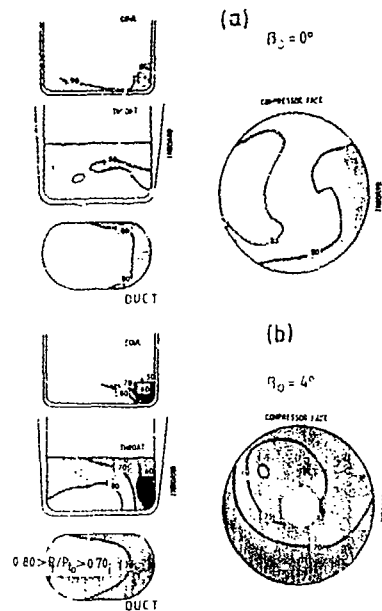


FIG 5.54 INLET TOTAL PRESSURE MAPS WITH BASELINE FUSELAGE  $M_0 = 2.2$ ,  $\alpha_0 = 15^\circ$   
(a)  $\beta_0 = 0^\circ$ , (b)  $\beta_0 = 4^\circ$

Figure 5-55 gives an example of throat flow variations associated with the different forebody influences. Influence of the forebody is seen in all three of the integrated configurations, but is by far the most prominent with the SQUARED forebody, where a substantial region of flow

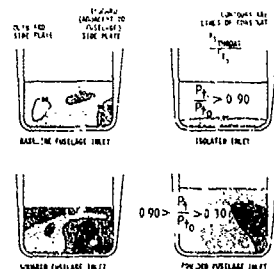


FIG 5.55 SIDE-MOUNTED INLET THROAT PRESSURE CONTOURS,  $M_0 = 2.2$ ,  $\alpha_0 = 15^\circ$ ,  $\beta_0 = 0^\circ$

separation dominates the lower inboard region of the throat. Thus, it is seen that the flow field differences between the BASELINE and SQUARED fuselage shapes do indeed make a difference in intake performance.

### 2.5.3.3 Performance of axisymmetric half-cone intakes on the side of a fuselage

The previous discussion and examples centred on the horizontal ramp intake. The choice of rectangular versus axisymmetric or vertical versus horizontal ramps depends upon the Mach number range and manoeuvrability required. At low angles of incidence, axisymmetric intakes can provide better pressure recovery than rectangular intakes at supersonic Mach numbers because of the smaller fundamental losses associated with conical shocks. Also, axisymmetric intakes tend to be much lighter because of the high load carrying capability of "hoop" tension. However, axisymmetric inlets and vertical ramp intakes exhibit nonsymmetry of the flow at high angles of incidence which result in lower pressure recovery. The manoeuvring horizontal ramp intake is able to deflect the oncoming flow and retain its quasi two-dimensional character. In addition, variable geometry to control shock position, spillage, and recovery is easier to accomplish. Variable geometry in axisymmetric intakes is usually confined to spike translation in single or twin cone configurations.

The Ref 5-14 programme employed half-axisymmetric intakes as well as rectangular intakes, offering a comparison of their relative performance in the side-mounted (and wing-shielded) configurations. Figure 5-56 shows the side-mounted axisymmetric intake with its instrumentation. These intakes were tested with the forebody having the ROUNDED lower shoulder shape (see Fig 5-46) so the flowfield approaching this intake was at least as good as that ahead of the BASELINE rectangular intake.

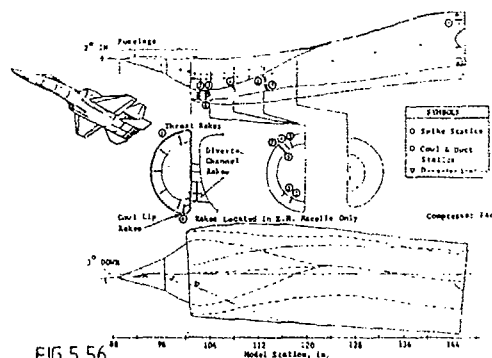


FIG 5.56 SIDE-MOUNTED HALF-AXISYMMETRIC INLET CONFIGURATION & INSTRUMENTATION

Flow progression through the side-mounted half-cone intake is shown in Fig 5-57 at  $\alpha_0 = 10^\circ$ . In this case, a massive flow separation originates in the upper part of the intake throat due to the oversped

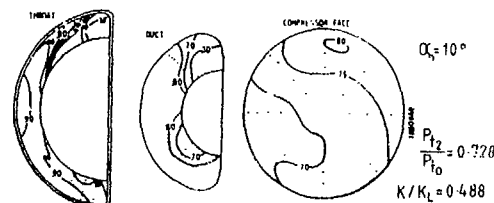


FIG 5.57 SIDE-MOUNTED HALF-AXI-SYMMETRIC INLET TOTAL PRESSURE CONTOURS,  $M_0 = 2.2$ ,  $\beta_0 = 0^\circ$

condition and hence strong normal shock in that region. Further down the duct the flow in this upper region is still separated, but has been joined by a separated flow region in the lower part of the throat, adjacent to the spike. At the compressor face evidence of separated flows is obvious in the low pressure regions and large distortion.

Based on this test data, the side-mounted half-axisymmetric intake would appear to be a poor candidate for highly manoeuvrable fighter aircraft. Yet several current aircraft systems employ this intake effectively, and it can be attractive from structure, system drag and reduced observables points of view. Design modifications to provide optimum compression surface angles, more efficient boundary layer removal and/or better variable geometry control can improve axisymmetric intake performance, possibly without giving up some of the important advantages noted. Care would also have to be taken with this type of an intake to design the diverter/sideplate carefully enough to avoid sideplate leading edge separation.

#### 2.5.3.4 Performance of a pitot intake on the side of a fuselage (Ref 5-15)

Although detailed body flow field data is not available in the following examples, the main influence of the increase in local angle of incidence due primarily to upwash around the body, particularly in the region of the upper shoulder, shows up in the performance of pitot intakes. The local variation of sidewash is probably not important for a pitot intake with blunt lip. Comparison of isolated pitot intake recovery with recovery measured on an installed pitot intake gives a relation between free stream incidence  $\alpha_0$  and local mean incidence  $\alpha_L$  for equal values of recovery and hence a derived upwash angle  $\alpha_L - \alpha_0$  as shown in Fig 5-58a at  $M_0 = 1.6$  can be obtained. This derived upwash angle varies quite rapidly as Mach number increases above 0.9 (Fig 5-58b).

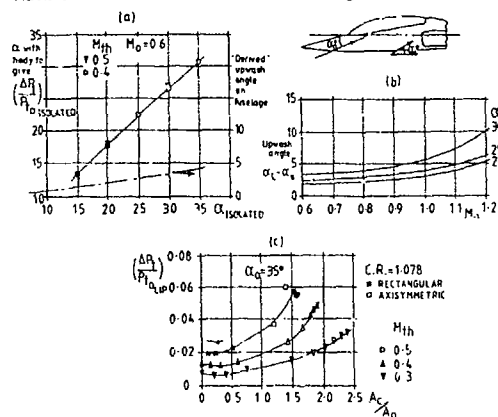


FIG. 5.58 SIDE BODY PITOT INTAKE PERFORMANCE

If corrections are made for upwash angle and for basic duct skin friction loss, then the derived lip loss associated with a long rectangular installed pitot intake at high incidence agrees quite well with that for a short isolated axisymmetric pitot intake with the same lip contraction ratio (Fig 5-58c).

The influence of stagger angle on the performance of a pitot intake is not only beneficial at incidence but also in sideslip. Both at positive and negative  $\beta$  a 50° staggered pitot intake has lower losses and better engine face distribution

than an unstaggered intake (Fig 5-59). There is also a small favourable effect under these conditions of increasing diverter height.

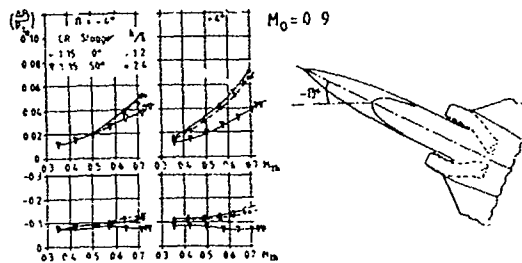


FIG 5.59  
EFFECT OF STAGGER ANGLE & DIVERTER HEIGHT  
ON PERFORMANCE OF A SIDE BODY INTAKE  
UNDER SIDESLIP CONDITIONS

At supersonic speeds (Ref 5-16) there can be a beneficial effect on the pressure recovery of a pitot intake to be derived from allowing the intake normal shocks to intersect with the body boundary layer provided the intake is mounted on a sufficiently high boundary layer diverter. The well known lambda shock formed as a result of the normal shock interaction with the boundary layer can give a theoretical shock recovery equivalent to a 10° ramp compression surface. However, this shock pattern only progressively encompasses the whole of the intake flow as flow ratio is reduced from the maximum value and eventually the theoretical advantage of the two shock pattern is increasingly overtaken (unless the boundary layer diverter is inordinately high) by the adverse effect of body boundary layer ingestion. This is if the flow pattern remains stable which is not always the case (depending on free stream Mach number and amount of flow spillage). The measured gain in recovery relative to normal shock recovery is shown in Fig 5-60 at  $M_0 = 1.4$  and 1.6 as a function of throat Mach number (spillage) compared to the theoretical gain from the two shock recovery. The measured gain is derived by adding a duct and lip loss (obtained at subsonic speeds) to the measured pressure recovery and subtracting the theoretical normal shock recovery. As can be seen at  $M_0 = 1.4$  the two shock recovery appears to influence the whole of the intake flow even at the smallest spillage condition (higher  $M_{th}$ ).

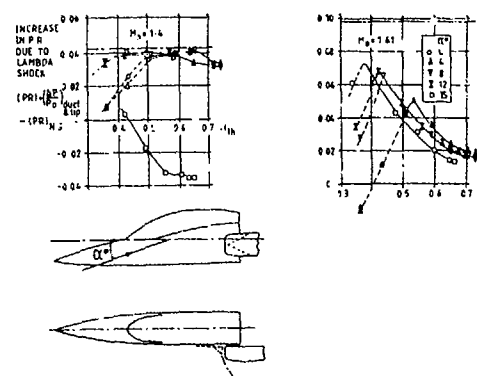


FIG 5.60 INCREASE IN PRESSURE RECOVERY DUE TO  
INTERACTION BETWEEN SIDE INTAKE  
NORMAL SHOCK & FUSELAGE BOUNDARY  
LAYER



At  $M_0 = 1.6$  the smaller shock wave angle of the  $10^\circ$  separated flow 'ramp' results in only a small part of the ingested intake flow being influenced by the two shock pattern at high  $M_{th}$  values but the effect progresses rapidly as spillage increases until some ingestion of the separated body boundary layer commences at values of  $M_{th}$  below 0.4-0.5.

For the staggered pitot intake, the gain progressively changes into a loss as stagger angle increases from  $20^\circ$  to  $50^\circ$ . At  $20^\circ$  stagger angle the majority of the intake and shock boundary layer intersection is upstream of the upper lip and swept endwalls and is therefore still on the body boundary layer. At  $50^\circ$  stagger this interaction is wholly on the surfaces of the intake and hence the lambda shock formation only results in wholly deleterious ingestion of separated flow into the intake which completely overwhelms the small favourable effect of the lambda shock pattern. Fig 5-61a,b show the progressive change in 'gain' due to lambda shock formation as stagger angle changes from  $20^\circ$  (similar to the unstaggered intake values of Fig 5-60) to  $50^\circ$  and Fig 5-61c summarises the change with stagger angle on a basis of losses other than the theoretical normal or two shock loss (which depends on angle of incidence and not on the formation of a lambda shock).

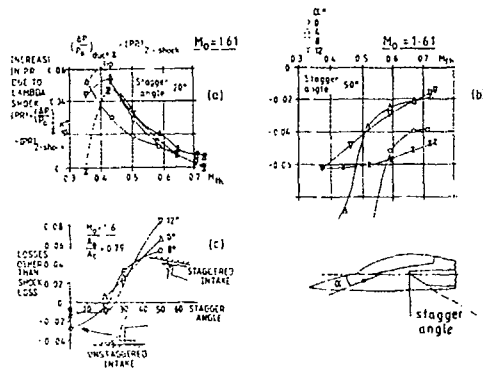


FIG 5.61 EFFECT OF INTAKE STAGGER AT SUPERSONIC SPEEDS

### 25.3.5 Fuselage/wing flow fields for shielded intake installations

The concept of sustaining intake performance at high angles of incidence by positioning an intake beneath a body or a wing applies to both subsonic and supersonic aircraft and has been used on a number of aircraft projects varying from Concorde to F16. When incidence is varied, airflow direction is controlled by the aircraft surface, so to that extent, the intake is not aware of a change of aircraft attitude. Additionally, at supersonic speeds, advantage can usually be taken of a reduction in local Mach number and hence a reduction in shock loss occurs as incidence increases.

Aircraft configurations incorporating shielded intakes can be either the "fuselage-shielded" configuration or the "wing-shielded" configurations depicted in Fig 5-62.

Flow field instrumentation for the shielded configurations was essentially identical to that for the side-mounted configurations (Fig 5-46).

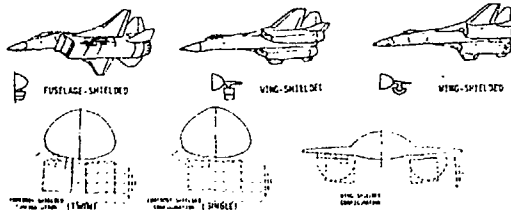


FIG 5.62 FOREBODY FLOW FIELD MODEL INSTRUMENTATION

All three of the installation types are shown in Fig 5-63. A comparison of vector flow fields for the two of the shielded and the baseline unshielded configuration forebodies at  $M_0 = 2.2$  and  $\alpha_0 = 15^\circ$  (Ref 5-10) shows the nature of two shielded flow fields.

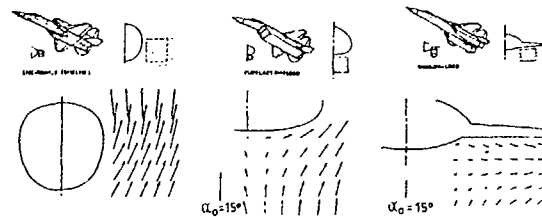


FIG 5.63 COMPARISON OF VECTOR FLOW FIELDS AT  $M_0 = 2.2$ ,  $\alpha_0 = 15^\circ$ ,  $\beta_0 = 0^\circ$  FOR BASELINE AND SHIELDED CONFIGURATIONS

In Fig 5-64 average levels of local Mach number and incidence  $M_L$  and  $\alpha_L$  are shown for the same three different airframe-intake integrations at  $M_0 = 1.6$  and 2.2. It is seen that there is a substantial reduction of average  $M_L$  and  $\alpha_L$  from free stream values associated with the shielded configurations in supersonic flight at incidence.

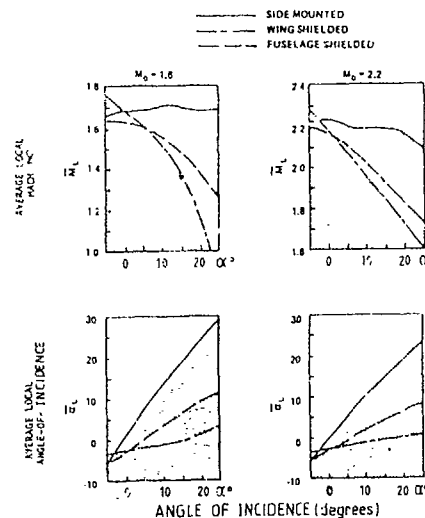


FIG 5.64 COMPARISON OF SHIELDED & UNSHIELDED CONFIGURATION FLOW FIELDS;  $M_0 = 2.2$ ,  $\alpha_0 = 15^\circ$ ,  $\beta_0 = 0^\circ$

Fig 5-65 shows the changing nature of shielded flow fields as  $4^\circ$  sideslip is added to the  $\alpha_0 = 15^\circ$  condition. The leeward flow field on the wing-shielded configuration now shows significantly higher levels of adverse inboard sideslip.

From these forebody flow fields, it might be anticipated that the shielded configurations could offer a considerable performance advantage at the higher values of aircraft incidence, but that this advantage could be tempered by sensitivity to sideslip for the wing-shielded concept.

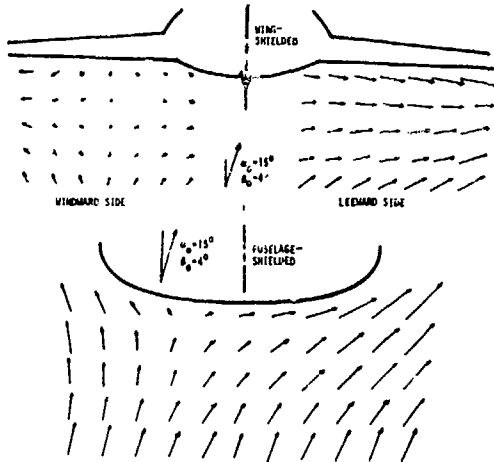


FIG 5-65 SHIELDED CONFIGURATION VECTOR FLOW FIELDS;  $M_0 = 2.2$ ,  $\alpha_0 = 15^\circ$ ,  $\beta_0 = 4^\circ$

#### 2.5.3.6 Performance of shielded compression surface intakes

##### (a) Rectangular Intakes

Fig 5-66 depicts shielded horizontal ramp intakes along with the locations of total and static pressure instrumentation. Instrumentation in the short ( $L/D = 2.92$ ) Mach 2.5 design wing-shielded intake is essentially the same as that used in the side-mounted inlet (Fig 5-62). The longer ( $L/D = 5.8$ ) Mach 2.2 design fuselage-shielded inlet, however, incorporates no throat or duct total pressure probes. Since this was a single intake/single engine concept, throat total pressure rakes could not be included without disturbing flow at the simulated compressor face.

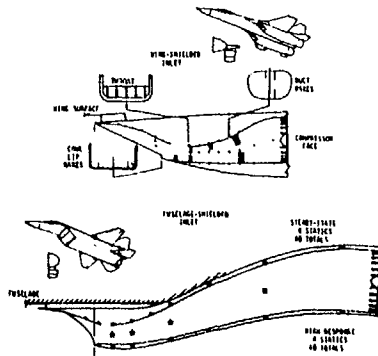


FIG 5-66 SHIELDED INLET CONFIGURATION AND INSTRUMENTATION

Values of intake pressure recovery, turbulence and flow distortion are plotted as a function of incidence for the three different installation types in Fig 5-67 (Ref 5-12 and 5-13). The BASELINE forebody intake configuration from previous illustrations is used to represent the side-mounted inlet installation. The lower Mach number design of the fuselage-shielded intake is revealed in its relatively low pressure recovery at low incidence ( $\alpha_0 < 5^\circ$ ). On the other hand, its pressure recovery continues to increase with  $\alpha_0$ , reaching a peak of  $P_{T2}/P_{T0} = 0.91$  at  $\alpha_0 = 20^\circ$ . The higher Mach number design and slightly better shielding of the wing-shielded inlet results in higher performance at high incidence, reaching a maximum  $P_{T2}/P_{T0} = .97$  at  $\alpha_0 = 20^\circ$ .

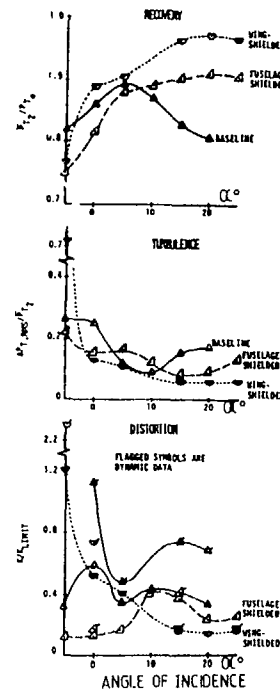


FIG 5-67 INLET PRESSURE RECOVERY, TURBULENCE AND FLOW DISTORTION FOR THREE INSTALLATIONS;  $M_0 = 2.2$ ,  $\beta_0 = 0^\circ$

Both shielded intakes significantly exceed the performance of the side-mounted inlet at high incidence although, in terms of compatibility, the simple, fuselage-shielded intake is the only concept which consistently ( $-5^\circ < \alpha_0 < 25^\circ$ ) exhibits acceptably low levels of turbulence and dynamic distortion index. The dynamic distortion index of the wing-shielded intake exceeds the limit level at  $\alpha_0 = -5^\circ$  where its  $K/K_{L, PEAK} = 2.3$ ; and the side-mounted intake (as noted previously) exceeds the limit at  $\alpha_0 = 0^\circ$  with  $K/K_{L, PEAK} = 1.12$ .

Examination of throat flow fields in Fig 5-68 shows that the wing-shielded intake at  $M_0 = 2.2$ ,  $\alpha_0 = 15^\circ$  produces much more uniform throat flow than either the side-mounted or the isolated intake. At  $\alpha_0 = -5^\circ$ , however, both flow field and inlet data show evidence of a strong vortex, possibly originating at the wing junction, lying near the wing leading edge and evidently intersecting the outboard sideplate of the wing-shielded intake to produce a large fall in performance at that point.

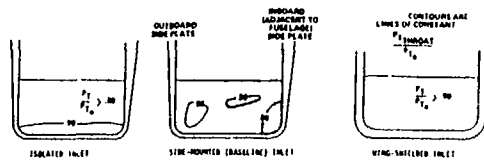


FIG 5.68 INLET THROAT TOTAL PRESSURE CONTOURS FOR DIFFERENT INLET INSTALLATIONS.  $M_0=2.2$ ,  $\alpha_0=15^\circ$ ,  $\beta_0=0^\circ$

The excellent performance of the wing-shielded intake at higher  $\alpha_0$  is negated by extreme sensitivity to sideslip. Values of pressure recovery, turbulence and distortion index over the sideslip range  $-8^\circ < \beta_0 < 8^\circ$  at Mach 2.2,  $\alpha_0 = 15^\circ$ , are shown in Fig 5-69 for the three installations. Here, the fuselage-shielded intake is seen to be essentially free from sideslip sensitivity while both the side-mounted and wing-shielded intakes exhibit extreme sensitivity in terms of all three performance parameters, exceeding distortion index limits at  $\beta_0 = 4^\circ$ .

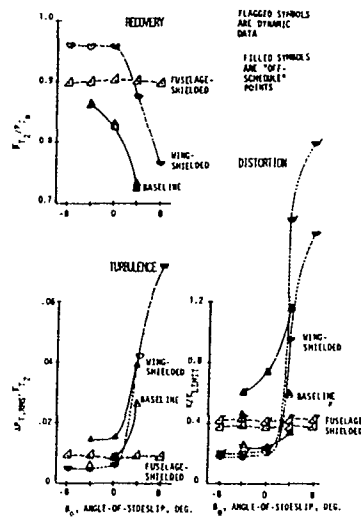


FIG 5.69 INLET PRESSURE RECOVERY, TURBULENCE AND FLOW DISTORTION FOR THREE INSTALLATIONS.  $M_0=2.2$ ,  $\beta_0=0^\circ$

Progression of flow in the wing-shielded intake at  $\alpha_0 = 15^\circ$ ,  $\beta_0 = 4^\circ$  is shown in Fig 5-70 where inboard flow separation at the cowl lip and throat is seen to expand to produce a near-classic 180° circumferential distortion pattern at the engine face.

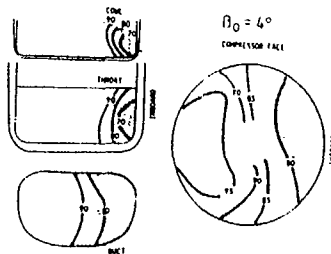


FIG 5.70 WING SHIELDED INLET TOTAL PRESSURE CONTOURS.  $M_0=2.2$ ,  $\alpha_0=15^\circ$

#### (b) Half axisymmetric intakes

In Fig 5-71 wing-shielded half axisymmetric intakes from Ref 5-14 are depicted. This intake and the one in Fig 5-56 share a common semi-conical compression surface with a fixed first cone angle of  $18^\circ$ . A porous boundary-layer bleed is provided on the second cone of each of these intakes, spanning the region of the normal shock location. Boundary layer bleed flow is routed through the diverter, discharging through the same secondary flow metering systems used for the rectangular intakes. Both intakes also employ l'p, throat and duct rakes.

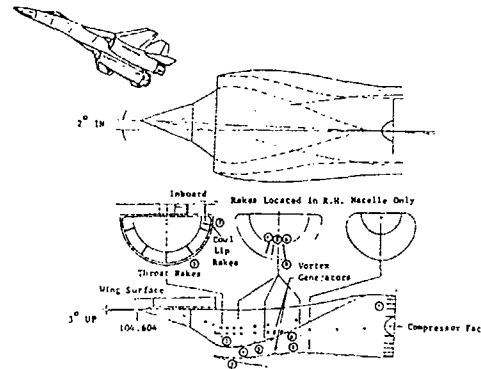


FIG 5.71 WING-SHIELDED HALF-AXISYMMETRIC INTAKE AND INSTRUMENTATION

The two half-axisymmetric intakes have different duct lengths; the side-mounted intake has an L/D of 2.99. As the shielded intake, "sees" less flow angularity than the side-mounted intake, it was designed with sharper cowl lips and it has less offset from intake to compressor face.

No flow fields are shown for the wing-shielded half-cone intake because it exhibited no significant sensitivity to manoeuvre conditions. Its superior performance is obvious in the summary charts shown in the comparisons in the following section.

#### 25.3.7 Comparison of performance of shielded and unshielded rectangular and half-axisymmetric intakes

This final section compares rectangular and half-axisymmetric intake performance. At Mach 2.2 it is seen (Fig 5-72) that total pressure recovery sensitivity to incidence  $\alpha_0$  and sideslip  $\beta_0$  for the five configurations varies greatly. Wing-shielding is effective for both rectangular and axisymmetric intakes, resulting in high pressure recovery from  $\alpha_0 = 0^\circ$  to  $25^\circ$ . On the other hand, both side-mounted intakes exhibit sensitivity to incidence, with the performance of the half-axisymmetric intake dropping off rapidly above  $\alpha_0 = 0^\circ$ . Fuselage shielding is also effective at incidence.

At  $\alpha_0 = 15^\circ$ , the performance of all but the fuselage-shielded intake deteriorate rapidly with increase in sideslip angle. In particular, the wing-shielded rectangular intake which produced the highest recovery in the range  $10^\circ < \alpha_0 < 25^\circ$  is extremely sensitive to sideslip.

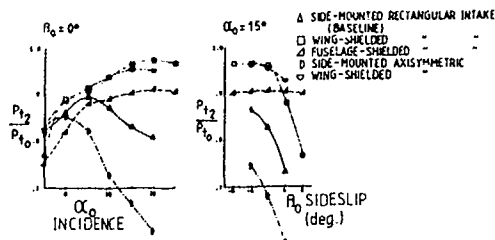


FIG 5.72 COMPARISON OF RECTANGULAR AND HALF-AXISYMMETRIC INTAKE PRESSURE RECOVERY AT  $M_0=2.2$

The wing-shielded rectangular intake is also shown to be much more sensitive to negative incidence than the other intakes in Fig 5-73. Here, the peak dynamic distortion parameter shows the seriousness of this intake's performance deficiency at moderate incidence and leeward (positive) sideslip.

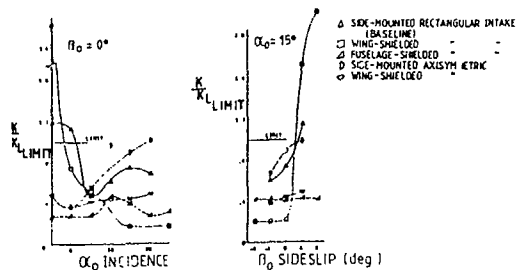


FIG 5.73 COMPARISON OF RECTANGULAR AND HALF-AXISYMMETRIC INLET PEAK FLOW DISTORTION;  $M_0 = 2.2$

Again, the side mounted half-axisymmetric inlet turbulence is much higher than other inlets at high incidence. All inlets except the fuselage-shielded inlet show some sensitivity to leeward sideslip.

Both steady state and dynamic distortion indices show the same trends except the wing-shielded half-axisymmetric inlet and the fuselage-shielded inlet which have low distortion. The importance of high response distortion is seen in that the  $(K/K_L)_{PEAK}$  values highlight side mounted inlets as having manoeuvre problems which is not obvious from steady state data.

#### 2.5.3.8 Performance of shielded pitot intakes (Ref 5.17)

The advantage of underbody shielding at subsonic speeds is shown in terms of both reduced losses compared to isolated pitot intake values (Fig 5-74a & b) and reduced mean local incidence (Fig 5-74c). At supersonic speeds the increase in recovery with increase in incidence is most marked at  $M_0 1.8$  (Fig 5-74d).

Shielding under a wing or strake for a side body intake is more difficult because of the presence of both body and wing boundary layers. Again, losses are shown compared to those for an isolated intake at  $M_0 1.9$  in Fig 5-75 and also, the reduction in effective incidence. In this case, the wing or strake reduces the mean local incidence but at the expense of some increase in sidewash angle.

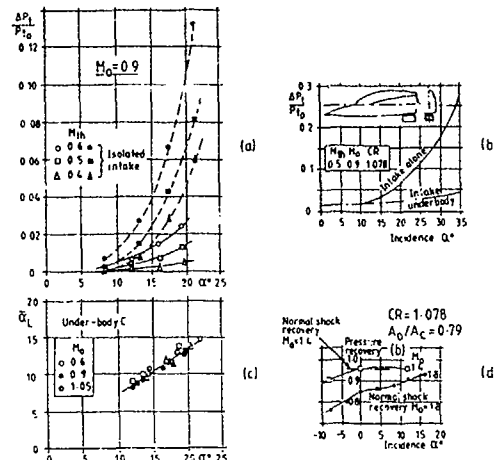


FIG 5.74 EFFECT OF UNDERBODY SHIELDING FOR A PITOT INTAKE AT SUBSONIC AND SUPERSONIC SPEEDS

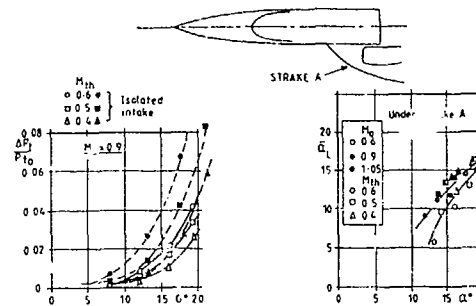


FIG 5.75 EFFECT OF UNDERSTRAKE SHIELDING AT  $M_0=0.9$

At supersonic speeds the lambda shock that forms on both the body and wing undersurface becomes complex in form where the two shock patterns intersect as illustrated in Fig 5-76. Recovery increases with increase in incidence due to the reduced local Mach number but engine face flow distortion is worse than for the isolated intake as a result of the complex shock and boundary layer interaction on body and wing undersurface.

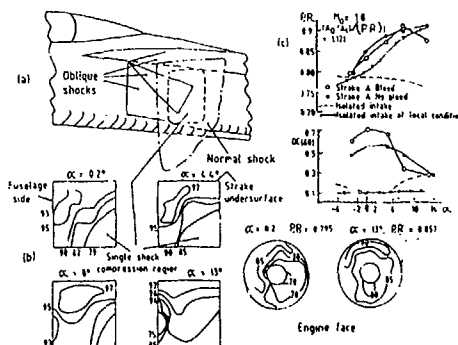


FIG 5.76 PRESSURE RECOVERY AND FLOW DISTORTION AT INCIDENCE FOR AN INTAKE UNDERNEATH A STRAKE AT  $M_0=1.8$  (REF 5.7)

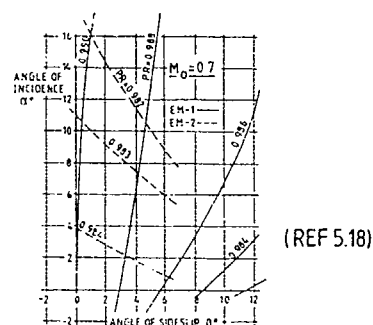
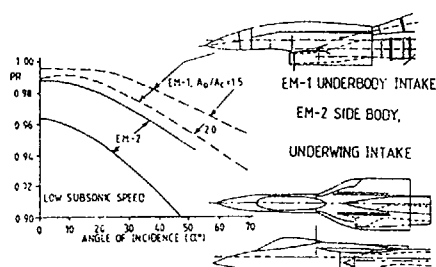


FIG 5.77 COMPARISON OF UNDERBODY & SIDEBODY/UNDERWING INTAKE PERFORMANCE

Post-1965, the response to the requirement for increased manoeuvrability of supersonic fighter aircraft, had a major impact on the design and development of many current aircraft. Whereas the drive for increased speed in earlier years had caused aircraft intakes to become more and more complex with time, there has been a conscious effort to keep complexity to a minimum in current aircraft. In Fig 5-78 the trend of correspondence between maximum Mach number and design complexity of the intake system is shown. This correspondence is due, in part, to the fact that US aircraft are being compared. European and Soviet designers sometimes tend to place greater value on simplicity and/or light weight than upon high pressure recovery and low drag.

FIGHTER	FLW	FLW	FLW	FLW	FLW	FLW	FLW	FLW	FLW	FLW	FLW
	FLW	FLW	FLW	FLW	FLW	FLW	FLW	FLW	FLW	FLW	FLW
F 80	✓										
F 89		✓									
F 5A		✓									
F 101		✓									
F 102		✓	✓								
F 16		✓									
F 18		✓	✓		✓						
F 104		✓			✓		✓				
F 105		✓	✓				✓		✓		
F 106		✓	✓		✓		✓		✓		
F 4		✓	✓		✓		✓		✓		
F 14		✓			✓		✓		✓		
F 15		✓			✓		✓		✓		
F 11		✓	✓	✓			✓		✓		

FIG 5.78 TREND OF INCREASING COMPLEXITY WITH INCREASE OF MAXIMUM MACH NUMBER

The F-111 airframe-intake (Fig 5-79) design represented one of the earliest attempts to improve airframe intake integration in a tactical aircraft and important lessons were learned (Ref 5.19). By tucking the inlet under the wing in an "armpit" location, the intake was shortened (for lighter weight) and the wing was used to shield the inlet and thus provide high pressure recovery and low distortion in supersonic manoeuvring flight.

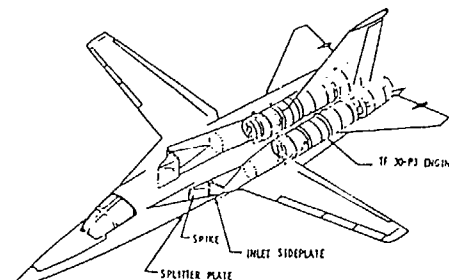


FIG 5.79 F-111A TACTICAL FIGHTER

Unfortunately, there was insufficient information at the time to alert the designers adequately concerning (a) the shedding of low energy fuselage air into the intake region at incidence, (b) the tendency for flow separation to occur inside the sharp cowl lip at high incidence and (c) the engine's response to time-varying distortion. The original complicated intake design also attempted to use boundary layer passing through upper and lower side-plate slots to act as engine cooling air on its way to the exhaust nozzle ejector. The tortuous flow path over the engine resulted in low cooling air flows so that much of the boundary layer air spilled into the intake. Eventually, General Dynamics was forced to (a) move the intake further outboard from the fuselage to avoid excessive ingestion of the low energy fuselage air, (b) thicken the cowl lip to avoid high incidence separation, (c) modify the conical compression surface boundary layer bleed and (d) place diverters in the side plate slots in place of the engine cooling scheme. The lessons of the F-111 flight test experience led to a major revival of research into airframe-propulsion in the following years.

The F-18 used a type of wing-shielding similar to the F-111, but (in the prototype YF-17 version) provided slots in the root of the wing leading edge extension which allowed the escape of fuselage boundary layer. These slots however caused high wing drag. McDonnell Douglas closed the slots and provided additional boundary layer control as necessary (Fig 5-80).

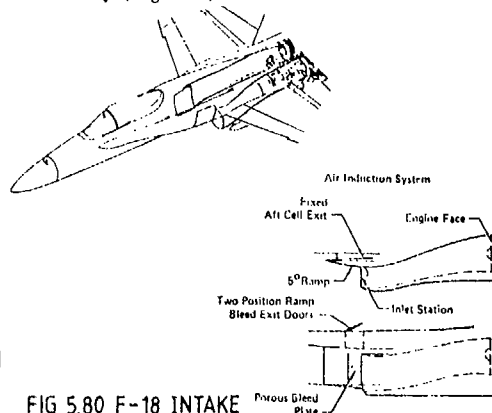


FIG 5.80 F-18 INTAKE

The F-16 employed fuselage-shielding and avoided the problem of fuselage boundary layer ingestion while maintaining the positive aspects of shielding.

A unique approach has been implemented in the French Rafale fighter aircraft (Fig 5-81) which would appear to share aspects of both the F-16 and F-18 shielding concepts. Rafale designers have avoided some of the subsystem interference problems of most fuselage-shielding concepts with two engines while still retaining what appears to be a significant amount of fuselage shielding. The unique fuselage shaping provides a considerable amount of boundary layer relief at high angles of incidence, allowing low energy air from the underbody to flow through the diverter region and be spilled above the inlet rather than be shed as vortices from the underbody into the intake region.

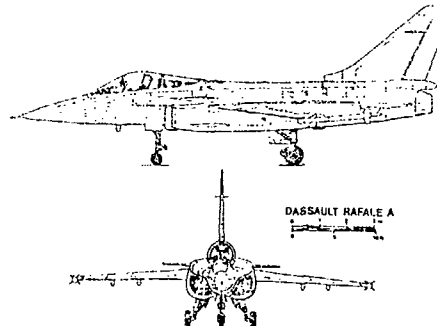


FIG 5.81 RAFALE - INTAKE & FUSELAGE SHAPING

The Northrop F-5 reduces maximum Mach number to 1.4-1.6 but puts a premium on high subsonic and transonic manoeuvrability and simplicity. The intakes only require a diverter and side plate to prevent boundary layer ingestion and shock-boundary layer interaction. The F-20 version with Mach 1.9 capability uses fixed vertical compression ramps with distributed suction bleed.

The use of side-mounted semi-conical intakes on France's Mirage series of fighters and Israel's Kfir (Fig 5-82) shows an approach emphasising light weight, low supersonic drag and simplicity. The use of side-mounted semi-conical intakes in highly manoeuvrable supersonic fighter aircraft would indicate high distortion levels, but both Mirage and Kfir are powered by turbojet engines with rather large stall margins.

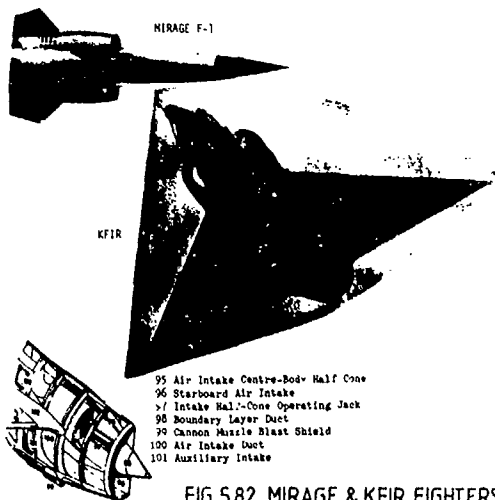


FIG 5.82 MIRAGE & KFIR FIGHTERS

Simple design measures can be taken in the detail design of intakes. The effect of lip contraction ratio on the performance of isolated pitot intakes at incidence has already been illustrated in section 5.2.1. Shaping the lower lip by cambering it outwards and increasing the thickness (with respect to the upper lip) can enhance the effect of a chosen overall contraction ratio as shown in the side intake performance at  $M_0$  0.9 of Fig 5-83.

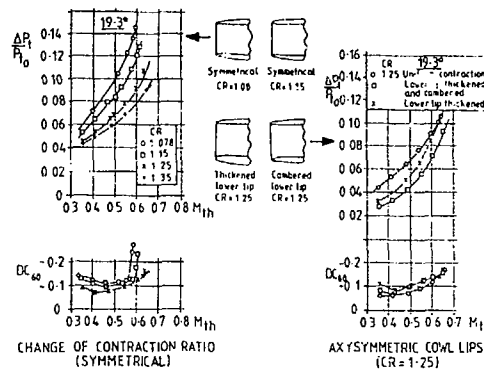


FIG 5.83 EFFECT OF SYMMETRIC & ASSYMMETRIC LIP THICKENING & OF LIP CAMBER (REF 5.15)

A small permanently open lower lip slot can also improve pitot intake performance at incidence as shown in Fig 5-84 at  $M_0$  0.9.

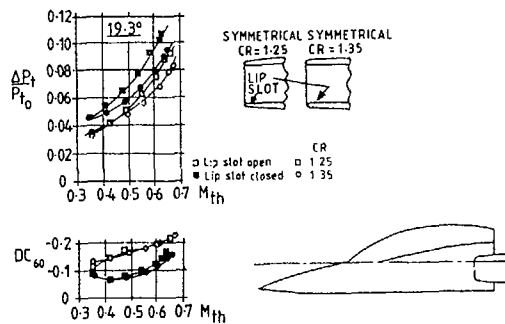


FIG 5.84 EFFECT OF AN OPEN LOWER LIP SLOT (REF 5.15)

The retrofitting of a blunt leading edge to the quarter circular centrebody intakes of the F-111 aircraft (Fig 5-44) to improve performance under subsonic manoeuvre conditions has already been noted.

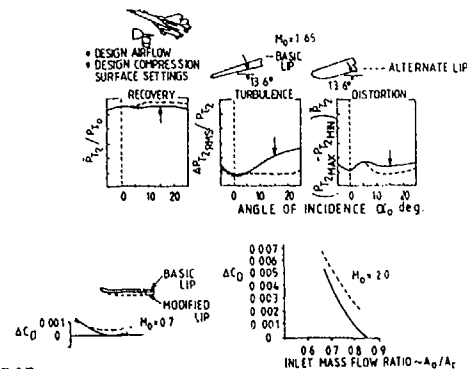


FIG 5.85 EFFECT OF LIP GEOMETRY ON INLET PERFORMANCE

There can also be a favourable effect at supersonic speeds on all internal performance parameters by changing from a sharp to a blunt lip but at the expense of an increase in external drag as would be expected (Fig 5-85).

Similar data was obtained in the course of designing the Tornado aircraft. A substantial decrease in instantaneous distortion was achieved in the Tornado intakes by blunting and decambering the cowl lip at subsonic speeds as shown in Fig 5-86a. Again, however, at supersonic speeds, the change in cowl shape resulted in decreased maximum mass flow and increase in cowl lip shock stand off distance (Fig 5-86b) and hence, penalties in external drag.

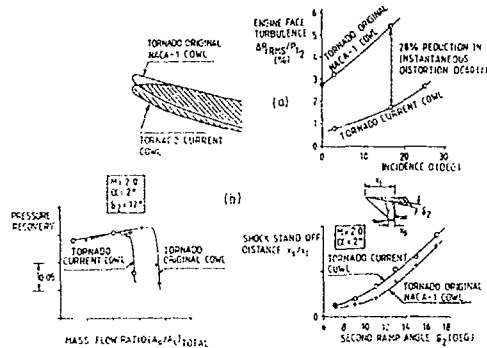


FIG 5.86  
EFFECT OF CHANGE OF COWL LIP SHAPE  
ON PERFORMANCE OF TORNADO INTAKE (REF 5.20)

Grumman and McDonnell Douglas both employed side-mounted, horizontal ramp external compression intakes to provide the built-in adjustment to manoeuvring flight on the F-14 and F-15. The overhead ramps help to align the flow with the intakes at incidence in the same manner as the use of entry plane stagger in pitot intakes noted in section 5.2.1.

Further examples of the effect of stagger angle and sidewall geometry at  $M_c$  0.9 and  $\alpha$  35° on side intake performance are shown in Fig 5-87. At 50° stagger angle because of the high shielding effect of the upper lip, this performance is virtually invariant with capture ratio (and hence  $M_0$ ) provided  $A_0/A_c < 1.0$  but as stagger angle decreases, this independence reduces and becomes similar to the dependence on  $M_{th}$  and  $A_c/A_0$  illustrated in Fig 5-58 for the unstaggered intake.

Much of the recent work in tactical intake variable geometry research has centred around increasing the manoeuvre/acceleration envelope of the aircraft. This requires high pressure recovery and low distortion over a wide range of flight conditions.

The most obvious active means of increasing performance at high incidence is to hinge the lower lip of the cowl. The European Fighter Aircraft (EFA) uses both underbody shielding and a hinged lower cowl lip (Fig 5-88). The favourable effect on losses at subsonic speed and high incidence is shown in Fig 5-89 and there is also a favourable effect of the hinged lip on intake efficiency at take off conditions (Fig 5-90).

The hinged lip can also be oriented in the opposite direction to affect drag in a favourable sense. The effect on spill drag is twofold as shown in Fig 5-91. Firstly the decrease in capture area as the cowl lip is hinged upwards towards the fuselage means that smaller amounts of flow need to be

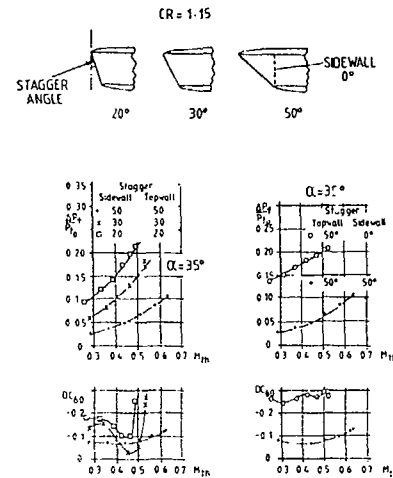


FIG 5.87 EFFECT OF INTAKE STAGGER AT  $M_0=0.9$   
( $A_0/A_c < 1.0$ ) (REF 5.15)

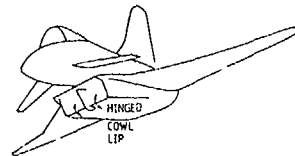


FIG 5.88  
BRITISH AEROSPACE EAP AIRCRAFT  
WITH HINGED COWL LIP

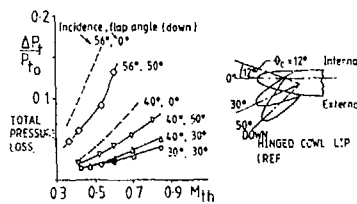


FIG 5.89  
PERFORMANCE OF INTAKE WITH HINGED COWL LIP  
AT SUPERSONIC SPEEDS (REF 5.7)

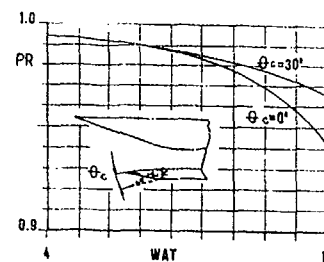


FIG 5.90 PERFORMANCE OF SUPERSONIC INTAKE  
WITH HINGED COWL LIP AT STATIC  
(TAKE-OFF) CONDITIONS

spilled. The shift of the curves to the left at  $\theta_c = 12^\circ$  is because the non-dimensionalising capture area  $A_c$  in the flow ratio  $A_0/A_c$  is based on the  $\theta_c = 0^\circ$  value. Secondly, there is a decrease in slope of the spill drag versus  $A_0/A_c$  curve resulting from the increase in cowl projected area and hence cowl suction force as  $\theta_c$  increases from  $0^\circ$  to  $12^\circ$ . At supersonic speeds however there is an increase in wave drag at full flow from this same increase in cowl projected area (Fig 5-92).

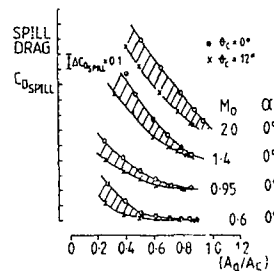


FIG 5.91 EFFECT OF COWL LIP INCLINATION ON SPILLAGE DRAG

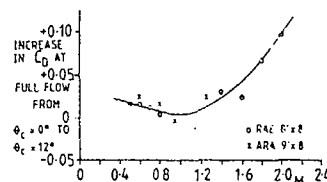


FIG 5.92 CHANGE IN COWL DRAG AT FULL FLOW DUE TO COWL LIP INCLINATION

Other variations to the lower cowl lip are possible in much the same vein as high lift devices on wing leading edges. Fig 5-93 shows a comparison of the internal performance of the simple hinged leading edge with a more complex cowl leading edge slot and a blown leading edge. Blowing is geometrically simple but uses high pressure air from the engine compressor which results in an engine thrust penalty.

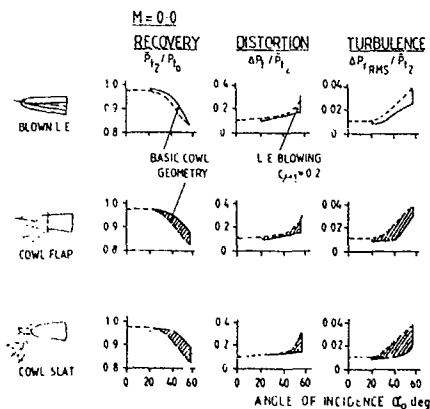


FIG 5.93 COWL LIP LEADING EDGE DEVICES

The benefits of optimising airflow matching, boundary layer control and variable geometry in a complex design at subsonic speeds can be seen in Fig 5-94. A rectangular advanced intake is compared with current fighter intakes at various conditions

where it can be seen that the advanced intake gives far superior performance at extreme manoeuvre points.

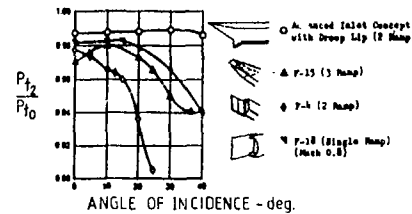


FIG 5.94 COMPARISON OF PERFORMANCE OF CURRENT & ADVANCED INTAKES (REF 5.8)

For ramp compression surface intakes at supersonic speeds, adjustment of the second ramp angle is made to compensate for the increased (or decreased) strength of the first oblique shock when incidence is changed. This enables the intake to retain a near optimum shock recovery but probably more importantly, contributes to better engine-inlet matching. For added flexibility of operation at incidence, the whole forward portion of the intake on the F15 aircraft (Fig 5-95) can incline downwards.

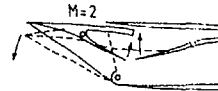


FIG 5.95 ROTATING FORWARD INTAKE (F-15)

For an axisymmetric centrebody intake, increases in performance can be obtained by both staggering the cowl lip so that the shock does not enter the lower lip and by pivoting the centrebody (Fig 5-26). Pivoting both centrebody and cowl however is necessary to achieve maximum insensitivity to increase in incidence.

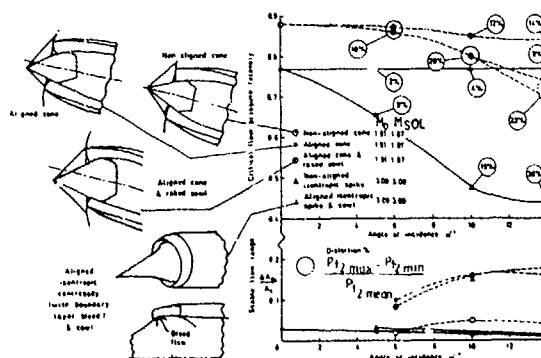


FIG 5.96 EFFECT OF CENTREBODY PIVOTING & COWL RAKING & PIVOTING ON AXISYMMETRIC INTAKE PERFORMANCE AT INCIDENCE (REF 5.7)



## 2.5.5 Concluding remarks

### Intake integration

The stream flow approaching a side-mounted intake is significantly distorted by the forebody, especially in manoeuvring flight. Horizontal ramp external compression intake designs are shown to have inherent advantages over vertical ramp or semi-conical intakes for agile fighters, but it is also shown that careful integration of the intake to provide appropriate shielding can make an enormous difference in pressure recovery performance and inlet-engine compatibility.

### Intakes

The design of a tactical fighter air intake results from a compromise of performance and stability against complexity and weight, driven by overall aircraft mission requirements. It is difficult to separate this design compromise from the consideration of inlet-airframe integration, yet there are a number of issues related directly to the inlet design itself.

It has been shown that the inlet configuration can reveal much about the intended aircraft mission application and the overall system design philosophy.

Intake design requires a thorough understanding of the various facets of inlet performance and the flow field phenomena which affect them. To this end, the discussion has dealt with the basic measures of performance and has outlined the primary flow field phenomena which must be controlled. Specific design considerations involved in maximising pressure recovery, minimising drag and controlling the flow for improved uniformity and steadiness have been discussed.

### REFERENCES

- 5-1 Fox, R W & Kline, S J, 'Flow regimes in curved subsonic diffusers', Journal of Basic Engineering, Transactions of the ASME, September 1962.
- 5-2 Tindell, R H, 'Highly compact inlet diffuser technology', AIAA-87-1747, July 1987.
- 5-3 Lee, C C & Boedicker, C, 'Subsonic diffuser design and performance for advanced fighter aircraft', AIAA-85-3073, October 1985.
- 5-4 Anderson, B H, 'CFD application to subsonic inlet airframe integration' Intake Aerodynamics, VKI Lecture Series, February 1988.
- 5-5 Goldsmith, E L, 'The internal performance at incidence of pitot intakes with circular cross section and elliptic lip shapes', ARA Report 76, Jan 1990.
- 5-6 Goldsmith, E L, 'Forces and pressure distributions at subsonic and supersonic speeds on circular section pitot intakes', ARA Report 75, Jan 1990.
- 5-7 Seddon, J & Goldsmith, E L, 'Intake aerodynamics', Collins, 1985.
- 5-8 Richey, G K, Surber, L E & Berler, B L, 'Airframe propulsion integration for fighter aircraft', 7th International Symposium on Air Breathing Engines, Sept 1985.
- 5-9 Brown, C S & Goldsmith, E L, 'Measurement of the internal performance of a rectangular air intake with variable geometry at Mach numbers from 1.7 to 2.5 Part I, RAE TR 71159, Aug 1971.
- 5-10 Surber, L E & Stava, D J, 'Supersonic inlet performance and distortion during maneuvering flight', AGARD CP-91-71, Inlets and Nozzles for Aerospace Engines, December 1971.
- 5-11 Antonatos, P P, Surber, L E & Stava, D J, 'Inlet/airplane interference and integration', AGARD LS-43, Airframe/Engine Integration, May 1972.
- 5-12 Richey, G K, Surber, L E & Laughrey, J A, 'Airframe/propulsion system flow field interference and the effect on air intake and exhaust nozzle performance', AGARD CP-150, Airframe/Propulsion Interference, March 1975.
- 5-13 Surber, L E, 'Effect of forebody shape and shielding technique on 2-D supersonic inlet performance', AIAA-75-1183, September 1975.
- 5-14 Surber, L E & Sedlock, D, 'Effects of Airframe-inlet integration on half-axisymmetric and two-dimensional supersonic inlet performance', AIAA-78-960, July 1978.
- 5-15 Goldsmith, E L, McGregor, I, 'The effect of intake geometry changes on the internal performance of a rectangular pitot intake on the side of a fuselage. Part I: Subsonic and Transonic Speeds', RAE TR 88070, November 1988.
- 5-16 Goldsmith, E L, McGregor, I, 'The effect of intake geometry changes on the internal performance of a rectangular pitot intake on the side of a fuselage. Part II: Supersonic Speeds', RAE TR 88071, November 1988.
- 5-17 Goldsmith, E L, McGregor, I, 'The effect of shielding on the performance of a rectangular pitot intake at subsonic and supersonic speeds' RAE TR 88018, March 1988.
- 5-18 Welte, D, Pitot-Selteneinlauf Dr 10/30-2673/84 Zwischenbericht zu BMV-Auftrag-Nr T/R42/D0018/D1418.
- 5-19 Surber, L E & Robinson, C P, 'Survey of inlet development for supersonic tactical aircraft', AIAA 83-1164, June 1983.
- 5-20 Stocks, C P & Bissinger, N C, 'The design and development of the Tornado engine air intake', AGARD CP 301, May 1981.

## 2.6 VSTOL AIRCRAFT INTAKES, DESIGN & PERFORMANCE

### CONTENTS

- 2.6.1 INTRODUCTION
- 2.6.2 GENERAL CONCEPTS, SPECIFIC EXAMPLES OF FLIGHT TESTED VEHICLES AND FUTURE POSSIBILITIES
  - 2.6.2.1 Fixed, Direct Lift Engine Intakes
  - 2.6.2.2 Rotating Engine Intakes
    - 2.6.2.2.1 State-of-the-Art Experience
    - 2.6.2.2.2 Future Possibilities
  - 2.6.2.3 Fixed Horizontal Engine with Flow Diverters
    - 2.6.2.3.1 State-of-the-Art Experience
    - 2.6.2.3.2 Future Possibilities
- 2.6.3 PERFORMANCE OF VSTOL INTAKES IN STATIC AND TRANSIENT CONDITIONS
  - 2.6.3.1 The Vertical Axis Inlet
    - 2.6.3.1.1 Inlet Physics
    - 2.6.3.1.2 The Lift Engines intakes of the Do 31 VSTOL Transport Aircraft
  - 2.6.3.2 The Fixed Horizontal Axis Intake - Harrier Type
    - 2.6.3.2.1 Design Problems
    - 2.6.3.2.2 Total Pressure Recovery
    - 2.6.3.2.3 Spillage Drag
    - 2.6.3.2.4 Velocity Distribution
    - 2.6.3.2.5 Low-Drag Cowi Section
  - 2.6.3.3 The Rotating Axis Intake - VJ-101

### REFERENCES

#### 2.6.1 INTRODUCTION

Over the past 30 or so years several approaches to the design of V/STOL aircraft have been taken, each with its own particular engine or fan air intake problems. (Ref 6.1 & 6.2). This section considers the various types of V/STOL aircraft intakes, their design and performance experience and some of their ancillary problems such as auxiliary air intakes. (Ref 6.3).

There appears to be three basic types of engine air intakes associated with V/STOL aircraft:

- Fixed, vertical axis inlets, for lift only thrust engines,
- the inlet whose axis rotates from vertical for lift to horizontal for cruise thrust, and
- the fixed horizontal-axis inlet which feeds a variable configuration engine for lift and cruise thrust.

Section 6.2. discusses these general concepts.

Consideration of the performance of V/STOL intakes, with respect to their design parameters is given in Section 6.3.

## 2.6.2 GENERAL CONCEPTS, SPECIFIC EXAMPLES OF FLIGHT TESTED VEHICLES AND FUTURE POSSIBILITIES

### 2.6.2.1 Fixed, Direct Lift engine intakes

One of the first design approaches to V/STOL was with fixed, direct lift engines, with engines located either in the fuselage or in wing mounted pods or nacelles, (Ref 6.4-6.6) as the podded lift engines of the Do 31 and the fuselage mounted lift engines of the VJ101. In this approach, specially designed, short engines, are mounted with their axes near vertical or with a small tilt forward to provide a small component of thrust in the forward direction. These engines operate only during lift-off or landing and are turned off during forward or cruise flight. Separate, horizontally mounted thrust engines, are used in cruise, which usually employ normal conventional inlets. The fixed direct lift engines must be carried as a non-useful load from point to point and subtract from the maximum useful load that might be carried otherwise.

The inlets of the vertical lift engines will have an incidence angle of about zero degrees at zero and very low forward speeds to almost 90 degrees incidence in transition to forward flight. These conditions must be met while maximum thrust is being demanded. The design and performance of the podded lift engines of the V/STOL transport Bomber 31 will be described in para. 6.3.1.

### 2.6.2.2 Rotating Engine Intakes

#### 2.6.2.2.1 State-of-the-Art Experience

The next conceptual step in the development of the V/STOL airplane appears to be the attempt to rotate the engines from a vertical attitude to horizontal so that these engines can serve both for lift and for forward propulsion. This approach introduces a measure of mechanical complexity and complicates aerodynamic control in transition from vertical to horizontal flight. However, in spite of the added mechanical and aerodynamic control complexity, this conceptual approach allows the engine air intake to rotate into the wind to maximize performance during transition.

The inlet must operate both at zero speed and maximum thrust and at a thrust for cruise speed. The single inlet must be tailored to handle two different design criteria and mass flow ratios. The V/STOL experimental fighter aircraft VJ101 from Messerschmitt-Bölkow-Blohm as an example of this category will be described in para. 6.3.3.

#### 2.6.2.2.2 Future Possibilities. (Ref 6.7-6.9)

Fig. 6.1 shows a Grumman concept using rotating, podded turbo-fan engines during rotation and landing. Such a design requires a very short or no inlet duct.

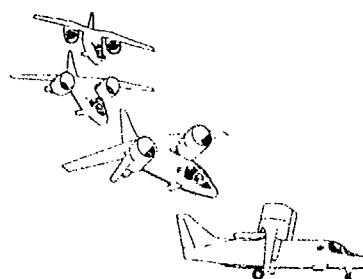


FIG 6.1 GRUMMAN ROTATING TURBOFAN DESIGN

The rotating aft-fuselage-with-engine concept is embodied in the Grumman "Nutcracker"-V/STOL concept for use on an aircraft carrier deck Fig. 6.2. Two large turbofan engines are mounted on either side of a hinged aft fuselage such that when rotating the thrust vector passes through the centre of gravity of the aircraft.

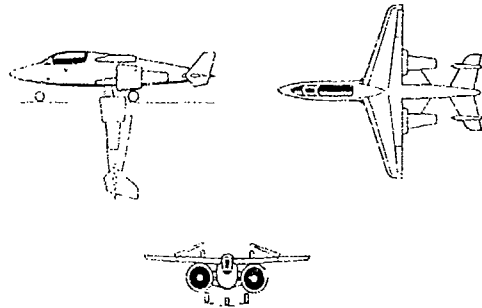


FIG 6.2 GRUMMAN "NUTCRACKER"

From the data available on this design the podded turbofan engines appear to have a normal nacelle intake with no allowance for spillage adjustment.

The ultimate in rotating thrust vector design appears to be to rotate the whole aircraft as in the very early "tail sitter" aircraft. The current proposal is the "wire hanger", a U.S. Navy design for use on a carrier deck, Fig. 6.3.

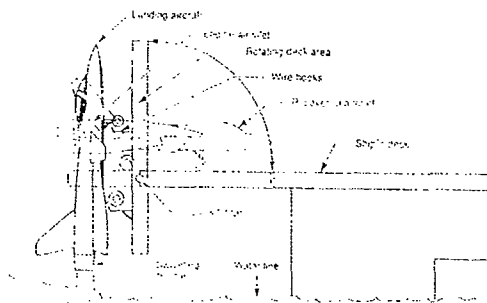


FIG 6.3 U.S. NAVY "WIRE HANGER" CONCEPT

The Wire Hanger concept is based on a F-18 type aircraft with an engine designed to have a gimballed nozzle which would tilt plus and minus ten degrees in any direction. It is to take off in the conventional way but would back down vertically to hook onto the side of a ship as shown in Fig. 6.3. It is somewhat similar to the Ryan X-13 tail sitter of 1956-1957.

X-13 experience suggests that the inlets may require auxiliary doors to enlarge the openings to prevent cross-flow stall of the engine air (Ref. 6.9).

#### 2.6.2.3 Fixed Horizontal Engines with Flow Diverters

##### 2.6.2.3.1 State-of-the-Art Experience

In the case of a fixed horizontal axis engine, vertical lift can be obtained by deflecting all or part of the engines' exhaust downwards by a

valve in the nozzle (Ref. 6.10-6.14). Air exhausting from the engine's compressor may also be bled to provide a lifting force. The Pegasus engine in the Harrier uses this arrangement to give two hot and two cold exhaust streams. The performance of the air intake of the Harrier will be described in para. 6.3.2.

The major intake design problem in this case is the great difference in the mass flow required between the lift mode and the forward cruise mode.

##### 2.6.2.3.2 Future Possibilities

A specially unique design, Rolls-Royce, Fig. 6.4, (Ref. 6.21) combines the exhaust from the two main engines into a plenum which can be deflected from a full-aft nozzle to a downwards deflected lift jet. Additional fan bleed from the two main engines are ducted through rotating nozzles from an aft direction to a downwards lifting jet.

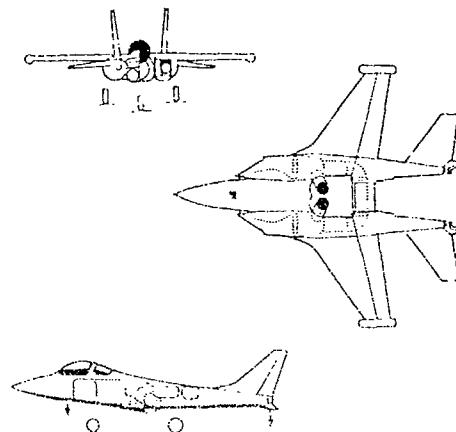


FIG 6.4 ROLLS-ROYCE DEFLECTED EXHAUST CONCEPT

The inlets on each side of the Rolls-Royce concept are square, 2-D intakes with wedge shaped ramps and a boundary layer diverter. The concept is unique in that it is configured around a twin tail boom design.

Several V/STOL concepts using the idea of slipstream deflection of pod mounted turbofan engines or tip driven fans have been proposed.

Fig. 6.5 illustrates a NASA design using a pair of tip driven fans with deflecting nozzles for vertical lift. A nose fan is used to balance the aircraft in hovering, lift-off and landing. The turbine engines serve as gas generators to feed the main and nose fans. The inlets for these engines are typical side mounted duct inlets.

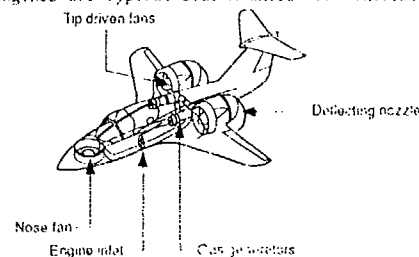


FIG 6.5 NASA TIP DRIVEN FAN DESIGN WITH DEFLECTING NOZZLES

The Dornier "LSK" PROJECT, (Ref 6.16), a light hovering combat airplane, as shown in Fig. 6.6, has a similar configuration except that the single engine, operating as a gas generator is supplied by an inlet at the base of the vertical tail and instead of using a deflecting nozzle it uses turning vanes in the slipstream.

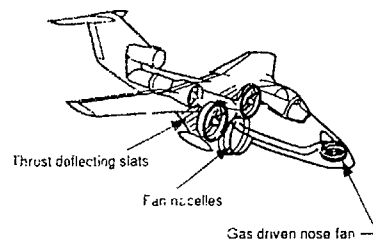


FIG 6.6 DORNIER "LSK" PROJECT

### 2.6.3 PERFORMANCE OF V/STOL INTAKES IN STATIC AND TRANSIENT CONDITIONS

The Dornier Do 31 (Ref 6.17) the MBB VJ-101C, (Ref's 6.18 & 19) and the Harrier, (Ref 6.20) have been chosen for purposes of performance considerations as representative of the three main categories of V/STOL intake design.

#### 2.6.3.1 The Vertical Axis Inlet

##### 2.6.3.1.1 Inlet Physics

The problem of intake design is unique for the fixed, vertical lift engine in that in forward flight the inlet air must turn through a large angle (near 90 degrees) from the free stream direction into the engine inlet duct. Such a turn requires a large turning force per air mass flow,  $K/wV_2$ . Fig. 6.7 shows a schematic diagram for the turning flow.

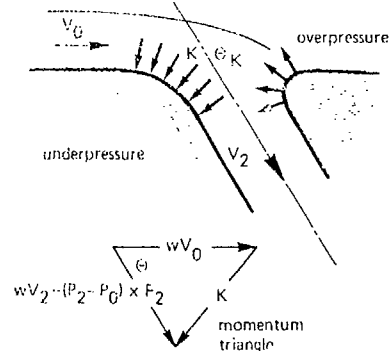


FIG 6.7 SCHEMATIC DIAGRAM OF AIRFLOW TURNING INTO INLET DUCT

A suction force on the near corner and a positive pressure force on the far corner is required to turn the flow through the angle  $\theta$ . A force diagram, using momentum theory, is shown on this figure from which the horizontal and vertical components of force can be determined. These two components can then be used to find the resultant force. The result is shown plotted in Fig. 6.8. The air velocity on the near and far surfaces of the inlet will vary as shown in Fig. 6.9 for  $V_0/V_2 = 2.0$ .

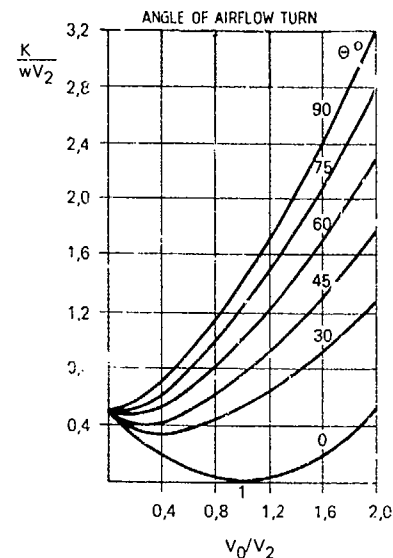


FIG 6.8 FORCE RATIO TO TURN AIRFLOW THROUGH  $\theta$  DEGREES

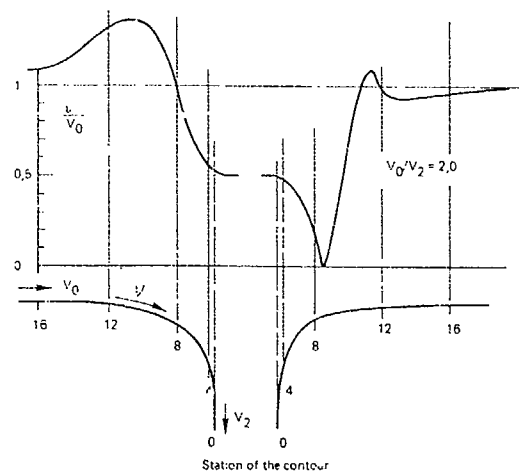


FIG 6.9 VARIATION OF FLOW VELOCITY ON SURFACE OF INLET

#### 2.6.3.1.2 The Lifting Engines Intakes of the Do 31 VSTOL Transport

Fig. 6.10 shows the aircraft configuration with pods for the lift engine at the wing tips. Wind tunnel tests were carried out on the Dornier Do 31, four-engine-vertical lift nacelle in early 1960 (Ref 6.17). A schematic diagram of the

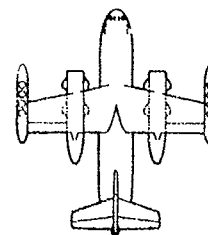


FIG 6.10 VTOL TRANSPORT AIRCRAFT "Do 31"

nacel 2 is shown in Fig. 6.11. Tests were made with and without a cascade of turning vanes in front of the first engine intake and with and without a spoiler at the engine exit.

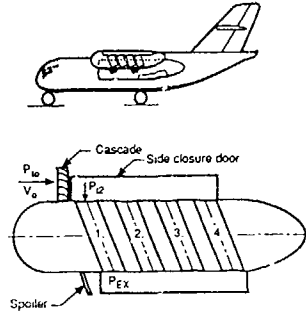


FIG 6.11

## SCHEMATIC OF THE VERTICAL LIFT NACELLE

Figs. 6.12 (a) and (b) compare the total pressure recovery measurements  $P_{t2}/P_{t0}$  without and with a cascade, at low inlet speeds,  $V_0/V_2 = \infty$ , corresponding to engine start at the beginning of transition for a vertical landing. The cascade improves the performance of the first intake but seemingly has little effect on the rearward engines.

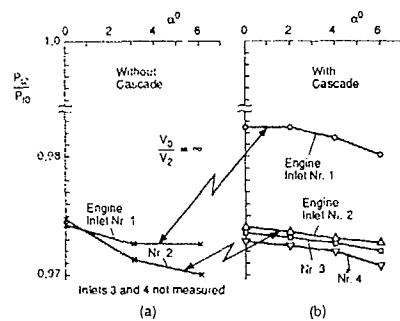


FIG 6.12 TOTAL PRESSURE RECOVERY VERSUS ANGLE OF INCIDENCE

A problem in the design of vertical lift engine aircraft is that of in-flight start of the engines prior to landing. For engine start-up in flight it is necessary to have a positive total pressure drop across the engine to provide air flow to windmill it up to starting rpm. That is,  $(P_{t1} - P_{EX})/P_{t0}$  must be greater than zero where  $P_{EX}$  is the static pressure at the exit of the engine.

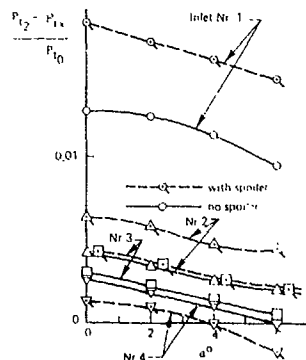


FIG 6.13 TOTAL PRESSURE DROP THROUGH ENGINE FOR STARTING VERSUS ANGLE OF INCIDENCE

Fig. 6.13 shows test results for the engine intake model tested, both without and with spoiler for the cascade equipped nacelle.

The spoiler, used to create a suction on the under-side of the nacelles, has a large effect on the first engine (about 40 percent). However, its influence decreases on engines 2 and 3 and give a negative effect on engine number 4 for an angle of incidence greater than 4°.

The row of intakes must finally be investigated for distortion at the engine face. Fig. 6.14 presents the test results for the  $DC_{60}$  distortion factor for engines 1 and 2 without a cascade. The dashed line shows the comparison of distortion level with a cascade for a 6° angle of incidence. The presence of the cascade gives a marked improvement at 6°, decreasing the distortion from -1.1 to -0.6 for engine no. 1 and from -0.7 to -0.3 for engine no. 2, both at  $V_0/V_2 = 1.5$ .

The measurement of a distortion figure below the limit curve for the configuration without a cascade,  $\alpha = 6^\circ$  and  $3^\circ$  yaw, as shown in Fig. 6.14, demonstrates the need for a cascade. The addition of a cascade brings the point upwards, into the operational range, even with a yaw angle of  $5^\circ$ .

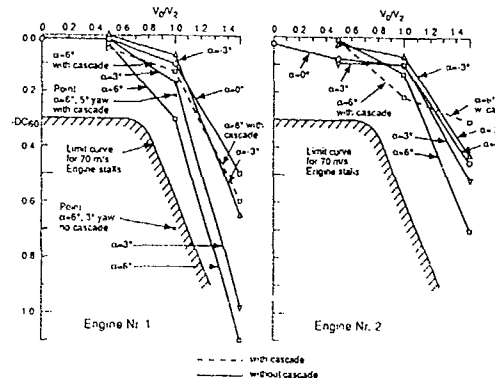


FIG 6.14 DC60 DISTORTION PARAMETER VERSUS VELOCITY RATIO AND ANGLE OF INCIDENCE, INFLUENCE OF CASCADE

### 2.6.3.2 The Fixed Horizontal Axis Intake-Harrier-Type (Ref. 6.20)

#### 2.6.3.2.1 Design Problems

Fig. 6.15 shows the general configuration of the Harrier. The special problems of horizontal V/STOL intakes arise from the mutually contradictory design requirements for cruise flight and vertical lift off conditions.

large mass flow at very low forward speeds  
comparatively low mass flow at high forward speed over a large range of incidence.

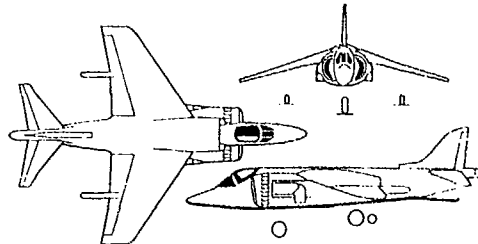


FIG 6.15 V/STOL LIGHT ATTACK AIRCRAFT "HARRIER"

The requirements are difficult to achieve with a fixed geometry inlet but can be obtained by means of variable geometry.

The large mass flow required at low speeds needs a large entry area for the intake. Thus, during high-speed cruise at low altitude the airflow spillage is large which leads to large preentry drag, which may be as great as 50 to 80 percent of the drag of the rest of the aircraft. Hence, for low altitude cruise, the cowl must be designed to achieve a large thrust to minimize this spillage drag. At high altitude the problem is much less important, although still significant. Finally, because the intakes are large, the forces on the intake are important for stability as well as the usual stress force on the cowl.

#### 2.6.3.2.2 Total pressure Recovery

The total pressure recovery in an intake with rounded entry lips varies with the mean entry Mach number as illustrated in Fig 6.16. A sharp lip intake at  $M_0 = 0$  and 0.2 is also shown.

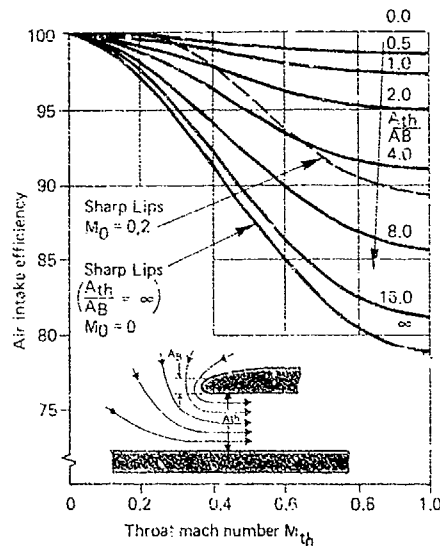


FIG 6.16 THEORETICAL EFFICIENCY OF ROUND-LIPPED AIR INLETS AT ZERO FLIGHT SPEED VERSUS THROAT MACH NUMBER AND AREA RATIO

The equation for pressure recovery is obtained from stream force and momentum considerations with zero onset velocity. These curves show directly that for a given pressure recovery, the suction intensity on the bellmouth is inversely proportional to the bellmouth area.

Since entry losses arise from the thickening or separation of the boundary layers on the bellmouth or near it, they vary with the suction, and therefore low losses require large bellmouth area  $A_B$ , and adequate throat area  $A_{th}$ .

Fig. 6.17 illustrates the relevant bellmouth areas for the auxiliary intakes which are projected in the direction of the appropriate throat flows and therefore do not add to the thickness of the cowl at the main entry.

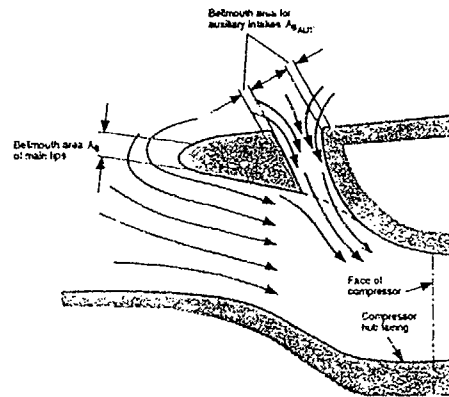


FIG 6.17 RELEVANT BELLMOUTH AREAS FOR THE AUXILIARY INTAKES

#### 2.6.3.2.3 Spillage Drag

When the stream force theorem is applied for forward speeds, when the spillage drag is low, the mean intensity of suction on the cowl is inversely proportional to the projected cowl area. Thus, low spillage drag requires both large cowl area and good shape.

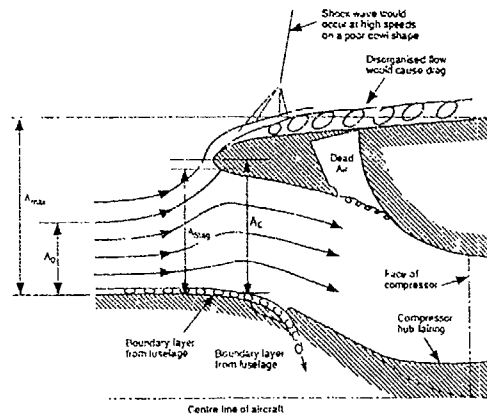


FIG 6.18 SOURCES OF SPILLAGE DRAG AT HIGH SUBSONIC SPEEDS

Fig. 6.18 shows an intake with spillage with auxiliary intake doors closed and its sources of drag. For typical rounded cowls the spillage drag varies roughly as shown in Fig. 6.19.

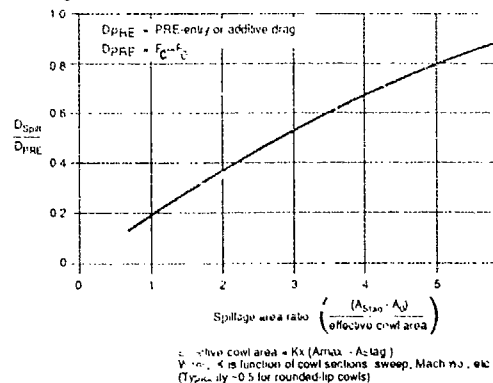


FIG 6.19 SPILLAGE DRAG AT HIGH SUBSONIC SPEEDS

Initially, the main inlets consisted of two side mounted inlets of "D" shape and a single row of six suck-in doors of  $0.585\text{m}^2$  and a throat area of  $0.855\text{m}^2$  and employing boundary layer bleed doors on the side of the fuselage. For the advanced version, the AV-8B, the throat area was increased to  $0.901\text{m}^2$  sq.ft. The inlet cross-section was changed from a half-round to a 2:1 ellipse with a double row of eight suck-in doors of  $0.780\text{m}^2$  sq.ft area to eliminate spillage (Ref 6.21).

Thus under vertical flight conditions a large bellmouth area and adequate throat area are required, while during low altitude cruise large cowl area and small throat area are necessary. Both conditions are vital so that some form of variable geometry is worthwhile in order to improve the efficiency in either condition.

At V/STOL, bellmouth area is more effective than throat area in improving efficiency, so it is usually possible to choose the minimum throat area suitable for conventional flight, then provide sufficient bellmouth area to achieve the target efficiency, preferably in such a way that the cowl area is not restricted at high speeds.

#### 2.6.3.2.4 Velocity Distribution

The problem of velocity distribution and total pressure distribution at the engine face are similar to those of conventional intakes, except that they are increased by the larger area and smaller length to diameter ratio. Adequate description of the distributions is sometimes complicated by variation of static pressure across the compressor face entry and uncertainties regarding the effect of the engine on this variation when measured on models (without an engine present) and the converse effect on the engine.

The worst velocity distributions are due to boundary layer separations caused by adverse pressure gradients in extreme conditions of flight. For example, in the case of a fuselage installation, if the flow is very much reduced, the adverse pressure gradient upstream of the entry acts on the boundary layer on the side of the fuselage and could cause separation forward of the intake entry plane. At extreme incidences particularly at high mass flow, the boundary layer may separate on the inside of the lower lip of the entry and on the adjacent fuselage wall.

#### 2.6.3.2.5 Low-Drag Cowl Section

The maximum area of the cowl tends to be determined by the aircraft's layout, so that the cowl area is given when this area has been chosen. This cowl area is unlikely to be generous, so the maximum velocities at low altitude may be supersonic. Cowl sections, therefore, have been developed which lead to largely isentropic recompressions from highly supersonic peak velocities. Some results of tests on an axisymmetric model are shown in Figs. 6.20a and b. Fig. 6.20a shows almost isentropic recompression from a peak local Mach number of about 1.9. Fig. 6.20b shows a typical curve of spillage drag for this cowl for  $M_0 = 0.9$ . Lower spillage drag will be obtained at lower Mach numbers.

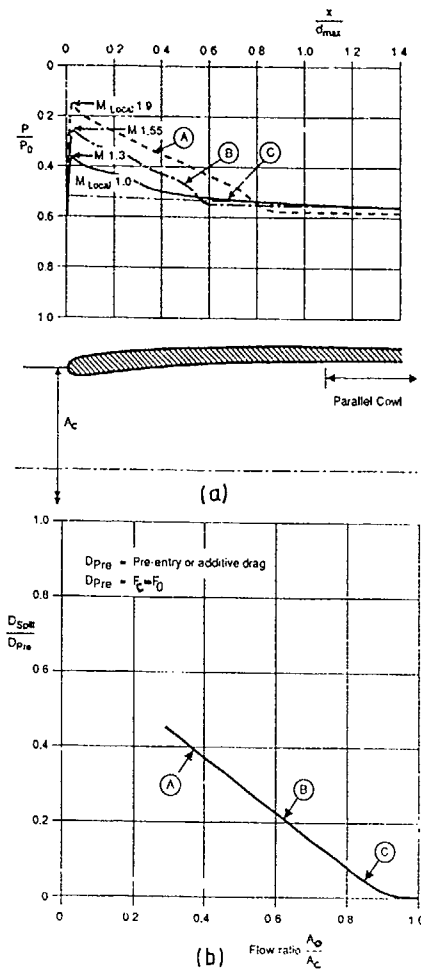


FIG 6.20 CIRCULAR COWL WITH 3 TYPES OF PEAKY PRESSURE DISTRIBUTION, a) PRESSURE DISTRIBUTION  $M=0.9$  b) SPILLAGE DRAG,  $M_0=0.9$

#### 2.6.3.3 Rotating Axis Intake of the VJ-101 (Ref 6.18)

Fig 6.21 shows the general configuration of the VJ 101. Fig. 6.22 shows the design of the VJ-101C lift/cruise engine intake installed on the tilting engine pods at the wing tips.

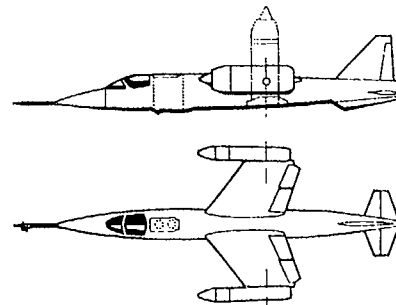


FIG 6.21 VTOL FIGHTER AIRCRAFT "VJ 101"

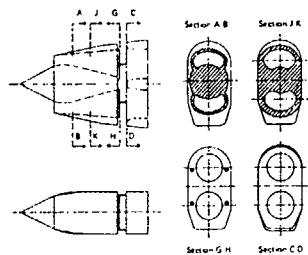


FIG 6.22 "VJ 101" LIFT/CRUISE ENGINE INTAKE

The inherently bad performance of an intake of this kind in the low speed range and at high intake incidence conditions is compensated in this case by the use of an auxiliary intake in the form of a circumferential opening around the nacelle about 15 cm wide. This opening is created by moving the forward part of the intake forward by means of four hydraulic actuators. Fig. 6.22 shows this auxiliary intake in the open position. This inlet was tested under various conditions.

Figs. 6.23 and 6.24 show the pressure loss factor vs.  $V_0/V_2$  and pressure recovery  $P_{t2}/P_{t0}$  vs. Mach number  $M_0$  for various inlet incidence angles,  $\alpha + \sigma$ .

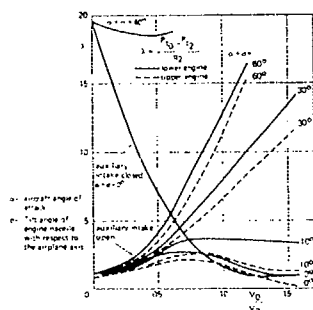


FIG 6.23 PRESSURE LOSS FACTOR VERSUS VELOCITY RATIO AND ANGLE OF INCIDENCE, INFLUENCE OF AUXILIARY INTAKE

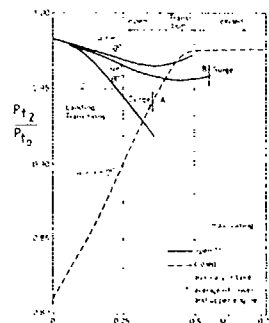


FIG 6.24 TOTAL PRESSURE RECOVERY VERSUS FLIGHT MACH NUMBER AND ANGLE OF INCIDENCE, INFLUENCE OF AUXILIARY INTAKE

Total pressure recovery on a sharp-lip intake is shown to be a function of throat Mach number and forward flight Mach number.

For the auxiliary inlet closed, pressure loss is high for low forward speeds,  $\alpha + \sigma = 0^\circ$  or  $60^\circ$  and pressure recovery is quite low for low flight Mach numbers, even with  $\alpha + \sigma = 0$ .

However, with the auxiliary slot open, losses drop markedly even for high  $\alpha + \sigma$  and total pressure recovery increases for  $0^\circ \leq \alpha + \sigma \leq 60^\circ$  up to  $M = 0.30$ .

These figures show clearly the advantage of changing the inlet geometry (opening the intake slot) with increasing aircraft forward speed and also the need to keep duct incidence,  $\alpha + \sigma$ , low.

#### REFERENCES

- 6.1 Book - Aerodynamics of V/STOL Flight by Mc.Cormick, Academic Press, New York, 1967, 328 pages
- 6.2 Book - Supersonic and Subsonic, CTOL & VTOL Airplane Design by Gerald Cornign, 4th ed., College Park, Md., 1976, 852 pages. (See especially Chapt. XIII, VTOL Aircraft Design, pages 13-1 to 13-51)
- 6.3 "V/STOL - Flugzeuge Entwicklung", MBB Information *Luftfahrttechnik*, BT 007 Nr. 4/82
- 6.4 "Jet Lift by Rolls-Royce", *The Aeroplane & Astronautics*, Jan. 25, 1962, pages 93 - 96
- 6.5 "Short SC-1 Cut-away Drawing", *The Aeroplane*, 10. June 1960
- 6.6 Advanced Aeronautical Concepts - Committee on Aeronautical and Space Sciences, United States Senate, 93rd Congress, July 16 and 18, 1974.
- 6.7 "Supersonic Vectored-Thrust Fighter Design Tested", *Aviation Week & Space Technology*, December 8, 1980, page 51
- 6.8 "Navy Unit to Demonstrate Vertical Attitude Landing", *Aviation Week & Space Technology*, December 15, 1980, page 69 (the "Wire Hanger")
- 6.9 Robinson Jr., C.L. "Navy Plans Emphasis on V/STOL", *Aviation Week and Space Technology*, March 1, 1976, pages 12 - 16.
- 6.10 *Harrier - Modern Combat Aircraft 13*, Bill Gunston, Ian Allan Ltd. London, 1981. See especially pages 40 and 100.
- 6.11 *Harrier: British Aerospace and McDonnell-Douglas AV-8A/B*, Wm. D. Siuru, Jr., Aero Series No.31, Aero Publishers, Inc. Fallbrook, Cal., 1985.
- 6.12 "British Design Ultra-Short Take-off and Landing Aircraft", *Aviation Week & Space Technology*, September 22, 1980, page 23
- 6.13 "McDonnell-Douglas AV-8B Advanced Harrier", *Jane's All the Worlds Aircraft*, pages 346 -
- 6.14 "Hawker P. 1127", *Flight International*, June 6, 1963, page 846.
- 6.15 Zabinsky and Burnham, "Design Consideration for a V/STOL Technology Airplane", *Jour. of Aircraft*, October 1976, page 745



- 6.16 "Dornier LSK", FLUG REVUE, December 1972, page 6.
- 6.17 "Modellversuche zur Gestaltung des Hubtriebwerks-einlaufs eines VTOL-Transportflugzeuges", Molleius and Uhrig, Deutsche Luft- und Raumfahrt Mitteilung; 65-14 ("Do 31")
- 6.18 Hans Redemann, "V/STOL-Waffensystem VJ-101", FLUG REVUE, January 1972
- 6.19 AGARD Conf. Papers No. 135, September 17-21, 1973, paper 28 "Propulsion System of the VJ-101 C VTOL Aircraft" by W. Biehl
- 6.20 Clark and Vasta, "Development of the AV-8B Propulsion System", AIAA-84-2426, October 31 - November 2, 1984.
- 6.21 "Rolls Royce to Test Propulsion System for Supersonic VTOLS", Aviation Week Space Technology, January 3, 1983, page 22

## 2.7 INTAKE DESIGN AND PERFORMANCE FOR MISSILES WITH AIRBREATHING PROPULSION

### CONTENTS

- 2.7.1 INTRODUCTION
  - 2.7.1.1 The relevance of air breathing engines for missiles
  - 2.7.1.2 Types of air breathing propulsion
  - 2.7.1.3 Specific problems of missile intakes
- 2.7.2 CONFIGURATION EVOLUTION AND CONSTRAINTS
  - 2.7.2.1 Early configurations
  - 2.7.2.2 Operational constraints
  - 2.7.2.3 More recent developments
- 2.7.3 ISOLATED INTAKES
  - 2.7.3.1 Intakes for subsonic or low supersonic speed missiles
    - 2.7.3.1.1 Pitot intakes
    - 2.7.3.1.2 Flush intakes
  - 2.7.3.2 Supersonic intakes
    - 2.7.3.2.1 Axisymmetric and derived intakes
    - 2.7.3.2.2 Rectangular and derived intakes
    - 2.7.3.2.3 Design Mach number
    - 2.7.3.2.4 Intake size
    - 2.7.3.2.5 Three dimensional intakes
- 2.7.4 FUSELAGE FLOW FIELD
  - 2.7.4.1 Fuselage with circular cross sections
    - 2.7.4.1.1 Zero incidence
    - 2.7.4.1.2 Non zero incidence
- 2.7.5 MISSILE CONFIGURATIONS
  - 2.7.5.1 Electromagnetic detection
  - 2.7.5.2 Types of steering
    - 2.7.5.2.1 Skid to turn steering
    - 2.7.5.2.2 Bark to turn steering
  - 2.7.5.3 Possible configurations with circular fuselages
    - 2.7.5.3.1 One intake
    - 2.7.5.3.2 Single intake at subsonic speeds
    - 2.7.5.3.3 Twin intakes
    - 2.7.5.3.4 Three intakes
    - 2.7.5.3.5 Four intakes
    - 2.7.5.3.6 More than four intakes
  - 2.7.5.4 Fuselages with wings or strakes
    - 2.7.5.4.1 Wings
    - 2.7.5.4.2 Strakes
- 2.7.5.5 Fuselages with non circular cross sections
- 2.7.6 PERFORMANCE PREDICTION
  - 2.7.6.1 Isolated intakes
  - 2.7.6.2 Flow field around the fuselage
  - 2.7.6.3 Mounted intakes
    - 2.7.6.3.1 One intake
    - 2.7.6.3.2 Several intakes
- 2.7.7 AIR BREATHING MISSILE DESIGN
- 2.7.8 CONCLUSIONS
- REFERENCES

## 2.7.1 INTRODUCTION

### 2.7.1.1 The relevance of air-breathing engines for missiles

For short ranges (430~40Km), the solid propellant rocket is the best means of propulsion because of its technological simplicity.

For medium to long ranges, air-breathing propulsion becomes increasingly advantageous because it is unnecessary to provide oxidant in the missile; intakes are then necessary to capture the external air.

Air-breathing propulsion has certain drawbacks:

- Intakes are necessary;
- missile geometry is more complex;
- engine development time is longer;
- If the missile has an expendable turbojet it will be more expensive (this will not be so if it has a ramjet) but an additional propulsion means may be necessary for a ramjet (boost rocket).

On the other hand it has the advantage that:

- for a given range, the missile is lighter and its overall dimensions are smaller;
- it can fly at low and constant altitude to ensure best penetration;
- its missions can be easily diversified.

### 2.7.1.2 Types of air-breathing propulsion

Two kinds of engine are possible for missile propulsion (Fig.7.1). The turbojet has advantages which increase with range because of the mass and cost of the expendable engine. It is very well suited to subsonic missiles (e.g. Cruise missiles such as OTOMAT, HARPOON...) and in some cases to low supersonic speed missiles  $M_0 < 1.8$ ). The ramjet is a very simple engine, without revolving parts and it is well suited to medium or long ranges but only for supersonic missiles. With subsonic combustion, flights from Mach 1.8 to about 6 are possible; above, supersonic combustion is more advantageous. The disadvantage of this engine is its very low thrust at low Mach numbers. An additional means of propulsion is therefore necessary to boost the missile up to Mach 1.8-2. A rocket booster provides this fast acceleration that also reduces missile response time.

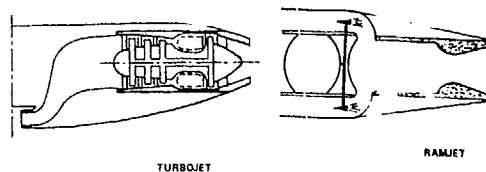


FIG 7.1 AIR BREATHING PROPULSION

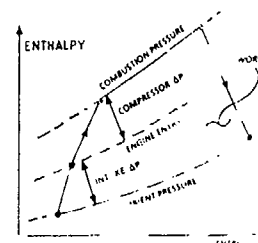


FIG 7.2 TURBOJET CYCLE

Fig 7.2 shows an enthalpy-entropy diagram for a turbojet; both intake and compressor contribute to the total compression of the cycle. For a

ramjet however the whole of the compression process takes place in the intake and the following duct. The intake has also to deliver the correct quantity and quality of flow to the engine throughout the flight envelope.

### 2.7.1.3 Specific problems of missile intakes

For a transport aircraft, the payload is in the fuselage, the wings provide lift and the engines in the nacelles give thrust; interactions exist but are limited in extent. For a fighter aircraft, there is a higher level of integration and fuselage and nacelles are often amalgamated but wings are still separate entities. For missile configurations, integration is carried a stage further and consequently, intakes perform their primary function of capturing the air flow but also produce a large share of the external aerodynamic forces (lift, drag) as shown in Fig.7.3.

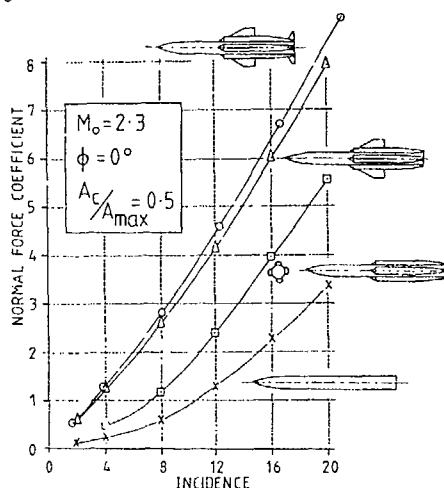


FIG 7.3 LIFT COMPONENTS ON A TYPICAL HALF AXI-SYMMETRIC INTAKE CONFIGURATION

The very high manoeuvrability required involves large loading factors which occur at high incidence and sideslip angles. The constraints imposed by a human presence for fighter aircraft disappears for missiles. For these very difficult situations intakes must still correctly perform their primary function. The missions being diverse, the flight envelope is wide and the intakes must supply the engine under all conditions of Mach number, altitude and attitude with the correct air quantity at high pressure recovery and with low distortion of the airflow.

Although there are no landing and take-off phases so that large mass flows at low speed are not a problem for missiles, some difficulties can appear during the boosted phase with the intakes closed either at the intake or at the engine face. However, missile intakes are required to perform for a single flight, possibly after a long storage time and therefore low cost and high reliability are essential.

### 2.7.2 CONFIGURATION EVOLUTION AND CONSTRAINTS

#### 2.7.2.1 Early configurations

The first air breathing missiles were experimental vehicles for testing ramjets, and therefore without operational size constraints.

Figure 7.4 shows a sketch of such a missile with separated functions (fuselage, wings, nacelles).

The payload is in the body and there is low interference between the fuselage flow field and the air flow captured by the intakes. The intakes have good performance, but on the other hand, the missile is heavy and bulky and its drag is high. Such missiles were developed: e.g. BOMARC (USA), BLOODHOUND (C.B.), SIRIUS CT 41 (Fr.) (Fig.7.5) in the 1950s.

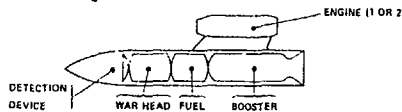


FIG 7.4 AIR BREATHING MISSILE WITH SEPARATED FUNCTIONS

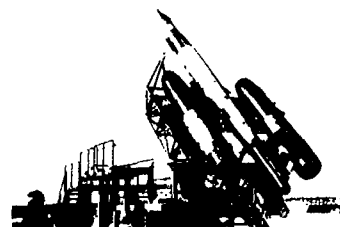


FIG 7.5 SIRIUS CT41(Fr.)

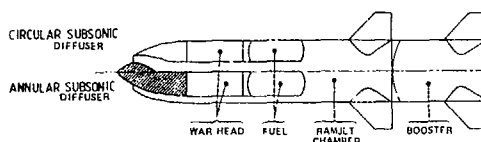


FIG 7.6 FIRST INTEGRATION FOR AIR BREATHING MISSILE

After that, a first integration appeared with an intake in the nose of the missile (Fig.7.6) and a jettisonable rocket booster located at the other end. This configuration has several advantages:

- compactness,
- good intake performance (without interference from wing or fuselage),
- low drag, and
- possible skid-to-turn steering, (see 27521) but also various drawbacks:
- poor diffuser integration (circular annular diffuser),
- lower warhead efficiency,
- difficulties for homing device integration, and
- tendency for missile configurations to have excessive length

Such missiles have been built e.g. TALOS (USA) Fig.7.7, SEA DART (C.B.) Fig.7.8, VEGA (Fr.) Fig.7.9 and STATALTIX (Fr.) Fig.7.10. The Russian missile SA4 CANEF (Fig.7.11) is unique in having an annular intake located after the payload.

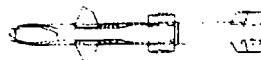


FIG 7.7 TALOS (US)

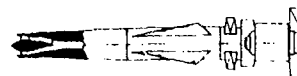


FIG 7.8 SEA DART (UK)

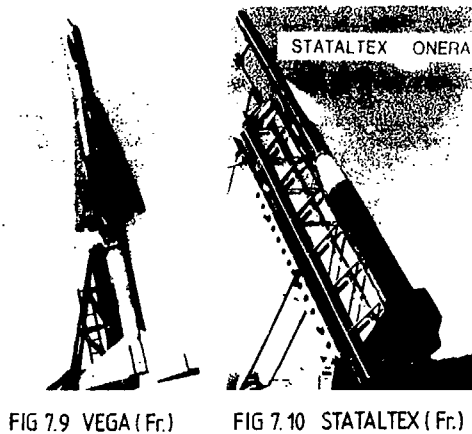


FIG 7.9 VEGA (Fr.)

FIG 7.10 STATALTIX (Fr.)



FIG 7.11 S4 GANEF (USSR)

#### 2.7.2.2 Operational Constraints

For medium to long range missiles, air-breathing propulsion is appropriate but the internal missile arrangement must take into account various constraints, which were solved without difficulties with a rocket engine.

A high degree of compactness is essential for aircraft carriage (especially by small European fighters) or container storage.

A modular design is the best means of separating the various functions:

- detection (hom'ing head),
- attack (warhead),
- propulsion (fuel tank, engine, booster)

Low visibility from electromagnetic, infrared, and optical detection and shapes and materials to give this are essential. Missiles must be increasingly manoeuvrable; two kinds of steering are possible: bank-to-turn or skid-to-turn (7.7.2).

Longer ranges impose new missile geometries with high lift-to-drag ratios and flight envelopes become wider.

For missiles, reliability, simplicity and low cost are essential and conventional industrial experience can sometimes be a handicap.

#### 2.7.2.3 More recent developments

Configurations have changed to respond to these operational constraints. Air flow captured by the intake depends strongly on the flow field around the fuselage; this can be an advantage or a disadvantage according to the location. Missiles have been built SA 422 (Fr.) Fig. 7.12, with one intake, or such as SCORPION (a French study)

Fig. 7.13, with four side intakes.

In a second step, compactness has been improved by integration of the rocket booster with the ramjet combustion chamber, which was left void in previous configurations (Fig. 7.14).



FIG 7.12 SA.422



FIG 7.13 SCORPION PROJECT (Fr.)

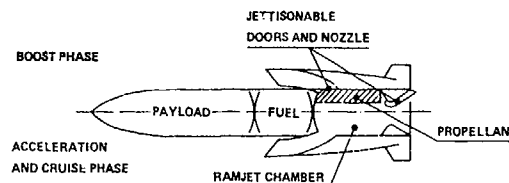


FIG 7.14 MISSILE WITH INTEGRATED BOOSTER

Two drawbacks appear with this integration:

- During the carriage and boost phases, the intake may be closed at the downstream end of the diffuser, this causes drag and can induce intake instabilities such as buzz (see Section 2 of Chapter 2).

- at the end of the boost phase, it is necessary to jettison both the booster nozzle and the diffuser doors and then to ignite the ramjet in a very short time to minimise deceleration.

Some variants of integration are possible. Figure 7.15 shows a missile configuration without jettisonable parts. The booster nozzle is located at the end of an axial extension tube connected to the booster. During the boost phase, the air flow captured by the intakes flows through the annular engine chamber and it is possible to ignite the ramjet during thrust decay to avoid any deceleration. During the cruise phase, the throat is annular and a separation appears at the base of the booster nozzle: good performance is obtained with such a nozzle but thrust alignment is difficult. Another drawback of this configuration is the limited compactness.

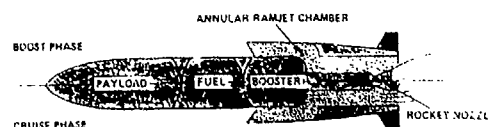


FIG 7.15 MISSILE WITHOUT JETTISONABLE PARTS

Another variant has been proposed in France by ONERA: the unsophisticated or "rustic" missile that does not have a jettisonable booster nozzle and for which only one igniter is necessary during the mission. This missile configuration, Fig. 7.16, is compact and simple. The solid fuel grain located in the ramjet chamber has a conical opening at its aft end, shaping the nozzle. Booster performance is lower and thrust alignment is more difficult but results in a lower cost missile. At the end of the boost phase, solid fuel is ignited and supplies gas which burns with the air captured by the intakes. Flight tests carried out in France have demonstrated the feasibility of such a concept.

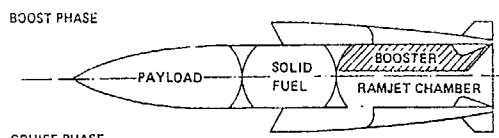


FIG 7.16 "RUSTIC" MISSILE

### 2.7.3 ISOLATED INTAKES

Before installing intakes on a fuselage, it is necessary to make a survey of different intake types and evaluate their advantages and disadvantages and performance.

#### 2.7.3.1 Intakes for subsonic or low supersonic speed missiles

##### 2.7.3.1.1 Pitot intakes

The Pitot intake is a slightly divergent tube located in the freestream (Fig. 7.17). When designed for subsonic or low supersonic Mach numbers, the lips are blunt and in a supersonic flow, a normal shock wave appears in front of the intake. At critical flow conditions, this shock is located in the intake entry plane. The pressure recovery obtained is just lower than the efficiency of the normal shock wave (Fig. 7.18), the difference resulting from viscous effects.

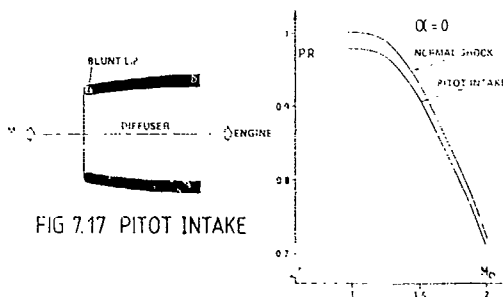


FIG 7.17 PITOT INTAKE

FIG 7.18 PITOT INTAKE PRESSURE RECOVERY

This type of intake has notable advantages:

- high simplicity with consequences on mass, cost, design...
- good integration with any possible front shape,
- low sensitivity to changes in incidence and sideslip angle.

##### 2.7.3.2 Flush intakes

The definition and working principle are described in Figure 7.19. These intakes can be wholly integrated in a fuselage, without external

protrusion; some advantages are:

- low drag,
- small overall dimensions,
- small Radar cross-section.

The working principle is based on the formation of two counter-rotating vortices along the sharp leading edges of the surfaces leading up to the entry plane. These vortices deflect the fuselage boundary layer out of the intake but drag the external flow into the intake by their rotation. These intakes also have some drawbacks:

- high attitude sensitivity (particularly at negative incidence),
- limited pressure recoveries, especially if the upstream Mach number exceeds unity,
- large internal volume requirement (the intakes are long)

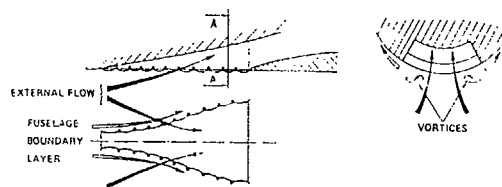


FIG 7.19 FLUSH INTAKE DEFINITION AND WORKING PRINCIPLE

It is possible to increase the performance of such intakes by moving out the lip giving a combined flush and Pitot intake; the American HARPOON missile is equipped with such an intake.

##### 2.7.3.2 Supersonic intakes

In this section, we consider missiles flying at Mach numbers above about 1.8-2 for which Pitot intakes are no longer efficient.

At the end of World War II, OSWATITCH proposed new supersonic compression concepts whose principles are recalled in Figure 7.20. Theoretically a compression ramp can progressively deflect the upstream flow, until sonic flow is obtained; after that, a subsonic diffuser continues the deceleration. This isentropic compression is realised without shock waves and only the friction on the walls increases the entropy. Three variants exist as shown in Figure 7.20: the compression can be completely external, completely internal or a mixture of the two.

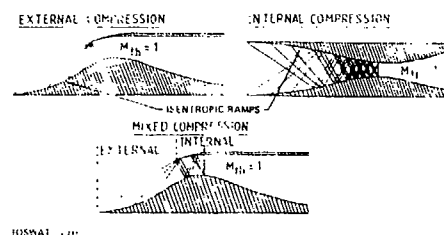


FIG 7.20 TYPES OF SUPERSONIC COMPRESSION

The pressure recoveries theoretically possible with these intakes are very high, but in practice, some modifications are necessary. For several reasons, the isentropic ramps are often changed into multi-wedge ramps because (a) the leading edge is too slender, and (b) the ramp is long and is too difficult to manufacture. The

compression profile is also only correct for one Mach number and incidence and a continuous compression cannot be achieved in practice with small intakes. Thus compression is often obtained by successive flow deflections initiated by a succession of inclined shock waves.

Another restriction is that in practice the Mach number at the end of supersonic compression must be greater than one (generally about 1.4). For external supersonic compression, this results from conditions at the focus point of the oblique compression waves which imposes a limited overall deflection. For internal compression, the minimum section must be larger than the sonic throat area to allow flow starting.

A mixed internal and external supersonic compression is a good compromise for upstream Mach numbers over about 2.5; the relative "merit" i.e. a combination of both internal efficiency and external drag for the various compression concepts is shown in Figure 7.21. This Figure also indicates the potential benefits on performance that can be available by incorporating variable geometry into an intake. By adapting the compression geometry, cowl angle or aft spill system to suit the flight conditions, increased performance and flow stability become available for the price of complexity, weight and cost.

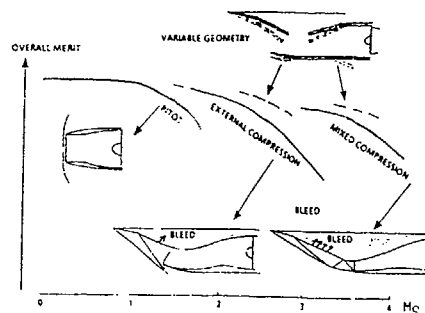


FIG 7.21 APPLICABILITY OF INTAKE TYPES OVER A RANGE OF MACH NUMBERS

For the design of compression ramps, it is much easier to choose two-dimensional flows; this leads to two main types of intake: axisymmetric and rectangular.

#### 2.7.3.2 Axisymmetric and derived intakes

A sectional view of an axisymmetric intake is given in Figure 7.22. It is possible to provide an internal boundary layer bleed at the end of the central body; the flow thus captured can be sucked out through hollow struts.

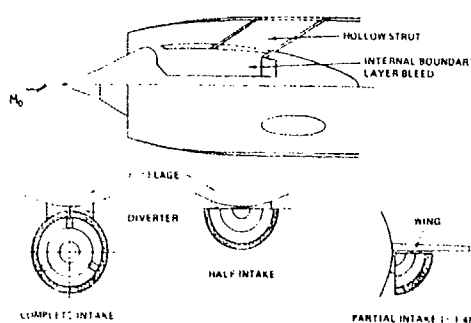


FIG 7.22 AXISYMMETRIC AND DERIVED INTAKES

Some variants are possible:

- a complete axisymmetric intake,
- a half intake,
- a partial intake, which can be located under a wing/body junction.

Figure 7.23 presents some axisymmetric intake geometries studied in France, with different compression profiles. Pressure recoveries obtained are compared in Figure 7.24; the advantage of an internal boundary layer bleed and of a progressive compression central body is highlighted. Figure 7.25 shows that the best intake at zero incidence (isentropic profile) is more sensitive to the angle of incidence and a compromise must therefore be established. It is also necessary that the cone shock is outside the cowl lip at  $\alpha = 0$  to obtain the best performance at incidence, but additional drag will result from the consequent flow spillage at  $\alpha = 0$ .

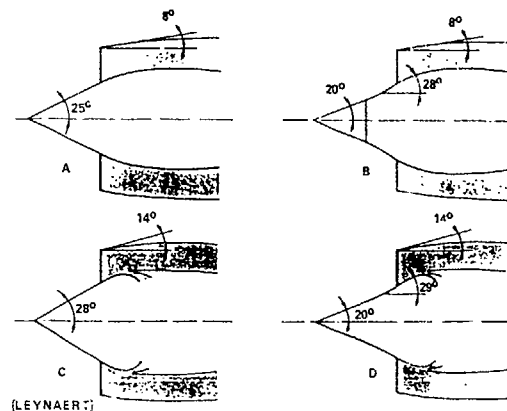


FIG 7.23 AXISYMMETRIC INTAKE GEOMETRIES

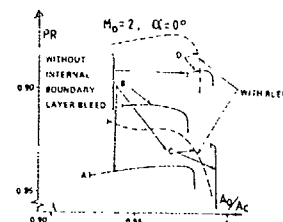


FIG 7.24 AXISYMMETRIC INTAKE PERFORMANCE

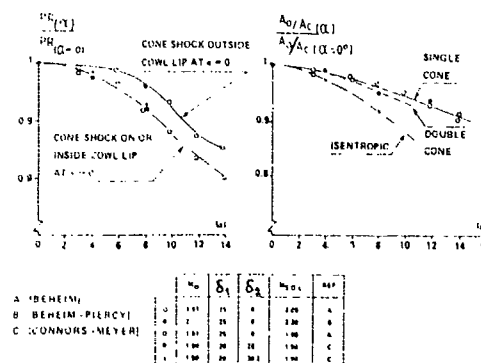


FIG 7.25 INCIDENCE EFFECT ON AXISYMMETRIC INTAKES

Other data on pressure recovery and flow capture for axisymmetric intakes are given in Section 5 of Chapter 1.

Axisymmetric intakes have a number of advantages:

- good structural rigidity, (and hence lower mass),
- possible high performance,
- no roll effects,
- medium incidence sensitivity,
- possibility of variable geometry by central body translation.

They must be compared with the drawbacks:

- maximum performance at zero incidence,
- difficulty of closing the intake during the aircraft carriage phase.

For the derived intakes, the incorporation of sidewalls leads to lower performance: the attitude sensitivity (incidence and sideslip angle) is higher, (which may or may not be favourable); and the integration with diverters is more difficult.

### 2.2.2.2 Rectangular and derived intakes

A sectional view of a rectangular intake is shown in Figure 7.26. It is possible to modify this geometry by wrapping the intake partially or completely around the fuselage. The latter case leads to an annular intake where its low height compared with the body radius leads to quasi two-dimensional flow locally.

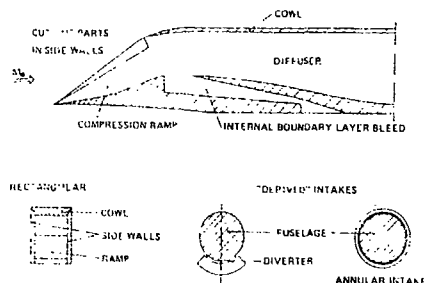


FIG 7.26 RECTANGULAR AND DERIVED INTAKES

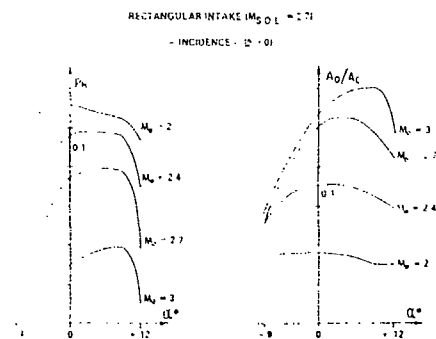


FIG 7.27 INCIDENCE EFFECT ON RECTANGULAR INTAKE PERFORMANCE

Contrary to axisymmetric intakes for which maximum pressure recovery is obtained at zero incidence, the performance of rectangular intakes (pressure recovery and mass flow ratio) can increase with increase in incidence (Fig. 7.27). A limit appears when the inclined shock waves become strong. The incidence effect is attenuated for upstream Mach numbers lower than the shock-on-lip value (design Mach number).

Rectangular intakes are very sensitive to sideslip angle (Fig. 7.28). This effect can be reduced by cutting out some parts of the sidewall as shown in Figure 7.29 but pressure recovery increases are accompanied by mass flow losses.

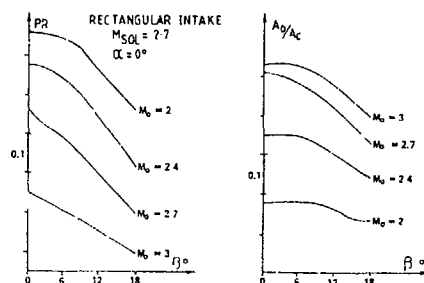


FIG 7.28 SIDESLIP ANGLE EFFECT ON RECTANGULAR INTAKE PERFORMANCE

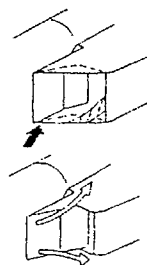


FIG 7.29 SIDEWALL SHAPE CHANGES

Internal boundary layer bleeds are even more necessary than for axisymmetric intakes to obtain high pressure recovery. One located at the end of the compression ramp is practically mandatory and others are useful: sidewalls can be perforated at the location of the shock wave, the cowl can be also perforated also or equipped with a large slot as shown in Figure 7.30. The advantage of boundary layer control increases when  $M_0 > M_{0,L}$  and the intake is 'overadapted' or operating above its design Mach number (see 2.3.2.3). It should be noted that internal boundary layer bleeds increase pressure recovery, at expense of mass flow losses, and improve internal flow stability if the ramjet generates low frequency instabilities.

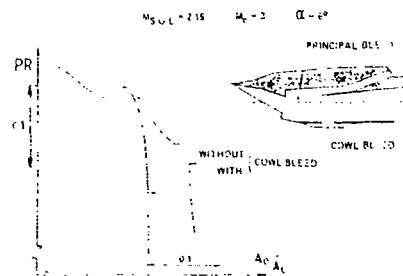


FIG 7.30 COWL BOUNDARY LAYER BLEED EFFECT ON RECTANGULAR INTAKE

Correct diffuser geometry is also very important for achieving high pressure recovery. Figs 7.31 to 7.33 show some results with an overadapted rectangular intake. In this case, the shock waves from the supersonic compression ramp penetrate the intake and impact the internal wall of the cowl and large separations generally appear. With a fixed geometry, very common for

missile intakes, these cases cannot be avoided. For such configurations, Figure 7.33 shows that large diffusion rates should be avoided.

Rectangular intakes have the following advantages:

- possible high performance,
- possibilities of variable geometry,
- possibilities of closing the intake by increasing the front ramp angle,
- favourable incidence effect.

Their disadvantages are:-

- structural rigidity problems, leading to increased mass,
- the necessity for internal boundary layer bleed(s) to obtain acceptable pressure recovery,
- high sensitivity to sideslip angle.

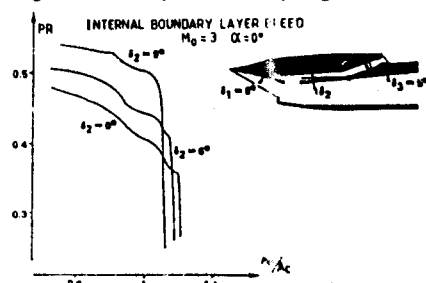


FIG 7.31 DIFFUSER PROFILE EFFECT ON RECTANGULAR INTAKE

RECTANGULAR INTAKE ( $M_{0.1} = 2.3$ )

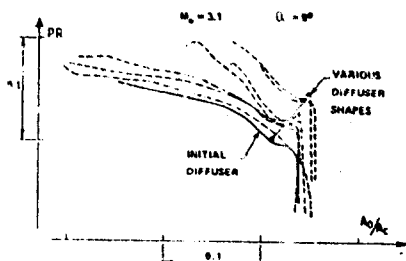


FIG 7.32 DIFFUSER SHAPE EFFECT

RECTANGULAR INTAKE ( $M_{0.1} = 2.3$ )

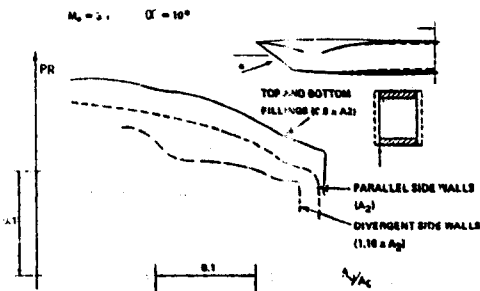


FIG 7.33 EFFECT OF CHANGE OF SUBSONIC DIFFUSER SHAPE

### 2.7.3.2.3 Design Mach Number

Very generally, missiles are equipped with fixed geometry intakes for reasons of cost and reliability but often they have to fly over a large Mach number range. Consequently, it is

necessary to choose a design Mach number  $M_D$  which is the result of a compromise. It is generally taken to be the Mach number at which it is first possible to operate the intake with all the compression system shocks focussed on the lip (ie  $M_D = M_{S.O.L.}$ ). At and above this design Mach number, the capture flow ratio may be unity if the engine demand is such as to match either at a critical or supercritical condition, without a spilled flow drag contribution. In pressure recovery terms, an increased rate of reduction of pressure recovery with Mach number results than is usual for critical type point operation. This follows from the increasingly swept back shock structure entering the intake which induces large boundary layer - shock wave interactions. (See Section 2 of Chapter 1).

Below the design Mach number, the standing off of any shocks from the lip leads to a spilled flow drag component, irrespective of engine demand. Such an operation is more likely to entail subcritical operation, thus requiring an assessment of flow stability margins, whilst at Mach numbers above design the matching dictates a progressively supercritical regime and hence increasing flow distortion problems.

If the design Mach number is low (Case 1 in Figure 7.34), the pre-entry drag is low below this Mach number, but above a thrust loss appears. For the opposite condition, (Case 2), with a high design Mach number the missile develops high thrust but acceleration is reduced when the high pre entry drag is taken into account.

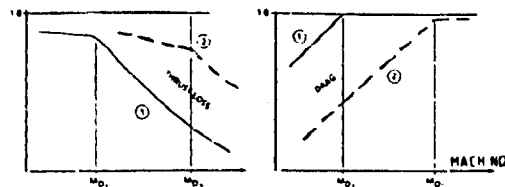


FIG 7.34 IMPLICATIONS OF DESIGN MACH NUMBER

Design Mach number choice is more difficult if the Mach number range is wide and if transonic flight is necessary (eg if a turbojet engine without rocket booster is used). For a large Mach number range, variable geometry for intake (and/or nozzle throat) has to be contemplated but this has to be weighed against the large increase in complexity.

### 2.7.3.2.4 Intake size

The selection of the size of an intake is an important optimisation procedure with implications for both missile performance and manoeuvre capability.

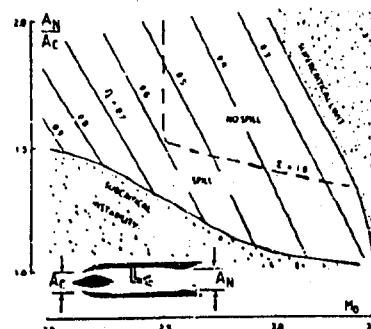


FIG 7.35 RAMJET INTAKE SIZING



It is necessary to obtain a compromise between internal performance and external drag, (without forgetting the pre-entry drag penalties at low Mach numbers). The intake must operate in a stable regime and low engine flow distortion is necessary if the engine is a turbomachine; for a ramjet, the sensitivity to distortion is lower. Some aspects of ramjet intake sizing are illustrated in the Figure 7.35 for a design Mach number of 2.5. It should be noted that a good choice for intake size is not easy.

### 27.3.2.5 Three-dimensional intakes

With three-dimensional intakes there are many possible geometries. There are however difficulties associated with:

- the theoretical optimisation of the compression ramp,
- manufacture of the model and wind tunnel testing.

This leads to more expensive research and development. Three types of three-dimensional intake are presented below.

(a) Chin intake These intakes use the windward upstream part of the missile ogival nose as a supersonic compression ramp. The nose can be inclined to increase the windward compression for the intake and to decrease the external drag of the leeward surface (Fig. 7.36). The diffuser follows the bottom of the ogival nose, the duct cross-section changing from an annular segment to a kidney-shaped duct. It is possible to add wedges just in front of the intake entry to increase the external compression.

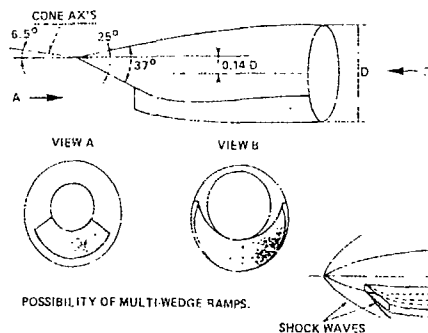


FIG 7.36 CHIN INTAKE GEOMETRIES

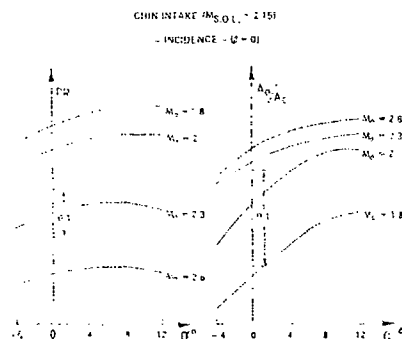


FIG 7.37 INCIDENCE EFFECT ON CHIN INLET

Located under the forebody, these intakes are sensitive to incidence as shown in Figure 7.37 but only slightly to sideslip angle (Fig. 7.38). These sensitivities are accentuated at Mach numbers above  $M_{0.OL}$ .

CHIN INTAKE ( $M_{0.OL} = 2.15$ )

SIDESLIP ANGLE ( $\alpha = 0$ )

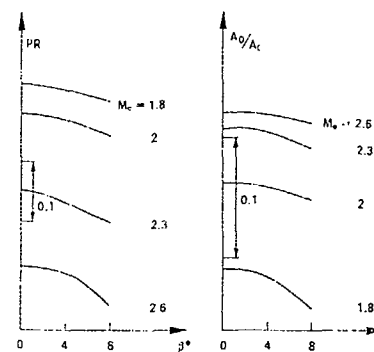


FIG 7.38 SIDESLIP ANGLE EFFECT ON CHIN INLET

(b) "Swedish" intakes. For four-intake missiles, side mounted intakes must exhibit satisfactory performance at a sideslip angle; this led Rosander to propose three-dimensional intakes. The first one is obtained by juxtaposition of two rectangular intakes. Therefore, in a side position, one of the two intakes works at a positive incidence (favourable effect) with very limited sideslip angles. Unfortunately, the second one is then at a negative incidence and consequently its performance is low. The mixture of both captured flows leads to a pressure recovery essentially imposed by the worst intake, which means that the final result is not good, as is shown in Figure 7.39.

The second type of three-dimensional intake proposed by Rosander is also a juxtaposition of two intakes with slightly rolled compression ramps. As above the results are not very satisfactory (Fig. 7.39).

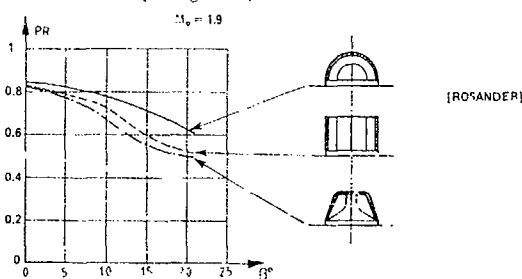


FIG 7.39 SIDESLIP ANGLE EFFECT ON "SWEDISH" INTAKES

(c) Hypersonic intakes Advanced studies are being carried out on hypersonic missiles in the USA. Figure 7.40 shows an example of a possible

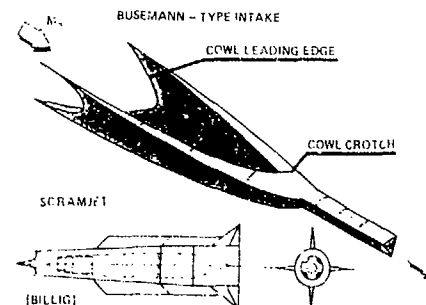


FIG 7.40 HYPERSONIC INTAKES

intake for such a missile powered by a scramjet (Supersonic Combustion Ramjet). It is based on internal supersonic compression but has had to have large amounts of the cowl cut away to allow starting of the internal flow.

#### 2.7.4 FUSELAGE FLOW FIELD

Operational constraints lead to locating the intake(s) downstream of the military payload and therefore in the fuselage flow field. Study of this flow field is necessary to determine favourable intake locations. To obtain high performance, low velocity fields are sought and low energy fields (boundary layers and vortices) are avoided.

##### 2.7.4.1 Fuselage with circular cross-sections

At the present time, this fuselage geometry is almost always chosen for reasons of ease of manufacture, simplicity, structural stiffness and habit. Therefore, it is useful to analyse its external flow field.

##### 2.7.4.1.1 Zero incidence

Zero and very low incidences are typical of cruise at low altitude and the inviscid flow can be analysed relatively easily.

A blunt nose causes a detached bow shock wave generating a loss in total pressure and consequently, intakes located downstream have limited performance (Fig. 7.41). This effect increases with increase in flight Mach number.

A fuselage has two parts: an ogival nose and a cylinder. A break in the curvature appears at the junction, and produces an over velocity region (Fig. 7.42) that is unfavourable for the location of intakes. According to the ogive shape, this discontinuity is more or less pronounced and therefore the effect on intake performance varies, as is shown in Figure 7.43. On the other hand actually on the ogive, there is an undervelocity area favourable for intake location (Fig. 7.44).

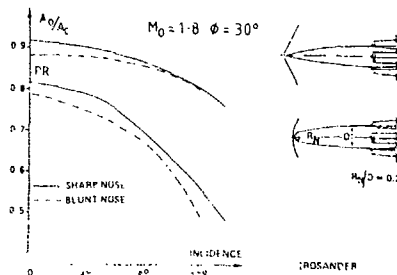


FIG 7.41 EFFECT OF NOSE BLUNTNESS

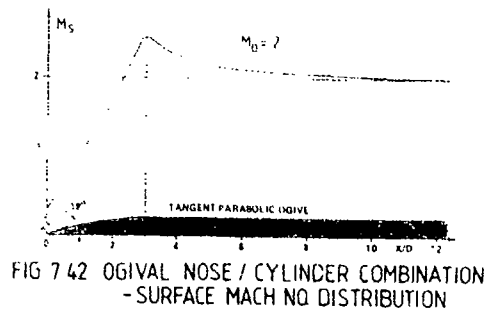


FIG 7.42 OGIVAL NOSE / CYLINDER COMBINATION - SURFACE MACH NO DISTRIBUTION

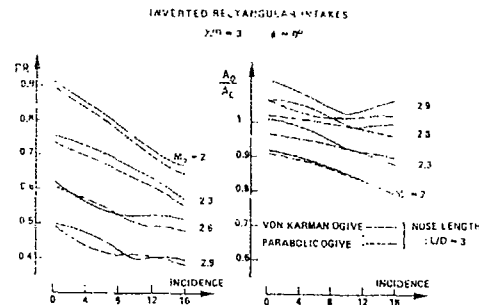


FIG 7.43 EFFECT OF OGIVE NOSE SHAPE

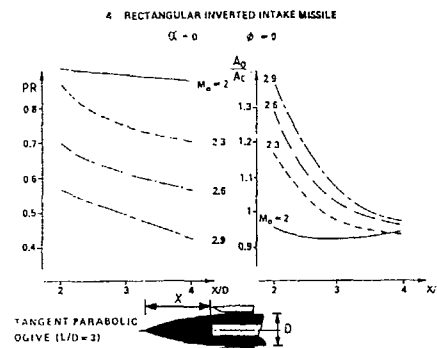


FIG 7.44 INTAKES AROUND THE OGIVAL NOSE

Viscous effects must be added to define the fuselage flow field completely. Along the surface, friction generates a boundary layer and diverters are necessary to spill this low energy air flow out of the intakes, thereby capturing a higher energy air flow. Figure 7.45 shows two examples of differing boundary layer thickness on a fuselage; when the intakes are moved downstream, higher diverters are required and cause a higher drag.

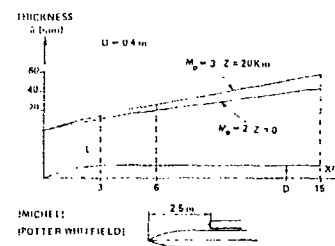


FIG 7.45 TURBULENT BOUNDARY LAYERS

For conventional missiles, Reynolds numbers are sufficient to obtain turbulent boundary layers that satisfactorily withstand the positive pressure gradients, that are created (for example) by diverters or incident shock waves. For missiles flying at high Mach numbers, and therefore at high altitude, it is possible to have laminar boundary layers on the fuselage surface just in front of side-mounted intakes (Fig. 7.46). In this case, the boundary layer is very sensitive to positive pressure gradients and separation can be generated modifying the flow field in front of the intakes. An example is given in Figure 7.47 with underadapted intakes. It is necessary to provide forward compression ramps spilling the fuselage boundary layer upstream of the intakes to limit interactions with shock waves from the intake compression

ramps; without these additional elements, is very performance much lower.

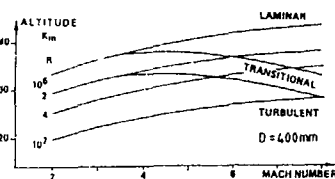


FIG 7.46 BOUNDARY LAYERS

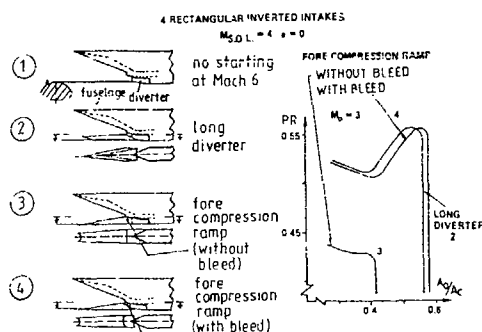


FIG 7.47 BOUNDARY LAYER / SHOCK WAVE INTERACTIONS

This analysis shows there are two interesting locations for intakes:

- around the ogival nose, upstream of the junction,
- around the cylindrical body two or three diameters downstream of the junction.

For the first location, some drawbacks appear:

- a long diffuser,
- mass and friction drag increases,
- forward location of the centre of pressure,
- combination of functions.

For the second location, there is a high sensitivity to incidence and sideslip angle that is generally but not always unfavourable.

#### 2.7.4.1? Nonzero incidence

This attitude is common to flights at high altitude and in manoeuvres. Figure 7.48 shows the nature of the inviscid transverse flow around a cylinder body at incidence. Slender body theory indicates that there are lateral overvelocity areas. The combination of these

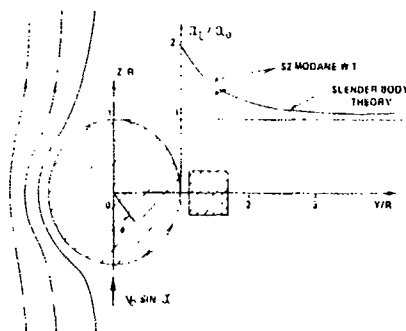


FIG 7.48 INVISCID TRANSVERSE FLOW

transverse overvelocities with the longitudinal velocity leads to the two unfavourable effects for intakes of higher total velocity and incidence.

On the other hand, missile incidence induces an undervelocity in the windward area (Fig.7.49). It should be noted that on the leeward side there is a small reduction in velocity downstream of the ogival nose-cylinder junction (Fig.7.50).

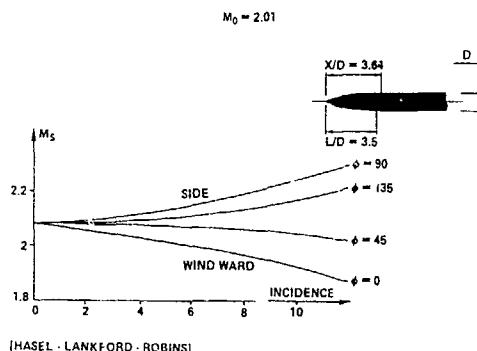


FIG 7.49 TRANSVERSAL FLOW EFFECTS

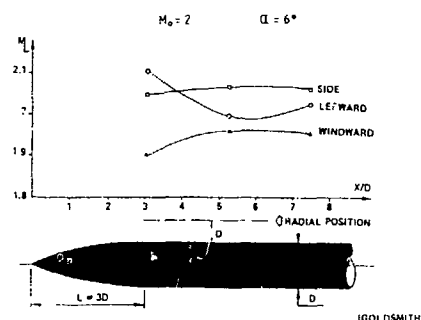


FIG 7.50 LONGITUDINAL MACH NO. DISTRIBUTION IN FLOWFIELD AT  $r = D$

With the fuselage at incidence, the boundary layer moves from the windward side to the leeward side. Consequently, at the bottom, the boundary layer is thinner and therefore favourable for intake location (Fig.7.51). At the top, it becomes thicker and then under the positive pressure gradient effect, separates from the surface to generate vortices (Fig.7.52). Figure 7.53 specifies the longitudinal location of vortex separation position versus incidence for various fuselages and Figure 7.54, the location of vortex cores.

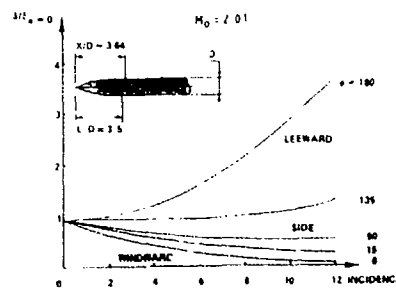


FIG 7.51 BOUNDARY LAYERS

$$M_0 = 2 \quad Re_0 = 2.3 \cdot 10^6$$

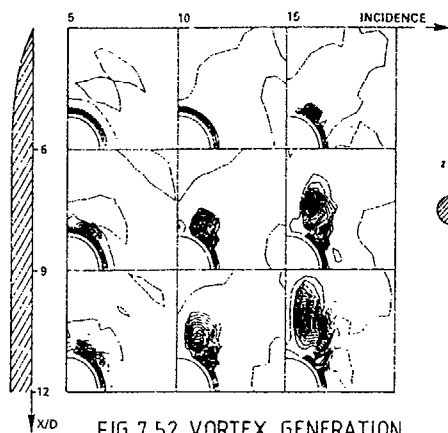


FIG 7.52 VORTEX GENERATION

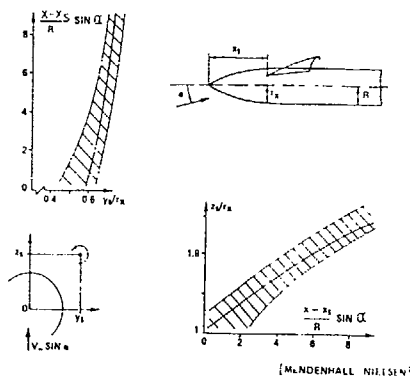


FIG 7.53 LONGITUDINAL LOCATION OF VORTEX SEPARATION POSITION

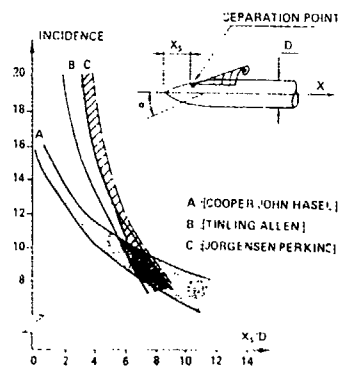


FIG 7.54 LOCATION OF VORTEX CORES

The foregoing analysis shows two unfavourable intake locations:

- the leeward side with its thick boundary layers and vortices,
- the sides with their overvelocities and high local incidences

It should be noted that at high incidence, where the vortices are well formed, an air intake can be supplied efficiently if it is located just between them, on the leeward side, this can be

seen on Figure 7.55 which synthesizes these results.

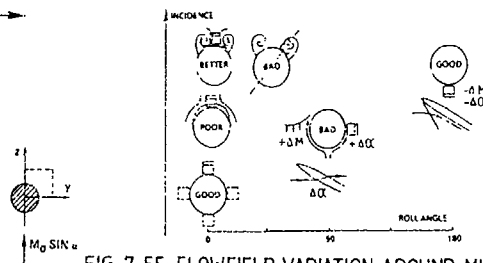


FIG 7.55 FLOWFIELD VARIATION AROUND MISSILE BODY

## 2.7.5 MISSILE CONFIGURATIONS

The location of intakes on a fuselage is the result of a trade-off between different constraints:

- high internal performance (pressure recovery and mass flow rate) depending on fuselage flow field and type of intake;
- external aerodynamic characteristics (drag, lift-to-drag ratio, cruise angle of attack, maximum lift...) often depending on the use of intakes with their diffuser as lifting surfaces;
- operational constraints:
  - overall dimensions (aircraft carriage),
  - separation of functions,
  - visibility;
- and the steering chosen depending on possible missions.

There are a large number of parameters and therefore many possible configurations.

### 2.7.5.1 Electromagnetic detection

In spite of the difficulty, a compromise must be made between performance and detection. Intakes contribute largely to overall Radar Cross-Section, by themselves and by their interactions with the body (Fig.7.56). The R.C.S. value differs according to the form of the intake. The presence of appropriate materials, suitably located both inside and outside the intake is very effective for decreasing the R.C.S. Reflections of electromagnetic waves from the intake/body interface can also be reduced by geometrical modifications and appropriate materials.

- ISOLATED INTAKES  
SCATTERING CENTRES:  
- POINT  
- COWL UP  
- DIFFUSER

- MOUNTED INTAKES  
REFLECTION OF THE  
ELECTROMAGNETIC WAVES

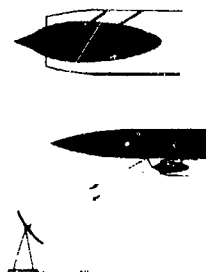


FIG 7.56 RADAR REFLECTION

### 2.7.5.2 Types of steering

#### 2.7.5.2.1 Skid-to-turn steering

With this type of steering, load factors are possible in any roll direction, missiles with axial symmetry (cruciform) are perfectly suited to this control mode (Fig.7.57)

For manoeuvres, response times are very short. Nevertheless, limits appear at high incidence with air-mounted intakes and configurations are not optimal because of the large wetted surfaces giving high friction drag.

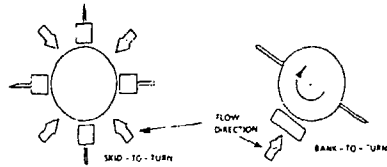


FIG 7.57 TYPES OF MISSILES STEERING

#### 27.5.2.2 Bank-to-turn steering

In this case, load factors are essentially in the pitch plane which imposes missile configurations with a plane of symmetry Fig. 7.57. This type of control has advantages:

- possible high load factors,
  - better lift-to-drag ratios,
  - favourable incidence effects at high altitude and high Mach number cruise flight.
- Obviously, some drawbacks appear:
- sensitivity to sideslip angle,
  - some limitations of negative incidence angle and
  - longer response times, but these may be amply compensated for by the higher load factors.

#### 27.5.3 Possible configurations with circular fuselages

##### 27.5.3.1 One intake

###### (c) Nose intake.

The nose intake is axisymmetric; its performance is described in 27.3.2.1. It is a suitable location for skid-to-turn steering. High pressure recoveries are possible with low incidence sensitivity and without roll effects. In practice, these intakes are no longer used for military applications because all the functions are combined; it has the worst possible integration.

###### (t) Chin intake.

This type of intake is described in 27.3.2.5.

It is suited to bank-to-turn steering with high performance, low drag at zero incidence and very limited overall dimensions.

Unfortunately, functions are partially combined; compatibility of the electromagnetic homing device and the intake is difficult to achieve. From the structural standpoint, the diffuser must have two fixed attachment points on the fuselage (intake and ramjet combustion chamber) creating problems of thermal expansion.

The intake provides no lift and consequently the normal force slope  $C_{N\alpha}$  is limited. Without added wings, this leads to higher cruise incidence and thereby to higher induced drag. Incidence limitations can also appear.

###### (i) Annular intake.

The annular intake is wrapped around the entire fuselage. For an entry section determined by the ramjet ( $A_1/A_2 < 0.5$ ), very small heights are necessary ( $H/D < 0.8$ ). Consequently, two options are possible:

- there is no fuselage boundary layer bleed and very low performance is obtained (Fig. 7.58), even if a small compression ramp is located just in front of the intake;

- the intake is isolated from the fuselage by a bleed and, in this case, difficulties appear in sucking away the boundary layer.

For both solutions, the intake is very close to the fuselage and the incidence effect is then very unfavourable. The Russians have reduced this difficulty with their "SA4 GANEF" missile by using movable wings which give lift while keeping the body at very low incidence (Fig. 7.59). It should be noted that integration is better than for nose intakes but performance is poor.

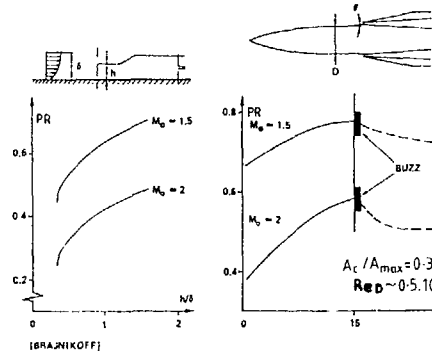


FIG 7.58 ANNULAR INTAKES

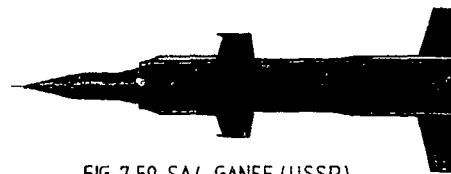


FIG 7.59 SA4 GANEF (USSR)

###### (d) Bottom-mounted intakes.

Locating the intakes at the bottom of the missile (windward side) is an excellent solution, well suited to bank-to-turn steering. Performance is high and it is possible to use the favourable incidence effect, especially for high Mach number cruise at high altitude.

Functions, such as detection, attack and propulsion, are well separated and a high degree of compactness is obtained.

Different types of intake can be adopted for this location (Fig. 7.60):

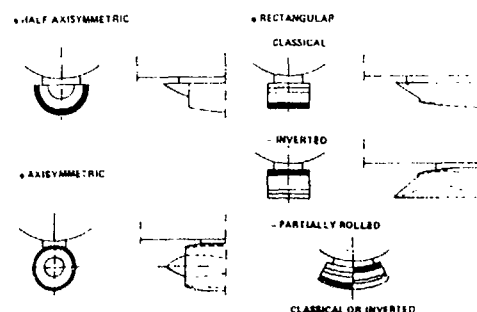


FIG 7.60 BOTTOM MOUNTED INTAKES

- half axisymmetric,
- axisymmetric,
- rectangular, partially wrapped or not.

For the last type, two options are possible:

- the classical position with the compression ramp close to the body,
- the inverted position in which the flow is deflected towards the body.

The second solution allows a gain in performance if negative incidence is required.

#### (c) Top-mounted intakes

From the results of the fuselage flow field study, it can be seen that there are few benefits to be gained from locating intakes at the top of the missile (leeward side), except for missiles with low manoeuvrability whose incidence variations are small.

Nevertheless, certain advantages are possible:

- low electromagnetic detection (the intake is hidden from ground based radars by the body),
- optimum overall dimensions.

The ALCM for instance is more easily stored in the Boeing B52 bomb bays (Fig.7.61).

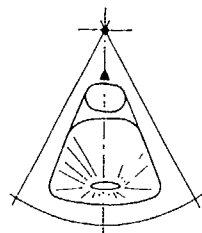


FIG 7.61 A.L.C.M. IN B52 BOMBING BAY

The following Figures show some results concerning single intake performance. Pressure recovery differences between windward and leeward sides increases with incidence (Fig.7.62). This effect can be put to advantage by moving intakes from the sides to the bottom (Fig.7.63). On the other hand, when the intakes are located near the top, and consequently in the vortices, this configuration is unfavourable (Fig.7.64). This effect is increased if the diverter height is small because the intakes capture the fuselage boundary layer (Fig.7.65).

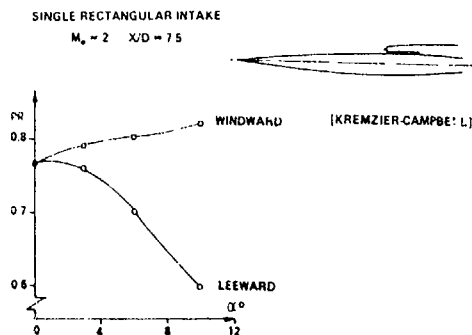


FIG 7.62 INCIDENCE EFFECT

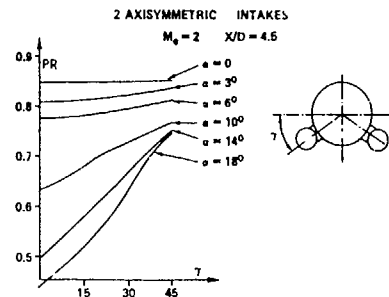


FIG 7.63 ROLL POSITION EFFECT

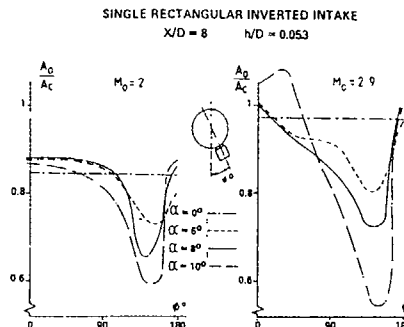


FIG 7.64 ROLL POSITION EFFECT

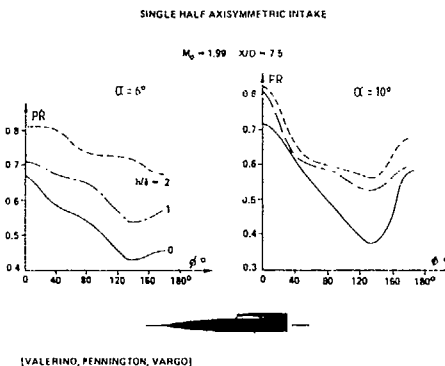


FIG 7.65 ROLL POSITION EFFECT

#### 7.5.2 Single intake at subsonic speeds

Pitot intakes have increasingly poor pressure recovery at Mach numbers above 1.5. However at subsonic speeds they are used universally on missiles with air breathing engines and are usually placed well to the rear of long bodies and feed air to a turbojet via a short S bend duct. Figure 7.66 shows such an example with some details of the SEA EAGLE missile developed by British Aerospace.

Subsonic missile intake studies have highlighted some particular points. Correct design of short S bend duct is very important to reduce the total pressure losses. The main parameters are throat Mach number, offset divergence, length and entry plane cant (See section 5 of Chapter 2)

The role of entry plane stagger or cant in reducing the sensitivity of aircraft fuselage

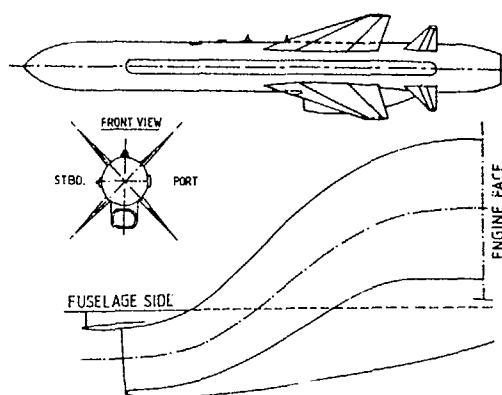


FIG 7.66 SEA EAGLE MISSILE

side intakes to the effects of incidence have been fully discussed in Section 5. Cant however can be used in a different way for an underbody intake. In this case the initial bend of the S duct is reduced in extent so naturally inclining the entry plane from its usual position at right angles to the free stream direction. Movement forward of the outer lip then staggers the intake and restores the entry plane to its original position. The effect of stagger is advantageous at both  $\alpha = 0^\circ$  and  $20^\circ$  (Fig 7.67) but the best performance is achieved by a combination of a small initial bend and a moderate amount of stagger (Fig 7.68).

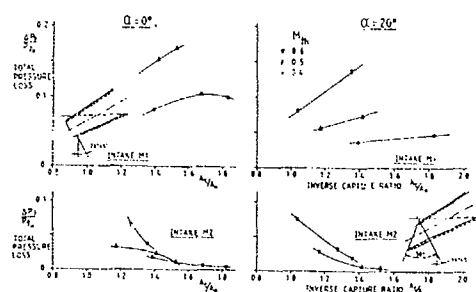


FIG 7.67 PERFORMANCE OF INSTALLED CANTED INTAKE WITH (M2) &amp; WITHOUT (M1) STAGGER

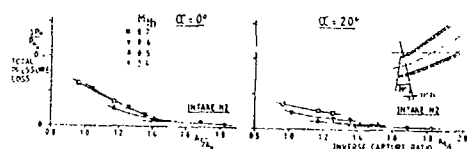


FIG 7.68 PERFORMANCE OF INSTALLED SEMI-CANTED INTAKE WITH STAGGER

### 2.7.5.3.3 Twin Intakes

With twin intakes, bank-to-turn steering is a natural choice. Generally, intakes are located in the windward flow field. The roll location results from a compromise:

If the intakes are diametrically opposed ( $\gamma = 0$ ) (Fig. 7.69), nacelle incremental normal force is a maximum and rectangular intakes are more favourable than axisymmetric ones. This configuration is also best for supplying air to the ramjet chamber.

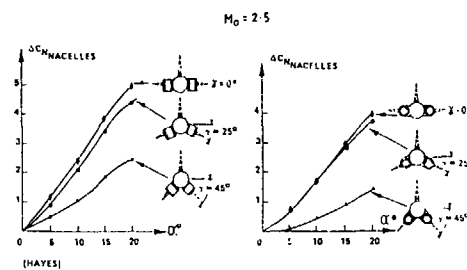


FIG 7.69 TWIN INTAKES: ROLL POSITION EFFECT ON INCREMENTAL NORMAL FORCE

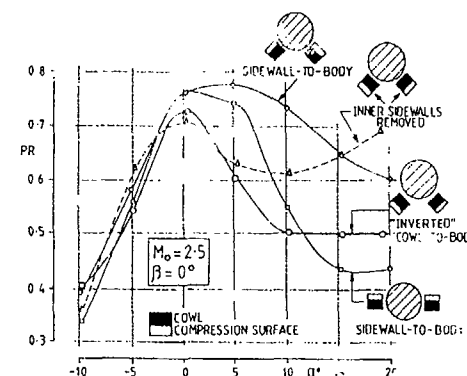


FIG 7.70 TWIN RECTANGULAR INTAKES: EFFECT OF ROLL POSITION AND INTAKE ORIENTATION

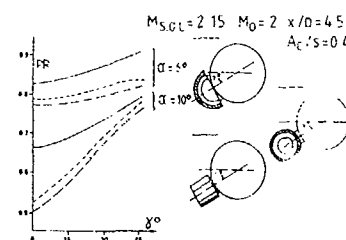


FIG 7.71 TWIN INTAKES: ROLL POSITION EFFECT FOR DIFFERENT INTAKE TYPES

On the other hand, if the intakes are moved towards the bottom, the internal performance increases (Fig. 7.70) and this effect is increased with incidence, more or less according to the type of intake (Fig 7.71).

$$M_{SOL} = 2.15 \quad M_0 = 2 \quad x/D = 8 \quad A_2/S = 0.4 \quad \gamma = 0$$

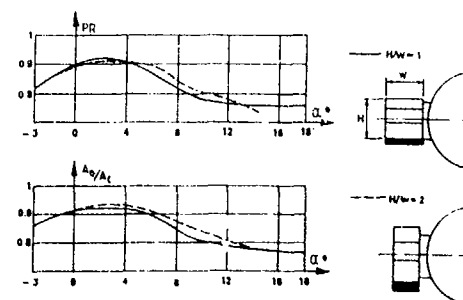


FIG 7.72 TWIN INTAKES: FRONTAL SHAPE EFFECT

Figures 7.72 and 7.73 show the effects of frontal shape and diverter height for two diametrically opposed rectangular intakes.

Longitudinal location has some effect on internal performance, centre of pressure and diffuser mass but normal force is only slightly modified.

As above, different types of intake are possible: half axisymmetric, axisymmetric, rectangular ... and their performance can be increased still more by shielding with wings or adding shields (2.7.5.4).

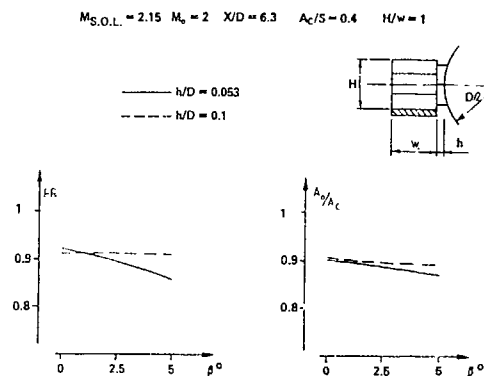


FIG 7.73 TWIN INTAKES: DIVERTER HEIGHT EFFECT

#### 2.7.5.3.4 Three intakes

Two types of three-intake configurations appear according to the chosen steering mode.

For bank-to-turn steering, configurations are obtained by adding one bottom-mounted intake to twin side intakes, not necessarily of the same type (Fig. 7.74).

For skid-to-turn steering, three identical intakes are mounted on the fuselage, at equal intervals. Control with three intakes and thereby with three fins is more complicated but partial integration in the aircraft fuselage can be an advantage (Fig. 7.74).

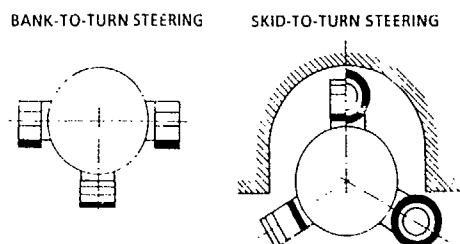


FIG 7.74 THREE INTAKES

#### 2.7.5.3.5 Four intakes

Cruciform configurations are well suited to skid-to-turn steering but possible load factors are limited by leeward intake performance.

It should be noted that lift-to-drag ratios of these configurations are not optimal, two intakes are sufficient to give the lift and the other two lead to additional, mainly frontal, drag.

Different types of intake can be mounted on cruciform missiles: half axisymmetric, axisymmetric, rectangular (classical or inverted\*) or others, like Swedish intakes. Figure 7.75 presents a comparison of these principal types, assuming entry areas and diverter heights to be identical.

\* The specific properties of inverted intakes are considered in 2.7.5.3.5(d)

Half axisymmetric intakes lead to a lower span and thereby a lower lift (Fig. 7.76) which, at a given load factor, imposes a higher incidence; lift is a maximum when two intakes are diametrically opposed. The broader intake, with a given diverter height, has a higher drag (half axisymmetric). For the inverted rectangular intake, the cowl is partially in the fuselage boundary layer and thereby drag is reduced. On the other hand, the half axisymmetric intake, for a given entry area, has greater cowl frontal area and consequently has higher drag.

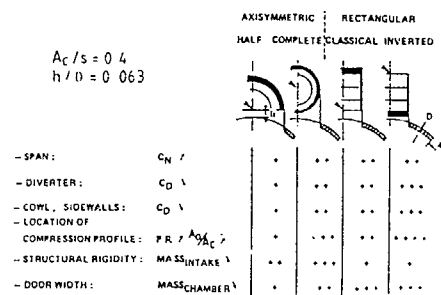


FIG 7.75 COMPARISON OF DIFFERENT TYPES OF INTAKE

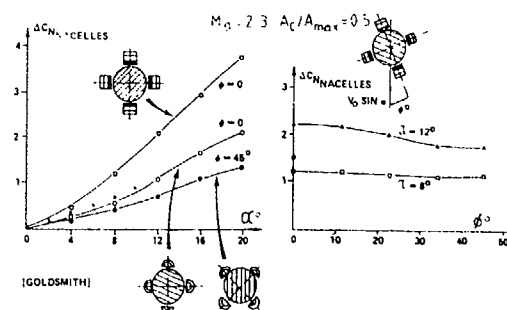


FIG 7.76 FOUR INTAKES: INCREMENTAL NORMAL FORCE

#### (d) Particular aspects of four intake configurations

Before presenting some effects of four intake configurations on internal performance, we have to define a new pressure recovery parameter allowing comparison of various configurations, which take into account every possible roll position. This parameter assumes that ramjet exit throat size as well as fuel-to-air ratio are fixed. Under these conditions, if maximum flight angle of incidence is  $\alpha_1$  (Fig. 7.77), the intake characteristic obtained for the worst roll position at this incidence determines ramjet exit throat size. Thus, at lower incidences, maximum intake performance cannot be used; the constant



engine demand fixes the "pressure recovery usable at zero incidence" for the range:  $0-\alpha_1$ . Obviously, if it is possible to control fuel-to-air ratio in flight with incidence and roll angle then higher pressure recoveries can be used.

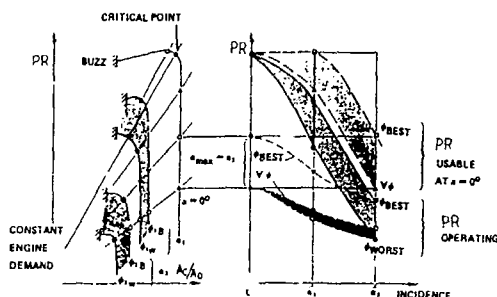


FIG 7.77 PRESSURE RECOVERY PARAMETERS

A further source of intake problems can arise from the use of multi-duct arrangements which join in a single duct at some internal position. At this confluence, it is found that the static pressure level is common to all ducts, which might imply that the total pressure recovery for the individual entries is similar also. In practice, however the overall system pressure recovery is determined by the pressure recovery of the lowest performing individual duct. Consequently, to obtain overall system pressure recovery increases, we have to improve the lowest performing intake by for example, moving the forebody entries away from the leeward intakes. This is considered in more detail in the next section where the effect of wings and strakes on the fuselage flow field is discussed.

Very generally, for multi-intake supersonic missiles, wind tunnel tests show that, when downstream compression increases, the worst operating intake operates subcritically and the other intakes operate in the supercritical regimes to obtain the same pressure recovery. In practice when, the stability limit of the subcritical intake is obtained it is not necessary to continue the test. Nevertheless, it is possible to continue and consecutive characteristics highlighting the limits of the different intakes of the missile (Fig. 7.78) are observed.

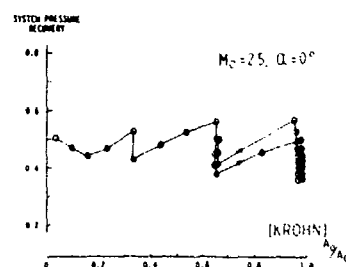


FIG 7.78 MULTIPLE INLET INSTABILITY

#### (b) Effect of diverter height variation

Figure 7.79 shows the effect of diverter height variation using the PR (usable) parameter; a compromise between drag and pressure recovery is necessary. Figure 7.80 shows that this effect is similar for all intake types.

#### 4 RECTANGULAR INTAKE MISSILE

$M_0 = 2$   $\alpha/D = 8$

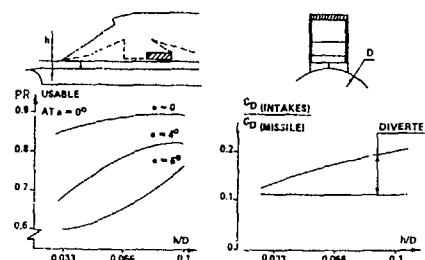


FIG 7.79 EFFECT OF DIVERTER HEIGHT VARIATION

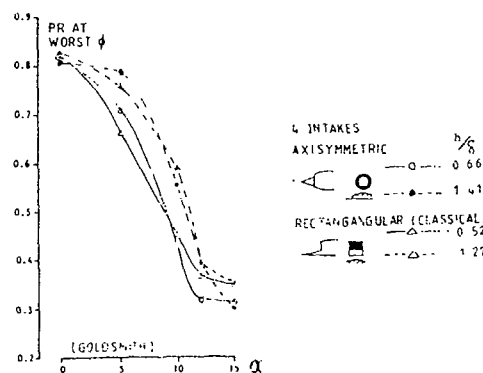


FIG 7.80 EFFECT OF DIVERTER HEIGHT VARIATION

#### (c) Effect of longitudinal location of intakes

The effect of longitudinal intake location appears in Figure 7.81. With upstream locations, over-velocities generated by the ogive-cylinder junction decrease the performance. The same result is obtained with downstream locations where vortices and fuselage boundary layer

#### 4 RECTANGULAR INTAKES

$M_0 = 2$   $\alpha = 0$   $h/D = 0.053$

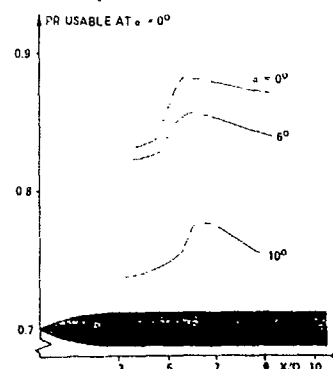


FIG 7.81 LONGITUDINAL INTAKE LOCATION (RECTANGULAR INTAKES)

increase in size. With about 3D ogival nose length, a good compromise between these two effects appears for an intake location at about 5-6D from the nose (Fig 7.82). This conclusion is correct for intakes having a compression ramp

near the fuselage (classical rectangular or axisymmetric intakes) which are sensitive to the flow field near the surface.

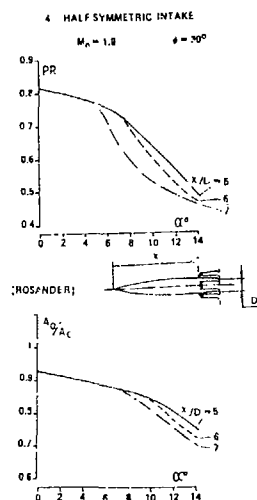


FIG 7.82 LONGITUDINAL INTAKE LOCATION  
(HALF AXISYMMETRIC INTAKES)

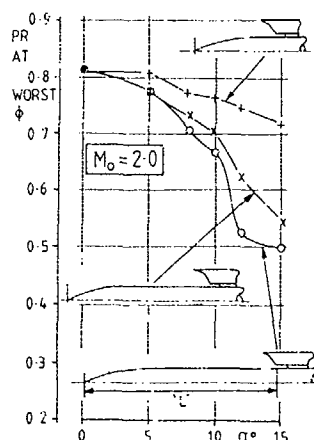


FIG 7.83 LONGITUDINAL INTAKE LOCATION

Figure 7.83 shows, for four inverted rectangular intakes, the overvelocity generated by the ogive cylinder junction is well compensated by increase of local incidence on the intake compression ramp. With these intakes, internal performance, for a forward location is good at high incidence. However, there are the effects on external aerodynamics of a slight variation of normal force coefficient and a forward incremental movement of the centre of pressure (Fig. 7.84) which is destabilizing. A mass increase appears also with these longer nacelles.

For intakes near the junction, some difficulties can appear, especially at high Mach numbers with a laminar fuselage boundary layer. Sharp pointed diverters, (Fig. 7.85), located in front of the cowl, allows inverted intakes to start, but interactions occur with the boundary layer. With intakes located upstream, at low incidence, the diverters are not aligned with the local incidence and partially mask the intake entry area, large mass flow losses are thus caused in

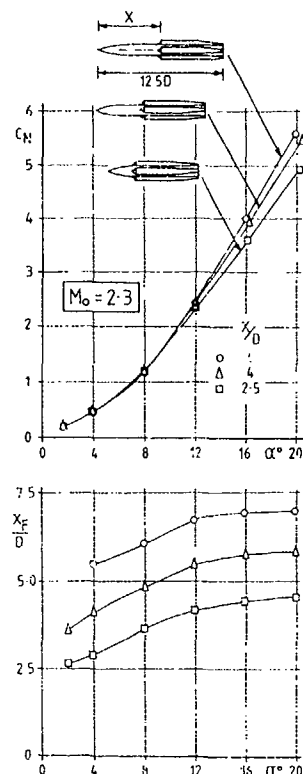


FIG 7.84 EFFECT OF INTAKE LOCATION ON NORMAL FORCE COEFFICIENT & CENTRE OF PRESSURE POSITION AT ZERO POLL ANGLE

the 0-5 degree incidence range. For higher incidences, the windward intake capturing the larger part of the mass flow is no longer obstructed by its diverter.

If the intake is located downstream, nozzles or diverters are located on the cylindrical body and are therefore correctly aligned. At zero incidence, intakes are supplied efficiently but at roughly 10 degrees, a leeward separation appears and leads to a large mass flow loss.

An intermediate location, with foreward compression ramps instead of diverters, allows intake starting and gives best internal performance.

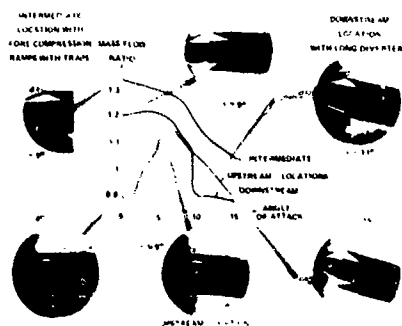
4. RECTANGULAR INVERTED INTAKE MISTRESSES (S. B. INDIAN) (MIST)  
 $M_0 = 0$   $\phi = 0$ 

FIG 7.85 LONGITUDINAL INTAKE LOCATION

### (d) Effect of intake inversion

It is possible to relate incidence sensitivity to location of the initial point of supersonic compression. Half axisymmetric and classical rectangular intakes initiate compression close to the fuselage; already, at low incidence, they capture the fuselage boundary layer and performance is low; higher diverters are necessary to limit this incidence effect but increase the drag. The half axisymmetric intake, the broader one, captures more of the low energy flow and is the poorer solution (Fig 7.86). Internal performance increases with height of the initial compression point: inverted rectangular and half axisymmetric intakes are less sensitive to incidence (Fig. 7.87 & 7.88). It should be noted that inverting half axisymmetric intakes does not give a large pressure recovery increase and can lead to various structural difficulties.

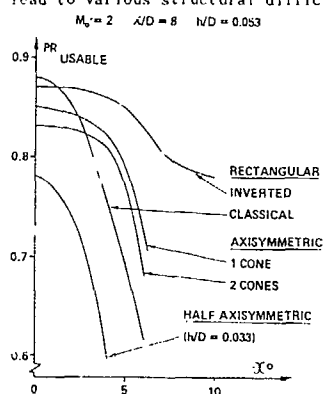


FIG 7.86 FOUR SIDE INTAKES: USABLE PRESSURE RECOVERY AT ZERO INCIDENCE

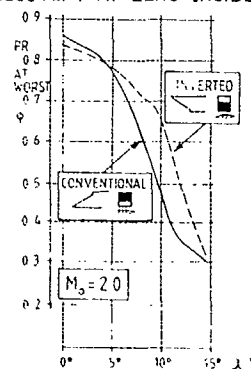


FIG 7.87 EFFECT OF RECTANGULAR INTAKE INVERSION

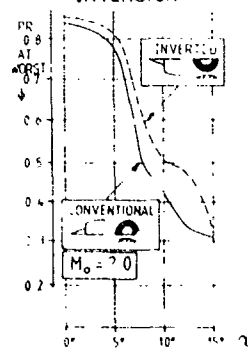


FIG 7.88 EFFECT OF HALF-AXISYMMETRIC INTAKE INVERSION

Figures 7.89 and 7.90 compare rectangular intake performance, respectively at Mach no 6 and 2, according as to whether they are classical or inverted. In both cases, inverted intakes are the best. Figure 7.89 shows, in particular, a large increase in pressure recovery (and mass flow ratio) for the intake located on the leeward side. It should be recalled that the worst intake imposes the overall pressure recovery. Concerning the structural rigidity of intakes, axisymmetric ones are lighter (Fig. 7.75). However if we consider the ramjet combustion chamber, the entry width is a minimum for rectangular intakes and thereby the chamber mass is also a minimum.

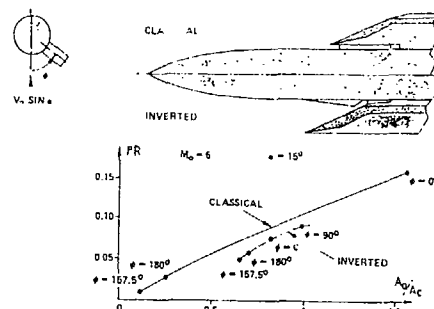


FIG 7.89 FOUR SIDE INTAKES: CLASSICAL & INVERTED

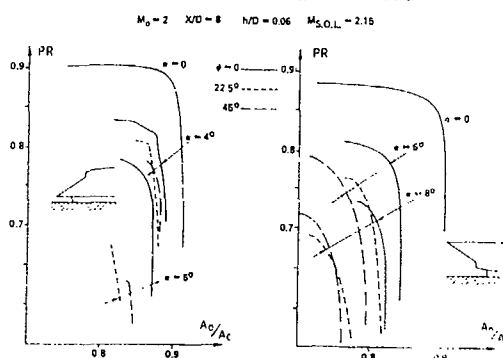


FIG 7.90 FOUR SIDE INTAKES: CLASSICAL & INVERTED

In conclusion, the chart of Figure 7.75 demonstrates the advantages of inverted rectangular intakes, or even axisymmetric ones for cruciform configurations.

Figure 7.91 presents, for a configuration with four inverted rectangular intakes, the effects of certain simplifications to obtain "rustic" or simplified intakes; diffuser length, internal boundary layer bleed and multi-wedge-ramps are very important elements for high performance. It

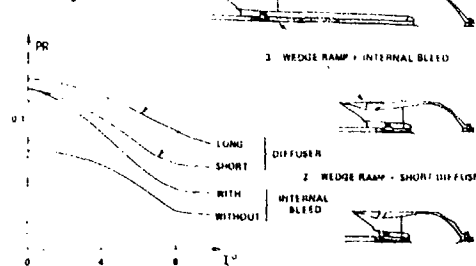


FIG 7.91 FOUR SIDE "RUSTIC" INTAKES

is possible to increase the pressure recovery of such intakes (Fig. 7.92) by cutting back the sidewalls to reduce the local sideslip angle sensitivity but mass flow losses appear.

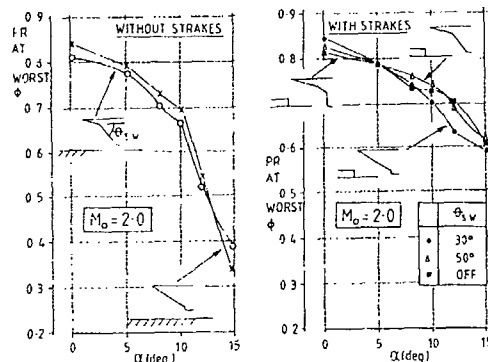


FIG 7.92 EFFECT OF SIDEWALL SHAPE FOR FOUR, INVERTED RECTANGULAR INTAKES

Figure 7.93 shows a small normal force increase and a smaller variation of centre of pressure position with incidence for a four rectangular intake missile by comparison with a twin intake missile. The same results are obtained with half axisymmetric intakes.

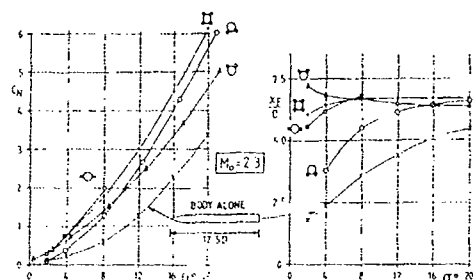


FIG 7.93 NORMAL FORCE COEFFICIENT & CENTRE OF PRESSURE LOCATION FOR RECTANGULAR INTAKES ON A BODY

As, for twin intakes, longitudinal location is a compromise taking into account:

- the fuselage flow field,
- diffuser length,
- centre of pressure,
- possibly, particular attachment points on the fuselage.

It is possible to increase the performance of four-intake configurations by mounting strakes along the fuselage or adding moving wings as for the Russian "SA6 GAINFUL" missile (Fig 7.94).

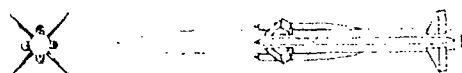


FIG 7.94 S.A. 6 GAINFUL (USSR)

#### 2.7.5.3c More than four intakes

Swedish studies have been carried out with eight-intake configurations. The possible advantages are:

- low overall dimensions,
- a "pseudo"-annular intake for which diverter

integration is easy and inverted rectangular intakes can be used, without starting flow problems.

They are counterbalanced by certain drawbacks:

- the large number of intakes, leading to a more expensive, heavier missile with a higher drag,
- the small intake height resulting in low internal performance and a high incidence sensitivity.

#### 2.7.5.4 Fuselage equipped with wings or strakes

##### 2.7.5.4.1 Wings

It is possible to add wings to a fuselage with the aim of improving the flow field uniformity in front of intakes when located in their windward flow field. This leads to a lower local Mach number, the wings effectively becoming first compression ramps.

These favourable effects for intake performance are counterbalanced by certain drawbacks:

- flow passes around the wings and induces a local sideslip angle which can be deleterious, especially for rectangular intakes.
- wing size must be sufficient to achieve a significant effect; Figure 7.95 compares pressure recoveries obtained with various wing shapes and shows the importance of the span.
- missile overall dimensions are thereby increased, and wings located upstream of intakes move the centre of pressure forward.

With the aim of limiting the local sideslip angle, it is possible to add a sidewall to the wing tip as shown in Figure 7.95.

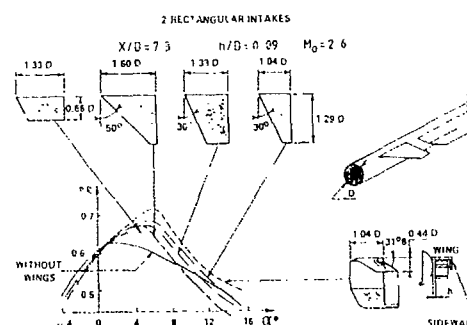


FIG 7.95 WING EFFECT

Under these conditions, the overall span is limited and pressure recovery is increased. A variant is presented in Figure 7.96, a shield integrated with the rectangular intake, replaces the wing with its sidewall. From a structural standpoint, it is easier to design an intake with a shield than to attach wings to a fuselage.

The favourable effect of wings or shields increases with positive incidence. A limit appears when the intake becomes underadapted as the local Mach number decreases. It is obvious that a fuselage equipped with wings leads to bank-to-turn steering.



FIG 7.96 INTAKE WITH SHIELD

### 2.754 Strakes

Strakes are located along the fuselage, upstream of the intakes. Four strakes allow axial symmetry of the missile, which is useful for maintenance of skid-to-turn steering.

The advantage of these strakes is to modify the structure of the vortices appearing at the top of a fuselage at incidence, four small vortices replace the two large ones. Figure 7.97 presents visualisation results showing these four vortices. UK studies suggest locating the strakes just in front of the intakes. Figure 7.98 shows the gain in performance increase so obtained with a four rectangular intake missile. It is possible to optimize the strake effect on intake performance; the main parameters are length, longitudinal location and span (Fig. 7.99). The roll location effect is discussed later.

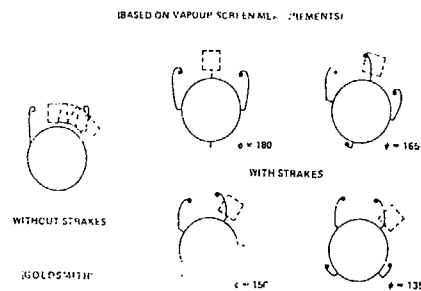


FIG 7.97 FLOW FIELD AROUND FUSELAGE EQUIPPED WITH STRAKES

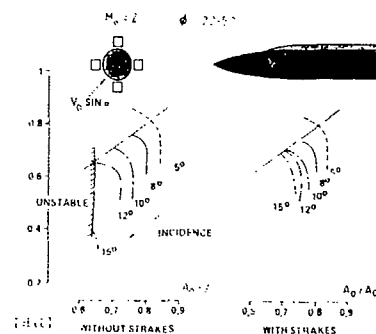


FIG 7.98 STRAKE EFFECT ON 4 RECTANGULAR INTAKES

In France, for the majority of tests, strakes have been located between intakes, as presented in Figure 7.100. With rectangular intakes, the results were not very good, but they were more promising with axisymmetric intakes as presented in Figure 7.101. In this last case, the roll angle effect is very small and the worst intake characteristic is clearly improved.

Recent wind tunnel testing with axisymmetric intakes has shown, for the chosen strakes, that location between intakes was the most favourable for the 0.8 degree incidence range.

As previously with wings, strakes slightly move the centre of pressure upstream and increase drag and normal force. Figure 7.102 shows such results for variation of roll angle for two four-intake missiles. The effects are the same for the rectangular or half axisymmetric intakes.

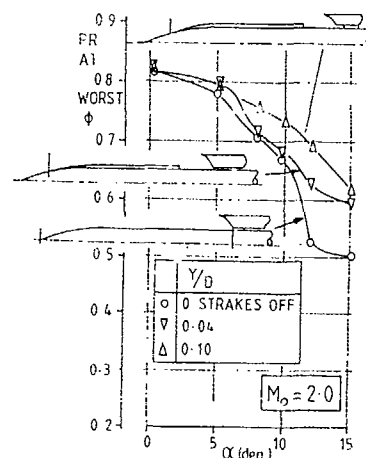
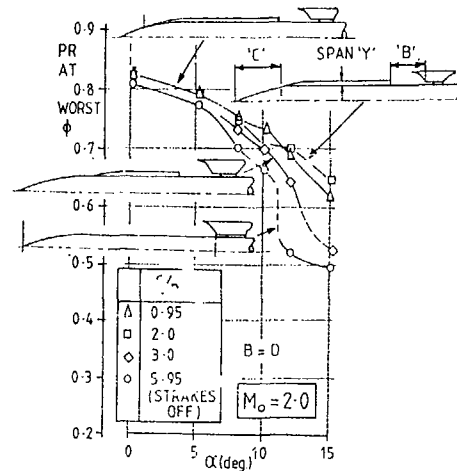


FIG 7.99 STRAKE GEOMETRY & LOCATION FOR OPTIMUM INTAKE PERFORMANCE

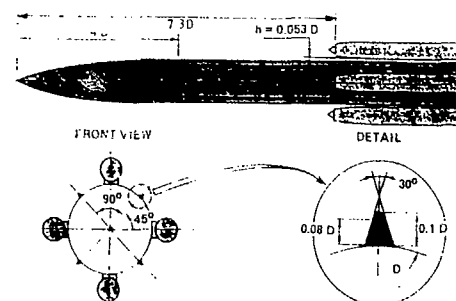


FIG 7.100 FUSELAGE EQUIPPED WITH STRAKES

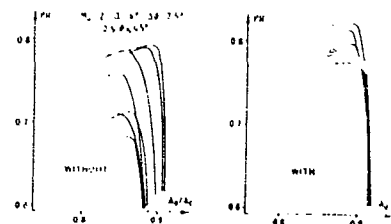


FIG 7.101 STRAKE EFFECT ON 4 AXISYMMETRIC INTAKES

If missile angle of incidence is limited to about 4-5 degrees, strakes are not worthwhile. Above this value, according to their location and size, strakes improve performance, but within a limited range.

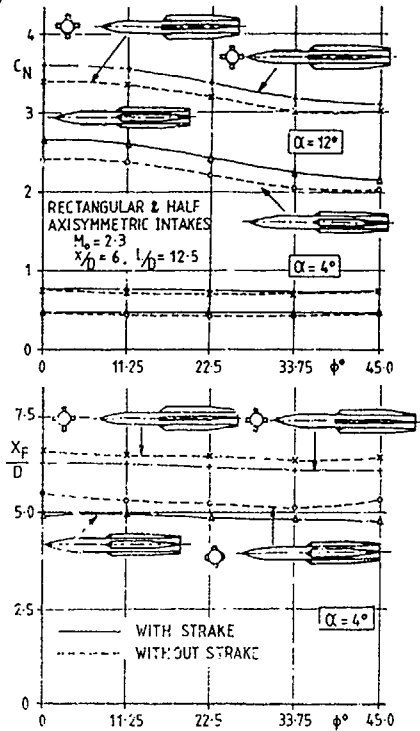


FIG 7.102 EFFECT OF FOREBODY STRAKES ON NORMAL FORCE COEFFICIENT & CENTRE OF PRESSURE POSITION

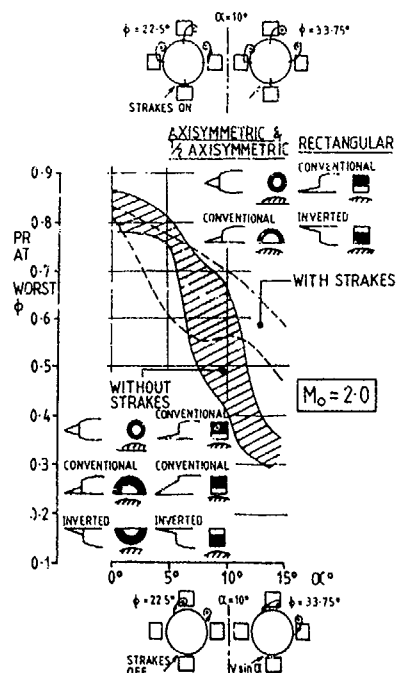


FIG 7.103 SUMMARY OF EFFECT OF FOREBODY STRAKES ON PRESSURE RECOVERY OF VARIOUS INTAKES IN CONVENTIONAL & INVERTED POSITIONS

Fig 7.103 summarises the results showing the effect of forebody strakes on intake pressure recovery for a wide range of intake configuration with sketches of the vortices entering or not the intakes according to incidence and the presence or absence of the strake.

#### 2.7.5.5 Fuselage with noncircular cross-sections

For manufacturing reasons, it is easier to build missiles with a cylindrical body. However, to increase performance and with the possibilities of new manufacturing methods, fuselages with noncircular cross-section can be envisioned and various objectives can be considered:

- optimum integration of the intake(s) in the fuselage flow field,
- a decrease in drag,
- an increase in lift-to-drag ratio,
- a smaller Radar Cross-Section,
- best design for carriage under aircraft.

Interest in these configurations increases with:

- long ranges,
- high flight Mach numbers,
- high flight altitudes,
- bank-to-turn steering.

Obviously, certain difficulties of internal arrangement appear and also manufacturing and structural problems, make the missile more expensive.

Different shapes of fuselage are possible. Figure 7.104 shows two examples but other cross-sections can also be considered: elliptical, square, etc.

Wave-riders are designed according two principles:

- the top is formed from the shape of non-deflected streamlines (minimum drag),
- the shock wave induced by the bottom surface is confined by the leading edges (maximum lift).

- WAVE RIDERS

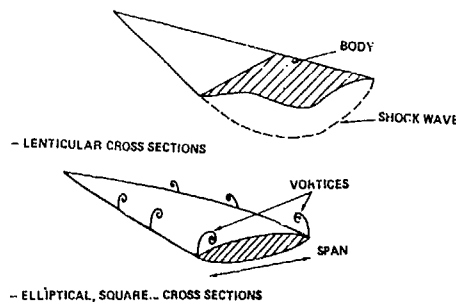


FIG 7.104 EXAMPLES OF FUSELAGE WITH NON-CIRCULAR CROSS SECTIONS

With this design, it is easier to locate an intake in the windward part to obtain high internal performance but the difficulty is that the design is for one angle of incidence and one upstream Mach number. It is not obvious how performance varies from this particular condition.

The other configuration presented in Figure 7.104 concerns a lenticular fuselage. It is designed with the following principles:

- to increase the span, with a constant cross-section (therefore the same volume) in order to obtain higher lift-to-drag ratios,
- to create sharp leading edges in order to generate strong vortices which will increase the lift.

Such a design, the "FIACRE" project, is now under study in France at ONERA (Fig. 7.105). It is obvious that the intake location looks similar to that on the F111 aircraft.

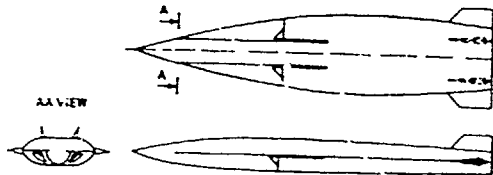


FIG 7.105 FRENCH FIACRE PROJECT

#### 276 PERFORMANCE PREDICTION

For missiles, prediction of internal performance requires considering many cases: generally, only one intake geometry is used, but over a very large flight envelope ( $M_0, \gamma, \beta$ ). In addition, high integration requires finding many compromises between internal and external flow considerations.

Three approaches can be considered: theoretical, experimental or semi-empirical.

The theoretical approach is not yet accurate enough because viscous effects are difficult to evaluate accurately. When that becomes possible, the calculation times will still be very long, even with future computers. In addition, there will be many cases to calculate.

In contrast, an experimental approach is accurate but expensive. In any case, such tests are necessary for air-breathing missile development.

The semi-empirical approach to reduce the number of wind-tunnel tests is very useful, despite its limited accuracy.

#### 276.1 Isolated intakes

A theoretical approach essentially for design is possible either with inclined shock wave theory or by solving the Euler equations, but it does not provide accurate data on pressure recovery. Examples of such results are given in Figures 7.106 and 7.107. Detailed adjustments such as boundary layer control or local shape modifications cannot be based, for the moment, on calculations.

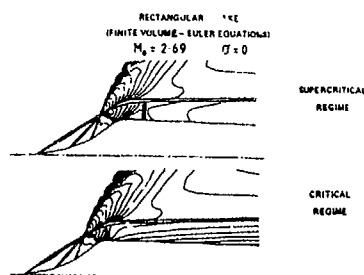


FIG 7.106 RESULTS FROM EULER CALCULATIONS

#### AXISYMMETRIC INTAKE (FINITE VOLUME - EULER EQUATIONS) $M_0 = 1.8 \quad \alpha = 0$

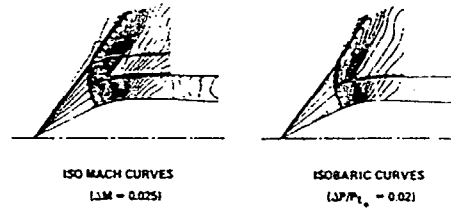


FIG 7.107 RESULTS FROM EULER CALCULATIONS

The semi-empirical approach is based on three components. The supersonic compression is calculated theoretically, the throat field with its boundary layer bleeds is estimated from data banks and semi-empirical methods are used for the diffuser (Fig. 7.108). The overall pressure recovery is estimated by multiplying the efficiencies previously calculated.

The experimental approach is based on models tested in wind tunnels. This method is perhaps expensive but is the only accurate one. Semi-empirical methods are used to limit the number of models to be tested.

- 1 THEORETICAL CALCULATIONS
- 2 DATA BANK
- 3 SEMI-EMPIRICAL METHODS

$$PR = PR_1 \times PR_2 \times PR_3$$

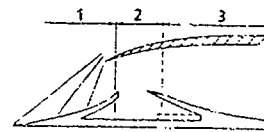


FIG 7.108 SEMI-EMPIRICAL APPROACH

#### 276.2 Flow field around the fuselage

A theoretical approach is possible without difficulties at low incidence; for different fuselage shapes the Euler equations can be solved and associated with boundary layer calculations. These results are necessary to choose the location of the intakes.

At moderate incidence, prediction of the vortex separation lines on the ogival nose is difficult and it is no longer possible to dissociate inviscid flow field calculation from boundary layer calculation. In addition, if separation is initiated correctly in the calculation, it is necessary to verify that viscous effects in the vortices are correctly taken into account by the method chosen.

At the moment, the experimental approach is the most accurate method for tracking the vortices and flow field analysis can be carried out with small five hole probes. An example of such a probing is shown in Figure 7.109; the diameters of the fuselage and probes were 100 and 3 millimeters respectively.

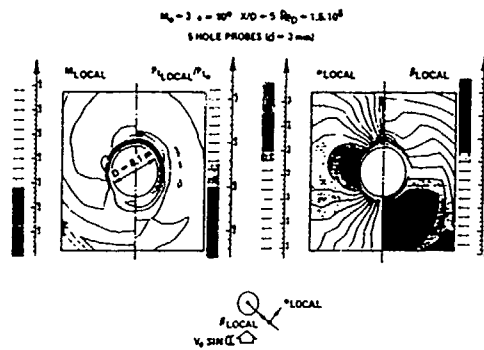


FIG 7.109 FLOWFIELD AROUND A CYLINDRICAL FUSELAGE

### 2.7.6.3 Mounted intakes

#### 2.7.6.3.1 One intake

Given the fuselage flow field, it is possible to calculate average values in the intake capture area  $A_c$  for Mach number  $M$ , total pressure  $P_t$ , incidence  $\alpha$  and sideslip angle  $\beta$ . The intake can then be regarded as located in this uniform flow field as an isolated intake.

Data from wind-tunnel tests can be used:

$$\left(\frac{A_0}{A_c}\right)_{\text{ISOLATED INTAKE}} = f(\bar{M}, \bar{\alpha}, \bar{\beta})$$

$$\text{and } PR_{I,1} = g(\bar{M}, \bar{\alpha}, \bar{\beta}).$$

The mounted intake performance is then given by:

$$\left(\frac{A_0}{A_c}\right)_{\text{MOUNTED INTAKE}} = \left(\frac{A_0}{A_c}\right)_{I,1} \times \left(\frac{\bar{P}_T}{P_{T_0}}\right) \times \frac{\sum(M_0)}{\sum(M)}$$

$$\text{where } \sum(M) = \frac{A(M)}{A^*} = \left(\frac{2}{\gamma+1}\right)^{\frac{\gamma+1}{2(\gamma-1)}} \times \frac{1}{M} \left[1 + \frac{\gamma-1}{2} M^2\right]^{\frac{\gamma+1}{2(\gamma-1)}}$$

$$\text{and } PR_{M,1} = PR_{I,1} \times \frac{P_t}{P_{t_0}}$$

Figures 7.110 and 7.111 show comparisons between such calculations and wind-tunnel test results.

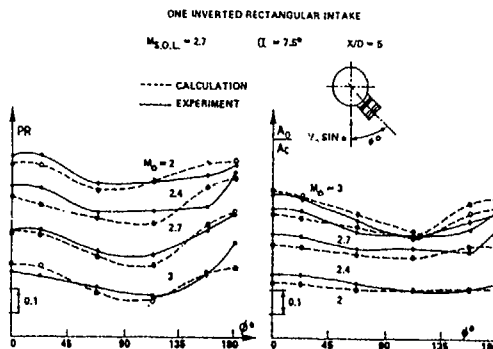


FIG 7.110 COMPARISON OF CALCULATION &amp; EXPERIMENT

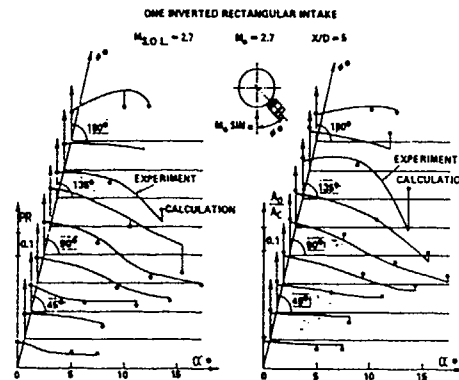


FIG 7.111 COMPARISON OF CALCULATION &amp; EXPERIMENT

A reasonable agreement is generally observed. Larger deviations are obtained when intakes are located in the vortices or at Mach numbers lower than the shock-on-lip Mach number. In this second case, interactions appear in front of the intake; they result from the impact of the shock waves created by the compression ramp on the fuselage boundary layer. For a large capture area, the average values account poorly for the flow distortions and deviations appear again.

#### 2.7.6.3.2 Several intakes

If several intakes ( $n$ ) are mounted on a fuselage and supply the same engine, the performance of each mounted intake ( $i$ ) is calculated first according to the previous method.

$$\left(\frac{A_0}{A_c}\right)_{M, I_i} \text{ \& } PR_{M, I_i} \text{ with } i < n$$

Then, the overall mass flow ratio is obtained by summing:

$$\left(\frac{A_0}{A_c}\right)_{\text{overall}} = \frac{1}{n} \left[ \left(\frac{A_0}{A_c}\right)_{M, I_1} + \dots + \left(\frac{A_0}{A_c}\right)_{M, I_i} + \dots + \left(\frac{A_0}{A_c}\right)_{M, I_n} \right]$$

and the overall pressure recovery is considered to be equal to the minimum pressure recovery of the different mounted intakes

$$(PR)_{\text{OVERALL}} = \min_{i=1, n} (PR_{M, I_i})$$

This method is not perfect and final tests are necessary with intakes mounted on the fuselage, but this semi-empirical approach for the missile design can now limit the wind-tunnel tests necessary to define the location of the intakes (longitudinal position, roll angle location and diverter height). Currently wind-tunnel tests can also be useful to validate this method for new configurations.

### 2.7.7 AIR-BREATHING MISSILE DESIGN

The previous sections gave a rapid survey of knowledge on missile intakes. A general synopsis must now be made to suggest design concepts for future supersonic air-breathing missile with high performance, taking into account four essential points: detection, manoeuvrability, penetration and range.

Some initial data are necessary at the beginning: mission(s), level of detection and overall dimensions.



According to the chosen type of steering, a sketch of the missile can be drawn; the number and type of intakes are generally determined at this juncture. It is then possible to estimate mass, overall external aerodynamic coefficients and possible maximum internal performance for intakes and engine.

Calculations of various trajectories are used to define an optimal "continuously flexible" missile whose internal sections ( $A_c$ ,  $A_{th}$ ,  $A_n$ ) could vary versus time, according to upstream Mach number and flight angle of incidence.

Intake design and its integration with the fuselage are then specified to satisfy, as closely as possible, requirements previously calculated. A compromise is necessary to obtain, if possible, a single fixed geometry. An estimate of intake performance can then be carried out. ( $PR$  and  $A_0/A_c = g(M_0, \alpha)$ ).

New calculations of various trajectories will give the optimal "inflexible" missile and aerodynamic models will be built. If the type of intake is new, tests with isolated intakes will be necessary; if not, tests in wind tunnels on mounted intakes will be sufficient. Overall external aerodynamic coefficients will be measured and Radar Cross-Sections will be specified.

From the experimental data, external missile geometry together with its internal arrangement will be settled and its performance will be estimated at this stage of the design.

Improvements will be necessary to obtain the specification values or to increase possible performance. Two remarks can be made:

- ultimate improvements are always minor but very expensive;
- modifications must be studied, making sure of the effective performance gains for the missions.

Some intake improvements can be unprofitable taking various adjustments into account. For example, if the missile must have high manoeuvrability, the ramjet exit throat size will be determined according to the intake performance at high incidence and sometimes, the best performance at zero incidence is not used, except at low Mach number during the acceleration phase.

## 2.7.8 CONCLUSION

Air-breathing propulsion, in particular for a ramjet, presents some new advantages for military applications. This results from obtaining low volume configurations and recent progress made in sensors, valves, engine control systems and airborne computers.

The existing realisations are mainly based on experimental data concerning:

- internal performance,
- external aerodynamics,
- and electromagnetic detection.

The design and development of future air-breathing missiles follow the current trends described below.

New computation codes will be very useful for design. Flow fields around fuselages with circular or noncircular sections will be accurately known. For intakes, major improvements are still necessary to take into

account viscous effects in these three-dimensional flow fields.

The use of semi-empirical methods is an excellent means for performance prediction and for reducing the number of wind-tunnel tests and models required.

Wind-tunnel tests will still be necessary for a very long time; although expensive, they are the only way of obtaining accurate data on performance at a number of attitudes and Mach numbers as soon as the model is built.

Research on new missile configurations imposes the need for low detection (electromagnetic and infrared) which can be obtained from studies on the intake geometry and materials. Longer ranges and higher flight Mach numbers will be possible with bank-to-turn steering and fuselages with non-circular cross-sections integrated with intakes.

## REFERENCES

- 7.1 M A BEHEIM, A preliminary investigation at Mach number 1.91 of a diffuser employing a pivoted cone to improve operation at angle of attack. NASA RM E53130
- 7.2 M A BEHEIM, T G PIERCY, Preliminary investigation of a shield to improve angle of attack performance of a nacelle type inlet. NACA RM E57G25a.
- 7.3 J G BENDOT, A E HEINS, T G PIERCY, Ramjet air induction system design for tactical missile application. AGARD LS 136 (Sep.84)
- 7.4 P BERTON, D REGARD, ONERA ramjet test facilities. La Recherche Aerospatiale No.197. English edition. ONERA 1980-4.
- 7.5 F S BILLIG, Ramjets with supersonic combustion. AGARD LS 136, 1984.
- 7.6 M BORREL, J L MONTAGNE, Numerical study of a non centred scheme with application to aerodynamics. 7th AIAA Computational Fluid Dynamics Conference, Cincinnati, July 1985.
- 7.7 C S BROWN, E L GOLDSMITH, Measurement of the internal performance of a rectangular air intake mounted on a fuselage at Mach numbers from 1.6 to 2.0. RAE-TR-72136. 1972.
- 7.8 P CARRIERE, R MARCUET, Aerodynamique interne des réacteurs-Prises d'air, statoréacteurs. Cours ENSA, 1977.
- 7.9 P CARRIERE, J LEYNAERT, Recherches sur les prises d'air supersoniques. Jahrbuch. WGL, 1959.
- 7.10 P CHAMPIGNY, Problèmes liés à l'aérodynamique externe des missiles aérobies. AGARD, Trondheim, Sept.82.
- 7.11 R J COMENZO, E A MACKLEY, Preliminary investigation of a rectangular supersonic scoop inlet with swept sides designed for low drag at a Mach number of 2.7. NACA RM L52J02, 1952.
- 7.12 J F CONNORS, R C MEYER, Performance characteristics of axisymmetric two-cone and isentropic nose inlets of Mach number 1.9. NACA RM E55F29.
- 7.13 E T CURRAN, F D STULL, Ramjet engines, highlights of past achievements and future promise. 2nd ISABE, 1974.

- 7.14 C L DAILEY, Supersonic diffuser instability. *Journal of the Aeronautical Sciences*, Vol.22 No.11 1955
- 7.15 I FARO, Supersonic inlets. *AGARDograph* 102, 1965.
- 7.16 E L GOLDSMITH, Some aspects of engine and airframe integration for ramjet and ramrocket powered missiles. *AGARD LS136*, Sept. 1984.
- 7.17 E L GOLDSMITH, Subsonic air intakes. *Weapon Aerodynamics Symposium Royal Aeronautical Society*, Dec. 1988
- 7.18 R GONIAU, Ecoulements supersoniques autour de cones en incidence. *La Recherche Aérospatiale* No.120, Sept., Oct. 1967
- 7.19 C R HALL, A criterion for prediction of airframe integration effect on inlet stability with application to advanced fighter Aircraft. *AGARD CP501* (1976)
- 7.20 L E HASEL, The performance of conical supersonic scoop inlets on circular fuselages. *NACA RM L53114a*, 1953.
- 7.21 L E HASEL, J L LANKFORD, A W ROBINS, Investigation of a half conical scoop inlet mounted at five alternative circumferential locations around a circular fuselage. Pressure recovery results at a Mach number of 2.01 *NACA L53D30*.
- 7.22 C HAYES, Aerodynamic characteristics of a series of single-inlet air-breathing missile configurations. *NASA TM 84557*.
- 7.23 C HAYES, Aerodynamic characteristics of a series of twin-inlet air-breathing missile configurations.  
I: Axisymmetric inlets at supersonic speeds - *NASA TM 84558*.  
II: Two-dimensional inlets at supersonic speeds - *NASA TM 85559*.
- 7.24 R HERMANN, Supersonic inlet diffusers and introduction to internal flow. Minneapolis - Honeywell Regulator Co., 1956.
- 7.25 C M JACKSON, Jr., W C SAWYER, Bodies with noncircular cross-sections and bank-to-turn missiles - Tactical missile aerodynamics. *Progress in Astronautics and Aeronautics*, Volume 104.
- 7.26 A L JAUMOTTE, A M ROTHROCK, A H LEFEBVRE, Combustion and propulsion. 4th *AGARD Colloquium: High Mach Number Air-Breathing Engines*, Milan, April 1960.
- 7.27 C S JELL, Air intake aerodynamics and operational and installation effects on missile powerplant performance. *VKI Course on Missile Aerodynamics*.
- 7.28 C S JELL, Air intake aerodynamics. *AGARD/FDP/VKI Course on Missile Aerodynamics*, March, May 1987.
- 7.29 D J JOHNSTON, J L HUNT, Mach 6 flow field and boundary layer surveys beneath the forebody of an air-breathing missile. *AIAA paper No. 84 0233*, Jan. 1984.
- 7.30 E J KREMIER, R C CAMPBELL, Angle of attack supersonic performance of a configuration consisting of a ramp-type scoop inlet located either on top or bottom of a body of revolution. *NACA TM E54C09*.
- 7.31 E O KROHN, K TRIESCH, Multiple intakes for ramrockets. *AGARD CP 307*, 1981.
- 7.32 G LARUELLE, Prises d'air d'engins supersoniques. *Discussion technique ONERA*, 1978.
- 7.33 G LARUELLE, Comparison of various configurations of supersonic missile air intakes. *AGARD CP307*, Oct. 1981.
- 7.34 G LARUELLE, Air intakes for a probative missile of rocket ramjet. *NASA TP 77407*. Traduction de "Prises d'air pour missile probatoire de stato fusée. *L'Aéronautique et l'Astronautique* No. 98, 1983.
- 7.35 G LARUELLE, C.SANS, R LEFEBVRE, Interest of internal bleed for a two-dimensional air intake operating in a wide Mach number range (1.8-3). *AGARD CP 365*, May 1984.
- 7.36 G LARUELLE, Synthesis of aerodynamic studies of air intakes of a highly manoeuvring missile at high Mach numbers. 7th *ISABE*, Beijing, Sept. 1985.
- 7.37 G LARUELLE, Air intakes for supersonic missiles, design criteria and development, 8th *ISABE*, Cincinnati, June 1987.
- 7.38 G LARUELLE, Prises d'air de missiles supersoniques, critères de choix et mise au point. *La Recherche Aérospatiale* No.6, 1987
- 7.39 G S LEYMAN, D P MORRIS, Concorde powerplant development. *AGARD CP91*, 1971.
- 7.40 C S LEYMAN, Review of the technical development of Concorde. *Progress in Aeronautical Sciences*, Vol. 23, No.3, 1986.
- 7.41 J LEYNAERT, Synthèse de résultats d'essais de prises d'air de révolution et de 1/2 révolution adaptées à Mach 2. *Note ONERA*, 1962.
- 7.42 J LEYNAERT, Engine installation aerodynamics. *AGARD LS 67*, 1964.
- 7.43 J LEYNAERT, B MASURE, Quelques problèmes d'expérimentation de prises d'air et de sortie de réacteurs. *AFITAE - Toulouse*, 1965.
- 7.44 J LEYNAERT, Fonctionnement du piège à couche limite interne d'une prise d'air à compression supersonique externe. *AGARDograph* 103, Tullahoma, 1965.
- 7.45 J LEYNAERT, T W BROWN, D COLLARD, A study of the Concorde air intake in yaw, *ICAS paper No. 74.50*, 1974.
- 7.46 J LEYNAERT, Problèmes d'interaction entre la prise d'air et l'avion. *AGARD CP 150*, 1974.
- 7.47 J LEYNAERT, D COLLARD, T W BROWN, Enseignement des prises d'air du Concorde pour un futur supersonique de croisière manoeuvrant. *AGARD*, Bruxelles, 1983.
- 7.48 J LEYNAERT, Fundamentals of fighter aircraft design; engine intake and afterbody *AGARD FDP-VKI*, 1986.
- 7.49 E MACKLEY, Effects of inlet aspect ratios on the starting and pressure recovery characteristics of a rectangular swept scoop inlet tested at a Mach number of 3.1. *NACA TM L57C07*, Jan. 1958.

- 7.50 R MARGUET, Etude et essais en vol d'un statoréacteur expérimental a Mach 5. N.T. ONERA No.94, 1966.
- 7.51 R MARGUET, C HUET, Recherche d'une solution optimale de statoréacteur a géométrie fixe de Mach 3 à Mach 7 avec combustion subsonique puis supersonique. 5e AFITAE, Poitiers, 1968.
- 7.52 R MARGUET, C HUET, G LARUELLE, Definition and performance of a one-stage rocket ramjet. 31st ISABE, Munich, March 1976.
- 7.53 R MARGUET, C ECARY, P CASIN, Studies and tests of rocket ramjets for missile propulsion. 4th ISABE, Orlando, April 1979.
- 7.54 N J MARTIN, C A HOLZHAUSER, Analysis of factors influencing the stability characteristics of symmetric twin-intake air induction systems. NACA TN 2049 (1950).
- 7.55 M R MENDENHALL, J N NIELSEN, Effect of symmetrical vortex shedding on the longitudinal aerodynamic characteristics of wing-body-tails configurations. NASA CR2473.
- 7.56 S MOLDER, E J SZPIRO, Buseman inlet for hypersonic speeds. Journal of Spacecrafts and Rockets, Vol.3, No.8, 1966.
- 7.57 E A MOSSMAN, L M RANDALL, An experimental investigation of the design variables for NACA submerged duct entrances. NACA RM 47130, 1947.
- 7.58 R K NANGIA, Three-dimensional wave interactions in supersonic intakes, 2nd ISABE, 1974.
- 7.59 K OSWATITCH, Pressure recovery for missiles with reaction propulsion at high supersonic speeds. NACA TM 1140, 1947.
- 7.60 T G PIERCY, H W JOHNSON, A comparison of several systems of boundary removal ahead of a typical conical external compression side inlet at Mach numbers of 1.88 and 2.93. NACA TM E53 F16, 1953.
- 7.61 C S RICHARDS, Supersonic air intakes for missiles. Weapons Aerodynamics Symposium Royal Aeronautical Society Dec. 1988.
- 7.62 G K RICHEY, L E SURBER, J A LAUGHREY, Airframe/propulsion system flow field interference, and the effect on air intake and exhaust nozzle performance, AGARD CP 150.
- 7.63 G ROSANDER, Development of aft-inlets for a ramjet powered missile. 1st ISABE, 1972.
- 7.64 J SEDDON, E L GOLDSMITH, Intake aerodynamics. Collins, 1985.
- 7.65 D B SMELTZER, N E SORENSEN, Investigation of a large scale mixed compression inlet system capable of high performance at Mach numbers 0.6 to 3.0. NASA TM X1507, 1968.
- 7.66 C SOULIER, J LAVERRE, Use of ONERA/S4MA hypersonic wind tunnel for supersonic combustion ramjet tests. 35th S.T.A. Dallas, March 1971.
- 7.67 L E SURBER, D J STAVA, Supersonic inlet performance and distortion during manoeuvring flight. AGARD CP91.
- 7.68 A N THOMAS, Inlets - Tactical missile aerodynamics. Progress in Astronautics and Aeronautics, Vol.104.
- 7.69 C A TREXLER, Inlet performance of the integrated Langley scramjet module (Mach 2.3 to 7.6). 11th Propulsion Conference AIAA 75-1212, Anaheim, Oct. 1975.
- 7.70 A S VALERINO, D B PENNINGTON, D J VARGO, Effect of circumferential location on angle of attack performance of twin half conical scoop type inlets mounted symmetrically on the RM10 body of revolution. NACA RM E53G09.
- 7.71 F F WERSTER, J A BUCY, ASALM-PTV chin inlet, technology overview. AIAA 79-1240, June 1979.
- 7.72 R WOOLLETT, F CONNORS, Zero angle of attack performance of two-dimensional inlets near Mach number 3. NACA RM E55K01, Feb. 1956.
- 7.73 Hypersonic boundary layers and flow fields. AGARD No 30, May 1968.
- 7.74 Inlets and nozzles for aerospace engines. AGARD CP91, 1971.
- 7.75 Aerodynamics of powerplant installation. AGARD CP301, 1981.
- 7.76 Aerodynamic inlets, A bibliography - Chemical propulsion Information Association, A.P.L. MD LS81-30, Dec. 1981.
- 7.77 Tactical missile aerodynamics. Progress in Astronautics and Aeronautics, Vol.104, 1986.

### CHAPTER 3

#### NUMERICAL SIMULATION OF INTAKES

##### 3.1 INTRODUCTION

The design of high speed air intakes for aircraft has been significantly affected by the recent development of computational fluid dynamics methods for analysis. CFD provides the designer with flow field solutions for air-intake geometries that are more detailed and provide more information than wind-tunnel-test-data. In general these solutions do not replace wind tunnel test but rather compliment the experimental methods to provide greater insight and understanding to the detailed flow interactions that greatly affect the performance of air intakes. As a result, the resulting designs can be expected to exhibit superior performance characteristics.

Since CFD provides such a powerful design tool, the Working Group elected to perform an evaluation of the current state-of-the-art in CFD analysis. The approach for this evaluation was to select a number of test cases for which rather detailed experimental data were available and to solicit investigators from the NATO countries to provide solutions to the selected test cases. These solutions were

compared with experimental data and with other solutions in order to provide the Working Group a global overview of the effectiveness and accuracy of CFD as a design tool. The comparisons were not intended to serve as a validation of CFD, but rather, give an indication of the viability of CFD for design application.

Eight test cases were selected for the evaluation as summarized briefly in Table 2.1. The test cases were chosen to range in complexity from normal-shock/boundary-layer interaction to full forebody-inlet combinations.

Computations were solicited from a large number of organizations and individual researchers within the NATO countries. A total of twenty-seven calculations were received from ten contributors. The Working Group wishes to express its sincere thanks to those who agreed to perform the calculations and followed through with the results that appear in this report.

TEST CASE	FLOW TYPE	NUMBER OF CALCULATIONS
1	Transonic Normal Shock/Turbulent Boundary Layer Interactions	2
2	Glancing Shock/Boundary Layer Interaction	5
3	Subsonic/Transonic Circular Intake	3
4	Subsonic/Transonic Semi-circular Intake	1
5	Supersonic Circular Pitot Intake	2
6	2D Hypersonic Intake	10
7	Mixed Compression Intake	2
8	Intake/Airframe Integration	2

TABLE 2.1 TEST CASES FOR CFD CALCULATIONS

## 3.2 CFD METHODS FOR INLETS

## LIST OF SYMBOLS FOR 3.2

Symbol	Meaning
$c_p$	coefficient of specific heat constant pressure
$c_v$	constant volume
$E_T$	total energy
$H$	total enthalpy
$p$	pressure
$q$	heat flow
$Re$	Reynolds number
$T$	temperature
$x, y, z$	directions
$u, v, w$	velocity components
$k$	coefficient of thermal conductivity
$\lambda$	second coefficient of viscosity
$\mu$	first coefficient of viscosity
$\rho$	density
$\tau$	stress

## 3.2.1 INTRODUCTION

In this section we shall discuss some of the aspects involved with computational fluid dynamics (CFD) analysis for intakes. CFD encompasses many related disciplines including grid generation, flow solvers, solution algorithms, turbulence models, processing and post-processing hardware and software. In each of these areas, the user must exercise careful judgement in choosing from several available methods to solve his particular flow problem. We will consider these aspects of CFD to provide the reader with an overview of the topic, and to provide a background for the following section in which comparisons will be made between computations and experimental results. The reader is referred to several excellent texts on CFD which have appeared in the literature recently, Ref 2.1 to 2.5, to provide more details involved in this discipline.

## 3.2.2 GRID GENERATION

The CFD analysis process begins with a numerical description of the physical problem to be studied. First, the physical objects around which or through which the air flows must be described numerically. This is commonly described as surface grid generation. After the surfaces have been described, the flow domain which is confined by the surface grid and any free surfaces must also be described numerically. This is commonly described as field grid generation. We will consider each of these grids separately and will also discuss possible problems which arise in the generation of these grids.

## 3.2.2.1 Surface Grids

The generation of accurate surface grids continues to be one of the most difficult, and time-consuming problems facing intake CFD users. As shown in Section 2.5.1, actual intake geometries are often quite complex with highly three dimensional contours. For many applications, small changes in this geometry can result in large changes in the flow field. This is particularly true in supersonic and hypersonic intakes which generate shock waves or expansion fans with change in surface geometry. The need for accurate modeling of physical surfaces is quite obvious. There are several ways in which surfaces can be specified for surface grid generation. For relatively simple geometries, the surface may be specified algebraically, i.e. with

polynomial spline curve fits which define the surface in space. For some complex geometries it is possible to prescribe local curve fits for parts of the configuration. This leads to a zonal method of prescribing each local feature and, in some logical way, patching them together to produce the total surface grid. This method works well with various block flow solvers and block field grid generation techniques. For some complex geometries, only local surface grid points are known. The person generating the grid is then left with the choice of either curve fitting these grid points (if possible) or of constructing a grid on the known points. The danger with curve fitting is that, in most cases, the curve fits only approximate the actual surface in some sense. For some applications that may be all that is required, for others it may introduce serious errors in the geometry and therefore in the flow field. On the other hand, to construct a grid using known points can be very expensive in terms of time and computer resources and may introduce other problems into the field grid which must match the surface grid at its boundaries. Because the generation of accurate complex surface grids is so labor intensive, many of the recently developed grid generation codes are designed for operation on interactive graphics workstations. This allows the person generating the grid to see and interact with the grid generation process in a timely fashion.

Fig 2.1 shows a surface grid generated for the computation of the Tailor-Mate intake/airframe compatibility test. This computation was performed by Aerospatiale in support of Test Case 8 reported in Section 3.3.8. This grid includes the forebody, canopy, intake, intake transition duct, and boundary layer diverter. The complex geometry, including square to round transition of the intake duct, is evident. Also apparent are the zonal boundaries where the grid density is changed.

### 3.2.2.2 Field Grids

Once the surface grid has been generated, the CFD user must generate a computational grid for the flow path of interest. Generation of the field grid introduces some additional problems and considerations for the CFD user. The current state of CFD demands a strong link between the flow solver and the grid structure. The quality of the final flow solution directly depends on certain aspects of the field grid, including sufficient grid resolution near high flow gradients, grid smoothness and minimum skewness, particularly near surfaces. The use of

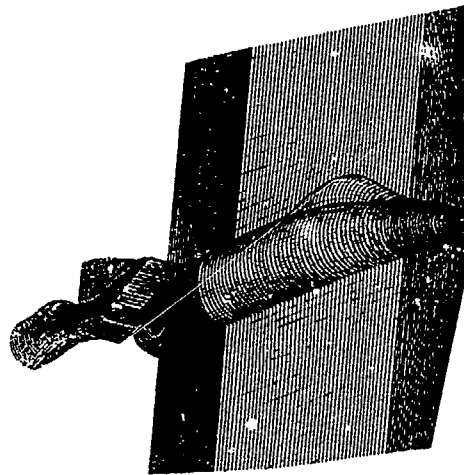


FIG 2.1 SURFACE GRID FOR COMPLETE TAILOR-MATE CONFIGURATION

solution adaptive grids, or multigrid algorithms, also causes a strong tie between the flow solver and the field grid. Often assumptions, or limitations, in the flow solver or its boundary condition specification impose additional constraints on the grid generation process. When generating the field grid, the surface grid will constitute part or all of the boundary for the field grid. Often the flow domain is decomposed into a number of regions which are each gridded separately and the interface between regions becomes new internal boundaries to the flow solver. There are many possible ways to generate a field grid for each region, but to maintain some degree of grid smoothness and orthogonality, the flow domain is usually mapped onto a Cartesian computational grid using a differential equation solver. Depending on the form of this mapping, different types of grids can be generated with different amounts of clustering in strategic locations. Unfortunately, the solution of the differential equations for grid generation can require computer resources which approach those required for the flow solution. Research continues to find ways to reduce the time and storage required for grid generation.

Figure 2.2 shows a sample of a field grid for the flow past a wedge for Test Case 2. Shown in the figure are three intersecting grid planes; one plane is near the wedge surface, one plane is near the wall surface to which the wedge is attached, and the third plane is

perpendicular to the wall and intersects the wedge. The flow in this figure would be from right to left. The clustering of the field grid to resolve boundary layers near the surface is clearly evident as is the streamwise clustering near the wedge leading edge. For this grid hyperbolic tangent packing functions were used to smoothly cluster the grid near surfaces.

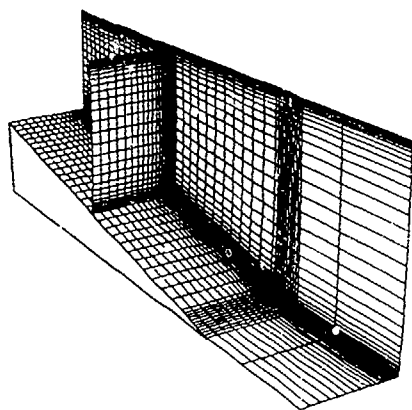


FIG 2.2 FIELD GRID FOR GLANCING SHOCK/BOUNDARY LAYER INTERACTION.

There are two areas of grid research which may have great future impact on the use of CFD for intake analysis. The first is solution adaptive gridding, which has been studied for some time and is beginning to be used in some analysis packages. In this technique, the grid used for solution is changed during the solution process to concentrate grid points in the areas of high flow gradients. This results in an improved solution using fewer grid points, although one must pay some overhead for adapting the grid. The second area of research is the use of unstructured grids. As the name implies, these grids have no set structure. Each grid cell need not be rectangular; in fact they may be three, four, five or more sided. There are usually no discernible planes of grid points; the points can be randomly distributed through the domain and connected through some algorithm. These grids are well suited for the complex geometries of modern aircraft. There are currently some algorithms available to generate these types of grids, and work is proceeding on the development of solution algorithms, turbulence models and stability parameters for this type of grid.

### 3.2.3 FLOW SOLVERS

Within the intake aerodynamics community there are many different computational schemes available to the user. In this section we will investigate some of these schemes to provide a background for the computational results to be discussed in the next section. The VKI has recently conducted a short course on intake aerodynamics, with a special emphasis on the CFD methods, Ref 2.6, which forms a basis for this section of the report.

#### 3.2.3.1 Flow Equations

The most general set of equations for the flow of air through intakes are the Navier-Stokes (NS) equations. These equations, given in Fig 2.3, simply express the conservation of mass, momentum and energy for a fluid system. For simplicity, the equations are shown here in two-dimensional conservation form for a Cartesian coordinate system. In order, these are the continuity, x-momentum, y-momentum, and energy equation. There are several different possible formulations of the energy equation; this is the total energy formulation. To complete the set of equations, some auxiliary equations describing the shear stress, heat transfer, and equation of state of the gas, are given in Fig 2.4. These equations are a coupled set of non-linear second-order partial differential equations and are therefore very difficult to solve. To solve this system of equations, one must specify some initial flow conditions and boundary conditions appropriate for the problem being considered. The choice of boundary conditions is particularly crucial for flow problem modeling because it is through the boundary conditions that the unique features of a problem are specified. The NS equations in the internal flow domain are the same for all problems, it is only the boundary surface and boundary equations on the surface that change from problem to problem. Within intakes, the specification of proper boundary conditions is even more important because one is ultimately interested in what happens on the surface or at the exit of the intake which typically falls on a computational boundary.

$$\begin{aligned}
\frac{\partial \rho}{\partial t} + \frac{\partial(\rho u)}{\partial x} + \frac{\partial(\rho v)}{\partial y} &= 0 \\
\frac{\partial(\rho u)}{\partial t} + \frac{\partial(\rho u^2)}{\partial x} + \frac{\partial(\rho uv)}{\partial y} &= -\frac{\partial p}{\partial x} + \frac{1}{Re} \left( \frac{\partial \tau_{xx}}{\partial x} + \frac{\partial \tau_{xy}}{\partial y} \right) \\
\frac{\partial(\rho v)}{\partial t} + \frac{\partial(\rho uv)}{\partial x} + \frac{\partial(\rho v^2)}{\partial y} &= -\frac{\partial p}{\partial y} + \frac{1}{Re} \left( \frac{\partial \tau_{xy}}{\partial x} + \frac{\partial \tau_{yy}}{\partial y} \right) \\
\frac{\partial(\rho E_T)}{\partial t} + \frac{\partial(u E_T)}{\partial x} + \frac{\partial(v E_T)}{\partial y} &= -\frac{\partial(u p)}{\partial x} - \frac{\partial(v p)}{\partial y} - \frac{1}{Re Pr} \left( \frac{\partial q_x}{\partial x} + \frac{\partial q_y}{\partial y} \right) \\
&\quad + \frac{1}{Re} \left[ \frac{\partial}{\partial x} (u \tau_{xx} + v \tau_{xy}) + \frac{\partial}{\partial y} (u \tau_{xy} + v \tau_{yy}) \right]
\end{aligned}$$

FIG 2.3 TIME-AVERAGED NAVIER-STOKES EQUATIONS.

$$\begin{aligned}
p &= \rho R T \\
\tau_{xx} &= 2\mu \frac{\partial u}{\partial x} + \lambda \left( \frac{\partial u}{\partial x} + \frac{\partial v}{\partial y} \right) \\
\tau_{yy} &= 2\mu \frac{\partial v}{\partial y} + \lambda \left( \frac{\partial u}{\partial x} + \frac{\partial v}{\partial y} \right) \\
\tau_{xy} &= \mu \left( \frac{\partial v}{\partial x} + \frac{\partial u}{\partial y} \right) \\
q_x &= -k \frac{\partial T}{\partial x} \\
q_y &= -k \frac{\partial T}{\partial y} \\
E_T &= \rho c_v T + \frac{1}{2} \rho (u^2 + v^2)
\end{aligned}$$

FIG 2.4 AUXILIARY EQUATIONS.

Researchers can often obtain meaningful solutions to specific problems by solving some subset of the full NS equations. If one is able to neglect the normal viscous forces in some principal flow direction the NS equations can be reduced, or "parabolized", to produce a set of equations which are much simpler to solve than the full NS equations. Fig 2.5 shows one formulation of the Parabolized Navier-Stokes (PNS) equations. This set still retains the continuity, x- and y-momentum, and energy equations. This particular set of equations has been written for steady flow in the x-direction, has folded in the auxiliary equations for the stresses and contains the total enthalpy formulation of the energy equation. Except for the pressure gradient term in the x-momentum equation, these equations are of mixed hyperbolic-parabolic type in x and can be solved by a forward marching scheme. The pressure gradient

term makes the x-momentum equation elliptic for subsonic portions of the flow. Various treatments of this pressure gradient term have produced various versions of the PNS analysis. PNS codes are typically faster and require less computer storage than equivalent full NS codes, but can only be used for those physics problems which do not violate any of the simplifying assumptions for the analysis.

$$\begin{aligned}
\frac{\partial(\rho u)}{\partial x} + \frac{\partial(\rho v)}{\partial y} &= 0 \\
\frac{\partial(\rho u^2)}{\partial x} + \frac{\partial(\rho uv)}{\partial y} &= -\frac{\partial p}{\partial x} + \frac{1}{Re} \frac{\partial}{\partial y} \left( \mu \frac{\partial u}{\partial y} \right) \\
\frac{\partial(\rho uv)}{\partial x} + \frac{\partial(\rho v^2)}{\partial y} &= -\frac{\partial p}{\partial y} + \frac{1}{Re} \frac{\partial}{\partial y} \left[ (2\mu + \lambda) \frac{\partial u}{\partial y} \right] \\
\frac{\partial(\rho u H)}{\partial x} + \frac{\partial(\rho v H)}{\partial y} &= -\frac{1}{Re Pr} \frac{\partial}{\partial y} \left( k \frac{\partial T}{\partial y} \right) \\
&\quad + \frac{1}{Re} \frac{\partial}{\partial y} \left[ \mu u \frac{\partial u}{\partial y} + (2\mu + \lambda) v \frac{\partial v}{\partial y} \right] \\
p &= \rho R T \\
H &= c_p T + \frac{1}{2} (u^2 + v^2)
\end{aligned}$$

FIG 2.5 PARABOLIZED NAVIER-STOKES EQUATIONS.

If one is able to neglect all viscous forces and heat conduction in the problem the NS equations can be reduced to the inviscid Euler equations. These equations are shown in Fig 2.6 for steady flow. While these equations cannot be used for viscous dominated flow problems, they can be used to study the inviscid portions of intakes, particularly with shock waves. Because the viscous portions of the flow have been neglected, fewer grid points are needed in an Euler solution and the solution is computed much faster than with a full NS. If the flow is supersonic, the Euler equations can be solved by the method of characteristics, an extremely fast solution technique often used for high speed intake design when coupled to a boundary layer analysis. The Euler equations are often used to test new CFD solution techniques before using the techniques in full NS because they maintain many of the numerical features of the NS equations.



$$\begin{aligned}\frac{\partial(\rho u)}{\partial x} + \frac{\partial(\rho v)}{\partial y} &= 0 \\ \frac{\partial(\rho u^2)}{\partial x} + \frac{\partial(\rho uv)}{\partial y} &= -\frac{\partial p}{\partial x} \\ \frac{\partial(\rho uv)}{\partial x} + \frac{\partial(\rho v^2)}{\partial y} &= -\frac{\partial p}{\partial y} \\ \frac{\partial(uE_T)}{\partial x} + \frac{\partial(vE_T)}{\partial y} &= -\frac{\partial(up)}{\partial x} - \frac{\partial(vp)}{\partial y}\end{aligned}$$

FIG 2.6 EULER EQUATIONS.

## 3.2.3.2 Solution Algorithm

We will now consider some numerical techniques to solve the equation sets described in the previous section. Once again, there are a variety of techniques currently available to the user and new techniques are being developed world wide. There are two principal classes of CFD analysis, differential and integral, and we shall now consider each of these separately.

The majority of CFD analysis currently employs finite difference techniques for the differential equations. In this method the differential equations are approximated by difference equations which are solved numerically. The differencing can take many different forms; forward, backward, central, two point, three point, etc., with each of the forms having certain advantages for certain types of problems. Once the equations have been differenced, there are several different forms of solution algorithm available to the user, again, with each having its own advantages. The explicit algorithms are relatively easy to code and easily adaptable to vector or parallel processing machines, but have certain stability limitations which can increase the amount of computing time. Implicit algorithms are harder to code but for certain problems have better stability characteristics than explicit schemes and converge faster. The problem of numerical instabilities has lead researchers to introduce artificial damping into many algorithms and to the development of new, more stable methods of differencing the equations. Slow convergence of certain relaxation algorithms have lead to acceleration schemes, such as multi-

gridding or matrix pre-conditioning, all with the intent of decreasing the total computational work load, time and expense. The many efforts to produce faster, more robust solvers have lead to many, different, specialized computer codes in the field, which can be confusing to a potential user.

A more recently developed algorithm for solution of the flow equations is the finite-volume method, Ref 2.7 to 2.9. In this method, the flow variables within a grid cell are integrated to produce an average flux across cell boundaries. These fluxes are then used in the evaluation of terms in the finite difference equations. Several different methods have been proposed for the treatment of the flux terms, producing several different formulations of the method. The different methods each have an advantage for a particular type of flow problem. These flow solvers are particularly well suited for shock capturing within high speed flow problems.

The finite element method, which is also an integral method, has its roots in structural analysis. This method solves the system of equations by discretizing the flow domain into a series of small elements which share common points or nodes. Within each element, a functional form of the variation of the flow variables is assumed. The constants multiplying these functions are then determined by solution of the variational form of the differential equations, i.e. the NS, PNS or Euler equations. This method has advantages and disadvantages relative to finite difference. The chief advantage is the inherent flexibility in the meshes which this method supports, including the new unstructured grids. The chief disadvantage is the overhead in computer storage required to define the elements and their nodes. In the future, we may see more applications of the finite element method for intake analysis.

## 3.2.3.3 Turbulence Models

In theory, the full Navier-Stokes equations could be solved for the continuum flow through an intake at any speed including turbulence effects. In reality, the length and time scales associated with turbulence are much too small to be resolved within a realistic configuration at this time, and so the CFD user normally models the effects of turbulence on the flow. There are currently several different methods for modeling turbulence effects available to the CFD user, Ref 2.10 to 2.13. Most of the models locally increase the

coefficient of viscosity and thermal conductivity to account for increased diffusion due to turbulence. The coefficient of viscosity and thermal conductivity are then referred to as "effective" viscosity and conductivity coefficients and the NS equations remain the same. Different techniques are employed to determine the magnitude of the change in coefficient ranging from simple algebraic equations to the solution of coupled differential equations. The more sophisticated models include more of the physics concerning turbulence than the simpler models, although they have a higher computational overhead. All current turbulence models require some type of empirical constants which are usually determined through correlation with experimental data. This, of course, introduces some levels of uncertainty concerning the accuracy of the model when it is applied to problems which are different from the correlation experiment. Turbulence modeling will continue to be an area for CFD research in years to come.

#### 3.2.3.4 Current Status

As described in Section 3.1, there have been eight proposed test cases for the CFD evaluation in this study, and there have been eleven contributors using a variety of computer codes and twenty two calculations. In this section we will provide a brief description of these codes for future reference. Table 3.2.1 gives an overview of the computer codes used in this study. The left column gives the name of the code, sometimes a meaningful acronym, sometimes not. The second column identifies the user of the code by affiliation, the third gives the type of code, and the fourth the particular test cases against which this code was applied. More details on the codes and the calculations can be found in the microfiche supplement to this report.

The PARC3D code, Ref 2.14 was used by several contributors in the US. This code is a derivative of the NASA Ames developed ARC codes, which employs a Beam-warming approximate factorization scheme to solve the NS equations by marching the time dependent equations to steady state and usually employs a Baldwin-Lomax algebraic turbulence model. The code used a diagonalized form of the implicit matrices for efficient execution times and a Jameson-style artificial dissipation scheme to stabilize the scheme near shock waves. There are many different versions of the PARC3D code in the field; users typically modify the turbulence model for their particular

Table 3.2.1 Codes used in CFD Assessment

CODE	USER	TYPE	TEST CASE
PARC3D	SVERDRUP-AEDC	NS	1 2 6 8
	SVERDRUP-CLEVE.		2 7
HAWK3D	GENERAL DYNAMICS	NS	2
FALCON	GENERAL DYNAMICS	NS	6
PEPSI-S	NASA-LEWIS	PNS	2 6 7
NS2D	ONERA	NS	2
	AEROSPATIALE		6
FLU3M	AEROSPATIALE	EU	6 8
	ARA	EU	4
		EUBL	5
ENSFL2D	DORNIER	NS	5
IKARUS	DORNIER	NS	3 6
RANSAC	BAE	NS	3
NSFLEX	MBB	NS	1 6

problem, and some have introduced block grid solvers into the basic code. The basic code supports a variety of boundary conditions which are solved explicitly. For subsonic outflow boundaries, a static pressure is specified and density and velocity are extrapolated in the basic code. The group at CALSPAN has used an implicit, approximate factorization scheme of Beam and Warming with a Chimera domain decomposition to study test case 3. This code supports both Baldwin-Lomax and two equation turbulence models. The HAWK3D code is a specially modified version of the PARC3D code which was used by General Dynamics. This code employs a two-equation k-k1 turbulence model, Ref 2.13, not available in the basic PARC3D code. The FALCON code was also used by General Dynamics to study test case 6. This code is a finite volume solver which uses Roe's flux difference splitting to solve the 2D or 3D NS equations. The code contains a multi-blocking capability and a Baldwin-Lomax algebraic turbulence model. For this supersonic test case, flow quantities were extrapolated at the downstream boundary. The PEPSI-S code, Ref 2.15, was used to solve several of the supersonic test cases. This code solves the PNS equations using a Briley-McDonald LBI scheme to make a single sweep in the predominately supersonic

flow direction. The code has a variety of turbulence models available, the algebraic McDonald-Camarata was used for case 2, a version modified for compressibility was used for case 6, and a one equation turbulent kinetic energy model was used for case 7. A variety of boundary conditions are also available to this code, including distributed mass removal for the bleed regions of test case 7. Because this code is used only for supersonic flows, and is a single sweep code, the downstream computational boundary is the last solution plane and is not specified by a boundary condition. The NS2D code, Ref 2.16, was adapted for air intakes (and used here for test case 6) from the code used by ONERA, Ref 2.17 and 2.18, for test case 2. This code solves the Reynolds averaged NS equations by a centered explicit finite difference scheme with a multigrid convergence accelerator. The discretization is performed using a two-step Lax-Wendroff type scheme with the dissipative terms being taken into account following Thommen's, Ref 2.19, ideas. The code employs an algebraic turbulence model developed by Michei et al., Ref 2.20. The FLU3M code, Ref 2.21 and 2.22, was used to analyze test case 6 and 8. This code was developed by ONERA and Aerospatiale for multiblock grids with an emphasis on supersonic and hypersonic flows. The code solves the Euler equations by an implicit upwind TVD finite volume scheme of van Leer's MUSCL type. Its implicit part consists of an ADI like inversion in cross-section planes coupled with a Gauss-Seidel relaxation in the third direction. The ARA Euler multiblock method is based on the scheme originally proposed by Jameson et al., Ref 2.23. It is a finite volume scheme with explicitly added artificial dissipation. The multi-stage - time-stepping scheme uses total enthalpy acceleration and a variable time step supported by residual smoothing, Ref 2.24. For test case 5, viscous effects were included by performing boundary layer calculations using results from the Euler calculations. Details of the boundary layer method can be found in Ref 2.25. Ikarus is a three-dimensional Navier-Stokes code derived from ENSFL2D which is a two-dimensional/axisymmetric code for the solution of the Euler and Navier-Stokes equations. Both codes are based on the finite volume spatial discretization and the Runge-Kutta type time integration presented by Jameson et al, Ref 2.22. The solution method is characterized by explicit artificial viscosity, local time stepping, implicit residual smoothing, multilevel grid technique accompanied by multigrid strategy within each grid level. The viscous terms in the Navier-Stokes

equations are simulated in full and their thin layer approximation. The Baldwin-Lomax turbulence model (with modifications) is used. Details for ENSFL2D can be found in Ref 2.26 and for Ikarus in Ref 2.27. RANSAC is a three dimensional, cell centered, finite volume, implicit, pressure correction method for the solution of the Reynolds averaged Navier-Stokes equations. A non-staggered grid pressure correction algorithm due to Rhie, Ref 2.28, is employed, in which the addition of explicit fourth order dissipation terms damp out pressure instabilities in the momentum equations. For the momentum equations, the scheme enforces central differencing for very slow flows and upwind differencing for fast flows. The linearization of the transport equation for all the cells creates a coefficient matrix that is septadiagonal. The matrix inversion is performed by an over-relaxation black/red iterative matrix inversion technique which takes two sweeps through the mesh on each iteration. For turbulent closure the standard k-e model is used, Ref 2.29. NSFLEX, Ref 2.30, is a finite volume Navier-Stokes code for subsonic, transonic and hypersonic flows developed at M3B. Its basis is the Euler method EUFLEX, Ref 2.31, for the conservative Euler equations. The fluxes at the cell faces are determined by a linear Riemann problem using a nominally third order accurate characteristic flux extrapolation scheme of MUSCL type, Ref 2.32. At strong shocks the method switches to a modified flux vector splitting method. The switching between the two methods is accomplished by an improved flux limiter of the van Albada type. The resulting unfactored difference equations are solved in their implicit and time depending form by a point Gauss-Seidel method. The viscous fluxes are approximated by central differences. The turbulence model is that of Baldwin-Lomax. The code has a block and real gas capability.

### 3.2.4 PROCESSING AND POST-PROCESSING

The increased use of CFD for intake analysis has been made possible by the increased availability, speed and storage of supercomputers. Central computing facilities, such as the NAS at NASA Ames, have pioneered the development of hardware required to solve complex flow problems. Some of the new chip and mainframe architectures are now being made available on less costly local computers. At the same time, new and improved compilers, operating systems, and other forms of software have enabled users to take advantage of the new computer architectures, particularly in the area

of code vectorization and parallelization. This increase in computational capability has spurred on the development of high speed graphics workstations for the post-processing and analysis of computed results. The workstation now provides the CFD user with the ability to visualize and understand complex flow fields which was not available even five years ago. Software packages, such as PLOT3D, GAS, and FAST, coupled to high speed workstations are revolutionizing the way engineers will design components. As previously mentioned, the generation of suitable grids for CFD has been greatly assisted by interactive graphic packages, such as GRIDGEN3D, which operate on workstations.

### 3.2.5 REFERENCES

- 2.1 Anderson, D.A., Tannehill, J.C., and Pletcher, R.H., Computational Fluid Mechanics and Heat Transfer, Hemisphere Publishing Corporation, McGraw-Hill Book Company, 1984.
- 2.2 Fletcher, C.A.J., Computational Techniques for Fluid Dynamics, Volumes 1 and 2, Springer-Verlag, 1988.
- 2.3 Hirsch, C., Numerical Computation of Internal and External Flows, Volume 1: Fundamentals of Numerical Discretization, John Wiley & Sons, Inc., 1988.
- 2.4 Hirsch, C., Numerical Computation of Internal and External Flows, Volume 2: Computational Methods for Inviscid and Viscous Flows, John Wiley & Sons, Inc., 1990.
- 2.5 Murthy, S.N.B., and Paynter, G. C., eds., Numerical Methods for Engine-Airframe Integration Progress in Astronautics and Aeronautics, Vol 102, AIAA, 1986.
- 2.6 Towne, C.E., "Computational Methods for Inlet Airframe Integration", Von Karman Institute for Fluid Dynamics, Lecture Series 1988-04, Intake Aerodynamics, Feb 26, 1988.
- 2.7 Godunov, S.K., "A Finite Difference Method for the Numerical Computation of Discontinuous Solutions of the Equations of Fluid Dynamics.", Mat. Sb., Vol 47, pp 357-393, 1959.
- 2.8 Roe, P.L., "Characteristic-Based Schemes for the Euler Equations", Ann. Rev. Fluid. Mech., Vol 18, pp 337-365, 1986.
- 2.9 van Leer, B., "Flux-vector splitting for the Euler Equations", Lect. Notes, Phys., Vol 170, pp 507-512, 1982.
- 2.10 Baldwin, B.S., and Lomax, H., "Thin Layer Approximation and Algebraic Model for Separated Turbulent Flows", AIAA Paper 78-257, 1978.
- 2.11 McDonald, H., and Camarata, F.J., "An Extended Mixing Length Approach for Computing the Turbulent Boundary Layer Development", Computation of Turbulent Boundary Layers -1968 AFOSR-IFP-Stanford Conference, S.J.Kiine, et. al. eds., Stanford University, pp 83-98, 1969.
- 2.12 Cebeci, T., and Smith, A.M.O., Analysis of Turbulent Boundary Layers, Academic Press, 1974.
- 2.13 Smith, B.R., "The k-k1 Turbulence Model and Wall Layer Model for Compressible Flows", AIAA 90-1482, June, 1990.
- 2.14 Cooper, G.K., "The PARC Code: Theory and Usage", AEDC-TR-87-24, Oct. 1987.
- 2.15 Buggeln, R.C., McDonald, H., Kreskovsky, J.P. and Levy, R., "Development of a Three-Dimensional Supersonic Inlet Flow Analysis", NASA CR 3218, 1979.
- 2.16 Cambrier, L. Veuillot, J.P., et Vuillot, A.M., "Developpements recents sur les methodes de calcul d'ecoulements internes par resolution des equations d'Euler ou de Navier-Stokes", Revue francaise de Mechanique No. 1988-4, 1988.
- 2.17 Cambrier, L. Couaillier, V. et Veuillot, J.P., "Resolution numerique des equations de Navier-Stokes a l'aide d'une methode multigrille", La Reserche Aerospaciale No.1988-2, english edition, pp23-42, 1988.
- 2.18 Cambrier, L., Couaillier, V. and Veuillot, J.P., "Simulation of a shock wave/turbulent boundary layer interaction in a three dimensional channel", AIAA 89-1851, 1989 and ONERA TP No 1989-82, 1989.
- 2.19 Thommen, H.U., "Numerical integration of the Navier-Stokes equations," ZAMP, Vol. 17, pp 369-384, 1966.
- 2.20 Michel, R., Quermard, C., and Durant, R., "Application d'un schema de longueur de melange a l'etude des couches limites turbulentes d'equilibre", ONERA NT No.154, 1969.

2.21 Guillen, Ph., Borrel, M., and Dormieux, M., "Numerical simulation of perfect fluid flows around complex 3D configurations by a multidomain solver using the MUSCL approach," Conference GAMNI/SMIA-IMA sur les Methodes de Calcul en Mecanique des Fluides Appliquees a l'Aeronautique, Antibes, Mai 1989.

2.22 Guillen, Ph., and Dormieux, M., "Design of a 3d multidomian Euler code," Supercomputing in Fluid Flow, Boston, October, 1989.

2.23 Jameson, A., Schmidt, W., and Turkel, E., "Numerical solutions of the Euler equations by finite volume methods using Runge-Kutta time-stepping scheme," AIAA 91-1259, 1981.

2.24 Doe, R.H. Brown, T.W. and Pagano, A., "The development of practical Euler methods for aerodynamic design," ICAS-86-1.4.2., 1986.

2.25 Green, J.E., Weeks, D.J. and Brodman, J.W.F., "Prediction of turbulent boundary layers and wakes in compressible flow by a lag entrainment method," A.R.C. R&M 3791, 1973.

2.26 Fritz, W., "Numerical simulation of 2D turbulent flow fields with strong separation," ICAS-88-4.6.4, 1988.

2.27 Leicher, S., "Fluxus a 3D Navier-Stokes solver for 3D-bodies in an arbitrary blockstructured grid, User manual", Dornier Report BF 4/89 B, 1989.

2.28 Rhie, C.M., "A pressure based Navier Stokes solver, using the multigrid method", AIAA-86-0207, 1986.

2.29 Mackenzie, C., "RINSAC: A pressure correction based Navier-Stokes code for afterbodies with jets", BAe SRC Report JS 11195, Dec, 1988.

2.30 Schmatz, M.A. NSFLEX - An implicit method for the Navier Stokes equations for a wide range of Mach numbers. Notes on Numerical Fluid Mechanics, Vol 30. Vieweg, Braunschweig, 1990.

2.31 Eberle, A., "Characteristic Flux Averaging Approach to the Solution of Euler's Equations", VKI Lecture Series 1987-04, March 1987.

2.32 Eberle, A. Schmatz, M.A., and Bissinger, N.C., "Generalized Flux Vectors for Hypersonic Shock Capturing", AIAA-90-0390, 1990.

### 3.3 ANALYSIS OF TEST CASES

#### 3.3.1 Test case 1 - Transonic Normal Shock/ Turbulent Boundary Layer Interactions

##### 3.3.1.1 INTRODUCTION

Flows around or inside high speed vehicles are usually accompanied by shocks interacting with boundary layers. Depending on shock strength these interactions can be the reason for boundary layer separations that can heavily degrade the performance of the propulsion systems of the vehicles. CFD methods therefore must be able to simulate these flow phenomena correctly.

The problem selected has been used for calculations before around 1983 (Ref 3.1.1 has been published in 1986). It was hoped that in the mean time progress in CFD methods made it possible to give better agreement between experiment and computations than at that time.

##### 3.3.1.2 PROBLEM DESCRIPTION

The experiments for this test case have been performed in a "two-dimensional" tunnel the main features of which are given in fig 3.1.1. All tests were performed at the same freestream conditions  $P_{\infty} = 96 \text{ kPa}$  and  $T_{\infty} = 300^\circ \text{ K}$ . For the formation of the shock interchangeable bumps are mounted on the upper and lower wall of the rectangular test section. The position of the shock on these bumps is determined by the adjustable second throat downstream of the test section. Flow variables at three different nominal Mach numbers at the shock of  $Ma = 1.3$  (called test case 1.1), 1.45 (called test case 1.2), and 1.37 (called test case 1.3) due to three differently shaped inserts had been measured by a two-color laser velocimeter. The flows depicted small to large separation respectively at the foot of the shock inside the boundary layer. The boundary layer is considered turbulent without any information from experiment about transition. The tunnel wall is assumed to be adiabatic.

The test data available from the experiments are the mean velocities, the mean Reynolds stress tensor components, the kinetic energy (assuming that  $w' = (u'^2 + v'^2)/2$ ), turbulent shear stress profiles and static wall pressures. The experiments can be considered two-dimensional for the small and moderately separated case. The case with larger separation showed a "rather strong distortion of the reattachment line" (Ref 3.1.2). So for this case three-dimensional calculations would have been appropriate.

Total pressure and total temperature are known from experiment and can be used at the entrance boundary condition for the calculations. Unfortunately the dimensions of the second throat downstream of the test section are not known. It was therefore recommended to use the static wall pressure measured during experiment at the exit boundary of the computational domain. The consequence of this is that the calculations had to be repeated with different exit pressures until the shock

location of the calculation agreed with that of the experiment. Details of the experiments can be found in Refs 3.1.3 to 3.1.5.

##### 3.3.1.3 CFD TECHNIQUES

This test case was attempted by two different research groups (see table 3.2.1 in section 3.2). Both used two-dimensional code versions for their calculations which solved the Navier-Stokes equations. The Sverdrup Tenn. group used the PARC2D code in which the algebraic Baldwin/Lomax turbulence model is incorporated. The results are designated (NS2) in the figures. The grid contained 9050 grid points with approximately fifty grid lines within the boundary layer. The flow case with large separation (test case 1.3) has not been calculated.

The group from MBB used their NSFLEX code together with the Baldwin/Lomax turbulence model. The calculations were performed assuming turbulent flow in all boundary layers. The results are designated (NS1) in the figures. Because the geometry for test cases 1.1 and 1.2 is symmetric only half of the actual flow field was simulated with a symmetry boundary condition on the center line. For test case 1.3 (one-sided bump) the complete flow field had to be simulated. The grid for test case 1.1 had 209 points in flow direction and 50 points normal to it. Results (i.e. static wall pressures, mean velocity profiles, Reynolds stress profiles and isolines of Mach number) with a grid with twice the number of points normal to the flow and a higher grid refinement at the wall agreed with those from the coarser grid. However, in order to reach the same shock location with the fine grid a reduction of the exit static pressure (from  $p/p_{\infty} = 0.6739$  to  $p/p_{\infty} = 0.6527$ ) was necessary (Ref 3.1.6). For test case 1.2 a grid with  $236 \times 50$  points for the half-model was used. The increase of points in flow direction (compared with test case 1.1) was considered necessary to be able to better resolve the separation region existing. The flow of test case 1.3 was calculated with a grid of  $239 \times 100$  and  $239 \times 200$  points, i.e. with the same grid resolution as the other test cases and again the same results for both grids. For a converged solution about 20000 iterations were necessary for test cases 1.1. and 1.3. Test case 1.2 was converged after approximately 30000 iterations. The computations required  $8.6 \times 10^{-3}$  seconds per grid point and iteration on a SIEMENS VP200 vectorcomputer.

##### 3.3.1.4 RESULTS

###### 3.3.1.4.1 Test Case 1.1 - $M = 1.3$

###### Static Wall Pressure Distributions

Figs. 3.1.2 and 3.1.3 show a comparison of the computed and experimental static wall pressure distributions (scaled by the tunnel total pressure  $P_{t0}$ ) along the lower and upper wall respectively. (The coordinate  $X$  along the tunnel wall is scaled by the tunnel height  $h_t = 0.1 \text{ m}$ ). Experimental data is shown by the symbol while the analysis are shown by different style lines. The static pressure is

plotted as a function of the coordinate  $X$  along the tunnel axis. As can be seen the shock standing at the downstream end of the tunnel wall insert spans the whole tunnel width with the same  $X$ -station at the lower and upper tunnel wall. The static pressure distribution ahead of the shock compares well between both solutions NS1 and NS2 and experiment. Whereas in the solution NS1 the foot of the shock is nearly exactly at the same  $X$ -station as in the experiment in solution NS2 the shock foot is slightly ahead of the experimental one. This is somewhat surprising because solution NS2 shows a lower static pressure at the exit of the test section (at  $X/h_t=3.5$ ) than solution NS1. From this pressure difference one would expect quite the opposite in shock location between NS1 and NS2. The pressure behind the shock (between  $X/h_t=1.6$  to  $2.1$ ) is overpredicted by both calculation methods.

#### Mean Velocity Profile

Here only a selection of mean velocity profiles (scaled by  $\bar{U}_{max} = 386$  m/sec - from experiment) at five  $X$ -stations is shown in Figs. 3.1.4 to 3.1.8; figures supplementary to the ones shown in this section can be found in Appendix 3.3.1. At the station just in front of the shock ( $X/h_t=1.4$ ) solution NS1 underpredicts the velocities whereas NS2 near the wall underpredicts and above that layer slightly overpredicts the velocities. This situation changes inside the shock (Figs. 3.1.5 and 3.1.6) in that now both solutions underpredict the velocities by a noticeable amount. That solution NS1 even produced negative velocities can be seen in Fig. 3.1.6. A separation of this small size could not be recognized in the measured data due to the larger distance of the first measuring point above the wall. The differences between calculations and experiment become smaller further downstream (Fig. 3.1.7). This figure also indicates differences in the laminar sublayer where the experiment depicts a fuller velocity profile than the calculation. Solution NS2 agrees better with the "free-stream" velocity which is underpredicted by NS1 (Fig. 3.1.8). This is in agreement with the static pressure difference at the exit of the test section. However, the boundary layer profile is fuller in solution NS1 and closer to experiment near the wall than in solution NS2 (Fig. 3.1.8).

#### Shear Stress Profiles

Shear stress data have been supplied for solution NS1 only. They are plotted in Figs. 3.1.9 to 3.1.13, for the same  $X$ -stations as the velocity profiles. Near the wall the Reynolds stress in the calculations is generally smaller than in experiment. The calculation delivers a maximum whose magnitude is lower in the upstream part, becomes higher inside the shock and reduces to values again that are smaller than that of the experiment. The distance of the maximum from the wall is larger in solution NS1 than in the experiment around the downstream side of the shock. Upstream and downstream of this area there is a good agreement in this variable. Figs. 3.1.12 and 3.1.13 seem to indicate some small scatter in the measurements closest to the wall.

#### CFD Flow Field

One variable to check the quality of a calculated intake flow is the variation of mass flow along the duct center line. For the solution NS1 this mass flow variation is plotted in Fig. 3.1.14. It can be seen that except in the shock region the mass flow in the test section does deviate from the mass flow entering the intake on the left by less than 0.1 percent. Figures showing lines of constant Mach numbers and pressure coefficient for solution NS1 can be found in the microfiche.

#### 3.3.1.4.2 Test Case 1.2 - $M = 1.45$

##### Static Wall Pressure Distributions

Figs. 3.1.15 and 3.1.16 show a comparison of the computed and experimental static wall pressure distributions (scaled by the tunnel total pressure  $p_{t0}$ ) along the lower and upper wall, respectively. (The coordinate  $X$  along the tunnel wall is scaled by the tunnel height  $h_t = 0.1$  m). Experimental data is shown by the symbol while the analysis are shown by different style lines. The static pressure is plotted as a function of the coordinate  $X$  along the tunnel axis. As can be seen the shock standing at the downstream end of the tunnel wall insert spans the whole tunnel width with the same  $X$ -station at the lower and upper tunnel wall. The static pressure distribution ahead of the shock compares well between both solutions NS1 and NS2 and experiment. Whereas in the solution NS1 the foot of the shock is nearly exactly at the same  $X$ -station as in the experiment in solution NS2 the shock foot is slightly ahead of the experimental one. This shock location difference is to be expected from the difference of the static pressures between the two solutions at the exit of the test section where the pressure of NS1 is higher than that of NS2. The pressure behind the shock indicates the beginning of a plateau which is to be expected in a flow just starting to separate. The pressure in this area is overpredicted by both calculation methods. NS1 exhibits a distinctive and longer plateau whereas NS2 seems to possess a shorter plateau than the experiment. After the separation region the pressure in NS1 is smaller than that of the experiment. Its positive slope indicates a steadily decelerated flow down to the intake exit. The pressure of solution NS2 behind the shock is larger than that of experiment but it is leveling off similar to the experiment. For  $X/h_t$  larger than about 3.5 both flows i.e. that of the experiment and of solution NS2 are no longer accelerated by the static pressure which is in contrast to solution NS1.

##### Mean Velocity Profiles

Here only a selection of mean velocity profiles (scaled by  $\bar{U}_{max} = 418$  m/sec - from experiment) at five  $X$ -stations is shown in Figs. 3.1.17 to 3.1.21; figures supplementary to the ones shown in this section can be found in Appendix 3.3.1. All velocities are scaled by the maximum velocity taken from experiment. At the station in front of the shock (see Fig. 3.1.17 -  $X/h_t=1.6$ ) solution NS1 under-

predicts the velocities even showing negative velocities, i.e. separation, near the wall. Solution NS2 near the wall does not produce negative velocities and overpredicts the velocities above the "wall layer". The measurements are not close enough to the wall to recognize separation. This situation changes closer and inside the shock (Figs. 3.1.18 and 3.1.19) in that now both solutions underpredict the velocities by a noticeable amount. The separation bubble in solution NS1 is steadily growing. Separation is indicated in solution NS2 at  $X/h_t = 1.95$  and  $X/h_t = 2.0$ . Negative velocities are reported from experiment at  $X/h_t = 2.0$  only. The differences between calculations and experiment become smaller further downstream (Fig. 3.1.21). Solution NS2 agrees better with the "free-stream" velocity which is underpredicted by NS1 (Fig. 3.1.21). The boundary layer profile is fuller in solution NS2 and somewhat closer to experiment near the wall than in solution NS1 which still shows negative velocities (Fig. 3.1.21).

#### Shear Stress Profiles

Shear stress data have been supplied for solution NS1 only. Representative plots are given in Figs. 3.1.22 and 3.1.23. In Appendix 3.3.1 the plots at the other X-stations can be found. Near the wall the Reynolds stress in the calculations is generally smaller than in experiment. In front and inside the shock the calculated maximum in the Reynolds stress is underpredicted and the distance from the wall where this maximum occurs is much larger than in the experiment (Fig. 3.1.22). Downstream of  $X/h_t = 2.0$  this distance from the wall of this maximum comes nearer to experimental one, however the magnitude of the Reynolds stress is still underpredicted (Fig. 3.1.23). This figure also shows that the boundary layer of solution NS1 is much thinner than that of the experiment (see also Fig. 3.1.21).

#### CFD Flow Field

For the solution NS1 the mass flow variation in the intake duct is plotted in Fig. 3.1.24. It can be seen that except in the shock region the mass flow in the test section does deviate from the mass flow entering the intake on the left by less than 0.1 percent. Figures showing lines of constant Mach numbers and pressure coefficient for solution NS1 can be found in the microfiche.

#### 3.3.1.4.3 Test Case 1.3 - $M = 1.37$

##### Static Wall Pressure Distributions

Figs. 3.1.25 and 3.1.26 show a comparison of the computed and experimental static wall pressure distributions (scaled by the tunnel total pressure  $p_{t0}$ ) along the lower and upper wall, respectively. (The coordinate  $X$  along the tunnel wall is scaled by the tunnel height  $h_t = 0.096$  m). Experimental data is shown by the symbol while solution NS1 is shown by a solid line. The static pressure is plotted as a function of the coordinate  $X$  along the tunnel axis. As can be seen the shock standing at the downstream end of the tunnel wall insert spans the whole

tunnel width. Because the insert in the tunnel is one-sided only the foot of the shock at the lower wall is more upstream than at the upper tunnel wall. The static pressure distribution ahead of the shock compares quite well between the calculation and the experiment. The pressure on the lower wall indicates the typical separation plateau both in experimental data and in the calculation (Fig. 3.1.25). However, the calculation overpredicts the plateau pressure. Between stations  $X/h_t = 3.2$  and  $4.2$  the calculated pressure on the lower wall is smaller than the measured one. For  $X/h_t$  larger than  $4.2$  the measured pressure drops considerably below the calculated one indicating a strong local acceleration of the flow which is much smaller in the calculation. The static pressure on the upper wall (without separation?) agrees with that of the experiment (Fig. 3.1.26).

#### Mean Velocity Profiles

Here only a selection of mean velocity profiles (scaled by  $\bar{U}_{max} = 403$  m/sec -

from experiment) at five X-stations is shown in Figs. 3.1.27 to 3.1.30; figures supplementary to the ones shown in this section can be found in Appendix 3.3.1. All velocities are scaled by the maximum velocity taken from experiment. The lateral extent of the separation bubble is overpredicted by NS1 for  $X/h_t$  less than 2.865 and underpredicted downstream of

that station. The "inviscid" core velocity is underpredicted in the whole flow field. The most downstream point of the separation bubble at about  $X/h_t = 3.385$  agrees between calculation and experiment (see figure in Appendix 3.3.1). The boundary layer thickness is underpredicted by NS1 for  $X/h_t$  larger than 2.969.

#### Shear Stress Profiles

Representative plots are given in Figs. 3.1.31 to 3.1.34. In Appendix 3.3.1 the plots at the other X-stations can be found. Near the wall the Reynolds stress in the calculations is generally smaller than in the experiment. At the beginning of the shock the calculated maximum in the Reynolds stress is underpredicted and the distance from the wall where this maximum occurs is larger than in the experiment (Fig. 3.1.31). Downstream of  $X/h_t = 2.917$  the distance from the wall of this maximum is smaller in the calculation than in experiment. The magnitude of this maximum is underpredicted always. Relaxation of the turbulence, i.e. reduction of the maximum of the Reynolds stress, becomes noticeable in the experiment downstream of  $X/h_t = 3.385$ . In the calculation the relaxation is negligible due to either the pressure gradient or to the turbulence model.

#### CFD Flow Field

For the solution NS1 the mass flow variation along the duct center line is plotted in Fig. 3.1.35. It can be seen that except in the shock region the mass flow in the test section does deviate from the mass flow entering the intake on the left by less than 0.1 percent. Figures



showing lines of constant Mach numbers and pressure coefficient for solution NS1 can be found in the microfiche.

### 3.3.1.5 CONCLUSIONS

Both methods applied used the Baldwin/Lomax turbulence model. It is known that this model is not very good for flows with separation. This general statement can be made for the flows analysed in this test case too. Unfortunately, from the fact that no calculation results with an alternate turbulence model have been presented, it can not be deduced that no better model exists. Definitely it is very badly needed.

On the other hand there are questions also for the experimental people. CFD needs detailed data on the boundaries of the computational domain, in this case at the entrance and exit of the test section. These data have not been collected for the flows considered. It would be worthwhile to repeat those tests and gather all the data needed for a more detailed comparison than was possible here. The question of the accuracy of the test data should also be raised. Raising this question does not mean that the data presented here are in doubt. But in a future effort, i.e. future comparison, the dependency of the measured data on, for example, particle size or laser power should be investigated. It should also be determined how close to the wall the measuring technique selected does deliver correct data.

### 3.3.1.6 References

- 3.1.1 Delery J., Marvin J.G., "Shock-Wave Boundary Layer Interactions", AGARD-AG-280, February 1986
- 3.1.2 Delery J.M., "Experimental Investigation of Turbulence Properties in Transonic Shock/Boundary-Layer Interactions", AIAA Journal Vol.21, No.2, February 1983, pp.180-185 and AIAA-81-1245, 1981
- 3.1.3 Delery J., Copy C., Reisz J., "Analyse au velocimetre laser bidirectionnel d'une interaction choc-couche limite turbulente avec decollement etendu", ONERA Rapport Technique No. 37/7078 AY 014, August 1980
- 3.1.4 Copy C., Reisz J., "Analyse experimentale d'une interaction choc-couche limite turbulente a Mach 1,30 (decollement naissant)", ONERA Rapport Technique No. 42/7078 AY 014, December 1980
- 3.1.5 Reisz J., "Analyse experimentale d'une interaction choc - couche limite turbulente a Mach 1,45", ONERA Rapport Technique No. 44/7078 AY 014, June 1981
- 3.1.6 Brenneis A., "Aerodynamische Einlaufrechnungen in Rahmen der AGARD Working Group 13 (Testfall TC1/6)", MBB/FE122/S/R/1627/A, 21.8.1990

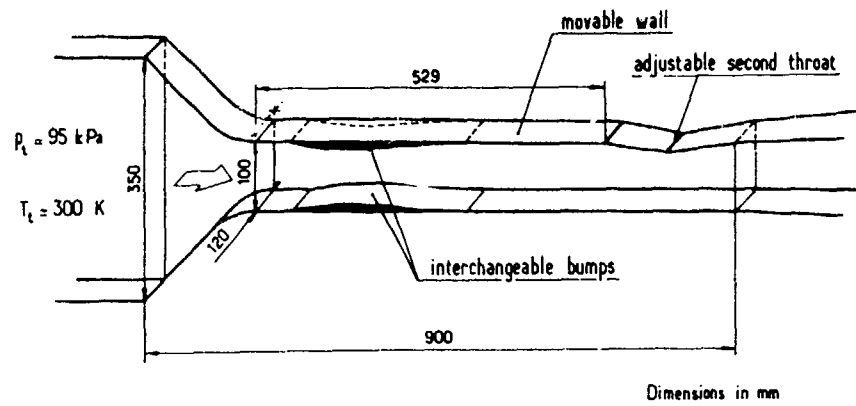


FIG. 3.1.1 EXPERIMENTAL ARRANGEMENT FOR TEST CASE 1

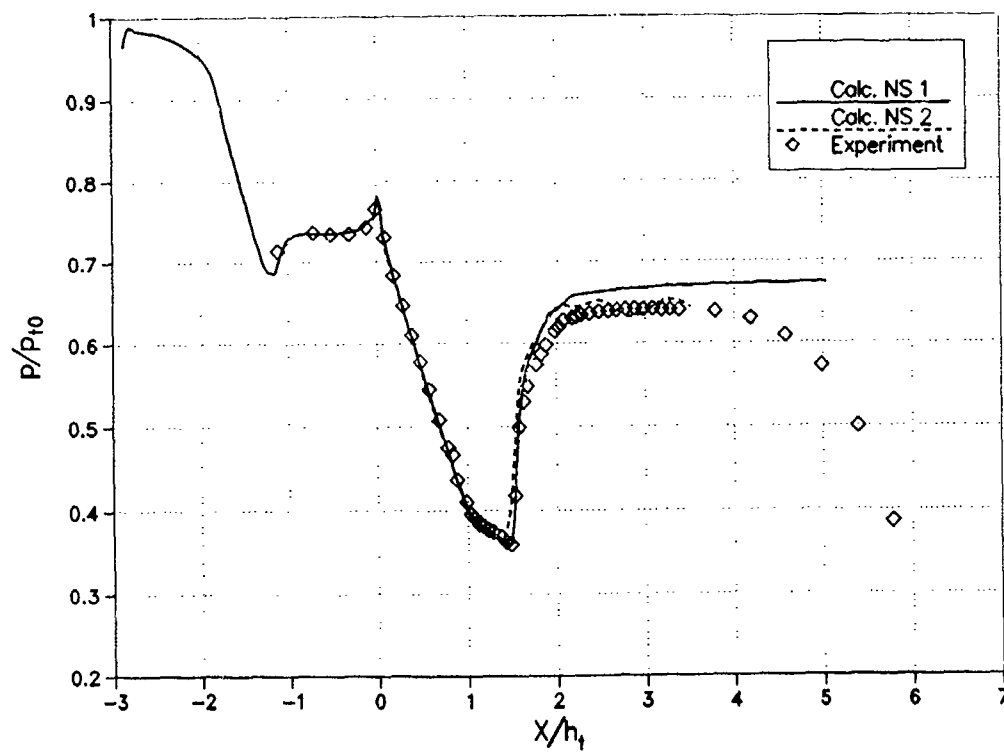


FIG. 3.1.2 TEST CASE 1.1: STATIC WALL PRESSURE ON LOWER TUNNEL WALL

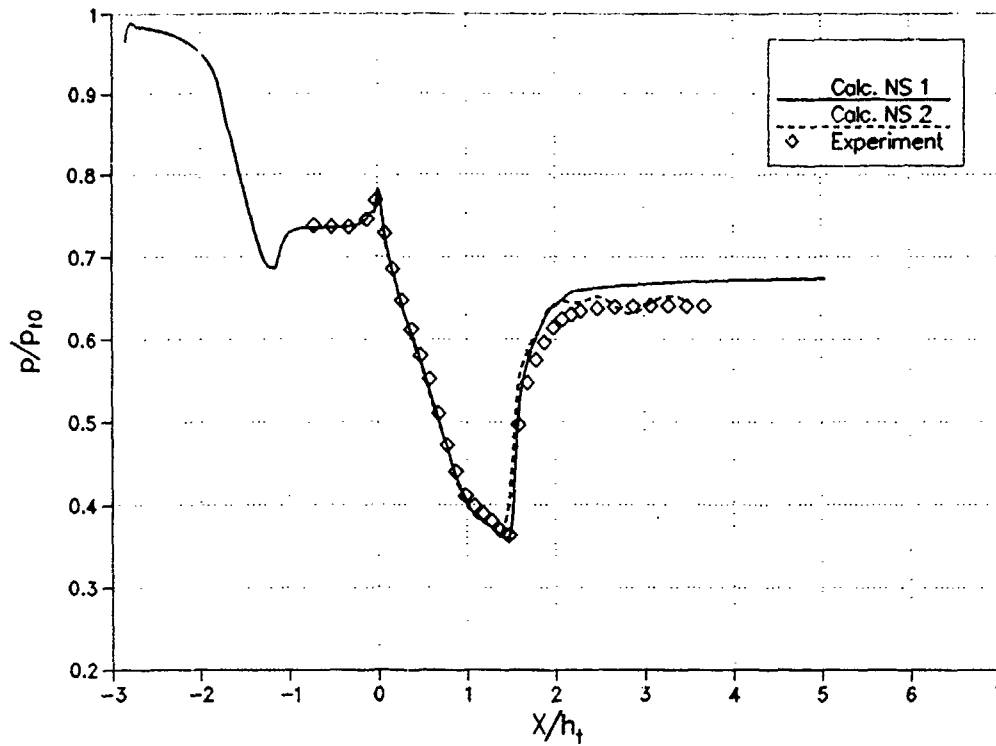
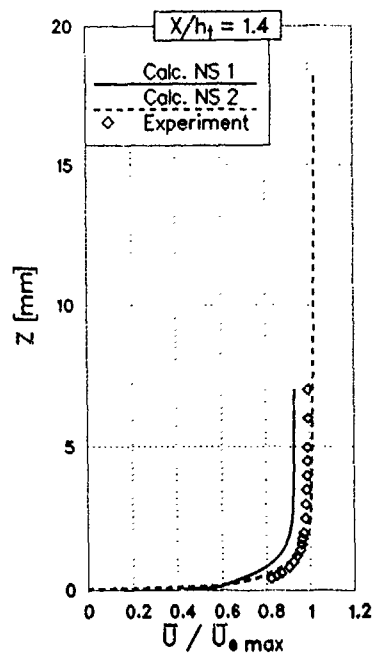
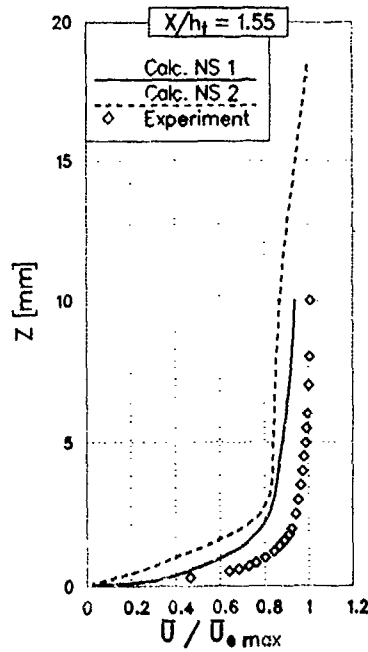


FIG. 3.1.3 TEST CASE 1.1: STATIC WALL PRESSURE ON UPPER TUNNEL WALL

FIG. 3.1.4  
MEAN VELOCITY PROFILES  
TEST CASE 1.1FIG. 3.1.5  
MEAN VELOCITY PROFILES  
TEST CASE 1.1

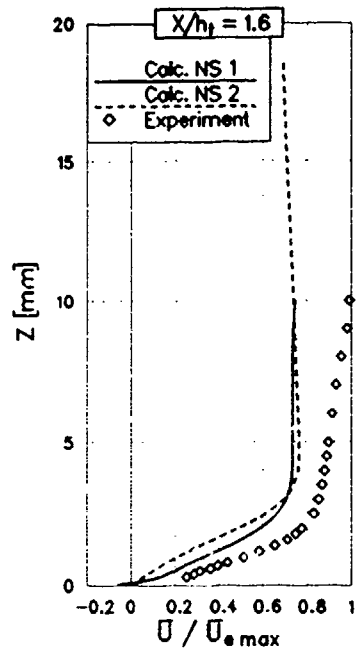


FIG. 3.1.6  
MEAN VELOCITY PROFILES  
TEST CASE 1.1

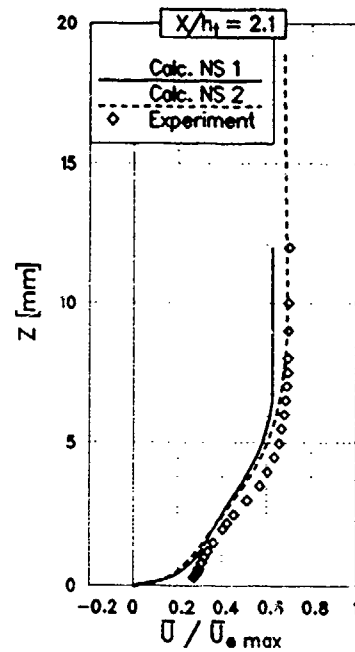


FIG. 3.1.7  
MEAN VELOCITY PROFILES  
TEST CASE 1.1

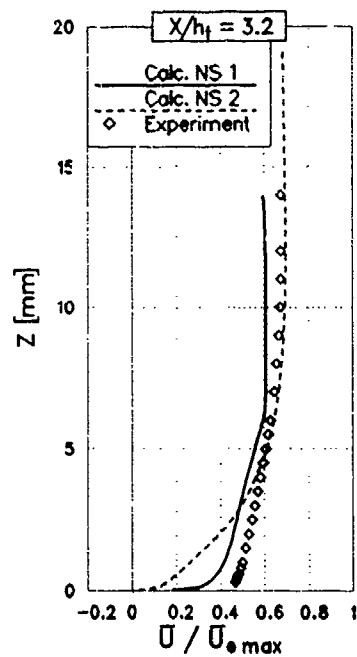


FIG. 3.1.8  
MEAN VELOCITY PROFILES  
TEST CASE 1.1

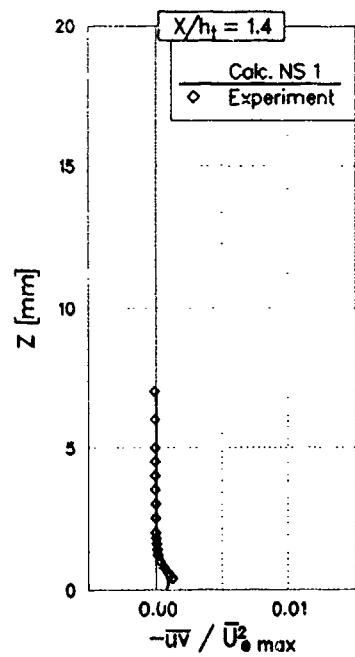


FIG. 3.1.9  
SHEAR STRESS PROFILES  
TEST CASE 1.1

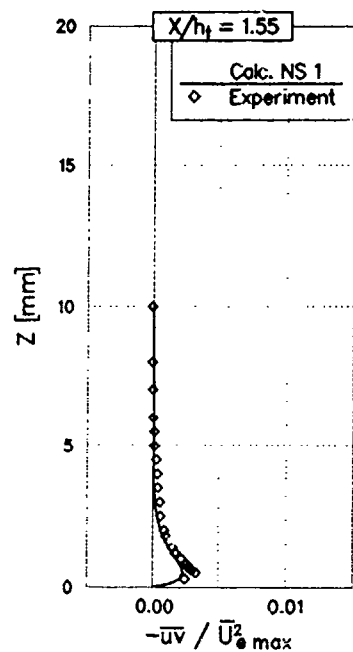


FIG. 3.1.10  
SHEAR STRESS PROFILES  
TEST CASE 1.1

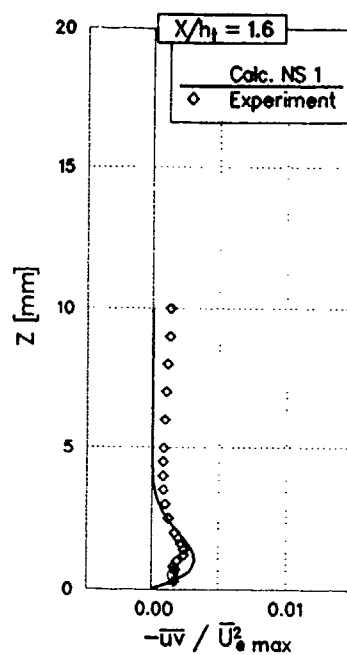


FIG. 3.1.11  
SHEAR STRESS PROFILES  
TEST CASE 1.1

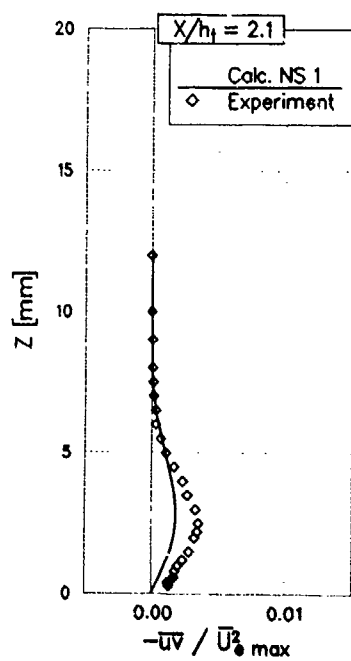


FIG. 3.1.12  
SHEAR STRESS PROFILES  
TEST CASE 1.1

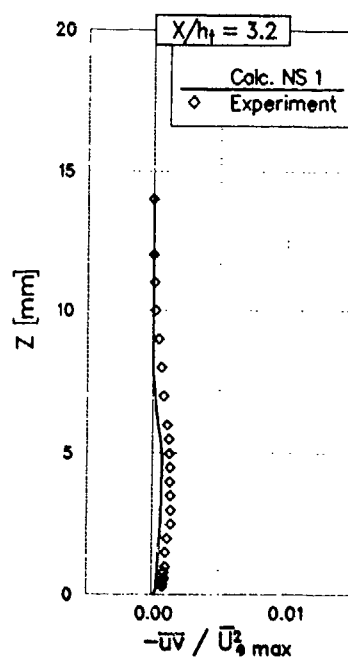


FIG. 3.1.13  
SHEAR STRESS PROFILES  
TEST CASE 1.1

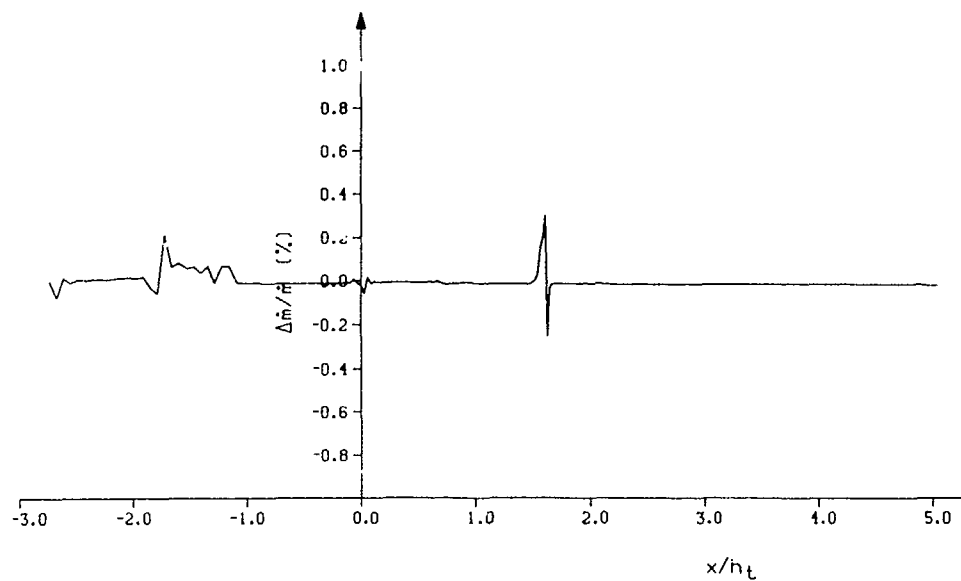


FIG. 3.1.14 TEST CASE 1.1: MASS FLOW LOSS ALONG DUCT IN SOLUTION NS1

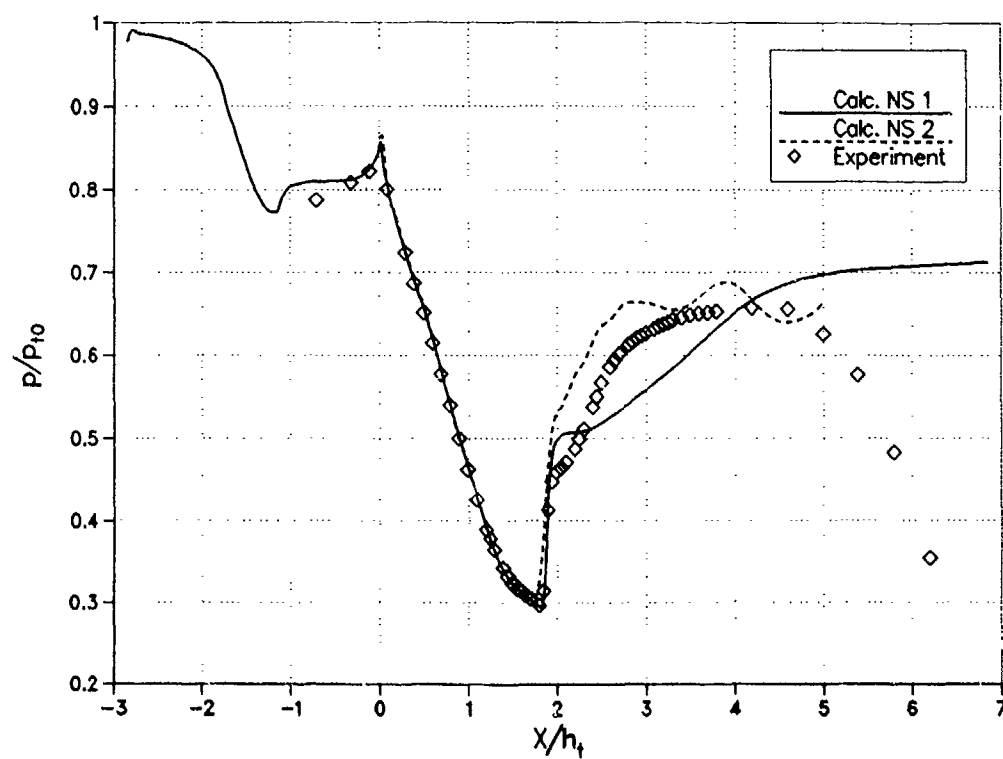


FIG. 3.1.15 TEST CASE 1.2: STATIC WALL PRESSURE ON LOWER TUNNEL WALL

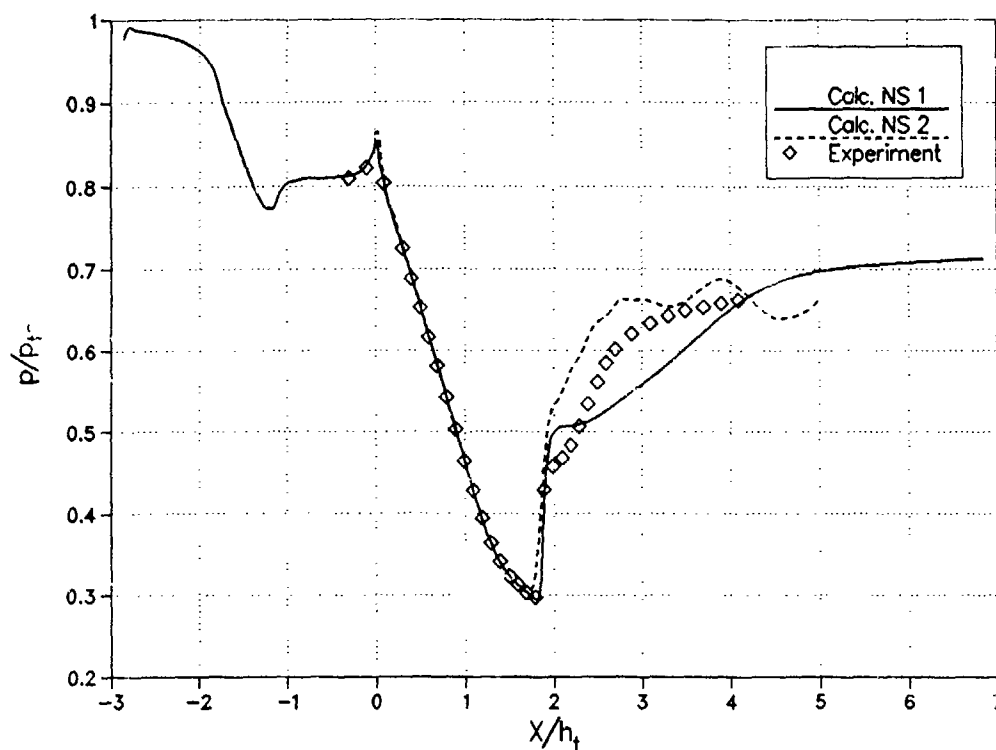
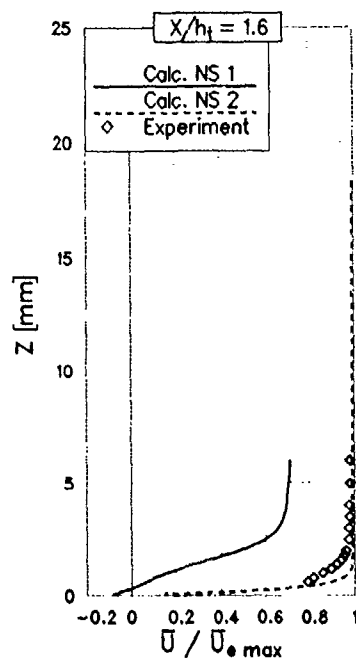
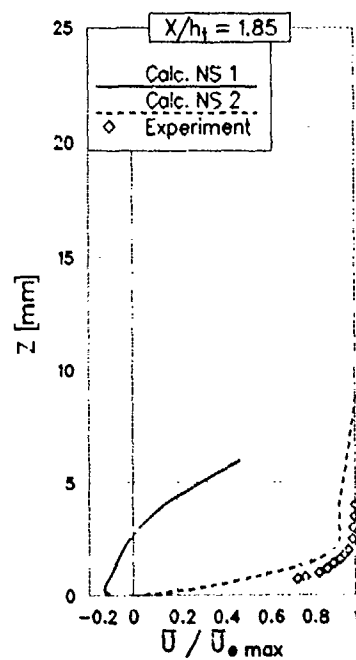


FIG. 3.1.16 TEST CASE 1.2: STATIC WALL PRESSURE ON UPPER TUNNEL WALL

FIG. 3.1.17  
MEAN VELOCITY PROFILES  
TEST CASE 1.2FIG. 3.1.18  
MEAN VELOCITY PROFILES  
TEST CASE 1.2

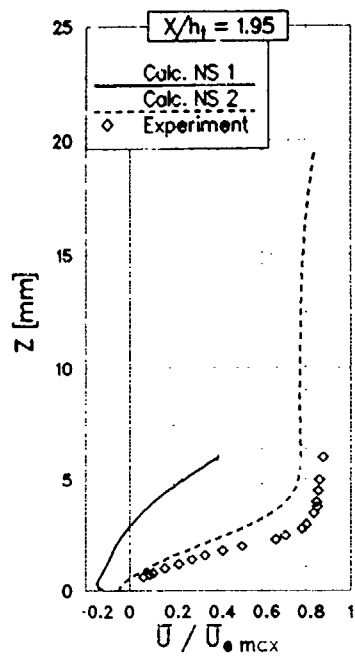


FIG. 3.1.19  
MEAN VELOCITY PROFILES  
TEST CASE 1.2

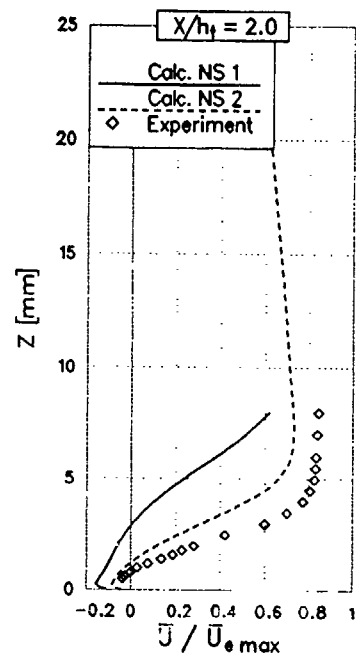


FIG. 3.1.20  
MEAN VELOCITY PROFILES  
TEST CASE 1.2

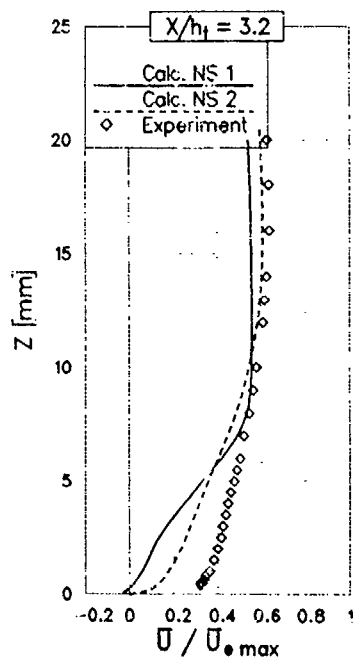


FIG. 3.1.21  
MEAN VELOCITY PROFILES  
TEST CASE 1.2

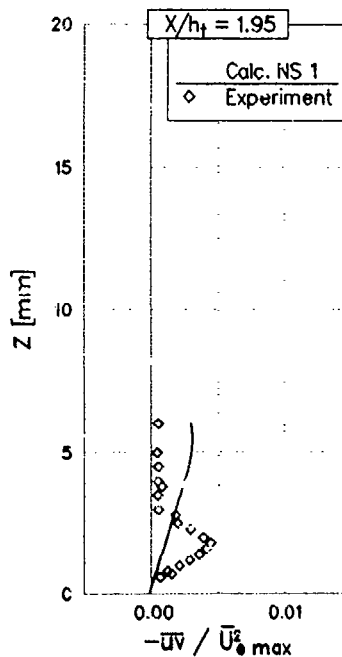


FIG. 3.1.22  
SHEAR STRESS PROFILES  
TEST CASE 1.2



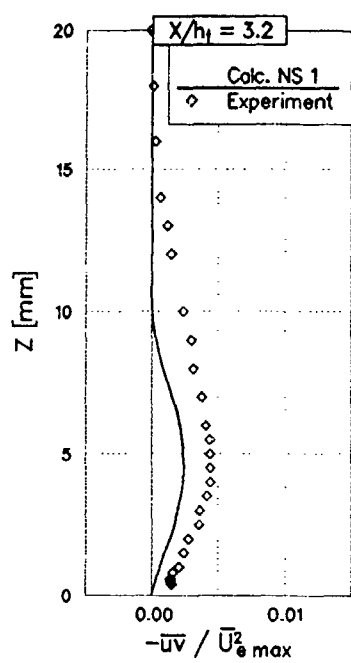


FIG. 3.1.23  
SHEAR STRESS PROFILES  
TEST CASE 1.2

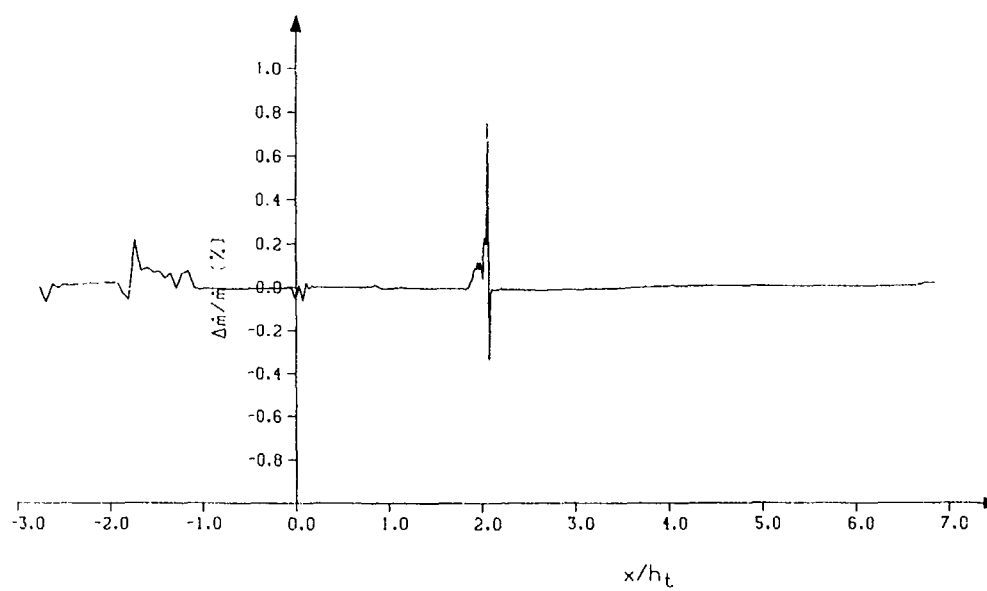


FIG. 3.1.24 TEST CASE 1.2: MASS FLOW LOSS ALONG DUCT IN SOLUTION NS1

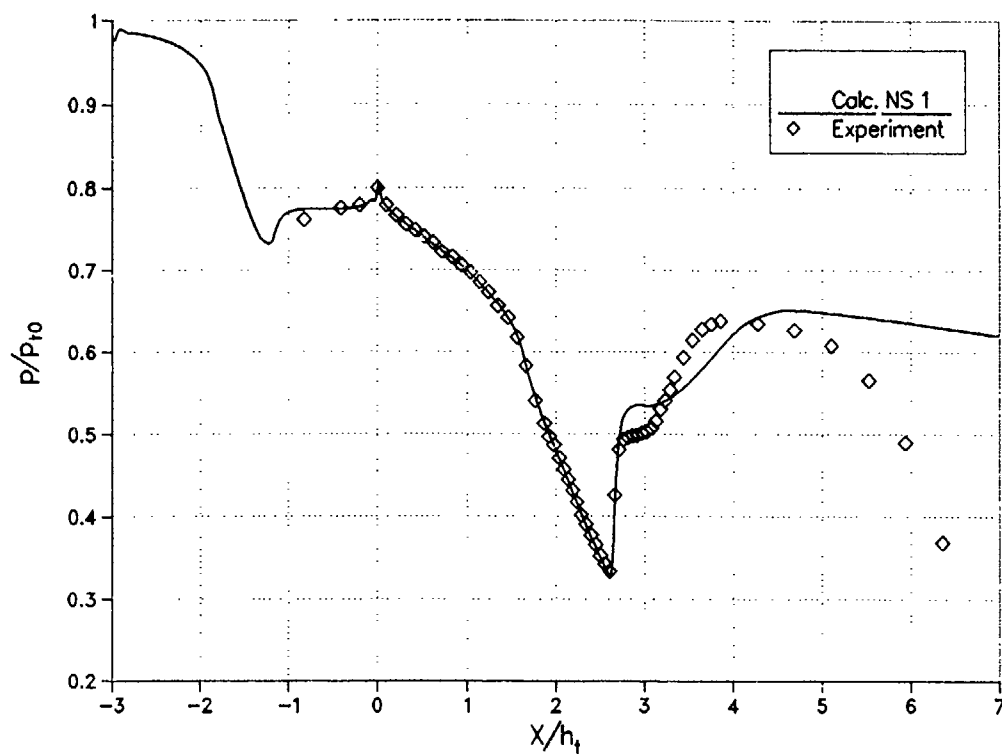


FIG. 3.1.25 TEST CASE 1.3: STATIC WALL PRESSURE ON LOWER TUNNEL WALL

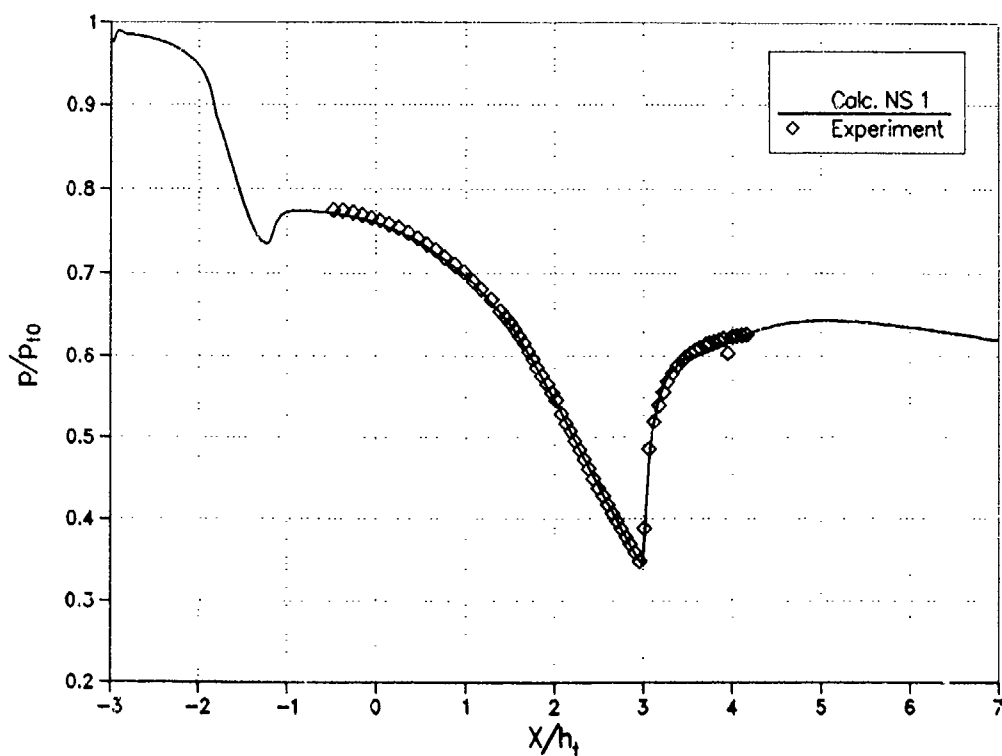


FIG. 3.1.26 TEST CASE 1.3: STATIC WALL PRESSURE ON UPPER TUNNEL WALL

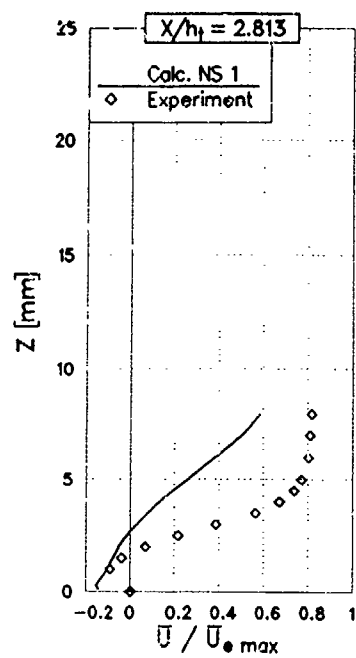


FIG. 3.1.27  
MEAN VELOCITY PROFILES  
TEST CASE 1.3

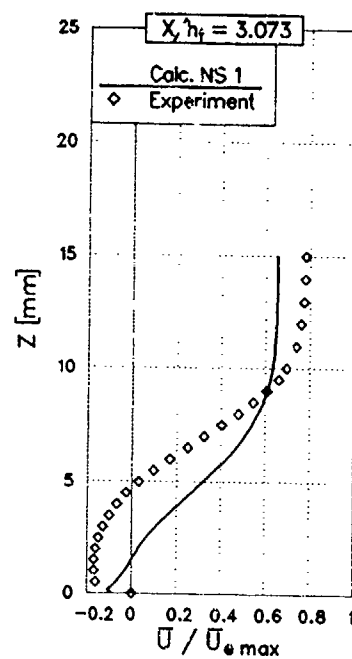


FIG. 3.1.28  
MEAN VELOCITY PROFILES  
TEST CASE 1.3

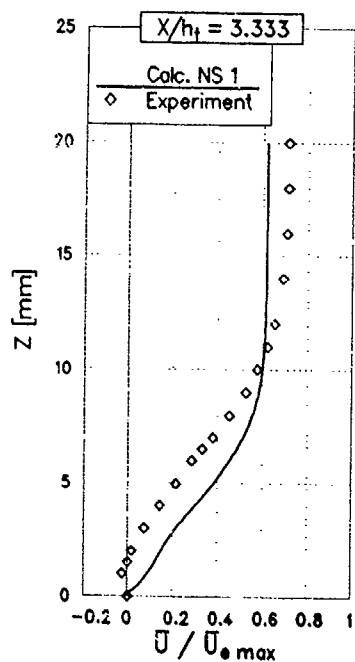


FIG. 3.1.29  
MEAN VELOCITY PROFILES  
TEST CASE 1.3

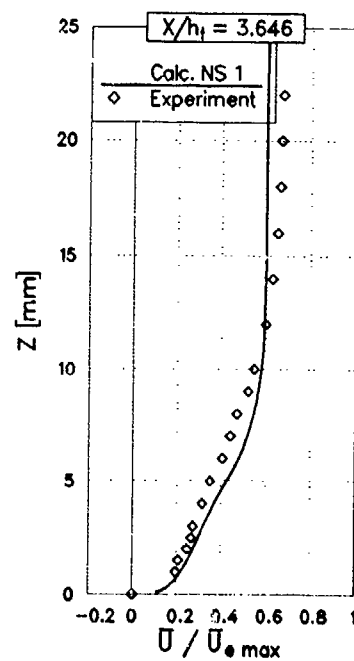


FIG. 3.1.30  
MEAN VELOCITY PROFILES  
TEST CASE 1.3

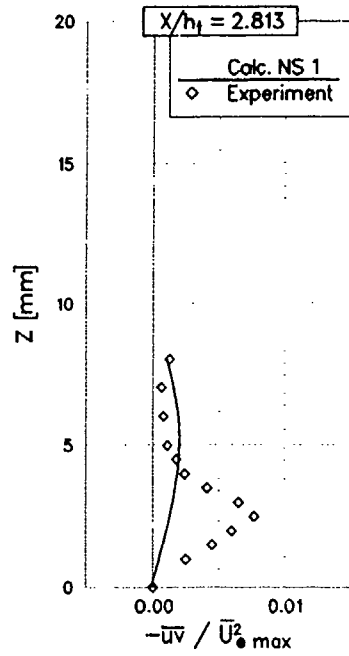


FIG. 3.1.31  
SHEAR STRESS PROFILES  
TEST CASE 1.3

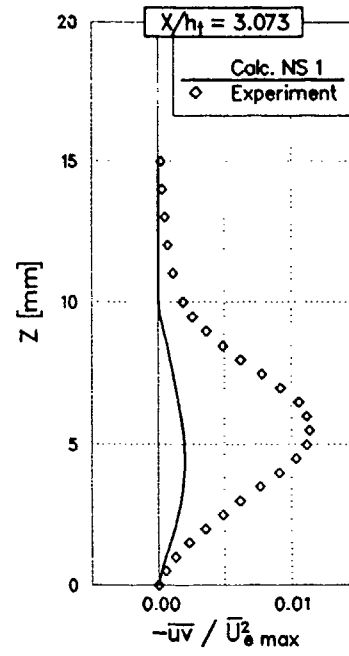


FIG. 3.1.32  
SHEAR STRESS PROFILES  
TEST CASE 1.3

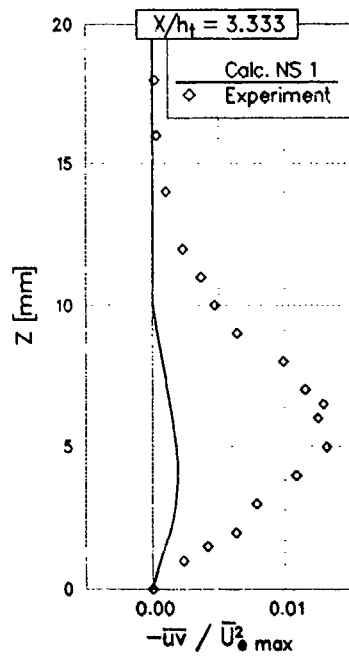


FIG. 3.1.33  
SHEAR STRESS PROFILES  
TEST CASE 1.3

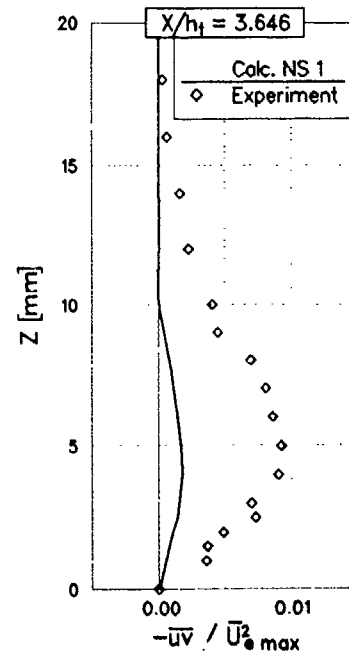


FIG. 3.1.34  
SHEAR STRESS PROFILES  
TEST CASE 1.3

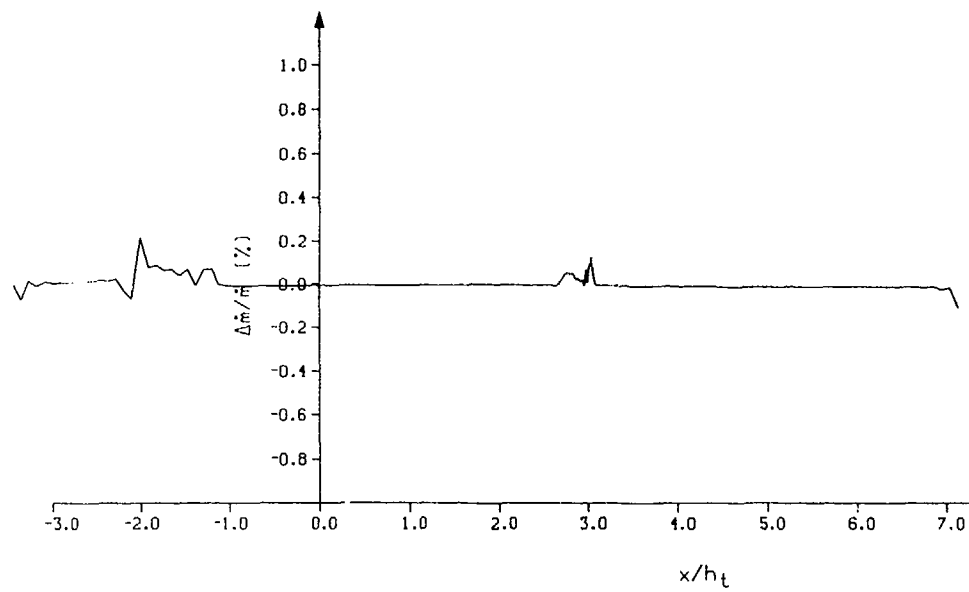
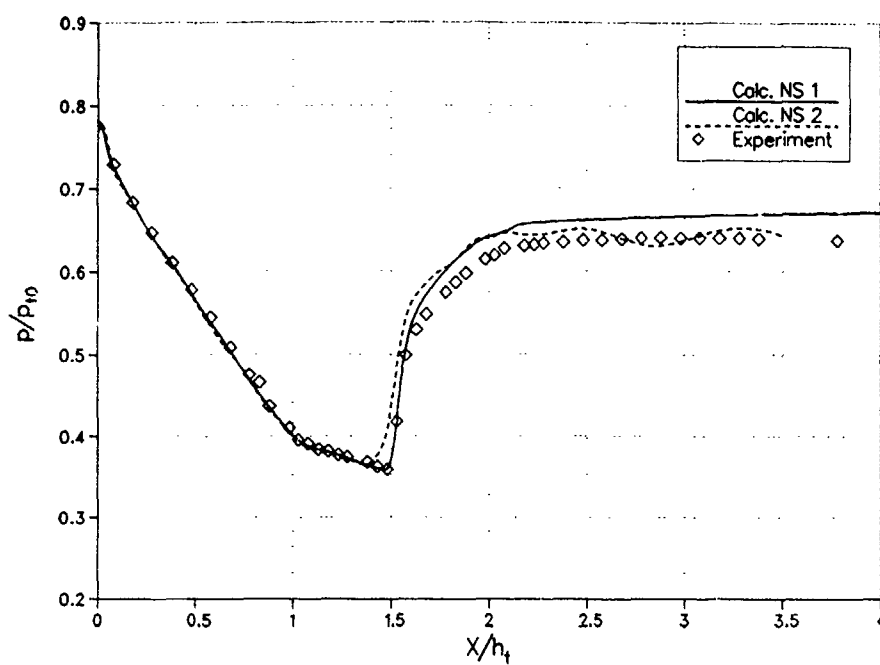


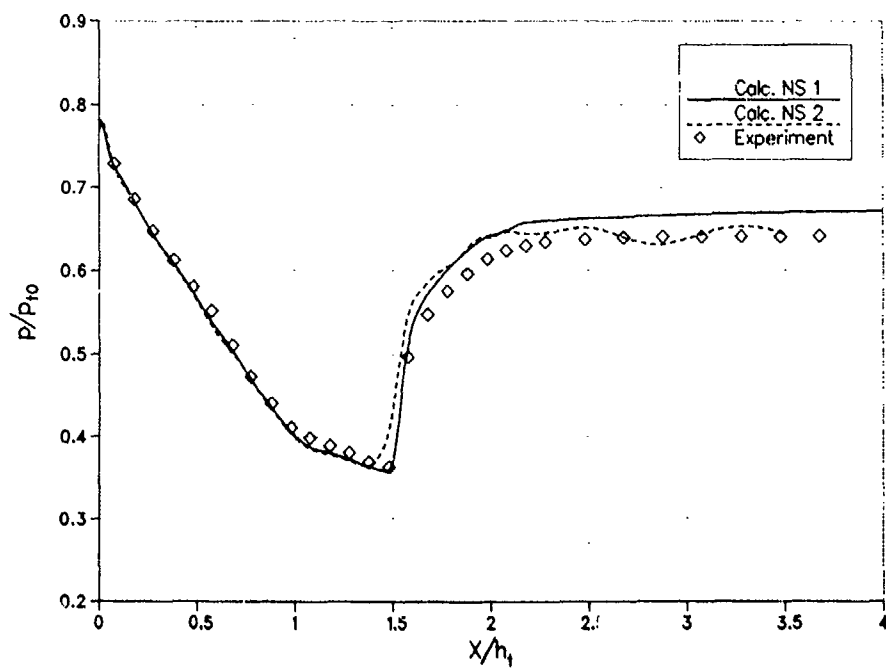
FIG. 3.1.35 TEST CASE 1.3: MASS FLOW LOSS ALONG DUCT IN SOLUTION NS1

Appendix 3.3.1  
Supplementary Figures for Test Case 1

AGARD WG13, Test Case 1.1  
Static Wall Pressure on Lower Tunnel Wall

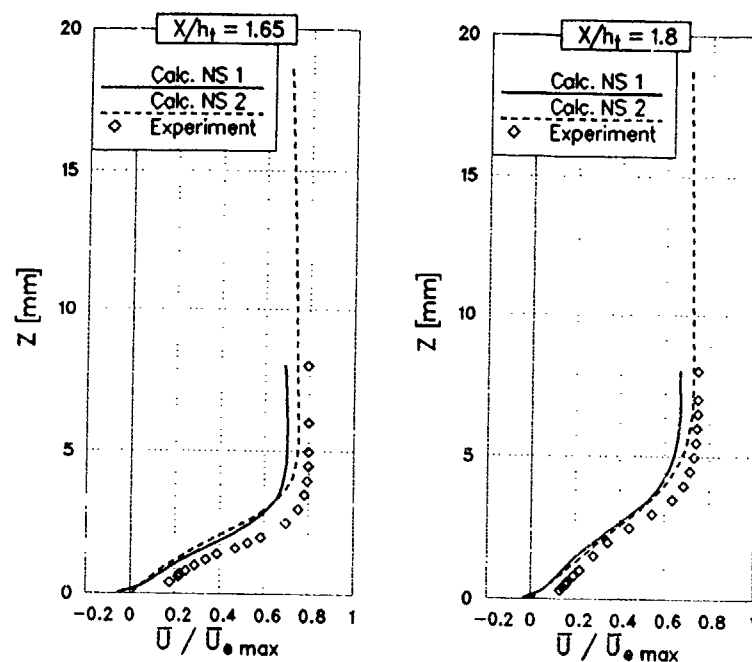


AGARD WG13, Test Case 1.1  
Static Wall Pressure on Upper Tunnel Wall



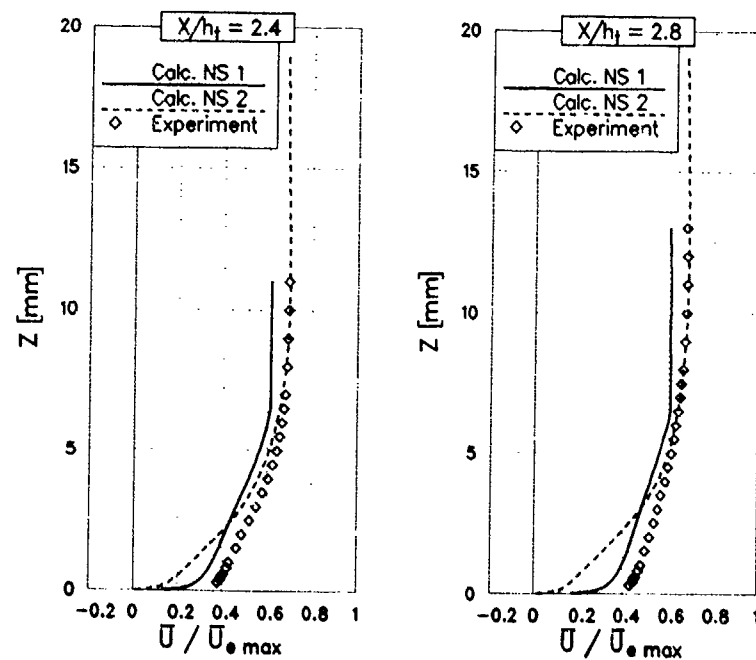
## AGARD WG 13, Test Case 1.1

## Mean Velocity Profiles



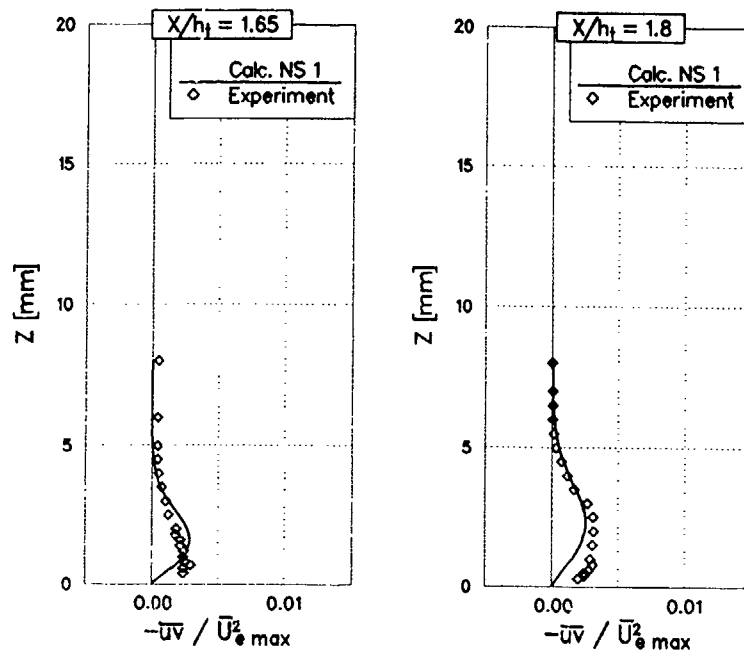
## AGARD WG 13, Test Case 1.1

## Mean Velocity Profiles



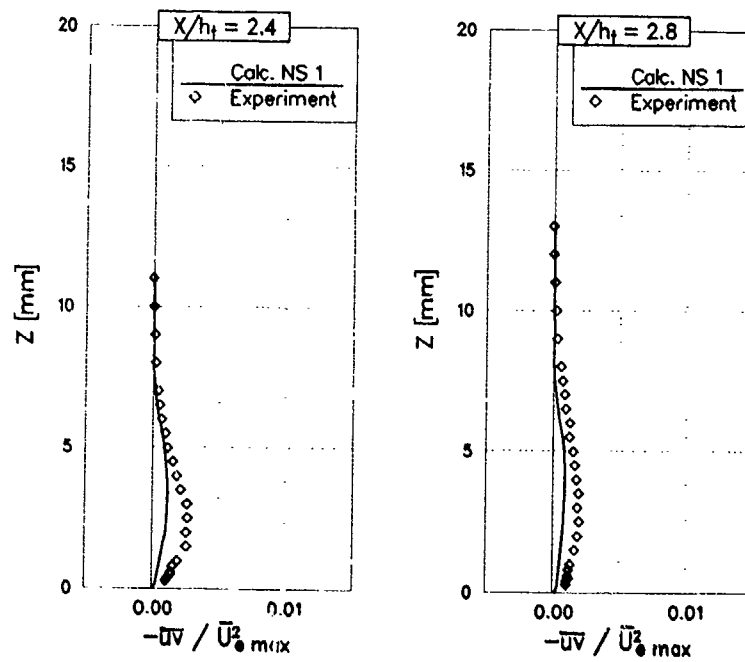
## AGARD WG13, Test Case 1.1

## Shear Stress Profiles



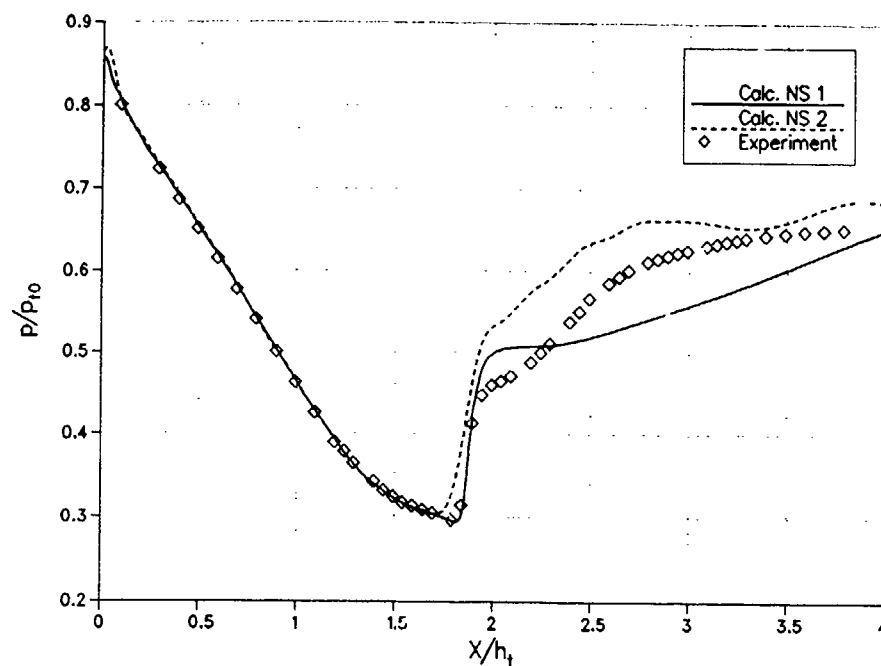
## AGARD WG13, Test Case 1.1

## Shear Stress Profiles

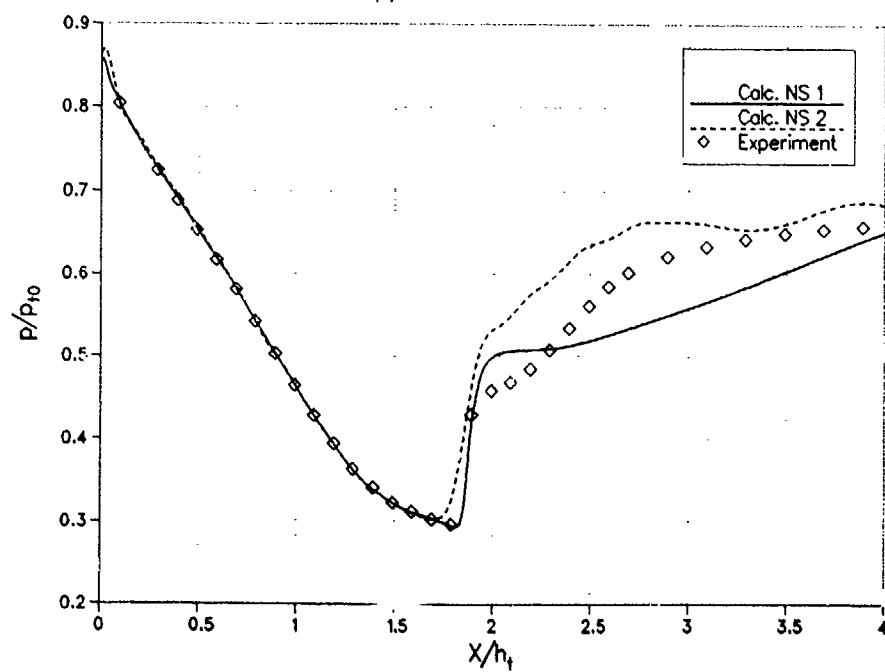




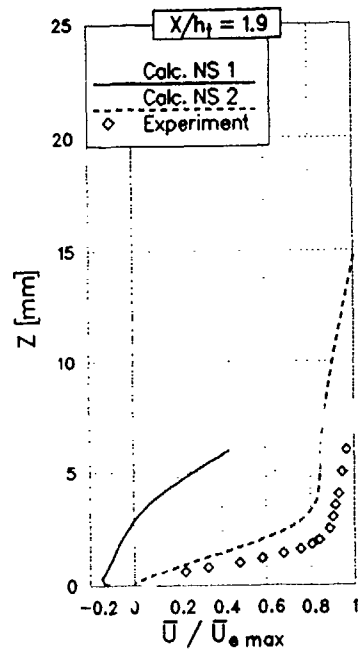
AGARD WG13, Test Case 1.2  
Static Wall Pressure on Lower Tunnel Wall



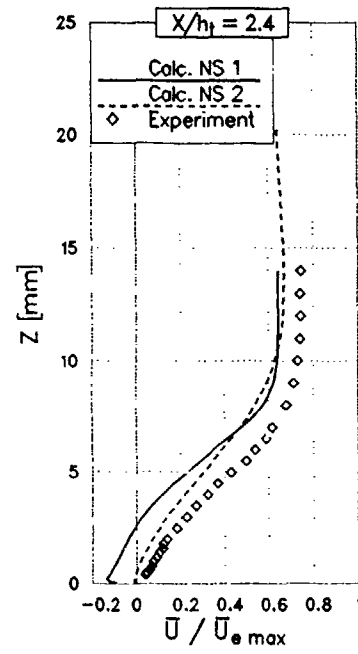
AGARD WG13, Test Case 1.2  
Static Wall Pressure on Upper Tunnel Wall



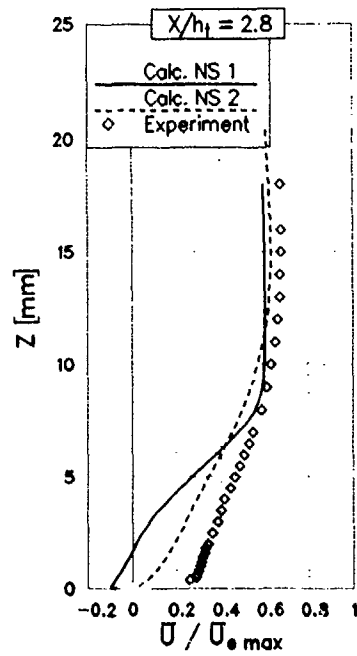
AGARD WG 13, Test Case 1.2  
Mean Velocity Profiles



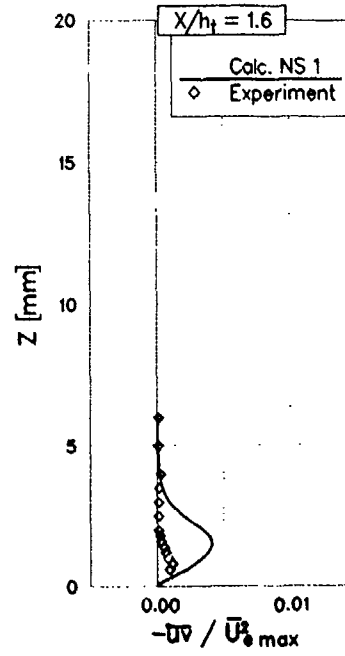
AGARD WG 13, Test Case 1.2  
Mean Velocity Profiles



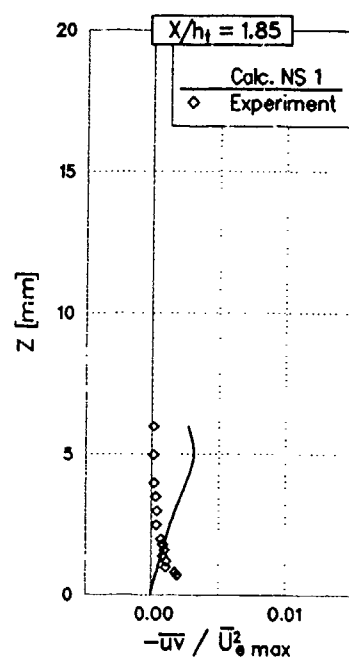
AGARD WG 13, Test Case 1.2  
Mean Velocity Profiles



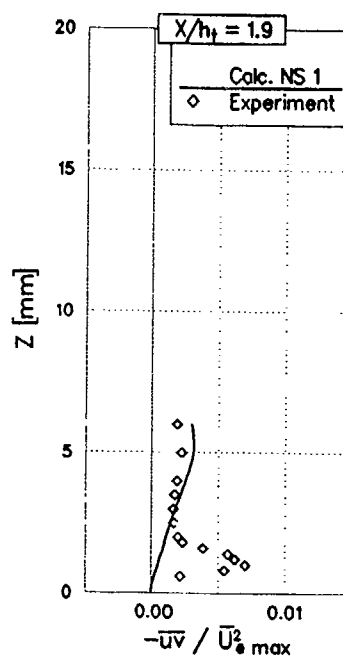
AGARD WG13, Test Case 1.2  
Shear Stress Profiles



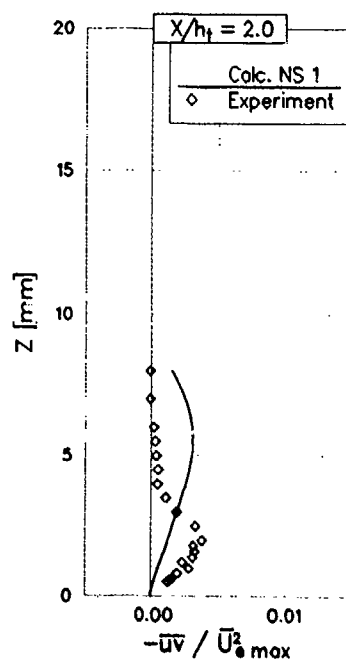
AGARD WG13, Test Case 1.2  
Shear Stress Profiles



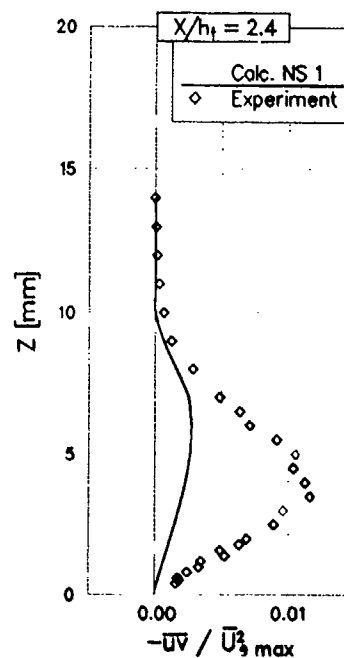
AGARD WG13, Test Case 1.2  
Shear Stress Profiles



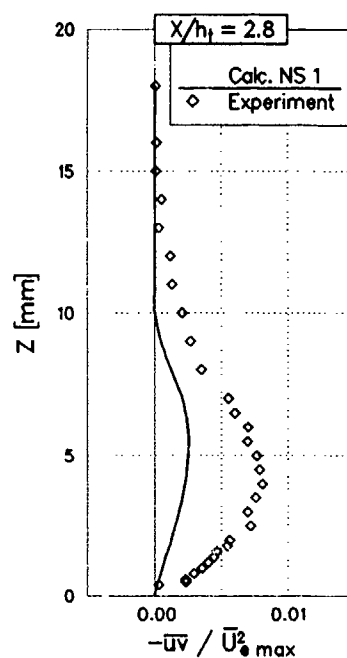
AGARD WG13, Test Case 1.2  
Shear Stress Profiles



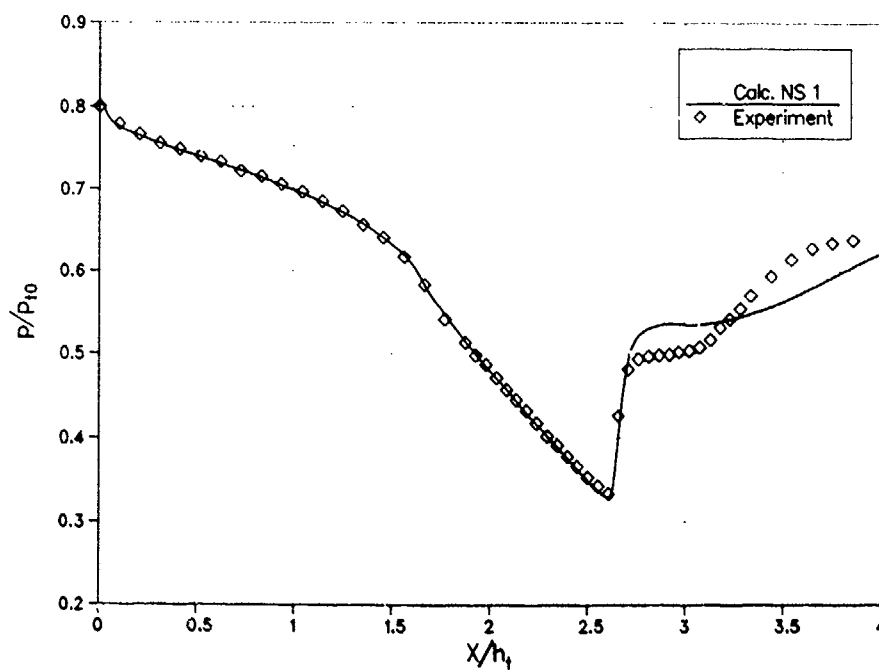
AGARD WG13, Test Case 1.2  
Shear Stress Profiles



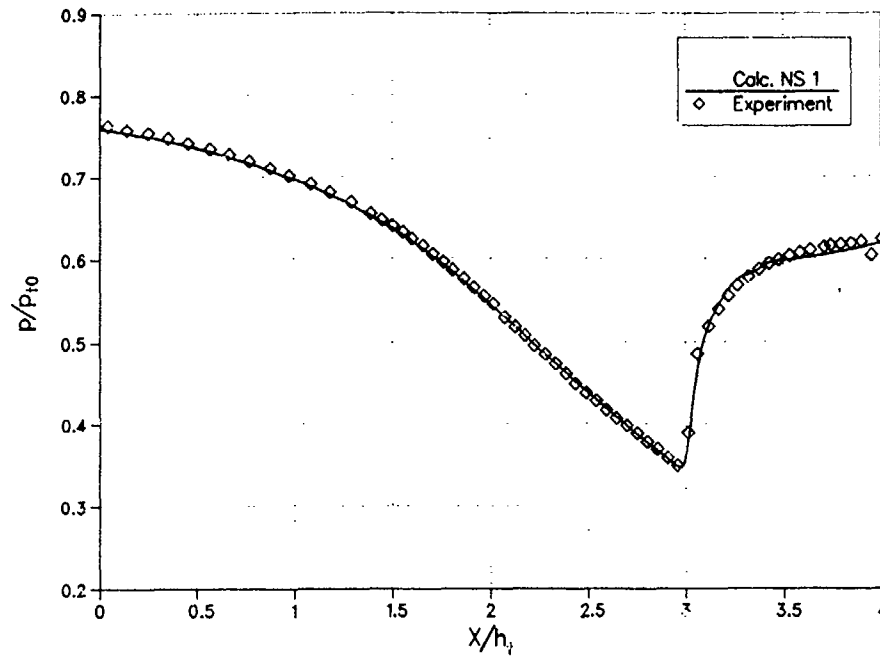
AGARD WG13, Test Case 1.2  
Shear Stress Profiles



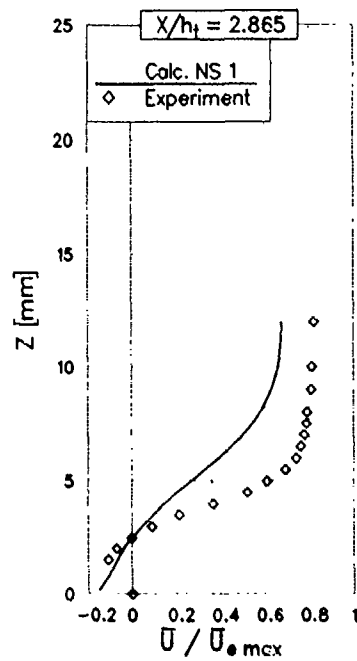
AGARD WG13, Test Case 1.3  
Static Wall Pressure on Lower Tunnel Wall



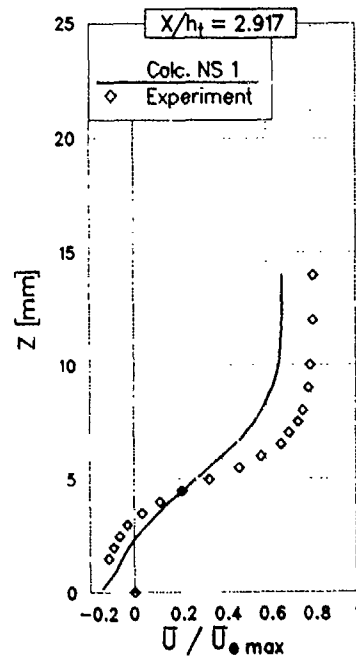
AGARD WG13, Test Case 1.3  
Static Wall Pressure on Upper Tunnel Wall



AGARD WG 13, Test Case 1.3  
Mean Velocity Profiles

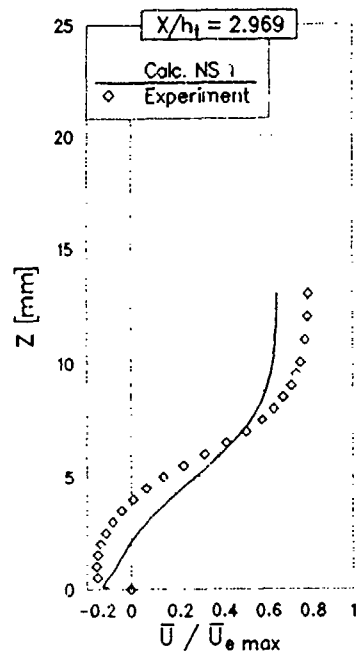


AGARD WG 13, Test Case 1.3  
Mean Velocity Profiles



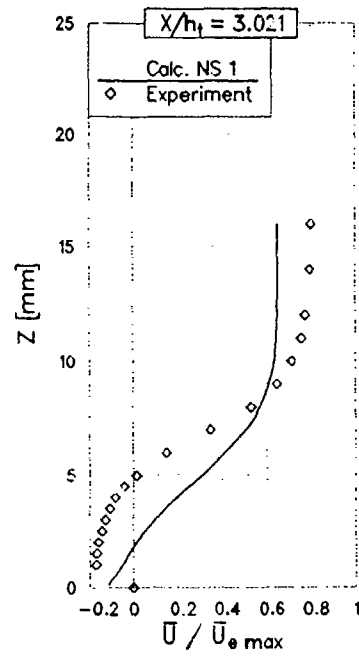
AGARD WG 13, Test Case 1.3

Mean Velocity Profiles



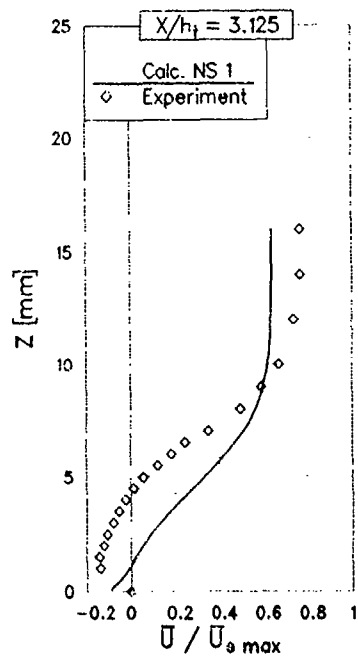
AGARD WG 13, Test Case 1.3

Mean Velocity Profiles



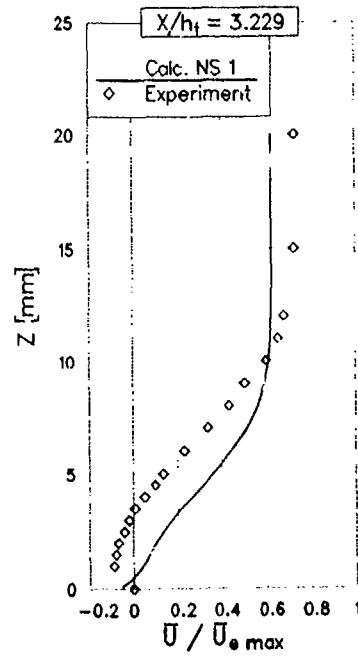
AGARD WG 13, Test Case 1.3

Mean Velocity Profiles

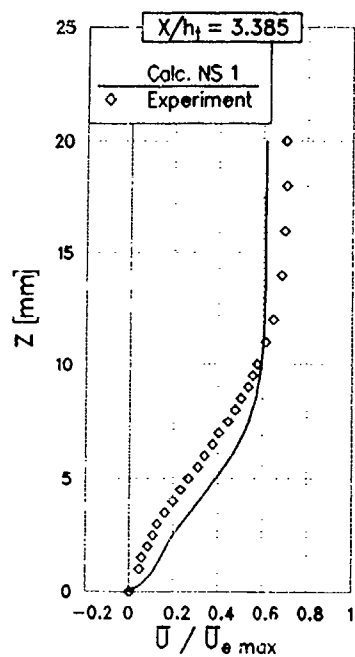


AGARD WG 13, Test Case 1.3

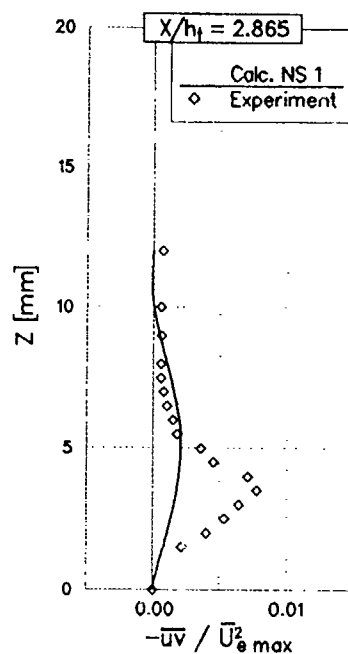
Mean Velocity Profiles



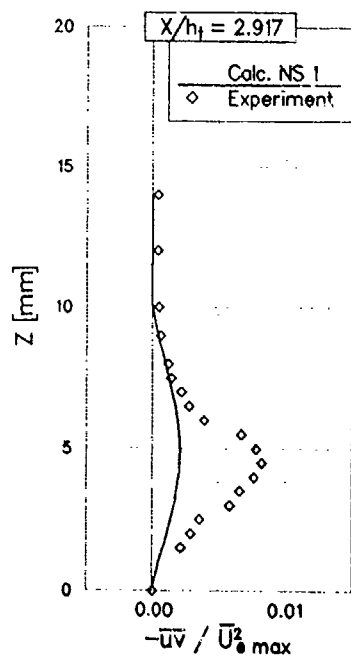
AGARD WG 13, Test Case 1.3  
Mean Velocity Profiles



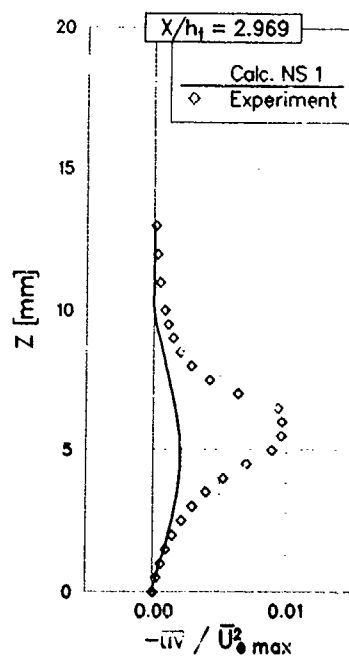
AGARD WG13, Test Case 1.3  
Shear Stress Profiles



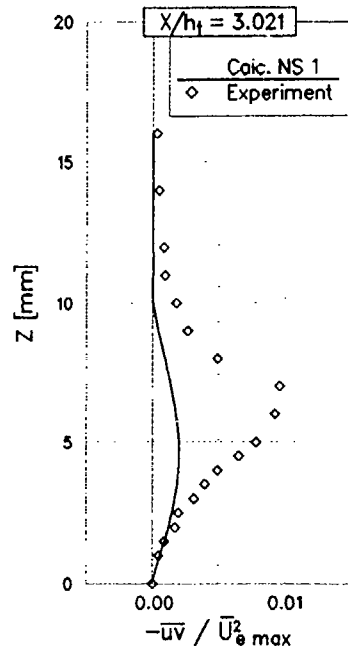
AGARD WG13, Test Case 1.3  
Shear Stress Profiles



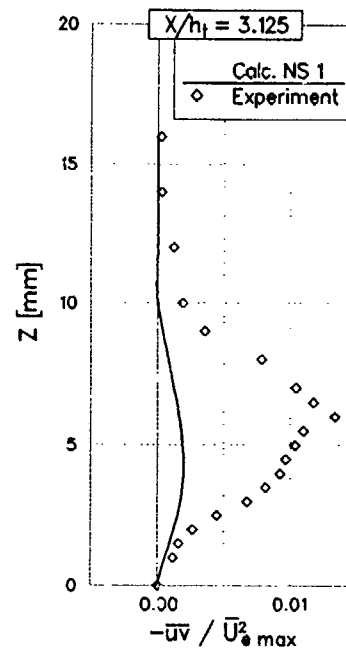
AGARD WG13, Test Case 1.3  
Shear Stress Profiles



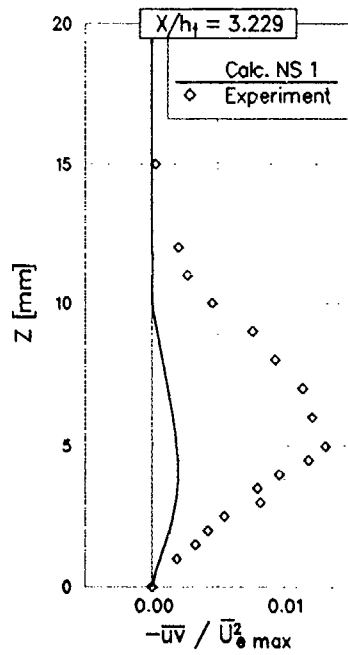
AGARD WG13, Test Case 1.3  
Shear Stress Profiles



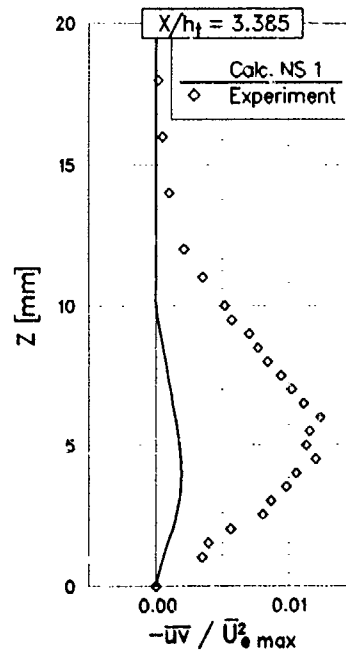
AGARD WG13, Test Case 1.3  
Shear Stress Profiles



AGARD WG13, Test Case 1.3  
Shear Stress Profiles



AGARD WG13, Test Case 1.3  
Shear Stress Profiles





### 3.3.2 Test Case 2 - Glancing Shock/Boundary Layer Interaction

#### 3.3.2.1 INTRODUCTION

The assessment of the ability of computational fluid dynamics (CFD) to accurately model intake flow fields is being conducted in a two step process. First, the ability of the codes to model simple flow fields which highlight only one basic flow mechanism will be assessed. Second, the ability of the codes to model actual intake flow fields with all of its complexity will be assessed. This initial assessment of codes for basic flow mechanisms is required because full component tests do not typically have the large quantities of data necessary to resolve all the features in the flow field. There are often interactions between basic flow mechanisms in full configurations which make interpretation of the results more difficult than with a single interaction. With this in mind, Test Case 2 has been chosen to assess the ability of CFD codes to model a single, three-dimensional shock wave/boundary layer interaction which often occurs in high speed rectangular intakes. The perspective here is not to do a detailed study of this interaction; this and other shock wave/boundary layer interactions have previously been the subject of AGARD studies, Ref 3.2.1. The purpose of this study is to assess the accuracy of CFD codes which are designed for full intake modeling by testing their ability to model a single flow phenomenon.

#### 3.3.2.2 PROBLEM DESCRIPTION

The problem to be considered is geometrically simple; a ten degree wedge is mounted on a flat plate which extends upstream of the wedge leading edge. A supersonic freestream flow sweeps along the plate and strikes the wedge. The shock wave generated by the wedge interacts with the boundary layer formed on the plate to produce a highly three-dimensional supersonic flow field. This type of interaction occurs in high speed intakes when the oblique shock wave formed by a compression wedge interacts with the boundary layer formed on a sidewall, as discussed in Section 2.4.5. The glancing shock/boundary layer interaction has been studied by numerous authors both experimentally and analytically, Refs. 3.2.1 through 3.2.5. The particular flow field to be modeled in this study has been experimentally investigated by Oskam, Vas and Bogdonoff, Ref 3.2.2. Fig. 3.2.1. presents a schematic diagram of their wind tunnel test section showing the

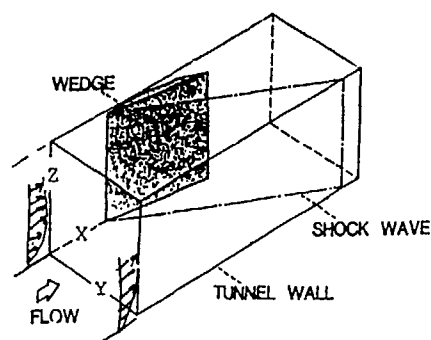


FIG 3.2.1 SCHEMATIC DRAWING OF  
GLANCING SHOCK/BOUNDARY LAYER  
INTERACTION TEST GEOMETRY.

location of the shock generating wedge, the flat plate and the incident and reflected shock waves. In this study, the nominal Mach number upstream of the wedge was 2.94 at a Reynolds number of  $1.76 \times 10^6$ .

Various models of this interaction have been proposed, although all of them contain the following features. In the inviscid core region, away from the plate and wedge boundary layers, the high energy fluid is turned parallel to the wedge surface. In the viscous region near the plate, the low energy fluid is turned much more than the wedge angle, nearly following the shock wave angle. In the lowest portion of the plate boundary layer, this turning occurs upstream of the inviscid shock location. A strong secondary flow is present in the viscous region with fluid moving along the plate from the wedge toward the shock wave. This cross flow near the plate causes the plate boundary layer to thicken in the vicinity of the shock and to thin down near the wedge. Previous computational models of this flow field, Refs 3.2.6 through 3.2.7 have indicated a vortex-like swirling of the flow near the plate and slightly downstream of the shock wave. Surface oil flows and static pressure distributions on the plate, downstream of the shock wave show a nearly conical flow distribution.

There were three principal types of data taken in the experiment. Surface static pressures were measured along the plate across the shock wave at a variety of distances from the wedge leading edge. Additionally, a traversing nulling pitot probe was used to determine both pitot pressure and flow yaw angle at selected locations through the interaction. The yaw angle was measured in a plane

parallel to the flat plate. Comparisons will be made between the results of calculations and these measurements. All of the comparisons for this case are presented in Appendix 3.3.2.

### 3.3.2.3 CFD TECHNIQUES

This test case was attempted by five different research groups as noted in Table 3.2.1 in section 3.2. The analysis techniques included Reynolds-Averaged Navier-Stokes (NS) and Parabolized Navier-Stokes (PNS). The NS analysis included three different versions of Beam-Warming solvers. The General Dynamics group used the HAWK3D code with a k-k1 turbulence model, designated (NS1) for comparison purposes, while the groups from Sverdrup-AEDC and Sverdrup-LERC used the PARC3D code with a Baldwin-Lomax turbulence model, designated (NS3) and (NS4) for comparisons. The group from ONERA, designated (NS2), used an explicit Lax-Wendroff solver with a Michel algebraic turbulence model. The PNS analysis was performed at NASA-Lewis using the PEPSIS code, a Briley-McDonald single sweep LBI solver with a McDonald-Camarata mixing length turbulence model. Details of the various analyses are to be found in the microfiche supplement of this report.

### 3.3.2.4 RESULTS

#### Static Pressure Distributions

Figs. 3.2.2 and 3.2.3 show a comparison of the computed and experimental static pressure distributions on the plate at two different locations. Experimental data is shown by the symbols while the various analyses are shown by different style lines. The static pressure distribution on the plate is shown as a function of distance from the wedge at a specified distance from the wedge leading edge. Fig. 3.2.2 is located at 5.1 inches from the leading edge of the wedge. Considering the figure from right to left, the pressure is seen to increase from a free stream value of one to a value of nearly two at the wedge surface. The pressure increase is not abrupt, as one would expect across a shock wave, but is seen to be a gradual, distributed increase to the wedge. A more careful examination shows that the initial increase in the pressure occurs upstream, to the right, of the shock wave. The pressure then reaches a plateau value in the vicinity of the shock and increases again downstream of the shock towards the wedge surface. Considering the CFD results, we see that, in general, both NS and PNS

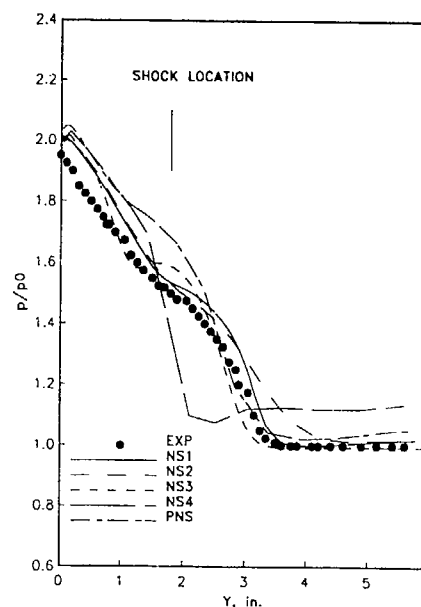


FIG 3.2.2 COMPARISON OF CFD AND EXPERIMENTAL WALL STATIC PRESSURE DISTRIBUTION AT X=5.1 INCHES.

calculations have qualitatively modeled this pressure variation. The NS1 solution has correctly predicted the upstream influence, the location and strength of the plateau, and the increase into the wedge. The NS2 solution does an excellent job in the plateau and near wedge region, but slightly overpredicts the upstream influence of the interaction. The PNS solution has correctly predicted the upstream influence while overpredicting the pressure levels downstream of the shock. The NS3 solution, while slightly underpredicting the upstream influence, has accentuated the plateau region near the shock wave. The NS4 solution has greatly underpredicted the upstream influence and has missed the pressure plateau. A similar pattern is seen farther downstream at X=9.1 as shown in Fig. 3.2.3. The shock has moved farther from the wedge surface at the left and the entire interaction has moved towards the right. The experimental data does not extend upstream far enough to allow detailed comparisons. Once again, the NS1 and NS2 analyses very closely predict the experimental results, the PNS analysis overpredicts the plateau

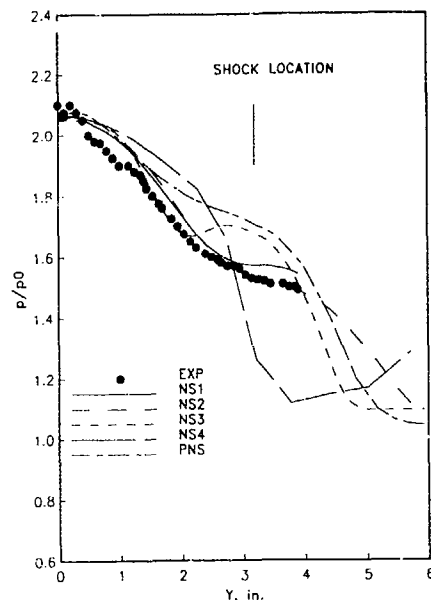


FIG 3.2.3 COMPARISON OF CFD AND EXPERIMENTAL WALL STATIC PRESSURE DISTRIBUTION AT X=9.1 INCHES.

region and the NS3 calculation has overaccentuated the formation of the plateau. The NS4 analysis continues to miss the upstream influence and the pressure plateau.

#### Pitot Profiles

Figs. 3.2.4 and 3.2.5 show comparison of CFD results and experimentally measured pitot profiles in the glancing shock/boundary layer interaction. These profiles were picked as representative of the CFD results; all of the comparisons are given in Appendix 3.3.2. As with the previous pressure plots, the experimental data is given by the symbols while the various style lines depict the CFD results. Fig. 3.2.4 shows a pitot profile normal to the plate and located 3.6 inches from the wedge leading edge and 2.9 inches from the corner formed by plate and the wedge. This rake location is upstream of the inviscid shock location and represents an inflow condition to the interaction. The flow calculations were to begin near the wedge leading edge, and therefore this rake location will test the codes ability to hold a prescribed, incoming, turbulent boundary layer profile. Considering the curve from left to right, the value of pitot pressure is given along the horizontal axis with increasing distance from the plate along the vertical axis. This

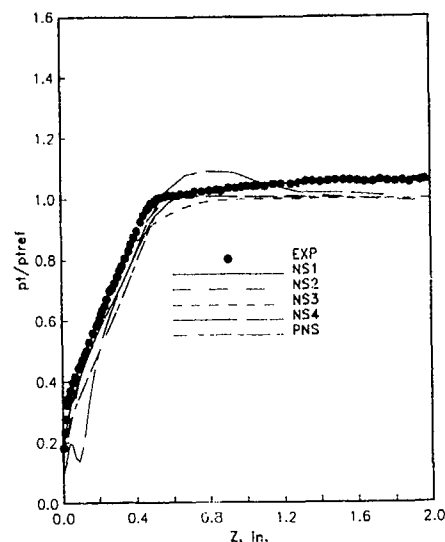


FIG 3.2.4 COMPARISON OF CFD AND EXPERIMENTAL PITOT PRESSURE DISTRIBUTION AT X=3.6 AND Y=2.9 INCHES.

orientation of the curves was chosen to be consistent with the data reports. The flattened profile is typical of a turbulent flat plate boundary layer. Considering the CFD results, we see that all five analyses agree fairly well with the data, although all of the analyses, except the NS2, are slightly overpredicting the boundary layer thickness. The NS1 analysis most correctly models the external flow, to the right, while maintaining the turbulent boundary layer profile. The NS2 analysis maintains a turbulent profile with the correct boundary layer thickness. The PNS analysis has also maintained the turbulent boundary layer shape, yet is overpredicting the thickness of the boundary layer. The NS3 analysis is also overpredicting boundary layer thickness, although its shape has become more like a rounded laminar profile. The NS4 analysis has a non-physical oscillation in the profile near the wall and overshoots the free-stream pitot pressure near the boundary layer edge. Both of the features may be symptoms of turbulence model problems. Fig. 3.2.5 shows a pitot profile normal to the plate and located 7.1 inches from the wedge leading edge and .75 inches from the corner formed by plate and the wedge. This rake location is far downstream of the inviscid shock location and represents an outflow condition from the interaction. This profile is somewhat similar to a turbulent boundary layer profile, except

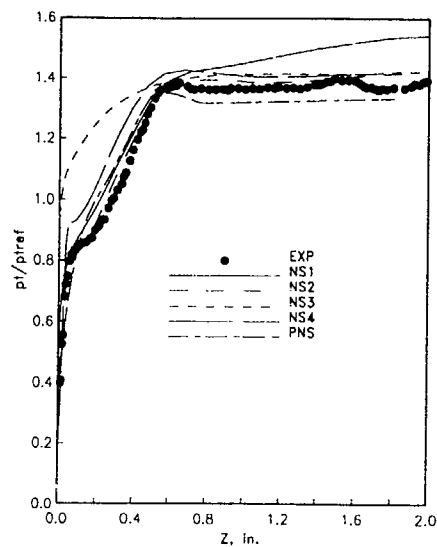


FIG 3.2.5 COMPARISON OF CFD AND EXPERIMENTAL PITOT PRESSURE DISTRIBUTION AT  $X=7.1$  AND  $Y=0.75$  INCHES.

near the wall, at the left. The near-horizontal portion of this curve resembles boundary layer profiles in the vicinity of flow separation. Considering the CFD results, we see that the NS1, NS2 and NS4 analyses have predicted this feature, with the NS4 analysis overpredicting the pressure level and the NS1 analysis smoothing the feature somewhat. The NS1, NS2, NS4 and PNS analyses have maintained the turbulent boundary layer shape through the interaction and, in general, give good prediction of the profile shape. The NS1 analysis overpredicts the pitot pressures near the free stream for reasons which are detailed in the microfiche. The NS2 analysis is slightly overpredicting the boundary layer thickness while correctly modeling the near wall region. The NS3 analysis has produced a laminar-type boundary layer profile and has returned little of the complex profile seen in the experiment.

#### Yaw Angle Surveys

A comparison of the CFD and experimental yaw angles is given in Figs. 3.2.6 and 3.2.7. As previously mentioned, the yaw angle is measured in a plane parallel to the flat plate. The particular profile of Fig. 3.2.6 was taken at 7.1 inches from the wedge leading edge and .75

inches from the corner formed by the plate and the wedge: the same location as the pitot profile Fig. 3.2.5. The figure shows the computed yaw angle along the vertical, versus distance above the flat plate along the horizontal. Considering the curve from right to left, one moves from external flow towards the wall. In the external flow, the yaw angle is seen to be nearly nine degrees, corresponding to the wedge angle and the inviscid turning of the flow by the shock wave. Near the wall, however, the flow is seen to turn nearly twenty-two degrees, with the break in the curve occurring near the edge of the boundary layer from Fig. 3.2.5. If we now consider the comparison of the CFD results, we see that all analyses properly model the external flow and predict increased turning near the plate. While the NS1, NS2, NS4 and PNS analyses nearly predict the wall flow turning angle, the NS3 analysis slightly underpredicts the flow turning. The NS3 analysis seems to predict the beginning of the flow turning too near to the

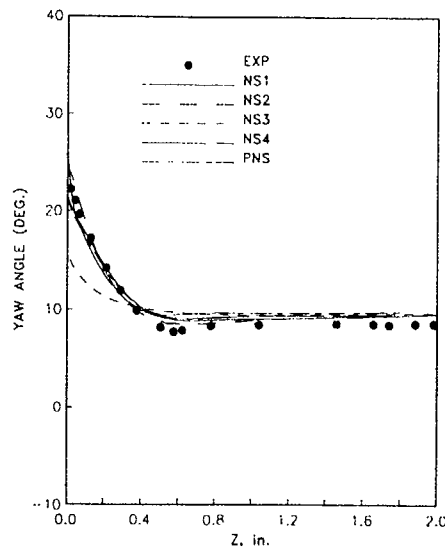


FIG 3.2.6 COMPARISON OF CFD AND EXPERIMENTAL YAW ANGLE DISTRIBUTION AT  $X=7.1$  AND  $Y=0.75$  INCHES.

wall. A similar trend is seen in Fig. 3.2.7, which is located nearer the inviscid shock at 1.25 inches from the corner formed by the plate and wedge. As before, the inviscid portion of the flow is turned nearly nine degrees. Near the wall, however, the flow is now turned nearly thirty degrees. All CFD results predict an increased amount of turning relative to the previous results with the NS1, NS2, NS4 and PNS analyses again nearly matching the data and the NS3 results underpredicting the turning.

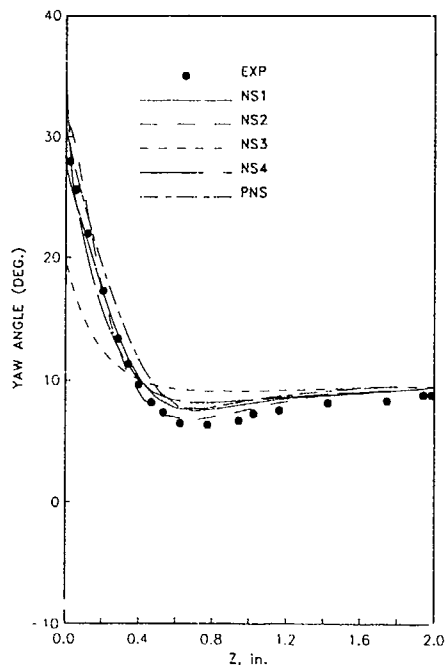


FIG 3.2.7 COMPARISON OF CFD AND EXPERIMENTAL YAW ANGLE DISTRIBUTION AT  $X=7.1$  AND  $Y=1.25$  INCHES.

#### CFD Flow Field

While the previous sections of this report have dealt with a quantitative comparison of CFD results with experiment, the CFD analysis also provides a powerful qualitative representation of the test case flow field. We have previously compared the experimental and computational values of flow yaw angle in this interaction. The results indicate that while the free stream is turned parallel to the wedge surface, the flow in the boundary layer

is turned much greater than the wedge angle. This feature of the interaction is clearly demonstrated in Fig. 3.2.8, which shows computed particle traces through the interaction from the analysis at NASA Lewis. The wedge is located on the left in this figure, with the wall at the bottom, and the view looking downstream. Two lines of particles have been released upstream of the wedge, perpendicular to the wall surface. One line is released near the wedge leading edge at the left, the other out near the center of the flow field at the right. In both cases, the lower portion of the traces are seen to be swept more sharply to the right than the upper portions. The lowest traces, which would correspond to surface oil flow patterns, are seen to coalesce into a single line; a feature which is also seen experimentally. For the line at the left, the upper traces are pulled down onto the wall surface far downstream from the wedge leading edge, while the upper traces at the right flow up and over the low energy flow on the surface. Such detail leads to better understanding of the three dimensional nature of this interaction

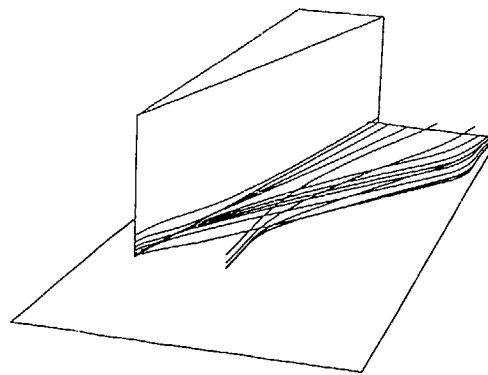


Figure 3.2.8 PARTICLE TRACES FROM CFD ANALYSIS OF GLANCING SHOCK BOUNDARY LAYER INTERACTION.

#### 3.3.2.5 CONCLUSIONS

In general, the CFD analyses used in this study, which have been designed and built for full intake calculations, have done a good job of modeling this

fundamental three dimensional interaction. It appears that the salient physical features of the interaction can be modeled with CFD. There are some interesting differences between the various computational results, particularly concerning the three similar NS calculations. Since the basic algorithms used here are the same, the differences can be attributed to differences in turbulence models, the way the problem was modeled and possible enhancements to the computer codes. In this case, one group chose to model this interaction with a plane of symmetry, thus doubling the grid resolution onto the plate, while another allowed the flow to slip along the wedge, thus increasing the resolution of the shock wave. These types of choices, which are often made in CFD analysis, are examples of user involvement in the flow solution. The current state of CFD analysis still requires user involvement in obtaining flow solutions. The same code run on the same computer by different users can often give different answers.

3.2.7. Knight, D.D., Horstman, C.C., Shaper, B., and Bogdonoff, S., "The Flowfield Structure of the 3-D Shock Wave-Boundary Layer Interaction Generated by a 20 Degree Sharp Fin at Mach 3", AIAA Paper No. 86-0343, 1986

#### 3.3.2.6 REFERENCES

3.2.1. Delery, J. and Marvin, J.G., "Shock-Wave Boundary Layer Interactions", AGARD-AG-280, February, 1986.

3.2.2. Oskam, B., Vas, I.E., and Bogdonoff, S.M., "Mach 3.0 Oblique Shock Wave/Turbulent Boundary Layer Interactions in Three-Dimensions," AIAA Paper No. 76-336.

3.2.3. Law, C.H., "Three-Dimensional Shock Wave-Turbulent Boundary Interactions at Mach 6," ARL TR 75-0191, Aerospace Research Laboratories, Wright-Patterson AFB, Ohio, June, 1975.

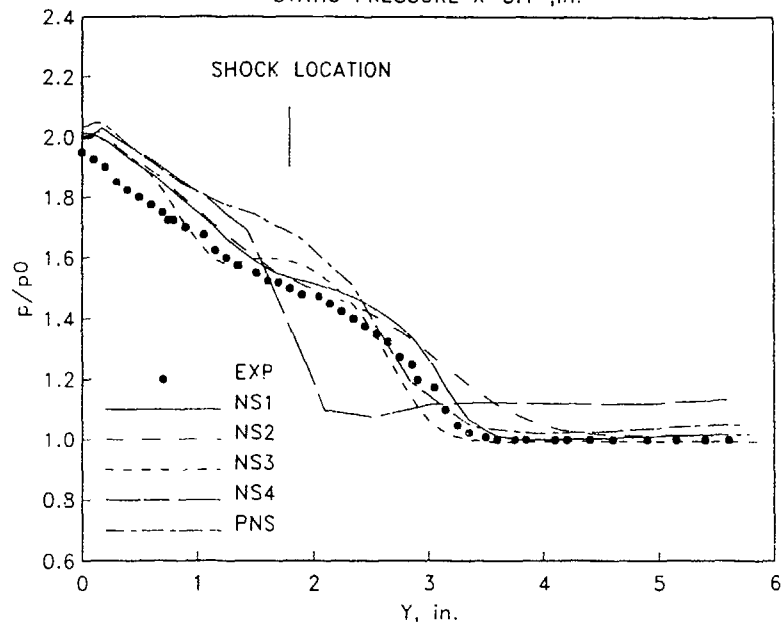
3.2.4. Hingst, W.R., and Jurkovich, M., "Flow Visualization of Shock-Boundary Layer Interaction", NASA Conference Publications 2243, March 1982.

3.2.5. Hung, C.M., and MacCormack, R. W. "Numerical Solution of Three-Dimensional Shock-Wave and Turbulent Boundary-Layer Interaction", AIAA J. Vol. 16, No. 12 December, 1978, pp. 1090-1096.

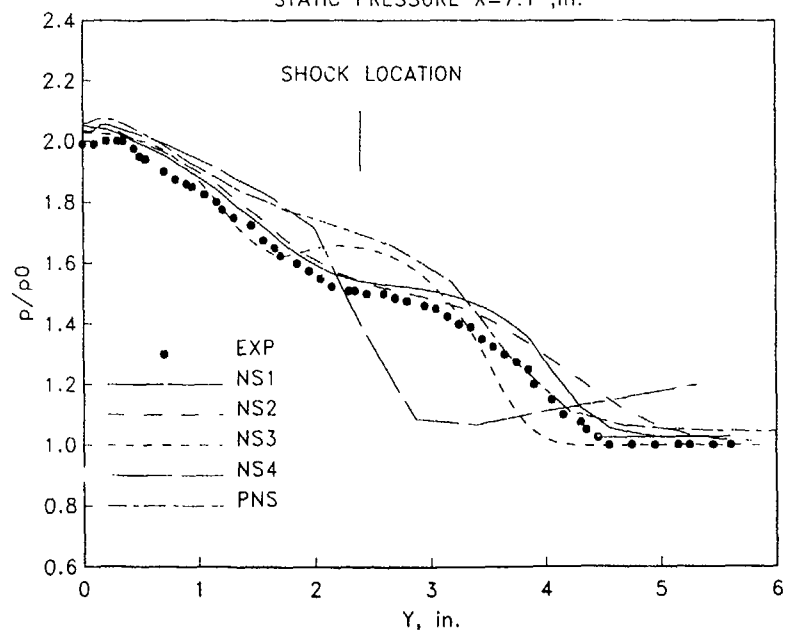
3.2.6. Anderson, B.H., and Benson, T.J., "Numerical Solution to the Glancing Sidewall Oblique Shock Wave/Turbulent Boundary Layer Interaction in Three Dimensions," AIAA Paper No. 83-0136, January 1983.

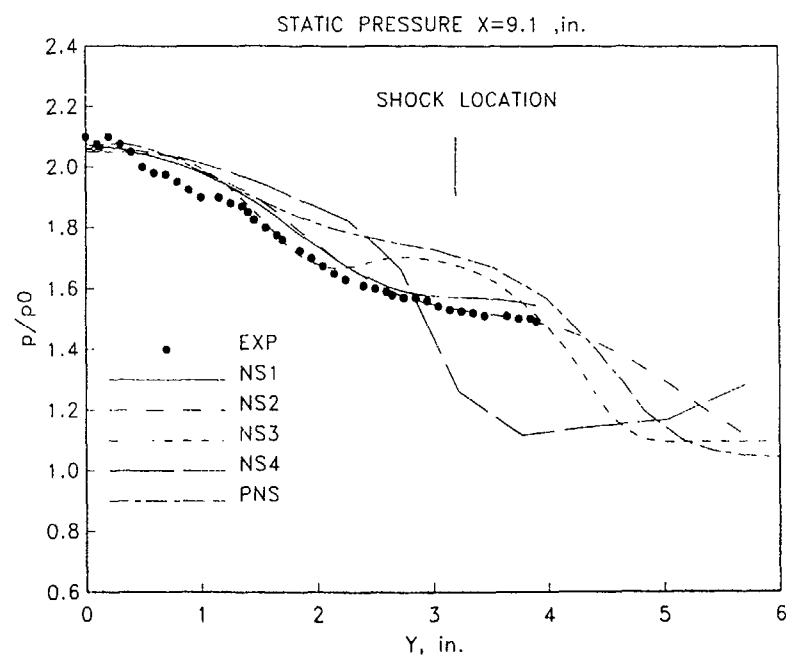
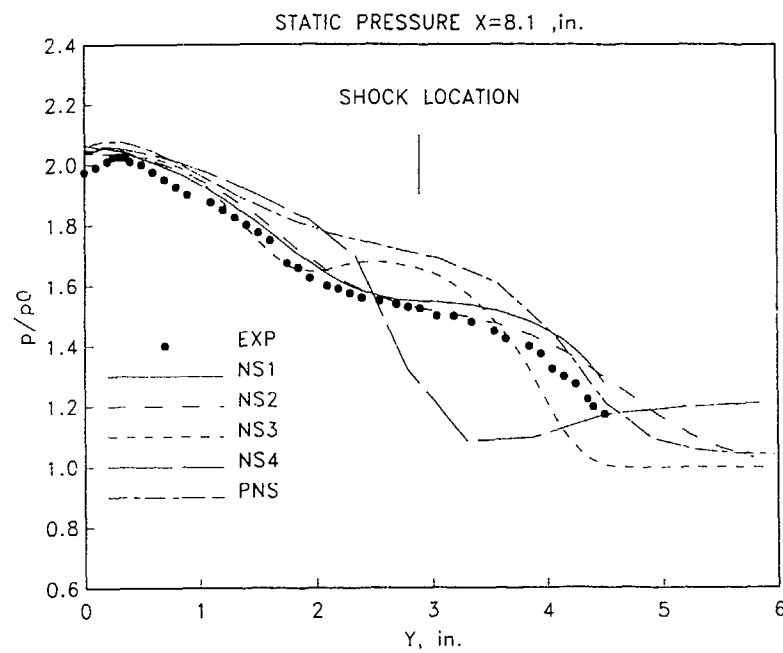
Appendix 3.3.2  
Full Comparison of CFD and Experiment

STATIC PRESSURE  $X=5.1$  ,in.

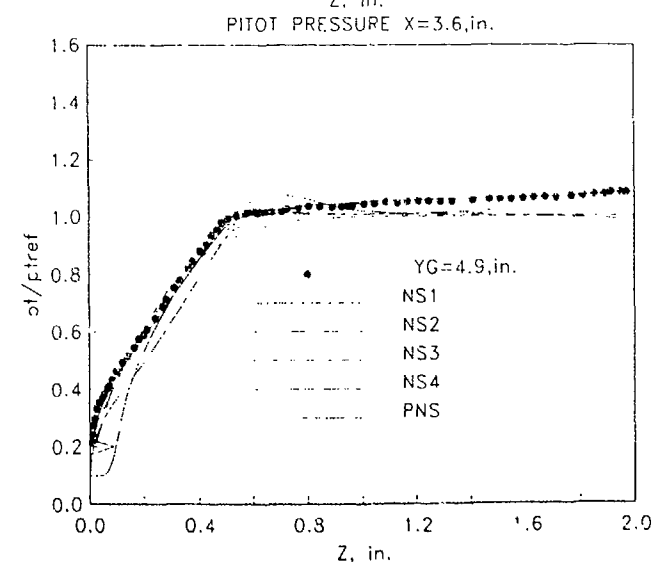
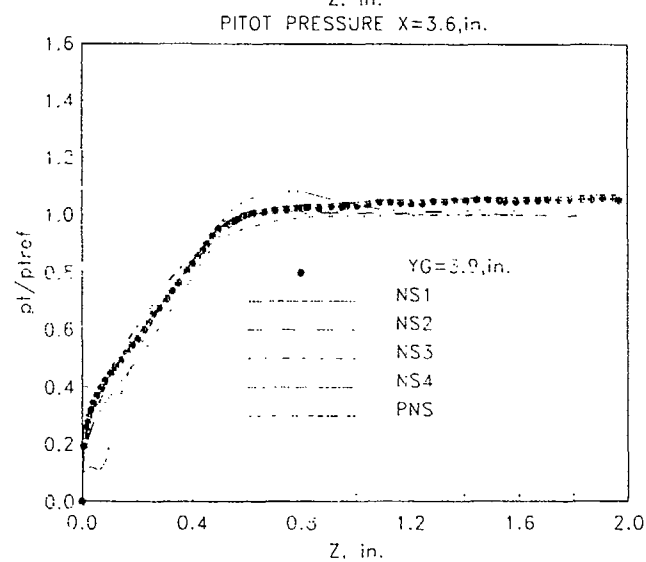
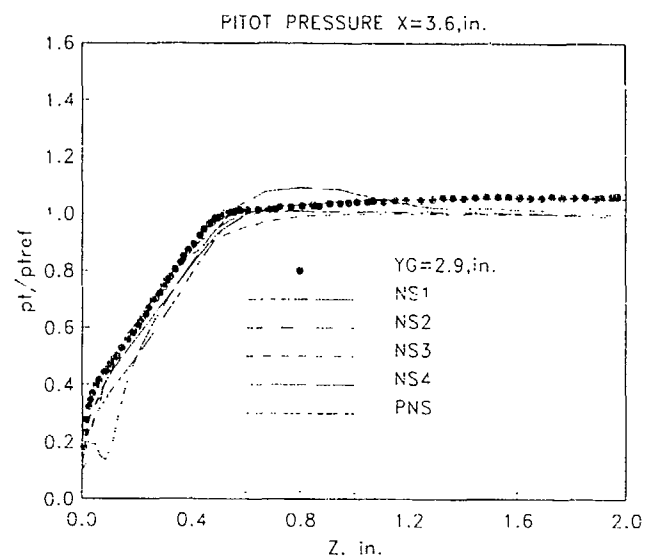


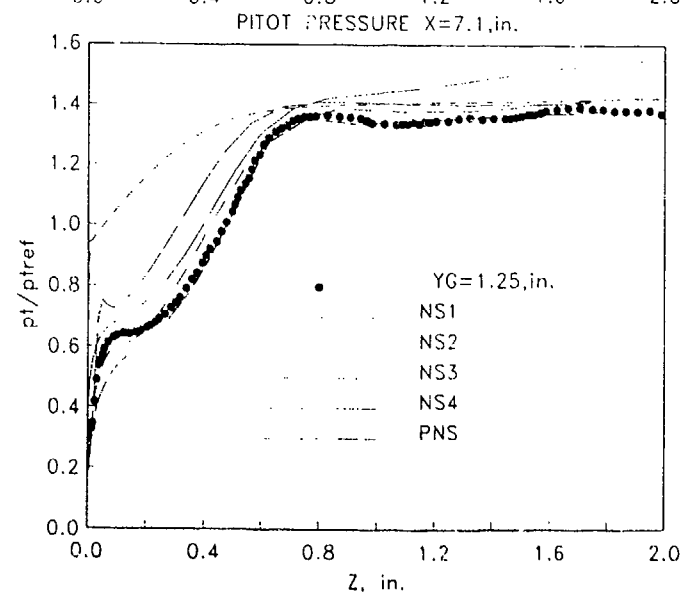
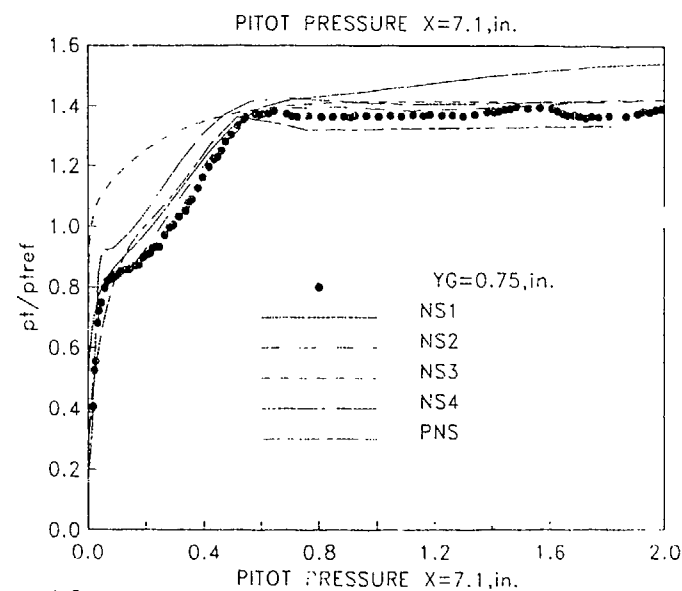
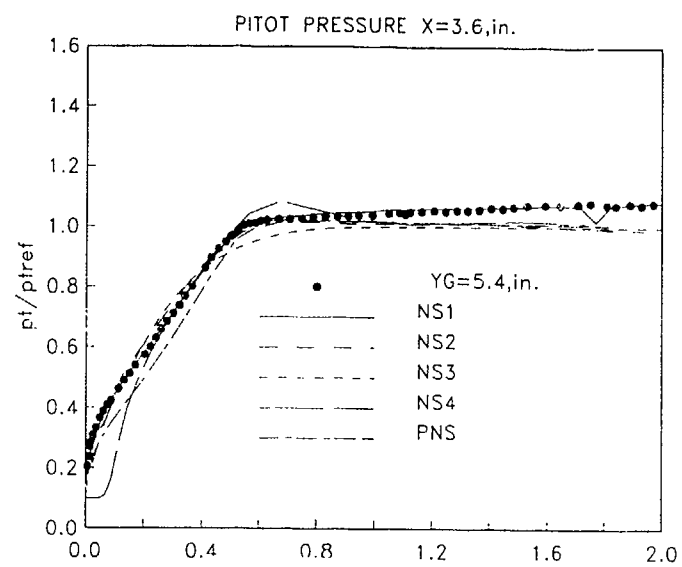
STATIC PRESSURE  $X=7.1$  ,in.

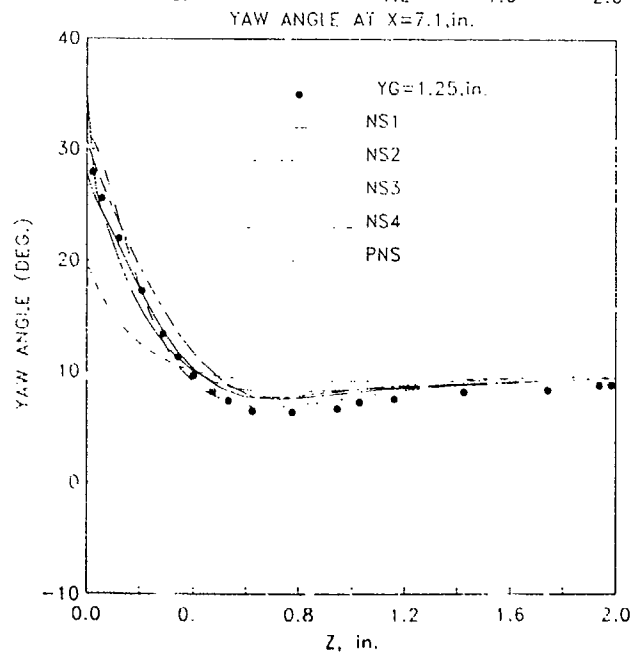
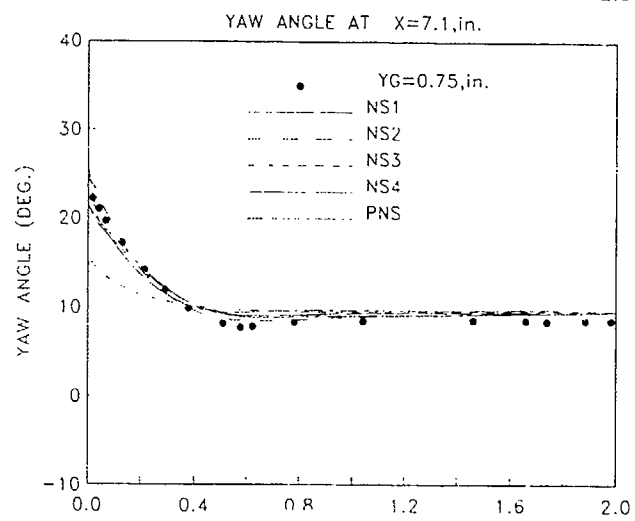
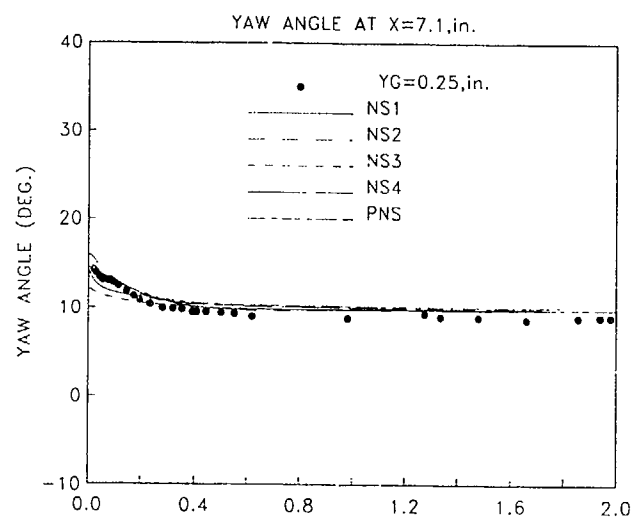












### 3.3.3 Test case 3 - Subsonic/Transonic Circular Intake

#### 3.3.3.1 INTRODUCTION

Many current military aircraft possess highly curved intake ducts. These ducts can exhibit boundary layer separation depending on mass flow and/or curvature. CFD could help in the design of those ducts by identifying possible problems of this nature at an early stage of a project.

#### 3.3.3.2 PROBLEM DESCRIPTION

The geometry for this test case consists of a circular intake followed by an S-bend diffuser (RAE intake model 2129). Fig 3.3.1 shows its shape (and at the same time the surface grid used by ARA Bedford). This intake is a side-mounted intake with a horizontal symmetry plane. The geometry of an "engine" bullet was specified too. Because tests with a serrated tape at different stations on the intake lip showed only a small effect on internal performance the tests for this test case were performed without any boundary layer trips attached. In order to eliminate the problem of differing entrance conditions within different codes the sollicitors were asked to calculate the complete flow from free-stream into the intake instead of just the duct flow.

The flow for two mass-flow ratios was to be calculated. The test conditions for test case 3.1 (high mass flow) and test case 3.2 (low mass flow) are summarized in the following table:

#### Test Case 3.1 (DP3532):

Total pressure	$H_0 = 29.889$ in Hg
Total temperature	$T_{t0} = 293$ °K
Flight Machnumber	$M_0 = 0.210$
Throat Machnumber	$M_{th} = 0.794$
'Non-dimensional' Weight Flow	$WAT_{cf} = 0.311 \frac{\text{in}^2 \sqrt{\text{°K}}}{\text{sec}}$
Compressor Face Machnumber	$M_{cf} = 0.536$
Pressure Recovery	$PR = 0.928$
Capture Flow Ratio $A_0/A_c$	$= 2.173$
Capture area	$A_c = 25.245$ in <sup>2</sup>

#### Test Case 3.2 (DP3537):

Total pressure	$H_0 = 29.865$ in Hg
Total temperature	$T_{t0} = 293$ °K
Flight Machnumber	$M_0 = 0.210$
Throat Machnumber	$M_{th} = 0.412$
'Non-dimensional' Weight Flow	$WAT_{cf} = 0.197 \frac{\text{in}^2 \sqrt{\text{°K}}}{\text{sec}}$
Compressor Face Machnumber	$M_{cf} = 0.304$
Pressure Recovery	$PR = 0.9897$
Capture Flow Ratio $A_0/A_c$	$= 1.457$
Capture area	$A_c = 25.245$ in <sup>2</sup>

For both test cases the free-stream Mach number was  $M_0 = 0.21$ . Angle of attack was  $\alpha = 0^\circ$  without sideslip.

The test data available from the experiments included static pressures, total pressures and some circumferential flow angles in the engine face plane. The total pressures within the boundary layer were scanned by total pressure probes at four circumferential stations just in front of the engine face plane. Along the duct walls four rows of static pressure taps were located.

All static and total pressures are scaled with the free stream total pressure  $P_{t0}$ . Coordinates are either scaled with the maximum diameter of  $D_{max} = 6.641$  in or with the engine face radius  $R_{ef} = 3.0$  in.

#### 3.3.3.3 CFD TECHNIQUES

This test case was attempted by four different research groups (see table 3.2.1 in section 3.2). BAe Filton used their RANSAC code which is a three dimensional, cell centred, finite volume, implicit pressure correction method for the Reynolds averaged Navier-Stokes equations. Turbulence is modeled by the standard k- $\epsilon$  model with a wall function in the near wall region which implies constant shear stress and no streamwise pressure gradient. In order to save computer effort only half of the S-bend diffuser was modelled. Initial conditions were estimated by assuming a constant total pressure up to the entrance plane of the calculations. The grid for this geometry consisted for both test cases of  $80 \times 24 \times 22$  cells (axial, circumferential, radial). To find this grid a limited grid dependency study was carried out. For the turbulent, isenthalpic flow calculation of test case 3.1 100 global iterations were needed. This took 16,544 seconds of CPU time on a CRAY-YMP. These numbers are the same for test case 3.2. Their results are designated (NS1) in the figures. ARA Bedford applied their Euler multiblock method whose flow solver is based on the explicit central difference scheme proposed by Jameson et al.. Because of the symmetry of the intake a grid for the half-model was constructed using 38 blocks with approximately 90,000 cells. A circular cylinder extension was added to bullet and diffuser. Also, the external part of the cowl was doubled in axial direction. It took 16,000 seconds on a CRAY2 to calculate the 5000 iterations considered necessary. To construct the grid one man needs about half a week and 1200 seconds computer time. Their results are designated (EU) in the figures. The Dornier group calculated the flow with their three-dimensional Navier-Stokes code FEARUS. This is an explicit finite volume code with the Runge-Kutta-type time integration proposed by Jameson et al.. The thin-layer approximation and the Baldwin-Lomax turbulence model were used. The assumption of fully turbulent boundary layers was applied. The grid was constructed for the half-model of the intake duct only. The boundary layer on the bullet is neglected. However, the computational domain is extended beyond the engine face plane. The fine mesh consists of 99,279 grid points. A sequence

of 3 mesh levels supported by up to 3 multigrid levels was used. Needing 500 cycles on each mesh level it took about 4 to 5 CPU hours on a CONVEX C220 (single processor) to arrive at a converged solution. Their results are designated (NS2) in the figures.

The CALSPAN Tenn. group used the implicit, approximate factorization scheme of Beam and Warming applying the Chimera domain decomposition technique. The right half of the duct was modeled by six meshes with a total of 399,404 points. A seventh mesh was used during the high mass flow calculations (test case 3.2) to obtain better resolution at the internal cowl. The exit plane of the computational domain was shifted by about five duct diameters downstream from the engine plane. Both the Baldwin/Lomax algebraic turbulence model and a two equation  $k-\epsilon$  turbulence model were applied. Approximately 2000 time steps were required to converge the flow field with the algebraic turbulence model. Starting from this converged solution 1000 additional time steps were needed to converge the  $k-\epsilon$  solution. Their results are designated (NS3) in the figures.

Details of the methods used and the results provided by the originators are given in the microfiche.

### 3.3.3.4 RESULTS

#### 3.3.3.4.1 Test Case 3.1 - High Mass Flow

##### Static Wall Pressures Along Duct

A description and interpretation of the flow of this test case using the experimental data is very difficult. As can be seen in Figs. 3.3.2 to 3.3.5 the static wall pressure drops from the stagnation point on the intake lip to supersonic values ( $p/p_{t0}$  less than approx. 0.52). All figures clearly show that the flow is supersonic in front of the throat ( $X/D_{max} < 0.09$ ). There is no explanation for the pressure increase on all four walls between the second and third data point from the left. It seems that the flow downstream of the pressure minimum goes subsonic again through a lambda shock system which could have been triggered by a separation bubble at the throat. There is a small pressure plateau in Fig. 3.3.4 at about  $S/D_{max} \sim 0.3$  which supports this supposition. At least the second leg of this shock system is hard to recognize in the pressure plots due to the relatively large distance between the pressure taps. The pressure level at the wall behind the shock system is already influenced by the first bend following the constant area duct piece with the port pressure reaching higher magnitudes than the starboard one. In addition the starboard, top and bottom pressures show a pressure drop that indicates the acceleration of the flow necessary to counteract the centrifugal forces inside the bend ( $X/D_{max} \sim 1.0$ ). On the starboard side the flow becomes supersonic again with a shock at about  $S/D_{max} = 1.0$ . In front of this shock the pressure depicts a somewhat erratic behaviour (the numerical people would talk of "wiggles"). This same behaviour can be observed in test case 4.1. The port pressure levels off at this station only (Fig. 3.3.3).

The further development of the pressure on the port side downstream in the duct is typical for an S-bend with constant area (Fig. 3.3.3) which shows a deceleration in the first bend and an acceleration in the second bend, i.e. a sinusoidal pressure distribution. The deceleration, i.e. pressure increase, close to the duct exit must be due to the highly three-dimensional flow around the engine bullet. The pressures at the other circumferential stations reveal a steadily decelerating flow with a sudden reduction in the deceleration magnitude at  $X/D_{max} \sim 1.4$ . This could be an indication for a further separation bubble the extent of which cannot be derived from these wall pressure plots.

The first comparison with calculations should be with the solution of ARA who did an Euler calculation (called EU in the figures) for this flow. As one can see in all figures the pressure drop at the cowl in the inviscid flow is not as large as that in the viscous flow. Qualitatively this is correct because the Euler calculations have been performed for the mass flow given in the experiment. This means that in the inviscid flow the velocities in the duct are lower and therefore the pressures are higher than in reality due to the missing displacement effect of the boundary layers. The pressure increase between the second and third data point in the experiment is not reproduced. The reason for this could be either an imperfection in the model surface or a grid in the calculation which is too coarse to resolve this flow detail sufficiently. There is only a small supersonic pocket on the cowl followed by a shock in front of the throat of the intake. From the position of the shock in front of the intake it can be deduced that it does not span the intake. Behind the shock the flow is subsonic, its pressure at all four circumferential duct stations is at nearly the same level as could be expected for this constant area duct. Because the inviscid Euler solution does not know separation (at least in theory) the shock system on the lip must be different from experiment. The pressure drop at the starboard wall at the beginning of the first bend, i.e. the acceleration of the flow, in solution EU is obviously not large enough for the flow to go supersonic again. There is no indication of a local shock. This

situation would have been different if instead of the mass flow the pressure at the engine face or at the throat of the experiment would have been simulated in the calculation. In that case the flow would have been somewhat closer to experiment.

The Navier-Stokes solution delivered by BAE (called NS1 in the figures) modelled the flow in the S-bend only. Their guess of the starting values gave a static wall pressure that is very close to that of the Euler solution EU. As can be seen in the figures the static wall pressure is the same on the port and starboard position but differs from the value at the top and bottom position. From that one could conclude that the inflow into the S-bend, although it is not uniform, misses all the losses due to the shocks on the cowl. This must lead to a totally different flow inside the duct. Although the pressures in

Figs. 3.3.4 and 3.3.5 seem to support this assumption it definitely needs a more detailed investigation and comparison of the results than is possible here to come to a final conclusion.

The pressure distribution on the cowl in the Navier-Stokes calculation performed by Dornier (called NS2 in the figures) shows a remarkable agreement with experiment. However, it reproduces neither the supersonic recompression close to the lip highlight nor the second branch of the lambda shock. Instead the flow in this solution stays supersonic in the constant area duct in front of the S-bend (Fig. 3.3.5). It even accelerates behind the first shock on the lip which could point to a shorter separation bubble. On the starboard wall this supersonic area ends with a relatively strong recompression or shock (Fig. 3.3.5) after the start of the S-bend diffuser. The pressure gradients on the other circumferential wall positions are not large enough to indicate the existence of another shock. This shock on the starboard wall is obviously very local only. The pressure distribution in the S-bend comes close to that of the experiment.

#### Static Pressures On Cowl Lip

There is only one figure shown here; figures supplementary to the ones shown in this section can be found in Appendix 3.3.3. The pressures are plotted in a coordinate system with the origin at the highlight of the lip. The Y-axis is normal to the intake centreline with positive Y values corresponding to the external shape of the lip. Fig. 3.3.6 depicts the underestimation of the pressure reduction inside the intake by the Euler solution EU. The location of the stagnation point seems to agree with that of the experiment. However, the pressure taps are not close enough to determine its location with good accuracy.

#### Total Pressures In Boundary Layer At Engine Face

The solution NS2 overestimates the total pressures on the top and bottom walls (Figs. 3.3.7 and 3.3.8). For this solution there is a good agreement on the port side but the results on the starboard side are too low (Figs. 3.3.9 and 3.3.10). The total pressures given from solution NS1 on the bottom and starboard side must be too high because this calculation did not simulate the losses in the lip shock system. The total pressures even exceed the total pressure of the free-stream.

#### Engine Face Static Wall Pressures And Circumferential Flow Angles

These results are plotted in Figs. 3.3.11 and 3.3.12. (The circumferential position is defined in figs. 3.3.1 and 3.3.29.) Although solution NS2 shows a good agreement with experiment in the static wall pressures there is a large deviation in the flow angles. The maximum flow angle in solution NS1 is close to that of solution NS2 both in magnitude and circumferential location.

#### Pressure Recovery And Steady State Distortion

The total pressures at the engine face rake have been integrated to give pressure recovery and steady state distortion values. Two distortion parameter have been calculated. DCA60 is a measure for the difference between the area weighted mean of the total pressure in the engine face and the smallest mean total pressure in a 60 degree sector in the engine face. DH represents the difference between the minimum and maximum pitot tube readings in the engine face. The pressure recovery specified here is the ratio between the area weighted mean of the total pressures in the engine face and the freestream total pressure. In solution NS1 the pressure recovery has been calculated twice. The first calculation used the total pressure values at the same position as in the experiment. This value can be compared directly with experiment. The second calculation used all the information on total pressure available from the calculation for the integration. This value is called "non-weighted" in table 3.3.1. As one can see there is a negligible difference between the two values in this calculated flow field. Solution NS2 did only the "non-weighted" integration and therefore differs from experiment. A comparison between the two is difficult. Although the pressure recovery of solution NS2 is closer to the experiment than that of solution NS1 the distortion values of NS2 are larger than that of NS1. Both calculation methods overpredict distortion.

#### CFD Flow Field

From solution NS2 the velocity vectors in the symmetry plane are plotted in Fig. 3.3.13. In this figure one recognizes that the separation in the S-bend is very large, its height reaching nearly the height of the annulus at the engine bullet. It is this large separation bubble that leads to the underestimation of the total pressure in Fig. 3.3.10. This low total pressure region can also be seen in the engine face (Fig. 3.3.15) in which the lowest total pressure shown is  $p_t/p_{t0}=0.74$ . This is much lower than the experimental value of  $p_t/p_{t0}=0.82$  shown in Fig. 3.3.14. The extent of the low and high total pressure areas is much larger in solution NS2 than in the experiment. The circumferential location of these two regions is reproduced correctly. That solution NS1 is different from experiment due to reasons stated above can again be recognized in Fig. 3.3.16. In order to show that CFD is able to give more insight into the flow than experimental data in Fig. 3.3.17 lines of constant Mach number

are plotted from solution NS2. The numbers attached to the lines indicate Mach number levels, i.e. increasing numbers mean increasing Mach numbers and vice versa. The expansion region on the starboard wall at the beginning of the S-bend can be seen clearly. However, there is no indication of a shock at the end of this expansion region as has been deduced above from the pressure distribution in Fig. 3.3.5. It is the opinion of the contributors of this

result that in regions where one could expect shocks their grid could be not fine enough. To resolve this "problem" more detailed calculations need to be performed.

### 3.3.3.4.2 Test Case 3.2 - Low Mass Flow

#### Static Wall Pressures Along Duct

Compared with test case 3.1 the flow of this test case is relatively simple. The flow stays subsonic in the whole intake duct. The top and starboard wall static pressure distributions are nearly identical. In Fig. 3.3.18 the top one is plotted. As before the pressures in the Euler solution EU are generally higher than the measured ones due to the missing displacement effects of the boundary layer. The Navier-Stokes solution NS2 underpredicts the pressure minimum on the intake lip which does mean that the boundary layer in the experiment is thinner than in the calculation for which a completely turbulent boundary layer has been assumed. Also, the pressure stays below the measured one far into the S-bend ( $X/D_{max} \sim 1.8$ ) where it becomes larger than the experimental one. At the engine face both are equal. The agreement between the experiment and the solution NS1 is very good. On the port wall (Fig. 3.3.19) the pressures in the S-bend of solution NS2 are very close to the measured ones although the entering flow, i.e. the pressures in the constant area piece, is different. There are bigger differences between measurement and solution NS1. The biggest differences between solution EU and the measurements inside the S-bend are experienced in Fig. 3.3.20. This could be interpreted as the effect of a separation on that wall which starts at about  $X/D_{max} \sim 1.7$ .

#### Static Pressures On Cowl Lip

There is a good agreement between the measured static pressures on the cowl and the inviscid solution EU (Fig. 3.3.21). More comparisons can be found in Appendix 3.3.3.

#### Total Pressures In Boundary Layer At Engine Face

The total pressures inside the boundary layer of solution NS2 either agree with experiment (Fig. 3.3.24) or are slightly underpredicted (Figs. 3.3.22 and 3.3.23). At the starboard wall (Fig. 3.3.25) the measurement presents a constant low total pressure area that is thicker than that of solution NS2. In Figs. 3.3.22 and 3.3.23 a slight shift in the measured data close to the wall sheds some doubt on the accuracy of the measurement there.

#### Engine Face Static Wall Pressures And Circumferential Flow Angles

The measured static wall pressure in the engine face is reproduced by solution NS2 except around the  $270^\circ$  degree position (Fig. 3.3.26). This is the same position as in Fig. 3.3.25 for which it was concluded above that the size of the low total pressure area is underpredicted by the calculation. In addition at this

location the circumferential flow angles of NS2 differ from measurement (Fig. 3.3.27). Although for solution NS1 the static wall pressures are close to measurement the flow angles are not.

#### Pressure Recovery And Steady State Distortion

These data are given in table 3.3.2. Again the values calculated by the full numerical results are designated "non-weighted". The pressure recovery of solution NS2 is nearly the same as in the experiment. However its distortion is different from experiment. Pressure recovery in solution NS1 is smaller than in the experiment. DCA60 of solution NS1 is about eight times larger than that of experiment.

#### CFD Flow Field

Velocity vectors plotted from solution NS2 in the symmetry plane (Fig. 3.3.28) clearly show a separation on the starboard wall inside the S-bend. This separation can be identified in the plot of constant total pressure lines in Fig. 3.3.30 as the area with decreasing total pressure on the starboard side. If one compares this figure with the measured data in Fig. 3.3.29 one recognizes that in solution NS2 the extent of the high total pressure area is overpredicted and the area with low total pressure is underpredicted. The result from NS1 has no resemblance with the measured data (Fig. 3.3.31).

### 3.3.3.5 CONCLUSIONS

It is very difficult to come to a reasonable conclusion from the comparison between experiment and calculations if the experimental data are so sparse as in this test case. However, from the difficulties experienced when interpreting the flow from measured data it became clear that there is a very large potential in CFD for flow diagnostics which are possible due to the increased amount of information on the flow. This information can be used for placing instrumentation in intake models and/or optimizing intake shapes for better performance.

Because intake flows with strong secondary flows are very sensitive to the onset flow it is very important for the calculations that the boundary conditions are specified as exact as possible. Detailed information on freestream flow conditions and duct exit flow conditions are needed. Only with correct transition and turbulence models will the results of CFD become good enough quantitatively to be used in actual project work.

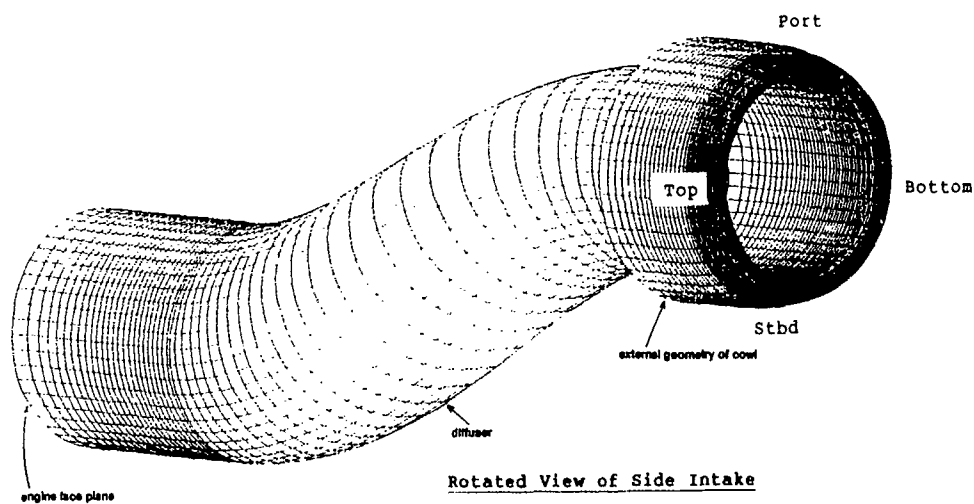
It still seems to be an art to produce very good results for complex intake flows. Only the engineer with good aerodynamic background can decide where in CFD grids need refinements to improve its results.

results from	pressure recovery	engine face mean static pressure	DCA60	DH
experiment	0.92798	0.725	-0.398	0.198
NS1	0.89000 0.88781 (non-weighted)	0.757	-0.417	0.286
NS2 (non-weighted)	0.92063	0.729	-0.884	0.351

TABLE 3.3.1 ENGINE FACE DATA FOR TEST CASE 3.1

results from	pressure recovery	engine face mean static pressure	DCA60	DH
experiment	0.98974	0.922	-0.226	0.041
NS1	0.96822	0.926	-1.724	0.082
NS2 (non-weighted)	0.99180	0.949	-0.157	0.090

TABLE 3.3.2 ENGINE FACE DATA FOR TEST CASE 3.2

FIG. 3.3.1 VIEW OF GEOMETRY FOR TEST CASE 3 -  
Surface grid from ARA Euler calculations



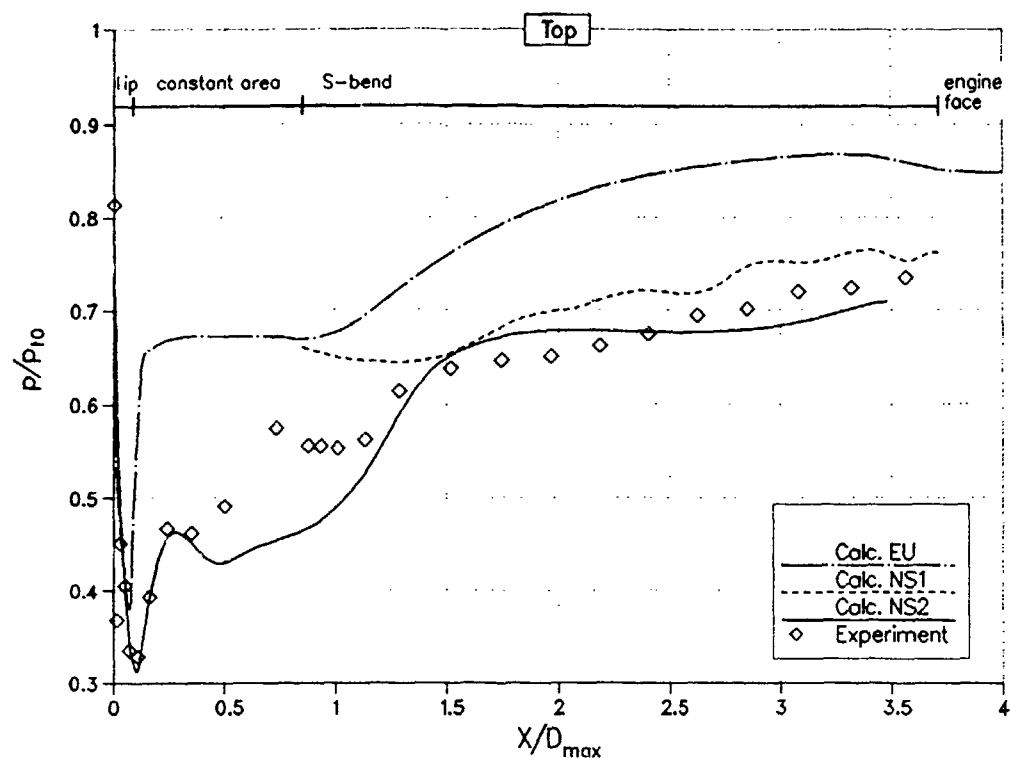


FIG. 3.3.2 TEST CASE 3.1: STATIC WALL PRESSURE ALONG DUCT - TOP

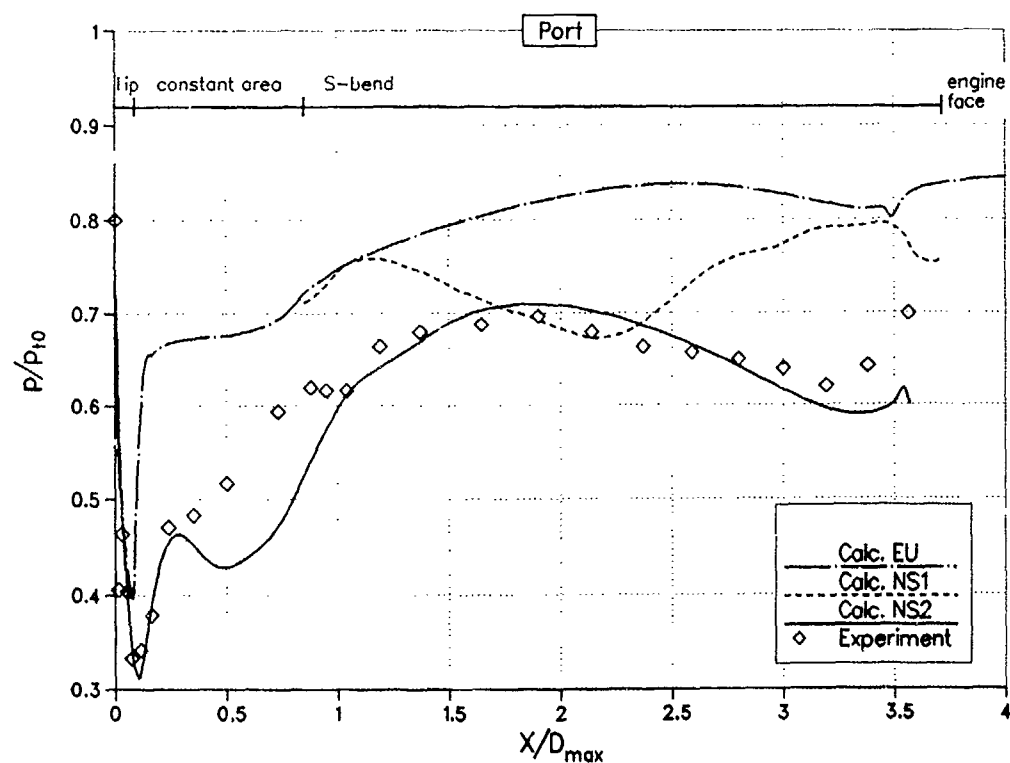


FIG. 3.3.3 TEST CASE 3.1: STATIC WALL PRESSURE ALONG DUCT - PORT

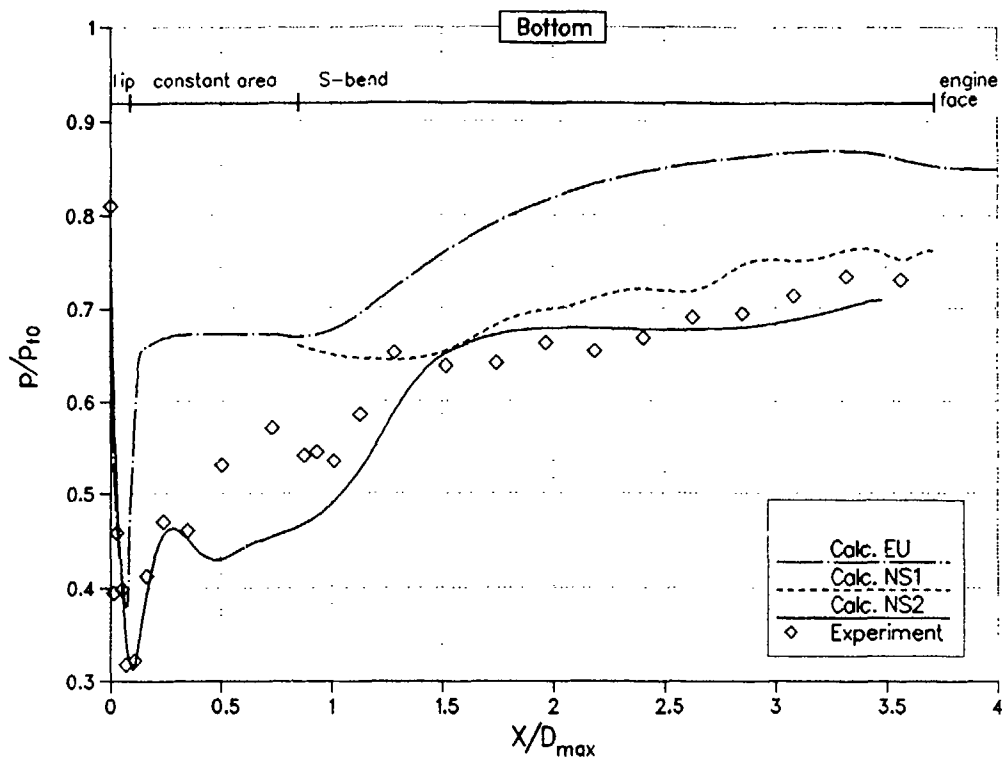


FIG. 3.3.4 TEST CASE 3.1: STATIC WALL PRESSURE ALONG DUCT - BOTTOM

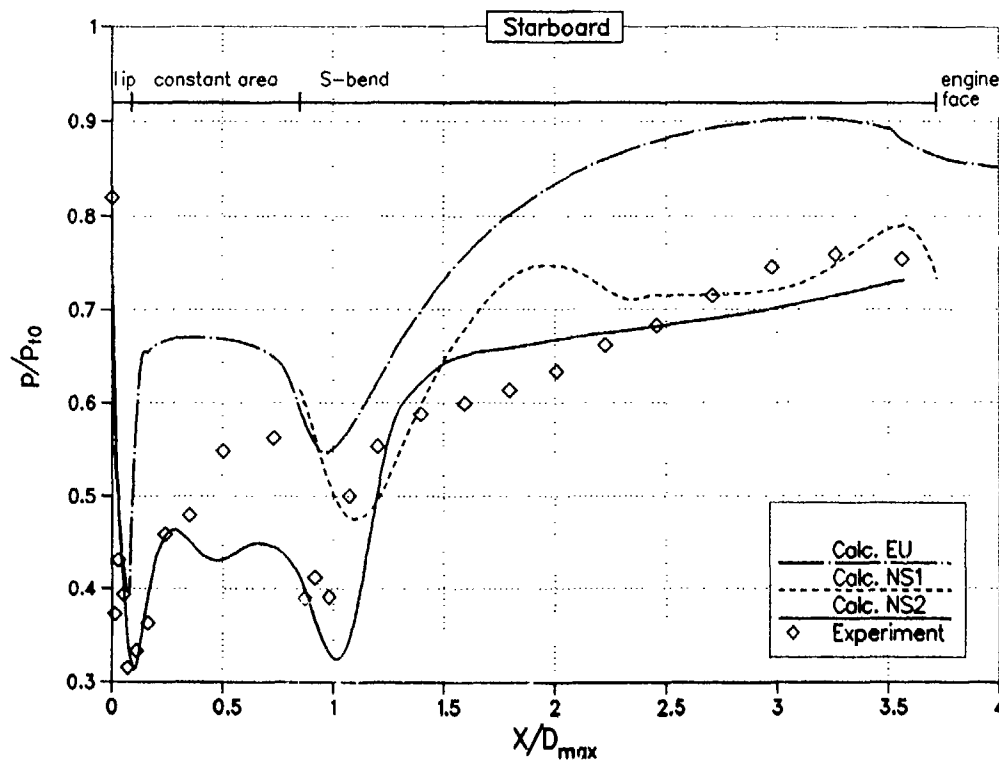


FIG. 3.3.5 TEST CASE 3.1: STATIC WALL PRESSURE ALONG DUCT - STBD

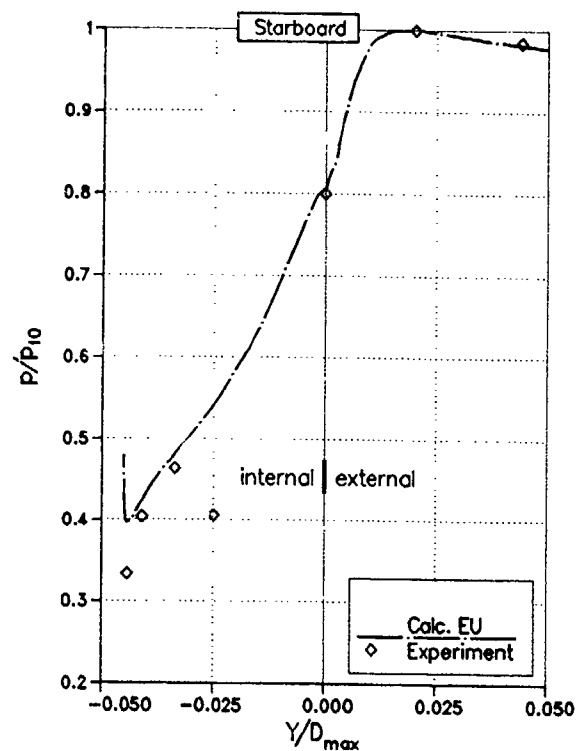


FIG. 3.3.6 STATIC PRESSURE ON COWL LIP - STBD  
TEST CASE 3.1

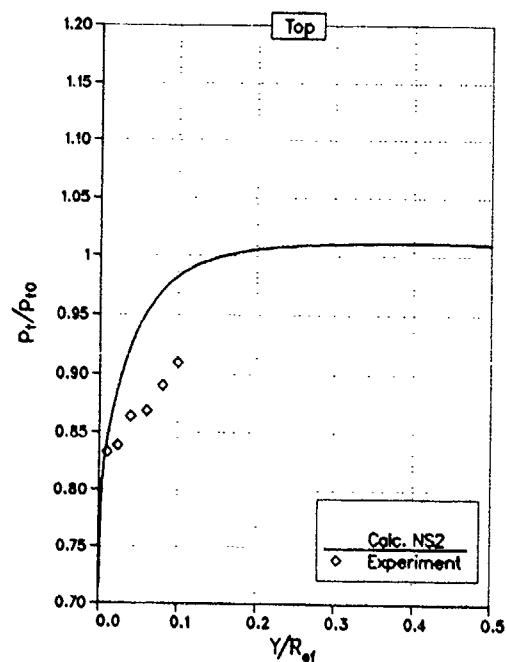


FIG. 3.3.7 TOTAL PRESSURE  
IN BOUNDARY LAYER  
AT ENGINE FACE - TOP  
TEST CASE 3.1

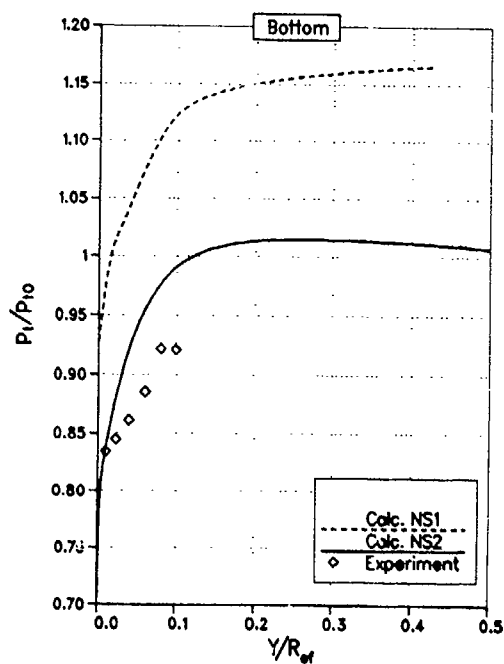


FIG. 3.3.8 TOTAL PRESSURE  
IN BOUNDARY LAYER  
AT ENGINE FACE - BOTTOM  
TEST CASE 3.1

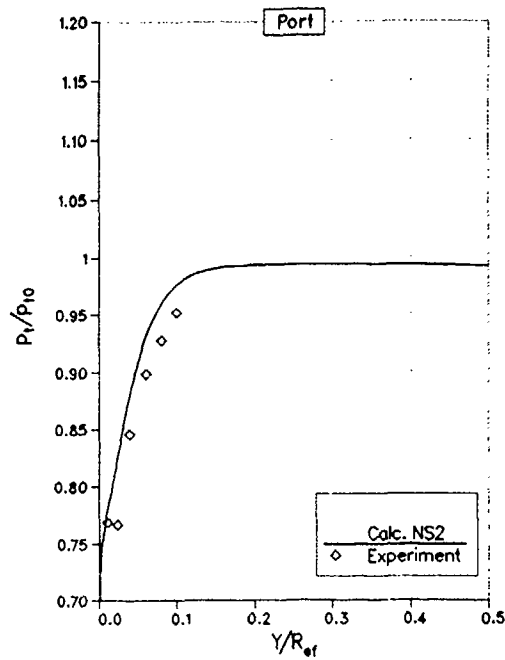


FIG. 3.3.9 TOTAL PRESSURE  
IN BOUNDARY LAYER  
AT ENGINE FACE - PORT

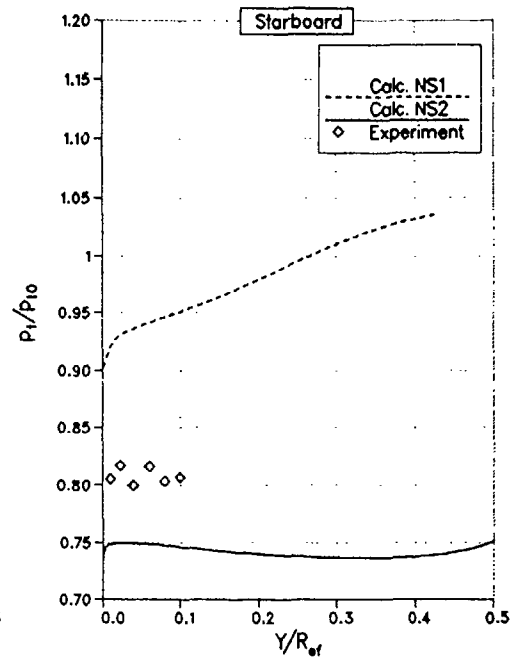


FIG. 3.3.10 TOTAL PRESSURE  
IN BOUNDARY LAYER  
AT ENGINE FACE - STBD

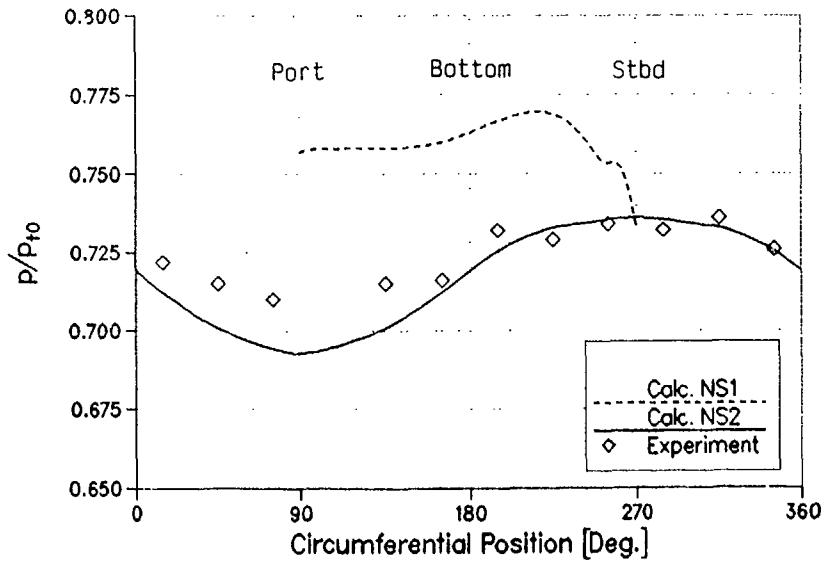


FIG. 3.3.11 TEST CASE 3.1: ENGINE FACE STATIC WALL PRESSURE

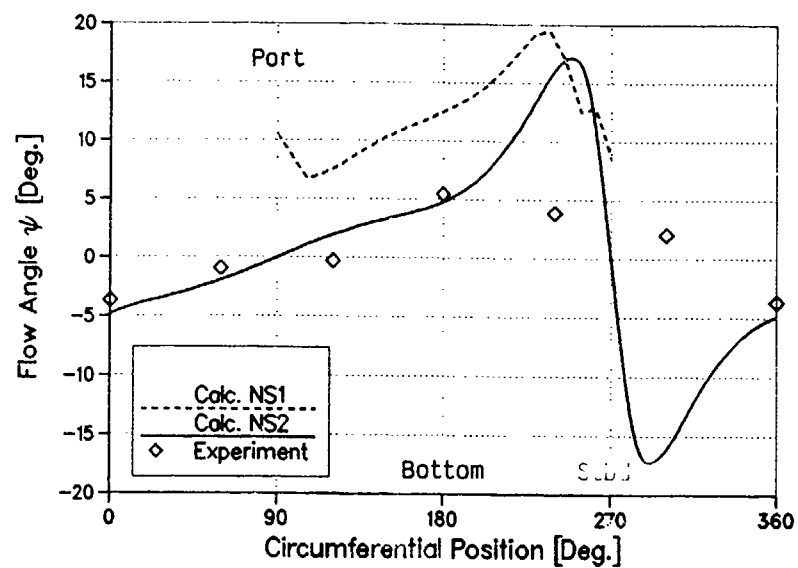


FIG. 3.3.12 TEST CASE 3.1: ENGINE FACE CIRCUMFERENTIAL FLOW ANGLES

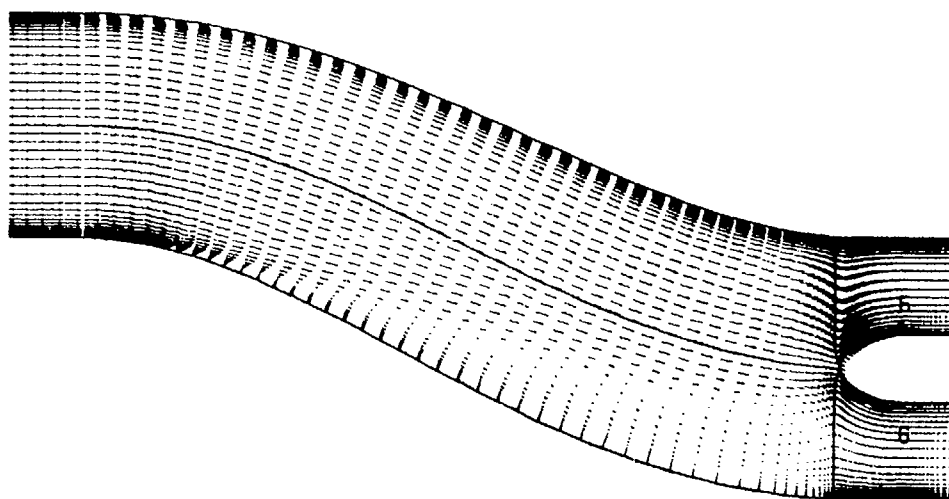


FIG. 3.3.13 TEST CASE 3.1: VELOCITY VECTORS IN THE SYMMETRY PLANE FROM SOLUTION NS2

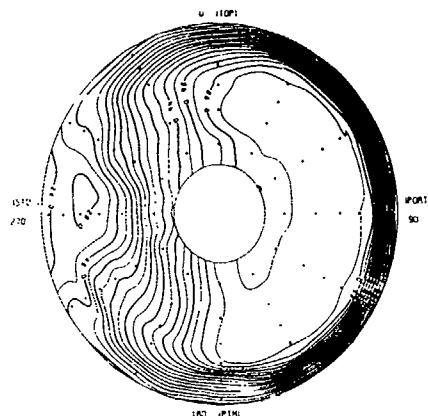


FIG. 3.3.14 TEST CASE 3.1: ENGINE FACE TOTAL PRESSURE DISTRIBUTION FROM EXPERIMENT

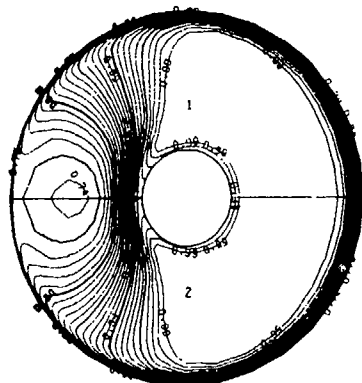


FIG. 3.3.15 TEST CASE 3.1: ENGINE FACE TOTAL PRESSURE DISTRIBUTION FROM SOLUTION NS2

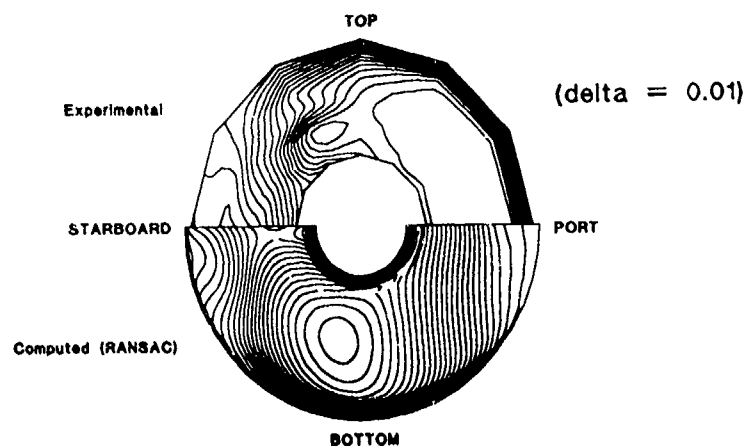


FIG. 3.3.16 TEST CASE 3.1: ENGINE FACE TOTAL PRESSURE DISTRIBUTION FROM SOLUTION NS1

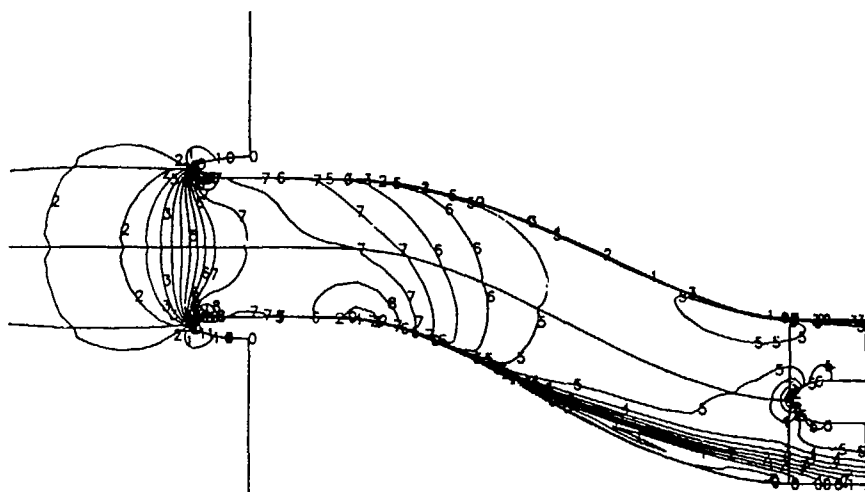


FIG. 3.3.17 TEST CASE 3.1: LINES OF CONSTANT MACH NUMBERS  
IN SYMMETRY PLANE FROM SOLUTION NS2

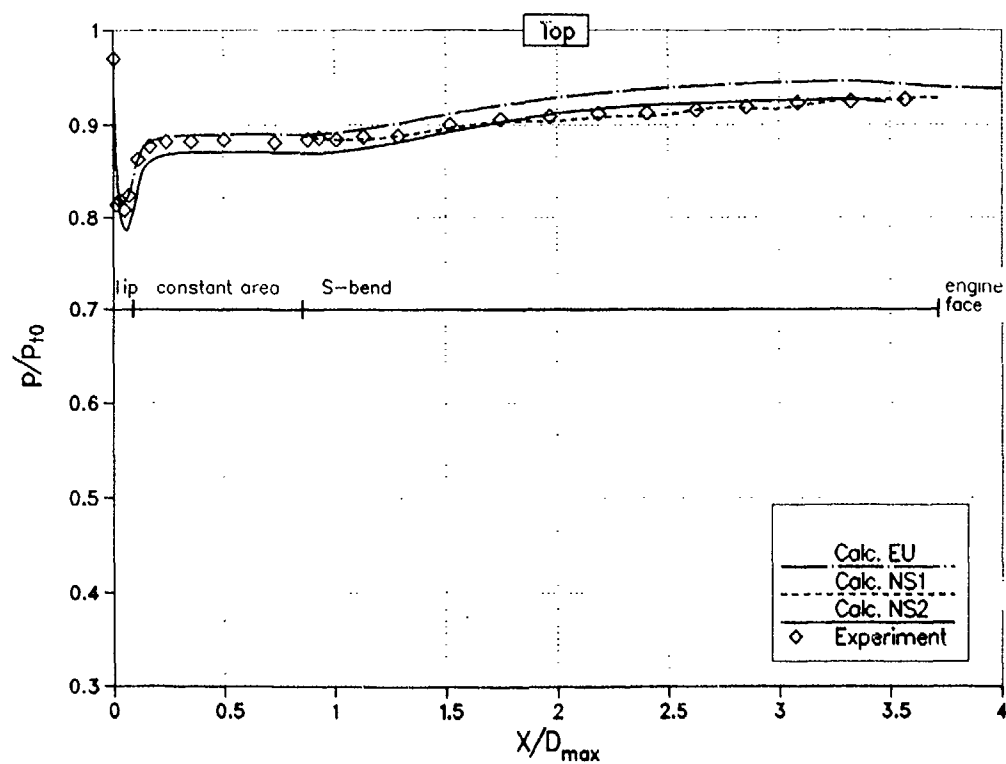


FIG. 3.3.18 TEST CASE 3.2: STATIC WALL PRESSURE ALONG DUCT - TOP

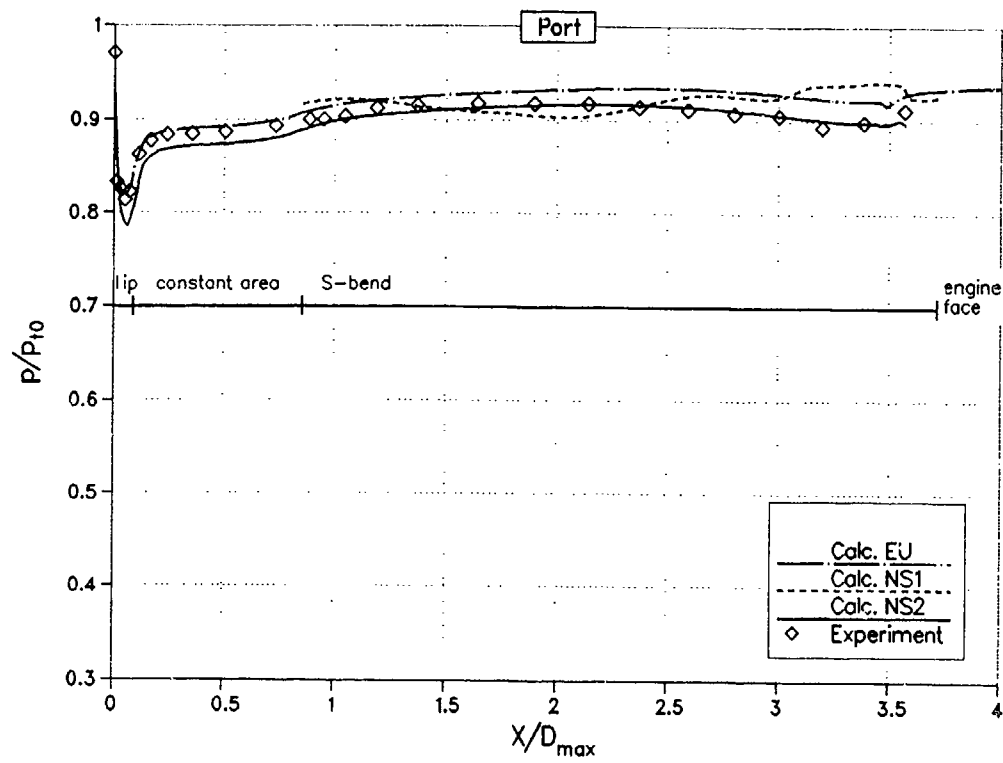


FIG. 3.3.19 TEST CASE 3.2: STATIC WALL PRESSURE ALONG DUCT - PORT

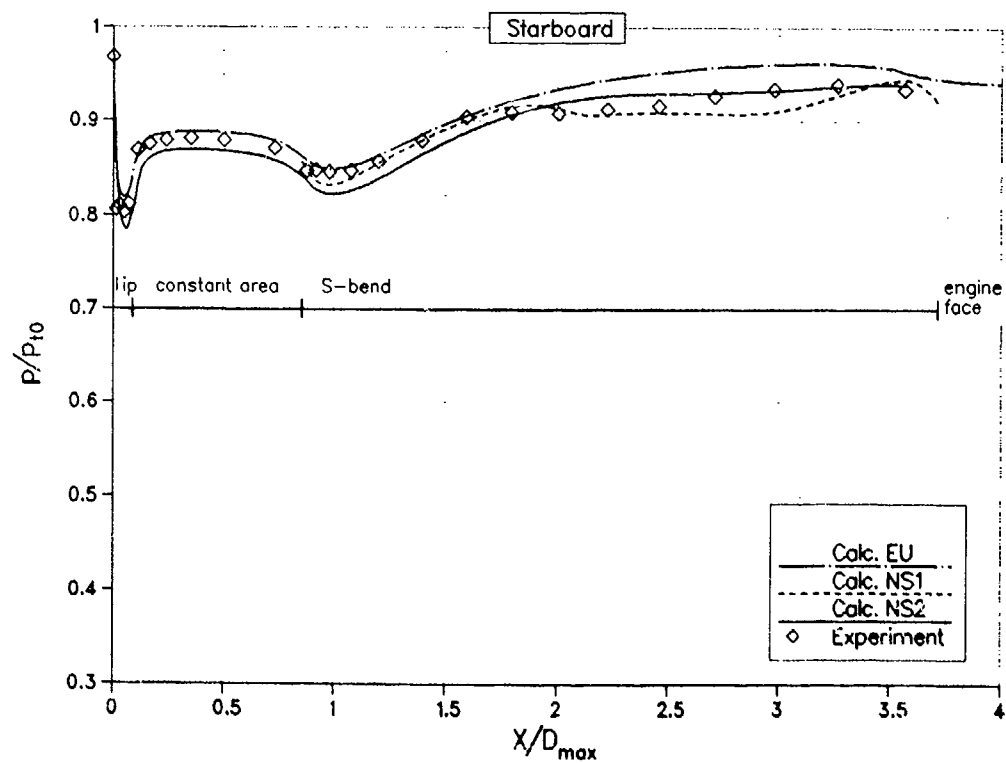


FIG. 3.3.20 TEST CASE 3.2: STATIC WALL PRESSURE ALONG DUCT - STBD



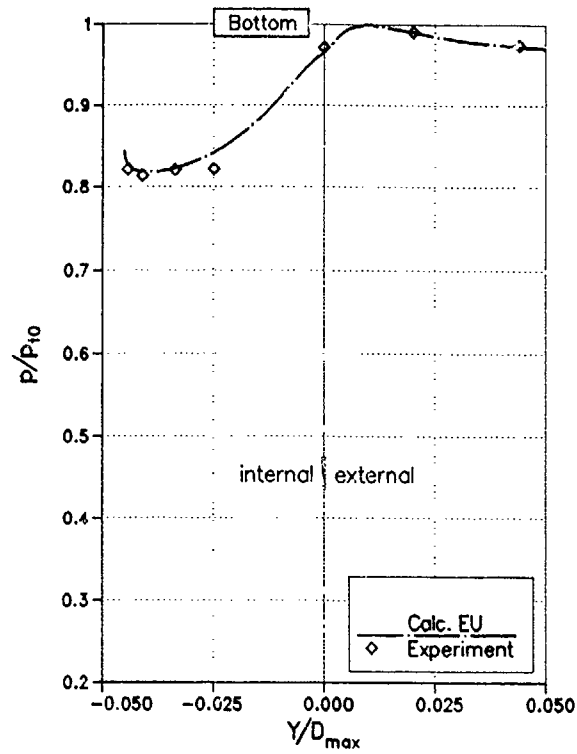
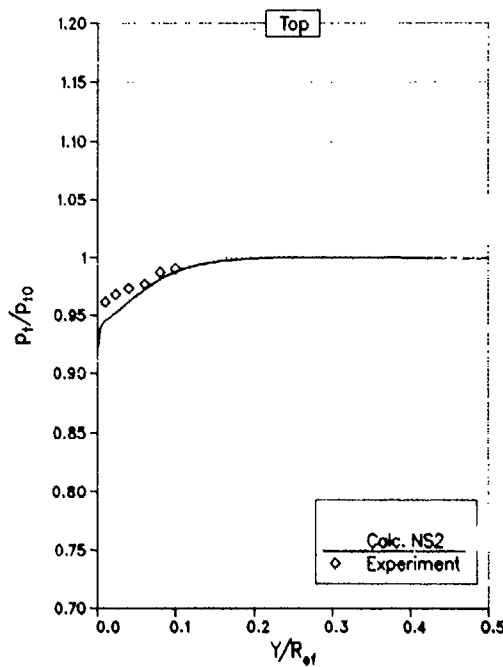
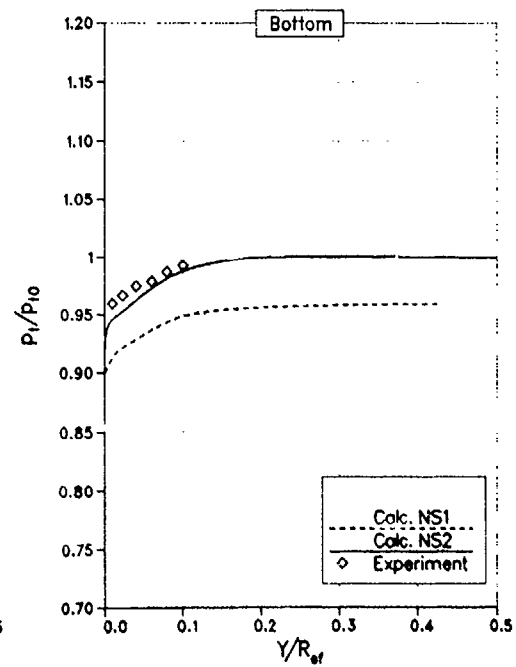


FIG. 3.3.21 TEST CASE 3.2: STATIC PRESSURE ON COWL LIP - BOTTOM

FIG. 3.3.22 TOTAL PRESSURE  
IN BOUNDARY LAYER  
AT ENGINE FACE - TOP  
TEST CASE 3.2FIG. 3.3.23 TOTAL PRESSURE  
IN BOUNDARY LAYER  
AT ENGINE FACE - BOTTOM  
TEST CASE 3.2

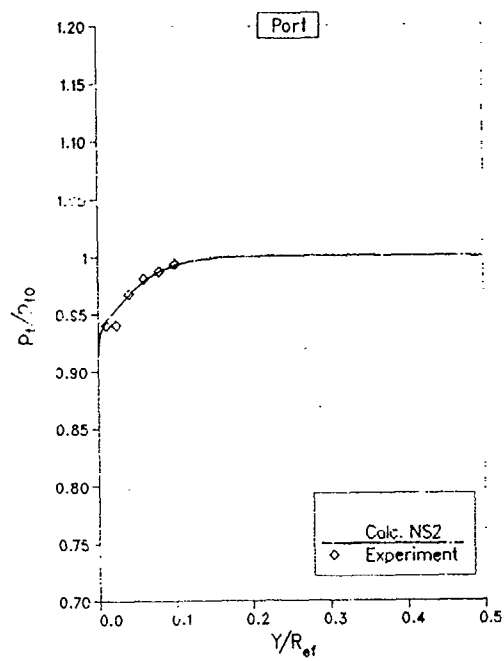


FIG. 3.3.24 TOTAL PRESSURE  
IN BOUNDARY LAYER  
AT ENGINE FACE - PORT  
TEST CASE 3.2

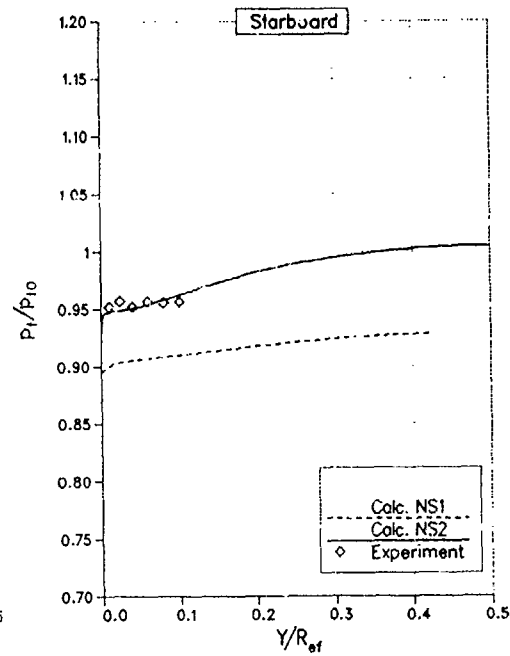


FIG. 3.3.25 TOTAL PRESSURE  
IN BOUNDARY LAYER  
AT ENGINE FACE - STBD  
TEST CASE 3.2

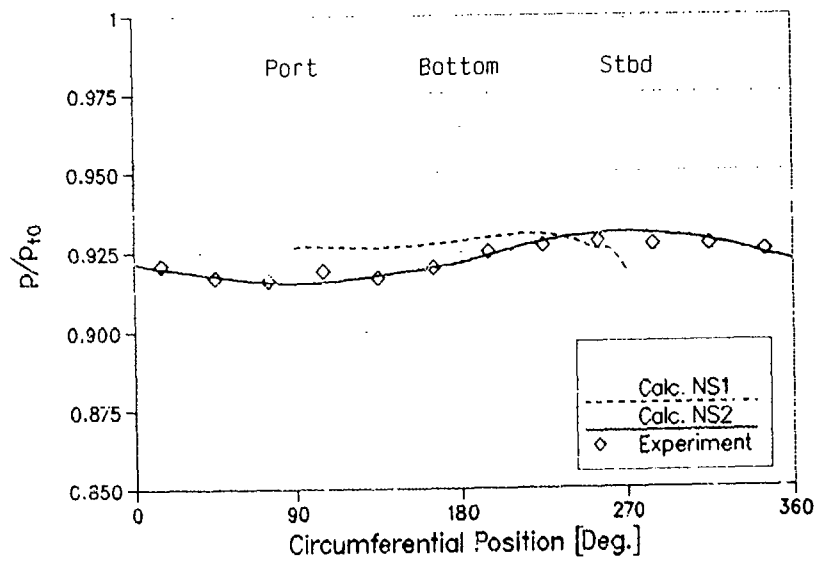


FIG. 3.3.26 TEST CASE 3.2: ENGINE FACE STATIC WALL PRESSURE

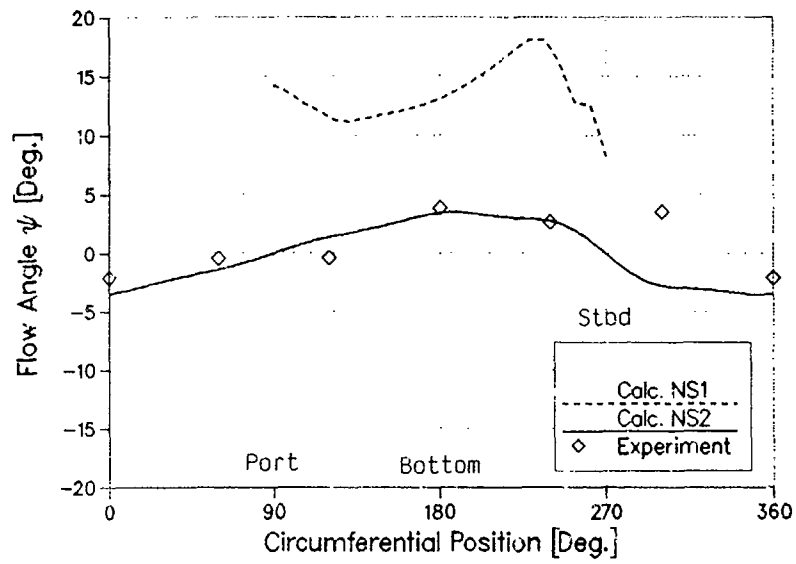


FIG. 3.3.27 TEST CASE 3.2: ENGINE FACE CIRCUMFERENTIAL FLOW ANGLES

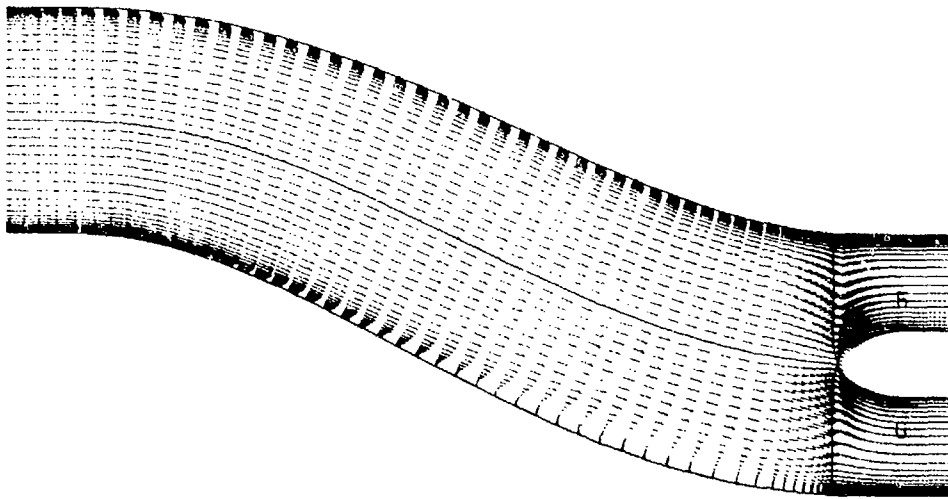


FIG. 3.3.28 TEST CASE 3.2: VELOCITY VECTORS IN THE SYMMETRY PLANE FROM SOLUTION NS2

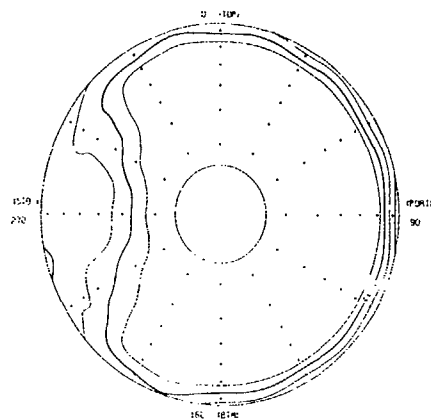


FIG. 3.3.29 TEST CASE 3.2: ENGINE FACE TOTAL PRESSURE DISTRIBUTION FROM EXPERIMENT

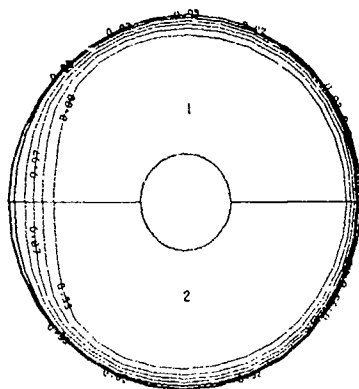


FIG. 3.3.30 TEST CASE 3.2: ENGINE FACE TOTAL PRESSURE DISTRIBUTION FROM SOLUTION NS2

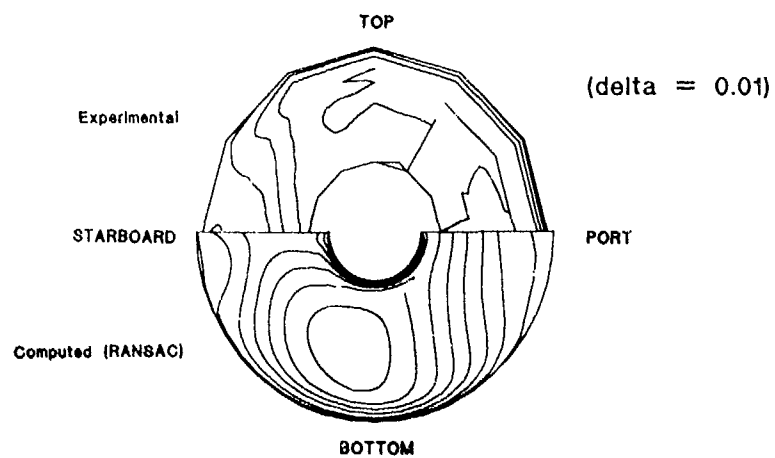
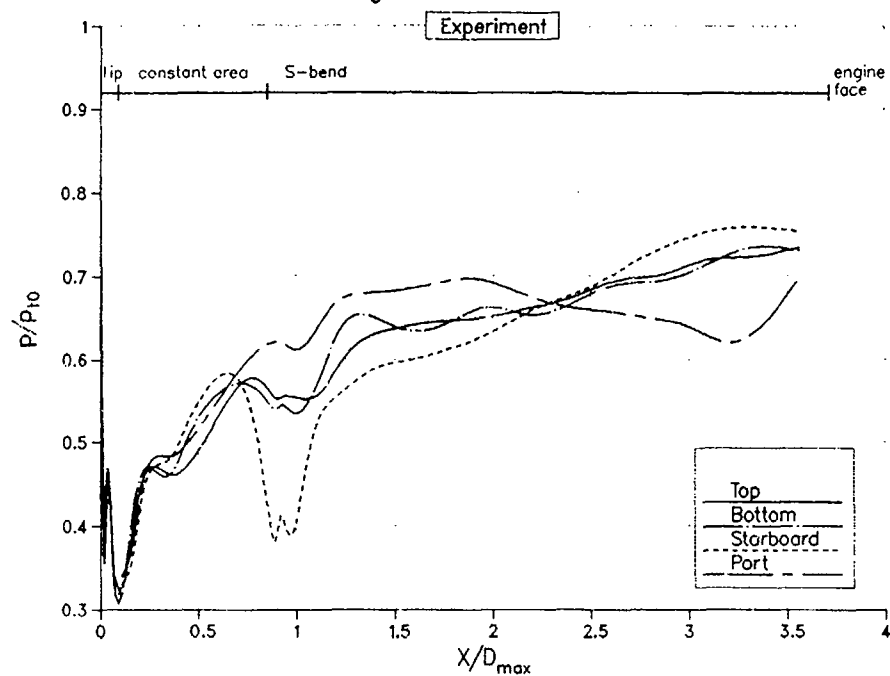


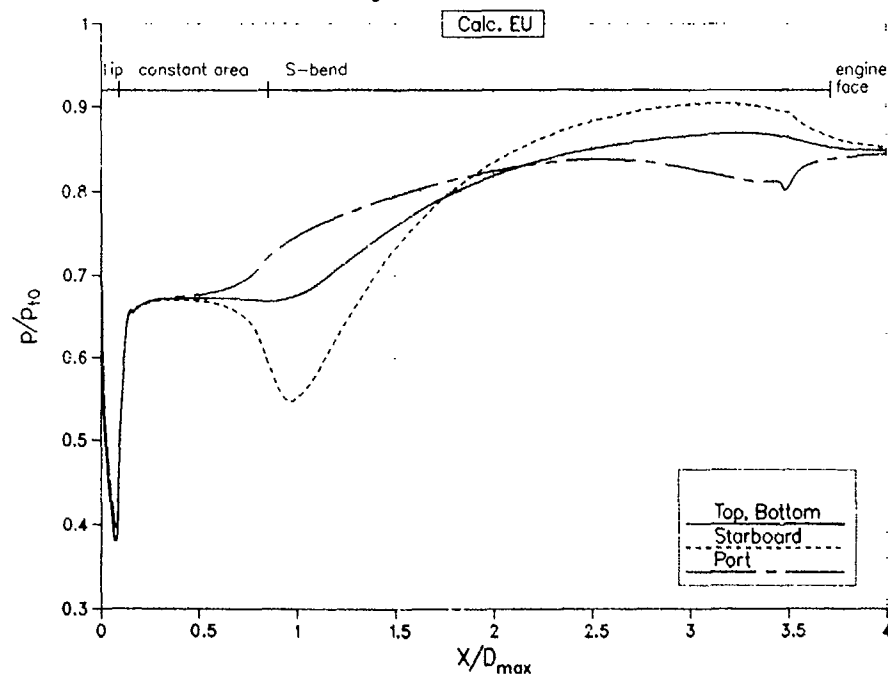
FIG. 3.3.31 TEST CASE 3.2: ENGINE FACE TOTAL PRESSURE DISTRIBUTION FROM SOLUTION NS1

Appendix 3.3.3  
Supplementary Figures for Test Case 3

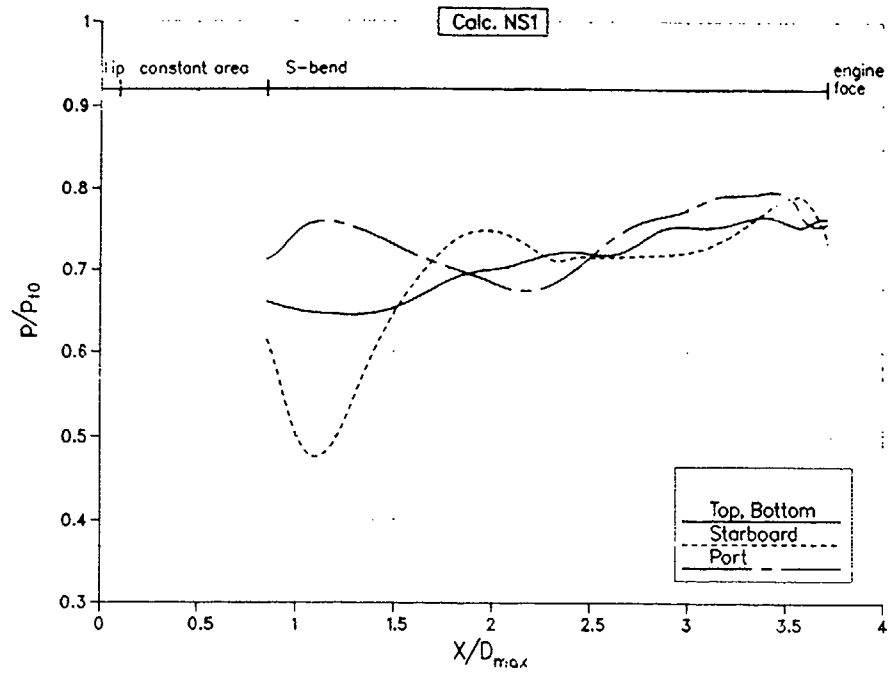
AGARD WG13, Test Case 3.1  
Static Wall Pressure along Duct



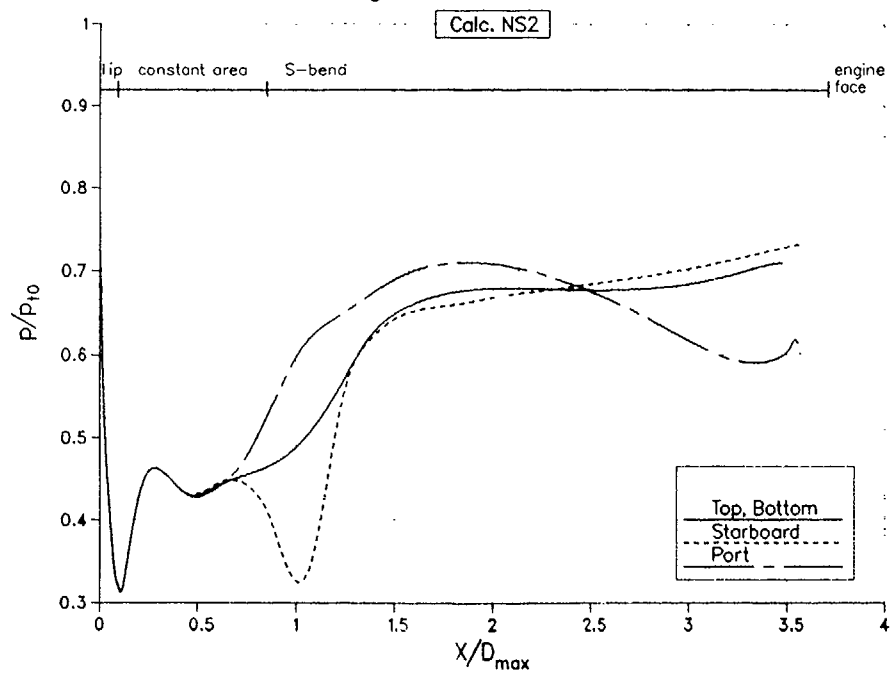
AGARD WG13, Test Case 3.1  
Static Wall Pressure along Duct



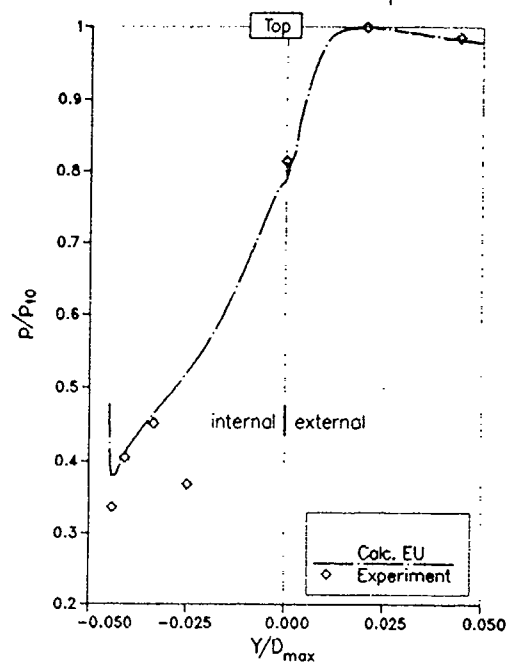
AGARD WG13, Test Case 3.1  
Static Wall Pressure along Duct



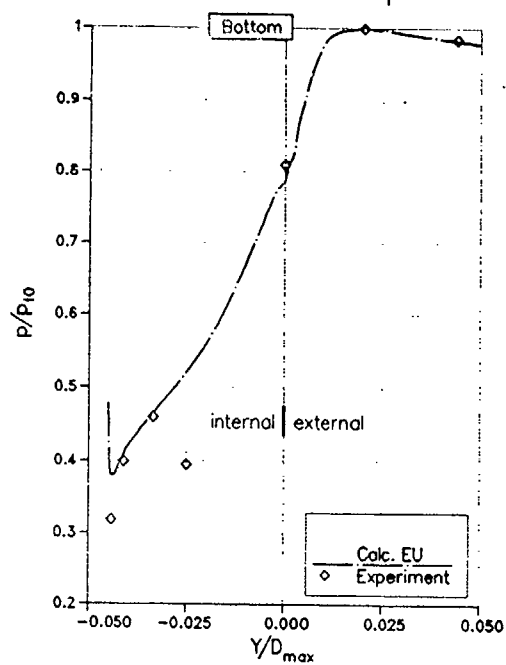
AGARD WG13, Test Case 3.1  
Static Wall Pressure along Duct



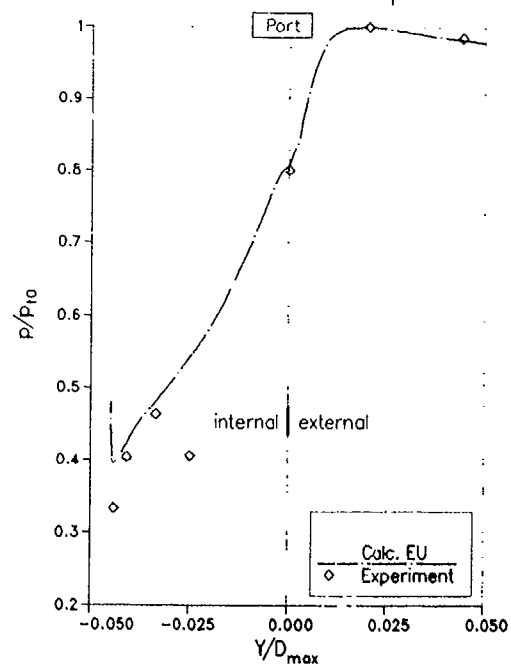
AGARD WG13, Test Case 3.1  
Static Pressures on Cowl Lip



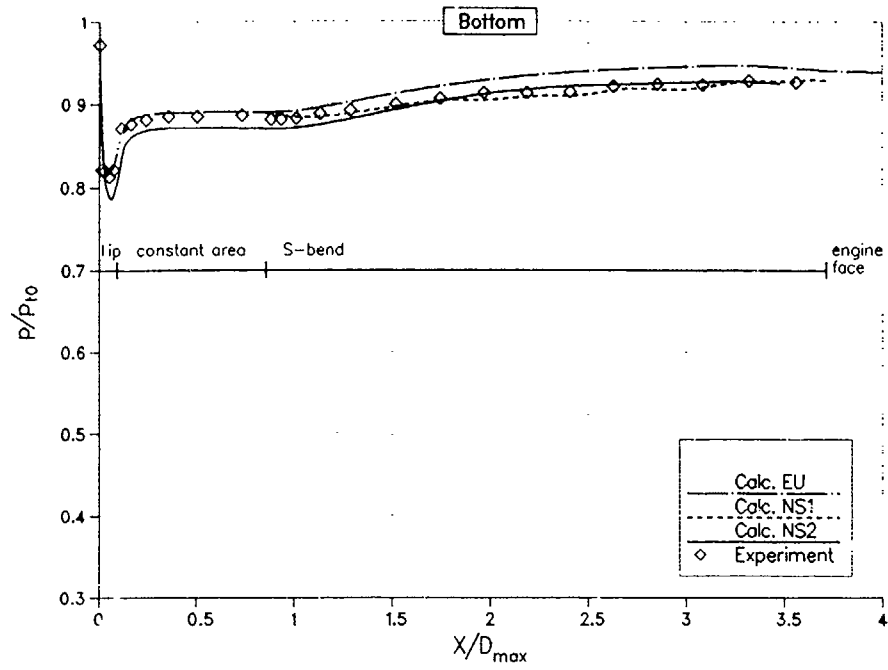
AGARD WG13, Test Case 3.1  
Static Pressures on Cowl Lip



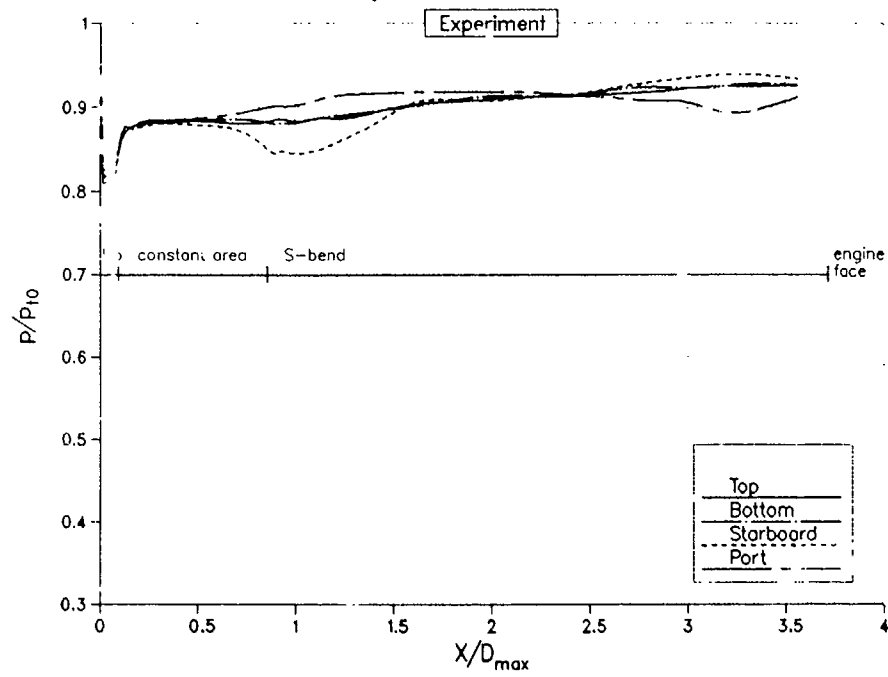
AGARD WG13, Test Case 3.1  
Static Pressures on Cowl Lip



AGARD WG13, Test Case 3.2  
Static Wall Pressure along Duct



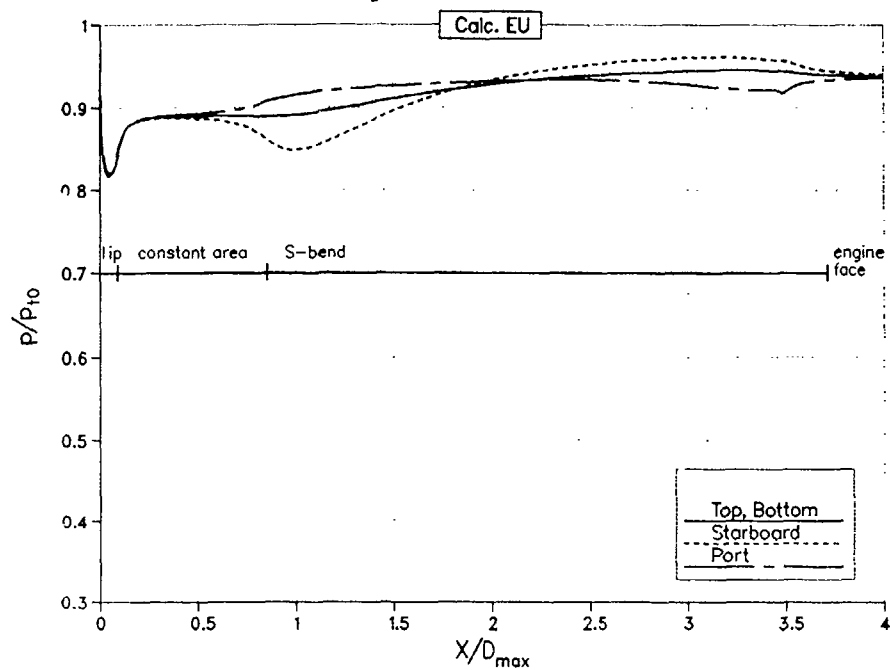
AGARD WG13, Test Case 3.2  
Static Wall Pressure along Duct





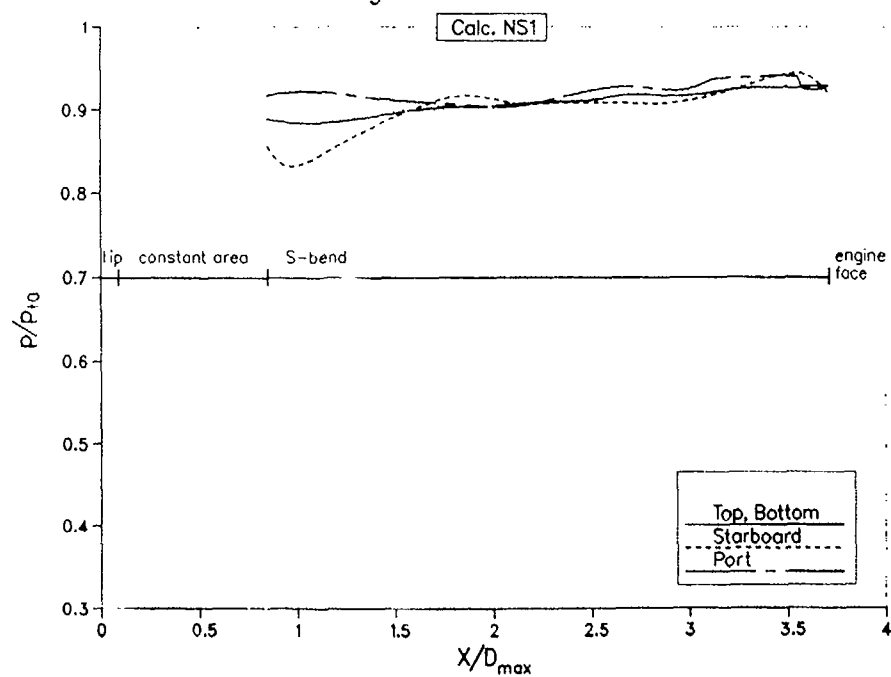
## AGARD WG13, Test Case 3.2

## Static Wall Pressure along Duct

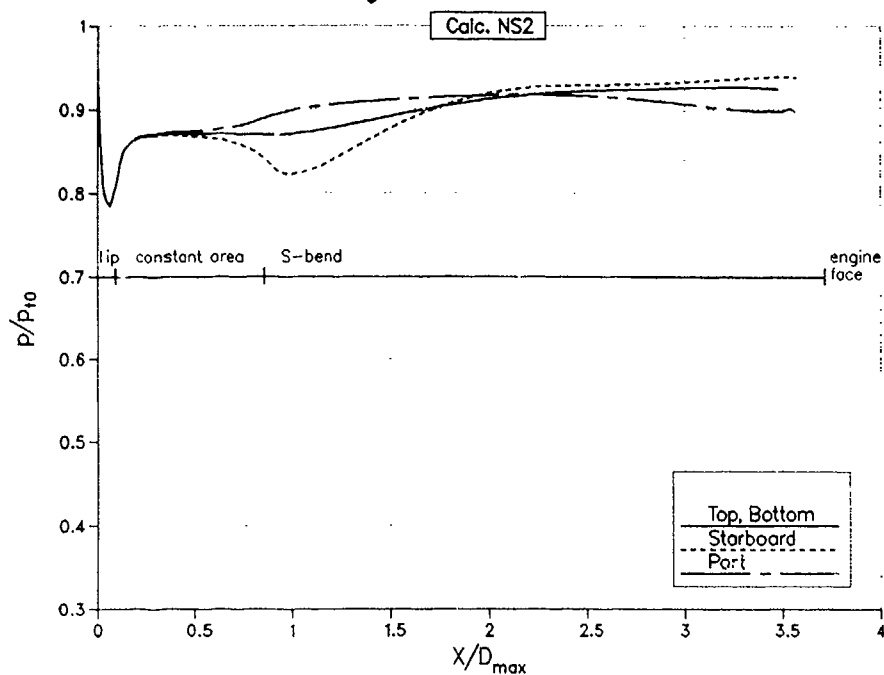


## AGARD WG13, Test Case 3.2

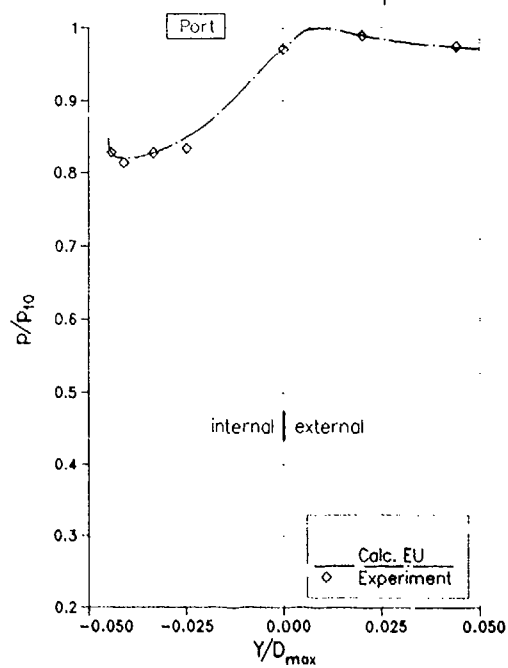
## Static Wall Pressure along Duct



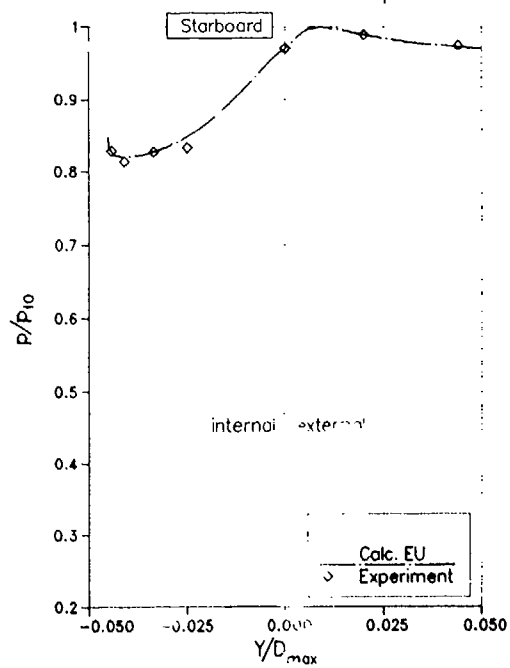
AGARD WG13, Test Case 3.2  
Static Wall Pressure along Duct



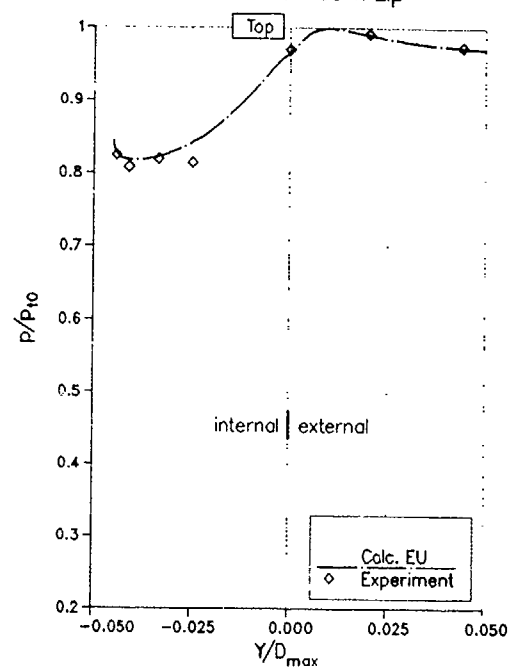
AGARD WG13, Test Case 3.2  
Static Pressures on Cowl Lip



AGARD WG13, Test Case 3.2  
Static Pressures on Cowl Lip



AGARD WG13, Test Case 3.2  
Static Pressures on Cowl Lip



### 3.3.4 Test case 4 - Subsonic/Transonic Semi-circular Intake

#### 3.3.4.1 INTRODUCTION

This test case is very similar to test case 3. However here the circular intake is replaced by a semi-circular one followed by an S-bend diffuser which ends in a circular engine face cross-section. CFD was expected to show the influence of the flow in the intake "corners" onto the duct flow. I.e., the flow of this test case is most likely more viscosity dominated than that of test case 3. It is also more challenging to find a "good" grid for the intake with its "corners" than for the round intake of test case 3.

#### 3.3.4.2 PROBLEM DESCRIPTION

The geometry for this test case consists of a semi-circular intake followed by an S-bend diffuser (RAE intake model 2129). Fig. 3.4.1 shows its shape (and at the same time the surface grid used by ARA Bedford). The geometry of an "engine" bullet was specified too. Because tests with a serrated tape at different stations on the intake lip showed only a small effect on internal performance the tests for this test case were performed without any boundary layer trips attached. In order to eliminate the problem of differing entrance conditions within different codes the sollicitors were asked to calculate the complete flow from free-stream into the intake instead of just the duct flow.

The flow for two mass-flow ratios was to be calculated. For test case 4.1 and test case 4.2 the test conditions are given in the following table:

#### Test Case 4.1 (DP18813):

Total pressure	$H_0 = 29.970$ in Hg
Total temperature	$T_{t0} = 293$ °K
Flight Machnumber	$M_0 = 0.211$
Throat Machnumber	$M_{th} = 0.701$
'Non-dimensional' Weight Flow	$WAT_{c,t} = 0.307 \frac{\text{in}^2 \sqrt{^\circ\text{K}}}{\text{sec}}$
Compressor Face Machnumber	$M_{c,t} = 0.526$
Pressure Recovery	$PR = 0.8865$
Capture Flow Ratio $A_0/A_c$	$= 2.14$
Capture area	$A_c = 24.326$ in <sup>2</sup>

#### Test Case 4.2 (DP18820):

Total pressure	$H_0 = 29.955$ in Hg
Total temperature	$T_{t0} = 293$ °K
Flight Machnumber	$M_0 = 0.211$
Throat Machnumber	$M_{th} = 0.538$
'Non-dimensional' Weight Flow	$WAT_{c,t} = 0.243 \frac{\text{in}^2 \sqrt{^\circ\text{K}}}{\text{sec}}$
Compressor Face Machnumber	$M_{c,t} = 0.387$
Pressure Recovery	$PR = 0.9781$
Capture Flow Ratio $A_0/A_c$	$= 1.837$
Capture area	$A_c = 24.326$ in <sup>2</sup>

For both test cases the free-stream Mach number was  $M_0 = 0.21$ . Angle of attack was  $\alpha = 0^\circ$  without sideslip.

The test data available from the experiments included static pressures, total pressures and some circumferential flow angles in the engine face plane. The total pressures within the boundary layer were scanned by total pressure probes at four circumferential stations just in front of the engine face plane. Along the duct walls two rows of static pressure taps were located.

All static and total pressures are scaled with the free stream total pressure  $p_{t0}$ . Coordinates are scaled with the maximum diameter of  $D_{max} = 6.641$  in.

#### 3.3.4.3 CFD TECHNIQUES

This test case was attempted only by the research group of ARA Bedford. They used their Euler multiblock method (Jameson type explicit central difference scheme) to calculate the inviscid flow within the intake. Because of the symmetry of the intake a grid for the half-model was constructed using 38 blocks with approximately 140,000 cells. A circular cylinder extension was added to bullet and diffuser. Also, the external part of the cowl was doubled in axial direction. Their results are designated (EU) in the figures.

#### 3.3.4.4 RESULTS

##### 3.3.4.4.1 Test Case 4.1 - High Mass Flow

Static Wall Pressures along Duct and Static Pressures on Cowl Lip

All results are plotted in Figs. 3.4.2 to 3.4.4. The experiment shows the following features. The stagnation point on the intake lip is on the outside of the intake. However, the experimental data available does not allow one to determine the exact position of the stagnation point nor of the point on the lip where the static pressure reaches its minimum. The flow accelerates around the lip to supersonic conditions which end in front of the throat with a shock (Fig. 3.4.2). The following subsonic flow is further decelerated until the pressure reaches a pressure level inside the constant area extension that is quite similar both on the port and starboard wall. In contrast to the flow of the circular duct of test case 3 the flow accelerates on both the top and starboard wall when it is entering the S-bend. Because the flow becomes supersonic again at the starboard wall during this acceleration there occurs another shock at about  $S/D_{max} \approx 1.2$ . In the S-bend the pressure distribution on the port wall is sinusoidal in shape (similar to a constant area S-bend). The pressure distribution on the starboard wall indicates a steady deceleration of the flow up to the engine face.

Because of the increased effective areas in the intake the pressures in the Euler solution EU must be higher than those in the experiment. Fig. 3.4.2 shows this

effect. In this solution the flow goes to subsonic conditions through a shock also. Behind this shock at  $X/D_{max} \sim 0.2$  the pressure in EU depicts a small waviness which sometimes signals errors in the surface definition. The difference between the measured and the calculated pressure in the constant area duct piece is much higher than in test case 3.1. This could be due to the neglect of the probably very thick boundary layers (which could be accompanied by local separation) in the corners of the half-circular intake in the Euler calculation. To deduce the reason for the differences between experiment and calculation inside the S-bend seems to be impossible because the flow becomes highly three-dimensional even before it enters the S-bend. Comparing the pressure distribution in the S-bend with that of test case 3.1 could lead to the conclusion that both ducts experience similar separations.

The pressures on the cowl lip are plotted in a coordinate system whose origin is at the highlight of the lip (Figs. 3.3.4.3 and 3.3.4.4). The Y axis is perpendicular to the centreline of the intake. Positive Y values correspond to the external part of the lip. The stagnation point is located on the external part of the intake lip. However, from the measurement it is very difficult to determine its exact position. The acceleration of the flow from the stagnation point into the intake differs considerably between the measurement and solution EU.

Total pressures in the boundary layer, static wall pressures and flow angles measured at the engine face are given in the supplementary figures in Appendix 3.3.4.

#### 3.3.4.4.2 Test Case 4.2 - Low Mass Flow

Static Wall Pressures along Duct and Static Pressures on Cowl Lip

The results are plotted in Figs. 3.4.5 and 3.4.7. From the measured data it is not

clear whether the flow stays subsonic throughout the duct. There could be a small supersonic region on the cowl lip. Again the calculated static wall pressures of the Euler solution are higher than the measured ones. The difference between the two is not as high as in test case 4.1. This is probably due to the fact that for the mass flow considered the boundary layers, especially those in the intake corners, are much thinner than in test case 4.1. The stagnation point is still located on the external side of the lip (Figs. 3.4.6 and 3.4.7). Compared with test case 4.1 the stagnation point did not move very much towards the highlight of the lip. For the calculation of the flow with an Euler or even Navier-Stokes code it requires an extremely fine grid on the lip to resolve this small movement of the stagnation point.

The extremely short acceleration region of the flow on the starboard wall before it enters the S-bend and its abrupt deceleration after it just entered the S-bend is not repeated in the Euler solution. In solution EU the acceleration is much weaker than in the experiment. The differences in the pressures inside the S-bend seem to be caused by the displacement of the steadily growing boundary layers.

Total pressures in the boundary layer, static wall pressures and flow angles measured at the engine face are given in the supplementary figures in Appendix 3.3.4.

#### 3.3.4.5 CONCLUSIONS

Due to the fact that only an Euler solution was contributed to this test case, there are no specific conclusions possible. However, from the limited comparison between solution EU and the experiment it is apparent that it would be a real challenge for the experimentalists to repeat the test in more details and the numeric people to calculate the flow with Navier-Stokes codes.

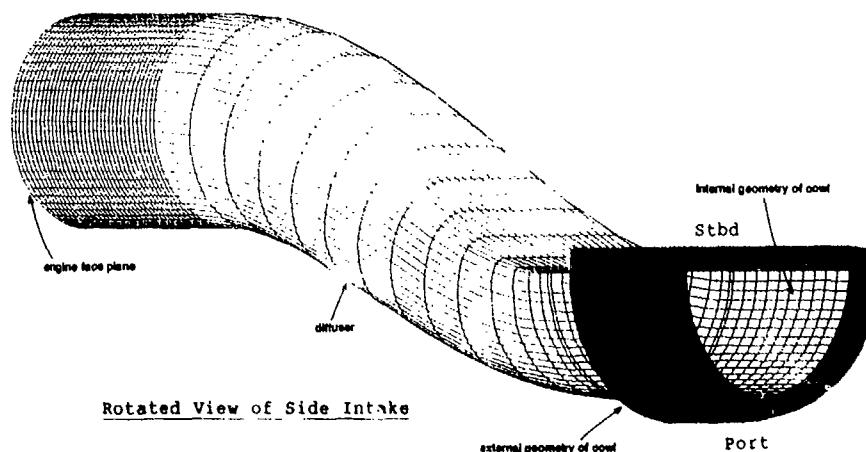


FIG. 3.4.1 VIEW OF GEOMETRY FOR TEST CASE 4 -  
Surface grid from ARA Euler calculations

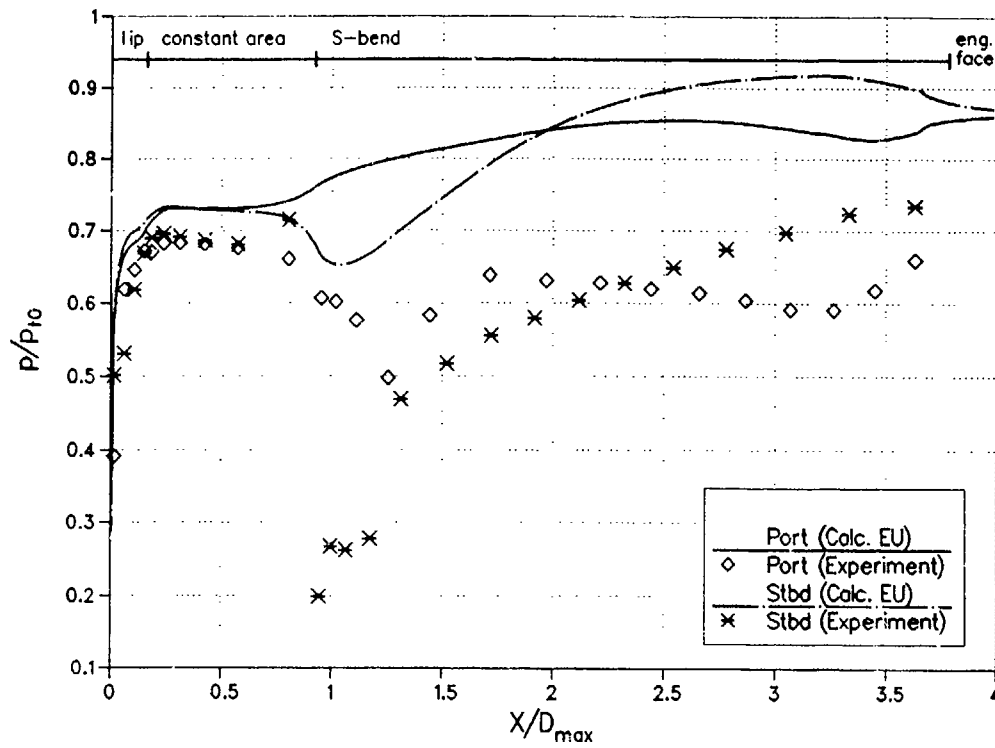


FIG. 3.4.2 TEST CASE 4.1: STATIC WALL PRESSURE ALONG DUCT PORT AND STARBOARD

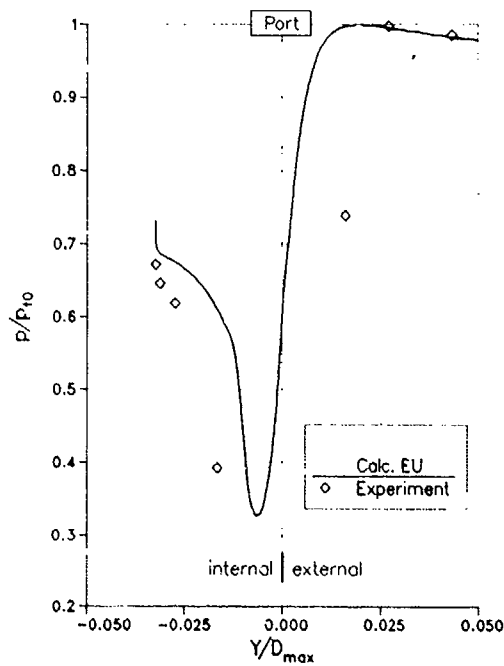


FIG. 3.4.3 STATIC PRESSURE ON COWL LIP - PORT TEST CASE 4.1

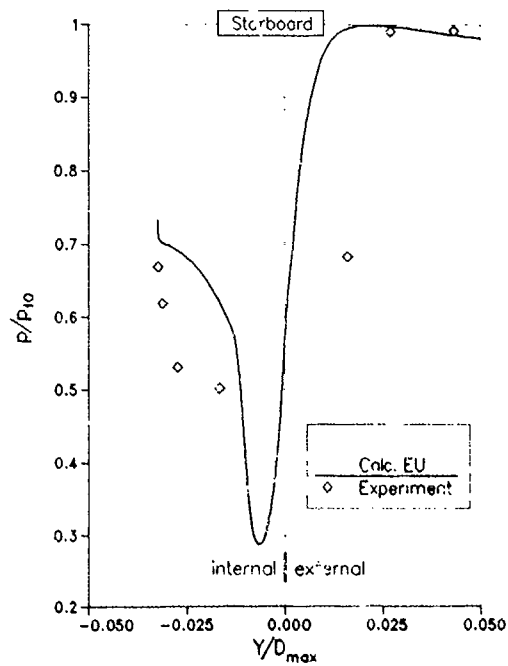


FIG. 3.4.4 STATIC PRESSURE ON COWL LIP - STBD TEST CASE 4.1

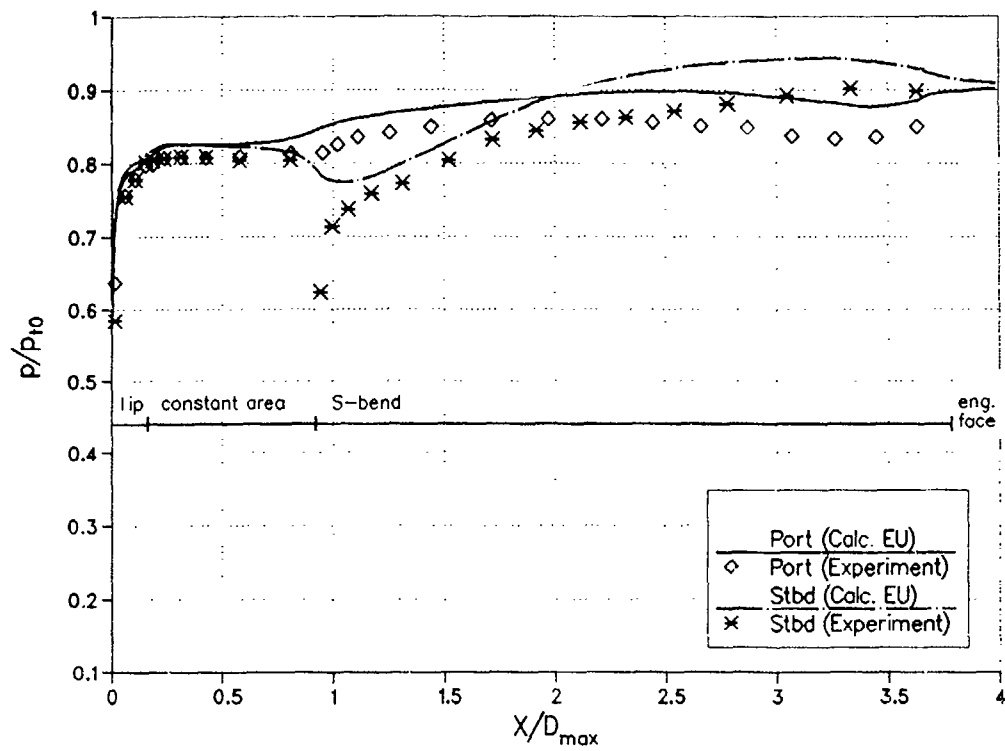


FIG. 3.4.5 TEST CASE 4.2: STATIC WALL PRESSURE ALONG DUCT PORT AND STARBOARD

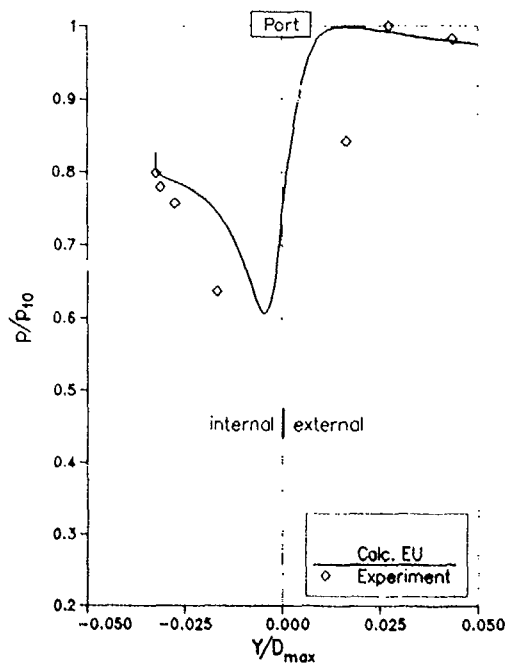


FIG. 3.4.6 STATIC PRESSURE ON COWL LIP - PORT TEST CASE 4.2

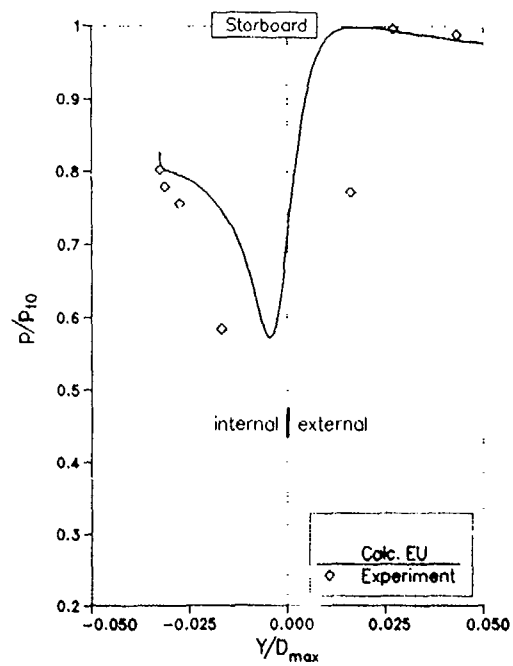
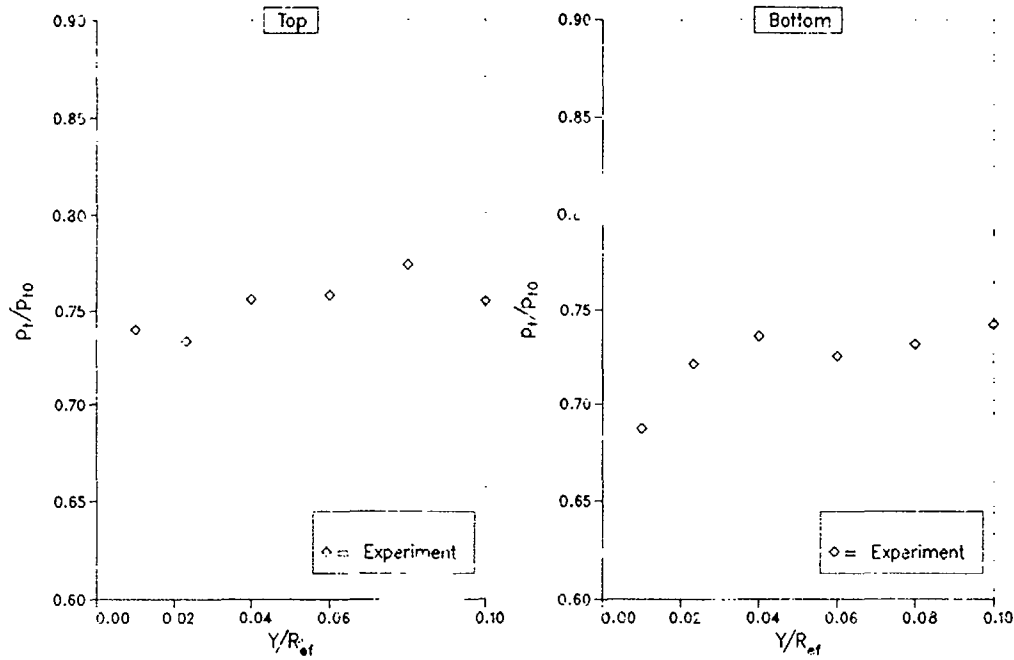


FIG. 3.4.7 STATIC PRESSURE ON COWL LIP - STBC TEST CASE 4.2

Appendix 3.3.4  
Supplementary Figures for Test Case 4

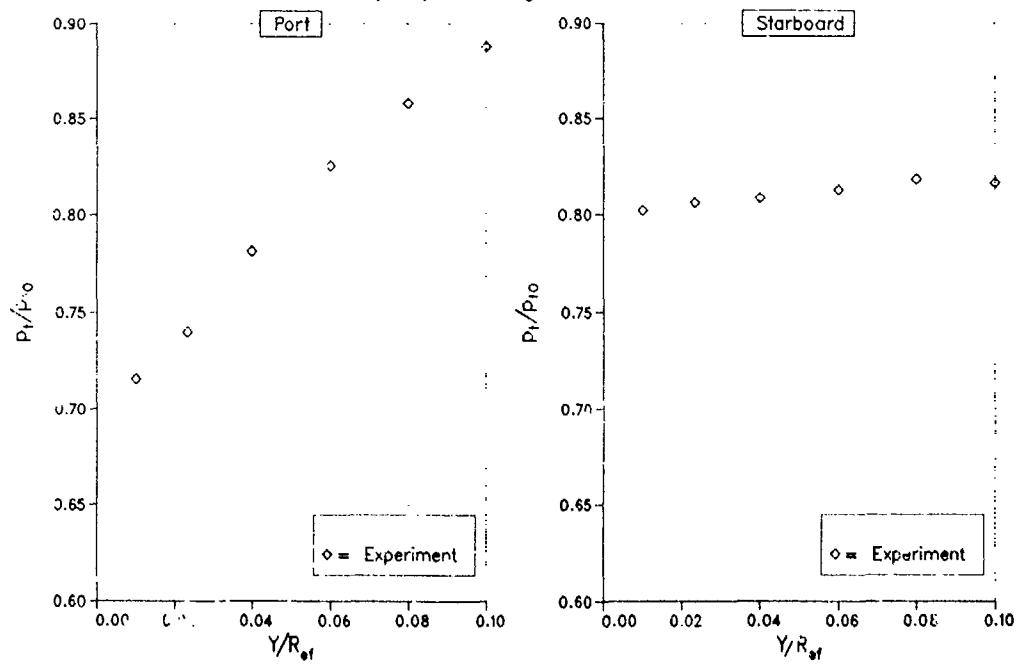
AGARD WG13, Test Case 4.1

Total Pressure in Boundary Layer at Engine Face Rake



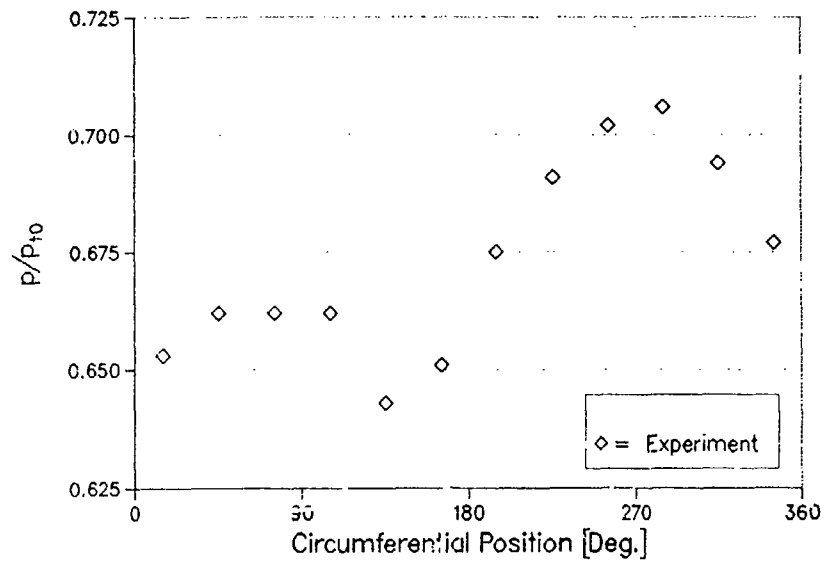
AGARD WG13, Test Case 4.1

Total Pressure in Boundary Layer at Engine Face Rake

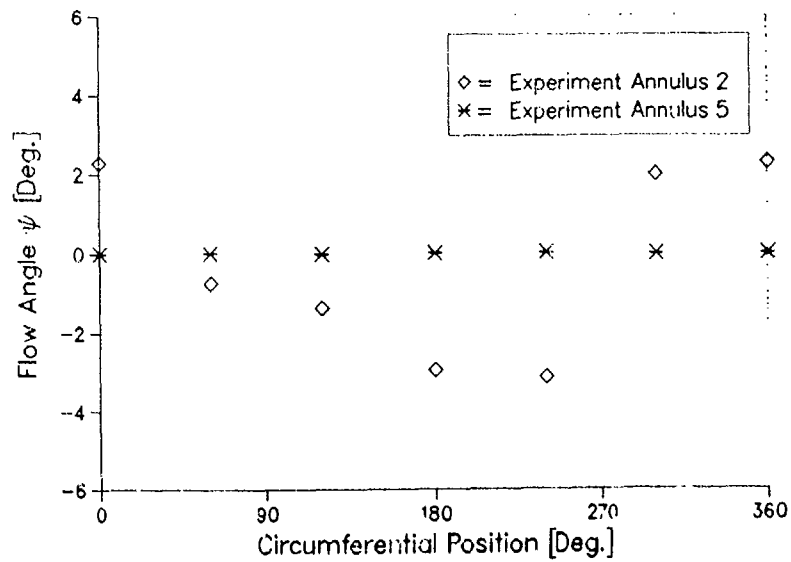




AGARD WG13, Test Case 4.1  
Engine Face Static Wall Pressure

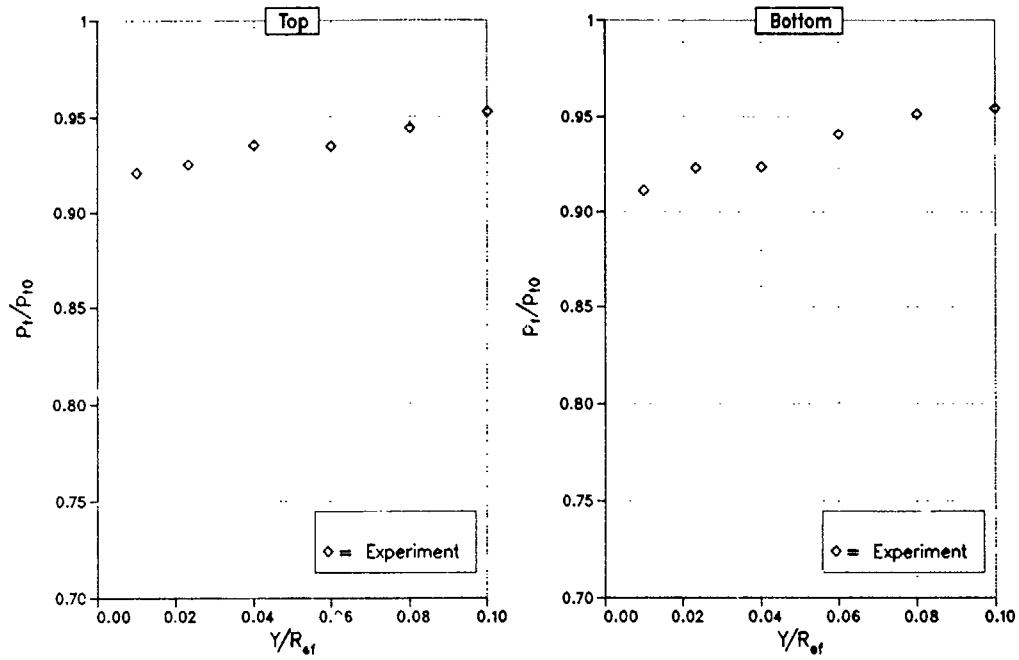


AGARD WG13, Test Case 4.1  
Circumferential Flow Angles at Engine Face



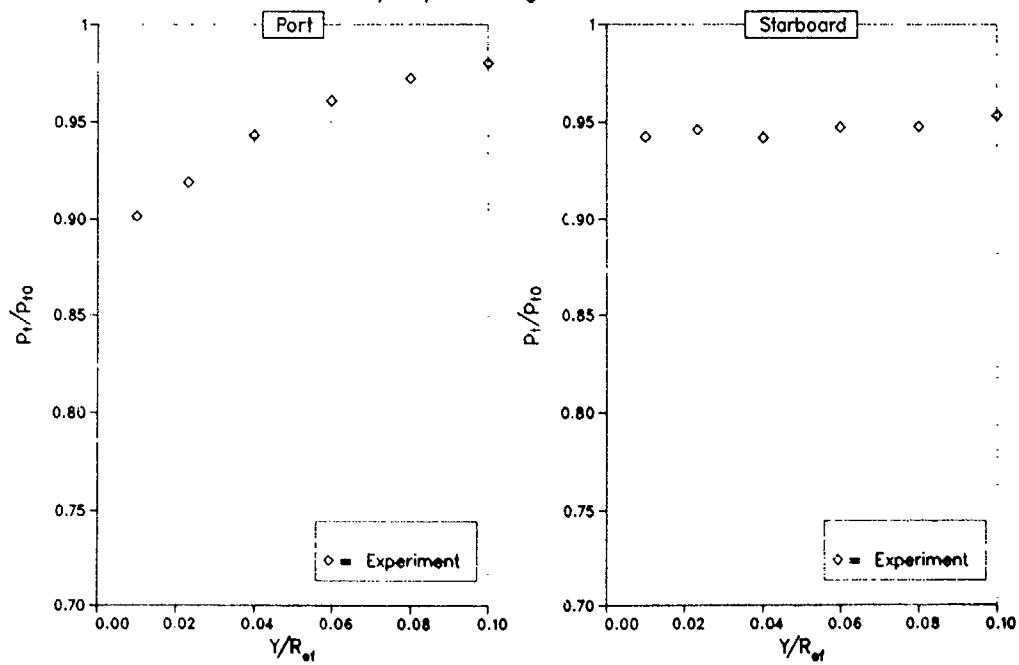
## AGARD WG13, Test Case 4.2

Total Pressure in Boundary Layer at Engine Face Rake

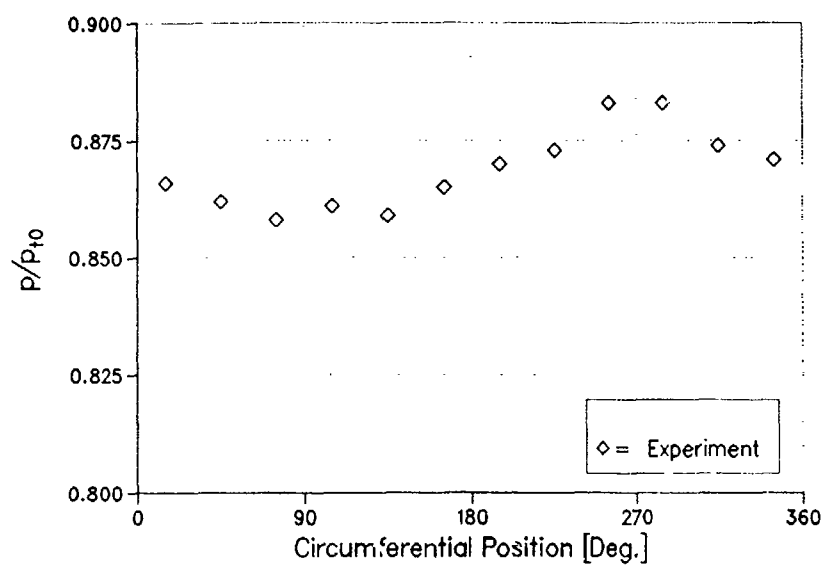


## AGARD WG13, Test Case 4.2

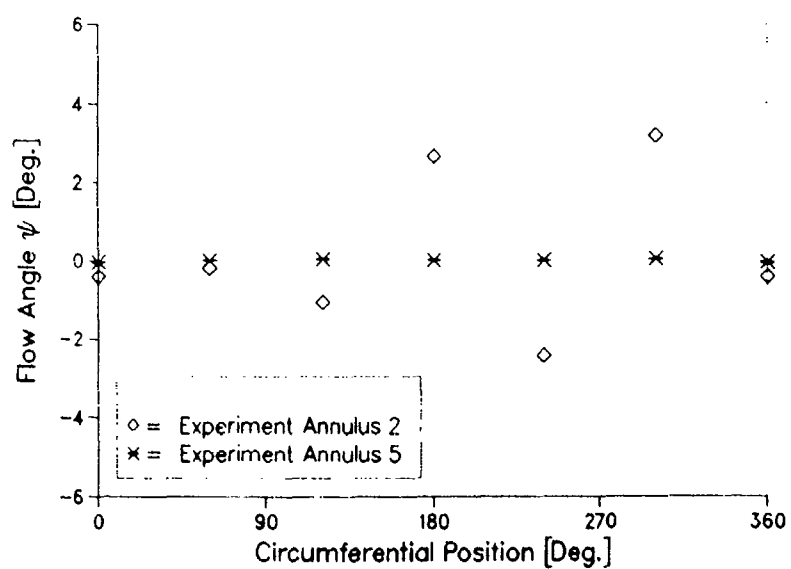
Total Pressure in Boundary Layer at Engine Face Rake



AGARD WG13, Test Case 4.2  
Engine Face Static Wall Pressure



AGARD WG13, Test Case 4.2  
Circumferential Flow Angles at Engine Face



### 3.3.5 Test case 5 - Supersonic Circular Pitot Intake

#### 3.3.5.1 INTRODUCTION

Whereas in test cases 3 and 4 the flow inside the intake was predominantly governed by the shape of the intake entrance and duct, in this test case the influence of the flow towards the intake onto the duct flow was to be investigated. The geometry therefore was kept as simple as possible in order to show just that effect. Variation of the flow was accomplished by variation of mass flow.

#### 3.3.5.2 PROBLEM DESCRIPTION

In this test case the flow into a straight circular pitot intake with a contraction ratio of 1.177 (RAE model 742L) at a supersonic flight Mach number of  $M_0=1.5$  was to be calculated. Fig. 3.5.1 gives an impression of its shape. The "engine bullet" was to be simulated in addition to the duct geometry.

The flow for three mass-flow ratios was to be calculated. For the three test cases 5.1, 5.2, and 5.3 the test conditions are summarized in the following tables:

##### Test Case 5.1:

Total pressure	$H_0 = 108426 \text{ Pa}$
Static pressure	$P_0 = 29535 \text{ Pa}$
Total temperature	$T_{t,0} = 292.2 \text{ }^\circ\text{K}$
Flight Machnumber	$M_0 = 1.5$
Pressure Recovery	$PR = 0.8978$
Capture Flow Ratio	$A_0/A_c = 0.9307$
Capture area	$A_c = 8.086 \text{ in}^2$

##### Test Case 5.2:

Total pressure	$H_0 = 108359 \text{ Pa}$
Static pressure	$P_0 = 29517 \text{ Pa}$
Total temperature	$T_{t,0} = 292.8 \text{ }^\circ\text{K}$
Flight Machnumber	$M_0 = 1.5$
Pressure Recovery	$PR = 0.9246$
Capture Flow Ratio	$A_0/A_c = 0.6256$
Capture area	$A_c = 8.086 \text{ in}^2$

##### Test Case 5.3:

Total pressure	$H_0 = 108525 \text{ Pa}$
Static pressure	$P_0 = 29507 \text{ Pa}$
Total temperature	$T_{t,0} = 292.8 \text{ }^\circ\text{K}$
Flight Machnumber	$M_0 = 1.5$
Pressure Recovery	$PR = 0.9267$
Capture Flow Ratio	$A_0/A_c = 0.2980$
Capture area	$A_c = 8.086 \text{ in}^2$

Transition during testing has been forced inside the intake duct by a 0.1" band of 0.005" to 0.006" ballotini placed 0.1" back from the highlight.

The test data available from the experiments included static pressures, total pressures, pressure recovery and steady state distortion values in the engine face plane. The total pressures within the boundary layer were scanned by total pressure probes at two circumferential stations just in front of the engine face plane. Along the duct wall one row of static pressure taps was located.

#### 3.3.5.3 CFD TECHNIQUES

This test case was attempted by two research groups. ARA Bedford applied their Euler multiblock method the flow solver of which is based on the explicit central difference scheme proposed by Jameson et al. and added a boundary layer calculation. Their results are designated (EU) for the Euler results and (EUBL) for the Euler results with the boundary layer results added in the figures. The Euler calculations are axisymmetric ones. The engine bullet was not simulated, however, the duct was extended behind the engine face. The grid possessed 7000 cells. The 8000 iterations (at a CFL=1.6) considered necessary for convergence needed 700 seconds on a CRAY2.

The Dornier group calculated the flow with their two-dimensional/axisymmetric Navier-Stokes code ENSFL2D using the axisymmetric mode. This is an explicit finite volume code with the Runge-Kutta-type time integration proposed by Jameson et al.. The Baldwin-Lomax turbulence model was used. The assumption of fully turbulent boundary layers was applied. Up to five grids with varying density have been used during the calculations. The finest grid with 30,720 cells in half of the duct was used only for test case 5.1, i.e. for the highest mass flow. Both the bullet and the intake duct were extended beyond the engine face plane. To arrive at a converged solution for one given engine face static pressure it took 20 to 25 minutes CPU-time on a CONVEX C220 (single processor). In order to calculate the flow for a given mass flow the flow for several engine face static pressures has to be calculated. The time for such a solution depends heavily on the skill of the code user. The results are designated (NS) in the figures.

Details of the methods used and the results provided by the originators are given in the microfiche.

#### 3.3.5.4 RESULTS

The stand-off of the shock ahead of the intake lip varied for the three engine mass flows selected thus producing varying spillage around the intake lip.

### 3.3.5.4.1 Test Case 5.1 - Highest Mass Flow

#### Static and Total Pressures

The static wall pressures are plotted in Figs. 3.5.2 to 3.5.5. The flow into the intake which is subsonic behind the shock in front of the intake lip is characterized by a strong acceleration from the stagnation point which is just inside the lip (Fig. 3.5.5). The static pressure reaches sonic values at the throat and goes slightly supersonic downstream of the throat. Somewhere at  $S/D_{in} \approx 0.6$  this supersonic flow goes subsonic again through a shock.

There is a good agreement between the pressures of EUBL and the experiment from the stagnation point towards the intake throat. Deviation starts shortly before the geometric throat (Fig. 3.5.2). This is due to the procedure by which this solution was determined. Because in the Euler solution the same mass flow has been simulated as in the experiment the calculated pressures must be generally higher than the measured ones. This means that the Euler flow does not go supersonic at the intake throat (Fig. 3.5.2). By just adding once a boundary layer solution onto the Euler result, i.e. without iterating between Euler and boundary layer calculation, this situation cannot be improved satisfactorily. It is, however, remarkable that downstream of the supersonic region in the intake duct solution EUBL is not too far off the experiment. That could mean that the flow in the downstream duct is not very much affected by the upstream flow.

In contrast to solution EUBL the pressure plateau at the throat inside the intake is nearly reached by solution NS (Fig. 3.5.2). The supersonic acceleration downstream of the throat is also reproduced. But, instead of showing a terminating shock the pressures of solution NS indicate a broad area where the pressure increases and the flow goes subsonic again. The contributors of this result explain this effect with the coarseness of the grid in this area. The deceleration of the flow in the diffuser takes place at about the same rate but at lower pressures, i.e. higher Mach numbers, than in the experiment. A possible reason for this could be that the displacement thickness of the boundary layer in NS has been larger than in the experiment necessitating a lower exit pressure to reach the same mass flow. This then results in lower duct pressures.

The pressures on the external wall downstream of the highlight of the lip agree quite well between experiment and solutions EUBL and NS. However, differences can be observed in Fig. 3.5.3 closer to the highlight of the intake lip. Details can best be seen in Fig. 3.5.4 which shows that both solution EUBL and NS miss the small region of constant pressure at  $Y/D_{in} < 0.026$ . It is interesting to see that both solutions deliver a wavy pressure distribution between this plateau and the highlight of the lip (Fig. 3.5.4). The stagnation point on the lip of the two solutions is close to but not at the correct location (Figs. 3.5.4 and 3.5.5).

Solution EUBL overpredicts the total pressure in the boundary layer at the engine face whereas solution NS underpredicts this total pressure at the intake wall and seems to overpredicts it closer to the engine bullet (Figs. 3.5.6 and 3.5.7 in which the total pressure is referenced with the free stream total pressure).

### 3.3.5.4.2 Test Case 5.2 - Medium Mass Flow

#### Static and Total Pressures

The static wall pressures are plotted in Figs. 3.5.8 to 3.5.11. As can be seen the pressures along the internal intake wall indicate completely subsonic flow in Fig. 3.5.8 and supersonic flow on the external wall in Fig. 3.5.9. Compared with test case 5.1 the stagnation point on the intake lip moved more into the intake (Figs. 3.5.10 and 3.5.11).

Solution EUBL very slightly overestimates the static wall pressures inside the duct whereas on the outside its pressures are slightly smaller than those of the experiment (Figs. 3.5.8 to 3.5.10). The location and pressure level of the stagnation point are reproduced correctly by EUBL (Figs. 3.5.10 and 3.5.11). The shape of the pressure distribution inside the boundary layer at the engine face is also slightly different from the experimental one. The boundary layer thickness is slightly larger in EUBL than in the experiment (Fig. 3.5.12).

Solution NS underpredicts the static pressures inside the intake duct (Fig. 3.5.8). This could be due to a boundary layer that is thicker than in the experiment. The recompression on the outside of the intake lip differs from the measured one (Fig. 3.5.10). However, the downstream static pressure values on the outside of the intake reach exactly the experimental ones. Figs. 3.5.10 and 3.5.11 show that the location of the stagnation point on the lip is reproduced very well. The total pressure (referenced with the free stream total pressure) in the boundary layer (Fig. 3.5.12) indicates a small but noticeable difference to the measured one. This figure does not confirm the speculation from above that the boundary layer might be thicker in the calculation than in the experiment. The shape of the total pressure curve of the calculation indicates a higher mass flow in the boundary layer which does also lead to lower static pressures inside the duct. Whether or not this is the only reason for the reduced duct pressure cannot be determined.

### 3.3.5.4.3 Test Case 5.3 - Small Mass Flow

#### Static and Total Pressures

For this mass flow the stagnation point on the lip moves even further into the intake. On the inside of the intake the acceleration of the flow is reduced. On the outside there appears an area with constant wall pressure before the flow is steadily decelerated to the freestream conditions. In Fig. 3.5.3 of test case 5.1 there occurred a similar constant pressure area on the outside of the intake.

Solution EUBL is not too far off from the measured static wall pressures on the inside wall of the intake (Fig. 3.5.13). The details on the lip can be observed in Figs. 3.5.15 and 3.5.16. There one sees that the calculated stagnation point pressure does not reach the measured one. Also the location of the stagnation point is shifted more to the inside in the calculation. On the outside of the lip solution EUBL does not reproduce the constant pressure region. This constant pressure region is most likely due to a separation. The deceleration pressures downstream of this area are slightly underestimated by EUBL. The total pressures inside the boundary layer at the engine face are very little smaller than the measured ones (Fig. 3.5.17) with a smaller core flow value.

The static wall pressures inside the intake of solution NS are slightly underestimated (Fig. 3.5.13) with some waviness in front of the throat. However, the location of the stagnation point inside the intake is represented quite well (Fig. 3.5.15). On the external wall the constant pressure plateau is not reproduced by NS (Fig. 3.5.14). The differences between this calculation and the experiment can best be seen in Figure 3.5.15. The total pressure in the boundary layer close to the engine face is slightly underestimated by NS as was the case with solution EUBL (Fig. 3.5.17).

#### 3.3.5.4.4 Intake Pressure Recovery

Intake pressure recovery values have been produced for solution NS only. However,

because NS is an axisymmetric calculation the integration of the engine face total pressures to form the pressure recovery was different from that of the experimentalists. It is therefore somewhat difficult to compare these data. The results are given in the following table:

	Experiment	SOLUTION NS
test case 5.1	0.8978	0.85684
test case 5.2	0.9246	0.91171
test case 5.3	0.9267	0.91089

The difference between measured and calculated pressure recovery of test case 5.1 is larger than for the other test cases. This reflects the large deviations between the measured and calculated internal flows already described in section 3.3.5.4.1.

#### 3.3.5.5. CONCLUSIONS

Concerning the Euler plus boundary layer approach the following conclusion can be drawn from this test case. This method gives reasonable results as long as there are no large separation regions and/or strong boundary layer shock interactions are not occurring in the flow. Even then an improvement of the results might be possible if an iteration cycle between Euler and boundary layer calculations is performed.

The results of the Navier-Stokes solution can be considered as good. However, even for such a "simple" geometry there exists a need for a locally refined grid. The results in the separation regions indicate the urgent need for improved turbulence models.

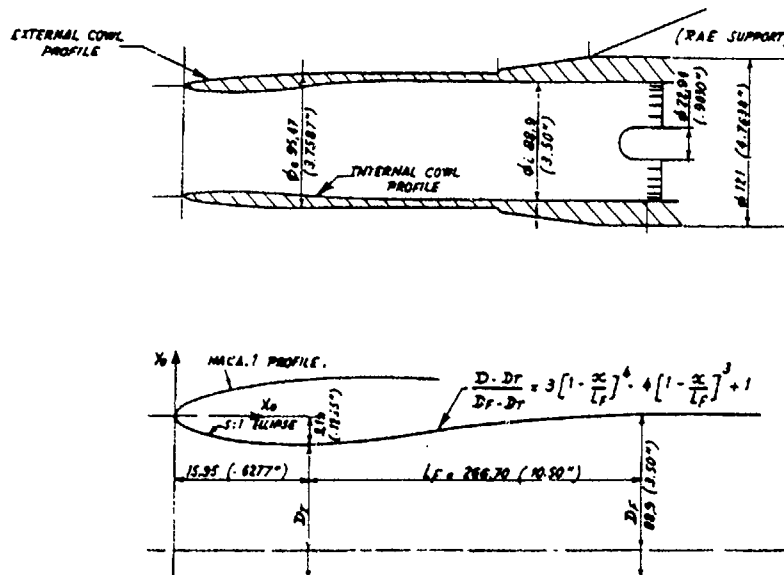


FIG. 3.5.1 INTAKE GEOMETRY FOR TEST CASE 5

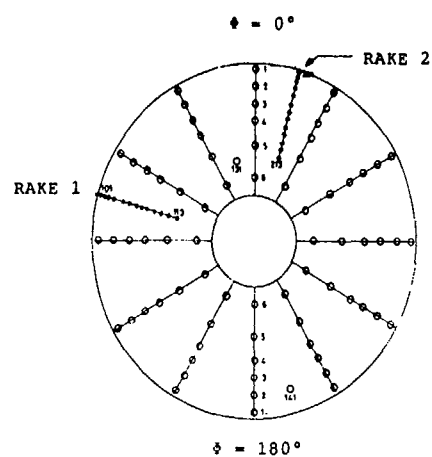
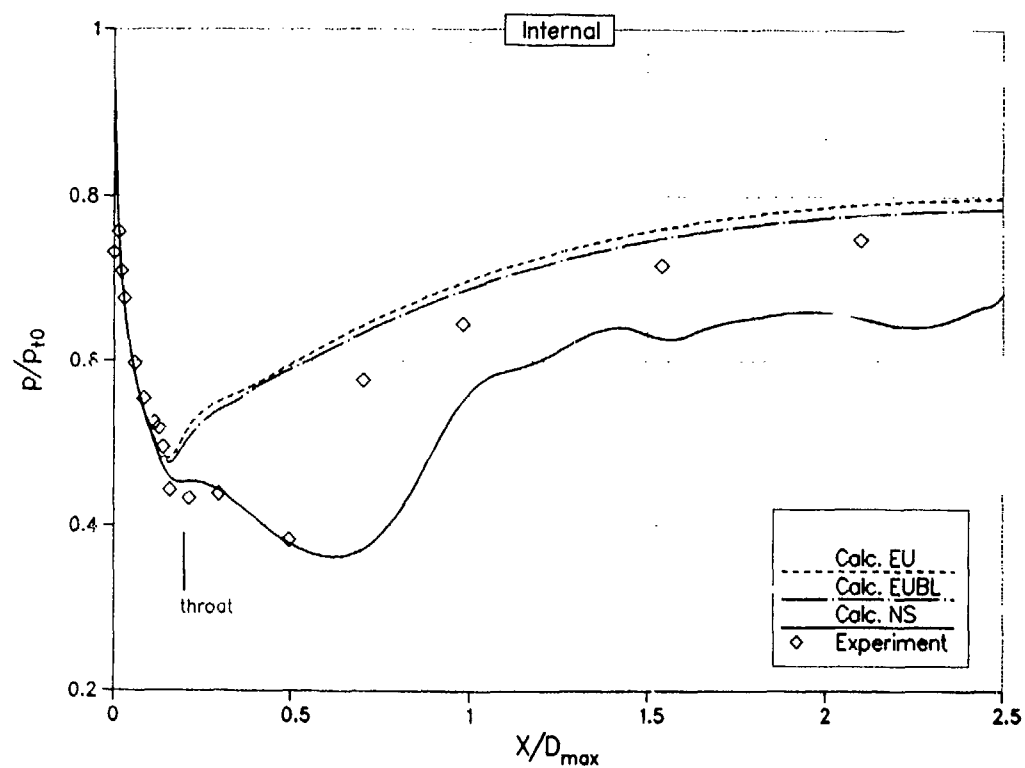
FIG. 3.5.1 CONT. ENGINE FACE RAKES AND DEFINITION OF  $\phi$ 

FIG. 3.5.2 TEST CASE 5.1: STATIC WALL PRESSURE ALONG DUCT - INTERNAL

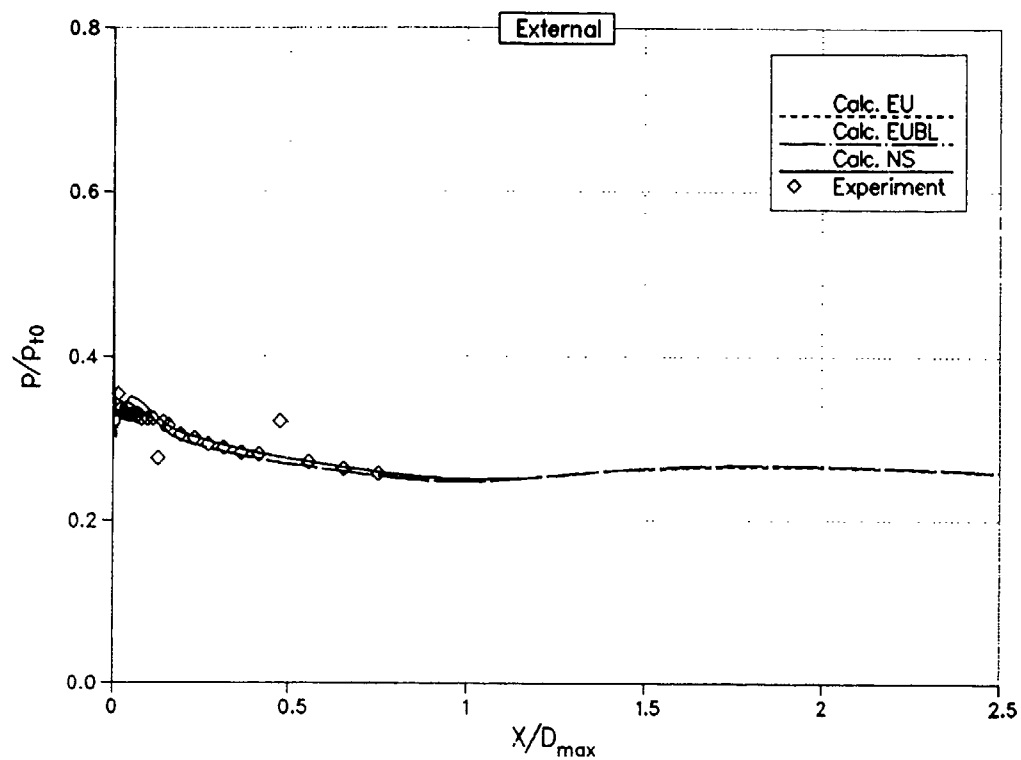


FIG. 3.5.3 TEST CASE 5.1: STATIC WALL PRESSURE - EXTERNAL

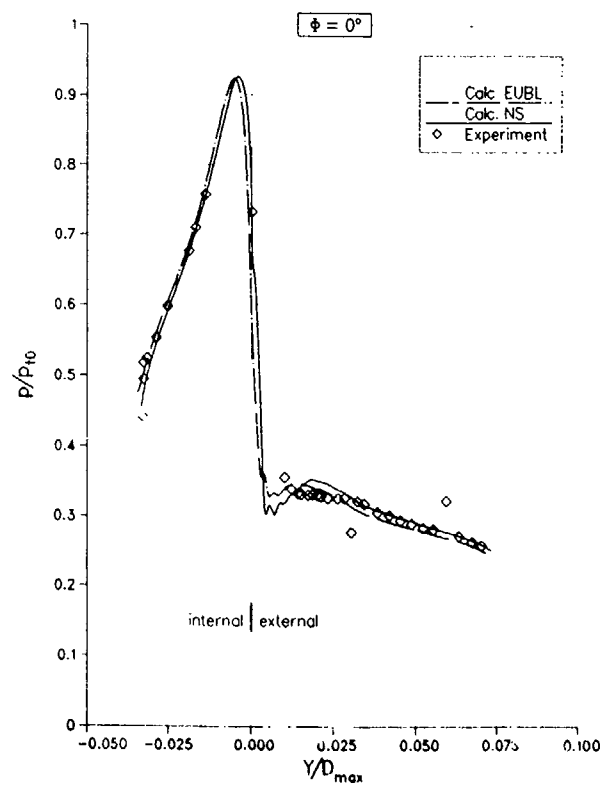


FIG. 3.5.4 TEST CASE 5.1: STATIC PRESSURE ON COWL LIP



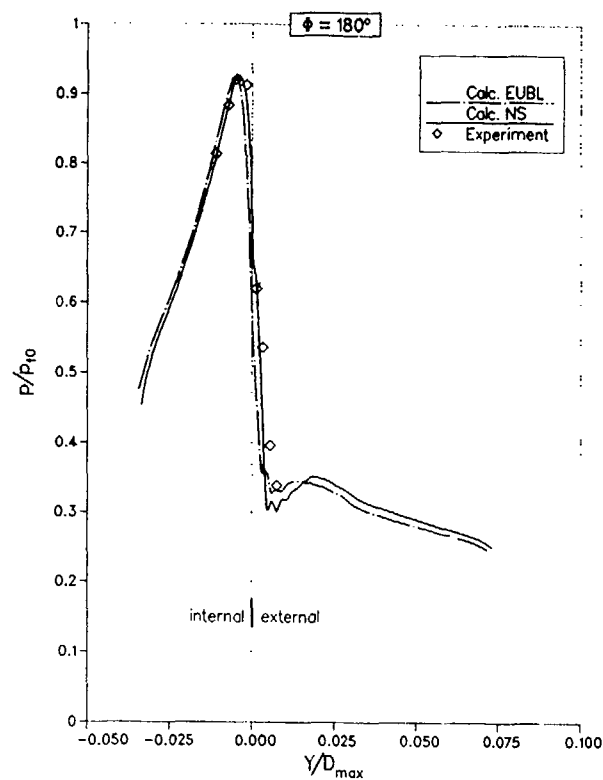
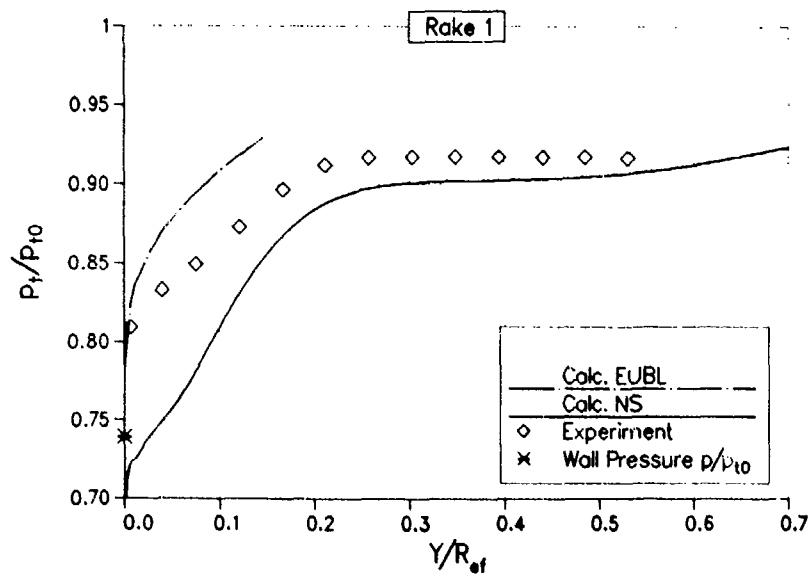


FIG. 3.5.5 TEST CASE 5.1: STATIC PRESSURE ON COWL LIP

FIG. 3.5.6 TEST CASE 5.1: TOTAL PRESSURE IN BOUNDARY LAYER  
AT ENGINE FACE - RAKE 1

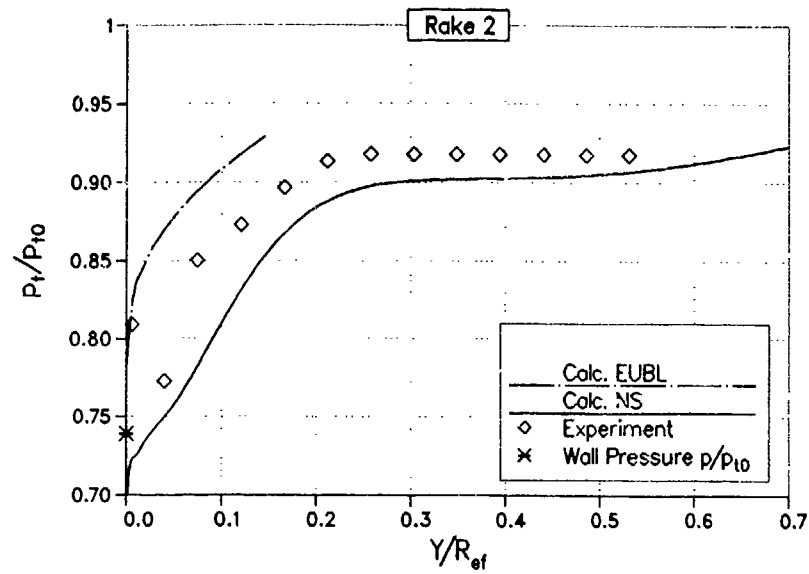


FIG. 3.5.7 TEST CASE 5.1: TOTAL PRESSURE IN BOUNDARY LAYER AT ENGINE FACE - RAKE 2

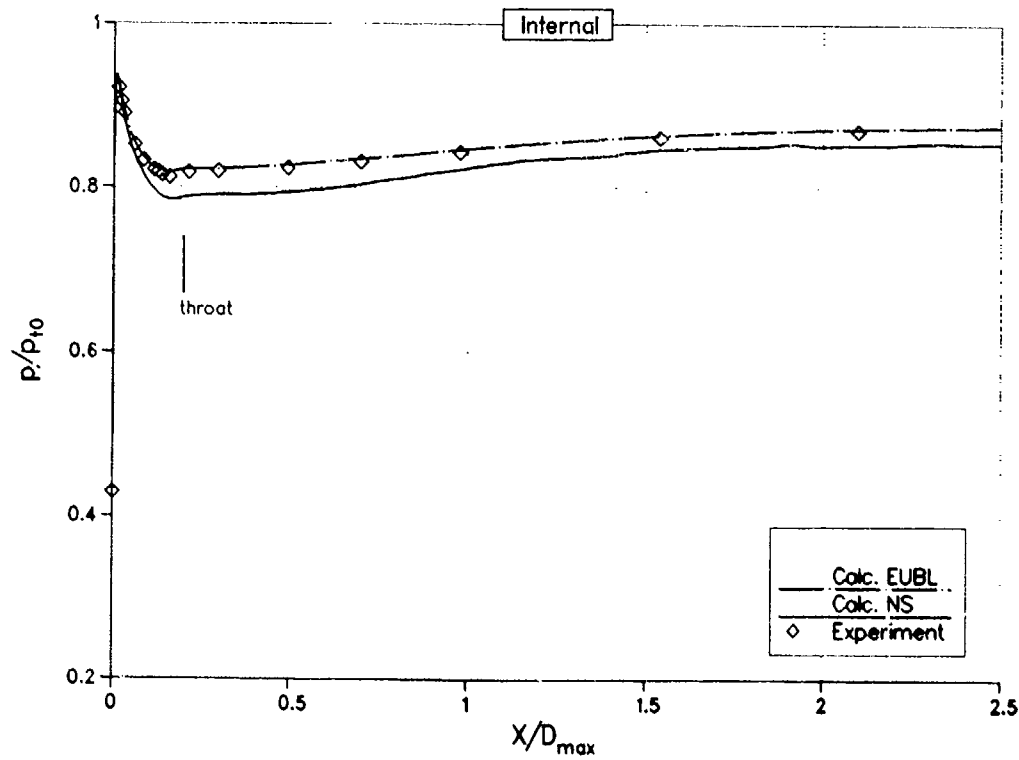


FIG. 3.5.8 TEST CASE 5.2: STATIC WALL PRESSURE ALONG DUCT - INTERNAL

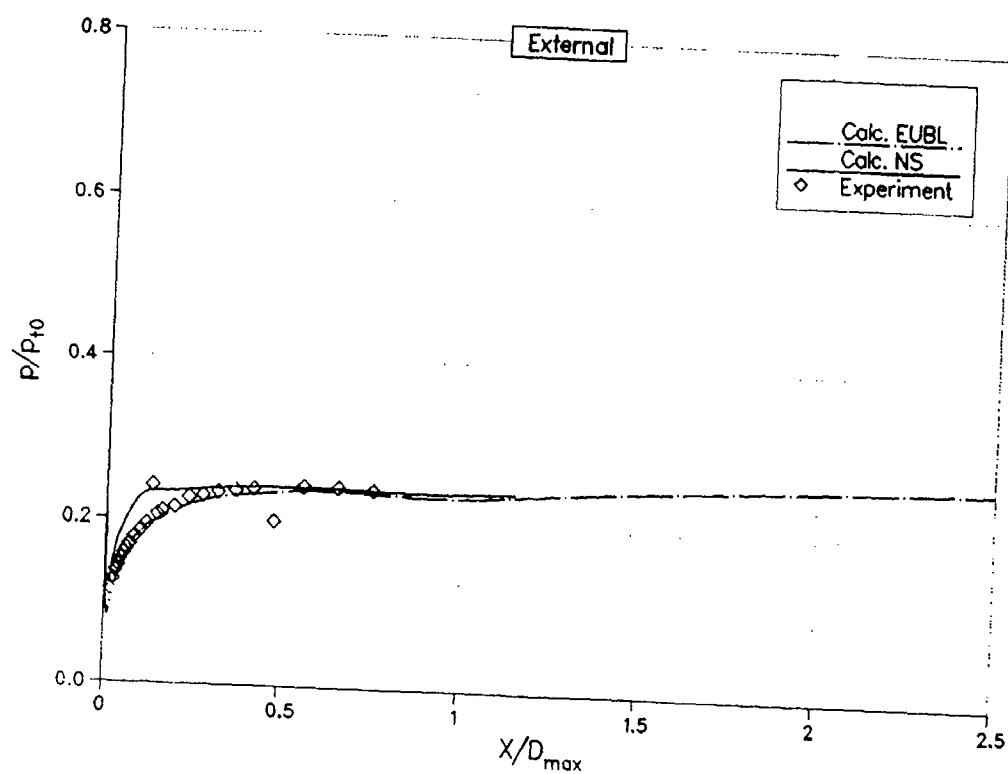


FIG. 3.5.9 TEST CASE 5.2: STATIC WALL PRESSURE - EXTERNAL

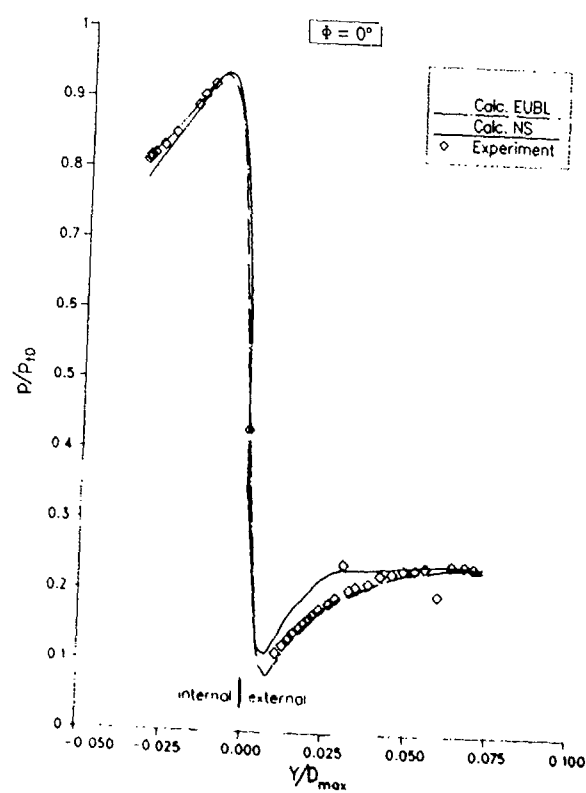


FIG. 3.5.10 TEST CASE 5.2: STATIC PRESSURE ON COWL LIP

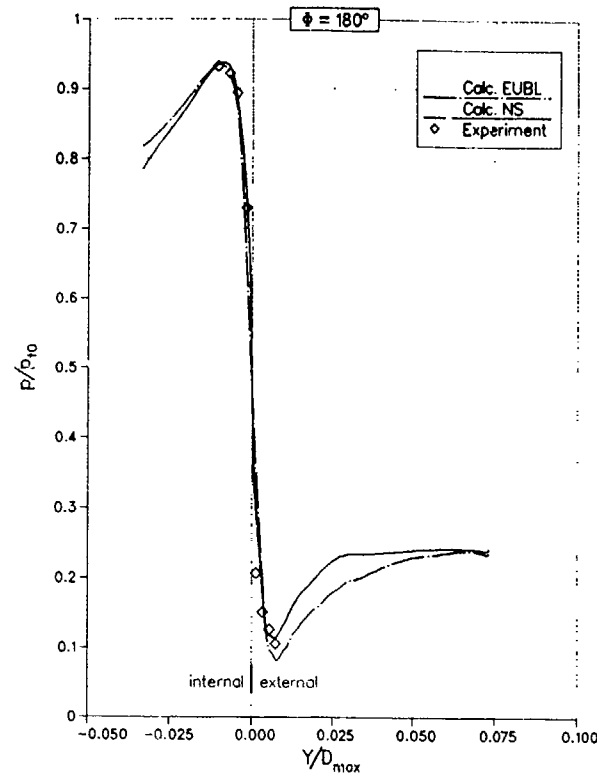
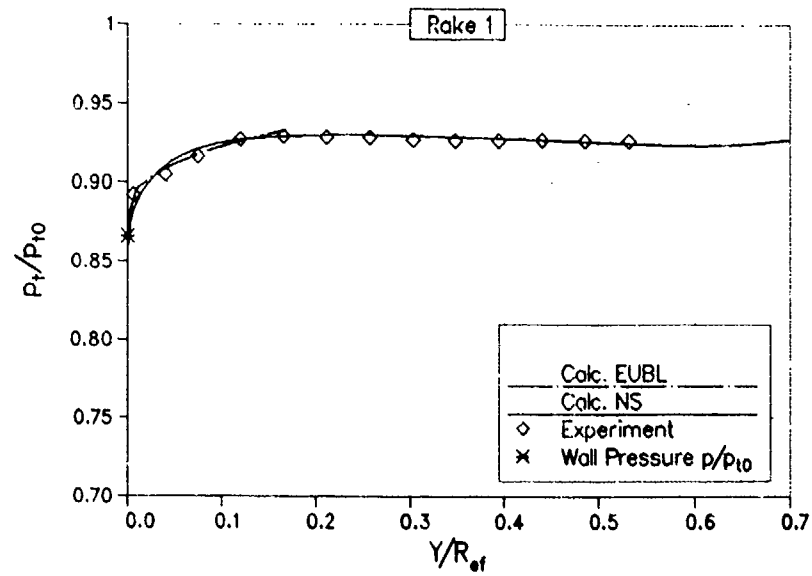


FIG. 3.5.11 TEST CASE 5.2: STATIC PRESSURE ON COWL LIP

FIG. 3.5.12 TEST CASE 5.2: TOTAL PRESSURE IN BOUNDARY LAYER  
AT ENGINE FACE - RAKE 1

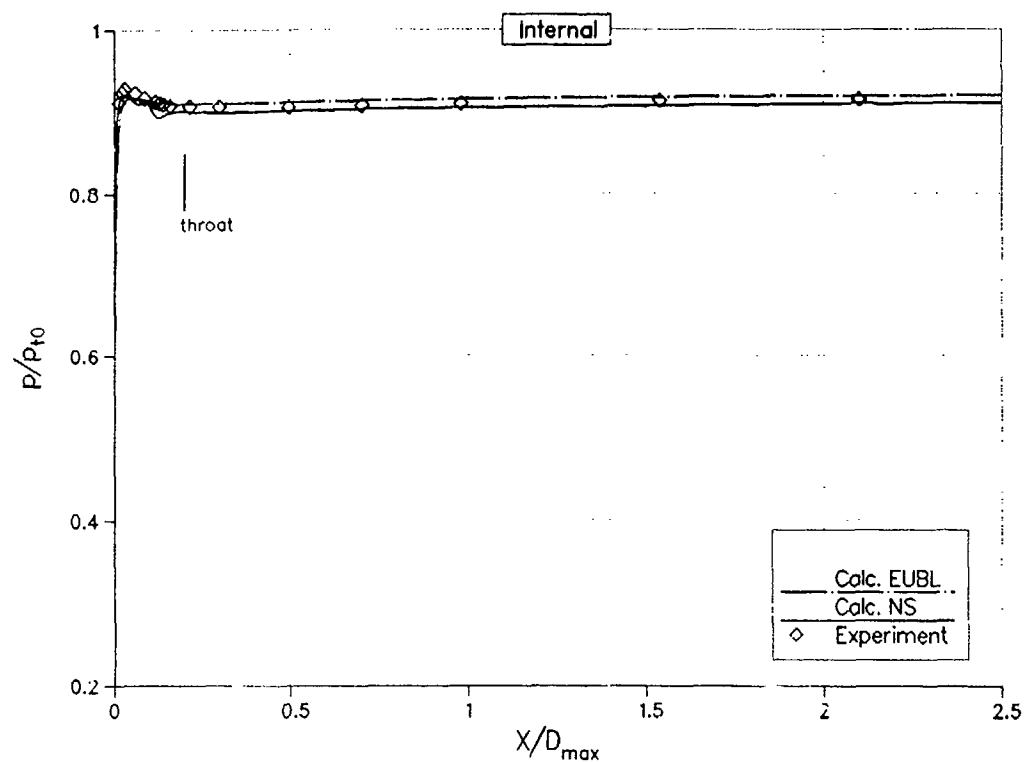


FIG. 3.5.13 TEST CASE 5.3: STATIC WALL PRESSURE ALONG DUCT - INTERNAL

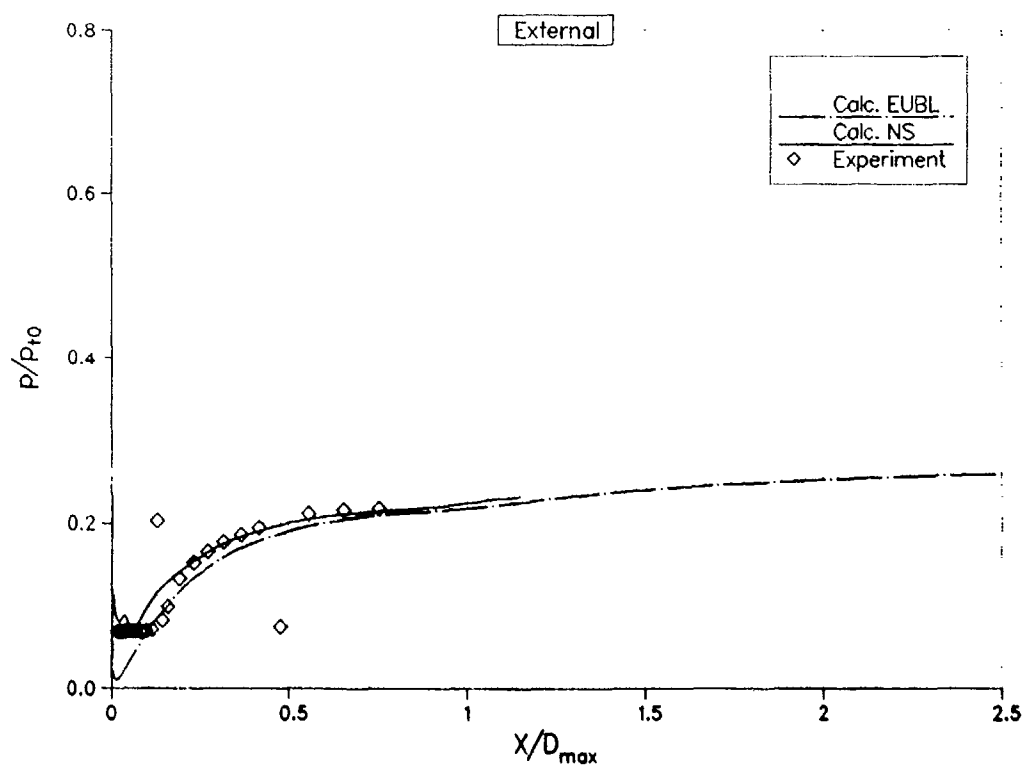


FIG. 3.5.14 TEST CASE 5.3: STATIC WALL PRESSURE - EXTERNAL

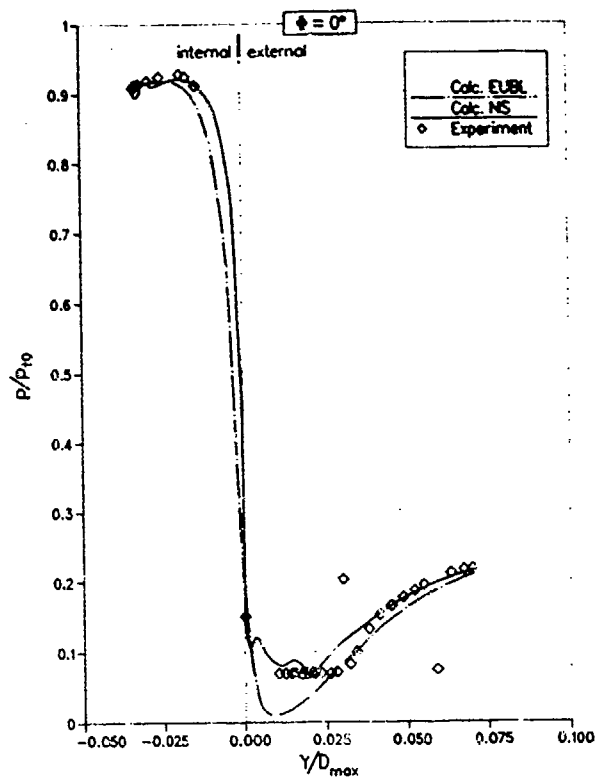


FIG. 3.5.15 TEST CASE 5.3:  
STATIC PRESSURE ON COWL LIP

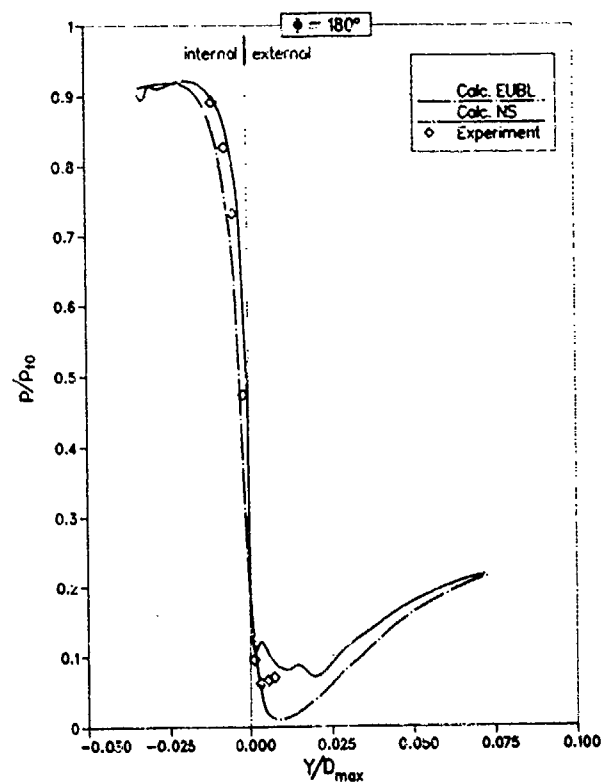


FIG. 3.5.16 TEST CASE 5.3:  
STATIC PRESSURE ON COWL LIP

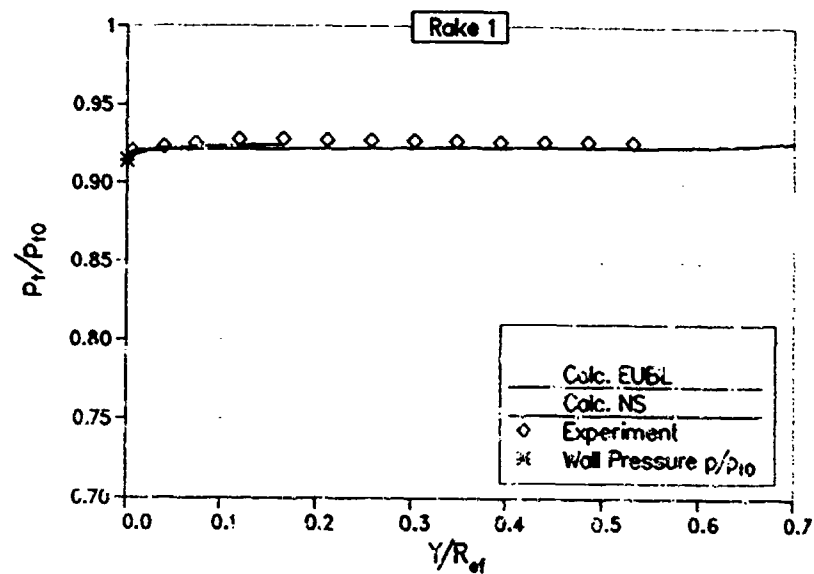


FIG. 3.5.17 TEST CASE 5.3: TOTAL PRESSURE IN BOUNDARY LAYER  
AT ENGINE FACE - RAKE 1

### 3.3.6 Test Case 6 - 2D Hypersonic Intake

#### 3.3.6.1 INTRODUCTION

International interest in hypersonic flight has been recently rejuvenated with the Hotol, Saenger, and National Aerospace Plane (NASP) projects spurring research efforts in high speed aerodynamics, propulsion and materials. In the propulsion area, highly integrated, non-conventional propulsion systems offer the greatest promise for sustained air-breathing flight. As described in Section 2.4, a highly integrated efficient intake is a key component of any proposed hypersonic or supersonic cruise vehicle. The intake must conduct high energy external flow into the combustion system as efficiently as possible. Much of the technology base for this effort depends on the progress in CFD for supersonic and hypersonic flows. Several factors affecting the accuracy of hypersonic intake calculations will be addressed in Test Case 6 by comparing the results of flow calculations with experimental results for the supersonic portion of a hypersonic intake system.

Hypersonic flows are characterized by high Mach numbers in the inviscid regions, high flow gradients in the vicinity of shock waves, and thick, heated boundary layers. To accurately model the flow in the high gradients near shocks, one must typically resolve these features computationally with large numbers of mesh points. Most flow calculations in this regime encounter some degree of post-shock numerical oscillations, which can be minimized either through some form of artificial viscosity, upwind differencing techniques, or increased grid resolution. To accurately model high temperature flows, one needs to model the real-gas effects. This model can take several forms from the simplest specific heats as a function of temperature to the more complex chemical kinetic models. To accurately model the thick boundary layers present in hypersonic flows, one may need to consider a variety of turbulence and transition models.

#### 3.3.6.2 PROBLEM DESCRIPTION

The hypersonic intake to be calculated for Test Case 6 was originally tested at the NASA Ames 3.5 Foot Hypersonic Wind Tunnel at a nominal test Mach number of 7.4, free stream Reynolds number of  $8.86 \times 10^6$  per meter, and total temperature of 811 degrees K, Ref 3.6.1. A schematic drawing of one configuration of the intake, designated P8, is shown in Fig. 3.6.1. The intake is a Mach 7.4

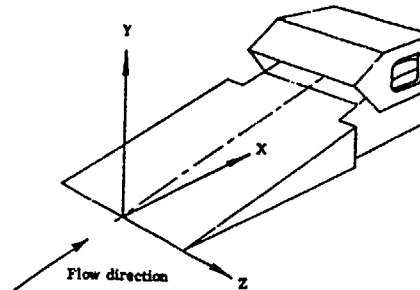


FIG 3.6.1 SCHEMATIC DRAWING OF P8 INTAKE FROM REF 3.6.1.

rectangular mixed-compression design with exiting supersonic flow. The cowl height is 8.89 cm, forebody length is 82.28 cm, overall length is 127 cm, and width is 35.56 cm. On design the nominal 6.5 degree wedge produces an oblique shock which passes just outside the cowl lip and delivers a Mach 6.0 flow at the entrance to the intake. Another shock is generated by the cowl lip and this shock traverses the internal flow passage and is reflected from the ramp surface back onto the cowl. The interior of the cowl is contoured to provide additional distributed compression. In the vicinity of the shock reflection, the flow field was surveyed with a traversing pitot pressure probe to obtain pressure profiles throughout the intake. Static pressures were measured along the ramp and cowl surfaces and some temperature profiles were obtained with the pitot pressure profiles.

While the high throat width to height ratio of this intake makes it possible to model the centerline flow two dimensionally, some comparison of 2D versus 3D modeling of the flow can also be assessed. The three dimensional effects are present in this intake due to the glancing shock/sidewall boundary layer, internally, and the outflow along the ramp surface, externally. In addition, while the free stream Mach number is sufficiently high to assess hypersonic flow calculations, the free stream total temperature is much too low to assess real-gas chemistry models. Ref 3.6.1 has determined that boundary layer transition occurs at  $X=35$  cm. on the wedge and  $X=107$  cm. on the cowl, so some assessment of transition and turbulence models can be made. This intake has



been previously analyzed by several authors, Refs 3.6.2 to 3.6.4, in support of high speed projects.

### 3.3.6.3 CFD TECHNIQUES

This test case was attempted by six different research groups, using seven different codes, as noted in Table 3.2.1 in section 3.2. The analysis techniques included both two and three dimensional Reynolds-Averaged Navier-Stokes (NS), two and three dimensional Parabolized Navier-Stokes (PNS), and two dimensional Euler (EU). The NS analysis was performed by five different groups using different types of flow solvers, and different turbulence models, including a laminar calculation. The group at Aerospatiale used the NS2D code, a centered explicit finite difference scheme with multigrid accelerator and an algebraic turbulence model by Michel. This solution is designated (ANS2) and they have not submitted total temperature profiles for comparison with experiment. Dornier has submitted a laminar three dimensional NS, designated (LNS3), and a turbulent three dimensional NS calculation, designated (DNS3). The General Dynamics group used the FALCON code, a finite volume, multi-block solver with Roe's flux difference splitting and a Baldwin-Lomax turbulence model. This group performed both two dimensional and three dimensional calculations, designated (GNS2) and (GNS3) respectively. The group at Messerschmitt-Boelkow-Blohm performed a two dimensional NS analysis using the NSFLEX code, a finite-volume, flux-extrapolation code, designated (MNS2), with a Baldwin-Lomax turbulence model. The Sverdrup group used the PARC code, a Beam-Warming ADI solver with Baldwin-Lomax turbulence model and designated (SNS2). The PNS analysis was performed at NASA-Lewis using the PEPSES code, a Briley-McDonald LBI solver with a McDonald-Camarata mixing length turbulence model. This group also performed both two dimensional and three dimensional calculations designated (PNS2) and (PNS3) respectively. The group at Aerospatiale also analyzed this intake using the FLU3M multi-block Euler solver. Only intake static pressure comparisons are possible with this analysis, designated (EU). Details of the various analyses are to be found in the microfiche supplement of this report.

### 3.3.6.4 RESULTS

#### Static Pressure Distributions

Detailed comparison of computed and experimental results for all requested

conditions are given in Appendix 3.3.6. We will now consider a few representative results from this larger group. Figs. 3.6.2 and 3.6.3 shows a comparison of the computed and experimental static pressure distributions on the ramp and cowl of the intake. Experimental data is shown by the filled symbols, all three dimensional calculations are shown by the symbolized lines, and all two dimensional calculations are given by plane, unsymbolized lines. The static pressures are all measured downstream of the intake cowl lip. Considering Fig. 3.6.2, the distribution on the ramp from the experimental data, and moving from left to right, we see that the pressure increases sharply at the location where the shock generated by the cowl strikes and reflects from the ramp surface, near  $X=6.2$ . The internal portion of the cowl has been contoured to produce a

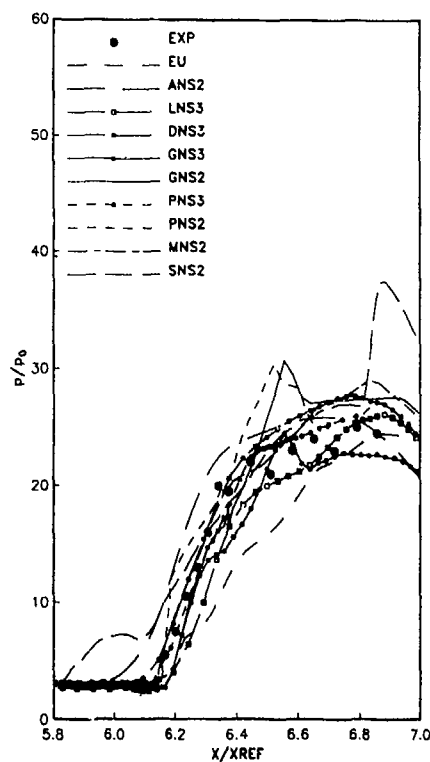


FIG 3.6.2 COMPARISON OF CFD AND EXPERIMENTAL RAMP STATIC PRESSURE DISTRIBUTION.

distributed compression near the shoulder of the intake. Because of this contouring and the interaction of the shock with a thick boundary layer, the pressure rise is spread from near  $X=6.2$  to  $X=6.4$ . Near  $X=6.4$  the flow turns over the shoulder of the intake and the pressure increases much more slowly with distance. Considering the CFD analyses, there appears to be a great deal of scatter about the experimental results. In general, the three dimensional computations more closely match the experimental results than the two dimensional calculations which would imply that three dimensional effects are quite important in this speed regime in spite of the high aspect ratio of the intake. The EU analysis has underpredicted the pressure rise, probably because it does not account for the additional compression effects of the cowl boundary layer displacement. The shock location was achieved by setting a virtual origin of the cowl as detailed in the microfiche supplement. The ANS2 analysis has predicted the shock impingement upstream of the experimental location while overpredicting the pressure rise through the shock reflection. The LNS3 analysis has slightly underpredicted the pressure rise and places the shock downstream of its actual location; both effects are consistent with underpredicting the boundary layer thickness. The DNS3 analysis does an excellent job of predicting both the pressure level and the shock location. The G.S analyses are nearly identical up through the early parts of the shock reflection; both predict the shock impingement point slightly downstream of the measured location. The two analyses split following the shock impingement which again indicates possible three dimensional effects present in this reflection. The GNS2 results significantly overpredict the pressure rise through the shock reflection. The MNS2 analysis correctly predicts the shock location and pressure rise, but slightly overpredicts the ramp pressure downstream. The PNS3 code has properly located the shock reflection location and strength while the PNS2 analysis locates the shock impingement correctly, but overpredicts the pressure rise substantially much like the GNS computations. The SNS2 analysis correctly locates the impingement of the cowl shock and closely models the distributed compression. At the shock impingement, this code predicts a small separation bubble, which accounts for the rise in pressure upstream of the impingement point. The experiment gives no indication of such a separation.

Considering the experimental pressure distribution on the cowl, Fig. 3.6.3, and again moving from left to right, the pressure slowly increases due to the internal contouring of the cowl. Near  $X=6.6$ , the pressure decreases due to the expansion from the ramp shoulder striking the cowl and then sharply increases as the cowl shock strikes this surface after being reflected from the ramp. Considering the CFD analyses, we again see substantial scatter from the experimental results and, in general, the three dimensional computations compare better with the experiment than the two dimensional computations. The EU analysis does a good job of predicting the distributed cowl compression, but does not model the impingement of the reflected shock very well. This again could be due to the lack of boundary layers in this analysis and therefore the neglect of displacement effects on the shock location. The ANS2 analysis correctly

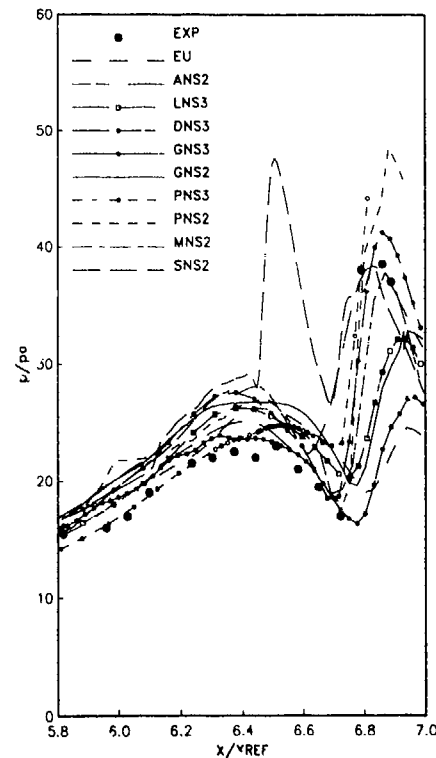


FIG 3.6.3 COMPARISON OF CFD AND EXPERIMENTAL COWL STATIC PRESSURE DISTRIBUTION.

models this feature of the flow, although the shock pressure rise is smeared over some distance. The LNS3 analysis has predicted the shock impingement but not the pressure rise because the laminar boundary layer is much thinner than the turbulent layer and does not properly model displacement effects. The DNS3 correctly predicts the pressure level across the shock, but slightly smears the pressure rise. The GNS analyses properly model the shape of the distributed compression and expansion, but predict the shock impingement downstream of the measured location which is entirely consistent with their ramp pressure distributions. The PNS analysis is able to correctly model the early pressure increase three-dimensionally and gets the slope, though not the level, two-dimensionally. The PNS2 analysis better models the expansion impingement, probably due to better grid resolution in this area. Both two and three dimensional analyses properly predict the reflected shock location, yet both overpredict its strength. The MNS2 analysis correctly models the reflected shock pressure levels, but smears the pressure rise relative to the data. The SNS2 code results closely track the PNS2 results and slightly overpredicts pressures in the distributed compression region. The spike near  $X=6.6$  is probably the result of an additional shock set up by the computed separation on the ramp. This analysis also correctly locates the reflected cowl shocks impingement and reflection.

#### Pitot Pressure Profiles

Figs. 3.6.5, 3.6.6, and 3.6.7 show comparison of the CFD and experimentally determined pitot profiles through the intake; there were nine such rakes in the intake. The location of the rakes are noted in Fig. 3.6.4. As before, the experimental data is given by filled symbols, three dimensional computations are given by symbolized lines, and two dimensional computations are given by plane lines. Considering the experimental data of Fig. 3.6.5 at intake station  $X=5.78$ , the lower part of the figure shows the thick boundary layer which has grown on the ramp surface; the thickness is indicated by the location where the curve turns vertical, at  $Y=.075$ . Continuing up the curve, the sharp turn to the right is indicative of the cowl shock location while the gradual rise to the right and up is caused by the distributed compression on the inside of the cowl. Near the top of the curve, it turns

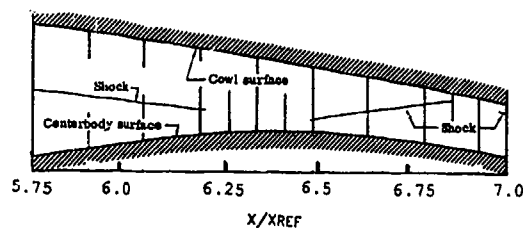


FIG 3.6.4 EXPERIMENTAL RAKE LOCATION WITHIN THE P8 INTAKE.

sharply back to the left which indicates the thickness of the boundary layer on the cowl. Noting the shapes of the boundary layer profiles, we see that the cowl profile is thin and curved which usually indicates a laminar profile. On the ramp, the profile is thick with a nearly linear section which usually indicates a turbulent boundary layer. Considering the CFD results, we again see substantial scatter between the analyses, although all of the CFD results fall to the right of the experimental results in the core flow. All of the analyses predict a similar, though different from experimental, value of pitot pressure upstream of the cowl shock. This is the nearly vertical portion of the profile. The ANS2 analysis has smeared the cowl shock pressure rise into a nearly smooth curve, although it does a good job of modeling the boundary layer thickness on the ramp. The thin laminar boundary layer of the LNS3 analysis is clearly indicated, while the DNS3 more correctly models the boundary layer thickness. The GNS3 analysis is able to correctly model the boundary layer height on the ramp, while the GNS2 results underpredicts this growth. A similar result is seen in the other two dimensional NS calculation. Both PNS analyses slightly overpredict the boundary layer thickness on the ramp. The MNS2 analysis slightly underpredicts the boundary layer thickness as does the SNS2 analysis. The pitot profile of the SNS2 calculation is becoming vertical on the ramp which is indicative of nearly separated flow. The PNS3 analysis has a similar type profile, while the PNS2 profile more closely matches the data. The middle portion of the curve, from  $Y=.13$  to  $Y=.22$ , shows a great deal of scatter between the computations. For the same types of codes, three dimensional calculations better match the data than two dimensional. The

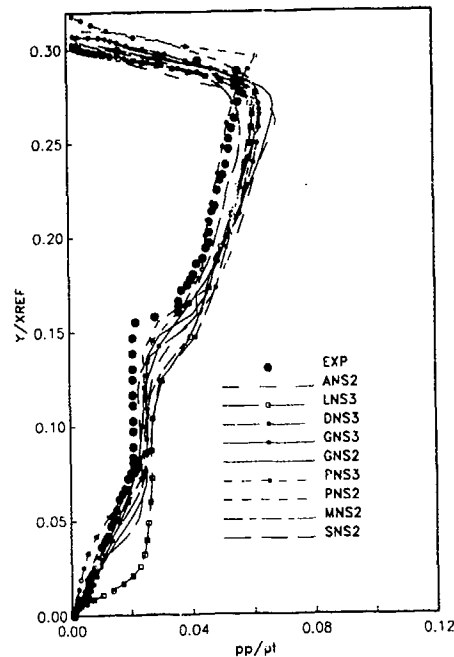


FIG 3.6.5 COMPARISON OF CFD AND EXPERIMENTAL PITOT PRESSURE DISTRIBUTION AT X=5.78.

upper portion of the curve describes the boundary layer on the cowl. In most cases, this boundary layer has been correctly modeled as being much thinner than the ramp boundary layer. The scatter at the upper left hand portion of this curve has several possible causes. Because the lowest portion of all of the curves have been fixed at  $Y=0.0$ , the  $Y$  value at the upper left portion of the curve indicates the computed height of the duct at this location. The vertical scatter at this point can be due to incorrect modeling of the intake geometry. It can also be caused by graphical errors in the post-processing of the computed results. The overall scatter at this location is much more evident in Appendix 3.6.1 at the various rake locations.

The next location to consider is at  $X=6.37$ , Fig. 3.6.6, a station just downstream of the reflection of the cowl shock from the ramp surface. Considering the experimental data, the lower portion of the figure shows that the ramp boundary layer has been compressed by the reflecting shock wave and is somewhat thinner than at the previous station. The reflected shock is just emerging from the boundary layer near  $Y=.025$  as shown by the break in the curve. The effect of the distributed

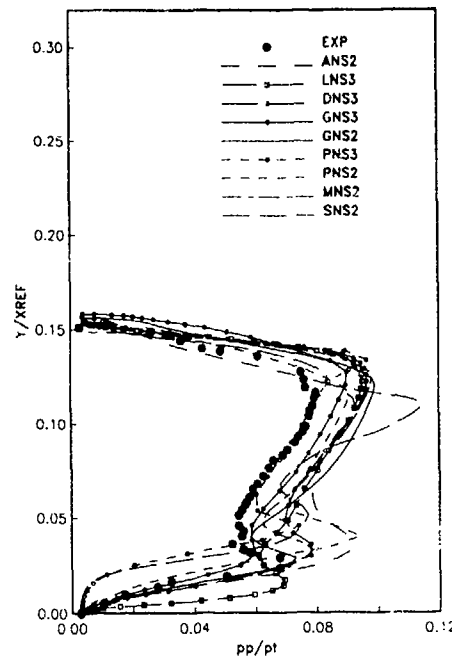


FIG 3.6.6 COMPARISON OF CFD AND EXPERIMENTAL PITOT PRESSURE DISTRIBUTION AT X=6.37.

cowl compression is seen in the sloping section of the curve from  $Y=.05$  to  $.125$ , while the cowl boundary layer is seen at the top. Considering the CFD results, we see again a great deal of scatter in the results with three dimensional calculations closer to the data than two dimensional calculations for the same code. The SNS2 and PNS3 analyses are predicting profiles near the ramp which indicate a flow separation which is not seen in the experimental results. The LNS3 analysis continues to underpredict the boundary layer thickness and the shock reflection because the analysis is laminar. The other computations do a reasonable job of predicting the shape of the boundary layer profile near the ramp. All of the codes pick up the emerging reflected shock wave, though each of the codes model this feature differently. The GNS2 analysis most closely predicts both the magnitude and location of this feature. All of the other analyses, except the LNS3, predict the break in the curve farther away from the ramp than the experiment. This would correspond to predicting the shock above its true location relative to the ramp. The various locations of the break in the curve between the analyses indicate the differences in the ability of these codes to model these features. Most of the codes correctly predict the slope of

the distributed compression region, but all of the analyses fall to the right of the experimental data. The large bulge in the SNS2 analysis is caused by the shock generated by the previously discussed separation on the ramp. The cowl boundary layer profile is fairly well modeled by all the codes, although we again see some variations in the height of the profiles at the extreme left part of the curve.

Moving now to Fig. 3.6.7, at  $X=6.65$ , a comparison is made near the end of the measuring stations. At this location, the reflected cowl shock is just striking the cowl boundary layer, as shown in the break in the experimental data near  $Y=0.10$ . The lower portion of the curve shows that the ramp boundary layer has been compressed thinner than

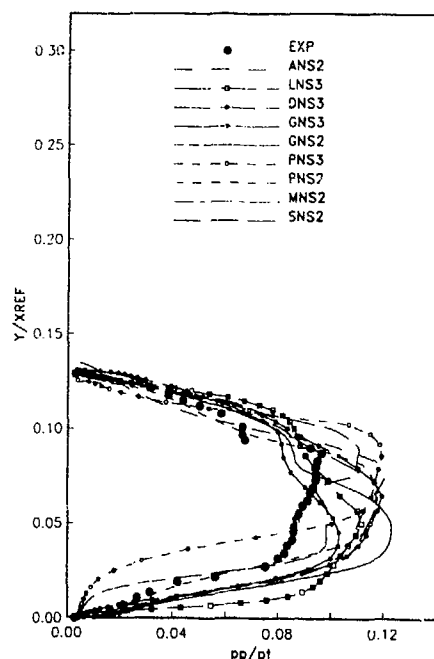


FIG 3.6.7 COMPARISON OF CFD AND EXPERIMENTAL PITOT PRESSURE DISTRIBUTION AT  $X=6.65$ .

at the previous station. The distributed compression is still evident by the sloping central portion of the experimental data. Considering the CFD results, we again see a great amount of scatter between the various computations. The LNS3 analysis continues to underpredict the ramp boundary layer thickness as previously discussed. The PNS3 and SNS2 results continue to indicate a separation on the

ramp which is not seen in either the experiment or the other analyses. All of the other codes overpredict the boundary layer pitot profile on the ramp, yet do a reasonable job of predicting the boundary layer thickness. Most of the analyses are still overpredicting the central portions of the curve. There is quite a bit of scatter in the predicted cowl boundary layer profiles because of the interaction of this profile with the incoming shock wave. As seen in the previous figure, each of the codes was predicting the shock wave in a slightly different location and with a different strength. As the shock hits the cowl, these variations are magnified in the profiles. In this type of intake, small variations at the beginning of an analysis can become larger variations as one proceeds downstream.

#### Total Temperature Profiles

Figs. 3.6.8, and 3.6.9 show comparison of the CFD and experimentally determined total temperature profiles through the intake. There were nine such rakes in the intake located at the same location as the pitot profiles. As before, the experimental data is given by filled symbols, three dimensional analyses by symbolized lines, and two dimensional analyses by plane lines. Considering

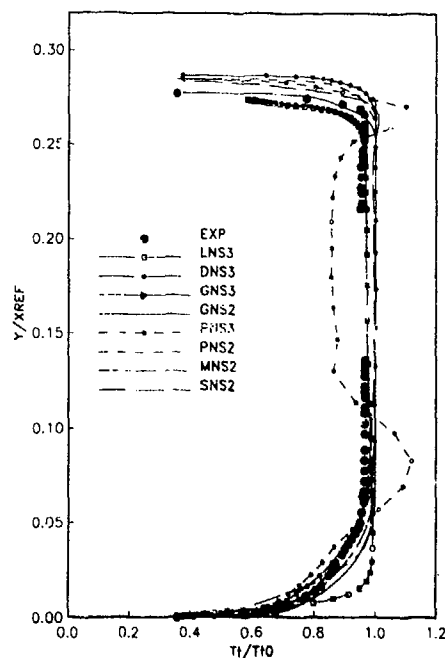


FIG 3.6.8 COMPARISON OF CFD AND EXPERIMENTAL TOTAL TEMPERATURE DISTRIBUTION AT  $X=5.78$ .

the experimental data in Fig. 3.6.8 at intake station  $X=5.78$ , we see that thermal boundary layers are generated on the ramp and cowl and that the central inviscid portion of the flow field has maintained a constant total temperature. Reference 3.6.1 indicates that this temperature ratio is less than one because it was not corrected due to uncertainties in other measurements. The corrected value should be one. Considering the CFD results, all of the analyses except the PNS3 and LNS3 have done an excellent job modeling this flow field. In general, the three dimensional analyses overpredict the thermal boundary layer thickness while the two dimensional results underpredict the thermal boundary layer thickness on the ramp. By the end of the intake duct, at  $X=6.65$  in Fig 3.6.9, the situation has changed somewhat. The PNS3 analysis still has some major problems, but most of the other analyses, two and three dimensional, are underpredicting the thermal boundary layer on the ramp. Along the cowl surface, the codes once again underpredict the thermal boundary layer thickness relative to the experiment.

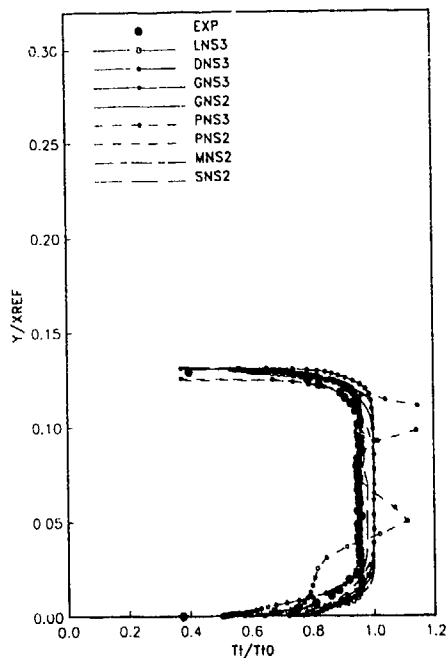


FIG 3.6.9 COMPARISON OF CFD AND EXPERIMENTAL TOTAL TEMPERATURE DISTRIBUTION AT  $X=6.65$ .

#### CFD Flow Field

In the previous sections we have noted evidence which suggests that three dimensional effects are present in this intake. While the experimental data was too sparse to quantify three dimensional effects, the full three dimensional CFD results gives some indication of the extent of these effects. Fig. 3.6.10 shows pitot pressure contour through the intake from the GNS3 analysis. The location of each plane is noted at the top of the figure by a letter, with the corresponding letter written next to the pitot contour plot. The contour plots are shown for half of the duct; a plane of symmetry exists along the left edge of each plot. The collection of horizontal lines at the top and bottom denotes the boundary layer on the ramp and cowl. The horizontal lines in the middle of each plot are indicative of the cowl shock wave, which is reflecting from the ramp back onto the cowl. To the right is the intake sidewall with its associated boundary layer. Because of shock/boundary layer interactions, such as the one studied in test case 2, low pressure regions develop in the corners of the intake. The effect of this corner phenomenon is seen to extend nearly a quarter of the distance across duct from the sidewall. It is this corner interaction which introduces the three dimensional effects into the intake, based on the CFD analysis.

#### 3.3.6.5 CONCLUSIONS

There are several interesting conclusions which can be drawn from a comparison of CFD and experimental results for this test case. First, there was a wide variation in the CFD results, both between different types of analysis and, within the same analysis, between two dimensional and three dimensional calculations. In general, a three dimensional calculation agreed better with the experimental results than a two dimensional calculation using the same code. Second, nearly all of the codes were able to match the experimental temperature profiles, although this result may be misleading. While this intake was designed for hypersonic testing, it was not tested at true flight enthalpies. The ability of the codes to match these wind tunnel results, while encouraging, should not be interpreted as a verification of the codes ability to model flight conditions. This is not the correct test case to assess intake code capability for real gas effects. Third, there is some evidence that the actual intake geometry as presented in the report is

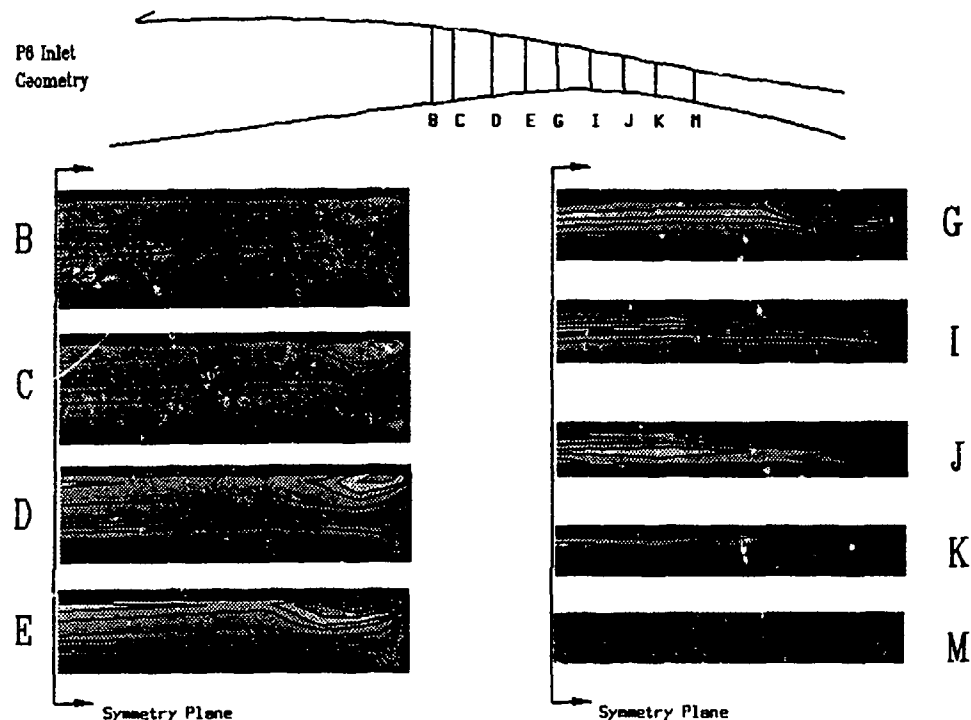


FIG 3.6.10 PITOT PRESSURE  
CONTOURS THROUGH THE P8 INTAKE.

not being modeled computationally. All of the analysis teams were provided with the same information concerning the intake geometry as provided in Ref 3.6.1, yet each modeled this geometry in a slightly different way. For hypersonic flows, even small differences in geometry can produce significant differences in flow properties. It would appear that additional work is required in hypersonic intake applications in the area of geometric specification and flow solver grid generation. Fourth, none of the CFD analyses were able to predict the pitot pressure downstream of the ramp shock, but upstream of the cowl shock. This is the vertical region of Fig. 3.6.5. In all of the calculations of this intake of which the author is aware, including the previously referenced papers, no one has ever matched the experimental data using the stated tunnel conditions of Ref 3.6.1. The many CFD analyses tend to agree with one another, but do not match the experimental data for a parameter which is relatively easy to compute, as evidenced by the results of test case 2. One is then lead to suspect that the conditions stated in the report were different in some way from the

conditions that were actually present in the tunnel. And fifth, for this class of intakes, it would appear that even small variations in the flow field upstream lead to large variations between codes downstream. This is perhaps a restatement of the sensitivity of hypersonic flow fields to small variations in flow parameters, be they geometric, or noise in the solution.

#### 3.3.6.6 REFERENCES

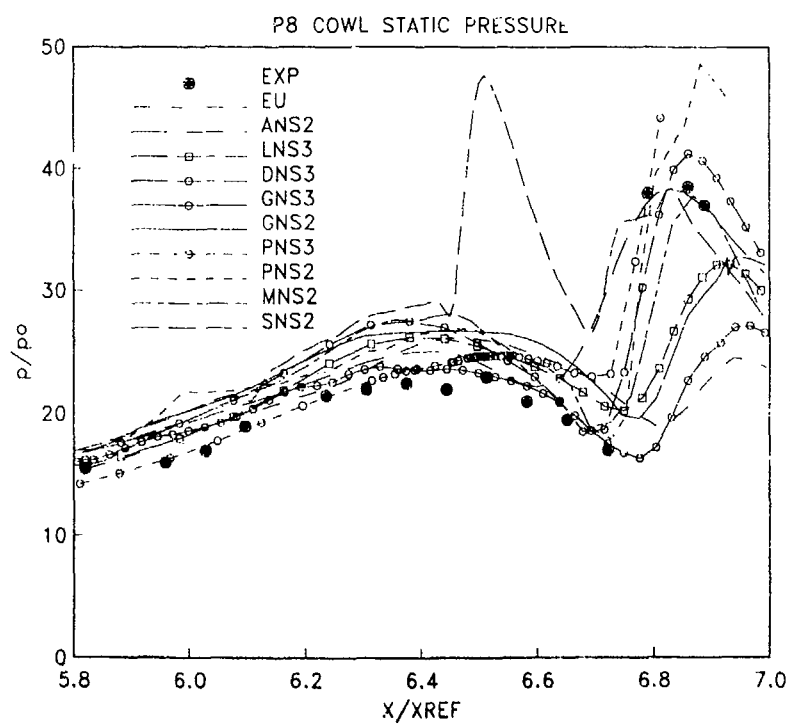
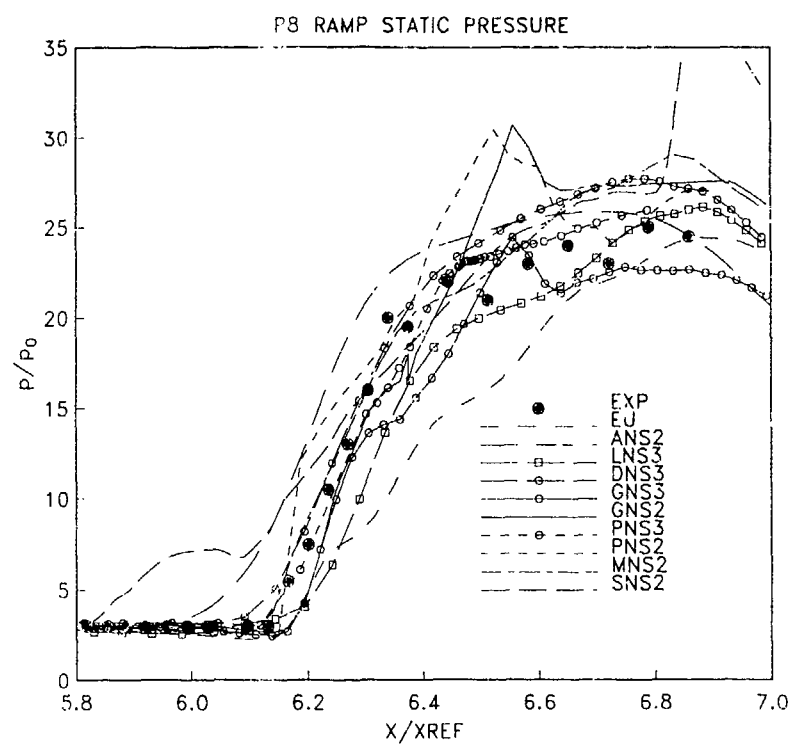
- 3.6.1. Gnos, A.V., Watson, E.C., Seebaugh, W.R., Sanator, R.J., and Decarlo, J.P. "Investigation of Flow Fields within Large-Scale Hypersonic Inlet Models," NASA TN D-7150, April, 1973.
- 3.6.2. Knight, D.D., "Improved Numerical Simulation of High Speed Inlets Using the Navier-Stokes Equations," AIAA Paper No. 80-0383, January 1980.

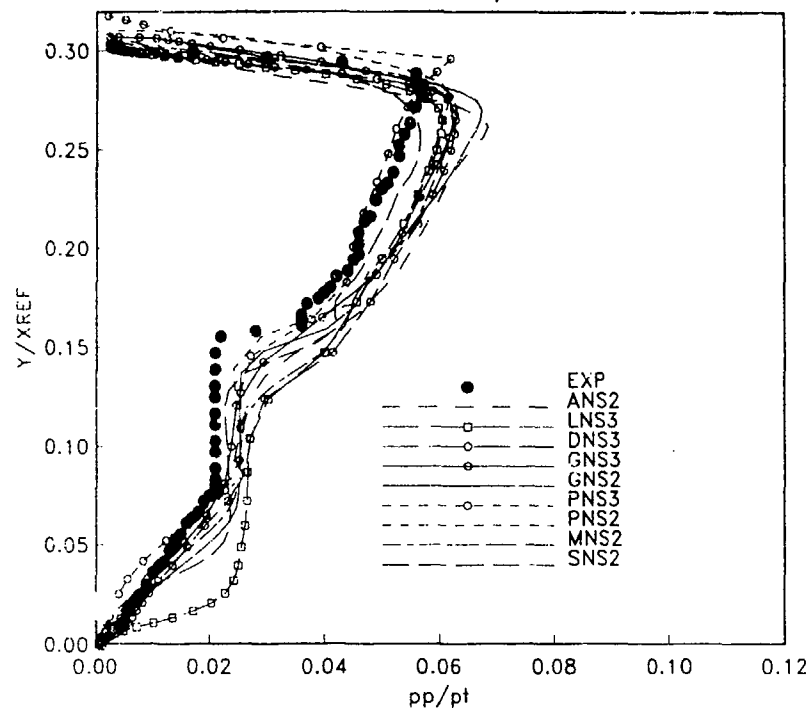
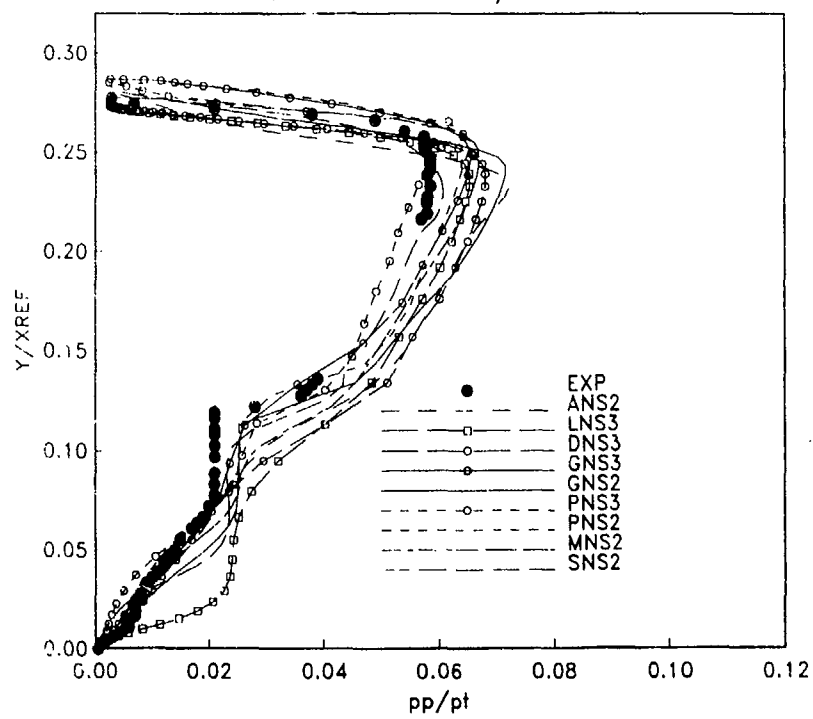
3.6.3. Kunik W.G., Benson, T.J., Ng, W.-F., and Taylor A., "Two- and Three-Dimensional Computations of a Hypersonic Inlet Flow", AIAA Paper No. 87-0283, January 1987.

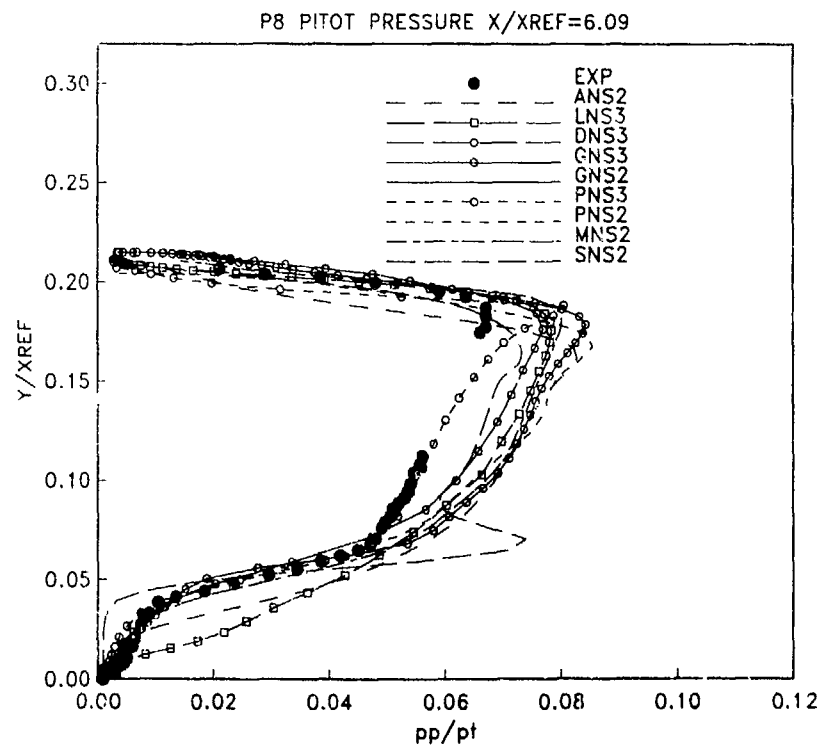
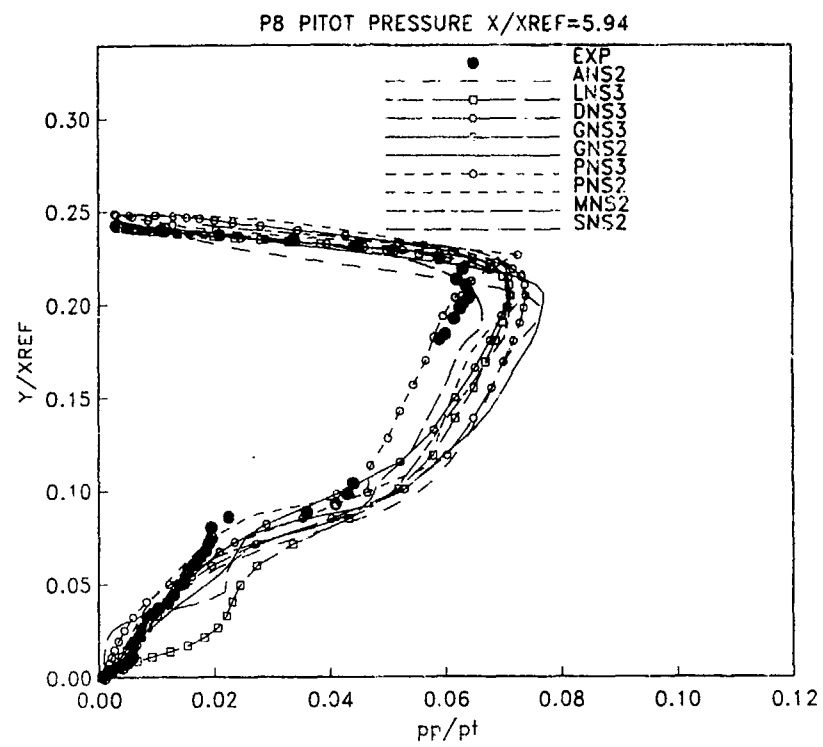
3.6.4. Rudy, D.H., Thomas, J.L., Kumar, A., Gnoffo, P. and Chakravarthy, S.R., "A Comparative Study of Navier-Stokes Codes for High-Speed Flows", NASA CP - 10038, March, 1989.

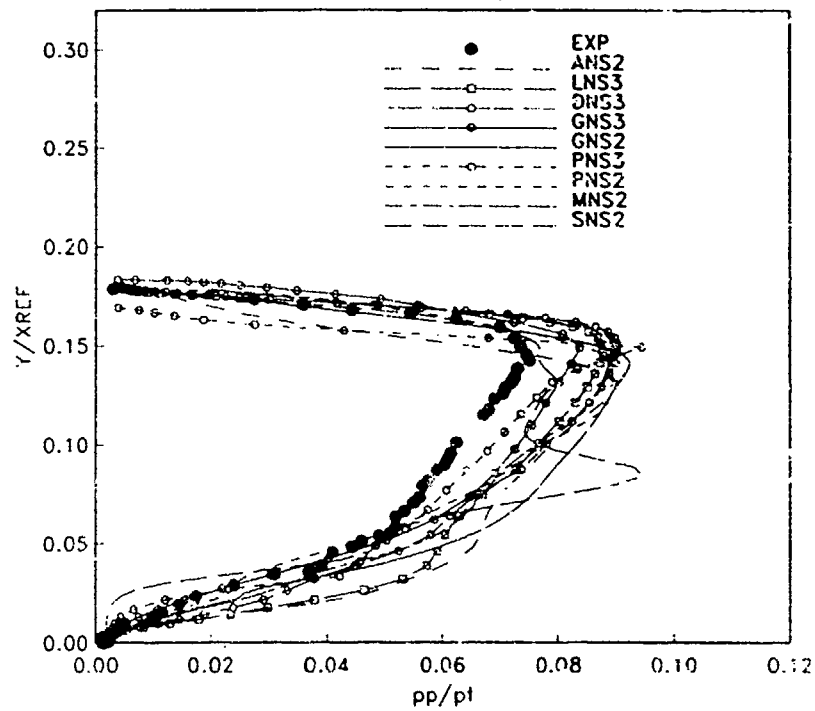
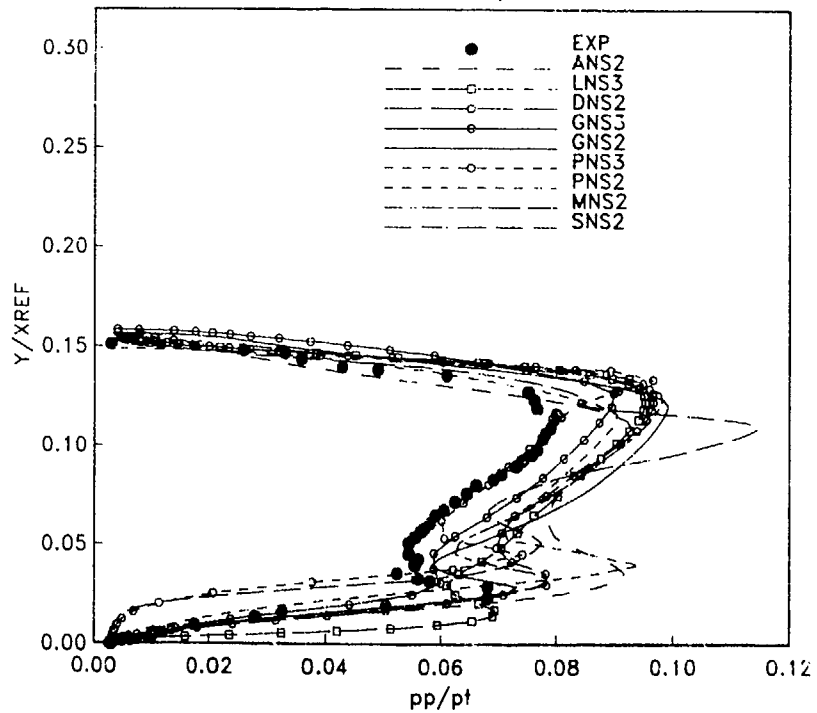


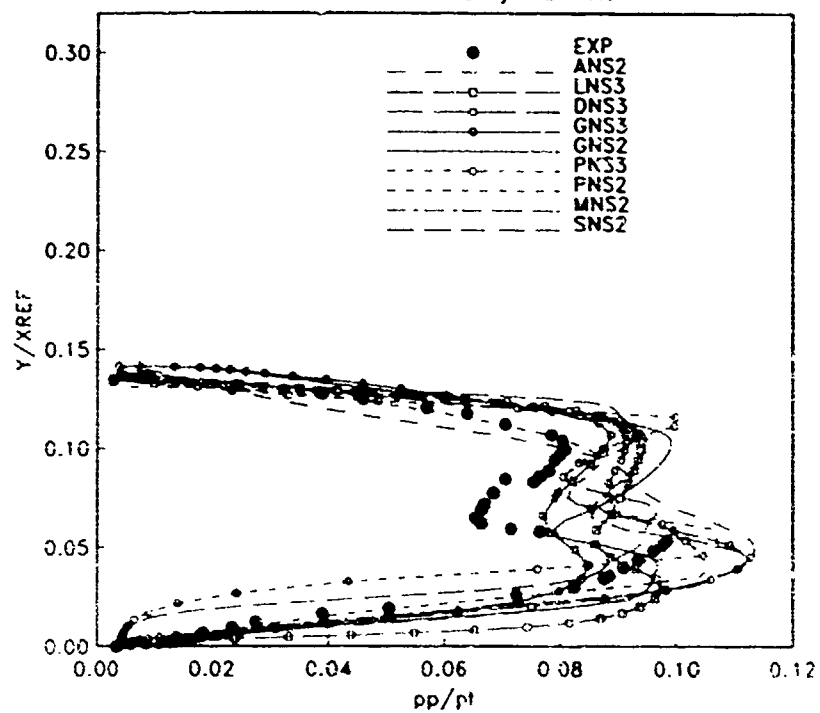
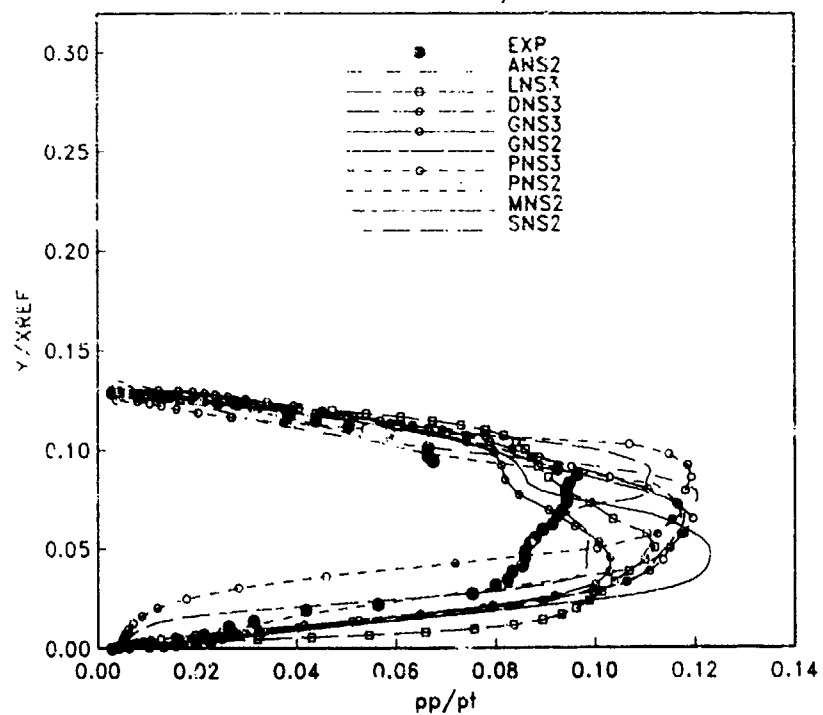
Appendix 3.3.6  
Full Comparison of CFD and Experiment

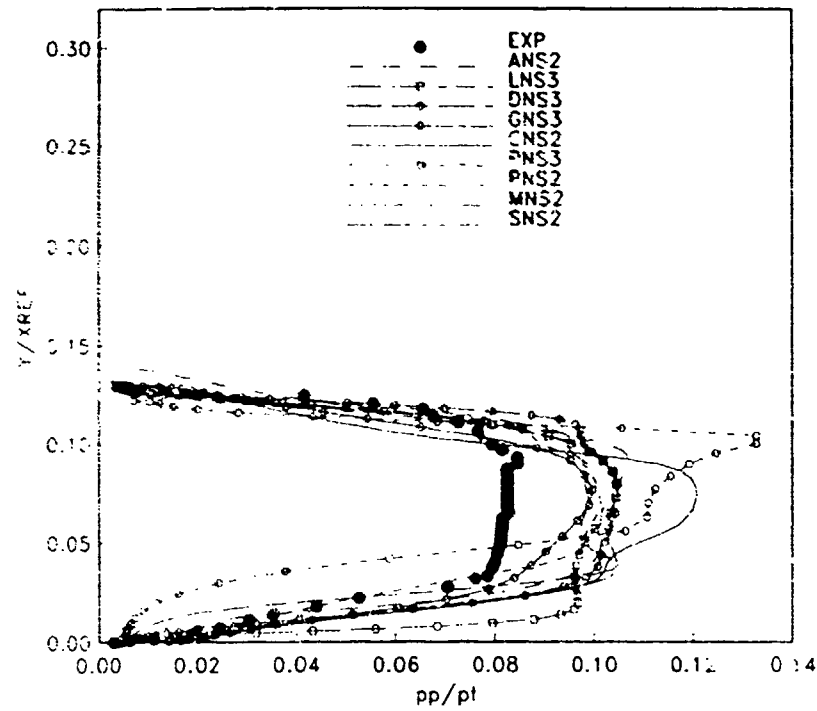
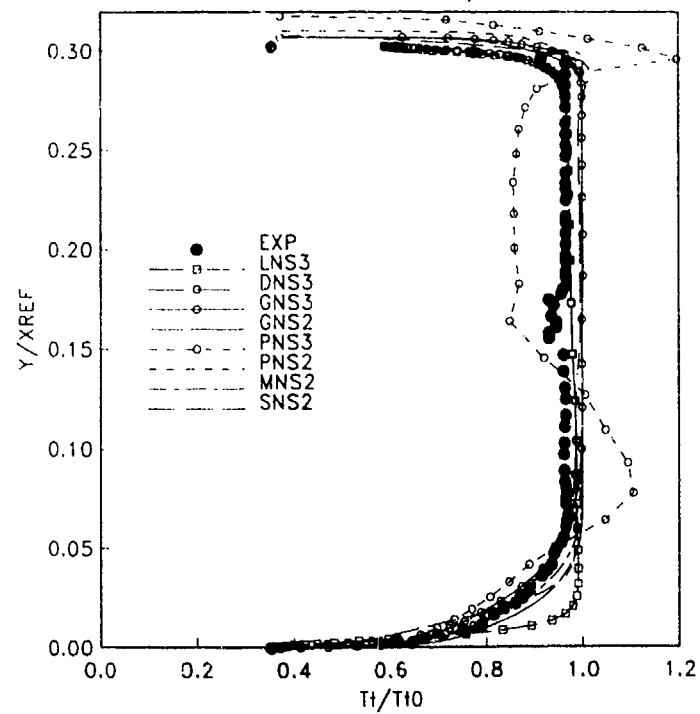


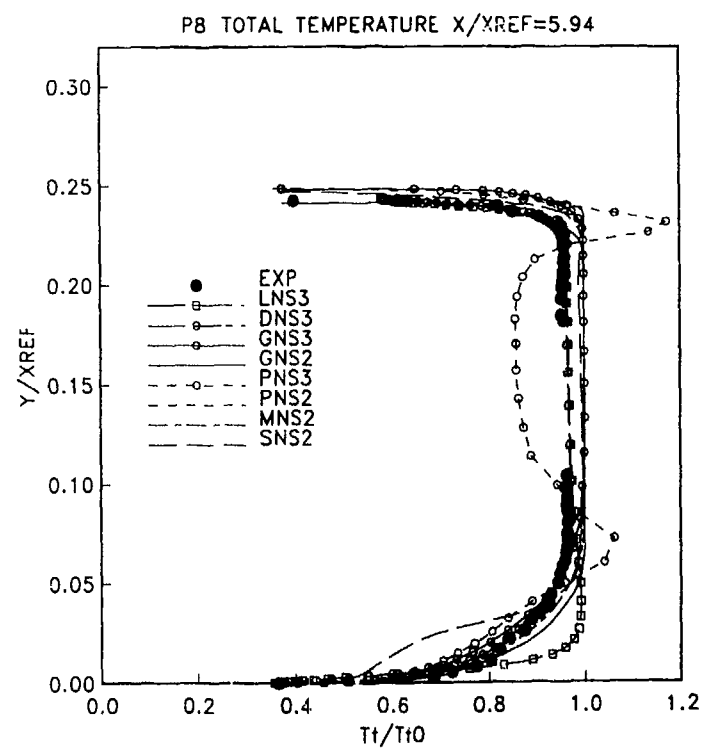
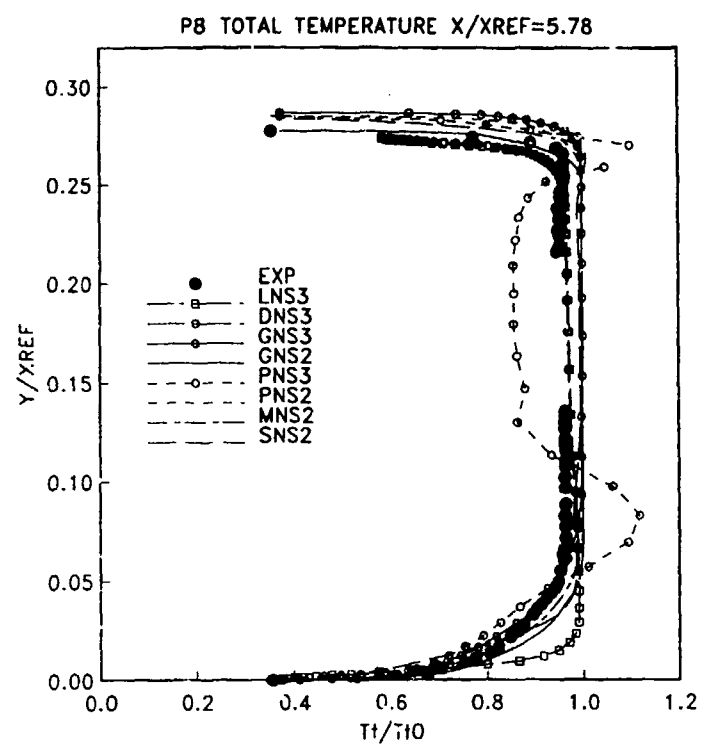
P8 PITOT PRESSURE  $X/X_{REF}=5.67$ P8 PITOT PRESSURE  $X/X_{REF}=5.78$ 

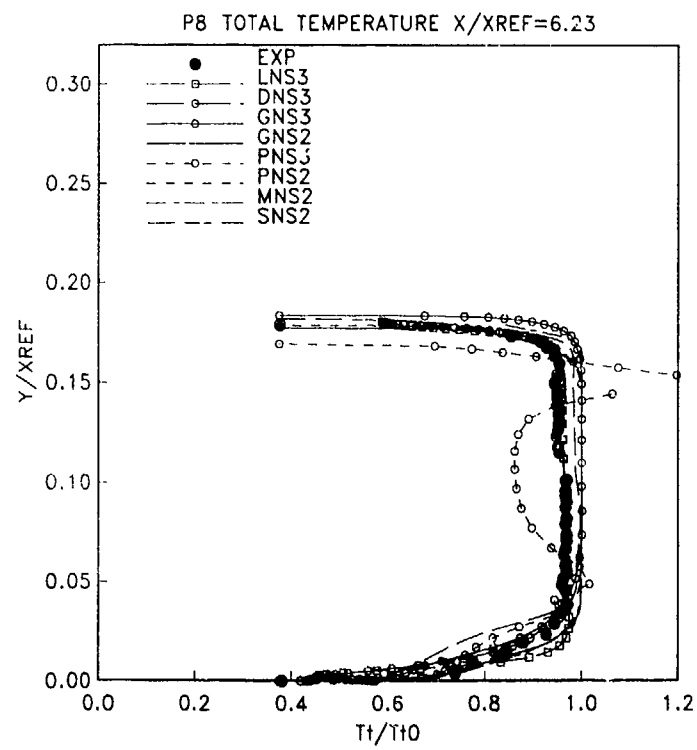
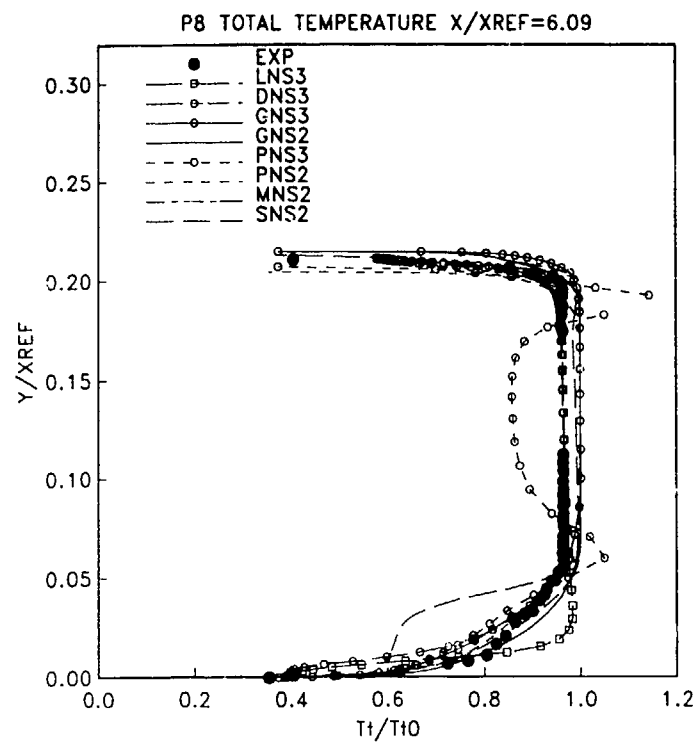


P8 PITOT PRESSURE  $X/X_{REF}=6.23$ P8 PITOT PRESSURE  $X/X_{REF}=6.37$ 

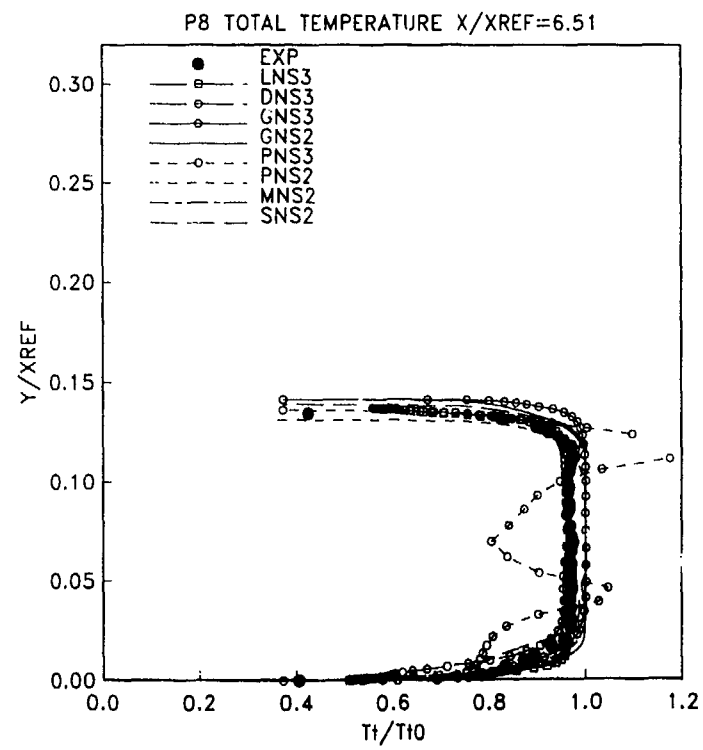
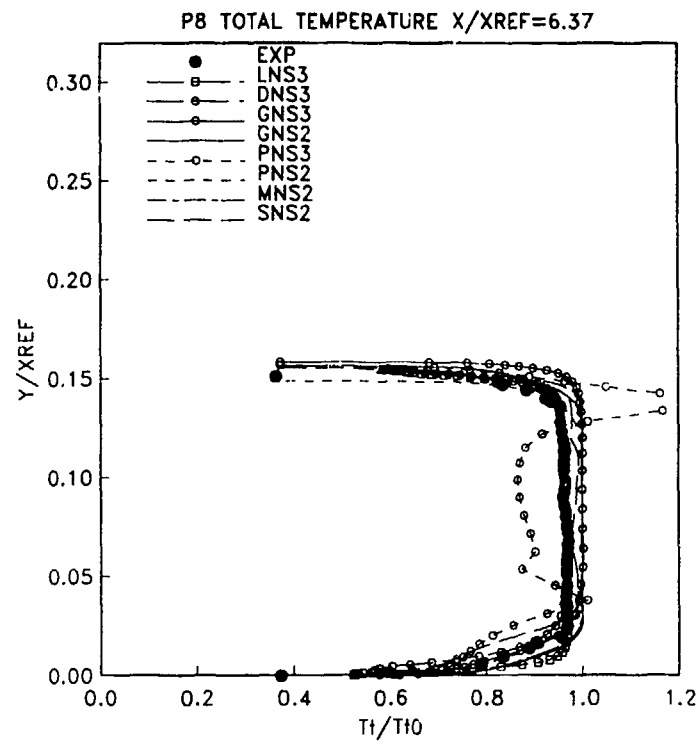
P8 PITOT PRESSURE  $X/X_{REF}=6.51$ P8 PITOT PRESSURE  $X/X_{REF}=6.65$ 

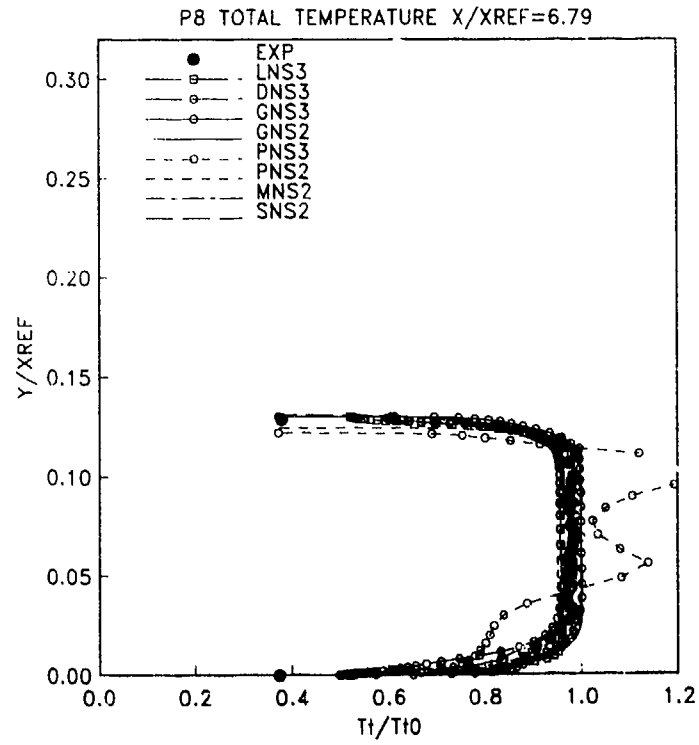
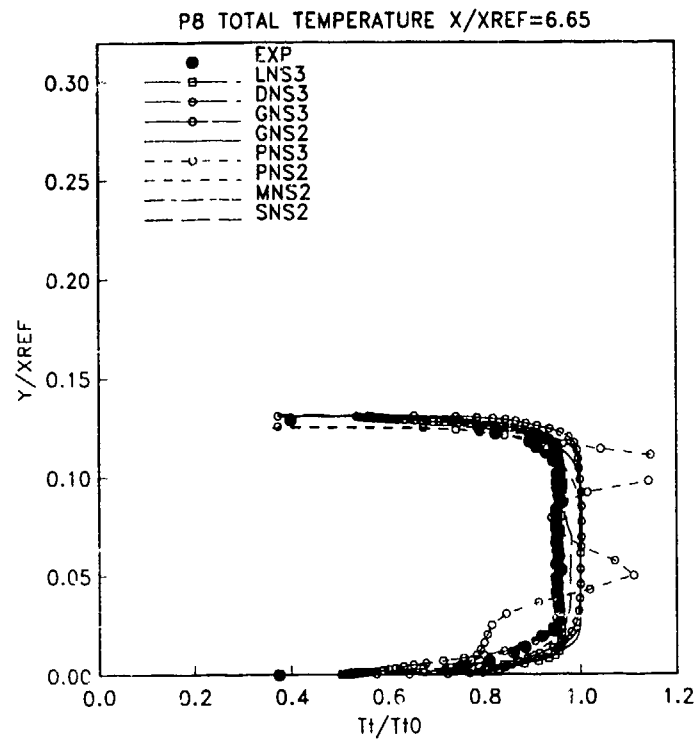
P8 PITOT PRESSURE  $X/X_{REF}=6.79$ P8 TOTAL TEMPERATURE  $X/X_{REF}=5.67$ 











### 3.3.7 Test Case 7 - Mixed Compression Intake

#### 3.3.7.1 INTRODUCTION

The late 1980's have witnessed a renewed interest in sustained supersonic flight for both military and civilian purposes. Experience with the SR-71 and the Concorde have shown that high propulsion system efficiency is an enabling technology for sustained high speed flight. As described in Section 2.4.2, the intakes for such propulsion systems must operate with high total pressure recovery, low levels of distortion, and low levels of associated spillage, bleed and by-pass drags. These represent serious challenges for intake designers of the 1990's. To meet this challenge, intake designers will rely heavily on the use of CFD for intake analysis. To assess the current ability of this new tool to aid in supersonic intake design, a representative mixed compression intake flow field will be calculated as Test Case 7 and the calculations compared with experimental results.

#### 3.3.7.2 PROBLEM DESCRIPTION

The intake to be analyzed is the 40-60 intake; a Mach 2.5 design which was extensively tested at the NASA Lewis Research Center during the late 1960's and early 1970's, Refs 3.7.1 to 3.7.5. The intake was built and tested principally in support of the American SST program to determine basic design parameters for axisymmetric mixed-compression intakes in this speed regime. The intake was also used for parametric studies of boundary layer control through bleed, considering many bleed patterns, distributions and locations. Some details of the inlet operation are given in Section 2.4.2.2 of this report. The intake, shown in Fig. 3.7.1, has a 12.5 degree half angle centerbody and cowl lip aligned with the intake axis. Variable geometry was provided by translating the centerbody cone along the intake axis. Forty per cent of the total intake compression occurs upstream of the cowl lip by a shock wave generated by the centerbody. The other sixty per cent of the intake compression occurs internally through a system of shock waves generated by reflecting the cowl shock from the centerbody back onto the cowl and again back onto the centerbody. Just downstream of the intake throat a terminal normal shock is formed and the resulting subsonic flow is further diffused to the engine compressor face. The centerbody is held in place by three struts in the subsonic diffuser spaced 120 degrees apart. To control shock/boundary layer interactions, boundary layer bleed is provided near

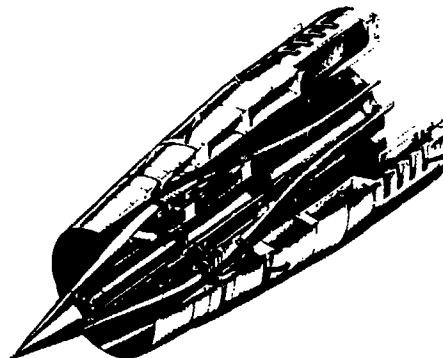


FIG 3.7.1 SCHEMATIC DRAWING OF  
40-60 INTAKE FROM REF 3.7.1.

each of the shock reflection locations by means of distributed, discrete-hole, porous plates. The flow through these bleed zones on the centerbody are routed overboard through the support struts. To provide operating margin and insure normal shock stability, an intake bypass system is provided in the subsonic diffuser.

Although the intake was tested with a variety of bleed configurations, bleed amounts, Mach number and mass flow conditions, the following conditions were recommended for computation:

Mach number = 2.5  
Angle of Attack = 0.0  
Bleed Configuration = DS  
Mass Flow Ratio = .886 + others  
Reynolds number =  $3.88 \times 10^6$   
No vortex generators  
Bleed doors closed  
Reference mass flow is 17.3 kg/sec.

These conditions correspond to test conditions reported in Refs 3.7.1 and 3.7.2. The principal experimental results available include surface static pressures along the cowl and centerbody, compressor face rake data, and seven Mach number profiles in the vicinity of the bleed zones.

#### 3.3.7.3 CFD TECHNIQUES

This test case was attempted by two research groups as noted in Table 3.2.1. One group used a Parabolized Navier-Stokes (PNS) technique, while the other used a Reynolds-Averaged Navier-Stokes (NS) code. The PNS analysis was performed at NASA Lewis and employed the PEPIS code, a single sweep LBI solver using a McDonald-Camarata mixing length

turbulence model. The PNS was only able to analyze the supersonic portion of the intake because such a technique is invalid across the terminal shock and in the subsonic diffuser where the flow is elliptic. The group at Sverdrup used the PARC code, a Beam-Warming ADI solver with a Baldwin-Lomax turbulence model, and designated NS on the following plots. Details of these analyses are found in the microfiche supplement of this report.

#### 3.3.7.4 RESULTS

##### Static Pressure Distributions

Detailed comparison of computed and experimental results for all requested conditions are given in Appendix 3.3.7. We will now consider a few representative results from this larger group. Figs. 3.7.2 and 3.7.3 shows a comparison of the computed and experimental static pressure distributions on the centerbody and cowl of the intake. Experimental data is shown by the symbols while the analyses are shown by different style lines. As shown in the figures of Appendix 3.3.7, there are three sets of experimental data corresponding to three different mass flow settings for the intake; mode A is the lowest mass flow ratio, mode C the highest. Both calculations were performed at conditions duplicating the high mass flow case, mode C. Therefore, for clarity in the plotting, we shall only display the mode C data in the report and the reader is referred to the appendix for the full comparison. All of the data was taken downstream of the intake cowl lip. Considering the experimental data for the centerbody plot, Fig. 3.7.2, at the left portion of the curve, the jump in the pressure corresponds to the first reflection point of the cowl shock on the centerbody. The sudden increase in pressure around  $X=3.4$  corresponds to the terminal normal shock. Comparing the CFD results for the centerbody, we see that the PNS analysis has correctly predicted the location and strength of the reflecting cowl shock. Up to the terminal shock, the inviscid flow is supersonic and the use of a single sweep PNS code properly captures the physics of the problem. In subsonic regions, across the terminal shock, in the diffuser, and for large separations, the single sweep PNS does not correctly model the elliptic nature of the flow. The PNS analysis does not properly predict the location of the terminal shock because this location is set by conditions at the compressor face and this type analysis cannot account for these elliptic effects. The NS analysis has predicted the impingement point of

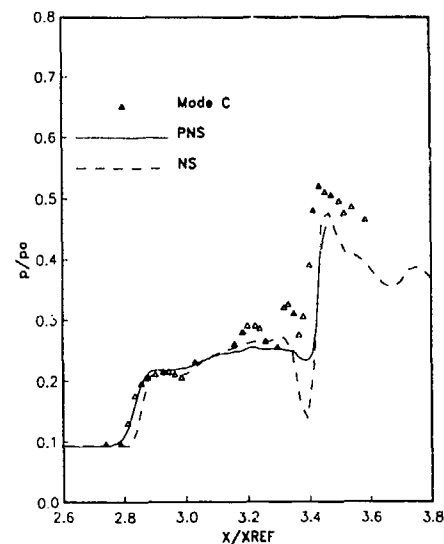


FIG 3.7.2 COMPARISON OF CFD AND EXPERIMENTAL CENTERBODY STATIC PRESSURE DISTRIBUTION.

the cowl shock slightly downstream of its experimental location. The normal shock location, however, is properly set by the NS analysis. At the centerbody bleed location the static pressure is decreased in both the experiment and analyses. The NS analysis overpredicts this decrease, but captures the pressure rise through the terminal shock quite well.

Considering now the cowl plot, Fig. 3.7.3, the jump in measured pressure near  $X=3.1$  corresponds to the second reflection of the cowl shock, while the increase near  $X=3.4$  indicates the terminal normal shock. Because of the plateau shape of the static pressure profile, it appears that, even with substantial bleed on the cowl, there is a separation on the cowl at the shock reflection with associated upstream influence. Comparing the CFD results for the cowl, we see that the PNS analysis has predicted the shock reflection location downstream from the test location as indicated by the Mode C symbols. The single sweep PNS code does not properly model the upstream influence in the separation and gives instead an attached flow pressure profile. The downstream pressure levels correctly correspond to the experimental values, but this analysis does not properly model the pressure plateau. In the NS analysis, the incoming reflected shock is predicted downstream of its

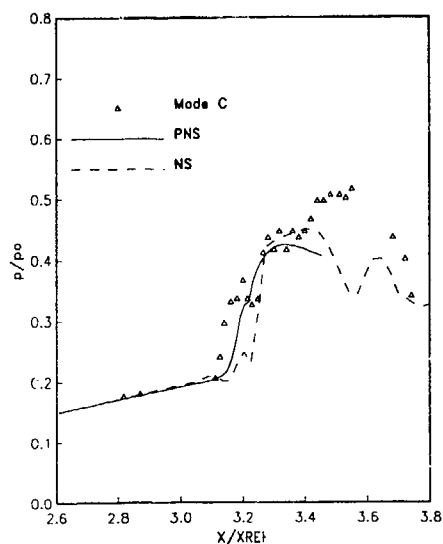


FIG 3.7.3 COMPARISON OF CFD AND EXPERIMENTAL COWL STATIC PRESSURE DISTRIBUTION.

measured location. This is consistent with the downstream prediction on the centerbody as previously discussed. The pressure rise across the shock is properly modeled by the NS analysis, although this analysis does not predict the flow separation.

#### Rake Profiles

Comparison has been made between the CFD results and experimentally measured Mach number profiles at seven locations through the intake. The rake locations are shown in Fig. 3.7.4, and the results for all seven rakes are given in Appendix 3.3.7. Here we shall present some representative cases to demonstrate the CFD results. Fig. 3.7.5 shows the Mach number profiles at rake location 2, on the centerbody, downstream of the first shock reflection. The symbols indicate the experimental results while the various lines present CFD results. In this plot, the Mach number has been plotted on the horizontal axis normalized by the external value at the edge of the boundary layer. The height is measured normal to the centerbody surface, in centimeters, along the vertical axis. Considering the CFD results, we see that the PNS analysis has correctly predicted the turbulent boundary layer shape, as compared with the data, but has overpredicted the boundary layer thickness. The NS analysis has also overpredicted the

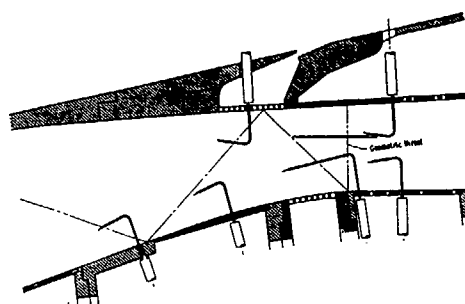


FIG 3.7.4 EXPERIMENTAL RAKE LOCATIONS WITHIN THE 40-60 INTAKE.

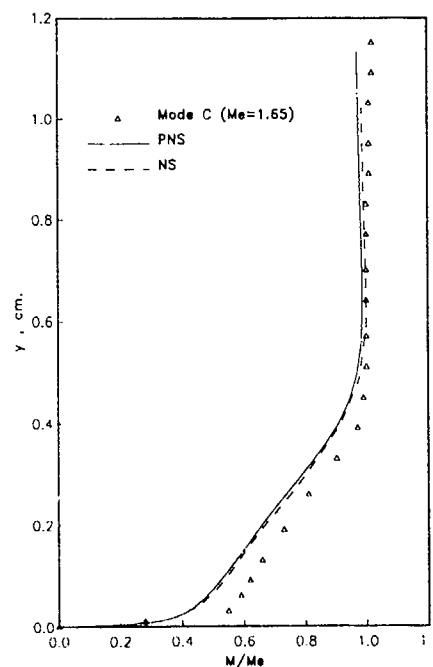


FIG 3.7.5 COMPARISON OF CFD AND EXPERIMENTAL MACH NUMBER DISTRIBUTION AT CENTERBODY PROBE 2.

boundary layer height while correctly predicting the shape. The computational profile has been normalized by an exterior Mach number equal to 1.65, so that comparisons can be made with Mode C. Both the NS and single sweep PNS have correctly predicted the external Mach number at this station for which

the flow is predominately supersonic. Moving downstream to probe 4, on the centerbody slightly upstream of the terminal shock in the vicinity of the throat, results are compared in Fig. 3.7.6. The computational profiles are nondimensionalized by Mach number equal 1.05 for comparison with Mode C mass flow ratio. Considering the experimental results, we see a turbulent boundary layer profile whose thickness is comparable to the previous rake. The lower portion of the profile shows the effects of the local bleed accelerating

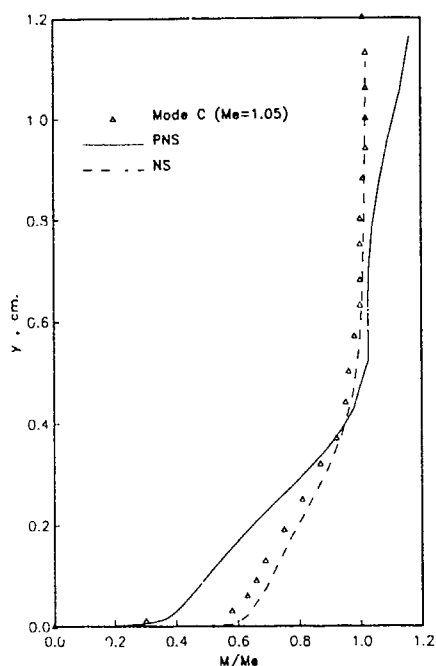


FIG 3.7.6 COMPARISON OF CFD AND EXPERIMENTAL MACH NUMBER DISTRIBUTION AT CENTERBODY PROBE 4.

the flow. Considering the CFD results, we see that the PNS code has not been able to predict the bleed effects near the wall, probably because of the elliptic nature of the flow in this region. The NS solution matches the profile quite well at this location. With the free stream Mach number approaching 1.0, an NS code is required; the PNS assumptions are beginning to break down at this location. Considering a rake on the cowl, Fig. 3.7.7 shows results at probe 6 which is located downstream of the shock reflection and the cowl bleed zone. The computational profile was

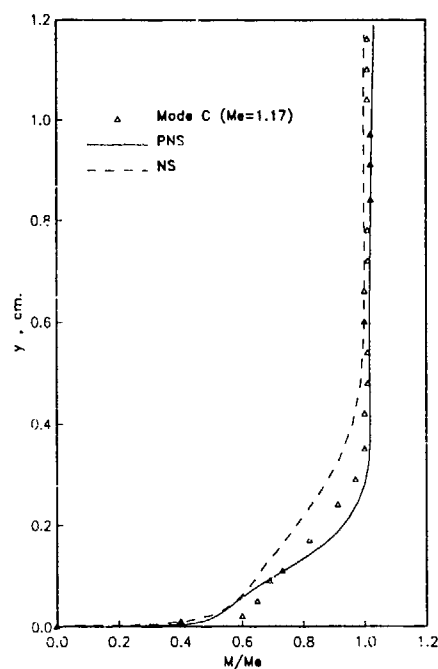


FIG 3.7.7 COMPARISON OF CFD AND EXPERIMENTAL MACH NUMBER DISTRIBUTION AT COWL PROBE 6.

nondimensionalized by Mach number equal 1.17 for comparison with Mode C mass flow ratio. The PNS analysis results compare quite closely with the experimental results with respect to farfield Mach number. The boundary layer thickness is underpredicted and some details of the lowest portion of the boundary layer are not captured. In view of a possible separation and reattachment on the cowl, such a discrepancy is again to be expected. The NS analysis is overpredicting the boundary layer thickness at this rake.

### 3.3.7.5 CONCLUSIONS

This test case was analyzed with two different types of codes, a fast running PNS code and a slower running NS code. In the predominately supersonic portions of the flow field, the single sweep PNS analysis was able to correctly predict major features present in this intake more efficiently than the NS analysis. However, in those places where elliptic effects are important, such as the lowest portions of the boundary layer and near the throat bleed zones, the NS code was clearly superior. For intake design purposes, it would appear that

the PNS analysis can provide useful information quickly, but that the NS analysis should be employed in those regions where it is truly required.

#### 3.3.7.6 REFERENCES

3.7.1. Cubbison, R.W., Meleason, E.T., and Johnson, D.F., "Effect of Porous Bleed in a High Performance Axisymmetric, Mixed-Compression Inlet at Mach 2.50", NASA TM X-1692, November 1968.

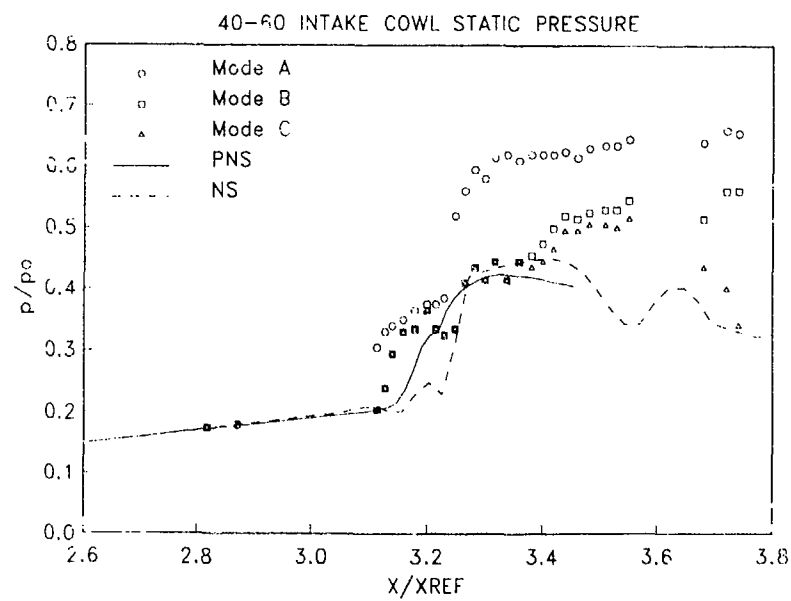
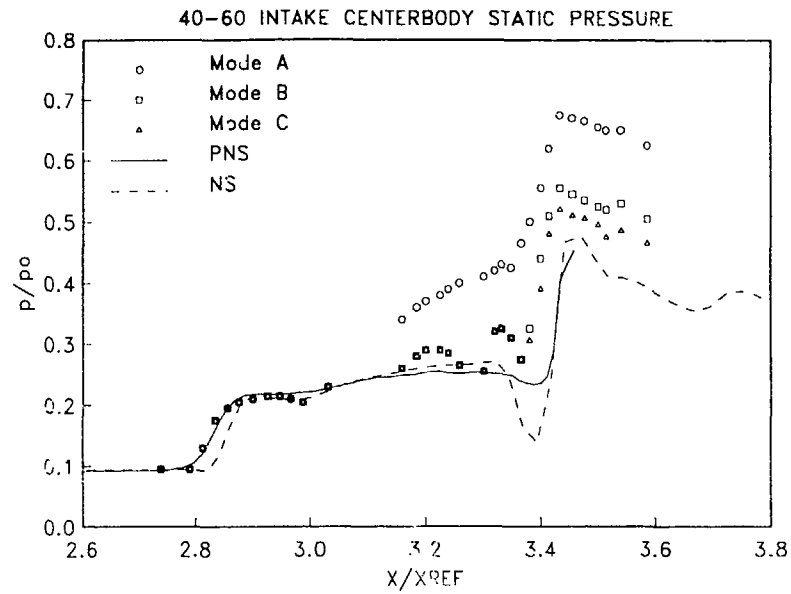
3.7.2. Hingst, W.R., and Johnson, D.F., "Experimental Investigation of Boundary Layers in an Axisymmetric, Mach 2.5, Mixed-Compression Inlet", NASA TM X-2902, October 1973.

3.7.3. Cubbison, R.W., Meleason, E.T., and Johnson, D.F., "Performance Characteristics from Mach 2.58 to 1.98 of an Axisymmetric Mixed-Compression Inlet System with 60-Percent Internal Contraction", NASA TM X-1739, February 1969.

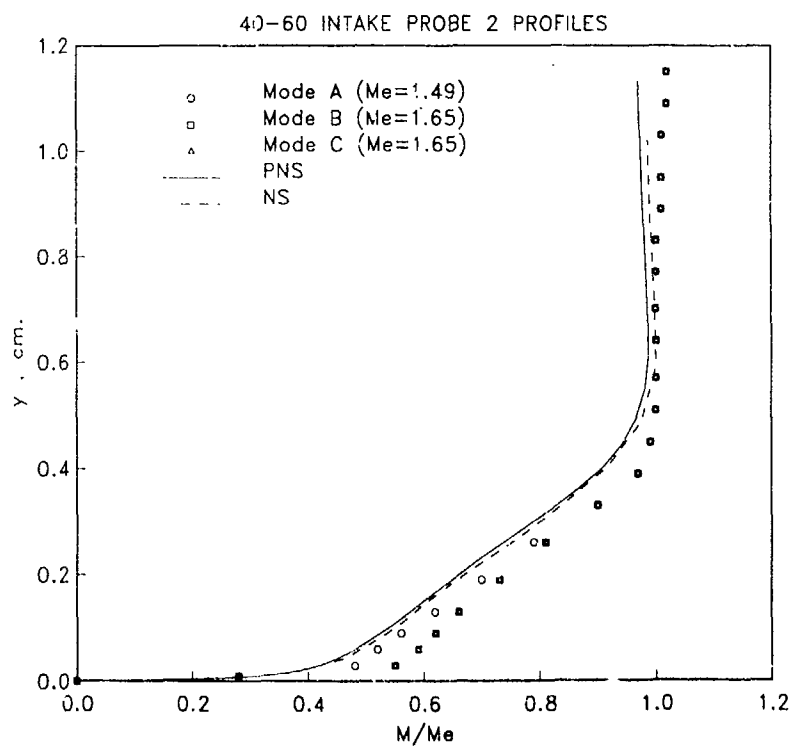
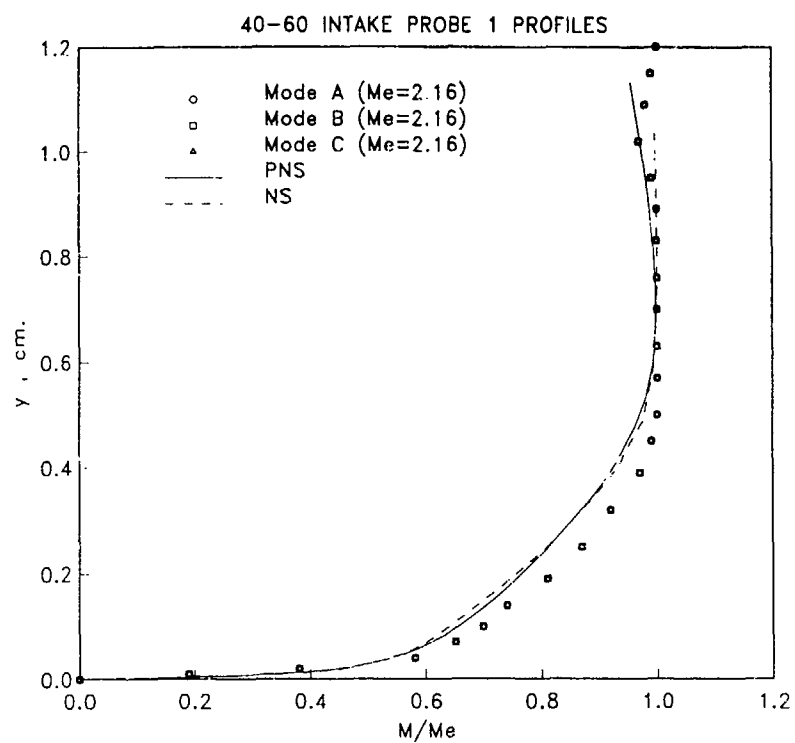
3.7.4. Woollett, R.R., Meleason, E.T., and Choby, D.A., "Transonic Off-Design Drag and Performance of Three Mixed-Compression Axisymmetric Inlets", NASA TM X-3215, June 1975.

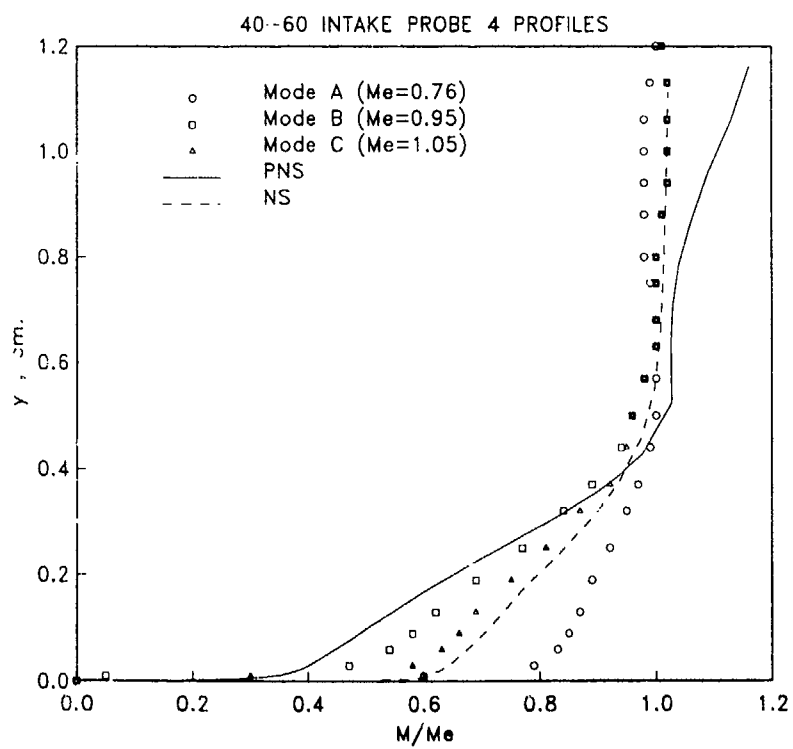
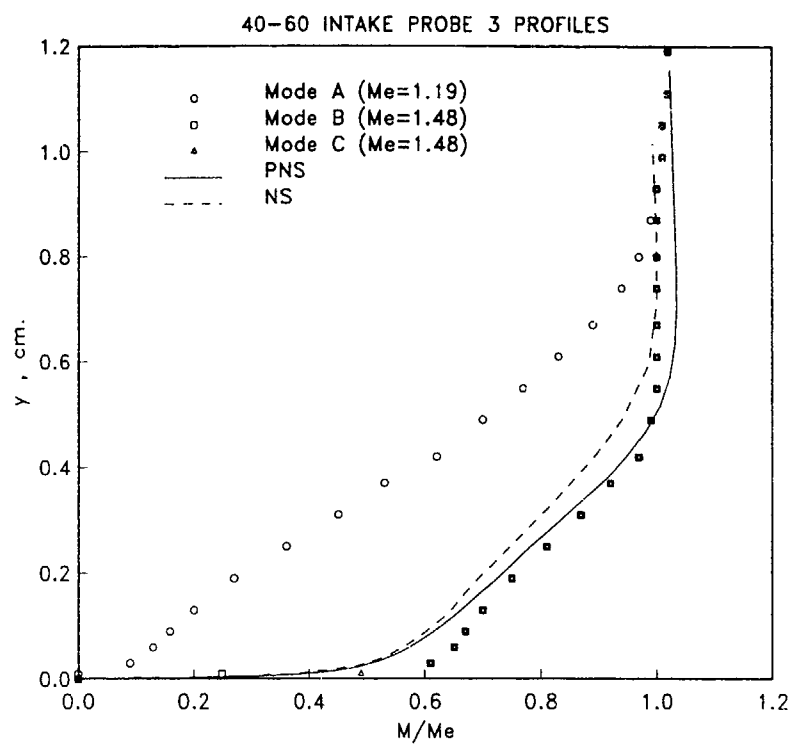
3.7.5. Fukuda, M.K., Hingst, W.G., and Reshotko, E., "Control of Shock Wave-Boundary Layer Interactions by Bleed in Supersonic Mixed Compression Inlets," NASA CR 2595, August 1975.

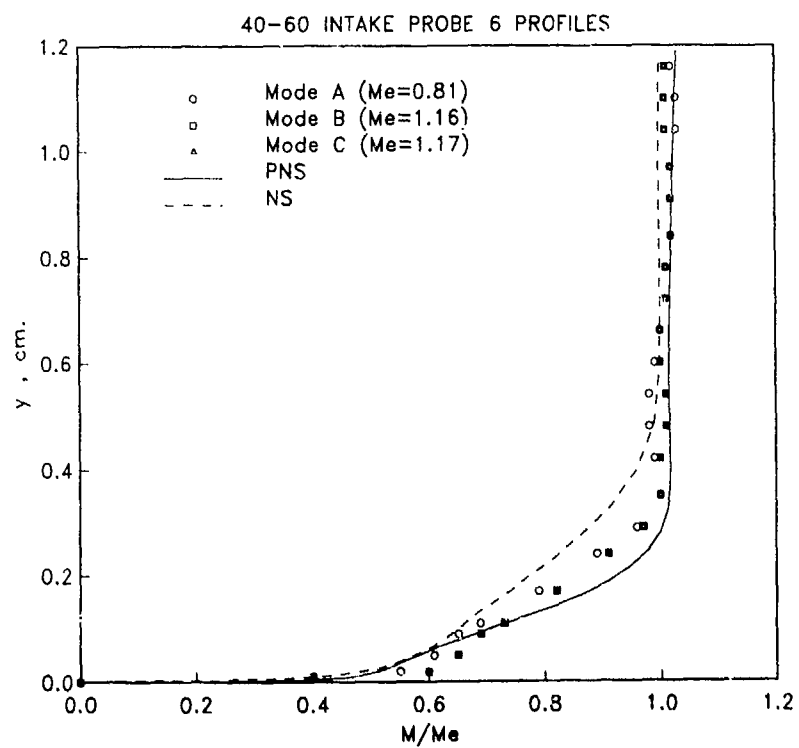
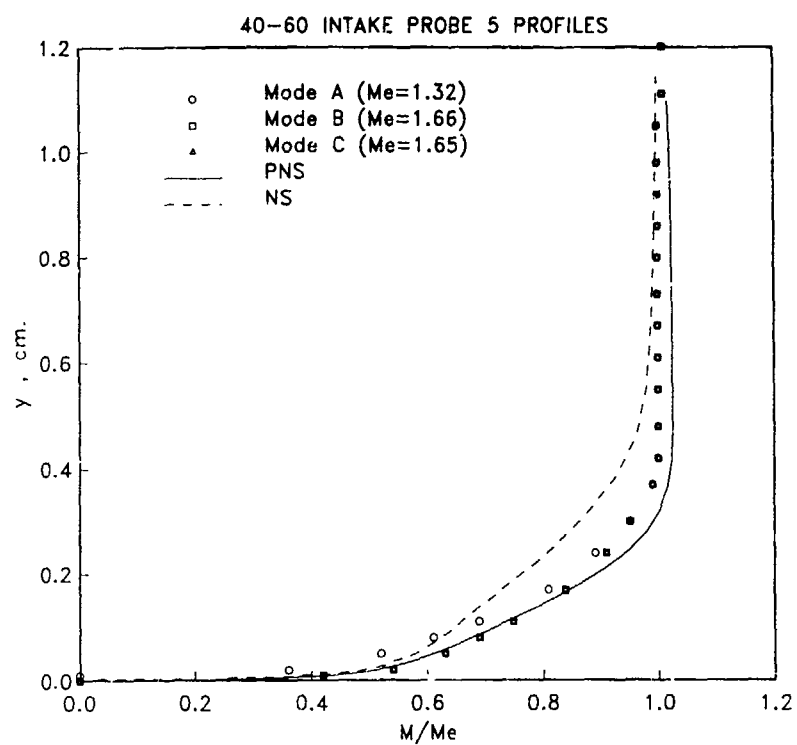
Appendix 3.3.7  
Full Comparison of CFD and Experiment

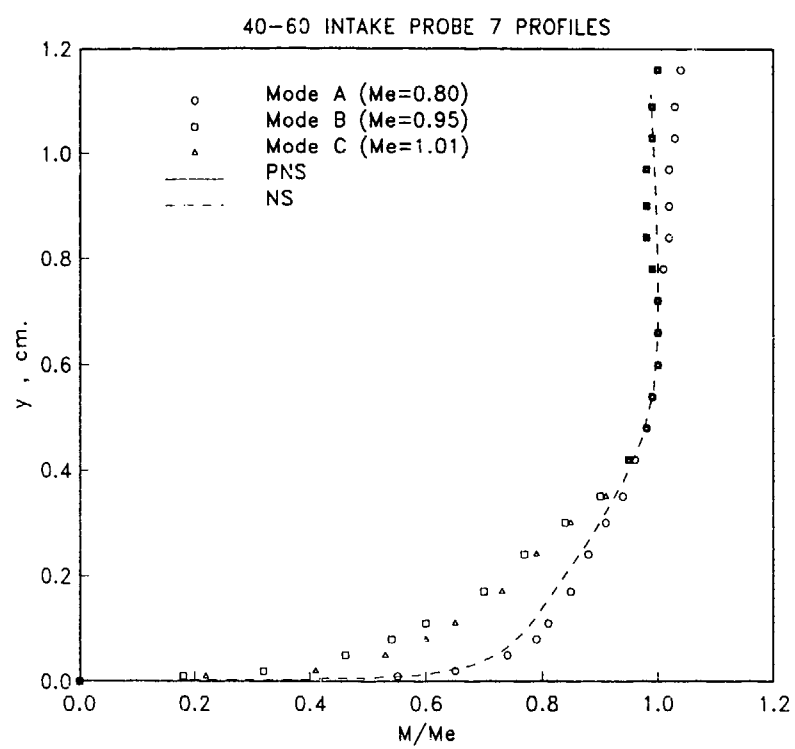












### 3.3.8 Test Case 8 - Intake/Airframe Integration

#### 3.3.8.1 INTRODUCTION

One of the ultimate goals of CFD analysis is the accurate modeling of an entire aircraft in flight including engine installation effects. Such a predictive capability would produce a more thorough understanding of the physics involved in engine/airframe integration and therefore a better designed aircraft. In the area of intake aerodynamics, the effects of intake installation on entire aircraft performance could be optimized. The test matrix for intake/airframe integration could be greatly reduced if accurate, fast, computer models of this problem can be generated. To assess the current state of CFD for predicting intake/airframe interactions, Test Case 8 was proposed for calculation. In this test case, CFD analysis of an experimental parametric study of intake/airframe integration will be assessed.

#### 3.3.8.2 PROBLEM DESCRIPTION

The test case chosen was the Tailor-Mate series of experiments conducted at AEDC by General Dynamics for the USAF Wright Patterson AFB, Ref 3.8.1. As described in Paragraph 2.5.3.1 of this report, these tests were a parametric study of different types and locations of intakes on various forebodies to experimentally determine intake/airframe integration effects. Tests were conducted across the speed regime with extensive instrumentation in the intake ducts, at the compressor face, and at the intake entrance. Measurements at the intake entrance included the effect of the forebody flow field on intake performance. Two of the many cases; one supersonic, one transonic, were chosen for comparison with CFD results. Fig. 3.8.1 shows a schematic picture of the model with the side mounted rectangular intakes chosen for this case. A thorough description of the model is given in Section 2.3.3 of this report.

#### 3.3.8.3 CFD TECHNIQUES

This test case was attempted by two research groups, as shown in Table 3.1. One group used Reynolds-Averaged Navier-Stokes (NS) analysis, while the other group used an Euler solver (EU). The group from Sverdrup-AEDC used the three-dimensional blocked version of the PARC NS code, with a Baldwin-Lomax turbulence model, to study the transonic test case. The group from Aerospatiale used the three-dimensional, multi-

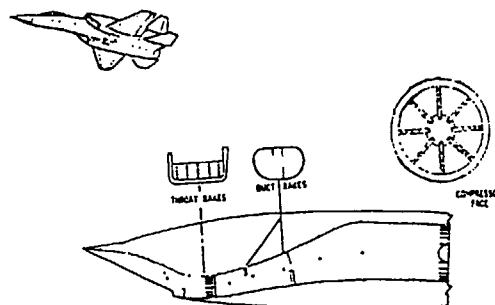


FIG 3.8.1 SCHEMATIC DRAWING OF TAILOR-MATE FOREBODY/INTAKE TEST.

domain, finite volume FLU3M EU code to analyze the supersonic test case. Details of these computations are to be found in the microfiche supplement of this report.

#### 3.3.8.4 RESULTS

##### Transonic Test

For the transonic test case, the free stream Mach number was set to 0.9. While a variety of intake mass flow ratios, bleed rates, and aircraft angle of attack and yaw were tested, only one set of conditions were requested for computation. This condition had zero angle of attack and yaw for the aircraft. The principal experimental data available for this case included pressure distributions in the duct and at the compressor face. Flow field data, including Mach number, total pressure variation and induced angle of attack and yaw were measured at the intake entrance. Sverdrup-AEDC has calculated the transonic case and comparison with experimental data is given in Figs. 3.8.2, 3.8.3 and 3.9.4 for their calculation. During the calculation, as detailed in the supplement, significant differences from the experimental results were calculated upstream of the intake. Because of the magnitude of these differences, it was decided that no comparison could be made with intake internal measurements. Fig. 3.8.2 illustrates the differences in induced Mach number at the intake entrance. This figure shows contour plots of Mach number with an outline drawing of the intake entrance and the forebody. The top of the figure shows the experimental results while the bottom gives the CFD

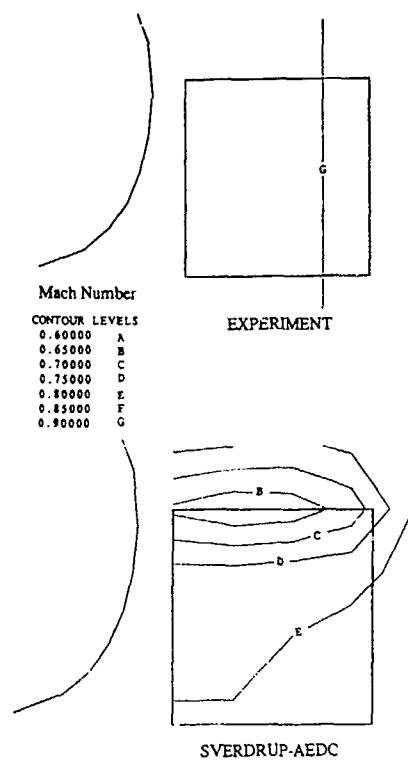


FIG 3.8.2 COMPARISON OF CFD AND EXPERIMENTAL MACH NUMBER CONTOURS AT THE INTAKE FACE FOR TRANSONIC CASE.

results. The experiment indicated a nearly uniform Mach distribution, while the analysis indicated a significant decrease in the vicinity of the ramp leading edge. The analysis predicted significant amounts of intake spillage at this test condition with an associated decrease in velocity at the ramp leading edge. This spillage is indicated even more in Fig. 3.8.3 which shows induced angle of attack at the intake entrance. The experiment measured a very small angle of attack as the flow wrapped around the forebody. The analysis predicts up to 8.0 degrees of flow spillage over the ramp leading edge. This value is better quantified and illustrated in Fig. 3.8.4 which shows angle of attack along a vertical line near the centerline of the intake. Again, the symbols give the measured values and the solid line the results from the analysis. The large increase in angle of attack near the ramp leading edge is easily noted.

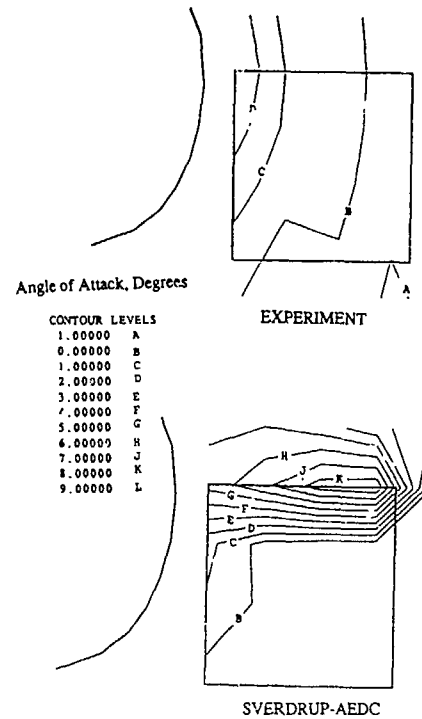


FIG 3.8.3 COMPARISON OF CFD AND EXPERIMENTAL INDUCED ANGLE OF ATTACK AT THE INTAKE FACE FOR TRANSONIC CASE.

#### Supersonic Test

For the supersonic test case, the free stream Mach number was set at 2.2. As before, several angles of attack and yaw, and engine and bleed mass flows were tested. The only condition to be modeled was the Mach 2.2, zero angle of attack and yaw case. Experimental data, as before, consisted of external flow field pitot pressure, Mach number, and induced angle of attack and yaw, as well as internal compressor face pitot pressure, duct static pressure and some duct rake data. Aerospatiale has computed the supersonic test case and comparisons between this computation and the test results are given in Figs. 3.8.5 to 3.8.6. Fig. 3.8.5 shows a comparison between the computed and measured flow fields near the intake face. This plot shows comparison of Mach

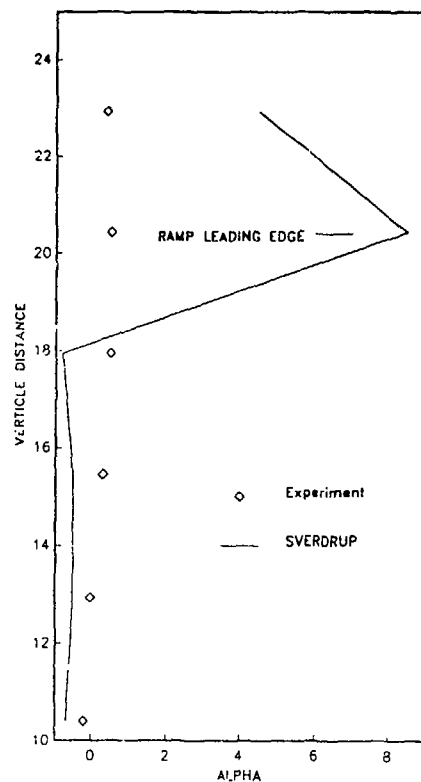


FIG 3.8.4 COMPARISON OF CFD AND EXPERIMENTAL ANGLE OF ATTACK ON INTAKE CENTERLINE AT THE INTAKE FACE.

number contours, with the experimental results at the top, and the computational at the bottom. The outline of the forebody on the intake leading edge is given for orientation purposes. In general, the comparison is quite good, particularly considering the use of an Euler solver in the analysis. It would appear that boundary layer effects of the forebody are very small for this zero angle of attack and yaw condition. Fig. 3.8.6 shows a similar comparison of the total pressure at this location. The comparison with this parameter is not as good as with the Mach number; this CFD results show a nearly uniform high recovery flow field while the experiment showed significant gradients near the body. It would appear that the CFD has not properly accounted for losses associated with the shock waves and expansion fans generated by the forebody.

#### CFD Flow Field

While the primary interest of this test

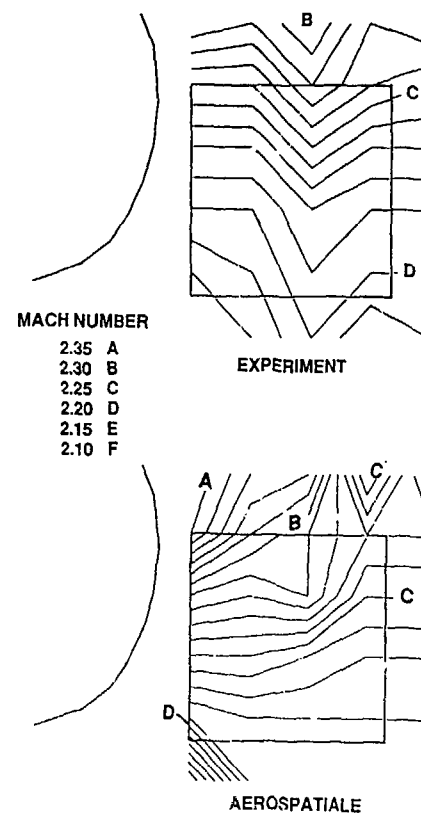
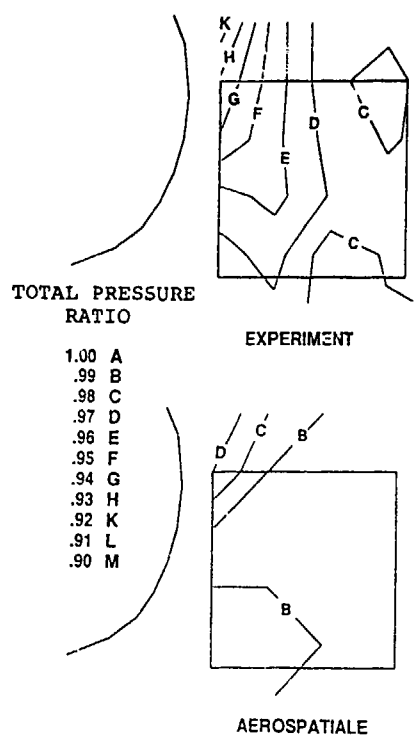


FIG 3.8.5 COMPARISON OF CFD AND EXPERIMENTAL MACH NUMBER CONTOURS AT THE INTAKE FACE FOR SUPERSONIC CASE.

case is to compare the results of the computations with the experimental results, it is also useful to consider the total flow field predicted by the CFD analysis. Fig. 3.8.7 shows the computed static pressures on the flow centerplane and the surface of the forebody and intake for the high speed case. The shock waves generated by the nose and canopy are clearly indicated, as are the shocks generated by the intake compression ramps. It appears that an oblique shock has been generated by the diverter between the intake and the forebody and this shock is seen to pass under the fuselage. These are exactly the airframe/intake integration features which one would hope to model properly for improved aircraft performance.



### 3.3.6.5 CONCLUSIONS/RECOMMENDATIONS

Because of the difficulty of the proposed test case and the scarcity of computational results for this case, it is difficult to make any assessment of the ability of CFD to model these types of problems. It would appear, however, that a significant disagreement between the attempted CFD calculation and the experiment exists for the transonic case. We would encourage future additional computations of this test case to help resolve these discrepancies.

### 3.3.8.6 REFERENCES

3.8.1 Antonatos, P.P., Surber, L.E., and Stava, D.J., "Inlet/Airplane Interference and Integration", AGARD LS-43, Airframe/Engine Integration, March 1975.

FIG 3.8.6 COMPARISON OF CFD AND EXPERIMENTAL TOTAL PRESSURE RATIO AT THE INTAKE FACE FOR SUPERSONIC CASE.

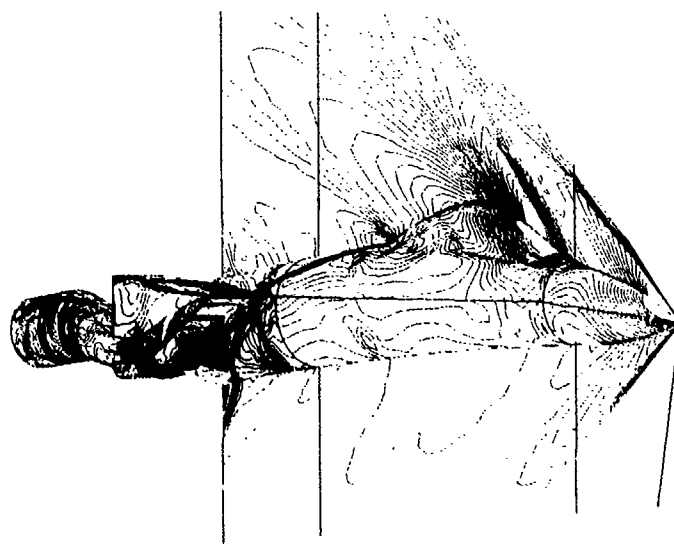


FIG 3.8.7 COMPUTED STATIC PRESSURE CONTOURS ON THE CENTERLINE AND ALONG BODY SURFACES.



### 3.4 CONCLUSIONS/RECOMMENDATIONS

In this study, experimental test cases have been proposed for calculation to assess the current ability of CFD to model inlet flow fields. The proposed test cases covered the speed regime from subsonic to hypersonic, and considered flow configurations from simple, benchmark experiments to full intake/airframe combinations. Computational techniques from 2D Euler to 3D Navier-Stokes have been employed. Having considered the computation of each of the test cases individually, the following general conclusions and recommendations can be drawn.

#### PARTICIPATION

The members of the AGARD Working Group 13 wish to thank and commend all of the contributors to this study. A great deal of donated time and effort was spent in the analysis and computation of these test cases. Of the eight proposed test cases, the greatest number of calculations was performed on test case 6, the 2D hypersonic intake. This probably reflects the increased interest in this speed regime and the important role that CFD could play in an area where experimental testing is most difficult. The test case with the fewest number of calculations was the D-shaped intake with offset diffusing duct, followed closely by the offset duct case and the intake/airframe case. It is ironic, and alarming, that the most calculations were performed on a configuration which has never flown, while the fewest calculations were done for configurations which exist on most aircraft.

#### RESULTS

From a comparison of CFD calculations and experimental results for eight test cases the following conclusions have been drawn. Not surprisingly, CFD has better modeled the simple benchmark experiments than the full intake/airframe configurations. This, of course, can be attributed to better definition of the problem, both computationally and experimentally. In general and as expected, the full

Navier-Stokes solvers have done a better job than the simpler Euler and Parabolized Navier-Stokes solvers, but with a greater computational expense. There is some evidence in these test cases that better, faster grid generation codes should be developed for intake applications. When comparing experimental and computational results, there are two chief sources of disagreement; the experiment and the computation. In some of the test cases

discussed here, it is clear that the experimental results were either incorrect or not completely described so that they could be calculated. In all fairness, most of the test cases chosen were completed before the rise in interest in CFD and the lack of detailed information for CFD comparison is understandable. However, in the future, all experimental programs should be conducted in a way which can benefit and be the benefit of CFD analysis. As pointed out in most of the test cases, CFD can provide additional information concerning the flow fields in intakes which one can not obtain in experiments. The codes must, however, be checked at some points to insure accurate calculations.

Between different calculations performed for the same test case one usually has seen variations in the results. These variations can be attributed to different computational techniques, different representations of the physics problem (i.e. different grids, different convergence levels, different boundary conditions), and ultimately different CFD users with different levels of experience. CFD is not yet, nor will it ever be, a mathematical genie in a bottle capable of returning accurate flow fields to any novice who rubs the lamp. CFD requires a lot of experience and physical insight to obtain meaningful results. When used in conjunction with an experiment, it can lead to a better understanding of complex physical flows.

#### OUTLOOK

It was the aim of the numerical subgroup of AGARD Working Group 13 to give an overview of today's numerical method's capability for calculating intake flows of high speed aircraft. The conclusions to be drawn are limited and can be given in general terms only. A more careful study is recommended in which the accuracy of CFD and its dependency on parameters like grids and turbulence models can be investigated. For this study, it is recommended that the number of test cases should be limited to a few cases where experimental data are plentiful and the accuracy of the measurements is well documented. The complexity of the problems should be restricted so that computers available in all NATO countries will be capable of modeling the flow. AGARD seems to be a good forum to initiate and bring together sufficient researchers and institutions necessary to provide a comprehensive study for a successful completion of such an exercise.

## Chapter 4

### AIR INTAKE TESTING

Symbols are those of Chapter 2, or are specified in the text

#### Section 4.1

#### SCOPE AND PURPOSE OF AIR INTAKE TESTS

##### Contents

- 4.1.1 - Validation of air intake tests run without an engine
- 4.1.2 - Test of the air intakes with engine
- 4.1.3 - Air intake interaction with the aircraft
- 4.1.4 - Similitude parameters

##### Scope and purpose of air intake tests

The purpose of testing air intakes is to qualify the flow they deliver to the engine, and to determine the effect they have (in terms of drag, lift and moment) on the external aerodynamics of the aircraft.

These tests are generally carried out using models with no engine, but with another device developing the same through-flow as the engine.

##### 4.1.1 - Validation of air intake tests run without an engine

This question of validation arises essentially in relation to the qualification of an internal flow. The best way of validating tests without an engine is to test the same air intake with a real engine and compare the results. According to bibliographical reference [1], "the effect the presence of the engine has on the pressure recovery  $P_R$ , on the level of turbulence and on the maximum instantaneous distortion is small, and is favorable."

Through this statement may be very encouraging, it should nonetheless be kept in mind that tests without engines may sometimes prove to be less than representative.

The same question of test validity also arises when the engine face flow conditions defined by a test on a given air intake model have to be transferred to an engine test rig. We will mention here only two reference solutions to this problem. The inflow distortion can be simulated either by grids or jets upstream in the supply pipe [2], or by constructing an air intake of appropriate form, that will recreate the static and dynamic distortion of certain extreme flight conditions [3].

The true response can of course be known by testing the full air intake-engine assembly whenever possible. We comment on this in the next section.

##### 4.1.2 - Tests of the air intakes with engine

It is rarely possible to test a real air intake-engine assembly in a wind tunnel under the same Mach number, incidence, and altitude conditions as in flight, because of the wind tunnel size this would require.

But there are certain possibilities of running such tests in very large facilities like ONERA's sonic S1MA wind tunnel (8 m in diameter) or the 16 foot

subsonic/supersonic wind tunnel of the AEDC [4].

Also, when large free-jet wind tunnels are used, the air intake can be placed in the jet flow in such a way as to simulate its actual operation and establish a representative air supply to the engine.

We may mention in this regard the CEP (Centre d'Essais et de Propulseurs) facilities in France, those of the RAE (Pyestock) in England, and the Aero-propulsion System Test Facility (ASTF) of the Arnold Engineering Development Center (AEDC) in the United States [4].

Such physical facilities can be highly useful in the final stages of air intake-engine compatibility design, e.g. to adjust the air intake-engine integration devices and to check how the engine operates at certain limits of the flight envelope. These facilities come into play only rarely through, and always at a late stage, in air intake definition studies. This is because of the large facilities involved, of the fact that the engines for a new aircraft are generally available at the required standard only late in the aircraft development, and also because of simulation limits.

Figure 1 illustrates the principle of the test setups used, with a free-jet wind tunnel test of the Concorde's Olympus engine-air intake assembly, run at the RAE (Pyestock) [5].

This type of test, which is closer to engine testing than to air intakes, will not be commented on further.

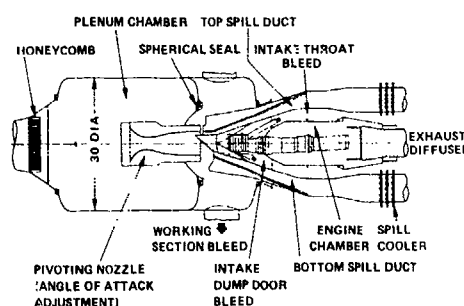


Fig. 1 - RAE (Pyestock) free jet test facility (Cell 4).  
(P.F. Ashwood - [5]).

##### 4.1.3 - Air intake interaction with the aircraft

A second line of investigation concerns the possibility of defining the effect the air intake has on the external aerodynamics of the aircraft.

Tests in which force measurements are made on the air intake either alone or with the forward part of the aircraft can provide a preliminary approximation of how much the air intake contributes to the overall drag and lift of the aircraft.

In certain cases, the specific contribution of the nacelles and the effect of various air intakes on the aircraft's aerodynamic characteristics can be defined by force measurements on full models of the aircraft, with and without the nacelles.

Generally, of course, the level of integration of the air intakes with the rest of the aircraft is such that it is difficult to establish a precise separate analysis for each. But it is often by combining these two types of tests, i.e. of the air intake alone and of the full model, that we manage to optimize the configuration of air intakes with the whole of the aircraft.

A few examples of these testing techniques will be given below.

#### 4.1.4 - Similitude parameters

The similitude parameters for wind tunnel tests of air intakes, generally run on small models, are the following :

- same geometry, to scale ;
- same Mach and Reynolds numbers ;
- same Mach number distribution and same velocity vector orientation at the engine face ;
- reduced frequencies,  $f/\sqrt{T_1}$ , at the engine face station, inversely proportional to the scale,  $\lambda$ .

If the test is run using an engine having the same characteristic as the engine that will be used in flight, the last two conditions are obtained by adjusting the engine rotation speed to the same reduced frequency,  $N/\sqrt{T_1} \times \lambda^{-1}$ .

If no engine is used, it is assumed that the third condition is met when the same mean Mach number  $M_2$  is set at the engine face station or, equivalently, the same reduced flowrate  $W(\sqrt{T_2})/P_{12} \times \lambda^2$ .

In this expression,  $W$  is the measured flowrate,  $T_{12}$  is equal to the upstream stagnation temperature  $T_{10}$  (see a few comments in [6]), and  $P_{12}$  is generally defined as the area mean of the stagnation pressure measured at the engine face (see the references in Chapter 2 and a few comments in [7] and [8]).

When we want to know the unsteady characteristics of the flow in the air intake (the fourth condition above), we should make a distinction between the unsteady distortion and the surging of the air intake. In the former case, as the distortion stems from the local instabilities of the inflow and depends little on how the internal flow valving system is arranged downstream, the unsteady characteristics measured in reduced frequencies are fairly representative. In the latter case, when the air intake surging is being studied, or for that matter any other relatively low-frequency characteristics involving wave propagation times between the intake and the engine, a valve system must be provided at the position of the first compressor stages, in order to reproduce the phenomena exactly, particularly in reduced frequency (see one example in section 4.5.2).

### Section 4.2

#### TESTS OF SUBSONIC TRANSPORT AIRCRAFT INTAKES

##### Contents

- 4.2.1 - General aspects
- 4.2.2 - Test of air intakes in high subsonic flow
  - 4.2.2.1 - Principle of the test setup
  - 4.2.2.2 - Engine face equipment and measurement of pressure recovery  $P_R$
  - 4.2.2.3 - Flow rate measurement
  - 4.2.2.4 - Drag measurement with external probes

#### 4.2.2.5 - Other drag measurement methods

#### 4.2.3. - Low velocity air intake tests

##### 4.2.3.1 - General conditions

##### 4.2.3.2 - Test setups

##### 4.2.3.3 - Engine face instrumentation, and measurement of the distortion

##### 4.2.3.4 - Flow rate measurement

##### 4.2.3.5 - Drag measurement

##### 4.2.3.6 - Effect of the aircraft aerodynamic field

#### 4.2.4 - Nacelle installation test using turbine power simulator (T.P.S.).

##### 4.2.1 - General aspects

It is difficult to investigate the air intake of a subsonic turbojet separately from the entire nacelle containing it, just as it is difficult to investigate the whole nacelle itself without considering its interaction with the wing - or with the fuselage, for those nacelles that are mounted on the rear of the aircraft.

The characteristics of the nacelle alone nonetheless provide the basis for addressing the problem as a whole, and it has been shown that the effect of the air intake of the entire nacelle can be well identified so long as a large part of the outer fairing of the nacelle is considered along with it. This would include the maximum cross section of the nacelle, plus enough of the narrower rear part of the boattail part so as to include any supersonic expansion there may be at the maximum cross section, plus the shock that bounds it [9].

To study the external flow and the drag, the test setup will have to provide its support from downstream and, insofar as possible, will follow the boattail of the nacelle, the boundary between the two being just the diameter needed to ensure the internal passage of the inlet flow. This means we use a support tube of minimum thickness, connected to the boattail part of the fairing by a short fillet.

A full investigation of the nacelle also calls for studying the afterbody characteristics on an appropriate test setup, as well as the wing installation or the rear of the aircraft, as the case may be.

Air intake and nacelle installation tests are described below.

#### 4.2.2 - Test of air intakes in high subsonic flow

##### 4.2.2.1 - Principle of the test setup

An example of a test setup is given in figures 2 and 3.

The internal flow is provided at the natural flow rate, which is possible starting at a Mach number of about 0.6. If we wanted the maximum flow at lower Mach numbers, forced suction would be needed.

The internal flow is measured by a set of total pressure probes installed at the engine face section. The flow then passes downstream through a honeycomb filter and a grid to remove non-uniformities, and then through a venturi to measure the flow rate. The flow rate is adjusted by a system of flaps controlling the area of the outlet.

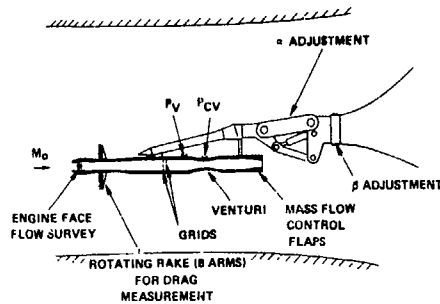


Fig. 2 - Example of subsonic intake high speed test rig. (ONERA - STMA).

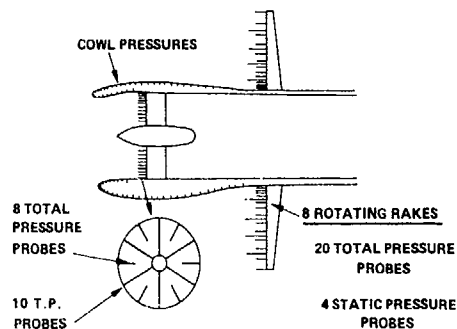


Fig. 3 - Internal flow survey and external drag measurement equipment.

The external drag is calculated from the external flow survey, which is made by a set of rotating pitot probe rakes.

Figure 4 is a photo of such an arrangement with forced flow suction, in the Aircraft Research Association transonic wind tunnel [10].

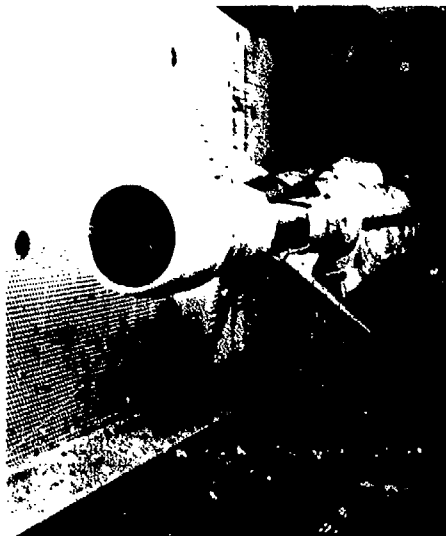


Fig. 4 - Drag measurement by rotating rake (ARA).

#### 4.2.2.2 - Engine face equipment and measurement of pressure recovery $P_R$

The degradation of the flow inside a subsonic air intake under cruising conditions essentially results from stagnation pressure losses near the wall surfaces. The pitot tubes should therefore be small, and closely spaced near the walls to get a precise value for the pressure recovery, defined by :

$$P_R = \int_{A_2} \frac{P_{t2}}{P_{t0}} \frac{dA}{A}$$

Figure 3 indicates a typical system including 108 pitot tubes and figure 5 shows a comparable system, complemented by a few static probes mounted on internal rakes, making a total of 136 pressures.

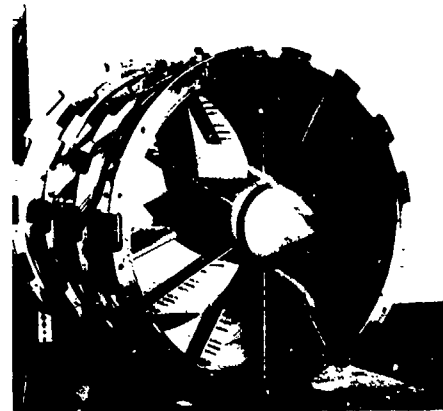


Fig. 5 - Engine face station equipment (Rolls-Royce).

The stagnation pressure losses under cruising conditions are of course very small and the objective is to measure  $P_R$  with a precision of  $\pm 0.001$ . The quality of the measurements can be verified by the pressure ratio values measured in the central, isentropic part of the flow, which should be equal to unity.

#### 4.2.2.3 - Flow rate measurement

The flow rate is measured by a venturi. But the precision of this measurement (about  $\pm 0.5\%$ ) cannot be guaranteed if the venturi is used under other than the standard conditions, which is often the case when the test setups restrict the dimensions of the pipes.

It is then possible to improve the result by calibrating the measurement. This is done by replacing the air intake in question with a sonic-throat intake, the flow of which can be calculated precisely beforehand.

In fact, several such sonic throats should be used if the experimenter has to cover a certain range of venturi operation and still avoid very supercritical regimes that might give rise to strong internal distortion and undermine the validity of the calibration.

A typical sonic throat used is shown schematically in figure 6.

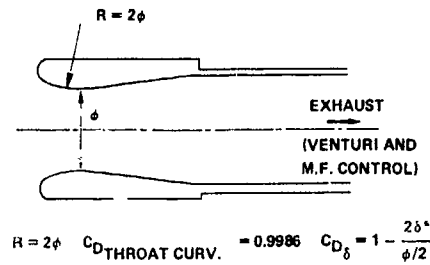


Fig. 6 - Reference sonic throat intake for mass flow measurement checking.

The sonic throat flow rates are calculated to a precision of better than 0.2 % [1]. Detailed formulae are given in section 4.3.2.3.

The calibration is made in the wind tunnel, under the same conditions as in the air intake test, and, using that calibration, the mass flow measurement is obtained with a precision of at least  $\pm 0.5\%$ .

#### 4.2.2.4 - Drag measurement with external probes

The measured drag is the sum of the pre-entry drag and the cowl drag (see Chapter 2, section 2).

This is done by measuring the external flow with rotating probe rakes as shown in figure 3 and as can be seen in figure 4.

Adopting the hypothesis of uniform static pressure in the plane of the rakes, the momentum theorem is applied to the flow outside the captured flow and cowl, leading to the following expression for the drag:

$$\text{air intake drag} = p_0 \gamma M_0^2 \int_{A_R} \left| \frac{p_{tr} \sum M_R^2}{p_0 \sum M_0^2} \right| dA_r$$

in which  $p_{tr}$  is the stagnation pressure measured by the rake probes;  $M_r$  the local Mach number calculated from the ratio  $p_0/p_{tr}$ ;  $\sum_r$  the function  $A/A^*$  of the Mach number  $M_r$ ;  $A_R$  the area of the probing plane.

The rakes are assumed to extend out to the isentropic outer flow.

From this expression we can verify that only those fluid streams having a degraded stagnation pressure contribute to the drag.

The probes on the rake must of course be more closely spaced near the model surface, to correctly measure the boundary layer profile.

Considering the large areas covered by the outer probes on the rake, a small error in the measurement by these probes, results in a significant error in the drag calculation, so special attention has to be paid to validating their measurements.

In addition to the stagnation pressure probes, the rakes include a few static pressure probes, for measuring the pressure profile in the measurement plane.

To account for the pressure deviations from  $p_0$ , a correction is made by adopting the hypothesis of an isentropic development of the flow to a fictitious measurement plane where the pressure is assumed to become uniform again. This is a classical

procedure when studying the drag of an airfoil by analyzing its wake (Betz method).

The possibility that the incidence of the flow in the rake plane might be anything other than zero is neglected. If it were not negligible, it could still be taken into account either by calculating it or by measuring it with yawmeters.

When all of the above precautions have been taken to obtain the best quality measurement, this external probe approach actually yields a very close evaluation of the drag. Its precision can be placed at less than 0.1 % of the total drag of the aircraft.

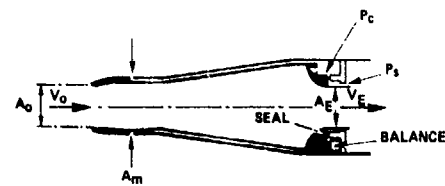
This method is appropriate for an air intake at zero incidence; but when the air intake is set at a modest angle of incidence, the same technique can be applied and still offers a good value for the configuration. But the exact meaning of the term obtained would call for fuller discussion.

#### 4.2.2.5 - Other drag measurement methods

Another way of determining the drag of an air intake is to measure the total internal and external force acting on the air intake and then subtract this from the thrust of the system comprising the captured tube of flow and the inner part of the air intake. The total force is measured by a balance, or by pressure measurements together with an evaluation of the friction, and the thrust is found by a momentum analysis. The difference between the two is the drag.

This approach is favoured for air intakes of complex shapes, or that are integrated into an assembly. It is also appropriate in supersonic tests, where the method using external probes is no longer practical once the external shocks extend far out into the flowfield.

One example of such an approach, applied to an isolated air intake of revolution, is shown in figure 7. This type of setup hinders the representation of the narrowed aft part of the nacelle, more than the first approach did. One difficult problem is the seals between the measured ('live') and unmeasured ('earthed') parts as their stiffness adds to the stiffness of the balance. Evaluating the momentum at the outlet throat also requires special precautions (boundary layer checks, etc.).



$$\text{INTAKE DRAG} = \text{MEASURED FORCE (BALANCE AND BASE FORCES)} + q_m (V_E - V_0) + P_E (A_E - A_0) - P_0 (A_m - A_0)$$

Fig. 7 - Intake drag measurement by a force balance. (E.C. Carter [10]).

Figure 8 shows how the previous test setup was arranged to study the drag of a two-dimensional air intake, or one adjacent to a wall. One of the difficulties encountered of this arrangement was evaluating the base drag precisely, as the base pressure is not uniform. Tests with several throat dimensions did determine the drag variation precisely though, as a function of the flow rate, at different Mach numbers.

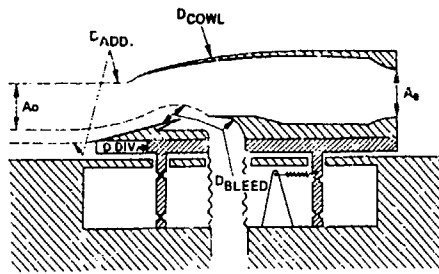


Fig. 8 - 2-D intake drag measurement (ONERA mounting).

The drag divergence limit as a function of the Mach number, which is an important parameter in qualifying an air intake, can sometimes be found by simple pressure measurements on the forward portion of the cowl. According to [12], integrating the external pressures, starting at the stagnation point, yields the suction force compensating the pre-intake drag (Chapter 2 above), and this passes through a maximum, exhibiting a very sharp drop at the divergence Mach number.

#### 4.2.3 - Low velocity air intake tests

##### 4.2.3.1 - General conditions

At the cruising Mach number, the essential parameters are the pressure recovery  $P_R$  and the drag. Under takeoff and landing conditions, though, the important parameters are rather the distortion and the stability of the internal flow. So we are more particularly interested in measuring :

- steady and unsteady internal distortion, in the most critical case of static conditions at take off, in a crosswind ;
- pressure recovery at takeoff ;
- distortion at the incidence and sideslip limits, at takeoff and landing ;
- the incidence limit at which an external separation appears, i.e. a sudden increase in drag, under reduced flow conditions (engine failure during climb).

Tests have also shown that limit conditions of internal or external separations affecting the operation of air intakes in these flight configurations are very sensitive to Reynolds number, and that these limits evolve practically right up to the flight Reynolds number. Figures 9 and 10 [13 and 14] illustrate this. Test facilities capable of reaching high Reynolds number should be used for these studies.

##### 4.2.3.2. - Test setups

Compared with the test setup used at high subsonic speeds, forced suction of the flow is necessary here.

This can be done with a suction pump or with an ejector nozzle, an example of which is given in the diagrams of the Rolls-Royce facilities at Hucknall (Figs. 11 and 12).

In a pressurized wind tunnel, the equivalent effect can also be had simply by discharging the flow to the atmosphere.

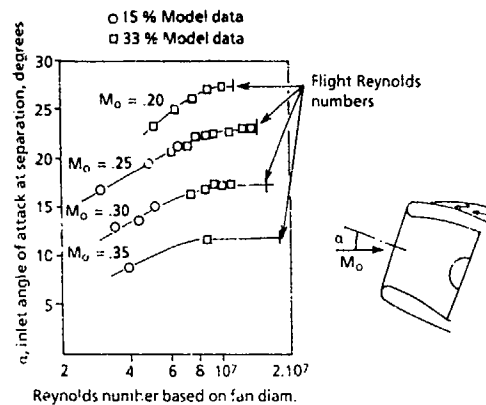


Fig. 9 - Reynolds number effect on angle of attack at upper external lip separation (W. Hoelmer - [13]).

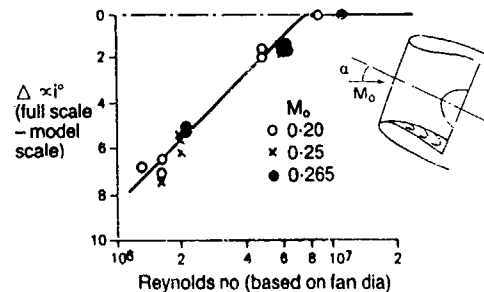


Fig. 10 - Reynolds number effect on angle of attack at lower internal lip separation (D.L. Motyka - [14]).

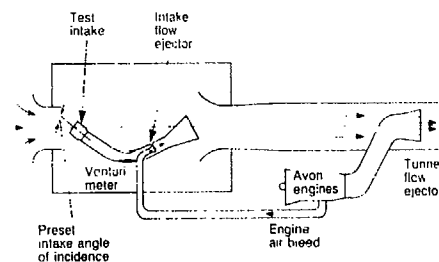


Fig. 11 - High incidence intake test tunnel (Rolls Royce - Hucknall).

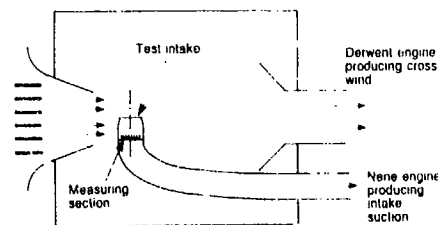


Fig. 12 - Cross wind intake test tunnel (Rolls Royce - Hucknall).

The test setups should also be capable of reproducing high angles of incidence and sideslip, to simulate a crosswind at static (90° sideslip) conditions. Considering the maximum dimensions that could be used to attain high Reynolds numbers, this may lead to two different test setups.

Figure 11 and 12 give examples where the "free jet" technique is also used, to take advantage of a maximum model dimension with a limited amount of wind tunnel power.

Figures 13 and 14, on the other hand, show the two high-Reynolds number setups at ONERA in the low-velocity F1 wind tunnel, operating at 4 bar, at Le Fauga Mauzac [15]. The air intake is supported by an extraction pipe that ejects the captured flow through a swivel joint to the atmosphere. The swivel joint is used to set angles of incidence and sideslip through ranges of 35° and 15°, respectively. The internal diameter at the engine face section is 0.35 m.

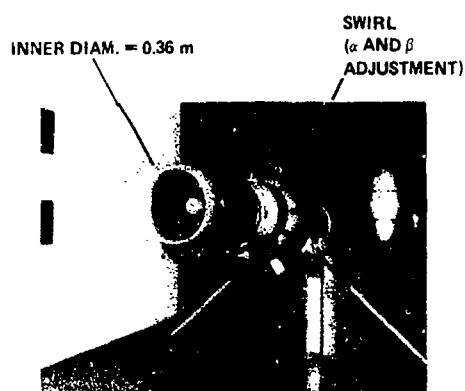


Fig. 13 - Low speed test mounting  
 $\Delta\alpha = 35^\circ$   $\Delta\beta = 15^\circ$  (ONERA - F1).

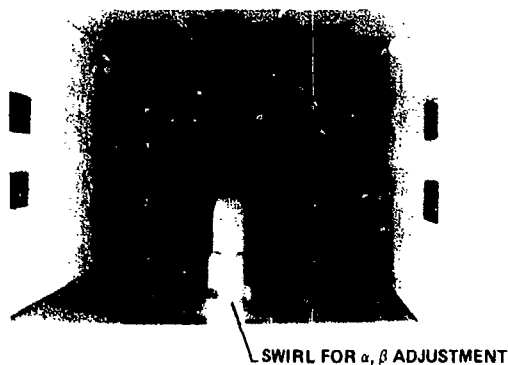


Fig. 14 - Cross flow test mounting

It should be pointed out that areas of hysteresis in the separation and reattachment conditions exist, and that means are therefore needed to vary continuously the different parameters involved - flow rate, angle of incidence; angle of sideslip - to reveal these phenomena.

#### 4.2.3.3 - Engine face instrumentation, and measurement of the distortion

The instruments mentioned for the high subsonic tests can evaluate not only the pressure

recovery  $P_R$ , but also the "steady" distortion of the internal flow.

The forty unsteady pressure probes that are defined later (in section 4.3.2.2) for fighter plane air intake tests may also be used for measuring maximum instantaneous distortion.

It is not easy to incorporate complete steady and unsteady instrumentation without running the risk of choking the internal flow, so special care is needed in defining the supports. Thus, the air intake is often equipped with only some of these dynamic probes, i.e. in the unstable area affected by the separations.

Various distortion indices are often calculated for different engine manufacturers. A few indications and references are given on this subject in Chapter 2 Section 2. The meaning of the indices and of the frequencies to be considered is briefly discussed in references [7] and [8]. The measurement technique is specified later in section 4.5.1.

#### 4.2.3.4 - Flow rate measurement

Flow rate is usually measured by use of a venturi. In the same way as with high subsonic tests, the venturi measurement can be calibrated precisely by replacing the air intake with a sonic throat whose known rate of flow can be ensured under calibration conditions.

#### 4.2.3.5 - Drag measurement

As indicated in section 4.2.3.1, the most useful drag measurement would be the one for an engine failure during a climb, i.e. at low flow rate and high incidence. The external probing technique is not, however, appropriate for a measurement at incidence. Moreover, external separation on the upper part of the nacelle, caused by a reduction in flow rate at high incidence, has more extensive consequences than a simple increase in the specific drag of the air intake. These overall consequences can be measured by testing a complete model equipped with a flow-through nacelle, the natural flow rate of which is sufficient at low velocity to be able to simulate an engine failure.

In the case of an air intake tested alone, we only determine the incidence limit of the increase in drag, or the incidence at which the external separation appears at the reduced flow rate. This phenomenon is generally sharply pronounced, and a measurement by external pressure taps or a few stagnation pressure probes on an external rake is enough to identify it.

It should also be recalled that the limiting incidence can exhibit 'arc' areas of hysteresis, and that it varies until very high Reynolds numbers are reached.

#### 4.2.3.6 - Effect of the aircraft aerodynamic field

The mean local flow conditions at the position of the air intake, which are reproduced in uniform flow in the test of the air intake alone, can be defined by calculations or by local probe measurements on a complete model.

When this seems to be inadequate (because of a non uniform flow field or a wake from a wing upstream, etc.), the air intake has to be tested in its real field. This calls for a partial or complete model of the aircraft, often to the detriment of scale, and thereby of Reynolds number.

Fig. 15 gives an example of such a test in the British Aerospace wind tunnel at Hatfield. This type of test is essentially no different from that of isolated air intakes.



Fig. 15 - Aft engine intake  
with suction test mounting (BAe - Hatfield).

#### 4.2.4 - Nacelle installation test using Turbine Power Simulator (TPS.)

Although these are not actually air intake tests per se, but rather concern the total effect of the nacelle and of the jets on the aerodynamics of the aircraft, they are still closely associated, and it is a technique that is coming more and more into use, which is why we will briefly comment on it here.

The principle is to establish an analysis by way of a series of experiments :

- A calibration test rig measurement of the flow rate and of the TPS thrust, as a function of the parameters determining them, which are the reduced frequency of the TPS ( $N/\sqrt{T}$ ) and the outlet expansion ratio of the fan and primary flows,  $P_{TF}/P_0$  and  $P_{TP}/P_0$ .

This calibration can be used to calculate the thrust of the TPS at the test Mach number, under the TPS operating conditions.

- Possibly a test using an isolated motorized nacelle supported by a strut from the wall of a wind tunnel. The end of the strut simulates the actual pylon holding the nacelle on the aircraft, and forces unit are measured along with the nacelle itself. The difference between the thrust of the TPS and the thrust of the assembly defines the reference drag on the nacelle-strut assembly.
- A test of a "clean" model of the aircraft, i.e. without nacelle.
- A test of a model of the aircraft, equipped with motorized nacelles. The difference between the thrust of the TPS units and the thrust of the motorized model measured by the balance yields the aircraft drag with nacelles included. The difference between this drag and the drag of the clean model yields the drag of the installed nacelles, and the difference between this nacelle drag and its reference drag is the installation drag.

In fact, we often settle for comparing the drags of installed nacelles, while the reference nacelle drag would be either not considered, or evaluated by calculation.

Through these tests may be simple in principle, they do require various corrections :

- The TPS units are driven by compressed-air turbines, which are fed by pipes passing through the balance, the support and the model itself, to the nacelle. This air forms the primary flow of the engine, and is therefore not captured by the air intake the way the primary flow of the real engine is.

The fact of operating with a reduced inflow rate means that the effect this reduction in the flow rate has on the drag has to be evaluated. This can be done by using a model fitted with a flow-through nacelle having an internal drag that is calibrated for two pressure drop grids that will be used to simulate the two flow rates, successively. However, the outer flow is less disturbed if the nacelle has an air intake of reduced dimensions, appropriate for a lower flow rate, which is why this alternative is often adopted. The difference in drag compared with the real air intake is evaluated in the same way, using flow-through nacelles.

- When the external flow modifies the blockage conditions of the jet exhausts, hypotheses have to be adopted concerning the effect this has on the thrust of the model engine, compared to its effect on the real engine. These hypotheses are intricate, and applying them may demand thrust calibration tests on a calibration test rig using variants of the jet exhaust sections.
- The sequence of TPS calibration and force measurement in the wind tunnel operations using balances with compressed air flow-through devices calls for measurements of the very highest quality, and very high-performance balance decoupling systems.
- Experience nonetheless shows that the necessary corrections are still small, that the repeatability of the motorized model tests can be excellent and that the precision sought can be attained.



Fig. 16 - Nacelle installation drag measurement.  
A 340 half model test with TPS (ONERA - S1MA).



More detailed analyses of the principles and techniques of testing models equipped with motorized nacelles are presented in a variety of papers in [16] and [17].

When the nacelles are placed under the wing, the nacelle installation tests are easier to run on a half-model mounted on a lateral wall balance, than they are on a complete model. Figure 16 illustrates a half-model of an Airbus A340 equipped with two motorized nacelles and mounted on the wall of ONERA's S1MA wind tunnel.

#### Section 4.3

#### SUPERSONIC AIR INTAKE TESTS

##### Contents

- 4.3.1 - General aspects
- 4.3.2 - Study of the internal flow
  - 4.3.2.1 - Test setups
  - 4.3.2.2 - Engine face instrumentation
  - 4.3.2.3 - Flow rate measurement
- 4.3.3 - Drag, lift and moment measurements

##### 4.3.1 - General aspects

All techniques for testing air intakes in supersonic flows resemble each other, regardless of whether the aircraft is a civilian transport, a fighter plane or an airbreathing missile.

The fact that a supersonic inlet flow is entirely determined by the domain of influence upstream of the model means that the characteristics of the internal flow can be studied using models of this upstream portion alone. So the scale of the model can be larger than that of a complete aircraft model, and the Reynolds number can be correspondingly increased.

As far as the outer flow is concerned, air intakes are generally very much a part of the complete aircraft design. Though their own drag and lift characteristics do have to be considered - chiefly for defining the upstream profile of the cowl starting at the leading edge of the lip - studying their general effect on the aircraft can be investigated only by force measurement on full aircraft models (with representative captured flows).

Moreover, one of the advantages of supersonic testing is that the ratio between the stagnation pressure of the internal flow and the external static pressure is such that it is easy to capture the natural flow with the intake, and then adjusting and measuring the flow rate by the formation of a sonic throat at the outlet.

##### 4.3.2 - Study of the Internal flow

##### 4.3.2.1 - Test setups

Figures 17 and 18 illustrate a few classical test setups. Figure 19 is a photograph of the test setup used for the Concorde air intakes in ONERA's S2MA wind tunnel. This setup is the one shown in figure 18.

Figure 17 is a typical free-jet test on an air intake alone, to maximize the model scale and thereby take advantage of a high Reynolds number.

These last tests are particularly useful for making preliminary analyses of air intake operation as a function of Mach number, angle of incidence or

sideslip in uniform flow, and for understanding the structure of the internal flow and the effect of various geometric or aerodynamic (e.g. boundary layer control) variations of the configuration.

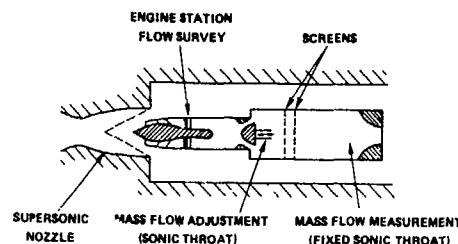


Fig. 17 - Isolated intake high Reynolds number test mounting.

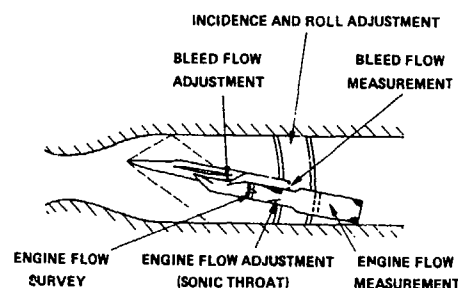


Fig. 18 - Integrated intake test set up.

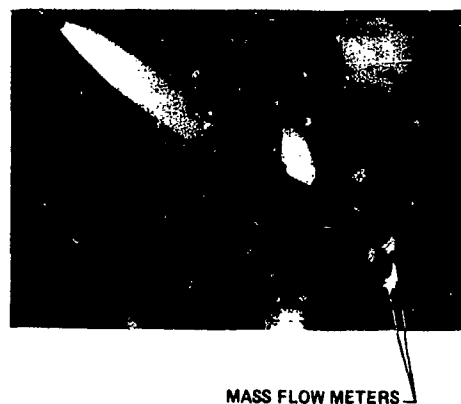


Fig. 19 - 1/15 Concorde intake test (ONERA - S2MA).

Schlieren visualization is a valuable tool for understanding the flow in front of the air intake, and sometimes the internal flow as well, when a two-dimensional air intake is being studied (in which case the lateral walls can be fitted with transparent windows).

Figure 18 shows a test setup used for studying an air intake in the field of the forward part of the aircraft.

The maximum scale is determined by the shock wave rhombus emanating from the apex of the

model nose cone, and within which the air intake must remain in order to avoid any disturbance of the inlet flow by reflections of waves off the wind tunnel walls.

The internal flow ducts in the two diagrams are first fitted with probes to measure the characteristics of the flow at the engine face station, then with flow adjustment equipment (represented here by an adjustable sonic throat, but which could just as well be a nonsonic variable pressure drop such as a butterfly valve), and lastly with a flow rate measurement system, consisting here of a flowmeter with sonic throat.

But frequently, when this system with two throats in series cannot be used because of the dimensional constraints of the test setup or because the internal pressure drops are limited for the sake of ensuring the desired flow, the flow adjustment and measurement functions are provided by the first throat alone, without the downstream flowmeter, as detailed in section 4.3.2.3.

#### 4.3.2.2 - Engine face instrumentation

The instrumentation requirements for defining the pressure recovery  $P_R$  of the air intake are not as strict here as they are for the air intake of a subsonic nacelle. Usually forty stagnation pressure probes distributed over eight radial arms covering equal area sections is enough to determine the mean stagnation pressure at the engine face station, by simple arithmetic mean.

The various steady distortion indices can also be found from measurements taken with the recommended standard rake carrying forty stagnation pressure probes [18].

For the sake of uniformity of measurement, an identical rake of 40 unsteady stagnation pressure transducers is well suited to measuring the maximum instantaneous distortions. Figure 20 shows such a rake with forty unsteady transducers from an ONERA model. These are differential pressure transducers. The gage bridges of the sensors are compensated for thermal drifts, so that the absolute value of the difference from the reference pressure can be measured precisely and the pressure recovery, the mean distortion and instantaneous distortion can all be measured by the same instrumentation.

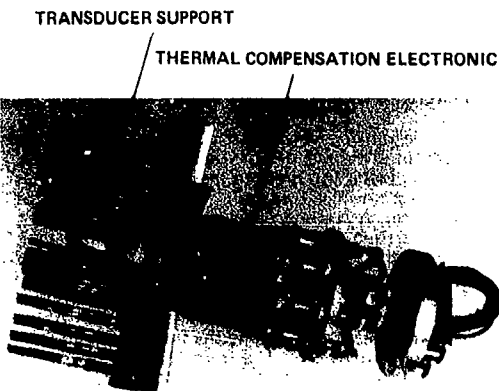


Fig. 20 - Engine face unsteady pressure rakes (ONERA).

In other cases, where unsteady transducers without special equipment cannot give a precise measurement of the absolute value of differential pressures, a stagnation pressure probe (whose mean

value is measured in the usual way) is associated with each unsteady transducer, for which the steady component is suppressed.

Various methods have been proposed for estimating the unsteady distortion from a smaller number of measurements. A very detailed discussion can be found in [19] and [20]. There is even a 'rule of thumb' correlating the unsteady distortion with the mean internal stagnation pressure drop of the air intake starting at the diffuser, in which case no unsteady measurement is made [20].

The way unsteady measurements are processed is commented on in section 4.5.1.

With aircraft that have engine inlet guide vanes, it has been felt up to now that we have only to know what the stagnation pressure distortion is at the engine inlet plane, in order to predict the effect the air intake has on the engine surge limits.

The particular case of the Tornado equipped with the Rolls Royce RB 199 engine, which has no such inlet guide vanes, has underscored the need to take the rotational aspect of the inlet flow into account.

Sixteen directional five-hole probes were used for this.

Figure 21 shows three examples of engine face probe configurations adopted by British Aerospace and MBB as part of a fighter intake design programme.

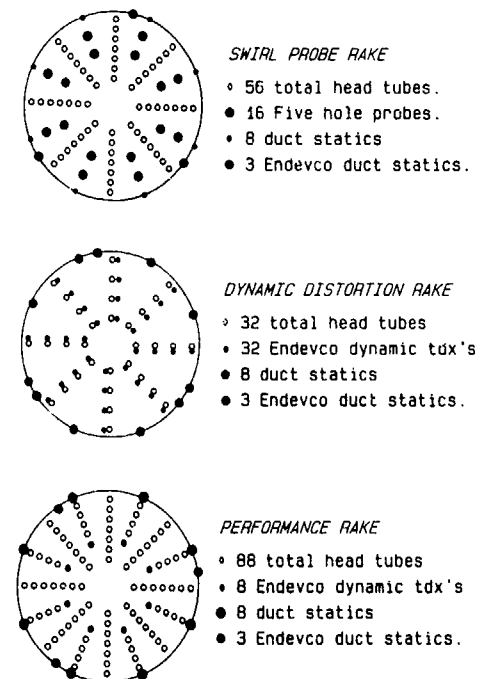


Fig. 21 - Dynamic and steady distortion rakes (British Aerospace - Warton divn).

In fact, as recommended in [21], the differences in relative incidence of the engine face fluid stream with respect to the rotating blades - i.e. the differences that give rise to the distortion effect - should normally be considered from a global point of view, by combining the flow deviation measure-

ments with the local deviation measurements found by measuring the stagnation pressure fluctuations and converting to axial velocity fluctuations. Such elaborate combinations have not yet been adopted.

One indicator has been proposed in [22], that quantifies the rotational deviation alone. It is defined analogously to the DC 60: the circumferential component of the velocity, divided by the axial velocity and averaged through a 60° sector yielding the mean maximum value, defines the DS 60 distortion index.

#### 4.3.2.3 - Flow rate measurement

When test conditions allow a flowmeter to be used as illustrated in figures 17 and 18, the flow rate can be measured directly and precisely this way. The determination uses the supposedly uniform static pressure, measured in the settling chamber of the flowmeter with a tap in the wall surface, and also depends on the calculated sonic section of the outlet throat. The stagnation temperature in the flowmeter is assumed to be equal to the stagnation temperature upstream, in a continuous wind tunnel. If heat transfers have to be considered, e.g. due to the flowmeter settling chamber grids, which may be at a different initial temperature from the upstream stagnation temperature in a blowdown wind tunnel, then the stagnation temperature in the flowmeter should be measured by use of thermocouples.

The sonic throat is calculated using the curvature of the throat profile and the boundary layer evaluation at the throat, which go into making the coefficients CDK and CD8 applied to the geometric cross section of the throat.

These calculations are discussed in [11].

Figure 22, which is constructed on the basis of references [23] and [24], gives the value of CDK as a function of the radius  $h$  of the throat section, divided by the radius  $R$  of the profile. An  $h/R$  value of 0.25 is sometimes chosen because the result is then a rather short throat, but one that has a small enough curvature for the calculation still to be exact. The corresponding CDK coefficient is 0.9987.

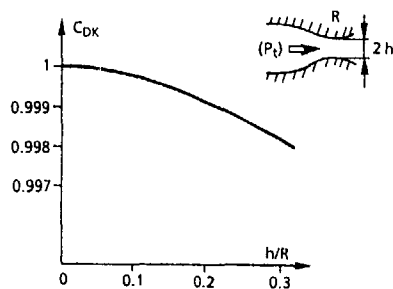


Fig. 22 -  $CD_K$  - sonic throat striction coefficient due to the throat curvature.

Figure 23 gives the value of CD8 calculated according to the hypothesis of a turbulent boundary layer. This formula is established on the basis of a boundary-layer similarity law at the throat, in [25], and by systematic calculations according to [26]. The results agree well with the calculation results reported in [27].

For  $h/R = 0.25$ , the indicated CD8 is  $1 - 0.045 (a_t/v_t)^{1/6}$ , in which  $a_t$  is the speed of sound and  $v_t$  the kinematic flow viscosity  $\mu_t/\rho_t$ , under the stagnation conditions of the flow through the flowmeter.

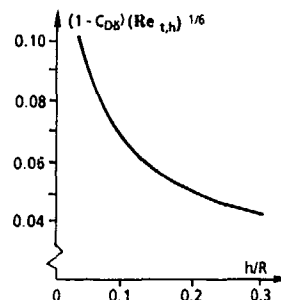


Fig. 23 -  $CD_8$  - sonic throat striction coefficient due to the boundary layer.

We also find [26] a formula for a Viriel-effect CDV coefficient, or real gas effect which comes into play when the pressures are high:

$$CDV = 1 + \frac{0.035 P_{t(atm)}}{T_{t(k)} - 210}$$

We can also use a sonic throat following the standard forms of ASME nozzles, with zero curvature at the throat [28]. The effect of the nozzle curvature is in this case neglected, and the boundary layer effect is calculated by the coefficient  $CD = 1 - 0.184 Re_t^{-0.2}$ , in which  $Re_t$  is the Reynolds number calculated using the throat diameter and the local flow conditions at the throat.

Comparisons made between measurements by two types of sonic throat exhibit differences of a few thousandths of measured mass flow and which are essentially due to uncertainties in the boundary layer calculation (throat relaminarization problems have not yet been solved by calculation).

When the test Mach number is not high enough (e.g. at transonic Mach number) for the flowmeter throat to be choked, or when the pressure loss accompanying a sharp reduction in the flow rate leads to an unchoking of the throat, the same setup can still be used, with the flowmeter throat then being considered like a venturi.

To measure the flow in this case, the static pressure at the throat also has to be measured. The flow rate can again be evaluated by a flow calculation; but it is preferable to use a calibration, by placing the flowmeter being studied in series with a reference flowmeter, in a separate installation.

When the very presence of the flowmeter is unacceptable (because it is too large, or the internal pressure loss is too great to insure the mass flow, as for example in a transonic test at high angle of incidence), it is done away with. The first throat, which is used to adjust the rate of flow, can then serve as the flowmeter sonic throat, as long as it is choked. The static pressure measured in the internal flow duct upstream of the throat is the second parameter measured (the first being the throat sectional area) to determine the flow rate, using the same hypothesis of a constant stagnation temperature from upstream, in adiabatic flow.

Reference [29] gives diagrams of conic plugs that can be adjusted by translational motion, along with data for the aerodynamic throat areas of the corresponding passages and the expansion ratios needed for choking.

A standard RAE test cell using such a conic plug is presented in figure 24.

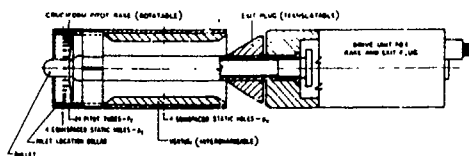


Fig. 24 - Unit for measuring mass flow and pressure recovery (RAE) - [29].

The fact that there is no settling chamber upstream of the throat, and that the aerodynamic definition of the throat is not as certain in this configuration, makes the flow measurement less precise; but again, this precision can be improved by a calibration where the flow rate is measured precisely, upstream or downstream. However, the measurement is sensitive to the inlet distortion, which cannot be simulated perfectly in a calibration test.

If the throat between the exit nozzle and the plug is not choked, the pressure ratio across the exit is used to calculate the mass flow, on the basis of calibration data. This ratio is defined as the ratio of the ambient external pressure to the flowmeter pipe static pressure. In such an unchoked flow condition, flow fluctuations have been observed in reference [30], which seem to be induced by a flow separation at the exit nozzle. Suggestions were made to avoid these fluctuations by use of a sharp-edged exit.

When the downstream throat can no longer be choked and the flow profile is not uniform, the recourse is to measure the flow rate by integrating the elementary flow rates calculated for the engine face, using the stagnation pressures measured by the rakes, and the static pressure found by measuring the pressures at the wall surface. The precision then depends on how finely the measurement section is explored. The method can again be calibrated, to refine the result. A precision of 1 % has been claimed [31] when a detailed exploration is made using a rotating rake and a flow matching hypothesis for the wall boundary layers.

#### 4.3.3 - Drag, lift and moment measurements

The external aerodynamic forces are measured according to the same principle as the overall method described in section 4.2.2.5, i.e. by overall force measurement of the model or of the model element considered, and then subtracting the resultant of the "internal" forces evaluated from the freestream section of the captured tube flow back to the outlet section of the same flow. These internal forces are calculated from a momentum balance between the outlet, where the flow characteristics are given by the measurements, and the freestream, where the momentum is determined from the flow rate (measured at the outlet).

Two types of tests are generally run. The first is a large-scale test of the air intake alone, or with the forward part of the aircraft including the air intake and the upstream part of the outer fairing. The purpose of this is to study the local effect of the various elements used in adjusting the geometry of the air intake, of the various boundary layer bleeds and of the flow rate. These tests require as representative as possible a Reynolds number, and a precise definition of the configuration. The second type of test is a small scale test of the whole aircraft, in which the model is equipped with the air intake operating at the nominal flow rate, to evaluate the overall characteristics of the aircraft and possibly verify the effect of a few geometric variations.

Figure 25 shows the principle of a test in which force measurements on the forward part of the aircraft are made. The difficult problem is the stiffness of the joint between the 'live' and 'earthed' parts, and how to evaluate the internal momentum at the junction, which is calculated from the probe measurements of the flow at the engine face. As the flow rate is also measured elsewhere, an adjustment can be defined for the probe measurements, to obtain the same flow rate by local integration, and using this adjustment to refine the momentum measurement.

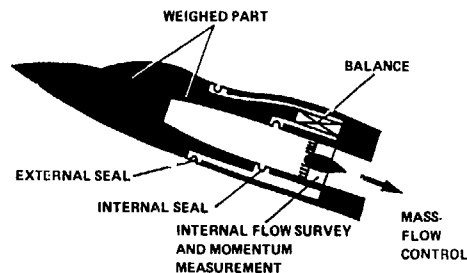


Fig. 25 - Internal flow survey and force measurement model.



Fig. 26 - 1/4 scale Rafale intake model in S2MA wind tunnel (ONERA).

The absolute precision of this measurement is nonetheless uncertain when the flow is not uniform at the engine face; but this can be accepted when we limit ourselves to comparing similar configurations, which is often the objective in such tests.

Figure 26 is a photograph of a test of the Rafale air intake on a 1:4 scale model in ONERA's S2MA wind tunnel, a test run according to the principle of figure 25.

Another solution using the same principle consists in limiting the model to the cutoff plane considered, which becomes a base plane. The whole assembly is then metric and avoids the problems of the seals, but no longer benefits from a downstream flowmeter to refine the measurement of the momentum and of the internal drag. It also requires a precise measurement of the base drag.

A non metric adjustable plug can be placed at the outlet of the captured flow duct to adjust the flow rate, (Fig. 27). In this case, the momentum is

evaluated a little upstream of the plug by measuring the static and stagnation pressure in a part of the duct where the flow is still cylindrical, and the internal drag evaluated on the basis of this momentum has only to be corrected for the drag of the cylindrical element of the tube downstream from the measured static pressures to the outlet section. This is a small friction term, found by calculation.

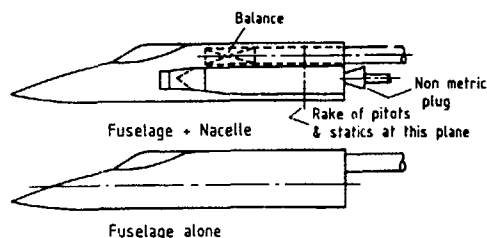


Fig. 27 - Intake and nacelle drag measurement using a non metric plug (RAE) - [29].

The flow rate measurement is calibrated on a separate setup, to refine the measurements.

The photograph in figure 28 shows a model in the ARA transonic tunnel using this principle.

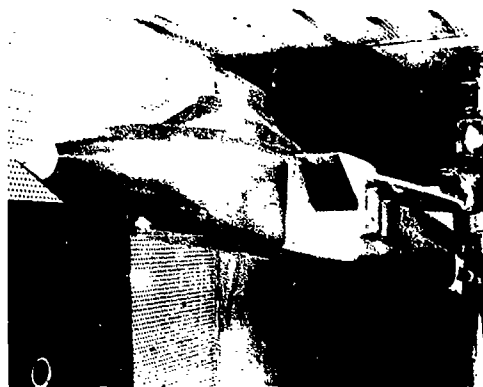


Fig. 28 - Typical arrangement for intake spillage drag measurement (Rolls-Royce/ARA).

A full model is measured in a similar way, with the air intake flow rate represented. The cutoff plane is simply the base of the aircraft. In these measurements, though, we are not generally concerned with the effect of adjusting the flow, which is studied on a partial model. So the internal tube of captured flow terminates at the base with a cylindrical nozzle forming a nonadjustable throat, and allowing the maximum flow rate. A test can be made with a reduced flow rate, if necessary, using a nozzle of lesser sectional area.

The principle of the setup used for testing and for calibrating the flow rate of the outlet throat is given in figure 29.

An error calculation, using  $M_0$  and the Mach number at nozzle exit area, is reported in [29] and [32]. This calculation indicates that a sonic nozzle is less sensitive to an error in the evaluation of the outlet conditions at Mach numbers  $M_0$  of the order of 1.5 to 2.5. At these Mach numbers, the condition of a sonic outlet is generally satisfactory in the above tests.

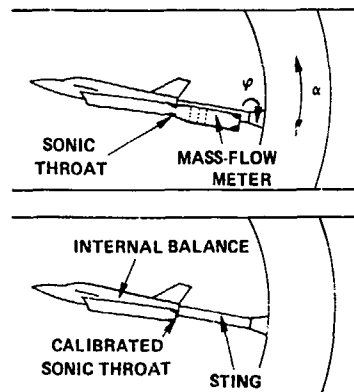


Fig. 29 - Complete model drag measurement.



Fig. 30 - 1/7 scale Rafale with internal flow for force measurement (ONERA - S1MA).

#### Section 4.4

##### TRANSONIC AND SUBSONIC TESTS OF FIGHTER PLANE AIR INTAKES

The special feature of these tests is that they cover a broad range of angles of incidence and sideslip.

Also, in subsonic tests, the aerodynamic field ahead of the air intake is affected by the entire aircraft; so if we want to analyze the characteristics of the internal flow precisely, it is no longer sufficient to test models that represent only the air intake and the forward part of the aircraft;

This means we have to test complete models. However, by comparing full-model tests with partial-model tests, we can still define Mach number and angle of incidence conditions for the partial models that will bring their test results rather close to those of the full model, since the effect of the rear parts of the aircraft are comparable, in a first approximation, to a far field that globally affects the upstream flow conditions.

Then again, testing full models at high angles of incidence in transonic flows places a severe limit on the scale of the models, because of the flow choking problems, and justifies the recourse to large wind tunnels.

To give an example, a 1:7 scale model of the complete Rafale, with a wing span of 1.5 m, is tested in high subsonic flows in the S1MA wind tunnel (a porous test section with a 40 m<sup>2</sup> sectional area, Fig. 30). The same model, but without the wings and with the canard surfaces truncated, can be tested in the S2MA wind tunnel, in a porous transonic test section with a cross sectional area of 3 m<sup>2</sup>.

How these models are instrumented for testing and characterizing the internal flow was spoken of in the section on supersonic tests.

At low velocity, the range of angle of incidence for fighter plane tests may go beyond 90°. Conventional test setups with their stingholder sectors adapt poorly to such angles, and a floor pivot with integral supports is more generally used.

The diagram in figure 31 shows just one such test setup, allowing continuous adjustments at angles of incidence from -20° to +200°, and sideslip angles from -20° to +20°. This is in the 4.50 m x 3.5 m test section of ONERA's F1 wind tunnel. This tunnel is pressurized, and the flow is provided by simply discharging the captured flow to the atmosphere. The evacuation pipe is designed with a pivoting elbow to adjust the sideslip, and a rotary joint centered on the turret to set the angle of attack.

Figure 32 is a view of another test setup on the wall pivot of the British Aerospace atmospheric wind tunnel (2.7 m x 2.1 m) at Warton. The air intakes are connected by hoses to ejectors.

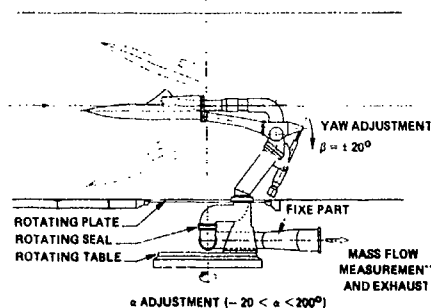


Fig. 31 - Low speed test set up for high angle of incidence and yaw (ONERA - F1).



Fig. 32 - Low speed high incidence test set up (British Aerospace, Warton).

## Section 4.5

### SPECIAL TEST DEVICES

#### Contents

#### 4.5.1 - Unsteady flow distortion acquisition system

##### 4.5.1.1 - Complete measurement

##### 4.5.1.2 - RMS analysis

#### 4.5.2 - Intake flow dynamic study

#### 4.5.3 - Complete internal flow probing

#### 4.5.1 - Unsteady flow distortion acquisition system

##### 4.5.1.1 - Complete measurement

The distortion indices come from the forty unsteady pressure transducers of the engine face rakes.

The highest frequency to be considered is of the order of 1000 Hz at scale 1 ([7], [2]), and must be divided by the model scale.

One way of obtaining a particular distortion index is to build an analog computer which delivers a signal proportional to the desired distortion index.

The advantage of this is that it provides the result in real time, which is very useful for monitoring a test program on the basis of the actual results.

Such analog computers are widely used, but they are unfortunately limited to the one distortion index for which they were designed. Then, as a complement, the transducer signals are usually recorded on magnetic tape for off-line complete analysis (to calculate the other distortion indices or to generate a sequence of instantaneous total pressure maps, etc.). It is not easy matter to synchronize the recording and readback of the forty channels, though. Better performance can be obtained with a PCM (Pulse-Code Modulation) record.

The distortion indices can also be computed digitally using analog-digital conversion with a suitable computer (array processor). A typical analog-digital measurement system is shown in figure 33 (British Aerospace Warton Division).

What is required first are the maximum values of the various distortion indices, which are recorded during a given length of time of the order of 1 minute at scale 1 ([7], [8]), for various flight conditions which initiate a high internal flow distortion.

The recorded distortion can be analyzed statistically to define those maximum values according to a given probability [33].

A detailed analysis of the instantaneous flow (pressure maps) may also be of interest ; but considering the volume of data, a selection must be made. This selection is based on the measured distortion indices. A conditional "quick acquisition system" has been developed at ONERA that limits the selection on the basis of a particular distortion index measured by an analog computer. This system gives a first evaluation of the various distortion indices in real time, and delivers a few selected instantaneous pressure maps (Fig. 34). A PCM is also provided for fuller off-line analysis.

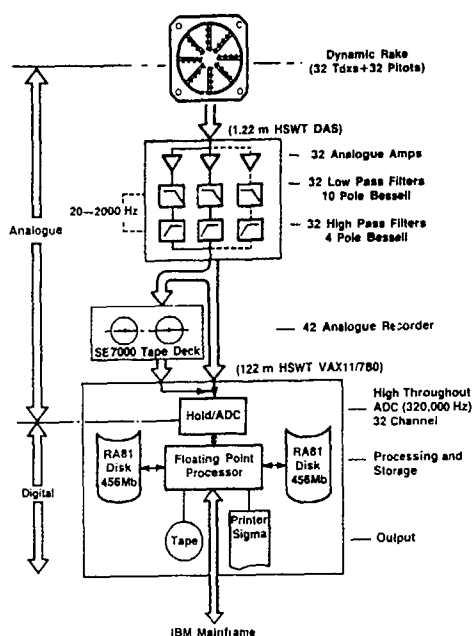


Fig. 33 - Dynamic distortion instrumentation package (B.Ae).

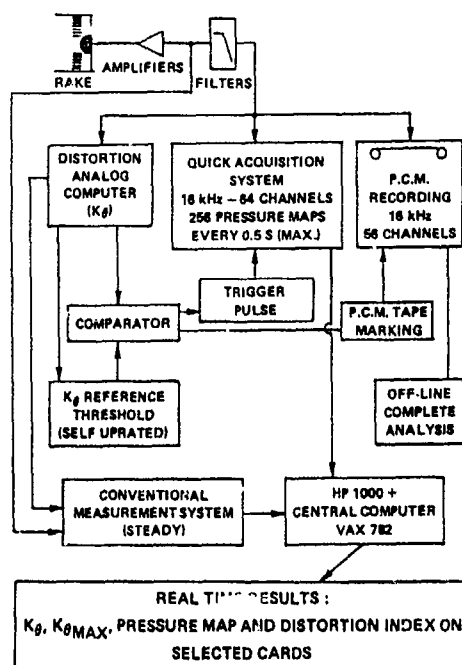


Fig. 34 - Unsteady distortion measurement, with conditional real time acquisition (ONERA)

A similar system is used at AEDC named DYNADEC (Dynamic Data Editing and Computing). (Figure 35) [19] - [34]:

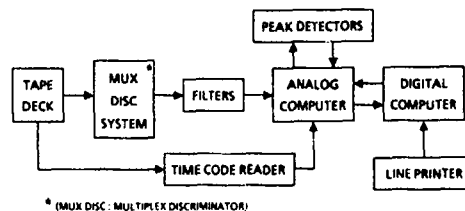


Fig. 35 - Block diagram of DYNADEC (U.S. Air Force) - [19 - 34].

The high response pressure transducer outputs are multiplexed and recorded on 14 track analog tape. The multiplexed pressure signals are fed into a 96 channel discriminator system which demultiplexes the data signals. Each pressure is filtered to account for model scale and engine sensitivity. The filters are AC coupled and therefore remove any steady state component or DC bias that might be present on the tape. The fluctuating pressures are sent to the analog board where they are gain-compensated to account for the individual pressure transducers response characteristics. Each fluctuating pressure is then combined with its steady state value to form the total pressure signal. These pressures and other parameters are used in the continuous solution of the engine distortion parameter equations on the analog computer. The screening parameter is fed into a peak detector network. Peak values of distortion above a preset threshold level generate a logic signal to hold the peak value of the screening parameter and the accompanying level of all other distortion parameters being computed. These parameter values and the time at which the peak occurs are transferred and stored in the digital computer. In addition, the compressor face total pressures for the maximum peak distortion level are held and stored for developing the pressure contour map at the conclusion of the screening of the data record.

#### 4.5.1.2 - RMS analysis

If no analog computers or high speed acquisition systems are available, a first estimate of the various distortion indices can be made, based on the only measurement of the RMS values of each individual total pressure probe of the rake

Such a simple process is defined in [35], based on an analytical study assuming a random distribution of discrete vortices.

A still simpler method is proposed in [36], by assuming a time random fluctuation of the individual total pressure probes.

The same method, named "statistical model" has been applied, and some improvements have been developed [19] - [37 - 38 - 39], the details of which are presented hereafter, issued from [19].

The basis for the statistical model development is that a synthesized fluctuating component can be constructed and added to the steady state pressure to form the dynamic total pressure. The fluctuating pressure is assumed to be stationary and random with a normal distribution.

The synthesized fluctuating pressure can be determined for each probe using a random number generator with a zero mean and the standard deviation derived from the measured turbulence levels.

The dynamic total pressures are input to the distortion parameter equations and the level is determined. The pressure distortion map is also generated. Forty new random numbers are then generated, providing a new set of dynamic total pressures that represents data from another equivalent time slice. The new distortion level is computed and compared to the current maximum value.

The calculated pressure levels from the higher distortion map are retained and the sequence is repeated until the appropriate sample size is reached.

When this point has been reached, the set of pressures which produced the maximum distortion level will have been retained, similarly to the DYNADEC procedure.

The improved statistical model is schematically represented in figure 36. The rms turbulence and random numbers are combined, as in the basic method. However, these synthesized pressures are now input into the two digital filters added to the basic model. The first filter provides a slight amplitude rolloff with frequency over the entire power spectrum (as inlets tend to do) and the second filter accounts for engine sensitivity. The second filter's output is the filtered, synthesized fluctuating pressure component that is added to the steady state pressure to form the dynamic total pressure. The dynamic total pressures are input to the distortion parameter equation where the distortion level is determined. Forty new random numbers are generated, providing 40 filtered dynamic pressures for another equivalent time slice. The distortion level is then computed and compared to the current maximum value. The larger value is retained, as well as the pressures for the distortion map. The sequence is repeated until a desired sample size is reached which is based on cutoff filter frequency. The entire solution is then restarted with another set of random numbers. The average maximum distortion map is achieved by repeating the entire solution process several times with different sets of random numbers to generate several maximum distortion maps. Individual probe pressures from the several maximum distortion maps are summed and averaged. In this way, the resulting 40 averaged pressures represent the data for the most probable or average maximum pressure distortion map.

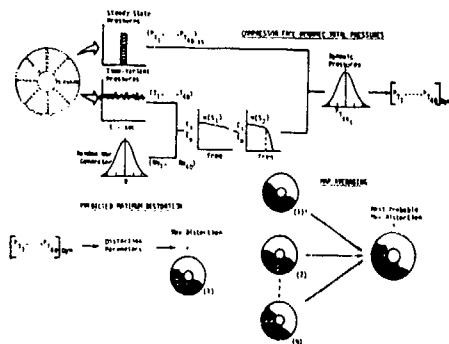


Fig. 36 - Improved statistical model [19 - 38 - 39].

An example of the statistical method capability is presented in figure 37.

Both the experimental and synthesized fluctuating pressure data are based on filtering the raw data at a frequency of 500 Hz.

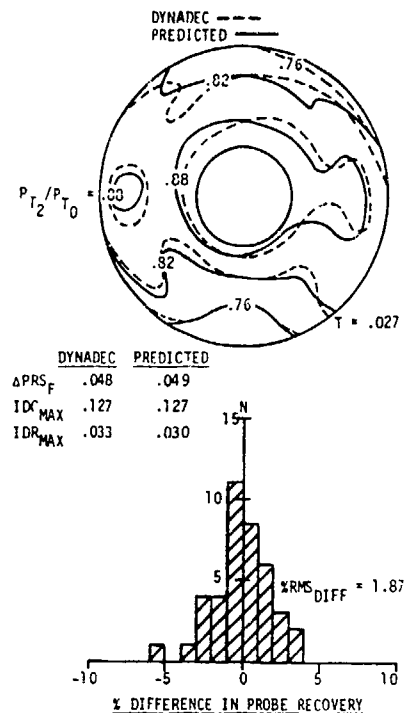


Fig. 37 - Pressure contour map and histogram, moderate turbulence, 40 turbulence measurements [19].

Excellent agreement has been achieved between the predicted and measured contour map and total distortion levels, including the circumferential and radial components. The distribution of probe recovery difference (the histogram) shows that 29 probe pressures are within  $\pm 2\%$  of their measured values, while the range has decreased from 17% for the basic model to 10% for the improved model. The rms difference for the 40 probes is 1.87%, a 44% improvement over results from the basic model.

As mentioned in section 4.2.3.3, a discussion of various processes is included in references [19] and [20].

#### 4.5.2 - Intake flow dynamic study

To design a control system for a variable-geometry air intake, the dynamic characteristic of the internal flow has to be studied. It is also important to identify the level of the wall pressure rise, in transient flow, for the design of the intake structure.

To perform such a study, high speed rotating vanes can be installed at the compressor face station to produce a periodic variation of the reduced mass flow. The intake is equipped with unsteady transducers which measure the amplitude and the phase lag of the pressure waves.

A sketch of such a device is reproduced in figure 38 [11]. There, to simulate the surge of the engine, a negative mass flow was periodically injected by compressed air supplied through the vane, as shown in the sketch. A good simulation of the engine surge phenomenon and its effect on the adjacent air intake was obtained, as indicated by the pulse traces shown in the figure, compared with the flight result.



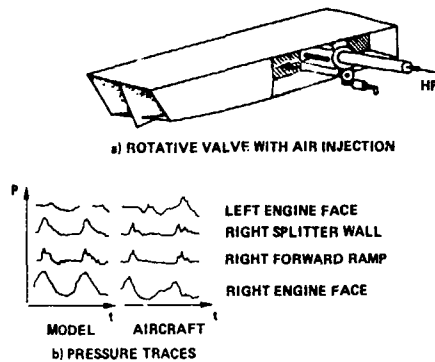


Fig. 38 - Engine surge simulation device  
(E.C. Carter - [10]).

The sudden stall of an engine and the resulting "hammer shock" in the intake duct has also been simulated the same way, but a pyrotechnical device was used to close the vane fast enough.

A similar device is presented in figure 39 [40]. A rotating hollow cylinder having spanwise slots 180° apart rotates around a hollow shaft with a forward facing slot. The shaft is fed with high pressure air.

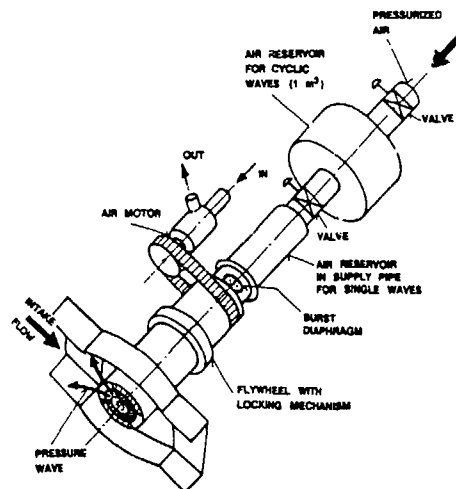


Fig. 39 - System display of MBB  
surge wave generator [40].

On that device, the suppression of the rotating butterfly vanes avoid intake flow degradation during valve acceleration.

To allow a single pressure wave to be simulated, a bursting diaphragm is installed in the supply pipe, and the valve is locked in the open slot position.

#### 4.5.3 - Complete internal flow probing

A detailed analysis of the whole internal flow may be of use in checking the validity of the CFD flow prediction, or to guide an experimental approach to flow improvement.

Figures 40 and 41 show an internal probing system developed at ONERA. The device can support

various types of probes (pitot, five-hole directional probe, hot-wire, etc.). By combining the three movements of the support, the probe can explore the all entire volume of the intake duct.

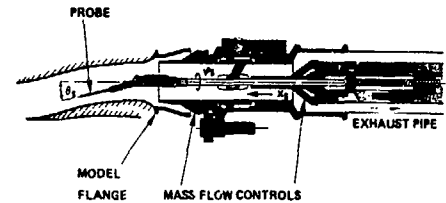


Fig. 40 - Internal probing device.

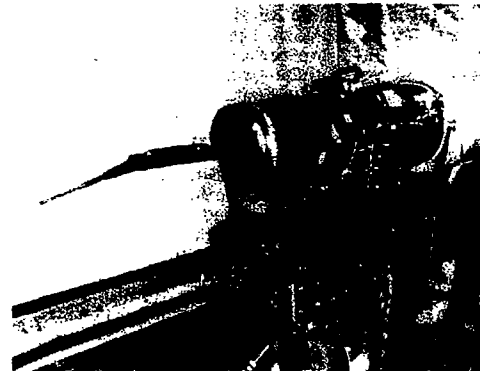


Fig. 41 - Probing device on checking bench (ONERA).

The displacement of the probe is programmed on a computer before the test, and is controlled automatically. It can explore successive cross sections, for each of them, along lines homothetical to the contour of the section - or it can follow a streamline through the duct, for instance, when studying the decay of the turbulence components.

### Section 4.6

#### MEASUREMENTS IN THREE EUROPEAN WIND TUNNELS AT SUBSONIC AND SUPERSONIC SPEEDS OF DYNAMIC DISTORTION AND STEADY STATE PERFORMANCE OF AN AXISYMMETRIC PITOT INTAKE

##### Contents

- 4.6.1 - Introduction
- 4.6.2 - Model geometries
- 4.6.3 - Instrumentation
- 4.6.4 - Test programmes and test conditions
- 4.6.5 - Data reduction and presentation
- 4.6.6 - Comparison of results
  - 4.6.6.1 - At subsonic speeds
  - 4.6.6.2 - At supersonic speeds
- 4.6.7 - Results unique to ONERA and DLR tests
- 4.6.8 - Repeatability study at RAE

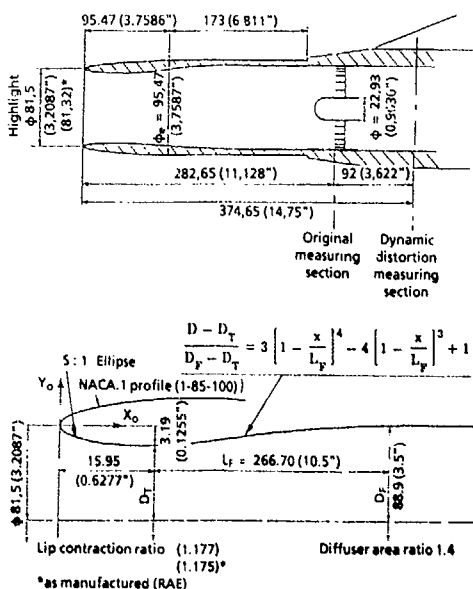
#### 4.6.1 - Introduction

Models to a common design have been manufactured in Britain, France and Germany to slightly different scales and tested in the 8' x 8' (2.44 m x 2.44 m) tunnel at the RAE (Bedford), the S2MA (1.75 m x 1.75 m) tunnel at ONERA (Modane) and the 1 m x 1 m tunnel at DLR (Göttingen). The common design (RAE Model 742L Cowl 2) is a simple subsonic-type pitot intake with a circular cross section and a blunt lip. The slightly different scales are necessary so as to fit to existing engine face instrumentation available (as supplied by MBB in the case of DLR) to the three tunnels. This resulted in engine face diameters of 88.9 mm (RAE) 94.18 mm (ONERA) and 107.36 mm (DLR). Although each contributor had a basic common engine face rake of 40 unsteady total pressure probes, each wind tunnel used its own nationally available instrumentation, data recording and data reduction systems. Further details of the model geometry, engine face instrumentation and data recording and reduction systems are given in 4.6.2 and 4.6.3.

The measurements include steady state values of the usual intake parameters such as pressure recovery, engine face flow distortion and intake mass flow as well as dynamic distortion of the flow at the engine face. The main aim of the tests has been to establish the dispersion of the steady and unsteady results at common test conditions.

The tests have concentrated on a common condition of incidence variation ( $0^\circ$  to  $25^\circ$ ) at  $M_0 = 0.8$  in all three wind tunnels. However other test conditions, principally change of free stream Mach number both at subsonic and supersonic speeds (up to  $M_0 = 1.8$ ) and change of Reynolds number have been made in two of the three wind tunnels.

Unfortunately due to lack of time within the WG13 reporting schedule it has not been possible to analyse completely the results from all the tests made. There also has been no time to identify the possible reasons for the source of the dispersion of the processed results that have been presented. This will be done and presented in a paper to the AGARD FDP Symposium on Aerodynamic Engine/Airframe Integration to be given at Fort Worth USA 7th - 10th October 1991.



#### 4.6.2 - Model geometries

The common model geometry was that of RAE Model 742L, Cowl 2. External and internal static pressures and steady state performance on this model was measured in 1983 and 1984 at the RAE and the ARA over the Mach number range 0.2 to 2 and incidence range  $0^\circ$  to  $40^\circ$ . This used an earlier version of the engine face instrumentation and was reported in refs. [41]-[42]. The earlier version of the engine face rakes had no dynamic pitot probes, had a bullet in the centre of the rake and was positioned upstream of present engine face rakes (Fig. 42). Details of the common lip, external cowl and diffuser shapes are shown in Fig. 42.

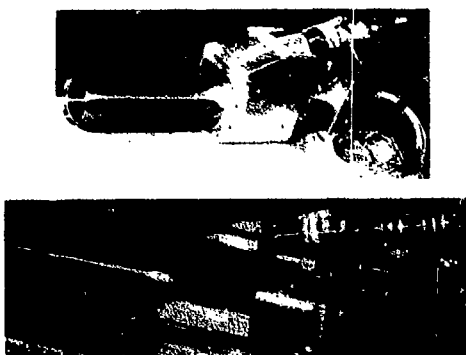
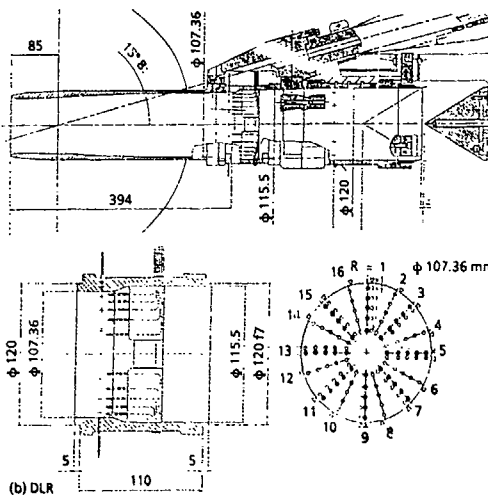
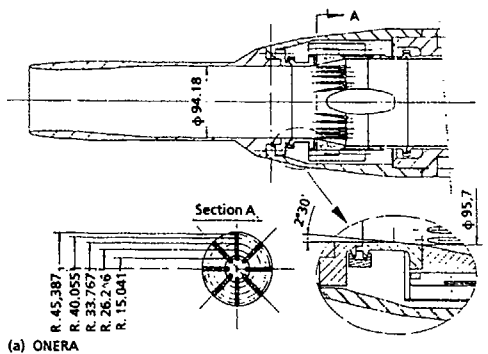


Fig. 43 (a) & (b) - ONERA and DLR models.

Fig. 43 (a) (b) & (c) shows longitudinal cross sections and photos of the three national models together with details of the engine face pitot probes. The small variation in absolute size of the models, the variations in rake geometry and duct geometry downstream of the measurement plane are evident. Fig. 44 (a) (b) & (c) show the outline of the models in relation to the supporting sting, tunnel quadrant and tunnel walls.

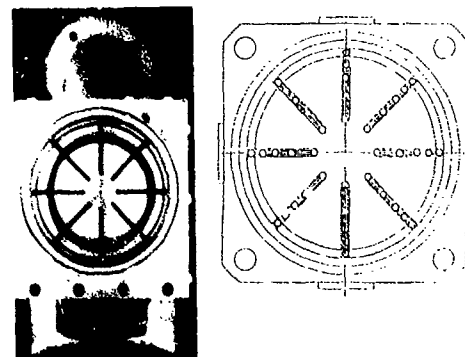
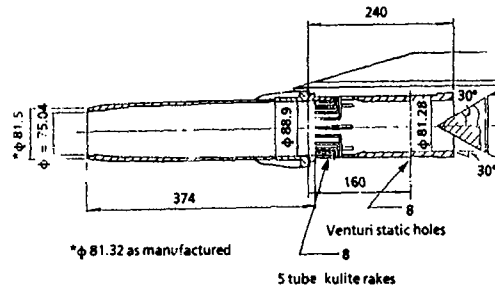


Fig. 43 (c) - RAE model.

#### 4.6.3 - Instrumentation

The form of the engine face instrumentation used by ONERA (Fig. 43 (a)) and RAE (Fig. 43 (c)) was similar. The only total pressure probes (used for both steady and unsteady measurements) were 40 Kulite transducers arranged 5 per arm in an 8 arm rake. DLR (Fig. 43 (b)) used a similar Kulite rake for the unsteady pressure measurements but steady state

measurements were made using 80 normal pitot tubes placed in 16 arms, 8 adjacent to the Kulite tubes and 8 interdigitated between them. The 80 pitot tubes were connected to individual PSI transducers arranged in groups of 32.

RAE and ONERA used 2.36 mm diameter  $\pm$  5 psi differential transducers together with a backing pressure near to the average total pressure in the duct.

The choice of only 40 probes at the engine face results in less blockage than if the probe quantity is doubled to accommodate simultaneous steady state measurements. Preliminary experiments at the RAE also indicated a superior accuracy for steady state values that are obtained by time averaging the DC coupled individual Kulite recordings over the use of adjacent pitot probes linked to one or two transducers via a Scanivalve system. Table I gives results from a preliminary investigation made on a different intake model for two conditions where considerable dynamic activity was present.

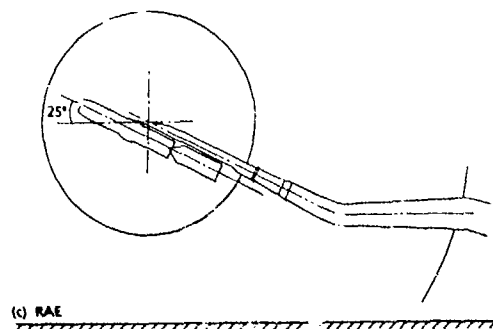
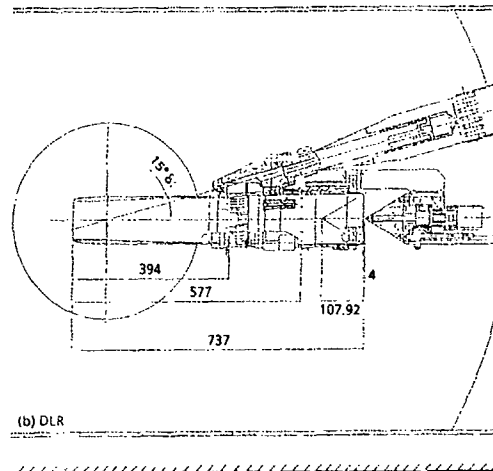
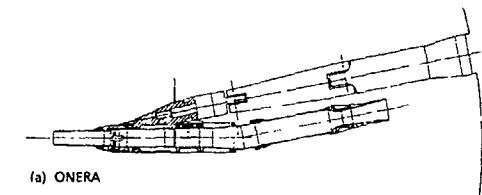


Fig. 44 (a), (b) & (c) - Models installed in ONERA, DLR & RAE wind tunnels.

Table 1 - Repeatability of DC90 measurements.  
DC90 values

M = 0.80 $\alpha = 40^\circ$ Repeat	Pitot tubes and scanis.	Kulites	M = 1.8 $\alpha = 5^\circ$ Repeat	Pitot tubes and scanis.	Kulites
		Time average			Time average
1	0.377	0.384	1	0.240	0.261
2	0.366	0.387	2	0.255	0.259
3	0.368	0.393	3	0.261	0.263
4	0.396	0.393	4	0.239	0.262
5	0.367	0.389	5	0.226	0.265
			6	0.269	0.260

Details of the pressure instrumentation and the data recording and signal conditioning systems follow under the headings of the different national centres.

#### (a) RAE

There was no bullet in the centre of the duct, the 8 rakes were inserted and supported from the duct wall Fig. 43 (c). The duct downstream of the rakes was unobstructed until the exit where the area was varied by means of a sliding cone throttle. The duct wall diameter decreased slightly downstream of the rakes and wall static pressures in this reduced section were used in conjunction with the rake total pressures (and a duct calibration) to obtain values for mass flow ratio  $A_0/A_c$  at subsonic speeds. At supersonic speeds the choked exit area (modified by an experimentally determined discharge coefficient) was used together with the rake total pressures to obtain mass flow.

The Kulites were fitted with Boeing screens and a 3 mm extension ensured that true total pressure was measured. The dynamic data signals were digitised and stored in real time on 67 Mbyte exchangeable discs. The maximum digitisation rate of the system was 300 K, 10 bit words per second. Sample and hold amplifiers were used to ensure that all pressures were measured at the same instant in time. Signal conditioning was achieved using 48 high stability variable gain DC amplifiers (which can be AC coupled if required) together with 48 low pass Butterworth filters (48 dB per octave roll-off). The cut off frequency was variable from 10 Hz to 2.5 kHz and was set to 1.7 kHz, which is equivalent to 200 Hz full scale for a model scale of 1/8.5. The sampling rate was three times the cut off frequency i.e. 5.1 k samples/sec on the evidence of Fig. 45 [43]. The record length was 4.016 secs.

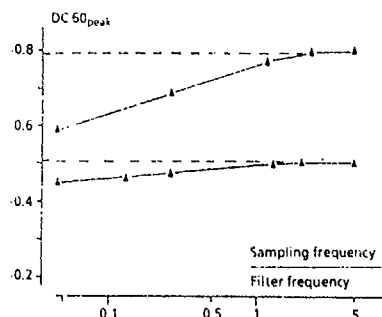


Fig. 45 - Effect of sampling frequency.

#### (b) ONERA

There was a bullet in the duct but this was positioned downstream of the Kulite rakes (Fig. 43(a)).

The Kulites are protected by ONERA screens, and a 7 mm extension ahead. The duct diameter increased slightly downstream of the rakes to account for the blockage effect of the bullet.

A butterfly valve is installed downstream of the engine face, to vary the mass flow. It is followed by two grids, to smooth the flow and reduce distortion. The flow is exhausted back to the free stream via a conv-div. nozzle which is used to measure the mass flow. When the nozzle is choked, mass flow measurement is based on theoretical discharge coefficient for the sonic throat. When it is not, (at low Mach number or low mass flow), Venturi formulae are used, with corrections derived from measurements in the choked flow conditions.

The filter cut-off frequency was set to 1.6 kHz and the sampling rate was five times the cut-off frequency i.e. 8 K samples/sec. The record length was 3.84 secs.

For a few points the cut-off frequency was doubled 3.2 kHz and then the sampling rate becomes 16 K samples/sec.

The record is obtained in real time by successive acquisitions (every 0.5 s) of batches of 256 pressure maps at the maximum frequency of 16 kHz, 12 bits words.

#### (c) DLR

There was no bullet in the duct but a thin walled ring of a diameter slightly less than that of the innermost probe joints all 16 arms of the rake as shown in Fig. 43 (b). The Kulite tubes were 1.6 mm in diameter arranged in 8 arms and are in the same angular position as those in the RAE and ONERA models but the 80 steady state pitots were positioned adjacent to and midway between the Kulite rake arms. The duct diameter increased just downstream of the probe entries to more than compensate for the blockage of the 16 arm rake. The duct remained unobstructed downstream of the rake until the exit where the duct exit area was varied using the common conical plug geometry.

The maximum digitisation rate was 200 K 12 bit words per second. The signal conditioning used DC/AC Bessel filters (48 dB per octave roll off) and the cut-off frequency could be varied from 0.1 Hz to 1.42 kHz. The cut-off frequency was set to 1.42 kHz for all characteristics except one, when it was doubled. The sampling rate was 80 K and 20 K (80 K for data storage, and 20 for on-line presentation) samples/sec and the record length 4 secs and 30 secs.

The MBB data gathering and signal conditioning equipment was operated by MBB personnel for the test under the direction of DLR.

MBB provided both model instrumentation (i.e. dynamic and steady state rakes and the mass flow throttling plug system) as well as data gathering and signal condition equipment.

DLR supplied the pitot intake, model support, the PSI modules and the wind tunnel and defined the test conditions.

#### 4.6.4 - Test programmes and test conditions

The tests were conducted in the RAE (Bedford) 8' x 8' subsonic and supersonic speed tunnel (Fig. 44 (c)) in October 1988, in the DLR (Göttingen) 1 m x 1 m transonic and supersonic speed tunnel in December 1989 (Fig. 44 (b)) and in the ONERA (Modane) (1.75 m x 1.75 m) tunnel in July 1990 (Fig. 44 (a)). The use of existing engine face instrumentation resulted in the smallest model being tested in the largest tunnel (RAE) and the largest in the smallest tunnel (DLR).

The test programmes were as follows :

(a) RAE

Angle of incidence effect			Reynolds number effect		
$M_o$	$\alpha^\circ$	$R_e$ (based on capture diameter $d_c = 81.5$ mm)	$M_o$	$\alpha^\circ$	$R_e$
0.8	0 10 15* 20 25	$1.25 \times 10^6$	1.8	0 5 10* 15 20	$1.25 \times 10^6$

\*10 repeatability check at this condition

\*13 repeatability check at this condition

The model had a transition strip 2 mm wide located on the duct inside surface 12 mm from the highlight position.

(b) ONERA

Angle of incidence effect		
$M_o$	$\alpha^\circ$	$R_e$ (based on capture diameter $d_c = 86.3$ mm)
0.8	0 10 15* 20 25	$1.25 \times 10^6$

\*Cut-off frequency varied from 1.6 kHz to 3.2 kHz.

Mach number effect			Reynolds number effect		
$M_o$	$\alpha^\circ$	$R_e$	$M_o$	$\alpha^\circ$	$R_e$
0.75 0.80 0.85 0.90 0.95	15	$1.25 \times 10^6$	0.80	15 20	$1.9 \times 10^6$ $1.9 \times 10^6$

(c) DLR

Angle of incidence effect		
$M_o$	$\alpha^\circ$	$R_e$ (based on $d_c = 97.9$ mm)
0.8	0 5 10 15 20	$1.027 \times 10^6$

Mach number effect			Reynolds number effect		
$M_o$	$\alpha^\circ$	$R_e$	$M_o$	$\alpha^\circ$	$R_e$
0.75 0.9 1.8	0° - 20°	$1.027 \times 10^6$	0.8 0.8 5 5 15		$0.388 \times 10^6$ $1.723 \times 10^6$

A transition strip was located on the duct inside surface 10 mm downstream of the highlight.

#### 4.6.5 - Data reduction and presentation

The usual format of steady state intake characteristic data is presented i.e. pressure recovery  $P_t/P_o$  and  $DC_{60}$  versus relative mass flow  $A_o/A_c$ . Unsteady  $DC_{60}$  can be presented as maximum values recorded  $DC_{60IX}$ , or using the Jacocks statistical method (ref. 33) as the maximum values, 2 min  $DC_{60}$  that would be predicted after 2 minutes of operation at full scale.

$DC_{60}$  has already been defined in Chapter 2, Section 2.

$DC_{60IX}$  is defined as :

$$\frac{\bar{P}_{t_2} - P_{t_2 \min 60}}{\bar{q}}$$

where now  $P_{t_2 \min 60}$  is the instantaneous value of the minimum total pressure of any sector of 60° at the engine face.

$\bar{P}_{t_2}$  is the mean steady state total pressure

$$\left[ \frac{1}{40} \sum_{i=1}^{40} P_{t_i} \text{ (RAE and ONERA)} = \frac{1}{80} \sum_{i=1}^{80} P_{t_i} \text{ (DLR)} \right]$$

at the engine face, and using the Rolls Royce recommendation,  $\bar{q}$  is the mean incompressible steady dynamic pressure as obtained from a mass flow derived mean Mach number at the engine face.

The Jacocks method is summarised as follows :

1. Peak  $DC_{60}$  values are calculated for each of the  $N$  blocks of data available in the 3-4 secs of recording time.  $N$  is normally in the range 15-25.
2. Peak  $DC_{60}$  are arranged in ascending order of value and assigned an index 'm' where  $m = 1, 2, \dots, N$ .
3. The reduced variable  $\gamma = -\ln \ln [(N+1)/m]$  is calculated.
4. Peak  $DC_{60}$  values are plotted versus  $\gamma$  and a least squares fit straight line through the points is calculated.
5. Extrapolation of this straight line allows estimation for a longer time period (e.g. 14 secs RAE model scale, 14.83 secs ONERA model scale, equivalent to 2 minutes full scale).

As 2 min  $DC_{60}$  values are not available at the present time for the DLR results, results for the three tunnels are compared on a  $DC_{60IX}$  basis.

#### 4.6.6 - Comparison of measurements

##### 4.6.6.1 - At subsonic speeds

##### (a) Effect of incidence variation

Pressure recovery-mass flow characteristics at  $M_o 0.8$  at all incidences (Fig. 46 (a)) except 20° show close agreement. If the value of maximum mass flow ratio is judged on points on the supercritical leg of the characteristic that are close to the critical point, then there is a tendency for the ONERA values to be slightly in excess of the RAE and DLR values at  $\alpha = 0^\circ$  and 10°. At  $\alpha = 0^\circ$ , the theoretical choking mass flow ratio is 0.882 which indicates a throat discharge coefficient  $C_d$  of 0.992 for the ONERA results 0.987 for DLR and 0.978 for RAE. At  $\alpha = 20^\circ$ , DLR and ONERA values are in close agreement for pressure recovery over the full mass flow range whereas RAE values are 1-2 % higher over the flow range 0.6 - 0.8.

At  $\alpha = 25^\circ$ , results are only available from RAE and ONERA and pressure recovery values differ by about 1 % again over the mass flow ratio range 0.6-0.8 but there is no consistent one way trend.

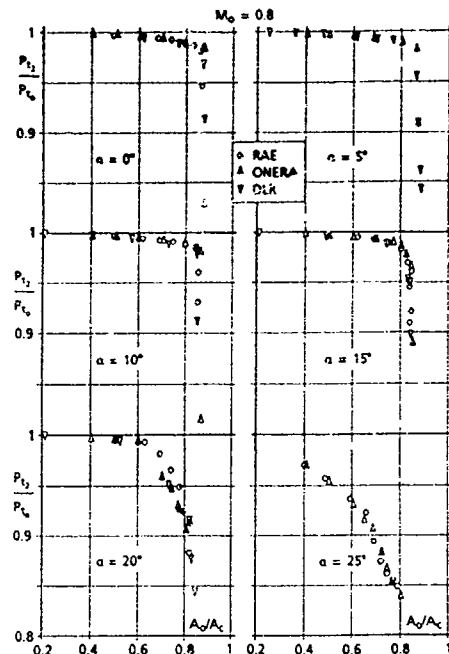


Fig. 46 (a) - Incidence variation : comparison of pressure recovery from RAE, ONERA, & DLR at  $M_0 = 0.8$ ,  $\alpha = 0^\circ - 25^\circ$ .

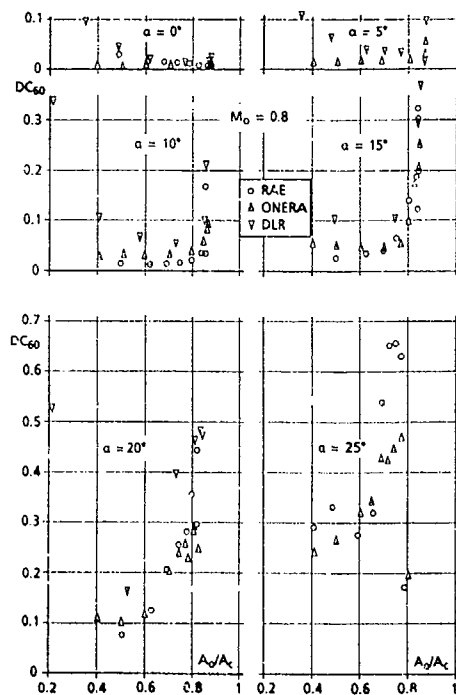


Fig. 46 (b) - Incidence variation : comparison of  $DC_{60}$  from RAE, ONERA, & DLR at  $M_0 = 0.8$ ,  $\alpha = 0^\circ - 25^\circ$ .

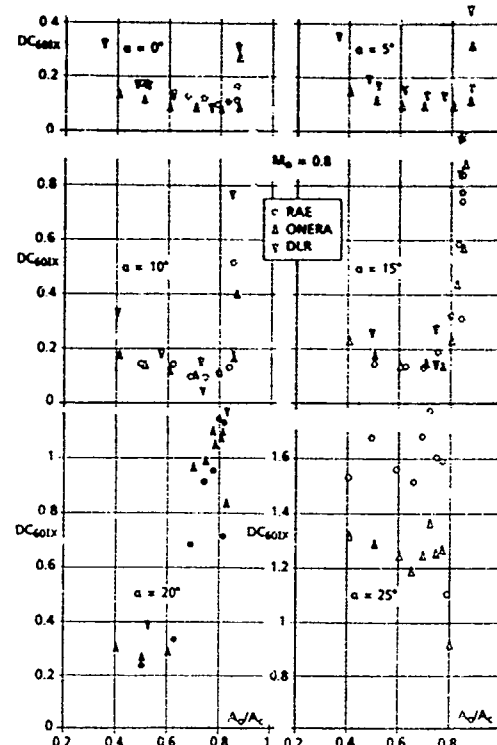


Fig. 46 (c) - Incidence variation : comparison of  $DC_{601x}$  from RAE, ONERA, & DLR at  $M_0 = 0.8$ ,  $\alpha = 0^\circ - 25^\circ$ .

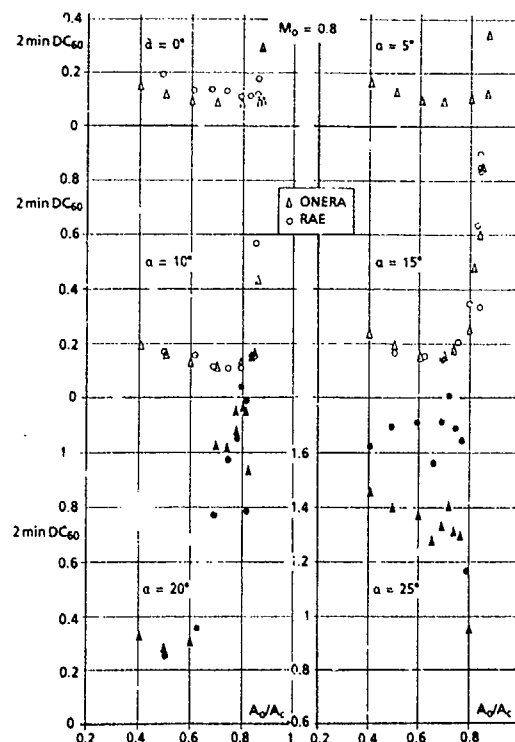


Fig. 46 (d) - Incidence variation : comparison of  $2 \min DC_{60}$  from RAE & ONERA.  $M_0 = 0.8$ ,  $\alpha = 0^\circ - 25^\circ$ .

Internal cowl lower lip surface Mach number plots at  $M_0 = 0.8$ ,  $\alpha = 20^\circ$  from ref. [41] show the collapse of the lip suction that occurs on changing flow ratio from 0.559 to 0.605 (Fig. 47 (a)) indicating the advent of lip separation. The steady increase in separation bubble Mach number as  $A_0/A_c$  varies from 0.65 to 0.796 (Fig. 47 (b)) then gives rise to rapidly increasing mixing losses and results in the observed deterioration in engine face pressure recovery. At  $\alpha = 25^\circ$ , the flow is separated from the lower lip of the cowl over the complete range of measured mass flow.

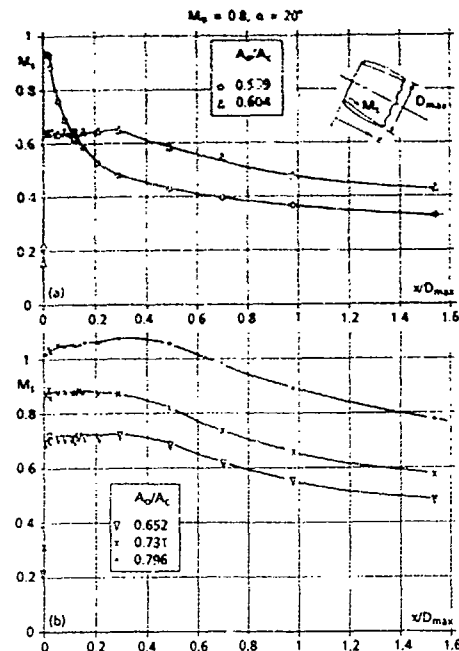


Fig. 47 (a) & (b) - Internal lower lip Mach no. distributions for RAE model 742L cowl 2 at  $M_0 = 0.8$ ,  $\alpha = 20^\circ$  (from ref. [41]).

Up to  $\alpha = 15^\circ$ , values for  $DC_{601X}$  from all three tunnels (Fig. 46 (c)) are in reasonably close agreement over the full flow range.  $DC_{60}$  values (Fig. 46 (b)) however show more variation between the three sets of tests. In particular at  $\alpha = 0^\circ$  theoretically,  $DC_{60}$  should be zero as any distortion of the engine face flow in an axisymmetric intake and duct should be purely radial. All three results approximate to this at flow ratios above 0.6 but RAE and DLR values tend to increase quite rapidly (though remaining small) below  $A_0/A_c = 0.6$ . DLR values show the same tendency at  $\alpha = 5-15^\circ$  but start increasing rapidly below  $A_0/A_c = 0.6-0.7$  whereas ONERA and RAE values remain below 0.05 over the full measured flow range. At  $\alpha = 20^\circ$ ,  $DC_{60}$  climbs rapidly above  $A_0/A_c = 0.6$  remarkably consistently from all three tunnels. At  $\alpha = 25^\circ$  values from  $A_0/A_c = 0.7$  upwards from RAE are considerably higher than ONERA values.

$DC_{601X}$  values become slightly more scattered between the three tunnel values at  $\alpha = 20^\circ$ . At  $\alpha = 25^\circ$  ONERA values are considerably lower than RAE values but both sets are, numerically, very high (note the false origin of the graph at  $\alpha = 25^\circ$ ). The 2 min  $DC_{60}$  values available from RAE and ONERA only (Fig. 46 (d)) show similar differences to the  $DC_{601X}$  values.

(b) Effect of variation of free stream Mach number ( $\alpha = 15^\circ$  only) (Fig. 48)

Comparisons at  $M_0 = 0.75$  and  $0.9$  are limited to DLR and ONERA results. Values of pressure recovery at  $M_0 = 0.75$  near to full flow are not in such close agreement at  $M_0 = 0.8$  with ONERA values being 1/2 - 1 % higher than those from DLR.  $DC_{60}$  values show the same (but opposite) trend throughout the flow range. At  $M_0 = 0.9$ , one value of the DLR pressure recovery-mass flow characteristic (at  $A_0/A_c = 0.57$ ) is much lower than the corresponding ONERA value. This is not accompanied by a correspondingly large increase in  $DC_{60}$  at this condition which may indicate that the pressure recovery value is in error. Again, as at  $M_0 = 0.8$ ,  $DC_{601X}$  values between the two tunnels are remarkably consistent.

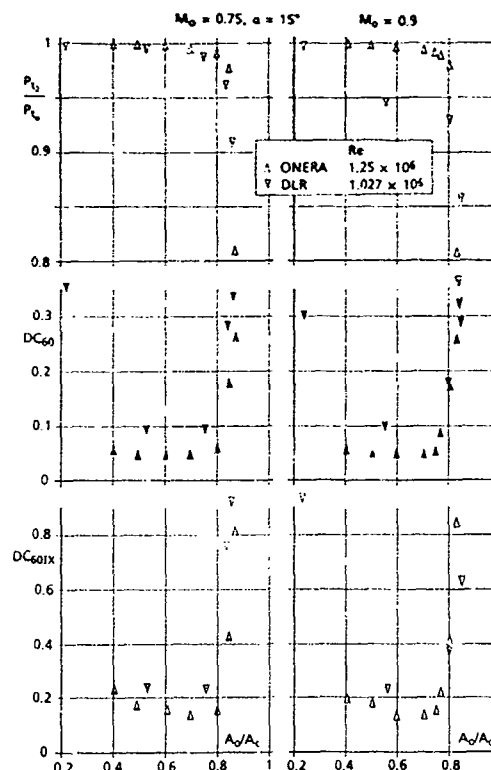


Fig. 48 - Variation of subsonic speed: comparison of pressure recovery,  $DC_{60}$  &  $DC_{601X}$ , from ONERA & DLR at  $\alpha = 15^\circ$ ,  $M = 0.75$  &  $0.90$ .

(c) Reynolds number variation ( $\alpha = 15^\circ$ ,  $M_0 = 0.8$ ) (Fig. 49)

Variation between  $Re = 1.25 \times 10^6$  and  $1.91 \times 10^6$  for all three (pressure recovery,  $DC_{60}$  and  $DC_{601X}$ ) ONERA results are negligible, as might be expected for this small Reynolds number change. DLR results are similar for the two higher Reynolds number. However, the values at the low Reynolds number of  $0.39 \times 10^6$  illustrate the large adverse effects of going below the well-known "rule of thumb" of intake testing that the Reynolds number based on intake diameter should if possible exceed  $1 \times 10^6$ .

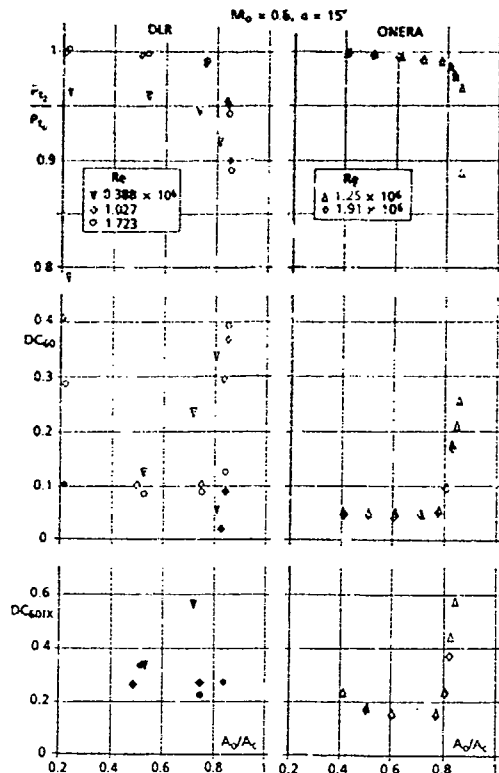


Fig. 49 - Variation of Reynolds no. : comparison of pressure recovery,  $DC_{60}$  &  $DC_{60IX}$  from ONERA & DLR at  $\alpha = 15^\circ, M_0 = 0.8$ .

#### 4.6.6.2 - At supersonic speeds

##### (a) Effect of incidence variation (Fig. 50 (a) - (d))

At  $M_0 = 1.8$ , results are only available from DLR and RAE. In general pressure recovery - mass flow characteristics are very similar at  $\alpha = 0^\circ$  and  $5^\circ$ . Pressure recovery at low mass flow at  $\alpha = 0^\circ$  is very close to the normal shock value of 0.813 at  $M_0 = 1.8$ ; maximum theoretical choking flow at this condition is 0.994 which compares with the measured value of 0.977 for both sets of results if DLR values in excess of unity at very supercritical conditions are ignored. This gives a throat discharge coefficient of 0.983. At  $\alpha = 10^\circ - 20^\circ$ , there is a tendency for DLR values of pressure recovery to be slightly higher than RAE values at flow ratios above 0.8 and for maximum flow ratios also to be slightly higher. This latter difference may be exaggerated by a lack of truly supercritical values for the RAE results at these incidences.

$DC_{60}$  values from DLR show the same tendency as at  $M_0 = 0.8$  of being slightly higher than RAE values at mass flow values below the critical point. There is a good agreement between DLR and RAE values for  $DC_{60IX}$  at  $\alpha = 0-15^\circ$ . The high peak values at  $0^\circ$  and  $15^\circ$  are probably the results of coincidence of lip separation and shock-boundary layer interaction in the region of the lip. The DLR results show that when the internal supersonic flow pattern has become properly established and the terminal shock has moved downstream of the lip  $DC_{60IX}$  values can drop considerably.

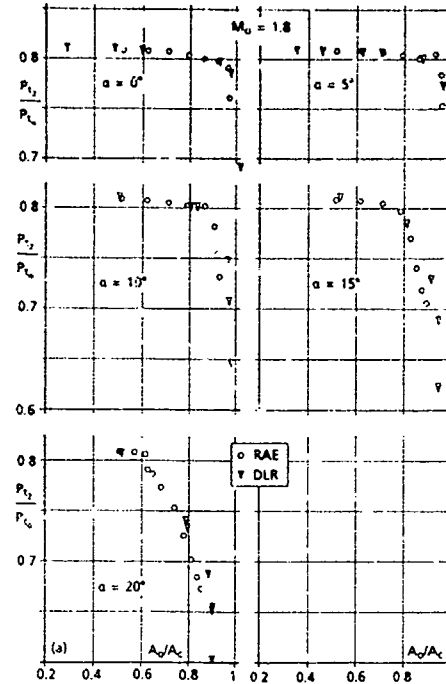


Fig. 50 (a) - Incidence variation : comparison of pressure recovery from RAE & DLR at  $M_0 = 1.8, \alpha = 0^\circ - 20^\circ$ .

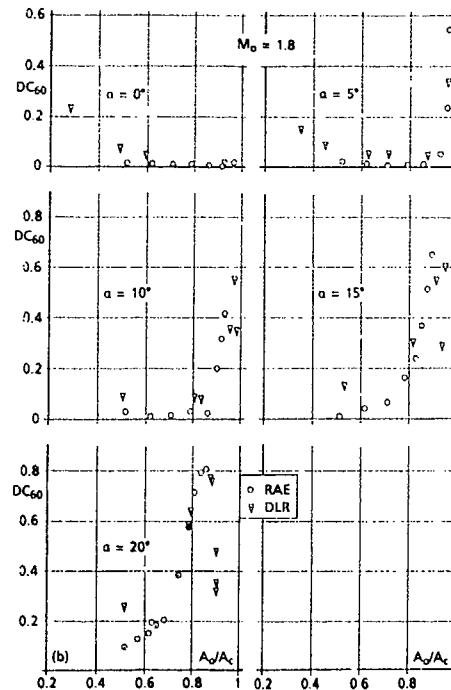


Fig. 50 (b) - Incidence variation : comparison of  $DC_{60}$  from RAE & DLR at  $M_0 = 1.8, \alpha = 0^\circ - 20^\circ$ .



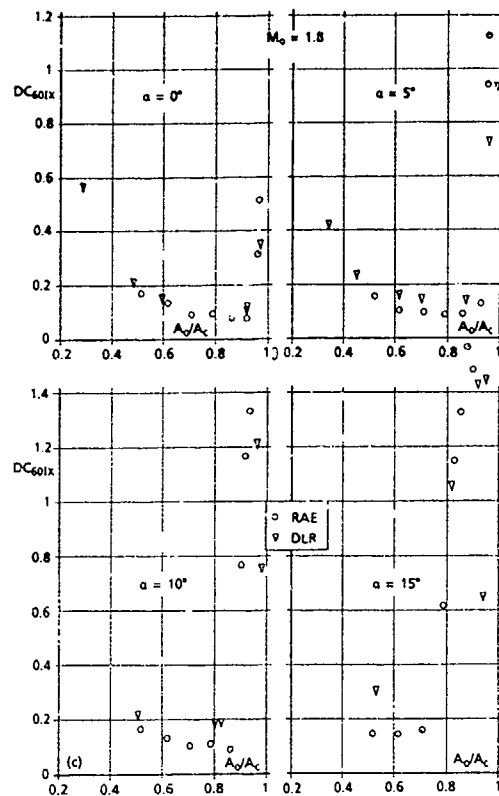


Fig. 50 (c) - Incidence variation : comparison of  $DC_{601x}$  from RAE & DLR at  $M_0 = 1.8, \alpha = 0^\circ - 15^\circ$ .

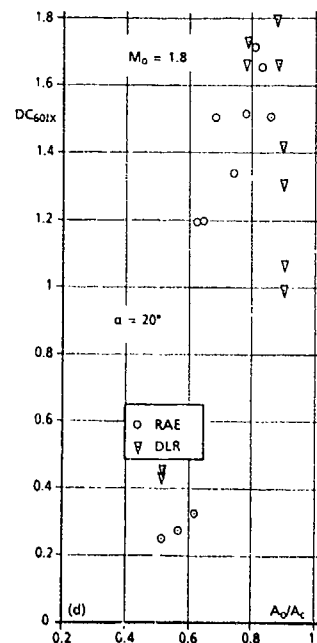


Fig. 50 (d) - Incidence variation : comparison of  $DC_{601x}$  from RAE & DLR at  $M_0 = 1.8, \alpha = 20^\circ$ .

#### 4.6.7 - Results unique to ONERA and DLR tests

For completeness, results from tests that were performed in one tunnel only are shown in Figs. 51-54. Results from ONERA at  $\alpha = 15^\circ, M_0 = 0.85$  and  $0.95$  in addition to those already discussed at  $M_0 = 0.75, 0.8$  and  $0.9$  are shown altogether in Fig. 51. Similarly results from DLR tests at  $\alpha = 5^\circ$  at  $M_0 = 0.75, 0.8$  and  $0.9$  are shown in Fig. 52.

The effect of Reynolds number variation at  $M_0 = 0.8, \alpha = 20^\circ$  is shown in Fig. 53.

Finally, the effect of change of cut-off frequency at  $\alpha = 15^\circ, M_0 = 0.8$  on 2 min  $DC_{60}$  is shown to be small (Fig. 54).

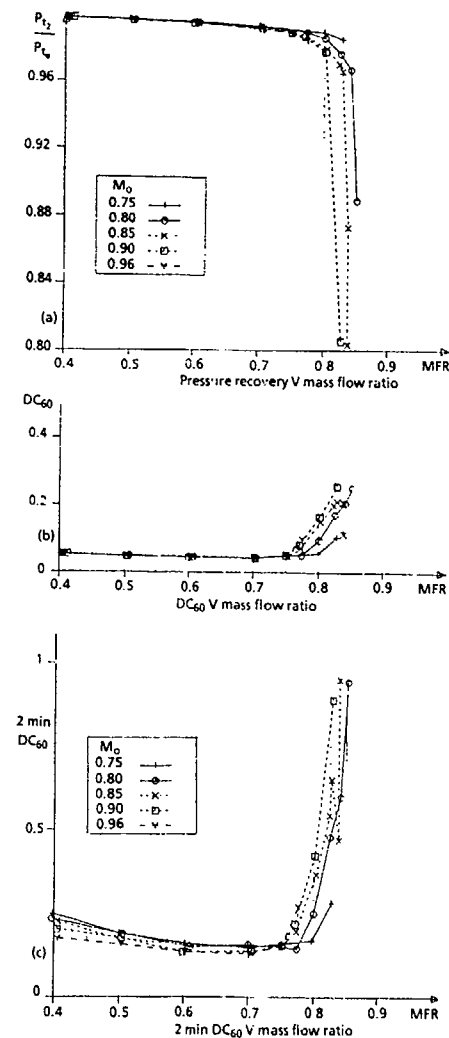
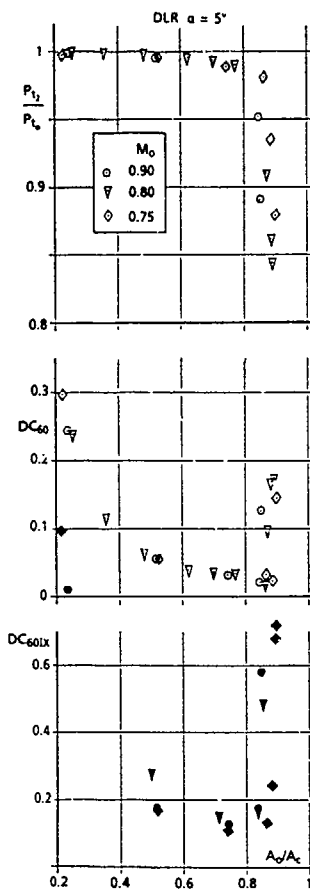


Fig. 51 - Mach number effect -  $\alpha = 15^\circ$  &  $Re = 1.25$ .



◀ Fig. 52 - Effect of change of subsonic Mach no. from DLR at  $\alpha = 5^\circ$ .

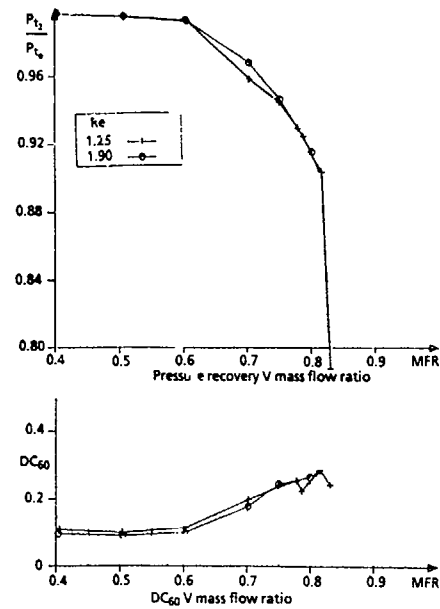
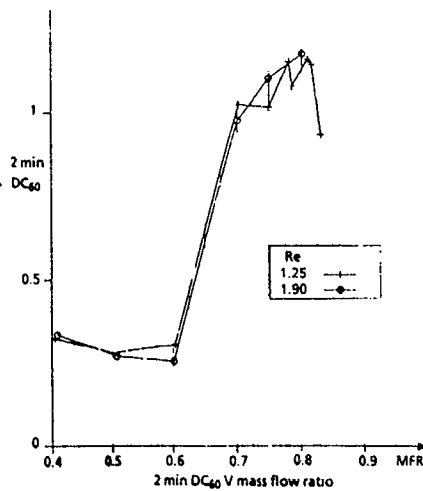
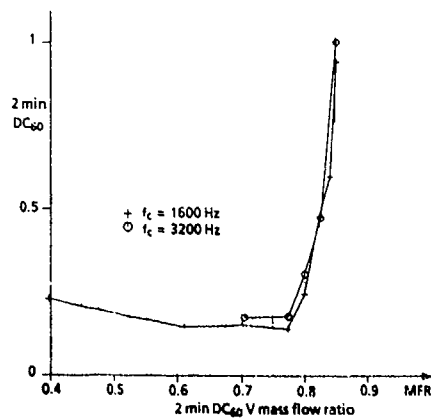


Fig. 53 - Reynolds number effect -  $M = 0.8$  &  $\alpha = 20^\circ$  ▶



◀ Fig. 54 - Cut-off frequency effect -  $M = 0.8$ ,  $\alpha = 15^\circ$  &  $Re = 1.25$ .

#### 4.6.8 - Repeatability study at RAE

The question of repeatability and accuracy is of much greater complexity in dynamic than in steady state measurements. Even assuming that the measuring and analysing equipment is 100 % accurate, measurements made in unsteady flow may show considerable variation. The flow may be 'stationary' in a statistical sense (i.e. samples taken at different times will have the same mean values) but peak values of flow distortion are not 'ergodic' (i.e. samples taken at different times will produce different peak  $DC_{60}$  values). This is clearly shown up in the RAE repeat tests at  $M_0 = 1.8$  (Table II).

Table II. - Repeatability of  $DC_{60}$  values.  
 $M = 1.8, \alpha = 10^\circ, A_0/A_c = 0.504,$   
 $P_R = 0. = 0.782$

Data point No	Time average $DC_{60}$	Dynamic $DC_{60}$		I-CEPT	Slope	2 min $DC_{60}$
		Lowest peak	Highest peak			
43	0.199	0.544	0.767	0.605	0.056	0.844
Repeat 68	0.200	0.530	0.758	0.606	0.049	0.813
69	0.203	0.547	0.724	0.612	0.044	0.801
70	0.200	0.563	0.709	0.620	0.035	0.771
71	0.201	0.558	0.741	0.619	0.044	0.806
72	0.201	0.532	0.787	0.611	0.060	0.867
73	0.203	0.574	0.708	0.630	0.033	0.771
74	0.202	0.577	0.781	0.617	0.052	0.836
75	0.201	0.574	0.810	0.622	0.055	0.855
76	0.201	0.559	0.729	0.618	0.048	0.822
77	0.204	0.566	0.721	0.612	0.043	0.798
78	0.203	0.545	0.920	0.609	0.082	0.959
79	0.201	0.555	0.776	0.639	0.043	0.824
80	0.205	0.598	0.713	0.639	0.030	0.769

The Jacock method of analysis attempts to overcome this in a logical manner but with only 20 peak values a single very high or very low peak can significantly distort the results. DP78 is a case in point where the slope of the least squares line is obviously affected by one very high peak value. Jacocks plots for the repeats with the highest and lowest slope (DPs 78 and 80) are shown in Fig. 55 (a) (b). It should be noted that though in general the slope does vary considerably, the intercept (the reduced variate  $y = 0$  value) remains remarkably consistent. A composite plot of all peak  $DC_{60}$  values from DP43 and repeat DPs 68-80 (regarding these as a continuous recording) can be produced as shown in Fig. 55 (c). It can be deduced from this plot that the very high peak value of DP78 corresponds to a return period of about 27 minutes full scale. Assuming the measurement to be correct, this clearly represents a rare event, but in principle it could occur only a fraction of a second after entering the relevant intake operating condition.

Ten repeat measurements at  $M_0 = 0.8, \alpha = 15^\circ$  show a similar variation in intercept value but with less variation of slope (0.027 to 0.037 compared to 0.030 to 0.082 at  $M_0 = 1.8$ ).

The main conclusion from this brief investigation is that in flows of moderate to high turbulence the naturally occurring random variations in peak distortion are likely to be of much greater significance than any other uncertainties due to different experimental techniques.

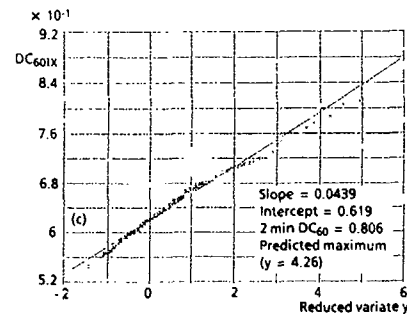
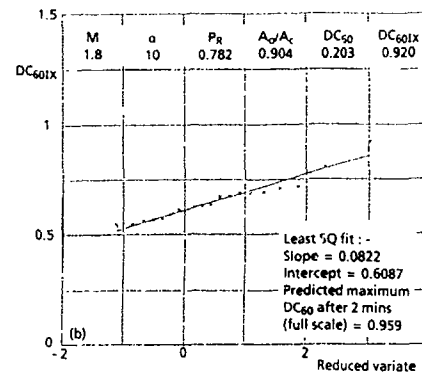
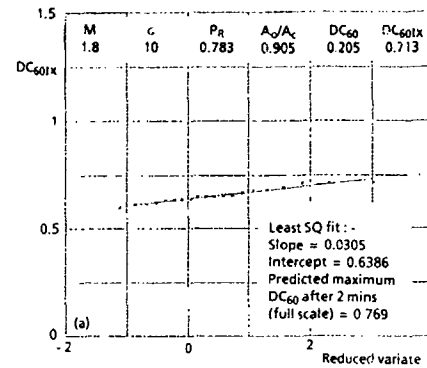


Fig. 55 (a) - (c) - Jacocks plots of  $DC_{60IX}$  to predict 2 min  $DC_{60}$ .

#### Section 4.7

#### CONCLUSIONS AND RECOMMENDATIONS

Many and varied means exist for studying air intakes experimentally.

Still today tests on models of modest scale constitute the most appropriate way of addressing the problems of defining a new aircraft configuration or choosing an air intake concept that will satisfy the given requirements.

So this approach can be developed further, with a constant emphasis on better identification and measurement of the parameters describing the internal flow - chiefly its unsteady distortion - and defining the external force balance better.

This is the motivation of the test program initiated by AGARD and described in the last section, in which the steady and unsteady distortion of the

internal flow is studied repeatedly for the same intake in a variety of test facilities, in order to evaluate the precision of the measurements.

At the same time, large scale testing, at close to flight Reynolds numbers and possibly with the actual aircraft air intake and engine too, is expected to be invested in heavily, for the purpose of predicting more precisely the compatibility limits between engine and intake, and adapting them to each other.

There is no fundamental difference between supersonic and hypersonic air intake tests, the latter of which have not been mentioned so far; but there are currently no testing facilities for large-scale hypersonic experimentation with engine, and this will have to be considered for the future.

Finally, to get better theoretical predictions of air intake performance, the validity of the calculation codes and their components have to be analyzed in greater depth, which means that new means have to be developed that are adapted to detailed analyses of these specific flows.

Results from measurements of pressure recovery, mass flow,  $DC_{60}$  and  $DC_{60IX}$  from three European wind tunnels using a common axisymmetric pitot intake have been compared. In general there has been a good measure of agreement at all the common test condition of  $M_0 = 0.75 - 0.9$  and  $1.8$  and incidences from  $0^\circ - 25^\circ$ . Even where absolute values are markedly different, the shape of the variation of  $DC_{60}$  and  $DC_{60IX}$  with mass flow is usually very similar. The exact source of discrepancies can be in the value of the original pressure signals, the form of the engine face instrumentation and/or the geometry of the duct (including the duct exit) downstream of it (Ref. 30). The means of signal conditioning and the subsequent processing to obtain  $DC_{60}$  and  $DC_{60IX}$  are also relevant.

A subsequent analysis in greater depth should lead to a cooperative effort to tighten and standardise on engine face instrumentation and data collection and analysis procedures, which will benefit all participants.

The undoubted success of this cooperative exercise, especially in the realm of dynamic distortion measurements with all its complication and manifold potential sources of variation, should be followed by further exercises of this nature. In particular, the use of a more complex model that involved shock boundary layer interaction on an adjacent surface to an intake or on an intake with a compression surface would be of great interest.

#### REFERENCES

- [1] C.H. Stevens, E.D. Spong, M.S. Hammock F15 inlet/engine test techniques and distortion methodologies studies. Vol. 1 - Technical Discussion NASA CR 144866 - June 1978.
- [2] Tate, Jack T., Inlet - Engine compatibility testing techniques in ground test facilities. AGARD CP 293 - 1981.
- [3] J.R. Bion - Steady and unsteady inlet flow simulation for engine ground test. 20th "Joint propulsion" Conference (AIAA/ASME/SAE) 1984 (ONERA TP 1984-35).
- [4] James G. Mitchell - Fluid dynamic aspects of turbine engine testing. AGARD CP 348 - 1983.
- [5] P.H. Ashwood - Free jet test of a full scale supersonic intake/engine combination. AGARD CP 91 - 1971.
- [6] J. Leynaert - Complément à prises d'air - Cours ENSAe 1985.
- [7] J. Leynaert - Fundamentals of fighter aircraft design : engine intake and afterbody. AGARD R 740 - 1986.
- [8] J. Leynaert - Les prises d'air et arrière-corps de moteur des avions subsoniques et supersoniques. Eléments généraux - ONERA TP 1988-132, 1986.
- [9] J. Leynaert - Entrées d'air et arrière-corps de fuselage moteurs en transsonique. AGARD CP 83 - 1971.
- [10] E. Carter - Experimental determination of inlet characteristics and inlet and airframe interference. AGARD LS 53, 1972.
- [11] B. Masure, J.L. Solignac, P. Laval - Mass flow rate measurements by means of a sonic throat; Pittsburg Symposium 1971 (ONERA TP 956-71).
- [12] Richard J. Re - An investigation of several NACA.1 series inlets at Mach numbers from 0.4 to 1.29 for mass flow ratio near 1.0. NASA TM X3324 - 1975.
- [13] W. Hoelmer, J.L. Younghans, J. Cl. Raynal - Effects of Reynolds number on upper cowl flow separation. ICAS Proceedings, 1984.
- [14] D.L. Motycka (Pratt and Whitney) - Comparison of model at full scale inlet distortion for subsonic commercial transport inlet. AIAA 84 2427 - 1984.
- [15] J. Leynaert - Essais de prises d'air à des nombres de Reynolds comparables au vol dans les souffleries F1 et S1MA de l'ONERA - AGARD CP 301 - 1981.
- [16] AGARD CP 301 - Aerodynamics of Power Plant Installation. 1981.
- [17] AGARD CP 348 - Wind Tunnels and Testing Techniques 1983.
- [18] SAE-ARP (Aerospace Recommended Practice) n° 1420 - 1978.
- [19] L.E. Surber and Clay Fugimura - Inlet engine compatibility. VKI lecture series 1988-04 - "Intake Aerodynamics", 1988.
- [20] F. Aulehla and D.M. Schmitz. Intake swirl and simplified methods for dynamic pressure distortion assessment. VKI Lecture Serie 1988-04. "Intake Aerodynamics", 1988.
- [21] P. Carrière - Aperçu de quelques problèmes aérodynamiques actuels posés par les prises d'air supersoniques. 1er Symposium international sur les Progrès des Réacteurs d'Avion. Marseille, 1972 - ONERA TP 1102.
- [22] R.W. Guo and J. Seddon - The swirl in a S. Duct of typical air intake proportions. Aeronautical Quarterly, May 1983.
- [23] I.M. Hall - Transonic flow in two-dimensional and axially symmetric nozzles. Mechanic of Fluid Department. Manchester University (January 1962).

- [24] J.P. Kliegel and J.N. Levine - Transonic flow in small throat radius of curvature nozzles - AIAA Journal n° 7, 1969.
- [25] P. Carrière - Viscous effects on propulsion nozzles. Short course on internal aerodynamics of rocket engines. VKI 1966.
- [26] B. Masure - Effets de la viscosité et effets de Viriel sur la mesure des débits par col sonique. La Recherche Aérospatiale n° 120 - 1967.
- [27] B.S. Stratford - The calculation of the discharge coefficient of profiled choked nozzles and the optimum profile for absolute airflow measurement. J. RAS n° 4, 1964.
- [28] Fluid Meters - Their theory and application - Report of the ASME Committee on fluid meters. 1971 - Bearn H.S. ed.
- [29] J. Seddon and E.L. Goldsmith - Intake Aerodynamics 1985. Collins ed.
- [30] Mc Gregor, J. Gibb, M. Cameron - Flow induced pressure fluctuations in model air intake flow metering device. RAE Unpublished March 1990.
- [31] P.A. Mackrodt, D.M. Schmitz - Experimentelle Untersuchungen an einem Unterumpf Rampeneinlauf bei Überschallströmung Jahrbuch 1986.1 der DGLR.
- [32] J.W. Britton - Measurements of the internal drag of air breathing installations on slender wing-body combinations at supersonic speed. RAE TR 65 275 - 1965.
- [33] J.L. Jacocks - Statistical analysis of distortions factors - AIAA paper 72-1100 - 1972..
- [34] J. Marous, D. Sedlock - An analog editing system for inlet dynamic flow distortion, DYNADEC. Past, present and future - AIAA 80-1108.
- [35] H. Cl. Melick, A.H. Ybarra and D.P. Bencze. Estimating maximum instantaneous distortion from inlet total pressure RMS measurements. AIAA paper 78-970 (2).
- [36] R. Borg, A synthesis method for estimating instantaneous inlet distortion based on measured inlet steady state and RMS pressures. AGARD CP 301, 1981.
- [37] Ch. Stevens, E.D. Spong et al., - Evaluation of a statistical method for determining peak inlet flow distortion using F15 and F18 data. AIAA 80-1109.
- [38] D. Sedlock - Improved statistical method for prediction of maximum inlet distortion - AIAA 84-1274.
- [39] D. Sedlock - Statistical analysis method for prediction of maximum inlet distortion - Journal of Propulsion and Power. Vol. 1, n° 5, p. 354, Sept. 1985.
- [40] K. Lotter, P.A. Mackrodt, R. Scherbaum - Engine surge simulation in wind-tunnel model inlet ducts. 16<sup>th</sup> ICAS 1988.
- [41] E.L. Goldsmith - The internal performance at incidence of pitot intakes with circular cross section and elliptic lip shapes. ARA Report 76. Jan. 1990.
- [42] E.L. Goldsmith - Forces and pressure distributions at subsonic and supersonic speeds on circular section pitot intakes. ARA Report 75. Jan. 1990.
- [43] D.E. Colbourne and J.E. Flucroft - Prediction and measurement of time variant three dimensional flows in military aircraft intakes. Aerodynamics of Power Plant Installation. AGARD CP 301. May 1981.

## CHAPTER 5

### Concluding Remarks

Since detailed summarizing and concluding remarks were given in the previous chapters for the various classes of configurations, only a few general remarks will be made here.

The Working Group compiled comprehensive information about transport and military aircraft as well as missile intakes covering

- design methodology and integration concepts
- computational tools
- wind tunnel testing techniques and testing limitations in the subsonic, transonic, and supersonic speed range.

No information has been gathered for hypersonic configurations exhibiting real gas effects. However, advanced computational tools allow for necessary extensions where physical models are available. Large scale testing facilities do not exist for hypersonic flight conditions.

Validation/calibration of computational tools is extremely difficult due to the limited amount of detailed experimental data.

Interaction between air intakes and engines need further consideration from both air vehicle and engine designers.

REPORT DOCUMENTATION PAGE			
1. Recipient's Reference	2. Originator's Reference	3. Further Reference	4. Security Classification of Document
	AGARD-AR-270	ISBN 92-835-0637-5	UNCLASSIFIED
5. Originator	Advisory Group for Aerospace Research and Development North Atlantic Treaty Organization 7 rue Ancelle, 92200 Neuilly sur Seine, France		
6. Title	AIR INTAKES FOR HIGH SPEED VEHICLES		
7. Presented on			
8. Author(s)/Editor(s)	Various		9. Date September 1991
10. Author's/Editor's Address	Various		11. Pages 258
12. Distribution Statement	This document is distributed in accordance with AGARD policies and regulations, which are outlined on the back covers of all AGARD publications.		
13. Keywords/Descriptors	<div style="display: flex; justify-content: space-between;"> <div> Jet engine inlets Computational fluid dynamics Flow distribution Wind tunnel tests Jet engines </div> <div> Aerodynamics Design Aircraft Missiles </div> </div>		
14. Abstract	<p>This report presents the results of a study by Working Group 13 of the AGARD Fluid Dynamics Panel which was formed to investigate the state-of-the-art of methodologies for aerodynamic design of engine intakes for high speed vehicles. The scope of the investigation included intake aerodynamics, intake/engine compatibility, and intake/airframe integration for both aircraft and missiles.</p> <p>The present capability of Computational Fluid Dynamics (CFD) methods was assessed through a comparative analysis of both CFD predictions and experimental data. This analysis was conducted for eight different flow field test cases designed to produce critical features of air-intake flow fields. Flow field results and comparisons are presented both in the report and in a microfiche appendix.</p> <p>Air-inlet wind tunnel testing techniques and limitations were also investigated and reported. Results from measurements of inlet performance from three European wind tunnels using a common axisymmetric pitot intake are also presented.</p> <p>The participants in Working Group 13 represented Belgium, France, Germany, Italy, the United Kingdom, and the United States.</p>		

<p>AGARD Advisory Report 270 Advisory Group for Aerospace Research and Development, NATO <b>AIR INTAKES FOR HIGH SPEED VEHICLES</b> Published September 1991 258 pages</p> <p>This report presents the results of a study by Working Group 13 of the AGARD Fluid Dynamics Panel which was formed to investigate the state-of-the-art of methodologies for aerodynamic design of engine intakes for high speed vehicles. The scope of the investigation included intake aerodynamics, intake/engine compatibility, and intake/airframe integration for both aircraft and missiles.</p> <p>PTO.</p>	<p>AGARD-AR-270</p> <p>Jet engine inlets Computational fluid dynamics Flow distribution Wind tunnel tests Jet engines Aerodynamics Design Aircraft Missiles</p>	<p>AGARD Advisory Report 270 Advisory Group for Aerospace Research and Development, NATO <b>AIR INTAKES FOR HIGH SPEED VEHICLES</b> Published September 1991 258 pages</p> <p>This report presents the results of a study by Working Group 13 of the AGARD Fluid Dynamics Panel which was formed to investigate the state-of-the-art of methodologies for aerodynamic design of engine intakes for high speed vehicles. The scope of the investigation included intake aerodynamics, intake/engine compatibility, and intake/airframe integration for both aircraft and missiles.</p> <p>PTO.</p>	<p>AGARD-AR-270</p> <p>Jet engine inlets Computational fluid dynamics Flow distribution Wind tunnel tests Jet engines Aerodynamics Design Aircraft Missiles</p>	<p>AGARD-AR-270</p> <p>Jet engine inlets Computational fluid dynamics Flow distribution Wind tunnel tests Jet engines Aerodynamics Design Aircraft Missiles</p>
<p>AGARD Advisory Report 270 Advisory Group for Aerospace Research and Development, NATO <b>AIR INTAKES FOR HIGH SPEED VEHICLES</b> Published September 1991 258 pages</p> <p>This report presents the results of a study by Working Group 13 of the AGARD Fluid Dynamics Panel which was formed to investigate the state-of-the-art of methodologies for aerodynamic design of engine intakes for high speed vehicles. The scope of the investigation included intake aerodynamics, intake/engine compatibility, and intake/airframe integration for both aircraft and missiles.</p> <p>PTO.</p>	<p>AGARD-AR-270</p> <p>Jet engine inlets Computational fluid dynamics Flow distribution Wind tunnel tests Jet engines Aerodynamics Design Aircraft Missiles</p>	<p>AGARD Advisory Report 270 Advisory Group for Aerospace Research and Development, NATO <b>AIR INTAKES FOR HIGH SPEED VEHICLES</b> Published September 1991 258 pages</p> <p>This report presents the results of a study by Working Group 13 of the AGARD Fluid Dynamics Panel which was formed to investigate the state-of-the-art of methodologies for aerodynamic design of engine intakes for high speed vehicles. The scope of the investigation included intake aerodynamics, intake/engine compatibility, and intake/airframe integration for both aircraft and missiles.</p> <p>PTO.</p>	<p>AGARD-AR-270</p> <p>Jet engine inlets Computational fluid dynamics Flow distribution Wind tunnel tests Jet engines Aerodynamics Design Aircraft Missiles</p>	<p>AGARD-AR-270</p> <p>Jet engine inlets Computational fluid dynamics Flow distribution Wind tunnel tests Jet engines Aerodynamics Design Aircraft Missiles</p>



<p>The present capability of Computational Fluid Dynamics (CFD) methods was assessed through a comparative analysis of both CFD predictions and experimental data. This analysis was conducted for eight different flow field test cases designed to produce critical features of air-intake flow fields. Flow field results and comparisons are presented both in the report and in a microfiche appendix.</p> <p>Air-inlet wind tunnel testing techniques and limitations were also investigated and reported. Results from measurements of inlet performance from three European wind tunnels using a common axisymmetric pitot intake are also presented.</p> <p>The participants in Working Group 13 represented Belgium, France, Germany, Italy, the United Kingdom, and the United States.</p> <p>ISBN 92-834-0637-5</p>	<p>The present capability of Computational Fluid Dynamics (CFD) methods was assessed through a comparative analysis of both CFD predictions and experimental data. This analysis was conducted for eight different flow field test cases designed to produce critical features of air-intake flow fields. Flow field results and comparisons are presented both in the report and in a microfiche appendix.</p> <p>Air-inlet wind tunnel testing techniques and limitations were also investigated and reported. Results from measurements of inlet performance from three European wind tunnels using a common axisymmetric pitot intake are also presented.</p> <p>The participants in Working Group 13 represented Belgium, France, Germany, Italy, the United Kingdom, and the United States.</p> <p>ISBN 92-834-0637-5</p>
<p>The present capability of Computational Fluid Dynamics (CFD) methods was assessed through a comparative analysis of both CFD predictions and experimental data. This analysis was conducted for eight different flow field test cases designed to produce critical features of air-intake flow fields. Flow field results and comparisons are presented both in the report and in a microfiche appendix.</p> <p>Air-inlet wind tunnel testing techniques and limitations were also investigated and reported. Results from measurements of inlet performance from three European wind tunnels using a common axisymmetric pitot intake are also presented.</p> <p>The participants in Working Group 13 represented Belgium, France, Germany, Italy, the United Kingdom, and the United States.</p> <p>ISBN 92-834-0637-5</p>	<p>The present capability of Computational Fluid Dynamics (CFD) methods was assessed through a comparative analysis of both CFD predictions and experimental data. This analysis was conducted for eight different flow field test cases designed to produce critical features of air-intake flow fields. Flow field results and comparisons are presented both in the report and in a microfiche appendix.</p> <p>Air-inlet wind tunnel testing techniques and limitations were also investigated and reported. Results from measurements of inlet performance from three European wind tunnels using a common axisymmetric pitot intake are also presented.</p> <p>The participants in Working Group 13 represented Belgium, France, Germany, Italy, the United Kingdom, and the United States.</p> <p>ISBN 92-834-0637-5</p>

### **Microfiche Appendix**

This Microfiche Appendix contains "Contributions to Test Cases" relating to Section 3.3 "Analysis of Test Cases" as listed in the Contents Pages ix, x, xi.

(Fiche No. 5 contains the colour reproductions referred to throughout Fiche No's 1 to 4.)

**AGARD**  
**NATO OTAN**  
**7 RUE ANCELLE - 92200 NEUILLY-SUR-SEINE**  
**FRANCE**  
Téléphone (1) 47.38.57.00 - Télex 610 176  
Télécopie (1) 47.38.57.99

**DIFFUSION DES PUBLICATIONS**  
**AGARD NON CLASSIFIEES**

L'AGARD ne détient pas de stocks de ses publications, dans un but de distribution générale à l'adresse ci-dessus. La diffusion initiale des publications de l'AGARD est effectuée auprès des pays membres de cette organisation par l'intermédiaire des Centres Nationaux de Distribution suivants. A l'exception des Etats-Unis, ces centres disposent parfois d'exemplaires additionnels; dans les cas contraire, on peut se procurer ces exemplaires sous forme de microfiches ou de microcopies auprès des Agences de Vente dont la liste suit.

**CENTRES DE DIFFUSION NATIONAUX**

<p><b>ALLEMAGNE</b>  Fachinformationszentrum,  Karlsruhe  D-7514 Eggenstein-Leopoldshafen 2</p> <p><b>BELGIQUE</b>  Coordonnateur AGARD-VSL  Etat-Major de la Force Aérienne  Quartier Reine Elisabeth  Rue d'Evere 1140 Bruxelles</p> <p><b>CANADA</b>  Directeur du Service des Renseignements Scientifiques  Ministère de la Défense Nationale  Ottawa, Ontario K1A 0K2</p> <p><b>DANEMARK</b>  Danish Defence Research Board  Ved Idrætsparken 4  2100 Copenhagen Ø</p> <p><b>ESPAGNE</b>  INTA (AGARD Publications)  Pintor Rosales 34  28008 Madrid</p> <p><b>ETATS-UNIS</b>  National Aeronautics and Space Administration  Langley Research Center  M/S 180  Hampton, Virginia 23665</p> <p><b>FRANCE</b>  O.N.F.R.A. (Direction)  29, Avenue de la Division Leclerc  92320, Châtillon sous Bagneux</p> <p><b>GRECE</b>  Hellenic Air Force  Air War College  Scientific and Technical Library  Dekelia Air Force Base  Dekelia, Athens TGA 1010</p>	<p><b>ISLANDE</b>  Director of Aviation  c/o Flugrad  Reykjavik</p> <p><b>ITALIE</b>  Aeronautica Militare  Ufficio del Delegato Nazionale all'AGARD  Aeroporto Pratica di Mare  00040 Pomezia (Roma)</p> <p><b>LUXEMBOURG</b>  Voir Belgique</p> <p><b>NORVEGE</b>  Norwegian Defence Research Establishment  Attn: Biblioteket  P.O. Box 25  N-2007 Kjeller</p> <p><b>PAYS-BAS</b>  Netherlands Delegation to AGARD  National Aerospace Laboratory NLR  Kluyverweg 1  2629 HS Delft</p> <p><b>PORTUGAL</b>  Portuguese National Coordinator to AGARD  Gabinete de Estudos e Programas  CLAFIA  Base de Alfragide  Alfragide  2700 Amadora</p> <p><b>ROYAUME UNI</b>  Defence Research Information Centre  Kentigern House  65 Brown Street  Glasgow G2 8EX</p> <p><b>TURQUIE</b>  Milli Savunma Başkanlığı (MSB)  ARGE Daire Başkanlığı (ARGE)  Ankara</p>
--	--

LE CENTRE NATIONAL DE DISTRIBUTION DES ETATS-UNIS (NASA) NE DETIENT PAS DE STOCKS  
DES PUBLICATIONS AGARD ET LES DEMANDES D'EXEMPLAIRES DOIVENT ETRE ADRESSEES DIRECTEMENT  
AU SERVICE NATIONAL TECHNIQUE DE L'INFORMATION (NTIS) DONT L'ADRESSE SUIT.

**AGENCES DE VENTE**

National Technical Information Service (NTIS) 5285 Port Royal Road Springfield, Virginia 22161 Etats-Unis	ESA/Information Retrieval Service European Space Agency 10, rue Mario Nikis 75015 Paris France	The British Library Document Supply Division Boston Spa, Wetherby West Yorkshire LS23 7BQ Royaume Uni
---	--	---

Les demandes de microfiches ou de photocopies de documents AGARD (y compris les demandes faites auprès du NTIS) doivent comporter la dénomination AGARD, ainsi que le numéro de série de l'AGARD (par exemple AGARD-AG-315). Des informations analogues, telles que le titre et la date de publication sont souhaitables. Veuillez noter qu'il y a lieu de spécifier AGARD-R-nnn et AGARD-AR-nnn lors de la commande de rapports AGARD et des rapports consultatifs AGARD respectivement. Des références bibliographiques complètes ainsi que des résumés des publications AGARD figurent dans les journaux suivants:

Scientific and Technical Aerospace Reports (STAR)  
publié par la NASA Scientific and Technical  
Information Division  
NASA Headquarters (NTT)  
Washington D.C. 20546  
Etats-Unis

Government Reports Announcements and Index (GRA&I)  
publié par le National Technical Information Service  
Springfield  
Virginia 22161  
Etats-Unis  
(accessible également en mode interactif dans la base de  
données bibliographiques en ligne du NTIS, et sur CD-ROM)



Imprimé par Specialised Printing Services Limited  
40 Chigwell Lane, Loughton, Essex IG10 3TZ

AGARD

NATO OTAN

7 RUE ANCELLE · 92200 NEUILLY-SUR-SEINE

FRANCE

Telephone (1)47.38.57.00 · Telex 610 176

Telefax (1)47.38.57.99

**DISTRIBUTION OF UNCLASSIFIED  
AGARD PUBLICATIONS**

AGARD does NOT hold stocks of AGARD publications at the above address for general distribution. Initial distribution of AGARD publications is made to AGARD Member Nations through the following National Distribution Centres. Further copies are sometimes available from these Centres (except in the United States), but if not may be purchased in Microfiche or Photocopy form from the Sales Agencies listed below.

**NATIONAL DISTRIBUTION CENTRES**

**BELGIUM**

Coordonnateur AGARD — VSL  
Etat-Major de la Force Aérienne  
Quartier Reine Elisabeth  
Rue d'Evere, 1140 Bruxelles

**CANADA**

Director Scientific Information Services  
Dept of National Defence  
Ottawa, Ontario K1A 0K2

**DENMARK**

Danish Defence Research Board  
Ved Idraetsparken 4  
2100 Copenhagen Ø

**FRANCE**

O.N.E.R.A. (Direction)  
29 Avenue de la Division Leclerc  
92320 Châtillon

**GERMANY**

Fachinformationszentrum  
Karlsruhe  
D-7514 Eggenstein-Leopoldshafen 2

**GREECE**

Hellenic Air Force  
Air War College  
Scientific and Technical Library  
Dekelia Air Force Base  
Dekelia, Athens TGA 1010

**ICELAND**

Director of Aviation  
c/o Flugrad  
Reykjavik

**ITALY**

Aeronautica Militare  
Ufficio del Delegato Nazionale all'AGARD  
Aeroporto Pratica di Mare  
00040 Pomezia (Roma)

**LUXEMBOURG**

See Belgium

**NETHERLANDS**

Netherlands Delegation to AGARD  
National Aerospace Laboratory, NLR  
Kluwerweg 1  
2629 HS Delft

**NORWAY**

Norwegian Defence Research Establishment  
Attn: Biblioteket  
P.O. Box 25  
N-2007 Kjeller

**PORTUGAL**

Portuguese National Coordinator to AGARD  
Gabinete de Estudos e Programas  
CLAFIA  
Base de Alfragide  
Alfragide  
2700 Amadora

**SPAIN**

INTA (AGARD Publications)  
Pintor Rosales 34  
28008 Madrid

**TURKEY**

Milli Savunma Başkanlığı (MSB)  
ARGE Daire Başkanlığı (ARGE)  
Ankara

**UNITED KINGDOM**

Defence Research Information Centre  
Kentigern House  
65 Brown Street  
Glasgow G2 8EX

**UNITED STATES**

National Aeronautics and Space Administration (NASA)  
Langley Research Center  
M/S 180  
Hampton, Virginia 23665

THE UNITED STATES NATIONAL DISTRIBUTION CENTRE (NASA) DOES NOT HOLD STOCKS OF AGARD PUBLICATIONS, AND APPLICATIONS FOR COPIES SHOULD BE MADE DIRECT TO THE NATIONAL TECHNICAL INFORMATION SERVICE (NTIS) AT THE ADDRESS BELOW.

**SALES AGENCIES**

National Technical  
Information Service (NTIS)  
5285 Port Royal Road  
Springfield, Virginia 22161  
United States

ESA/Information Retrieval Service  
European Space Agency  
16, rue Mario Nikis  
75015 Paris  
France

The British Library  
Document Supply Centre  
Boston Spa, Wetherby  
West Yorkshire LS23 7BQ  
United Kingdom

Requests for microfiches or photocopies of AGARD documents (including requests to NTIS) should include the word 'AGARD' and the AGARD serial number (for example AGARD-AG-315). Collateral information such as title and publication date is desirable. Note that AGARD Reports and Advisory Reports should be specified as AGARD-R-nnn and AGARD-AR-nnn, respectively. Full bibliographical references and abstracts of AGARD publications are given in the following journals:

Scientific and Technical Aerospace Reports (STAR)  
published by NASA Scientific and Technical  
Information Division  
NASA Headquarters (NTT)  
Washington D.C. 20546  
United States

Government Reports Announcements and Index (GRA&I)  
published by the National Technical Information Service  
Springfield  
Virginia 22161  
United States

(also available online in the NTIS Bibliographic  
Database or on CD-ROM)



Printed by Specialised Printing Services Limited  
40 Chigwell Lane, Loughton, Essex IG10 3TZ

ISBN 92-835-0637-5

# AR 270

## Air Intakes for High Speed Vehicles

### Microfiche Appendix to Section 3.3 "Analysis of Test Cases"

#### CONTENTS

Sub-Section		Page No.	Fiche No.
3.3.1	Contributions to Test Case 1 — Transonic normal shock/turbulent	A1	1
3.3.2	Contributions to Test Case 2 — Glancing shock/boundary layer interaction	A33	1
3.3.3/3.3.4	Contributions to Test Case 3 and 4 — Case 3 Subsonic/transonic circular intake — Case 4 Subsonic/transonic semi-circular intake	A103	2
3.3.5	Contributions to Test Case 5 — Supersonic circular pitot intake	A184	2
3.3.6	Contributions to Test Case 6 — 2D hypersonic intake	A209	3
3.3.7	Contributions to Test Case 7 — Axisymmetric mixed compression inlet	A339	4
3.3.8	Contributions to Test Case 8 — Intake/airframe integration	A346	4

**Note:** Fiche No.5 contains the colour reproductions referred to throughout Fiche No's 1 to 4.

# **AR 270**

## **Microfiche Appendix to Sub-Section 3.3.1**

### **Contributions to Test Case 1**

#### **Transonic normal shock/turbulent**

**Sverdrup -- AEDC**

**MBB**

**Page No's**

**A2 to A8**

**A9 to A32**

## MEMORANDUM

SVERDRUP TECHNOLOGY, INC.

Date: May 8, 1990

Organization

Mail Stop

To: Record

From: D.H. Huddleston

EL2

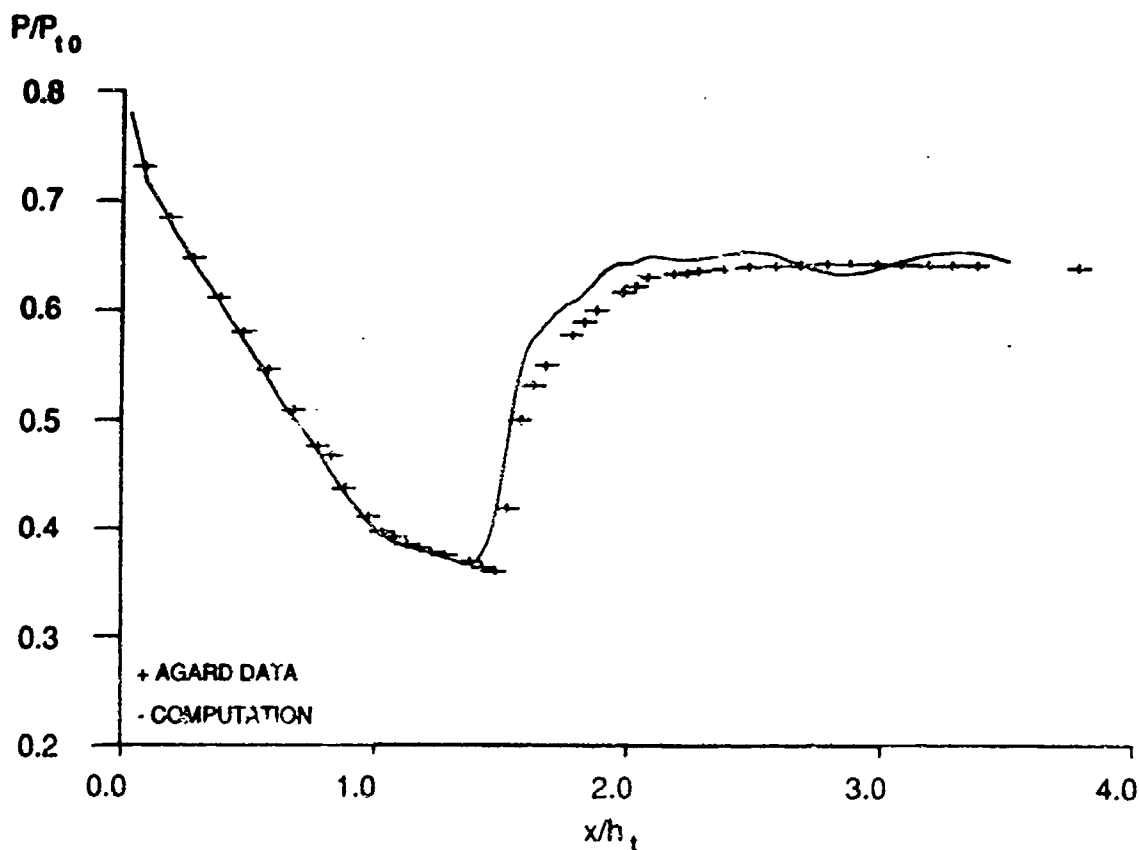
900

Thru:

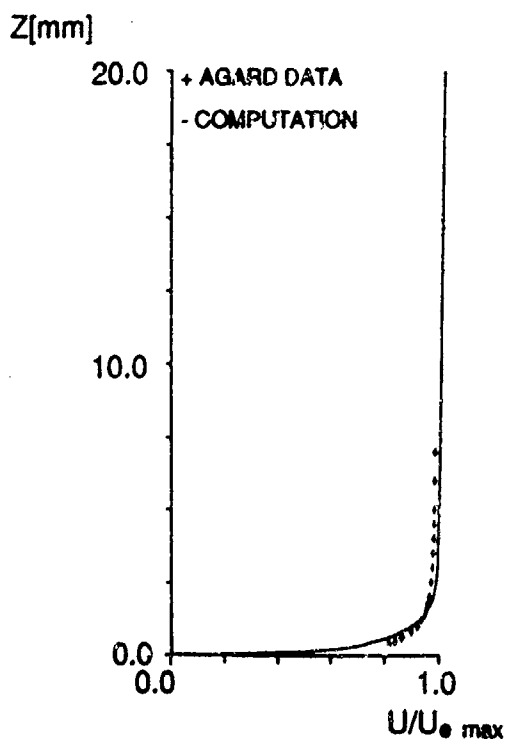
Subject: AGARD WG13 Test Case 1: Transonic normal shock/turbulent  
boundary layer interactions

---

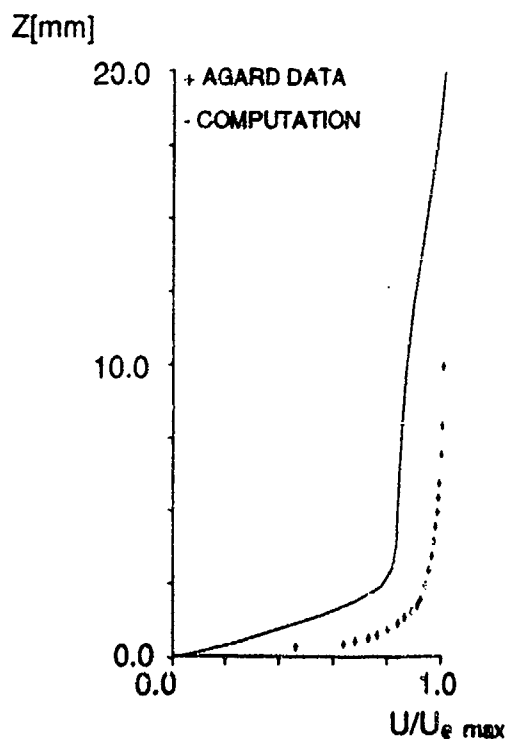
The requested preliminary comparisons of axial pressure distribution and boundary layer velocity profiles are attached, for the subject test cases 1.1 and 1.2. Computations for each test case were made by application of the PARC2D Navier-Stokes code. The algebraic turbulence model available in PARC2D was applied without modification. Computations were made on a grid containing 9050 grid points with approximately fifty grid lines within the boundary layer. Preliminary comparisons with AGARD data for test case 1.3 is not yet available. The AGARD data, as received for test case 1.3, requires interpolation of the data in order to produce the comparisons at the requested axial stations. This does not seem consistent since the purpose of the AGARD test cases is to evaluate currently available CFD codes relative to detailed turbulent flow measurements.



Static wall pressure on lower tunnel wall.  
Test Case 1.1

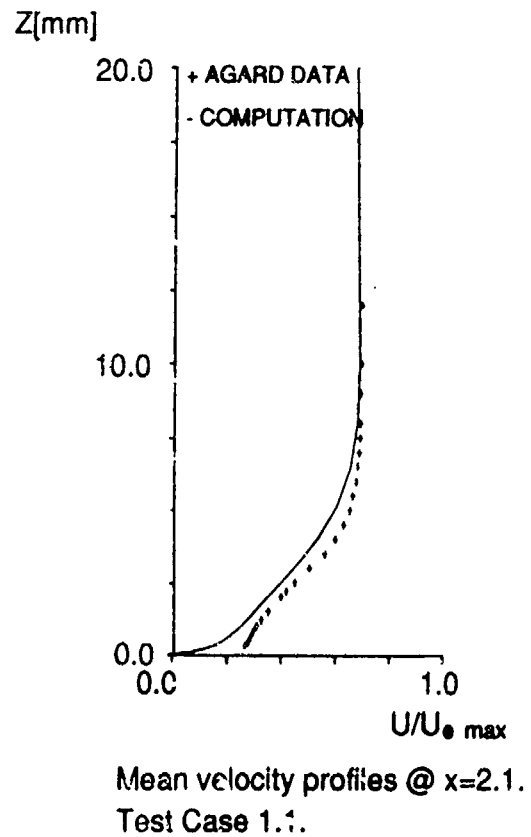
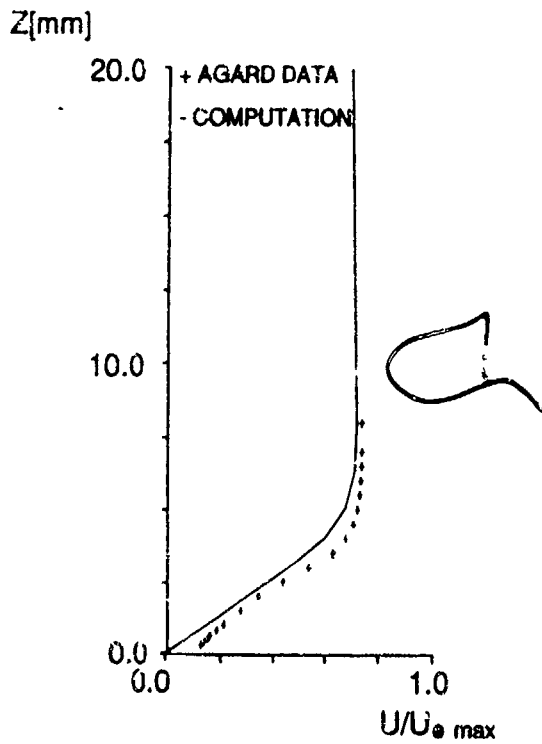
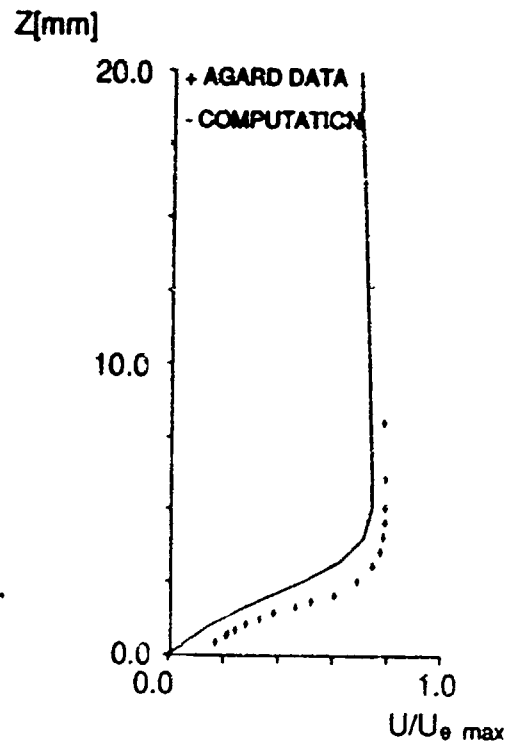
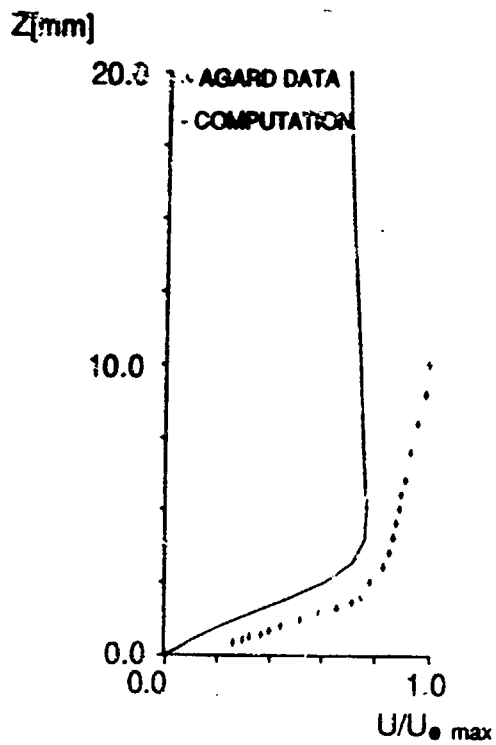


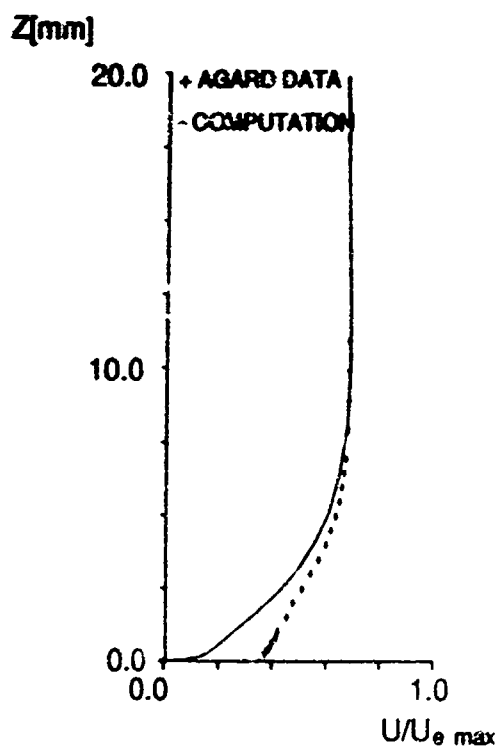
Mean velocity profiles @  $x=1.4$ .  
Test Case 1.1.



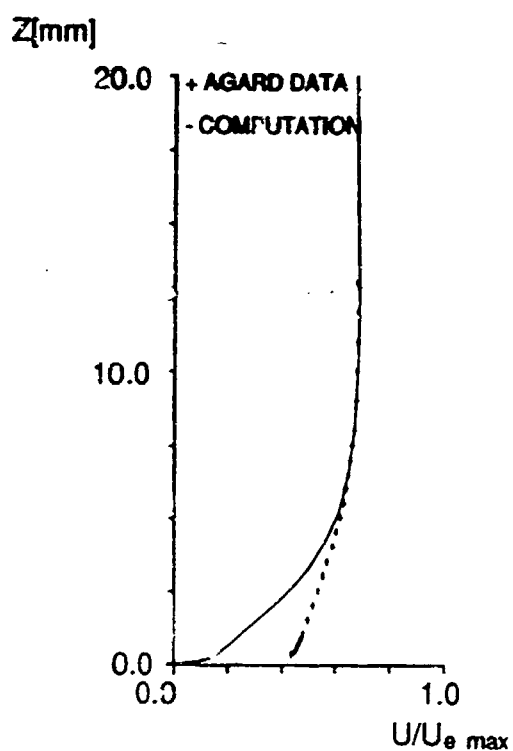
Mean velocity profiles @  $x=1.55$ .  
Test Case 1.1.



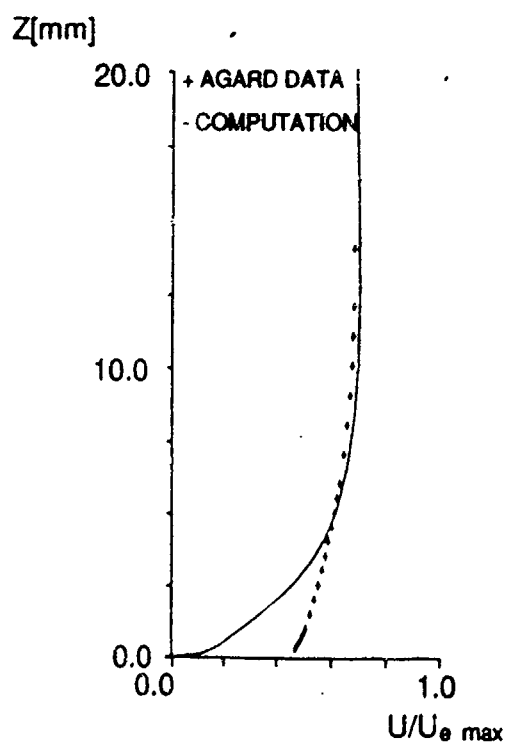




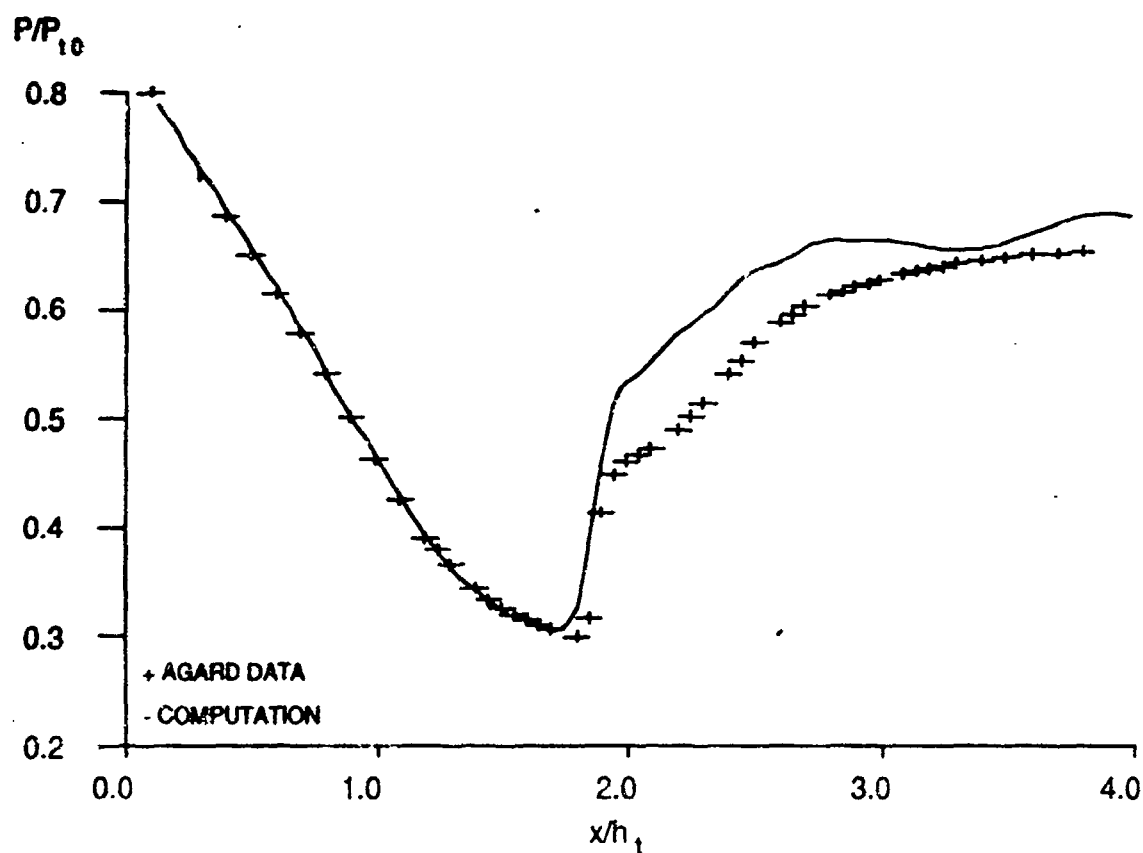
Mean velocity profiles @  $x=2.4$ .  
Test Case 1.1.



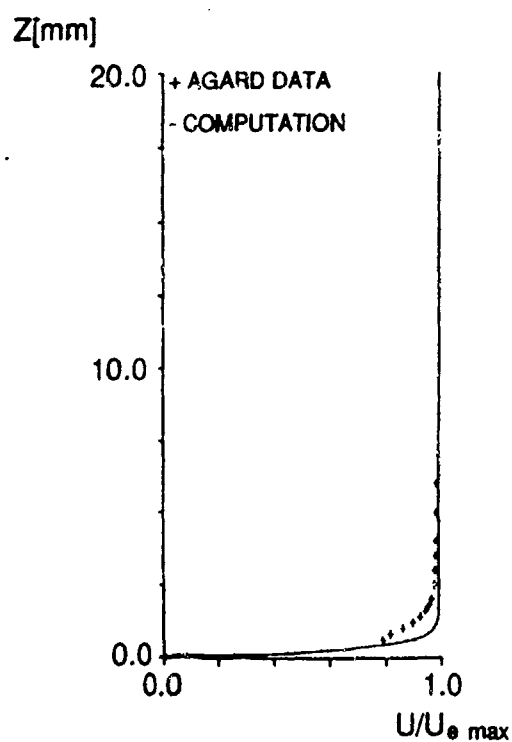
Mean velocity profiles @  $x=2.8$ .  
Test Case 1.1.



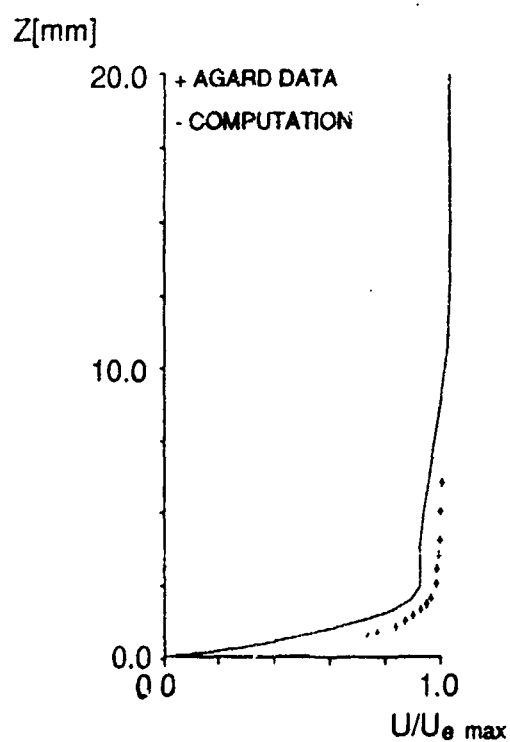
Mean velocity profiles @  $x=3.2$ .  
Test Case 1.1.



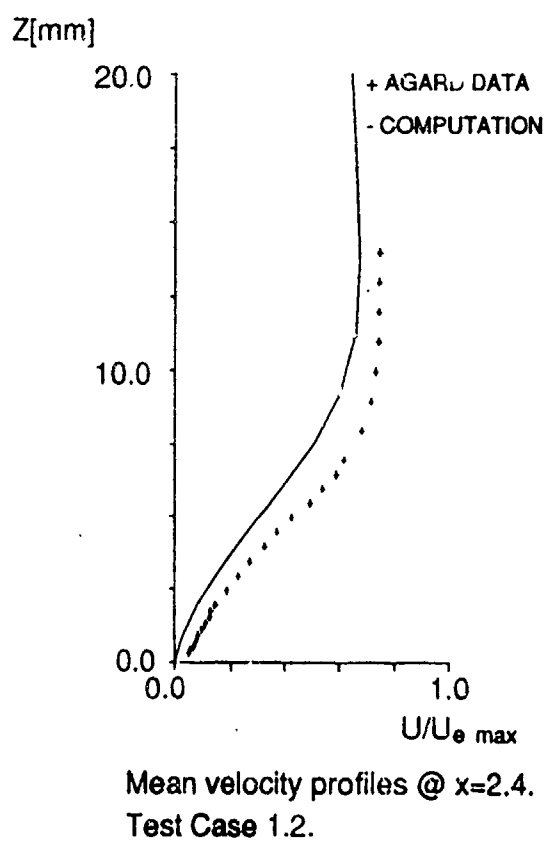
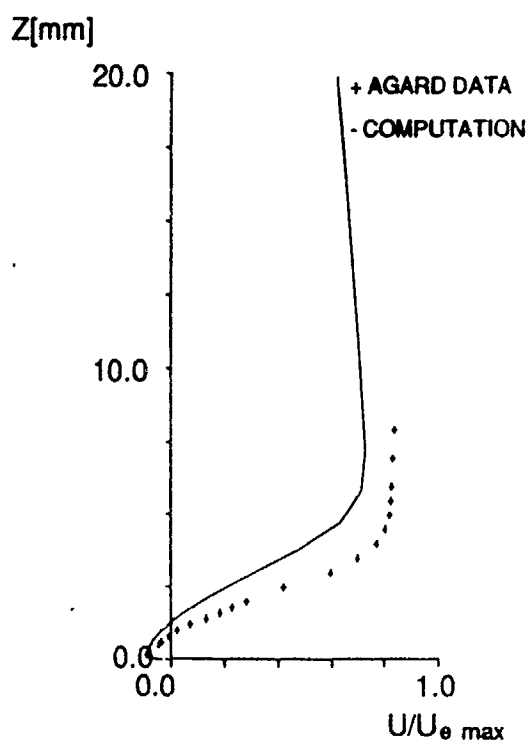
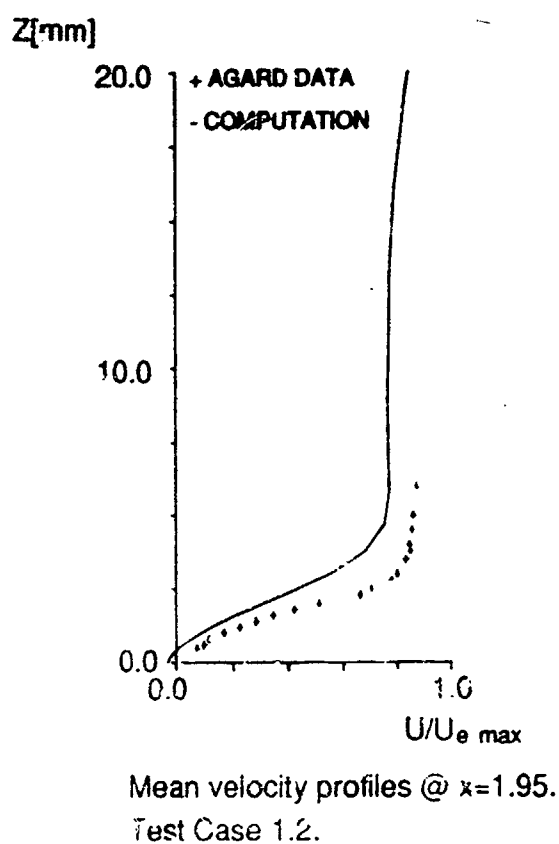
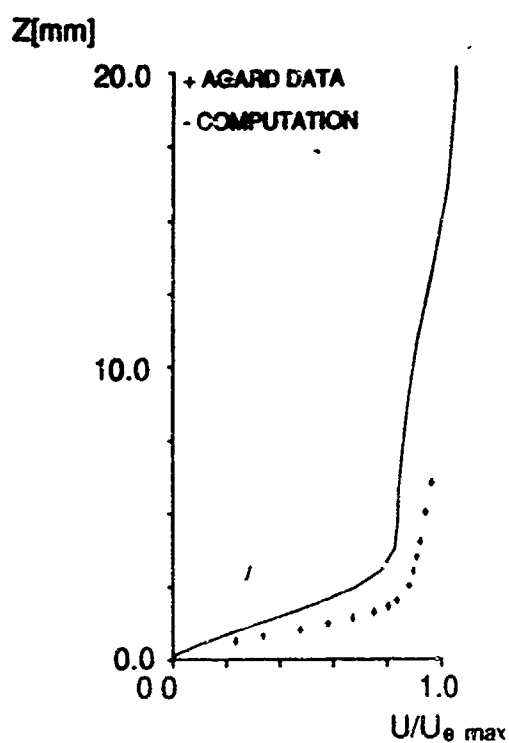
Static wall pressure on lower tunnel wall.  
Test Case 1.2

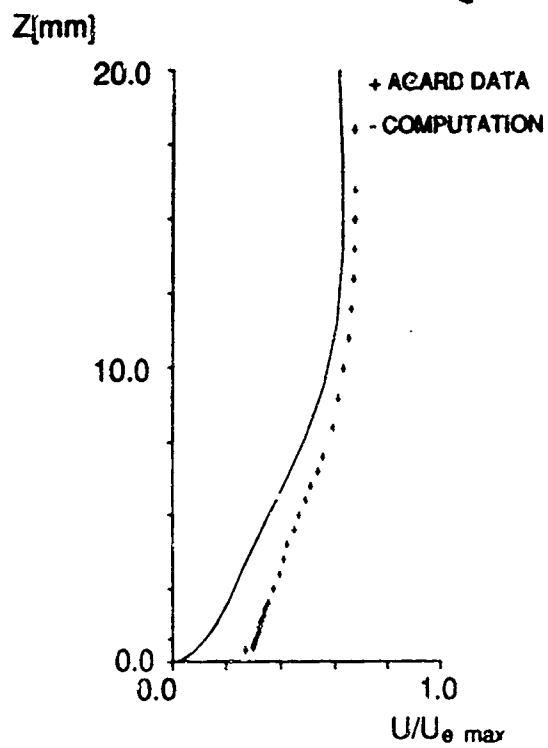


Mean velocity profiles @  $x=1.60$ .  
Test Case 1.2.

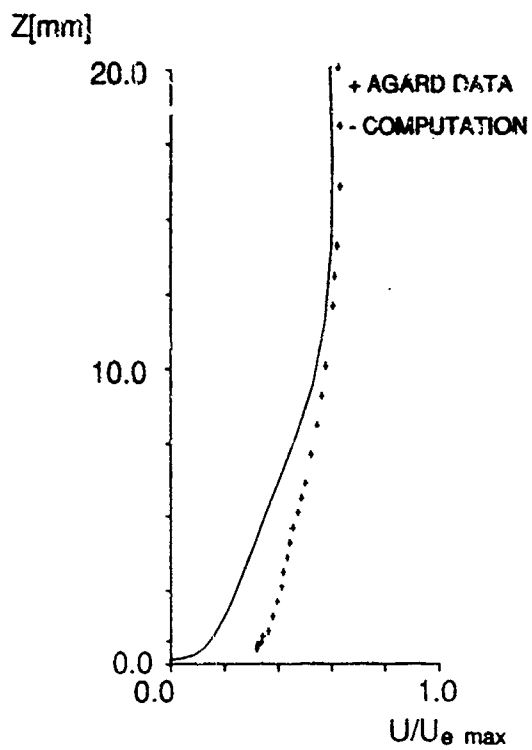


Mean velocity profiles @  $x=1.85$ .  
Test Case 1.2.





Mean velocity profiles @  $x=2.8$ .  
Test Case 1.2.



Mean velocity profiles @  $x=3.2$ .  
Test Case 1.2.

Messerschmitt-Bölkow-Blohm GmbH  
 FE211, P.O. Box 801160  
 D-8000 München 80, FRG

October 4, 1990

Input for AGARD Working Group 13, Test Case 1:

### Transonic shock-wave/turbulent boundary-layer interactions

The solutions of the transonic-flows in the S8 transonic channel of the ONERA Fluid Mechanics Laboratory were obtained using the two-dimensional Navier-Stokes code NSFLEX (Navier-Stokes solver using characteristic flux extrapolation) [1]. It is a finite-volume method applicable to sub-, trans- and hypersonic flows. The inviscid fluxes at the finite-volume faces are evaluated by solving a Riemann problem [2]. A third-order accurate local characteristic flux extrapolation scheme of type MUSCL [3] is employed. For capturing strong shock waves (especially in hypersonic flows) a flux vector splitting is used [4]. For the interpolation between the two ways (MUSCL flux-difference splitting and a modified Steger/Warming flux-vector splitting) to form cell face fluxes a sharpened high-order limiter derived from the van Albada limiter has been incorporated. The viscous fluxes are approximated with central differences. The numerical method utilizes the algebraic turbulence model of Baldwin and Lomax [5]. The unfactored implicit equations are solved in time-dependent form by a point Gauss-Seidel relaxation technique. By applying the so-called checkerboard scheme, in which points are divided into black and white ones, a high degree of vectorization is achieved. The code contains multi-blocking capability and real gas effects are incorporated.

The computational grids used are shown in Fig. 1 to Fig. 3. Because of the symmetric geometry of the nozzle of the test case TC1.1 and TC1.2 one half of the flow fields with symmetry condition were calculated only. Each of the grids consists of one block and was generated with an algebraic mesh generator ensuring perpendicular intersection of the grid lines with the surfaces. The inner-law variable  $z^+$  can be varied. The results shown in Fig. 4 to Fig. 21 were produced on grids with  $209 \times 100$  points (TC1.1),  $236 \times 100$  points (TC1.2) and with  $239 \times 100$  points (TC1.3). Grid refinements from 100 to 200 points in  $z$ -direction with  $z^+(200 \text{ points}) = 0.1 \cdot z^+(100 \text{ points})$  did not show any change neither in the wall pressures, in the mean velocity profiles nor in the shear stress profiles.

All calculations were performed on the SIEMENS supercomputer VP200. They were started with the initial conditions of  $p_{t,e} = 96000 \text{ N/m}^2$ ,  $T_{t,e} = 300 \text{ K}$  and  $T_e$  in the first cell row of the entrance. The static pressure  $p/p_{t,e}$  at the exit face of the channel was used to adjust the shock position.

The mass loss along the duct, Fig. 7, Fig. 13 and Fig. 19, was used both for quality check of the code and convergence criterion.  $\Delta \dot{m}$  was referred to the mass flux  $\dot{m}$  in the third-cell in  $x$ -direction. About 20000 iterations for TC1.1 and TC1.3 and 30000 iterations for TC1.2 were necessary to obtain converged solutions. The computations required  $8.0E-5$  seconds per point and iteration. The calculation was done turbulent starting from the entrance.

### References

- [1] Schmatz, M.A.: NSFLEX - An implicit relaxation method for the Navier-Stokes equations for a wide range of Mach numbers. Notes on Numerical

Fluid Mechanics, vol. 30, Vieweg, Braunschweig (1990).

- [2] Eberle, A.: Characteristic flux averaging approach to the solution of Euler's equations. VKI-Lecture Series 1987-04 (1987).
- [3] Anderson, W.K., Thomas, J.L. van Leer, B.: A comparison of finite volume flux vector splittings for the Euler equations. AIAA Paper 85-0122 (1985).
- [4] Eberle, A., Schmatz, M.A., Bissinger, N.C.: Generalized flux vectors for hypersonic shock capturing. AIAA Paper 90-0290 (1990).
- [5] Baldwin, B.S., Lomax, J.: Thin layer approximation and algebraic model for separated turbulent flows. AIAA Paper 78-0257 (1978).

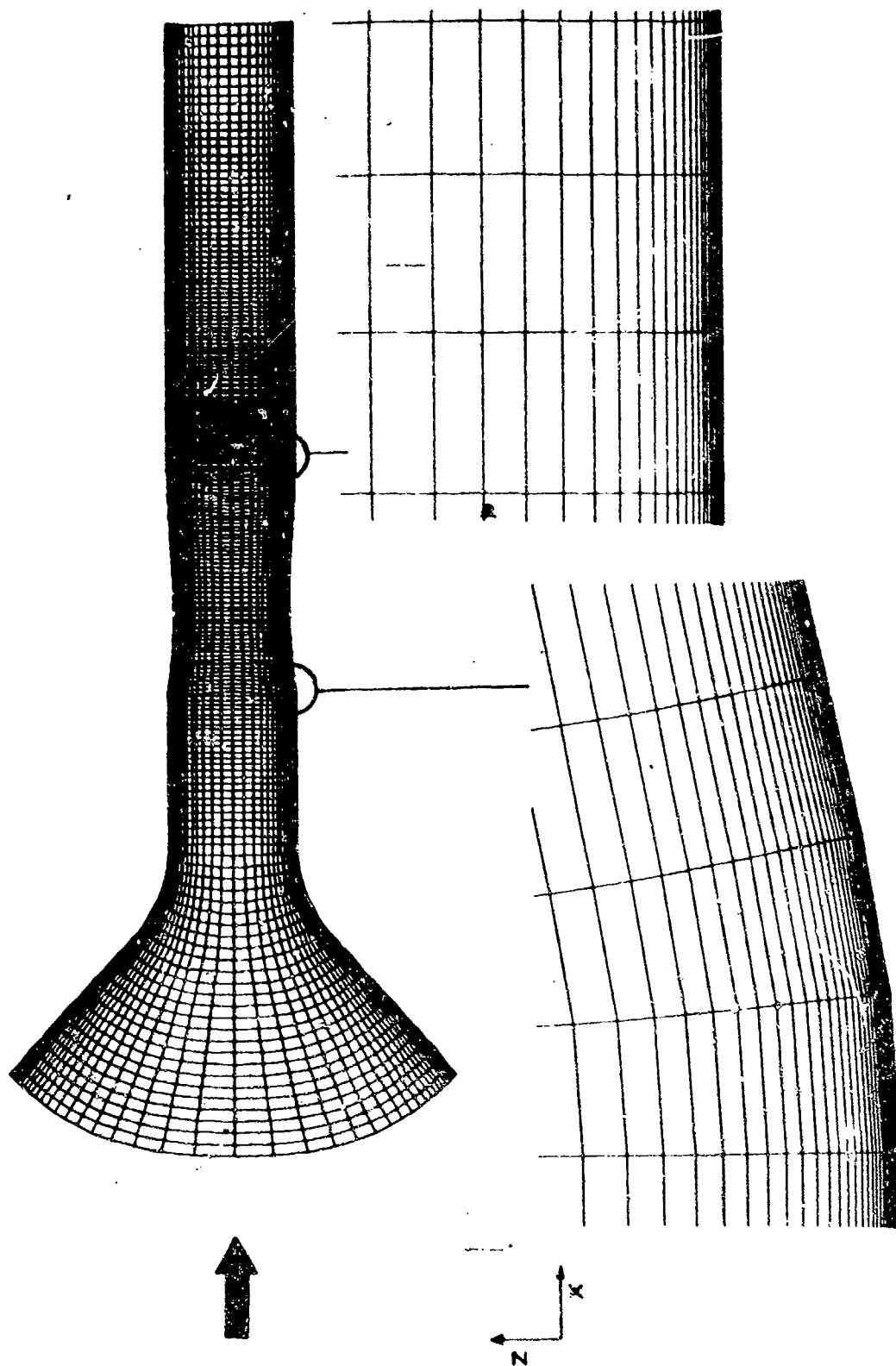


Fig. 1 Computational mesh for the test case 1.1 (209\*500 points)



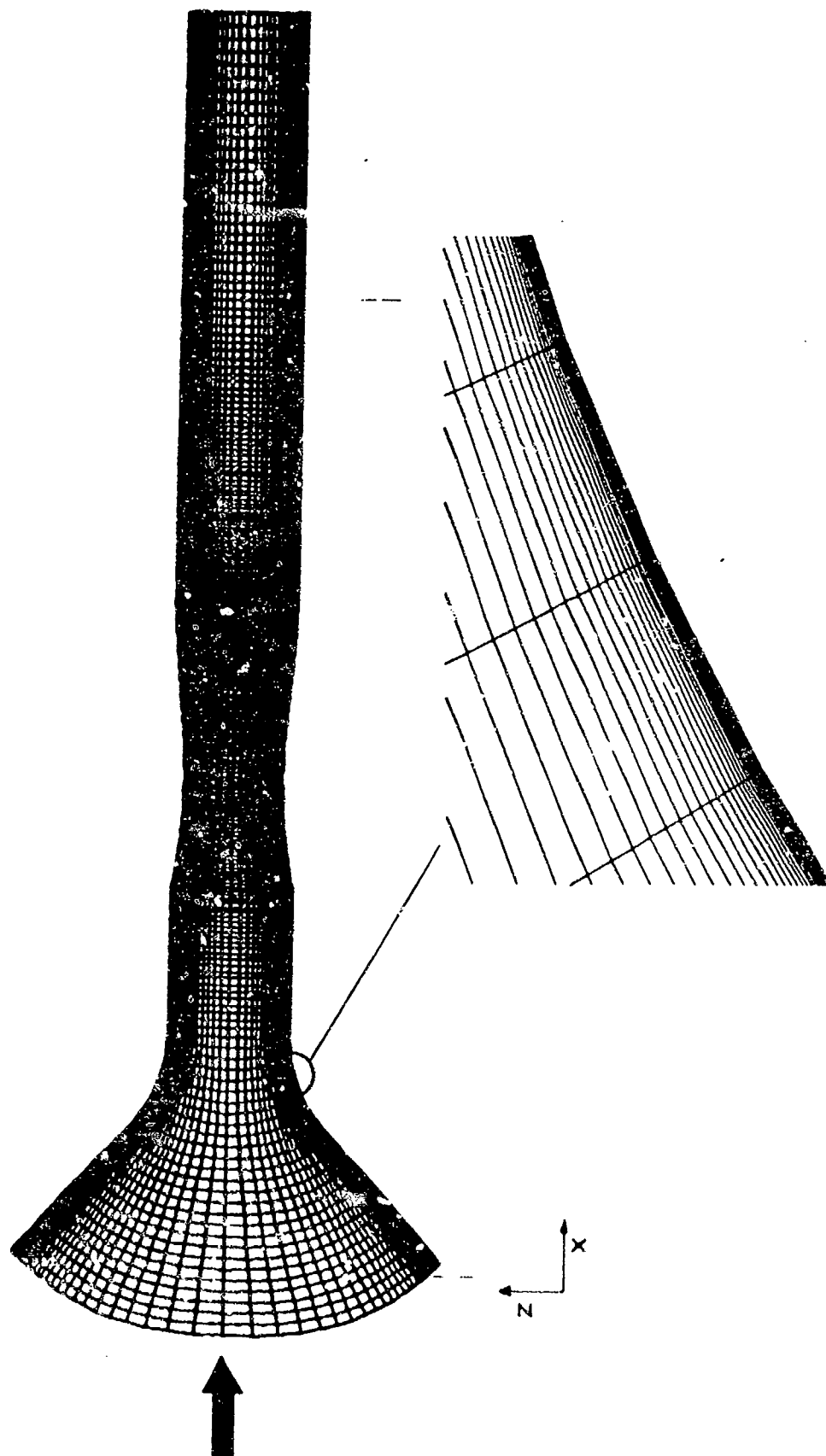


Fig. 2 Computational mesh for the test case 1.2 (236\*100 points)

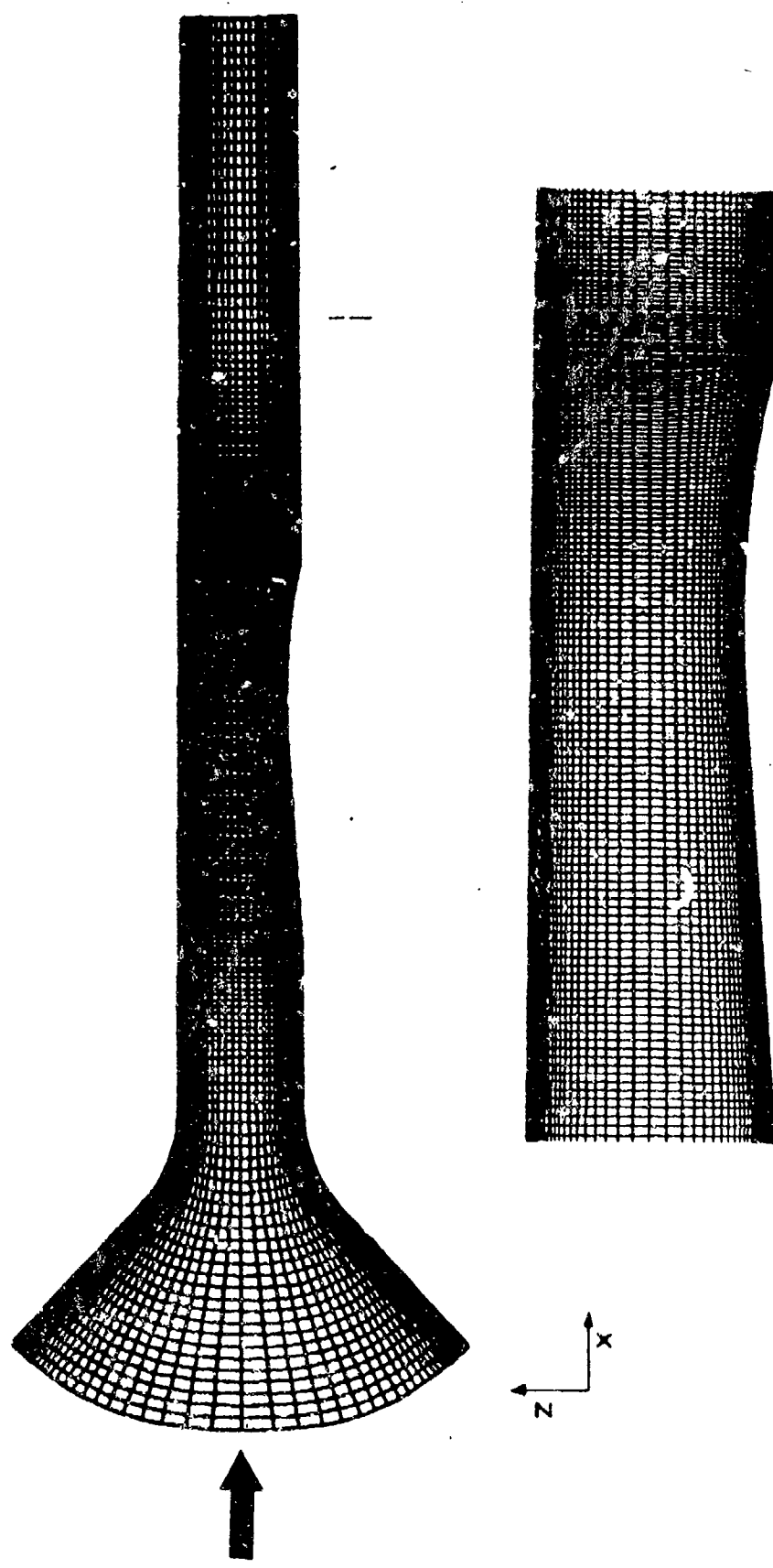


Fig. 3 Computational mesh for the test case 1.3 (239\*100 points)

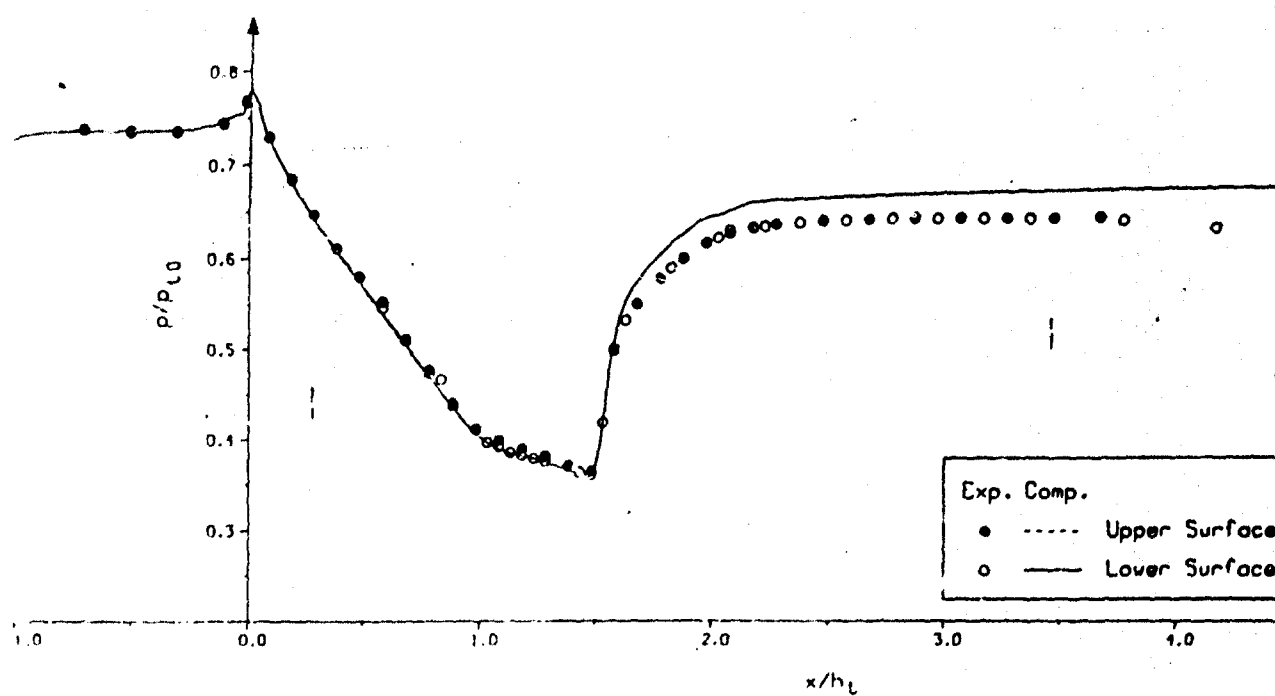


Fig. 4 Static wall-pressure distribution, test case 1.1

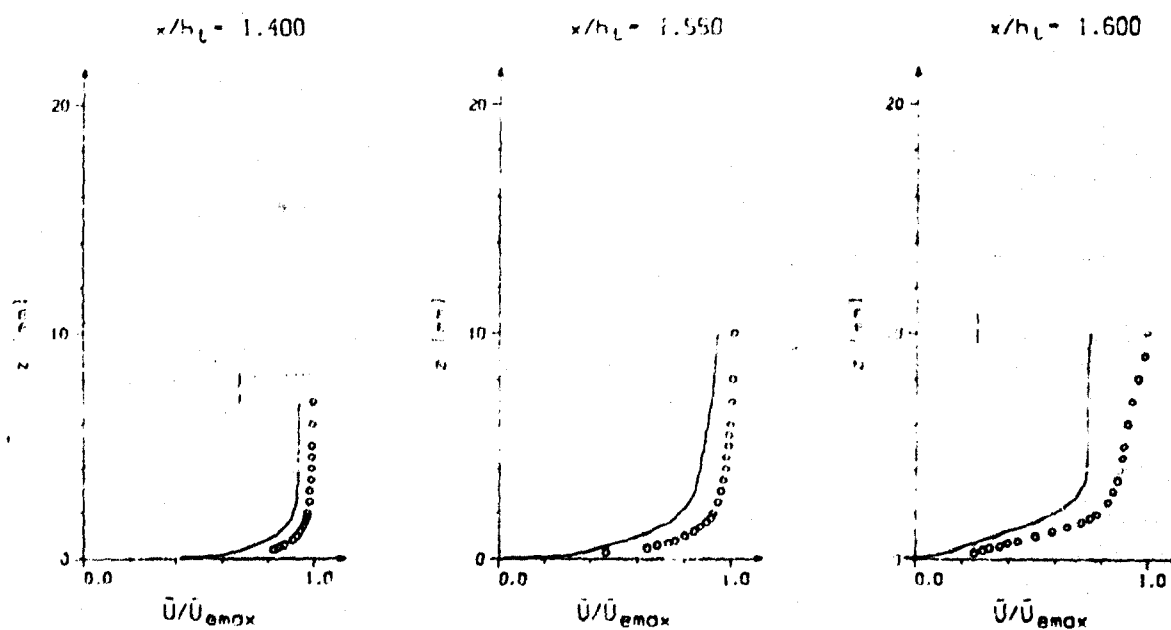


Fig. 5 Mean velocity profiles, test case 1.1

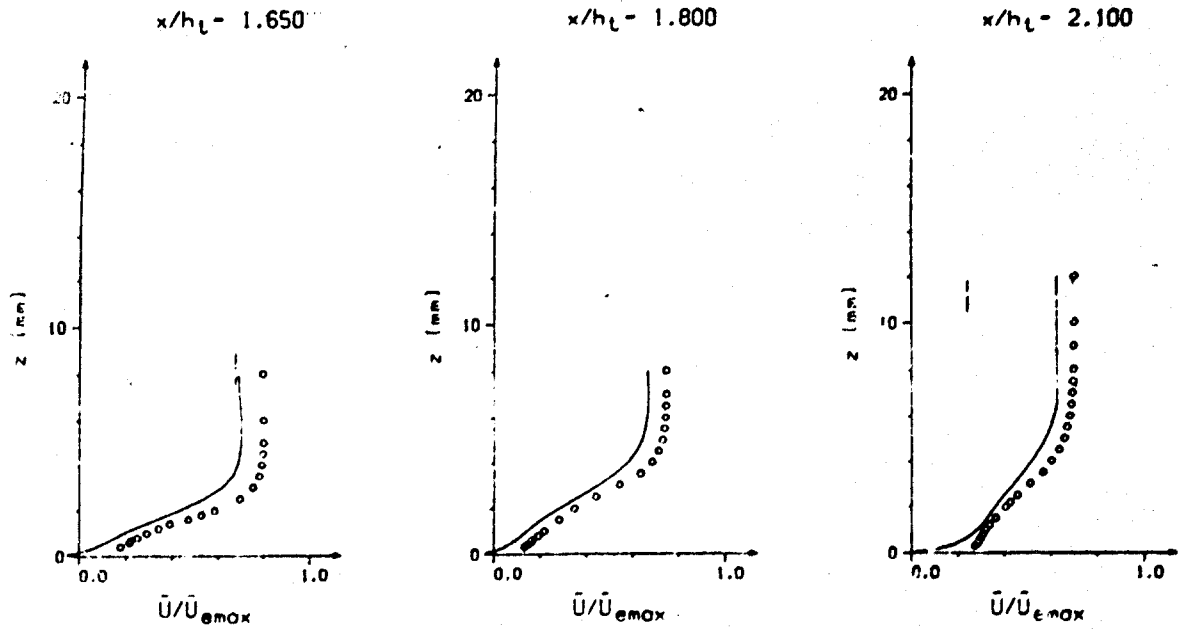


Fig. 5 Continued

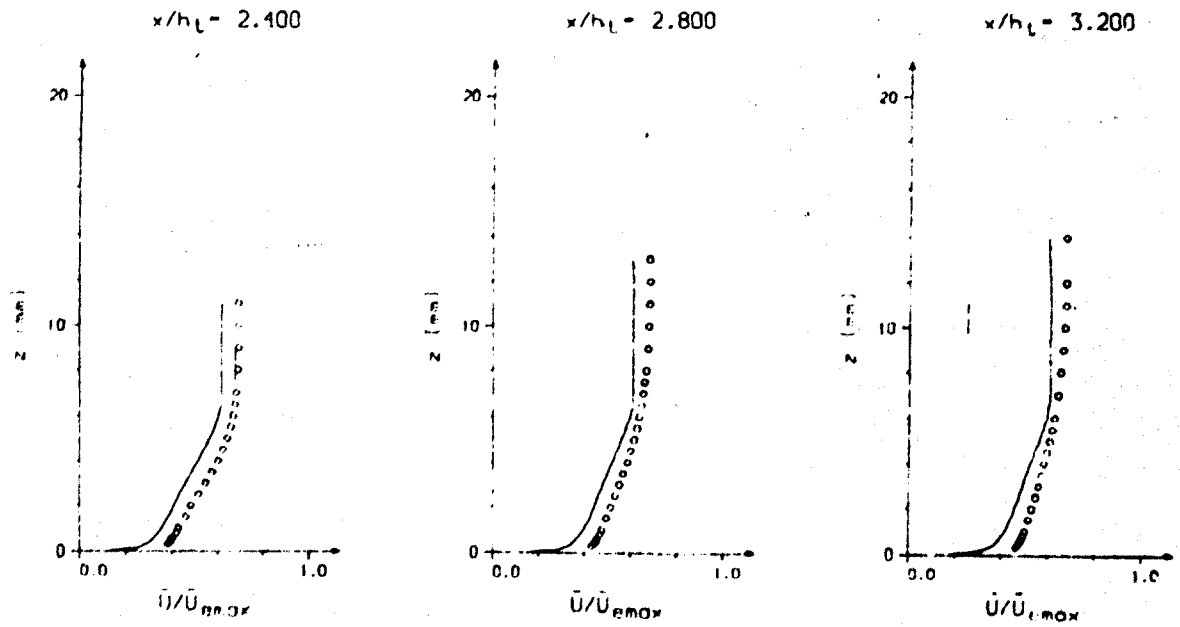


Fig. 5 Continued

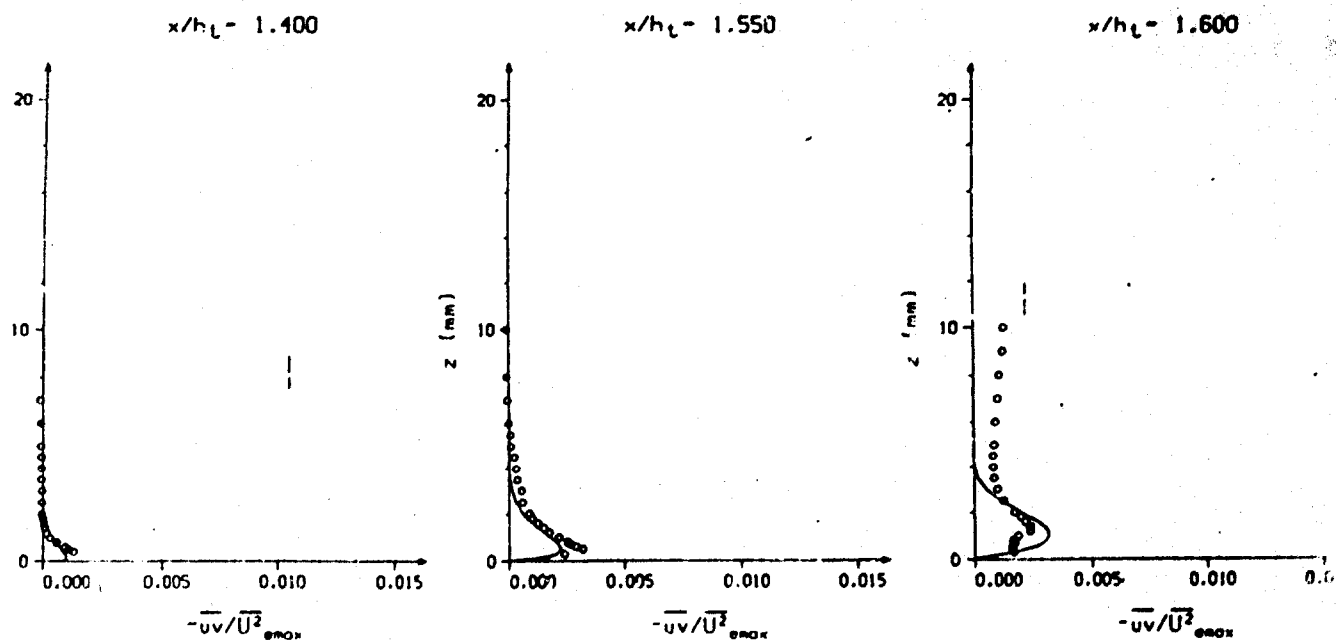


Fig. 6 Reynolds stress profiles, test case 1.1

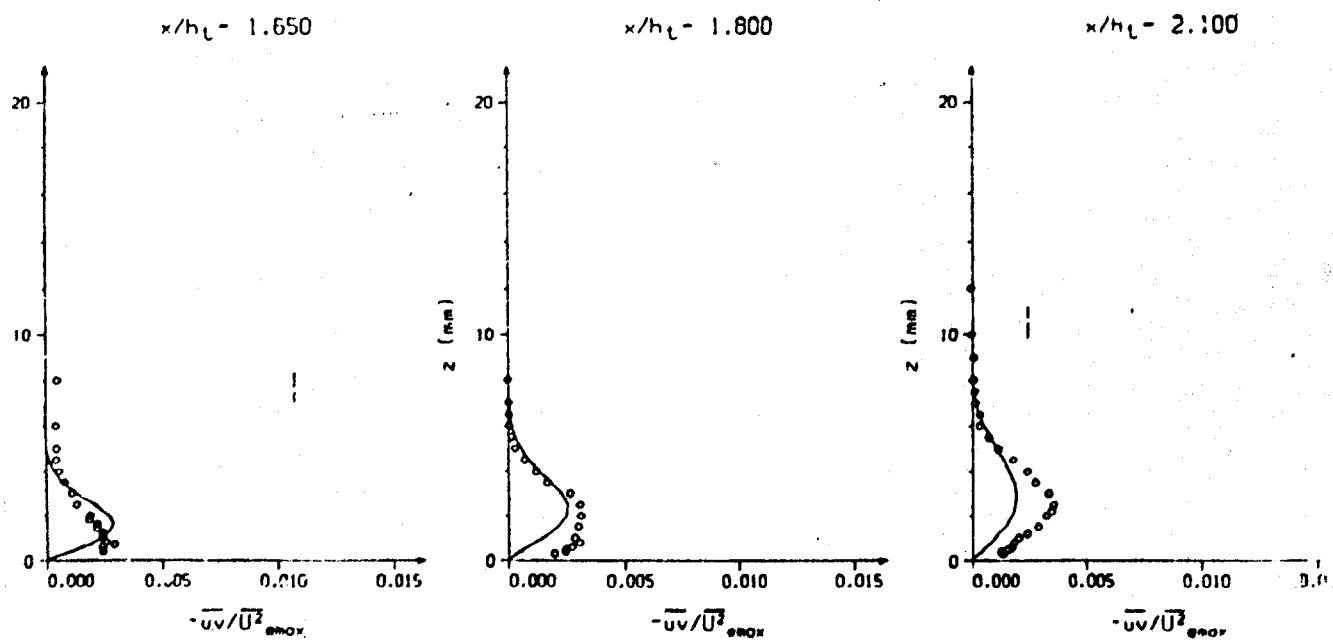


Fig. 6 Continued

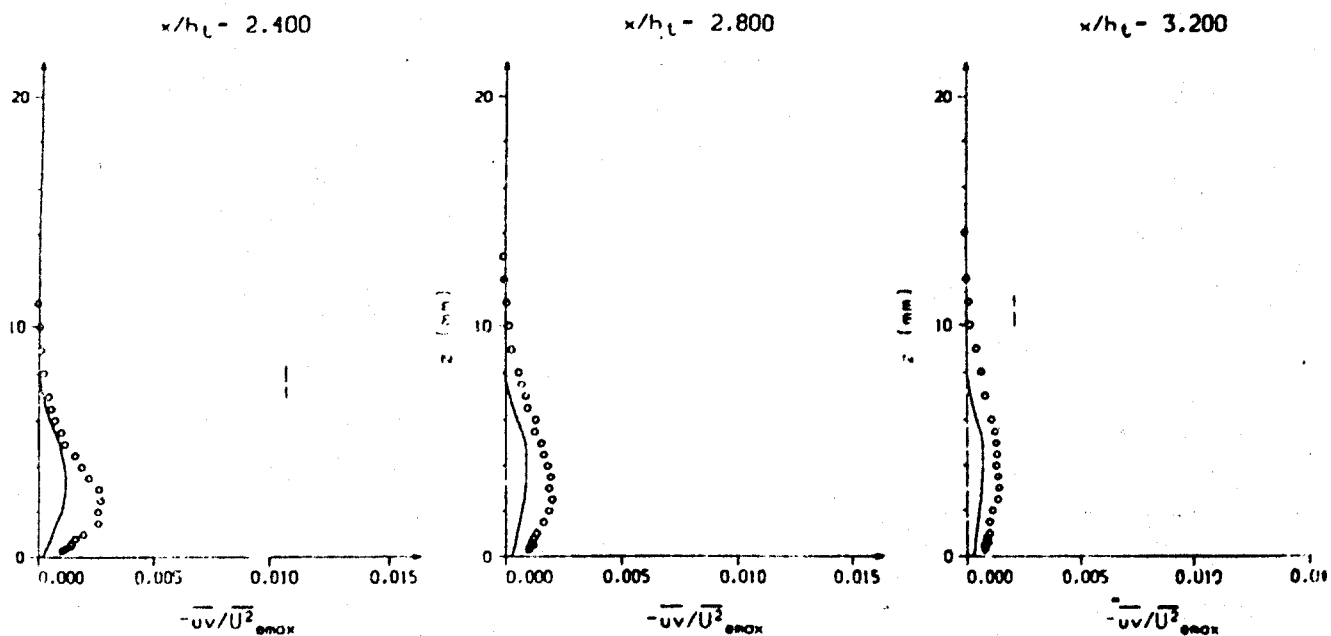


Fig. 6 Continued

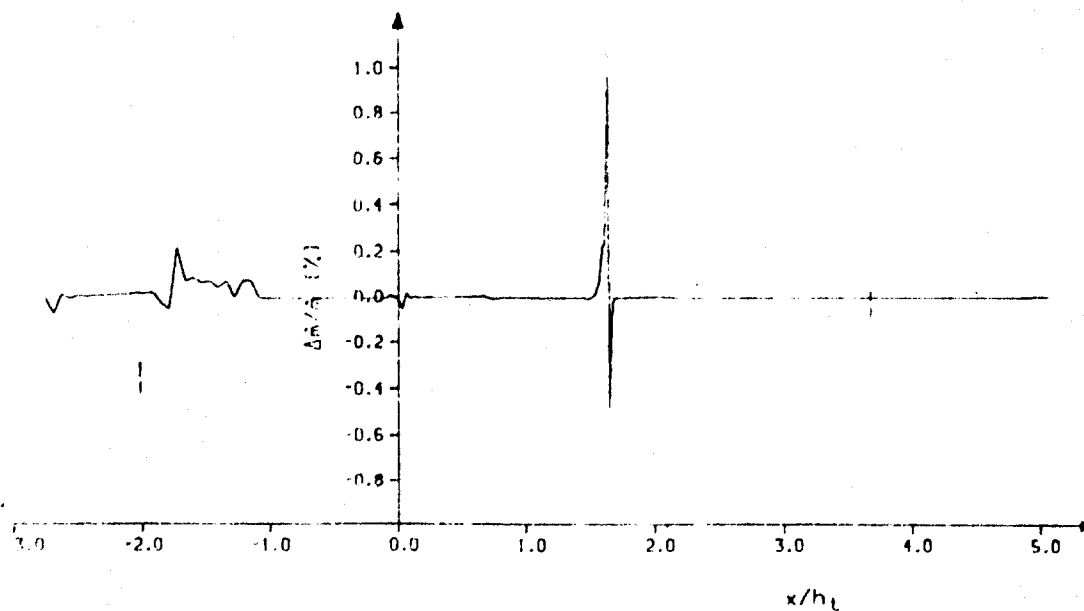


Fig. 7 Mass loss along duct, test case 1.1

A colour reproduction of this  
illustration can be found on  
fiche number 5.

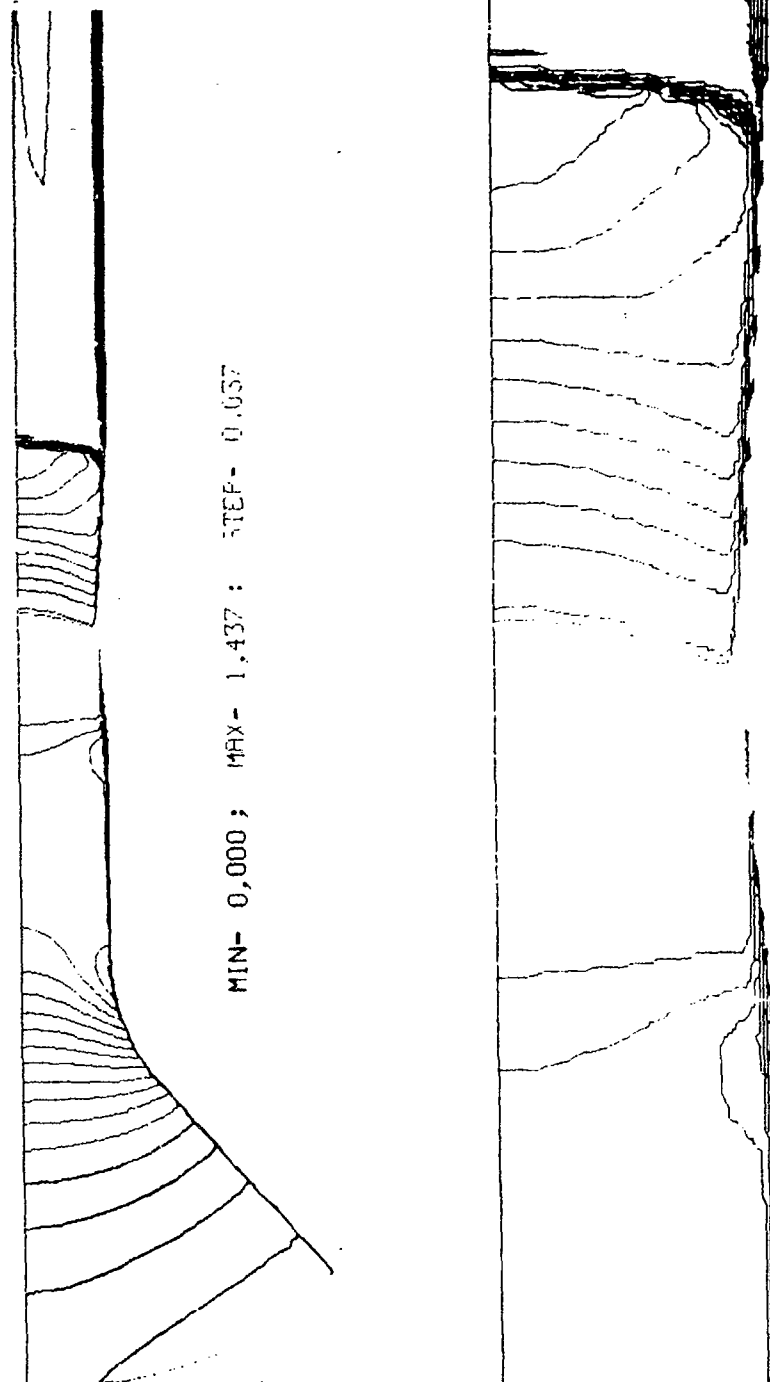


Fig. 8 Isolines of Mach number, test case 1.1

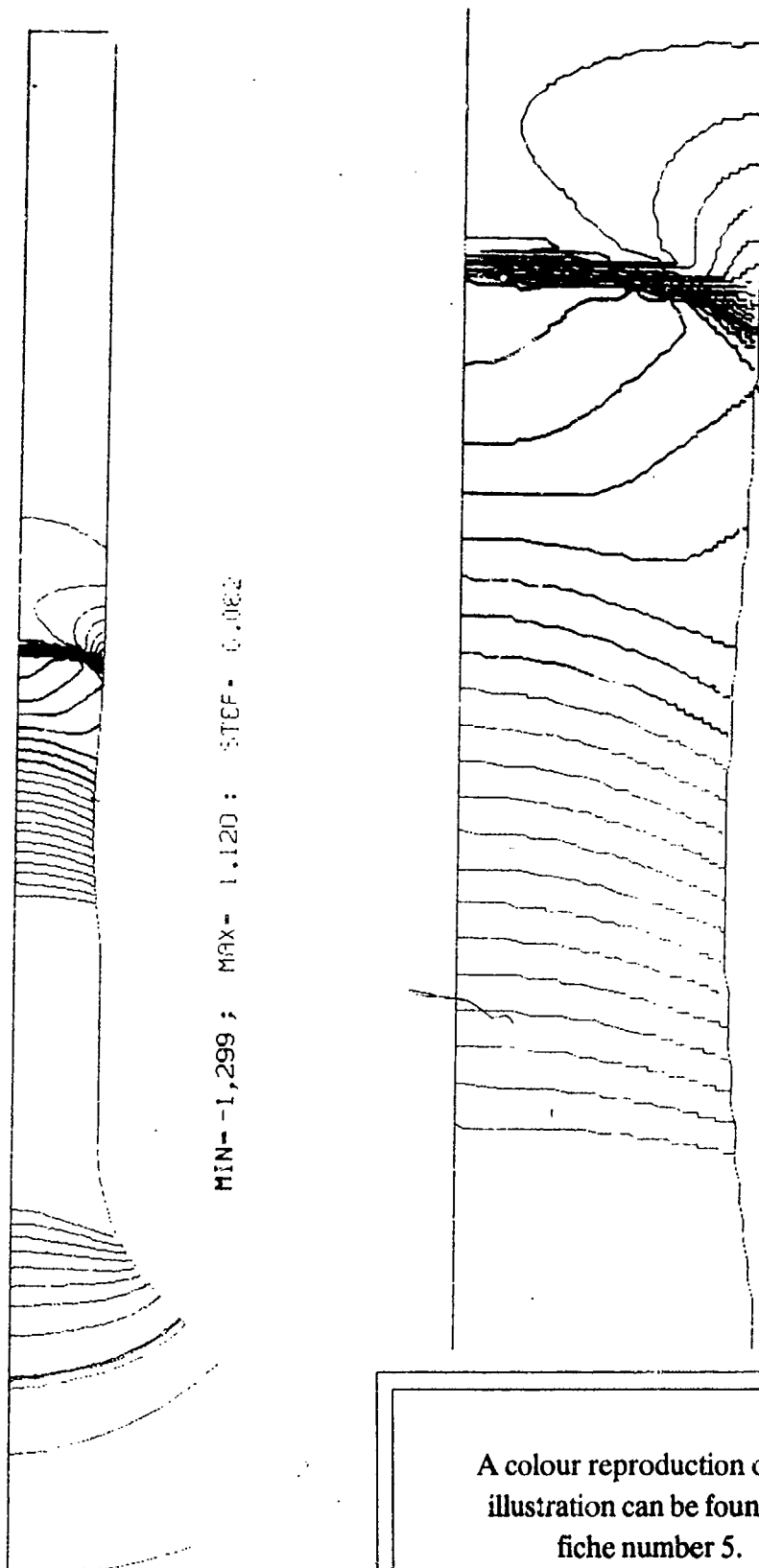


Fig. 9 Isolines of pressure coefficient  $C_p$ , test case 1.1

A colour reproduction of this  
illustration can be found on  
fiche number 5.



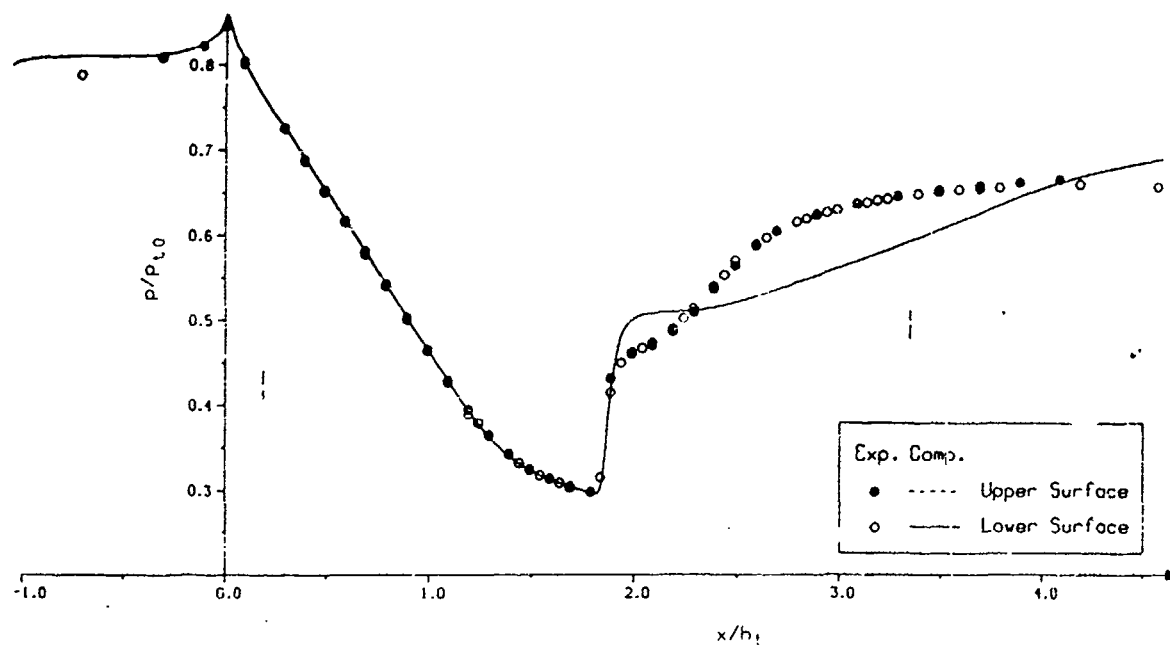


Fig. 10 Static wall-pressure distribution, test case 1.2

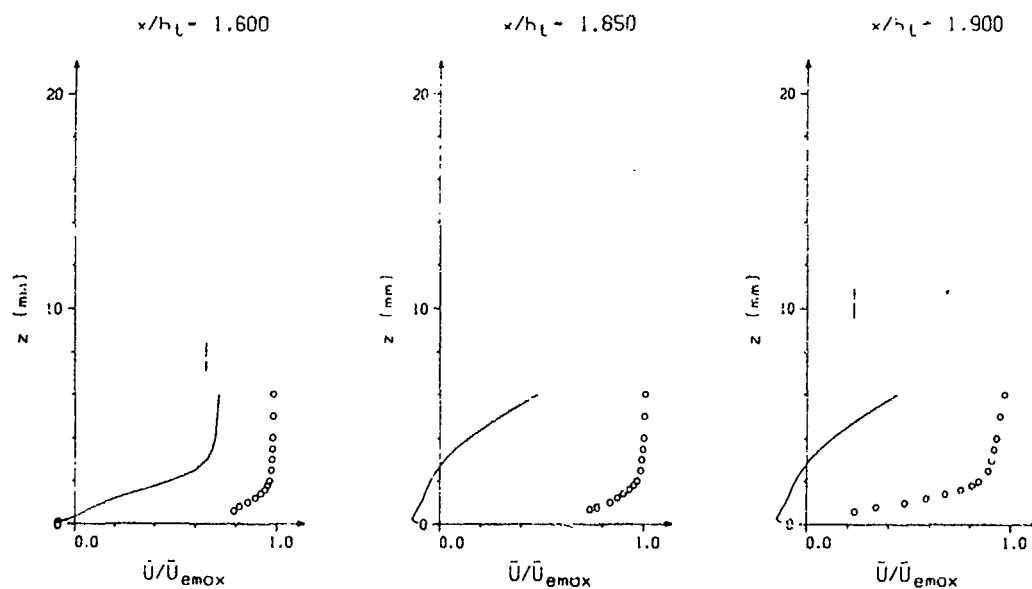


Fig. 11 Mean velocity profiles, test case 1.2

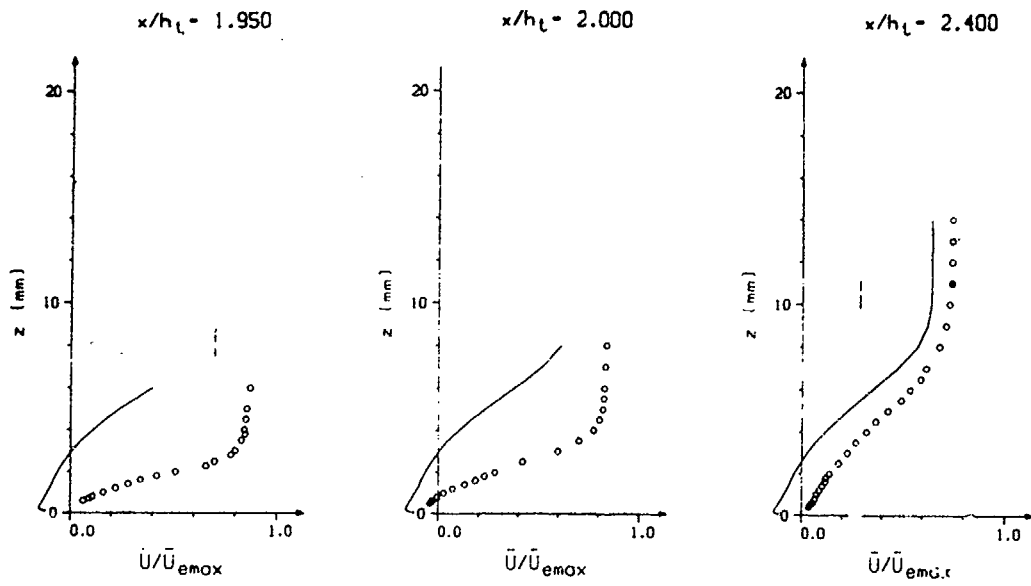


Fig. 11 Continued

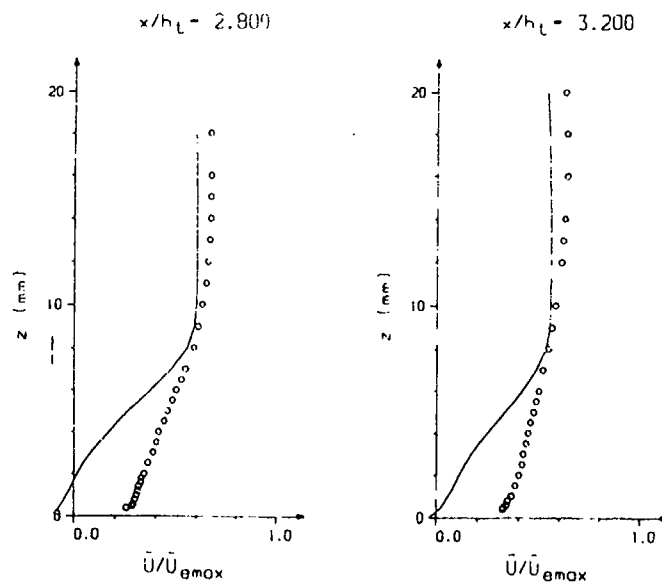


Fig. 11 Continued

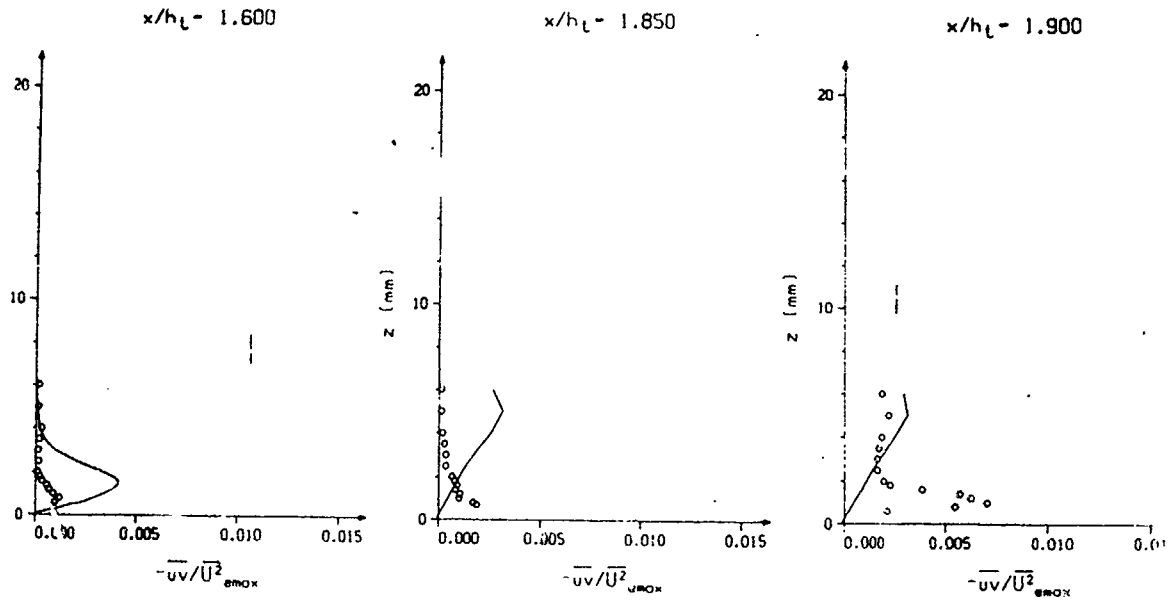


Fig. 12 Reynolds stress profiles, test case 1.2

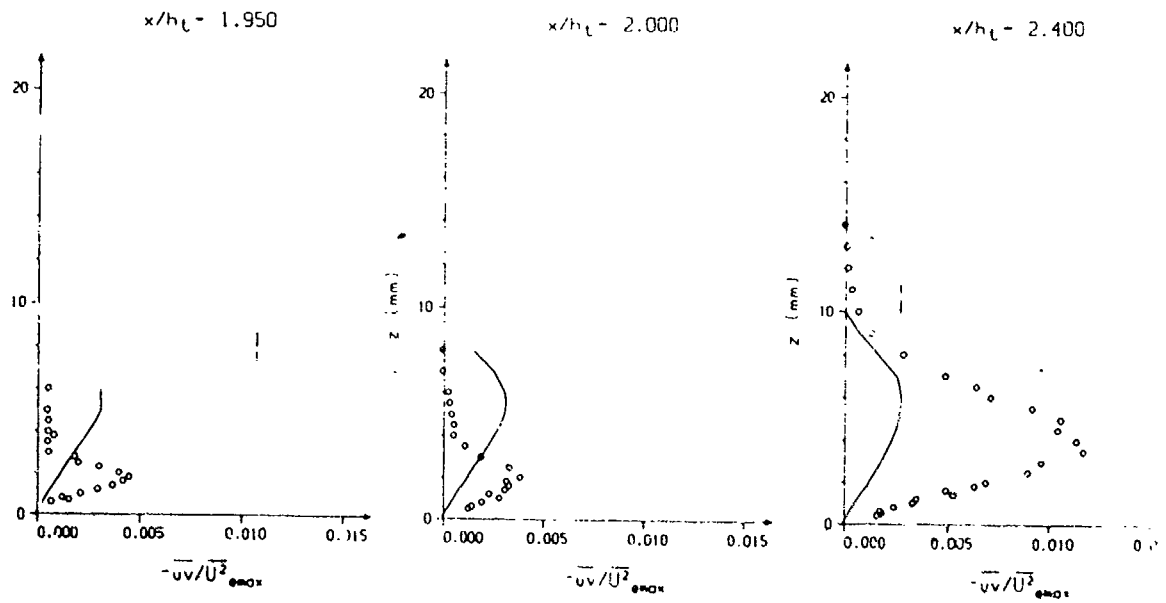


Fig. 12 Continued

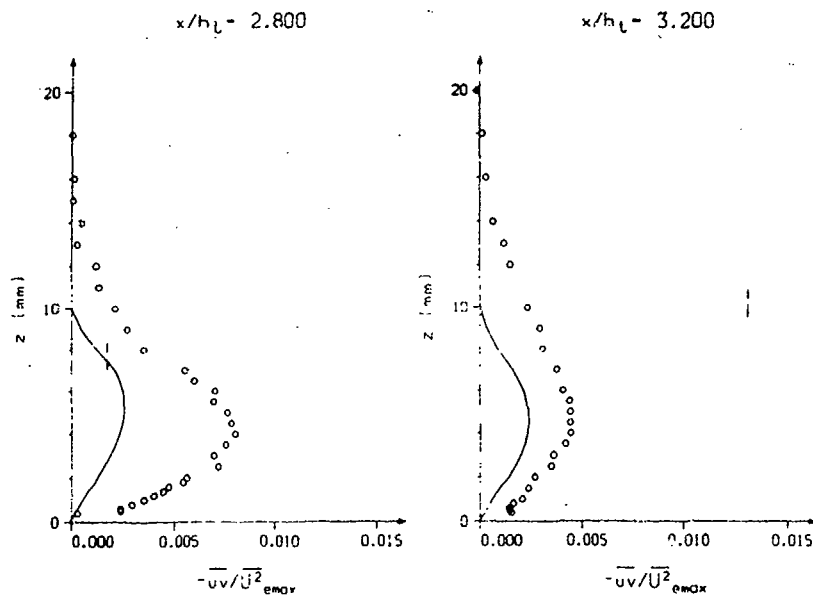


Fig. 12 Continued

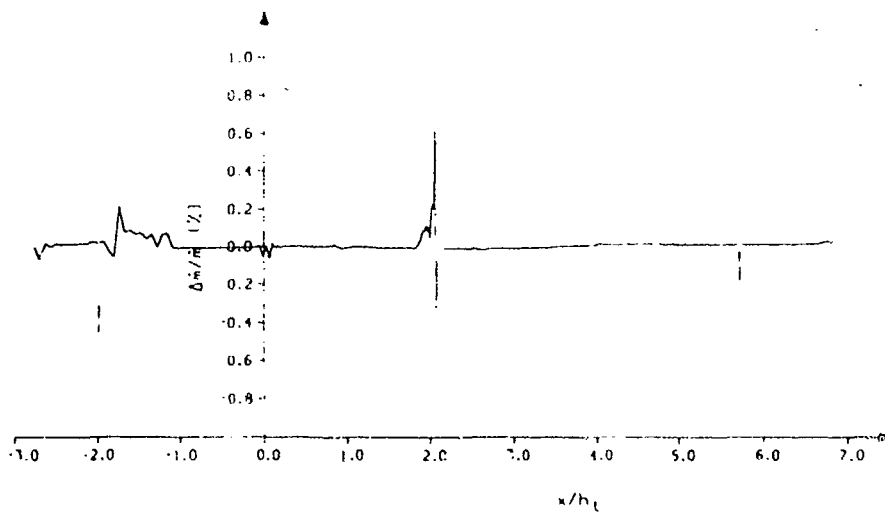


Fig. 13 Mass loss along duct, test case 1.2

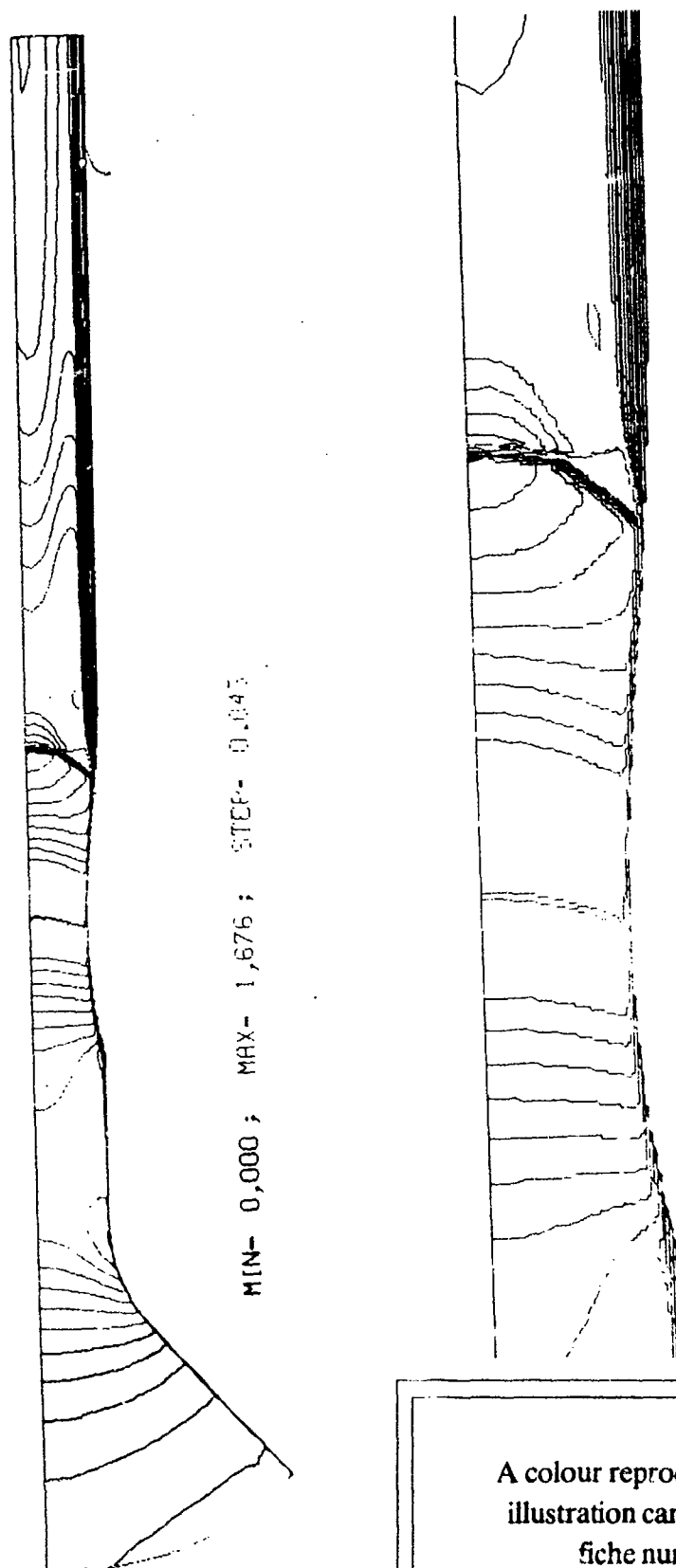
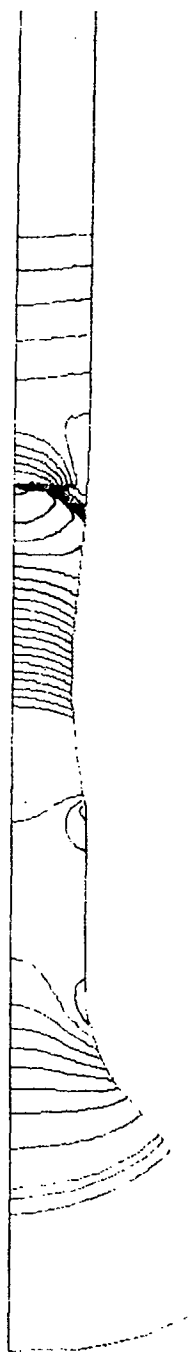


Fig. 14 Contourlines of Mach number, test case 1.2

A colour reproduction of this  
illustration can be found on  
fiche number 5.

A colour reproduction of this  
illustration can be found on  
fiche number 5.



MIN=-1,917 ; MAX= 1,100 ; STEP= 0,025

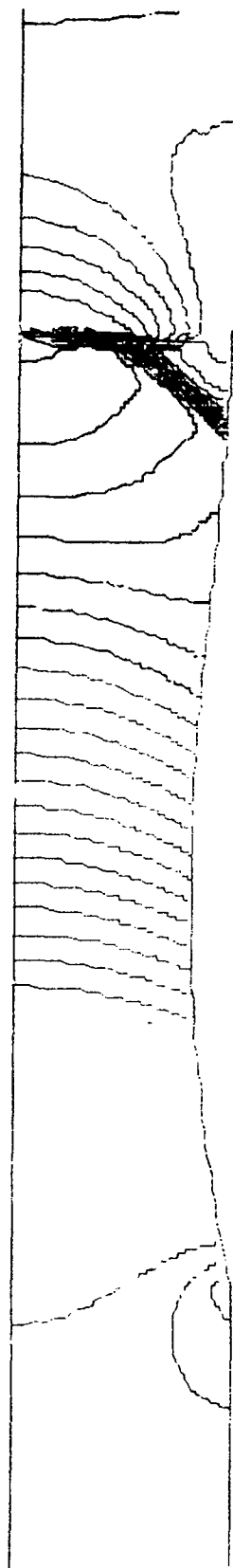


Fig. 15 Isolines of pressure coefficient  $c_p$ , test case 1.2

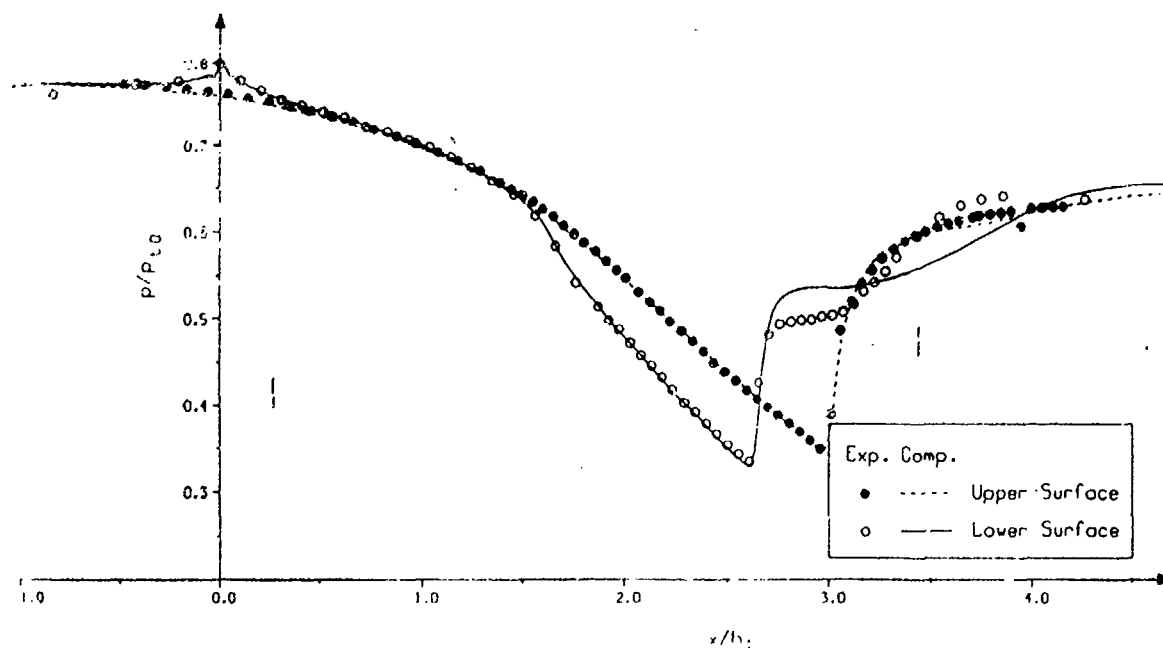


Fig. 16 Static wall-pressure distribution, test case 1.3

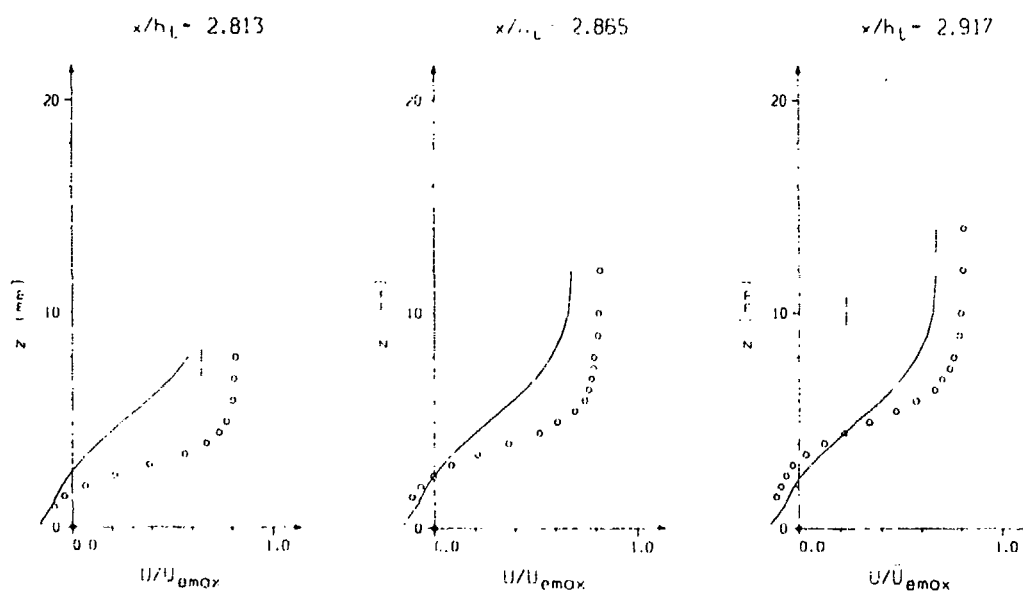


Fig. 17 Mean velocity profiles, test case 1.3

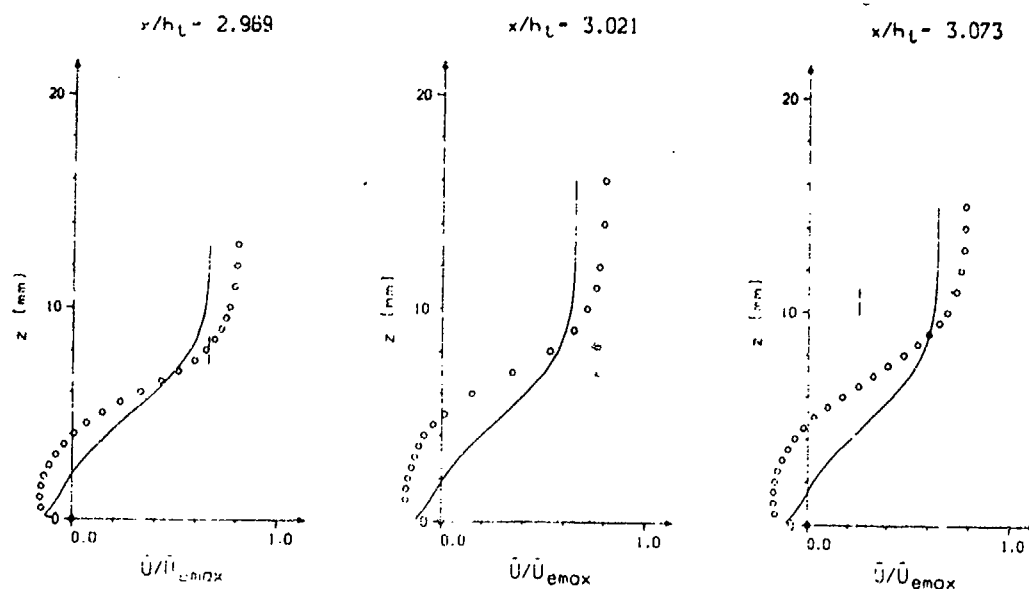


Fig. 17 Continued

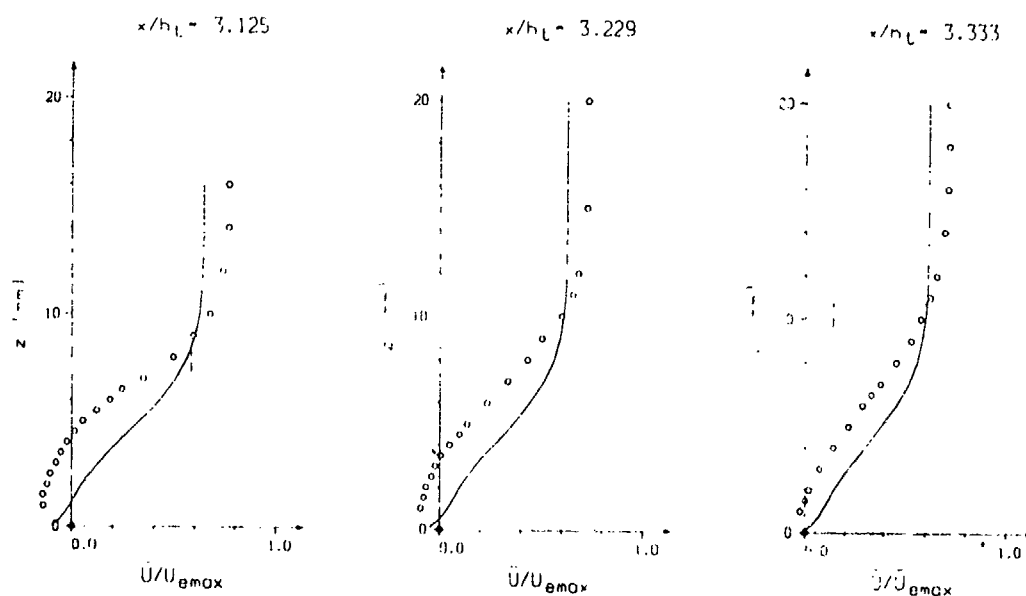


Fig. 17 Continued



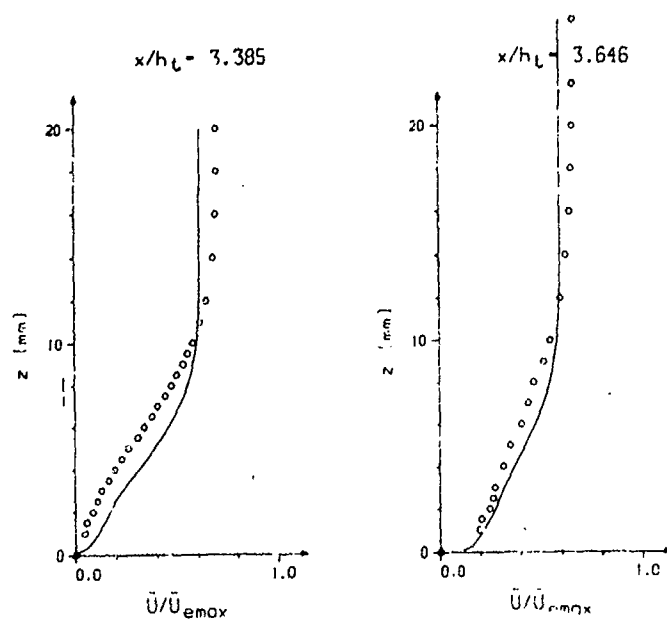


Fig. 17 Continued

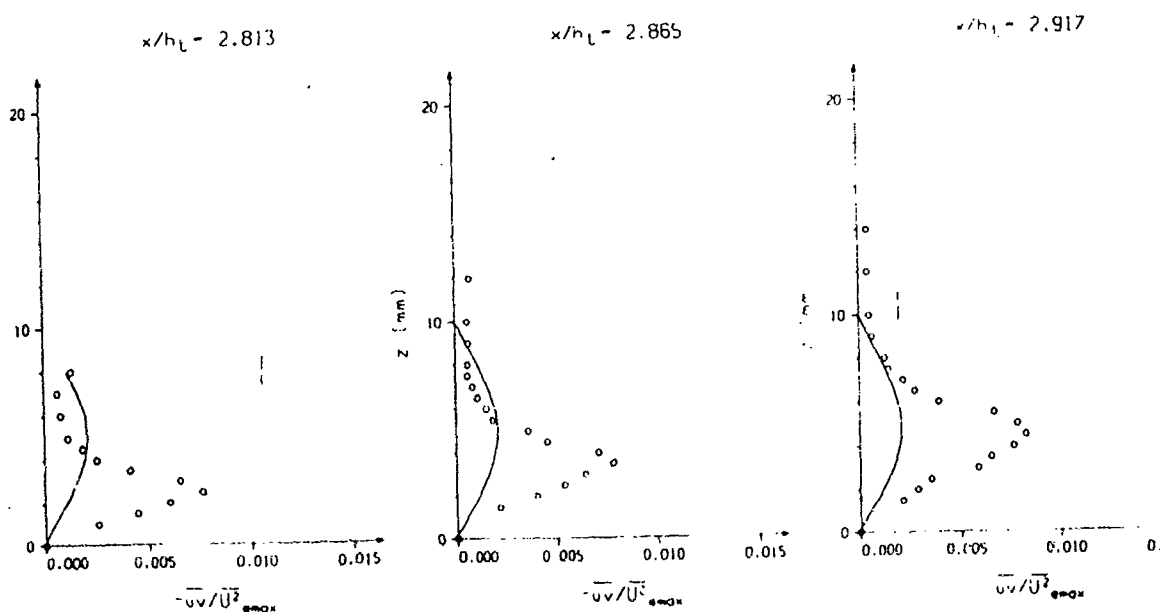


Fig. 18 Reynolds stress profiles, test case 1.3

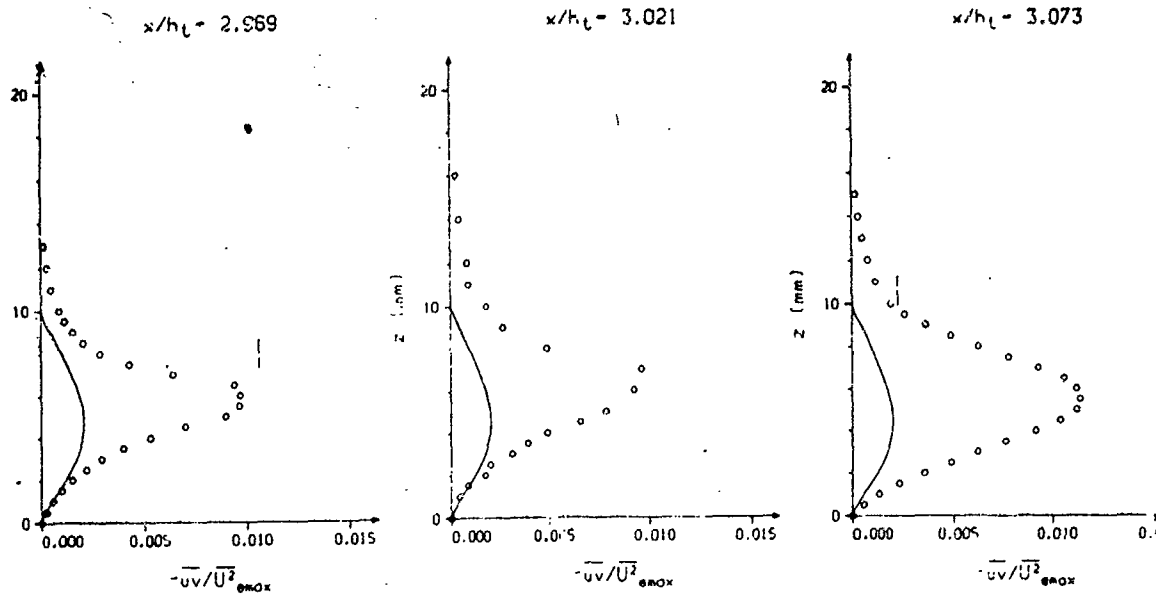


Fig. 18 Continued

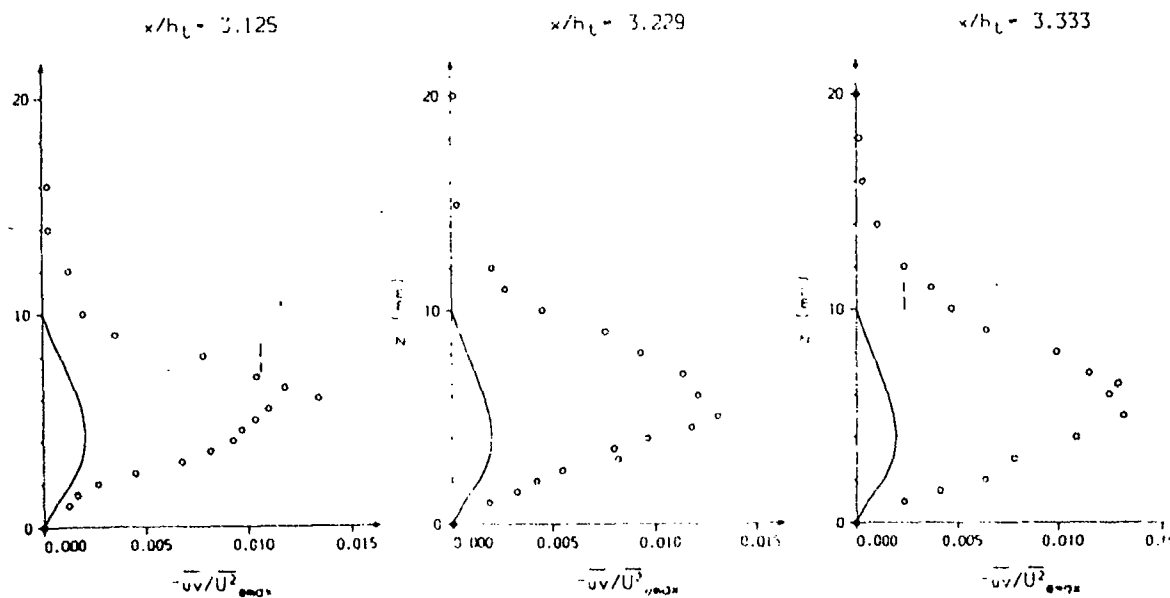


Fig. 18 Continued

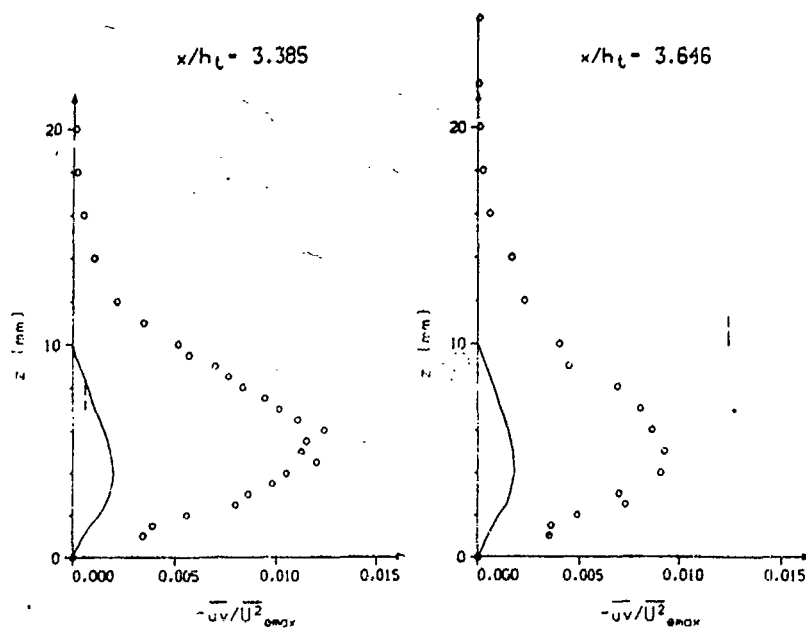


Fig 18 Continued

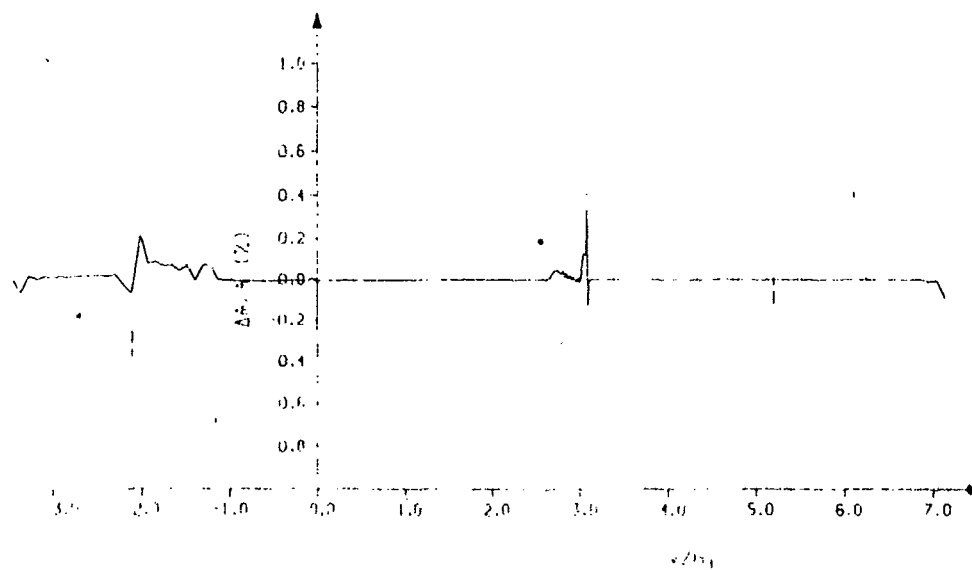


Fig. 19 Mass loss along duct, test case 1.3

A colour reproduction of this  
illustration can be found on  
fiche number 5.

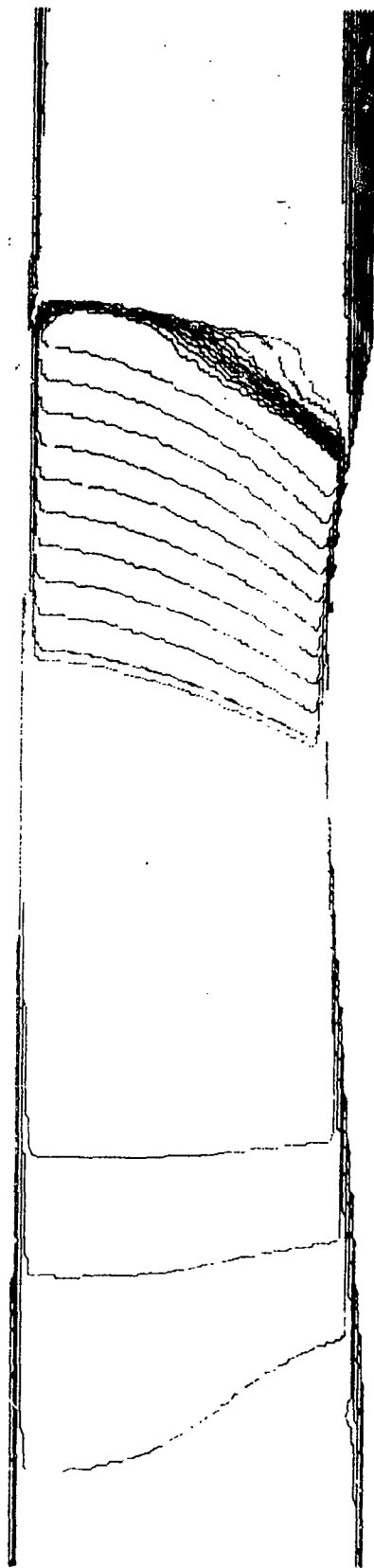
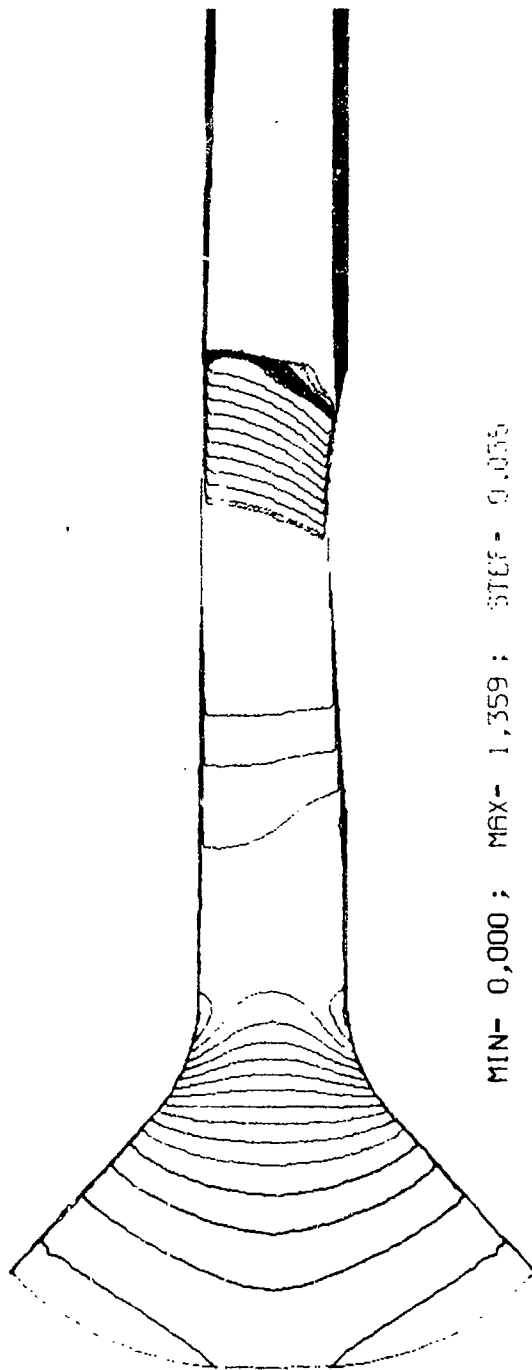


Fig. 20 Isolines of Mach number, test case 1.3

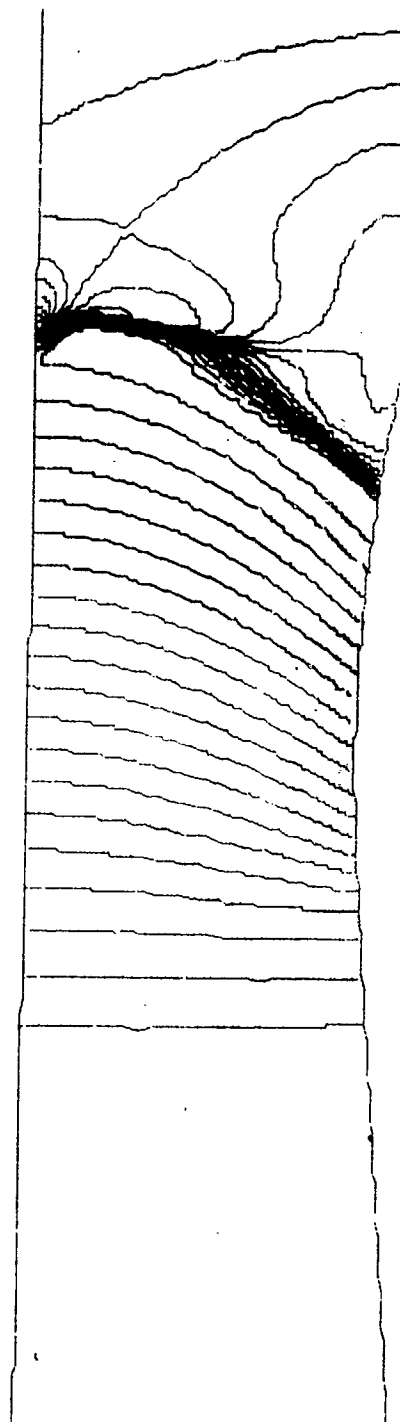
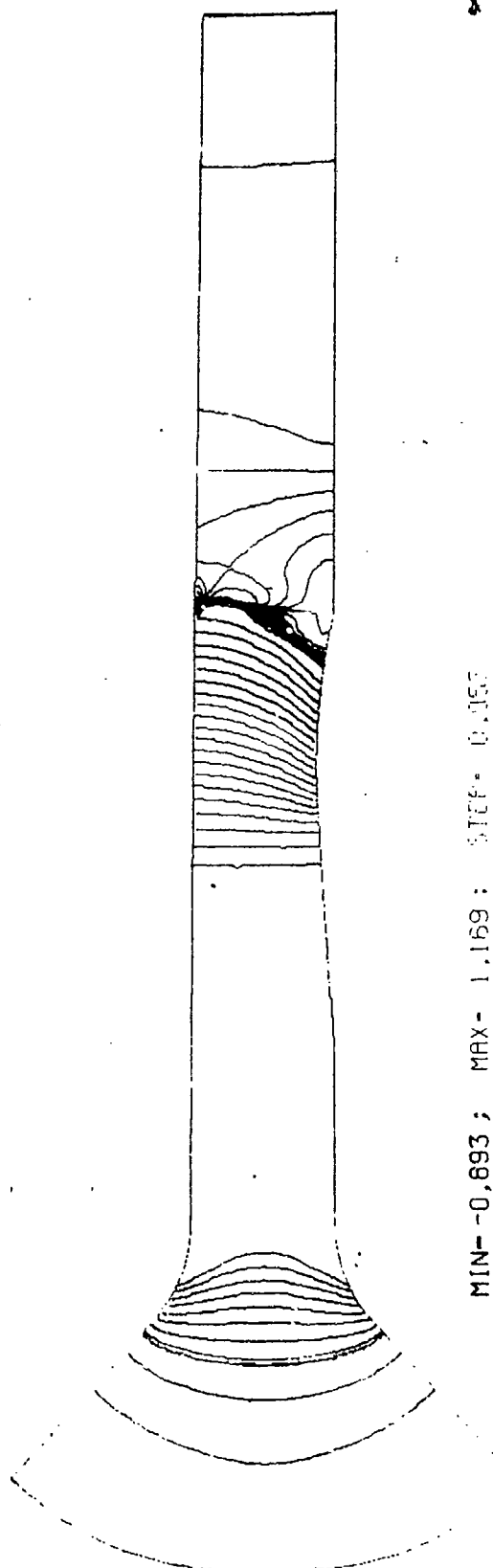


Fig. 21 Isolines of pressure coefficient  $C_p$ , test case 1.3

A colour reproduction of this  
illustration can be found on  
fiche number 5.

# AR 270

## Microfiche Appendix to Sub-Section 3.3.2

### Contributions to Test Case 2

#### Glancing shock/boundary layer interaction

	Page No's
General Dynamics	A34 to A50
ONERA	A51 to A61
Sverdrup, AFDC	A62 to A69
Sverdrup, Cleveland	A70 to A94
NASA Lewis	A95 to A102

GENERAL DYNAMICS  
FORT WORTH DIVISION

**HAWK3D CFD RESULTS:**  
**GLANCING SHOCK/BOUNDARY LAYER INTERACTION**

The CFD results from a HAWK3D Analysis of the AGARD Test Case #2 (Glancing Shock/Boundary Layer Interaction) are presented in tabular and graphical formats. The graphs have the corresponding experimental data for comparison while the tables list only the CFD data.

The CFD solution was obtained without knowledge of some details of the experimental set up, because the given details of the problem were somewhat vague. Accordingly, there are minor (yet possibly significant) differences between the experimental and CFD analyses (summarized in Table 1).

A major point of concern is that the experimental Pitot pressures given to start the CFD solution had values greater than 1.0 in the freestream. The Pitot pressure values (nondimensionalized by freestream Pitot pressure supposedly) were as great as 1.08 in the freestream. No explanation to this concern has been found. Some question as to the nondimensionalization of Pitot pressures downstream results from these given Pitot pressures. Although most results from the HAWK3D analysis compare well with experimental data, the downstream Pitot pressures are up to 8% greater than the experimental data.

The grid size used was 100 X 70 X 50 with corresponding x,y,z dimensions of 11.5" X 8" X 4". A symmetry plane was used in the Z-direction. (The actual tunnel height was 8"). The initial CFD solution was started 0.5 inches upstream of the wedge tip.

The HAWK3D code was run on the NAS CRAY YMP (before the February 1990 upgrades to the YMP). A converged solution was reached in 2000 iterations. The runs used approximately 12.7 seconds per iteration.

The results presented in this package represent a "first look" at the Glancing Shock Problem. Limited time and funding reduced the CFD analysis to one sparse grid and the assumptions shown in Table 1.

If there are any questions, comments or concerns please contact:

Ben Smith (817) 763-3069  
General Dynamics/Fort Worth Division  
P.O. Box 748  
Fort Worth, Texas 76101

Table 1

EXPERIMENT	CFD
<ul style="list-style-type: none"><li>• WEDGE TIP WITH NO INITIAL BOUNDARY LAYER (BL)</li><li>• TUNNEL FLOOR BEGINS WITH 0.55 INCH BL</li><li>• FULL TUNNEL CROSS SECTION: 8" X 8" (WEDGE OFFSET FROM TUNNEL WALL)</li><li>• BL's ON ALL TUNNEL WALLS (BUT NOT ON WEDGE)</li></ul>	<ul style="list-style-type: none"><li>• NO SLIP WALL BEGINS 0.5 INCHES UPSTREAM OF WEDGE</li><li>• TUNNEL FLOOR BEGINS WITH EXPERIMENTAL DATA FROM <math>X=3.6"</math></li><li>• SOLUTION DOMAIN 11.5" X 8" X 4" (SYMMETRY PLANE USED IN Z-DIRECTION)</li><li>• BL INITIALIZED ONLY ON TUNNEL FLOOR</li><li>• INITIALIZED WITH EXPERIMENTAL PROFILES FROM <math>X = 3.6"</math></li></ul>



## TEST CASE #2: SURFACE STATIC PRESSURES;

Y(in)	P/PREF	X=5.1"; GD/FW HAWK3D
0.000	2.014	
0.100	2.006	
0.200	1.989	
0.300	1.962	
0.400	1.934	
0.500	1.906	
0.600	1.878	
0.700	1.848	
0.750	1.833	
0.800	1.817	
0.900	1.784	
1.050	1.733	
1.150	1.698	
1.250	1.663	
1.350	1.630	
1.500	1.587	
1.600	1.565	
1.700	1.548	
1.800	1.535	
1.900	1.525	
2.050	1.511	
2.150	1.500	
2.250	1.486	
2.350	1.470	
2.450	1.452	
2.550	1.431	
2.650	1.406	
2.750	1.377	
2.850	1.340	
2.900	1.319	
3.050	1.241	
3.150	1.175	
3.250	1.119	
3.350	1.068	
3.500	1.032	
3.600	1.013	
3.750	1.003	
3.850	0.999	
4.100	1.000	
4.200	1.001	
4.400	1.003	
4.600	1.006	
4.900	1.010	
5.150	1.014	
5.400	1.017	
5.600	1.019	

## TEST CASE #2: SURFACE STATIC PRESSURES;

Y(in)	P/PREF	X=7.1"; GD/FW HAWK3D
0.000	2.053	
0.100	2.045	
0.200	2.039	
0.300	2.026	
0.350	2.018	
0.450	2.000	
0.500	1.992	
0.550	1.983	
0.700	1.954	
0.800	1.932	
0.900	1.908	
0.950	1.895	
1.050	1.869	
1.150	1.841	
1.200	1.826	
1.300	1.796	
1.450	1.750	
1.550	1.719	
1.650	1.689	
1.700	1.674	
1.850	1.632	
1.950	1.607	
2.050	1.586	
2.150	1.569	
2.300	1.550	
2.350	1.545	
2.450	1.538	
2.600	1.530	
2.700	1.526	
2.800	1.522	
2.950	1.513	
3.050	1.506	
3.150	1.497	
3.250	1.487	
3.350	1.473	
3.450	1.457	
3.550	1.438	
3.650	1.415	
3.750	1.388	
3.850	1.357	
3.900	1.331	
4.050	1.247	
4.150	1.200	
4.300	1.122	
4.350	1.109	
4.450	1.085	
4.550	1.055	
4.750	1.039	
4.950	1.028	
5.150	1.025	
5.250	1.025	
5.450	1.025	
5.600	1.026	

## TEST CASE #2: SURFACE STATIC PRESSURES;

Y(in)	P/PREF	X=8.1"; GD/FW HAWK3D
0.000	2.065	
0.100	2.057	
0.200	2.054	
0.250	2.050	
0.300	2.045	
0.350	2.040	
0.400	2.033	
0.500	2.020	
0.600	2.006	
0.700	1.991	
0.800	1.974	
0.900	1.956	
1.100	1.912	
1.200	1.888	
1.300	1.862	
1.400	1.834	
1.500	1.806	
1.600	1.777	
1.750	1.733	
1.850	1.705	
1.950	1.677	
2.100	1.640	
2.200	1.618	
2.300	1.599	
2.400	1.583	
2.550	1.566	
2.700	1.555	
2.800	1.551	
2.900	1.549	
3.050	1.546	
3.200	1.542	
3.350	1.536	
3.550	1.520	
3.650	1.510	
3.850	1.483	
3.950	1.465	
4.050	1.443	
4.150	1.419	
4.250	1.386	
4.350	1.350	
4.400	1.328	
4.500	1.278	

## TEST CASE #2: SURFACE STATIC PRESSURES;

Y(in)	P/PREF	X=9.1"; GD/FW HAWK3D
0.000	2.076	
0.100	2.067	
0.200	2.066	
0.300	2.060	
0.400	2.052	
0.500	2.043	
0.600	2.034	
0.700	2.023	
0.800	2.011	
0.900	1.997	
1.000	1.981	
1.150	1.953	
1.250	1.932	
1.350	1.910	
1.400	1.898	
1.450	1.886	
1.550	1.860	
1.650	1.834	
1.700	1.820	
1.850	1.779	
1.950	1.752	
2.050	1.726	
2.150	1.700	
2.250	1.676	
2.400	1.643	
2.500	1.625	
2.600	1.609	
2.650	1.603	
2.750	1.591	
2.850	1.583	
2.950	1.577	
3.050	1.574	
3.150	1.572	
3.250	1.571	
3.350	1.570	
3.450	1.568	
3.650	1.561	
3.750	1.555	
3.850	1.547	
3.900	1.543	

TEST CASE #2: PITOT PRESSURES, X=3.6"; YG=2.4";  
S (in) PT/PTREF GD/FW HAWK3D

S (in)	PT/PTREF	GD/FW HAWK3D
0.0000000E+00	0.9636966E-01	
0.3029734E-02	0.1316063E+00	
0.6122216E-02	0.1762247E+00	
0.9262144E-02	0.1989655E+00	
0.1251434E-01	0.2184726E+00	
0.1582376E-01	0.2345725E+00	
0.1921533E-01	0.2502682E+00	
0.2269408E-01	0.2644354E+00	
0.2626538E-01	0.2782466E+00	
0.2993435E-01	0.2908514E+00	
0.3370654E-01	0.3039622E+00	
0.3758746E-01	0.3153103E+00	
0.4158282E-01	0.3271519E+00	
0.4569852E-01	0.3388152E+00	
0.4994046E-01	0.3496476E+00	
0.5431471E-01	0.3609321E+00	
0.5882776E-01	0.3721441E+00	
0.6348582E-01	0.3825894E+00	
0.6829566E-01	0.3934625E+00	
0.7326417E-01	0.4047844E+00	
0.7839799E-01	0.4150226E+00	
0.8370463E-01	0.4255737E+00	
0.8919108E-01	0.4365545E+00	
0.9486528E-01	0.4475709E+00	
0.1007346E+00	0.4577963E+00	
0.1068074E+00	0.4684367E+00	
0.1130915E+00	0.4794101E+00	
0.1195953E+00	0.4905785E+00	
0.1263276E+00	0.5009789E+00	
0.1332971E+00	0.5118004E+00	
0.1405129E+00	0.5230609E+00	
0.1479842E+00	0.5346215E+00	
0.1557207E+00	0.5451977E+00	
0.1637321E+00	0.5562027E+00	
0.1720283E+00	0.5676548E+00	
0.1806197E+00	0.5795723E+00	
0.1895168E+00	0.5912105E+00	
0.1987303E+00	0.6030055E+00	
0.2082713E+00	0.6152762E+00	
0.2181510E+00	0.6280412E+00	
0.2283809E+00	0.6411053E+00	
0.2389730E+00	0.6533210E+00	
0.2499391E+00	0.6660828E+00	
0.2612916E+00	0.6793584E+00	
0.2730431E+00	0.6931673E+00	
0.2852065E+00	0.7074985E+00	
0.2977945E+00	0.7223629E+00	
0.3108208E+00	0.7378041E+00	
0.3242989E+00	0.7538425E+00	
0.3382424E+00	0.7704990E+00	
0.3526654E+00	0.7887301E+00	
0.3675824E+00	0.8070349E+00	
0.3830077E+00	0.8263785E+00	
0.3989561E+00	0.8464232E+00	
0.4154426E+00	0.8670393E+00	
0.4324824E+00	0.8885546E+00	
0.4500906E+00	0.9047143E+00	
0.4682832E+00	0.9245385E+00	
0.4870759E+00	0.9450451E+00	
0.5064845E+00	0.9630170E+00	
0.5265253E+00	0.9733182E+00	
0.5472147E+00	0.9839605E+00	
0.5685689E+00	0.9949529E+00	
0.5906052E+00	0.1006305E+01	
0.6133402E+00	0.1012920E+01	
0.6367909E+00	0.1015397E+01	
0.6609744E+00	0.1017952E+01	
0.6859084E+00	0.1020587E+01	
0.7116103E+00	0.1023303E+01	
0.7380980E+00	0.1026049E+01	
0.7653893E+00	0.1028872E+01	
0.7935025E+00	0.1031781E+01	
0.8224557E+00	0.1034777E+01	
0.8522675E+00	0.1037506E+01	
0.8829572E+00	0.1040240E+01	
0.9145432E+00	0.1043055E+01	
0.9470451E+00	0.1045712E+01	
0.9804828E+00	0.1047391E+01	
0.1014876E+01	0.1049118E+01	
0.1050245E+01	0.1050895E+01	
0.1086611E+01	0.1051860E+01	
0.1123996E+01	0.1052744E+01	
0.1162430E+01	0.1053654E+01	
0.1201907E+01	0.1053738E+01	
0.1242479E+01	0.1053694E+01	
0.1284161E+01	0.1053830E+01	
0.1326977E+01	0.1056149E+01	
0.1370952E+01	0.1058533E+01	
0.1416113E+01	0.1060224E+01	
0.1462488E+01	0.1061132E+01	
0.1510104E+01	0.1062021E+01	
0.1558993E+01	0.1062134E+01	
0.1609185E+01	0.1062249E+01	
0.1660713E+01	0.1061051E+01	
0.1713612E+01	0.1059423E+01	
0.1767918E+01	0.1058502E+01	
0.1823668E+01	0.1058027E+01	
0.1880903E+01	0.1058098E+01	
0.1939666E+01	0.1058580E+01	
0.2000000E+01	0.1059698E+01	

TEST CASE #2: PITOT PRESSURES, X=3.6"; YG=2.9";  
Z (in) PT/PTREF GD/FW HAWK3D

Z (in)	PT/PTREF	GD/FW HAWK3D
0.0000000E+00	0.1631470E+00	
0.3029734E-02	0.8391627E-01	
0.6122216E-02	0.1509170E+00	
0.9262144E-02	0.1857831E+00	
0.1251434E-01	0.2080654E+00	
0.1582376E-01	0.2266079E+00	
0.1921533E-01	0.2421094E+00	
0.2269407E-01	0.2556512E+00	
0.2626538E-01	0.2685792E+00	
0.2993435E-01	0.2800722E+00	
0.3370654E-01	0.2912450E+00	
0.3758746E-01	0.3020305E+00	
0.4158282E-01	0.3120384E+00	
0.4569852E-01	0.3224468E+00	
0.4994046E-01	0.3319668E+00	
0.5431471E-01	0.3414764E+00	
0.5882776E-01	0.3513604E+00	
0.6348582E-01	0.3605394E+00	
0.6829566E-01	0.3697802E+00	
0.7326417E-01	0.3793828E+00	
0.7839799E-01	0.3887627E+00	
0.8370463E-01	0.3978218E+00	
0.8919108E-01	0.4072336E+00	
0.9486528E-01	0.4170151E+00	
0.1007346E+00	0.4261804E+00	
0.1068074E+00	0.4355101E+00	
0.1130915E+00	0.4452045E+00	
0.1195953E+00	0.4552791E+00	
0.1263276E+00	0.4647746E+00	
0.1332971E+00	0.4745676E+00	
0.1405129E+00	0.4847422E+00	
0.1479842E+00	0.4953144E+00	
0.1557207E+00	0.5055141E+00	
0.1637321E+00	0.5158925E+00	
0.1720283E+00	0.5266743E+00	
0.1806197E+00	0.5378758E+00	
0.1895168E+00	0.5493506E+00	
0.1987303E+00	0.5610616E+00	
0.2082713E+00	0.5732227E+00	
0.2181510E+00	0.5858513E+00	
0.2283809E+00	0.5989633E+00	
0.2389730E+00	0.6119726E+00	
0.2499391E+00	0.6254435E+00	
0.2612916E+00	0.6394271E+00	
0.2730431E+00	0.6539412E+00	
0.2852065E+00	0.6691328E+00	
0.2977945E+00	0.6851526E+00	
0.3108208E+00	0.7017700E+00	
0.3242989E+00	0.7190045E+00	
0.3382424E+00	0.7368756E+00	
0.3526654E+00	0.7555635E+00	
0.3675824E+00	0.7750205E+00	
0.3830077E+00	0.7951794E+00	
0.3989561E+00	0.8160619E+00	
0.4154426E+00	0.8376893E+00	
0.4324824E+00	0.8571540E+00	
0.4500906E+00	0.8770011E+00	
0.4682832E+00	0.8975388E+00	
0.4870759E+00	0.9187862E+00	
0.5064845E+00	0.9391645E+00	
0.5265253E+00	0.9518593E+00	
0.5472147E+00	0.9649795E+00	
0.5685689E+00	0.9785360E+00	
0.5906052E+00	0.9925409E+00	
0.6133402E+00	0.1002892E+01	
0.6367909E+00	0.1008232E+01	
0.6609744E+00	0.1013742E+01	
0.6859084E+00	0.1019426E+01	
0.7116103E+00	0.1025280E+01	
0.7380980E+00	0.1027413E+01	
0.7653893E+00	0.1028661E+01	
0.7935025E+00	0.1029948E+01	
0.8224557E+00	0.1031273E+01	
0.8522675E+00	0.1033700E+01	
0.8829572E+00	0.1036566E+01	
0.9145432E+00	0.1039516E+01	
0.9470451E+00	0.1042345E+01	
0.9804828E+00	0.1043627E+01	
0.1014876E+01	0.1044947E+01	
0.1050245E+01	0.1046305E+01	
0.1086611E+01	0.1047059E+01	
0.1123996E+01	0.1047595E+01	
0.1162430E+01	0.1048348E+01	
0.1201907E+01	0.1049562E+01	
0.1242479E+01	0.1050940E+01	
0.1284161E+01	0.1052329E+01	
0.1326977E+01	0.1052423E+01	
0.1370952E+01	0.1052520E+01	
0.1416113E+01	0.1052857E+01	
0.1462488E+01	0.1053522E+01	
0.1510104E+01	0.1054205E+01	
0.1558993E+01	0.1054899E+01	
0.1609185E+01	0.1055611E+01	
0.1660713E+01	0.1056445E+01	
0.1713612E+01	0.1057340E+01	
0.1767918E+01	0.1057091E+01	
0.1823668E+01	0.1055954E+01	
0.1880903E+01	0.1054352E+01	
0.1939666E+01	0.1052328E+01	
0.2000000E+01	0.1052207E+01	

TEST CASE #2: PITOT PRESSURES, X=3.6"; YG=3.9";  
Z (in) PT/PTREF  
GD/FW HAWK3D

0.0000000E+00 0.1320639E+00  
0.3029734E-02 0.9029478E-01  
0.6122216E-02 0.1644758E+00  
0.9282144E-02 0.1945995E+00  
0.1251434E-01 0.2146004E+00  
0.1582376E-01 0.2322771E+00  
0.1921533E-01 0.2481913E+00  
0.2269408E-01 0.2613004E+00  
0.2626538E-01 0.2745820E+00  
0.2993435E-01 0.2859123E+00  
0.3370054E-01 0.2974568E+00  
0.3758746E-01 0.3082190E+00  
0.4158282E-01 0.3185408E+00  
0.4569851E-01 0.3292745E+00  
0.4994046E-01 0.3388405E+00  
0.5431471E-01 0.3486771E+00  
0.5882776E-01 0.3589000E+00  
0.6348582E-01 0.3681050E+00  
0.6829566E-01 0.3775757E+00  
0.7326417E-01 0.3874161E+00  
0.7839799E-01 0.3968483E+00  
0.8370464E-01 0.4061203E+00  
0.8919108E-01 0.4157524E+00  
0.9486528E-01 0.4257614E+00  
0.1007346E+00 0.4349161E+00  
0.1068074E+00 0.4443736E+00  
0.1130915E+00 0.4541996E+00  
0.1195953E+00 0.4643740E+00  
0.1263276E+00 0.4739831E+00  
0.1332971E+00 0.4835649E+00  
0.1405129E+00 0.4943349E+00  
0.1479342E+00 0.5051090E+00  
0.1557207E+00 0.5154254E+00  
0.1637321E+00 0.5260171E+00  
0.1720283E+00 0.5370193E+00  
0.1806198E+00 0.5484491E+00  
0.1895168E+00 0.5601902E+00  
0.1987303E+00 0.5722604E+00  
0.2082713E+00 0.5847943E+00  
0.2181510E+00 0.5978093E+00  
0.2283810E+00 0.6113133E+00  
0.2389730E+00 0.6246076E+00  
0.2499391E+00 0.6384090E+00  
0.2612916E+00 0.6527361E+00  
0.2730431E+00 0.6676069E+00  
0.2852065E+00 0.6833256E+00  
0.2977945E+00 0.7000837E+00  
0.3108208E+00 0.7174661E+00  
0.3242889E+00 0.7354933E+00  
0.3382424E+00 0.7541863E+00  
0.3526654E+00 0.7733477E+00  
0.3675824E+00 0.7931072E+00  
0.3830077E+00 0.8135800E+00  
0.3989561E+00 0.8347882E+00  
0.4154426E+00 0.8567529E+00  
0.4324824E+00 0.8766308E+00  
0.4500906E+00 0.8970528E+00  
0.4682837E+00 0.9181871E+00  
0.4870099E+00 0.9400551E+00  
0.5064845E+00 0.962641E+00  
0.5261253E+00 0.9712209E+00  
0.5472146E+00 0.9825436E+00  
0.5685689E+00 0.9942414E+00  
0.5906051E+00 0.1006325E+01  
0.6133403E+00 0.1014275E+01  
0.6367909E+00 0.1017275E+01  
0.6609744E+00 0.1020370E+01  
0.6859085E+00 0.1023564E+01  
0.7116103E+00 0.1026856E+01  
0.7380980E+00 0.1029566E+01  
0.7653893E+00 0.1032223E+01  
0.7935024E+00 0.1034960E+01  
0.8224558E+00 0.1037777E+01  
0.8522675E+00 0.1039109E+01  
0.8829571E+00 0.1039997E+01  
0.9145432E+00 0.1040911E+01  
0.9470451E+00 0.1042030E+01  
0.9804828E+00 0.1043434E+01  
0.1014876E+01 0.1046723E+01  
0.1050245E+01 0.1049471E+01  
0.1086611E+01 0.1050962E+01  
0.1123996E+01 0.1052665E+01  
0.1162420E+01 0.1054416E+01  
0.1201907E+01 0.1054744E+01  
0.1242479E+01 0.1054765E+01  
0.1284161E+01 0.1054836E+01  
0.1326977E+01 0.1056206E+01  
0.1370952E+01 0.1057613E+01  
0.1416113E+01 0.1058732E+01  
0.1462488E+01 0.1059465E+01  
0.1510105E+01 0.1060217E+01  
0.1558993E+01 0.1060551E+01  
0.1609185E+01 0.1061706E+01  
0.1660714E+01 0.1062757E+01  
0.1713612E+01 0.1063938E+01  
0.1767918E+01 0.1066116E+01  
0.1823668E+01 0.1069044E+01  
0.1880903E+01 0.1071469E+01  
0.1939666E+01 0.1073475E+01  
0.2000000E+01 0.1075556E+01

TEST CASE #2: PITOT PRESSURES, X=3.6"; YG=4.9";  
Z (in) PT/PTREF  
GD/FW HAWK3D

0.0000000E+00 0.9268330E-01  
0.3029735E-02 0.1036875E+00  
0.6122217E-02 0.1731731E+00  
0.9282144E-02 0.2012541E+00  
0.1251471E-01 0.2217849E+00  
0.1582376E-01 0.2383185E+00  
0.1921533E-01 0.2540985E+00  
0.2269408E-01 0.2671460E+00  
0.2626538E-01 0.2804042E+00  
0.2993436E-01 0.2917829E+00  
0.3370654E-01 0.3036328E+00  
0.3758747E-01 0.3142349E+00  
0.4158282E-01 0.3248429E+00  
0.4569851E-01 0.3356285E+00  
0.4994046E-01 0.3453066E+00  
0.5431471E-01 0.3553473E+00  
0.5882776E-01 0.3656031E+00  
0.6348582E-01 0.3748945E+00  
0.6829566E-01 0.3845445E+00  
0.7326417E-01 0.3945698E+00  
0.7839799E-01 0.4038784E+00  
0.8370462E-01 0.4132053E+00  
0.8919109E-01 0.4228936E+00  
0.9486528E-01 0.4328288E+00  
0.1007346E+00 0.4419875E+00  
0.1068073E+00 0.4515005E+00  
0.1130915E+00 0.4613836E+00  
0.1195953E+00 0.4714754E+00  
0.1263276E+00 0.4810300E+00  
0.1332971E+00 0.4909551E+00  
0.1405129E+00 0.5012652E+00  
0.1479342E+00 0.5119766E+00  
0.1557207E+00 0.5222744E+00  
0.1637321E+00 0.5329574E+00  
0.1720283E+00 0.5440544E+00  
0.1806197E+00 0.5555814E+00  
0.1895168E+00 0.5673437E+00  
0.1987303E+00 0.5794242E+00  
0.2082713E+00 0.5919685E+00  
0.2181510E+00 0.6049944E+00  
0.2283809E+00 0.6184817E+00  
0.2389730E+00 0.631266E+00  
0.2499391E+00 0.64626E+00  
0.2612916E+00 0.6609532E+00  
0.2730431E+00 0.6761994E+00  
0.2852065E+00 0.6923590E+00  
0.2977945E+00 0.7095283E+00  
0.3108208E+00 0.7273375E+00  
0.3242889E+00 0.7458081E+00  
0.3382424E+00 0.7649603E+00  
0.3526654E+00 0.7844178E+00  
0.3675824E+00 0.8044496E+00  
0.3830077E+00 0.8252066E+00  
0.3989561E+00 0.8467106E+00  
0.4154426E+00 0.8689850E+00  
0.4324824E+00 0.88871E+00  
0.4500905E+00 0.9091297E+00  
0.4682832E+00 0.9302592E+00  
0.4870739E+00 0.9521208E+00  
0.5064845E+00 0.9716226E+00  
0.5265253E+00 0.9817703E+00  
0.5472146E+00 0.9922550E+00  
0.5685689E+00 0.1003087E+01  
0.5906052E+00 0.1014275E+01  
0.6133402E+00 0.1020779E+01  
0.6367909E+00 0.1022477E+01  
0.6609745E+00 0.1024229E+01  
0.6859084E+00 0.1026036E+01  
0.7116104E+00 0.1027899E+01  
0.7380980E+00 0.1030947E+01  
0.7653893E+00 0.1034265E+01  
0.7935025E+00 0.1037683E+01  
0.8224556E+00 0.1041204E+01  
0.8522676E+00 0.1042608E+01  
0.8829572E+00 0.1043480E+01  
0.9145432E+00 0.1044378E+01  
0.9470451E+00 0.1045530E+01  
0.9804828E+00 0.1047928E+01  
0.1014876E+01 0.1050395E+01  
0.1050245E+01 0.1052933E+01  
0.1086611E+01 0.1054240E+01  
0.1123996E+01 0.1055379E+01  
0.1162420E+01 0.1056550E+01  
0.1201907E+01 0.1057687E+01  
0.1242479E+01 0.1058844E+01  
0.1284161E+01 0.1059987E+01  
0.1326977E+01 0.1060388E+01  
0.1370952E+01 0.1060799E+01  
0.1416113E+01 0.1061601E+01  
0.1462488E+01 0.1062871E+01  
0.1510104E+01 0.1064197E+01  
0.1558993E+01 0.1066145E+01  
0.1609185E+01 0.1068144E+01  
0.1660714E+01 0.1068271E+01  
0.1713612E+01 0.1067762E+01  
0.1767918E+01 0.1069570E+01  
0.1823668E+01 0.1072992E+01  
0.1880903E+01 0.1076808E+01  
0.1939666E+01 0.1080963E+01  
0.2000000E+01 0.1082478E+01

TEST CASE #2: PITOT PRESSURES, X=3.6"; YG=5.4";  
Z (in) PT/PTREF GD/FW HAWK3D

0.0000000E+00 0.8593464E-01  
0.3029734E-02 0.1147712E+00  
0.6122216E-02 0.1772659E+00  
0.9282144E-02 0.2035314E+00  
0.1251434E-01 0.2240167E+00  
0.1582376E-01 0.2395799E+00  
0.1921533E-01 0.2547361E+00  
0.2269408E-01 0.2677236E+00  
0.2626538E-01 0.2805610E+00  
0.2993435E-01 0.2918852E+00  
0.3370654E-01 0.3036792E+00  
0.3758746E-01 0.3139862E+00  
0.4158282E-01 0.3245565E+00  
0.4569852E-01 0.3351066E+00  
0.4994046E-01 0.3447488E+00  
0.5431471E-01 0.3547475E+00  
0.5882776E-01 0.3648118E+00  
0.6348582E-01 0.3740851E+00  
0.6829566E-01 0.3837163E+00  
0.7326417E-01 0.3937230E+00  
0.7839799E-01 0.4028775E+00  
0.8370463E-01 0.4121883E+00  
0.8919108E-01 0.4218442E+00  
0.9486528E-01 0.4316558E+00  
0.1007346E+00 0.4408186E+00  
0.1068073E+00 0.4503361E+00  
0.1130915E+00 0.4602243E+00  
0.1195953E+00 0.4702374E+00  
0.1263276E+00 0.4797696E+00  
0.1332971E+00 0.4896713E+00  
0.1405129E+00 0.4999585E+00  
0.1479842E+00 0.5106093E+00  
0.1557207E+00 0.5209149E+00  
0.1637321E+00 0.5316195E+00  
0.1720283E+00 0.5427398E+00  
0.1806197E+00 0.5542896E+00  
0.1895168E+00 0.5660433E+00  
0.1987303E+00 0.5780415E+00  
0.2082713E+00 0.5905361E+00  
0.2181510E+00 0.6035107E+00  
0.2283809E+00 0.6169472E+00  
0.2389730E+00 0.6306694E+00  
0.2499391E+00 0.6449151E+00  
0.2612916E+00 0.6597034E+00  
0.2730431E+00 0.6750523E+00  
0.2852065E+00 0.6912627E+00  
0.2977945E+00 0.7083684E+00  
0.3108208E+00 0.7261136E+00  
0.3242989E+00 0.7445180E+00  
0.3382424E+00 0.7636033E+00  
0.3526654E+00 0.7829812E+00  
0.3675824E+00 0.8029516E+00  
0.3830077E+00 0.8236465E+00  
0.3989561E+00 0.8450888E+00  
0.4154426E+00 0.8672177E+00  
0.4324824E+00 0.8871233E+00  
0.4500906E+00 0.9077284E+00  
0.4682832E+00 0.9290521E+00  
0.4870759E+00 0.9511156E+00  
0.5064845E+00 0.9706451E+00  
0.5265253E+00 0.9815043E+00  
0.5472147E+00 0.9927250E+00  
0.5685689E+00 0.1004316E+01  
0.5906052E+00 0.1016288E+01  
0.6133402E+00 0.1023161E+01  
0.6367909E+00 0.1025235E+01  
0.6609744E+00 0.1027374E+01  
0.6859084E+00 0.1029580E+01  
0.7116103E+00 0.1031855E+01  
0.7380980E+00 0.1034454E+01  
0.7653893E+00 0.1037166E+01  
0.7935025E+00 0.1039961E+01  
0.8224557E+00 0.1042800E+01  
0.8522675E+00 0.1044389E+01  
0.8829572E+00 0.1045474E+01  
0.9145432E+00 0.1046673E+01  
0.9470451E+00 0.1048107E+01  
0.9804828E+00 0.1050540E+01  
0.1014876E+01 0.1053045E+01  
0.1050245E+01 0.1055620E+01  
0.1086611E+01 0.1056494E+01  
0.1123996E+01 0.1057142E+01  
0.1162420E+01 0.1057889E+01  
0.1201907E+01 0.1058983E+01  
0.1242479E+01 0.1060274E+01  
0.1284161E+01 0.1061547E+01  
0.1326977E+01 0.1062114E+01  
0.1370952E+01 0.1062697E+01  
0.1416113E+01 0.1063762E+01  
0.1462488E+01 0.1065382E+01  
0.1510104E+01 0.1067039E+01  
0.1558993E+01 0.1068593E+01  
0.1609185E+01 0.1070188E+01  
0.1660713E+01 0.1070513E+01  
0.1713612E+01 0.1070431E+01  
0.1767918E+01 0.1071611E+01  
0.1823668E+01 0.1073655E+01  
0.1880903E+01 0.1077181E+01  
0.1939666E+01 0.1081666E+01  
0.2000000E+01 0.1083306E+01

TEST CASE #2: PITOT PRESSURES, X=7.4"; YG=0.25";  
Z (in) PT/PTREF GD/FW HAWK3D

0.0000000E+00 0.5404502E+00  
0.3029734E-02 0.6216704E+00  
0.6122216E-02 0.6830189E+00  
0.9282144E-02 0.7264388E+00  
0.1251434E-01 0.7682944E+00  
0.1582376E-01 0.8006199E+00  
0.1921533E-01 0.8333157E+00  
0.2269408E-01 0.8585165E+00  
0.2626538E-01 0.8845474E+00  
0.2993435E-01 0.9072117E+00  
0.3370654E-01 0.9281114E+00  
0.3758746E-01 0.9497067E+00  
0.4158282E-01 0.9676271E+00  
0.4569852E-01 0.9851796E+00  
0.4994046E-01 0.1003330E+01  
0.5431471E-01 0.1019134E+01  
0.5882776E-01 0.1033999E+01  
0.6348582E-01 0.1049330E+01  
0.6829566E-01 0.1064647E+01  
0.7326417E-01 0.1077020E+01  
0.7839799E-01 0.1089848E+01  
0.8370463E-01 0.1103130E+01  
0.8919108E-01 0.1115783E+01  
0.9486528E-01 0.1126442E+01  
0.1007346E+00 0.1137490E+01  
0.1068073E+00 0.1148945E+01  
0.1130915E+00 0.1160177E+01  
0.1195953E+00 0.1169480E+01  
0.1263276E+00 0.1179128E+01  
0.1332971E+00 0.1189137E+01  
0.1405129E+00 0.1199521E+01  
0.1479842E+00 0.1208229E+01  
0.1557207E+00 0.1217023E+01  
0.1637321E+00 0.1226149E+01  
0.1720283E+00 0.1235619E+01  
0.1806197E+00 0.1244772E+01  
0.1895168E+00 0.1253221E+01  
0.1987303E+00 0.1261989E+01  
0.2082713E+00 0.1271088E+01  
0.2181510E+00 0.1280531E+01  
0.2283809E+00 0.1289287E+01  
0.2389730E+00 0.1298033E+01  
0.2499391E+00 0.1307104E+01  
0.2612916E+00 0.1316513E+01  
0.2730431E+00 0.1326230E+01  
0.2852065E+00 0.1334651E+01  
0.2977945E+00 0.1343379E+01  
0.3108208E+00 0.1352425E+01  
0.3242989E+00 0.1361800E+01  
0.3382424E+00 0.1370979E+01  
0.3526654E+00 0.1378672E+01  
0.3675824E+00 0.1386638E+01  
0.3830077E+00 0.1394886E+01  
0.3989561E+00 0.1403422E+01  
0.4154426E+00 0.1410896E+01  
0.4324824E+00 0.1416631E+01  
0.4500906E+00 0.1422559E+01  
0.4682832E+00 0.1428691E+01  
0.4870759E+00 0.1435028E+01  
0.5064845E+00 0.1439411E+01  
0.5265253E+00 0.1442414E+01  
0.5472147E+00 0.1445517E+01  
0.5685689E+00 0.1448720E+01  
0.5906052E+00 0.1452027E+01  
0.6133402E+00 0.1453683E+01  
0.6367909E+00 0.1454965E+01  
0.6609744E+00 0.1456288E+01  
0.6859084E+00 0.1457654E+01  
0.7116103E+00 0.1458497E+01  
0.7380980E+00 0.1459934E+01  
0.7653893E+00 0.1460903E+01  
0.7935025E+00 0.1461901E+01  
0.8224557E+00 0.1462935E+01  
0.8522675E+00 0.1464154E+01  
0.8829572E+00 0.1465409E+01  
0.9145432E+00 0.1466702E+01  
0.9470451E+00 0.1468102E+01  
0.9804828E+00 0.1469661E+01  
0.1014876E+01 0.1471266E+01  
0.1050245E+01 0.1472966E+01  
0.1086611E+01 0.1475577E+01  
0.1123996E+01 0.1478264E+01  
0.1162420E+01 0.1481027E+01  
0.1201907E+01 0.1483877E+01  
0.1242479E+01 0.1486808E+01  
0.1284161E+01 0.1490156E+01  
0.1326977E+01 0.1494811E+01  
0.1370952E+01 0.1499594E+01  
0.1416113E+01 0.1502834E+01  
0.1462488E+01 0.1505093E+01  
0.1510104E+01 0.1507412E+01  
0.1558993E+01 0.1509776E+01  
0.1609185E+01 0.1512206E+01  
0.1660713E+01 0.1515244E+01  
0.1713612E+01 0.1518436E+01  
0.1767918E+01 0.1522762E+01  
0.1823668E+01 0.1527382E+01  
0.1880903E+01 0.1532211E+01  
0.1939666E+01 0.1537037E+01  
0.2000000E+01 0.1538510E+01

TEST CASE #2: PITOT PRESSURES, X=7.1", YG=0.75",  
 Z (in) PT/PTREF GD/FW HANK3D

0.000000E+00 0.4370119E+00  
 0.302973E-02 0.517728E+00  
 0.6122217E-02 0.517728E+00  
 0.9282144E-02 0.633432E+00  
 0.1251434E-01 0.6609429E+00  
 0.1582376E-01 0.6862570E+00  
 0.1921533E-01 0.7054020E+00  
 0.2269408E-01 0.7236413E+00  
 0.2626538E-01 0.7370733E+00  
 0.2993435E-01 0.7507441E+00  
 0.3370654E-01 0.7669231E+00  
 0.3758746E-01 0.7783481E+00  
 0.4138282E-01 0.7883655E+00  
 0.4569052E-01 0.7987308E+00  
 0.4994045E-01 0.8080435E+00  
 0.5431471E-01 0.8159532E+00  
 0.5882775E-01 0.8241343E+00  
 0.6348582E-01 0.8326296E+00  
 0.6829566E-01 0.8393279E+00  
 0.7326417E-01 0.8461890E+00  
 0.7839799E-01 0.8533054E+00  
 0.8370463E-01 0.8604595E+00  
 0.8919108E-01 0.8667227E+00  
 0.9485528E-01 0.8730762E+00  
 0.1007346E+00 0.8799600E+00  
 0.1068074E+00 0.8863545E+00  
 0.1130915E+00 0.8934052E+00  
 0.1195953E+00 0.9001670E+00  
 0.1263276E+00 0.9071270E+00  
 0.1332971E+00 0.9145105E+00  
 0.1405129E+00 0.9223996E+00  
 0.1479842E+00 0.9297607E+00  
 0.1557207E+00 0.9378391E+00  
 0.1637321E+00 0.9462491E+00  
 0.1720283E+00 0.9551255E+00  
 0.1806197E+00 0.9646634E+00  
 0.1895168E+00 0.9745933E+00  
 0.1987203E+00 0.9849343E+00  
 0.2082713E+00 0.9957020E+00  
 0.2181510E+00 0.1007504E+01  
 0.2283809E+00 0.1020081E+01  
 0.2389730E+00 0.1033171E+01  
 0.2499391E+00 0.1046797E+01  
 0.2612916E+00 0.1060977E+01  
 0.2730431E+00 0.1076115E+01  
 0.2852065E+00 0.1092503E+01  
 0.2977945E+00 0.1109231E+01  
 0.3108208E+00 0.1126322E+01  
 0.3242989E+00 0.1144605E+01  
 0.3382424E+00 0.1162811E+01  
 0.3526654E+00 0.1181771E+01  
 0.3675824E+00 0.1201334E+01  
 0.3830077E+00 0.1221697E+01  
 0.3989561E+00 0.1242474E+01  
 0.4154426E+00 0.1259498E+01  
 0.4324824E+00 0.1278163E+01  
 0.4500905E+00 0.1297502E+01  
 0.4682032E+00 0.1317531E+01  
 0.4870759E+00 0.1338688E+01  
 0.5064845E+00 0.1360444E+01  
 0.5265253E+00 0.1380664E+01  
 0.5472147E+00 0.1397465E+01  
 0.5685639E+00 0.1389285E+01  
 0.5906052E+00 0.1357223E+01  
 0.6133402E+00 0.1403250E+01  
 0.6367909E+00 0.1409470E+01  
 0.6609744E+00 0.1415886E+01  
 0.6859848E+00 0.1422086E+01  
 0.7116103E+00 0.1444444E+01  
 0.7380980E+00 0.1426876E+01  
 0.7653892E+00 0.1429384E+01  
 0.7935025E+00 0.1431970E+01  
 0.8224556E+00 0.1434859E+01  
 0.8522676E+00 0.1437834E+01  
 0.8829572E+00 0.1440900E+01  
 0.9145431E+00 0.1444295E+01  
 0.9470451E+00 0.1448256E+01  
 0.9804820E+00 0.1452332E+01  
 0.1014976E+01 0.1456530E+01  
 0.1050245E+01 0.1461021E+01  
 0.1086611E+01 0.1465641E+01  
 0.1123996E+01 0.1470390E+01  
 0.1162420E+01 0.1475237E+01  
 0.1201937E+01 0.1480219E+01  
 0.1242479E+01 0.1485294E+01  
 0.1284161E+01 0.1490310E+01  
 0.1326977E+01 0.1495466E+01  
 0.1370952E+01 0.1500648E+01  
 0.1416113E+01 0.1504875E+01  
 0.1462480E+01 0.1509107E+01  
 0.1510104E+01 0.1513774E+01  
 0.1558093E+01 0.1518568E+01  
 0.1605185E+01 0.1523264E+01  
 0.1660713E+01 0.1527921E+01  
 0.1713612E+01 0.1531773E+01  
 0.1767818E+01 0.1535323E+01  
 0.1823650E+01 0.1537416E+01  
 0.1880803E+01 0.1538796E+01  
 0.1939666E+01 0.1540639E+01  
 0.2000000E+01 0.1546399E+01

 TEST CASE #2: PITOT PRESSURES, X=7.1", YG=1.25",  
 Z (in) PT/PTREF GD/FW HANK3D

0.000000E+00 0.2880501E+00  
 0.3029734E-02 0.3970541E+00  
 0.6122216E-02 0.4459572E+00  
 0.9282144E-02 0.4839489E+00  
 0.1251434E-01 0.5106327E+00  
 0.1582376E-01 0.5344175E+00  
 0.1921533E-01 0.5530592E+00  
 0.2269408E-01 0.5700154E+00  
 0.2626538E-01 0.5829145E+00  
 0.2993435E-01 0.5962670E+00  
 0.3370654E-01 0.6054919E+00  
 0.3758746E-01 0.6147346E+00  
 0.4138282E-01 0.6237827E+00  
 0.4569052E-01 0.6301215E+00  
 0.4994045E-01 0.6367903E+00  
 0.5431471E-01 0.6435372E+00  
 0.5882775E-01 0.6483462E+00  
 0.6348582E-01 0.6533321E+00  
 0.6829566E-01 0.6585092E+00  
 0.7326417E-01 0.6628898E+00  
 0.7839799E-01 0.6668196E+00  
 0.8370463E-01 0.6709083E+00  
 0.8919108E-01 0.6751630E+00  
 0.9485528E-01 0.6787452E+00  
 0.1007346E+00 0.6823354E+00  
 0.1068074E+00 0.6860824E+00  
 0.1130915E+00 0.6899944E+00  
 0.1195953E+00 0.6937109E+00  
 0.1263276E+00 0.6975163E+00  
 0.1332971E+00 0.7014996E+00  
 0.1405129E+00 0.7056700E+00  
 0.1479842E+00 0.7101821E+00  
 0.1557207E+00 0.7150298E+00  
 0.1637321E+00 0.7201138E+00  
 0.1720283E+00 0.7254403E+00  
 0.1806197E+00 0.7311413E+00  
 0.1895168E+00 0.7381496E+00  
 0.1987203E+00 0.7454936E+00  
 0.2082713E+00 0.7531890E+00  
 0.2181510E+00 0.7612542E+00  
 0.2283809E+00 0.7708182E+00  
 0.2389730E+00 0.7819263E+00  
 0.2499391E+00 0.7935469E+00  
 0.2612916E+00 0.8057016E+00  
 0.2730431E+00 0.8184159E+00  
 0.2852065E+00 0.8340521E+00  
 0.2977945E+00 0.8510187E+00  
 0.3108208E+00 0.8686835E+00  
 0.3242989E+00 0.8871171E+00  
 0.3382424E+00 0.9064782E+00  
 0.3526654E+00 0.9291893E+00  
 0.3675824E+00 0.9528350E+00  
 0.3830077E+00 0.9774508E+00  
 0.3989561E+00 0.1003069E+01  
 0.4154426E+00 0.1029806E+01  
 0.4324824E+00 0.1057842E+01  
 0.4500905E+00 0.1086955E+01  
 0.4682032E+00 0.1117180E+01  
 0.4870759E+00 0.1148551E+01  
 0.5064845E+00 0.1178331E+01  
 0.5265253E+00 0.1205868E+01  
 0.5472147E+00 0.1230375E+01  
 0.5685639E+00 0.1263888E+01  
 0.5906052E+00 0.1294428E+01  
 0.6133402E+00 0.1315750E+01  
 0.6367909E+00 0.1333174E+01  
 0.6609744E+00 0.1351161E+01  
 0.6859848E+00 0.1369766E+01  
 0.7116103E+00 0.1388523E+01  
 0.7380980E+00 0.1396184E+01  
 0.7653892E+00 0.1404084E+01  
 0.7935025E+00 0.1412227E+01  
 0.8224556E+00 0.1420619E+01  
 0.8522676E+00 0.1424089E+01  
 0.8829572E+00 0.1427347E+01  
 0.9145431E+00 0.1430712E+01  
 0.9470451E+00 0.1434109E+01  
 0.9804820E+00 0.1437428E+01  
 0.1014976E+01 0.1440055E+01  
 0.1050245E+01 0.1444383E+01  
 0.1086611E+01 0.1448277E+01  
 0.1123996E+01 0.1452291E+01  
 0.1162420E+01 0.1456424E+01  
 0.1201937E+01 0.1461459E+01  
 0.1242479E+01 0.1466673E+01  
 0.1284161E+01 0.1472220E+01  
 0.1326977E+01 0.1478920E+01  
 0.1370952E+01 0.1485804E+01  
 0.1416113E+01 0.1492157E+01  
 0.1462480E+01 0.1498101E+01  
 0.1510104E+01 0.1504307E+01  
 0.1558093E+01 0.1511416E+01  
 0.1605185E+01 0.1518718E+01  
 0.1660713E+01 0.1523965E+01  
 0.1713612E+01 0.1528912E+01  
 0.1767818E+01 0.1534440E+01  
 0.1823650E+01 0.1540330E+01  
 0.1880803E+01 0.1544909E+01  
 0.1939666E+01 0.1548771E+01  
 0.2000000E+01 0.1551914E+01

## TEST CASE #2: YAW ANGLES,

X=7.1"; YG=0.25";  
GD/FW HAWK3D

Z (in)	Yaw Angle
0.000000E+00	0.1169802E+02
0.3028734E-02	0.1482148E+02
0.6122217E-02	0.1454788E+02
0.9282144E-02	0.1447733E+02
0.1251434E-01	0.1441131E+02
0.1582376E-01	0.1434191E+02
0.1921533E-01	0.1428747E+02
0.2269408E-01	0.1422006E+02
0.2626538E-01	0.1416944E+02
0.2993436E-01	0.1411177E+02
0.3370654E-01	0.1405371E+02
0.3758746E-01	0.1399607E+02
0.4158282E-01	0.1393550E+02
0.4569852E-01	0.1387504E+02
0.4994045E-01	0.1381409E+02
0.5431471E-01	0.1374931E+02
0.5882775E-01	0.1368209E+02
0.6348582E-01	0.1361429E+02
0.6829566E-01	0.1354489E+02
0.7326417E-01	0.1346634E+02
0.7839799E-01	0.1339069E+02
0.8370463E-01	0.1331196E+02
0.8919108E-01	0.1322983E+02
0.9486523E-01	0.1314122E+02
0.1007346E+00	0.1305047E+02
0.1068074E+00	0.1295967E+02
0.1130915E+00	0.1286449E+02
0.1195953E+00	0.1276442E+02
0.1263276E+00	0.1266216E+02
0.1332971E+00	0.1255771E+02
0.1405129E+00	0.1245103E+02
0.1479842E+00	0.1234320E+02
0.1557207E+00	0.1222944E+02
0.1637321E+00	0.1212010E+02
0.1720283E+00	0.1200467E+02
0.1806187E+00	0.1189024E+02
0.1895168E+00	0.1177869E+02
0.1987303E+00	0.1166464E+02
0.2082713E+00	0.1154745E+02
0.2181510E+00	0.1142771E+02
0.2283879E+00	0.1131893E+02
0.2389730E+00	0.1121193E+02
0.2499391E+00	0.1110237E+02
0.2612916E+00	0.1099022E+02
0.2730431E+00	0.1087614E+02
0.2852065E+00	0.1076040E+02
0.2977945E+00	0.1064245E+02
0.3108208E+00	0.1052262E+02
0.3242989E+00	0.1040988E+02
0.3382424E+00	0.1040803E+02
0.3526654E+00	0.1034021E+02
0.3675824E+00	0.1027071E+02
0.3830077E+00	0.1019951E+02
0.3989561E+00	0.1012660E+02
0.4154426E+00	0.1006703E+02
0.4324824E+00	0.1002793E+02
0.4500936E+00	0.9987794E+01
0.4682832E+00	0.9946609E+01
0.4870759E+00	0.9904369E+01
0.5064845E+00	0.9879162E+01
0.5265233E+00	0.9865973E+01
0.5472147E+00	0.9852401E+01
0.5685689E+00	0.9838442E+01
0.5906052E+00	0.9824088E+01
0.6133402E+00	0.9822785E+01
0.6367909E+00	0.9824705E+01
0.6609714E+00	0.9826684E+01
0.6859084E+00	0.9828720E+01
0.7116103E+00	0.9831109E+01
0.7380980E+00	0.9835588E+01
0.7653893E+00	0.9840197E+01
0.7935025E+00	0.9844938E+01
0.8224557E+00	0.9849733E+01
0.8522675E+00	0.9851915E+01
0.8829572E+00	0.9854159E+01
0.9145432E+00	0.9856464E+01
0.9470451E+00	0.9857424E+01
0.9804828E+00	0.9858975E+01
0.1014876E+01	0.9854486E+01
0.1050245E+01	0.9852960E+01
0.1086611E+01	0.9851375E+01
0.1123996E+01	0.9849751E+01
0.1162420E+01	0.9848134E+01
0.1201907E+01	0.9846689E+01
0.1242479E+01	0.9845255E+01
0.1284161E+01	0.9843961E+01
0.1326977E+01	0.9842758E+01
0.1370952E+01	0.9841612E+01
0.1416113E+01	0.9840538E+01
0.1462488E+01	0.9839688E+01
0.1510104E+01	0.9838724E+01
0.1558993E+01	0.9838363E+01
0.1609185E+01	0.9838511E+01
0.1660713E+01	0.9839682E+01
0.1713512E+01	0.9839719E+01
0.1767918E+01	0.9839241E+01
0.1823666E+01	0.9838565E+01
0.1880903E+01	0.9838183E+01
0.1939666E+01	0.9837956E+01
0.2000000E+01	0.9838785E+01

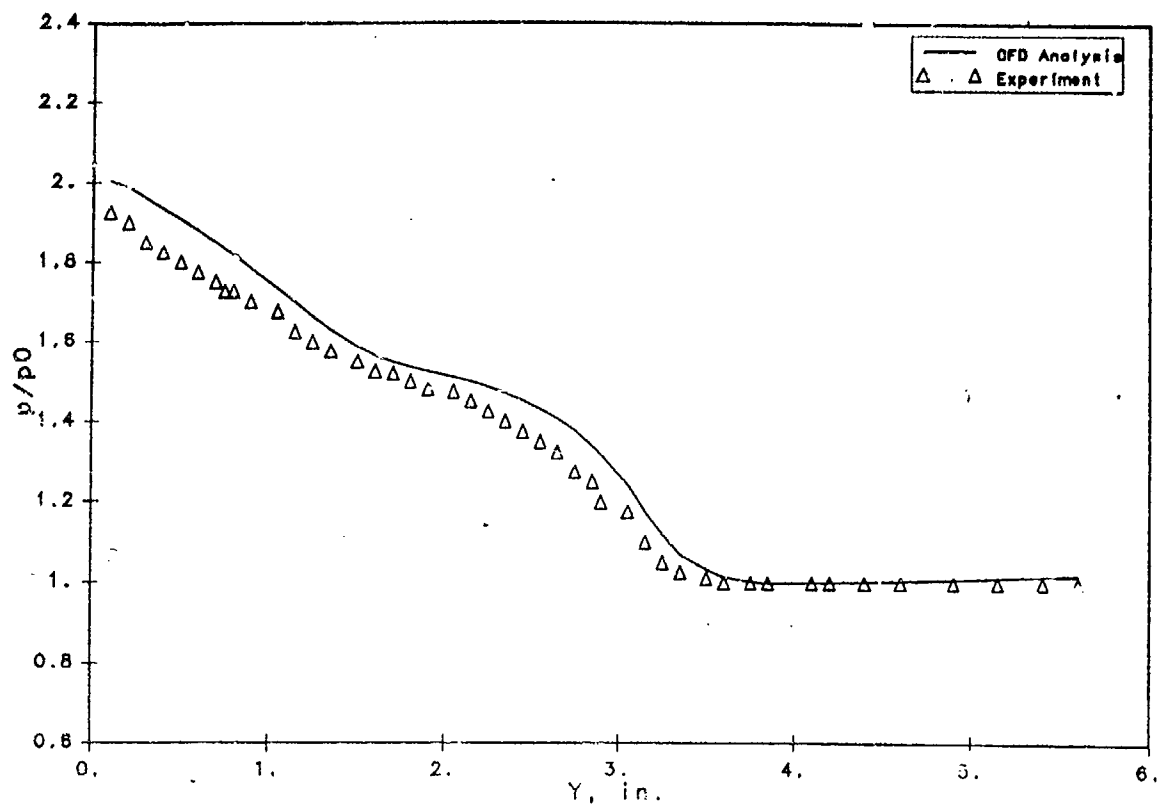
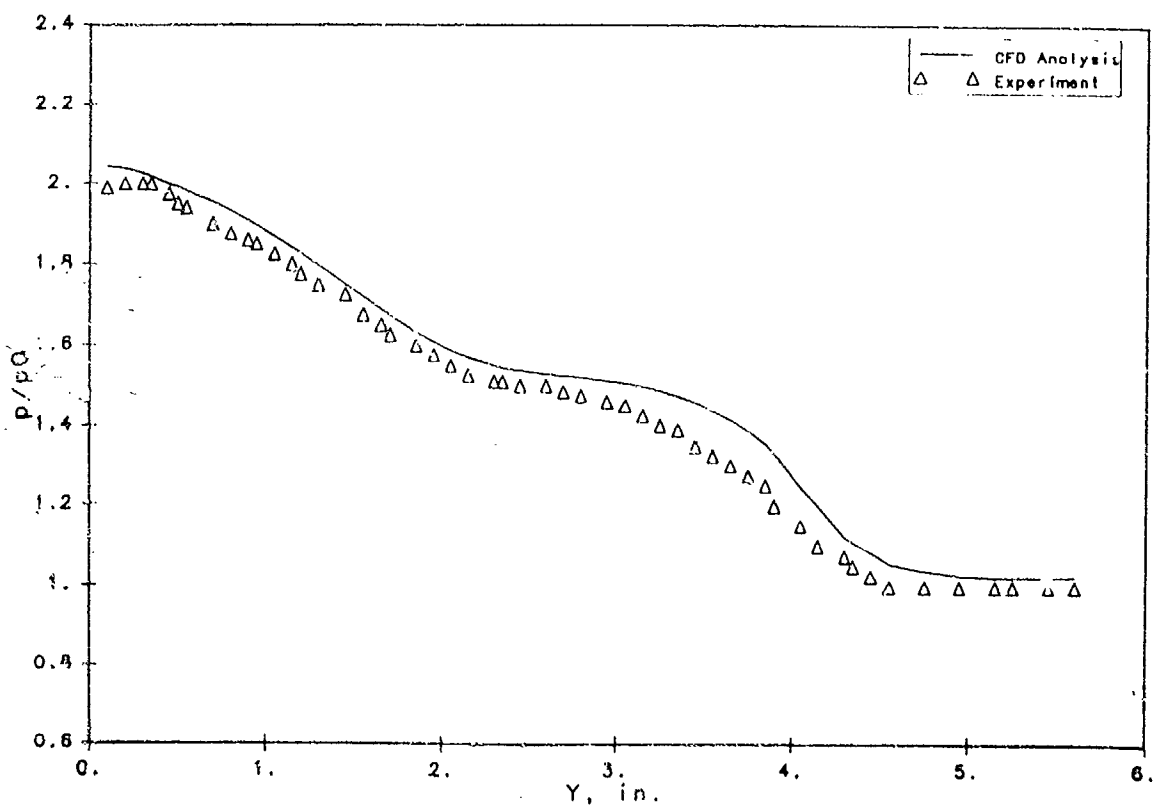
## TEST CASE #2: YAW ANGLES,

X=7.1"; YG=0.75";  
GD/FW HAWK3D

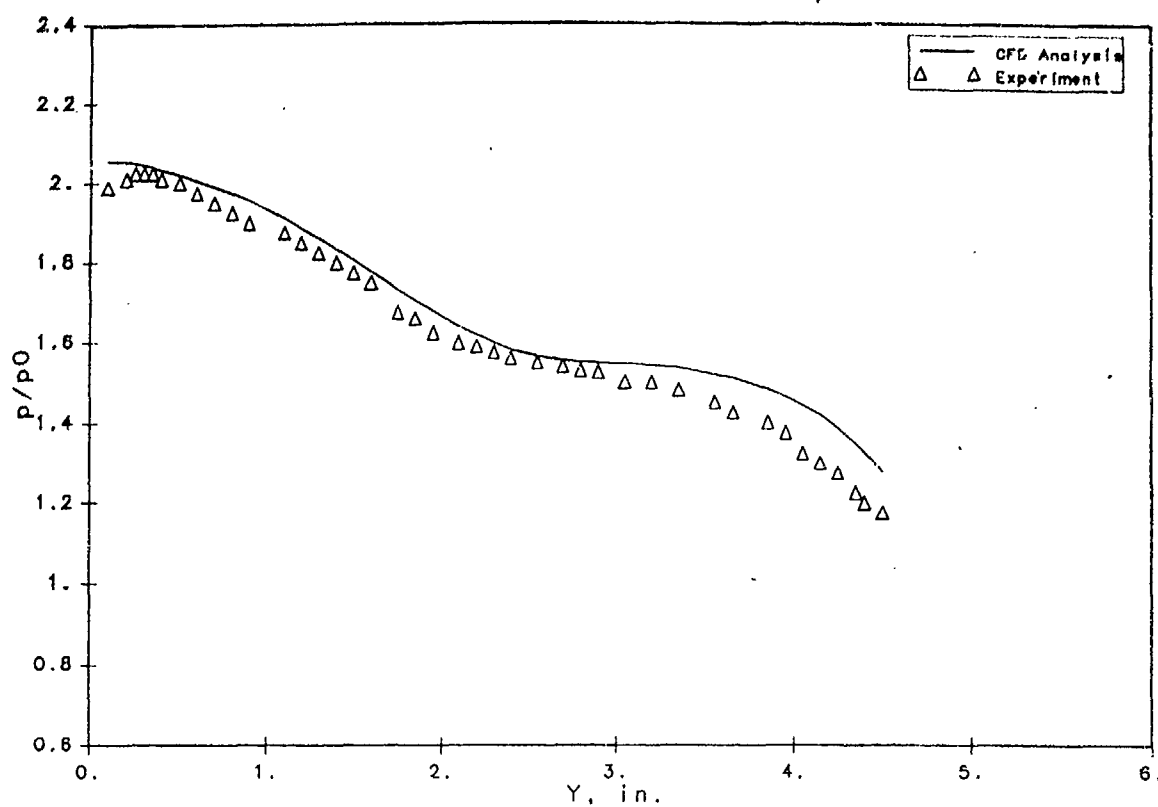
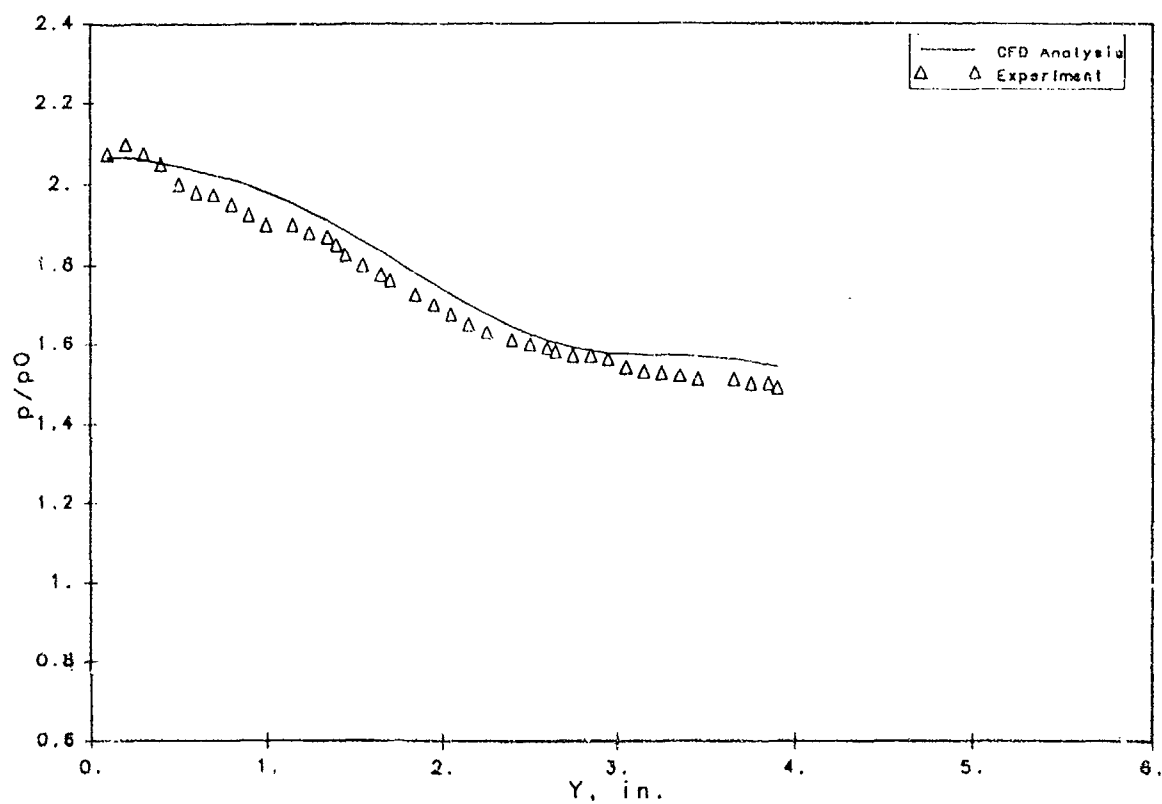
Z (in)	Yaw Angle
0.000000E+00	0.2163254E+02
0.3029734E-02	0.2145164E+02
0.6122217E-02	0.2126200E+02
0.9282144E-02	0.2108015E+02
0.1251434E-01	0.2090525E+02
0.1582376E-01	0.2073537E+02
0.1921533E-01	0.2057083E+02
0.2269408E-01	0.2041211E+02
0.2626538E-01	0.2025582E+02
0.2993436E-01	0.2010303E+02
0.3370654E-01	0.1995306E+02
0.3758746E-01	0.1980301E+02
0.4158282E-01	0.1965497E+02
0.4569852E-01	0.1950715E+02
0.4994045E-01	0.1936781E+02
0.5431471E-01	0.1920766E+02
0.5882775E-01	0.1905616E+02
0.6348582E-01	0.1890218E+02
0.6829566E-01	0.1874655E+02
0.7326417E-01	0.1858450E+02
0.7839799E-01	0.1841597E+02
0.8370463E-01	0.1825208E+02
0.8919108E-01	0.1807984E+02
0.9486528E-01	0.1789862E+02
0.1007347E+00	0.1771330E+02
0.1068074E+00	0.1752383E+02
0.1130915E+00	0.1732933E+02
0.1195953E+00	0.1712132E+02
0.1263276E+00	0.1690843E+02
0.1332971E+00	0.1669082E+02
0.1405129E+00	0.1646821E+02
0.1479842E+00	0.1623210E+02
0.1557207E+00	0.1598632E+02
0.1637321E+00	0.1573924E+02
0.1720283E+00	0.1548485E+02
0.1806187E+00	0.1522335E+02
0.1895168E+00	0.1495228E+02
0.1987303E+00	0.1467603E+02
0.2082713E+00	0.1439462E+02
0.2181510E+00	0.1410813E+02
0.2283879E+00	0.1382134E+02
0.2389730E+00	0.1353237E+02
0.2499391E+00	0.1323912E+02
0.2612916E+00	0.1294173E+02
0.2730431E+00	0.1264037E+02
0.2852065E+00	0.1236184E+02
0.2977945E+00	0.1208165E+02
0.3108208E+00	0.1179860E+02
0.3242989E+00	0.1151287E+02
0.3382424E+00	0.1123367E+02
0.3526654E+00	0.1099655E+02
0.3675824E+00	0.1075757E+02
0.3830077E+00	0.1051690E+02
0.3989561E+00	0.1027468E+02
0.4154426E+00	0.1005902E+02
0.4324824E+00	0.9892222E+01
0.4500936E+00	0.9723928E+01
0.4682832E+00	0.9554246E+01
0.4870759E+00	0.9393286E+01
0.5064845E+00	0.9262583E+01
0.5265233E+00	0.9183418E+01
0.5472147E+00	0.9103036E+01
0.5685689E+00	0.9021474E+01
0.5906052E+00	0.8938760E+01
0.6133402E+00	0.8916835E+01
0.6367909E+00	0.8913333E+01
0.6609714E+00	0.8909745E+01
0.6859084E+00	0.8906071E+01
0.7116103E+00	0.8903129E+01
0.7380980E+00	0.8931228E+01
0.7653893E+00	0.8958036E+01
0.7935025E+00	0.8985561E+01
0.8224557E+00	0.9013813E+01
0.8522675E+00	0.9031527E+01
0.8829572E+00	0.9049682E+01
0.9145432E+00	0.9068300E+01
0.9470451E+00	0.9083731E+01
0.9804828E+00	0.9092460E+01
0.1014876E+01	0.9101389E+01
0.1050245E+01	0.9110691E+01
0.1086611E+01	0.9125311E+01
0.1123996E+01	0.9140255E+01
0.1162420E+01	0.9155523E+01
0.1201907E+01	0.9172841E+01
0.1242479E+01	0.9190526E+01
0.1284161E+01	0.9203115E+01
0.1326977E+01	0.9230247E+01
0.1370952E+01	0.9251814E+01
0.1416113E+01	0.9274777E+01
0.1462488E+01	0.9298811E+01
0.1510104E+01	0.9323082E+01
0.1558993E+01	0.9346277E+01
0.1609185E+01	0.9369949E+01
0.1660713E+01	0.9395974E+01
0.1713512E+01	0.9422015E+01
0.1767918E+01	0.9456607E+01
0.1823666E+01	0.9493760E+01
0.1880903E+01	0.9539863E+01
0.1939666E+01	0.9591153E+01
0.2000000E+01	0.9629323E+01

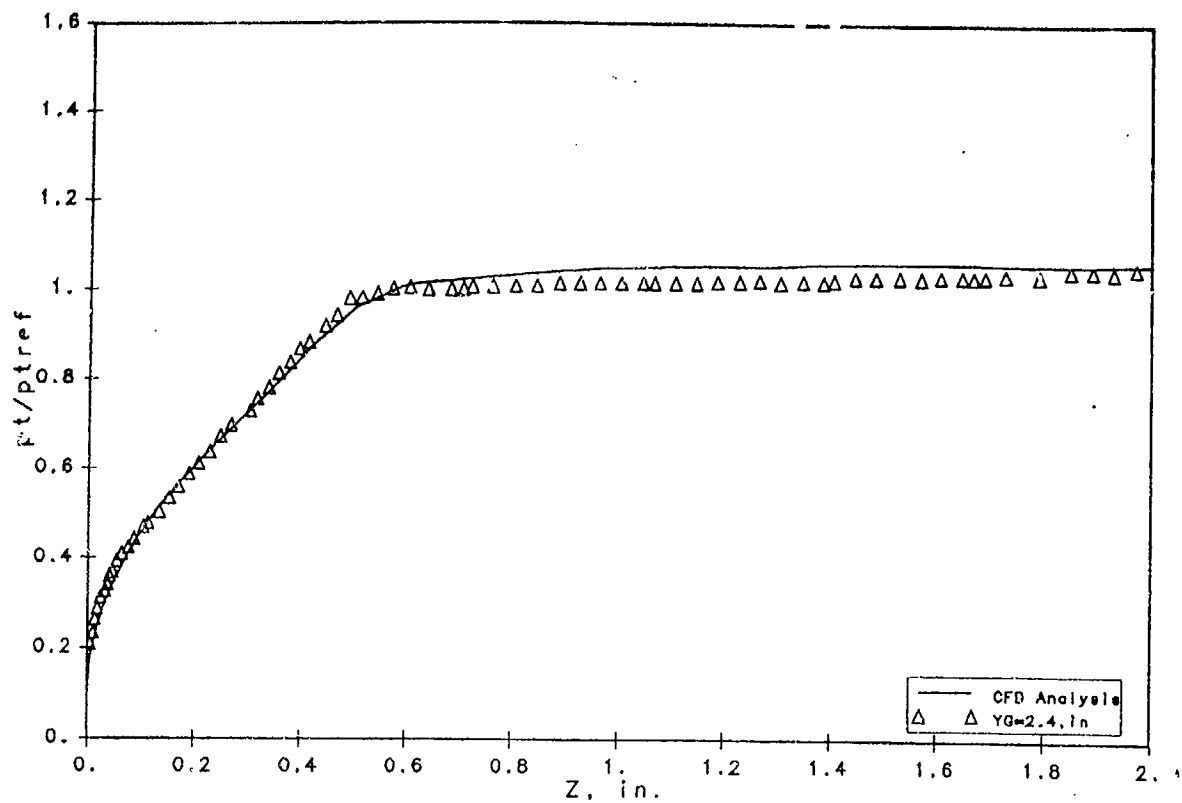
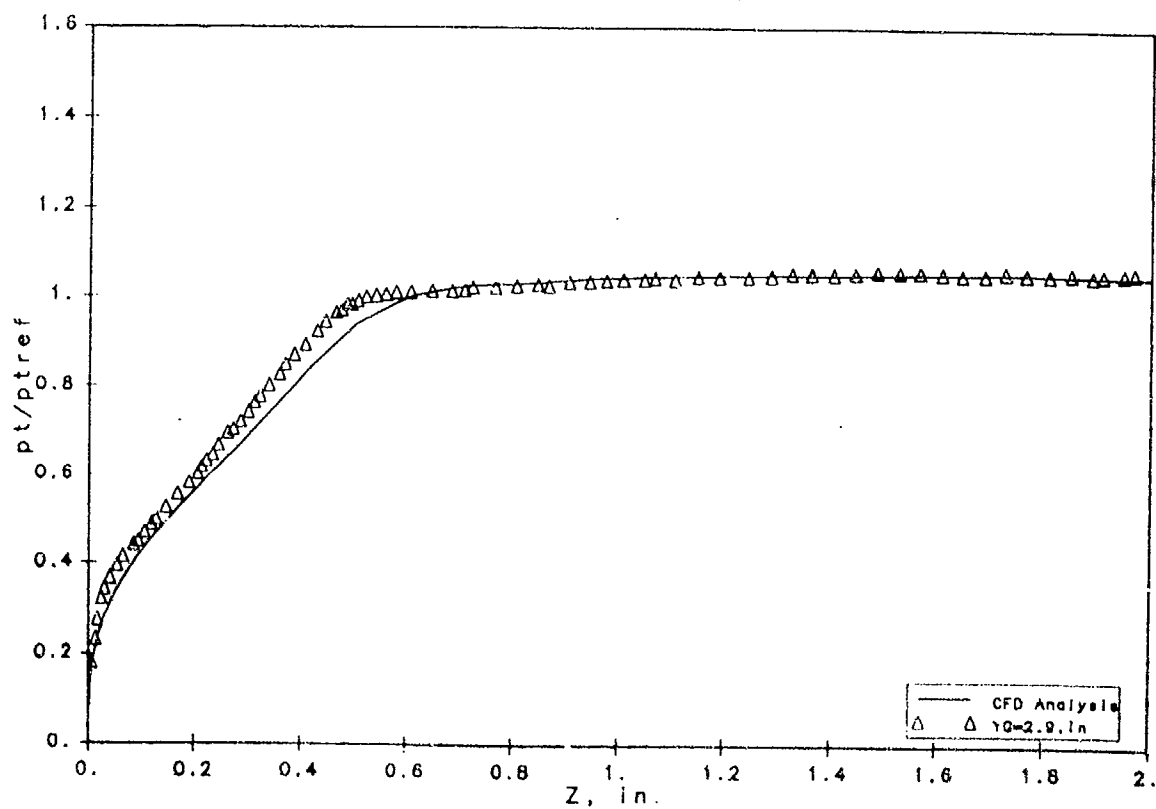
TEST CASE #2: YAW ANGLE, X=7.1"; YG=1.25"; GD/TW HAWK3D

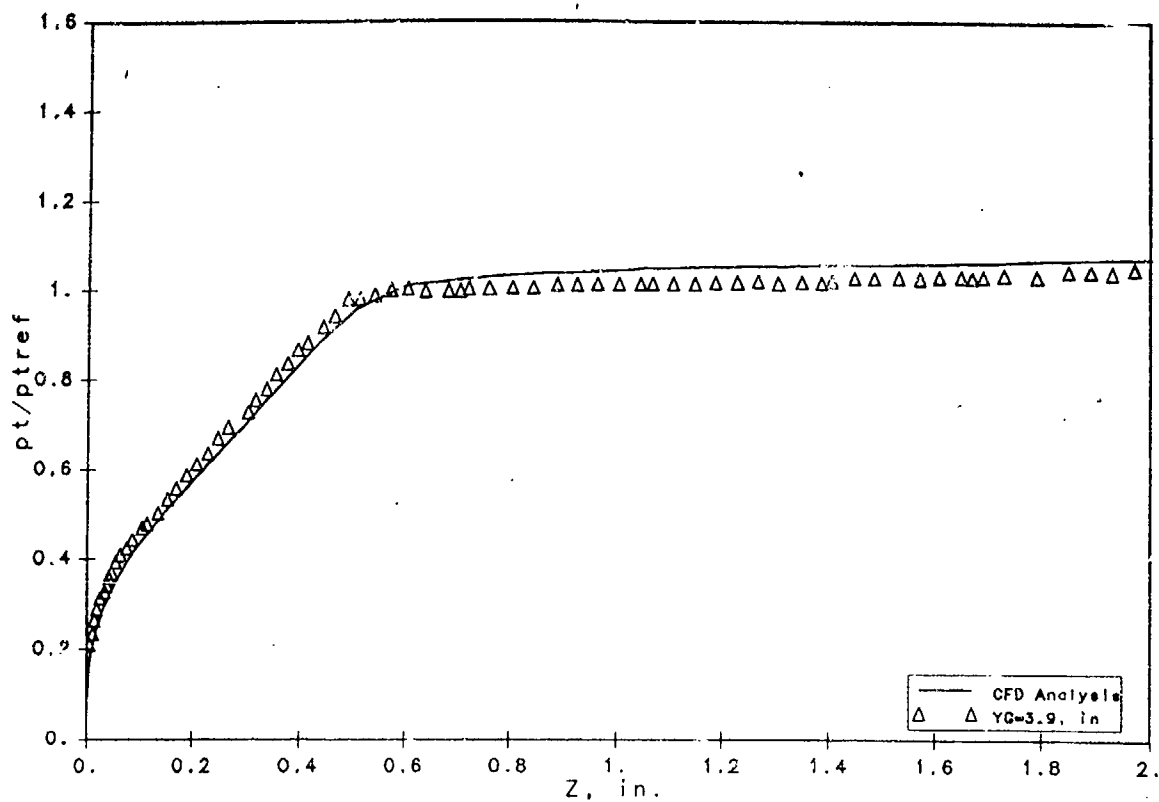
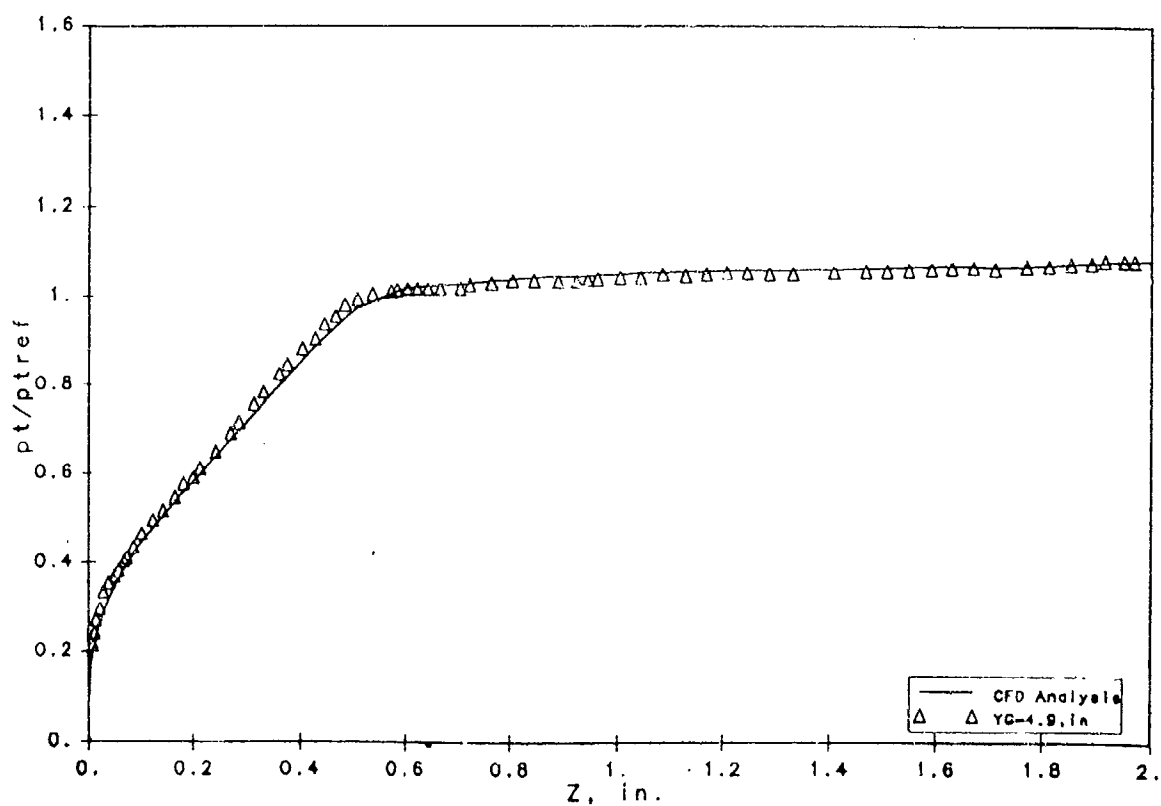
Z (in)	Yaw Angle
0.000000E+00	0.2800730E+02
0.3029734E+02	0.2775989E+02
0.6122216E-02	0.2748203E+02
0.9282144E-02	0.2721251E+02
0.1251434E-01	0.2694916E+02
0.1582376E-01	0.2670077E+02
0.1921533E-01	0.2646107E+02
0.2269408E-01	0.2623042E+02
0.2626538E-01	0.2600778E+02
0.2993435E-01	0.2578690E+02
0.3370654E-01	0.2557513E+02
0.3758746E-01	0.2536282E+02
0.4158282E-01	0.2515056E+02
0.4567852E-01	0.2494145E+02
0.4994446E-01	0.2472935E+02
0.5431471E-01	0.2451430E+02
0.5882776E-01	0.2429694E+02
0.6348582E-01	0.2407519E+02
0.6829566E-01	0.2384895E+02
0.732417E-01	0.2361473E+02
0.7839799E-01	0.2337295E+02
0.8370463E-01	0.2312533E+02
0.8919108E-01	0.2287175E+02
0.9486528E-01	0.2260099E+02
0.1007346E+00	0.2232131E+02
0.1068073E+00	0.2203432E+02
0.1130915E+00	0.2173987E+02
0.1195953E+00	0.2142201E+02
0.1263276E+00	0.2109720E+02
0.1332971E+00	0.2077369E+02
0.1405129E+00	0.2044063E+02
0.1479842E+00	0.2003801E+02
0.1557207E+00	0.1965060E+02
0.1637321E+00	0.1925375E+02
0.1720283E+00	0.1884738E+02
0.1806197E+00	0.1842989E+02
0.1895168E+00	0.1798939E+02
0.1987303E+00	0.1754014E+02
0.2082715E+00	0.1708221E+02
0.2181510E+00	0.1661573E+02
0.2283809E+00	0.1614334E+02
0.2389730E+00	0.1566691E+02
0.2499391E+00	0.1518483E+02
0.2612916E+00	0.1469743E+02
0.2730431E+00	0.1420500E+02
0.2852065E+00	0.1373708E+02
0.2977945E+00	0.1327437E+02
0.3108208E+00	0.1281080E+02
0.3242977E+00	0.1234673E+02
0.3382424E+00	0.1189565E+02
0.3526654E+00	0.1144915E+02
0.3675824E+00	0.1108523E+02
0.3829077E+00	0.1068920E+02
0.3989561E+00	0.1029635E+02
0.4154426E+00	0.9927373E+01
0.4324824E+00	0.9621465E+01
0.4500906E+00	0.9319007E+01
0.4682832E+00	0.9020172E+01
0.4870759E+00	0.8725122E+01
0.5064845E+00	0.8484272E+01
0.5265253E+00	0.8304563E+01
0.5472147E+00	0.8126103E+01
0.5685689E+00	0.7949015E+01
0.5906052E+00	0.7773404E+01
0.6133402E+00	0.7687548E+01
0.6367909E+00	0.7640477E+01
0.6609744E+00	0.7593037E+01
0.6859084E+00	0.7545251E+01
0.7116103E+00	0.7499775E+01
0.7380980E+00	0.7538557E+01
0.7653893E+00	0.7578105E+01
0.7935025E+00	0.7618418E+01
0.8224557E+00	0.7659490E+01
0.8522675E+00	0.7735413E+01
0.8829572E+00	0.7815300E+01
0.9145432E+00	0.7897111E+01
0.9470451E+00	0.7979478E+01
0.9804828E+00	0.8060378E+01
0.1014873E+01	0.8143173E+01
0.1050245E+01	0.8227879E+01
0.1086611E+01	0.8303033E+01
0.1123996E+01	0.8379661E+01
0.1162420E+01	0.8457952E+01
0.1201907E+01	0.8533683E+01
0.1242479E+01	0.8569410E+01
0.1284161E+01	0.8624654E+01
0.1326977E+01	0.8672352E+01
0.1370952E+01	0.8720905E+01
0.1416113E+01	0.8766809E+01
0.1462484E+01	0.8810738E+01
0.1510104E+01	0.8856389E+01
0.1558993E+01	0.8909015E+01
0.1609185E+01	0.8962529E+01
0.1660713E+01	0.9024076E+01
0.1713612E+01	0.9088219E+01
0.1767918E+01	0.9150776E+01
0.1823668E+01	0.9213175E+01
0.1880903E+01	0.9277355E+01
0.1939666E+01	0.9343236E+01
0.2000000E+01	0.9399715E+01

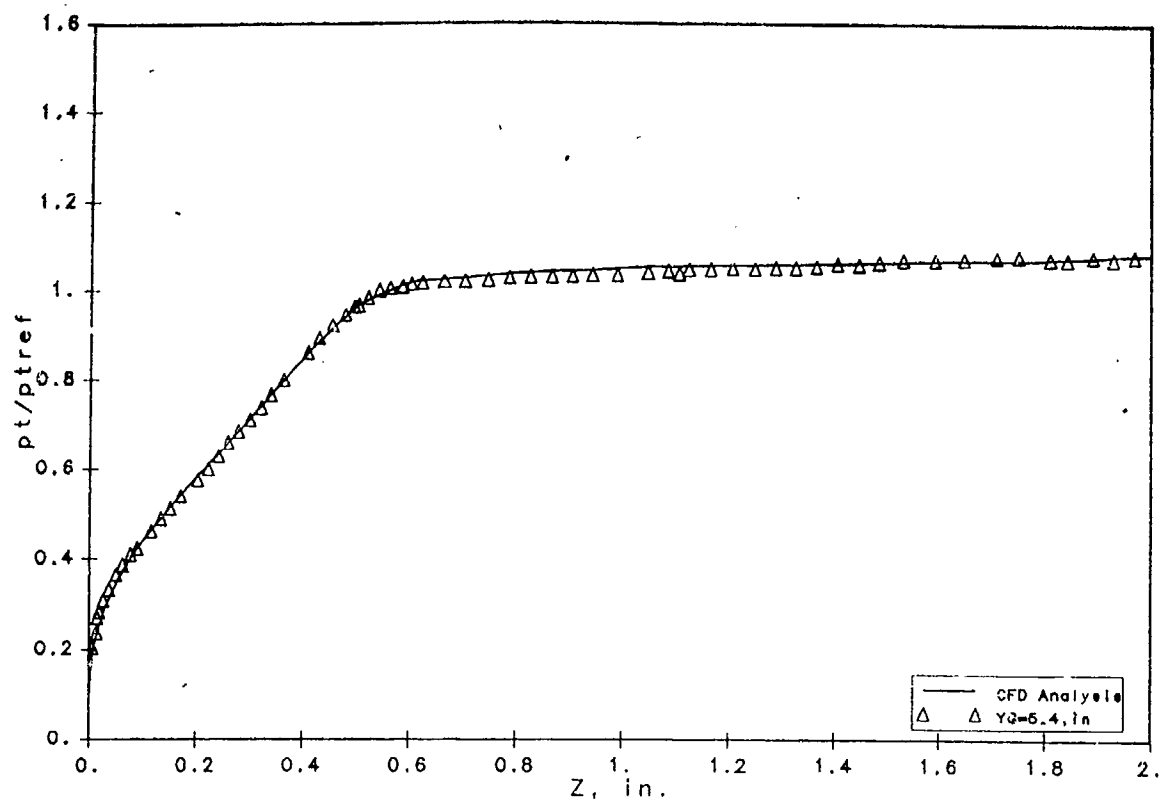
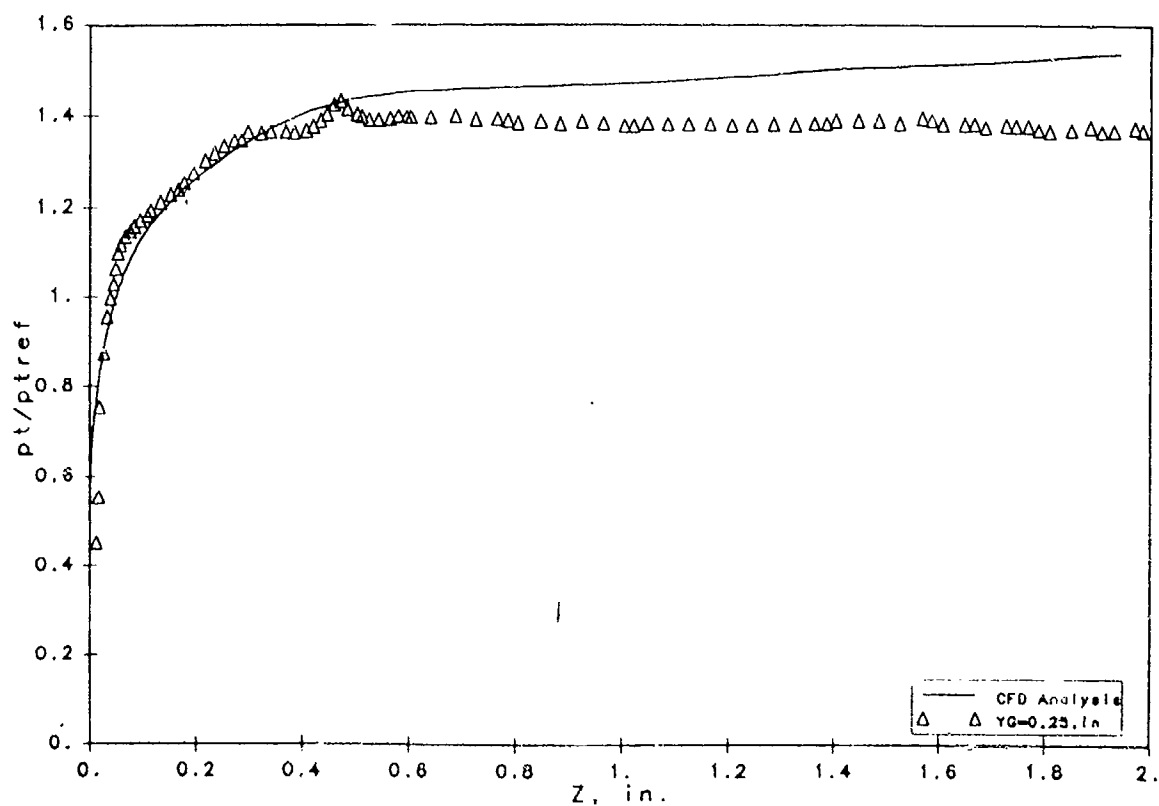
SURFACE STATIC PRESSURE  $X=5.1$  , in.SURFACE STATIC PRESSURE  $X=7.1$  , in.

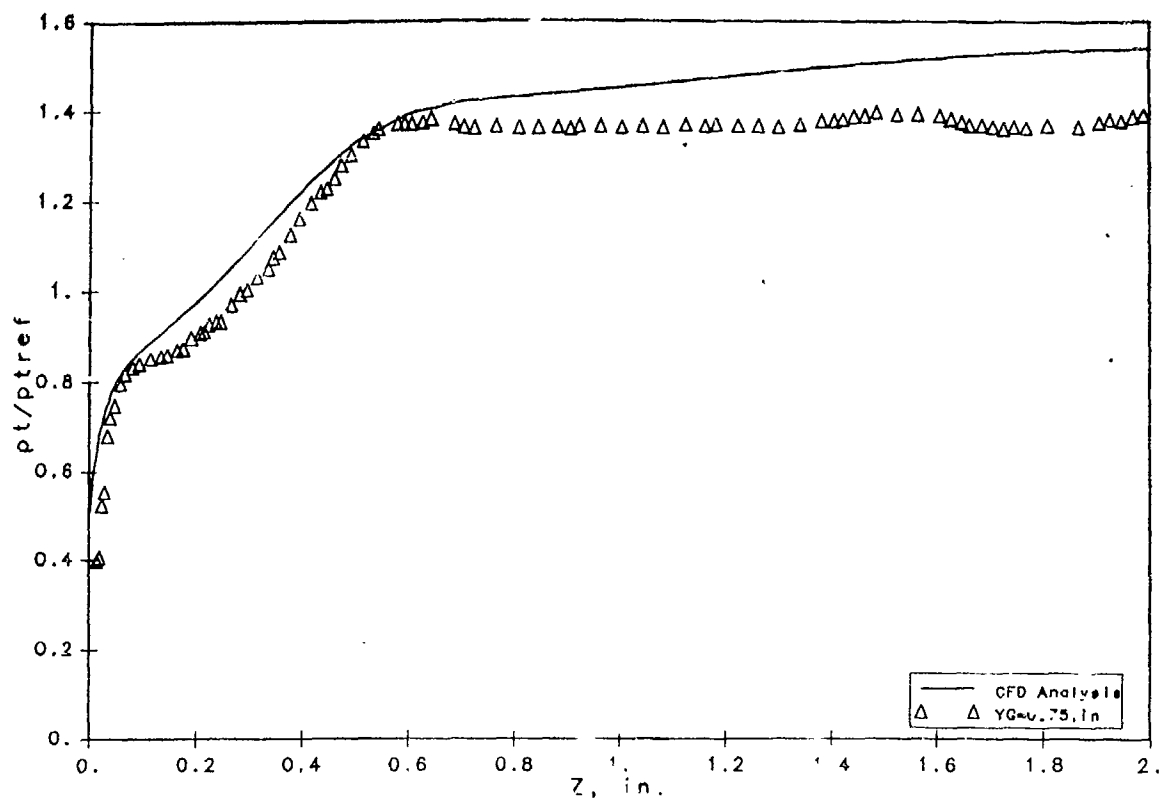
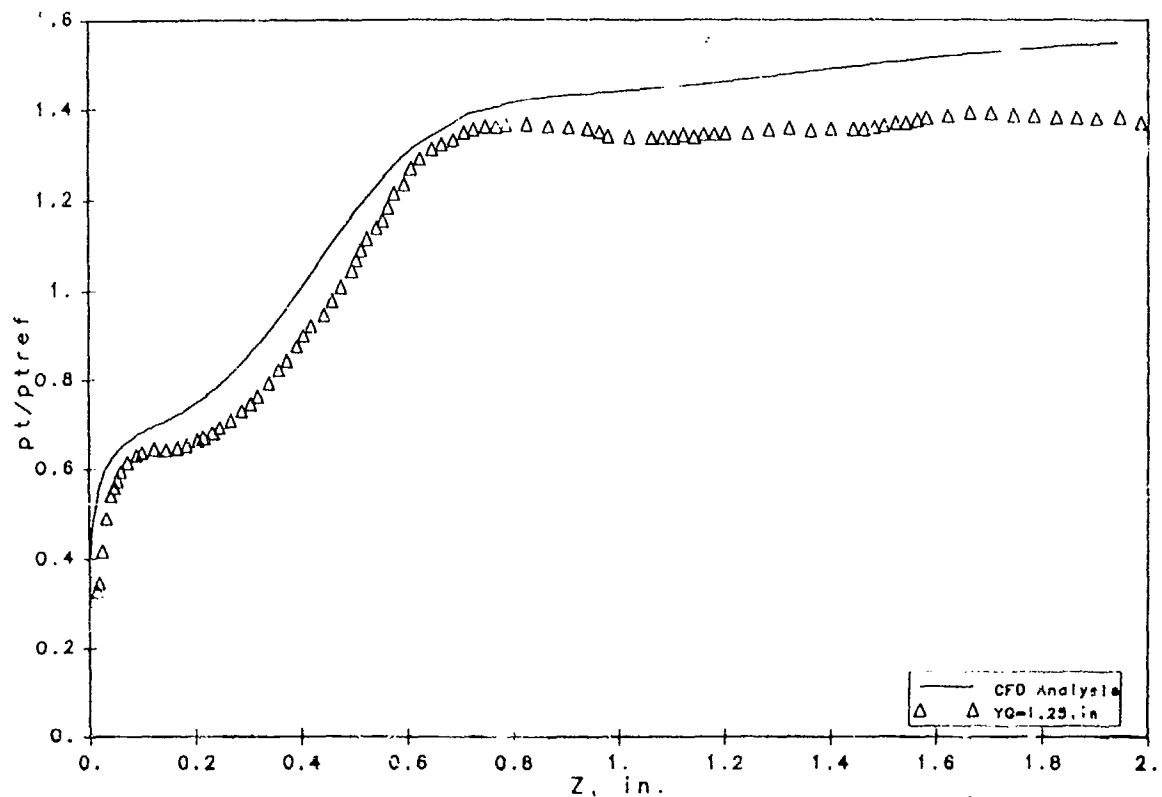


SURFACE STATIC PRESSURE  $X=8.1$  , in.SURFACE STATIC PRESSURE  $X=9.1$  , in.

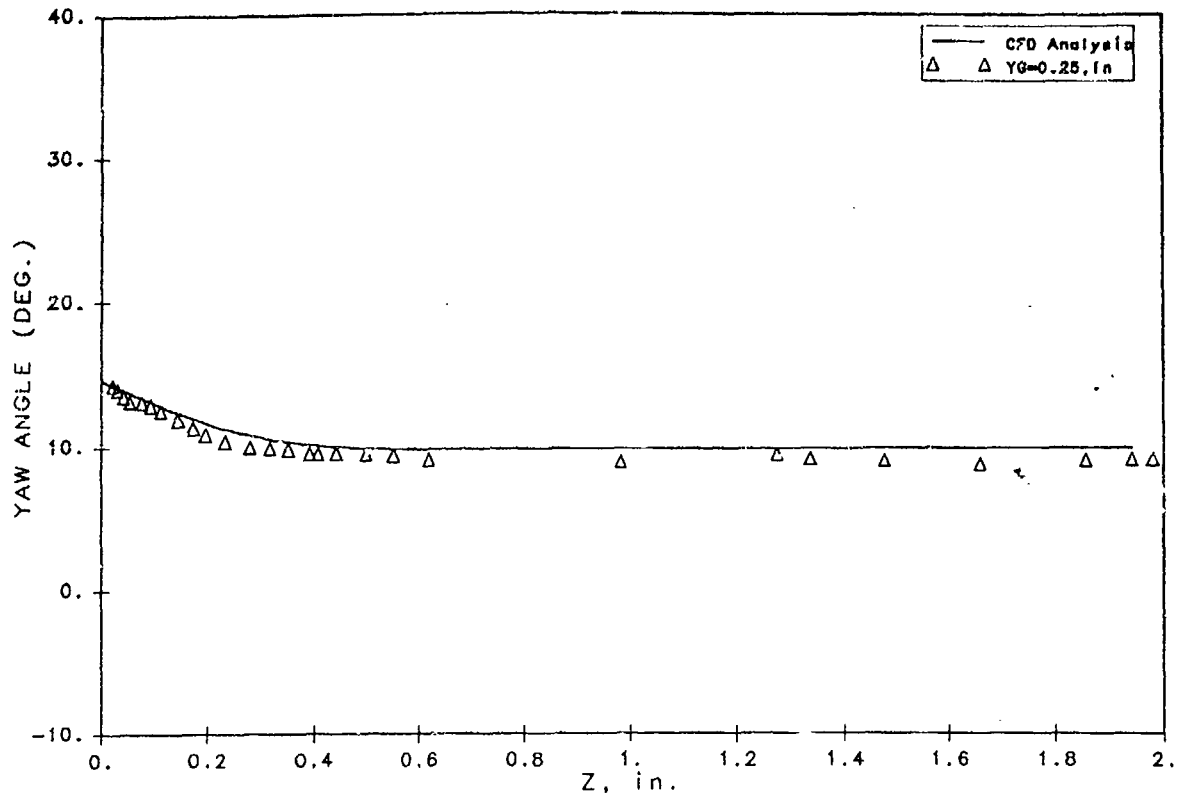
PITOT PRESSURE  $X=3.6$  , in.PITOT PRESSURE  $X=3.6$  , in.

PITOT PRESSURE  $X=3.6$  , in.PITOT PRESSURE  $X=3.6$  , in.

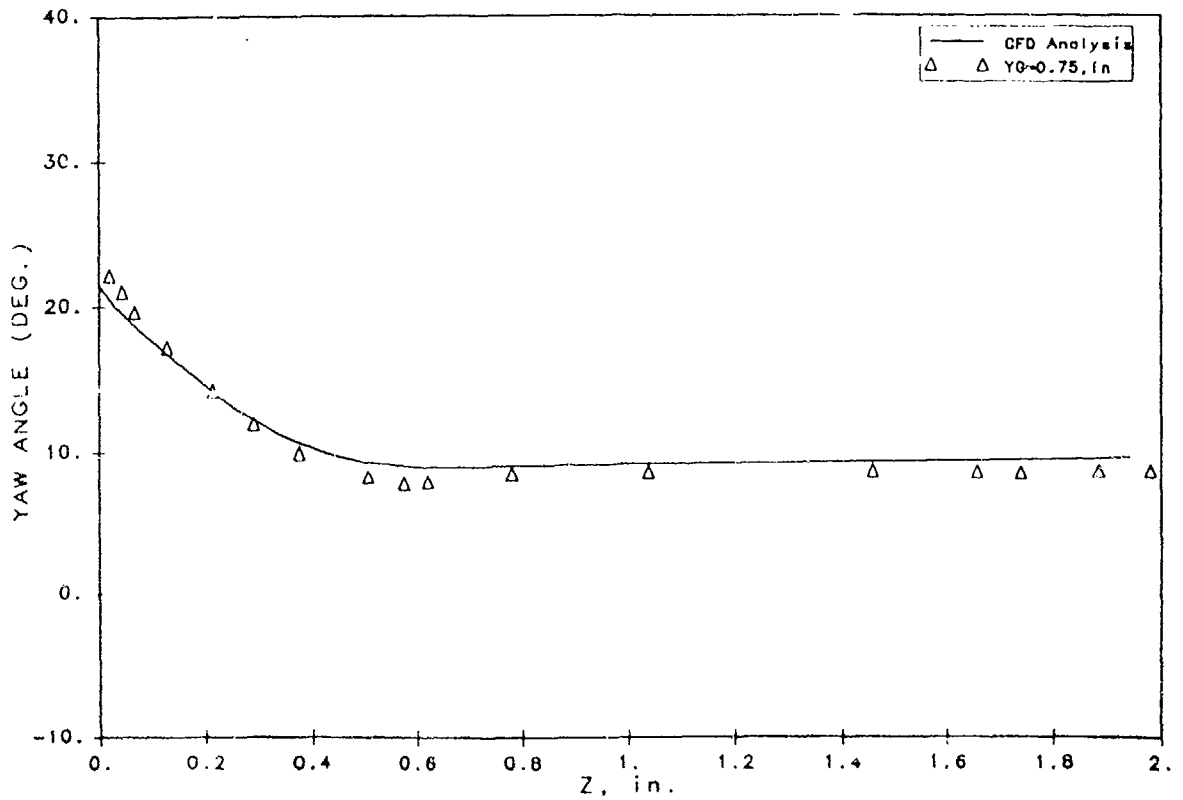
PITOT PRESSURE  $X=3.6$  , in.PITOT PRESSURE  $X=7.1$  , in.

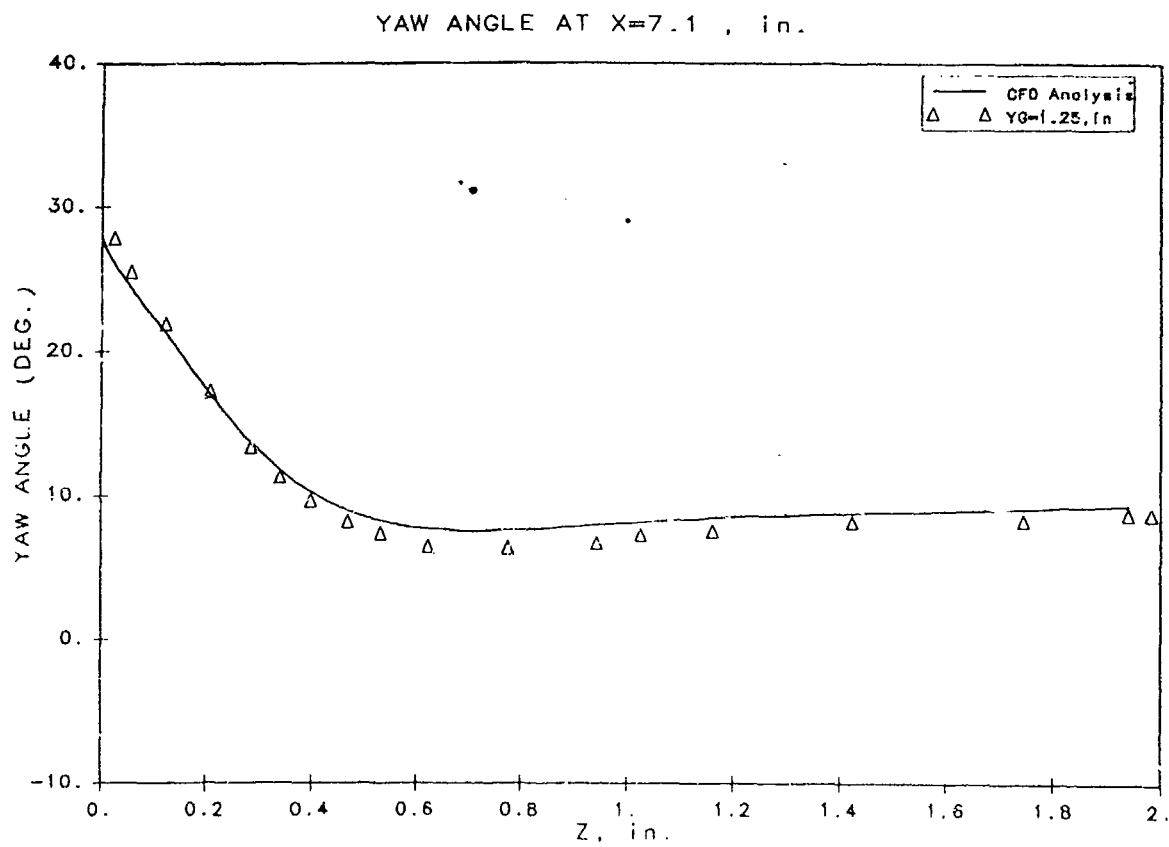
PITOT PRESSURE  $X=7.1$  , in.PITOT PRESSURE  $X=7.1$  , in.

YAW ANGLE AT X=7.1 , in.



YAW ANGLE AT X=7.1 , in.





ONERA

R. THEROT - P. CHAMPIGNY

Direction de l'Aérodynamique

## 1 INTRODUCTION.

This paper deals with the numerical simulation of a shock-wave turbulent boundary layer interaction in a tridimensionnal channel. This calculation has been performed with the configuration defined in the test case n° 2 by the AGARD working group 13 : 'Air Intakes for High Speed Vehicles'.

This paper shortly describes the numerical method used and presents some results concerning the pitot pressure, static pressure and yaw angle distributions.

## 2 NUMERICAL METHOD.

The theoretical model for this study is the compressible Reynolds averaged Navier-Stokes equations associated with an algebraic mixing-length type turbulence model [1]-[3].

The numerical method is characterized by an explicit centered finite difference scheme associated with a multigrid convergence acceleration.

The equations are discretized using a two-step Lax-Wendroff type scheme, the dissipative terms being taken into account according to Thommen's idea [4].

The method uses an algebraic mixing-length type turbulence model developed by Michel et al. [5].

The local time step used in the computation takes into account the CFL and diffusion limitations.

## 3 BOUNDARY CONDITIONS.

In the upstream boundary of the domain the density, the three components of the velocity and the total energy are imposed at each mesh-point. These distributions are constant in the  $j$ -direction. As the boundary layer characteristics (such as density, velocity and energy distributions) were not given by the experiment in the initial plane  $X=0$ , but only in the plane  $X=3.6$  in , a 2D boundary layer solver [6] has been used to calculate them.

On both wedge surface and tunnel wall surface a no slip condition is applied and the temperature is set at the wall-temperature  $T_w = 1.1 T_{io}$ .

On the other boundaries of the domain a 0-order extrapolation is made.

The flow used in the starting condition is constant in  $i$ -direction and equal to the upstream flow in  $j$ - and  $k$ -directions.



## 4 GRID.

The computational domain extends from  $X=-0.275$  to  $X=10.725$  in., from  $Y_g=0.$  to  $Y_g=7.5$  in. and from  $Z=0.$  to  $7.5$  in.

The three families of mesh planes have been defined such that the i-planes and the k-planes correspond respectively to x-planes and z-planes, and the j-planes to planes parallel to the wedge surface. Figure 1 shows the three families of mesh planes. The number of mesh-points is equal to  $41 \times 60 \times 60 = 147,600$ .

The mesh is highly stretched in the j- and k-directions near the wedge surface and the tunnel wall surface for an adequate resolution of the viscous layer. The mesh size at the wall is equal to  $0.55 \cdot 10^{-4}$  in., whereas the spacing in the streamwise direction is equal to  $0.275$  in.

## 5 DESCRIPTION OF THE COMPUTATION.

The CPU time on a CRAY-2 computer is equal to 2.7 seconds for one iteration (that is to say  $18.4 \mu s$  for one iteration and one mesh-point). A plotting accuracy and a three-decade decrease of the residuals are obtained after 6,000 iterations.

## 6 RESULTS.

Figures 2 to 5 present the static pressure distributions in the plane  $Z=0$ . They show some differences between calculation and experiment, particularly in the viscous area near the shock.

Figures 6 to 12 present the pitot pressure distributions in the planes  $X=3.6$  in. and  $X=7.1$  in. There is a rather good agreement between calculation and experiment except in the laminar part of the boundary layer near the wedge surface.

Figures 13 to 15 present the yaw angle distributions in the plane  $X=7.1$  in. Here the agreement between calculation and experiment is better though the yaw angle is difficult to measure and calculate, being the quotient of two velocities that approach zero near the walls.

## 7 REFERENCES.

- [1] L. CAMBIER, V. COUAILLER et J.P. VEUILLLOT. Résolution numérique des équations de Navier-Stokes à l'aide d'une méthode multigrille. La Recherche Aérospatiale n° 1988-2, pp 23-42, 1988.

- [2] - L. CAMBIER, V. COUAILLER et J.P. VEUILLOT. Calculs d'écoulements turbulents tridimensionnels par résolution des équations de Navier-Stokes moyennées. ONERA Rapport technique de synthèse n° 33/7077 AY, 1988.
- [3] - L. CAMBIER, V. COUAILLER et J.P. VEUILLOT. Simulation of a Shock Wave/Turbulent Boundary Layer Interaction in a Three Dimensional Channel. AIAA Paper 89-1851, 1989 and ONRERA TP n° 1989-82, 1989.
- [4] - H.U. THOMMEN. Numerical Integration of the Navier-Stokes Equations. ZAMP, Vol. 17, pp. 369-384, 1966.
- [5] - R. MICHEL, C. QUEMARD et R. DURANT. Application d'un schéma de longueur de mélange à l'étude des couches limites turbulentes d'équilibre. ONERA NT n° 154, 1969.
- [6] - C. QUEMARD et J.P. ARCHAMBAUD. Différences finies en couches limites bidimensionnelles avec flux de chaleur.
  - A) Principe de la méthode et applications.
  - B) Mode d'utilisation du programme numérique.ONERA (DERAT) NT n° 11/5005 DN, Dec. 1974.

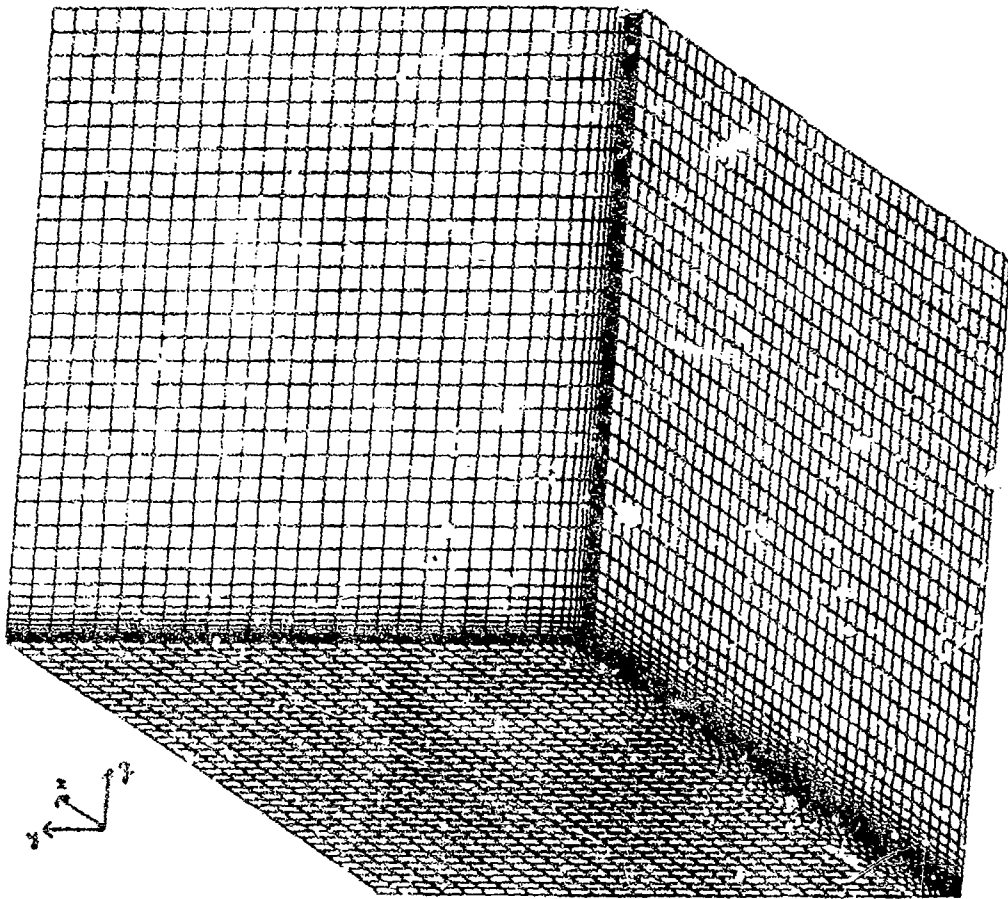
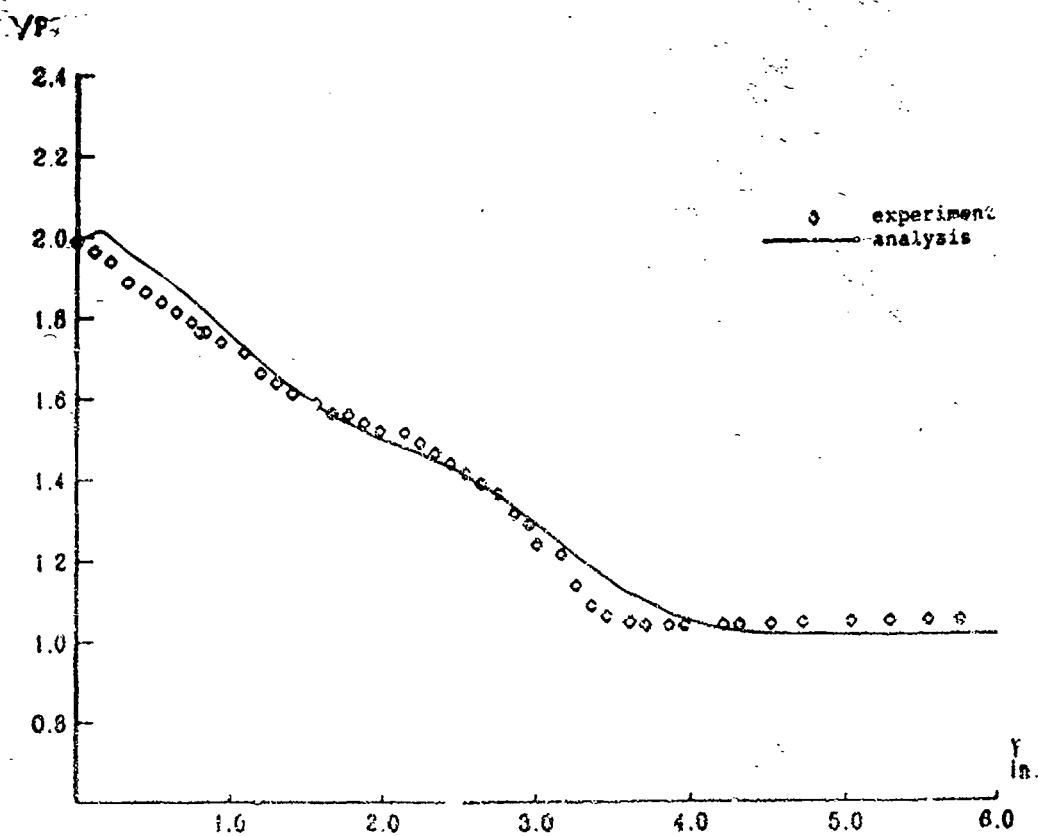
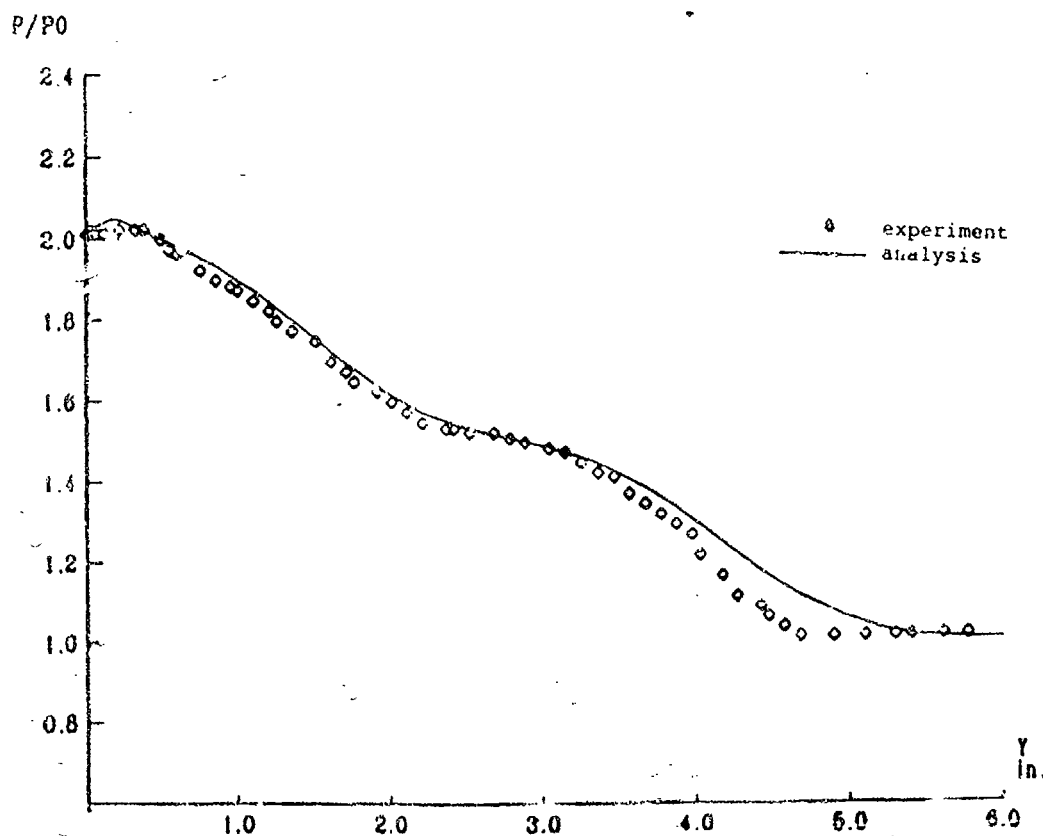
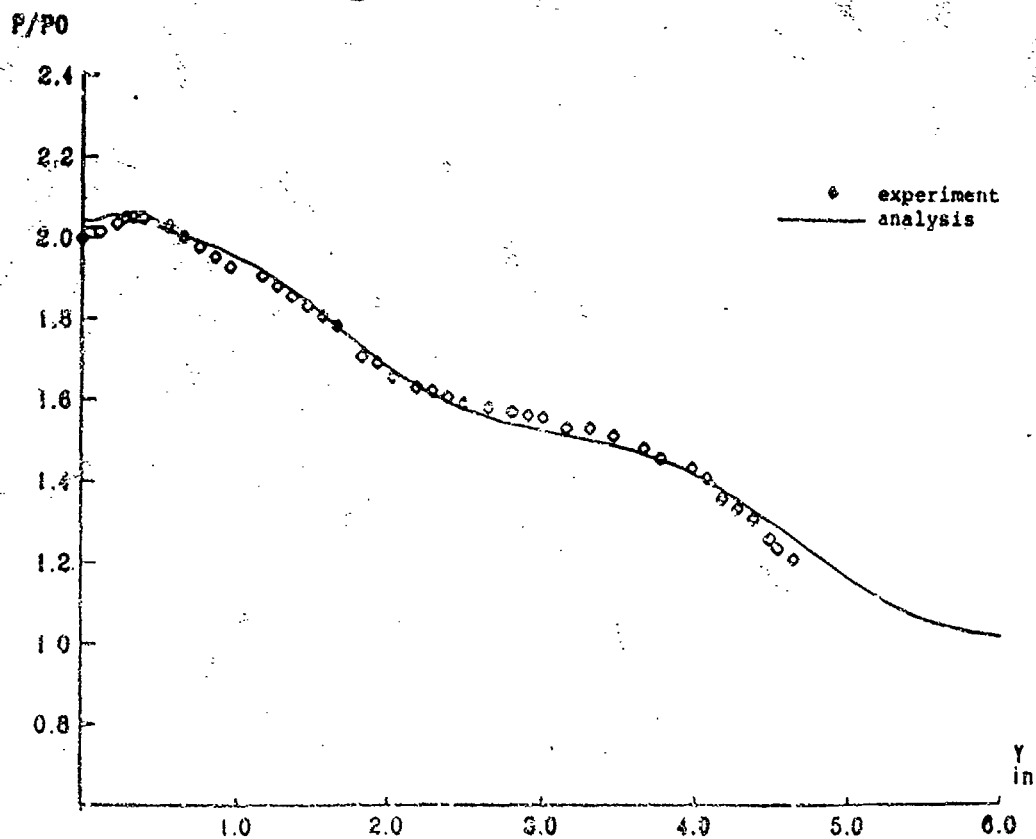
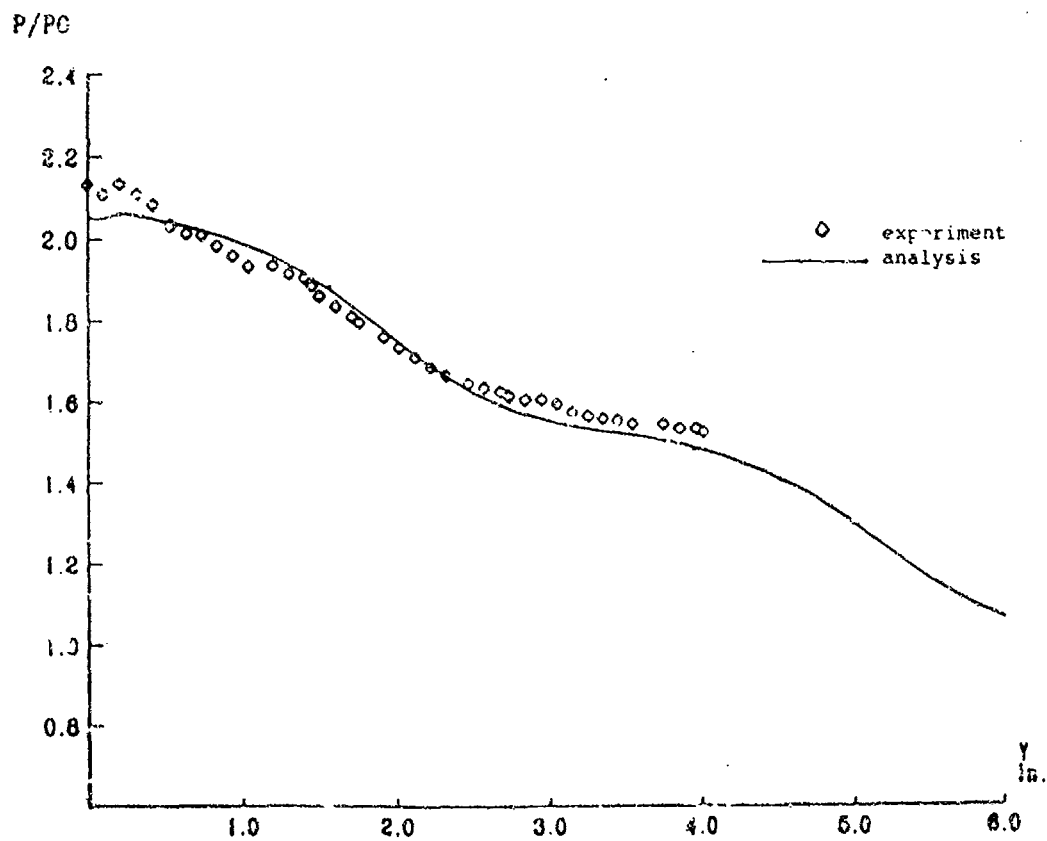


Figure 1 : Mesh planes.

Figure 2 : Static pressure  $X=5.1$  in.Figure 3 : Static pressure  $X=7.1$  in.

Figure 4 : Static pressure  $X=8.1$  in.Figure 5 : Static pressure  $X=9.1$  in.

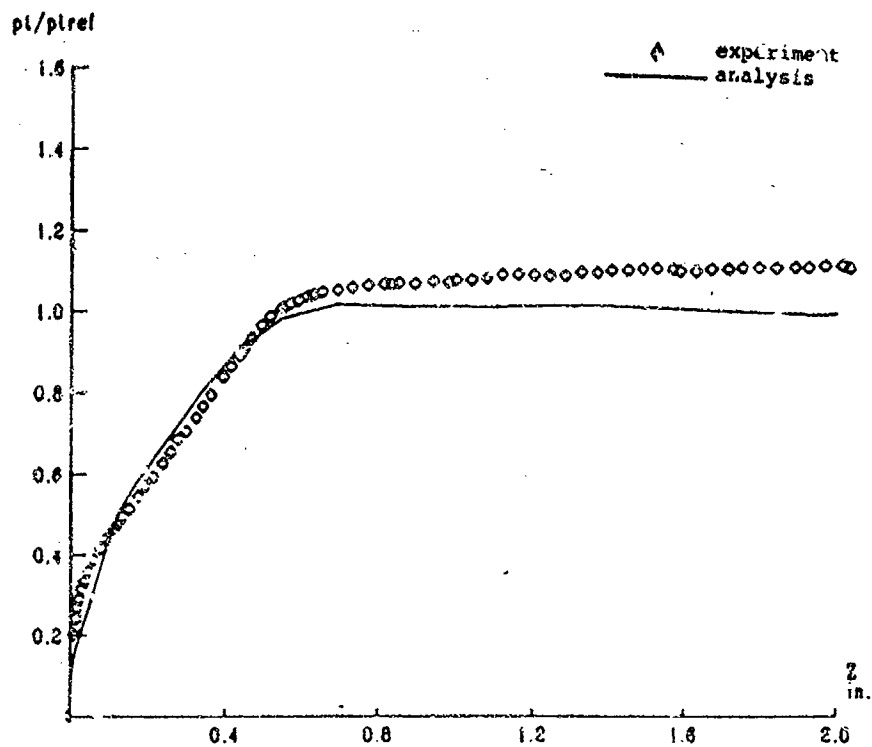


Figure 6 : Pitot pressure  $X=3.6$  in.,  $Y_q=2.9$  in.

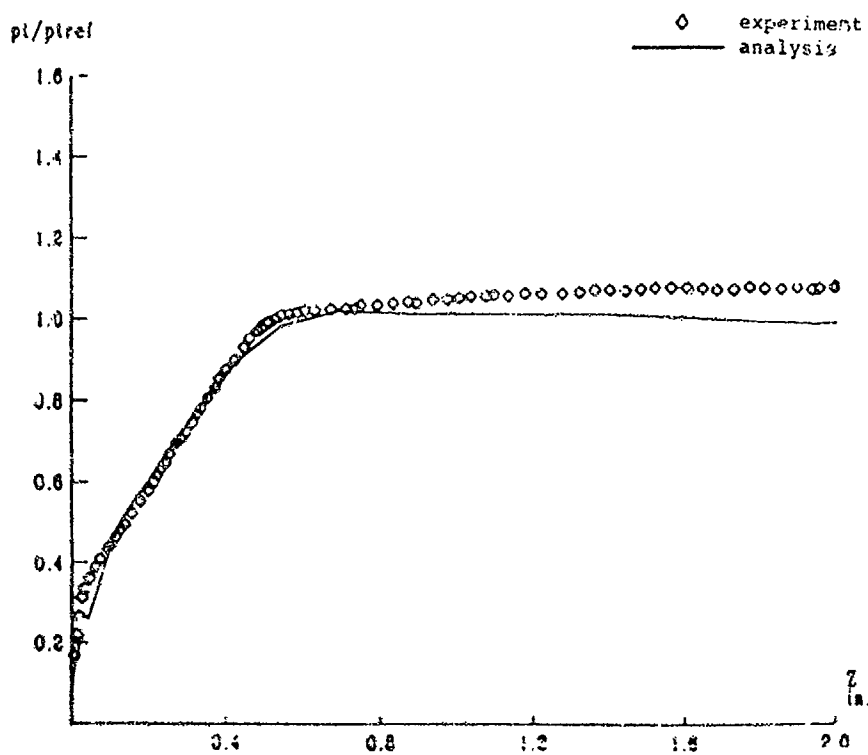


Figure 7 : Pitot pressure  $X=3.6$  in.,  $Y_q=3.9$  in.

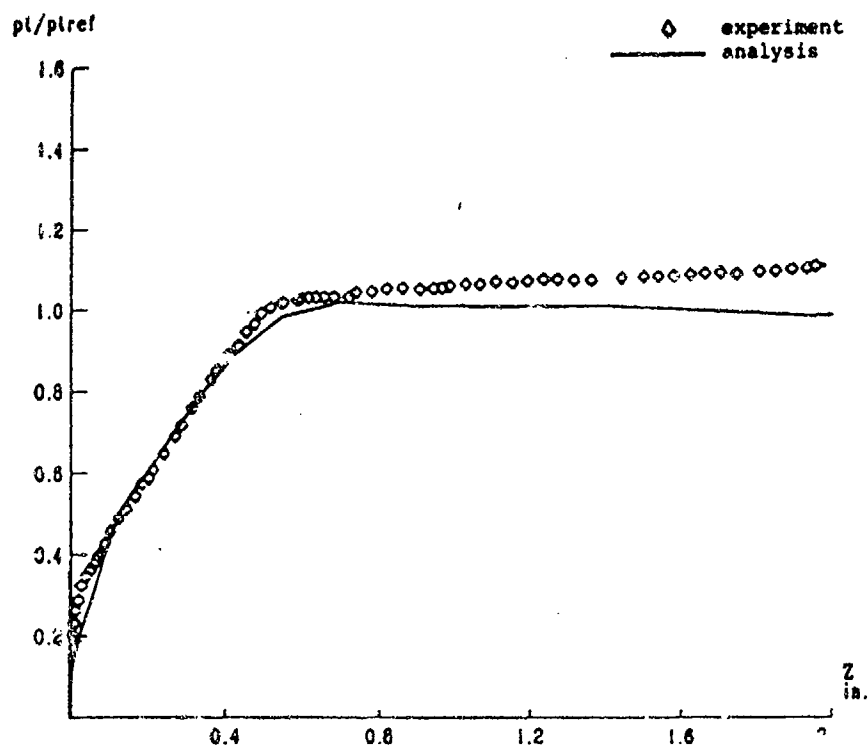


Figure 8 : Pitot pressure  $X=3.6$  in.,  $Y_g=4.9$  in.

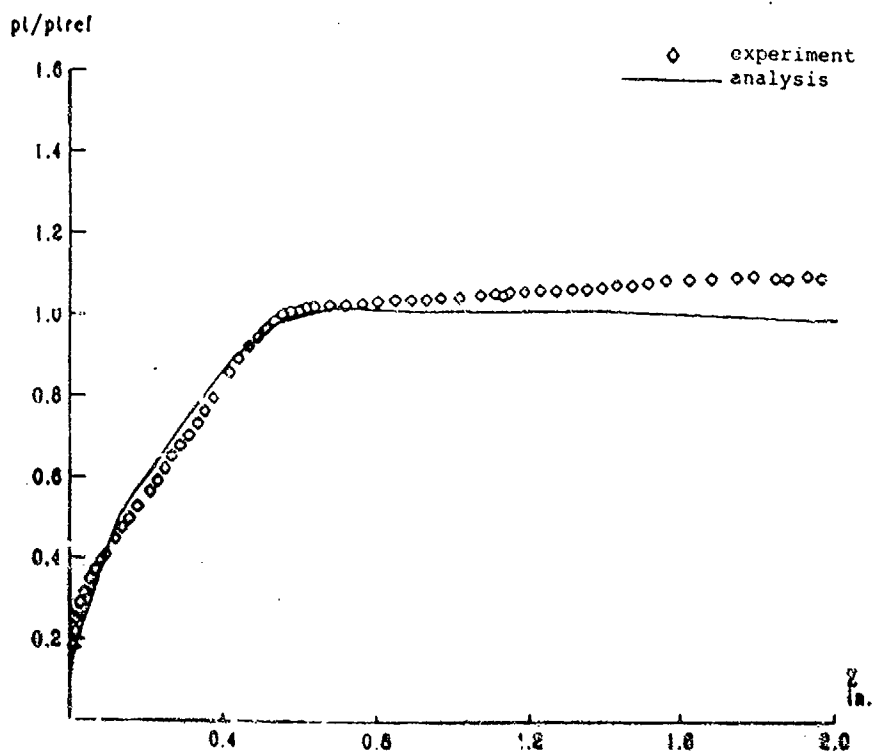


Figure 9 : Pitot pressure  $X=3.6$  in.,  $Y_g=5.4$  in.

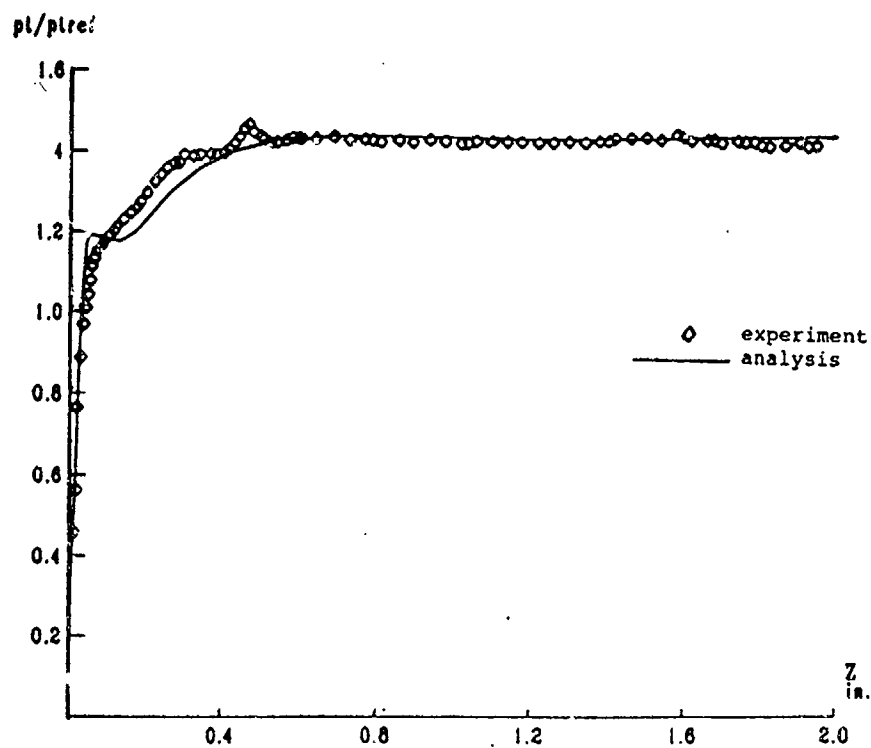


Figure 10 : Pitot pressure  $X=7.1$  in.,  $Yq=0.25$  in.

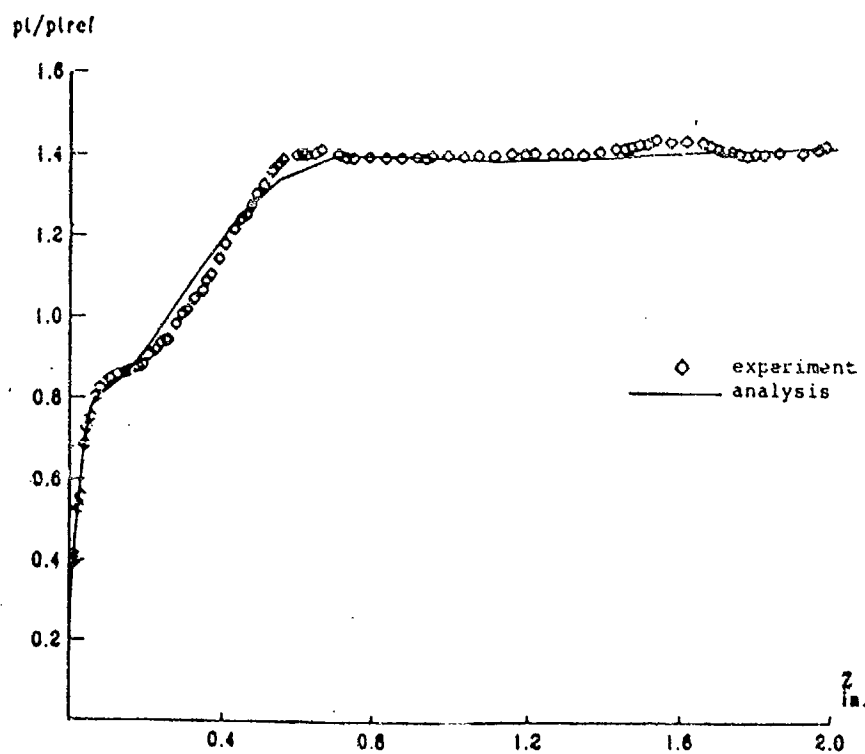


Figure 11 : Pitot pressure  $X=7.1$  in.,  $Yq=0.75$  in.



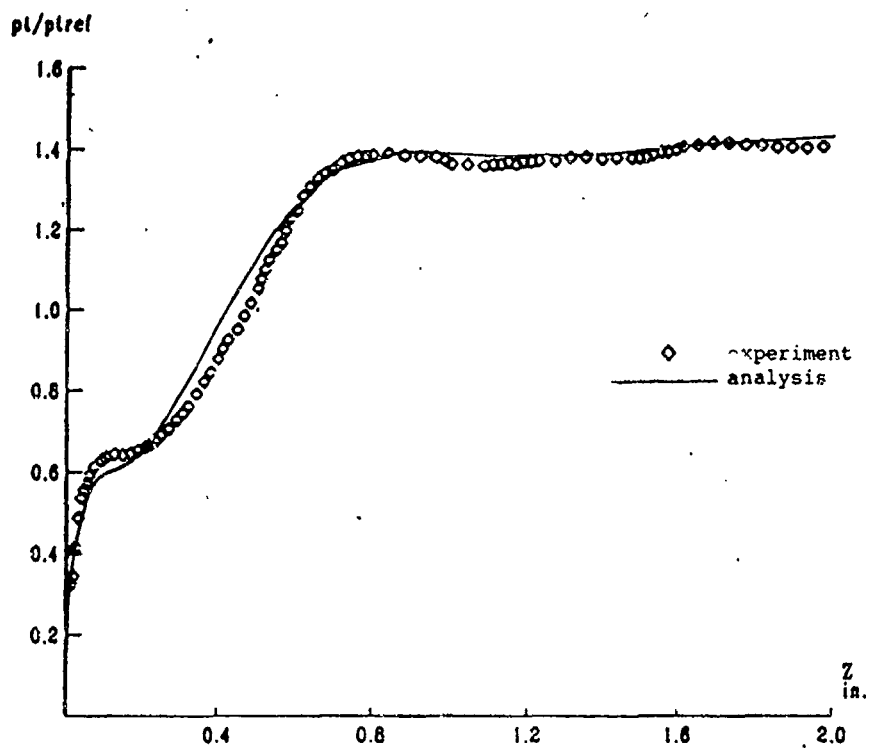


Figure 12 : Pitot pressure  $X=7.1$  in.,  $Y_g=1.25$  in.

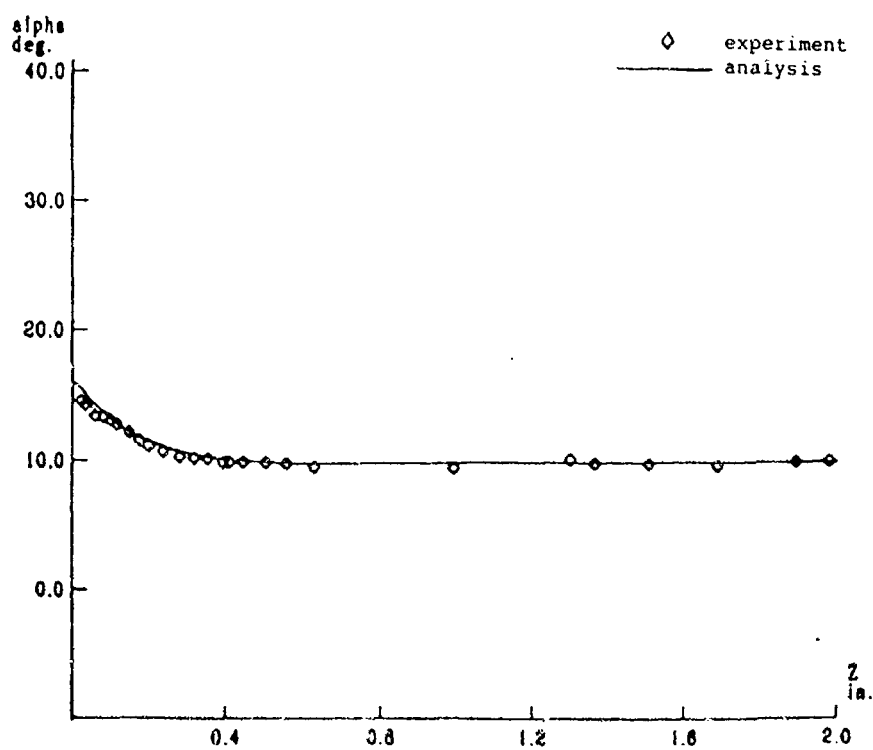
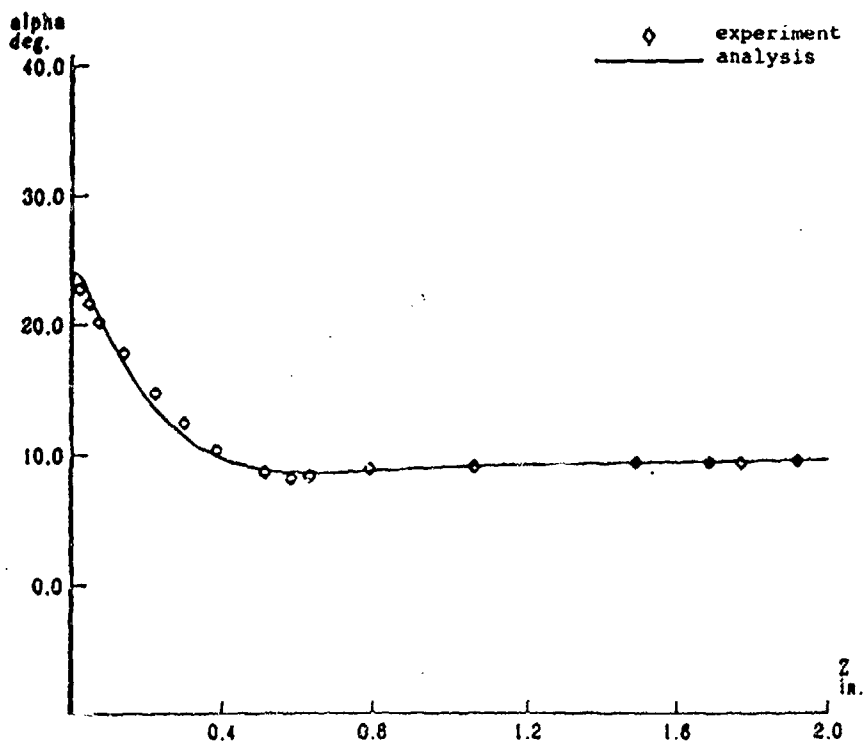
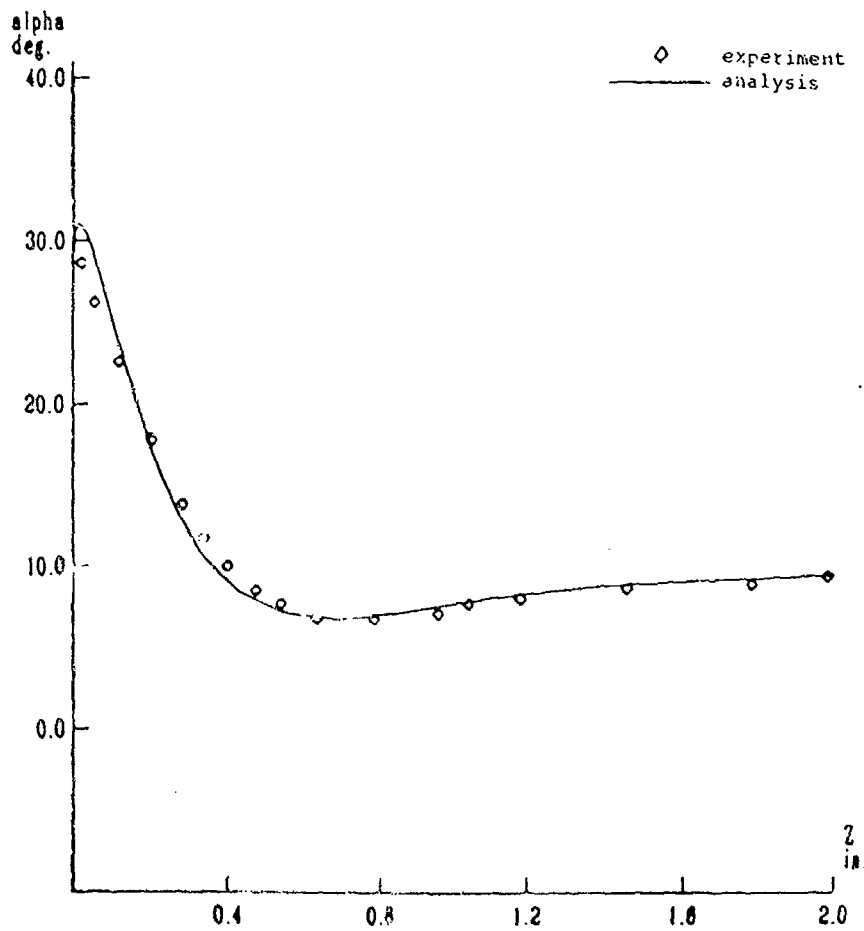


Figure 13 : Yaw angle  $X=7.1$  in.,  $Y_g=0.25$  in.

Figure 14 : Yaw angle  $X=7.1$  in.,  $Yq=0.75$  in.Figure 15 : Yaw angle  $X=7.1$  in.,  $Yq=1.25$  in.

## A. CFD Methodology

Applied code - AEDC PARC3D (Version 5.0). Reference AIAA-90-2002.

Standard ideal gas assumptions

P. D. Thomas type implementation of algebraic Baldwin & Lomax model. Reference NACA-CR-3147 & AIAA-78-257.

## B. Computer Resources

7.75 cpu hours on a CRAY XMP-12

2000 iterations

7 computational blocks each requiring approximately 1.8 megawords of memory. Each block contained approximately 50000 grid points.

## C. Boundary Conditions

Inflow plane held fixed to a boundary layer profile generated from the total pressure profile supplied by AGARD

outflow subsonic static pressure adjusted to match the supersonic outflow static pressure. Supersonic outflow conditions were extrapolated.

Wedge and tunnel side walls were treated as viscous. Tunnel top and bottom walls were slip surfaces.

## D. Convergence

3 orders of magnitude reduction in the  $L_2$  norm

Asymptotic convergence of the  $P_{TOTAL}$  plots along surfaces of interest

## E. Calculation Integrity Checks

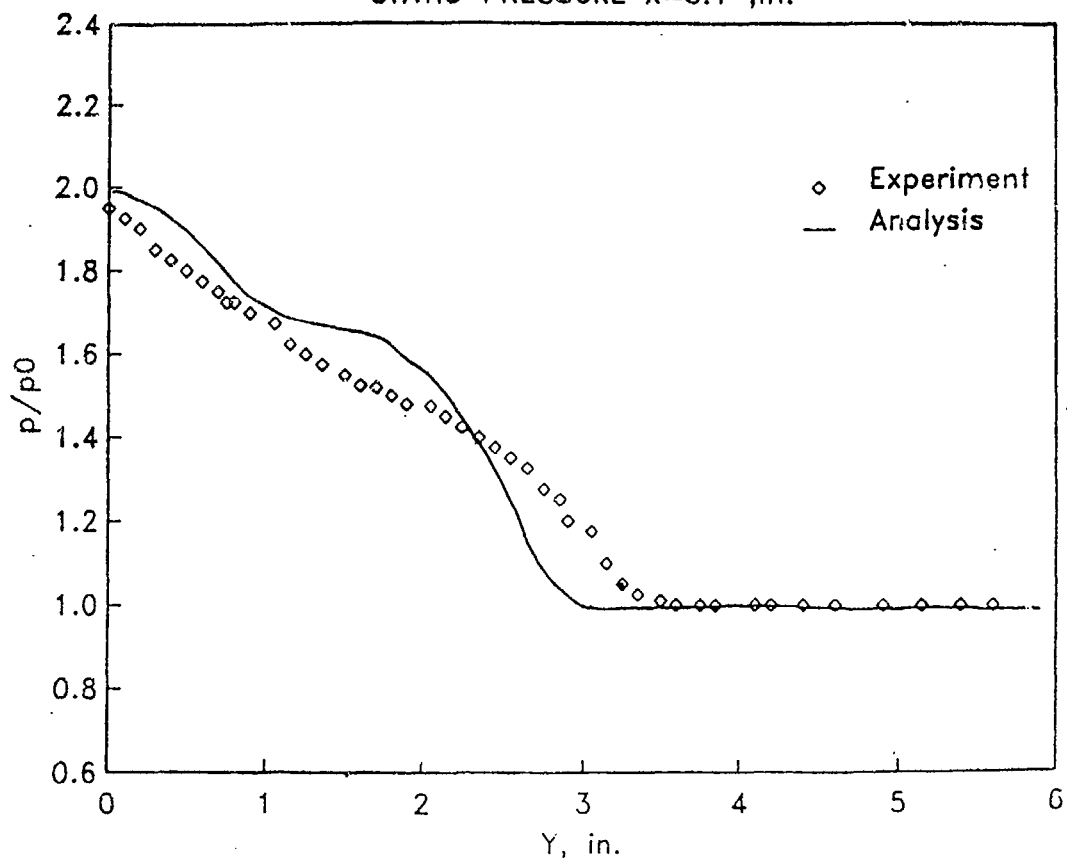
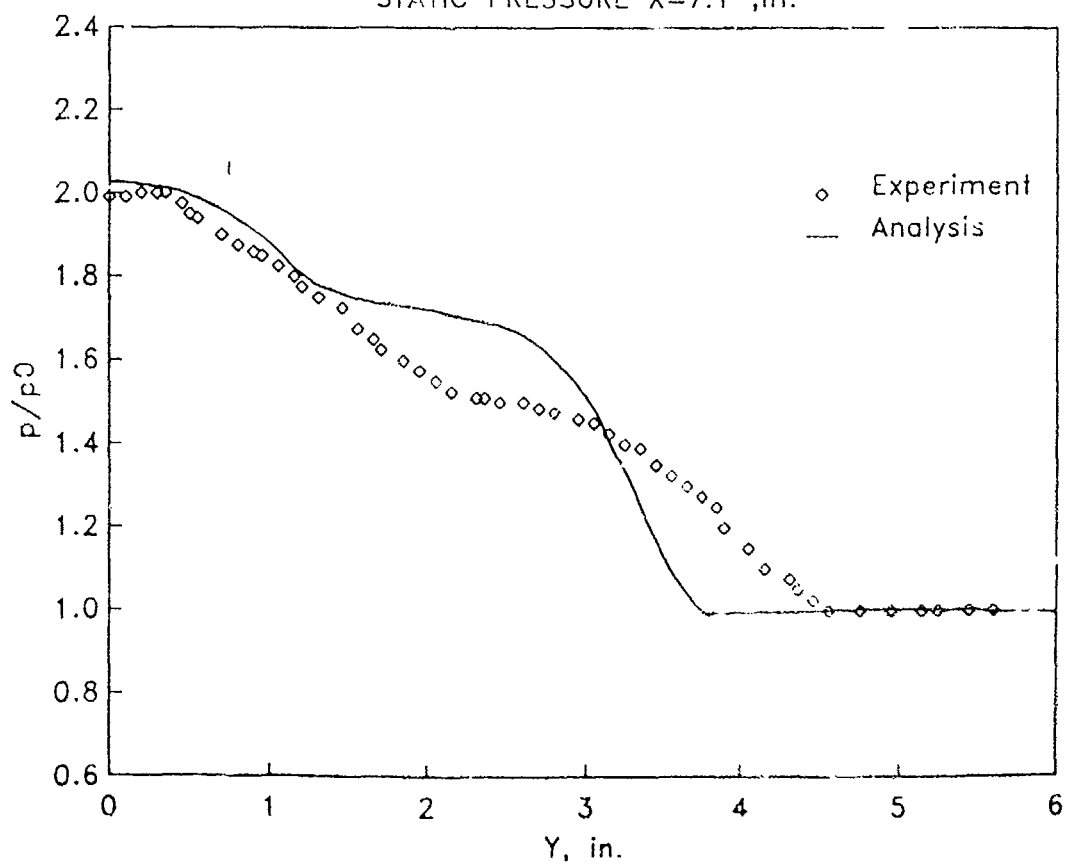
No global mass conservation checks were performed.

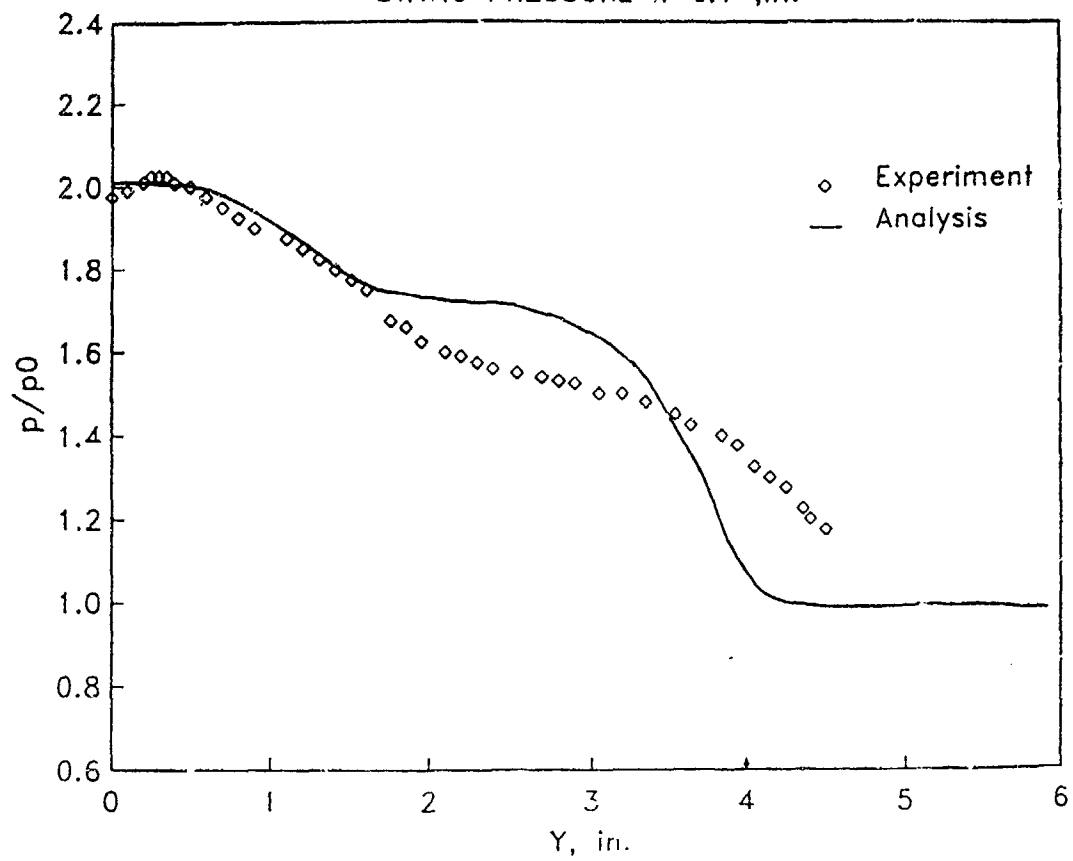
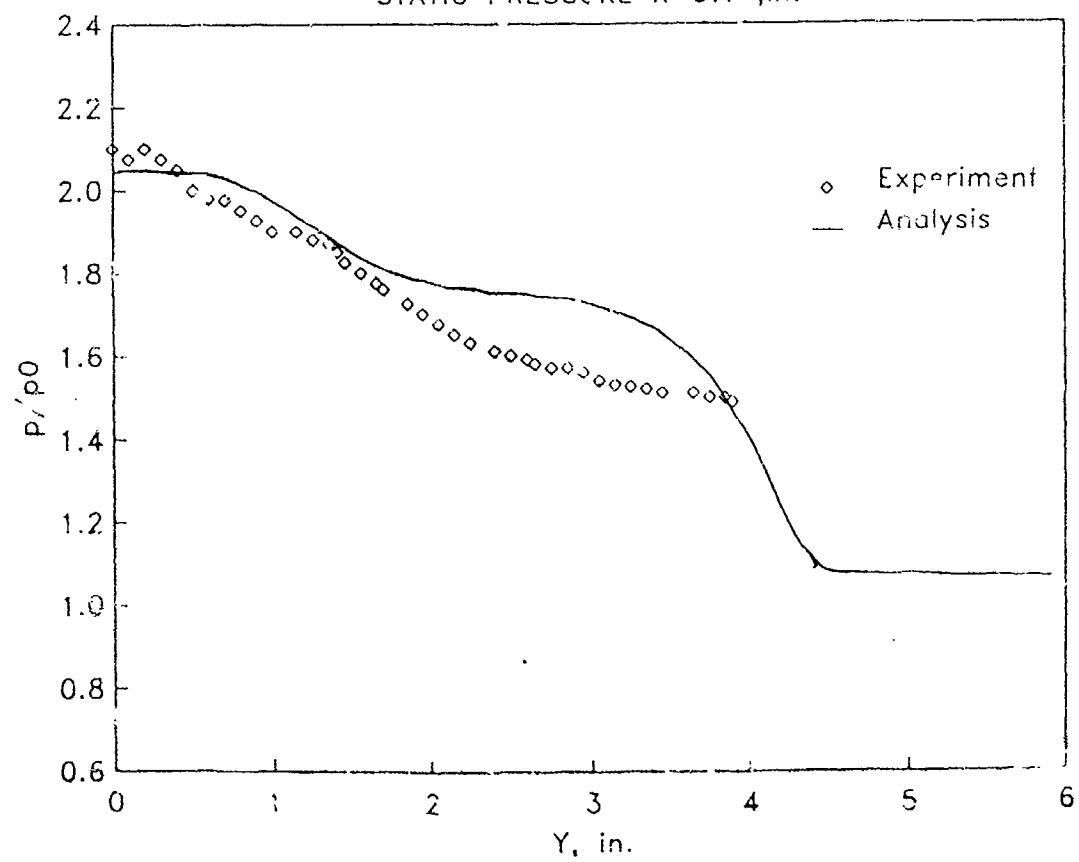
## F. Experience/Difficulties

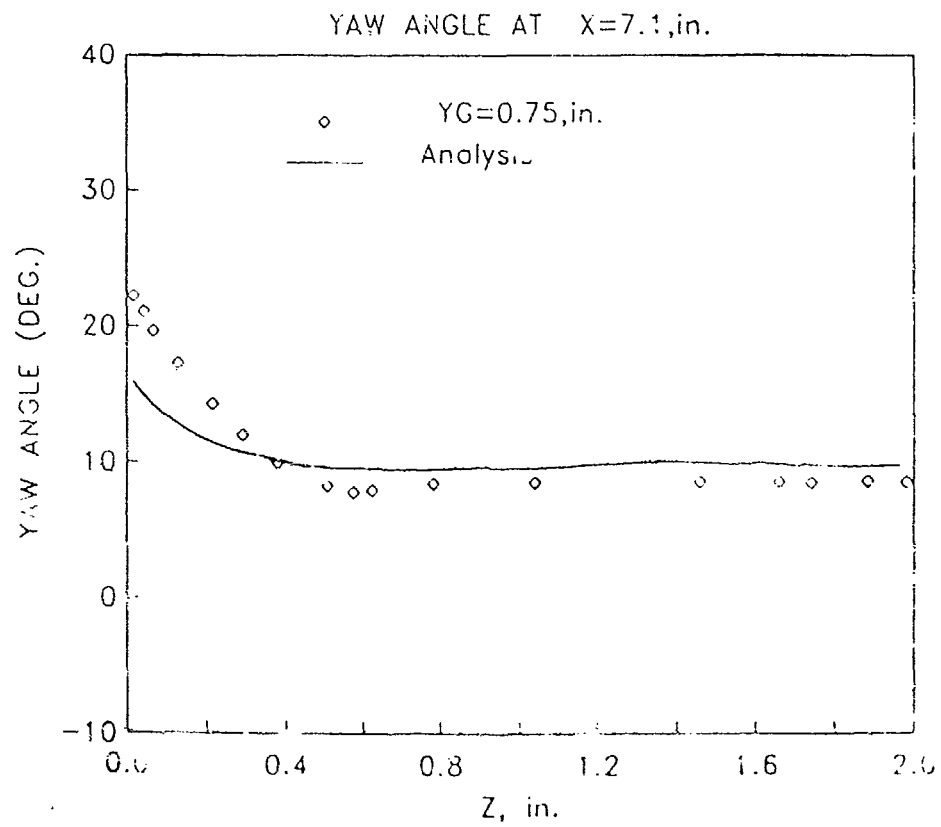
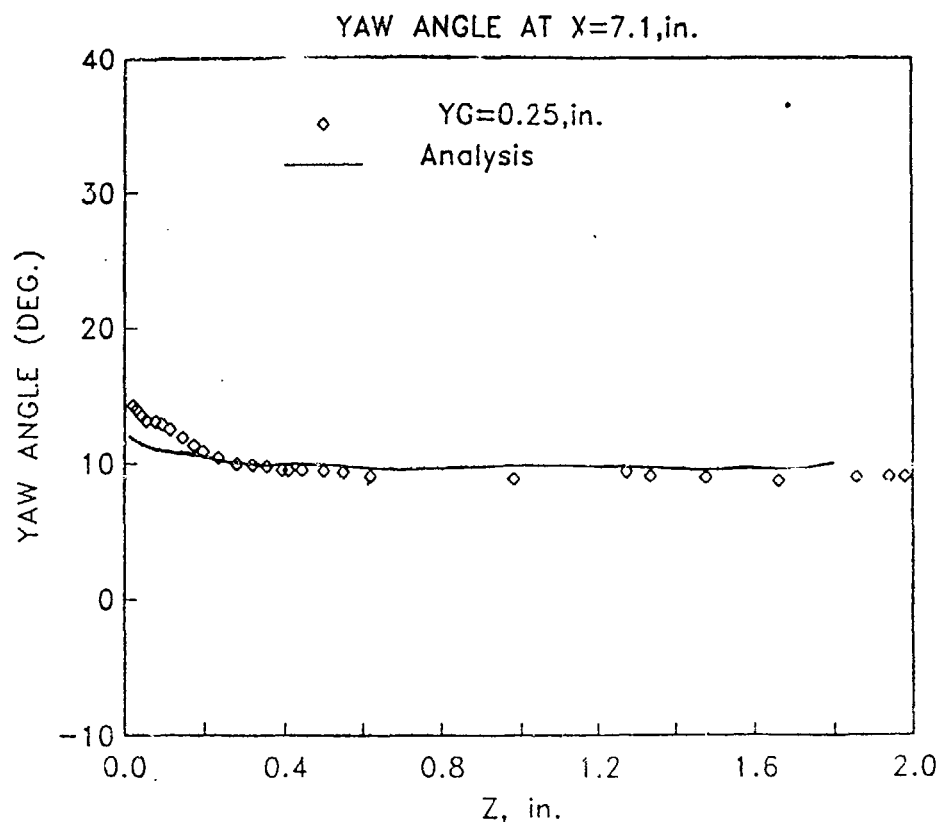
Results exhibited sensitivity to grid packing/cell aspect ratio in the boundary layer.

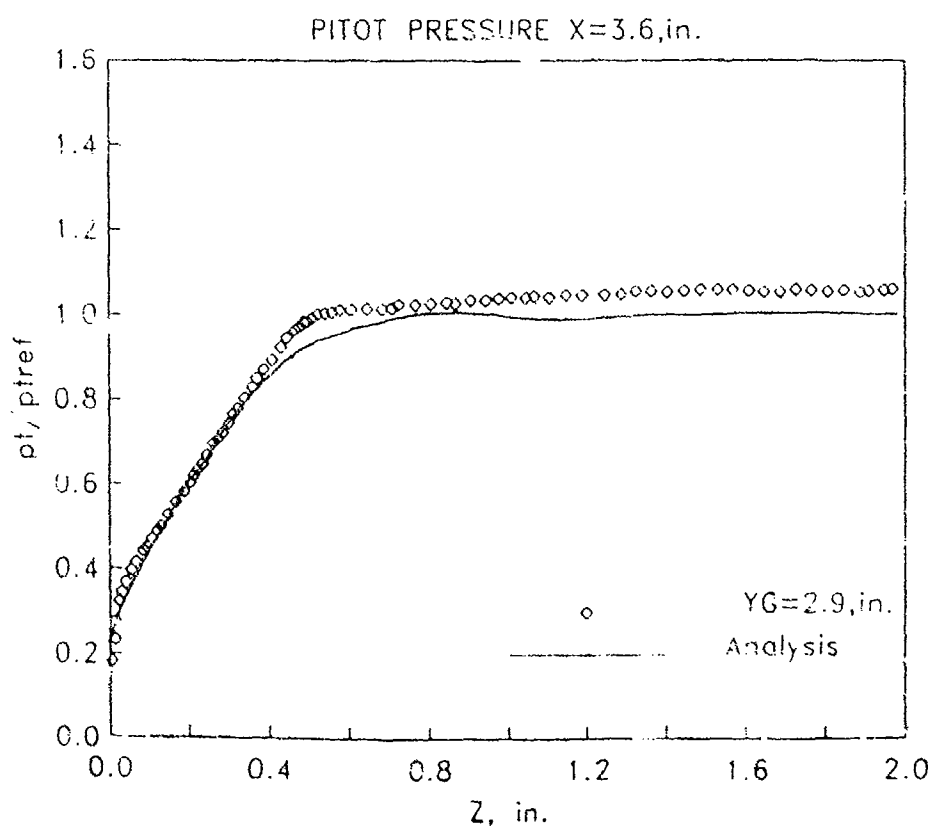
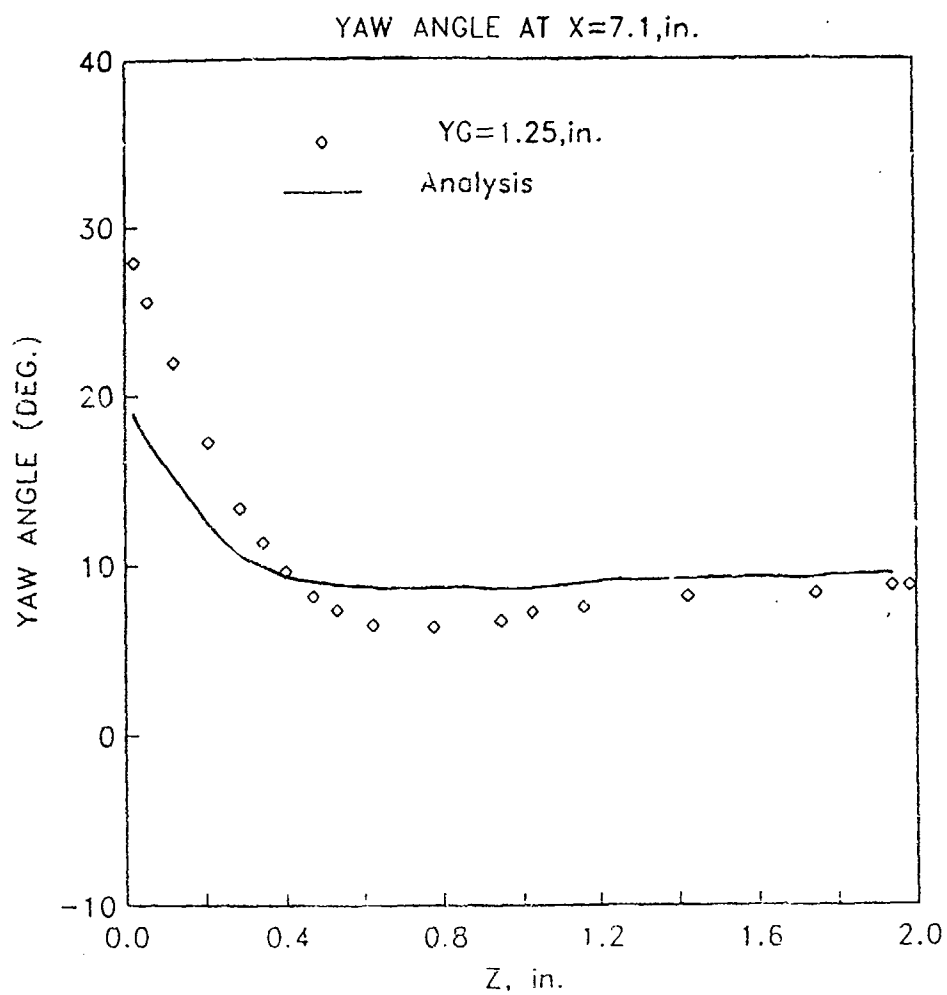
Cell Reynolds number scaling was applied to artificial viscosity coefficients.

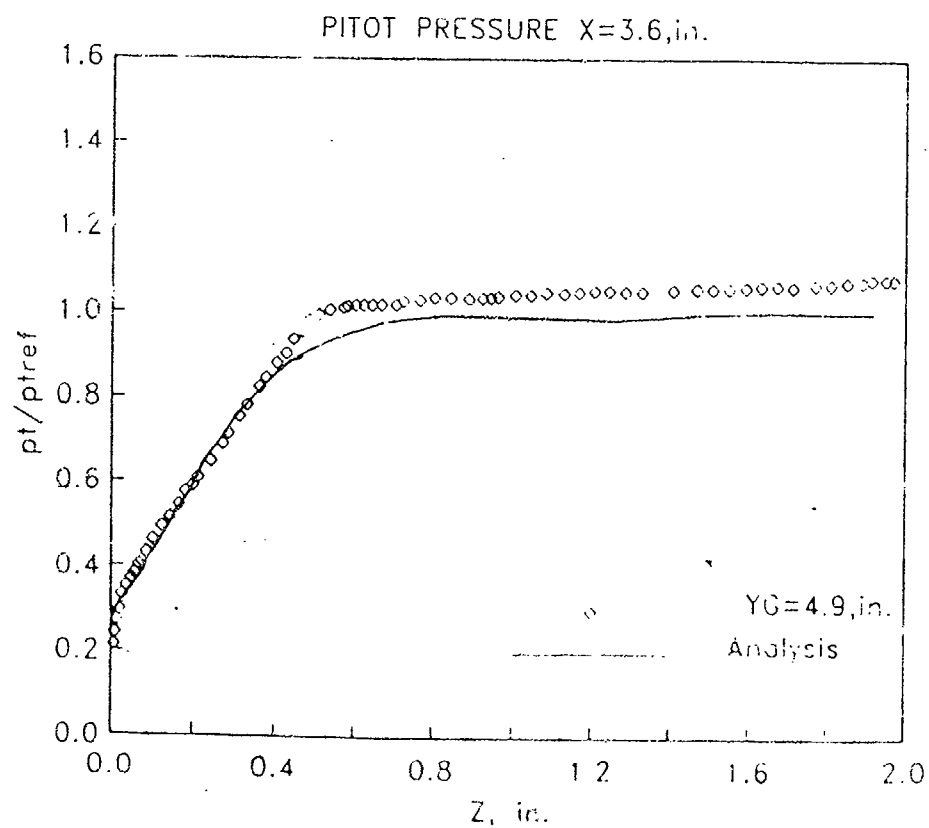
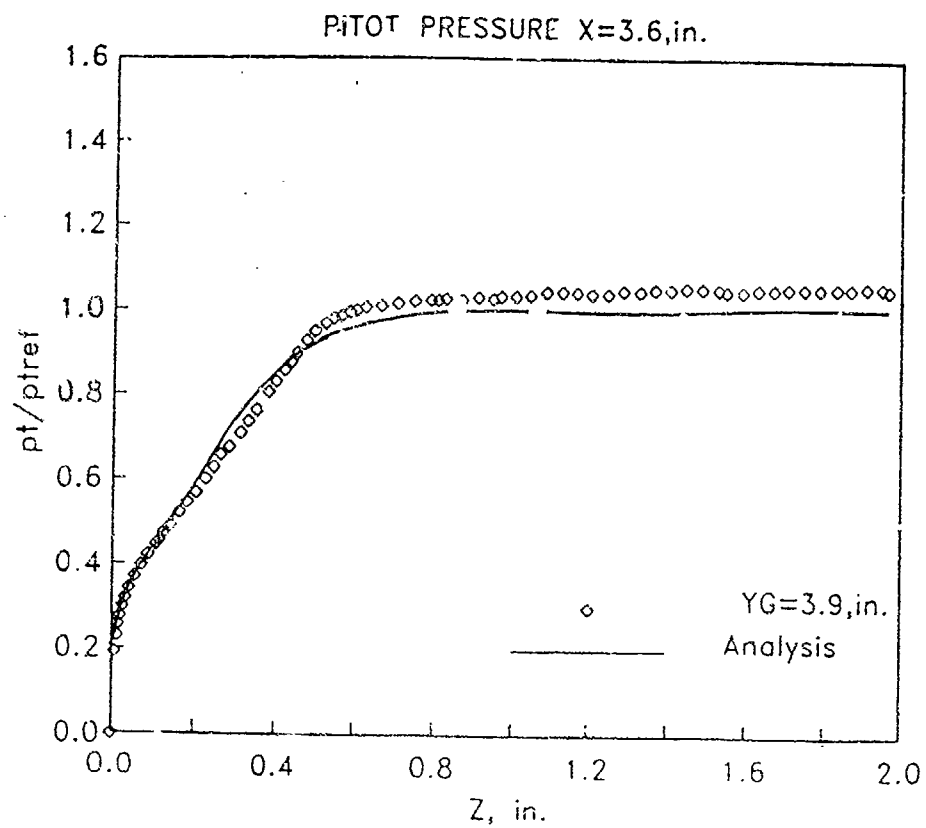
A solutions was generated for this test case using the AEDC PARC code. A single grid with dimensions of 83 x 71 x 67 covered the entire flow domain. Due to limited in-core memory, the flow domain was decomposed into seven nearly equal subdomains. Communications between subdomains is handled automatically by the PARC code. The upstream inflow boundary was held fixed using turbulent layer information provided in the initial information package. The surface of the wedge was modeled as a slip surface, while the tunnel side wall was a no-slip surface. Additional information on the code and solutions may be obtained by contacting either Kyle Cooper (615) 454-5821 or Jim Sirbaugh (615) 454-3478.

STATIC PRESSURE  $X=5.1$  ,in.STATIC PRESSURE  $X=7.1$  ,in.

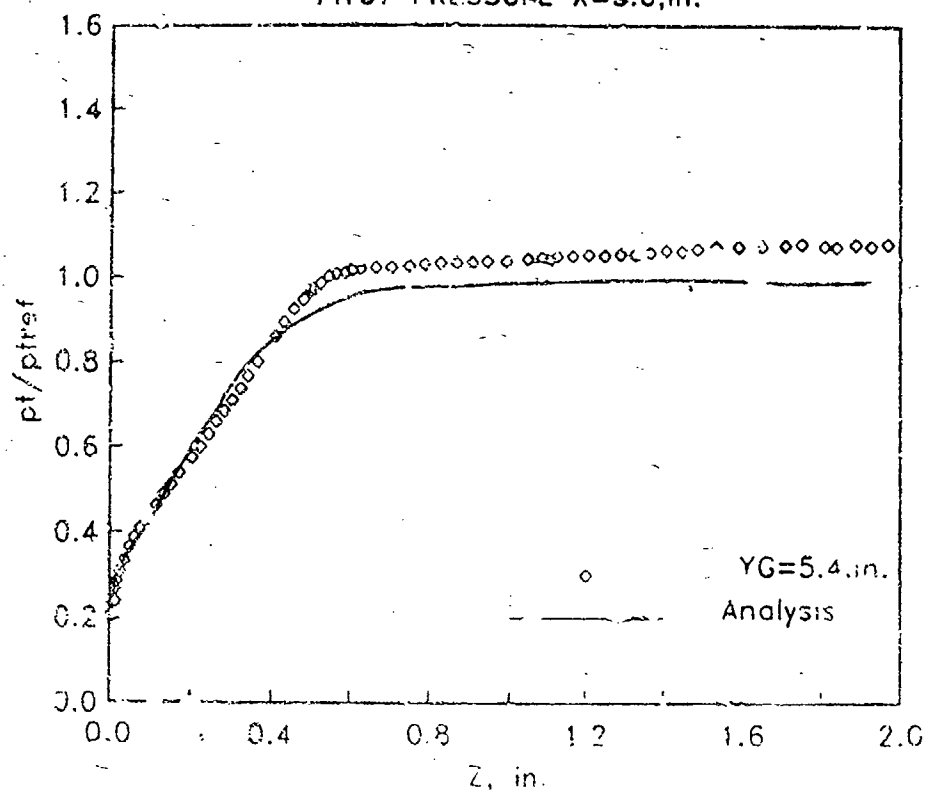
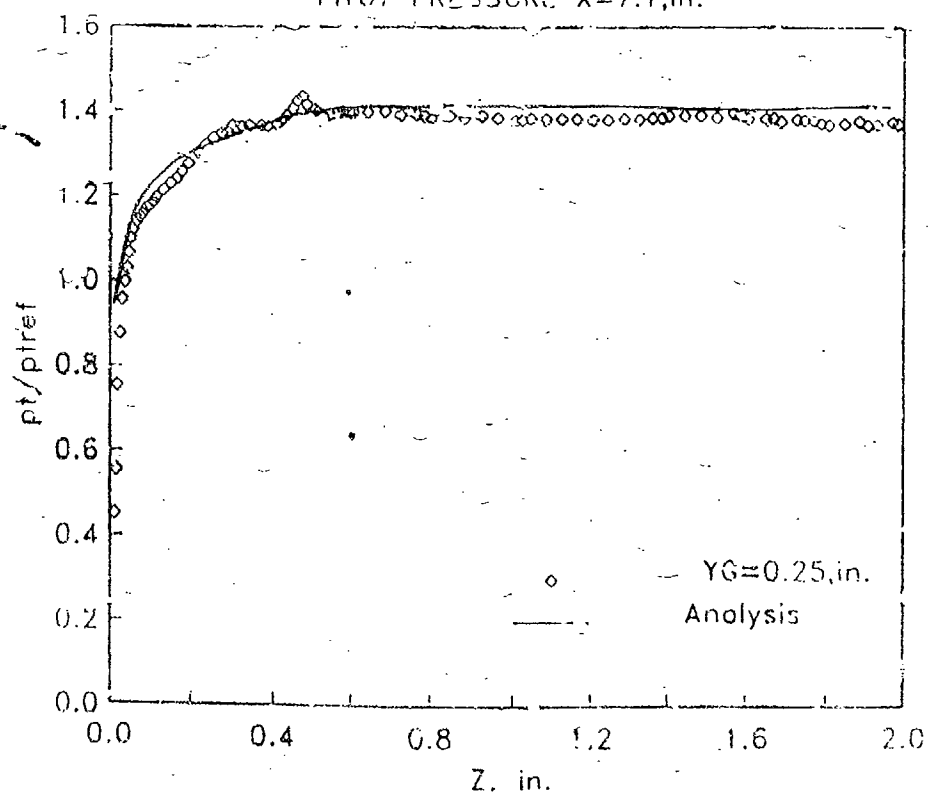
STATIC PRESSURE  $X=8.1$  ,in.STATIC PRESSURE  $X=9.1$  ,in.

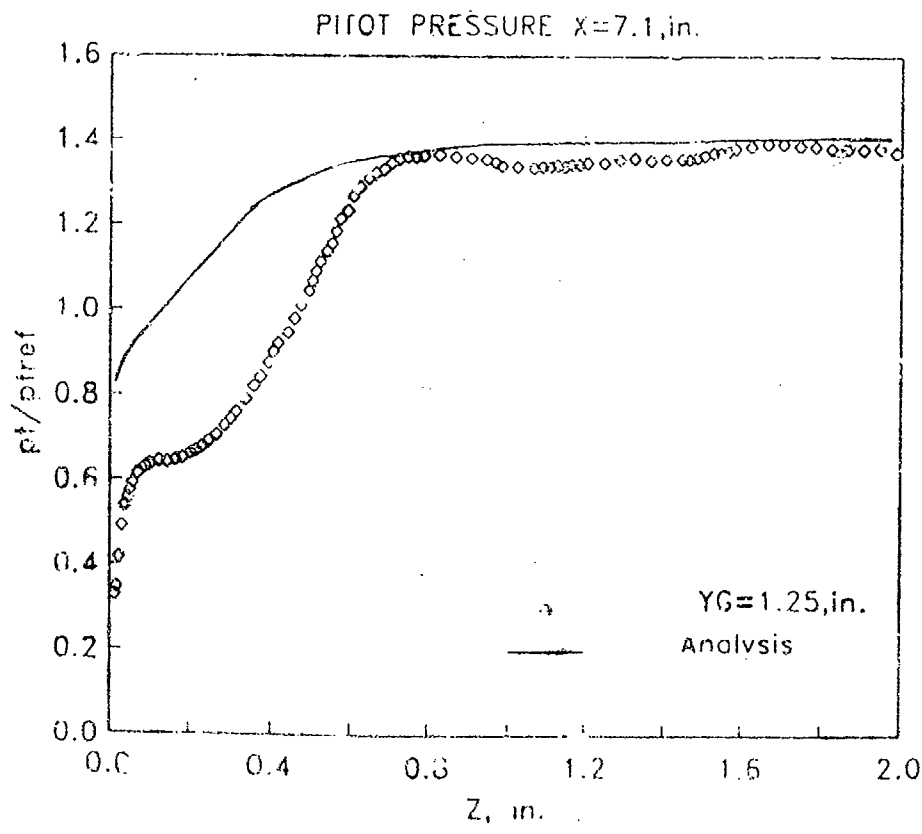
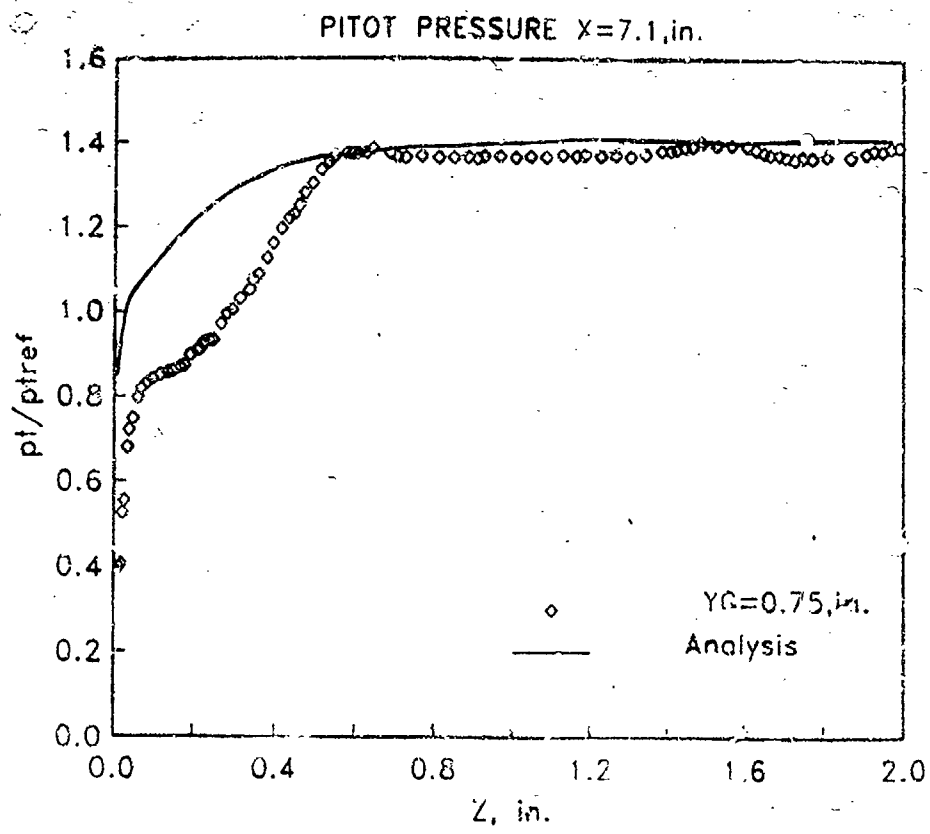








PITOT PRESSURE  $X=3.6$ , in.PITOT PRESSURE  $X=7.1$ , in.



## Three-Dimensional Viscous Flow Computations of High Area Ratio Nozzles for Hypersonic Propulsion

D.R. Reddy\* and G.J. Harloff\*\*

Sverdrup Technology Inc., NASA Lewis Research Center Group  
Cleveland, Ohio

### Abstract

The PARC3D code was selected by the authors to analyze a variety of complex and high speed flow configurations. Geometries considered for code validation include ramps and corner flows which are characteristic of inlets and nozzles. Flows with Mach numbers of 3 to 14 were studied. Both two- and three-dimensional experimental data for shock-boundary layer interaction were considered to validate the code. A detailed comparison of various flow parameters with available experimental data is presented; agreement between the solutions and the experimental data in terms of pitot pressure profiles, yaw angle distributions, static pressures and skin friction is found to be very good. In addition, two and three-dimensional flow calculations were performed for a hypersonic nozzle. Comparison of the wall pressure results with the published solutions is made for the two-dimensional case.

---

\*Supervisor, Turbomachinery Analysis Section, Member AIAA.

\*\*Senior Staff Scientist, Associate Fellow AIAA.

## Introduction

Accurate evaluation of nozzle performance is essential in hypersonic propulsion because the net thrust is very sensitive to nozzle performance. Highly integrated fuselage/nozzle configurations may experience complex interactions of shocks, turbulent mixing, differing levels of under/over expansion, and possibly boundary layer separation. A numerical method has been selected and used to examine the flow phenomena mentioned above. The model is calibrated herein using available experimental data in two and three dimensions.

The PARC3D<sup>1</sup> code, selected by the authors for this study, solves the full, three-dimensional, Reynolds-averaged Navier-Stokes equations in strong conservation form with the Beam and Warming approximate factorization algorithm. The implicit scheme uses central differencing for a curvilinear set of coordinates. The code was originally developed as AIR3D by Pulliam and Steger<sup>2</sup>; Pulliam<sup>3</sup> later added the Jameson<sup>4</sup> artificial dissipation and called the code ARC3D.

Cooper<sup>1</sup> adapted the ARC3D code for internal propulsion applications and named the code PARC3D. Cooper et. al.<sup>5</sup> applied a two dimensional version of PARC to a trumpet and a conical nozzle with a throat Reynolds number of 12,000. The ground-tested nozzles had

expansion ratios of 362 and 400, and exhausted into low pressures of  $3.8 \times 10^{-7}$  to  $6.2 \times 10^{-8}$  psia. They concluded that the PARC code provided reasonable flowfields for the cases studied.

In order to gain confidence with the IARC3D code for high speed applications, some shock-boundary layer experimental data and a published nozzle flowfield results were selected in the present study for code validation. Both two and three-dimensional experimental data for shock-boundary layer interaction were considered; a detailed comparison of various flow parameters is presented. In addition, two and three-dimensional flow calculations were performed for a hypersonic nozzle. Comparison of the wall pressure results with the published solutions were made for the two-dimensional case; the solutions agree very well with the experimental data for the shock-boundary layer interaction cases and with other numerical solutions for the hypersonic nozzle configuration.

## Previous Studies

### Shock-Boundary Layer Interaction

Many researchers have studied two and three-dimensional shock boundary layer interactions in the past. For example, Visbal<sup>6</sup> evaluated the Baldwin-Lomax turbulence model for a two-dimensional Mach 3 compression corner with a Reynolds-averaged Navier-Stokes

computer program. He examined attached and separated flows and concluded that some of the constants in the outer formulation of the Baldwin-Lomax model are dependent on the flow Mach number. Horstman<sup>7</sup> presented experimental and theoretical three-dimensional solutions for a family of fin-induced shock wave turbulent boundary layer interactions with separated flow at Mach number 2.94 with fin angles from 10 to 20 degrees; he used the MacCormack explicit second order predictor-corrector finite volume method. Knight<sup>8,9</sup> used a hybrid explicit-implicit method to solve the three-dimensional sharp fin interaction at Mach 3 with a wedge angle of 10 degrees. Lawrence et. al.<sup>10</sup> presented an upwind scheme for parabolized Navier-Stokes equations and calculated the flowfields for a 15 degree compression corner and a hypersonic inlet.

Anderson and Benson<sup>1</sup> studied three-dimensional shock boundary layer interactions in calibrating a single sweep space marching code, PEPSIS. They showed good comparisons for the Oskom et. al.<sup>12</sup> three-dimensional shock boundary layer configuration.

Holden and Moselle<sup>13</sup> studied experimentally several two-dimensional ramp configurations in hypersonic flow. Hung and MacCormack<sup>14</sup>, as well as Lawrence and Tannehill<sup>10</sup> have previously computed the flowfield for a few of Holden and Moselle's<sup>13</sup> ramp configurations.

## Nozzles

Dash et. al.<sup>15</sup> presented a parabolized Navier-Stokes nozzle capability in two and three-dimensions to calculate mixed super and subsonic flows. Pressure-split and sublayer approximations were used to obtain solutions by spatial marching. A method of characteristics study by Lewis<sup>16</sup> examined a cutoff nozzle to investigate the effect of internal to external expansion on thrust-vectored lift of asymmetric nozzles with a truncated lower cowl.

## Code Validation

In order to assess the capability of the PARC3D code in simulating the interaction phenomena characteristic of hypersonic nozzle flow, some shock-boundary layer experimental data and a published nozzle flowfield study were selected for comparison. Both two and three-dimensional shock-boundary layer interaction experimental data were considered. Two sets of data were examined, the three-dimensional flowfields of Oskam, Vas, and Bogdonoff<sup>17</sup> at Mach 2.94, and the two-dimensional flow of Holden and Moselle<sup>18</sup> at Mach 14.1.

## Results and Discussion

### Three-Dimensional Shock-Boundary Layer Calculations at Mach 2.94

Figure 1 shows the schematic of the experimental three-dimensional configuration from reference 12. The details of the experimental rake locations can be found in references 11 and 12. The data measured include yaw angle as well as static and pitot pressure profiles. In the experimental setup, the wedge was mounted off the wall to avoid the wall boundary layer at the leading edge of the wedge; however, the boundary layer on the side wall ( $Z=0$ ), was undisturbed in the entry plane. The wedge angle was 10 degrees as shown in Figure 1. The freestream Mach number was 2.94, and the Reynolds number, based on wind tunnel test section height (3. in or 20.32 cm.) and total conditions, was  $58.9 \times 10^6$ .

The computational grid used in this study was  $121 \times 81 \times 4$ . To assess grid resolution effects on the solution, a finer mesh of  $121 \times 101 \times 61$  was also used. Symmetry was assumed in the transverse  $Z$  direction in the computations. In these computations, a small flow angularity in the  $Y$  direction, up to a maximum of 1 degree, was specified to account for the normal velocity due to the boundary layer growth upstream of the wedge.

Plots of static pressure rake surveys are shown in Figure 2-a for



the coarse grid case, for the rake location of 5.1 in. (12.95 cm.) and for different distances from the wedge, YG (see Figure 1). Reasonable agreement of the solutions with the experimental data can be seen from the comparison. The corresponding fine grid solution is shown in Figure 2-b. As expected, the agreement between the solution and the data improves with the finer grid, especially near the wall. Yaw angle distributions for rake locations of 5.1 and 7.1 in. (12.95 and 18.03 cm.) are shown in Figures 3-a and 4-a for the coarse grid. Good agreement is also evident for the yaw angles. In the near wall region, the finer grid results show much better agreement as shown in Figures 3-b and 4-b respectively. Note that the 20 degree variation of yaw angles through the sidewall boundary layer is well predicted by the theory. Pitot pressures, presented as the ratio of local pitot pressure to the freestream pitot pressure, through the boundary layer at rake locations of 5.1 and 7.1 in. (12.95 and 18.03 cm.) are presented for the coarse grid case in Figures 5-a and 6-a: the computed and experimental pitot pressure values agree well in the outer portion of the boundary layer, farther than 0.25 in. (0.63 cm.) from the wall. The fine grid results presented in Figures 5-b and 6-b show much better agreement near the wall than the coarse grid results. Additional grid refinement in the shock-boundary layer interaction region away from the wall should further improve the comparison. Studies involving different amounts of artificial viscosity were performed with little effect on the results.

## Two-Dimensional Shock-Boundary Layer Interaction at Mach 14

The two-dimensional experimental data of Holden and Moselle<sup>13</sup> at Mach 14 were used as a hypersonic test case. The leading edge flat plate was 1.44 ft. (43.89 cm.) long, the ramp angle 18 degrees, and the ramp length 1.14 ft. (34.75 cm.). The Reynolds number per foot based on total conditions was  $22.2 \times 10^6$ . The computational grid used in the present study was  $399 \times 99$ .

The predicted surface pressure coefficient is shown in Figure 7 compared to the test data; good agreement is evident from the comparison. The flow was assumed to be laminar in these calculations. The skin friction distribution along the ramp surface is shown in Figure 8; the agreement with experimental data is very good. Note that a small region of reversed flow, just upstream of the ramp corner, can be seen from the negative skin friction values in Figure 8.

## Nozzle Flowfield Calculations

### Geometry

The three-dimensional nozzle is shown schematically in Figure 9 (from Spradley et al.<sup>18</sup>). The nozzle length is six entrance nozzle

heights and the upper wall is linear with a 20 degree slope. The lower splitter length is three. The lower wall is horizontal up to one nozzle height where the wall expands at a six degree angle (see Figure 9). The 2-D geometry expressions were taken from ref. 19, and the 3-D geometry considered for the computations was taken from ref. 18. Note that the aft portion of the nozzles differs from that of ref. 19.

### Two-Dimensional Flowfield Calculations

Two dimensional nozzle flowfield calculations are presented for the nozzle analyzed by Spradley et. al.<sup>18</sup>. The same region of flow that was analyzed by Spradley et. al. is analyzed here, i.e., to six nozzle entrance heights in the flow direction. The grid used in the present computation was 199 x 99.

The nozzle entrance flow was assumed to be uniform. The ratio of specific heats was 1.27 for both streams. The nozzle entrance velocity was 1610 m/sec, the static pressure 9206.3 Pa, the static temperature 2311 deg. K, and the Mach number 1.657. The corresponding freestream values were 1765 m/sec, 506.2 Pa, 261 deg K, and 5.0, respectively<sup>18</sup>. The upper wall static pressures are shown in Figure 10. Also shown in the figure are values from the GIM code, the Seagull code, and a method of characteristics code (MOC). The pressures near the nozzle entrance are in agreement

with the GIM results, and are higher in the aft region. The inviscid results of Seagull and MOC lie between the current viscous solution and the GIM solution in this region.

The predicted flowfield is presented in terms of Mach number, static pressure, total pressures contours, and velocity vectors in Figures 11 to 14, respectively. The contact surface between the nozzle flow and the freestream is evident in the total pressure contour plot. The corresponding variation in the Mach lines is shown in the Mach number contours. Note that the jet is deflected downward, as shown in the velocity vectors, indicating that the nozzle flow is underexpanded.

### Three-Dimensional Nozzle Flowfield Calculations

The 3-D geometry is similar to the 2-D geometry in that the lower cowl has a 6-degree expansion and a 20-degree upper wall. The outer nozzle wall expands by 6 degrees.

The following boundary conditions were used:

- 1) no slip on all walls, adiabatic wall temperature (no slip was specified all along the top surface)
- 2) freestream boundary at  $Z = 6$  (out = boundary in Z direction)
- 3) freestream boundary at  $Y = -3$  (lower boundary in Y direction)

- 4) extrapolated conditions at the exit
- 5) symmetry at  $Z = 0$  (inner boundary in  $Z$  direction)

The same nozzle entrance and freestream conditions as those of the 2-D configuration are used here. The computational grid used for this configuration was  $111 \times 61 \times 51$ .

The flowfield is presented in terms of Mach and static pressure contours in Figures 15 to 18, at planes  $Z = 0.473$  and  $1.06$  nozzle heights, respectively. The nozzle width is one nozzle height. The  $0.473$  plane is close to the nozzle center and the  $1.06$  plane is just outside the nozzle. The center plane flowfield is similar to the 2-dimensional flowfield presented in Figures 11 and 12. The  $1.06$  plane shows the effect of the side relief on the flowfield.

#### Summary

The PARC3D code has been validated for a variety of complex and high speed flow configurations. The results were compared with experimental data where possible with very good agreement and reveal that the code can handle a wide variety of geometries, including ramps and corner flows characteristic of inlets and nozzles. Flows with Mach numbers of 3 to 14 were studied; phenomena of shock-boundary layer interaction and shear layer mixing were considered. Thus, this study demonstrates the capability of the PARC code to analyze three-dimensional viscous flows through high

speed propulsion components of practical interest.

#### Acknowledgement

Prepared for the NASA Lewis Research Center under Contracts NAS 3-24105 and NAS 3-25266, project managers Mr. B. Anderson and Mr. T. Benson. Mr. Benson's assistance in providing the digitized data for the Oskam et. al. configuration and support with the plotting software are appreciated. A major portion of the computational results were obtained using the Numerical Aerodynamic Simulation (NAS) computation facility located at NASA Ames Research Center, Moffett Field, California.

#### References

1. Cooper, G.K., "The Parc Codes," Arnold Engineering Development Center, Tennessee, AEDC-TR-87-24, October 1987.
2. Pulliam, T.H., and Steger, J.L., "Implicit Finite -Difference Simulations of Three Dimensional Compressible flow " AIAA Journal, Vol. 18, February 1980, pp. 159-167.
3. Pulliam, T.H., "Euler and Thin Layer Navier-Stokes Codes: ARC2D, ARC3D," Notes for Computational Fluid Dynamics User's Workshop.

The University of Tennessee Space Institute, Tullahoma, TN., UTSI  
Pub. B02-4005-023-84, 1984, pp. 15.1-15.85.

4. Jareson, A. Schmidt, W. and Turkel, E., "Numerical Solutions of the Euler Equations by Finite Volume Methods Using Runge-Kutta Time-Stepping Schemes," AIAA Paper 81-1259, AIAA 14th Fluid and Plasma Dynamics Conference, Palo Alto California, June 1981.

5. Cooper, G.K., Jordan, J.L., and Phares, W.J., "Analysis Tool for Application to Ground Testing of Highly Underexpanded Nozzles," AIAA Paper 87-2015, AIAA, SAE, ASME, and ASEE 23rd Joint Propulsion Conference, San Diego, California, June-July 1987.

6. Visbal, M. "Numerical Simulation of Shock/Turbulent Boundary Layer Interactions Over 2-D Compression Corners," Ph.D. Dissertation, Rutgers University, October 1983.

7. Horstman, C.C., "Computation of Sharp-Fin Induced Shockwave/Turbulent Boundary Layer Interactions," AIAA Paper 86-1032, 4th AIAA and ASME Fluid Mechanics, Plasma Dynamics, and Lasers Conference, Atlanta, Georgia, May 1986.

8. Knight, D.D., "Numerical Simulation of 3-D Shock-Turbulent Boundary Layer Interaction Generated by a Sharp Fin," AIAA Paper 84-1559, 17th AIAA Fluid Dynamics, Plasma Dynamics, and Lasers Conference, Snowmass, Colorado, June 1984.

9. Knight, D.D., "A Hybrid Explicit-Implicit Numerical Algorithm for the Three- Dimensional Compressible Navier-Stokes Equations," AIAA 83-0223, Presented at the AIAA 21st Aerospace Science Meeting, January 1983.
10. Lawrence, S.L., Tannhill, J.C., Chaussee, D.S., "An Upwind Algorithm for the Parabolized Navier-Stokes Equations," AIAA - 86-1117, Presented at AIAA/SSME 4th Fluid Mechanics, Plasma Dynamics and Laser Conference, Atlanta, Ga., May 1986.
11. Anderson, B.H., and Benson, T.J., "Numerical Solution to the Glancing Sidewall Oblique Shock Wave/Turbulent Layer Interaction in Three Dimension," NASA TM 83056, AIAA Paper 83-0136, Twenty-First Aerospace Sciences Conference, AIAA, Reno, Nevada, January 1983.
12. Oskam, B., Vas, I.E., and Bogdonoff, S.M., "Oblique Shock Wave/Turbulent Boundary Layer Interactions in Three Dimensions at Mach 3, Part I," Princeton University, New Jersey, AFFDL-TR-76-48, Part I, June 1976.
13. Holden, M.S., Mosello, J.R., "Theoretical and Experimental Studies of the Shock Wave- Boundary Layer Interaction on Compression Surfaces in Hypersonic Flow," CAL Report No. AF-2410-A-1, October 1969.



14. Hung, C.H., and MacCormack, R.W., "Numerical Solutions of Supersonic and Hypersonic Laminar Flows Over a Two-Dimensional Compression Corner," AIAA Paper 75-2, Presented at the AIAA 13th Aerospace Sciences Meeting, Pasadena, California, January 1975.

15. Dash, S.M., Wolf, D.E., Sinha, N., Lee, S.H., "Progress in the Development of Parabolized Navier-Stokes (PNS) Methodology for Analyzing Propulsive Jet Mixing Problems," AIAA Paper 86-1115, Presented at the AIAA/ASME 4th Fluid Mechanics, Plasma Dynamics and Lasers Conference, Atlanta, Ga., May 1986.

16. Lewis, W.G.E., Herd, R.J., Herbert, M.V., "Lift Characteristics of Asymmetric Exhaust Nozzles at High Flight Speeds," Journal Royal Aeronautical Society Vol. 70, November 1966, pp. 1036-1040.

17. Baldwin, B., Lomax, H., "Thin Layer Approximation and Algebraic Model for Separated Flows," AIAA Paper 78-257, Jan. 1978.

18. Spradley, L.W., Anderson, P.G., and Pearson, M.L., "Computations of Three-Dimensional Nozzle-Exhaust Flow Fields With the GIM Code," NASA CR-3042, August 1978.

19. Oman, R.A., Forman, K.M., Leng, J. and Hopkins, H.B., "Simulation of Hypersonic Scramjet Exhaust," NASA CR-2494, March 1975.

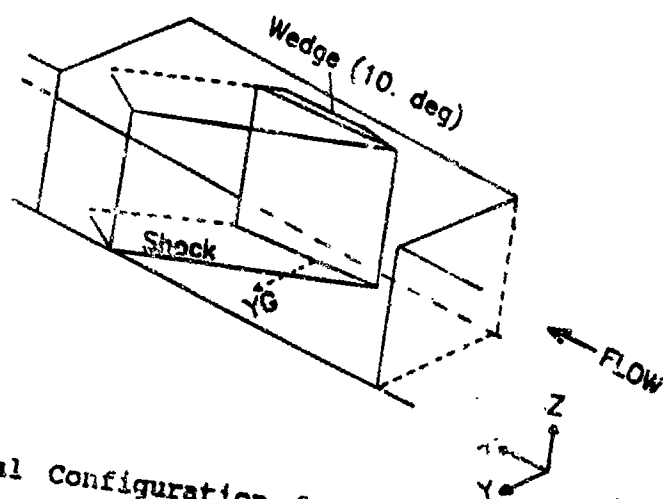


Fig. 1 Experimental Configuration for 3-D Shock Boundary Layer Interaction

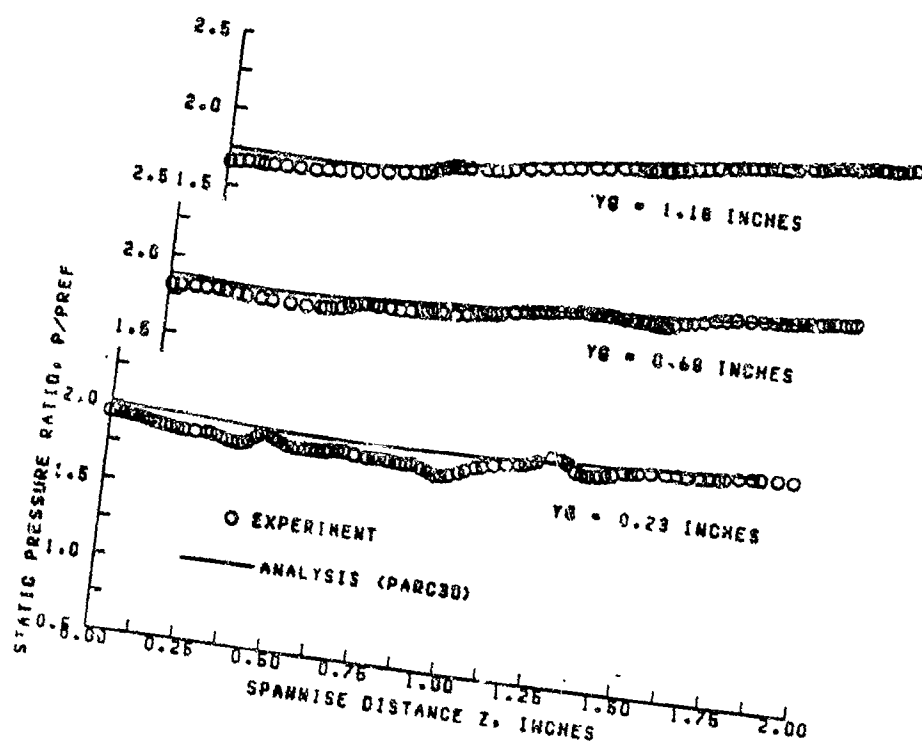


Fig. 2-a Static Pressure Surveys for coarse grid,  $X = 5.10$  inches

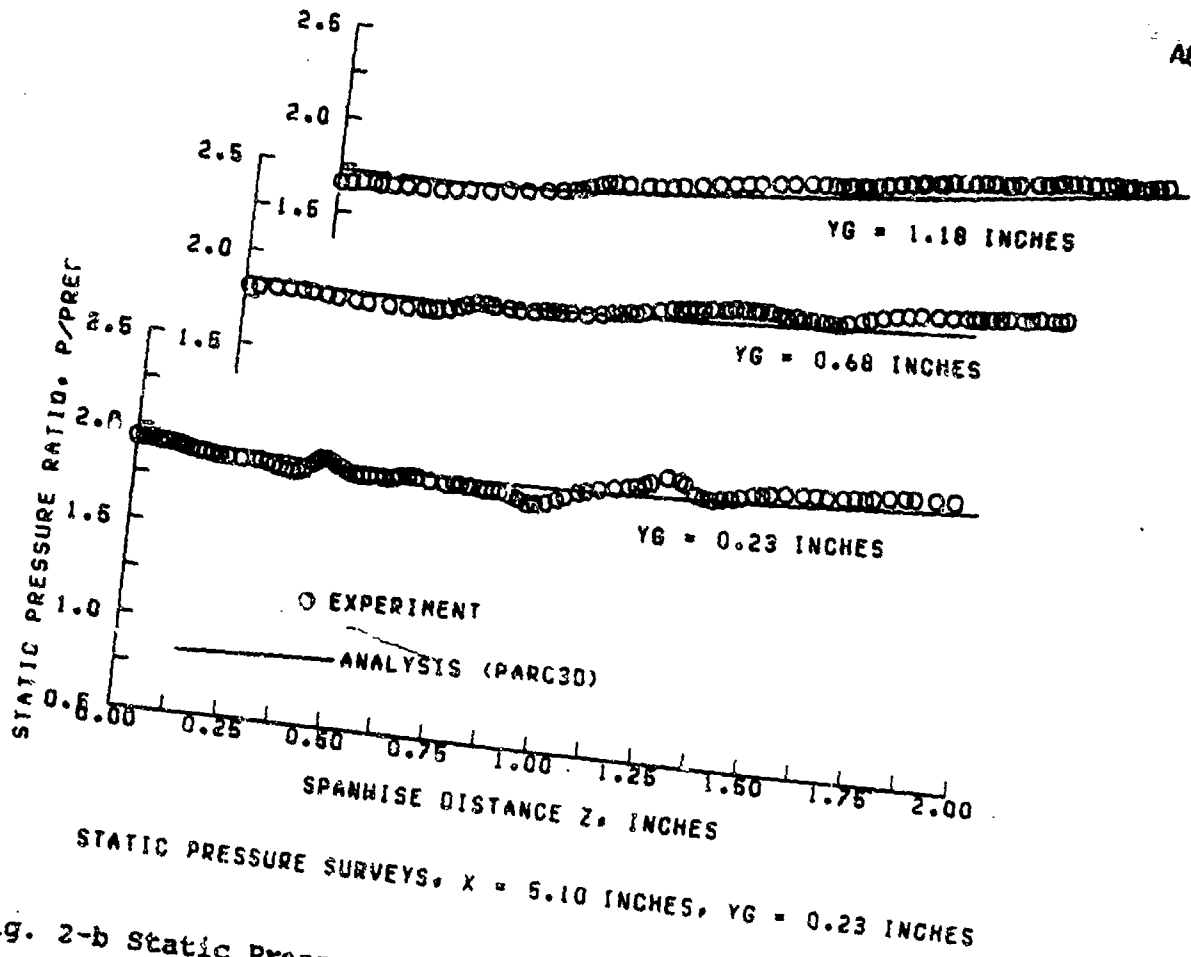


Fig. 2-b Static Pressure Surveys for fine grid,  $X = 5.10$  inches

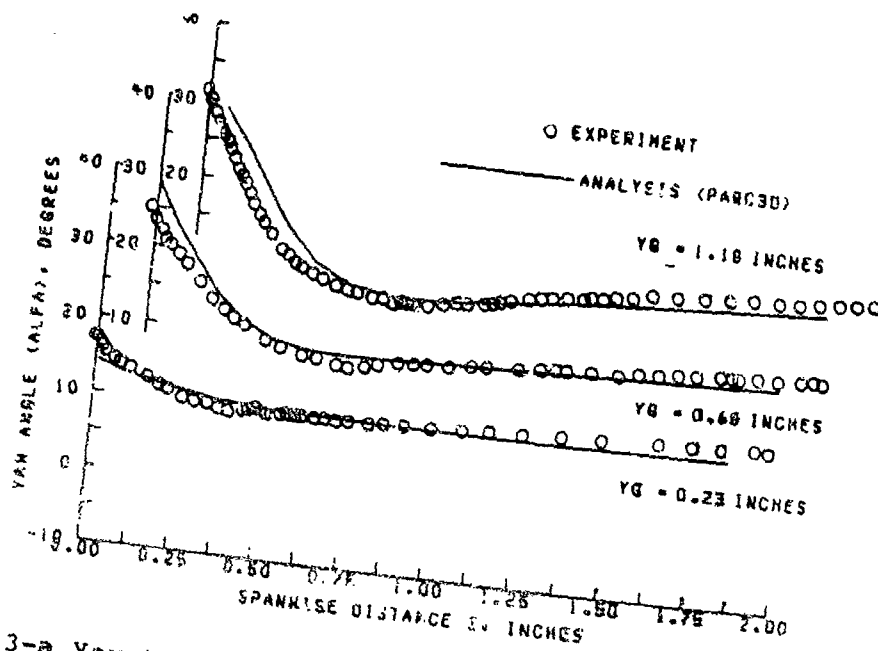


Fig. 3-a Yaw Angle Surveys for coarse grid,  $X = 5.10$  Inches

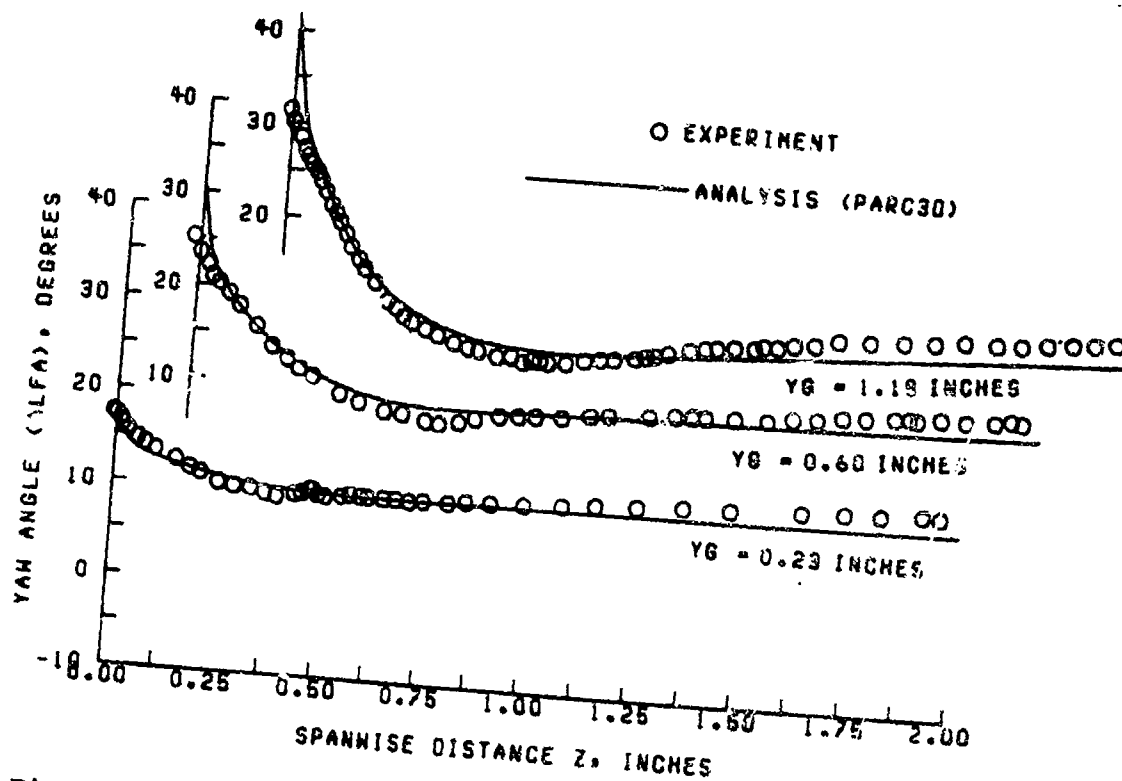


Fig. 3-b Yaw Angle Surveys for fine grid,  $X = 5.10$  Inches

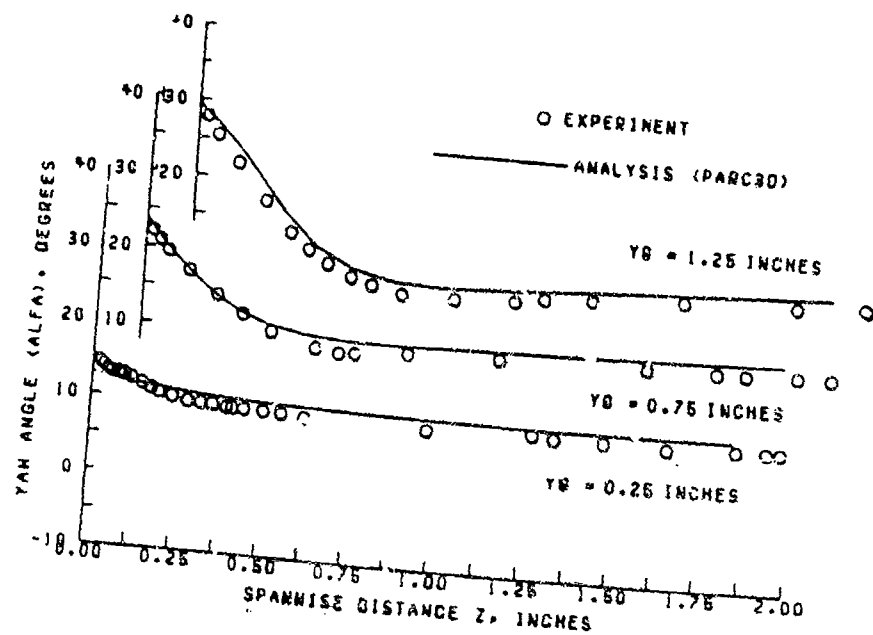


Fig. 4-a Yaw Angle Surveys for coarse grid,  $X = 7.10$  Inches

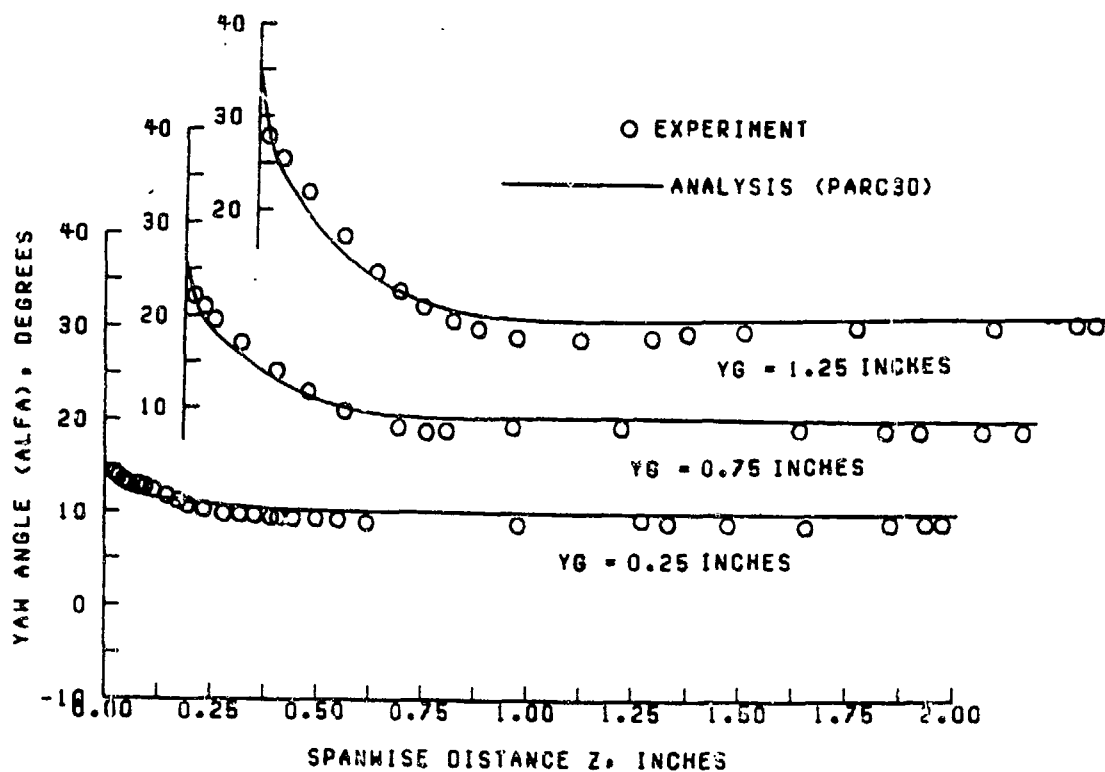


Fig. 4-b Yaw Angle Surveys for fine grid,  $X = 7.10$  Inches

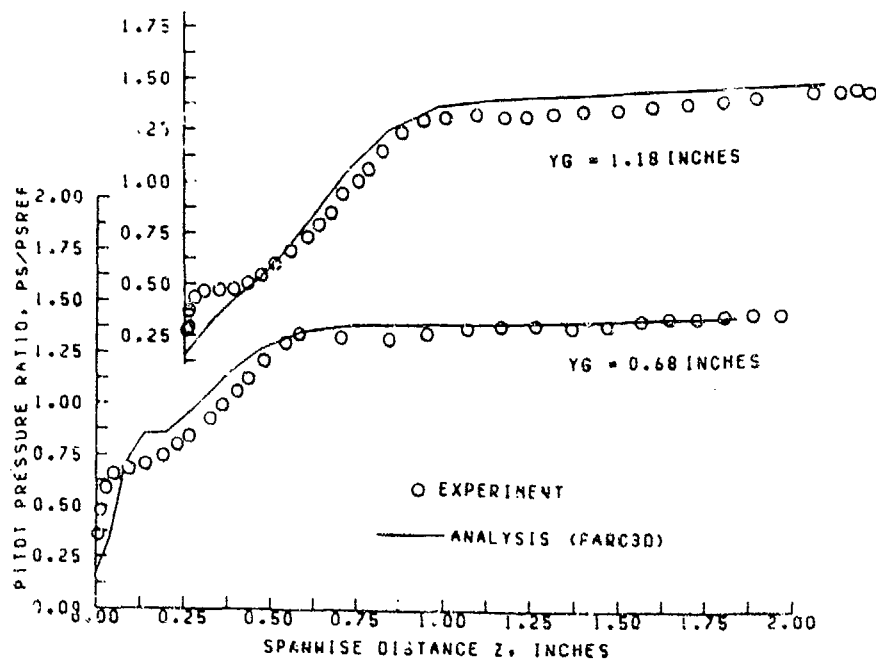


Fig. 5-a Pitot Pressure Surveys for coarse grid,  $X = 5.1$  Inches

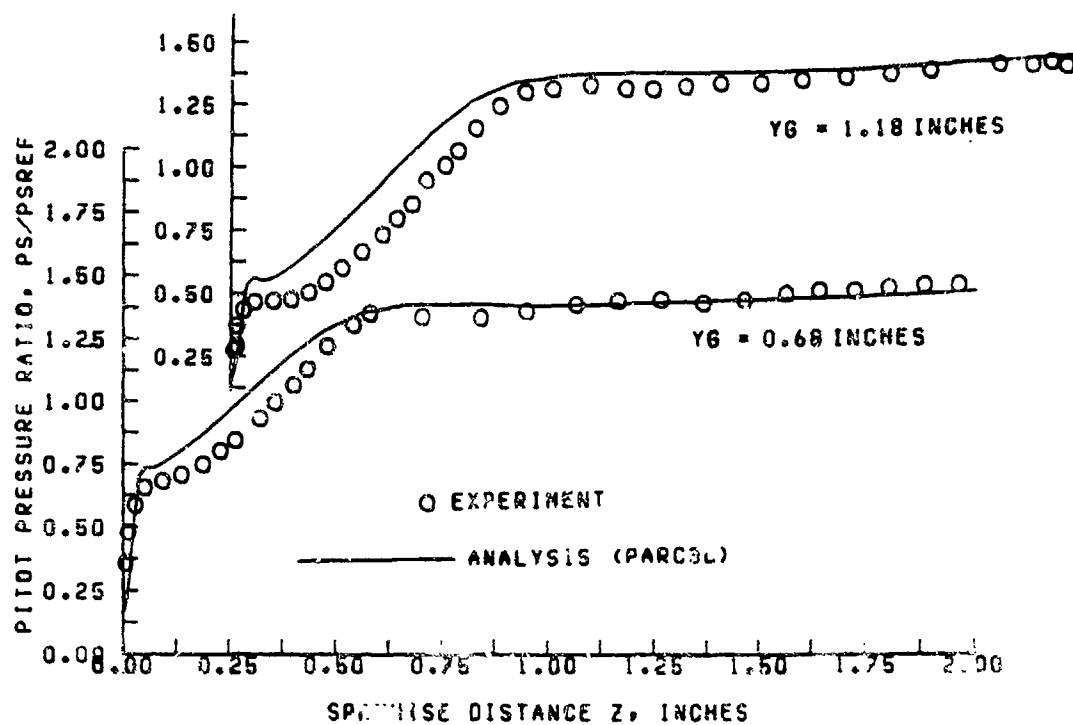


Fig. 5-b Pitot Pressure Surveys for fine grid, X = 5.1 Inches

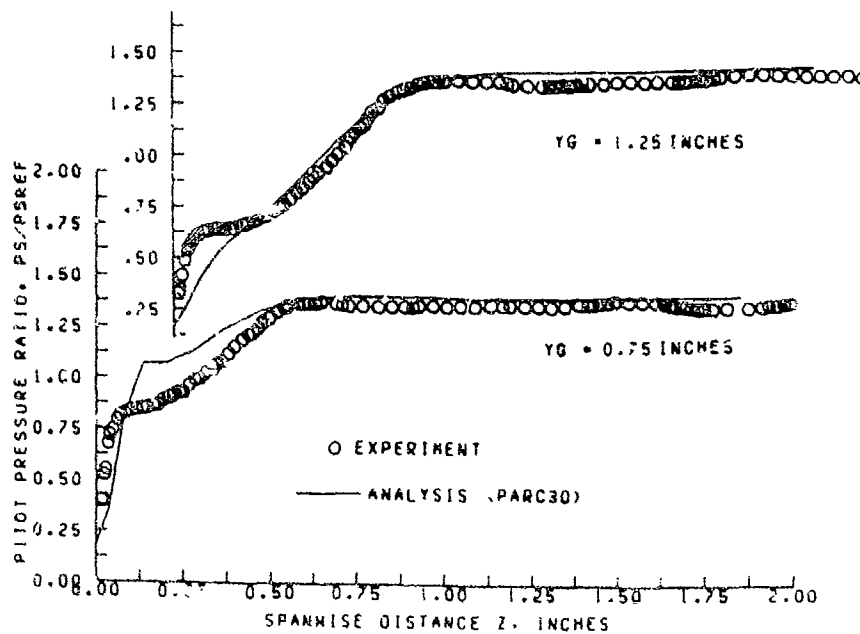


Fig. 6-a Pitot Pressure Surveys for coarse grid, X = 7.1 Inches

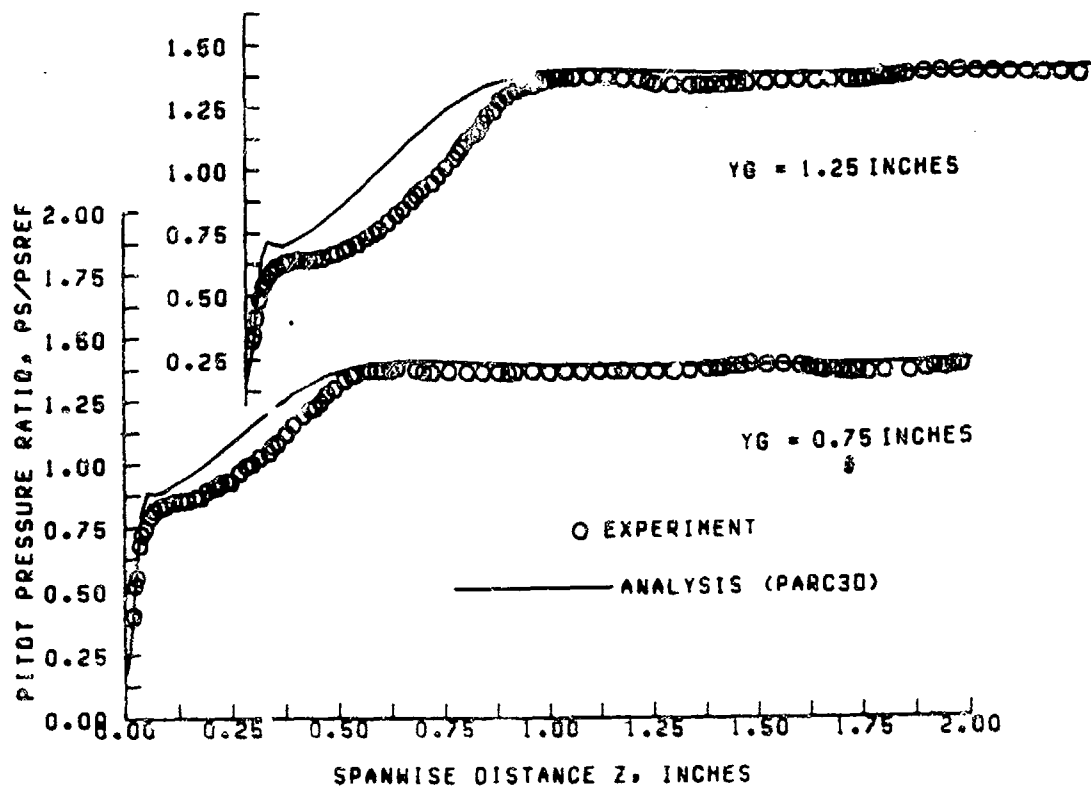


Fig. 6-b Pitot Pressure Surveys for fine grid,  $X = 7.1$  Inches

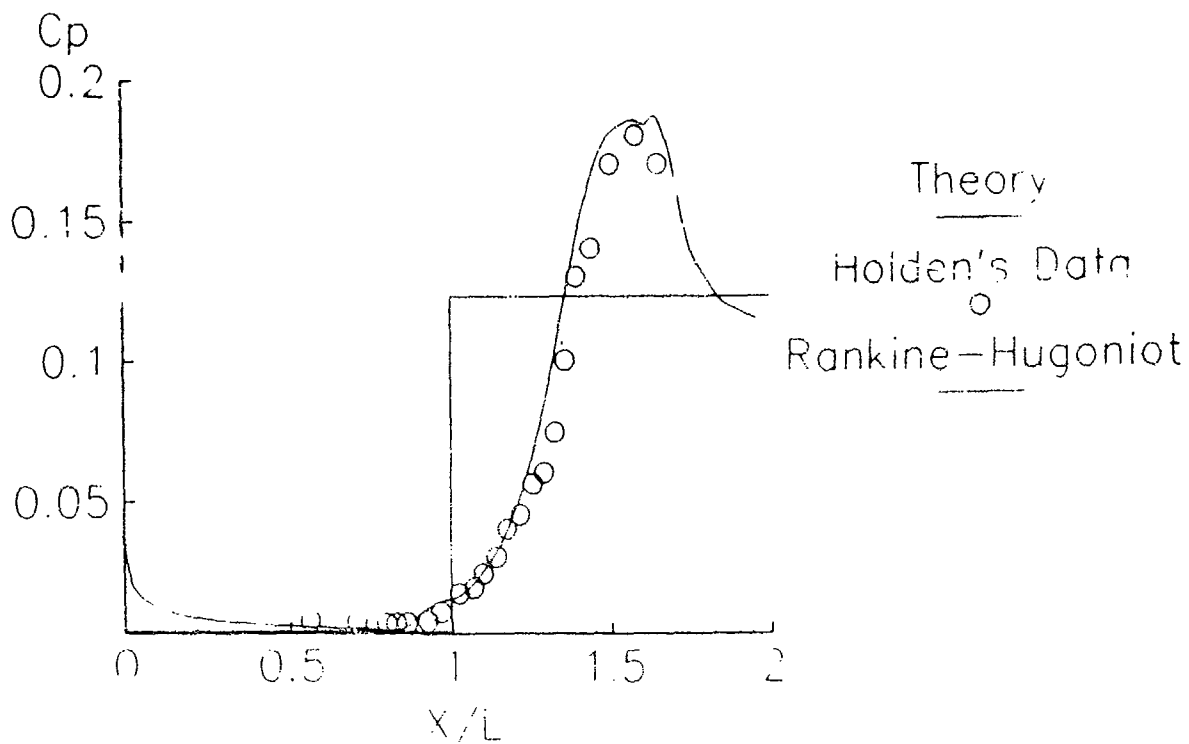


Fig. 7  $C_p$  on 18 Deg Ramp at Mach = 14.1

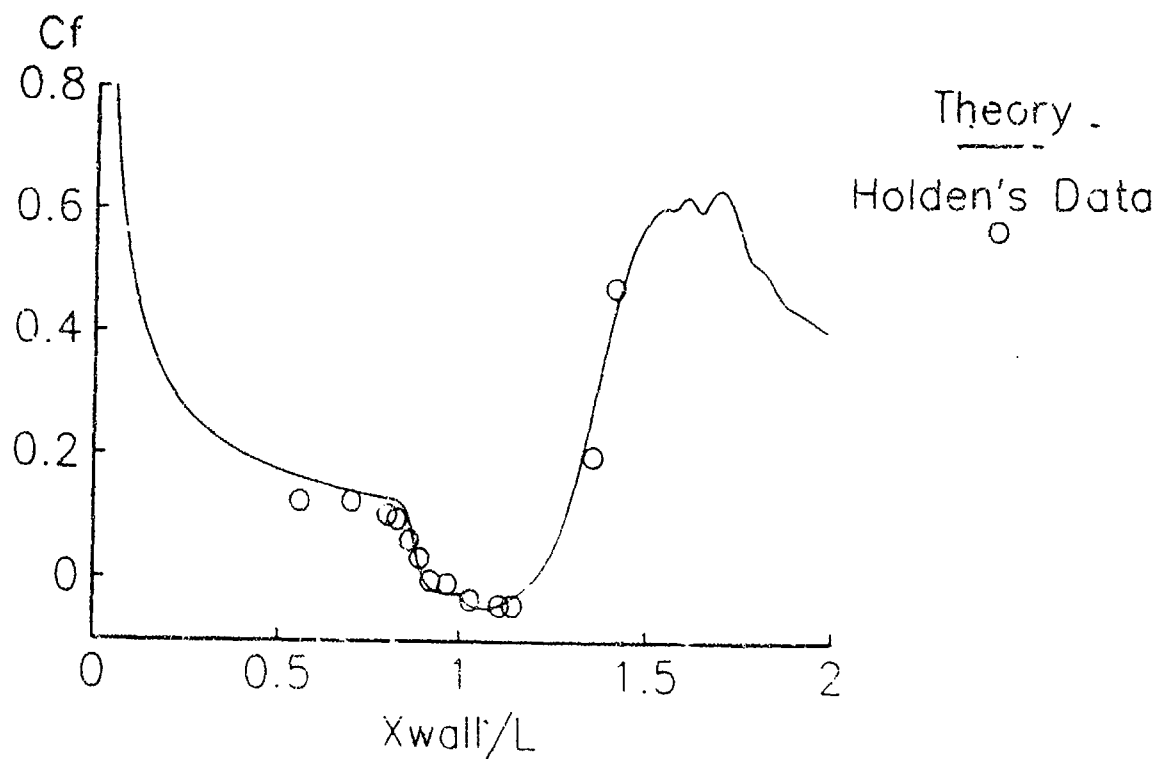


Fig. 8  $C_f$  on 18 Deg Ramp at Mach = 14.1

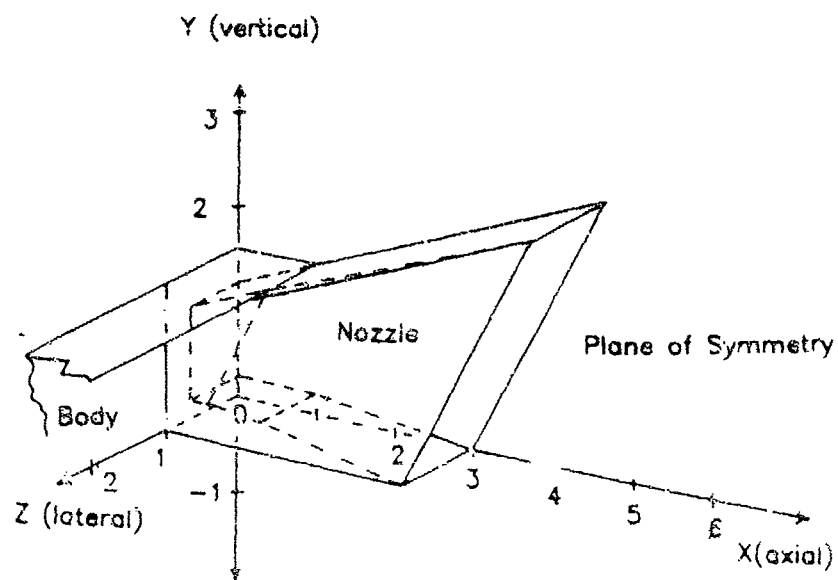


Fig. 9 Schematic of 3-Dimensional Nozzle



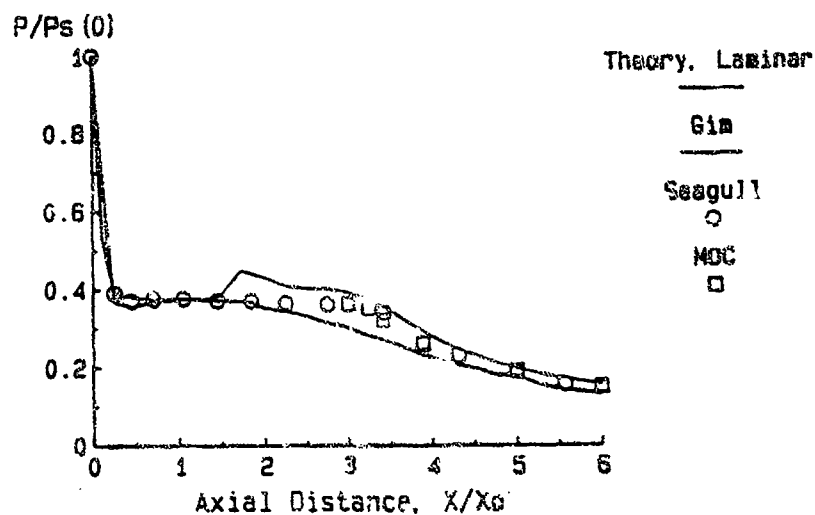
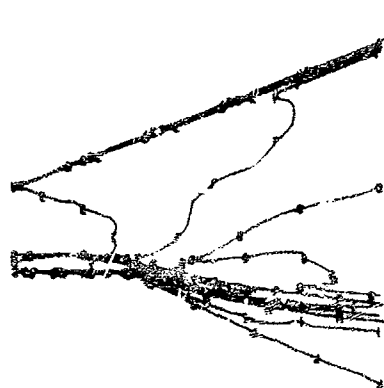
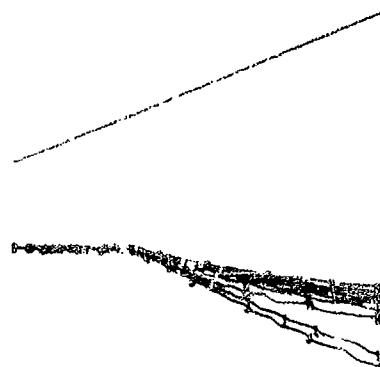


Fig. 10 Upper Wall Static Pressure vs. Distance, 2-D Nozzle Calculations

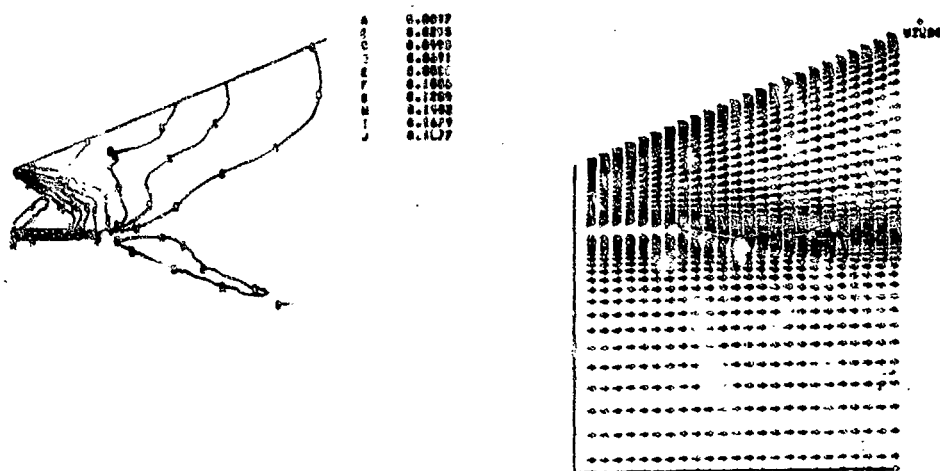


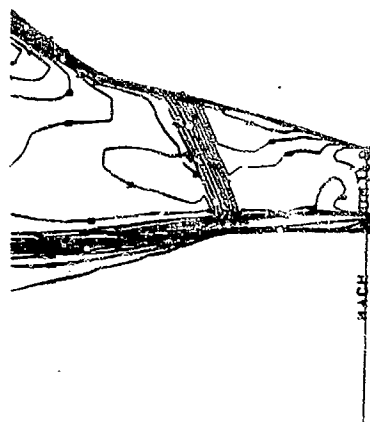
A	0.9900
B	0.6910
C	1.0830
D	1.6331
E	2.6041
F	2.6041
G	3.4041
H	1.6372
I	1.0807
J	0.6910



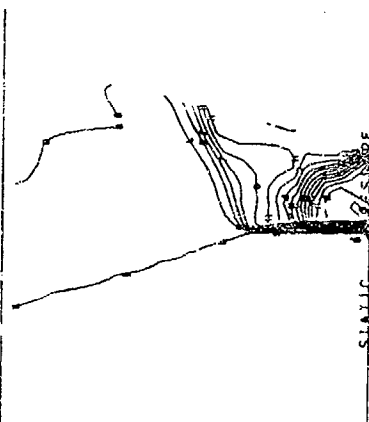
A	0.6101
B	1.0131
C	2.0231
D	3.1231
E	4.1231
F	5.1231
G	6.1231
H	7.1231
I	8.1231
J	9.1231

Fig. 11 Mach Numbers for 2-D Nozzle      Fig. 12 Total Pressure for 2-D Nozzle





A	8.2800
B	8.2812
C	8.2824
D	8.2837
E	1.0060
F	1.2462
G	1.1874
H	1.2487
I	1.2079
J	2.2512
K	2.1575
L	2.2694
M	1.2199
N	3.2661
O	2.1179
P	3.2686
Q	4.0150
R	4.2711
S	4.6223
T	4.7736



A	0.0510
B	0.0132
C	0.0233
D	0.0398
E	0.0509
F	0.0867
G	0.0679
H	0.0798
I	0.0602
J	0.1013
K	0.1125
L	0.1236
M	0.1348
N	0.1457
O	0.1570
P	0.1682
Q	0.1793
R	0.1906
S	0.2016
T	0.2128
V	0.2239

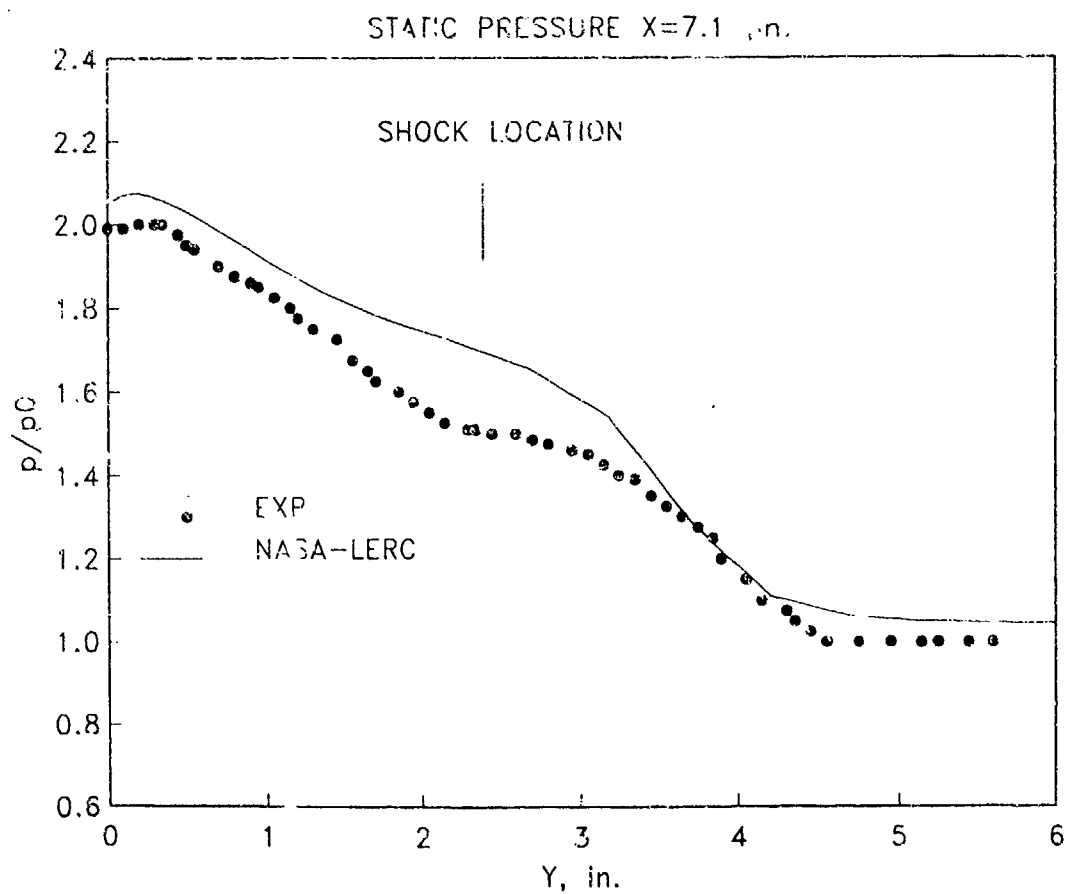
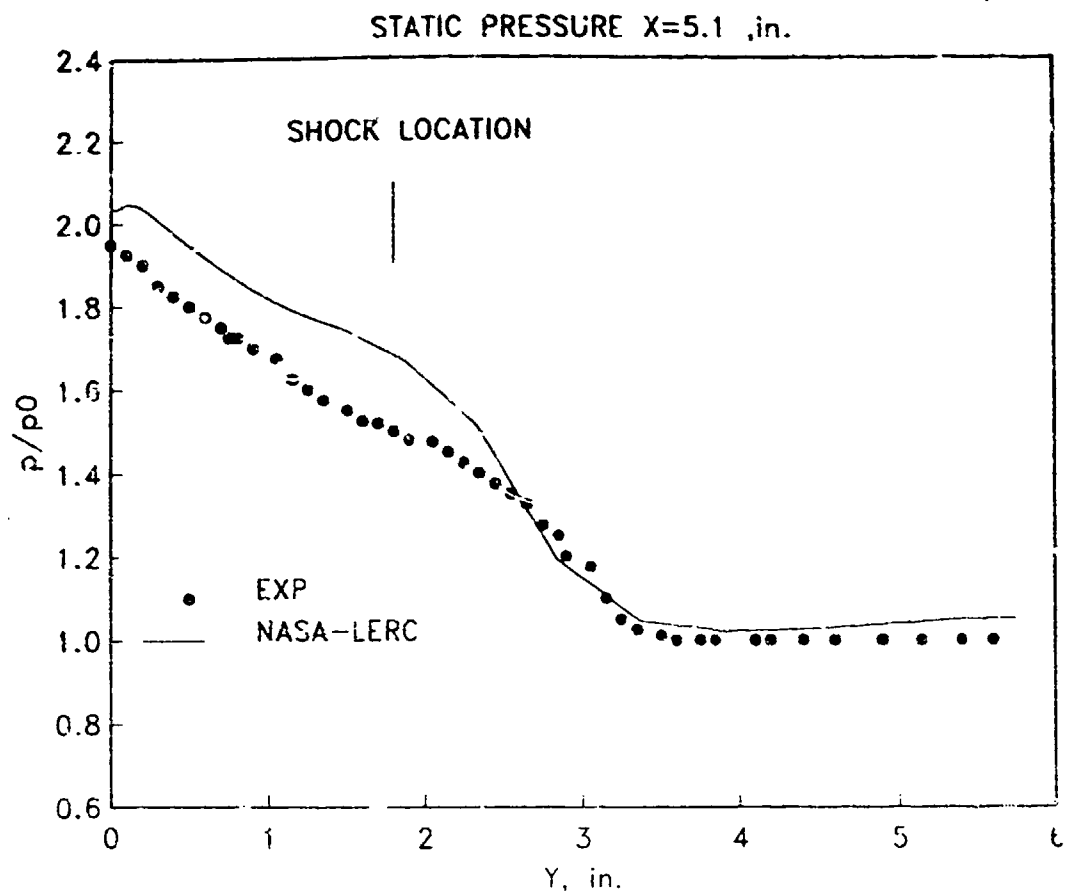
Fig. 17 Mach Numbers at  $Z = 1.06$ Fig. 18 Static Pressures at  $Z = 1.06$

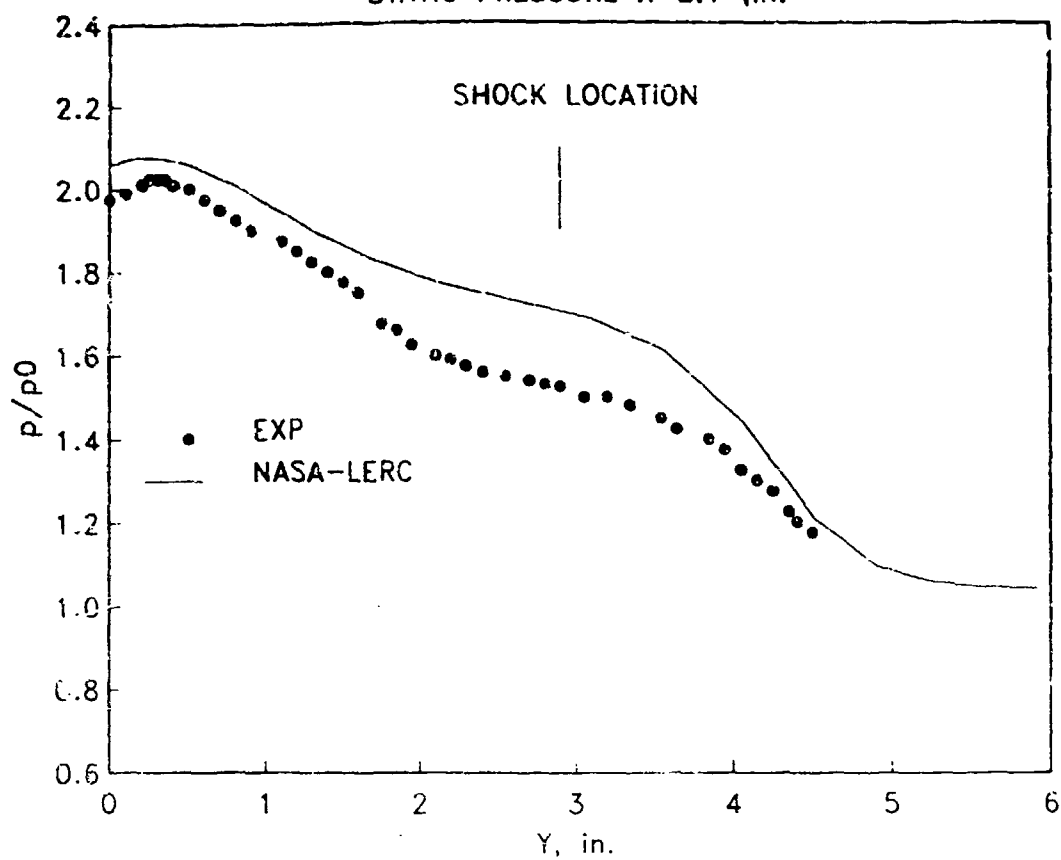
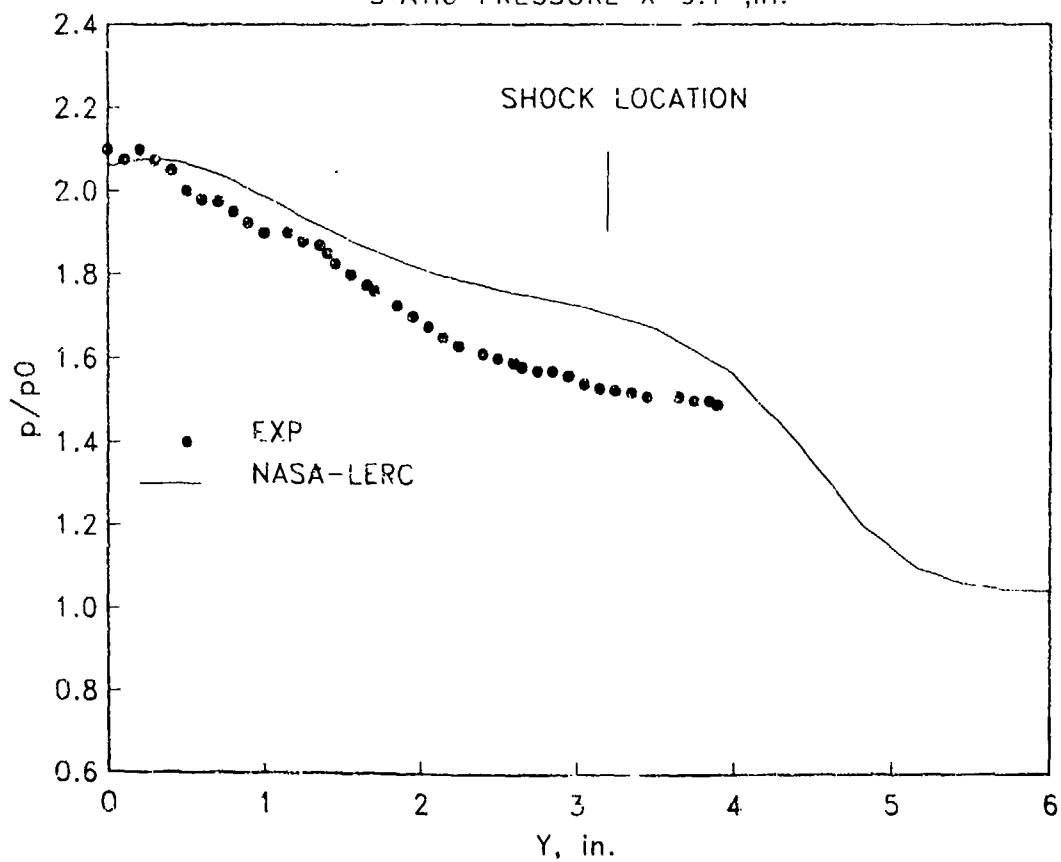
Thomas J. Benson  
National Aeronautics and Space Administration  
Lewis Research Center  
Cleveland, Ohio 44135

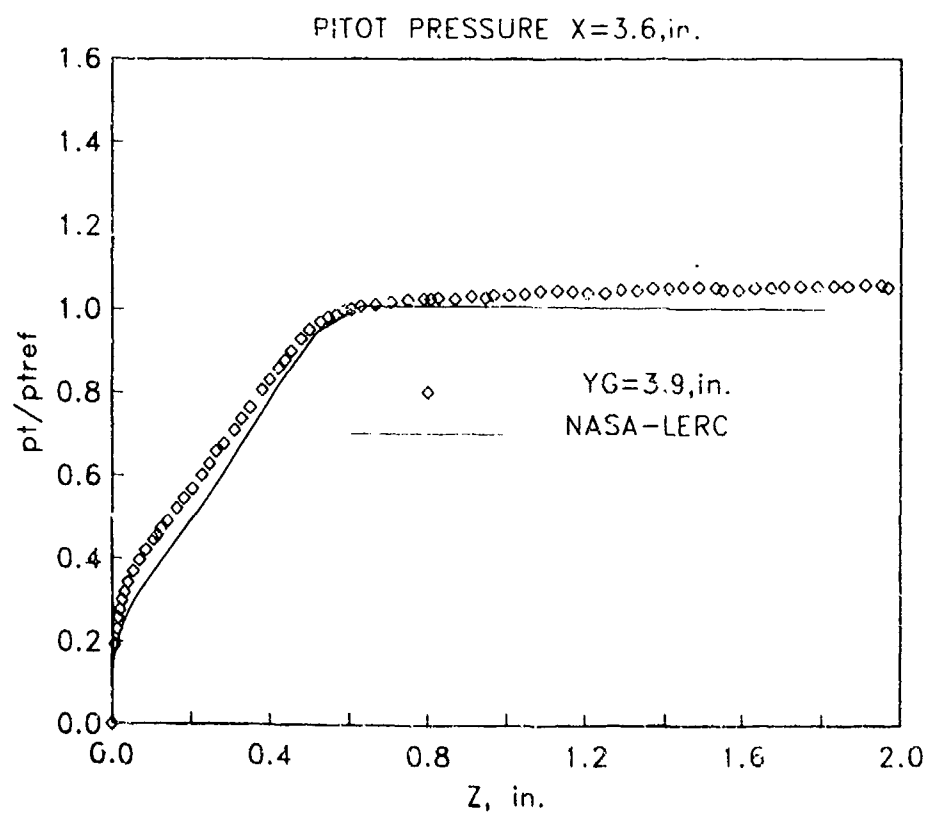
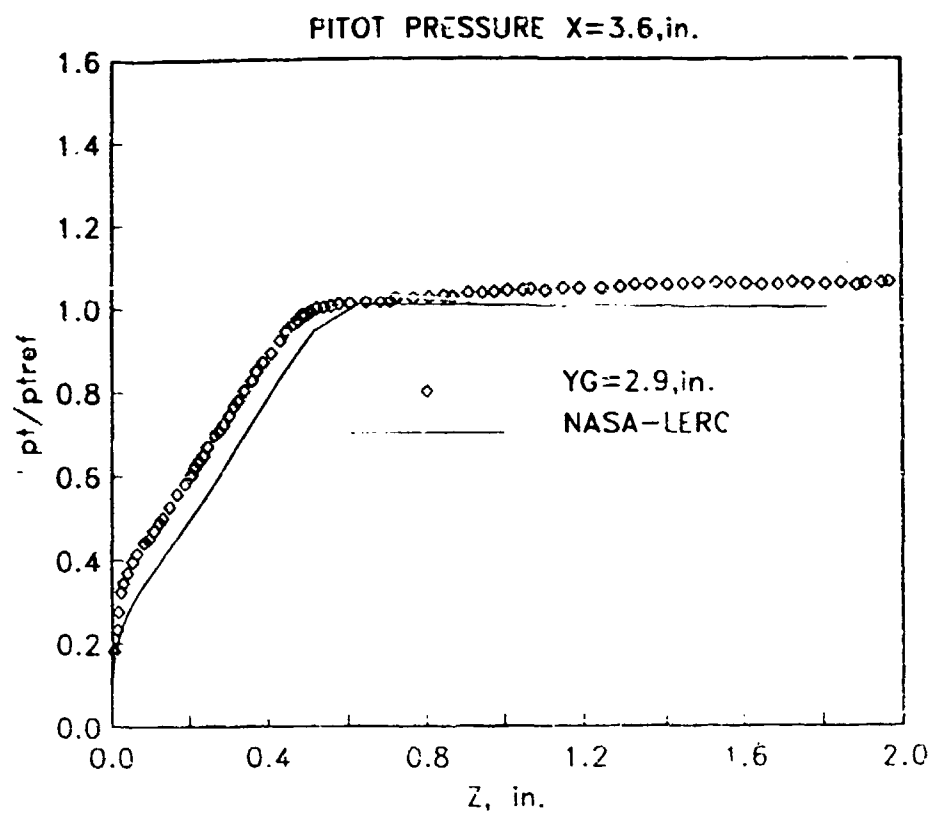
A three-dimensional supersonic Parabolized Navier-Stokes code has been used to investigate the glancing shock/boundary layer interaction of Oskan.. Vas and Bogdonoff.. Parametric studies of grid resolution, boundary conditions, and turbulence modeling have been conducted, although the results presented here represent the best of these calculations. The results indicate a significant three dimensional effect exists for this simple two dimensional geometry. The comparison with experimental data is quite good, if sufficient grid resolution is used.

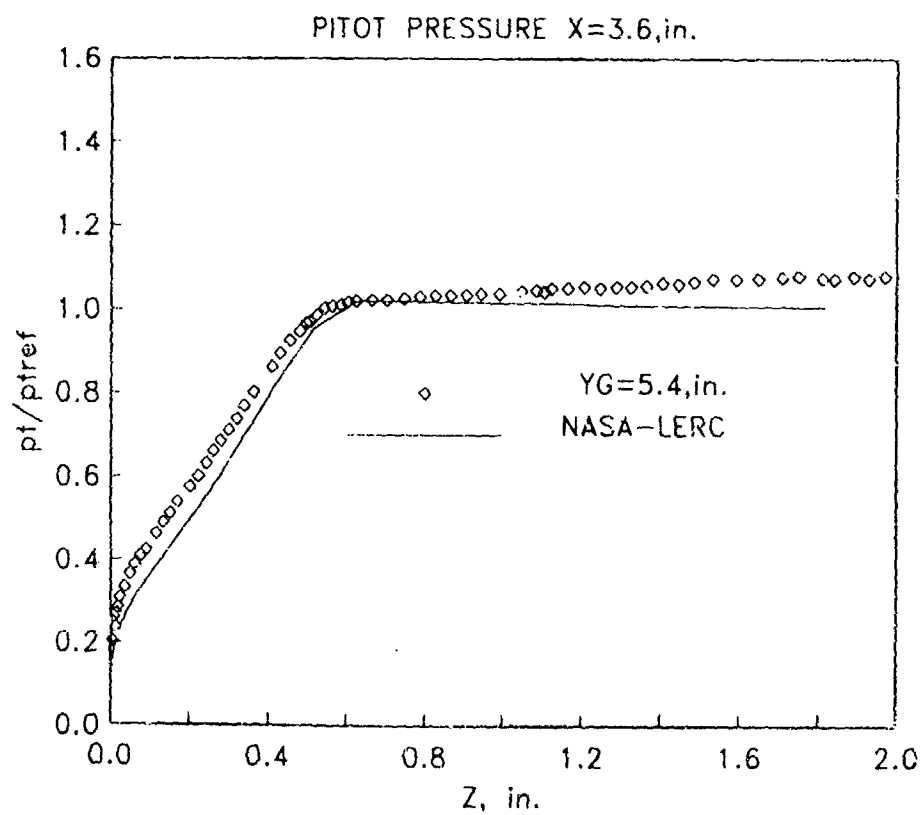
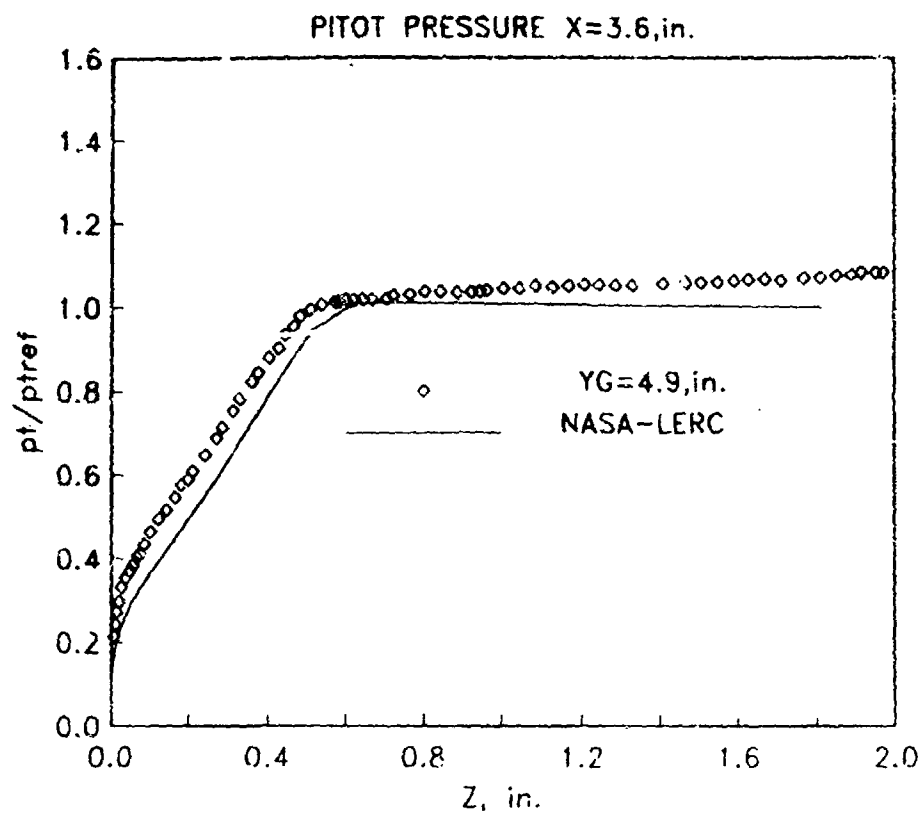
The three-dimensional supersonic viscous marching analysis used in this study is the PEPSIS code. The code solves the PNS equations for supersonic flow by an efficient Briley-McDonald, linearized block implicit scheme. The code solves for the flowfield in a single sweep, can be run with a variety of turbulence models, in either two or three dimensional mode, and can either solve the energy equation or impose constant stagnation enthalpy. The two dimensional result presented in the enclosed figures was run on a CRAY-1S at the Lewis Research Center on a 61X41X200 grid with constant stagnation enthalpy imposed. Each flow computation required about 25 minutes of CPU time with much more time used to refine grids, post process results, etc. The turbulence model used in this calculation is the standard McDonald-Camarata mixing length model. The calculation was started with uniform free stream conditions and a turbulent boundary layer profile on the wall as specified in the report. This case was run fully turbulent. The grid generated for this case was an orthogonal-curvelinear grid which fillets the sharp leading edge of the wedge.

While providing comparisons with the experimental results, we have included an additional particle tracing plot of this interaction to demonstrate some of the power of CFD in visualizing and understanding complex three-dimensional flow problems. In this figure, particles are released upstream of the wedge leading edge and in a line normal to wall. Those particles released closest to the wedge are seen to be splayed out and dispersed over the entire plate downstream. Those that are released far from the wedge, but low in the boundary layer, are swept up and spread by the cross flow. Those that are released far from the wedge but out of the boundary layer rise up and over the cross flow and are turned by the inviscid shock wave.

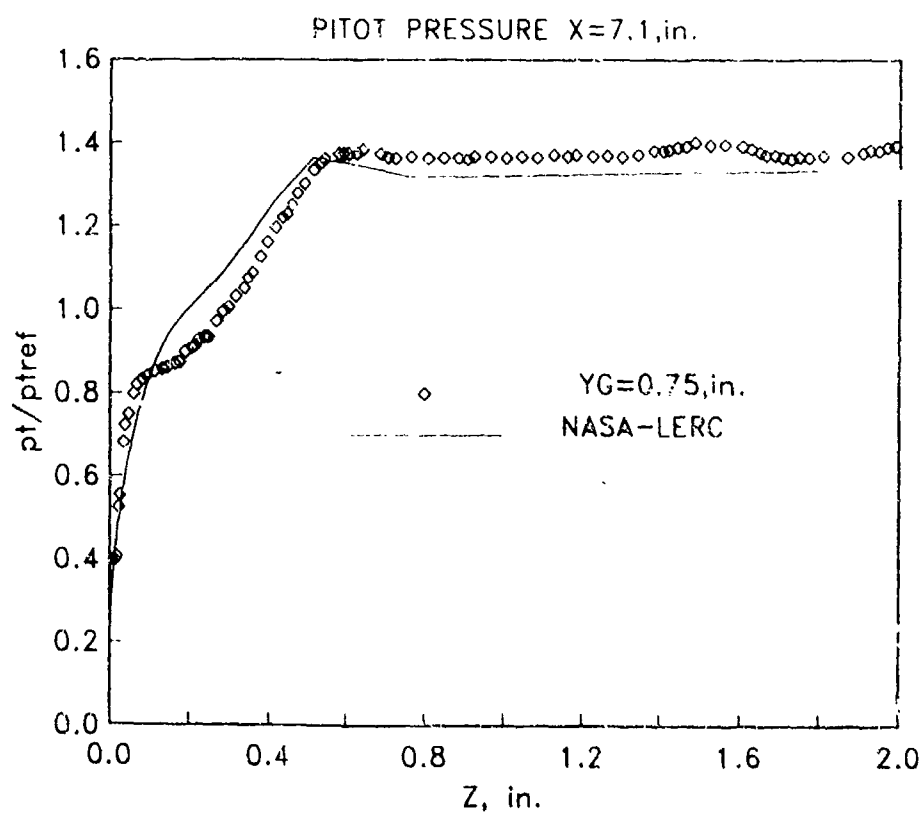
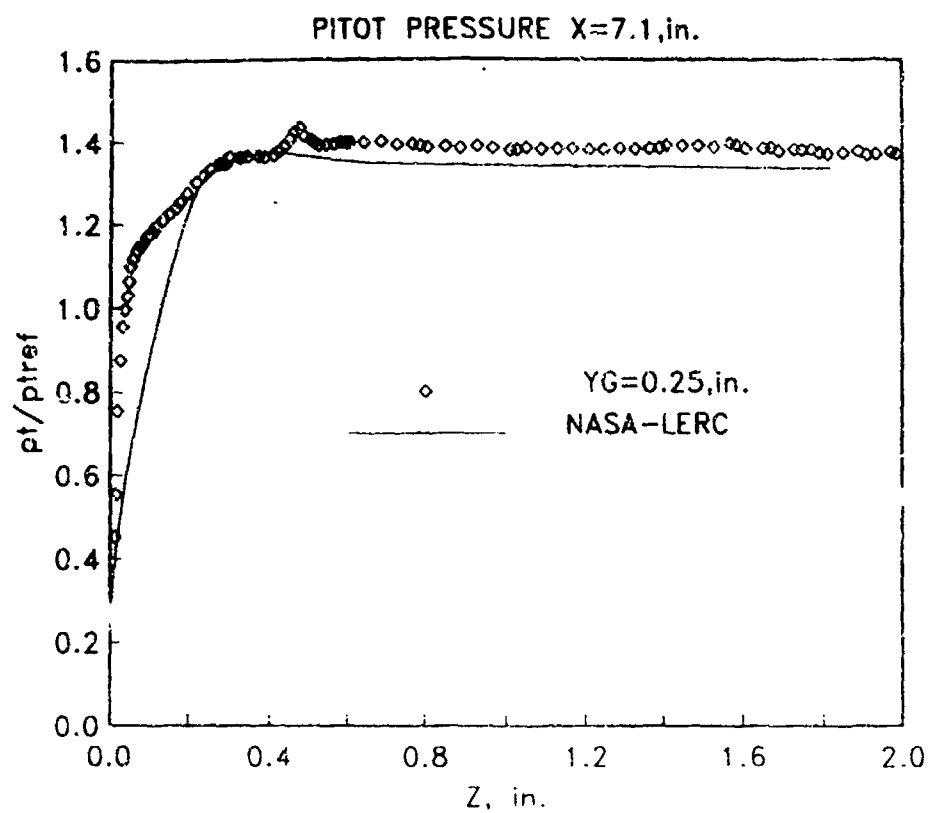


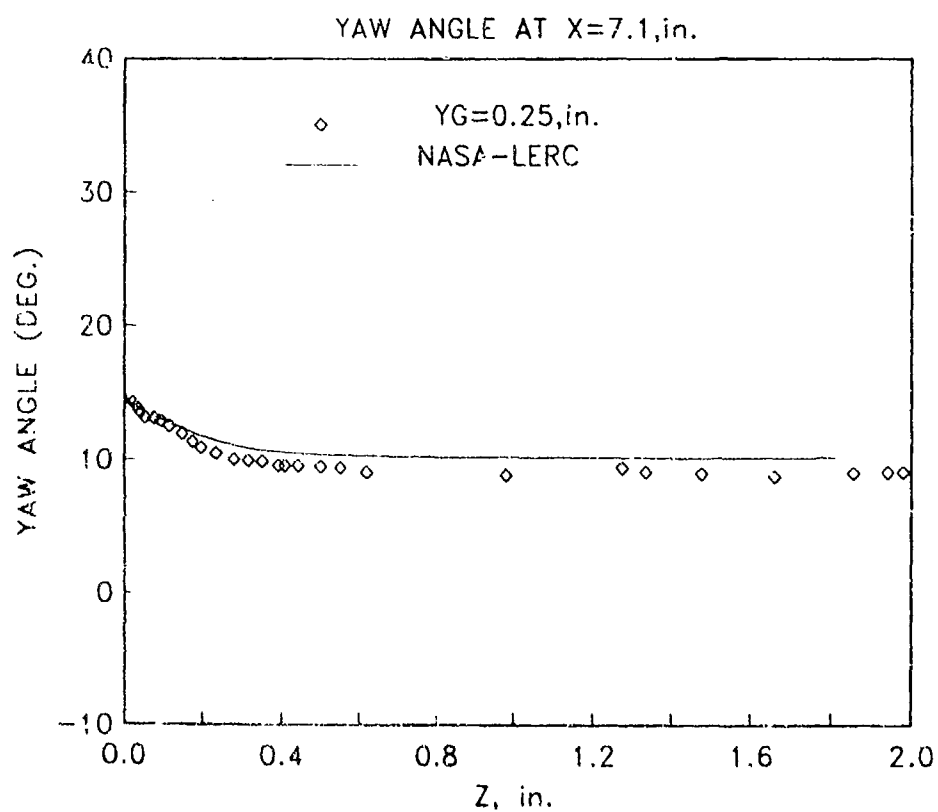
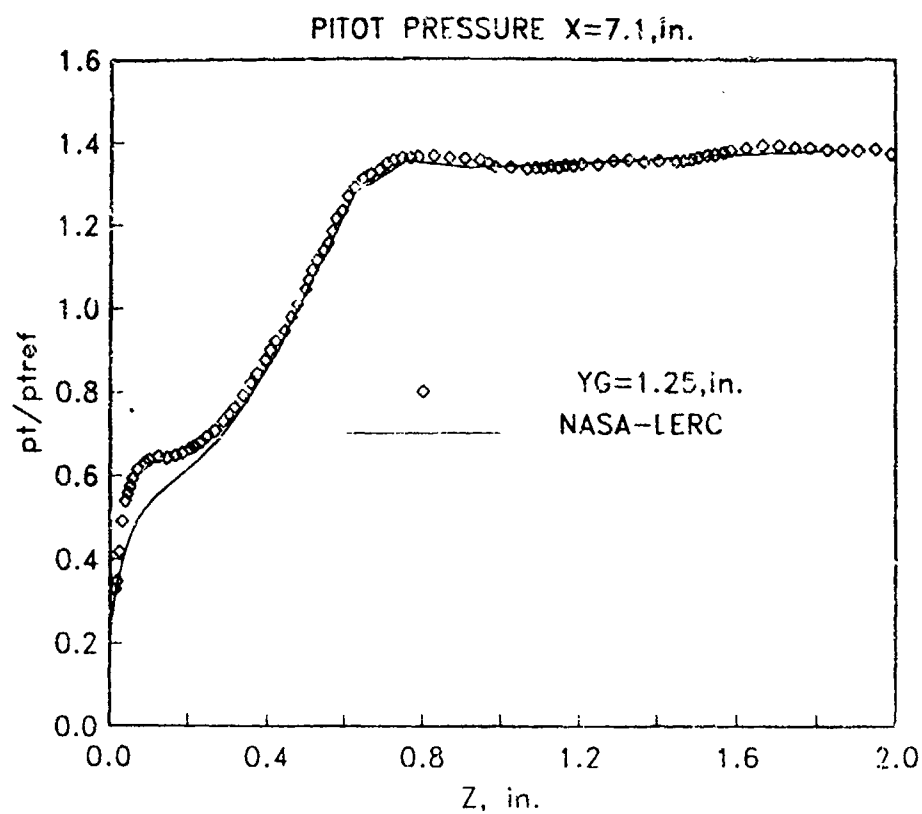
STATIC PRESSURE  $X=8.1$  ,in.STATIC PRESSURE  $X=9.1$  ,in.

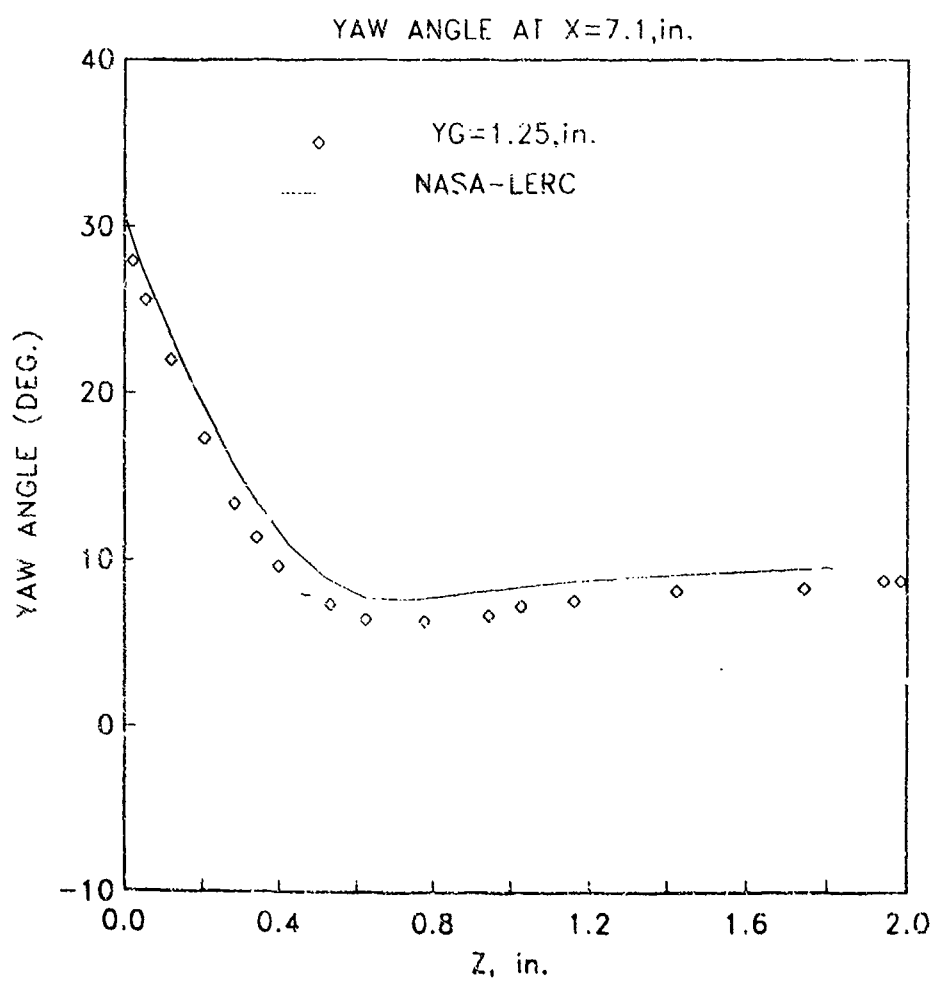
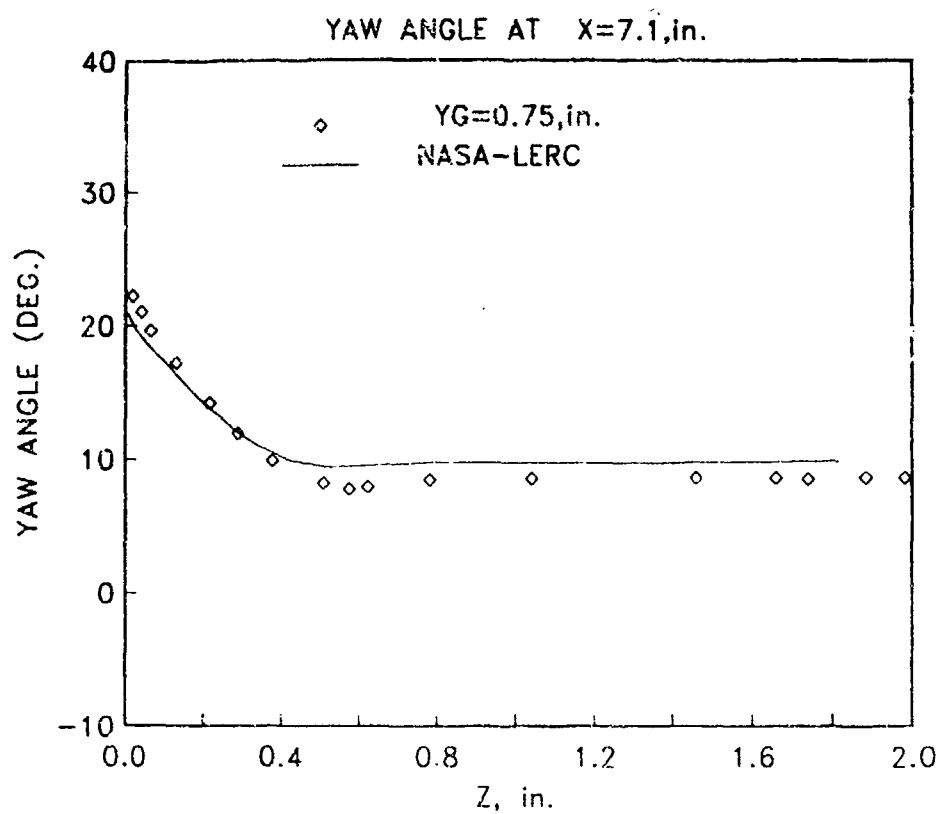












# **AR 270**

## **Microfiche Appendix to Sub-Section 3.3.3/3.3.4**

### **Contributions to Test Cases 3 and 4**

**Case 3 Subsonic/transonic circular intake**

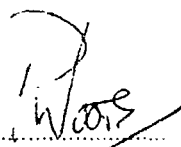
**Case 4 Subsonic /transonic semi-circular intake**

	<b>Page No's</b>
<b>BAe</b>	<b>A104 to A128</b>
<b>Dornier</b>	<b>A129 to A150</b>
<b>ARA</b>	<b>A151 to A183</b>

# THE COMPUTATIONAL WORKINGS OF THE REYNOLDS AVERAGED NAVIER-STOKES CODE RANSAC

'Evaluation of RANSAC on Test Cases 3.1 & 3.2'

Prepared by:

  
PD WOODS

Section Leader (Applied CFD)  
Aerodynamics & Vulnerability Research  
Sowerby Research Centre  
British Aerospace

Approved by:

  
PG CHERRING

Head of Department  
Aerodynamics & Vulnerability Research  
Sowerby Research Centre  
British Aerospace.

## ABSTRACT

This report details the evaluation of RANSAC (a Reynolds averaged Navier-Stokes afterbody code, developed by the CFD group at Sowerby Research Centre, British Aerospace) on two flows through a single geometry, circular cross section, s-shaped diffuser. Results are compared with experiment wherever possible and it is shown that agreement is good for the Mach 0.412 case and less quantitative for the Mach 0.794 case. For both flows the qualitative characteristics are predicted well. It is thought that much of the discrepancy is due to the coarseness of the computational mesh.

### 1. Introduction

The CFD group at the Sowerby Research Centre, British Aerospace has developed a three dimensional, finite volume, Reynolds averaged Navier-Stokes afterbody code (RANSAC). Originally designed for use with afterbodies and jets it is sufficiently general to model most aerodynamic flows. Two different mass flow rates through a single geometry diffuser were studied :

- 1) AGARD test case 3.1/3537  
Inflow Mach number (at onset of s-bend) = 0.412
- 2) AGARD test case 3.2/3532  
Inflow Mach number (at onset of s-bend) = 0.794

For brevity these cases will be referred to as 'slow' and 'fast' respectively.

All calculations have been performed on the British Aerospace CRAY-YMP.

### 2. The Model and Conditions Considered.

The model consists of an s-sectioned diffuser of circular cross-section with a cowl lip and a forward parallel extension at inlet and a 'bullet' shaped insert at the engine face (outlet). In order to simplify calculations and to reduce the required run times, the geometry modelled consisted of only the s-sectioned diffuser with the engine bullet. The symmetry of the duct rendered it necessary to model only half the full three dimensional configuration. All geometry specifications were taken from [ 1 ], due to apparent errors with the data stored on magnetic tape, reference [ 2 ].

Inlet conditions required by the code are static pressure, static temperature, the three components of velocity and the turbulent energy all across the entire inlet plane. Inlet

conditions were therefore estimated by assuming a constant total pressure thus giving static conditions at the onset of the s-bend. These conditions were then assumed constant over the inlet plane and the boundary conditions adopted within the code were allowed to alter these values as downstream conditions dictated. Full potential plus boundary layer calculations (supplied by Dr. L. Goldsmith of ARA) demonstrated little velocity variation or deviation from the parallel across the pane concerned and thus the inlet conditions adopted were deemed sufficient.

### 3. Grid Generation

Initial grids generated were 70 x 12 x 12 cells (axial, radial, circumferential) and included the forward extension pipe and a crude representation of the cowl lip. It was clear however that in order to accurately model the flow over the cowl lip and through the forward extension a large area surrounding the lip needed to be included in the computational domain. As this would necessitate the use of a large number of cells and consequently greatly increase the computer effort required, the cowl lip and forward extension models were abandoned and the mesh begun at the onset of the s-bend.

A limited grid dependency study was carried out eventually arriving at a single grid for both the fast and slow calculations. It consists of 80 x 24 x 22 cells (axial, circumferential, radial).

### 4. Run Times

Test case : 3.1/3537 (slow)  
 Cray CPU : 16,544 seconds  
 Case : 100 global iterations, turbulent, isenthalpic.

Test case : 3.2/3532 (fast)  
 Cray CPU : 16,500 seconds  
 Case : 100 global iterations, turbulent, isenthalpic.

### 5. References.

1. 'Pitot Intake Model 2129 (R10); Calculation of inlet Losses'

BAe Aircraft Group Report B59R/R&D/620/12893  
 D.C Greenman, June 1983.

2. 'Magnetic Tape containing diffuser geometry data'

Dr. N.C. Bissinger, MEB, August 1989.

## ABSTRACT

This paper outlines the basic algorithm implemented within the Reynolds Averaged Navier-Stokes code RANSAC. The algorithm is a three dimensional, cell centred, finite volume, implicit, pressure correction method. The pressure correction procedure is taken from that of C.M. Rhie (Ref.1). RANSAC uses a 'multiblock' input geometry whereby the flow field is split into many simple 'blocks' to enable the modelling of complex designs and a multigrid solver is available for use with the pressure equations. This paper will detail the basic flow field equations, the differencing schemes, the pressure correction procedure, the treatment of boundary conditions and the dissipation type.



## CONTENTS

SECTION 1	THE FLOW FIELD EQUATIONS
SECTION 2	THE DIFFERENCING SCHEME
SECTION 3	THE PRESSURE CORRECTION TECHNIQUE
SECTION 4	THE TREATMENT OF BOUNDARY CONDITIONS
SECTION 5	DISSIPATION
SECTION 6	THE MULTIBLOCK CONCEPT
SECTION 7	RELAXATION TECHNIQUES
7.1	MATRIX INVERSION
7.2	INERTIAL RELAXATION
SECTION 8	MULTIGRID TECHNIQUE
SECTION 9	CONVERGENCE
APPENDIX	
Appendix	
A	NOMENCLATURE

# 1 THE FLOW FIELD EQUATIONS

The Reynolds Averaged Navier-Stokes equations can be written in the form:

## CONTINUITY

$$\frac{\partial}{\partial x_j} (\rho u_j) = 0 \quad (1.1)$$

## MOMENTUM

$$\frac{\partial}{\partial x_j} (\rho u_i u_j) = \frac{\partial}{\partial x_j} \left\{ (\mu + \mu_t) \frac{\partial u_i}{\partial x_j} \right\} + S^u_i \quad (1.2)$$

## ENERGY

$$\frac{\partial}{\partial x_j} (\rho u_j H) = \frac{\partial}{\partial x_j} \left\{ \frac{(\mu_t + \mu_l)}{Pr} \frac{\partial H}{\partial x_j} \right\} + S^H \quad (1.3)$$

The Standard k-ε model of Launder & Spalding (Ref. 2) gives equations for the turbulent energy k and the turbulent dissipation ε as

$$\frac{\partial}{\partial x_j} (\rho u_j k) = \frac{\partial}{\partial x_j} \left\{ \frac{\mu_t}{\sigma_k} \frac{\partial k}{\partial x_j} \right\} - S^k \quad (1.4)$$

$$\frac{\partial}{\partial x_j} (\rho u_j \epsilon) = \frac{\partial}{\partial x_j} \left\{ \frac{\mu_t}{\sigma_\epsilon} \frac{\partial \epsilon}{\partial x_j} \right\} + S^\epsilon \quad (1.5)$$

The above five sets of equations may all be written in the form of a general transport equation:

$$\frac{\partial}{\partial x_j} (\rho u_j \phi) = \frac{\partial}{\partial x_j} \left\{ \Gamma \frac{\partial \phi}{\partial x_j} \right\} + S^\phi \quad (1.6)$$

for the dependant variable  $\phi$  and the corresponding non-linear source term  $S^\phi$

The general transport equation (1.6) can be written in computational coordinates ( $\xi, \eta, \zeta$ ) as

$$\begin{aligned} & \frac{1}{J} \left\{ \left[ \rho G_1 \phi \right]_\xi + \left[ \rho G_2 \phi \right]_\eta + \left[ \rho G_3 \phi \right]_\zeta \right\} \\ &= \frac{1}{J} \left\{ \left[ \mathcal{M} a_1 \phi \right]_\xi + \left[ \mathcal{M} a_2 \phi \right]_\eta + \left[ \mathcal{M} a_3 \phi \right]_\zeta + S \right\} + S^\phi \end{aligned} \quad (1.7)$$

where  $J$  is the Jacobian of the transformation.

The source term  $S$  incorporates all the non-normal diffusive fluxes through the faces:

$$S = \left[ J\Gamma\beta_1\phi_\eta \right]_\xi + \left[ J\Gamma\beta_1\phi_\xi \right]_\eta + \left[ J\Gamma\beta_2\phi_\zeta \right]_\eta \\ + \left[ J\Gamma\beta_2\phi_\eta \right]_\zeta + \left[ J\Gamma\beta_3\phi_\xi \right]_\zeta + \left[ J\Gamma\beta_3\phi_\zeta \right]_\xi \quad (1.8)$$

The general transport equation can then be integrated over each finite volume. The resulting equation is a form of difference equation which may be linearised and solved by application of a suitable differencing scheme.

## 2 THE DIFFERENCING SCHEME

In terms of the linearised coefficients the general transport equation (1.6) becomes

$$A_P\phi_P = A_E\phi_E + A_W\phi_W + A_N\phi_N + A_S\phi_S + A_T\phi_T \\ + A_B\phi_b + \left[ S_{\text{general}} + S^\phi \right]_{\text{volume}} \quad (2.1)$$

where  $A_i$  are the influence coefficients at cell centres ( $E$  = East cell,  $W$  = West cell, etc)

The differencing scheme applied is termed the 'hybrid' difference, whereby central differences are taken for slow flows and upwinding is ensured for fast flows. The influence coefficients are defined as follows.

$$A_W = \max \{ F_w, D_w + 1/2 F_w, 0 \} \\ A_E = \max \{ -F_e, D_e - 1/2 F_e, 0 \} \\ A_N = \max \{ -F_n, D_n - 1/2 F_n, 0 \} \\ A_S = \max \{ F_s, D_s + 1/2 F_s, 0 \} \\ A_T = \max \{ F_t, D_t - 1/2 F_t, 0 \} \\ A_B = \max \{ F_b, D_b + 1/2 F_b, 0 \} \\ A_P = A_E + A_W + A_N + A_S + A_T + A_B$$

where lower case subscripts refer to cell faces,  
upper case subscripts refer to cell centres.

$F$  is the convective flux and

$D$  is the diffusive flux

An over relaxed red-black (ORBR) matrix solver is used to solve for the dependant variable.

### 3 THE PRESSURE CORRECTION TECHNIQUE

After obtaining solutions to the momentum equations (the 3 components of velocity) it is necessary to satisfy conservation of mass flow (the continuity equation). This is achieved by means of the pressure correction procedure due to C.M. Rhie (Ref.1) and is detailed in Mackenzie (Ref.3). It serves to update the pressure, density and velocity fields in such a manner that continuity is satisfied

The correction to the pressure density and velocity is found by perturbation. For step one:

$$\begin{aligned} p_{NEW} &= p_{OLD} + p' \\ \rho_{NEW} &= \rho_{OLD} + \rho' \\ u_{i,NEW} &= u_{i,OLD} + u_i' \end{aligned} \quad (3.1)$$

The pressure and density updates are linked via the ideal gas equation such that:

$$\rho' = \frac{\beta p'}{\gamma RT} \quad (3.2)$$

Mackenzie (Ref.3) details the derivation of the velocity at the centre of a cell  $\Phi$  as:

$$u_{1c} = \left[ \sum \frac{A_i u_i}{A_p} + \frac{S^*}{A_p} \right]_p - \left[ \frac{R^{u1}}{A_p} p_t + \frac{C^{u1}}{A_p} p_n + \frac{D^{u1}}{A_p} p_l \right] \quad (3.3)$$

with similar expressions for  $u_{2c}$ ,  $u_{3c}$ , the other components of velocity.

The continuity error (the difference in mass flux entering and leaving the cell) may then be expressed in terms of  $p'$ . By assuming for a first approximation that all cross derivatives of the pressure perturbation are negligible and that:

$$\sum_{j=1}^6 \frac{A_j u_j}{A_p} = 0 \quad (3.4)$$

the resulting equation may then be converted into the general transport format of (1.6). It can then be solved in a like manner to those of momentum.

The second pressure correction takes account of non-zero cross derivatives of the pressure perturbation (arising from grid non-orthogonalities).

$$P_{NEW} = P_{OLD} + p' + p'' \quad (3.5)$$

By assuming that cross derivatives of the second pressure perturbation are negligible and that:

$$\sum_{j=1}^6 \frac{A_j}{A_P} (U_{ij}' + U_{ij}'') = 0 \quad (3.6)$$

then again the resulting equation may be expressed in the general transport format of (1.6) and solved as for the first pressure correction.

The third pressure step allows for the effect of the velocity variations on the mass flow field:

$$P_{NEW} = P_{OLD} + p' + p'' + p''' \quad (3.7)$$

As in previous pressure steps it is assumed that cross derivatives of the second and third pressure perturbations are negligible and that:

$$U_i''' = 0 \quad (3.8)$$

Again the resulting equation can be expressed in the form of (1.6) and solved as in previous pressure steps.

#### 4 THE TREATMENT OF BOUNDARY CONDITIONS

There are four types of boundary condition considered within the code:

- (1) Solid surface
- (2) Far field (free stream)
- (3) Symmetry plane
- (4) Inflow/Outflow

On solid surfaces the velocity is set to zero and hence the convective and diffusive fluxes also, while a zero pressure gradient is enforced between the cell centre and the surface (for which it is assumed that the first cell lies within the boundary layer). A  $w_2^2$  function is introduced to deal with the turbulent quantities in the near wall region (where the  $k-\epsilon$  turbulence model breaks down). The function adopted is based on a one dimensional Couette flow assumption which implies a constant shear stress and no streamwise pressure gradient in the near wall region (where the  $k-\epsilon$  turbulence model breaks down).

Far field require a fixed pressure and a zero normal gradient for all other flow variables.

Symmetry planes force a zero normal gradient on the dependant variable  $\phi$

Inflows and outflows are treated as entropy conserving Riemann invariants except for supersonic inflows where all static conditions are specified. Each individual cell is interrogated to determine its state (inflow or outflow, sub or supersonic) in order to allow variations across these planes

All boundary conditions are implemented by the use of halo cells. These halo cells are internally generated and surround the entire working domain

On interblock boundaries no explicit boundary condition is applied. The halo values are accessed as real cells but are not updated in the normal process of the solution

## 5 DISSIPATION

In order to stabilise the pressure solver a fourth order explicit dissipation term is included. This term takes the form.

$$DISS_e^{u1} = \left\{ \frac{1}{2} \left[ \left( \frac{B^{u1}}{A_p} p_i + \frac{C^{u1}}{A_p} p_\eta + \frac{D^{u1}}{A_p} p_\zeta \right)_P + \left( \frac{B^{u1}}{A_p} p_i + \frac{C^{u1}}{A_p} p_\eta + \frac{D^{u1}}{A_p} p_\zeta \right)_E \right] \right. \quad (5.1)$$

$$\left. - \left[ \frac{B^{u1}}{A_p} p_i + \frac{C^{u1}}{A_p} p_\eta + \frac{D^{u1}}{A_p} p_\zeta \right]_e \right\}$$

and serves as a flux corrector creating a non-linear feedback between the linearised flux and the pressure gradient. Similar expressions exist for  $DISS_e^{u2}$ ,  $DISS_e^{u3}$  etc.

## 6 THE MULTIBLOCK CONCEPT

Multiblocking is a procedure to enable the modelling of complex geometries without the need of large in-core memory. A large, complex domain is split into smaller and simpler blocks, the flow through each being solved separately. Communication between the blocks is achieved via the 'halo' cells (the virtual cells which surround the entire block). Values in the halo cells are determined by the boundary conditions. On interblock boundaries the values put into the halo cells are simply the values in the real cells (of adjoining blocks) which they overlap. The solution procedure is thus:

- (a) Read block one into core memory.
- (b) Set up halo cell values
- (c) Solve for momentum, pressure, energy and turbulence.
- (d) Put updated block one values into storage
- (e) Feed block two data into core memory
- (f) Set up halo cell values (accessing updated block one)
- (g) Solve for momentum, pressure, energy and turbulence.
- (h) etc.

This is repeated for each block in turn until all blocks have converged

## 7 RELAXATION TECHNIQUES

Two types of relaxation are implemented within RANSAC, a relaxation during the matrix inversion and on inertial relaxation on the dependant variable

## 7.1 MATRIX INVERSION

An over relaxed black red (ORBR) matrix inverter has been adopted within the code.

$$\phi_{PNEW} = \phi_{POLD} + \Omega \left[ \frac{\sum A_i \phi_i + S^\phi}{A_p} - \phi_{POLD} \right]$$

Where  $\Omega$  is the relaxation parameter.

Values of  $\Omega = 1.2$  have been used on the momentum equations while for pressure and turbulent quantities  $\Omega = 1.0$ .

## 7.2 INTERNAL RELAXATION

This process involves under relaxing the dependant variable by the addition of artificial inertia:

$$A_p (1 + \alpha_I) \phi_{PNEW} = \sum A_i \phi_i + S^\phi + \alpha_I \phi_{POLD}$$

It has the effect of increasing diagonal dominance and thus damping any large transient changes.

Value of  $\alpha_I = 0.8$  have been used for the momentum and energy equations,  $\alpha_I = 0.5$  for the pressure equations and  $\alpha_I = 0.0$  for the turbulent quantities.

## 8 MULTIGRID TECHNIQUE

A multigrid acceleration procedure has been implemented within RANSAC for use with the pressure correction equations. The multigrid procedure is to solve the residual equation on a coarse (reduced) grid where it is cheap to compute. The errors are then interpolated back up to the fine grid where they are used to correct the solution.

Best results are obtained for 'slow' flows where there is no strong preferred direction but speedups of up to 5 have been achieved for 'realistic' flows.



## 9 CONVERGENCE

There are two areas where 'convergence' has to be obtained in the matrix inverter itself and globally for each block. For the momentum, energy and turbulent equations the matrix inverter (ORBR) iterates until the sum of all the normalised residuals of each cell falls below an externally specified degree (usually  $10^{-10}$ ). For the pressure equations this was considered too strict (in most cases) and instead the inverter iterates until the sum of the normalised residuals on each cell falls below some factor (usually  $\approx 0.3$ ) of the residual at the onset of the inversion.

Globally, convergence is obtained when the residual for each equation solved (momentum, energy, continuity, turbulence) for every block falls below the externally specified value of  $10^{-10}$ .

## REFERENCES

- 1 Rhie, C M. 'A pressure Based Navier Stokes Solver, Using the Multigrid Method'  
AIAA Paper 86-0267 (1986)
- 2 Launder, B E 'The Numerical Calculations of Turbulent Flows'  
Spalding, D B. Computer Methods Applied Mechanical Engineering Journal, Vol.269  
(1974)
- 3 Mackenzie, C 'RANSAC A Pressure Correction Based Navier-Stokes code for  
Afterbodies with Jets'  
BAe SRC Report JS 11195 (Dec 1988)

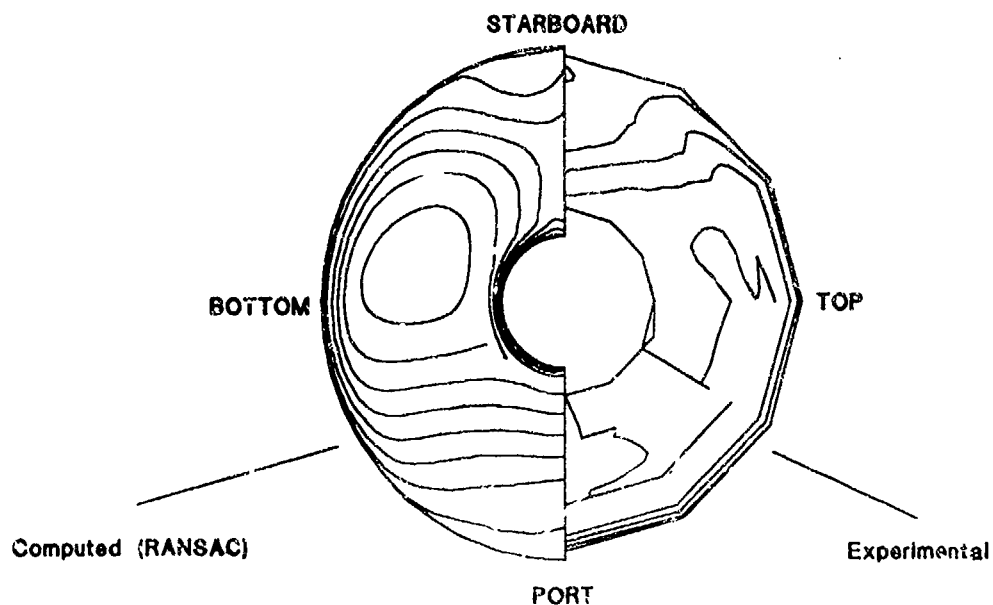
## APPENDIX A: NOMENCLATURE

$A_i$	influence coefficient for cell faces ( $i = e, w, n, s, t, b$ ) or cell centres ( $i = E, W, N, S, T, B$ )
$B''$	grouping Constant made up of Cell face areas and metric coefficients multiplying $dp/d\xi$
$C''$	grouping constant made up of cell face areas and metric coefficients multiplying $dp/d\eta$
$D_{wi}$	grouping constant made up of cell face areas and metric coefficients multiplying $dp/d\xi$
$DIS$	pressure based dissipation
$D_i$	diffusive flux through a cell face ( $i = e, w, n, s, t, b$ )
$F_i$	convective flux through a cell face ( $i = e, w, n, s, t, b$ )
$G_1$	$J(\xi x_1 u_1 + \xi x_2 u_2 + \xi x_3 u_3)$
$G_2$	$J(\eta x_1 u_1 + \eta x_2 u_2 + \eta x_3 u_3)$
$G_3$	$J(\zeta x_1 u_1 + \zeta x_2 u_2 + \zeta x_3 u_3)$
$P$	pressure
$p'$	first pressure update
$p''$	second pressure update
$p'''$	third pressure update
$R$	Gas constant (287.06 for air)
$T$	absolute temperature
$H$	enthalpy

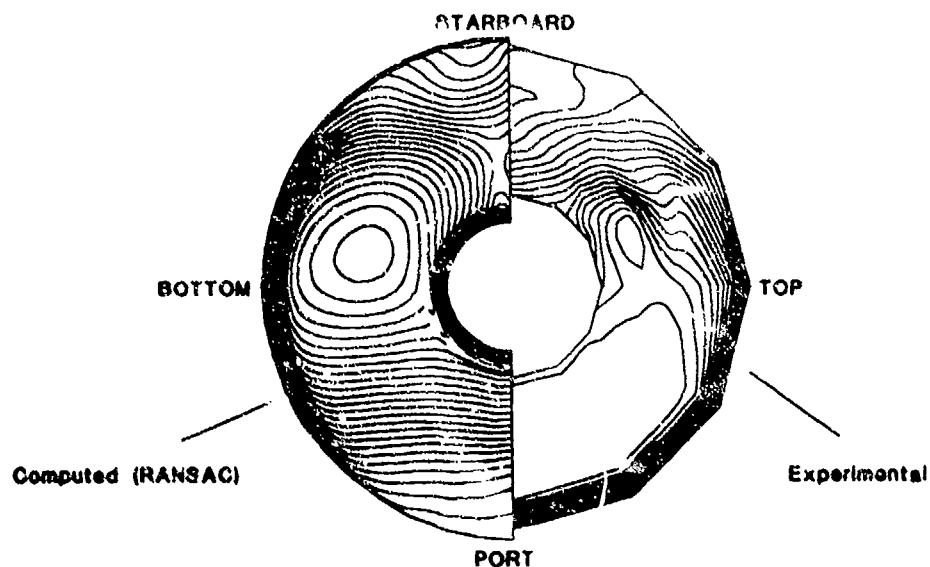
## NOMENCLATURE (continued)

Pr	Prandtl number
$S^\phi$	general source term for variable $\phi$
$u_i$	velocity component
$\alpha_1$	$(\xi_{x_1})^2 + (\xi_{x_2})^2 + (\xi_{x_3})^2$
$\alpha_2$	$(\eta_{x_1})^2 + (\eta_{x_2})^2 + (\eta_{x_3})^2$
$\alpha_3$	$(\zeta_{x_1})^2 + (\zeta_{x_2})^2 + (\zeta_{x_3})^2$
$\beta_1$	$\xi_{x_1} \eta_{x_1} + \xi_{x_2} \eta_{x_2} + \xi_{x_3} \eta_{x_3}$
$\beta_2$	$\eta_{x_1} \zeta_{x_1} + \eta_{x_2} \zeta_{x_2} + \eta_{x_3} \zeta_{x_3}$
$\beta_3$	$\zeta_{x_1} \xi_{x_1} + \zeta_{x_2} \xi_{x_2} + \zeta_{x_3} \xi_{x_3}$
$\alpha$	Ratio of specific heats $C_p/C_v$
$\rho$	density
$\mu$	laminar viscosity
$\mu_t$	turbulent viscosity
$k$	turbulent kinetic energy
$\varepsilon$	turbulent dissipation
$\sigma_k$	Effective Prandtl number for turbulent energy
$\sigma_\varepsilon$	Effective Prandtl number for turbulent dissipation

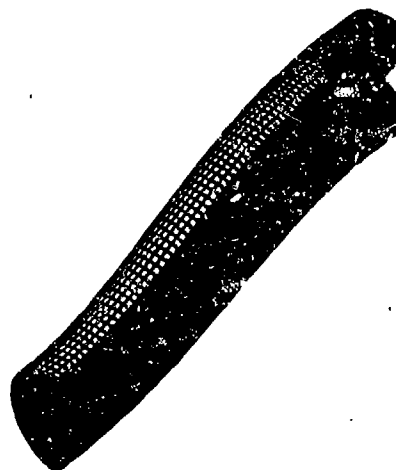
ENGINE FACE TOTAL PRESSURES  
CONTOURS OF  $P_t/P_{t0}$  ( $\delta = 0.01$ )  
TEST CASE 3.2/3537 (SLOW)



ENGINE FACE TOTAL PRESSURES  
CONTOURS OF  $P_t/P_{t0}$  ( $\delta = 0.01$ )  
TEST CASE 3.1/3532 (FAST)



## THE COMPUTATIONAL GRID

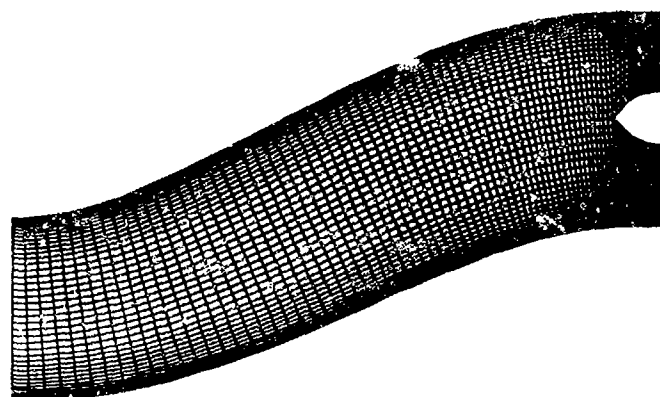


No. of Axial Cells = 81

No. of Radial Cells = 206

No. of Circumferentialw

Cells = 22



## COMPUTED DISTORTION COEFFICIENTS :

TEST CASE	PR (Non-weighted)	PR (weighted)	PEF	DCA60	DH
FAST	0.887809	0.89000	0.757	-0.417	0.286
SLOW	0.967213	0.96822	0.926	-1.724	0.082

## EXPERIMENTAL DISTORTION COEFFICIENTS :

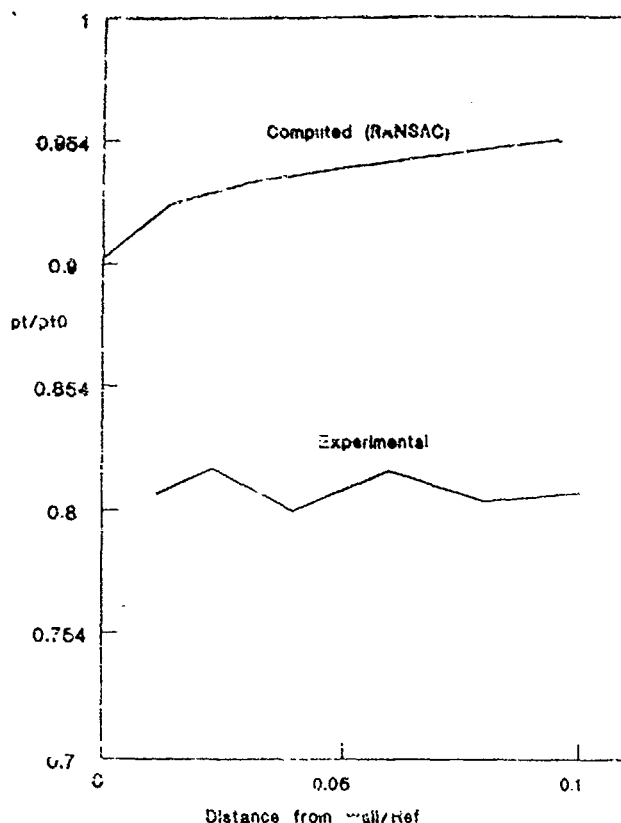
TEST CASE	PR (Non-weighted)	PR (weighted)	PEF	DCA60	DH
FAST	-----	0.92798	0.725	-0.398	0.198
SLOW	-----	0.98974	0.922	-0.226	0.041

## COMPUTED MASS FLOW :

TEST CASE MASS FLOW (Kg/s)

FAST 2.408

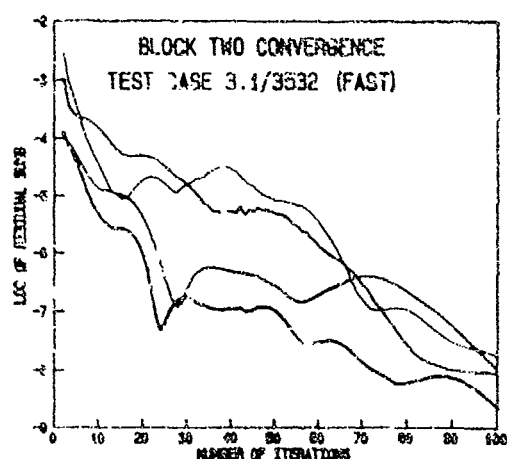
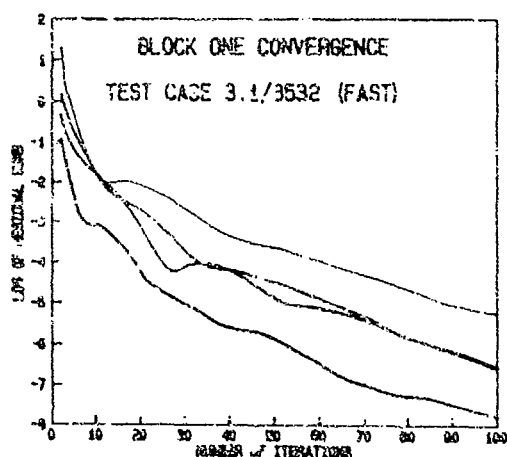
SLOW 1.481



BOUNDARY TOTAL PRESSURES  
TEST CASE 3.1/3532 (FAST)  
(STARBOARD RAKE)

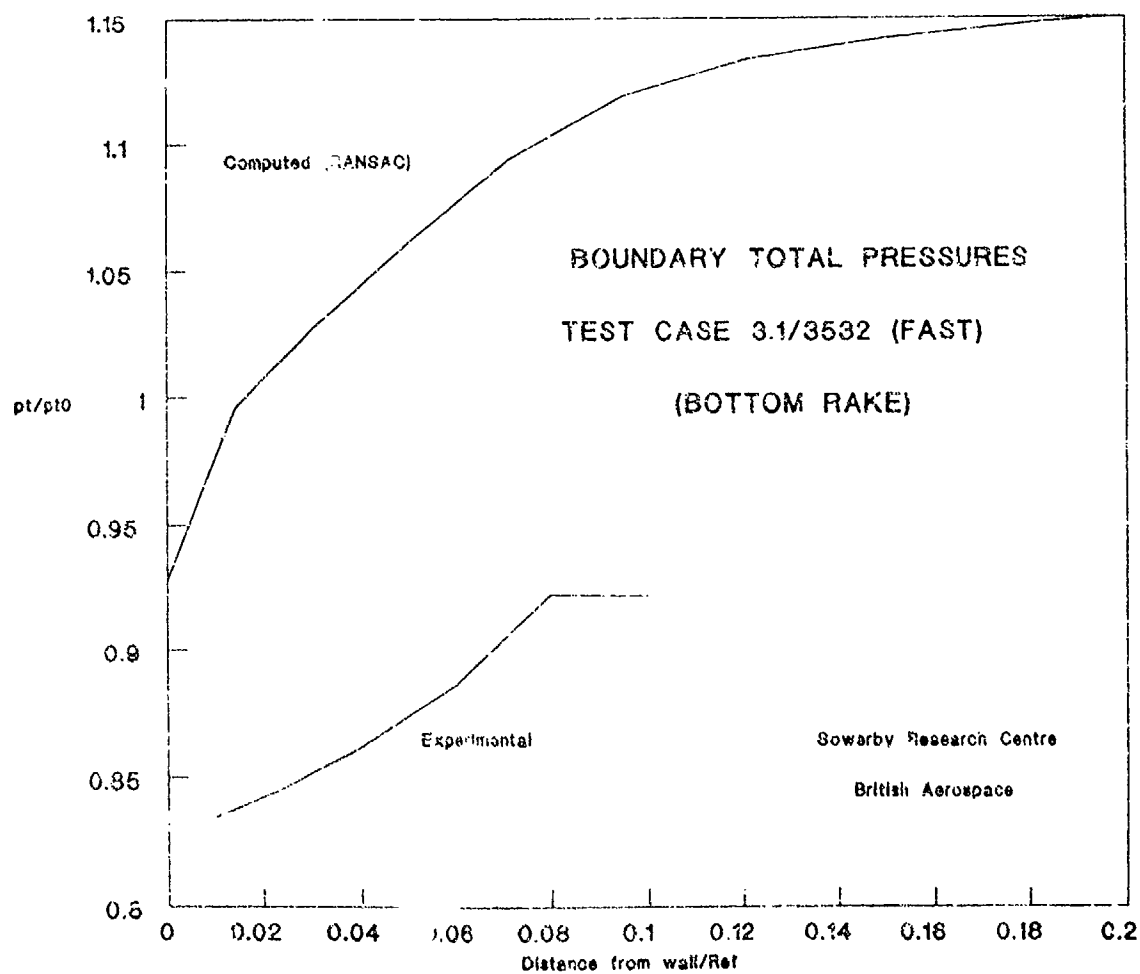
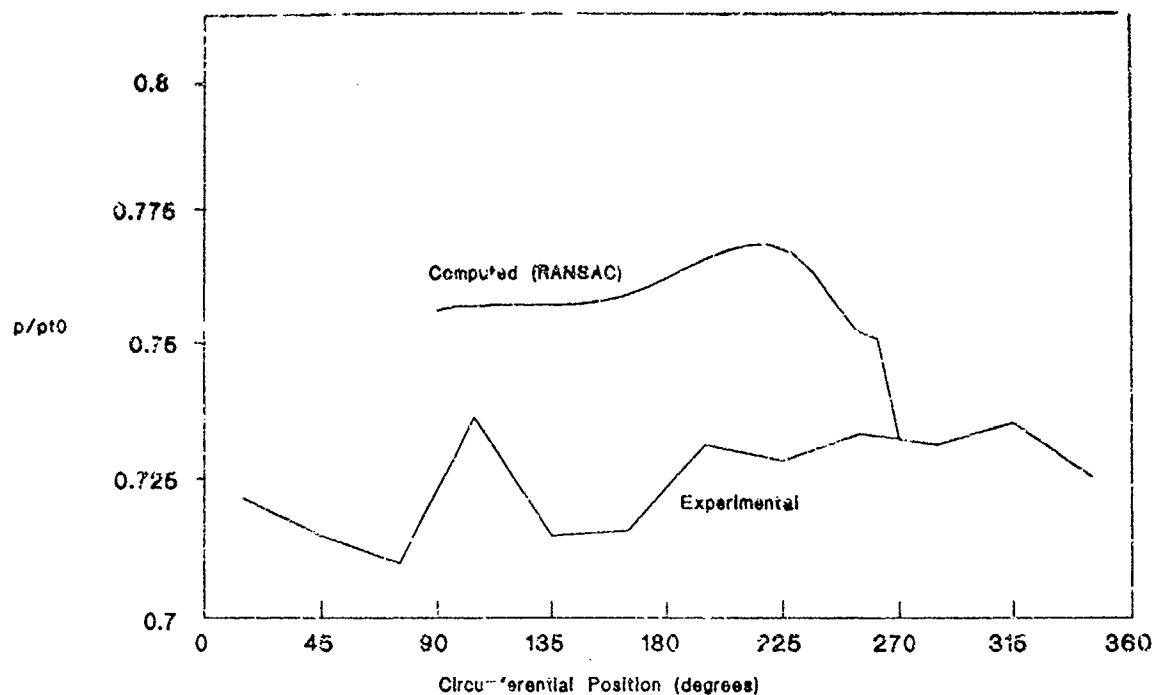
(Ref = 0.0762 m)

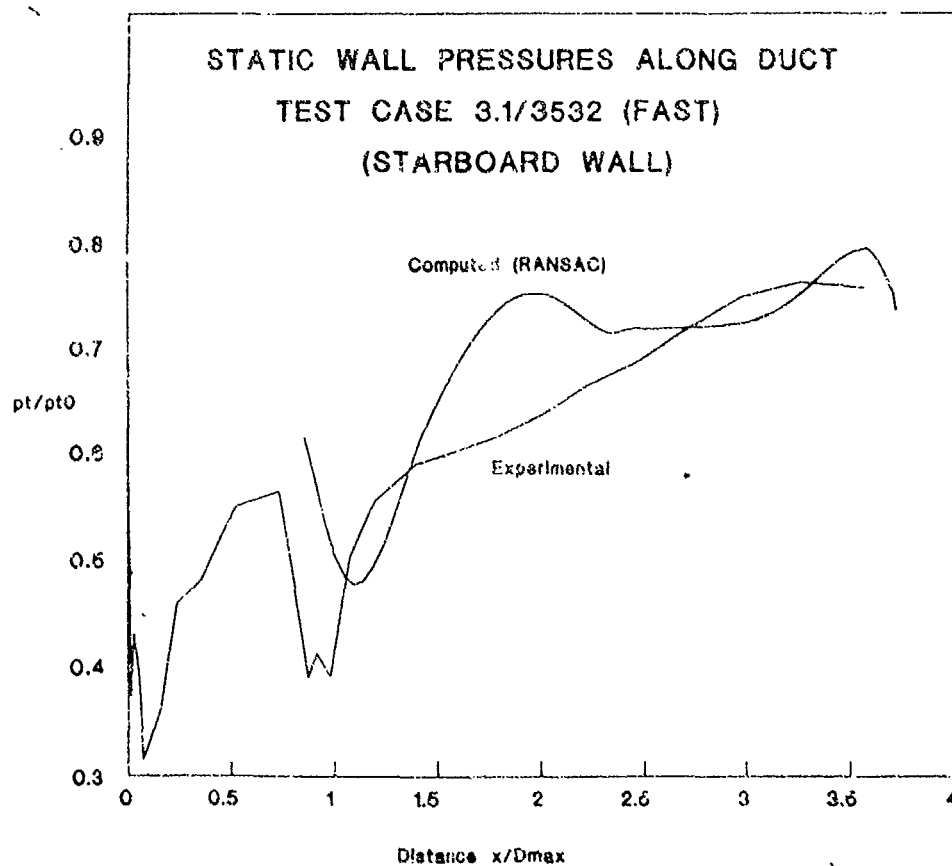
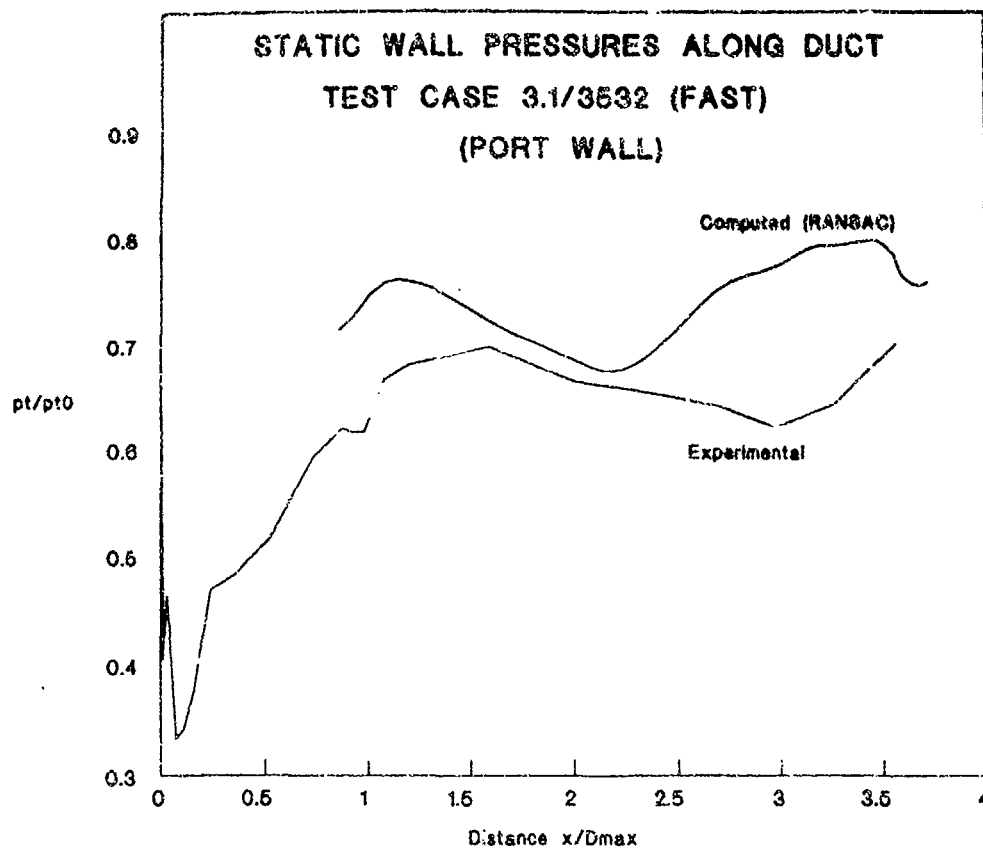
### CONVERGENCE HISTORIES



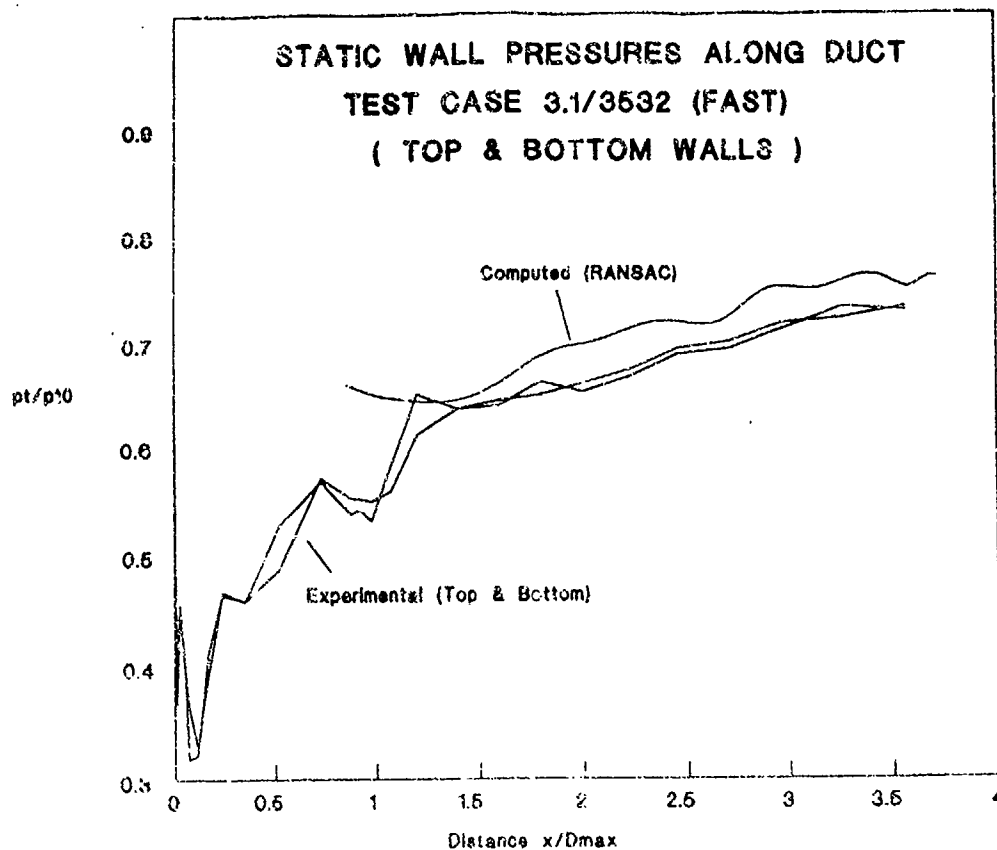
## ENGINE FACE STATIC PRESSURES

TEST CASE 3.1/3532 (FAST)

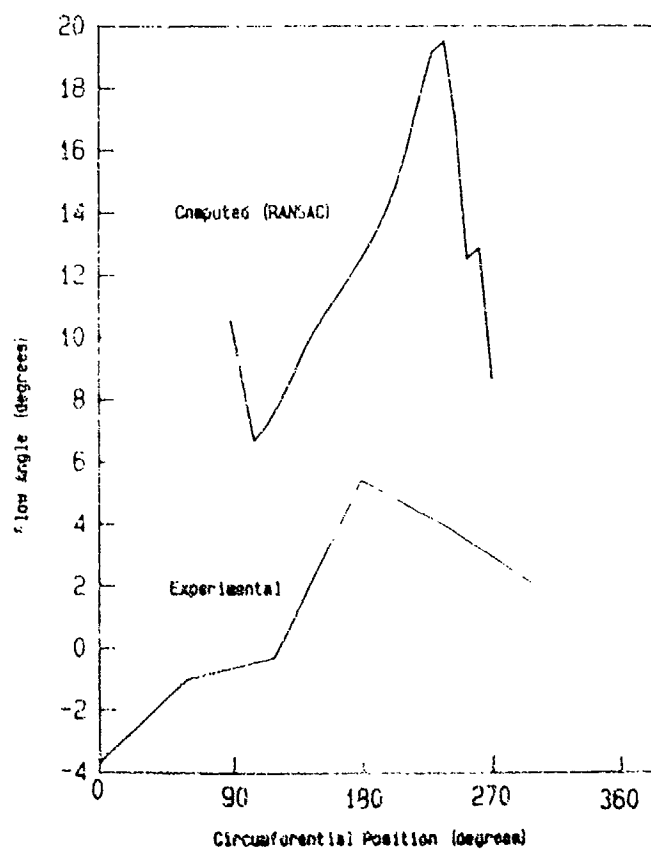


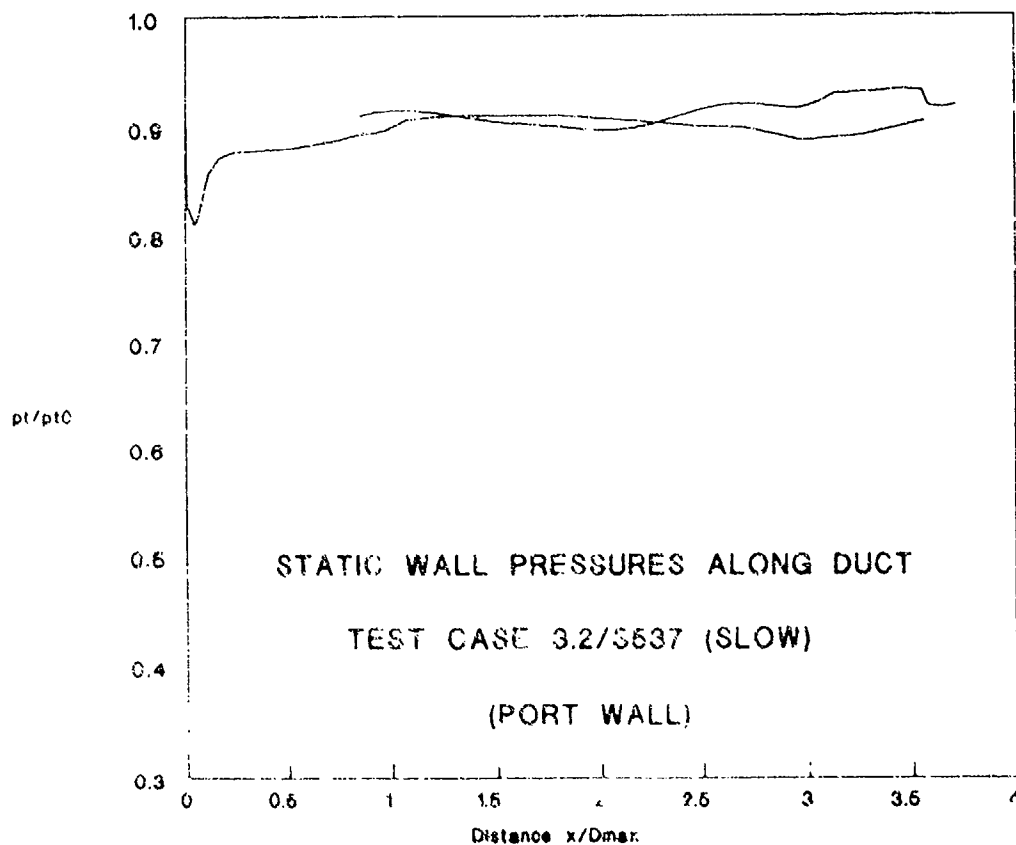
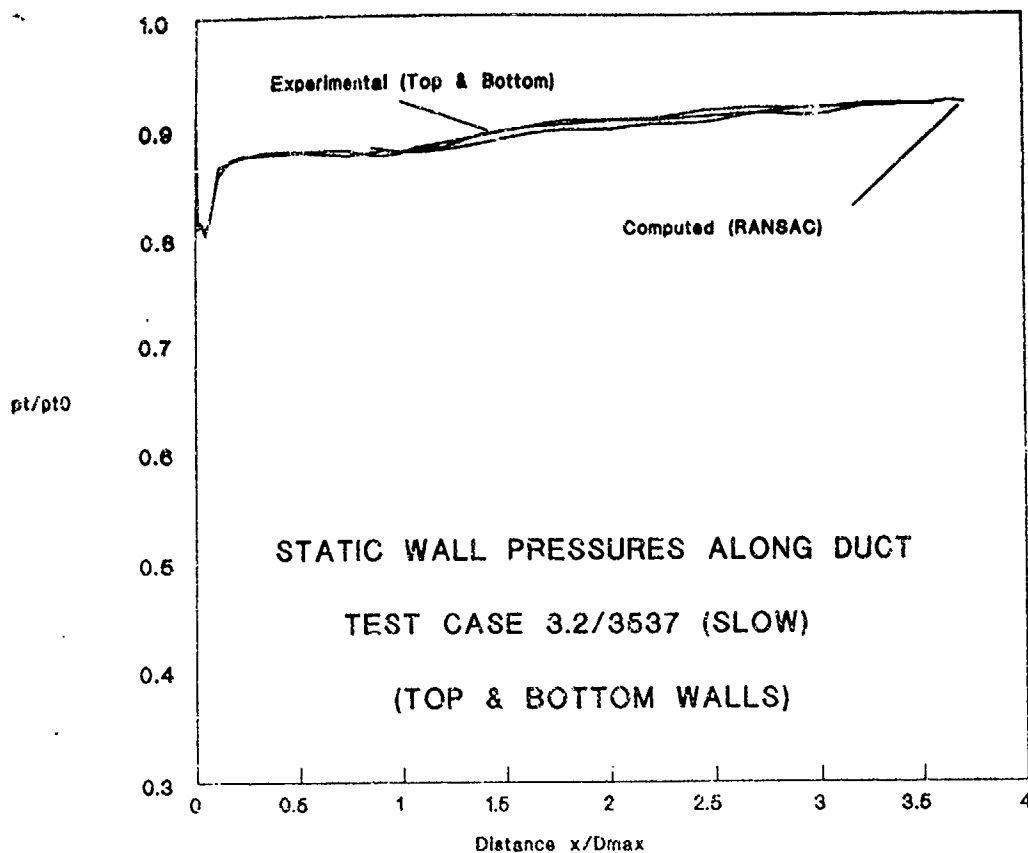


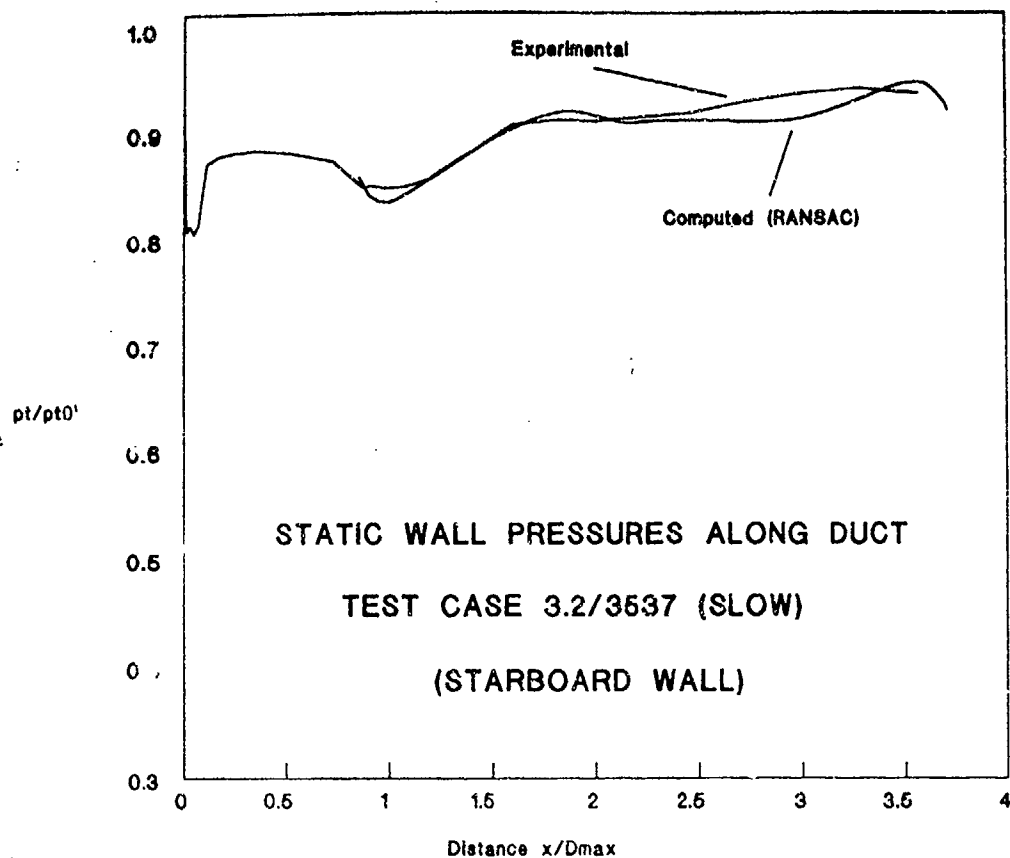




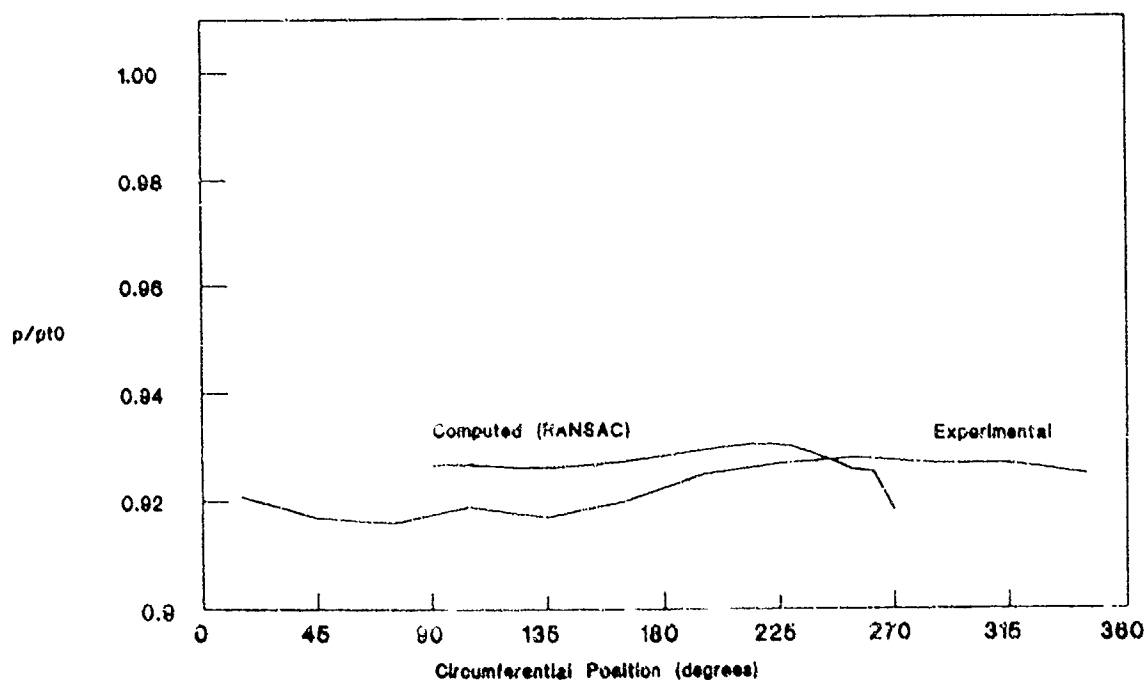
**ENGINE FACE CIRCUMFERENTIAL FLOW ANGLES**  
**TEST CASE 3.1/3532 (FAST)**





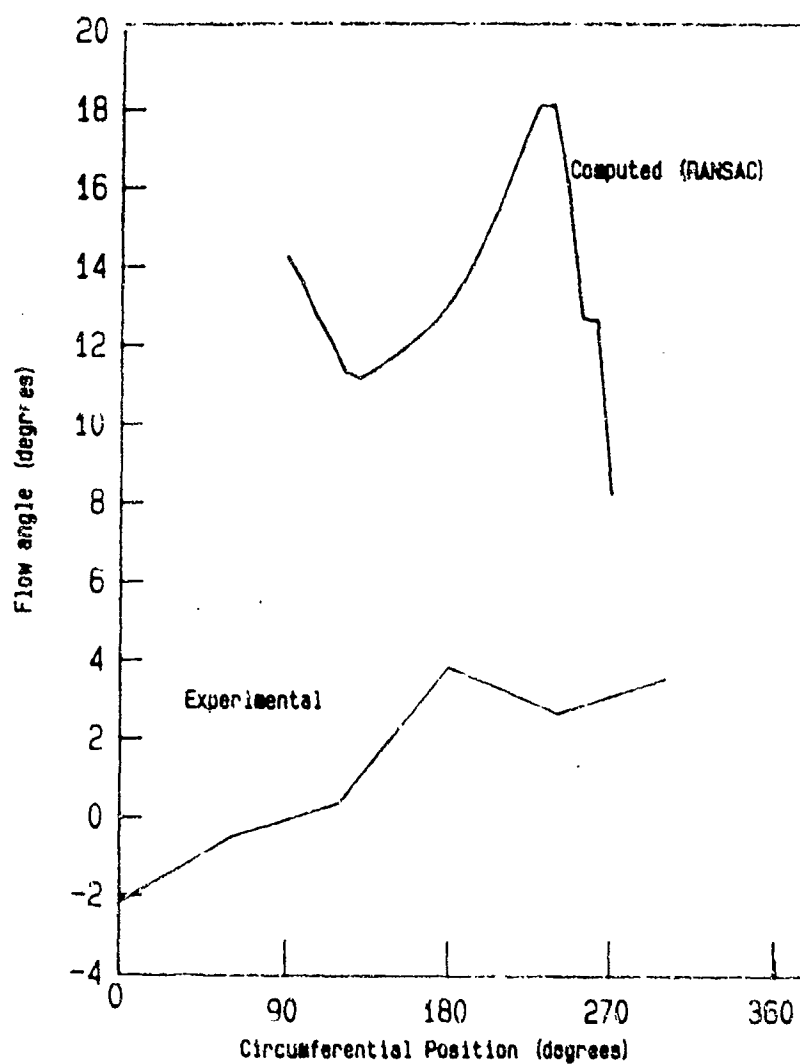


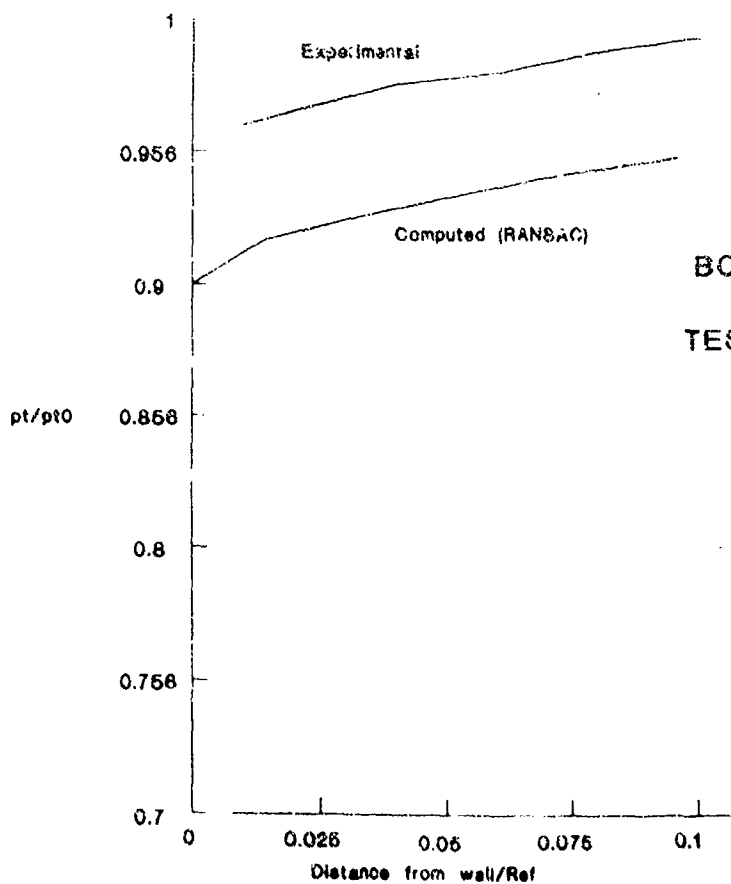
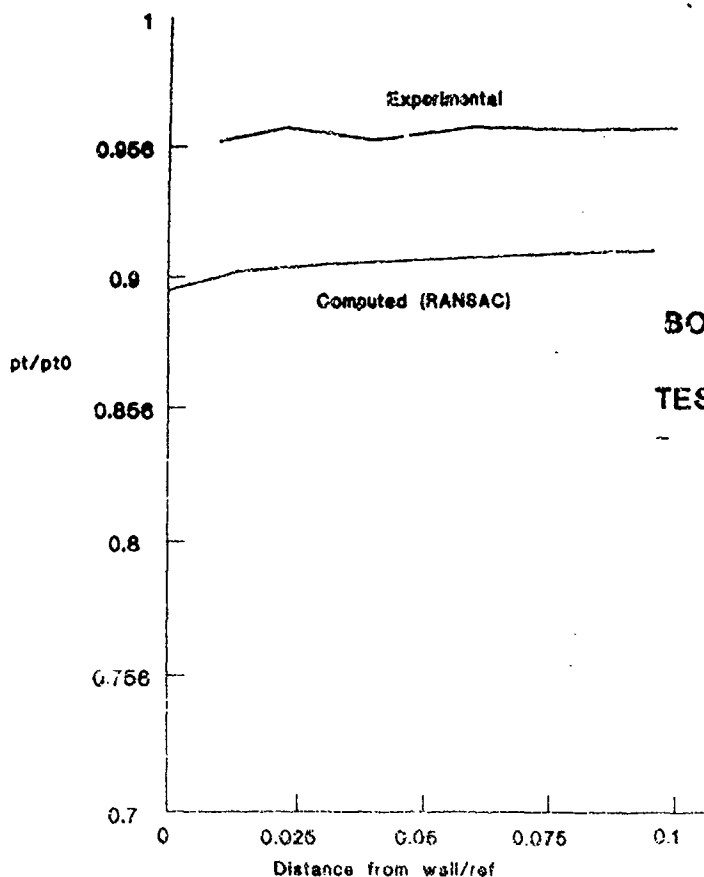
ENGINE FACE STATIC PRESSURES  
TEST CASE 3.2/3537 (SLOW)



## ENGINE FACE CIRCUMFERENTIAL FLOW ANGLES

TEST CASE 3.2/3537 (SLOW)





## Contribution of DORNIER to the Test Case 3

M. Lötzerich, F. Magagnato

### Introduction

The computations for the test cases has been carried out using Dornier's 3D blockstructured Navier-Stokes-code Ikarus. The flow solutions are obtained using an explicit version of the code based on a finite volume spatial discretisation and a Runge-Kutta-type integration in time, first presented by Jameson et. al.(1).

In order to speed up convergence, local time stepping and implicit residual averaging are applied. Furthermore a sequence of 3 mesh levels supported by up to 3 multigrid grid levels was used to achieve the steady state solution in an efficient way.

For the viscous effects the thin-layer approximation was chosen and the turbulent stresses were estimated via the Baldwin-Lomax turbulence model. For both test cases effects caused by the laminar to turbulent transition were neglected, and therefore the assumption of a fully turbulent boundary layer has been made. In order to avoid odd and even point decoupling and to reduce the numerical scheme to first order in the vicinity of shock waves an artificial viscosity term constructed as a blend of second and fourth order derivatives has been used.

Detailed descriptions of the numerical scheme can be found in (2,3).

### Meshes

With regard to the symmetry of the problem and in order to reduce the computational efforts a symmetry condition is employed in circumferential direction. Applying a slip

boundary condition on the surface of the bullet, the influence of the thin boundary layer developing on the bullet is neglected. Furthermore the computational domain is extended in the axial direction behind the engine face, in order to avoid a feed back of the constant pressure boundary condition on the measurement plane. The fine mesh consists of 99279 gridpoints and is subdivided into 3 blocks. The mesh resolution in radial direction is granted by 33, in circumferential by 17 and in axial direction by 145 gridpoints. The final mesh is depicted in Fig. 1.

### **Computer and CPU Times**

The calculations were done on a CONVEX C220. Using a single processor the required CPU times varied between 4 and 5 hours for a complete run, 500 cycles on each mesh level, depending on the workload of the machine.

### **Starting Conditions and Convergence History**

For both test cases the initial conditions for the coarse mesh has been set to freestream values, for the successive mesh levels initial conditions are obtained from the previous one by interpolation. Typical convergence plots for test case 3.2 are indicating a reduction of the residual by four orders of magnitude on each mesh level. With regard to the complex flow situation corresponding to test case 3.1 the turbulence model and the amount of artificial viscosity has to be adjusted carefully. Doing this without starting from the initial conditions causes convergence plots, which are not comparable to those of test case 3.2. However the same residual level as for test case 3.2 is obtained on the fine mesh. Furthermore the quality of the solution is checked by integration of the fluxes in cross-sections along the duct. For the transonic case a small error is introduced over the shock.

## Results

To summarize, the results obtained for test case 3.2 seem to be reasonable even for the relative coarse mesh used in the computations. Test case 3.1 describes a much more complex flow including features as shock boundary-layer-interaction or large regions of separated flow. Numerical tests upon mesh resolution and downstream pressure level indicated a very sensitive behaviour of the flow. Compared to the measurements the size of the separation bubble appears unrealistic large. The reason for this discrepancy may be thought to be due to the poor turbulence modelling, the inaccurate resolution of the shock boundary-layer-interaction, causing a too early separation of the flow, or the missing information about the laminar to turbulent transition. For a better understanding of these deviations from the measurements detailed experimental results would be helpful. With regard to the integral parameters describing the flow non-uniformity it should be mentioned, that these values are sensitive to the step size used in the integration process, and may therefore only be comparable to those obtained from a similar resolution. However the main features of the flow are described qualitatively correct for both test cases.

## References

- (1) Jameson A., Schmidt W. and Turkel E.  
 Numerical Solutions For Euler Equations By Finite Volume Method using Runge Kutta  
 Time Stepping  
 AIAA 81-1259, 1981.



(2) Jameson, A.

A Non Oscillatory Shock Capturing Scheme Using Flux Limited Dissipation

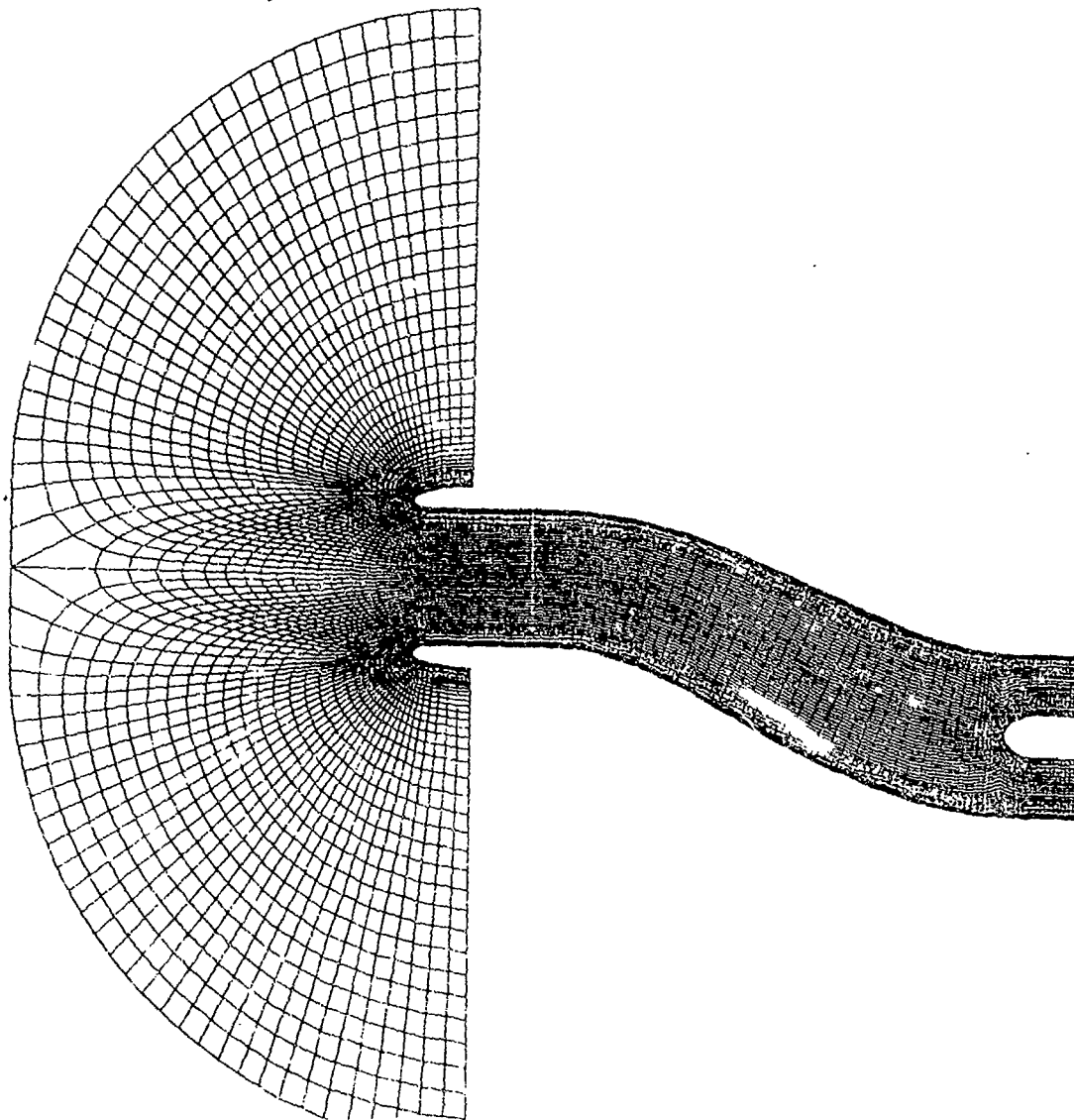
MAE Report 1653

(3) Leicher, S.

Ikarus a 3D Navier Stokes Solver For 3D-Bodies in an Arbitrary Blockstructured Grid

User Manual

Dornier Report BF 4/89 B



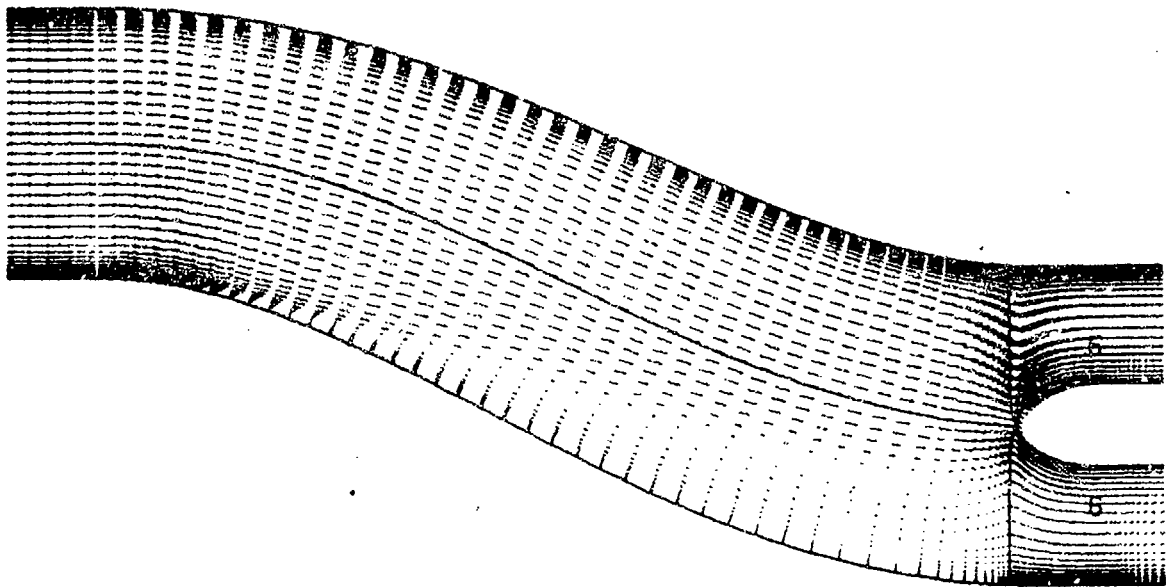


FIG. 1 : GESCHWINDIGKEITSVERTEILUNG IN DER SYMMETRIEEBENE  
TEST CASE 3.1

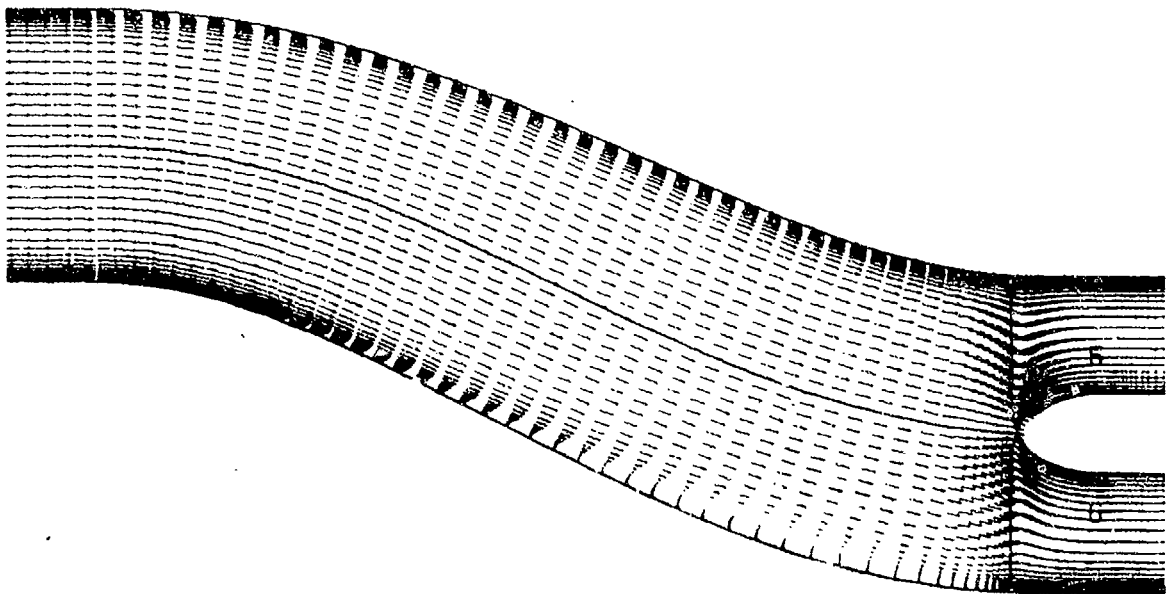


FIG. 1 : GESCHWINDIGKEITSVERTEILUNG IN DER SYMMETRIEEBENE  
TEST CASE 3.2

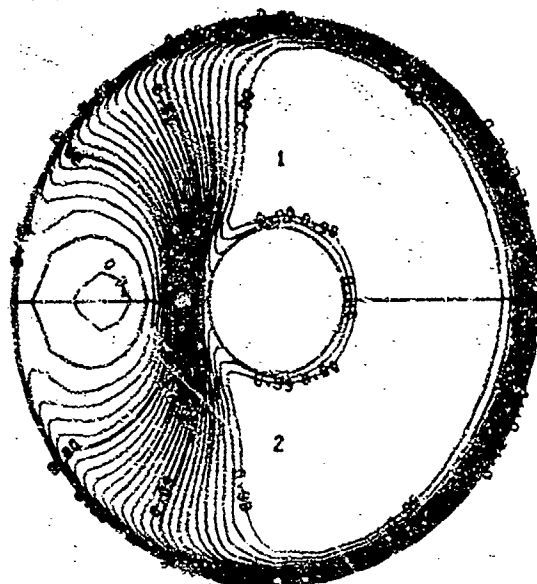


FIG. 3.1 : LINES OF CONSTANT ENGINE FACE TOTAL PRESSURES  $P_T/P_{T0}$   
TEST CASE 3.1 (DORNIER)

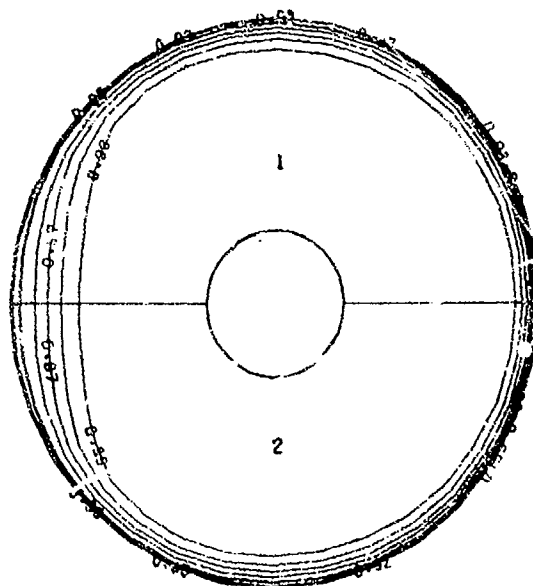
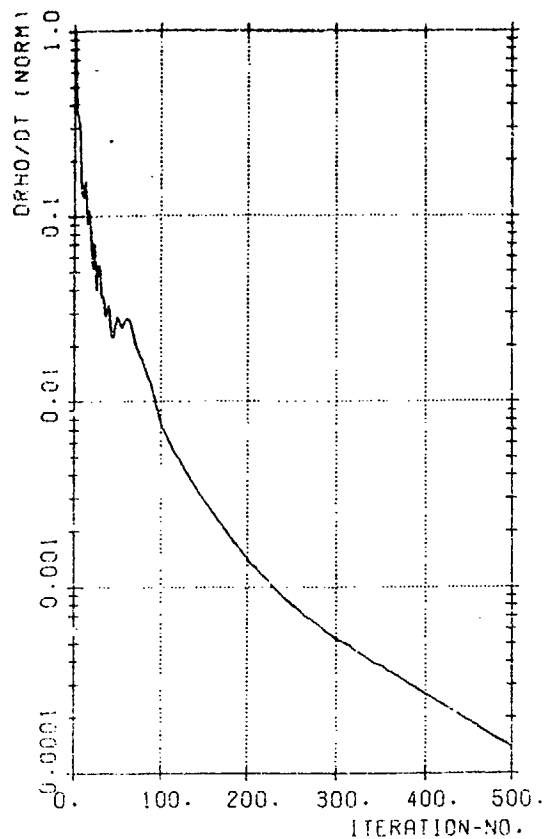
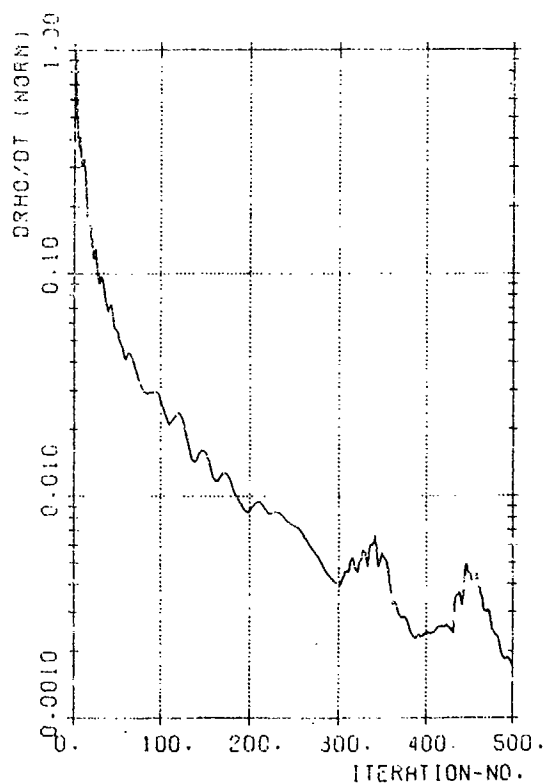


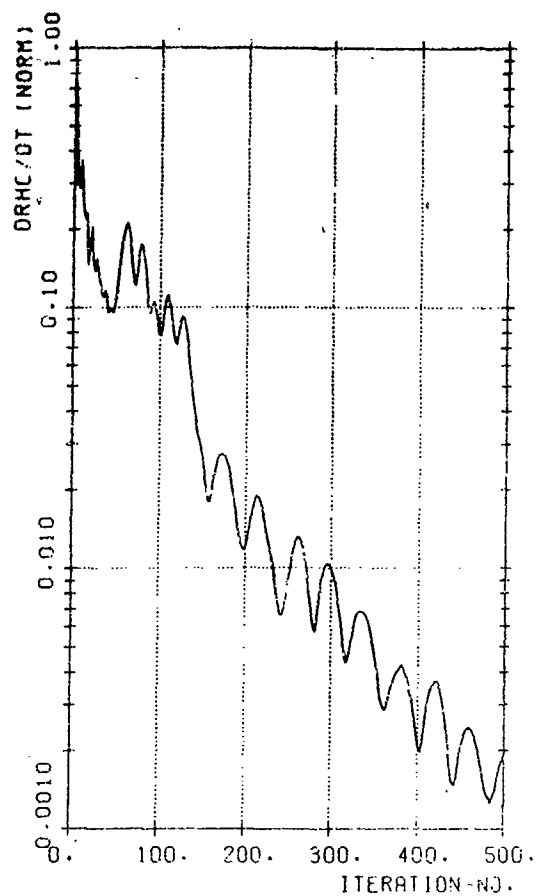
FIG. 3.1 : LINES OF CONSTANT ENGINE FACE TOTAL PRESSURES  $P_T/P_{T0}$   
TEST CASE 3.2 (DORNIER)



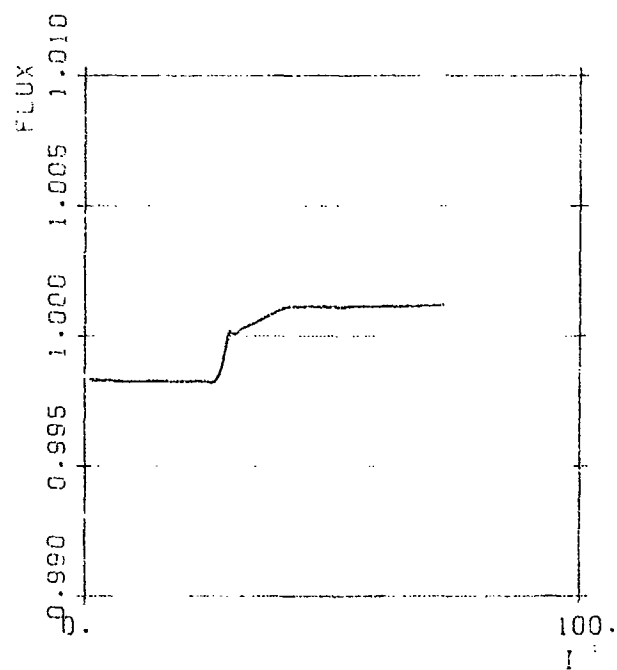
CONVERGENCE HISTORY TEST CASE 3.2  
COARSE MESH



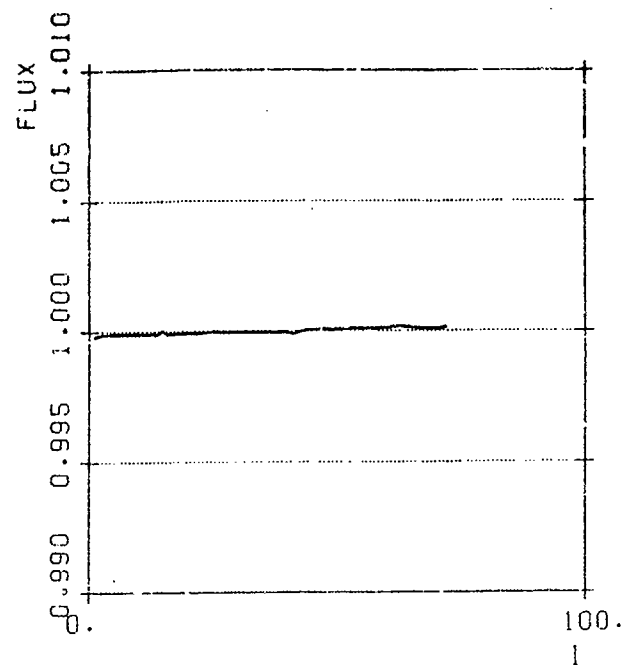
CONVERGENCE HISTORY TEST CASE 3.2  
SECOND MESH LEVEL



CONVERGENCE HISTORY TEST CASE 3.2  
FINE MESH



MASS FLUX IN CROSS-SECTIONS ALONG THE AXIS  
TEST CASE 3.1 (DORNIER)



MASS FLUX IN CROSS-SECTIONS ALONG THE AXIS  
TEST CASE 3.1 (DORNIER)

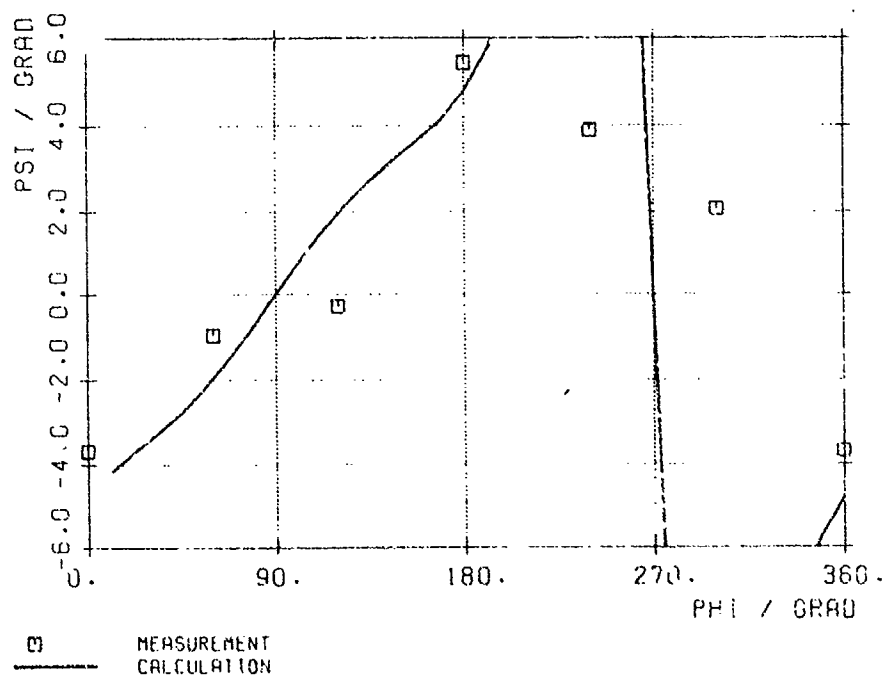


FIG. 3.4: CIRCUMFERENTIAL FLOW ANGLES AT ENGINE FACE  
TEST-CASE 3.1 (DORNIER)

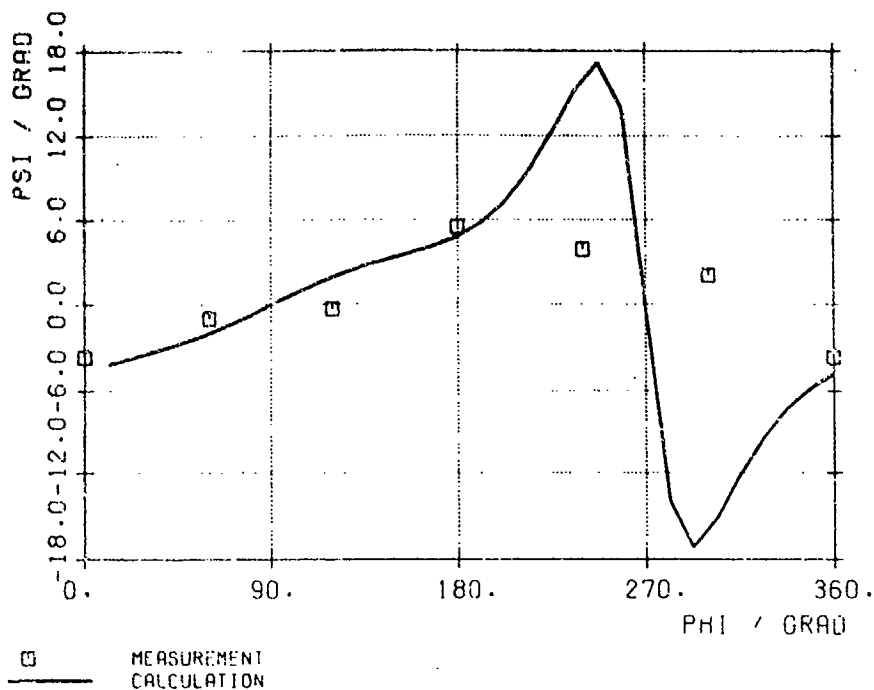


FIG. 3.4: CIRCUMFERENTIAL FLOW ANGLES AT ENGINE FACE  
TEST-CASE 3.1 (DORNIER)

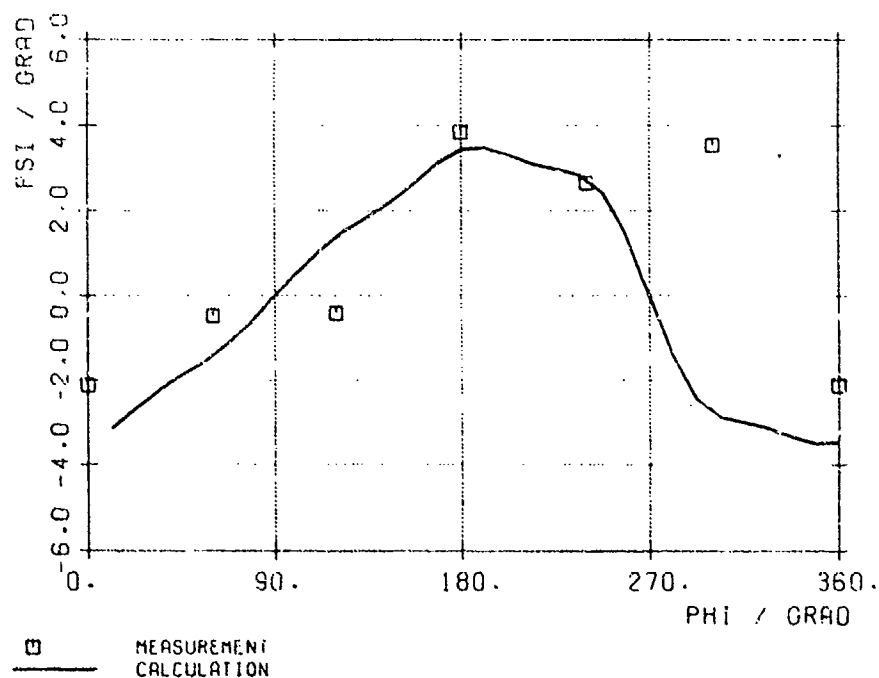
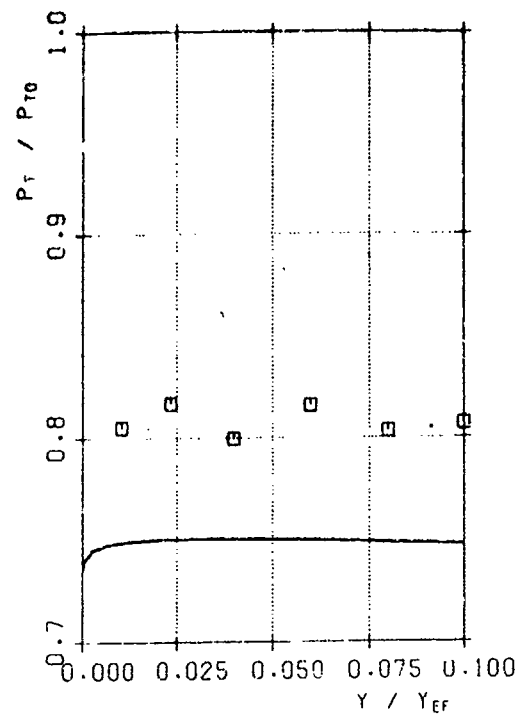


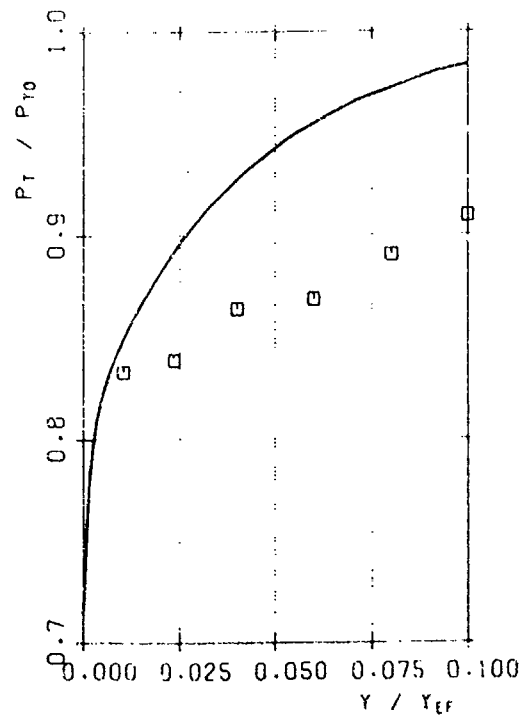
FIG. 3.4: CIRCUMFERENTIAL FLOW ANGLES AT ENGINE FACE  
TEST-CASE 3.2 (DORNIER)





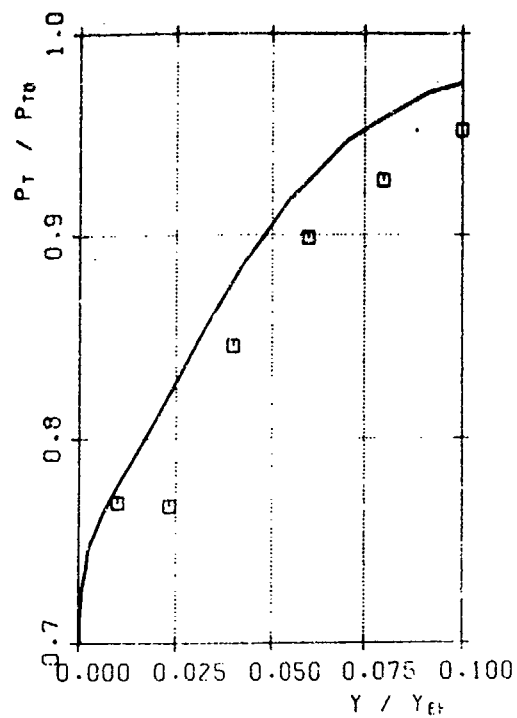
— CALCULATION  
□ MEASUREMENT

FIG. 3.2.1: TOTAL PRESSURE IN BOUNDARY LAYER AT ENGINE FACE RAKE  
TEST-CASE 3.1 STARBOARD (DORNIER)



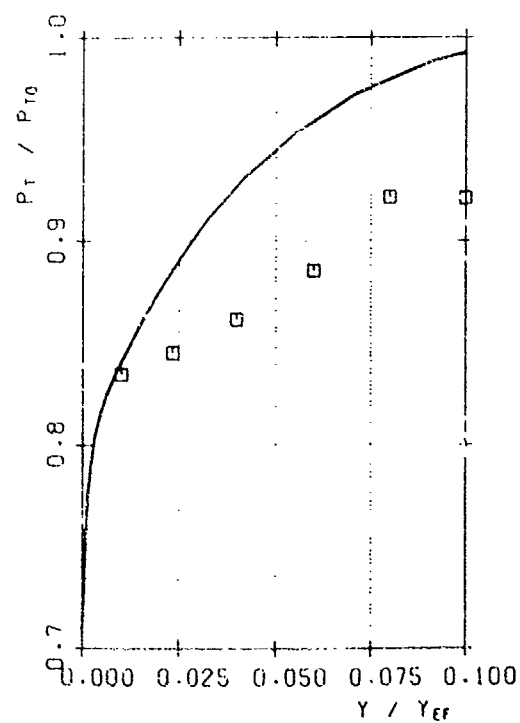
— CALCULATION  
□ MEASUREMENT

FIG. 3.2.2: TOTAL PRESSURE IN BOUNDARY LAYER AT ENGINE FACE RAKE  
TEST-CASE 3.1 TOP (DORNIER)



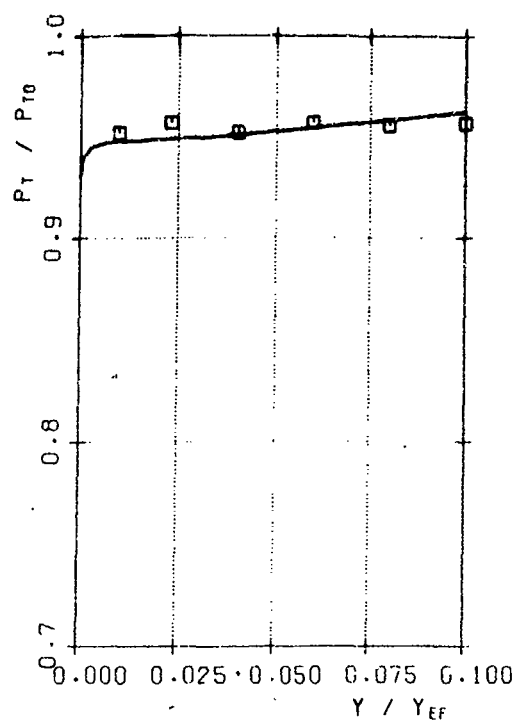
— CALCULATION  
 □ MEASUREMENT

FIG. 3.2.3: TOTAL PRESSURE IN BOUNDARY LAYER AT ENGINE FACE RAKE  
 TEST-CASE 3.1 PORT  
 (DORNIER)



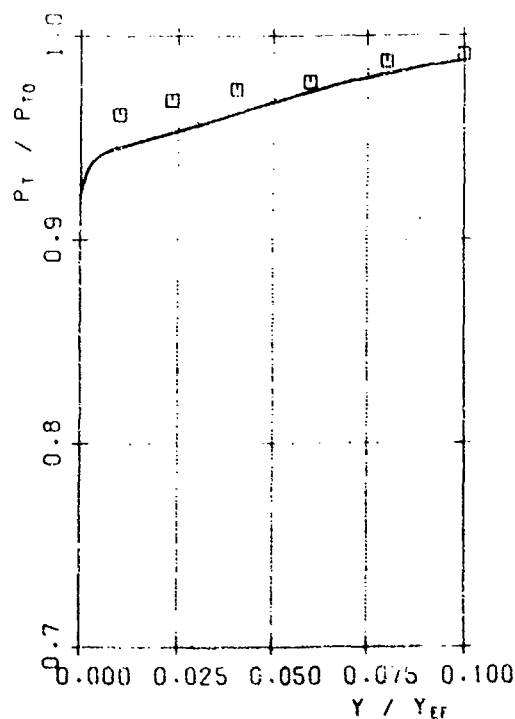
— CALCULATION  
 □ MEASUREMENT

FIG. 3.2.4: TOTAL PRESSURE IN BOUNDARY LAYER AT ENGINE FACE RAKE  
 TEST-CASE 3.1 BOTTOM  
 (DORNIER)



— CALCULATION  
 □ MEASUREMENT

FIG. 3.2.1: TOTAL PRESSURE IN BOUNDARY LAYER AT ENGINE FACE RAKE  
 TEST-CASE 3.2 STARBOARD  
 (DORNIER)



— CALCULATION  
 □ MEASUREMENT

FIG. 3.2.2: TOTAL PRESSURE IN BOUNDARY LAYER AT ENGINE FACE RAKE  
 TEST-CASE 3.2 TOP (DORNIER)

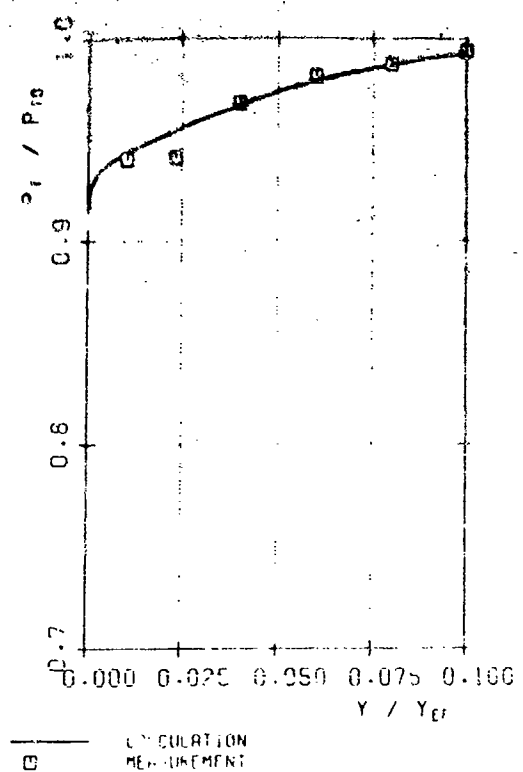


FIG. 3.2.3: TOTAL PRESSURE IN BOUNDARY LAYER AT ENGINE FACE RAKE  
TEST-CASE 3.2 PORT  
(DORNIER)

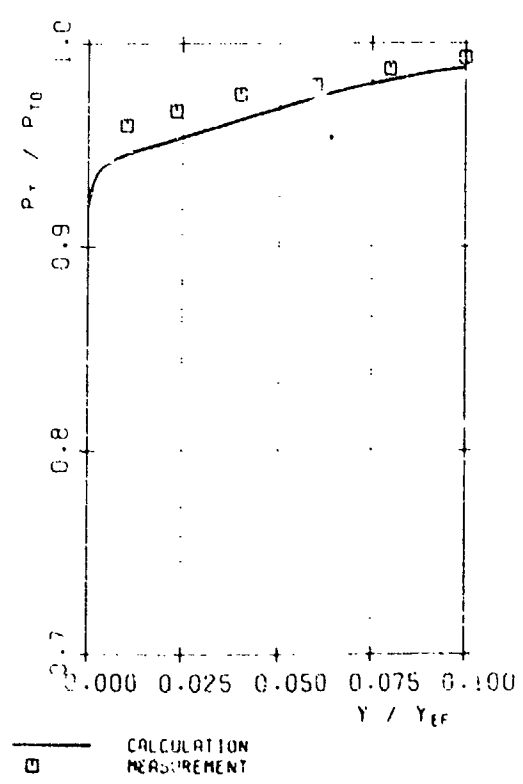


FIG. 3.2.4: TOTAL PRESSURE IN BOUNDARY LAYER AT ENGINE FACE RAKE  
TEST-CASE 3.2 BOTTOM  
(DORNIER)

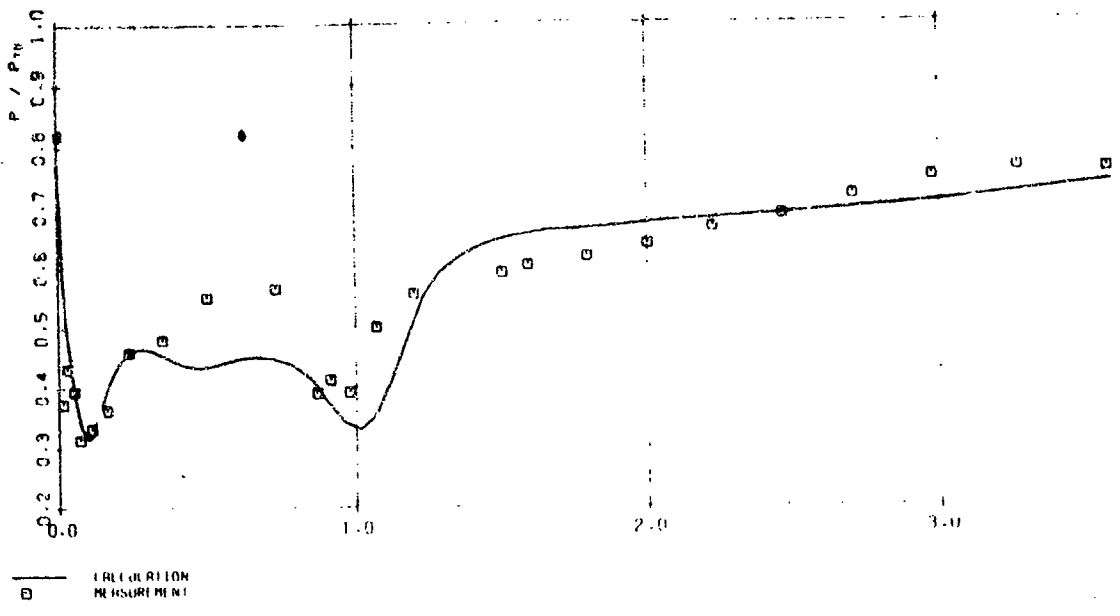


FIG. 3.5.1: STATIC WALL PRESSURE ALONG DUCT  
 TEST CASE 3.1 STARBOARD ROW (DOWNRIVER)

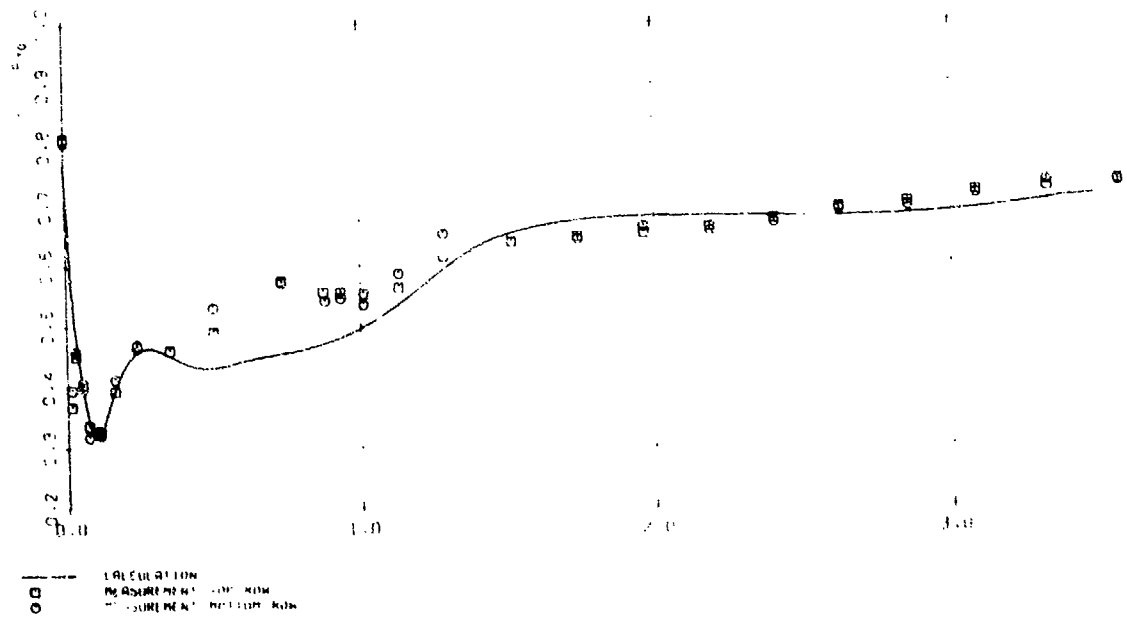


FIG. 3.5.2: STATIC WALL PRESSURE ALONG DUCT  
 TEST CASE 3.1 TOP AND BOTTOM ROW (DOWNRIVER)

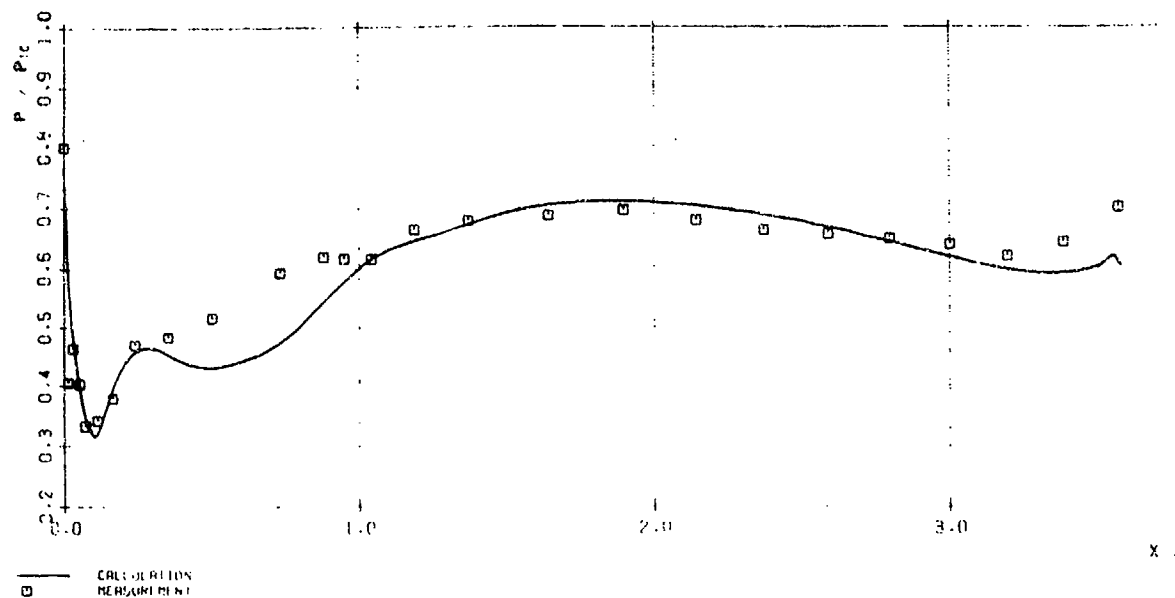


FIG. 3.5.31: STATIC WALL PRESSURE ALONG DUCT  
TEST CASE 3.1 PORT ROW 100RNER)

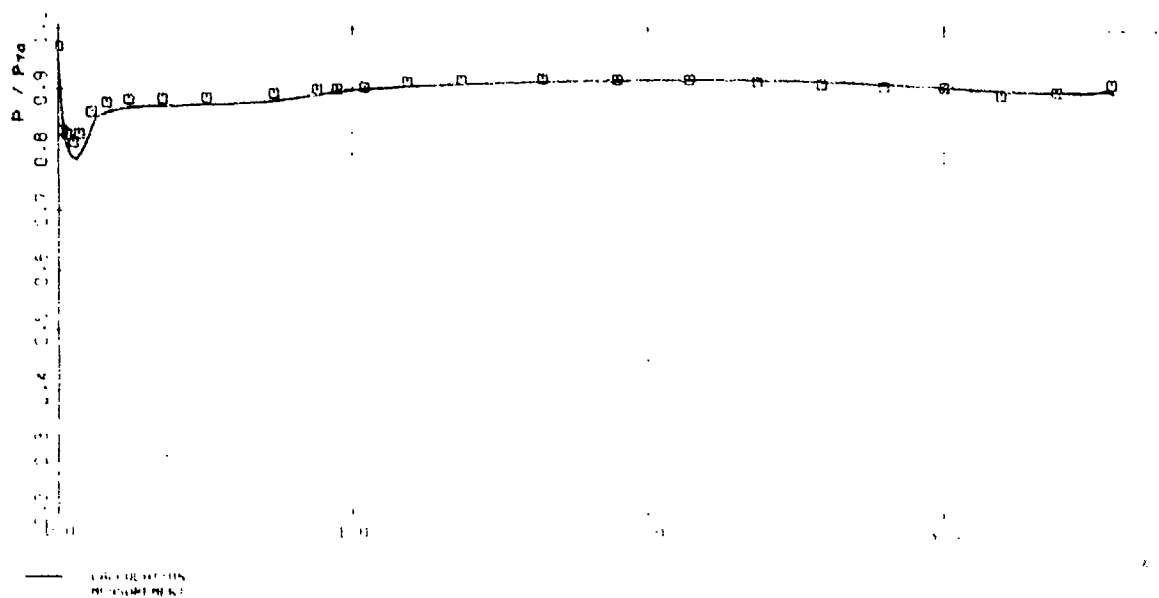


FIG. 3.5.32: STATIC WALL PRESSURE ALONG DUCT  
TEST CASE 3.2 PORT ROW 100RNER)

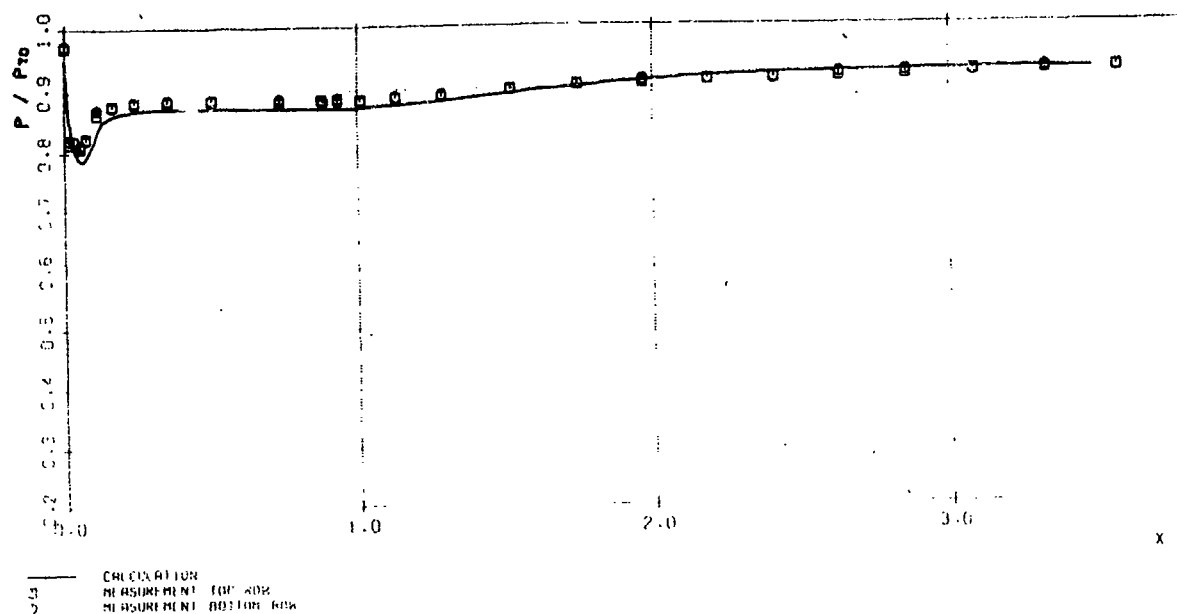


FIG. 3.5.2: STATIC WALL PRESSURE ALONG DUCT  
TEST CASE 3.2 TOP AND BOTTOM ROW (TUORNIER)

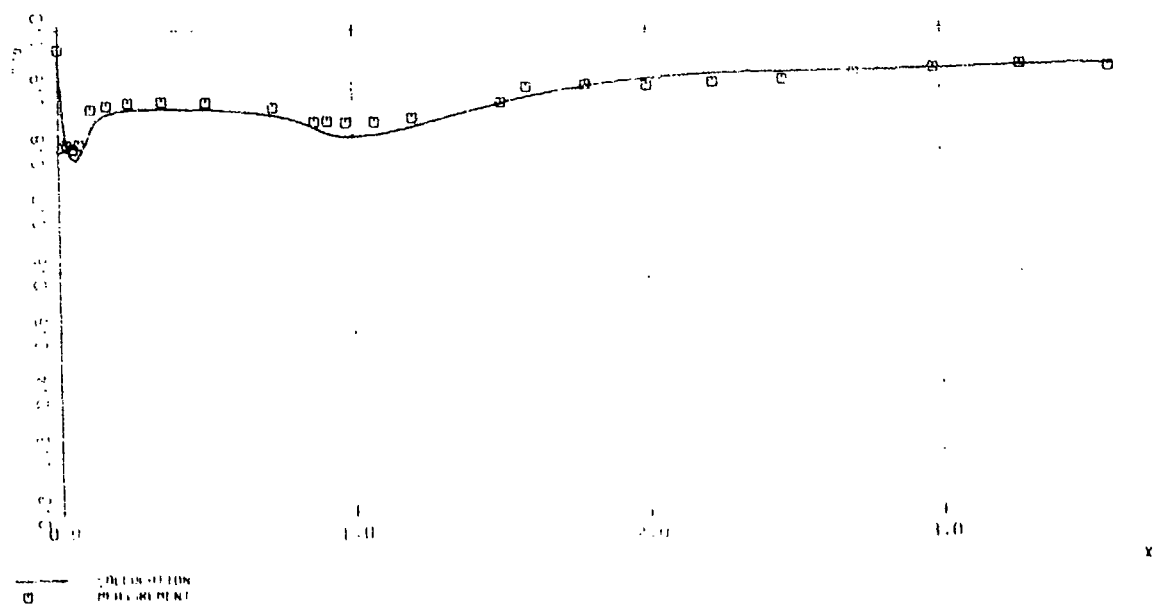


FIG. 3.5.1: STATIC WALL PRESSURE ALONG DUCT  
TEST CASE 3.2 STARBOARD ROW (TUORNIER)

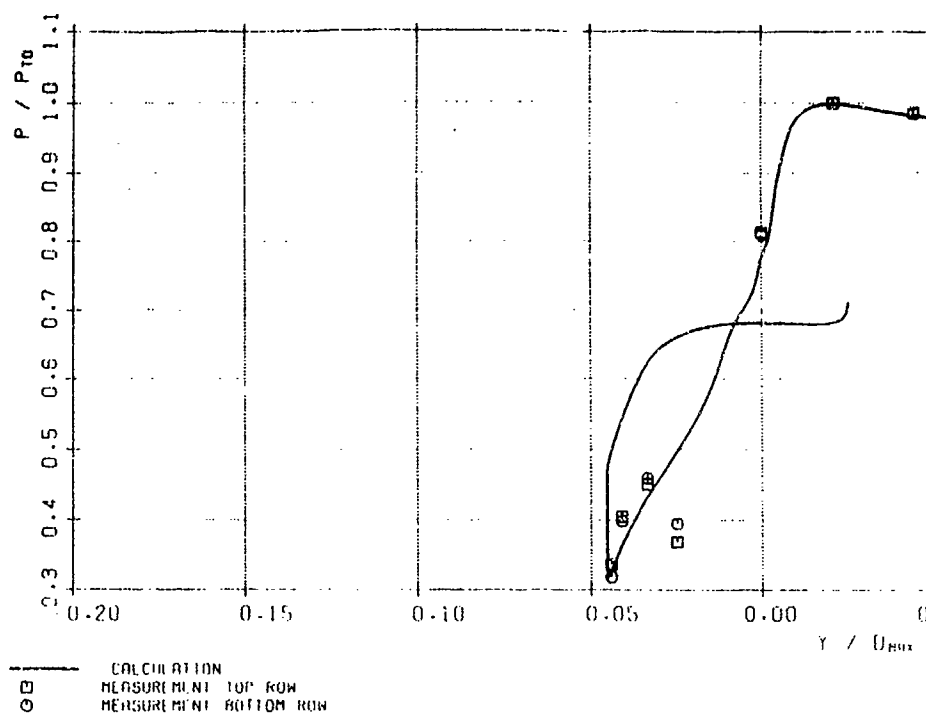


FIG. 3.6.2: STATIC WALL PRESSURES AROUND COWL LIP TEST CASE 3.1  
TOP AND BOTTOM ROW (DORNIER)

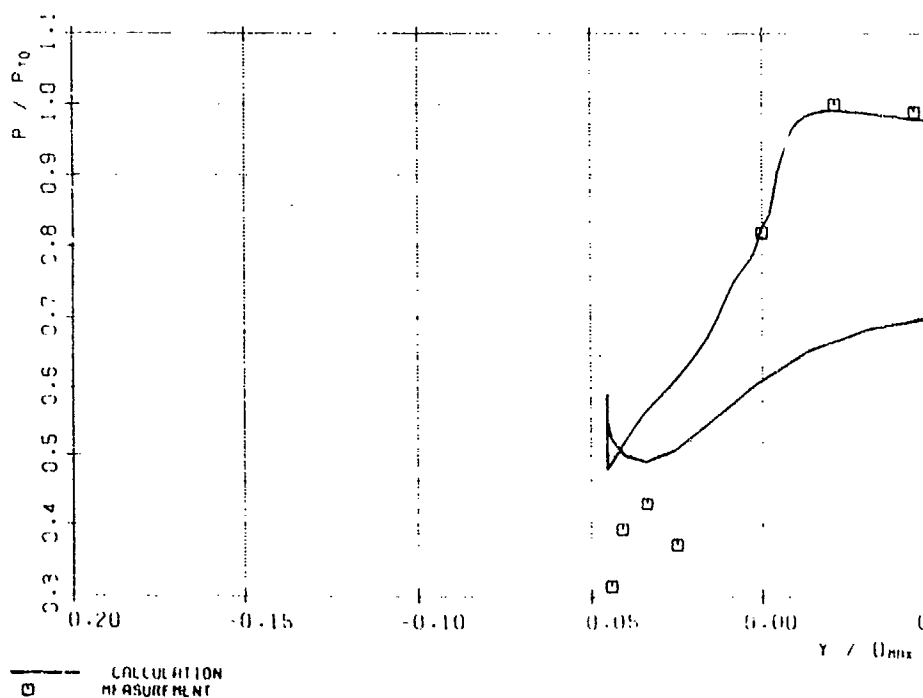


FIG. 3.6.1: STATIC WALL PRESSURES AROUND COWL LIP TEST CASE 3.1  
STARBOARD ROW (DORNIER)



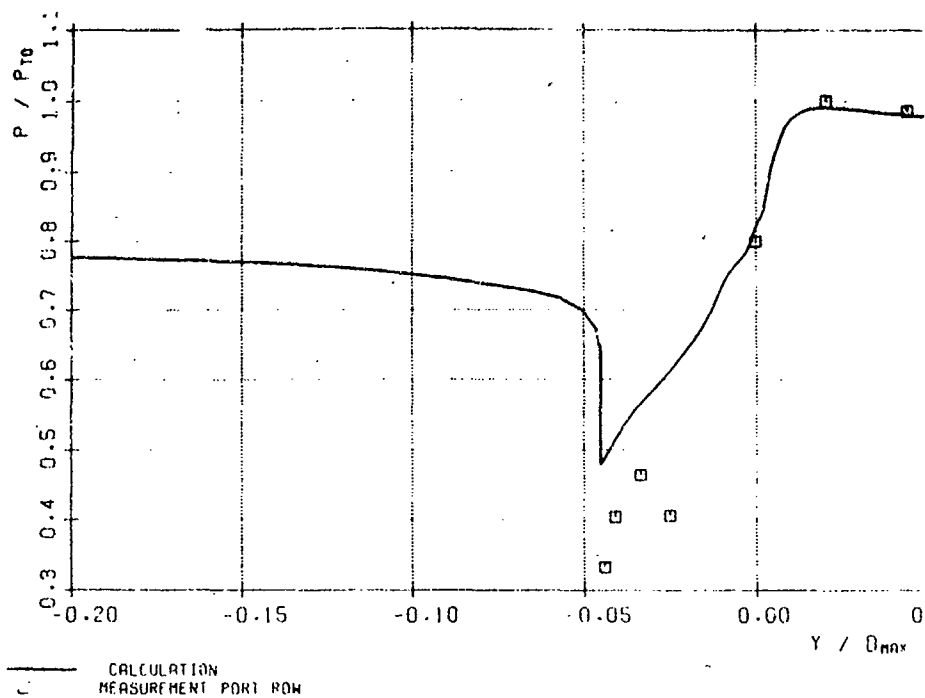


FIG. 3.6.3: STATIC WALL PRESSURES AROUND COWL LIP TEST CASE 3.1  
PORT ROW (DORNIER)

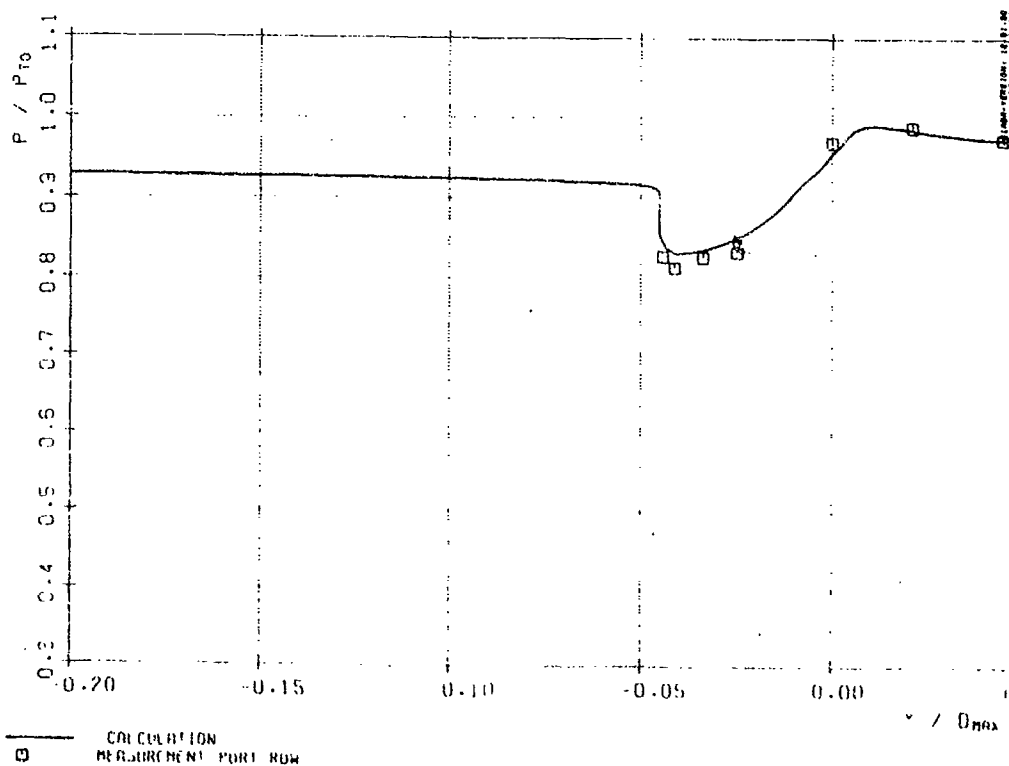


FIG. 3.6.3: STATIC WALL PRESSURES AROUND COWL LIP TEST CASE 3.2  
PORT ROW (DORNIER)

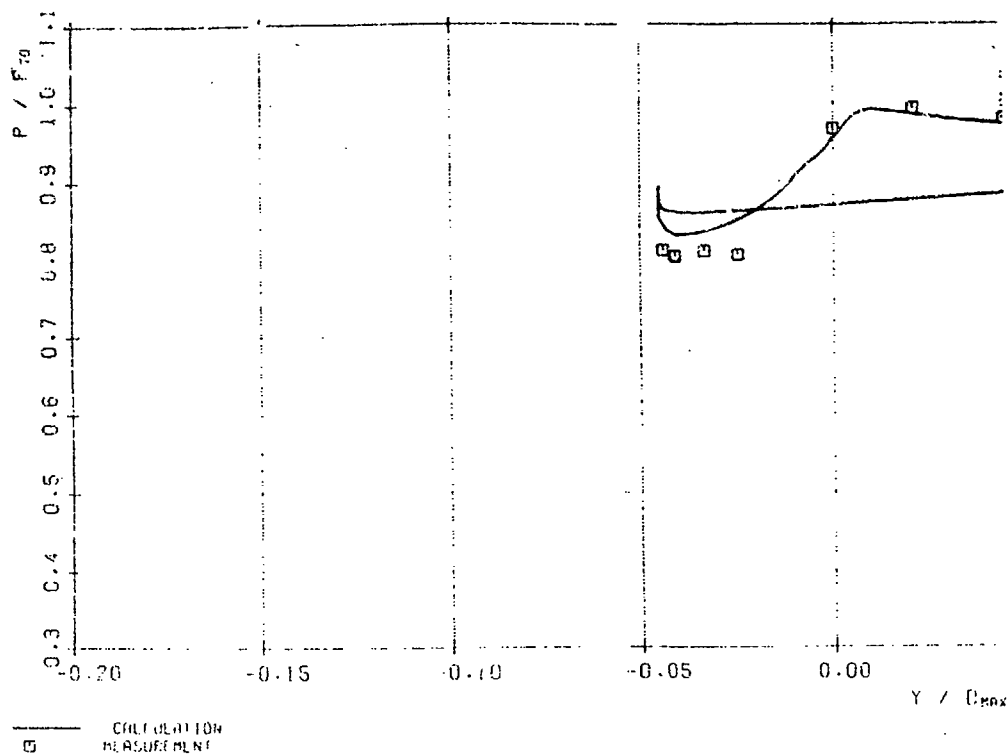


FIG. 3.6.1: STATIC WALL PRESSURES AROUND COWL LIP TEST CASE 3.2  
STARBOARD ROW (DORNIER)

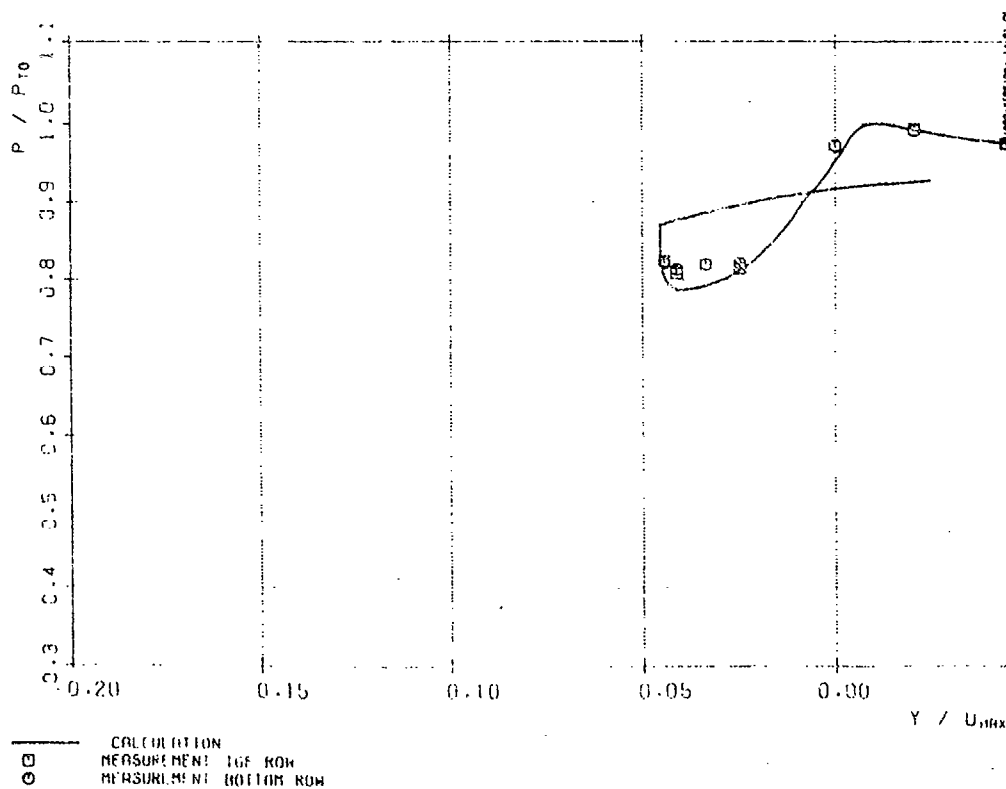


FIG. 3.6.2: STATIC WALL PRESSURES AROUND COWL LIP TEST CASE 3.2 TOP  
AND BOTTOM ROW (DORNIER)

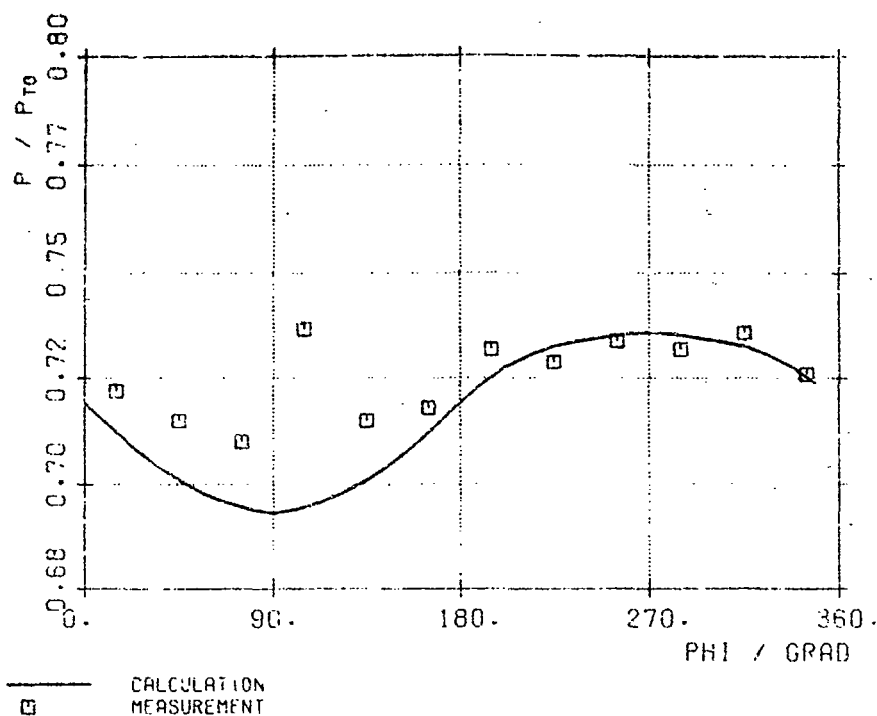


FIG. 3.3: STATIC WALL PRESSURE AT ENGINE FACE TEST-CASE 3.1 (DORNIER)

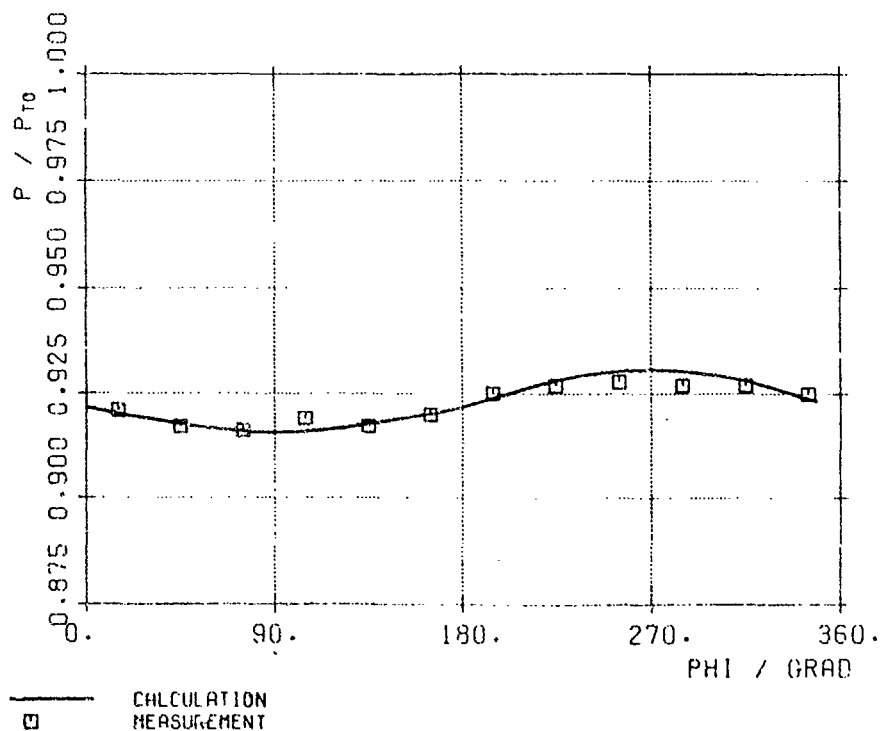


FIG. 3.3: STATIC WALL PRESSURE AT ENGINE FACE TEST-CASE 3.2 (DORNIER)



# AIRCRAFT RESEARCH ASSOCIATION LIMITED

MANTON LANE  
BEDFORD MK41 7PF

Tel: 0234 350681 Telex: 825056  
Fax Groups 2&3 0234 328584

## THE ADAPTATION OF THE ARA EULER MULTIBLOCK METHOD

### FOR CALCULATING TWO INTAKE/S-BEND DIFFUSER GEOMETRIES -

### CONTRIBUTION TO AGARD WG13 (TEST CASES 3 AND 4)

by

J A Shaw

A J Peace

S E Bounds

---

#### SUMMARY

The ARA Euler multiblock method is used to predict the flow about two intake/S-bend diffuser geometries. One configuration has a circular intake whilst the other has a semi-circular intake: the diffuser in each case terminates at a circular engine face plane. These geometries are part of a number of test cases defined by AGARD Working Group 13, whose purpose is to assess the current capabilities of relevant computer based calculation methods for air intakes. The generation by the multiblock approach of what are considered high quality grids is described in some detail, as these geometries possess features which have hitherto not been considered by the method. Inviscid solutions are presented at two mass-flow ratios for each geometry, and comparison with experimental data shows the importance of viscous effects in flows of this type.

NOVEMBER 1990

Prepared for Procurement Executive, Ministry of Defence Contract No  
A94C/2694

## 1. INTRODUCTION

In recent years, the ARA multiblock method has been applied to a wide variety of aerodynamic configurations, with two of the most geometrically complex examples to date being the fighter aircraft with intakes and nozzles and the wing/body/pylon/store model described by Shaw et al<sup>1</sup>. Such examples demonstrate the geometric versatility of the method and also the accuracy of flow solutions which can be obtained from the accompanying Euler algorithm.

This Note describes a further application of the multiblock method, namely to two intake/S-bend diffuser geometries. The geometries are a subset of a number of propulsion related configurations which were defined by AGARD Working Group (WG) 13, entitled 'Air Intakes for High Speed Vehicles', with a view to soliciting associated flow predictions from state-of-the-art computer based methods. The first of these geometries, denoted Test Case 3 by WG13, consists of an axisymmetric intake whose throat joins smoothly onto an S-bend diffuser of circular cross section, and the second, denoted Test Case 4, consists of a semi-circular intake with semi-circle- to-circle S-bend diffuser. Such geometries have obvious application to side and chin engine intakes on current military aircraft.

Each of the above test cases consists of two separate flow conditions at the same free-stream Mach number ( $M_\infty \approx 0.21$ ). The two flow conditions differ in the mass flow which is passed through the duct in each case, with the Mass Flow Ratio (MFR) characterising each of the situations. It is well known that, for even moderate mass flows through S-bend ducts of this type, where the boundary layer remains attached throughout, viscous effects are important in determining the flow. For high mass flows, flow separation may take place and secondary flows may be set up in the duct. Because the modelling of viscous effects is critical in giving an accurate picture of certainly the internal flow component of these WG test cases, it is not surprising that the majority of the contributors will be using computer methods based on solution of the Navier-Stokes equations. However, interpretation of predictions of highly viscous flows can be extremely difficult, and it was thus considered desirable by the WG that high quality inviscid solutions should be available for each of the flow conditions. Such solutions were solicited from ARA, and these were obtained from the ARA Euler multiblock method.

A brief description of the multiblock approach is given in section 2 of this document, and it will become clear from the following sections on the means of generating a computational grid around the two geometries addressed here, that a complex arrangement of grid blocks is required to 'optimally' model each of the geometrical features involved, eg intake lip, duct surface and core etc. The Euler algorithm used to obtain the required inviscid flow solutions is also briefly described. The four flow solutions (two for each test case) are presented and analysed in section 7, including a comparison with experimental data, although, as will be apparent from the above discussion, it is not expected that high absolute accuracy will be a feature of such a comparison. The value of the results herein will hopefully become apparent when all contributions to WG13 have been collected and collated.

## 2 MULTIBLOCK APPROACH

The approach to grid generation and flowfield simulation around complex aerodynamic geometries being pursued at the Aircraft Research Association is based on the multiblock concept<sup>2</sup>. For each component of a configuration, there is an optimal grid topology which mostly conforms to the geometry of the component. The qualitative features (orthogonality, aspect ratio and smoothness) of such a grid topology will provide the most efficient discretisation of a flow domain on which to construct a numerical algorithm for simulating the equations which describe the motion of a fluid. Since, in general, it is not possible to generate a single block structured grid which satisfies the above requirement, the approach adopted is to split the flow domain between the configuration and some farfield boundary into a number of blocks, based on the constraint that only one type of flow boundary condition can be applied on each face of each block.

The blocks fill the domain without overlapping each other. Each block has six faces and eight corners and can be mapped into its own unit cube in computational space without change in topological structure. All points lying within a given block can be directly referenced with respect to each other (ie the grid is locally structured) but bear no direct structural relationship to any of the grid points which lie within other blocks (ie the grid is globally unstructured). This sacrifice of global structure within a grid allows the flexibility required to construct grids whose topological structure local to each component is compatible with the particular geometric characteristics of the component.

The structure of the ARA multiblock system can be readily broken down into five parts as shown in Figure 1. Accordingly, the remainder of this memo is broken down into five sections, each one describing the techniques used and work undertaken, within each individual section of the multiblock system, for the AGARD WG13 test cases.

### 3 GEOMETRY DEFINITION AND MODELLING

The geometry of Test Case 3 (TC3) of AGARD WG13 is an intake cowl, attached to an S-bend diffuser whose centreline is offset by 0.3 times its length, inside part of which lies an axisymmetric bullet that is positioned at the centre of a nominal engine face. Throughout its length, the geometry is circular in cross-section. The geometry of Test Case 4 (TC4) is made up of similar components. However, for TC4, both the interior and exterior parts of the cowl are semi-circular in cross-section. Thus, the diffuser is defined to allow a smooth variation in cross-sectional shape from the semi-circular cowl to the circular engine face. For both test cases, the profile of the engine face bullet is the same and is given, along with the geometry of the cowl lips and diffusers, by a discrete set of points<sup>3</sup>.

In aerodynamics, the influence of the solid boundaries on the flow field is of paramount importance. It follows, therefore, that for an accurate representation of the fluid dynamics, it is necessary to define the geometry of the solid boundaries as accurately as possible. The approach to geometry modelling adopted in the work described here requires each component to be defined by a rectangular array of points. Such a network is given in Figure 2. The two families of intersecting curves through these geometry data points can be represented by parametric curves. Thus, the surface can be viewed as a rectangular plane in the independent parametric coordinates,  $s$  and  $t$ , say.

Parametric cubic spline curves are fitted through the rectangular array of points in the two parametric directions  $s$  and  $t$ . Each cubic spline consists of a series of points in a given parametric direction. Boundary conditions impose continuity of position, first derivative and second derivative between adjacent segments of the spline curve and zero curvature at the end points of the spline, which are the first and last point of the relevant parametric coordinate. The slopes at, and position vectors of, each of the geometry data points provide the necessary boundary conditions required to construct a bi-cubic patching of the surface of the geometry<sup>4</sup>.

Thus, given a set of geometry points, defined in terms of Cartesian coordinates and arranged in a regular manner, a continuous representation of the surface of a configuration can be obtained. To this end, programs were written which read in the given discrete data points (defining the profile of the cowl lip, the local radii of the axisymmetric bullet and the shape of the S-bend diffusers) and output the TC3 and TC4 geometries in a form appropriate to constructing a bi-cubic patch of the surfaces.

Some important modifications to the geometries were also made. For both test cases, the engine face was positioned further downstream than originally defined<sup>3</sup> by adding on circular cylinder extensions to the bullets and diffusers. Also, the external part of both cowls was doubled in axial length by extrapolating downstream from, and parallel to, the original geometry. These changes effectively moved the boundaries of the flow domain at which outflow boundary conditions were to be applied. They were made to alleviate concerns about the inappropriateness of applying the outflow boundary conditions described in section 6 at the original boundaries. The derived geometries for TC3 and TC4 are given in Figures 3 and 4 respectively.

As will be seen in section 5, the technique adopted for the modelling of surfaces has an important influence on the approach to the generation of computational meshes on surfaces.

#### 4 TOPOLOGY DEFINITION

The flexibility of the multiblock approach allows a wide range of alternative grid topologies to be constructed. However, this flexibility is gained at the expense of having

- a) to visualise a block decomposition of the domain around a given geometry, and
- b) to define the grid and flow boundary conditions imposed on each block face and, where necessary, details relating to adjoining blocks.

Obviously, step (a) precedes step (b). The information defined in step (b), the grid topology, is stored in a data bank known as a topology file. This file drives the multiblock system, providing the structure necessary to allow grid and flowfield information to be transferred between blocks.



As described earlier, the geometry of TC2 is circular in cross-section throughout its streamwise extent. A polar, 'O'-mesh topology is therefore suitable for modelling the circumferential profile of the geometry (see Figure 5a). The cowl lip has a rounded leading edge, it being defined internally by an ellipse and externally by a NACA section (1-854-35). A 'C'-mesh topology conforms to this feature of the cowl (see Figure 5b). The large internal angle at the nose of the axisymmetric engine face bullet suggests the use of a C-grid topology in an azimuthal plane through the bullet (see Figure 5c). These considerations can be readily combined to yield the azimuthal block structure shown in Figure 6. (Note the five-point singularity that arises from embedding the C-grid topology local to the bullet). This block structure can be rotated locally about the centre-line axis to give the required polar topology in the circumferential plane. This rotation would yield a polar singularity along the centre-line axis (see Figure 5a). However, it has been demonstrated in Reference 5 that such a singularity can adversely affect the convergence rate of the explicit time-stepping flow algorithm to be used in this work. (This is primarily because the volume of the cells, and hence maximum permissible local time-step, decreases as the centre-line is approached). To overcome this, the centre-line region can be modelled by a Cartesian topology. This results in the azimuthal and circumferential block structures given in Figures 7a and b respectively. As can be seen from Figure 7a, the blocks modelling the internal region from the cowl lip to just upstream of the bullet are split into three blocks in the axial direction. This ultimately allows a sufficiently dense mesh to be generated in this region. (The multiblock system has a limit on the number of points that can be used in any one coordinate direction of a block). Since the geometry of TC3 is symmetrical, and the flow cases to be run do not require sideslip to be simulated, the configuration can be modelled using 38 blocks. The above discussion covers step (a) of the topology definition process.

Step (b) involves specifying the information that links the blocks together and the boundary conditions on each block face. To do this, the convention adopted is to assign to each block a computational coordinate system and a unique number ranging from 1 to the number of blocks, 38 in this case (see Figure 7). Also, each block face is assigned a number, with 1, 3 and 5 denoting the computational planes  $I = 1$ ,  $J = 1$  and  $K = 1$  respectively, and 2, 4 and 6 denoting the planes  $I = I_{MAX}$ ,  $J = J_{MAX}$  and  $K = K_{MAX}$  respectively. The block connectivity and boundary condition data is then specified using the block faces as a basis.

For the grid generation, boundary conditions include a Dirichlet type, where a fixed set of data points is given, and a continuity condition. Many faces within the block structure are boundaries between blocks in the interior of the flow domain and, as such, are purely notional boundaries which, provided grid lines pass smoothly through the junction, have no physical significance. At such boundaries, the continuity condition is imposed which ensures that grid lines pass through the interface of two adjacent blocks with continuity of position, slope and curvature. For block faces on which a continuity condition is applied, block connectivity data must be specified. This takes the form of a unique number associated with the adjacent block, a number depicting the common face of the adjacent block and the relative orientation of the local axis systems on adjoining block faces.

For the flow solver, a wider range of boundary conditions are available which are consistent with solving the Euler equations of motion for both the internal and external regions of the flow domain. The block connectivity data required for the mesh generators is also used by the flow solvers. If a face of a block lies on the surface of a geometric component, a four character alpha-numeric string must be specified for that face, for example, COWL.

Thus, in total, six items of data (boundary condition for the grid generator, boundary condition for the flow solver, adjacent block, adjoining face, relative orientation and a name) must be specified for each block face. With each block having six faces and requiring the number of mesh points in each coordinate direction to be defined, 39 amounts of data must be specified per block. Thus, in total, the topology file will contain 1482 (ie  $39 \times 38$ ) items of data. To facilitate the potentially labour intensive task of preparing this data, a program was written to create the topology file, with simple input allowing the block dimensions to be altered as required.

Note that although the mesh generators are vertex based, no additional data defining boundary conditions for, and connections between corners and edges of the blocks is required. All this data is derived using the face connectivity data and internal program logic within the multiblock system. This completes the topology definition process for TC2.

The task of simulating the flow over TC4 geometry represents a severe challenge, even to an approach with the flexibility of multiblock. The main

problem in modelling the inviscid flow over this configuration arises from the transition of the semi-circular cowl to the circular engine face. Step (a) of the topology definition process can be readily visualised for both the interior and exterior of the cowl in isolation (see Figure 8). The topology for the domain local to the engine face can be the same as for TC3, since the geometries are similar in this region. However, these three topologies are incompatible with each other since they cannot be readily combined in the axial direction. Consideration was therefore given to the implications of extending each of the three topologies, in turn, in the axial direction. In other words, how would the topology best suited to the interior of the cowl model the exterior region of the cowl and the engine face region? On balance, it was concluded that the topology best suited to the engine face would be likely to provide the least distorted grid for the other regions of the geometry (see Figure 9). Hence, the block structure already defined for TC3 was also used for TC4. The block dimensions in the circumferential direction were increased from 7 to 11 in all cases in an attempt to limit the grid distortion and model the higher cross-flow gradients expected with the TC4 geometry.

The above topology definitions, whilst being suitable for geometries similar to those addressed here, would require modification before they could be integrated into a topology for an aircraft type geometry.

## 5 GRID GENERATION

The generation of a three-dimensional multiblock grid for a given configuration is a two step process. It involves first the generation of grids on the surface of the geometry, and on the other boundary surfaces of the flow domain, and second the generation of the grid in the field.

The generation of grids on the actual surfaces of a configuration represents one of the most difficult aspects of the total grid generation problem. Its importance, in two respects, is undoubted, however. Firstly, it is the response of the flow to the precise shaping of the configuration's surfaces that has a major influence on the total flow field. Secondly, the surface grids act as boundary conditions for the generation of field grids. Consequently, surface grids exert a strong influence upon the field grids, particularly in the neighbourhood of a configuration, the very region where flow gradients need to be resolved accurately. Surface grids have the same requirement for smoothness and continuity as field meshes and, in addition, are required to conform to the configuration surfaces, including lines of component intersection, and to model regions of high surface curvature.

The approach to surface grid generation to be described here makes use of the discussion in section 3 where parametric coordinates are employed and a surface is continuously representable via the bi-cubic patching technique. Such a description of a surface is important for the generation of surface meshes which, in general, are not coincident with the network of points defining the geometry. The parametric approach utilises the fact that a surface in three-dimensional Euclidean space can be expressed in terms of two independent parametric coordinates,  $\underline{S} = \underline{S}(s,t)$ . Surface mesh generation can then be viewed as a transformation  $S(s,t) \rightarrow X(x,y,z)$ , where the mesh is generated in the two-dimensional parametric space and mapped to physical space via the bi-cubic patches, which ensures mathematical consistency with the geometry definition.

The surface grids are generated by solving the coupled set of non-linear elliptic partial differential equations, originally proposed by Thompson, Thames and Mastin<sup>6</sup>,

$$\alpha(s_{\xi\xi} + Ps_{\xi}) - 2\beta s_{\xi\eta} + \gamma(s_{\eta\eta} + Qs_{\eta}) = 0 \quad (1)$$

$$\alpha(t_{\xi\xi} + Pt_{\xi}) - 2\beta t_{\xi\eta} + \gamma(t_{\eta\eta} + Qt_{\eta}) = 0$$

where

$$\alpha = s_{\eta}^2 + t_{\eta}^2$$

$$\beta = s_{\eta}s_{\xi} + t_{\eta}t_{\xi}$$

$$\gamma = s_{\xi}^2 + t_{\xi}^2$$

and P and Q are source terms used to control the mesh.  $\xi$  and  $\eta$  are the computational coordinates.

These equations are approximated using second-order accurate finite differences to obtain a non-linear set of algebraic equations for the positions of grid points in parametric space. The equations are then solved iteratively using a successive line over-relaxation algorithm.

The source terms can be evaluated in a number of ways. The technique employed here is an essentially automatic procedure whereby the source terms are constructed from two terms, one which reflects the boundary point spacing into the field, the other which drives the grid towards orthogonality at the boundary<sup>7</sup>. For example, P is evaluated by

$$P = \frac{-\underline{S}_{\xi} \cdot \underline{S}_{\xi\xi}}{|\underline{S}_{\xi}|^2} - \frac{-\underline{S}_{\xi} \cdot \underline{S}_{\eta\eta}}{|\underline{S}_{\eta}|^2}$$

The first term, which contains only  $\xi$  derivatives, is evaluated solely from the point distribution on  $\eta = \text{constant}$  boundaries, using second-order accurate central differences. The orthogonality term contains both  $\xi$  and  $\eta$  derivatives. The second derivative term can be replaced by a first derivative and the orthogonality term reformulated as

$$\frac{-S_{\xi} \cdot S_{\eta\eta}}{|S_{\eta}|^2} = \frac{-2S_{\xi} \cdot S_{\eta}}{|S_{\eta}|^2}$$

The orthogonality term can be evaluated for nodes on  $\eta = \text{constant}$  boundaries by using second-order accurate central differences along the boundary for the  $\xi$  derivative and first-order accurate one-sided differences into the interior of the domain for the  $\eta$  derivative (see Figure 10). Thus, since the position of the interior nodes evolves with the iterative solution process, the orthogonality term must be updated regularly, every iteration being used in this work. Once the source terms have been evaluated on all the boundaries, they are interpolated through the mesh to control the position of the interior nodes.

In previous multiblock surface grid generation work, the orthogonality term has been neglected because it is known to significantly increase the run time for generating the grid, by factors of say 4, and its success can be geometry and topology dependent. It was coded into the surface grid generator for this work due to concerns about the quality of the grid obtained using only the term which reflects the boundary point spacing and because a limited number of surface grids needed to be generated.

To produce a valid multiblock surface grid, the topology of the surface grid must be consistent with the topology of the multiblock field grid. The multiblock system includes a program which automatically extracts all the required topology data for generating surface grids from the field grid topology. The configuration and boundaries of the flow domain were broken down into eight surfaces:

- 1) Cowl
- 2) Duct
- 3) Internal extension of duct
- 4) Engine face bullet
- 5) Engine face

- 6) Downstream boundary of the flow domain
- 7) Plane of symmetry
- 8) Farfield boundary.

Note, the first three surfaces in this list could have been modelled as one surface, but were represented as three to allow for detailed control of the point distribution on the geometry.

To generate the surface grids using an elliptic set of equations requires the point distribution to be specified along all boundary edges of the surface. Furthermore, since this boundary point distribution is to be used to control the surface grid, the boundary nodes must be specified carefully.

Consider Figure 11 which shows the block structure for generating the grid on the engine face surface. The surface grid topology file describes how the surface blocks relate to each other in computational space. Specifying the correct boundary point distribution along the Dirichlet boundary edges, and then solving the grid generation equations for the interior of the domain, will ensure that the surface blocks relate to each other in the correct manner in physical space. Thus, for example, the boundary point distribution along the line  $I = IMIN$  of surface block 1 must conform to the top octant of the engine face circumference. In addition, to produce a valid multiblock grid, it must also match exactly the point distribution that will be specified along the topologically equivalent edge of the surface grid generated on the extension of the duct. To this end, a number of subroutines were written for distributing grid points and appended to the basic multiblock surface grid generation program.

Figure 12 shows the surface grids generated for TC3 on the cowl, duct, extension of duct, engine face and bullet in physical space. In Figure 13 the corresponding surface grids for TC4 are shown. The surface grid on the plane of symmetry and the grid on the ellipsoidal outer boundary are shown for TC4 in Figures 14 and 15 respectively. These surface grids act as boundary conditions for the field grid generation. The equivalent grids for TC3 are similar.

The field grids are generated from the elliptic equations

$$\partial^2 X_i / \partial \xi^2 = -p^i X_i$$

where  $g^{ij}$  are the metric terms,  $p^i$  the source functions,  $X$  the grid point coordinates and  $\xi^i$  the computational coordinates with the tensor notation taking values 1, 2 and 3. No development work was required for this stage of the multiblock system and the standard multiblock field grid generator was used. Figure 16 illustrates a cross section of the field grid through the throat region for TC4. Note the tendency for the grid lines to be repelled from the corner regions of the semi-circle. This is indicative of the topology structure being non-optimum in this plane, as discussed previously in section 3. The field grids for test cases 3 and 4 are composed of approximately 90,000 and 140,000 cells respectively.

## 6 FLOW ALGORITHM FOR SOLVING THE EULER EQUATIONS

The flow algorithm used to solve the Euler equations of motion is based on the scheme originally proposed by Jameson et al<sup>8</sup>. This finite volume method, with explicitly added artificial dissipation, uses a multi-stage time-stepping scheme. Convergence to a steady state is accelerated by the introduction of a forcing term proportional to the difference between the local total enthalpy and its freestream value and the use of a variable time step supported by residual smoothing<sup>9</sup>.

On the external farfield boundaries of the domain, Riemann invariant boundary conditions are applied. At solid surfaces, the normal-momentum relation derived by Rizzi<sup>10</sup> is used to ensure there is no flow normal to the surface. The representation of powered effects at the engine face is included by specifying a mass flow ratio and area contraction ratio. These are then used to give an engine face static pressure<sup>5</sup>, the velocity components and total energy being extrapolated from the interior and the density evaluated so as to be consistent with the freestream total enthalpy. This procedure assumes subsonic flow at the engine face, which is valid for the flow conditions of interest.

## 7 ANALYSIS OF FLOWFIELD RESULTS

The results of four Euler calculations are analysed below, two for each test case, and comparison is drawn with experimental data<sup>3</sup> in each case. Table 1 gives the details of Mach number and mass-flow ratio.

Test Case	$M_0$	MFR
3 (a)	0.210	1.457
3 (b)	0.210	2.173
4 (a)	0.211	1.837
4 (b)	0.211	2.140

TABLE 1

Each of the calculations was run at a CFL = 2.8 for 5000 cycles, to ensure a high level of convergence. The number of cycles may seem large compared with those generally required for a three-dimensional external flow calculation using the multiblock method, but past experience<sup>5</sup> has indicated that duct flows are particularly slow at converging to a steady state, and the higher the mass-flow ratio the slower the convergence rate (for the free-stream initial conditions used here).

Test case 3 is examined first. Figures 17 and 18 show the variation of the ratio of surface static to free-stream total pressure for the low and high mass-flow ratio cases, respectively. Part (a) of each figure gives the axial variation from an external downstream station, around the lip and downstream to the engine face plane, and part (b) gives the radial variation in the immediate lip region. The definition of port and starboard on all figures is best visualised by assuming both test case geometries correspond to side intakes on the starboard side of an aircraft. Port and starboard are thus labelled in Figure 14: the definition of top and bottom follows naturally. Figure 17a reveals that the agreement between theory and experiment at the lower MFR in the lip and throat region is excellent and that the qualitative flow behaviour in the diffuser at each of the measuring planes is similar. It is apparent, however, that the pressure as predicted by the Euler method is uniformly higher within the diffuser, including at the engine face plane. This is almost certainly due to the neglect of the modelling of the diffuser surface boundary layer in the inviscid results. The boundary layer reduces the effective duct area, via its displacement effect, thus increasing the axial velocity and reducing the static pressure. This pressure shift due to viscous effects would improve the comparison between theory and experiment, and a more precise agreement in the diffuser would be expected from a high quality Navier-Stokes or even an Euler/interactive boundary layer solution.



Figure 17b, with its expanded radial scale, enables a more detailed analysis of the lip region to be made. Agreement is seen to be favourable, which is a good indication that the stagnation point predicted by the theory closely matches that observed in the real flow.

Turning to Figures 18 at the higher MFR, an immediate contrast in the quality of predictions is observed. It is expected that viscous effects are particularly severe at this MFR, probably including flow separation and secondary flow structures within the diffuser, but the level of mismatch, especially in Figure 18a, is so great that it is difficult to envisage that the whole of the discrepancy can be attributed to this cause. Examination of the qualitative features of the theoretical and experimental diffuser flows reveals a broad similarity between the two, with the obvious very large shift in pressure level. As the peak suction levels are not reproduced, Figure 18b suggests that, in contrast to the previous case, the stagnation point is not correctly positioned in the theory. These observations give some credence to the suggestion that the experimental MFR may be incorrectly specified\*. Other contributions to WC13, particularly Navier-Stokes predictions, may shed more light in this area.

Test case 4 is examined through similar plots in Figures 19 (low MFR) and 20 (high MFR). At the lower MFR, equivalent comments can be made as those associated with Figures 17, except that the pressure level in the throat region is slightly more in error and the rapid expansion downstream of the throat on the starboard plane is not reproduced particularly well. However, the small pressure shift associated with the constriction due to an attached boundary layer is again present in the experimental data. As stated in previous sections, the modelling of the semi-circular intake of this test case via the associated surface and field grids is somewhat difficult, particularly in the corner regions, and the quality of the flow prediction in these areas must be drawn to question. Experimental pressure readings would have facilitated conclusions in this respect. Figure 19b indicates that the stagnation point is not well predicted, and it is observed that the experimental data is consistent with an increased mass flow as would be expected from the error in the throat pressure levels.

---

\*Comparison of the theoretical results in Figure 18a with data from an experimental MFR which is 5% smaller than that specified for test case 3(b) shows a much closer match between theory and experiment, particularly for  $x/d_{\max} < 1.0$ , where viscous effects are probably relatively insignificant.

Similarly, Figures 20 show the same features as Figures 18, and again it must be considered that the given experimental MFR for this case may be in error. In some respects, however, the theoretical predictions do not qualitatively match the experimental results. For example, the experimental pressures on the port side show an expansion immediately downstream of the throat, whereas the theory shows a compression. Again, a high quality Navier-Stokes prediction would indicate whether this anomaly is due to viscous effects.

## 8 CONCLUSIONS

The ARA Euler multiblock method has been used to predict the flow about two intake/S-bend diffuser geometries, as defined by ACARD Working Group 13. An attempt has been made to define an optimal block structure for each of the configurations, although the second configuration posed particular problems in this respect, with its semi-circle-to-circle diffuser, and ultimately a block structure involving some compromise has been created for this case.

The inviscid results presented herein were solicited by ACARD WG13, in the main, to better assess the quality of Navier-Stokes predictions from other contributors. However, certain conclusions can be drawn by comparison of experimental data with surface pressures as calculated by the present Euler method, at two mass flows for each geometry, at  $M_\infty = 0.21$ . The flowfield for the lower mass flow in each case appears to have been modelled reasonably well, particularly on the exterior and interior of the intake, including the throat region. The diffuser flow is consistent with the neglect of an attached surface boundary layer. At the higher mass flow in each case, the predictions, at most, possess the correct qualitative features of the flow. It is presumed that the real flow is grossly affected by viscous effects, including secondary structures, for these cases.

## Acknowledgements

The authors would like to thank Mr E. L. Goldsmith for his advice during this work, and also for the comparisons referred to in the footnote of page 13.

REFERENCES

- 1     SHAW J A                     The construction of component adaptive grids for  
        GEORGALA J M               aerodynamic geometries.  
        WEATHERILL N P            Proc Second International Conference on Numerical  
    Grid Generation in Computational Fluid Mechanics,  
    Florida, pp 383-394, Pineridge Press            1988
  
- 2     WEATHERILL N P             Grid generation and flow calculations for aircraft  
        FORSEY C R                 geometries.  
    J Aircraft, Vol 22, No 10, pp 855-860.  
    October 1985
  
- 3                                     Data supplied to contributors to AGARD Working  
    Group 13, 'Air Intakes for High-Speed Vehicles'.  
    See also  
        BARKER A F                 Low Speed Pitot Intake tests in the BAe Filton  
    12' x 10' wind tunnel.  
    BAe Filton WT 734                                     October 1979
  
- 4     COONS S A                     Surfaces for computer aided design.  
    MID MAC-TR-41                                     1967
  
- 5     SHAW J. A                     Inviscid solutions over an advanced combat aircraft  
        PEACE A J                     including intake and jet effects using an Euler  
        FORSEY C R                   multi-block approach.  
    ARA Memo 299                                     June 1988
  
- 6     THOMPSON J F                 Automatic numerical generation of body-fitted  
        THAMES F C                 curvilinear coordinate system for field containing  
        MASTIN C W                 any number of arbitrary two-dimensional bodies.  
    J Comp Phys, Vol 15                                     1974
  
- 7     THOMPSON J F                 Composite grid generation for general 3D regions.  
    Proc First International Conference on Numerical  
    Grid Generation in Computational Fluid Mechanics,  
    Landshut, W Germany, pp 271-290, Pineridge Press  
    1986

REFERENCES (contd)

- 8 JAMESON A                      Numerical solutions of the Euler equations by  
SCHMIDT W                      finite volume methods using Runge-Kutta time-  
TURKEL E                      stepping scheme.  
AIAA Paper 81-1254                      1981
- 9 JAMESON A                      Solution of the Euler equations for complex  
BAKER T J                      configurations.  
Proc AIAA 6th Computational Fluid Dynamics  
Conference, Danvers, pp 293-302                      1983
- 10 RIZZI A W                      Numerical implementation of solid body boundary  
   conditions for the Euler equations.  
ZAMM, vol 58, pp T301-T304                      1978

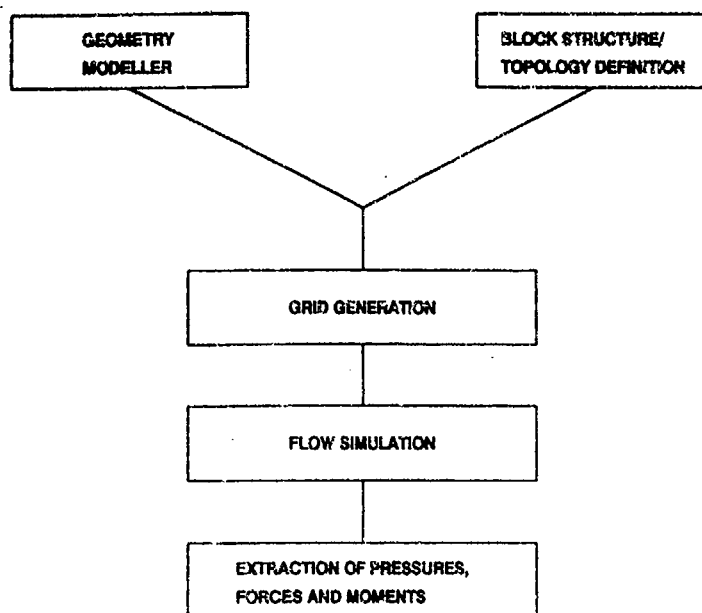
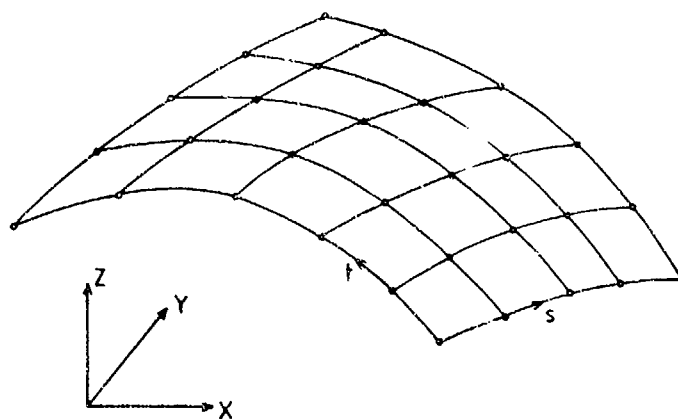
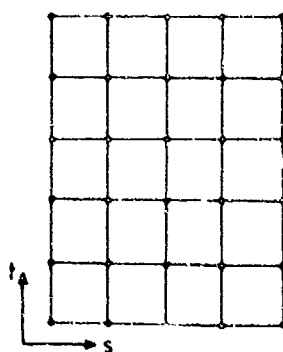


FIGURE 1 OVERVIEW OF MULTI-BLOCK SYSTEM



PHYSICAL SPACE



PARAMETRIC SPACE

FIGURE 2 RECTANGULAR ARRAY OF GEOMETRY DATA POINTS

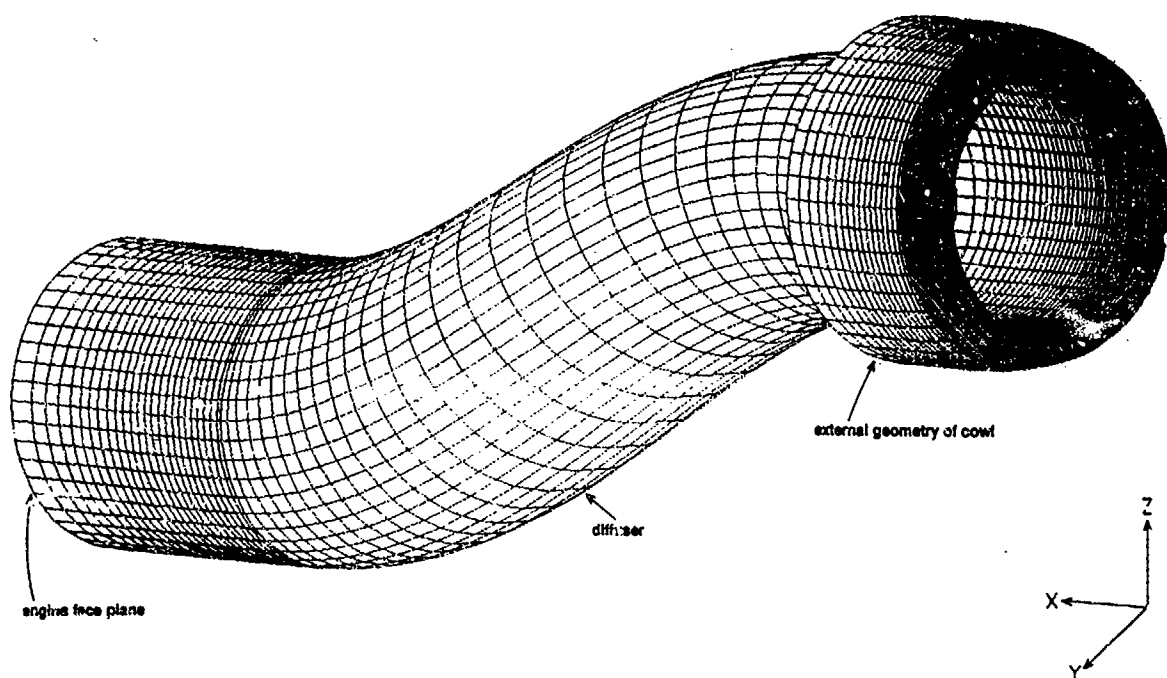


FIGURE 3 VIEW OF GEOMETRY FOR TEST CASE 3 (BULLET NOT SHOWN)

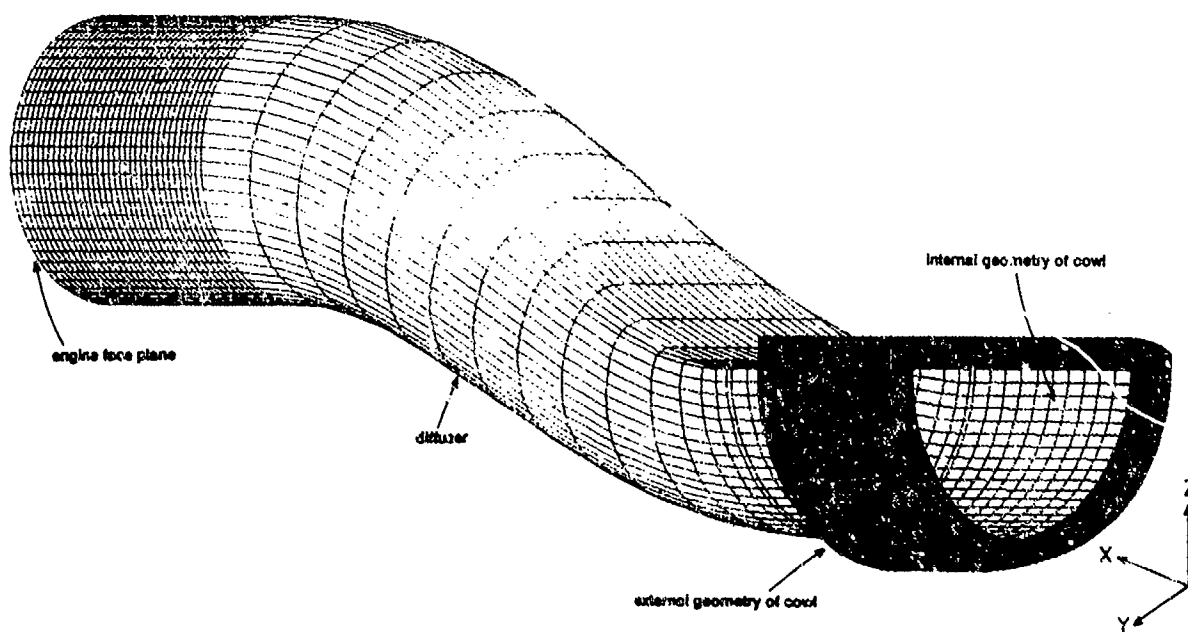
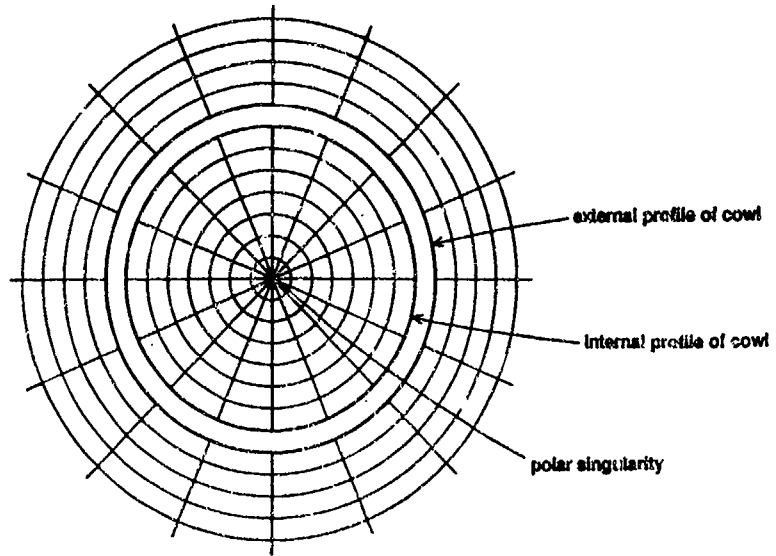
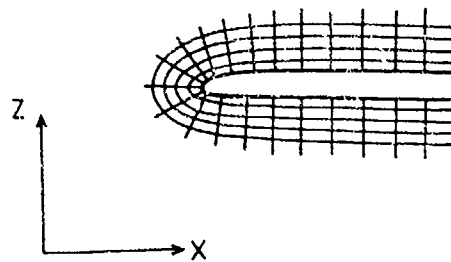


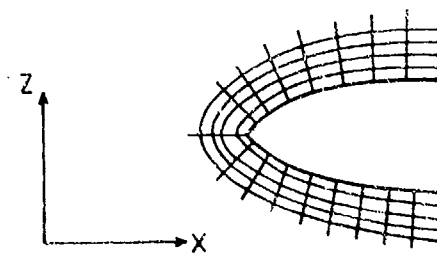
FIGURE 4 VIEW OF GEOMETRY FOR TEST CASE 4 (BULLET NOT SHOWN)



a) CIRCUMFERENTIAL SECTION (POLAR DEFINITION)



b) AZIMUTHAL SECTION OF COWL



c) AZIMUTHAL SECTION OF BULLET

FIGURE 5 COMPONENT GRID TOPOLOGIES FOR TEST CASE 3

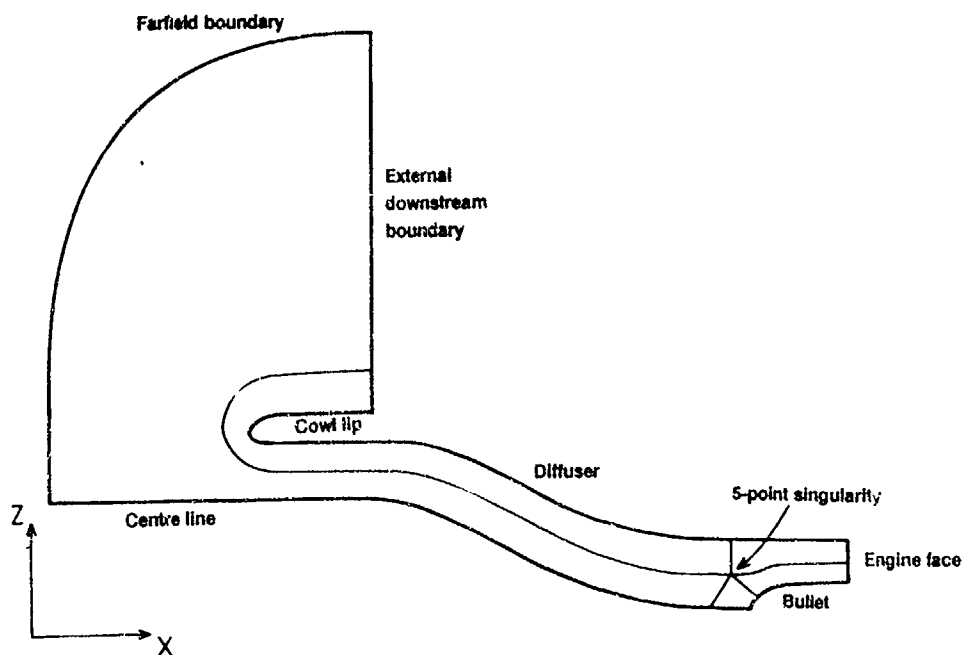
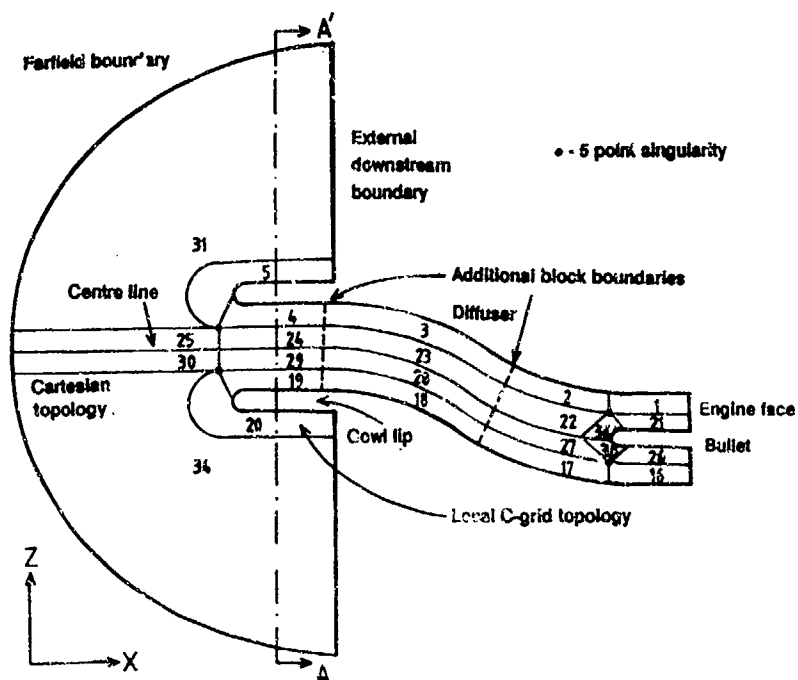
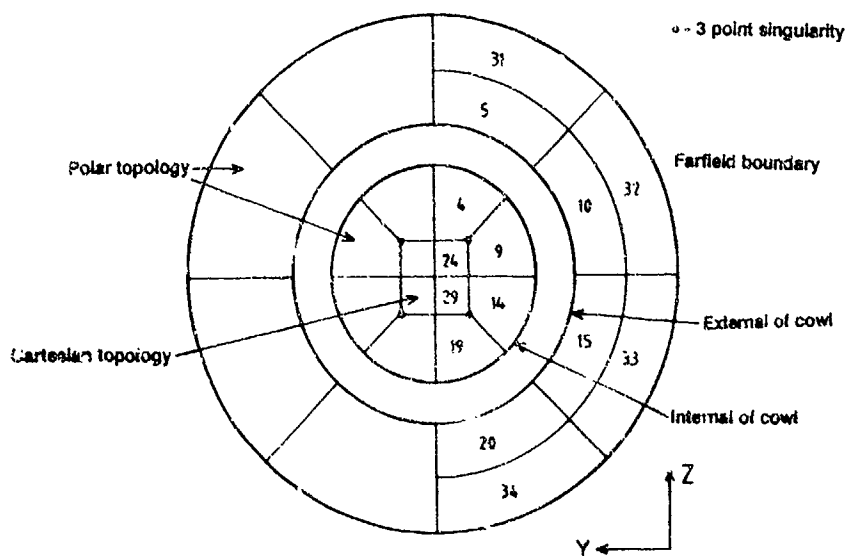


FIGURE 6 SKETCH OF AZIMUTHAL BLOCK STRUCTURE FOR TEST CASE 3 (POLAR DEFINITION)





a) AZIMUTHAL SECTIONS



b) CIRCUMFERENTIAL SECTION AT AXIAL STATION AA

FIGURE 7 SKETCH OF FINAL BLOCK STRUCTURE FOR TEST CASE 3

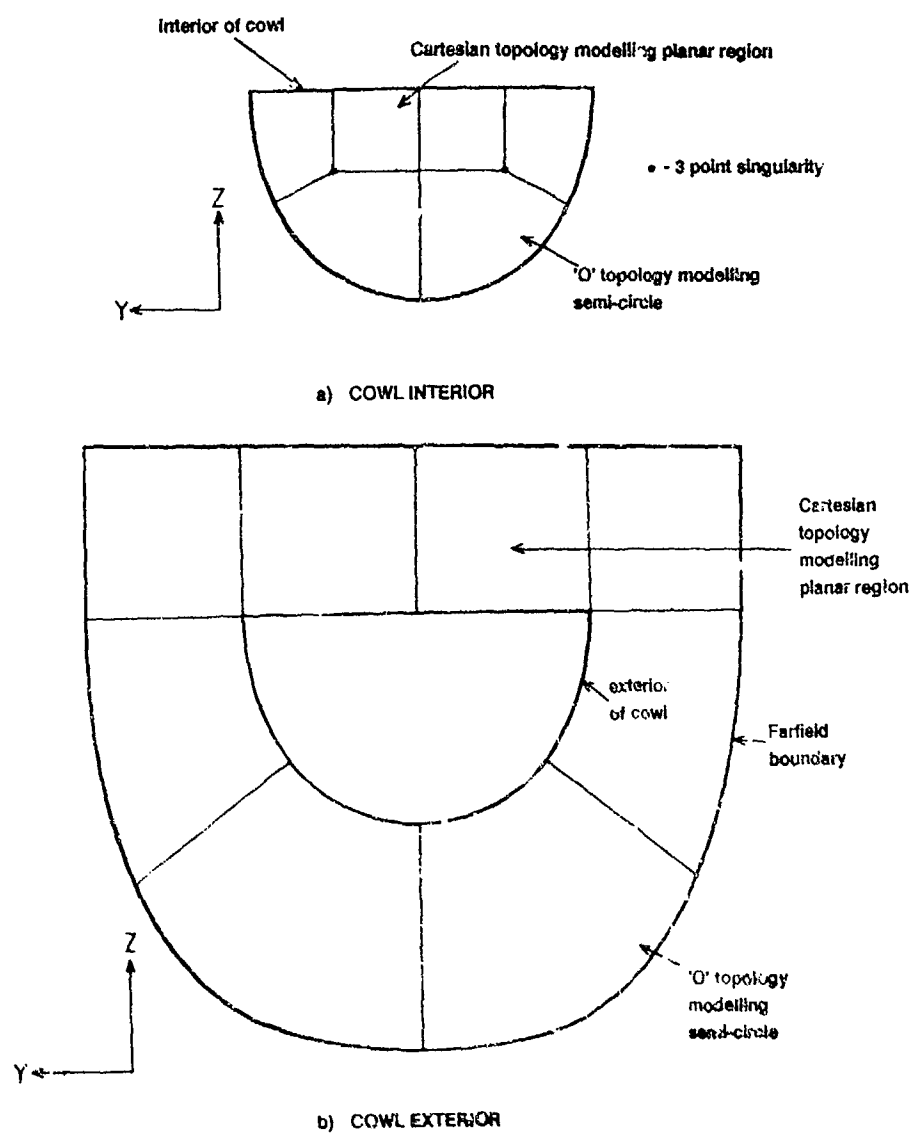


FIGURE 8 OPTIMAL CIRCUMFERENTIAL BLOCK STRUCTURE FOR TEST CASE 4

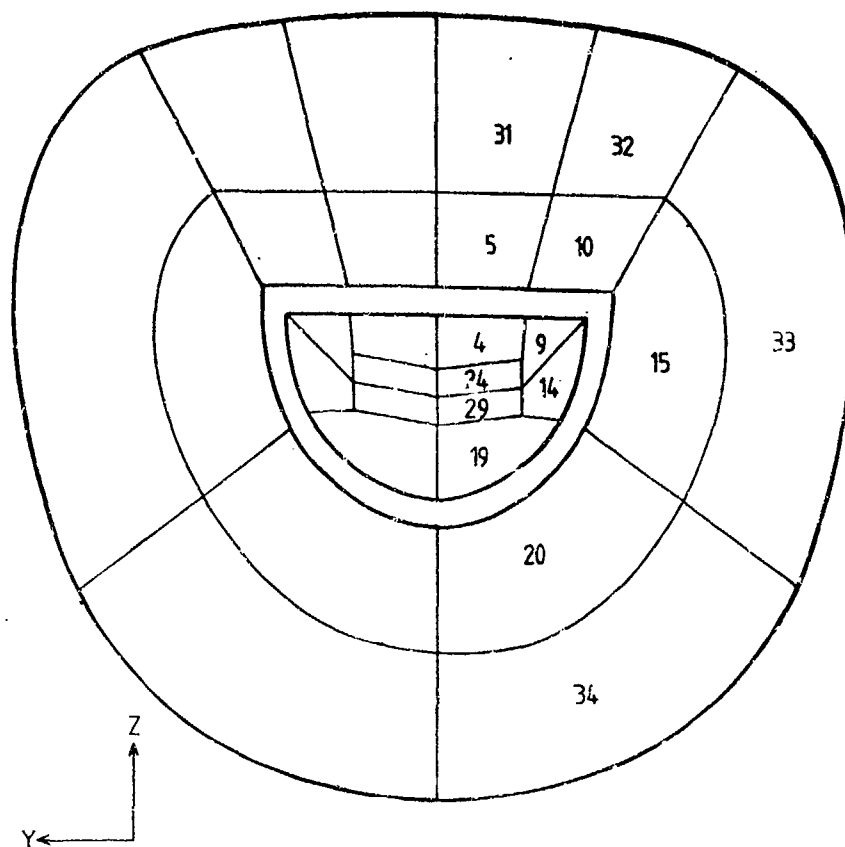
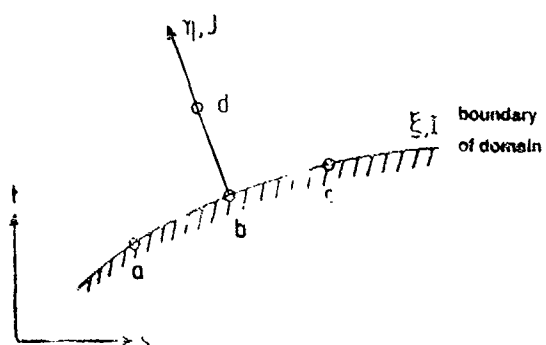


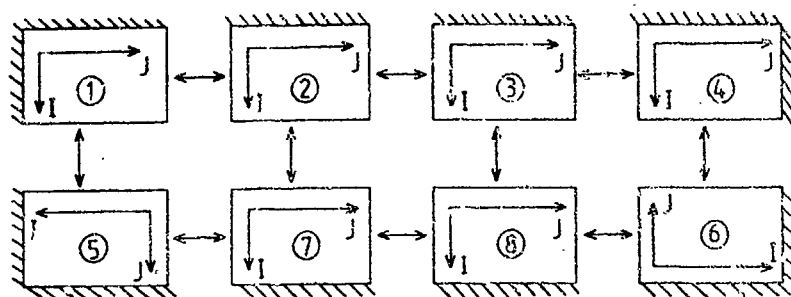
FIGURE 9 SKETCH OF FINAL CIRCUMFERENTIAL BLOCK STRUCTURE FOR TEST CASE 4



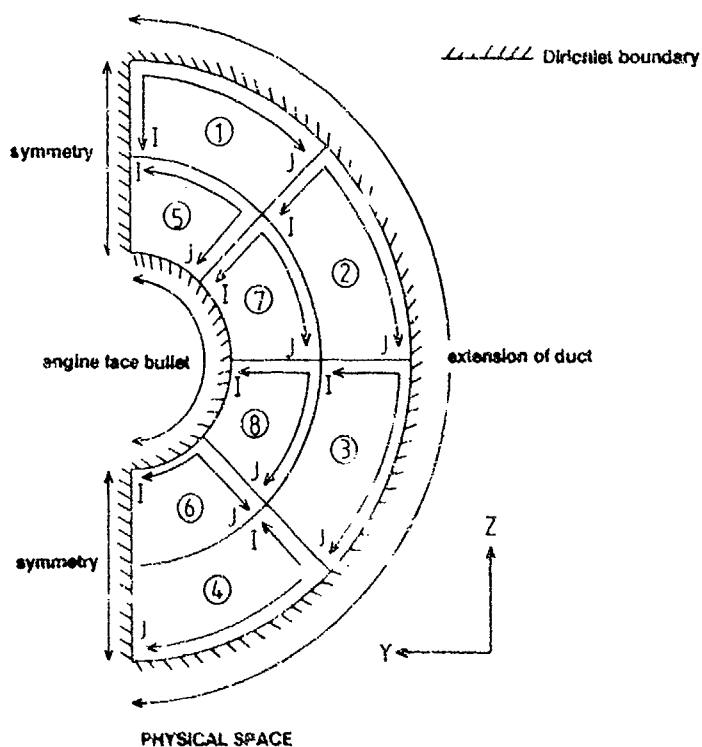
$$\Delta \xi = (\xi_c - \xi_0) / 2$$

$$\Delta \eta = \Delta d - 2b$$

FIGURE 10 EVALUATION OF ORTHOGONALITY TERM



COMPUTATIONAL SPACE



PHYSICAL SPACE

FIGURE 11 TOPOLOGY FOR ENGINE FACE

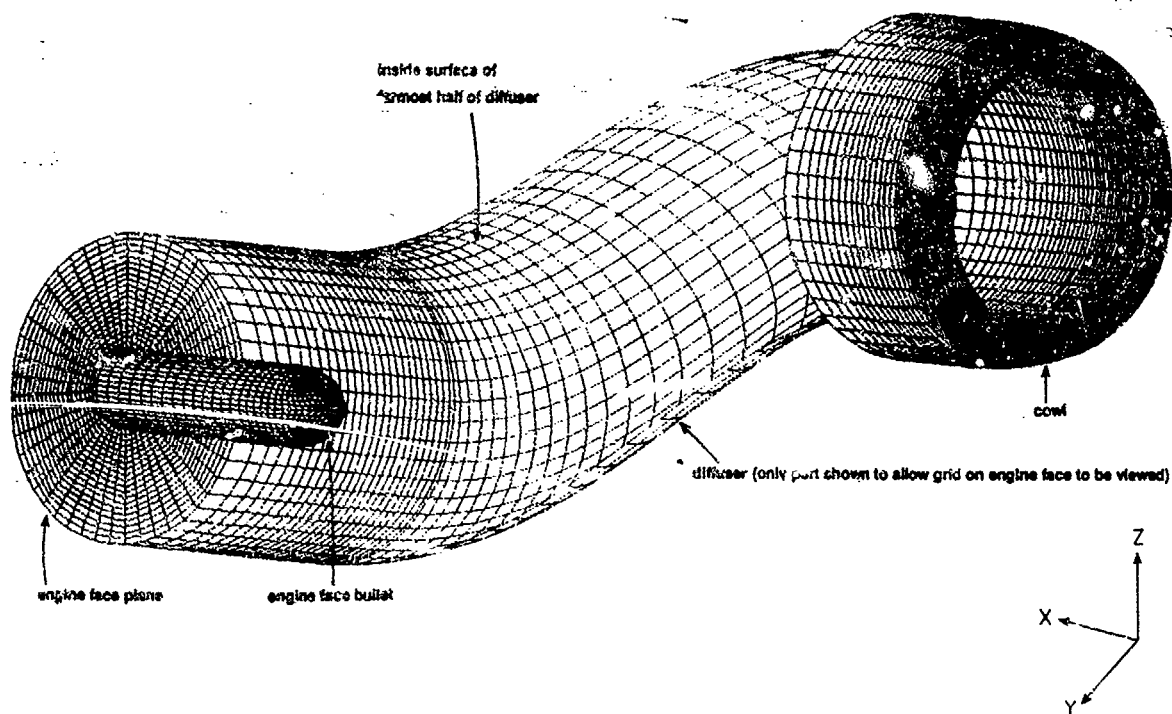


FIGURE 12 GRID ON SURFACE OF TEST CASE 3 GEOMETRY

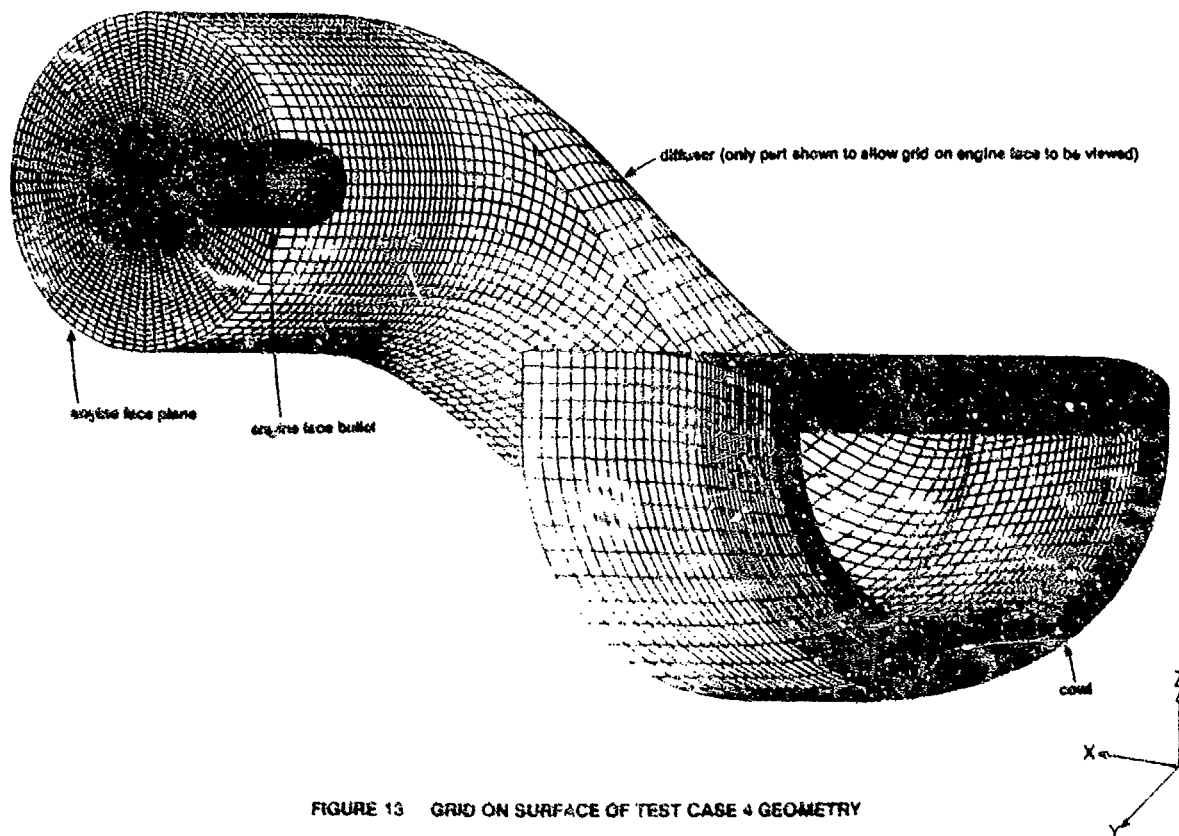


FIGURE 13 GRID ON SURFACE OF TEST CASE 4 GEOMETRY

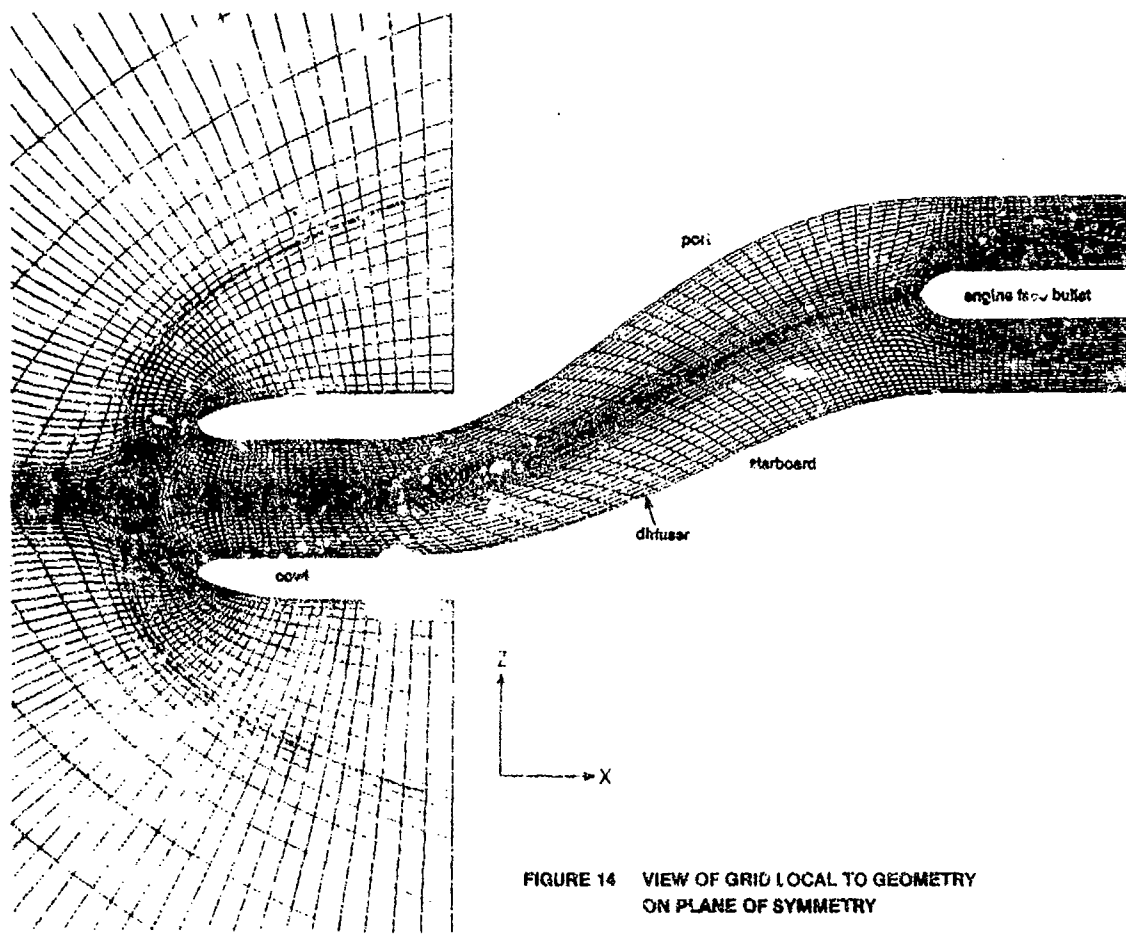


FIGURE 14 VIEW OF GRID LOCAL TO GEOMETRY  
ON PLANE OF SYMMETRY

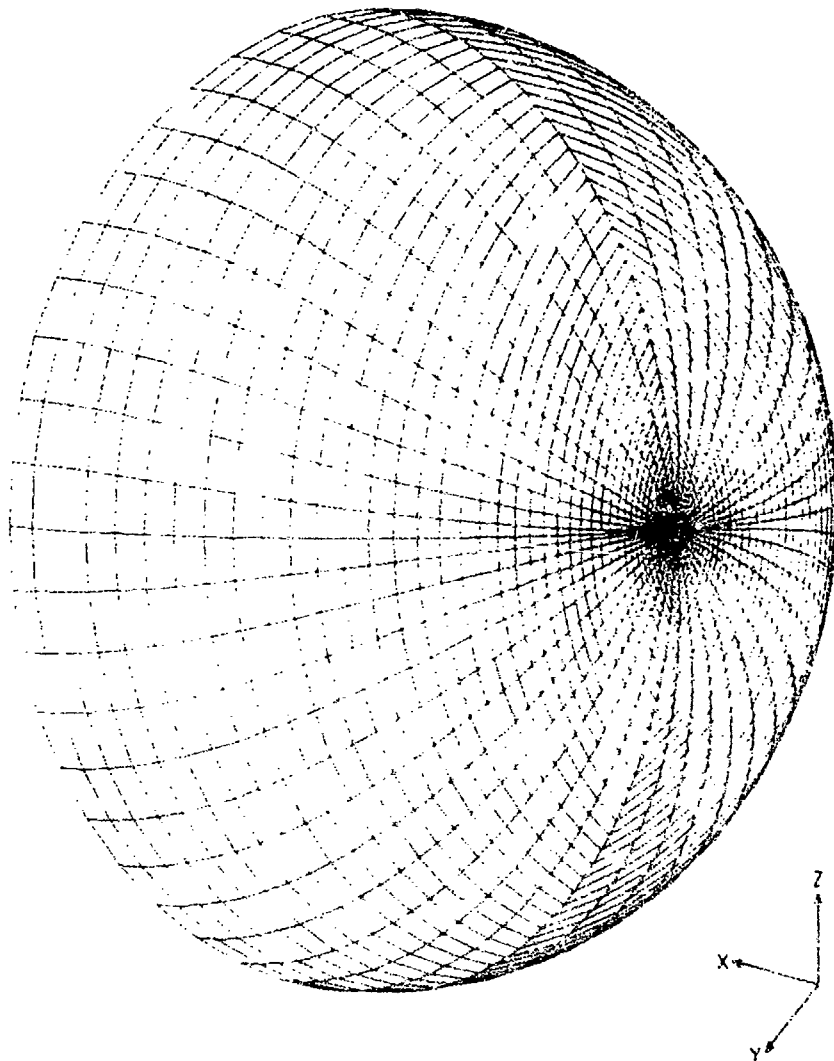


FIGURE 15 GRID ON FARFIELD BOUNDARY

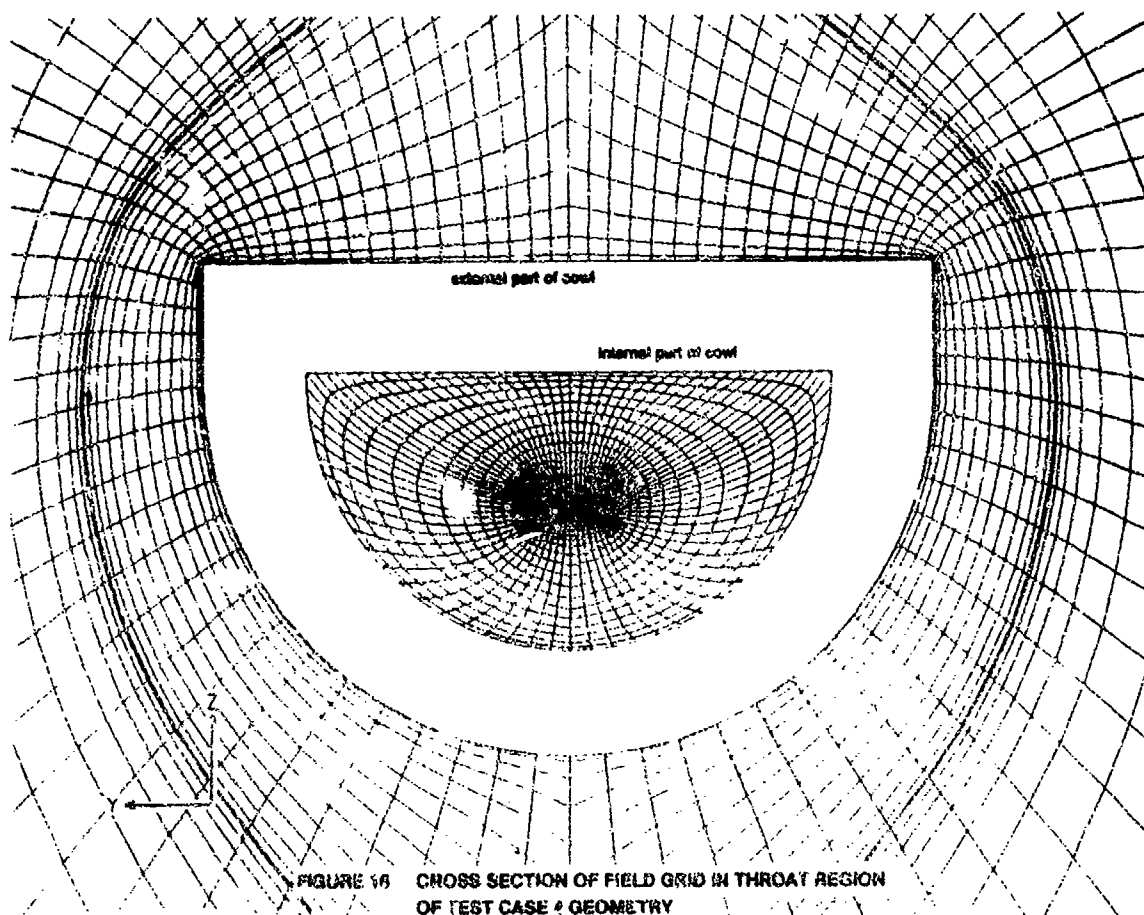


FIGURE 16 CROSS SECTION OF FIELD GRID IN THROAT REGION  
OF TEST CASE 4 GEOMETRY



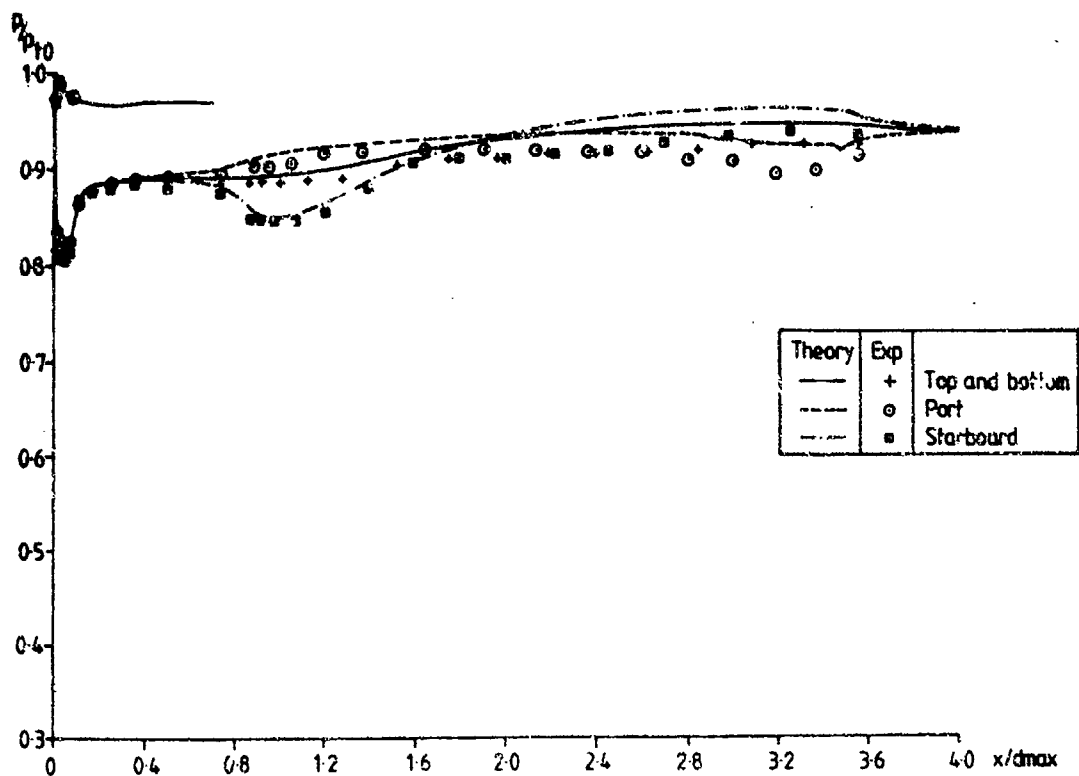


FIGURE 17(a) TEST CASE 3(a) - AXIAL PRESSURE VARIATION

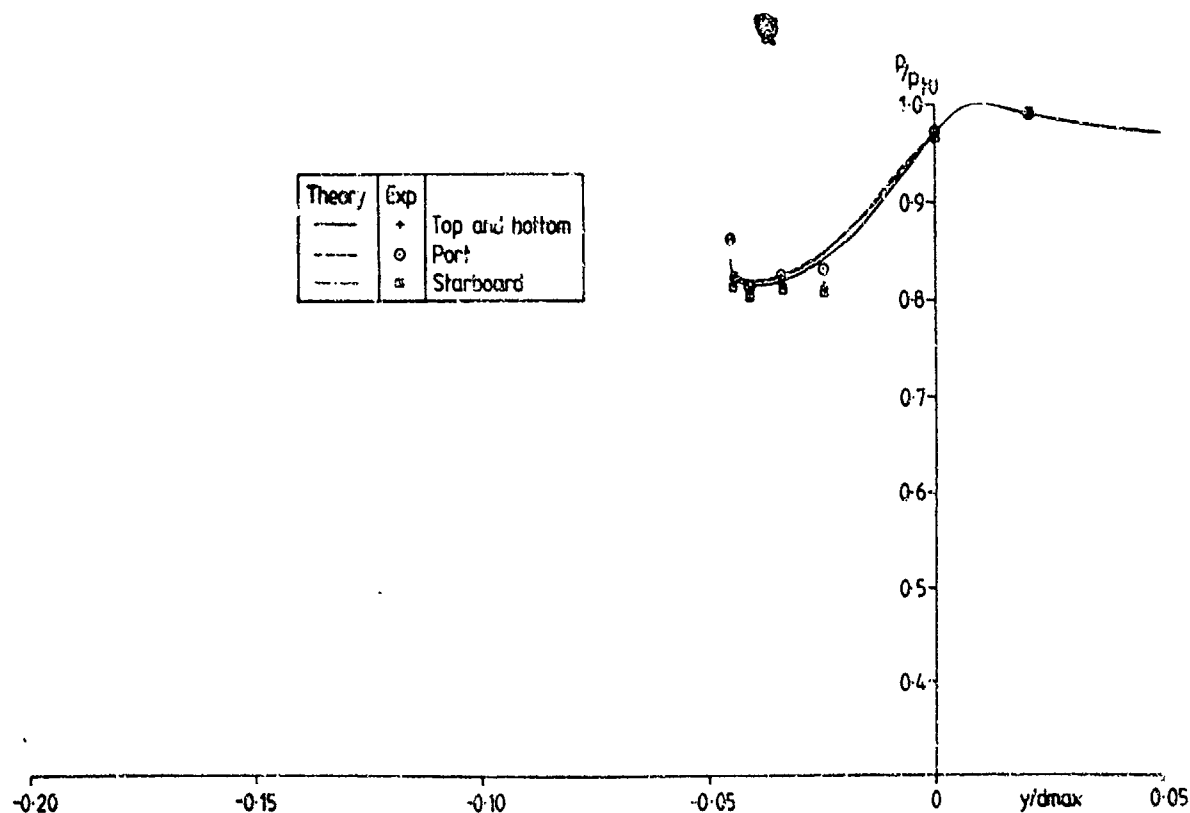
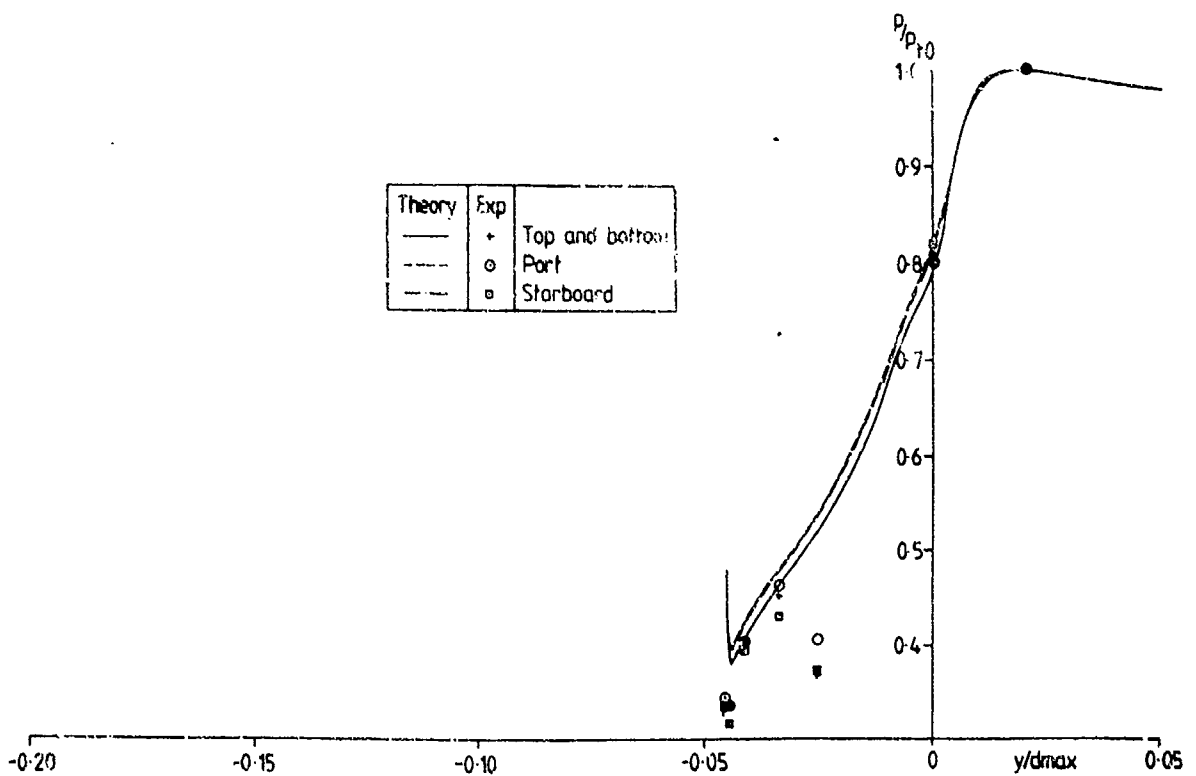
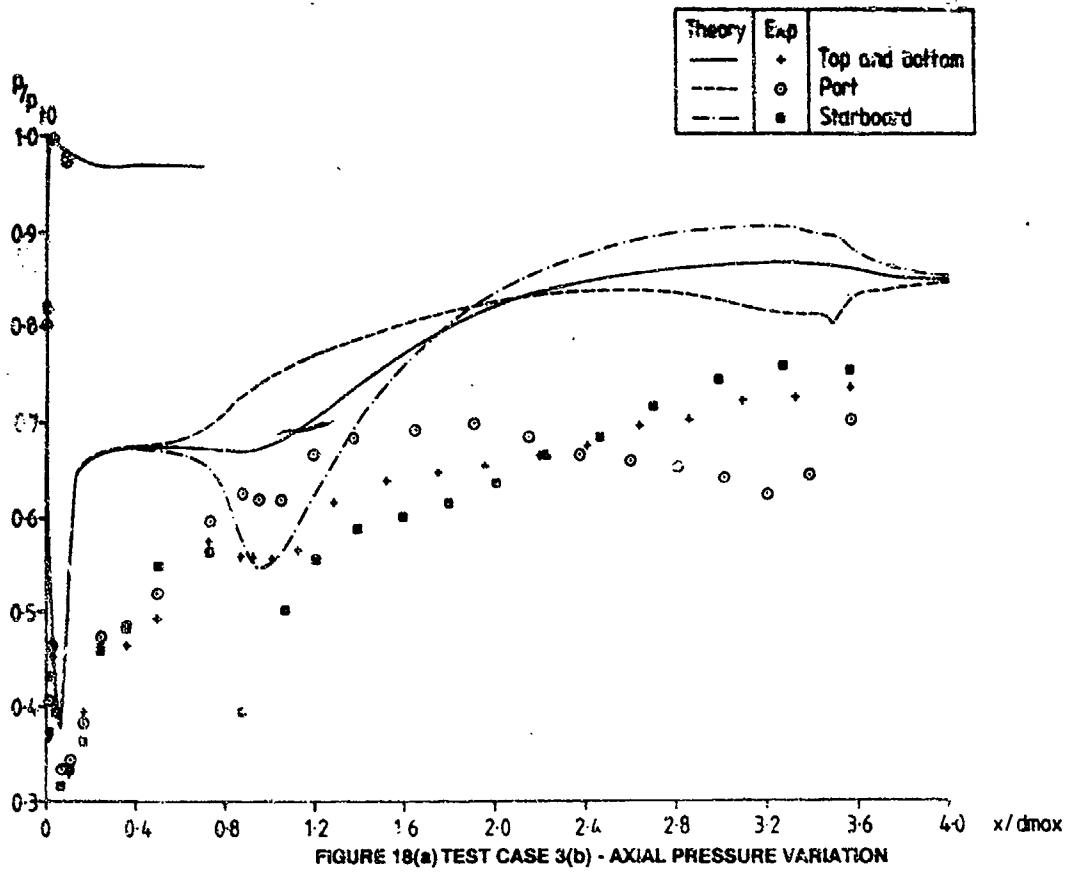


FIGURE 17(b) TEST CASE 3(a) - RADIAL PRESSURE VARIATION



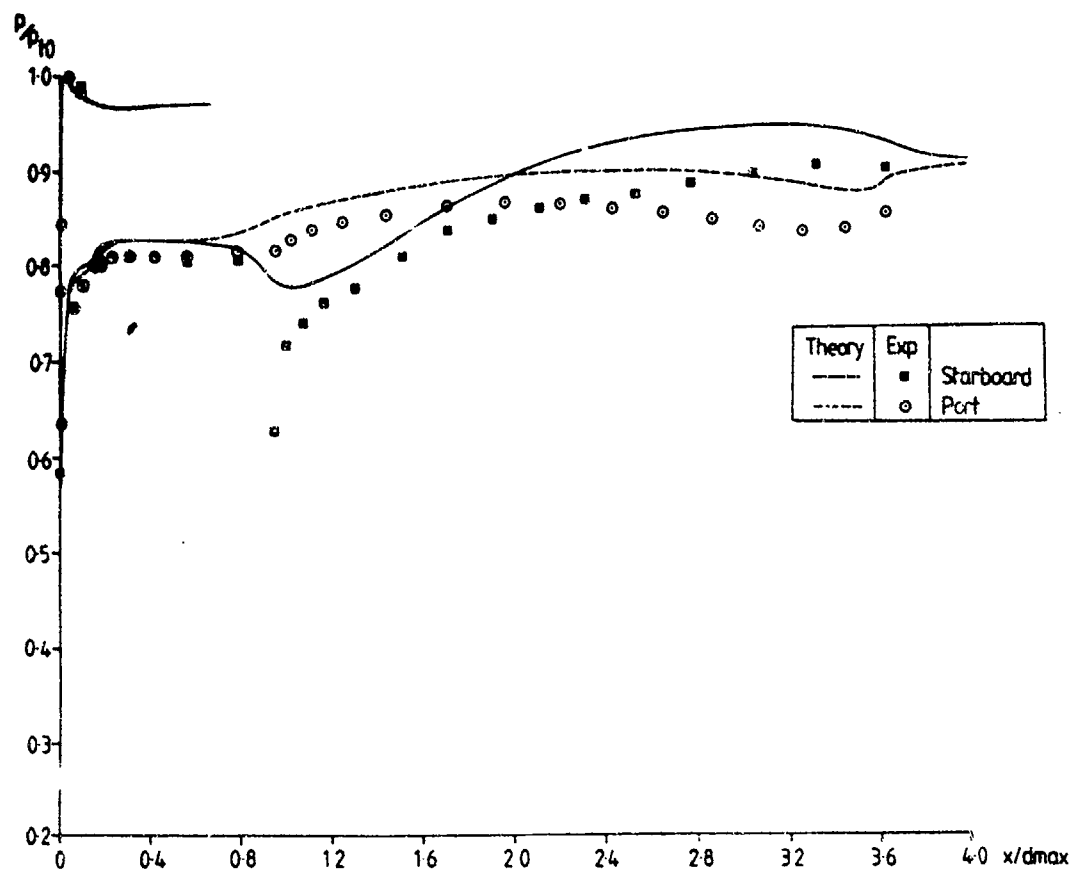


FIGURE 19(a) TEST CASE 4(a) - AXIAL PRESSURE VARIATION

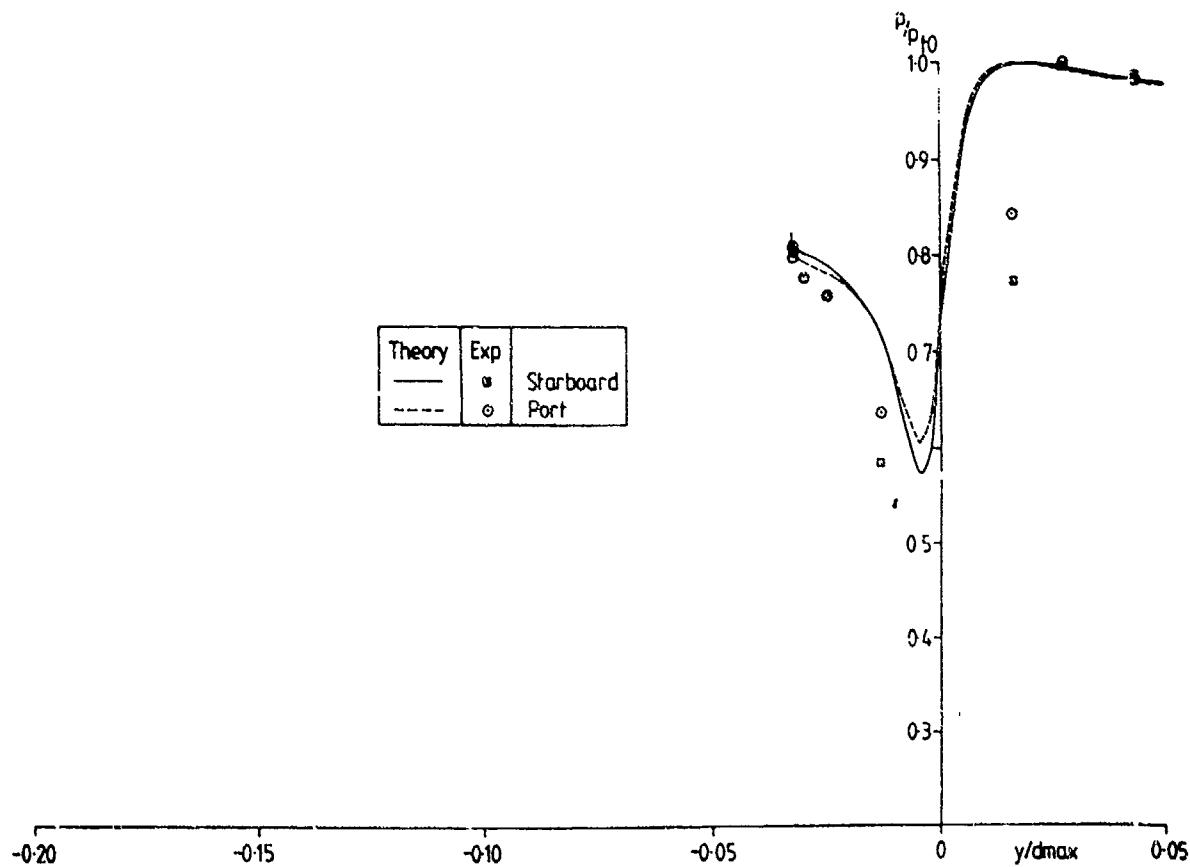


FIGURE 19(b) TEST CASE 4(a) - RADIAL PRESSURE VARIATION

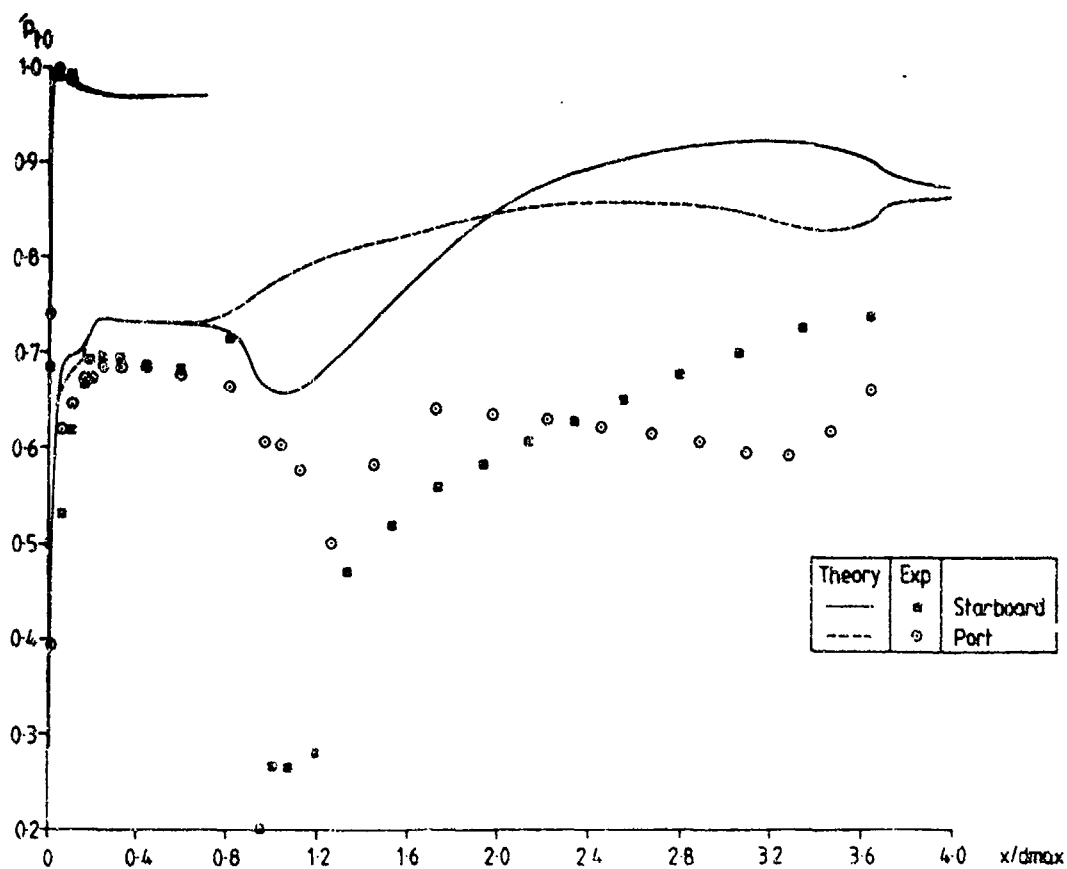


FIGURE 20(a) TEST CASE 4(b) - AXIAL PRESSURE VARIATION

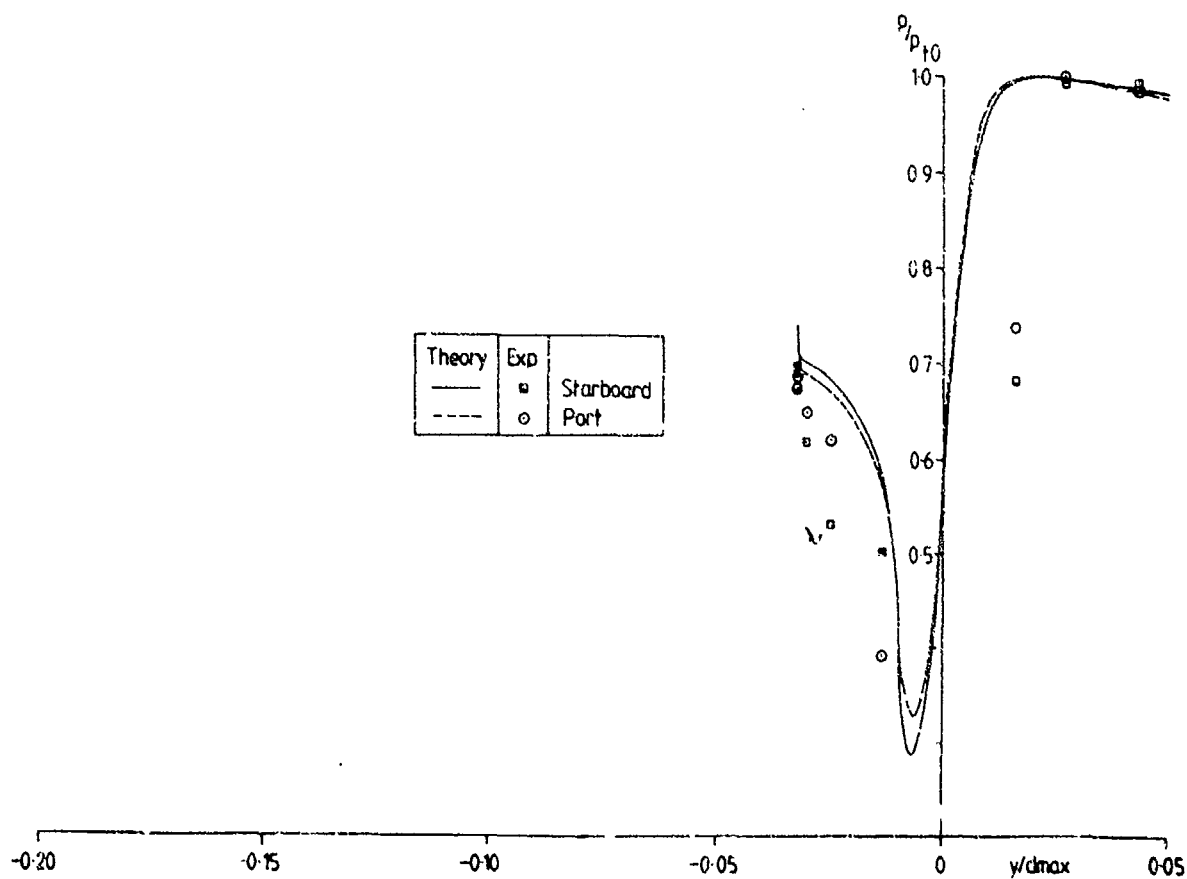


FIGURE 20(b) TEST CASE 4(b) - RADIAL PRESSURE VARIATION

# **AR 270**

**Microfiche Appendix to Sub-Section 3.3.5**

**Contributions to Test Case 5**

**Supersonic circular pitot intake**

**Dornier**

**Page No's  
A185 to A208**

## Contribution of DORNIER to the Test Case 5

### W. Fritz

### Introduction

The testcase 5 consists of three mass flows for the circular pitot intake AGARD M742L. Following there is a listing of the test conditions and the initial conditions.

#### Test Case 5.1:

Total pressure	$H_0$	=	108426 Pa
Static pressure	$p_0$	=	29535 Pa
Total temperature	$T_0$	=	292.2° K
Flight Machnumber	$M_0$	=	1.5
Pressure Recovery	$PR$	=	0.8978
Capture Flow Ratio	$A_0/A_c$	=	0.9307
Capture area	$A_c$	=	8.086 in <sup>2</sup>

#### Test Case 5.2:

Total pressure	$H_0$	=	108359 Pa
Static pressure	$p_0$	=	29517 Pa
Total temperature	$T_0$	=	292.8° K
Flight Machnumber	$M_0$	=	1.5
Pressure Recovery	$PR$	=	0.9246
Capture Flow Ratio	$A_0/A_c$	=	0.6256
Capture area	$A_c$	=	8.086 in <sup>2</sup>

#### Test Case 5.3:

Total pressure	$H_0$	=	108525 Pa
Static pressure	$p_0$	=	29507 Pa
Total temperature	$T_0$	=	292.8° K
Flight Machnumber	$M_0$	=	1.5
Pressure Recovery	$PR$	=	0.9267
Capture Flow Ratio	$A_0/A_c$	=	0.2980
Capture area	$A_c$	=	8.086 in <sup>2</sup>

By prescribing the Mach number, the total temperature and the total pressure for the outer flow field and the intake mass flow ratio for the internal flow, the complete flow field is defined sufficiently. Whereas the Mach number, the total temperature and the total pressure define concrete boundary and initial conditions also for a discrete set of points, the mass flow ratio is an integral value and there is no possibility to use the mass flow ratio itself as boundary condition at a discrete set of points. Therefore, the mass flow ratio was approximated by an iterative variation of the static pressure at the downstream boundary until the desired mass flow ratio was obtained as exactly as possible. For all three test cases only the mass flux ratio nothing else was fitted.

## Grid Generation

For the grid generation, the given geometry was extended cylindrically behind the engine face area, to ensure one dimensional flow conditions at the downstream boundary during the calculation. The grid was generated using conformal mapping with the Maxwell transformation. The Maxwell curves describe contour conformal coordinate lines which are very suitable for inlet configurations. In the complex space, those curves are defined by:

$$z = \frac{a}{\pi} (w + 1 + e^w)$$

with  $z = x + iy$  as the complex coordinates of the physical space and  $w = u + iv$  as the evenly spaced coordinates of the transformed space. The coordinates of the grid lines in the physical space are given by the relations

$$x = \frac{a}{\pi} (1 + ue^u \cos v)$$

$$y = \frac{a}{\pi} (v + e^u \sin v)$$

where the parameter  $a$  is defined by the internal diameter of the inlet. The grid is defined by geometric stretching functions along the cowl and along the diameter; the field grid coordinates are smoothed by elliptical differential equations in the complex space. The final grid is nearly exactly orthogonal. In the figures 5.1 - 5.5 five different grid levels which have been used during the calculations are depicted. The number of volumes indicated in each of the figures, means the number of volumes in one half of the grid. The finest grid consists of 281 points along the cowl from the cowl lip to outflow boundary and of 97 points from the centerline to the cowl. The finest grid starts with  $y^+$  values of 0.3 at the cowl and there are at least three points within  $y^+ = 1.0$ . The finest grid was only used for the test case 5.1 with the high intake mass flow ratio, as for this case a normal shock inside the inlet required a high mesh resolution. In all other test cases only 4 grid levels have been used.

## Flow Solution

The flow solutions were obtained by using Dornier's 2-D and/or axisymmetric block structured flow solver. This method solves the 2-D and/or axisymmetric Reynolds averaged Navier Stokes equations using the finite volume approach and an explicit Runge-Kutta-type time stepping scheme. For convergence acceleration and reduction of the computational effort, local time stepping, implicit residual averaging, the multilevel grid technique and the multigrid strategy within each grid level have been applied. A modified version of the Baldwin-Lomax algebraic turbulence model was used as closure of the Reynolds equations. Turbulent flow was assumed only in those blocks, which are bounded by a fixed wall, in all the other blocks laminar flow was assumed. To prevent an odd-even decoupling, an artificial viscosity term constructed as a blend of second and fourth order derivatives was used.

## Initial Conditions

For all test cases the calculation was started in the coarsest mesh assuming the freestream values as initial conditions. At the downstream boundary the static pressure was prescribed. To get an idea of the magnitude of that static pressure, there was performed a one dimensional calculation using the continuity equation, the definition of the pressure recovery and the relations for a perfect gas with the values, which are given for each test case as input values. Under the assumption of a constant total temperature it is possible to get an equation for the static pressure at the outflow boundary.

The mass flux is given by the capture flow ratio. With the index  $\infty$  for the freestream values and the index  $a$  at the outflow boundary the continuity equation gives:

$$(\rho w)_{\infty} A_{\infty} = (\rho w)_c A_c = (\rho w)_a A_a$$

and the mass flux at the outflow boundary is:

$$(\rho w)_a A_a = (\rho w)_{\infty} \frac{A_{\infty}}{A_c} A_c$$

This mass flux will be approximated by an iterative variation of the static pressure.

In the engine face area (index  $f$ ) there are known (either as given value or by gasdynamic relations):

- $\rho_f w_f$  (continuity equation)
- The mean value of the total pressure  $p_t$  (defined by  $p_w$  and the pressure recovery PR).
- The total temperature  $T_t$  (the total temperature is constant for flows without heat transfer)

With the definition of the total temperature,

$$w_f^2 = 2c_p T_t \left(1 - \frac{T_f}{T_t}\right)$$

the definition of the total pressure,

$$\frac{p_f}{p_t} = \left(\frac{T_f}{T_t}\right)^{\frac{\gamma}{\gamma-1}}$$

the continuity equation

$$\rho_f w_f A_f = \rho_{\infty} w_{\infty} \left(\frac{A_{\infty}}{A_c}\right) A_c$$

and the equation of state for a perfect gas

$$p_f = \rho_f R T_f$$

one can get the relation

$$\frac{1}{\rho_f^2} \left(\frac{p_f}{p_t}\right)^{\frac{2\gamma(\gamma-1)}{\gamma}} = \frac{(\rho_{\infty} w_{\infty} R T_t \frac{A_{\infty}}{A_c} \frac{A_c}{A_f})^2}{2c_p^2 T_t^2} = 1 - \left(\frac{p_f}{p_t}\right)^{\frac{\gamma-1}{\gamma}}$$

or with the substitutions

$$u = \frac{p_f}{p_t}$$

and



$$a_1 = \frac{(\rho_0 u_0 \left(1 + \gamma \frac{A_0}{A_c} \frac{A_c}{A_f}\right)^2)}{2c_p T_{f1}}$$

the above equation can be written as

$$a_1 u^{-\frac{2}{\gamma}} + u^{\frac{\gamma-1}{\gamma}} - 1 = 0$$

This equation can be solved iteratively by the Newton Method. The solution of this equation gives the static pressure in the engine face area under the assumption of one dimensional flow. The pressure at the outflow boundary is assumed to be the same as at the engine face area.

In the following table there is a comparison of the static pressure at the outflow boundary as it was estimated by the above equation and that value which was obtained at the end of the calculation. Also included are capture flow ratios as they were approximated in the calculation compared with the definition values.

	test case 1	testcase 2	testcase 3
$\left(\frac{A_0}{A_c}\right)_{\text{Calculation}}$	0.930	0.630	0.297
$\left(\frac{A_0}{A_c}\right)_{\text{Definition}}$	0.9307	0.6256	0.298
Error:	0.07 %	0.7 %	0.3 %
$\frac{p_0}{p_0}$ Calculation:	2.47	3.12	3.36
$\frac{p_0}{p_0}$ Initial:	2.67	3.15	3.35

As it can be seen, the desired mass flow ratios were approximated very accurately. Except the test case 5.1, the static pressures at the outflow boundary have been predicted extremely well by the one-dimensional precalculation.

During the calculation it was found, that the test case 5.1 with the high intake mass flow ratio was a very critical one. Two solutions for the prescribed mass flow ratio were possible:

- Subsonic flow at the engine face area and the outflow boundary.
- Supersonic flow at the engine face area and the outflow boundary.

Both solutions are very close together and a too low value of the static pressure at the outflow boundary leads to the supersonic solution. Especially at the changes from a coarser to a finer grid the static pressure has to be varied very carefully, as the same static pressure at the outflow boundary gives a higher mass flow ratio in the finer grid. That means, that either the mass flow ratio is kept smaller in the coarse subgrids, or the static pressure at the outflow boundary had to be decreased at the changes from a coarser to a finer grid. If the pressure is decreased too much, the supersonic solution

with a complex shock system around the engine bullet will be obtained. So it was very important, to ensure that the flow at the engine face area was subsonic, and if necessary, the static pressure has to be increased. The test cases 5.2 and 5.3 were run without those problems, as for those mass flow ratios it was impossible to get a supersonic solution.

### *Computer and CPU Times*

The calculations were done on a Convex C220. Using a single processor, the required CPU time for one complete run was 30 - 35 minutes for the test cases 5.2 and 5.3 and 50 minutes for the test case 5.1 with one additional finer grid level. The computing time depends very much on the initial guess of the static pressure at the downstream boundary and on the skill of the user during the variation of that static pressure in order to capture the desired mass flow ratio. If the static pressure at the outflow boundary is fixed, the computing time towards a converged solution is 20 - 25 minutes CPU time. So far, the computing time for a test case at which the mass flow has to be approximated, is not very suitable for a comparison.

### *Convergence and Mass Flow Check*

The convergence plots on each mesh level for all the three test cases are included in the figures 5.6-5.17. They indicate a reduction of the residual by three to four orders of magnitude on each mesh level. Another quality check of the solution is the mass flux along the inlet. Figures 5.18 to 5.20 show that mass flux, obtained by integration of the fluxes in the cross sections, along the inlet. The value  $x/x_{max}=0$  is at the inlet lip,  $x/x_{max}=1$  is at the outflow boundary. In all cases, the mass flux along the inlet is normalized with that value of the outflow boundary. As it can be seen, the error is less than 0.5 %, a value which can also be seen as an accuracy limit of the numerical integration.

## **Results**

### *Flow Fields*

The figures 5.21 to 5.26 show the pressure and Mach number contours of the different flow fields. There is a detached shock in front of the inlet which moves in upstream direction with decreasing mass flow ratio. At the high intake mass flow ratio, there is a supersonic region inside the inlet which is terminated by a normal shock. In the calculation this normal shock is washed out, as even in the finest grid the resolution is not fine enough at the (unknown) position of the normal shock. In the plot of the Mach number contours, it is noticed, that the boundary layer thickness increases considerably behind that normal shock. At the other mass flow ratios the flow inside the inlet is purely subsonic.

### *Pressure Distributions*

The figures 5.27 to 5.41 present the engine face total pressure and static pressure, the boundary layer rake total pressure and static pressure and the static pressure along the cowl compared with the experimental data as they were available. The agreement between the theoretical values and the experimental data is very good for the low and the medium intake mass flow ratio. At the high mass flow ratio, in the calculation the boundary layer along the cowl seems to be too thick as it is indicated by the engine face and the boundary layer rake pressure distributions. A comparison of the static pressure

distribution along the cowl yields, that the pressure behind the shock is too low in the calculation. In the calculation the boundary layer behind the normal shock becomes too thick. This results in a too small net cross section for the inviscid part of the intake flow. To get the desired mass flow by this the static pressure has to be decreased to get the desired mass flow. The reasons therefore may be seen in the inaccurate resolution of the shock layer-interaction. Therefore the grid should be adapted to the flow field, as the position of the shock is a priori unknown at the beginning of the calculation.

A comparison of the computed and the experimental pressure recovery PR in the engine face area is given in the table below. PR was obtained by a numerical integration of the engine face pressure distribution.

Test case	$PR_{comp}$	$PR_{exp}$
5.1	0.85763	0.8978
5.2	0.91137	0.9246
5.3	0.91300	0.9267

As the calculation was performed as an axisymmetric one, the steady state pressure distortion DC60 = 0.0 for all the three test cases in the calculation.

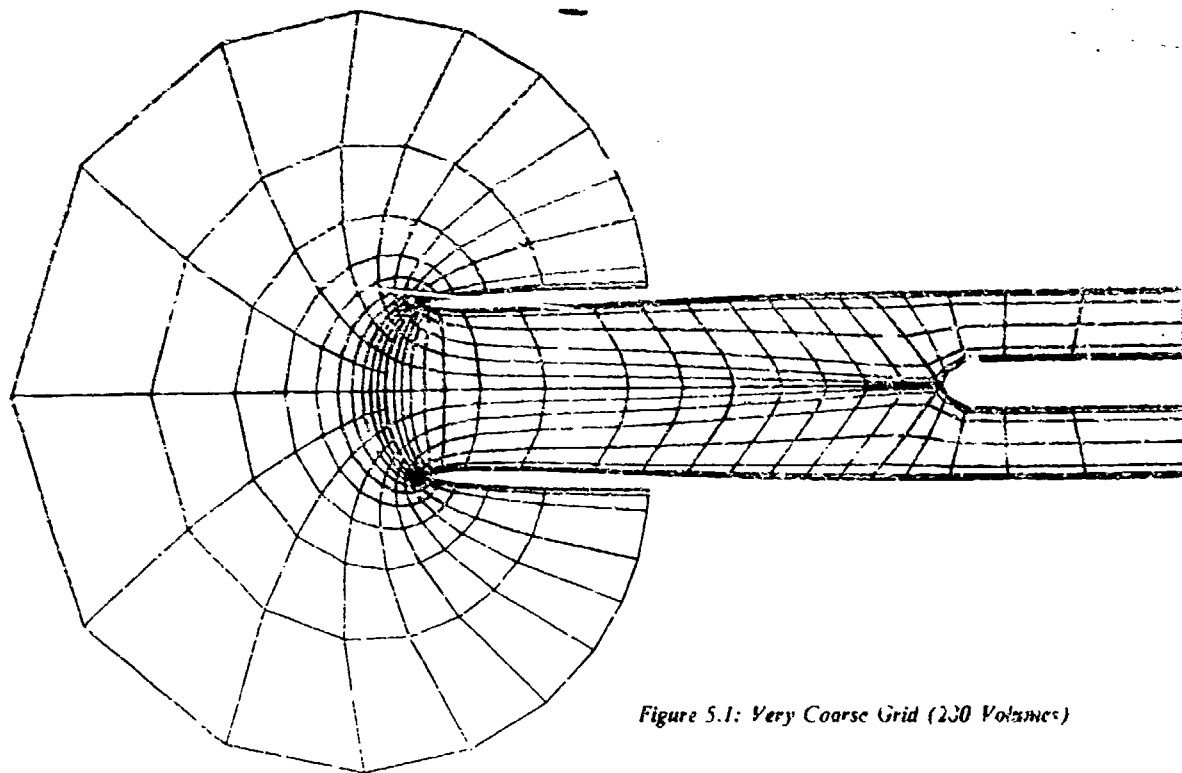


Figure 5.1: Very Coarse Grid (230 Volumes)

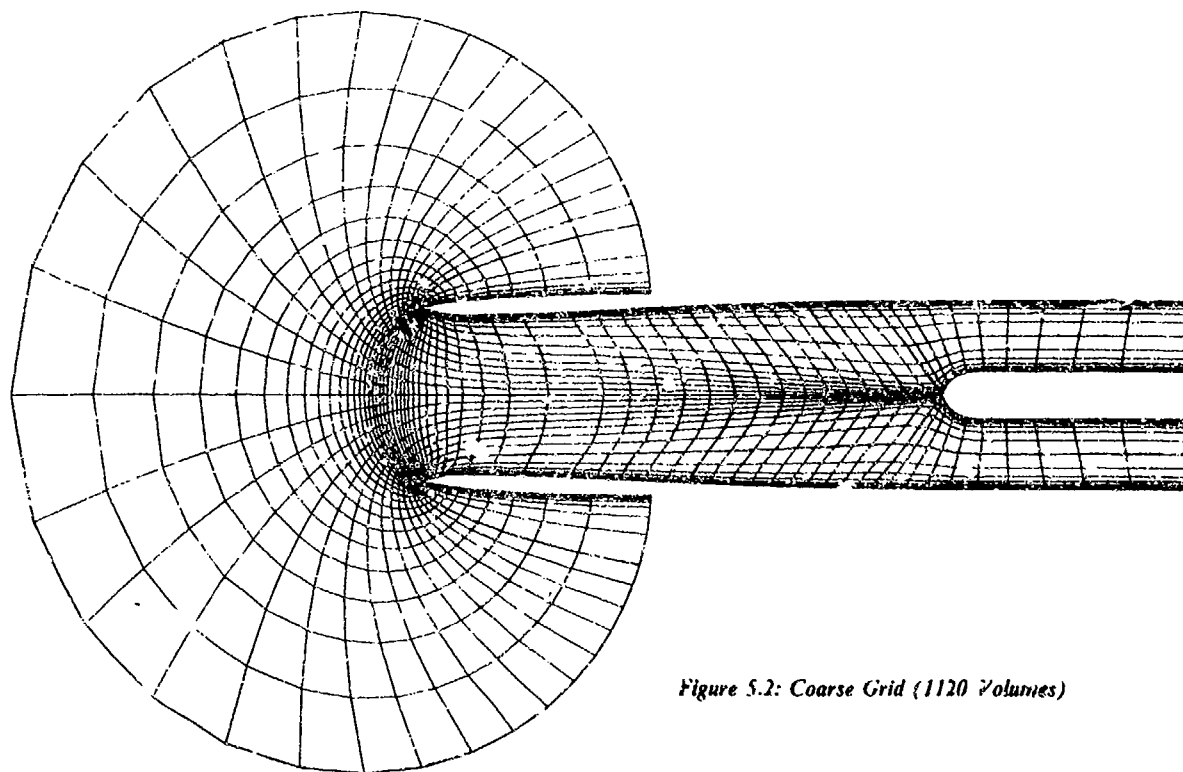


Figure 5.2: Coarse Grid (1120 Volumes)

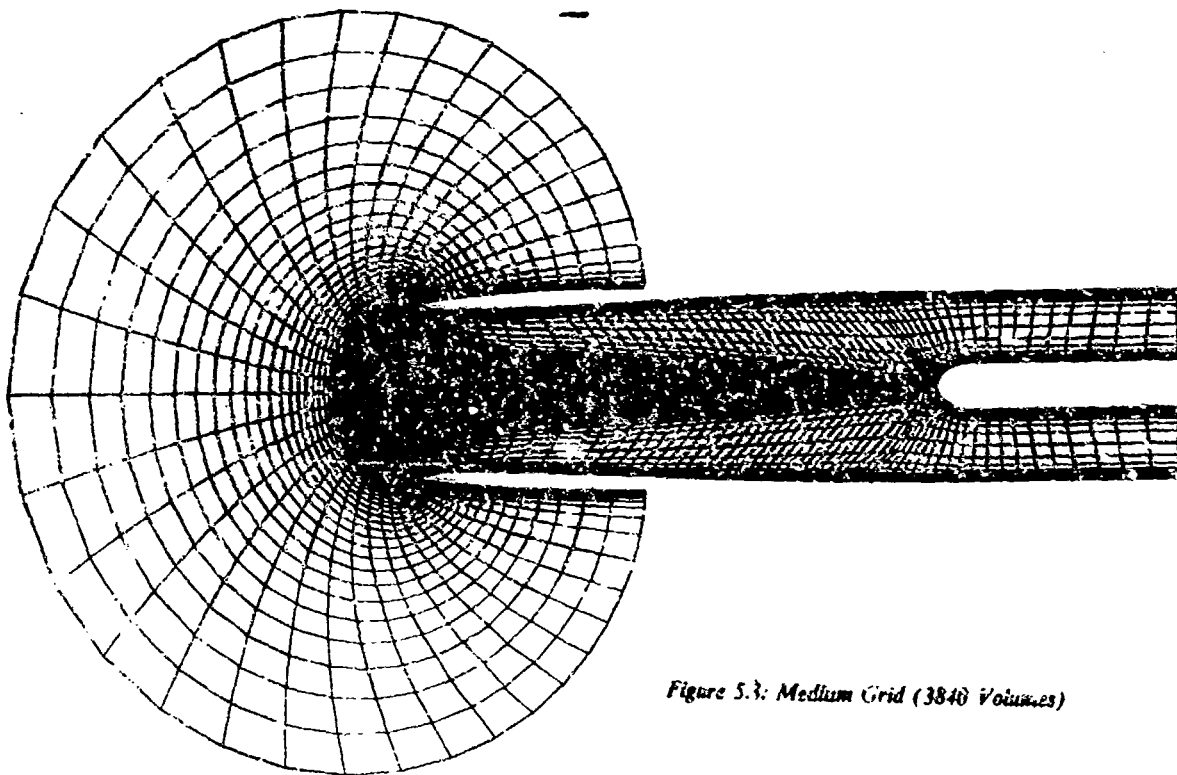


Figure 5.3: Medium Grid (3840 Volumes)

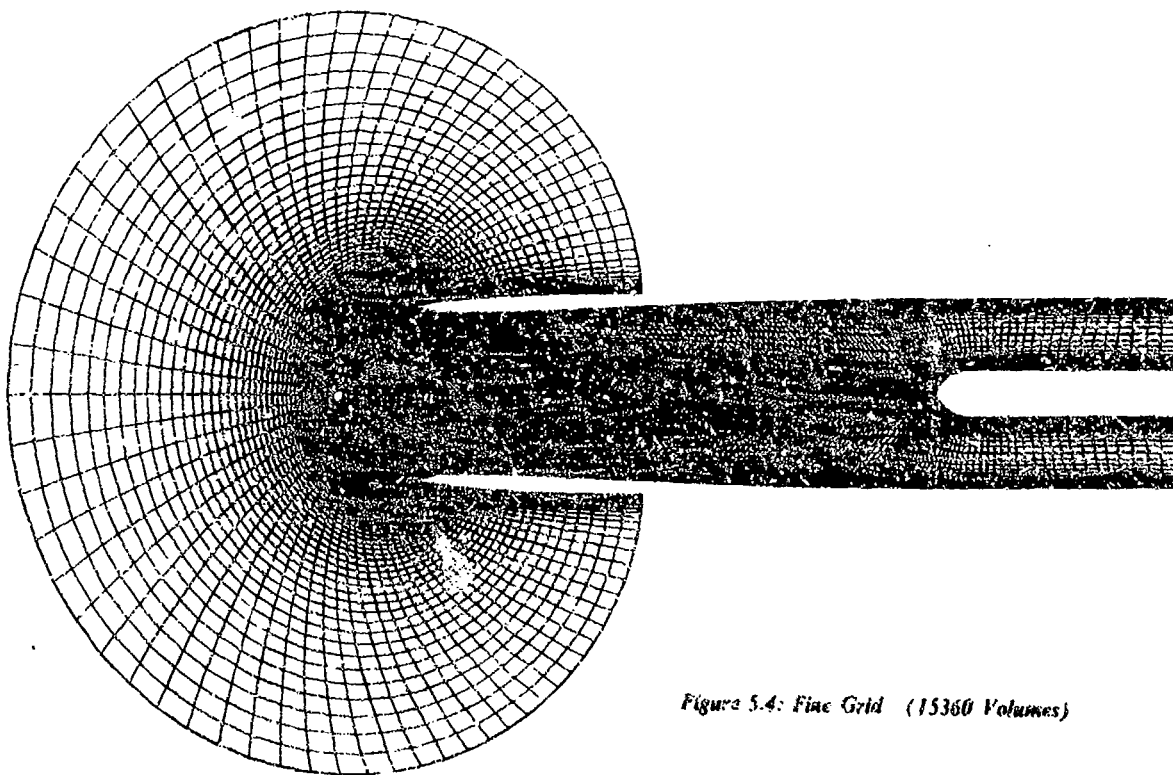


Figure 5.4: Fine Grid (15360 Volumes)

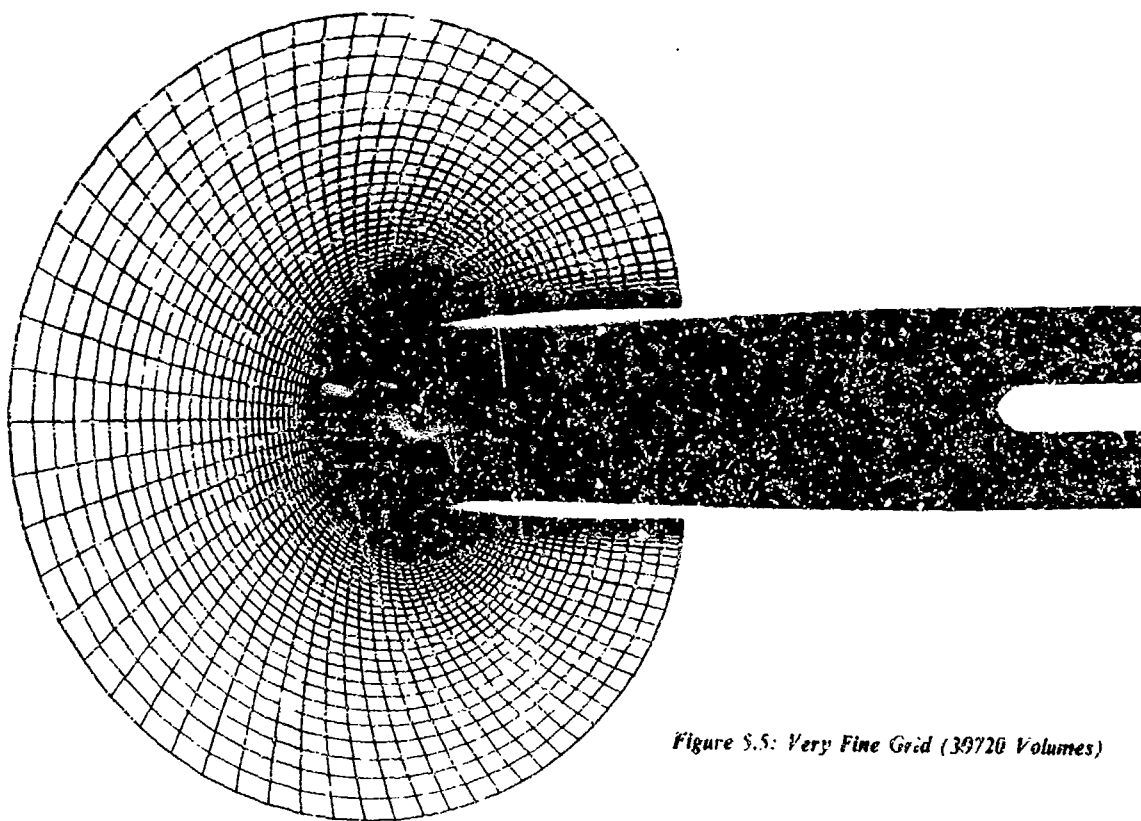
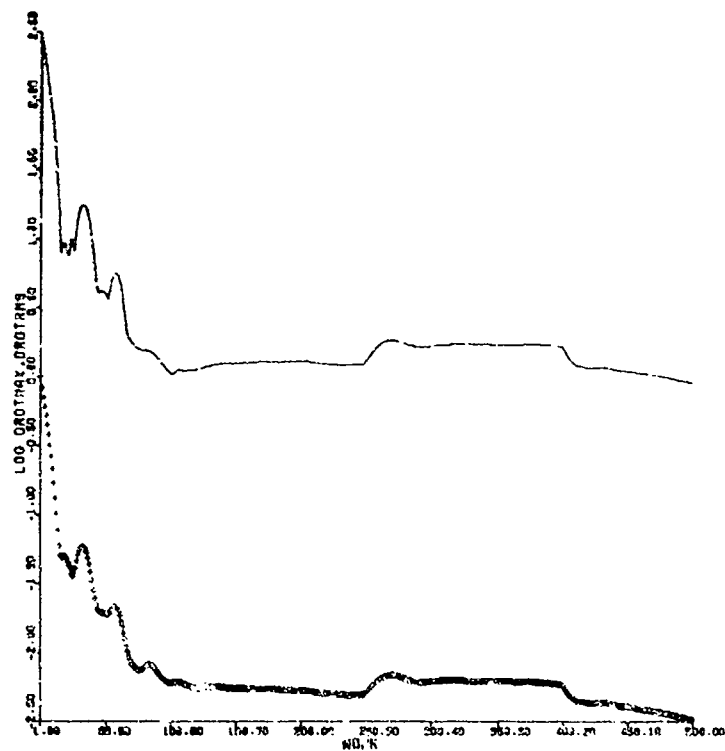


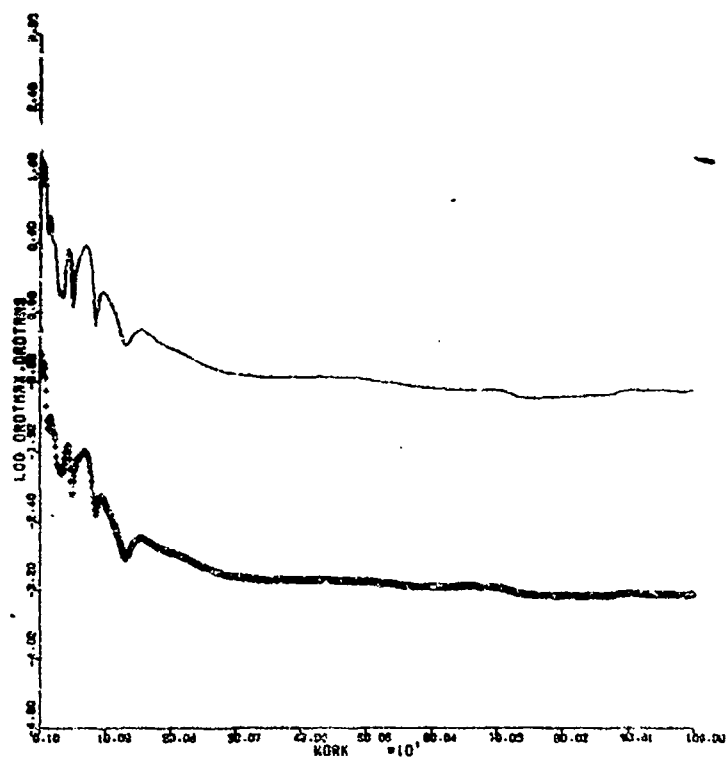
Figure S.5: Very Fine Grid (39720 Volumes)



— DRDTMAX  
+ DRDTRMS

*Figure 5.6*

TESTCASE 5.1 VERY COARSE MESH  
CONVERGENCE BEHAVIOUR  
M=1.50 AO/AC = 0.9307



— DRDTMAX  
+ DRDTRMS

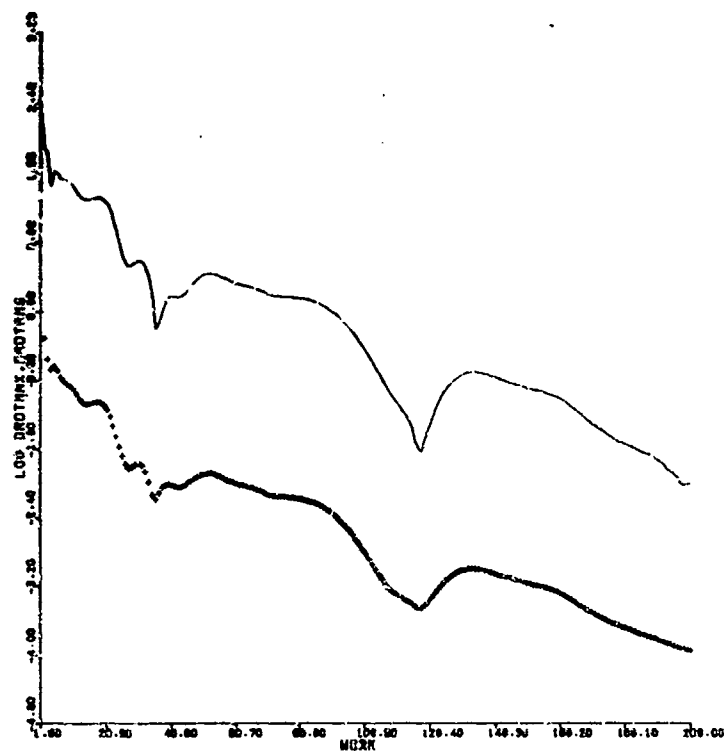
**Figure 5.7**

TESTCASE 5.1 COARSE MESH

CONVERGENCE BEHAVIOUR

$M = 1.50$   $RO/AC = 0.9307$





— DRDTMAX  
+ DRDTRMS

**Figure 5.8**

TEST CASE 5.1 MEDIUM GRID  
CONVERGENCE BEHAVIOUR  
 $M = 1.50$   $A0/AC = 0.9307$

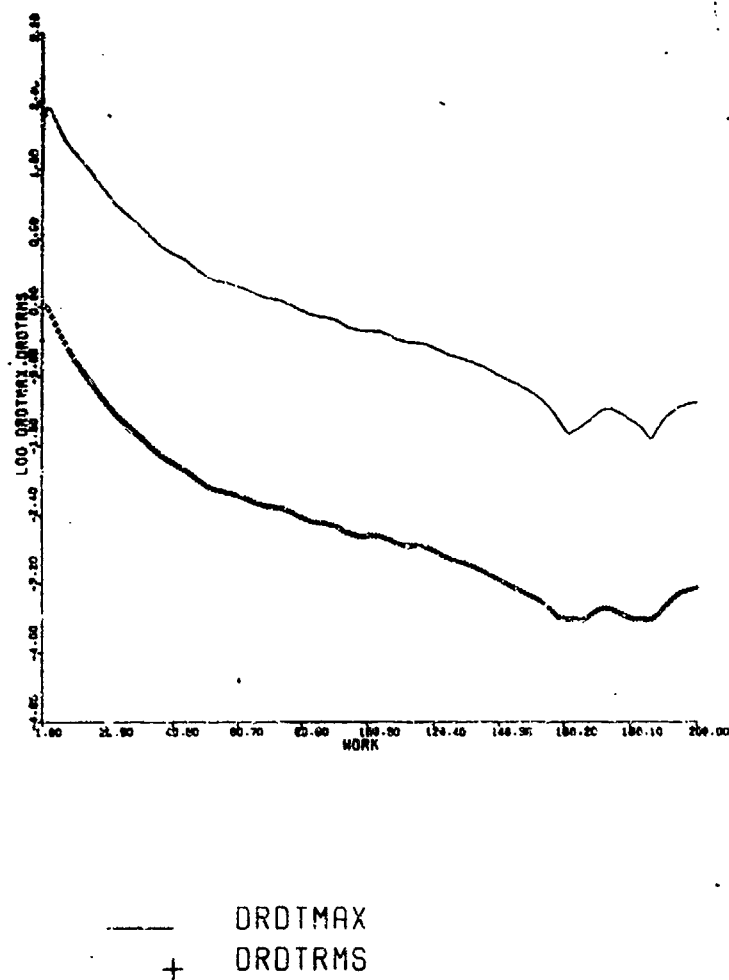
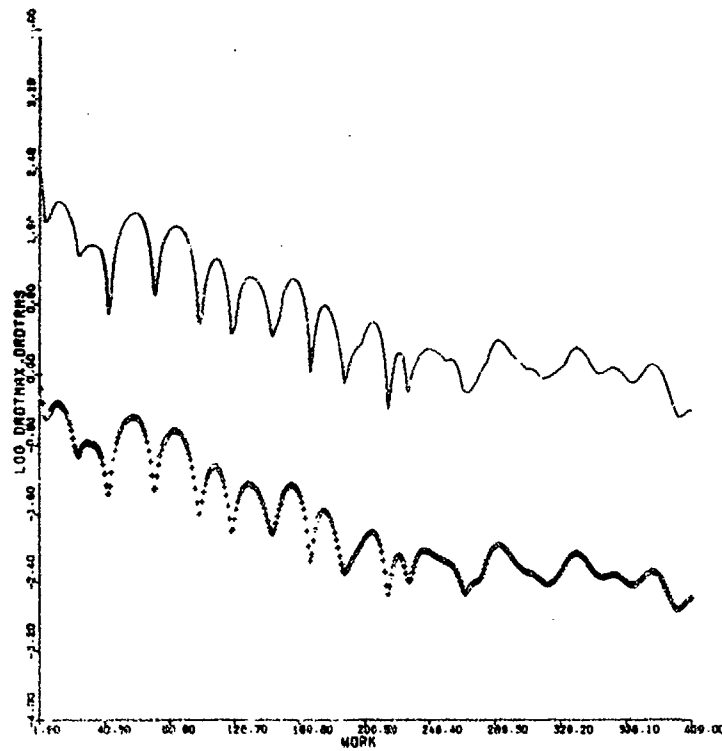


**Figure 5.9**

TESTCASE 5.1 FINE MESH

CONVERGENCE BEHAVIOUR

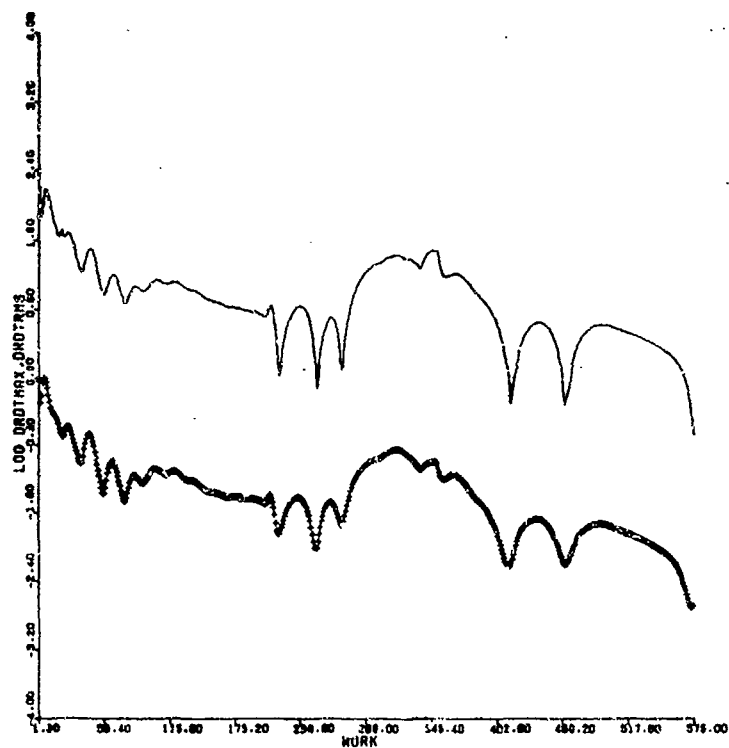
M = 1.50 AO/AC = 0.9307



— DROTMAX  
+ DROT RMS

*Figure 5.10*

TESTCASE 5.2 VERY COARSE MESH  
CONVERGENCE BEHAVIOUR  
 $M = 1.50$   $A0/AC = 0.6256$



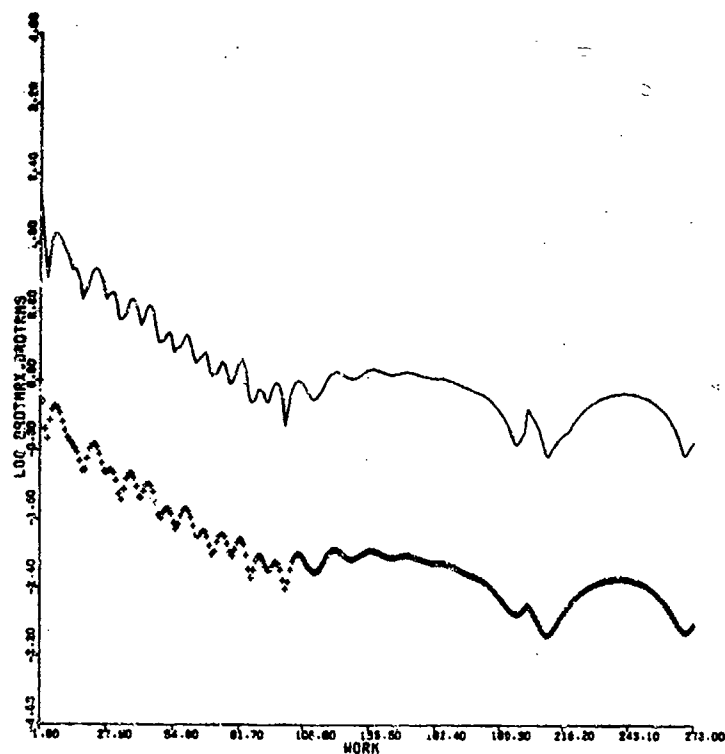
— DRDTMAX  
+ DRDTRMS

*Figure 5.11*

TESTCASE 5.2 COARSE MESH

CONVERGENCE BEHAVIOUR

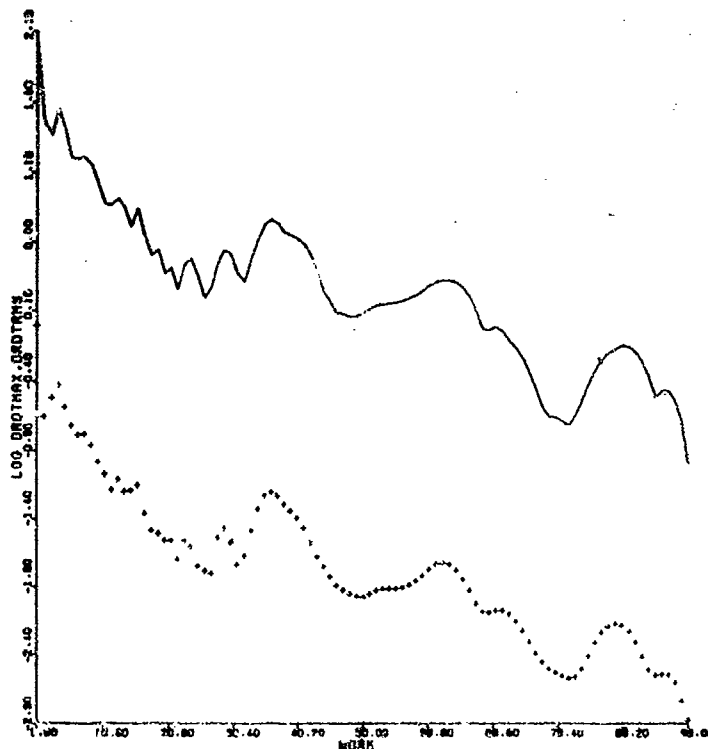
$M = 1.50$      $AO/AC = 0.6256$



— DRDTMAX  
+ DRDTRMS

**Figure 5.12**

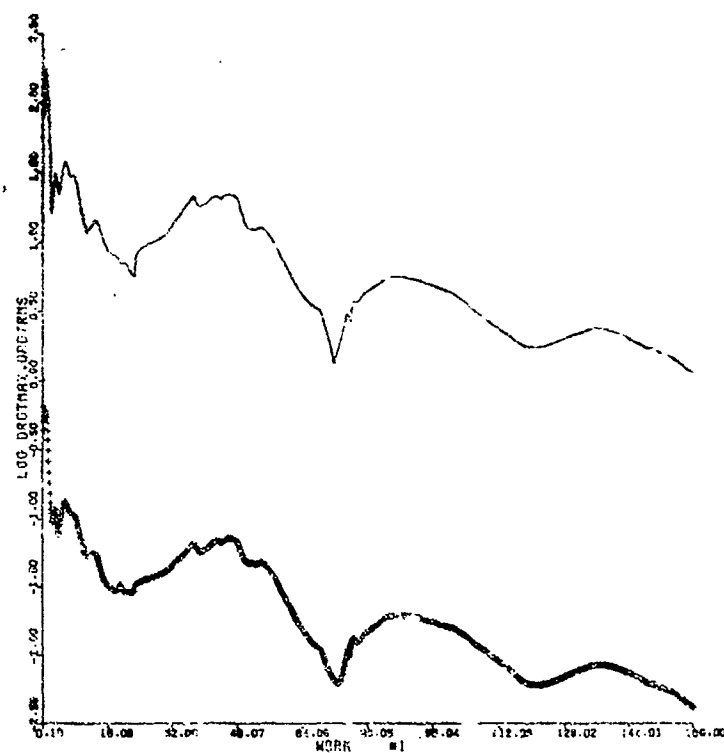
TESTCASE 5.2 MEDIUM MESH  
CONVERGENCE BEHAVIOUR  
 $M = 1.50$   $AO/AC = 0.6256$



— DROTMAX  
 + DROT RMS

**Figure 5.13**

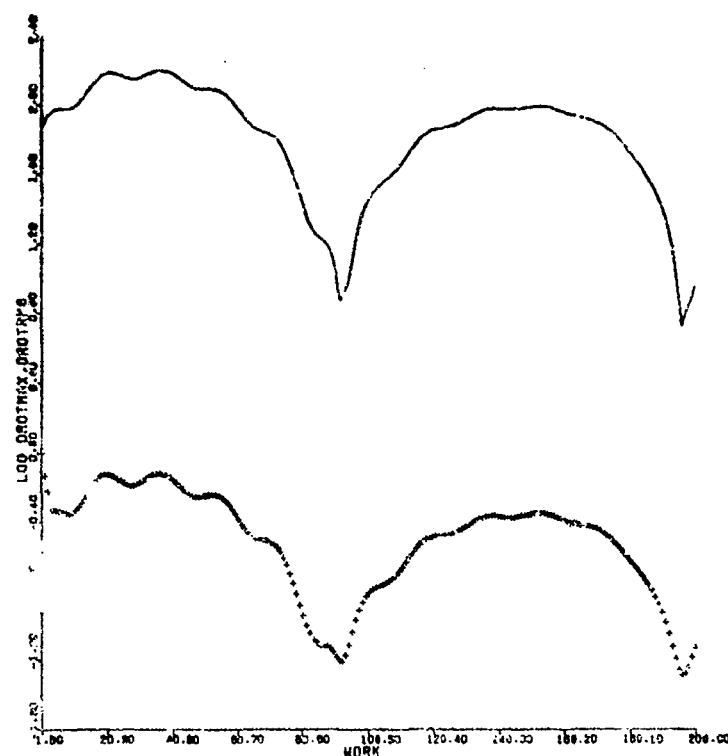
TESTCASE 5.2 FINE MESH  
 CONVERGENCE BEHAVIOUR  
 $M = 1.50$      $A0/AC = 0.6256$



---- DROTMAX  
 + DROT RMS

*Figure 5.14*

TESTCASE 5.3 VERY COARSE MESH  
 CONVERGENCE BEHAVIOUR  
 M = 1.50 AO/AC = 0.298



— DROTMAX  
+ DRDTRMS

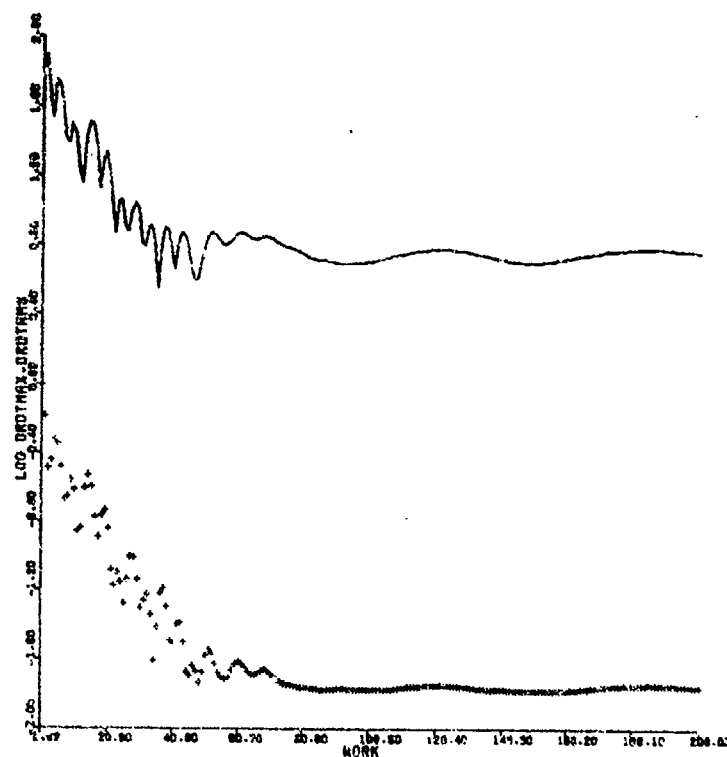
*Figure 5.15*

TESTCASE 5.3 COARSE MESH

CONVERGENCE BEHAVIOUR

$M = 1.50$   $AO/AC = 0.298$





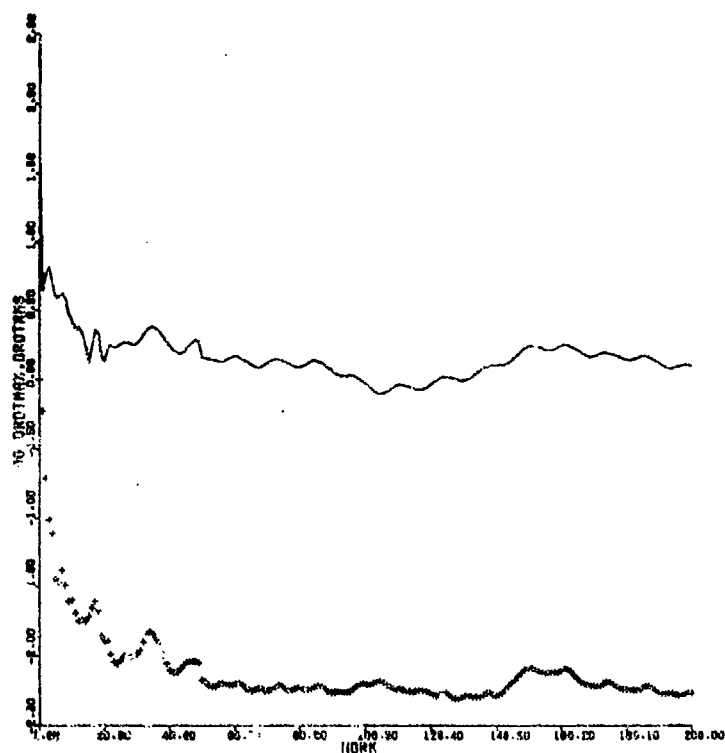
— DRDTMAX  
+ DRDTRMS

**Figure 5.16**

TESTCASE 5.3 MEDIUM MESH

CONVERGENCE BEHAVIOUR

$M = 1.50$   $AO/AC = 0.298$



— DROTMAX  
+ DROTMS

*Figure 5.17*

TESTCASE 5.3 FINE MFSH  
CONVERGENCE BEHAVIOUR  
M = 1.50 RO/AC = 0.298

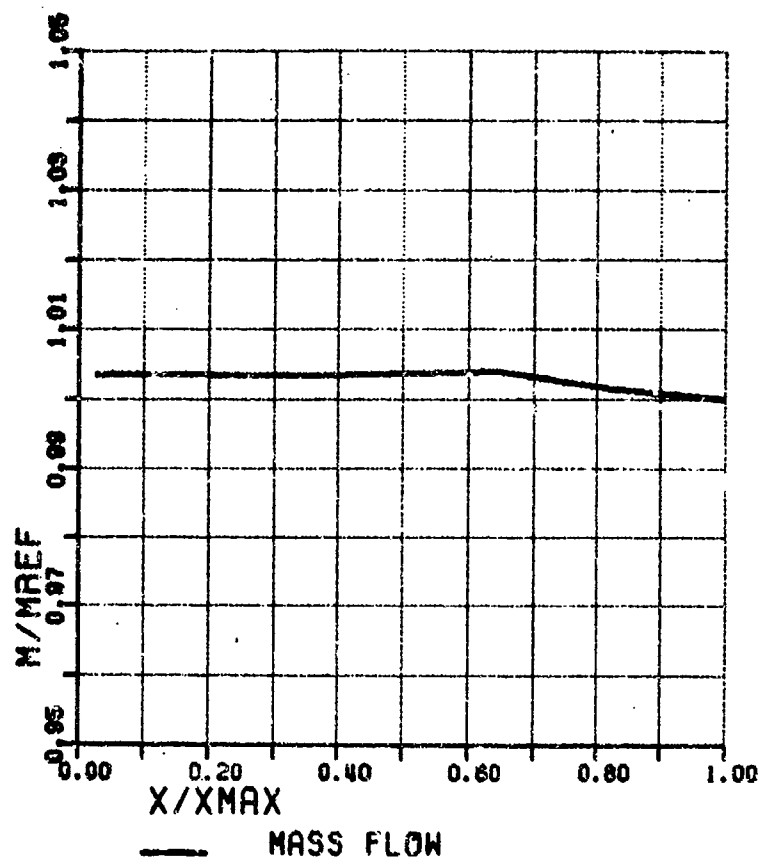
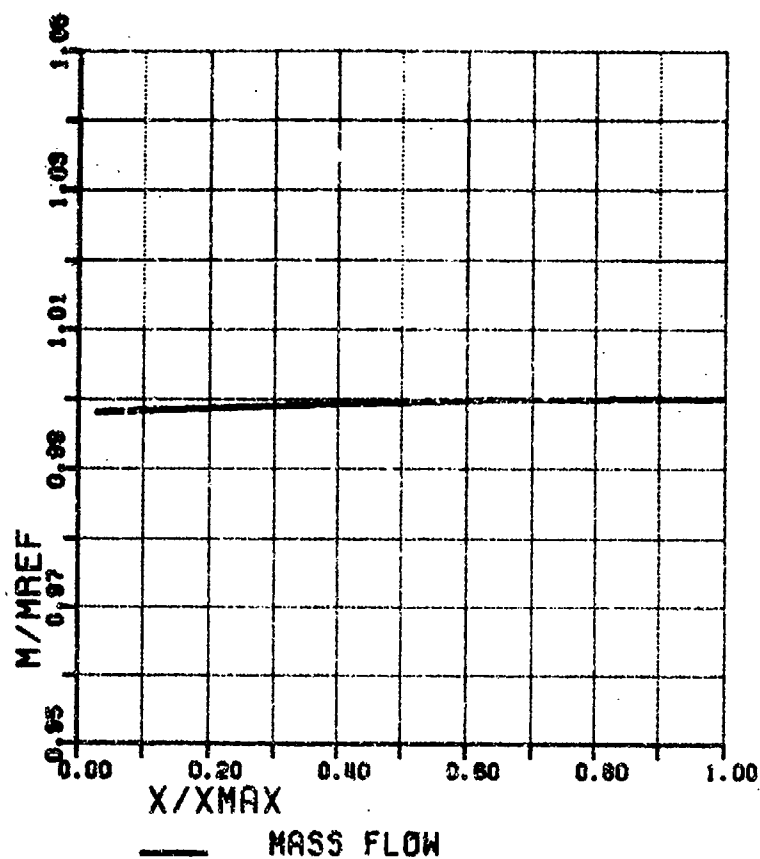


Figure 5.18

AGARD WG 13 TEST CASE 5.1  
 NORMALIZED MASS FLOW RATIO  
 MASS FLUX RATIO MREF = 0.930



*Figure 5.19*

AGARD WG 13 TEST CASE 5.2  
NORMALIZED MASS FLOW RATIO  
MASS FLUX RATIO  $M_{REF} = 0.630$

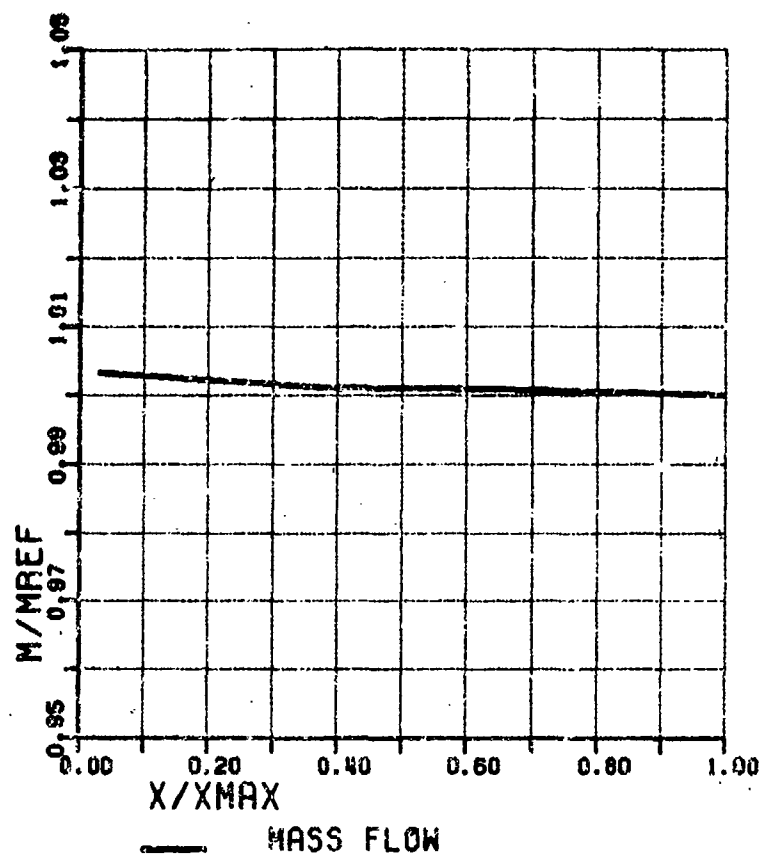


Figure 5.20

AGARD WG 13 TEST CASE 5.1  
 NORMALIZED MASS FLOW RATIO  
 MASS FLUX RATIO MREF = 0.297

# AR 270

## Microfiche Appendix to Sub-Section 3.3.6

### Contributions to Test Case 6

#### 2D hypersonic intake

	Page No's
Aérospatiale	A210 to A231
Dornier	A232
General Dynamics	A233 to A262
MBB	A263 to A295
Sverdrup, AEDC	A296 to A309
NASA Lewis	A310 to A338

**V. BRUMEAU - P. GARNERO**  
**Service Aérodynamique Théorique**  
**Les Gâtines - 91370 Verrières le Buisson**

**TEST CASE 6**  
**NASA P8 high aspect ratio mixed compression intake**  
**( supersonic part only )**

Flow calculations are based on two different models :

- a perfect gaz model with resolution of Euler's equations,
- a viscous gaz model with resolution of averaged Navier-Stokes equations completed by a turbulence model.

**1. Euler results**

**1.1 Code used:**

The Euler multi domain code FLU3M, which has been developed by ONERA in collaboration with ~~a~~ **aérospatiale**, applies to numerically simulated flows of gazes around and in complex configurations with an emphasis on supersonic and hypersonic flows.

The code organisation is built around 3 key units : a command interpreter which assumes the user interface, a plan monitoring unit which decides of the type of the computation, and a plane processor including the numerical scheme.

**1.2 Computer used:**

The FLU3M code runs on a CONVEX C220 bi-processor with 512 M-octets of central memory.

### 1.3 Grid:

As the flow in the air intake could be considered to be bidimensional, the simulation was 2D with 3 identical plans in order to use the 3D code FLU3M.

The treatment of the air intake geometrie has led us to adopt a multiblock grid made of 3 structured domains on each plan.

The first domain, composed by 100x60 points, represents the ramp; the second one of 115x40 points dimension defines the volume between the centerbody and the cowl, whereas the third one 100x20 structures the external part of the cowl. ( figure 1 )

### 1.4 Initial conditions:

$$M_0 = 7.4 \quad \alpha = 0^\circ \text{ and } \beta = 0^\circ$$

Each domain was initialised with the infinite upstream conditions.

We use a dynamic data file included algorithm and flow parameters, the definition of each grid and its initialisation.

### 1.5 Difficulties:

The difficulties we met were mainly due to the grid quality imposed by the flow nature. Boundaries were splined to avoid undesirable pressure rates.

Because of mesh constraints, cowl extremity couldn't be blunted enough to make the cowl shock detached; The effective upstream displacement of the cowl shock is achieved by moving the cowl leading edge to the "virtual origin" defined by the tangent to the cowl surface and the experimental shock location downstream of the inlet entrance. As the figure 2 indicates, the virtual origin is placed 1.1 in. upstream of the actual origin. ( figure 3 and 4 )  
( ref 1 )

### 1.6 Results:

The quality check of calculations is tested with a controle of residues, which reache  $10^{-4}$  for 5000 iterations in the present case.



We present the results we have obtained compared to experimental measures given by AGARD.

Figure 5 presents static pressures contours in the inlet.

Figures 6 and 7 represent static pressures on the centerbody surface and on the cowl surface.

Results with advanced cowl leading edge are compared to results with actual origin and experimental measures.

Figures 8 and 9 represent static pressures contours in the inlet with the actual origin and with the virtual origin.

Figures 10 and 11 represent Mach numbers contours in the inlet with the actual origin and with the virtual origin.

Figure 12 represents Mach numbers in the entrance section.

Figure 13 represents pitot pressures in the cowl entrance section. Euler simulation don't compute boundary layer effects that explains the difference between calculations and experimental measures near boundaries. Because of that difference, the comparison for further sections doesn't present from our point of view the interest that Navier-Stokes results may have, that's why these results are not presented here.

## 2. Navier-Stokes Results

### 2.1 Code used:

The Navier-Stokes code NS2D was adapted for air intakes cases from a model developed by ONERA. Internal flows calculations are based on the resolution of the Reynolds averaged Navier-Stokes equations ( viscous flows ) with an algebraic turbulence model ( ref 2 and 3 ).

The numerical method of MICHEL is characterised by the use of a centered explicit finite difference scheme combined with a multigrid convergence acceleration technique.

### 2.2 Computer used:

The NS2D code runs on a convex C220 bi-processor.

### 2.3 Grid:

Although this bidimensional code copes with multi domain calculations, the case was treated on a single domain, structured by 247x73 points ( figure 14 ). A high density of points on boundaries is needed to capture boundary layer thickness. Boundaries were also splined and the cowl nose lightly blunted ( figure 15 ).

### 2.4 Initial conditions:

$M_0 = 7.4$  ,  $\alpha = 0^\circ$  and  $\beta = 0^\circ$

Calculations were initialised with the upstream infinite Mach number.

### 2.5 Results:

Figure 16 represents static pressure contours in the inlet.

Figures 17 and 18 represent static pressure on the centerbody and on the cowl

Figure 19 represents static pressure contours in the inlet.

Figure 20 represents Mach numbers contours in the whole domain and specially in the inlet.

Figure 21 represents the Mach numbers in the entrance section.

Figure 22 to 30 represent pilot pressure in different sections of the inlet.

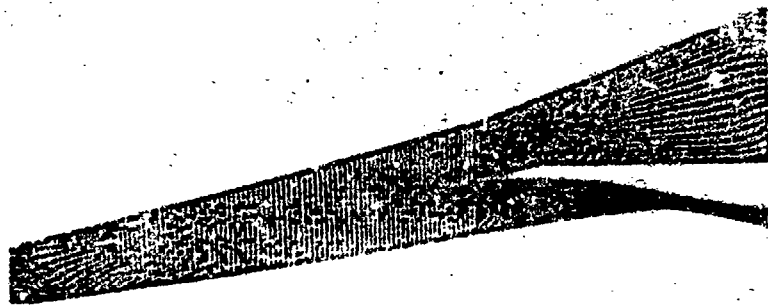


Figure 1: Mesh of the actual cowl leading edge

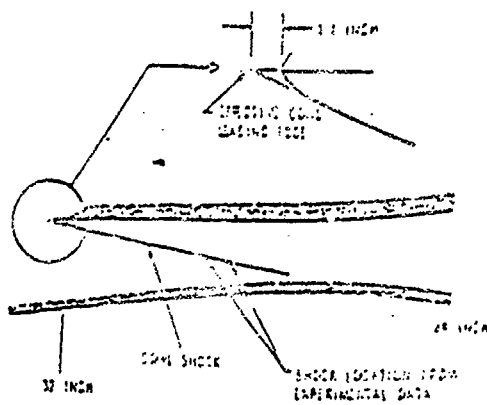


Figure 2: Determining effective cowl leading edge.

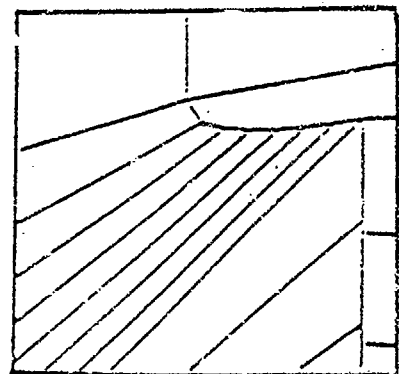


Figure 3  
Definition of the cowl leading edge mesh

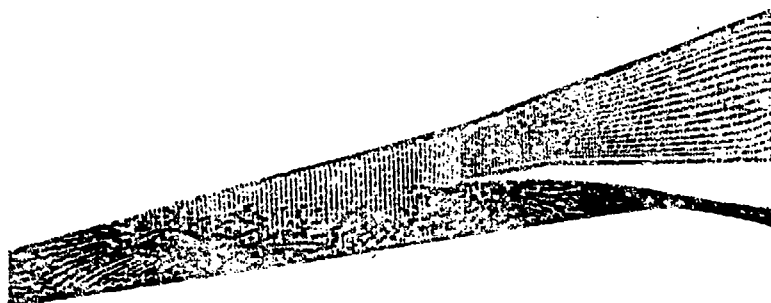


Figure 4  
Mesh of the advanced cowl leading edge

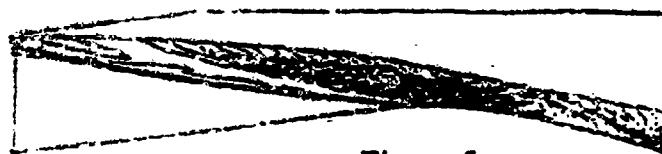


Figure 5  
Static pressure contours

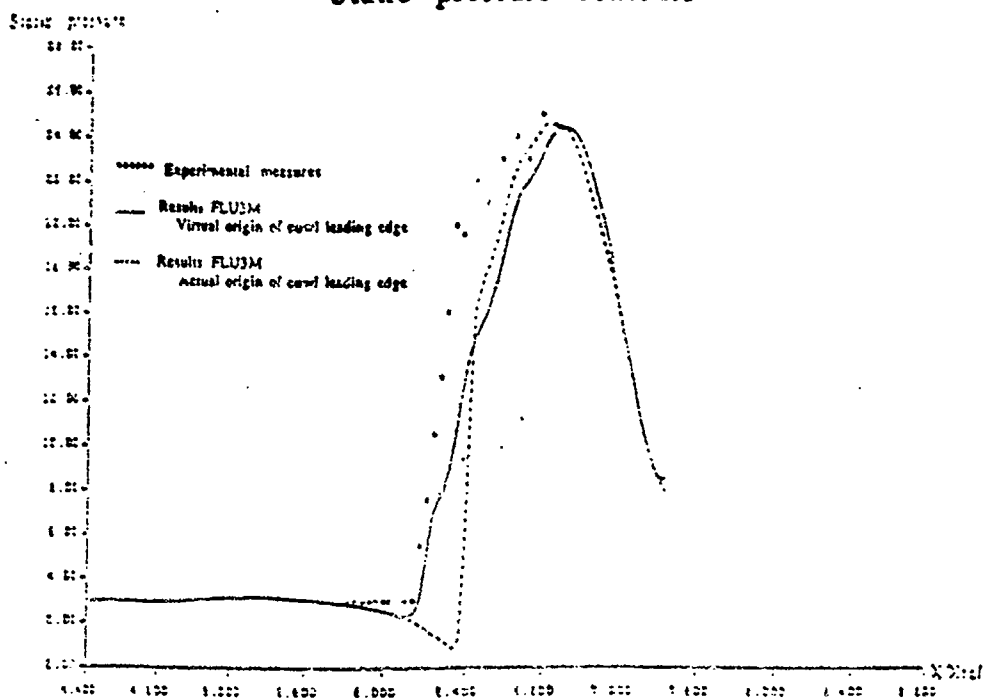


Figure 6: P8 FLU3M results  
Static pressure on the centerbody

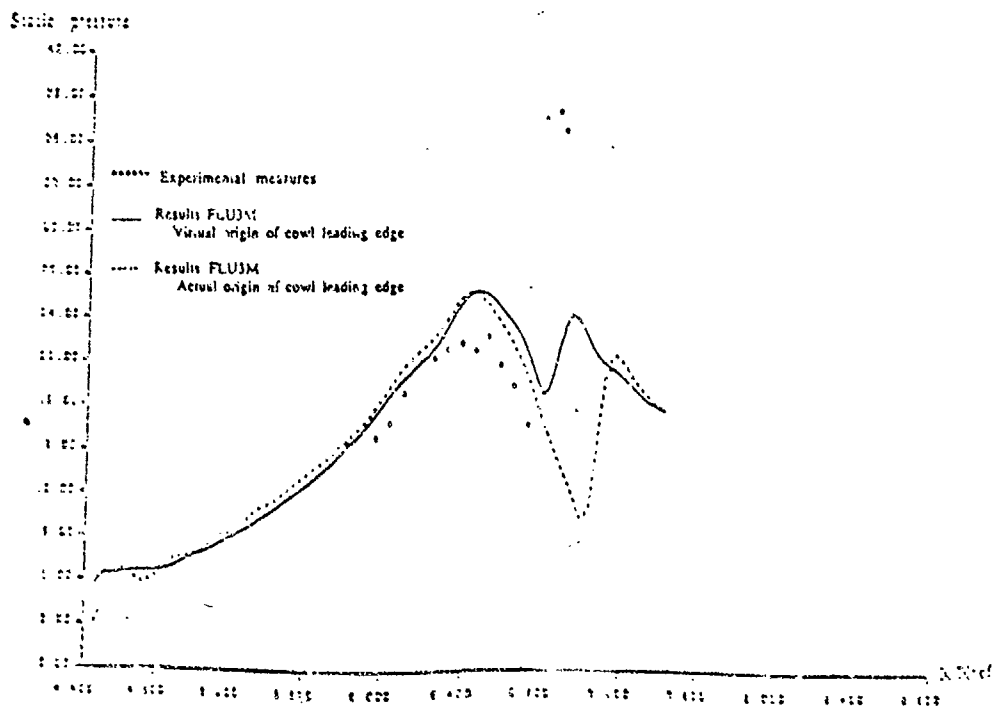
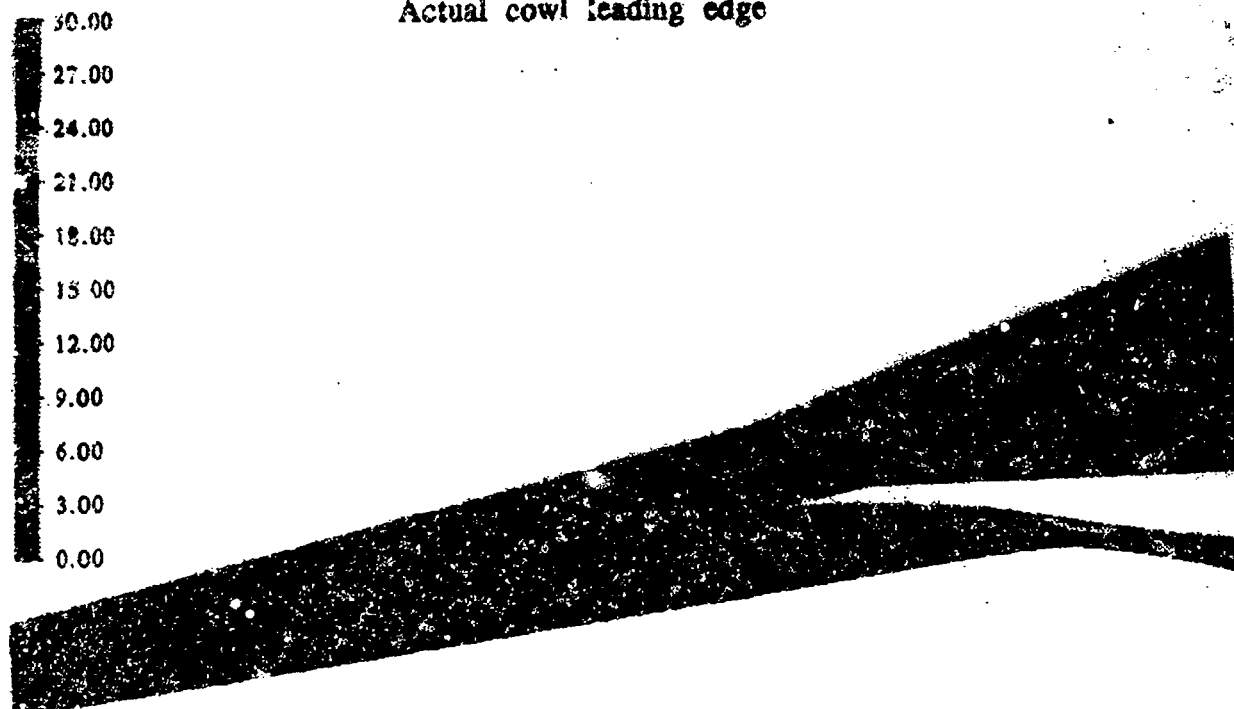


Figure 7: P8 FLU3M results  
Static pressure on the cowl

Figure 8 : FLU3M results  
Visualization of static pressure contours  
Actual cowl leading edge



A colour reproduction of this  
illustration can be found on  
fiche number 5.

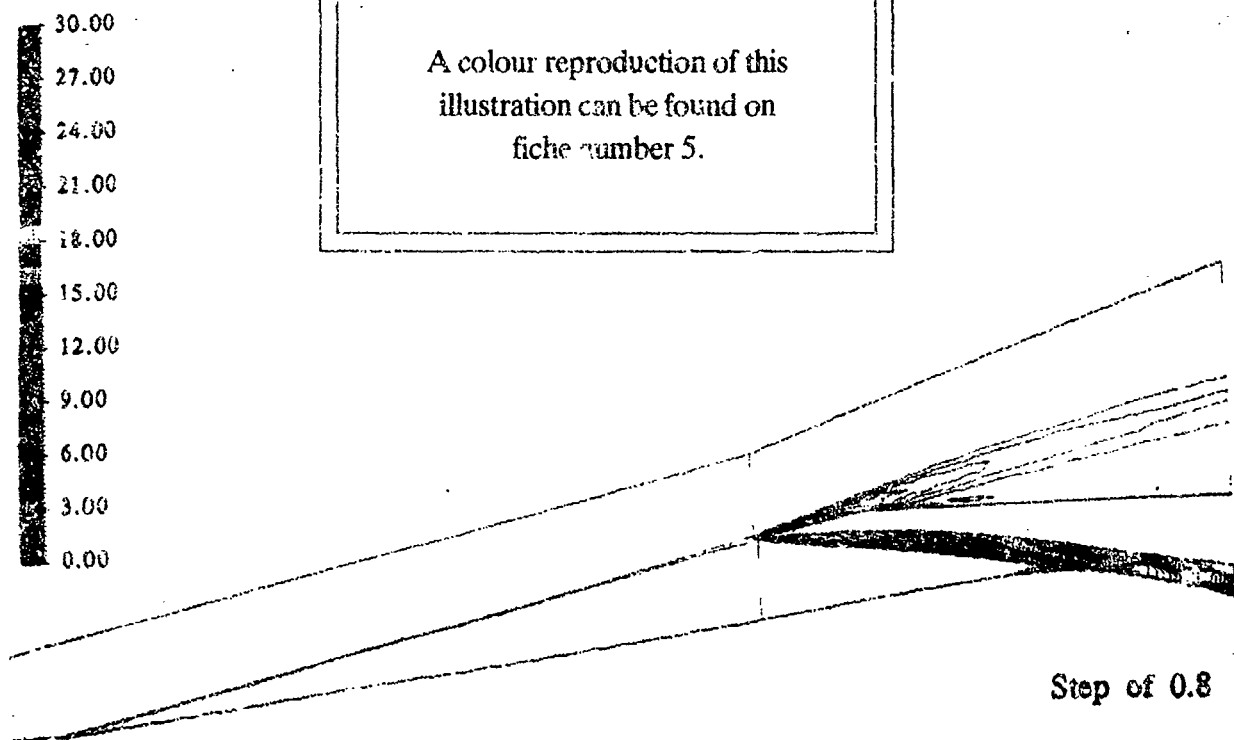
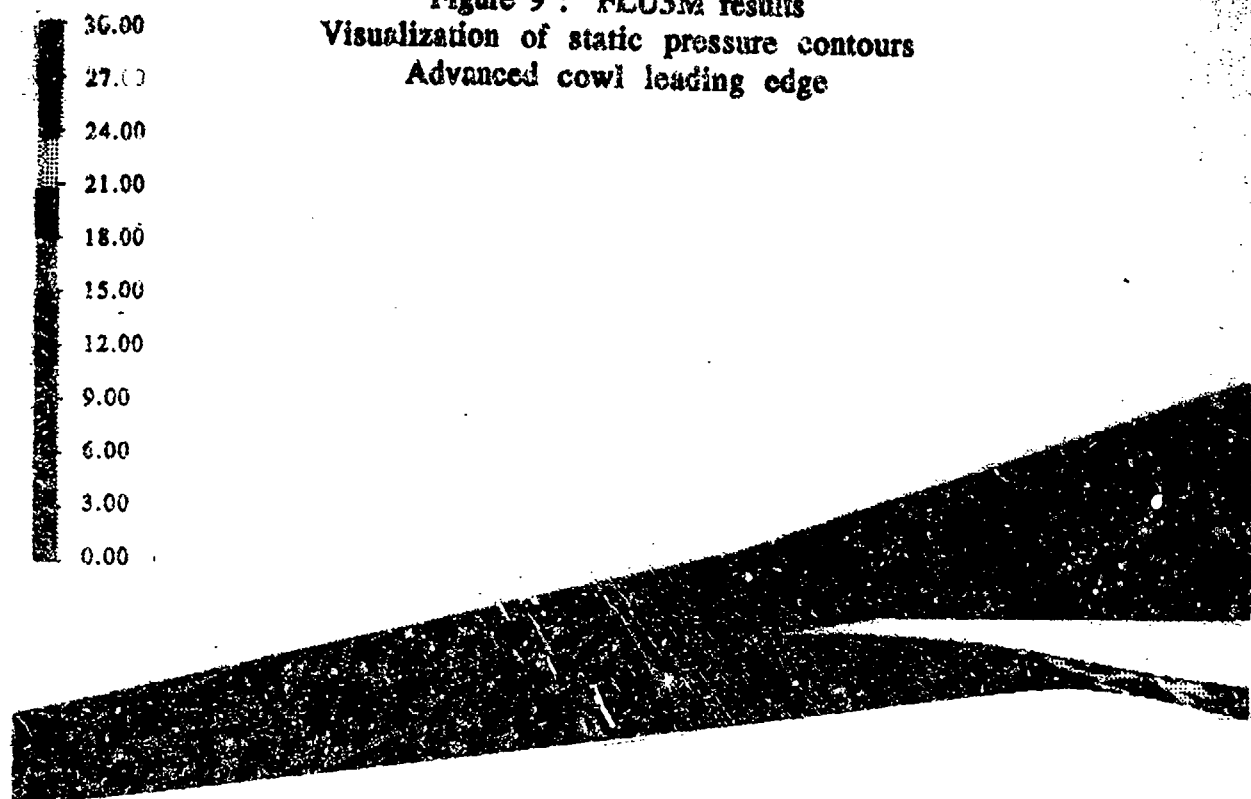
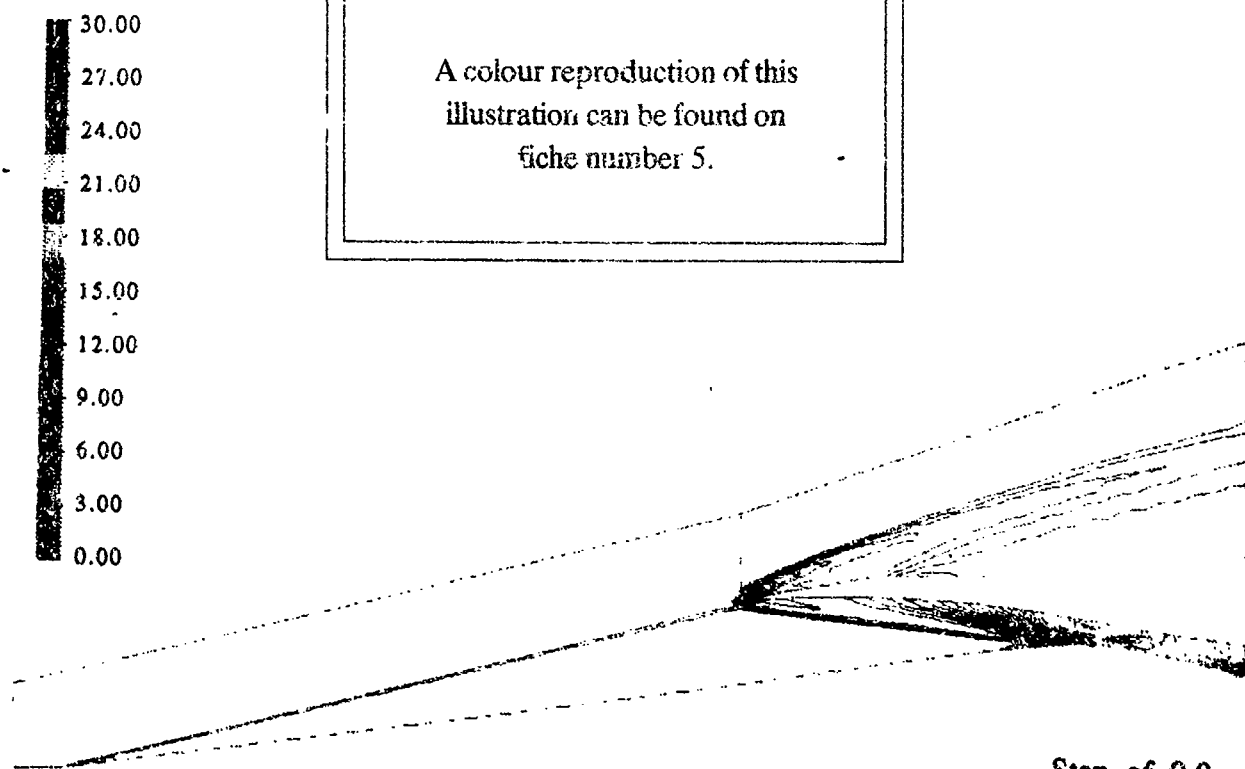


Figure 9 : FLU3M results  
Visualization of static pressure contours  
Advanced cowl leading edge

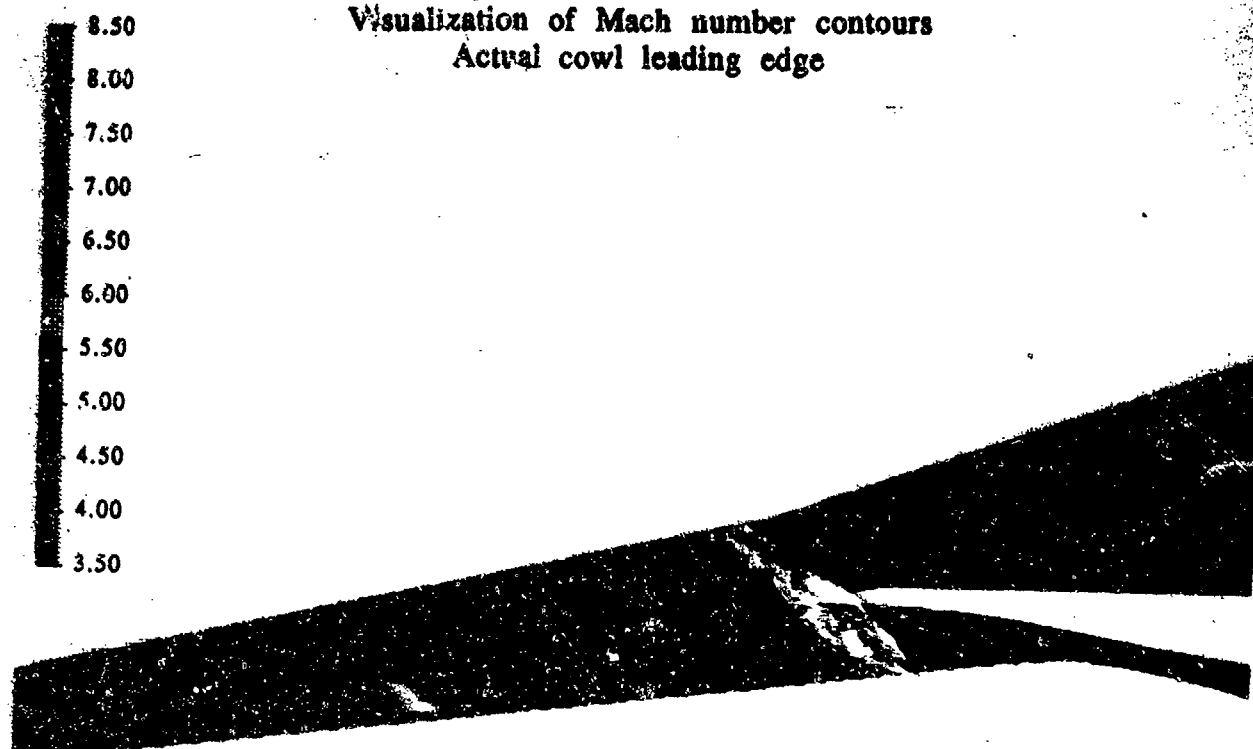


A colour reproduction of this  
illustration can be found on  
fiche number 5.

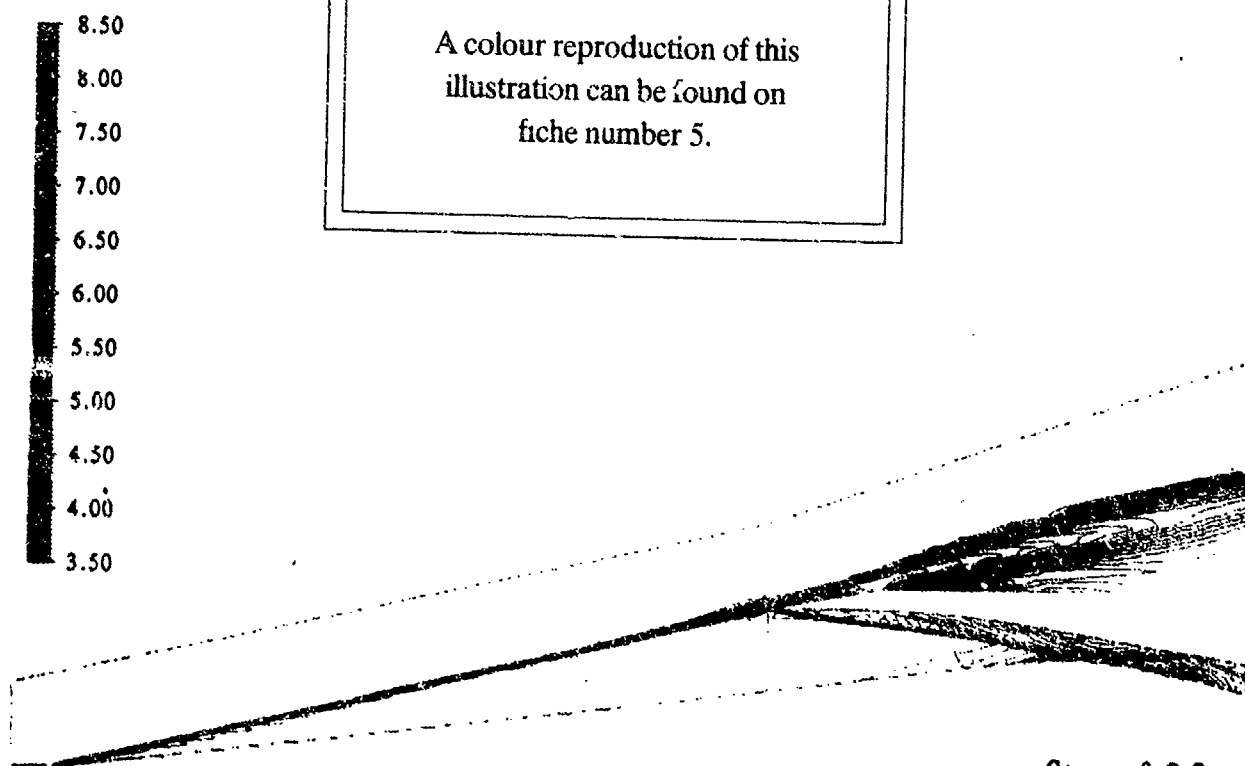


Step of 0.9

Figure 10 : FLU3M results  
Visualization of Mach number contours  
Actual cowl leading edge



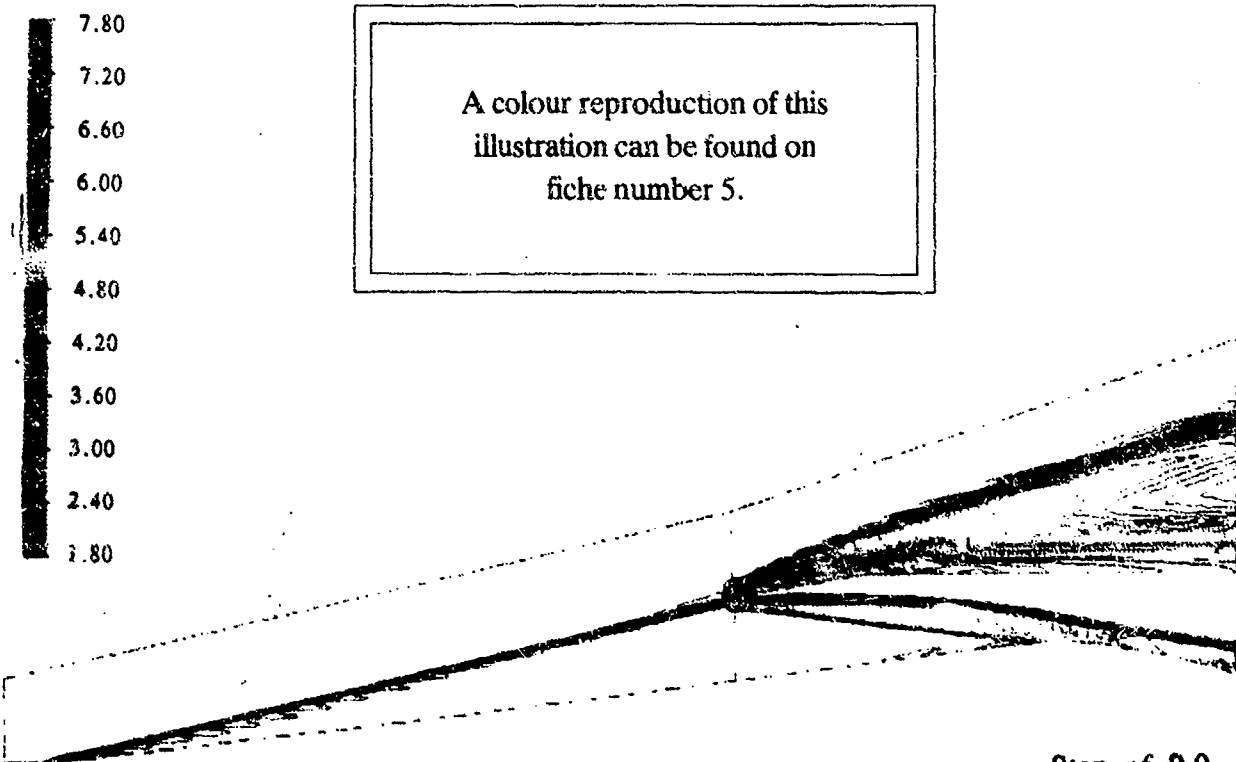
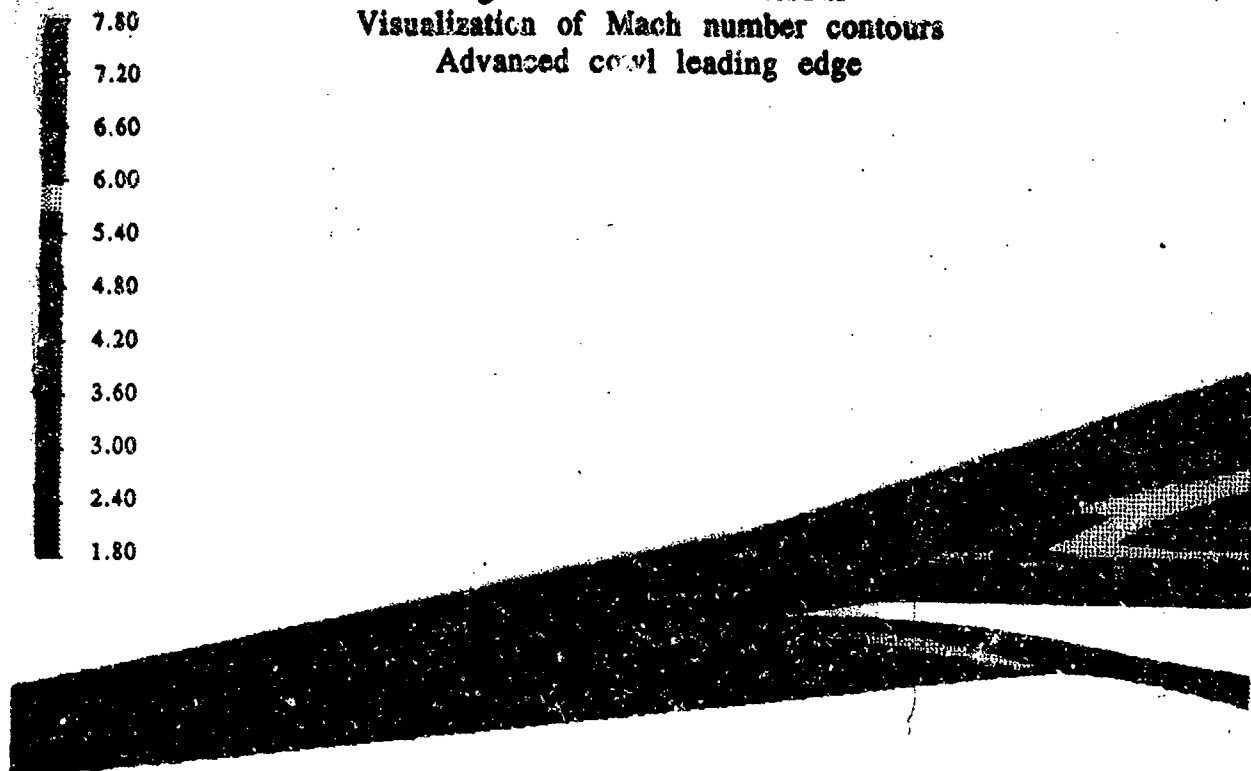
A colour reproduction of this  
illustration can be found on  
fiche number 5.



Step of 0.8



Figure 11 : FLU3M results  
Visualization of Mach number contours  
Advanced cowl leading edge



A colour reproduction of this  
illustration can be found on  
fiche number 5.

Step of 0.9

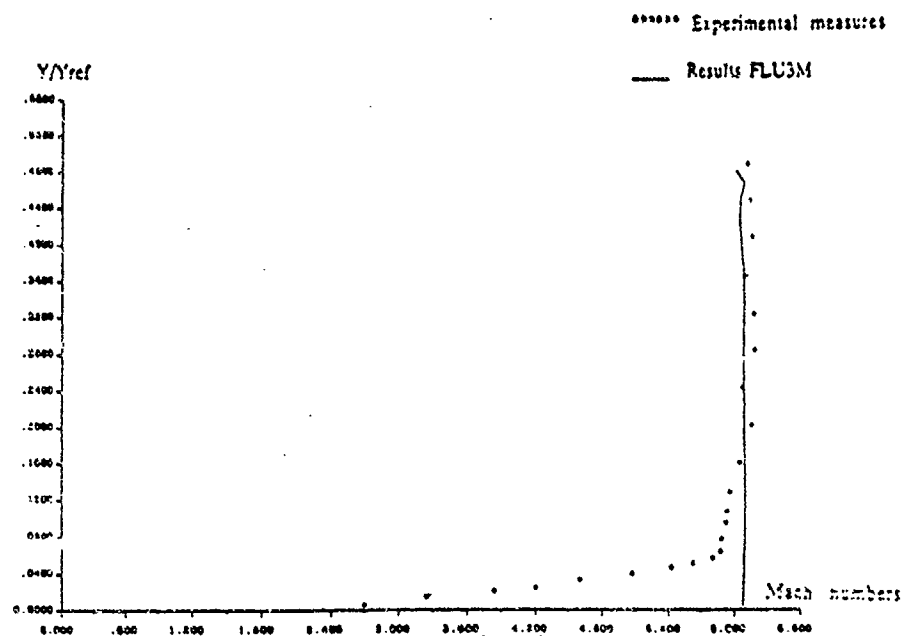


Figure 12: Results FLU3M  
Mach numbers in cowl entrance section

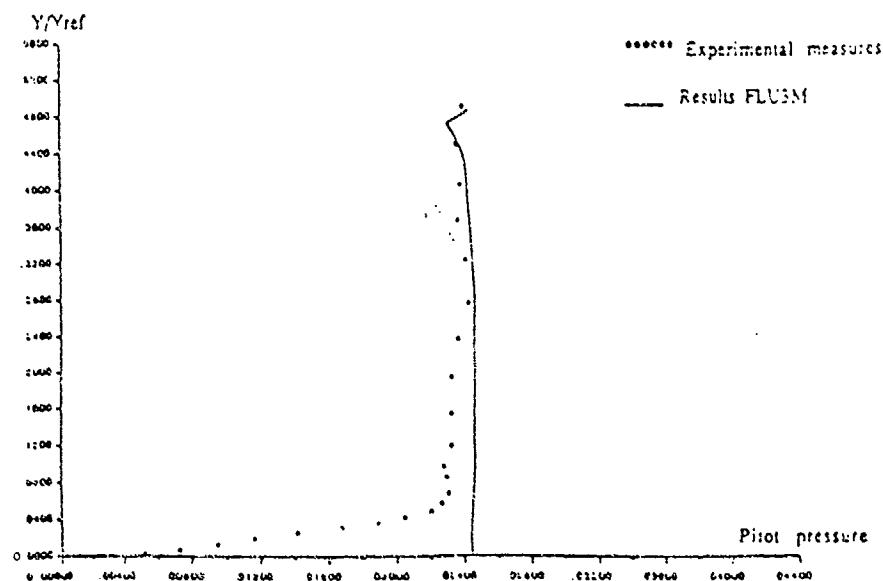


Figure 13: Results FLU3M  
Pitot pressure in the cowl entrance section

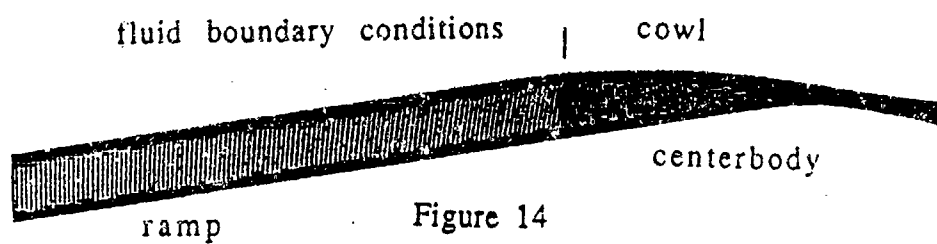


Figure 14  
NS2D calculation mesh

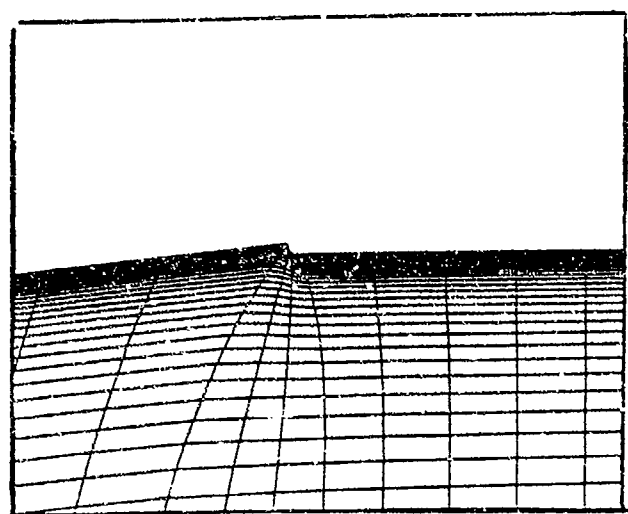


Figure 15  
NS2D calculation mesh

## P8 NS2D results

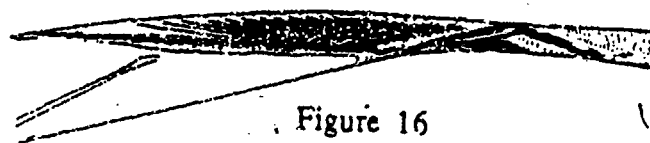


Figure 16  
Static pressure contours

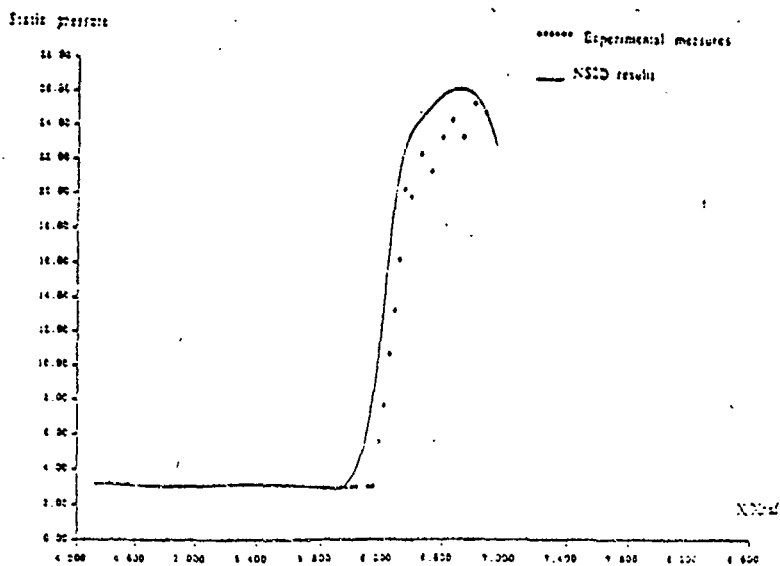


Figure 17: Static pressure on the centerbody

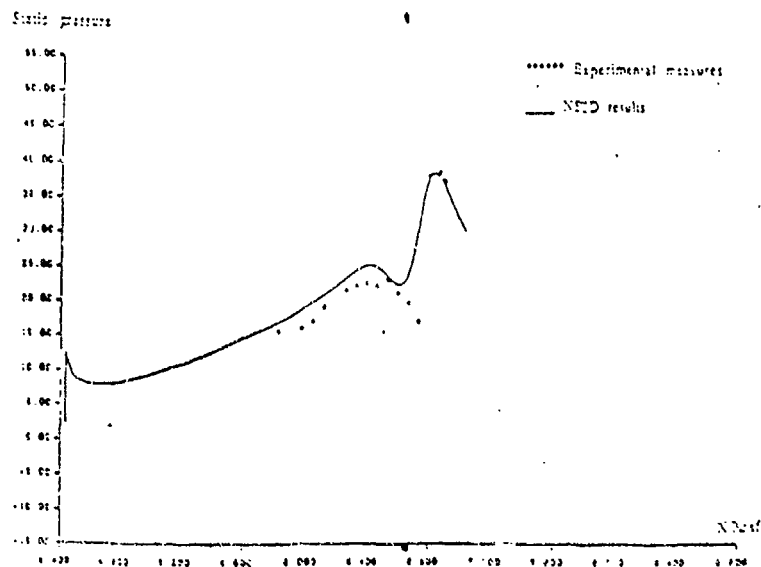


Figure 18: Static pressure on the cowl

1.000  
2.000  
3.000  
4.000  
5.000  
6.000  
7.000  
8.000  
9.000  
10.000  
11.000  
12.000  
13.000  
14.000  
15.000  
16.000  
17.000  
18.000  
19.000  
20.000  
21.000  
22.000  
23.000  
24.000  
25.000  
26.000  
27.000  
28.000  
29.000  
30.000  
31.000  
32.000  
33.000  
34.000  
35.000  
36.000  
37.000  
38.000  
39.000  
INLET  
Minf = 7.40  
Incidence = 0

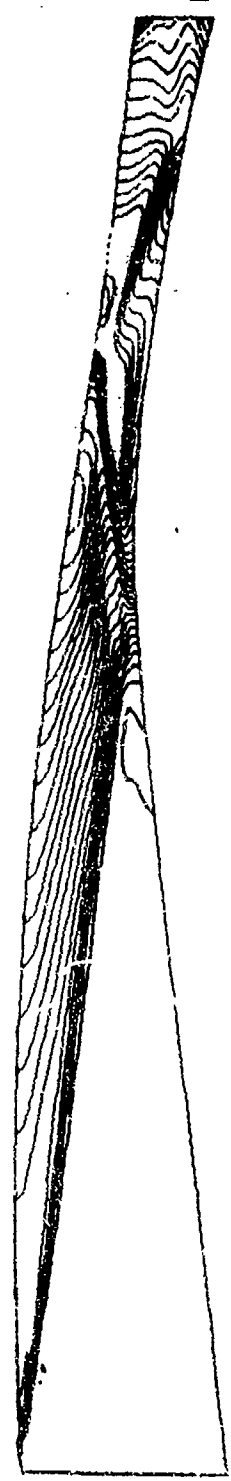


Figure 19 :  
NS2D Results  
Static pressure contours in the inlet

A colour reproduction of this illustration can be found on fiche number 5.



# P8 NS2D results

A220

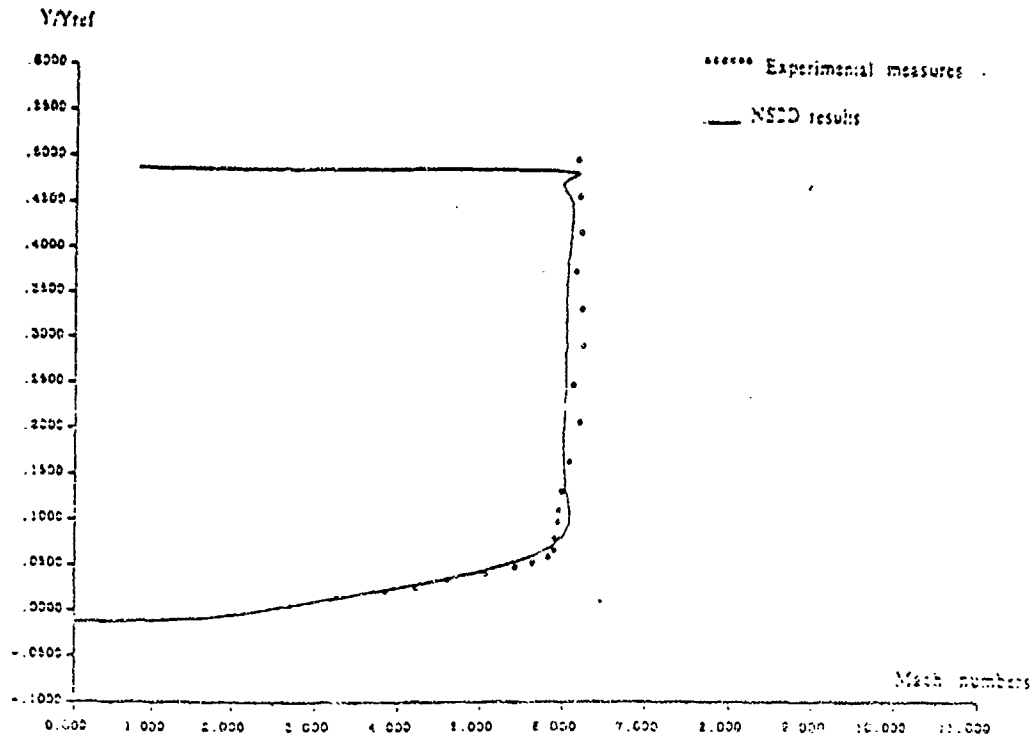


Figure 21: Mach numbers in cowl entrance section

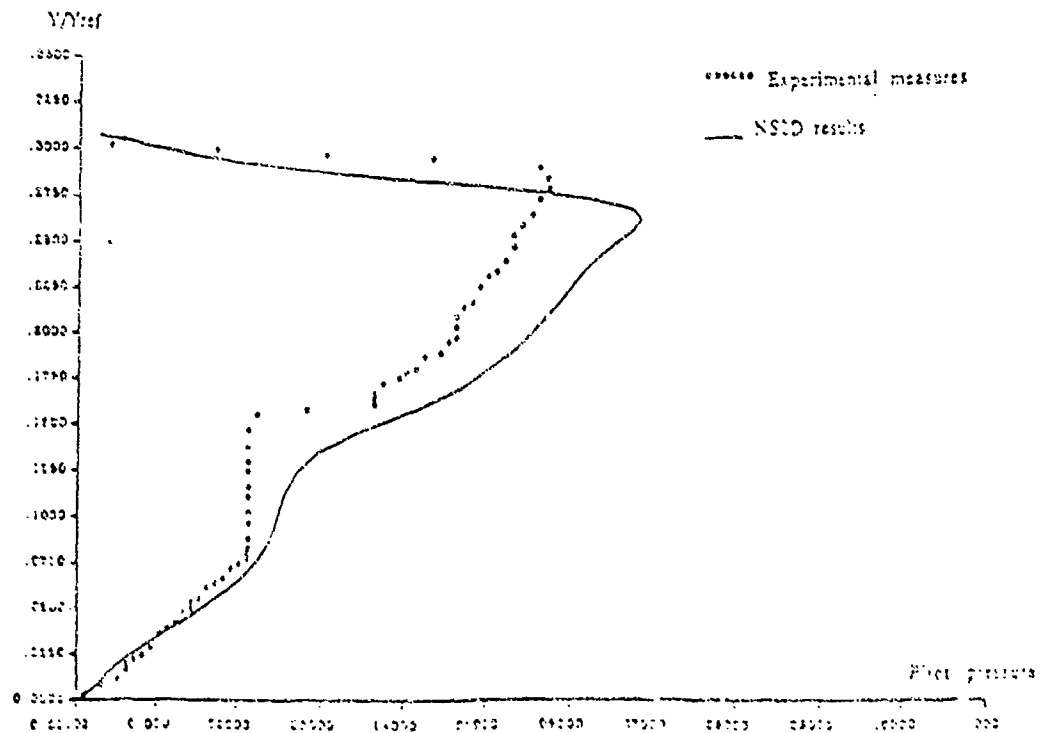


Figure 22: P8 Pitot pressure  $X/X_{ref} = 5.67$

# P8 NS2D results

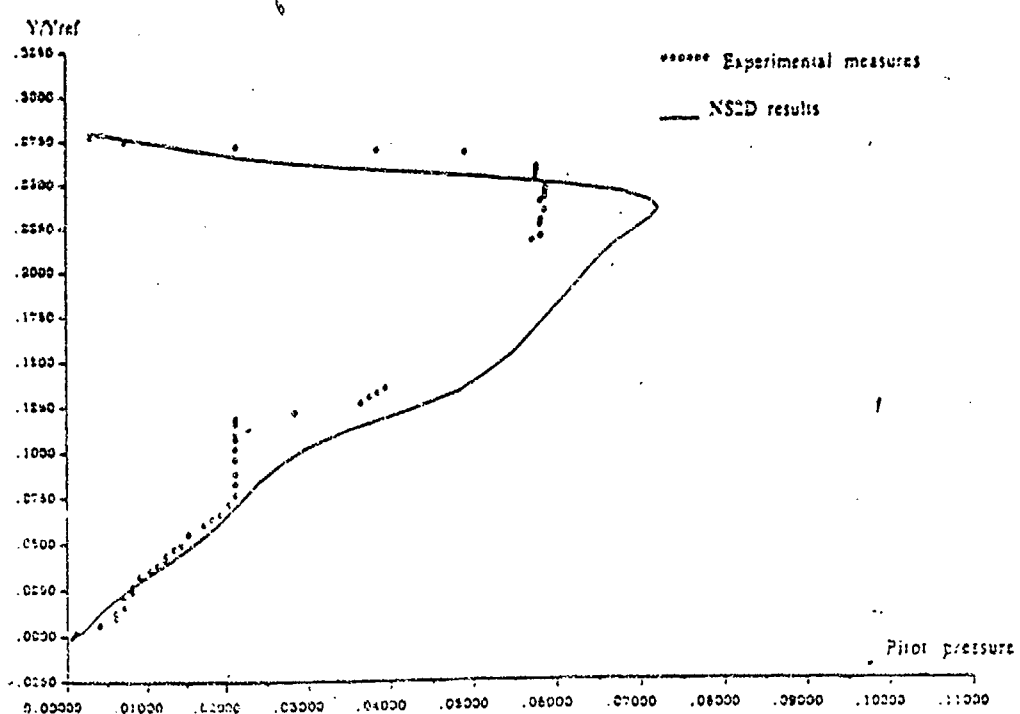


Figure 23: P8 Pitot pressure  $X/X_{ref} = 5.78$

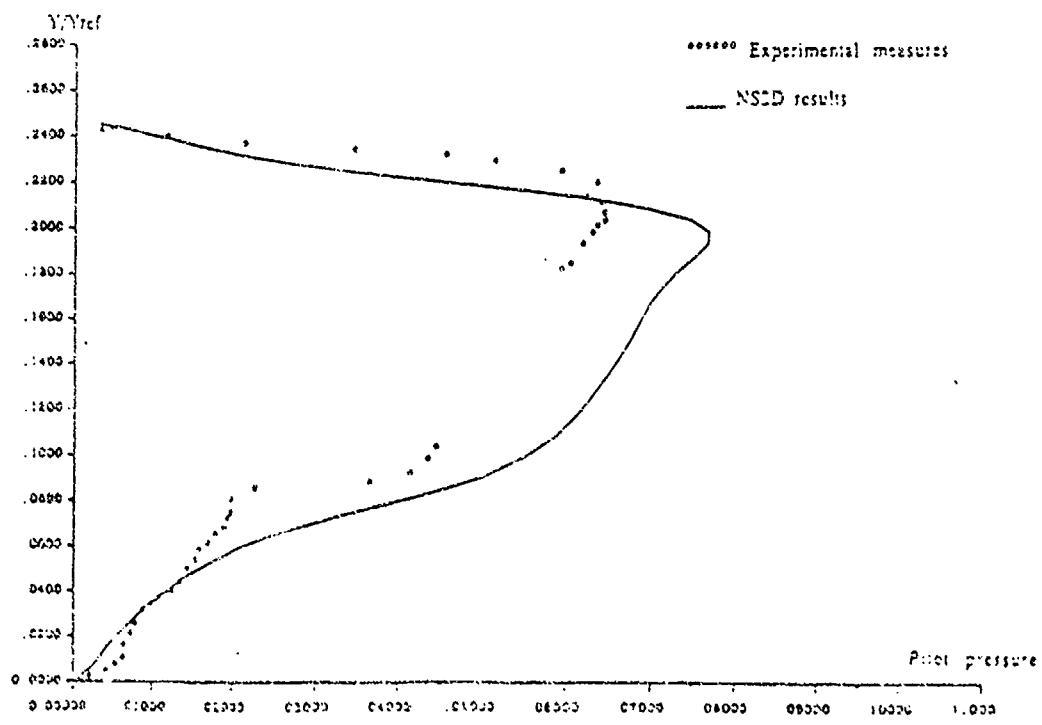


Figure 24 P8 Pitot pressure  $X/X_{ref} = 5.94$



# P8 NS2D results

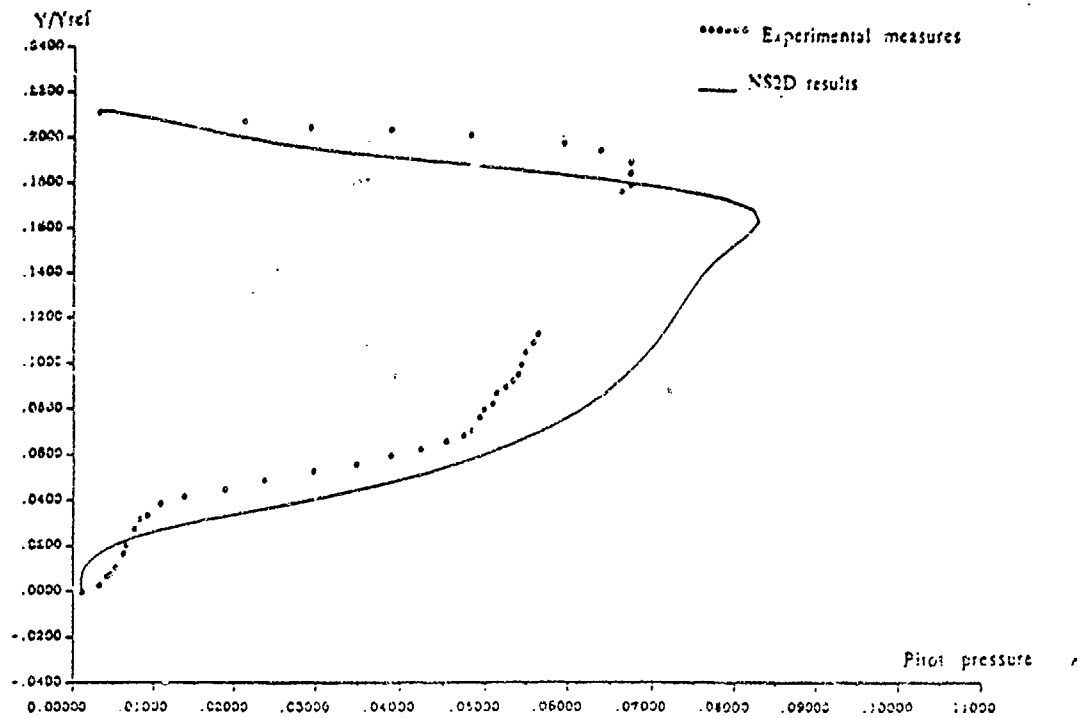


Figure 25: P8 Pitot pressure  $X/X_{ref} = 6.09$

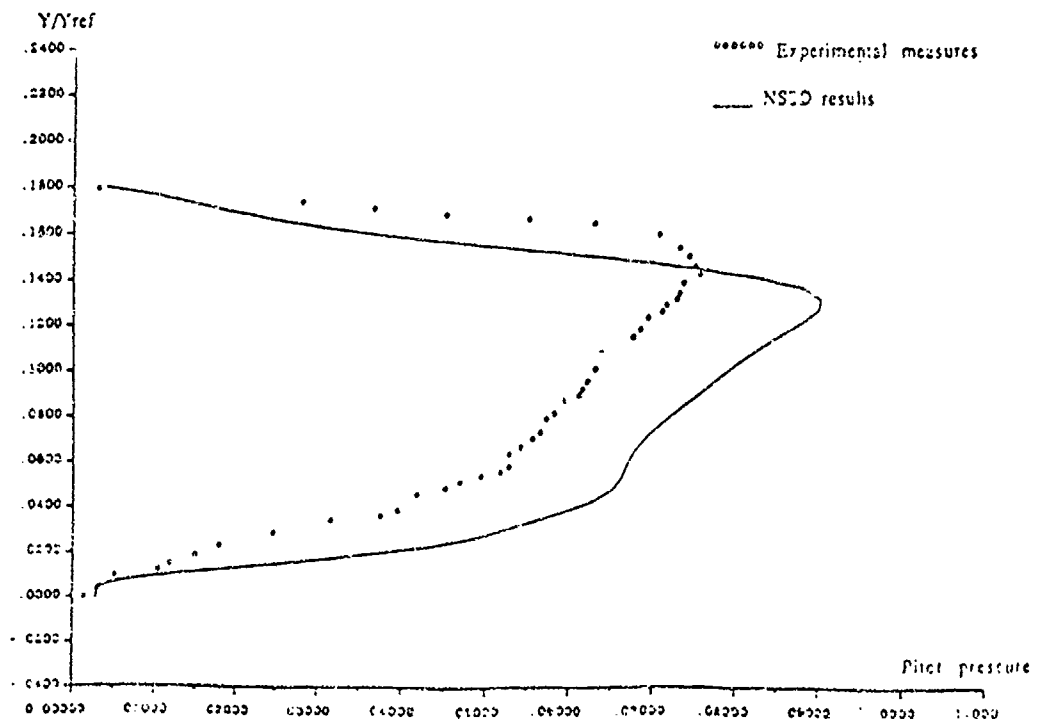
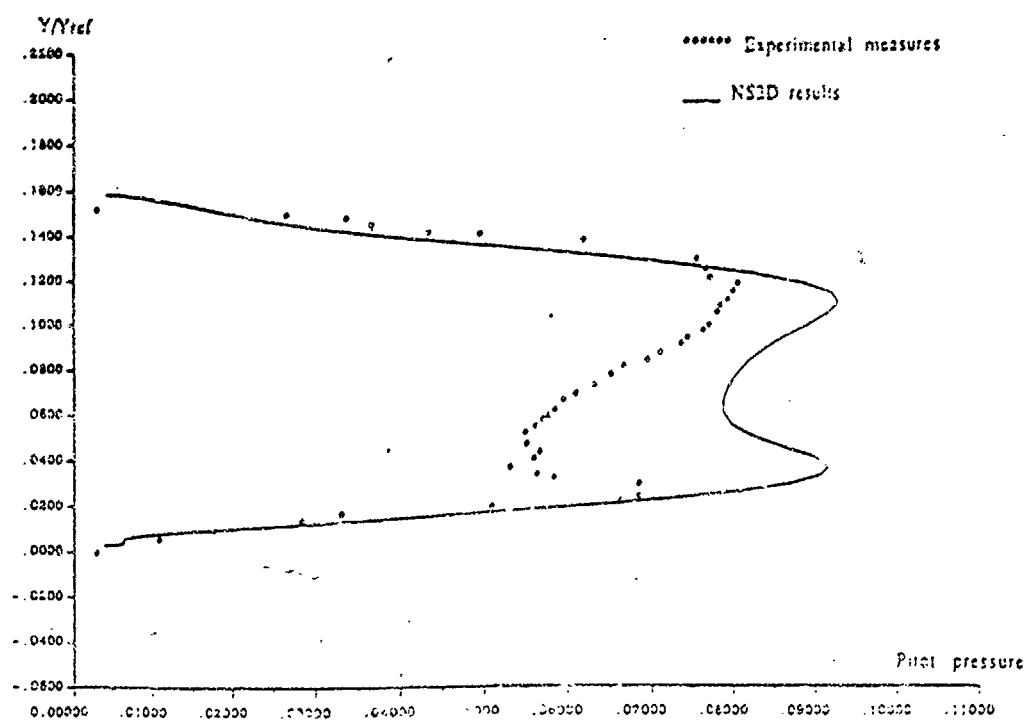
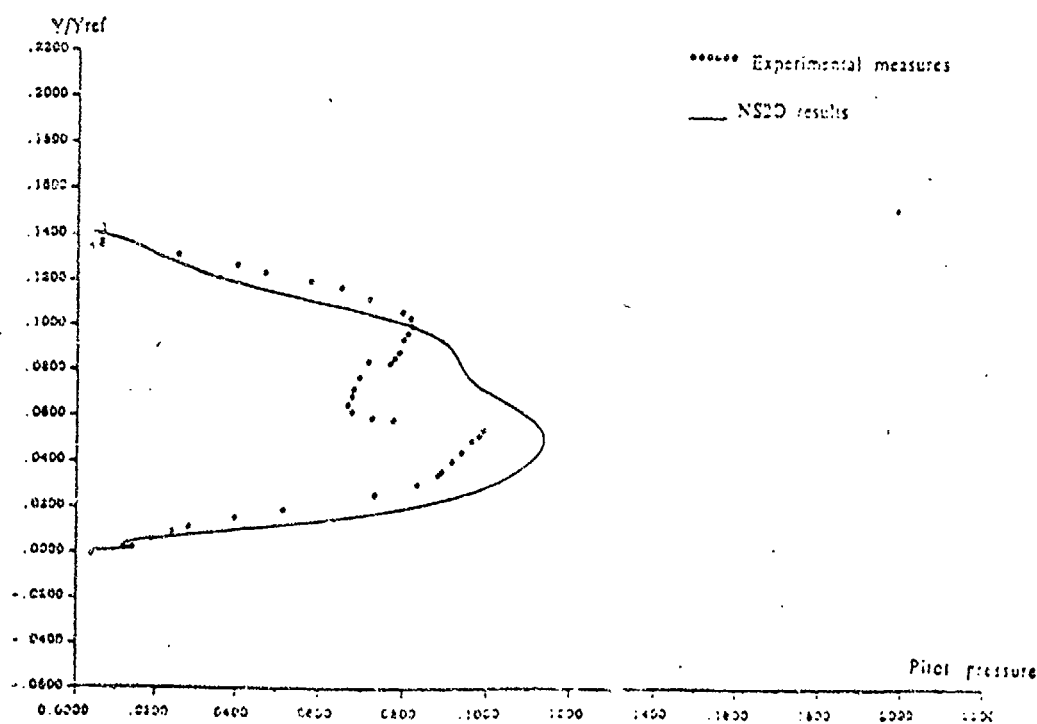
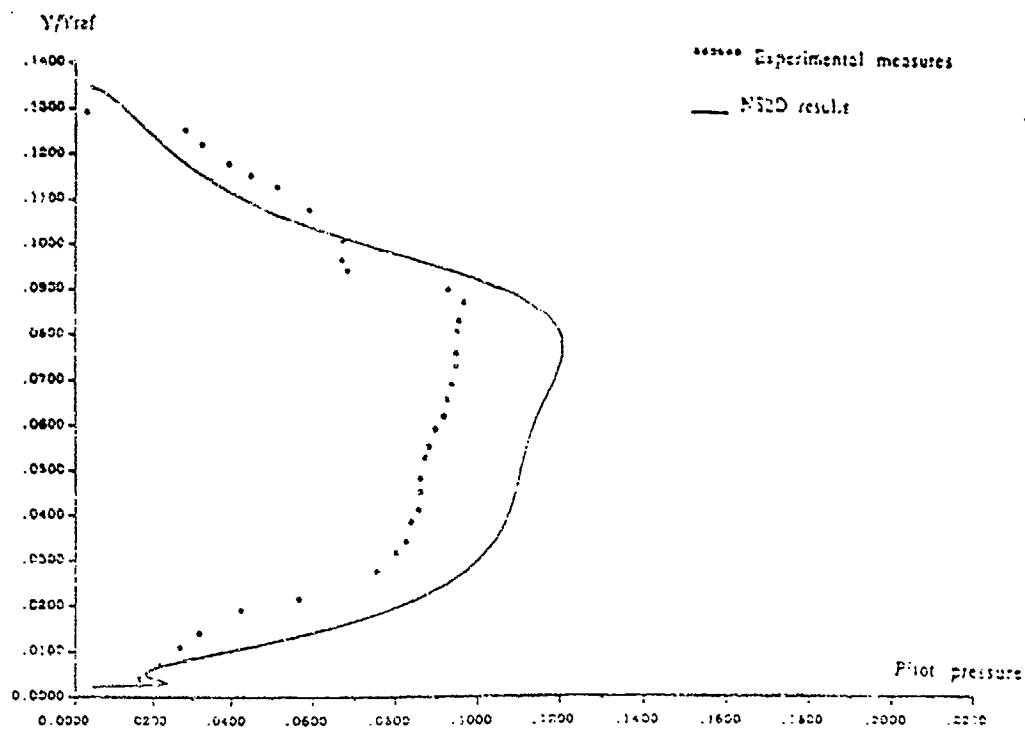
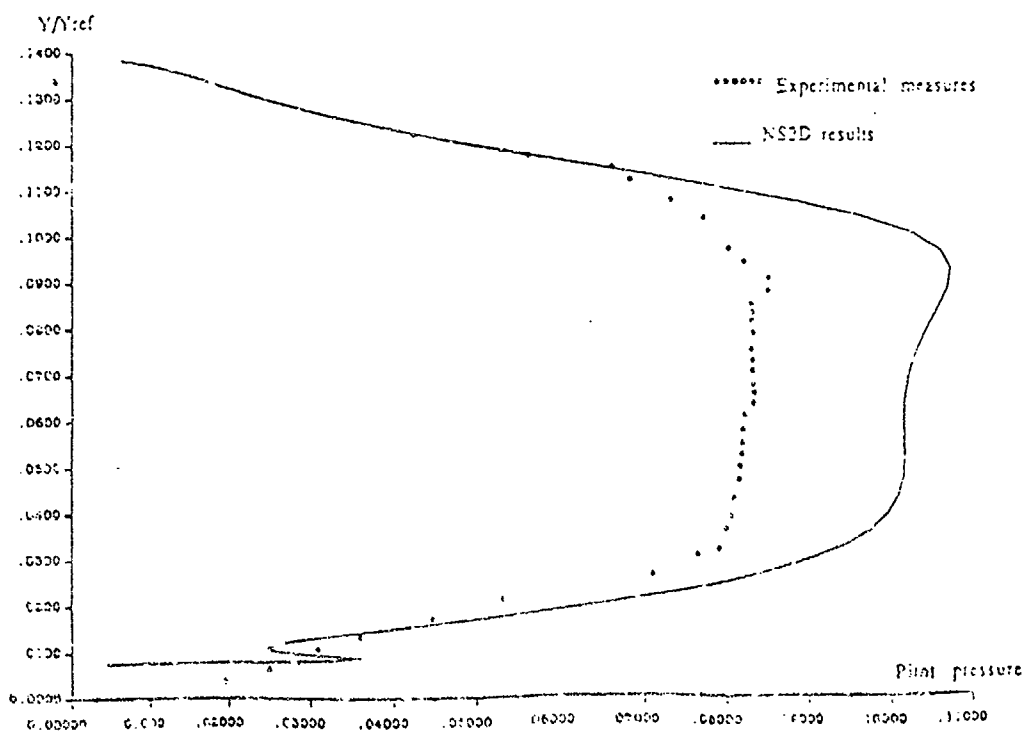


Figure 26: P8 Pitot pressure  $X/X_{ref} = 6.23$

## P8 NS2D results

Figure 27: P8 Pitot pressure  $X/X_{ref} = 6.37$ Figure 28: P8 Pitot pressure  $X/X_{ref} = 6.51$

## P8 NS2D results

Figure 29; P8 Pitot pressure  $X/X_{ref} = 6.65$ Figure 30; P8 Pitot pressure  $X/X_{ref} = 6.79$

## REFERENCES

1. "Numerical Simulation of Realistic High-Speed Inlets Using the Navier-Stokes Equations" 1977  
D.D. Knight Air Force Flight Dynamics Laboratory  
Wright-Patterson Air Force Base, Ohio
2. "Développements récents sur les méthodes de calcul d'écoulements internes par résolution des équations d'Euler ou de Navier-Stokes" 1988  
L.Cambier, J.P.Veuillot et A.M.Vuillot  
Office National d'Etudes et de Recherches Aérospatiales  
Chatillon
3. "Application d'un schéma de longueur de mélange à l'étude des couches limites turbulentes d'équilibre" R.Michel  
Office National d'Etudes et de Recherches Aérospatiales  
Chatillon

Friedrichshafen, Oct. 12, 1990

Stefan Leicher  
Dornier Luftfahrt  
Abt.: BF30  
Postfach 1330  
7990 Friedrichshafen  
Tel.: 07545/84819

Mr. R.J. Benson  
INTERNAL FLUID MECHANICS DIVISION  
MAIL STOP 5 - 7  
NASA LEWIS RESEARCH CENTER  
CLEVELAND, OH 44135  
USA

Reference : AGARD WG13 TESTCASE 6 ( P8 INLET )

Dear Mr. Benson

according to an agreement with Dr. Bissinger we directly mail you our computational results for the working group 13 testcase 6 ( P8 hypersonic inlet ). The disc contains data of a laminar and a turbulent calculation.

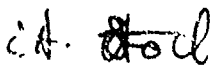
The grid used is a blockstructured grid with about 860.000 grid points. We use 169 points along the centerline for the compression ramp and the inlet; The cowl surface is approximated by 137 grid points while the channel contains 73 points in normal and 49 ( half configuration ) in the crossflow direction.

We just finished these calculation today and in a first comparison we recognize that our grid inside the inlet channel seems to be too coarse to resolve the shocks sharp enough. Therefore we are preparing an additional computation with an increased number of grid points in streamwise and the normal direction for the weekend.

If the computation is succesful and the results look reasonable we will send you these data immediately.

Also you can await some further written information, some plots of the grid we are using and some figures showing flow results.

Yours sincerely  
Dornier Luftfahrt GmbH



I.V. Dr. Wagner



I.A. Dr. Rieger

Enclosed: DISC  
Listing of file contents

General Dynamics  
Fort Worth Division

April 18, 1990

Dr. R. G. Bradley, Chairman  
AGARD Working Group 13  
General Dynamics / Fort Worth Division

Dear Dr. Bradley,

Enclosed are the intermediate results of the P8 Inlet Analysis (AGARD Test Case #6) as called for in your letter dated March 4, 1990. The solutions contained herein are the 2D results, for which the L2 Norm Residual has decreased 3 orders of magnitude, and the 3D results, for which the L2 Norm Residual has decreased 1 order of magnitude.

The solutions were obtained using the 2D and 3D versions of the GD/FW FALCON code. FALCON is a finite volume, viscous/inviscid flow solver that uses Roe's flux difference splitting algorithm. The code contains multi-blocking capability with point-to-point matching required at the block boundaries. Both the 2D and 3D analysis utilize the Baldwin-Lomax turbulence model.

The grid structure and part of the grid used in the analysis is shown in Figure 1. The 3D grid consists of 6 blocks and 480K points. The 2D grid is the centerline cut of the 3D grid with 2 times the number of points in the normal direction. The 2D analysis was performed on a CONVEX C210 computer and required  $3.5 \times 10^{-4}$  seconds/point/iteration. The 3D analysis is being performed on the NAS computer system using the CRAY YMP computer and requires  $1.0 \times 10^{-4}$  seconds/point/iteration.

The 2D results are complete and need only one point of clarification. The FALCON code does not currently allow for multiple regions of transition. As such, transition was set at  $x=35$  cm on the ramp surface. This condition establishes turbulent flow over the entire length of the cowl.

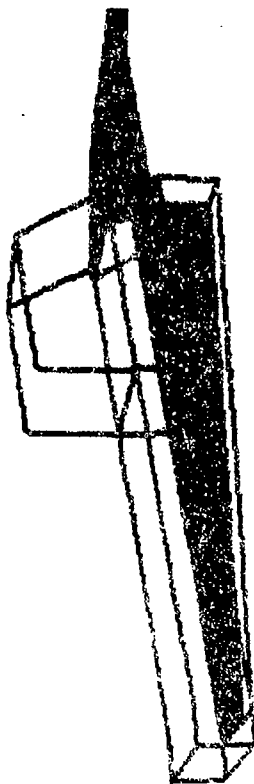
The 3D results, though not converged to a satisfactory state, are included for completeness. The same transition criterion was used as with the 2D case. Additional color plots are included to show the overall nature of the flowfield. These plots also aid in analyzing the differences between the 2D and 3D solutions. Mach number and pitot pressure contours are shown along the centerline for the 2D and 3D cases in Figure 2 and Figure 3. Pitot pressure contours are shown at the axial cuts to show the three-dimensional nature of the flow (Figure 4.) The data comparison requested is presented graphically in the format specified. Greyscale versions of the color charts (Figures 1-4) are included for use in duplicating.

The information in this packet represents the results obtained for the P8 Inlet Analysis at this time. It is expected to have complete results to you by the June 15 deadline. Should there be any questions regarding this test case, please do not hesitate to contact me.

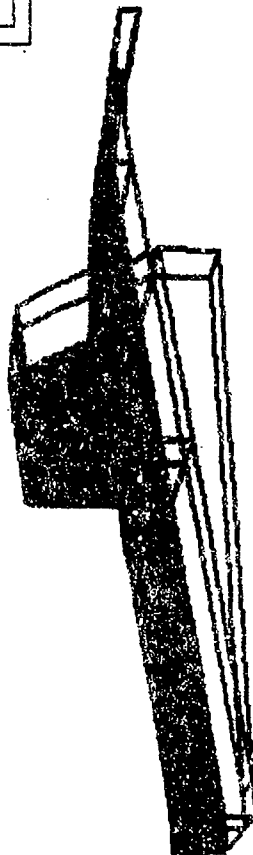
Keith M. Kisielewski  
Senior Engineer  
Computational Fluid Dynamics

# Grid and Block Structure Utilized in P8 Inlet Analysis with the FALCON Navier-Stokes Solver

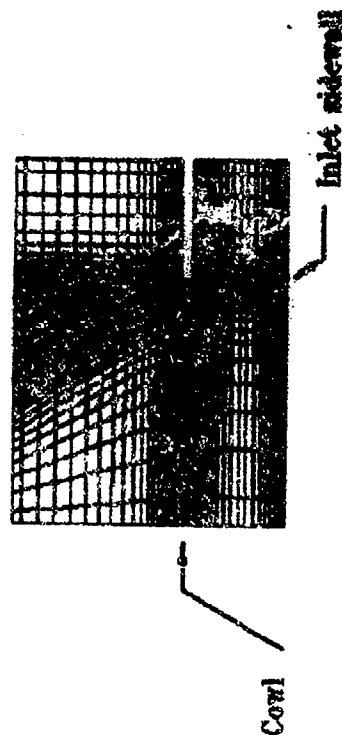
Block Structure of the grid used for the P8 Inlet analysis. The grid represents the right-half of the test configuration. The surface cells are shaded.



Grid lines are shown along the plane of symmetry (centerline.) Dimensions along this cut are 251 x 41 for the 3D analysis and 251 x 81 for the 2D case.



The grid at the entrance to the inlet shows the clustering of lines to the surfaces. Dimensions in this plane are 51 x 41 for the 3D analysis with 31 points on the ramp and cowl surfaces.



A colour reproduction of this illustration can be found on fiche number 5.

2D PB INLET ANALYSIS (AGARD TEST CASE #6)  
FALCON 2D with Baldwin-Lomax Turbulence

Converged Solution

- Contour Levels
- 0.00000
- 0.25000
- 0.50000
- 0.75000
- 1.00000
- 1.25000
- 1.50000
- 1.75000
- 2.00000
- 2.25000
- 2.50000
- 2.75000
- 3.00000
- 3.25000
- 3.50000
- 3.75000
- 4.00000
- 4.25000
- 4.50000
- 4.75000
- 5.00000
- 5.25000
- 5.50000
- 5.75000
- 6.00000
- 6.25000
- 6.50000
- 6.75000
- 7.00000
- 7.25000
- 7.50000



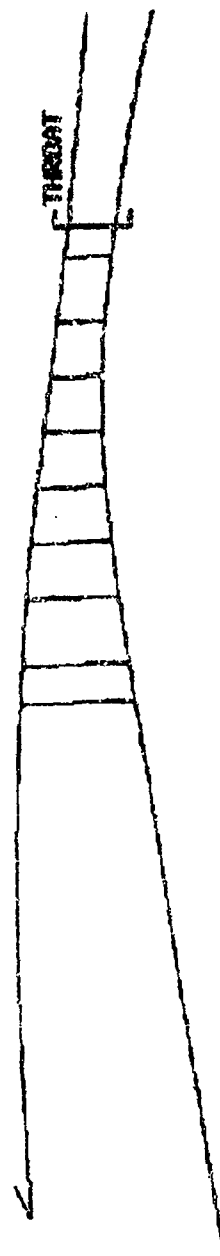
Mach Number Contours

Contour Levels  
x 1.0



Pitot Pressure Ratio Contours

Contour Levels  
x 100.



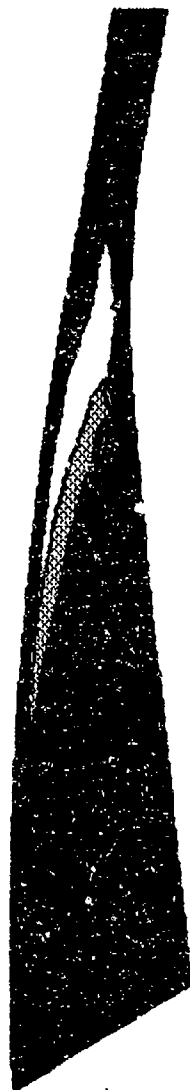
A colour reproduction of this illustration can be found on  
fiche number 5.



A colour reproduction of this illustration can be found on fiche number 5.

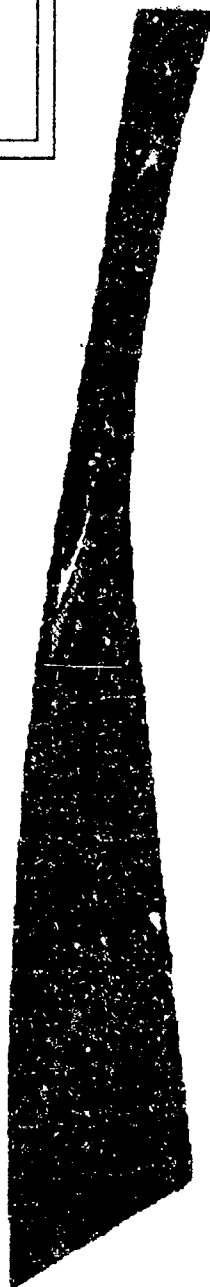
# 3D PB INLET ANALYSIS (AGARD TEST CASE #6) FALCON 3D with BALDWIN-LONG TUBULENCE

Results after 5250 Iterations



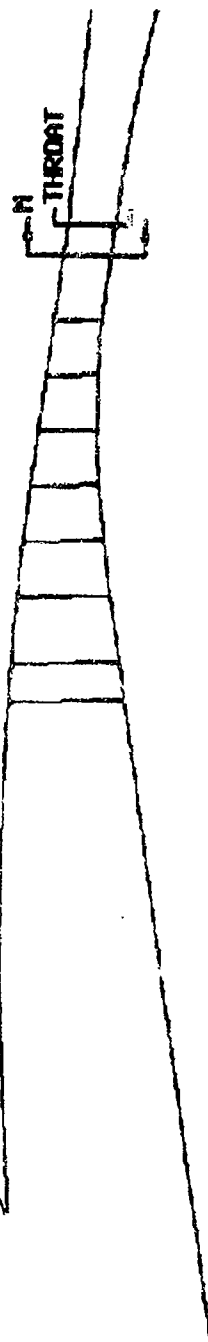
Contour  
Levels  
x 1.0

Centerline Mach Number Contours



Contour  
Levels  
x 100.

Centerline Pitot Pressure Ratio Contours



Contour  
Levels  
x 100.

Pitot Pressure Ratio Profiles at Station M

Symmetry

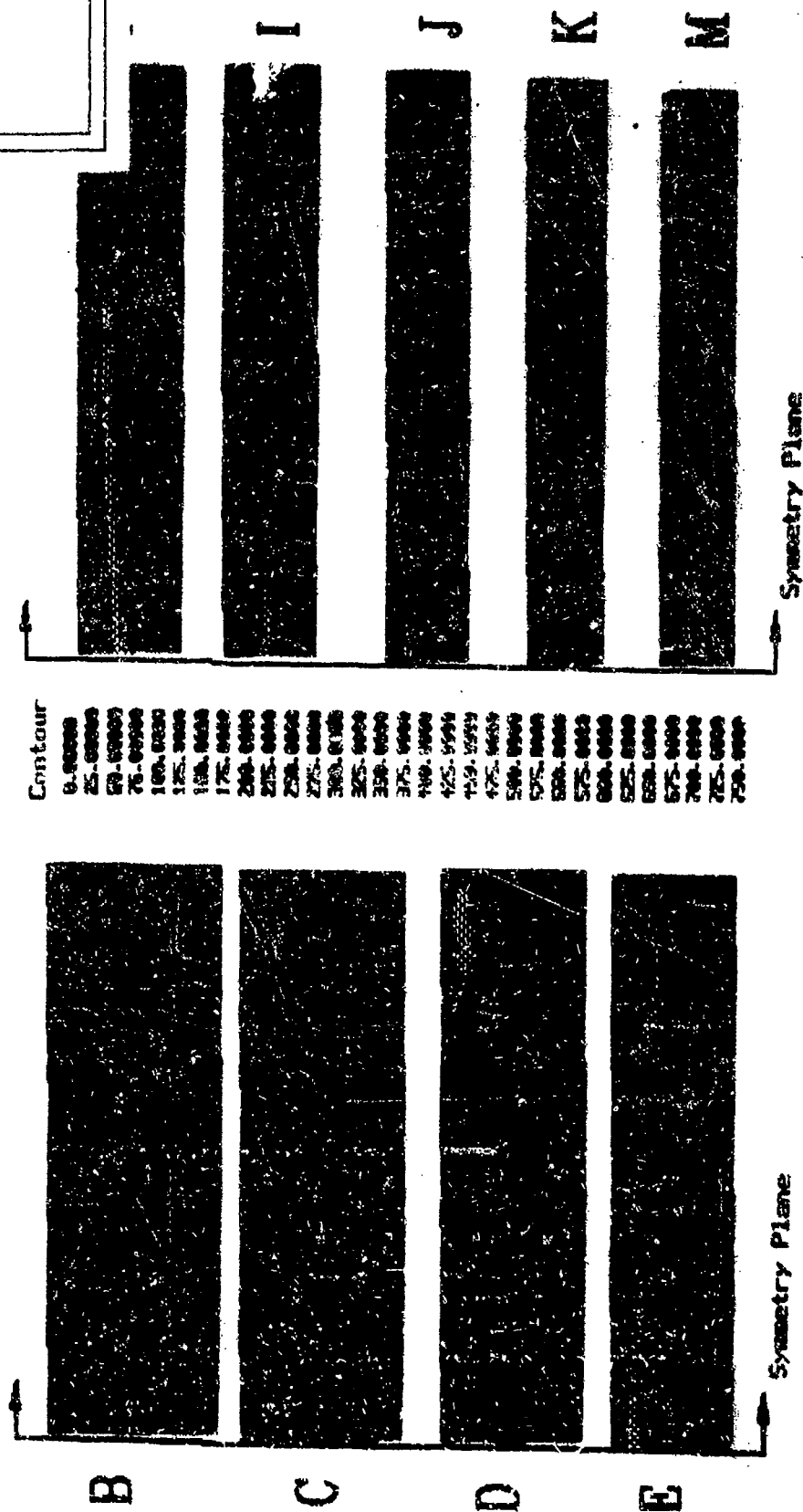
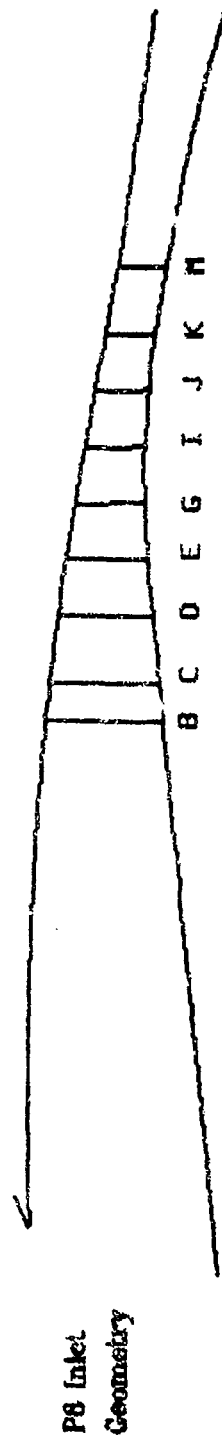
- Contour Levels
- 0.00000
- 0.25000
- 0.50000
- 0.75000
- 1.00000
- 1.25000
- 1.50000
- 1.75000
- 2.00000
- 2.25000
- 2.50000
- 2.75000
- 3.00000
- 3.25000
- 3.50000
- 3.75000
- 4.00000
- 4.25000
- 4.50000
- 4.75000
- 5.00000
- 5.25000
- 5.50000
- 5.75000
- 6.00000
- 6.25000
- 6.50000
- 6.75000
- 7.00000
- 7.25000
- 7.50000

A colour reproduction of this  
illustration can be found on  
fiche number 5.

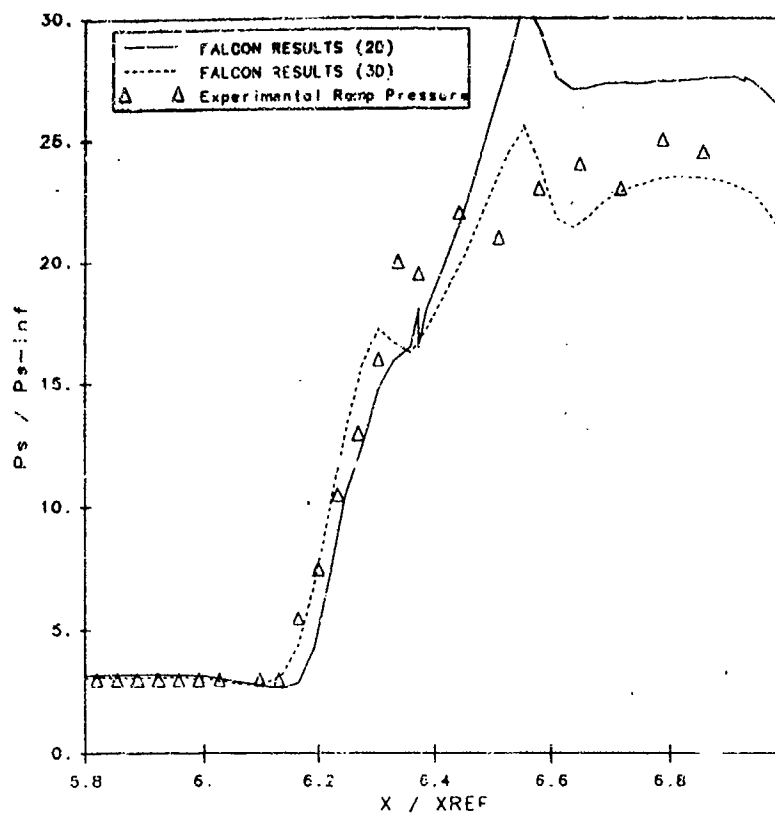
### 3D Falcon P8 Inlet Analysis (AGARD Case # 6)

Pitot Pressure Ratio Contours

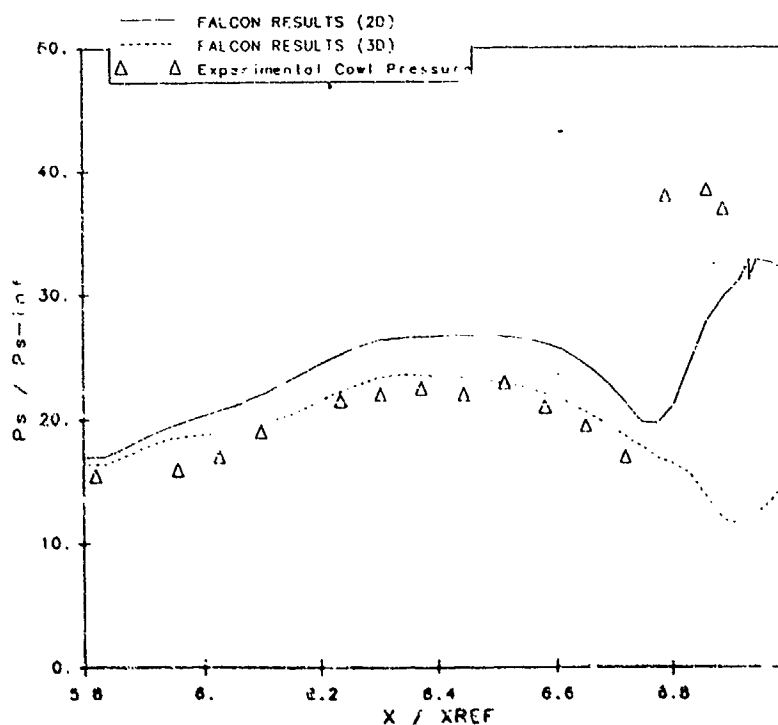
5250 Iterations



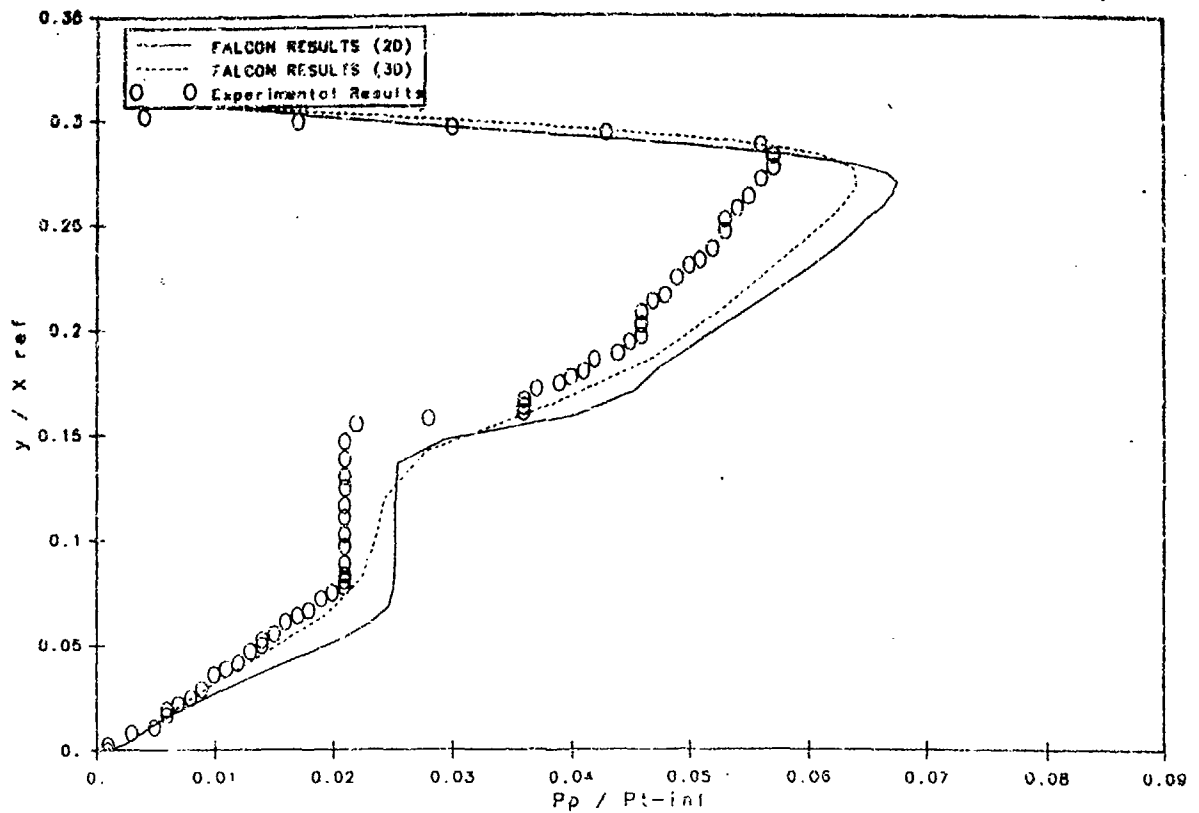
FALCON-3D ANALYSIS w/BALDWIN-LOMAX TURBULENCE MODEL  
Centerbody Static Pressure Ratio vs Axial Distance



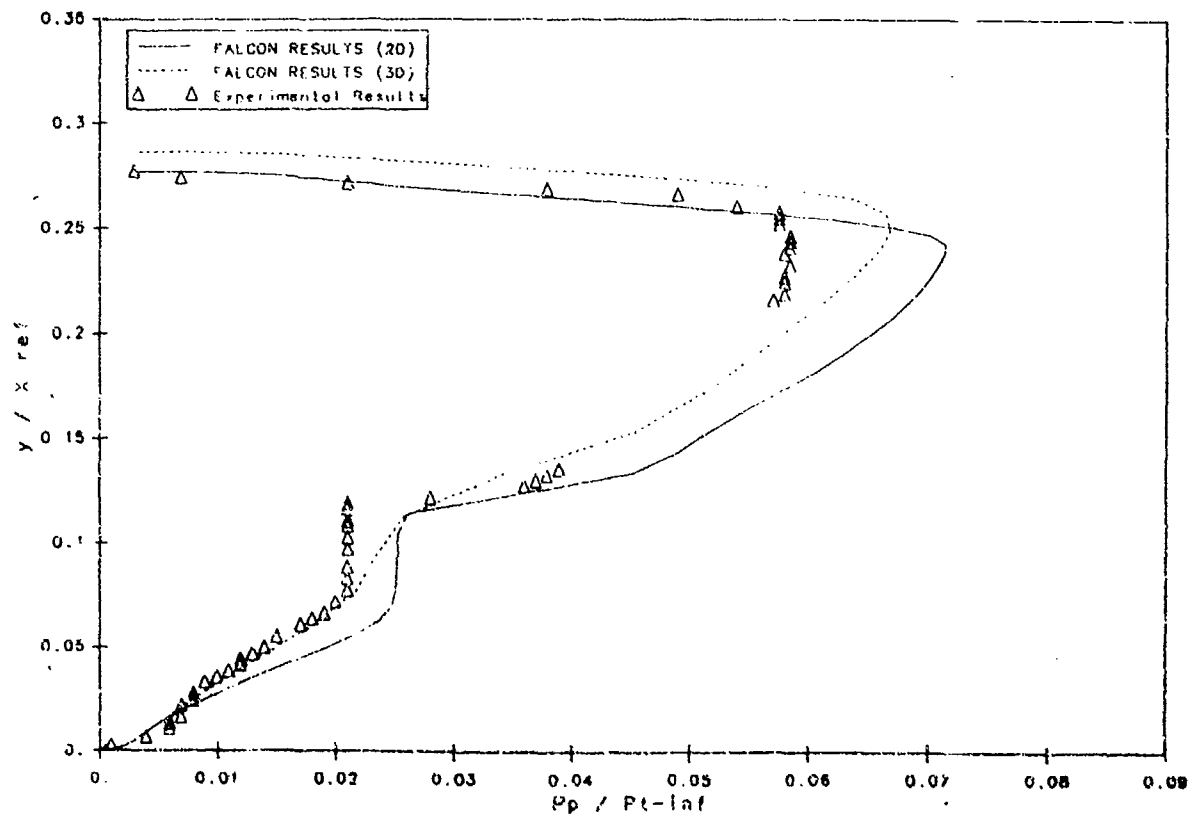
FALCON-3D ANALYSIS w/BALDWIN-LOMAX TURBULENCE MODEL  
Cowl Static Pressure Ratio vs Axial Distance



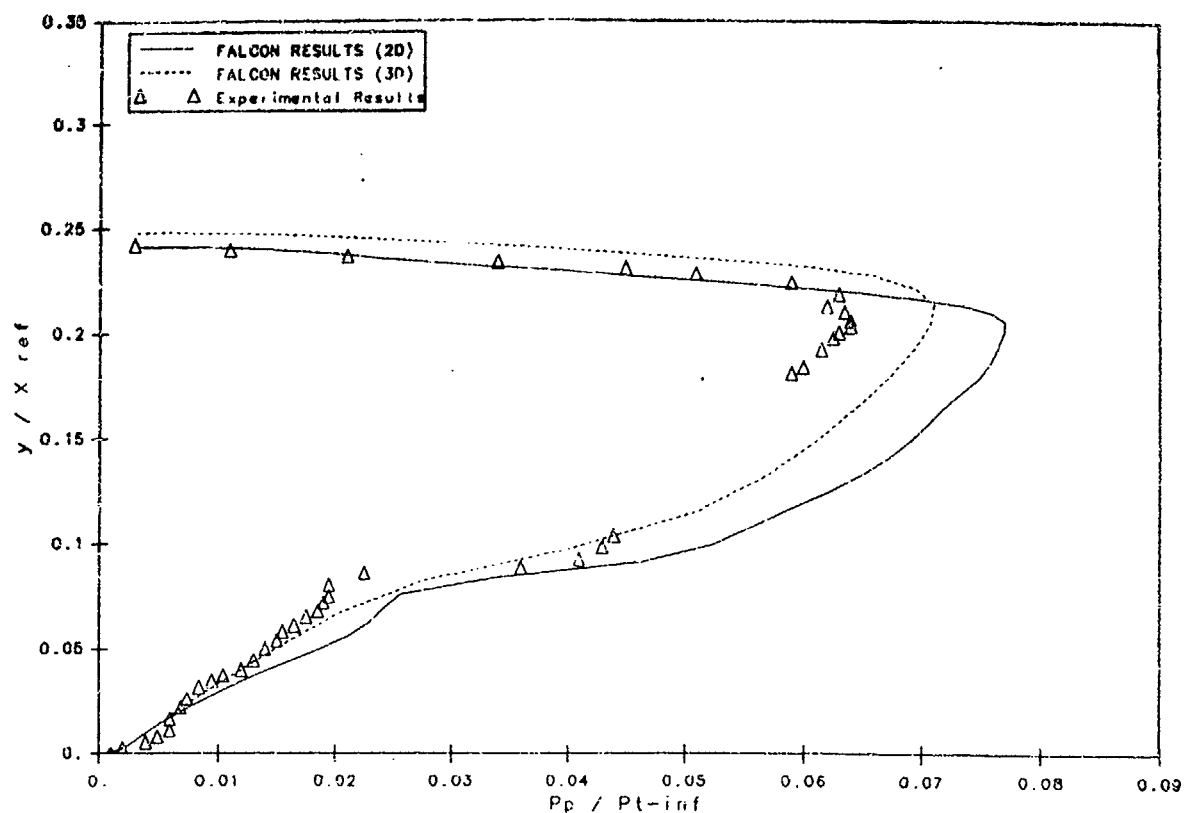
FALCON ANALYSIS w/BALDWIN-LOMAX TURBULENCE MODEL  
Pitot Pressure Ratio Profiles at  $X/X_{REF} = 5.67$



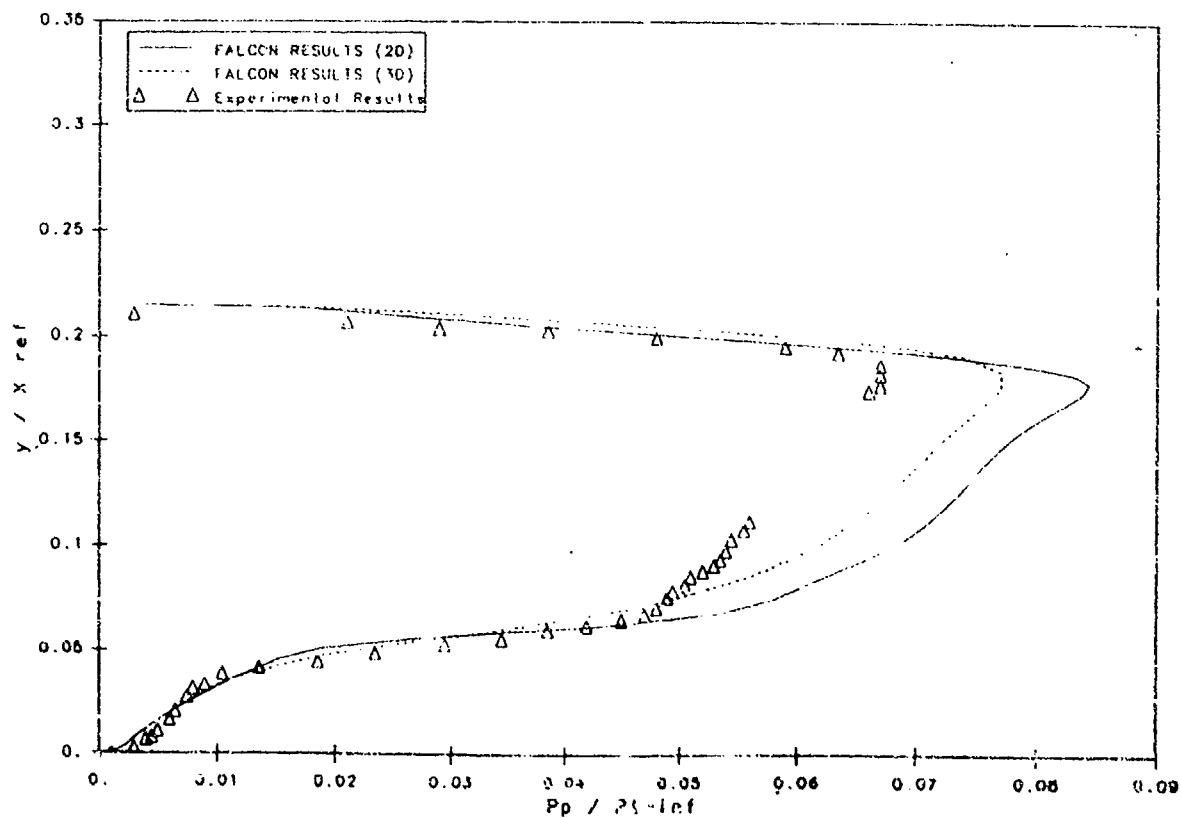
FALCON ANALYSIS w/BALDWIN-LOMAX TURBULENCE MODEL  
Pitot Pressure Ratio Profiles at  $X/X_{REF} = 5.78$



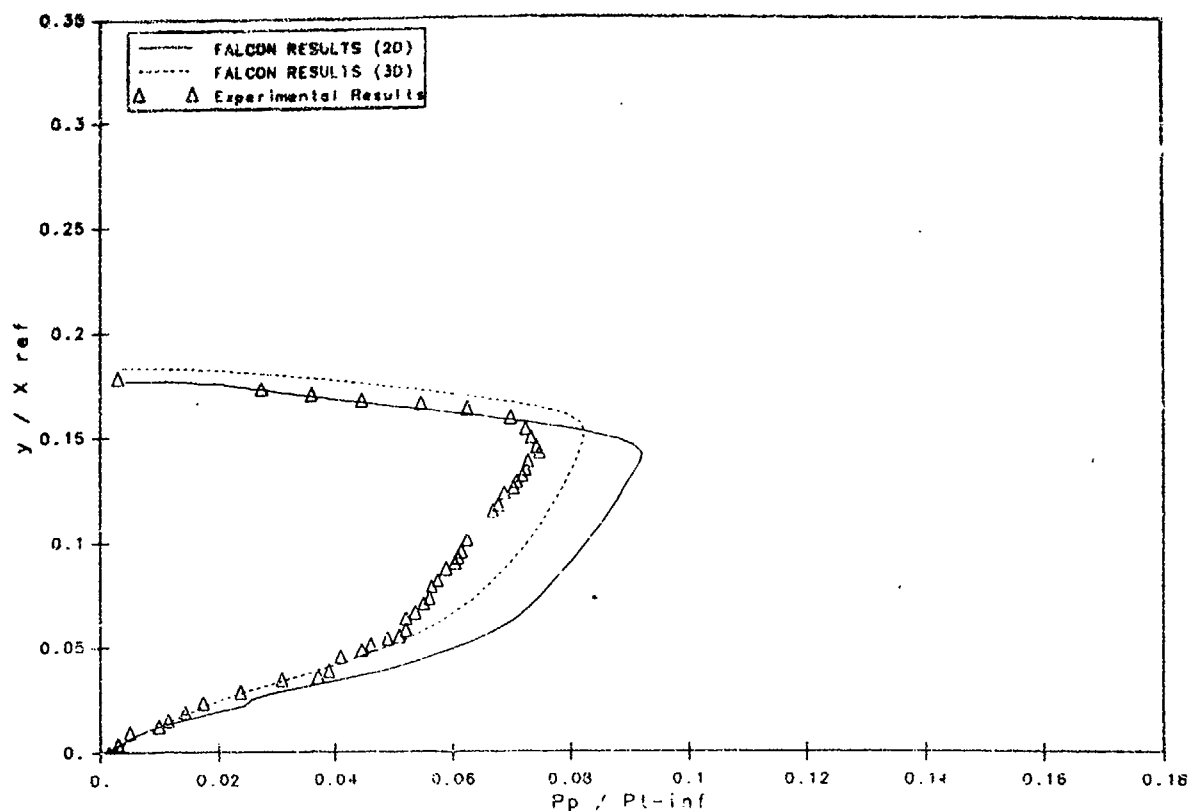
FALCON ANALYSIS w/BALDWIN-LOMAX TURBULENCE MODEL  
Pitot Pressure Ratio Profiles at  $X/X_{REF} = 5.94$



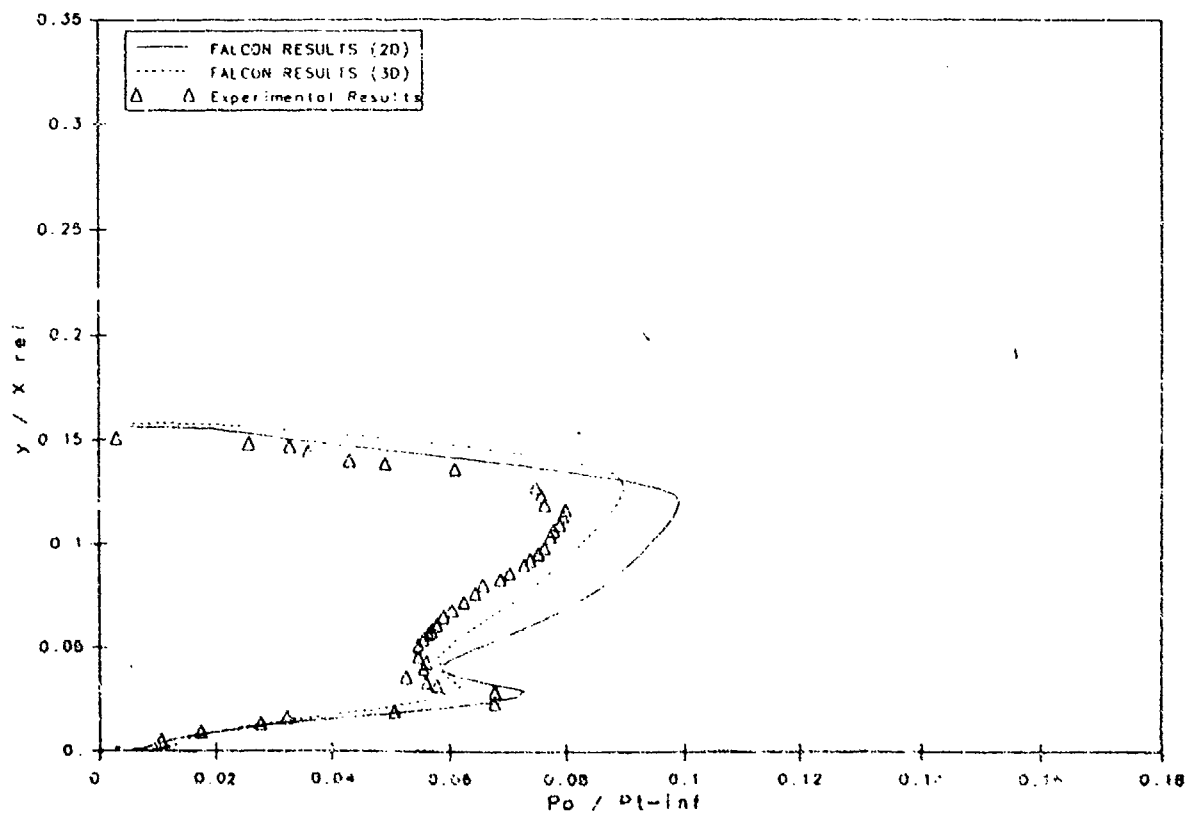
FALCON ANALYSIS w/BALDWIN-LOMAX TURBULENCE MODEL  
Pitot Pressure Ratio Profiles at  $X/X_{REF} = 6.09$



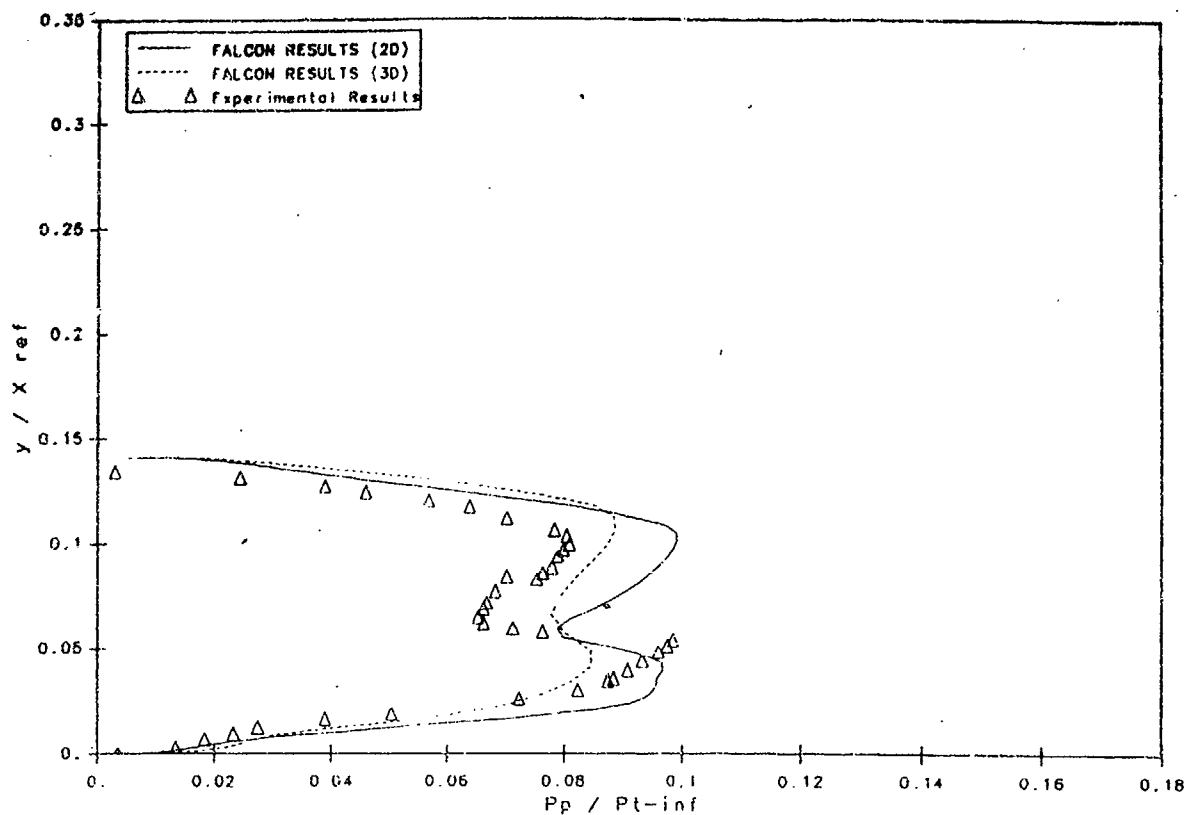
FALCON ANALYSIS w/BALDWIN-LOMAX TURBULENCE MODEL  
Pitot Pressure Ratio Profiles at  $X/X_{REF} = 6.23$



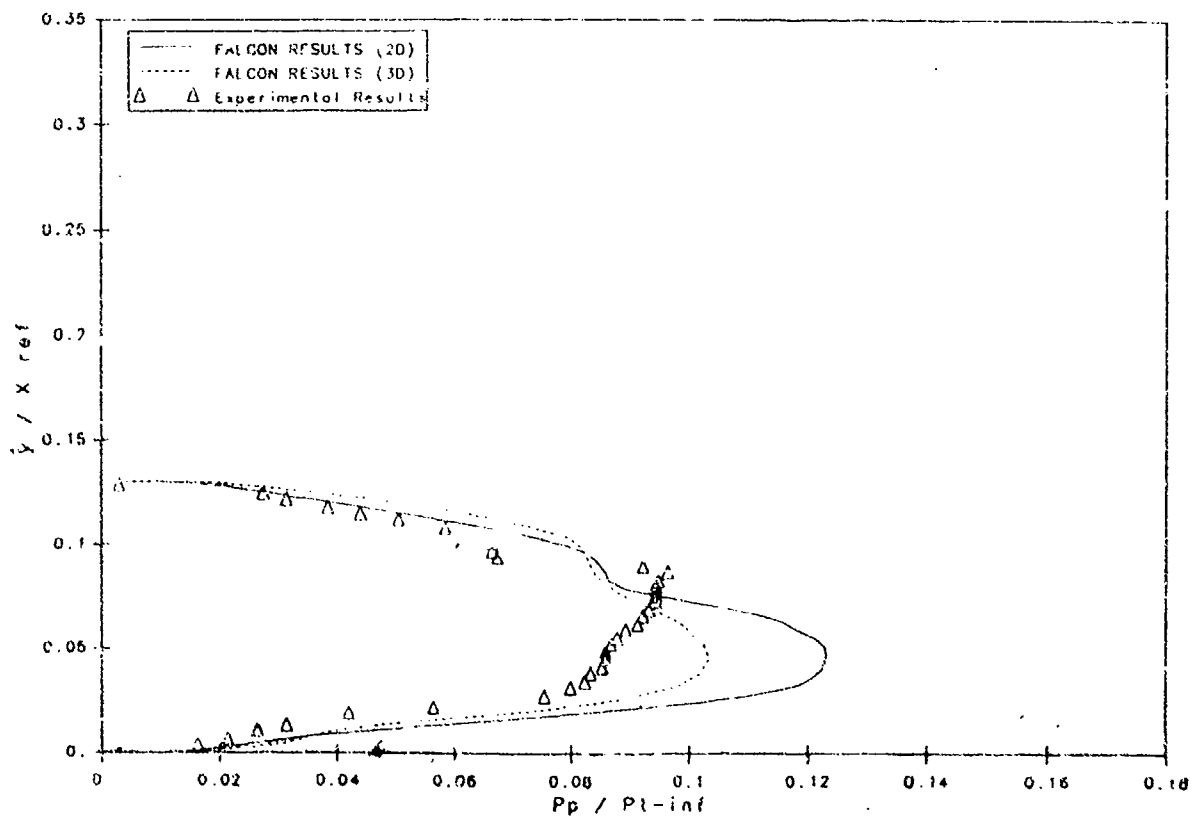
FALCON ANALYSIS w/BALDWIN-LOMAX TURBULENCE MODEL  
Pitot Pressure Ratio Profiles at  $X/X_{REF} = 6.37$



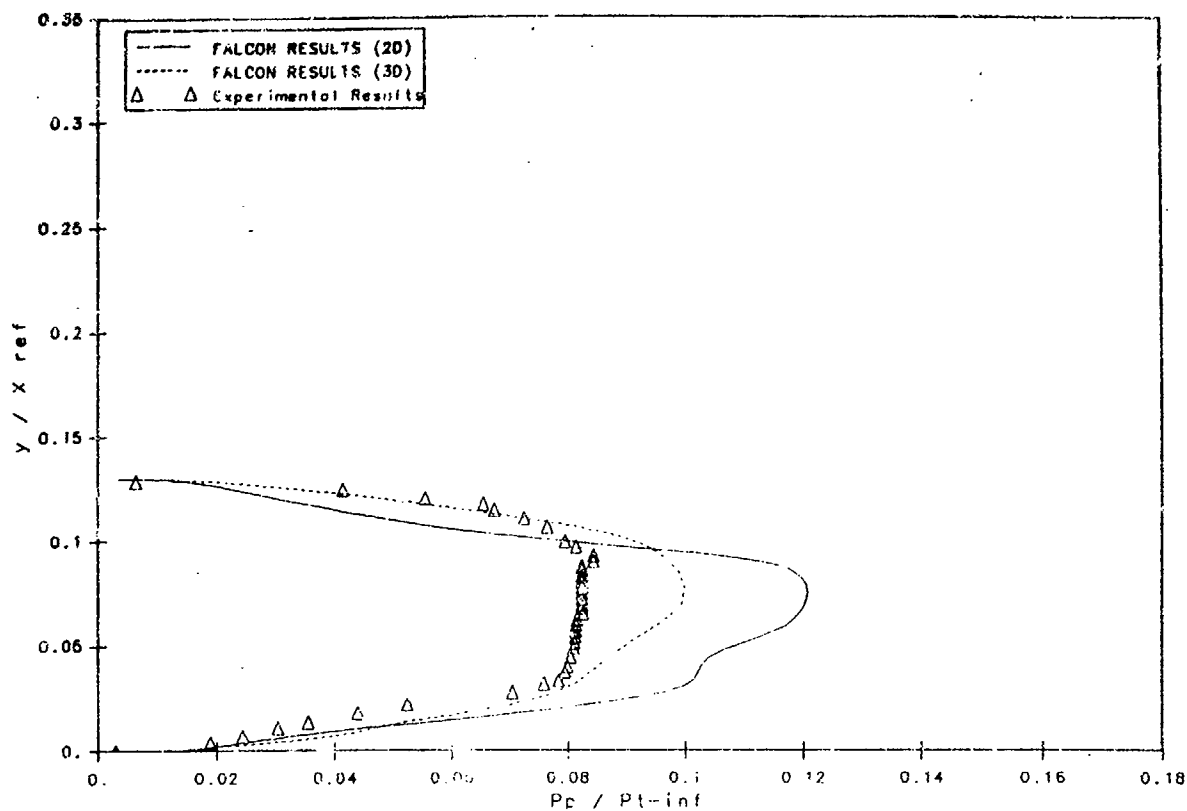
FALCON ANALYSIS w/BALDWIN-LOMAX TURBULENCE MODEL  
Pitot Pressure Ratio Profiles at  $X/X_{REF} = 6.51$



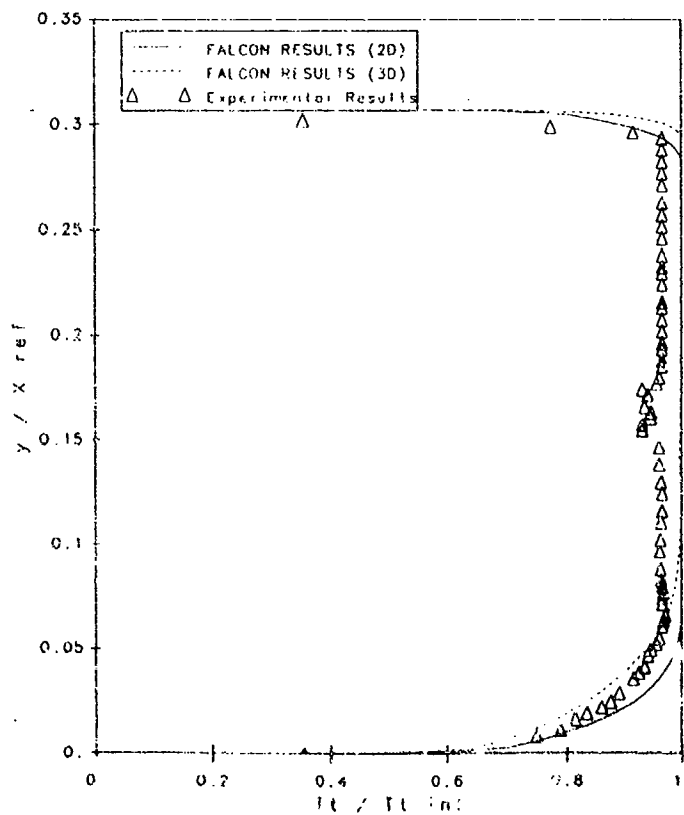
FALCON ANALYSIS w/BALDWIN-LOMAX TURBULENCE MODEL  
Pitot Pressure Ratio Profiles at  $X/X_{REF} = 6.65$



FALCON ANALYSIS w/BALDWIN-LOMAX TURBULENCE MODEL  
 Pitot Pressure Ratio Profiles at  $X/X_{REF} = 6.79$

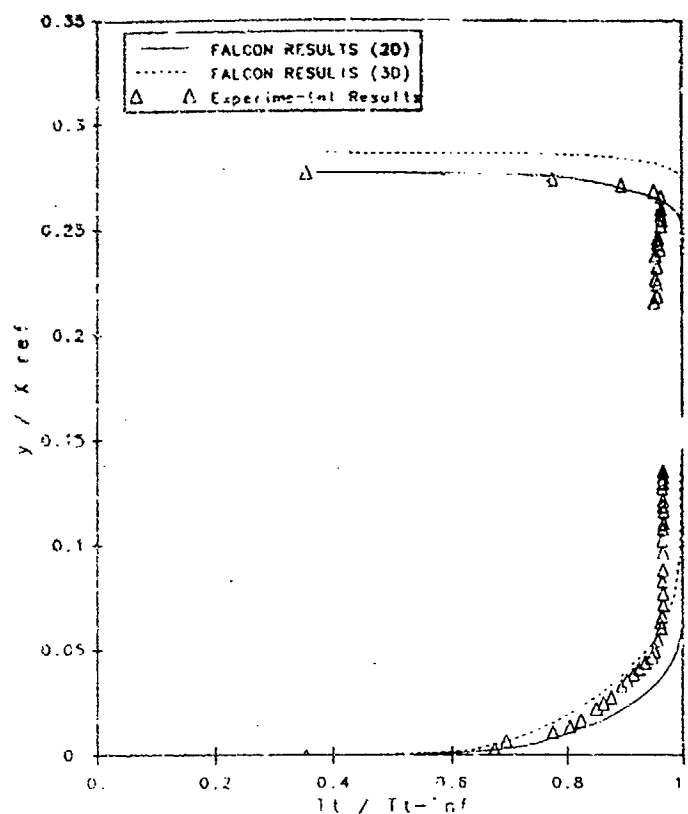


FALCON ANALYSIS w/BALDWIN-LOMAX TURBULENCE MODEL  
 Total Temperature Ratio Profiles at  $X/X_{REF} = 6.67$

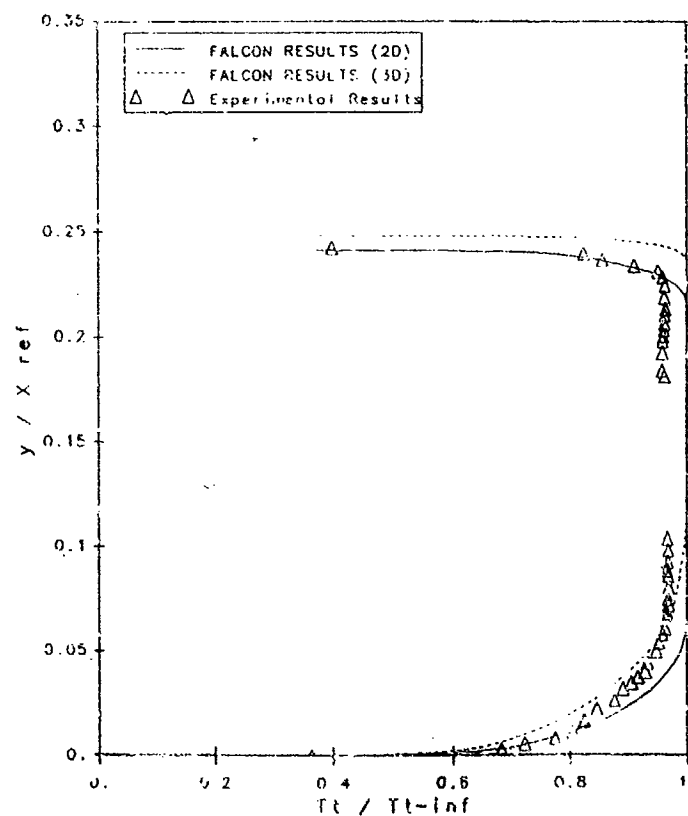




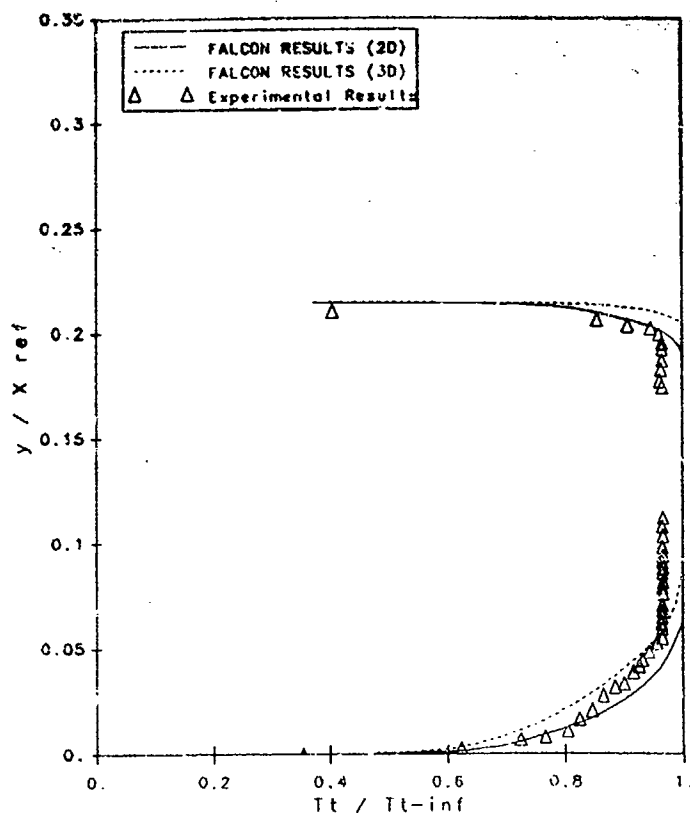
FALCON ANALYSIS w/BALDWIN-LOMAX TURBULENCE MODEL  
Total Temperature Ratio Profiles at  $x/x_{ref} = 5.78$



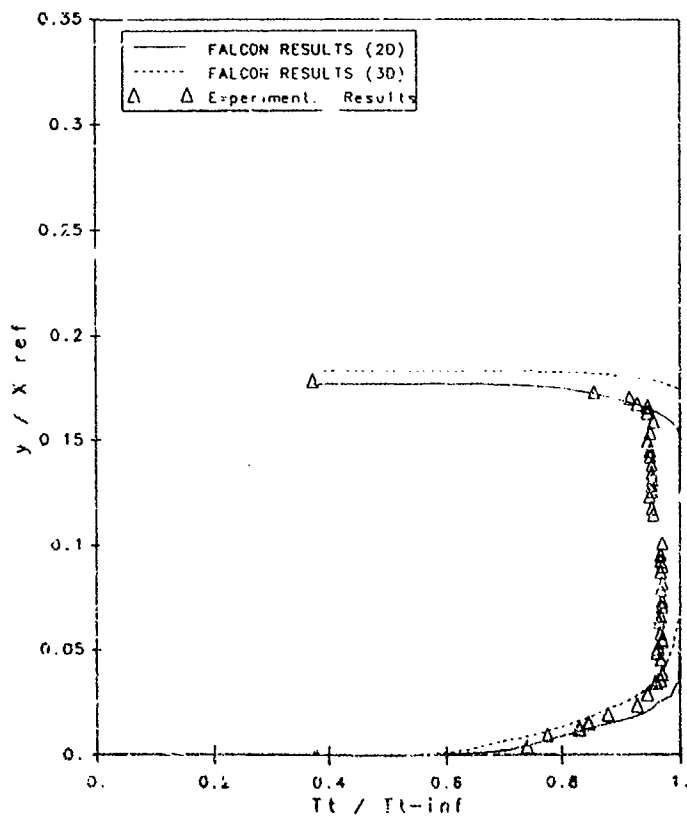
FALCON ANALYSIS w/BALDWIN-LOMAX TURBULENCE MODEL  
Total Temperature Ratio Profiles at  $x/x_{ref} = 5.94$



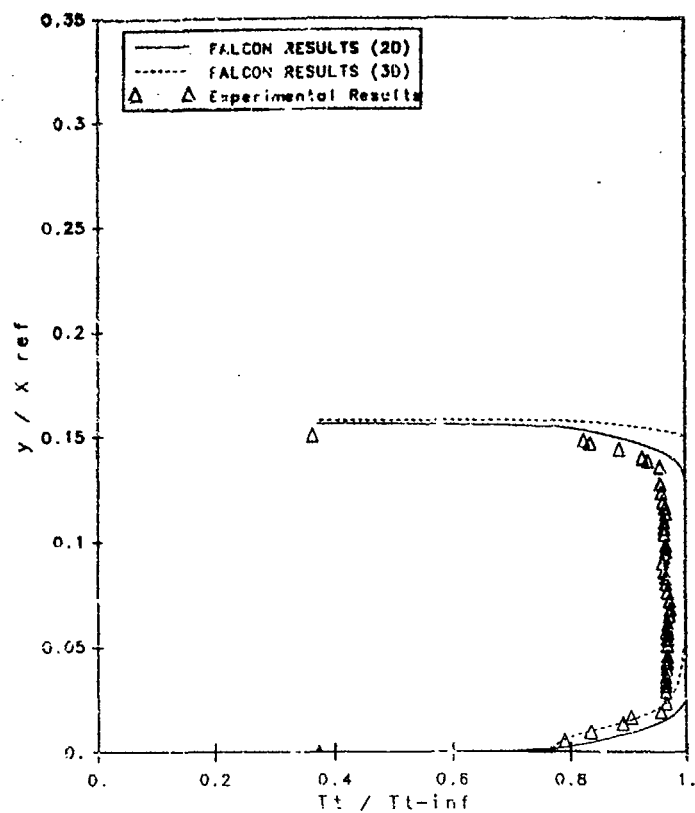
FALCON ANALYSIS w/BALDWIN-LOMAX TURBULENCE MODEL  
Total Temperature Ratio Profiles at  $X/X_{REF} = 6.09$



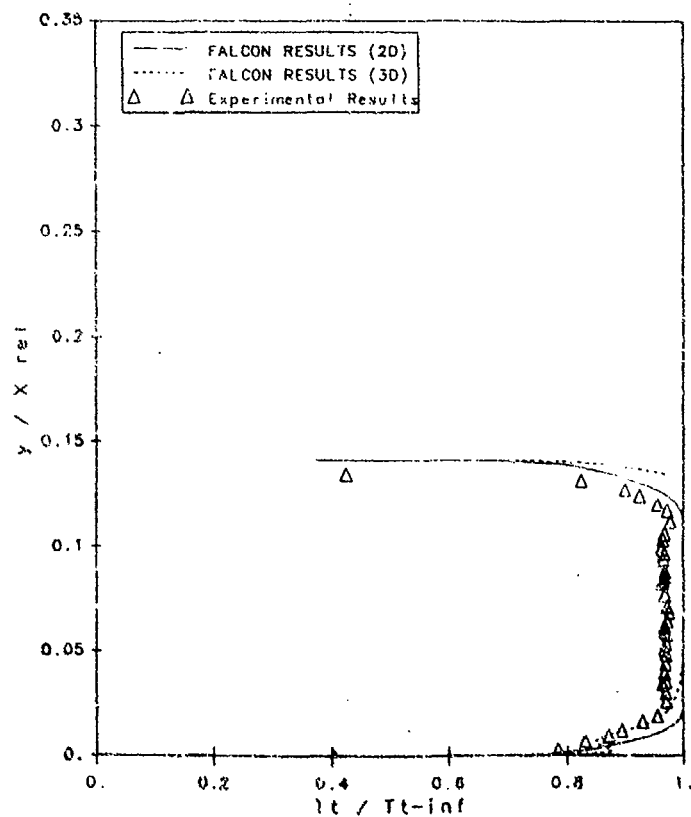
FALCON ANALYSIS w/BALDWIN-LOMAX TURBULENCE MODEL  
Total Temperature Ratio Profiles at  $X/X_{REF} = 6.23$



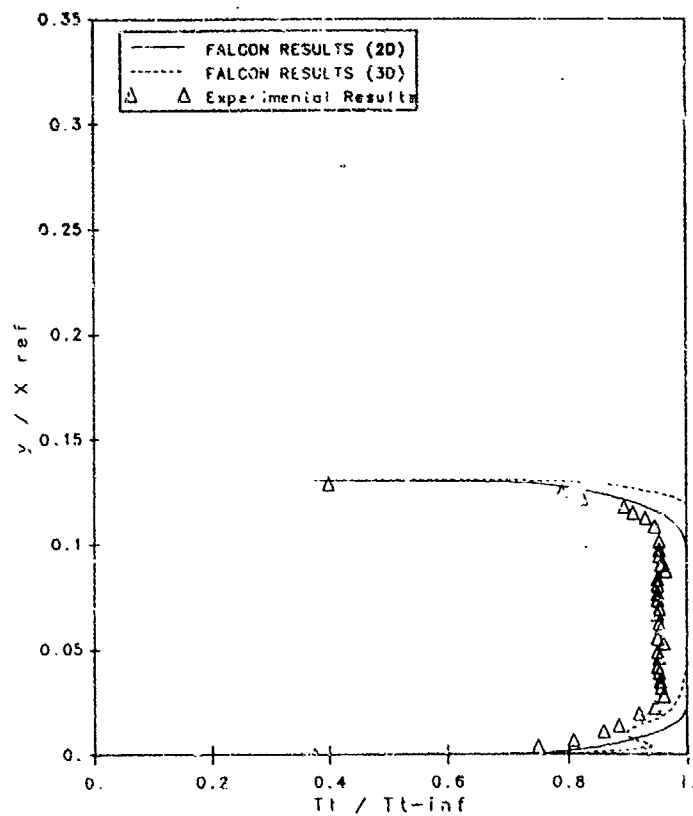
FALCON ANALYSIS w/BALDWIN-LOMAX TURBULENCE MODEL  
Total Temperature Ratio Profiles at  $X/X_{REF} = 6.37$



FALCON ANALYSIS w/BALDWIN-LOMAX TURBULENCE MODEL  
Total Temperature Ratio Profiles at  $X/X_{REF} = 6.51$



FALCON ANALYSIS w/BALDWIN-LOMAX TURBULENCE MODEL  
Total Temperature Ratio Profiles at  $X/X_{REF} = 6.65$



## FALCON RESULTS (2D) X/XREF = 5.67

Y/XREF	PP/PTINF	TT/TTINF
0.0000E+00	5.4268E-04	3.7369E-01
6.6554E-05	5.4747E-04	3.8994E-01
2.1617E-04	5.8512E-04	4.2327E-01
3.9908E-04	6.6851E-04	4.6180E-01
5.9659E-04	8.0864E-04	5.0378E-01
8.3136E-04	1.0088E-03	5.4530E-01
1.0975E-03	1.2563E-03	5.8285E-01
1.4135E-03	1.5183E-03	6.1510E-01
1.7793E-03	1.7777E-03	6.4243E-01
2.1950E-03	2.0287E-03	6.6564E-01
2.6772E-03	2.2705E-03	6.8561E-01
3.2425E-03	2.5040E-03	7.0307E-01
3.8744E-03	2.7310E-03	7.1856E-01
4.6060E-03	2.9541E-03	7.3257E-01
5.4541E-03	3.1717E-03	7.4521E-01
6.4332E-03	3.4051E-03	7.5778E-01
7.5493E-03	3.6820E-03	7.7156E-01
8.8297E-03	4.0136E-03	7.8662E-01
1.0310E-02	4.4119E-03	8.0293E-01
1.1989E-02	4.8907E-03	8.2038E-01
1.3918E-02	5.4675E-03	8.3879E-01
1.6115E-02	6.1608E-03	8.5788E-01
1.8607E-02	6.9930E-03	8.7726E-01
2.1434E-02	7.9831E-03	8.9647E-01
2.4660E-02	9.1536E-03	9.1453E-01
2.8285E-02	1.0519E-02	9.3230E-01
3.2359E-02	1.2104E-02	9.4822E-01
3.6948E-02	1.3949E-02	9.6229E-01
4.2053E-02	1.6153E-02	9.7592E-01
4.7740E-02	1.8692E-02	9.8758E-01
5.4009E-02	2.1148E-02	9.9432E-01
6.0893E-02	2.3279E-02	9.9826E-01
6.8426E-02	2.4712E-02	1.0001E+00
7.6574E-02	2.5110E-02	1.0002E+00
8.5337E-02	2.5216E-02	1.0003E+00
9.4699E-02	2.5254E-02	1.0003E+00
1.0458E-01	2.5273E-02	1.0002E+00
1.1494E-01	2.5287E-02	1.0002E+00
1.2568E-01	2.5307E-02	1.0002E+00
1.3672E-01	2.5505E-02	9.9994E-01
1.4791E-01	2.9321E-02	9.9821E-01
1.5918E-01	4.0446E-02	9.9952E-01
1.7039E-01	4.5264E-02	9.9998E-01
1.8142E-01	4.7498E-02	1.0000E+00
1.9216E-01	5.0351E-02	9.9994E-01
2.0252E-01	5.3007E-02	1.0001E+00
2.1241E-01	5.5637E-02	9.9941E-01
2.2176E-01	5.8140E-02	9.9891E-01
2.3052E-01	6.0432E-02	9.9979E-01
2.3868E-01	6.2357E-02	1.0005E+00
2.4620E-01	6.3789E-02	1.0003E+00
2.5310E-01	6.5099E-02	9.9952E-01
2.5937E-01	6.6351E-02	9.9944E-01
2.6506E-01	6.7154E-02	1.0002E+00
2.7015E-01	6.7386E-02	1.0006E+00
2.7473E-01	6.6597E-02	1.0007E+00

2.7883E-01	6.3986E-02	1.0005E+00
2.8245E-01	5.9661E-02	9.9926E-01
2.8566E-01	5.4311E-02	9.9611E-01
2.8850E-01	4.8588E-02	9.9011E-01
2.9100E-01	4.2993E-02	9.8141E-01
2.9319E-01	3.7849E-02	9.6977E-01
2.9512E-01	3.3281E-02	9.5543E-01
2.9680E-01	2.9346E-02	9.3890E-01
2.9828E-01	2.6054E-02	9.2129E-01
2.9956E-01	2.3344E-02	9.0316E-01
3.0067E-01	2.1134E-02	8.8556E-01
3.0166E-01	1.9339E-02	8.6883E-01
3.0250E-01	1.7877E-02	8.5333E-01
3.0324E-01	1.6680E-02	8.3923E-01
3.0387E-01	1.5640E-02	8.2584E-01
3.0443E-01	1.4645E-02	8.1196E-01
3.0491E-01	1.3656E-02	7.9706E-01
3.0533E-01	1.2664E-02	7.8094E-01
3.0570E-01	1.1649E-02	7.6310E-01
3.0601E-01	1.0582E-02	7.4271E-01
3.0628E-01	9.4199E-03	7.1828E-01
3.0651E-01	8.0917E-03	6.8689E-01
3.0671E-01	6.4986E-03	6.4266E-01
3.0689E-01	4.5771E-03	5.7206E-01
3.0704E-01	2.9323E-03	4.5843E-01
3.0713E-01	2.5945E-03	3.7363E-01

FALCON RESULTS (2D) COWL SURFACE PRESSURE  
X/XREF P/PZERO

0.0000E+00	1.0000E+00
6.8843E-04	1.0000E+00
2.1998E-03	1.0000E+00
4.0064E-03	1.0000E+00
6.1655E-03	1.0000E+00
8.7455E-03	1.0000E+00
1.1828E-02	1.0000E+00
1.5509E-02	1.0000E+00
1.9904E-02	1.0000E+00
2.5150E-02	1.0000E+00
3.1409E-02	1.0000E+00
3.8872E-02	1.0000E+00
4.7765E-02	1.0000E+00
5.8352E-02	1.0000E+00
7.0950E-02	1.0000E+00
8.5919E-02	1.0000E+00
1.0369E-01	1.0000E+00
1.2474E-01	1.0000E+00
1.4965E-01	1.0000E+00
1.7905E-01	1.0000E+00
2.1369E-01	1.0000E+00
2.5435E-01	1.0000E+00
3.0192E-01	1.0000E+00
3.5736E-01	1.0000E+00
4.2168E-01	1.0000E+00
4.9589E-01	1.0000E+00
5.8098E-01	1.0000E+00
6.7784E-01	1.0000E+00
7.8721E-01	1.0000E+00

9.0959E-01 1.0000E+00  
 1.0451E+00 1.0000E+00  
 1.1936E+00 1.0000E+00  
 1.3541E+00 1.0000E+00  
 1.5254E+00 1.0000E+00  
 1.7056E+00 1.0000E+00  
 1.8925E+00 1.0000E+00  
 2.0830E+00 1.0000E+00  
 2.2746E+00 1.0000E+00  
 2.4638E+00 1.0000E+00  
 2.6481E+00 1.0000E+00  
 2.8247E+00 1.0000E+00  
 2.9106E+00 1.0000E+00  
 2.9106E+00 1.0000E+00  
 2.9959E+00 1.0000E+00  
 3.1637E+00 1.0000E+00  
 3.3240E+00 1.0000E+00  
 3.4738E+00 1.0000E+00  
 3.6114E+00 1.0000E+00  
 3.7352E+00 1.0000E+00  
 3.8450E+00 1.0000E+00  
 3.9409E+00 1.0000E+00  
 4.0237E+00 1.0000E+00  
 4.0944E+00 1.0000E+00  
 4.1541E+00 1.0000E+00  
 4.2043E+00 9.9745E-01  
 4.2462E+00 9.7340E-01  
 4.2808E+00 2.1402E+00  
 4.3094E+00 2.8554E+00  
 4.3330E+00 3.1124E+00  
 4.3523E+00 3.0804E+00  
 4.3681E+00 3.0386E+00  
 4.3809E+00 3.0297E+00  
 4.3914E+00 3.0412E+00  
 4.3999E+00 3.0534E+00  
 4.4069E+00 3.0573E+00  
 4.4125E+00 3.0532E+00  
 4.4170E+00 3.0481E+00  
 4.4207E+00 3.0439E+00  
 4.4237E+00 3.0391E+00  
 4.4261E+00 3.0352E+00  
 4.4281E+00 3.0333E+00  
 4.4296E+00 3.0310E+00  
 4.4310E+00 3.0279E+00  
 4.4320E+00 3.1690E+00  
 4.4328E+00 4.1845E+00  
 4.4335E+00 1.1754E+01  
 4.4341E+00 4.8147E+01  
 4.4345E+00 8.8473E+01  
 4.4348E+00 1.0386E+02  
 4.4351E+00 1.0413E+02  
 4.4355E+00 9.7002E+01  
 4.4356E+00 9.3554E+01  
 4.4358E+00 9.2313E+01  
 4.4358E+00 9.2313E+01  
 4.4358E+00 9.2313E+01  
 4.4360E+00 8.7365E+01  
 4.4361E+00 6.1904E+01

4.4363E+00 5.0933E+01  
 4.4366E+00 3.8298E+01  
 4.4373E+00 2.2982E+01  
 4.4385E+00 1.7086E+01  
 4.4404E+00 1.4903E+01  
 4.4429E+00 1.3668E+01  
 4.4459E+00 1.4037E+01  
 4.4496E+00 1.3578E+01  
 4.4542E+00 1.2785E+01  
 4.4597E+00 1.2130E+01  
 4.4666E+00 1.1237E+01  
 4.4747E+00 9.0367E+00  
 4.4845E+00 8.8495E+00  
 4.4962E+00 8.1871E+00  
 4.5096E+00 7.7600E+00  
 4.5253E+00 7.4940E+00  
 4.5429E+00 7.3223E+00  
 4.5623E+00 7.2335E+00  
 4.5838E+00 7.1247E+00  
 4.6064E+00 7.0394E+00  
 4.6298E+00 6.9616E+00  
 4.6536E+00 6.8962E+00  
 4.6771E+00 6.8496E+00  
 4.6995E+00 6.8345E+00  
 4.7206E+00 6.8344E+00  
 4.7401E+00 6.8500E+00  
 4.7576E+00 6.8613E+00  
 4.7730E+00 6.8617E+00  
 4.7802E+00 7.0717E+00  
 4.7802E+00 6.8617E+00  
 4.7837E+00 7.0717E+00  
 4.7908E+00 7.1235E+00  
 4.7988E+00 7.1380E+00  
 4.8076E+00 7.1528E+00  
 4.8172E+00 7.1791E+00  
 4.8277E+00 7.2055E+00  
 4.8394E+00 7.2317E+00  
 4.8518E+00 7.2487E+00  
 4.8656E+00 7.2687E+00  
 4.8806E+00 7.2847E+00  
 4.8969E+00 7.5058E+00  
 4.9145E+00 7.6870E+00  
 4.9236E+00 7.7705E+00  
 4.9541E+00 7.8449E+00  
 4.9762E+00 7.8966E+00  
 4.9997E+00 8.2786E+00  
 5.0249E+00 8.5216E+00  
 5.0515E+00 8.6831E+00  
 5.0800E+00 8.8096E+00  
 5.1097E+00 8.9284E+00  
 5.1410E+00 9.0479E+00  
 5.1726E+00 9.7615E+00  
 5.2075E+00 1.0074E+01  
 5.2426E+00 1.0392E+01  
 5.2787E+00 1.0651E+01  
 5.3156E+00 1.1291E+01  
 5.3532E+00 1.1837E+01  
 5.3911E+00 1.2119E+01

5.4293E+00 1.2554E+01  
 5.4674E+00 1.3222E+01  
 5.5053E+00 1.3489E+01  
 5.5429E+00 1.3793E+01  
 5.5797E+00 1.4627E+01  
 5.6157E+00 1.4856E+01  
 5.6507E+00 1.5090E+01  
 5.6846E+00 1.5306E+01  
 5.7172E+00 1.6288E+01  
 5.7483E+00 1.6616E+01  
 5.7780E+00 1.6820E+01  
 5.8083E+00 1.6958E+01  
 5.8199E+00 1.7048E+01  
 5.8199E+00 1.6958E+01  
 5.8337E+00 1.7048E+01  
 5.8615E+00 1.7534E+01  
 5.8891E+00 1.8212E+01  
 5.9167E+00 1.8843E+01  
 5.9443E+00 1.9400E+01  
 5.9719E+00 1.9850E+01  
 5.9995E+00 2.0268E+01  
 6.0270E+00 2.0694E+01  
 6.0546E+00 2.1119E+01  
 6.0822E+00 2.1648E+01  
 6.1096E+00 2.2248E+01  
 6.1372E+00 2.2906E+01  
 6.1646E+00 2.3566E+01  
 6.1921E+00 2.4216E+01  
 6.2195E+00 2.4848E+01  
 6.2470E+00 2.5452E+01  
 6.2744E+00 2.5984E+01  
 6.3018E+00 2.6353E+01  
 6.3291E+00 2.6506E+01  
 6.3585E+00 2.6617E+01  
 6.3742E+00 2.6644E+01  
 6.3742E+00 2.6617E+01  
 6.3881E+00 2.6644E+01  
 6.4157E+00 2.6715E+01  
 6.4435E+00 2.6733E+01  
 6.4711E+00 2.6732E+01  
 6.4989E+00 2.6721E+01  
 6.5265E+00 2.6623E+01  
 6.5543E+00 2.6473E+01  
 6.5820E+00 2.6139E+01  
 6.6096E+00 2.5610E+01  
 6.6374E+00 2.4849E+01  
 6.6650E+00 2.3884E+01  
 6.6928E+00 2.2590E+01  
 6.7205E+00 2.1378E+01  
 6.7431E+00 1.9832E+01  
 6.7739E+00 1.9635E+01  
 6.8035E+00 2.1169E+01  
 6.8311E+00 2.4504E+01  
 6.8589E+00 2.7947E+01  
 6.8867E+00 2.9752E+01  
 6.9146E+00 3.1226E+01  
 6.9286E+00 3.2819E+01  
 6.9286E+00 3.1226E+01

6.9410E+00 3.2818E+01  
 6.9661E+00 3.2631E+01  
 6.9912E+00 3.2136E+01  
 7.0164E+00 3.1240E+01  
 7.0415E+00 2.9973E+01  
 7.0666E+00 2.8604E+01  
 7.0917E+00 2.7256E+01  
 7.1168E+00 2.6087E+01  
 7.1417E+00 2.5152E+01  
 7.1668E+00 2.4433E+01  
 7.1919E+00 2.3897E+01  
 7.2171E+00 2.3504E+01  
 7.2422E+00 2.3216E+01  
 7.2673E+00 2.3015E+01  
 7.2924E+00 2.2882E+01  
 7.3175E+00 2.2782E+01  
 7.3426E+00 2.2702E+01  
 7.3677E+00 2.2620E+01  
 7.3928E+00 2.2520E+01  
 7.4179E+00 2.2255E+01  
 7.4304E+00 2.2237E+01  
 FALCON RESULTS (2D) X/XREF = 5.78  
 Y/XREF PP/PTINF TT/TTINF  
 0.0000E+00 5.4239E-04 3.7369E-01  
 6.6505E-05 5.4675E-04 3.8914E-01  
 2.1617E-04 5.8105E-04 4.2089E-01  
 3.8253E-04 6.5697E-04 4.5757E-01  
 5.8199E-04 7.8456E-04 4.9777E-01  
 8.1481E-04 9.6711E-04 5.3797E-01  
 1.0642E-03 1.1961E-03 5.7477E-01  
 1.3801E-03 1.4435E-03 6.0669E-01  
 1.7293E-03 1.6902E-03 6.3388E-01  
 2.1284E-03 1.9295E-03 6.5703E-01  
 2.5940E-03 2.1598E-03 6.7696E-01  
 3.1095E-03 2.3821E-03 6.9438E-01  
 3.7248E-03 2.5972E-03 7.0980E-01  
 4.4232E-03 2.8076E-03 7.2369E-01  
 5.2379E-03 3.0121E-03 7.3622E-01  
 6.1524E-03 3.2294E-03 7.4860E-01  
 7.2168E-03 3.4845E-03 7.6207E-01  
 8.4140E-03 3.7883E-03 7.7677E-01  
 9.8107E-03 4.1504E-03 7.9268E-01  
 1.1374E-02 4.5834E-03 8.0971E-01  
 1.3186E-02 5.1008E-03 8.2770E-01  
 1.5215E-02 5.7197E-03 8.4641E-01  
 1.7543E-02 6.4566E-03 8.6552E-01  
 2.0170E-02 7.3312E-03 8.8460E-01  
 2.3130E-02 8.3589E-03 9.0320E-01  
 2.6472E-02 9.5590E-03 9.2083E-01  
 3.0230E-02 1.0949E-02 9.3748E-01  
 3.4404E-02 1.2571E-02 9.5215E-01  
 3.9077E-02 1.4488E-02 9.6599E-01  
 4.4232E-02 1.6841E-02 9.7962E-01  
 4.9918E-02 1.9355E-02 9.9000E-01  
 5.6138E-02 2.1675E-02 9.9524E-01  
 6.2905E-02 2.3648E-02 9.9883E-01  
 7.0222E-02 2.4812E-02 1.0001E+00  
 7.8070E-02 2.5104E-02 1.0002E+00

8.6434E-02	2.5196E-02	1.0002E+00	2.0454E-03	1.7992E-03	6.4479E-01
9.5248E-02	2.5246E-02	1.0003E+00	2.4943E-03	2.0112E-03	6.6437E-01
1.0444E-01	2.5272E-02	1.0002E+00	2.9932E-03	2.2150E-03	6.8147E-01
1.1399E-01	2.6076E-02	9.9877E-01	3.5586E-03	2.4115E-03	6.9859E-01
1.2377E-01	3.3429E-02	9.9818E-01	4.2237E-03	2.6025E-03	7.1019E-01
1.3371E-01	4.5327E-02	9.9977E-01	4.9720E-03	2.7869E-03	7.2241E-01
1.4369E-01	4.9023E-02	9.9992E-01	5.8200E-03	2.9810E-03	7.3444E-01
1.5363E-01	5.1668E-02	9.9987E-01	6.8011E-03	3.2067E-03	7.4748E-01
1.6341E-01	5.4644E-02	1.0002E+00	7.8986E-03	3.4729E-03	7.6169E-01
1.7295E-01	5.7623E-02	9.9966E-01	9.1623E-03	3.7875E-03	7.7704E-01
1.8216E-01	6.0578E-02	9.9863E-01	1.0592E-02	4.1594E-03	7.9345E-01
1.9098E-01	6.2983E-02	9.9900E-01	1.2222E-02	4.5999E-03	8.1065E-01
1.9932E-01	6.5041E-02	9.9994E-01	1.4068E-02	5.1201E-03	8.2848E-01
2.0717E-01	6.6827E-02	1.0004E+00	1.6146E-02	5.7311E-03	8.4684E-01
2.1449E-01	6.8159E-02	1.0004E+00	1.8491E-02	6.4480E-03	8.6544E-01
2.2126E-01	6.9306E-02	9.9997E-01	2.1135E-02	7.2839E-03	8.8389E-01
2.2749E-01	7.0277E-02	9.9949E-01	2.4095E-02	8.2551E-03	9.0179E-01
2.3318E-01	7.0895E-02	9.9967E-01	2.7404E-02	9.3777E-03	9.1879E-01
2.3833E-01	7.1422E-02	1.0004E+00	3.1079E-02	1.0684E-02	9.3505E-01
2.4299E-01	7.1421E-02	1.0008E+00	3.5169E-02	1.2198E-02	9.4918E-01
2.4718E-01	7.0160E-02	1.0008E+00	3.9659E-02	1.4043E-02	9.6300E-01
2.5092E-01	6.7038E-02	1.0004E+00	4.4614E-02	1.6330E-02	9.7721E-01
2.5426E-01	6.2108E-02	9.9842E-01	5.0002E-02	1.8732E-02	9.8802E-01
2.5724E-01	5.6321E-02	9.9373E-01	5.5855E-02	2.0998E-02	9.9383E-01
2.5987E-01	5.0393E-02	9.8666E-01	6.2157E-02	2.2940E-02	9.9759E-01
2.6218E-01	4.4598E-02	9.7664E-01	6.8908E-02	2.4201E-02	1.0001E+00
2.6423E-01	3.9329E-02	9.6381E-01	7.6075E-02	2.5713E-02	9.9912E-01
2.6602E-01	3.4709E-02	9.4866E-01	8.3624E-02	3.3630E-02	9.9926E-01
2.6760E-01	3.0786E-02	9.3181E-01	9.1490E-02	4.6378E-02	9.9914E-01
2.6898E-01	2.7519E-02	9.1415E-01	9.8638E-02	5.2457E-02	9.9949E-01
2.7019E-01	2.4830E-02	8.9646E-01	1.0797E-01	5.5600E-02	1.0003E+00
2.7126E-01	2.2626E-02	8.7948E-01	1.1645E-01	5.8775E-02	1.0001E+00
2.7217E-01	2.0829E-02	8.6369E-01	1.2495E-01	6.1952E-02	9.9948E-01
2.7297E-01	1.9363E-02	8.4925E-01	1.3341E-01	6.4913E-02	9.9800E-01
2.7369E-01	1.8147E-02	8.3607E-01	1.4176E-01	6.7305E-02	9.9904E-01
2.7429E-01	1.7040E-02	8.2303E-01	1.4991E-01	6.9156E-02	9.9986E-01
2.7482E-01	1.5951E-02	8.0916E-01	1.5777E-01	7.0565E-02	1.0004E+00
2.7528E-01	1.4881E-02	7.9446E-01	1.6532E-01	7.1868E-02	1.0004E+00
2.7568E-01	1.3812E-02	7.7863E-01	1.7249E-01	7.3365E-02	1.0003E+00
2.7603E-01	1.2724E-02	7.6121E-01	1.7924E-01	7.4815E-02	1.0004E+00
2.7633E-01	1.1587E-02	7.4145E-01	1.8554E-01	7.5805E-02	1.0003E+00
2.7660E-01	1.0353E-02	7.1789E-01	1.9139E-01	7.6356E-02	9.9996E-01
2.7683E-01	8.9462E-03	6.8780E-01	1.9680E-01	7.6702E-02	9.9981E-01
2.7703E-01	7.2560E-03	6.4557E-01	2.0174E-01	7.7052E-02	1.0001E+00
2.7720E-01	5.1761E-03	5.7769E-01	2.0624E-01	7.7024E-02	1.0006E+00
2.7735E-01	3.2893E-03	4.6368E-01	2.1032E-01	7.5965E-02	1.0009E+00
2.7741E-01	2.8746E-03	3.7369E-01	2.1401E-01	7.3218E-02	1.0003E+00
FALCON RESULTS (2D) X/XREF = 5.94			2.1730E-01	6.8893E-02	9.9849E-01
Y/XREF	PP/PTINF	TT/TTINF	2.2026E-01	6.3684E-02	9.9466E-01
0.0000E+00	5.4214E-04	3.7369E-01	2.2290E-01	5.7887E-02	9.8853E-01
6.6554E-05	5.4611E-04	3.8831E-01	2.2525E-01	5.1979E-02	9.7961E-01
2.1617E-04	5.7727E-04	4.1837E-01	2.2733E-01	4.6335E-02	9.6793E-01
3.8249E-04	6.4566E-04	4.5295E-01	2.2917E-01	4.1239E-02	9.5404E-01
5.6529E-04	7.5956E-04	4.9086E-01	2.3080E-01	3.6793E-02	9.3849E-01
7.9814E-04	9.2182E-04	5.2909E-01	2.3223E-01	3.3002E-02	9.2193E-01
1.0476E-03	1.1262E-03	5.6447E-01	2.3350E-01	2.9821E-02	9.0510E-01
1.3303E-03	1.3519E-03	5.9548E-01	2.3461E-01	2.7182E-02	8.8860E-01
1.6629E-03	1.5787E-03	6.2206E-01	2.3557E-01	2.4995E-02	8.7293E-01



2.3644E-01	2.3186E-02	8.5833E-01
2.3719E-01	2.1684E-02	8.4495E-01
2.3784E-01	2.0409E-02	8.3260E-01
2.3840E-01	1.9226E-02	8.2025E-01
2.3892E-01	1.8047E-02	8.0706E-01
2.3935E-01	1.6880E-02	7.9304E-01
2.3973E-01	1.5709E-02	7.7792E-01
2.4006E-01	1.4514E-02	7.6130E-01
2.4035E-01	1.3270E-02	7.4251E-01
2.4061E-01	1.1924E-02	7.2025E-01
2.4083E-01	1.0396E-02	6.9201E-01
2.4103E-01	8.5582E-03	6.5262E-01
2.4120E-01	6.2348E-03	5.8865E-01
2.4133E-01	3.9360E-03	4.7427E-01
2.4141E-01	3.3548E-03	3.7369E-01

FALCON RESULTS (2D) X/XREF = 6.09

Y/XREF	DP/PTINF	TT/TTINF
0.0000E+00	4.8261E-04	3.7369E-01
6.6455E-05	4.8575E-04	3.8647E-01
2.1617E-04	5.1043E-04	4.1286E-01
3.8248E-04	5.6449E-04	4.4335E-01
5.6539E-04	6.5533E-04	4.7739E-01
7.8151E-04	7.8754E-04	5.1281E-01
1.0309E-03	9.5913E-04	5.4676E-01
1.3136E-03	1.1359E-03	5.7736E-01
1.6295E-03	1.3578E-03	6.0407E-01
1.9954E-03	1.5556E-03	6.2717E-01
2.4112E-03	1.7460E-03	6.4710E-01
2.8934E-03	1.9280E-03	6.6460E-01
3.4421E-03	2.1022E-03	6.8006E-01
4.0574E-03	2.2699E-03	6.9383E-01
4.7558E-03	2.4299E-03	7.0599E-01
5.5539E-03	2.5954E-03	7.1800E-01
6.4685E-03	2.7839E-03	7.3071E-01
7.4994E-03	3.0011E-03	7.4433E-01
8.6800E-03	3.2520E-03	7.5887E-01
9.9937E-03	3.5460E-03	7.7431E-01
1.1490E-02	3.8897E-03	7.9063E-01
1.3186E-02	4.2939E-03	8.0775E-01
1.5082E-02	4.7708E-03	8.2555E-01
1.7227E-02	5.3336E-03	8.4371E-01
1.9621E-02	5.9968E-03	8.6186E-01
2.2299E-02	6.7712E-03	8.7970E-01
2.5275E-02	7.6806E-03	8.9694E-01
2.8584E-02	8.7333E-03	9.1370E-01
3.2225E-02	1.0025E-02	9.3056E-01
3.6250E-02	1.1448E-02	9.4568E-01
4.0640E-02	1.3142E-02	9.6106E-01
4.5429E-02	1.5173E-02	9.7713E-01
5.0600E-02	1.8828E-02	9.8169E-01
5.6154E-02	2.7584E-02	9.9003E-01
6.2090E-02	4.2859E-02	9.9768E-01
6.8293E-02	5.2491E-02	1.0001E+00
7.4994E-02	5.7923E-02	9.9967E-01
8.1873E-02	6.0632E-02	9.9962E-01
8.8925E-02	6.3652E-02	9.9944E-01
9.6278E-02	6.6548E-02	9.9919E-01
1.0360E-01	6.9035E-02	9.9891E-01

1.1109E-01	7.0885E-02	9.9922E-01
1.1849E-01	7.2326E-02	9.9886E-01
1.2578E-01	7.3534E-02	1.0003E+00
1.3289E-01	7.4643E-02	1.0004E+00
1.3978E-01	7.5694E-02	1.0003E+00
1.4640E-01	7.6739E-02	1.0003E+00
1.5268E-01	7.7987E-02	1.0004E+00
1.5862E-01	7.9459E-02	1.0004E+00
1.6419E-01	8.1039E-02	1.0002E+00
1.6936E-01	8.2554E-02	9.9984E-01
1.7415E-01	8.3846E-02	1.0000E+00
1.7854E-01	8.4320E-02	1.0005E+00
1.8256E-01	8.3185E-02	1.0008E+00
1.8620E-01	8.0096E-02	1.0005E+00
1.8951E-01	7.5524E-02	9.9917E-01
1.9249E-01	6.9950E-02	9.9591E-01
1.9517E-01	6.3906E-02	9.9048E-01
1.9756E-01	5.7756E-02	9.8277E-01
1.9971E-01	5.1866E-02	9.7250E-01
2.0160E-01	4.6445E-02	9.5980E-01
2.0330E-01	4.1627E-02	9.4541E-01
2.0480E-01	3.7439E-02	9.2968E-01
2.0611E-01	3.3876E-02	9.1346E-01
2.0729E-01	3.0871E-02	8.9733E-01
2.0832E-01	2.8364E-02	8.8182E-01
2.0922E-01	2.6278E-02	8.6726E-01
2.1003E-01	2.4547E-02	8.5384E-01
2.1073E-01	2.3108E-02	8.4167E-01
2.1135E-01	2.1820E-02	8.2993E-01
2.1190E-01	2.0563E-02	8.1765E-01
2.1236E-01	1.9323E-02	8.0467E-01
2.1278E-01	1.8094E-02	7.9088E-01
2.1314E-01	1.6863E-02	7.7605E-01
2.1348E-01	1.5608E-02	7.5981E-01
2.1376E-01	1.4362E-02	7.4130E-01
2.1399E-01	1.2890E-02	7.1991E-01
2.1421E-01	1.1281E-02	6.9270E-01
2.1441E-01	9.3631E-03	6.5482E-01
2.1457E-01	6.8982E-03	5.9324E-01
2.1471E-01	4.3480E-03	4.7971E-01
2.1477E-01	3.6695E-03	3.7369E-01

FALCON RESULTS (2D) X/XREF = 6.23

Y/XREF	DP/PTINF	TT/TTINF
0.0000E+00	1.7824E-03	3.7369E-01
6.6505E-05	1.7824E-03	3.9659E-01
1.9946E-04	1.7818E-03	4.4186E-01
3.6578E-04	1.7851E-03	4.8772E-01
5.4869E-04	1.7994E-03	5.3265E-01
7.6485E-04	1.8323E-03	5.7495E-01
9.9762E-04	1.8914E-03	6.1241E-01
1.2637E-03	1.9823E-03	6.4266E-01
1.5797E-03	2.1054E-03	6.6554E-01
1.8122E-03	2.2616E-03	6.8249E-01
2.3113E-03	2.4519E-03	6.9523E-01
2.7602E-03	2.6807E-03	7.0584E-01
3.2592E-03	2.9511E-03	7.1565E-01
3.8412E-03	3.2642E-03	7.2523E-01
4.4897E-03	3.6353E-03	7.3557E-01

```

5.2047E-03 4.0669E-03 7.4650E-01
6.0361E-03 4.5722E-03 7.5809E-01
6.9673E-03 5.1758E-03 7.7055E-01
8.0149E-03 5.9533E-03 7.8507E-01
9.1955E-03 6.9753E-03 8.0232E-01
1.0509E-02 8.2443E-03 8.2056E-01
1.1989E-02 9.8418E-03 8.401E-01
1.3635E-02 1.1857E-02 8.6176E-01
1.5481E-02 1.4384E-02 8.8717E-01
1.7543E-02 1.7469E-02 9.1415E-01
1.9821E-02 2.1152E-02 9.3811E-01
2.2349E-02 2.4760E-02 9.5328E-01
2.5125E-02 2.5921E-02 9.6394E-01
2.8169E-02 2.9416E-02 9.8559E-01
3.1494E-02 3.5263E-02 9.8937E-01
3.5119E-02 4.1864E-02 9.9622E-01
3.9043E-02 4.8387E-02 9.9842E-01
4.3250E-02 5.3825E-02 9.9825E-01
4.7757E-02 5.8731E-02 9.9775E-01
5.2546E-02 6.3293E-02 9.9790E-01
5.7601E-02 6.7257E-02 9.9877E-01
6.2889E-02 7.0423E-02 9.9881E-01
6.8376E-02 7.2960E-02 9.9940E-01
7.4046E-02 7.5115E-02 1.0003E+00
7.9816E-02 7.6948E-02 1.0005E+00
8.5685E-02 7.8676E-02 1.0004E+00
9.1573E-02 8.0447E-02 1.0001E+00
9.7426E-02 8.2185E-02 1.0001E+00
1.0321E-01 8.3842E-02 1.0001E+00
1.0887E-01 8.5423E-02 1.0002E+00
1.1437E-01 8.6858E-02 1.0002E+00
1.1966E-01 8.8016E-02 1.0003E+00
1.2471E-01 8.9013E-02 1.0004E+00
1.2950E-01 9.0028E-02 1.0003E+00
1.3401E-01 9.1073E-02 1.0000E+00
1.3823E-01 9.2007E-02 1.0002E+00
1.4216E-01 9.2380E-02 1.0004E+00
1.4578E-01 9.1168E-02 1.0007E+00
1.4911E-01 8.8200E-02 1.0004E+00
1.5217E-01 8.3810E-02 9.9912E-01
1.5494E-01 7.8333E-02 9.9596E-01
1.5745E-01 7.2256E-02 9.9072E-01
1.5973E-01 6.5967E-02 9.8342E-01
1.6179E-01 5.9821E-02 9.7384E-01
1.6364E-01 5.4057E-02 9.6229E-01
1.6529E-01 4.8834E-02 9.4905E-01
1.6679E-01 4.4193E-02 9.3464E-01
1.6808E-01 4.0166E-02 9.1962E-01
1.6926E-01 3.6707E-02 9.0445E-01
1.7031E-01 3.3776E-02 8.8963E-01
1.7124E-01 3.1293E-02 8.7544E-01
1.7205E-01 2.9201E-02 8.6212E-01
1.7279E-01 2.7434E-02 8.4979E-01
1.7343E-01 2.5938E-02 8.3850E-01
1.7400E-01 2.4563E-02 8.2752E-01
1.7450E-01 2.3252E-02 8.1602E-01
1.7495E-01 2.1329E-02 8.0380E-01
1.7535E-01 2.0606E-02 7.9077E-01

```

```

1.7568E-01 1.9273E-02 7.7672E-01
1.7599E-01 1.7909E-02 7.6129E-01
1.7626E-01 1.6486E-02 7.4394E-01
1.7649E-01 1.4951E-02 7.2358E-01
1.7671E-01 1.3214E-02 6.9810E-01
1.7689E-01 1.1122E-02 6.6299E-01
1.7704E-01 8.3862E-03 6.0578E-01
1.7719E-01 5.2829E-03 4.9403E-01
1.7726E-01 4.3144E-03 3.7369E-01
FALCON RESULTS (2D) X/XREF = 6.37
Y/XREF PP/PTINF TT/TTINF
0.0000E+00 2.8001E-03 3.7369E-01
6.6503E-05 2.9148E-03 4.3744E-01
2.1621E-04 3.4970E-03 5.3803E-01
3.8248E-04 4.2058E-03 6.1168E-01
5.8199E-04 4.8553E-03 6.6101E-01
7.9821E-04 5.4483E-03 6.9591E-01
1.0310E-03 6.0047E-03 7.2229E-01
1.2970E-03 6.5363E-03 7.4330E-01
1.6130E-03 7.0592E-03 7.6076E-01
1.9622E-03 7.5881E-03 7.7580E-01
2.3613E-03 8.1355E-03 7.8912E-01
2.7935E-03 8.7121E-03 8.0120E-01
3.2924E-03 9.3297E-03 8.1236E-01
3.8578E-03 9.9943E-03 8.2281E-01
4.4897E-03 1.0733E-02 8.3290E-01
5.1881E-03 1.1638E-02 8.4373E-01
5.9663E-03 1.2820E-02 8.5590E-01
6.8842E-03 1.4358E-02 8.6930E-01
7.8819E-03 1.6337E-02 8.8368E-01
8.9959E-03 1.8857E-02 8.9878E-01
1.0243E-02 2.2049E-02 9.1438E-01
1.1623E-02 2.6019E-02 9.3013E-01
1.3170E-02 3.0869E-02 9.4546E-01
1.4887E-02 3.6665E-02 9.5926E-01
1.6761E-02 4.3427E-02 9.7096E-01
1.8840E-02 5.0952E-02 9.8124E-01
2.1118E-02 5.8981E-02 9.8987E-01
2.3629E-02 6.6410E-02 9.9641E-01
2.6356E-02 7.1677E-02 9.9969E-01
2.9299E-02 7.3114E-02 9.9984E-01
3.2492E-02 6.7334E-02 9.9891E-01
3.5934E-02 6.1478E-02 9.9759E-01
3.9592E-02 5.8155E-02 9.9971E-01
4.3500E-02 5.9711E-02 1.0007E+00
4.7624E-02 6.2883E-02 9.9829E-01
5.1947E-02 6.6912E-02 1.0005E+00
5.6453E-02 7.0622E-02 9.9999E-01
6.1109E-02 7.4498E-02 1.0002E+00
6.5898E-02 7.8077E-02 9.9980E-01
7.0767E-02 8.1351E-02 9.9973E-01
7.5726E-02 8.4259E-02 1.0001E+00
8.0681E-02 8.6780E-02 1.0003E+00
8.5616E-02 8.8949E-02 1.0001E+00
9.0508E-02 9.0897E-02 1.0002E+00
9.5344E-02 9.2723E-02 1.0003E+00
9.9708E-02 9.4305E-02 1.0002E+00
1.0440E-01 9.5769E-02 1.0004E+00

```

1.0880E-01	9.6997E-02	1.0004E+00	1.0692E-02	4.1477E-02	9.5115E-01
1.1292E-01	9.8049E-02	1.0001E+00	1.2105E-02	4.7939E-02	9.6385E-01
1.1681E-01	9.8839E-02	1.0002E+00	1.3652E-02	5.5243E-02	9.7482E-01
1.2049E-01	9.9205E-02	1.0006E+00	1.5381E-02	6.3134E-02	9.8402E-01
1.2391E-01	9.9415E-02	1.0010E+00	1.7260E-02	7.1236E-02	9.9121E-01
1.2711E-01	9.9526E-02	1.0000E+00	1.9339E-02	7.9057E-02	9.9572E-01
1.3007E-01	9.9534E-02	9.9956E-01	2.1600E-02	8.5981E-02	9.9846E-01
1.3279E-01	8.4881E-02	9.9696E-01	2.4061E-02	9.1189E-02	9.9915E-01
1.3529E-01	7.8667E-02	9.9245E-01	2.6738E-02	9.3959E-02	9.9899E-01
1.3758E-01	7.2242E-02	9.8627E-01	2.9632E-02	9.5113E-02	9.9949E-01
1.3966E-01	6.5869E-02	9.7809E-01	3.2723E-02	9.5659E-02	1.0004E+00
1.4154E-01	5.9841E-02	9.6789E-01	3.6034E-02	9.5791E-02	1.0012E+00
1.4325E-01	5.4276E-02	9.5589E-01	3.9542E-02	9.6733E-02	1.0005E+00
1.4478E-01	4.9297E-02	9.4249E-01	4.3250E-02	9.6655E-02	9.9999E-01
1.4618E-01	4.4910E-02	9.2827E-01	4.7141E-02	9.4026E-02	1.2013E+00
1.4743E-01	4.1103E-02	9.1371E-01	5.1182E-02	8.7383E-02	1.0008E+00
1.4854E-01	3.7825E-02	8.9926E-01	5.5372E-02	7.9877E-02	1.0008E+00
1.4954E-01	3.5015E-02	8.8524E-01	5.9679E-02	7.8998E-02	1.0016E+00
1.5042E-01	3.2611E-02	8.7184E-01	6.4069E-02	8.1041E-02	1.0000E+00
1.5122E-01	3.0556E-02	8.5921E-01	6.8509E-02	8.4752E-02	1.0010E+00
1.5193E-01	2.8797E-02	8.4744E-01	7.2949E-02	8.7937E-02	1.0003E+00
1.5257E-01	2.7289E-02	8.3658E-01	7.7389E-02	9.0675E-02	1.0010E+00
1.5313E-01	2.5921E-02	8.2606E-01	8.1778E-02	9.2971E-02	1.0011E+00
1.5363E-01	2.4581E-02	8.1509E-01	8.6085E-02	9.4252E-02	1.0008E+00
1.5406E-01	2.3240E-02	8.0342E-01	9.0275E-02	9.6450E-02	1.0009E+00
1.5446E-01	2.1891E-02	7.9093E-01	9.4316E-02	9.7746E-02	1.0008E+00
1.5481E-01	2.0524E-02	7.7744E-01	9.8207E-02	9.8686E-02	1.0008E+00
1.5511E-01	1.9117E-02	7.6260E-01	1.0192E-01	9.9222E-02	1.0008E+00
1.5539E-01	1.7644E-02	7.4591E-01	1.0542E-01	9.9086E-02	1.0004E+00
1.5563E-01	1.6500E-02	7.2631E-01	1.0873E-01	9.7175E-02	1.0007E+00
1.5584E-01	1.4247E-02	7.0200E-01	1.1183E-01	9.3503E-02	9.9901E-01
1.5602E-01	1.2067E-02	6.6859E-01	1.1472E-01	8.8668E-02	9.9851E-01
1.5619E-01	9.1702E-03	6.1403E-01	1.1740E-01	8.3086E-02	9.9522E-01
1.5634E-01	5.7021E-03	5.0442E-01	1.1986E-01	7.7099E-02	9.9003E-01
1.5642E-01	4.5119E-03	3.7369E-01	1.2212E-01	7.1054E-02	9.8351E-01
FALCON RESULTS (20) X/XREF = 6.51			1.2420E-01	6.5207E-02	9.7492E-01
Y/XREF	PP/PTINF	TT/TTINF	1.2609E-01	5.9645E-02	9.6471E-01
0.0000E+00	4.3856E-03	3.7369E-01	1.2781E-01	5.4495E-02	9.5309E-01
6.6505E-05	4.8164E-03	4.7246E-01	1.2935E-01	4.9818E-02	9.4031E-01
1.9946E-04	6.3653E-03	5.8956E-01	1.3077E-01	4.5647E-02	9.2672E-01
3.4913E-04	7.8176E-03	6.5669E-01	1.3203E-01	4.1571E-02	9.1270E-01
5.3209E-04	9.0366E-03	6.9038E-01	1.3316E-01	3.8758E-02	8.9863E-01
7.3155E-04	1.0097E-02	7.2799E-01	1.3419E-01	3.5963E-02	8.8478E-01
9.6437E-04	1.1060E-02	7.5104E-01	1.3511E-01	3.3533E-02	8.7139E-01
1.2138E-03	1.1974E-02	7.7014E-01	1.3592E-01	3.1421E-02	8.5858E-01
1.4965E-03	1.2872E-02	7.8664E-01	1.3665E-01	2.9582E-02	8.4647E-01
1.8125E-03	1.3777E-02	8.0132E-01	1.3730E-01	2.7978E-02	8.3511E-01
2.1783E-03	1.4707E-02	8.1444E-01	1.3788E-01	2.6575E-02	8.2451E-01
2.5939E-03	1.5673E-02	8.2687E-01	1.3841E-01	2.5293E-02	8.1426E-01
3.0596E-03	1.6691E-02	8.3824E-01	1.3888E-01	2.4034E-02	8.0364E-01
3.5750E-03	1.7760E-02	8.4978E-01	1.3924E-01	2.2760E-02	7.9229E-01
4.1576E-03	1.8956E-02	8.5915E-01	1.3965E-01	2.1467E-02	7.8010E-01
4.8055E-03	2.0423E-02	8.7027E-01	1.3996E-01	2.0147E-02	7.6691E-01
5.5371E-03	2.2293E-02	8.8246E-01	1.4024E-01	1.8781E-02	7.5239E-01
6.3519E-03	2.4660E-02	8.9555E-01	1.4051E-01	1.7347E-02	7.3598E-01
7.2665E-03	2.7644E-02	9.0938E-01	1.4073E-01	1.5772E-02	7.1663E-01
8.2975E-03	3.1369E-02	9.2349E-01	1.4093E-01	1.3583E-02	6.9255E-01
9.4282E-03	3.5954E-02	9.3752E-01	1.4111E-01	1.1899E-02	6.5880E-01

1.4126E-01 8.9362E-03 6.0395E-01  
 1.4139E-01 5.6059E-03 4.9535E-01  
 1.4148E-01 4.5294E-03 3.7369E-01

FALCON RESULTS (2D) X/XREF = 6.65

Y/XREF	PP/PTINF	TT/TTINF
0.0000E+00	4.6001E-03	3.7369E-01
6.6505E-05	5.3864E-03	4.8662E-01
1.9956E-04	7.9071E-03	6.0049E-01
3.4918E-04	1.0161E-02	6.6120E-01
5.1544E-04	1.1923E-02	6.9871E-01
7.1505E-04	1.3373E-02	7.2574E-01
9.3122E-04	1.4647E-02	7.4722E-01
1.1806E-03	1.5821E-02	7.6537E-01
1.4467E-03	1.6941E-02	7.8135E-01
1.7626E-03	1.8035E-02	7.9579E-01
2.0951E-03	1.9123E-02	8.0907E-01
2.4942E-03	2.0216E-02	8.2139E-01
2.9266E-03	2.1329E-02	8.3292E-01
3.4254E-03	2.2455E-02	8.4362E-01
3.9742E-03	2.3692E-02	8.5429E-01
4.5894E-03	2.5169E-02	8.6576E-01
5.2713E-03	2.6943E-02	8.7797E-01
6.0528E-03	2.9077E-02	8.9081E-01
6.9009E-03	3.1650E-02	9.0439E-01
7.8653E-03	3.4745E-02	9.1744E-01
8.9295E-03	3.8452E-02	9.3047E-01
1.0110E-02	4.2870E-02	9.4294E-01
1.1424E-02	4.8058E-02	9.5469E-01
1.2870E-02	5.4038E-02	9.6567E-01
1.4467E-02	6.0809E-02	9.7605E-01
1.6229E-02	6.8200E-02	9.8498E-01
1.8142E-02	7.6354E-02	9.9175E-01
2.0237E-02	8.4470E-02	9.9552E-01
2.2515E-02	9.3275E-02	9.9775E-01
2.4976E-02	1.0225E-01	9.9971E-01
2.7636E-02	1.0966E-01	1.0004E+00
3.0480E-02	1.1530E-01	1.0009E+00
3.3527E-02	1.1896E-01	9.9952E-01
3.6732E-02	1.2092E-01	9.9965E-01
4.0124E-02	1.2230E-01	9.9969E-01
4.3683E-02	1.2291E-01	1.0000E+00
4.7391E-02	1.2311E-01	1.0002E+00
5.1215E-02	1.2284E-01	9.9981E-01
5.5140E-02	1.2175E-01	1.0008E+00
5.9131E-02	1.1871E-01	1.0003E+00
6.3188E-02	1.1595E-01	1.0016E+00
6.7245E-02	1.1122E-01	1.0027E+00
7.1286E-02	1.0380E-01	1.0001E+00
7.5277E-02	9.5506E-02	9.9985E-01
7.9201E-02	8.9124E-02	9.9981E-01
8.3076E-02	8.6593E-02	1.0000E+00
8.6734E-02	8.6122E-02	1.0000E+00
9.0292E-02	8.5183E-02	1.0012E+00
9.3684E-02	8.4790E-02	1.0019E+00
9.6894E-02	8.2267E-02	9.9921E-01
9.9937E-02	7.9275E-02	9.9779E-01
1.0278E-01	7.5435E-02	9.9432E-01
1.0544E-01	7.1102E-02	9.9036E-01

1.0790E-01 6.6498E-02 9.8477E-01  
 1.1018E-01 6.1906E-02 9.7713E-01  
 1.1227E-01 5.7420E-02 9.6910E-01  
 1.1419E-01 5.3133E-02 9.5774E-01  
 1.1595E-01 4.9102E-02 9.4615E-01  
 1.1755E-01 4.5379E-02 9.3354E-01  
 1.1899E-01 4.1984E-02 9.2023E-01  
 1.2031E-01 3.8919E-02 9.0652E-01  
 1.2149E-01 3.6172E-02 8.9267E-01  
 1.2255E-01 3.3719E-02 8.7891E-01  
 1.2352E-01 3.1531E-02 8.6545E-01  
 1.2436E-01 2.9582E-02 8.5241E-01  
 1.2515E-01 2.7847E-02 8.3988E-01  
 1.2583E-01 2.6303E-02 8.2795E-01  
 1.2644E-01 2.4927E-02 8.1666E-01  
 1.2701E-01 2.3701E-02 8.0604E-01  
 1.2749E-01 2.2584E-02 7.9591E-01  
 1.2792E-01 2.1495E-02 7.8556E-01  
 1.2832E-01 2.0380E-02 7.7445E-01  
 1.2867E-01 1.9239E-02 7.6250E-01  
 1.2897E-01 1.8065E-02 7.4953E-01  
 1.2925E-01 1.6838E-02 7.3517E-01  
 1.2949E-01 1.5530E-02 7.1804E-01  
 1.2970E-01 1.4088E-02 6.9942E-01  
 1.2990E-01 1.2423E-02 6.7480E-01  
 1.3007E-01 1.0383E-02 6.4042E-01  
 1.3022E-01 7.7105E-03 5.8398E-01  
 1.3035E-01 4.8424E-03 4.7744E-01  
 1.3042E-01 4.0485E-03 3.7369E-01

FALCON RESULTS (2D) X/XREF = 6.79

Y/XREF	PP/PTINF	TT/TTINF
0.0000E+00	4.6399E-03	3.7369E-01
6.6554E-05	5.5511E-03	4.9252E-01
2.1617E-04	8.3205E-03	6.0443E-01
3.6583E-04	1.0733E-02	6.6254E-01
5.3209E-04	1.2594E-02	6.9836E-01
7.1352E-04	1.4120E-02	7.2418E-01
9.6442E-04	1.5462E-02	7.4177E-01
1.2138E-03	1.6598E-02	7.6221E-01
1.4965E-03	1.7874E-02	7.7759E-01
1.7959E-03	1.9021E-02	7.9154E-01
2.1617E-03	2.0155E-02	8.0437E-01
2.5607E-03	2.1287E-02	8.1610E-01
3.0097E-03	2.2427E-02	8.2748E-01
3.5085E-03	2.3578E-02	8.3794E-01
4.0573E-03	2.4836E-02	8.4849E-01
4.6692E-03	2.6323E-02	8.5989E-01
5.3475E-03	2.8086E-02	8.7210E-01
6.1691E-03	3.0180E-02	8.8501E-01
7.0534E-03	3.2611E-02	8.9847E-01
8.0149E-03	3.5623E-02	9.1221E-01
9.0956E-03	3.9106E-02	9.2586E-01
1.0293E-02	4.3178E-02	9.3919E-01
1.1607E-02	4.7869E-02	9.5189E-01
1.3070E-02	5.3183E-02	9.6328E-01
1.4682E-02	5.9098E-02	9.7301E-01
1.6445E-02	6.5525E-02	9.8111E-01
1.8358E-02	7.2287E-02	9.8779E-01

2.0470E-02	7.9058E-02	9.9296E-01	0.0000E+00	1.0000E+00
2.2740E-02	8.5655E-02	9.9681E-01	6.8827E-04	5.4476E+00
2.5209E-02	9.1618E-02	9.9943E-01	2.1533E-03	5.0597E+00
2.7853E-02	9.6641E-02	1.0012E+00	4.0054E-03	4.3464E+00
3.0696E-02	9.9936E-02	1.0018E+00	6.1641E-03	4.0463E+00
3.3722E-02	1.0158E-01	1.0010E+00	8.7435E-03	3.8650E+00
3.6915E-02	1.0222E-01	1.0002E+00	1.1825E-02	3.7032E+00
4.0291E-02	1.0273E-01	9.9982E-01	1.5505E-02	3.5913E+00
4.3816E-02	1.0391E-01	1.0000E+00	1.9899E-02	3.5082E+00
4.7491E-02	1.0641E-01	9.9996E-01	2.5145E-02	3.4424E+00
5.1299E-02	1.1004E-01	1.0001E+00	3.1401E-02	3.3797E+00
5.5190E-02	1.1391E-01	1.0006E+00	3.8862E-02	3.3270E+00
5.9147E-02	1.1704E-01	9.9980E-01	4.7753E-02	3.2886E+00
6.3155E-02	1.1880E-01	9.9921E-01	5.8339E-02	3.2560E+00
6.7179E-02	1.2001E-01	9.9934E-01	7.0933E-02	3.2210E+00
7.1176E-02	1.2046E-01	9.9931E-01	8.5899E-02	3.1957E+00
7.5144E-02	1.2076E-01	9.9923E-01	1.0366E-01	3.1736E+00
7.9035E-02	1.2048E-01	9.9905E-01	1.2471E-01	3.1502E+00
8.2843E-02	1.1962E-01	9.9972E-01	1.4962E-01	3.1326E+00
8.6518E-02	1.1745E-01	1.0009E+00	1.7902E-01	3.1159E+00
9.0043E-02	1.1288E-01	1.0021E+00	2.1364E-01	3.1005E+00
9.3418E-02	1.0364E-01	1.0037E+00	2.5428E-01	3.0880E+00
9.6628E-02	9.1784E-02	9.9203E-01	3.0186E-01	3.0749E+00
9.9637E-02	8.0031E-02	9.8822E-01	3.5728E-01	3.0651E+00
1.0248E-01	6.9515E-02	9.8683E-01	4.2160E-01	3.0544E+00
1.0512E-01	6.1900E-02	9.7874E-01	4.9578E-01	3.0465E+00
1.0760E-01	5.5352E-02	9.6992E-01	5.8085E-01	3.0382E+00
1.0988E-01	5.0346E-02	9.5991E-01	6.7767E-01	3.0318E+00
1.1198E-01	4.6019E-02	9.4874E-01	7.8702E-01	3.0252E+00
1.1390E-01	4.2311E-02	9.3607E-01	9.0937E-01	3.0202E+00
1.1565E-01	3.8928E-02	9.2235E-01	1.0449E+00	3.0150E+00
1.1726E-01	3.6060E-02	9.0884E-01	1.1933E+00	3.0112E+00
1.1873E-01	3.3496E-02	8.9520E-01	1.3538E+00	3.0072E+00
1.2004E-01	3.1219E-02	8.8157E-01	1.5250E+00	3.0043E+00
1.2124E-01	2.9185E-02	8.6815E-01	1.7052E+00	3.0015E+00
1.2232E-01	2.7364E-02	8.5503E-01	1.8970E+00	2.9992E+00
1.2328E-01	2.5720E-02	8.4231E-01	2.0825E+00	2.9893E+00
1.2416E-01	2.4236E-02	8.2996E-01	2.2739E+00	2.9734E+00
1.2495E-01	2.2895E-02	8.1798E-01	2.4632E+00	2.9781E+00
1.2564E-01	2.1680E-02	8.0646E-01	2.6474E+00	2.9966E+00
1.2628E-01	2.0576E-02	7.9547E-01	2.8240E+00	3.0282E+00
1.2682E-01	1.9574E-02	7.8504E-01	2.9100E+00	3.0599E+00
1.2732E-01	1.8667E-02	7.7518E-01	2.9100E+00	3.0282E+00
1.2777E-01	1.7790E-02	7.6541E-01	2.9788E+00	3.0599E+00
1.2817E-01	1.6894E-02	7.5501E-01	3.1207E+00	3.1480E+00
1.2854E-01	1.5960E-02	7.4371E-01	3.2691E+00	3.1693E+00
1.2885E-01	1.4982E-02	7.3132E-01	3.4205E+00	3.1737E+00
1.2912E-01	1.3945E-02	7.1746E-01	3.5705E+00	3.1743E+00
1.2937E-01	1.2822E-02	7.0145E-01	3.7166E+00	3.1733E+00
1.2960E-01	1.1565E-02	6.8293E-01	3.8540E+00	3.1725E+00
1.2980E-01	1.0101E-02	6.5711E-01	3.9805E+00	3.1724E+00
1.2997E-01	8.2995E-03	6.2156E-01	4.0944E+00	3.1734E+00
1.3013E-01	6.0193E-03	5.6322E-01	4.1950E+00	3.1747E+00
1.3027E-01	3.8354E-03	4.6015E-01	4.2825E+00	3.1757E+00
1.3033E-01	3.3283E-03	3.7369E-01	4.3570E+00	3.1768E+00
			4.4198E+00	3.1775E+00
			4.4724E+00	3.1784E+00
			4.5156E+00	3.1794E+00

FALCON RESULTS (20) RAMP SURFACE PRESSURE  
X/XREF P/PZERO

4.5510E+00 3.1838E+00  
 4.5800E+00 3.1823E+00  
 4.6034E+00 3.1837E+00  
 4.6222E+00 3.1848E+00  
 4.6375E+00 3.1861E+00  
 4.6496E+00 3.1871E+00  
 4.6593E+00 3.1878E+00  
 4.6671E+00 3.1887E+00  
 4.6734E+00 3.1890E+00  
 4.6782E+00 3.1897E+00  
 4.6822E+00 3.1900E+00  
 4.6854E+00 3.1910E+00  
 4.6879E+00 3.1903E+00  
 4.6899E+00 3.1915E+00  
 4.6914E+00 3.1907E+00  
 4.6927E+00 3.1914E+00  
 4.6937E+00 3.1920E+00  
 4.6944E+00 3.1927E+00  
 4.6950E+00 3.1909E+00  
 4.6955E+00 3.1926E+00  
 4.6959E+00 3.1931E+00  
 4.6962E+00 3.1938E+00  
 4.6965E+00 3.1938E+00  
 4.6967E+00 3.1950E+00  
 4.6969E+00 3.1947E+00  
 4.6969E+00 3.1948E+00  
 4.6969E+00 3.1947E+00  
 4.6970E+00 3.1948E+00  
 4.6972E+00 3.1954E+00  
 4.6974E+00 3.1956E+00  
 4.6975E+00 3.1957E+00  
 4.6979E+00 3.1971E+00  
 4.6982E+00 3.1974E+00  
 4.6987E+00 3.1997E+00  
 4.6994E+00 3.1999E+00  
 4.7000E+00 3.2018E+00  
 4.7008E+00 3.2025E+00  
 4.7020E+00 3.2049E+00  
 4.7033E+00 3.2060E+00  
 4.7050E+00 3.2078E+00  
 4.7070E+00 3.2093E+00  
 4.7093E+00 3.2111E+00  
 4.7120E+00 3.2129E+00  
 4.7153E+00 3.2151E+00  
 4.7199E+00 3.2170E+00  
 4.7243E+00 3.2181E+00  
 4.7280E+00 3.2195E+00  
 4.7331E+00 3.2198E+00  
 4.7384E+00 3.2177E+00  
 4.7441E+00 3.2195E+00  
 4.7497E+00 3.2188E+00  
 4.7554E+00 3.2176E+00  
 4.7609E+00 3.2169E+00  
 4.7659E+00 3.2152E+00  
 4.7705E+00 3.2143E+00  
 4.7747E+00 3.2127E+00  
 4.7783E+00 3.2127E+00  
 4.7802E+00 3.2127E+00

4.7802E+00 3.2127E+00  
 4.7837E+00 3.2127E+00  
 4.7908E+00 3.2128E+00  
 4.7988E+00 3.2126E+00  
 4.8074E+00 3.2123E+00  
 4.8171E+00 3.2120E+00  
 4.8277E+00 3.2117E+00  
 4.8392E+00 3.2110E+00  
 4.8518E+00 3.2103E+00  
 4.8655E+00 3.2098E+00  
 4.8804E+00 3.2089E+00  
 4.8967E+00 3.2079E+00  
 4.9144E+00 3.2067E+00  
 4.9333E+00 3.2059E+00  
 4.9538E+00 3.2051E+00  
 4.9757E+00 3.2045E+00  
 4.9993E+00 3.2040E+00  
 5.0244E+00 3.2034E+00  
 5.0512E+00 3.2031E+00  
 5.0793E+00 3.2030E+00  
 5.1091E+00 3.2026E+00  
 5.1403E+00 3.2024E+00  
 5.1729E+00 3.2024E+00  
 5.2065E+00 3.2022E+00  
 5.2419E+00 3.2026E+00  
 5.2780E+00 3.2034E+00  
 5.3149E+00 3.2033E+00  
 5.3523E+00 3.2030E+00  
 5.3903E+00 3.2032E+00  
 5.4285E+00 3.2031E+00  
 5.4666E+00 3.2026E+00  
 5.5047E+00 3.2026E+00  
 5.5421E+00 3.2026E+00  
 5.5799E+00 3.2020E+00  
 5.6151E+00 3.2018E+00  
 5.6502E+00 3.2018E+00  
 5.6841E+00 3.2015E+00  
 5.7168E+00 3.2007E+00  
 5.7481E+00 3.2004E+00  
 5.7795E+00 3.2002E+00  
 5.8108E+00 3.1998E+00  
 5.8419E+00 3.2028E+00  
 5.8719E+00 3.1999E+00  
 5.9037E+00 3.2028E+00  
 5.9313E+00 3.2078E+00  
 5.9591E+00 3.2100E+00  
 5.9867E+00 3.2090E+00  
 6.0143E+00 3.2073E+00  
 6.0419E+00 3.1984E+00  
 6.0697E+00 3.1605E+00  
 6.0972E+00 3.0665E+00  
 6.1248E+00 2.9524E+00  
 6.1523E+00 2.8471E+00  
 6.1798E+00 2.7376E+00  
 6.2073E+00 2.6532E+00  
 6.2348E+00 2.5883E+00  
 6.2623E+00 2.4757E+00  
 6.2898E+00 2.3113E+00

6.2495E+00	1.0515E+01
6.2774E+00	1.2564E+01
6.3052E+00	1.4777E+01
6.3331E+00	1.5938E+01
6.3608E+00	1.6519E+01
6.3742E+00	1.8042E+01
6.3742E+00	1.6519E+01
6.3881E+00	1.8042E+01
6.4162E+00	1.9679E+01
6.4442E+00	1.1504E+01
6.4721E+00	2.3542E+01
6.5000E+00	2.5872E+01
6.5280E+00	2.8038E+01
6.5559E+00	3.0696E+01
6.5837E+00	2.9499E+01
6.6115E+00	2.7534E+01
6.6391E+00	2.7056E+01
6.6667E+00	2.7138E+01
6.6943E+00	2.7304E+01
6.7219E+00	2.7327E+01
6.7495E+00	2.7294E+01
6.7771E+00	2.7373E+01
6.8045E+00	2.7409E+01
6.8321E+00	2.7448E+01
6.8597E+00	2.7499E+01
6.8872E+00	2.7549E+01
6.9148E+00	2.7586E+01
6.9285E+00	2.7416E+01
6.9286E+00	2.7586E+01
6.9412E+00	2.7416E+01
6.9666E+00	2.7886E+01
6.9919E+00	2.6269E+01
7.0174E+00	2.5602E+01
7.0420E+00	2.4732E+01
7.0679E+00	2.3676E+01
7.0932E+00	2.2462E+01
7.1185E+00	2.1155E+01
7.1436E+00	1.9747E+01
7.1638E+00	1.8415E+01
7.1939E+00	1.7298E+01
7.2191E+00	1.6334E+01
7.2440E+00	1.5551E+01
7.2691E+00	1.4936E+01
7.2940E+00	1.4490E+01
7.3190E+00	1.4195E+01
7.3439E+00	1.3994E+01
7.3687E+00	1.3888E+01
7.3935E+00	1.4017E+01
7.4183E+00	1.4134E+01
7.4307E+00	1.4134E+01

## FALCON RESULTS (3D) X/REF = 5.67

X/XREF	PT/PTREF	TT/TTREF
0.0000E+00	5.0866E-04	3.7369E-01
1.4966E-04	5.3573E-04	4.1028E-01
4.9887E-04	6.8918E-04	4.7893E-01
9.8107E-04	1.0805E-03	5.3219E-01
1.6130E-03	1.6323E-03	5.8641E-01
2.4610E-03	2.1463E-03	6.2543E-01
3.5751E-03	2.6247E-03	6.5517E-01
5.0117E-03	3.0678E-03	6.7863E-01
7.0338E-03	3.5590E-03	7.0184E-01
9.6278E-03	4.1909E-03	7.2773E-01
1.3020E-02	5.0443E-03	7.5700E-01
1.7443E-02	6.1824E-03	7.8961E-01
2.3147E-02	7.6918E-03	8.2523E-01
3.0447E-02	9.6750E-03	8.6344E-01
3.9642E-02	1.2250E-02	9.0270E-01
5.1016E-02	1.5551E-02	9.4079E-01
6.4813E-02	1.9513E-02	9.7347E-01
8.1113E-02	2.2341E-02	9.8905E-01
9.9770E-02	2.3539E-02	9.9657E-01
1.2039E-01	2.4377E-02	9.9923E-01
1.4234E-01	2.7815E-02	9.9551E-01
1.6475E-01	3.8527E-02	9.9875E-01
1.8670E-01	4.7153E-02	1.0010E+00
2.0734E-01	5.2261E-02	1.0013E+00
2.2600E-01	5.6303E-02	1.0012E+00
2.4229E-01	5.9691E-02	1.0013E+00
2.5608E-01	6.2410E-02	1.0013E+00
2.6747E-01	6.4076E-02	1.0008E+00
2.7666E-01	6.3910E-02	1.0003E+00
2.8396E-01	6.0669E-02	1.0000E+00
2.8967E-01	5.3817E-02	1.0015E+00
2.9409E-01	4.4640E-02	1.0012E+00
2.9748E-01	3.6281E-02	9.9150E-01
3.0008E-01	2.8644E-02	9.7467E-01
3.0204E-01	2.4358E-02	9.5114E-01
3.0353E-01	2.0234E-02	9.2240E-01
3.0465E-01	1.6961E-02	8.9061E-01
3.0550E-01	1.4346E-02	8.5737E-01
3.0613E-01	1.1897E-02	8.2123E-01
3.0661E-01	8.7944E-03	7.8981E-01
3.069E-01	4.6159E-03	6.7473E-01
3.0713E-01	2.4867E-03	3.7369E-01

## FALCON RESULTS (3D) COWL SURFACE PRESSURE

X/REF	P/PSRO
4.4358E+00	0.3907E+01
4.4360E+00	7.8677E+01
4.4361E+00	5.8447E+01
4.4363E+00	4.7583E+01
4.4366E+00	3.6798E+01
4.4373E+00	2.2035E+01
4.4385E+00	1.4192E+01
4.4404E+00	1.4706E+01
4.4429E+00	1.3703E+01
4.4459E+00	1.2969E+01
4.4496E+00	1.2213E+01

4.4542E+00	1.1607E+01
4.4597E+00	1.0979E+01
4.4666E+00	1.0206E+01
4.4747E+00	9.3055E+00
4.4845E+00	8.4606E+00
4.4962E+00	7.9888E+00
4.5096E+00	7.7535E+00
4.5253E+00	7.4204E+00
4.5429E+00	7.2893E+00
4.5623E+00	7.2432E+00
4.5838E+00	7.1589E+00
4.6064E+00	7.1201E+00
4.6298E+00	7.0957E+00
4.6536E+00	7.0735E+00
4.6771E+00	7.0584E+00
4.6995E+00	7.0618E+00
4.7206E+00	7.0904E+00
4.7401E+00	7.1233E+00
4.7576E+00	7.1479E+00
4.7730E+00	7.1529E+00
4.7837E+00	7.1426E+00
4.7908E+00	7.1440E+00
4.7988E+00	7.14650E+00
4.8076E+00	7.1456E+00
4.8172E+00	7.1445E+00
4.8277E+00	7.15784E+00
4.8394E+00	7.1652E+00
4.8518E+00	7.1687E+00
4.8656E+00	7.1707E+00
4.8806E+00	7.1763E+00
4.8969E+00	8.0360E+00
4.9145E+00	8.2247E+00
4.9336E+00	8.2466E+00
4.9541E+00	8.3114E+00
4.9762E+00	8.3759E+00
4.9997E+00	8.8332E+00
5.0249E+00	9.0786E+00
5.0515E+00	9.2323E+00
5.0800E+00	9.3367E+00
5.1097E+00	9.4107E+00
5.1410E+00	9.4693E+00
5.1736E+00	1.0786E+01
5.2075E+00	1.0510E+01
5.2425E+00	1.0657E+01
5.2787E+00	1.0756E+01
5.3156E+00	1.1320E+01
5.3532E+00	1.1807E+01
5.3911E+00	1.1964E+01
5.4293E+00	1.2376E+01
5.4674E+00	1.3034E+01
5.5053E+00	1.3244E+01
5.5429E+00	1.3556E+01
5.5797E+00	1.4393E+01
5.6157E+00	1.4673E+01
5.6507E+00	1.4801E+01
5.6846E+00	1.4939E+01
5.7172E+00	1.5972E+01
5.7483E+00	1.6251E+01



5.7780E+00 1.6372E+01  
 5.8063E+00 1.6418E+01  
 5.8199E+00 1.6405E+01  
 5.8337E+00 1.6405E+01  
 5.8615E+00 1.6866E+01  
 5.8891E+00 1.7469E+01  
 5.9167E+00 1.8018E+01  
 5.9443E+00 1.8425E+01  
 5.9719E+00 1.8619E+01  
 5.9995E+00 1.8728E+01  
 6.0270E+00 1.8863E+01  
 6.0546E+00 1.9057E+01  
 6.0822E+00 1.9344E+01  
 6.1096E+00 1.9725E+01  
 6.1372E+00 2.0179E+01  
 6.1646E+00 2.0683E+01  
 6.1921E+00 2.1297E+01  
 6.2195E+00 2.1936E+01  
 6.2470E+00 2.2453E+01  
 6.2744E+00 2.2926E+01  
 6.3018E+00 2.3354E+01  
 6.3291E+00 2.3540E+01  
 6.3585E+00 2.3518E+01  
 6.3881E+00 2.3511E+01  
 6.4157E+00 2.3481E+01  
 6.4435E+00 2.3336E+01  
 6.4711E+00 2.3162E+01  
 6.4989E+00 2.3010E+01  
 6.5265E+00 2.2785E+01  
 6.5543E+00 2.2499E+01  
 6.5820E+00 2.2107E+01  
 6.6096E+00 2.1581E+01  
 6.6374E+00 2.0944E+01  
 6.6650E+00 2.0223E+01  
 6.6928E+00 1.9401E+01  
 6.7205E+00 1.8641E+01  
 6.7481E+00 1.7835E+01  
 6.7759E+00 1.6881E+01  
 6.8035E+00 1.6427E+01  
 6.8311E+00 1.5631E+01  
 6.8589E+00 1.3689E+01  
 6.8867E+00 1.1903E+01  
 6.9146E+00 1.1554E+01  
 6.9410E+00 1.2325E+01  
 6.9661E+00 1.3399E+01  
 6.9912E+00 1.5022E+01  
 7.0164E+00 1.6392E+01  
 7.0415E+00 1.7229E+01  
 7.0666E+00 1.7707E+01  
 7.0917E+00 1.7996E+01  
 7.1168E+00 1.8109E+01  
 7.1417E+00 1.8193E+01  
 7.1658E+00 1.8278E+01  
 7.1919E+00 1.8413E+01  
 7.2171E+00 1.8561E+01  
 7.2422E+00 1.8663E+01  
 7.2673E+00 1.8719E+01  
 7.2924E+00 1.8733E+01

7.3175E+00 1.8663E+01  
 7.3426E+00 1.8553E+01  
 7.3677E+00 1.8219E+01  
 7.3928E+00 1.7992E+01  
 7.4179E+00 1.7283E+01  
 7.4304E+00 1.7283E+01  
 FALCON RESULTS (3D) X/XREF = 5.78  
 X/XREF PT/PTREF TT/TTREF  
 0.0000E+00 5.0688E-04 3.7369E-01  
 1.4977E-04 5.2989E-04 4.0821E-01  
 4.9889E-04 6.7262E-04 4.6647E-01  
 9.6442E-04 1.0445E-03 5.2583E-01  
 1.5797E-03 1.5684E-03 5.7989E-01  
 2.3945E-03 2.0686E-03 6.1927E-01  
 3.4919E-03 2.5338E-03 6.4940E-01  
 4.9220E-03 2.9617E-03 6.7316E-01  
 6.8176E-03 3.4317E-03 6.9659E-01  
 9.3119E-03 4.0319E-03 7.2256E-01  
 1.2554E-02 4.8291E-03 7.5165E-01  
 1.6761E-02 5.8909E-03 7.8369E-01  
 2.2182E-02 7.2918E-03 8.1926E-01  
 2.9083E-02 9.1168E-03 8.5492E-01  
 3.7730E-02 1.1487E-02 8.9302E-01  
 4.8405E-02 1.4541E-02 9.3093E-01  
 6.1276E-02 1.8315E-02 9.6603E-01  
 7.6424E-02 2.1662E-02 9.8487E-01  
 9.3701E-02 2.3354E-02 9.9453E-01  
 1.1276E-01 2.5762E-02 9.9617E-01  
 1.3301E-01 3.4198E-02 9.9544E-01  
 1.5366E-01 4.5490E-02 1.0004E+00  
 1.7382E-01 5.1745E-02 1.0012E+00  
 1.9297E-01 5.6284E-02 1.0011E+00  
 2.1025E-01 6.0191E-02 1.0014E+00  
 2.2540E-01 6.3386E-02 1.0016E+00  
 2.3829E-01 6.5633E-02 1.0013E+00  
 2.4894E-01 6.6710E-02 1.0008E+00  
 2.5761E-01 6.6362E-02 1.0005E+00  
 2.6449E-01 6.3647E-02 1.0003E+00  
 2.6991E-01 5.6868E-02 1.0018E+00  
 2.7414E-01 4.7492E-02 1.0010E+00  
 2.7738E-01 3.9824E-02 9.9212E-01  
 2.7987E-01 3.1821E-02 9.7567E-01  
 2.8177E-01 2.6258E-02 9.5215E-01  
 2.8320E-01 2.1877E-02 9.2342E-01  
 2.8428E-01 1.9420E-02 8.9188E-01  
 2.8511E-01 1.5609E-02 8.5921E-01  
 2.8573E-01 1.3000E-02 8.2411E-01  
 2.8619E-01 9.7274E-03 7.7488E-01  
 2.8654E-01 5.2173E-03 6.8387E-01  
 2.8669E-01 2.7222E-03 3.7369E-01  
 FALCON RESULTS (3D) X/XREF = 5.94  
 X/XREF PT/PTREF TT/TTREF  
 0.0000E+00 5.0673E-04 3.7369E-01  
 1.4971E-04 5.2675E-04 4.0475E-01  
 4.9889E-04 6.5130E-04 4.5845E-01  
 9.4787E-04 9.7547E-04 5.1383E-01  
 1.5298E-03 1.4559E-03 5.6649E-01  
 2.3113E-03 1.9231E-03 6.0573E-01

3.3423E-03	2.3576E-03	6.3607E-01
4.6726E-03	2.7537E-03	6.6004E-01
6.4187E-03	3.1848E-03	6.8370E-01
8.6967E-03	3.7287E-03	7.0985E-01
1.1640E-02	4.4422E-03	7.3897E-01
1.5431E-02	5.3799E-03	7.7059E-01
2.0270E-02	6.6022E-03	8.0401E-01
2.6356E-02	8.1786E-03	8.3869E-01
3.3939E-02	1.0220E-02	8.7458E-01
4.3217E-02	1.2868E-02	9.1123E-01
5.4325E-02	1.6221E-02	9.4652E-01
6.7312E-02	2.0500E-02	9.7464E-01
8.2045E-02	2.7489E-02	9.8447E-01
9.8241E-02	4.0555E-02	9.9358E-01
1.1538E-01	5.1061E-02	9.9988E-01
1.3288E-01	5.6931E-02	1.0009E+00
1.5002E-01	6.1201E-02	1.0010E+00
1.6622E-01	6.4643E-02	1.0011E+00
1.8095E-01	6.7470E-02	1.0014E+00
1.9394E-01	6.9488E-02	1.0013E+00
2.0506E-01	7.076 E-02	1.0009E+00
2.1432E-01	7.1131E-02	1.0004E+00
2.2191E-01	6.9455E-02	1.0002E+00
2.2801E-01	6.5932E-02	1.0006E+00
2.3283E-01	5.9188E-02	1.0035E+00
2.3662E-01	4.9555E-02	1.0014E+00
2.3957E-01	4.1719E-02	9.9253E-01
2.4184E-01	3.5128E-02	9.7853E-01
2.4359E-01	2.9309E-02	9.5669E-01
2.4494E-01	2.4409E-02	9.2770E-01
2.4595E-01	2.0483E-02	8.9619E-01
2.4673E-01	1.7726E-02	8.6875E-01
2.4733E-01	1.5160E-02	8.3813E-01
2.4778E-01	1.1322E-02	7.8988E-01
2.4811E-01	6.2424E-03	7.0305E-01
2.4826E-01	3.0244E-03	3.7369E-01

FALCON RESULTS (3D) X/XREF = 6.09

X/XREF	PT/PTREF	TT/TTREF
0.0000E+00	4.5741E-04	3.7369E-01
1.4961E-04	4.7181E-04	3.9887E-01
4.8218E-04	5.6481E-04	4.4414E-01
9.1457E-04	8.1279E-04	4.9395E-01
1.4799E-03	1.2214E-03	5.4486E-01
2.2282E-03	1.6389E-03	5.8443E-01
3.1761E-03	2.0284E-03	6.1545E-01
4.4231E-03	2.3788E-03	6.3998E-01
6.0361E-03	2.7532E-03	6.6410E-01
8.1313E-03	3.2128E-03	6.9030E-01
1.0792E-02	3.8024E-03	7.1884E-01
1.4201E-02	4.5726E-03	7.4930E-01
1.8491E-02	5.6009E-03	7.8130E-01
2.3862E-02	7.0124E-03	8.1552E-01
3.0497E-02	9.0711E-03	8.5296E-01
3.8545E-02	1.2501E-02	8.9053E-01
4.8106E-02	1.9500E-02	9.3059E-01
5.9214E-02	3.3635E-02	9.6880E-01
7.1768E-02	4.7269E-02	9.8820E-01
8.5487E-02	5.5809E-02	9.9741E-01

1.0000E-01	6.1570E-02	1.0007E+00
1.1477E-01	6.5497E-02	1.0010E+00
1.2929E-01	6.8356E-02	1.0010E+00
1.4300E-01	7.0757E-02	1.0011E+00
1.5556E-01	7.3021E-02	1.0012E+00
1.6667E-01	7.5292E-02	1.0013E+00
1.7624E-01	7.7030E-02	1.0010E+00
1.8429E-01	7.7059E-02	1.0002E+00
1.9093E-01	7.4166E-02	1.0000E+00
1.9630E-01	6.8177E-02	1.0022E+00
2.0059E-01	5.9169E-02	1.0059E+00
2.0400E-01	5.0295E-02	1.0015E+00
2.0666E-01	4.2107E-02	9.9029E-01
2.0874E-01	3.5165E-02	9.7160E-01
2.1035E-01	3.0111E-02	9.5197E-01
2.1160E-01	2.5903E-02	9.2935E-01
2.1256E-01	2.1942E-02	9.0065E-01
2.1329E-01	1.8877E-02	8.7178E-01
2.1387E-01	1.5902E-02	8.3790E-01
2.1431E-01	1.2118E-02	7.9170E-01
2.1464E-01	6.7231E-03	7.0718E-01
2.1477E-01	3.2796E-03	3.7369E-01

FALCON RESULTS (3D) X/XREF = 6.23

X/XREF	PT/PTREF	TT/TTREF
0.0000E+00	1.2709E-03	3.7369E-01
1.4961E-04	1.3688E-03	4.3928E-01
4.8218E-04	1.7193E-03	5.1272E-01
8.9791E-04	2.1470E-03	5.6157E-01
1.4467E-03	2.5826E-03	5.9458E-01
2.1451E-03	3.0331E-03	6.1911E-01
3.0596E-03	3.5188E-03	6.3997E-01
4.2236E-03	4.0567E-03	6.5959E-01
5.7202E-03	4.7883E-03	6.8301E-01
7.6158E-03	5.9710E-03	7.1516E-01
1.0044E-02	7.8049E-03	7.5517E-01
1.3087E-02	1.0337E-02	7.9659E-01
1.6894E-02	1.3542E-02	8.3647E-01
2.1600E-02	1.7343E-02	8.7821E-01
2.7327E-02	2.2842E-02	9.2242E-01
3.4221E-02	3.1411E-02	9.5504E-01
4.2353E-02	4.1135E-02	9.7559E-01
5.1698E-02	5.0416E-02	9.8830E-01
6.2174E-02	5.8138E-02	9.9545E-01
7.3581E-02	6.3906E-02	9.9969E-01
8.5586E-02	6.8482E-02	1.0012E+00
9.8780E-02	7.2360E-02	1.0009E+00
1.0991E-01	7.5579E-02	1.0010E+00
1.2122E-01	7.7947E-02	1.0012E+00
1.3176E-01	7.9838E-02	1.0013E+00
1.4106E-01	8.1373E-02	1.0012E+00
1.4919E-01	8.2401E-02	1.0009E+00
1.5607E-01	8.2082E-02	1.0000E+00
1.6183E-01	7.8691E-02	9.9980E-01
1.6653E-01	7.0456E-02	1.0049E+00
1.7032E-01	6.0858E-02	1.0051E+00
1.7337E-01	5.2269E-02	1.0001E+00
1.7578E-01	4.4909E-02	9.9105E-01
1.7769E-01	3.8314E-02	9.7459E-01

1.7917E-01	3.2590E-02	9.5178E-01
1.8034E-01	2.7629E-02	9.2297E-01
1.8123E-01	2.3630E-02	8.9209E-01
1.8195E-01	2.0491E-02	8.6256E-01
1.8250E-01	1.7399E-02	8.2849E-01
1.8291E-01	1.3378E-02	7.8311E-01
1.8324E-01	7.7011E-03	7.0359E-01
1.8338E-01	3.6939E-03	3.7369E-01

FALCON RESULTS (3D) X/XREF = 6.37

X/XREF	PT/PTREF	TT/TTREF
0.0000E+00	2.5455E-03	3.7369E-01
1.4976E-04	4.3695E-03	6.1316E-01
4.8228E-04	6.9687E-03	6.9920E-01
9.1461E-04	8.9796E-03	7.3669E-01
1.4334E-03	1.0478E-02	7.5652E-01
2.1618E-03	1.1716E-02	7.6716E-01
3.0430E-03	1.2633E-02	7.7370E-01
4.1739E-03	1.3961E-02	7.7978E-01
5.6039E-03	1.5185E-02	7.8849E-01
7.3997E-03	1.6970E-02	8.0321E-01
9.6612E-03	2.0230E-02	8.2956E-01
1.2455E-02	2.5884E-02	8.6803E-01
1.5897E-02	3.4652E-02	9.1129E-01
2.0104E-02	4.6240E-02	9.4552E-01
2.5159E-02	5.6875E-02	9.7106E-01
3.1145E-02	6.1901E-02	9.8486E-01
3.8096E-02	5.8926E-02	9.9016E-01
4.5994E-02	5.8174E-02	9.9475E-01
5.4757E-02	6.1734E-02	9.9944E-01
6.4219E-02	6.6850E-02	1.0002E+00
7.4129E-02	7.2330E-02	1.0003E+00
8.4193E-02	7.6758E-02	1.0008E+00
9.4100E-02	8.0597E-02	1.0010E+00
1.0356E-01	8.3954E-02	1.0011E+00
1.1232E-01	8.6785E-02	1.0009E+00
1.2022E-01	8.8909E-02	1.0006E+00
1.2719E-01	8.9949E-02	1.0005E+00
1.3318E-01	8.8874E-02	9.9975E-01
1.3825E-01	8.2733E-02	1.0005E+00
1.4242E-01	7.3913E-02	1.0052E+00
1.4588E-01	6.5553E-02	1.0064E+00
1.4867E-01	5.5969E-02	1.0055E+00
1.5092E-01	4.7868E-02	9.9436E-01
1.5272E-01	4.0732E-02	9.7119E-01
1.5415E-01	3.4531E-02	9.3775E-01
1.5528E-01	2.9642E-02	9.0468E-01
1.5616E-01	2.5658E-02	8.7259E-01
1.5686E-01	2.2309E-02	8.4216E-01
1.5740E-01	1.9116E-02	8.1118E-01
1.5784E-01	1.4997E-02	7.7096E-01
1.5817E-01	8.8533E-03	6.9978E-01
1.5830E-01	3.9833E-03	3.7369E-01

FALCON RESULTS (3D) X/XREF = 6.51

X/XREF	PT/PTREF	TT/TTREF
0.0000E+00	3.4617E-03	3.7369E-01
1.3296E-04	6.9474E-03	6.8142E-01
4.4888E-04	1.0685E-02	7.7484E-01
8.4801E-04	1.3739E-02	8.2325E-01

1.3634E-03	1.6441E-02	8.5552E-01
2.0120E-03	1.9101E-02	8.7414E-01
2.8434E-03	2.1522E-02	8.7680E-01
3.8744E-03	2.3429E-02	8.6863E-01
5.1880E-03	2.5039E-02	8.5671E-01
6.8341E-03	2.6857E-02	8.4820E-01
8.8961E-03	3.0414E-02	8.5789E-01
1.1440E-02	3.7154E-02	8.9105E-01
1.4550E-02	4.7683E-02	9.3236E-01
1.8341E-02	5.9482E-02	9.5763E-01
2.2881E-02	6.9294E-02	9.7536E-01
2.8235E-02	7.6316E-02	9.8675E-01
3.4437E-02	8.1327E-02	9.9359E-01
4.1438E-02	8.4682E-02	9.9780E-01
4.9203E-02	8.4795E-02	9.9954E-01
5.7551E-02	8.0133E-02	9.9995E-01
6.6297E-02	7.7952E-02	1.0008E+00
7.5160E-02	7.9549E-02	1.0007E+00
8.3907E-02	8.2142E-02	1.0010E+00
9.2254E-02	8.5173E-02	1.0012E+00
1.0002E-01	8.7589E-02	1.0008E+00
1.0704E-01	8.3801E-02	1.0002E+00
1.1322E-01	8.8472E-02	9.9950E-01
1.1858E-01	8.5005E-02	9.9927E-01
1.2312E-01	7.6656E-02	1.0028E+00
1.2691E-01	6.8254E-02	1.0052E+00
1.3002E-01	6.0103E-02	1.0069E+00
1.3256E-01	5.2187E-02	9.9666E-01
1.3462E-01	4.4868E-02	9.7490E-01
1.3627E-01	3.8650E-02	9.4792E-01
1.3758E-01	3.3519E-02	9.1910E-01
1.3863E-01	2.9322E-02	8.9094E-01
1.3945E-01	2.5826E-02	8.6449E-01
1.4009E-01	2.2671E-02	8.3893E-01
1.4061E-01	1.9349E-02	8.0970E-01
1.4101E-01	1.5040E-02	7.7106E-01
1.4132E-01	8.7040E-03	6.9833E-01
1.4146E-01	3.9505E-03	3.7369E-01

FALCON RESULTS (3D) X/XREF = 6.65

X/XREF	PT/PTREF	TT/TTREF
0.0000E+00	3.4871E-03	3.7369E-01
1.3301E-04	6.3684E-03	6.7937E-01
4.3233E-04	1.1200E-02	7.6545E-01
8.3151E-04	1.4470E-02	8.1565E-01
1.3137E-03	1.7060E-02	8.4063E-01
1.9290E-03	2.0058E-02	8.8158E-01
2.7105E-03	2.3904E-02	9.1361E-01
3.6915E-03	2.8229E-02	9.3866E-01
4.9387E-03	3.1521E-02	9.5872E-01
6.4851E-03	3.3607E-02	9.7161E-01
8.4144E-03	3.5894E-02	9.8198E-01
1.0792E-02	3.9733E-02	9.9192E-01
1.3685E-02	4.7441E-02	9.1139E-01
1.7210E-02	6.0323E-02	9.5194E-01
2.1417E-02	7.6108E-02	9.7239E-01
2.5356E-02	8.8994E-02	9.8416E-01
3.2960E-02	9.7839E-02	9.9157E-01
3.8511E-02	1.0194E-01	9.9638E-01

October 4, 1990

Input for AGARD Working Group 13, Test Case 6:

### Hypersonic Inlet - P8

The solution of the hypersonic flow of the NASA P8 inlet were obtained using the two-dimensional Navier-Stokes code NSFLEX (Navier-Stokes solver using characteristic flux extrapolation) [1]. It is a finite-volume method applicable to sub-, trans- and hypersonic flows. The inviscid fluxes at the finite-volume faces are evaluated by solving a Riemann problem [2]. A third-order accurate local characteristic flux extrapolation scheme of type MUSCL [3] is employed. For capturing strong shock waves (especially in hypersonic flows) a flux vector splitting is used [4]. For the interpolation between the two ways (MUSCL flux-difference splitting and a modified Steger/Warming flux-vector splitting) to form cell face fluxes a sharpened high-order limiter derived from the van Albada limiter has been incorporated. The viscous fluxes are approximated with central differences. The numerical method utilizes the algebraic turbulence model of Baldwin and Lomax [5]. The unfactored implicit equations are solved in time-dependent form by a point Gauss-Seidel relaxation technique. By applying the so-called checkerboard scheme, in which points are divided into black and white ones, a high degree of vectorization is achieved. The code contains multi-blocking capability and real gas effects are incorporated.

The computational grid used is shown in Fig. 1. It consists of two blocks (block 1: 50\*145 points, block 2: 129\*100 points) and was generated with an algebraic mesh generator ensuring perpendicular intersection of the grid lines with the surfaces. The inner-law variable  $z^+$  can be varied.

The surface static pressures on the centerline of the ramp and on the cowl of the inlet are plotted in Fig. 2 and Fig. 3. The pitot pressure and total temperature contours at nine  $x/x_{ref}$  locations are shown in Fig. 4 and Fig. 5. Additionally, the isolines of Mach number, pitot pressure and pressure coefficient  $c_p$  are included in Fig. 6 to Fig. 8.

The mass loss along the duct, Fig. 9, was used both for quality check of the code and convergence criterion.  $\Delta m$  was referred to the mass in the entrance of the inlet. 10000 iterations were necessary to obtain a converged solution. The computation performed on the SIEMENS supercomputer VP200 required 5.0E-5 seconds per point and iteration.

The calculation was started with parallel flow with a Mach number of 7.4 and a temperature  $T_\infty = 67$  K. The wall temperature condition was isothermal with  $T_w = 303$  K.

Boundary layer transition was fixed at  $x = 35$  cm on the wedge and  $x = 107$  cm on the cowl like in the experiment [6].

Investigations were made to demonstrate first the influence of the numerical viscosity and secondly the wall temperature condition to the result. Fig. 10 shows the surface static pressure on the centerline of the ramp and Fig. 11 the pitot pressure contours due to a high numerical viscosity introduced by a higher rate of flux-vector splitting. The result obtained by using adiabatic wall condition is compared with experiment in Fig. 12 and Fig. 13 (surface static pressures on centerline and cowl). The

appropriate Mach isolines showing flow separation, are plotted in Fig. 14.

#### References

- [1] Schmatz, M.A.: NSFLEX - An implicit relaxation method for the Navier-Stokes equations for a wide range of Mach numbers. Notes on Numerical Fluid Mechanics, vol. 30, Vieweg, Braunschweig (1990).
- [2] Eberle, A.: Characteristic flux averaging approach to the solution of Euler's equations. VKI-Lecture Series 1987-04 (1987).
- [3] Anderson, W.K., Thomas, J.L., van Leer, B.: A comparison of finite volume flux vector splittings for the Euler equations. AIAA Paper 85-0122 (1985).
- [4] Eberle, A., Schmatz, M.A., Bissinger, N.C.: Generalized flux vectors for hypersonic shock capturing. AIAA Paper 90-0390 (1990).
- [5] Baldwin, B.S., Lomax, J.: Thin layer approximation and algebraic model for separated turbulent flows. AIAA Paper 78-0257 (1978).
- [6] Gnos, A.V., Watson, E.C., Seebaugh, W.R., Sanator, R.J., DeCarlo, J.P.: Investigation of flow fields within large-scale hypersonic inlet models. NASA TN D-7150 (1973).

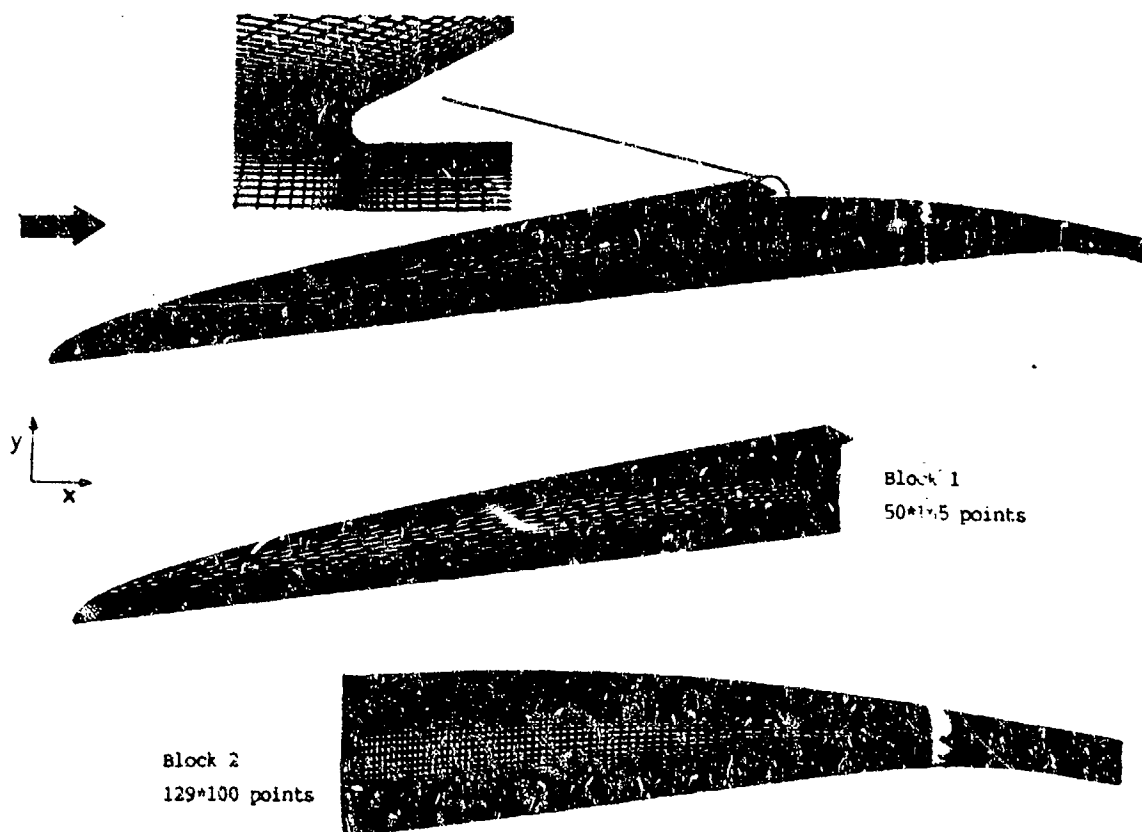


Fig. 1 Grid and block structure of the hypersonic NASA P8 inlet

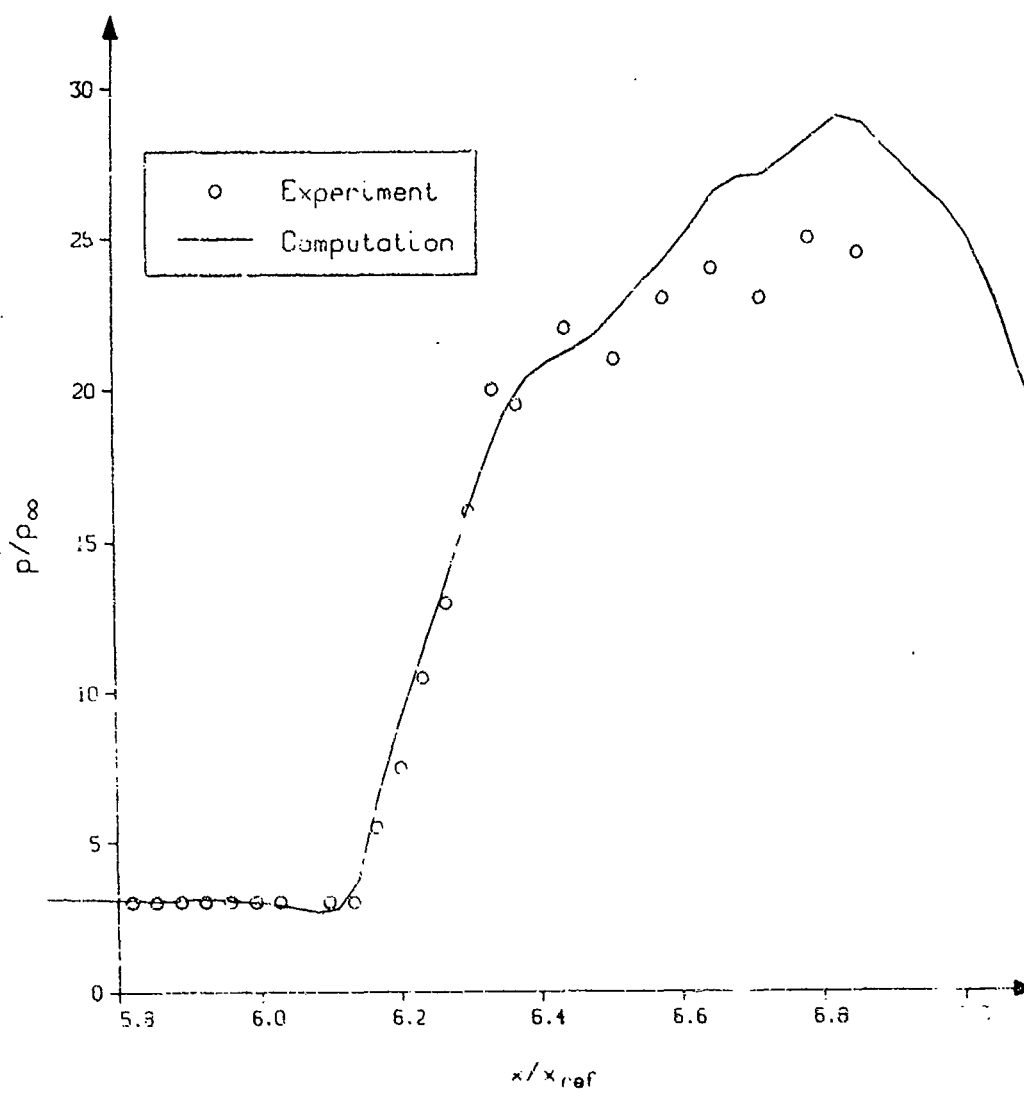


Fig. 2 Surface static pressure on the centerline of the ramp

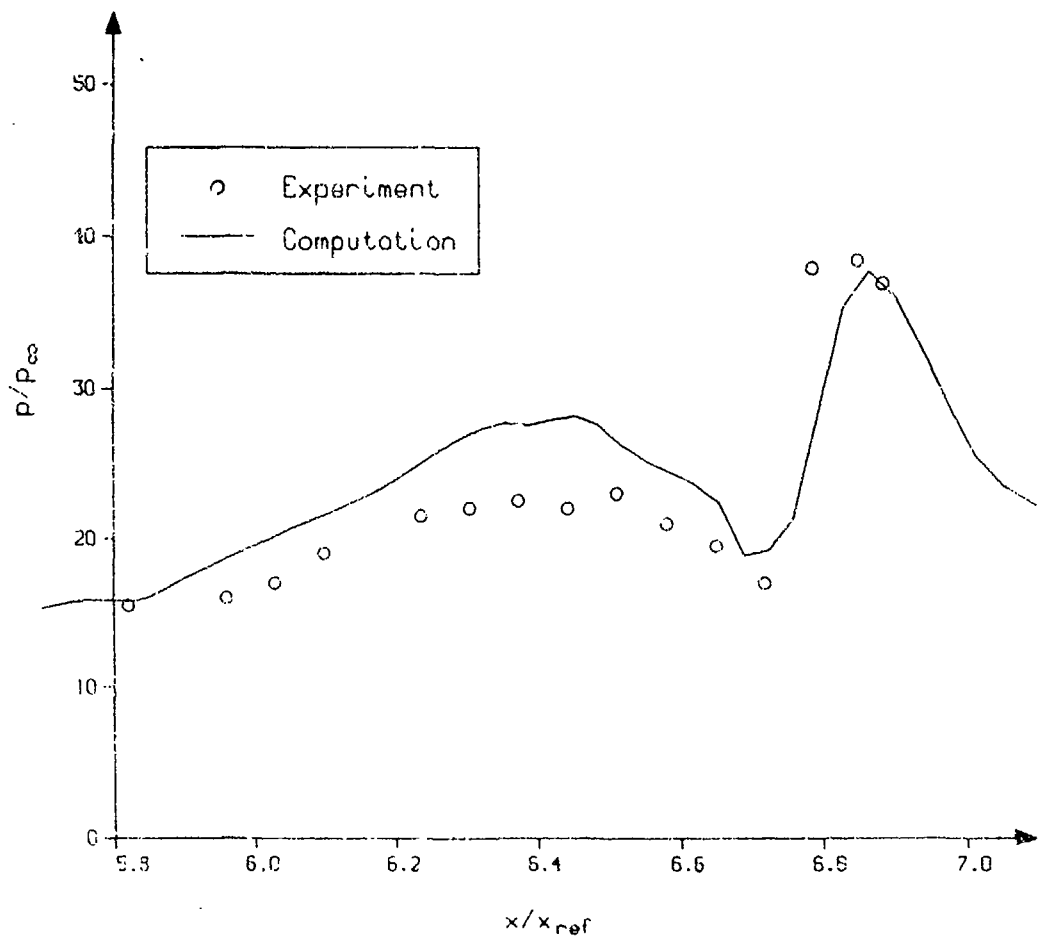


Fig. 3 Surface static pressure on the cowl of the inlet



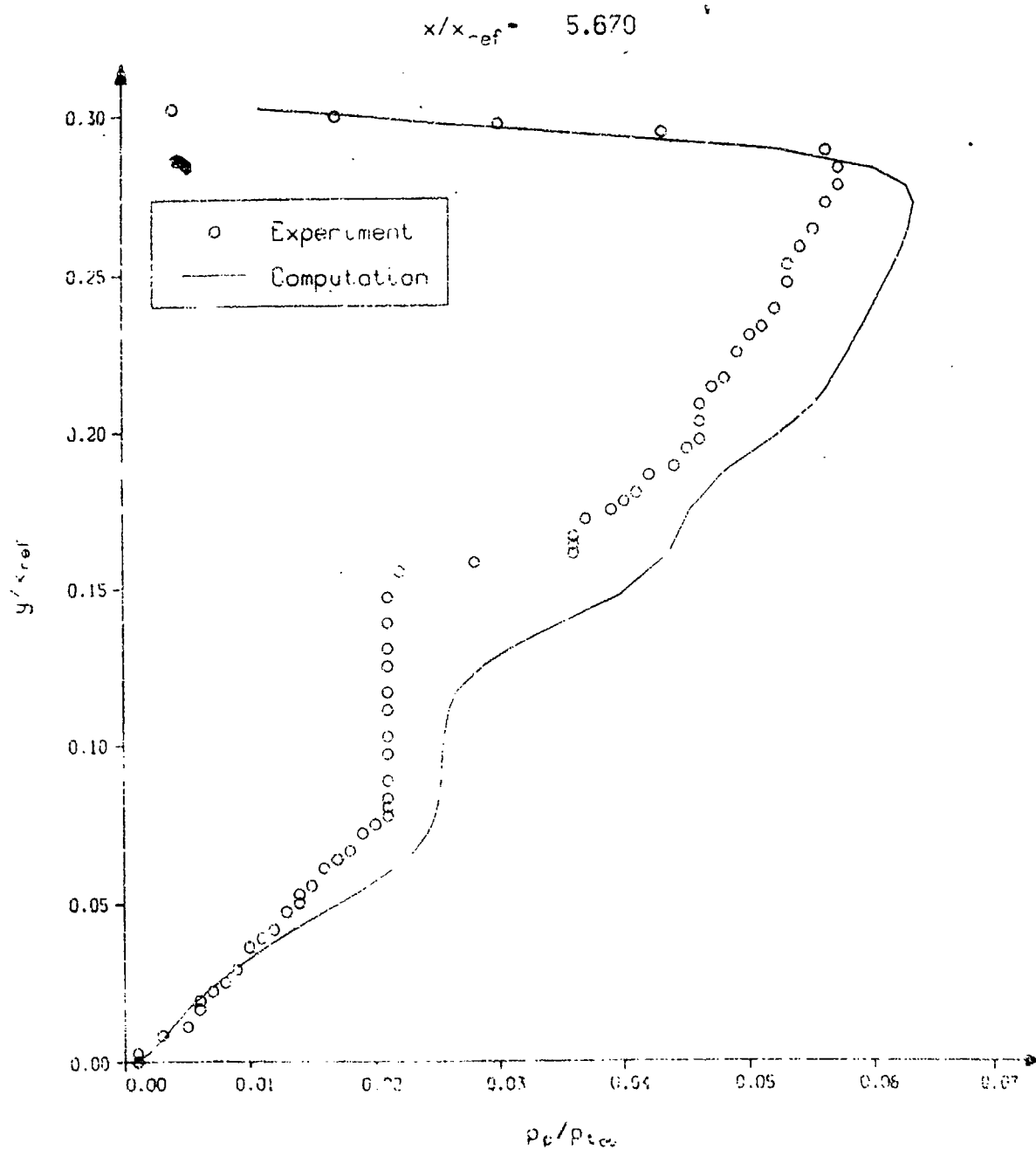


Fig. 4 Pitot pressure contours

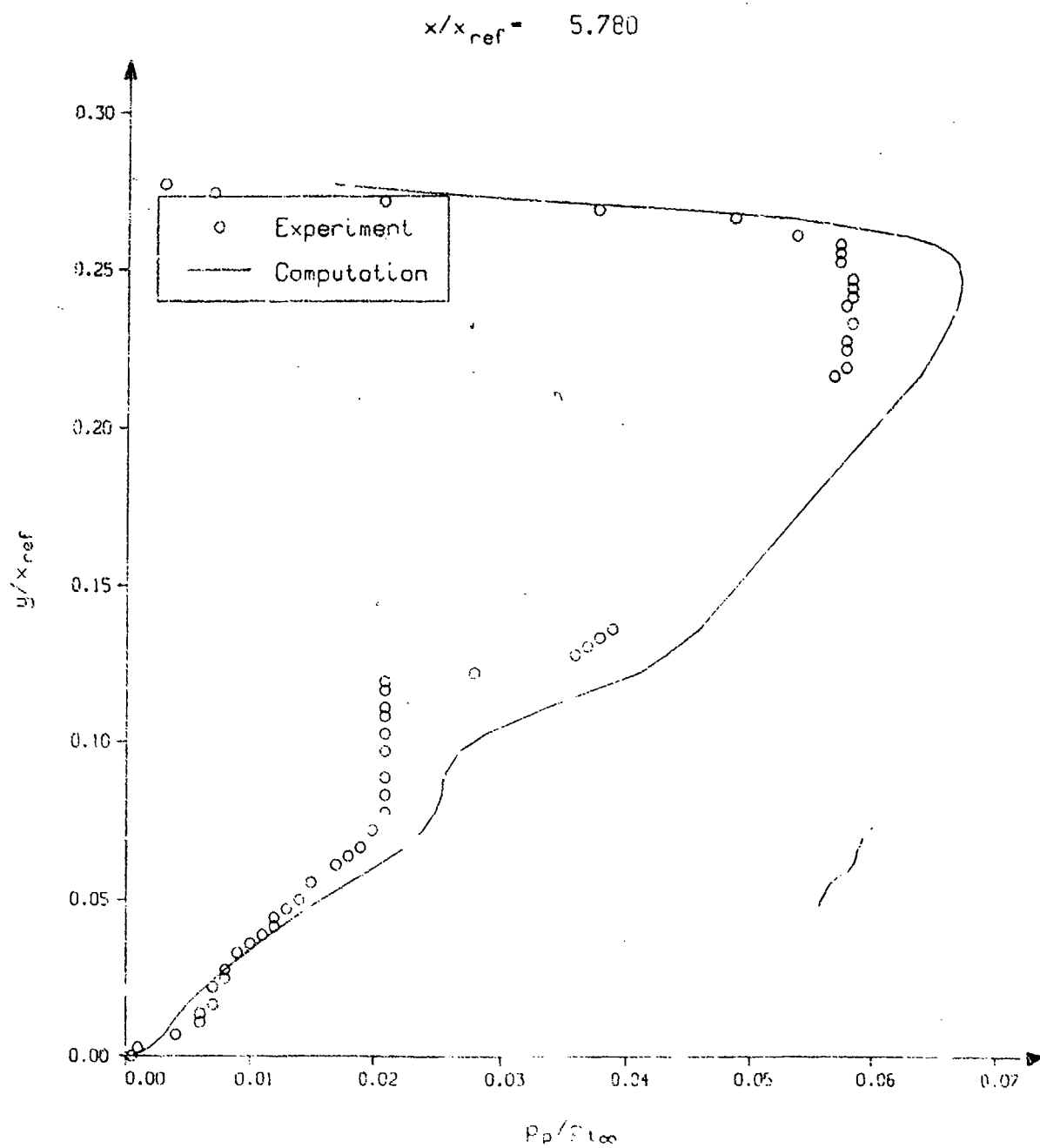


Fig. 4 Pitot pressure contours (continued)

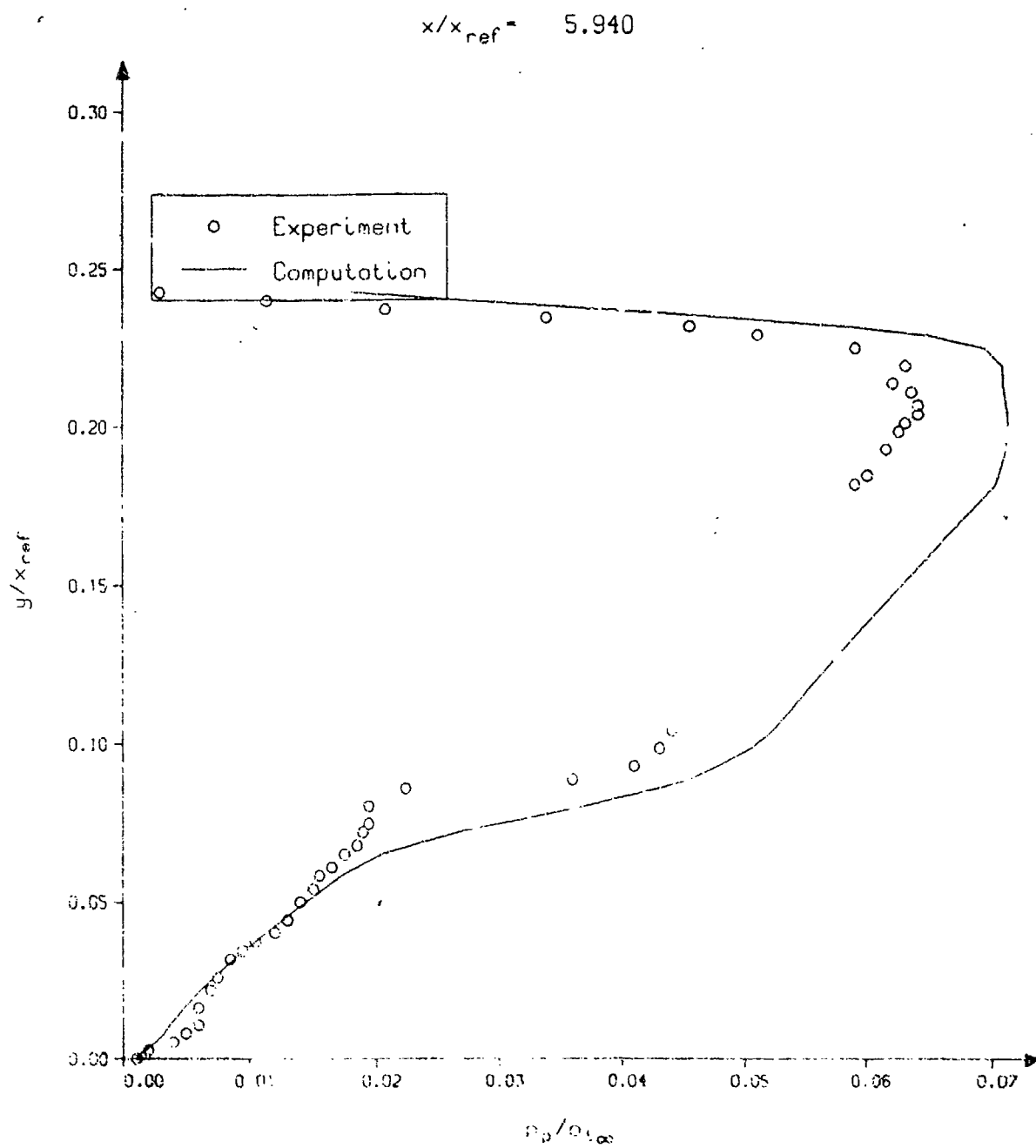


Fig. 4 Pitot pressure contours (continued)

$$\lambda/x_{ref} = 6.090$$

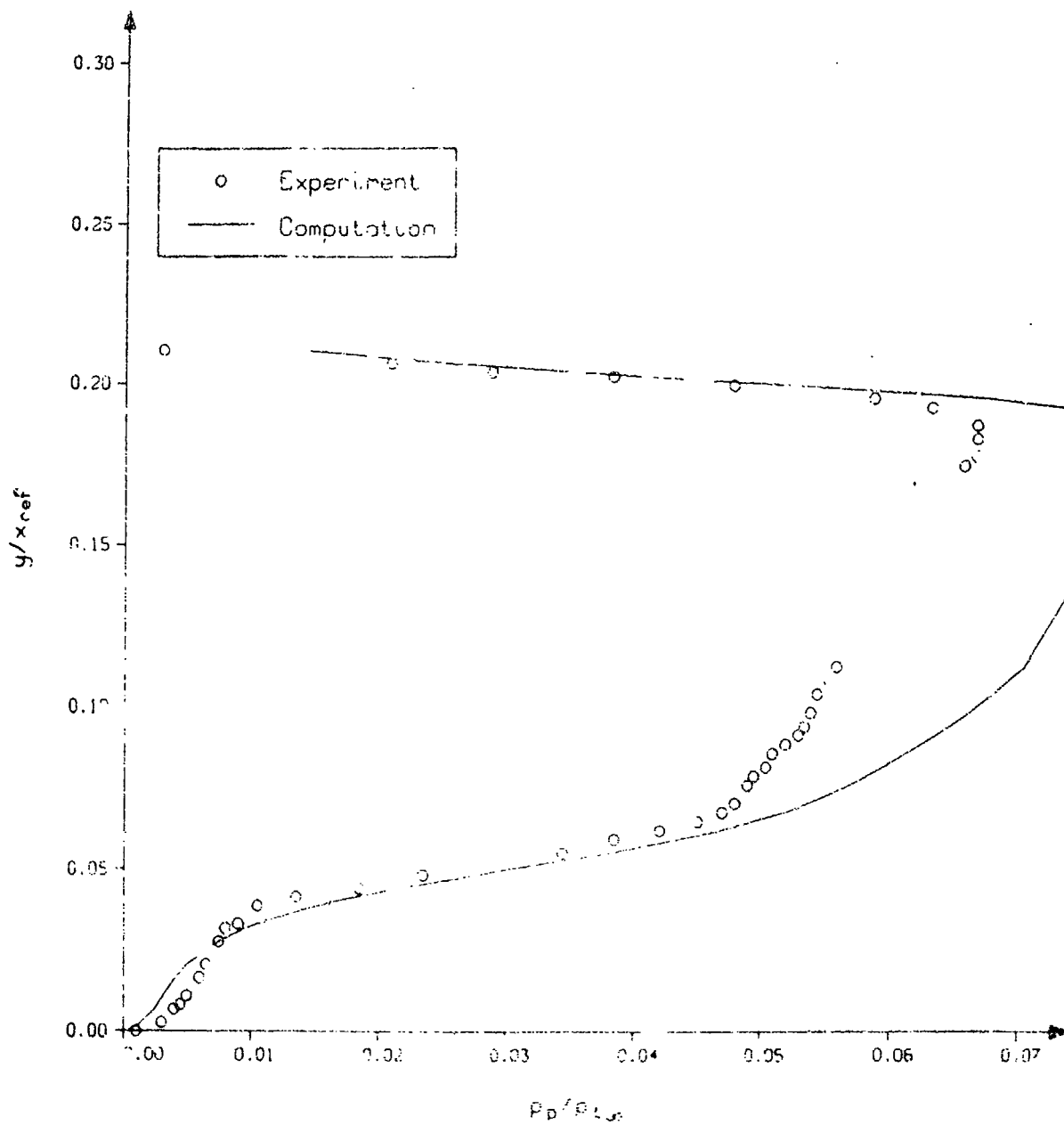


Fig. 4 Pitot pressure contours (continued)

$x/x_{ref} = 6.230$

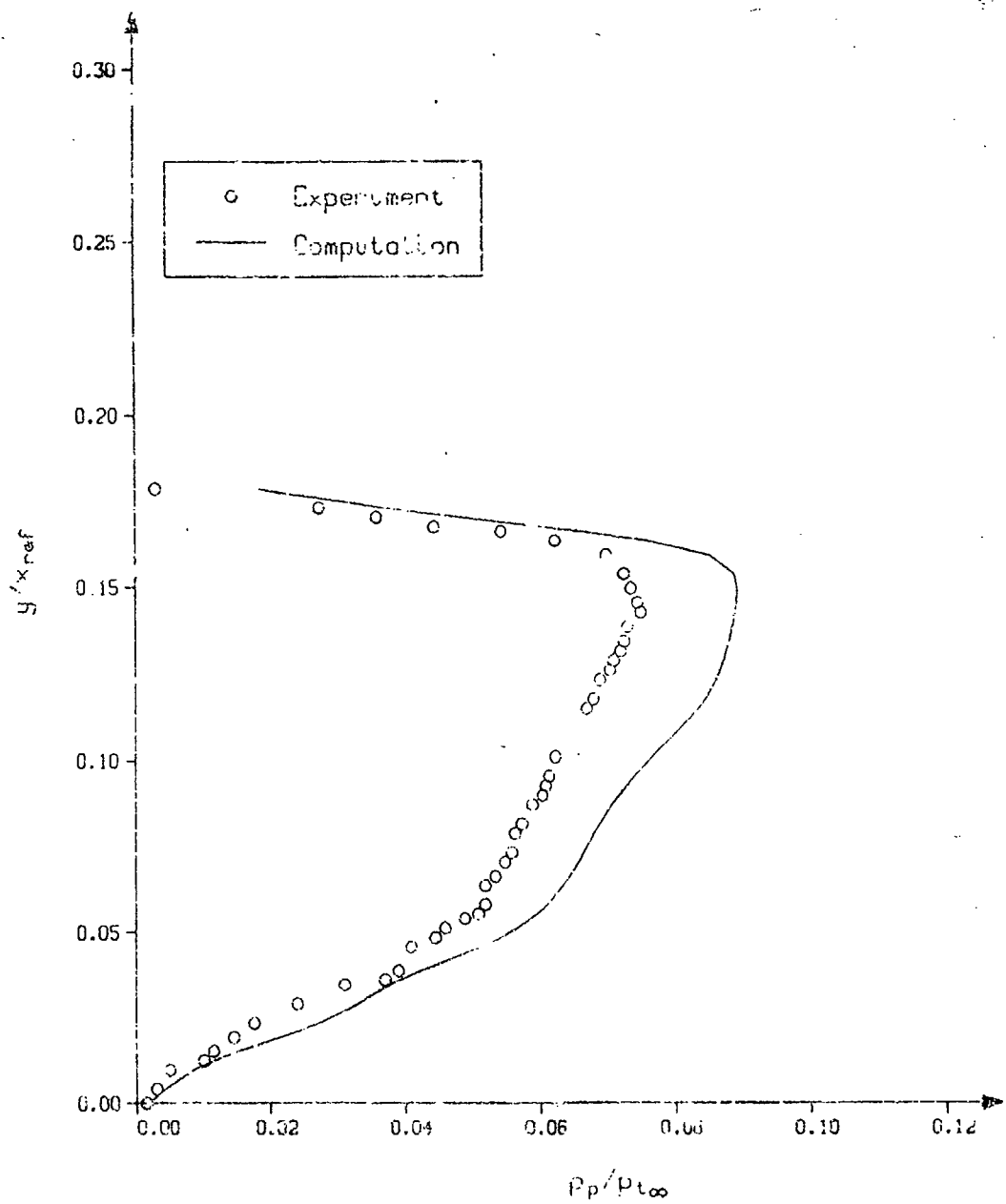


Fig. 4 Pitot pressure contours (continued)

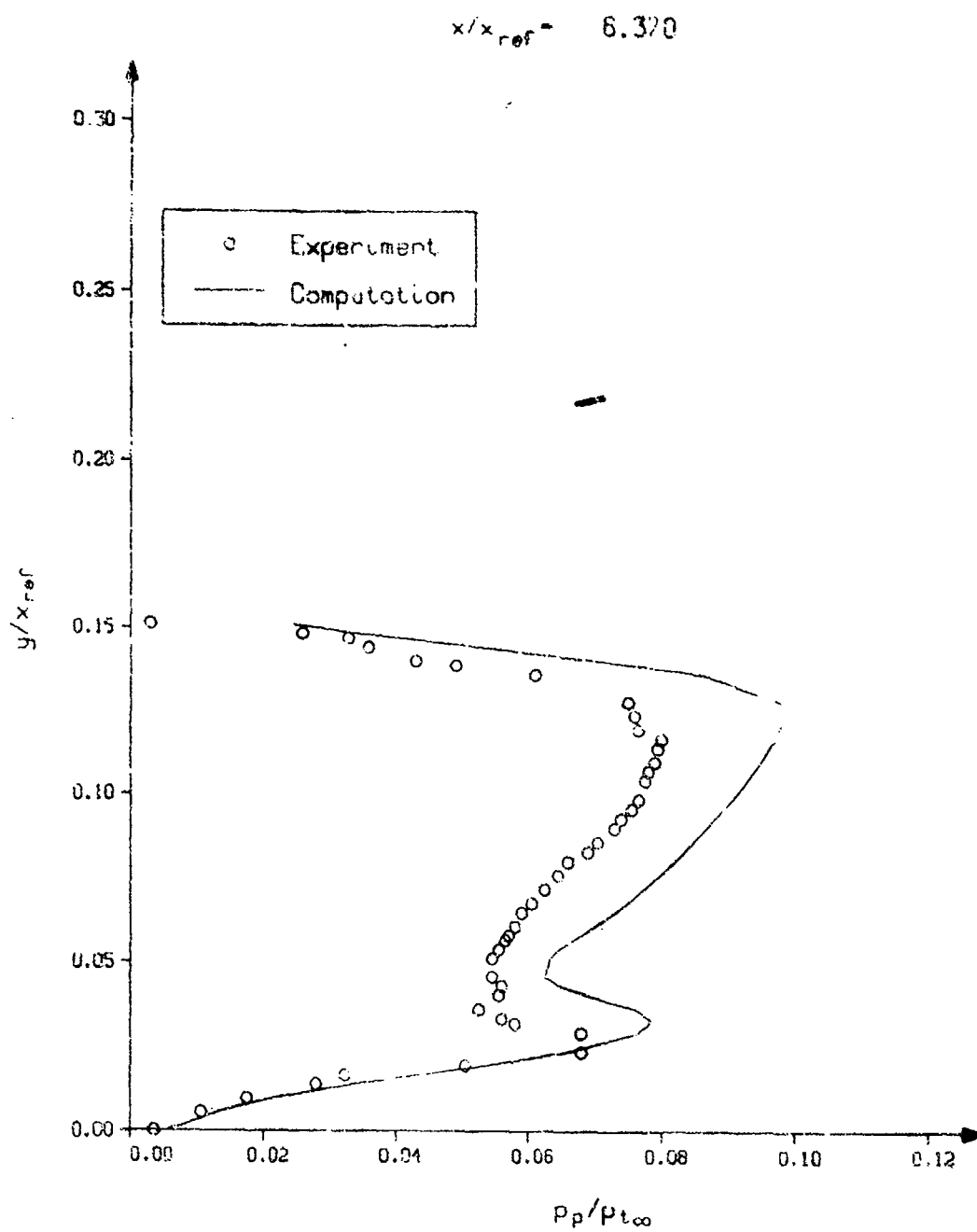


Fig. 4 Pitot pressure contours (continued)

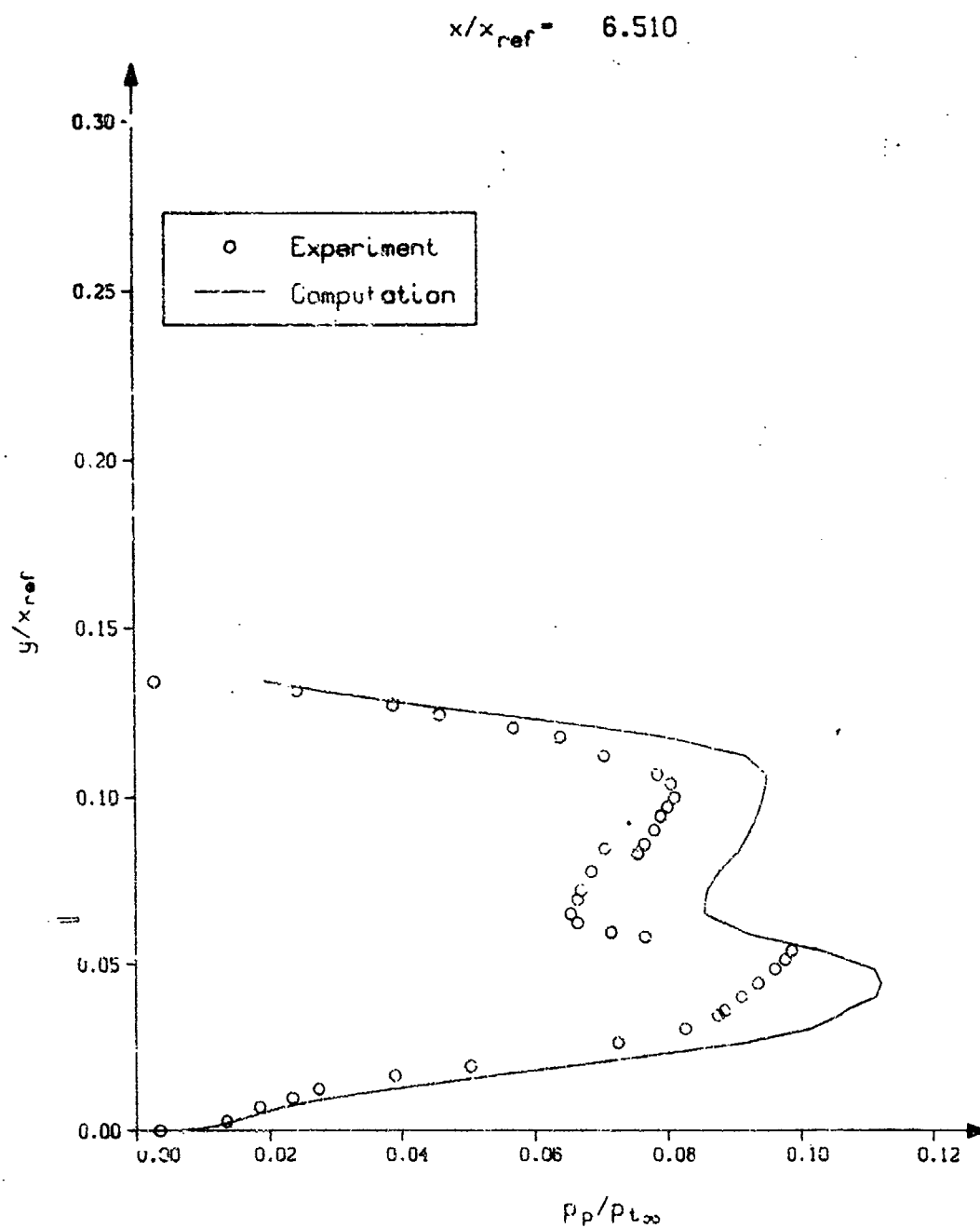


Fig. 4 Pitot pressure contours (continued)

$$x/x_{ref} = 6.650$$

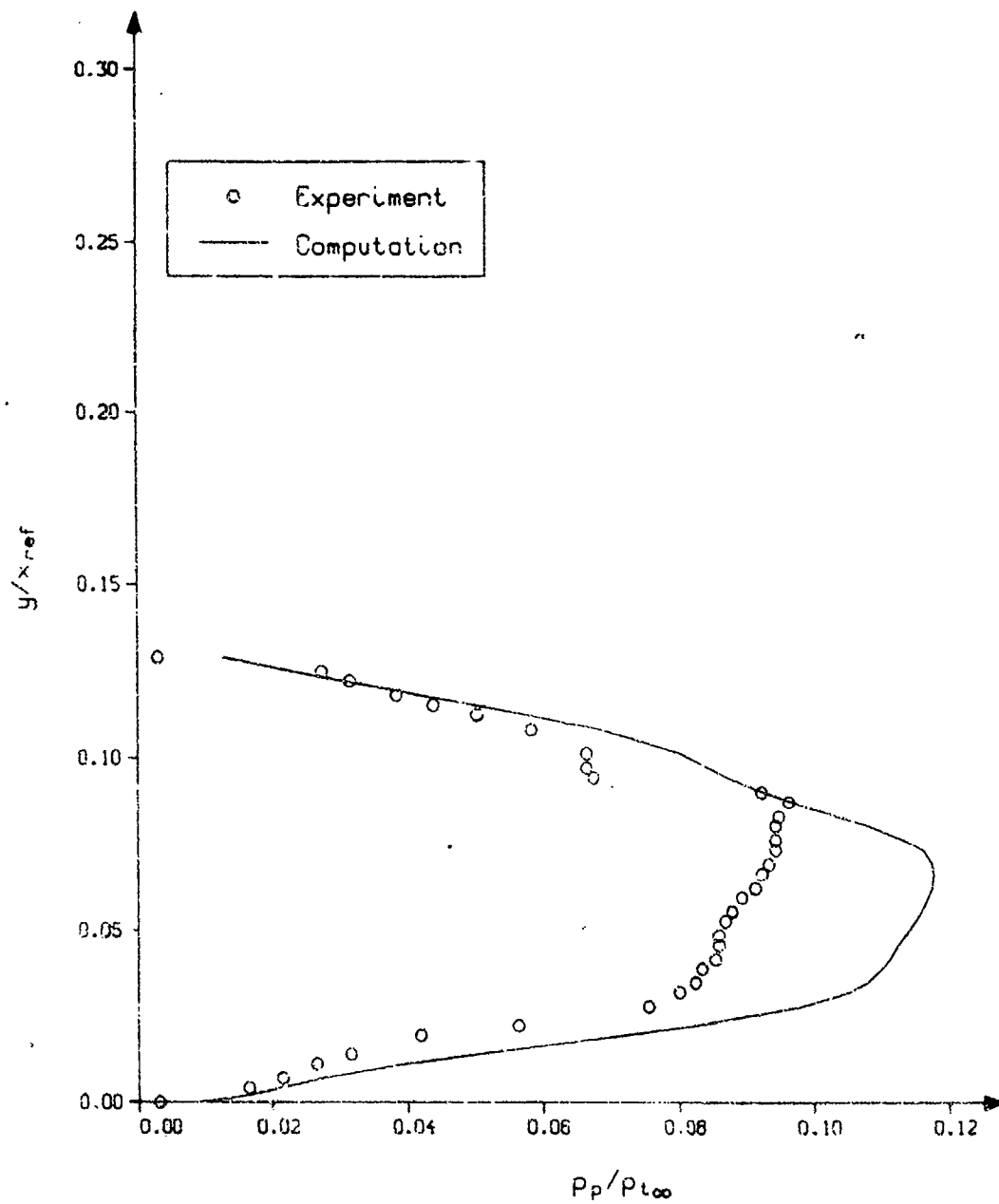


Fig. 4 Pitot pressure contours (continued)



$$x/x_{ref} = 6.790$$

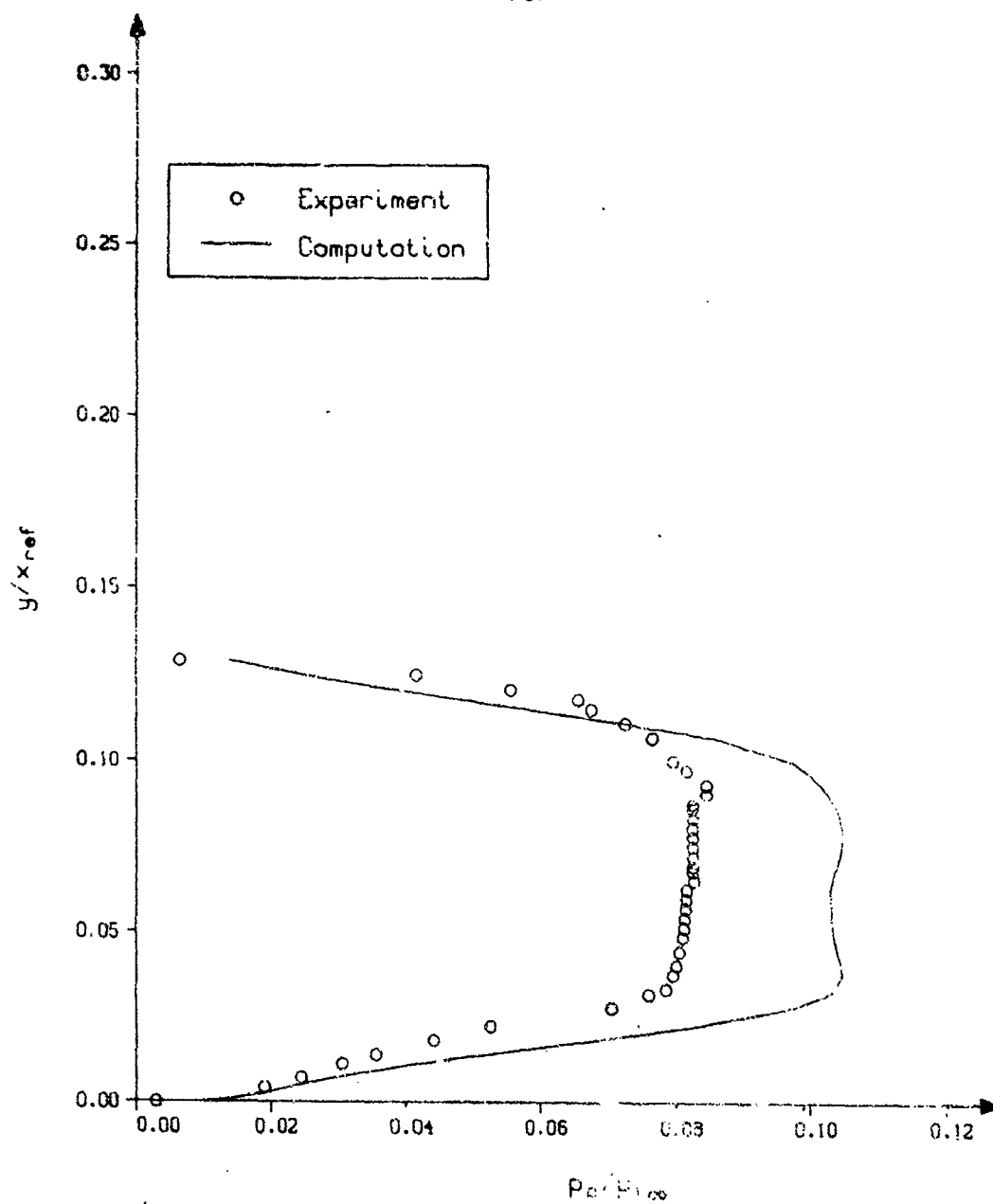


Fig. 4 Pitot pressure contours (continued)

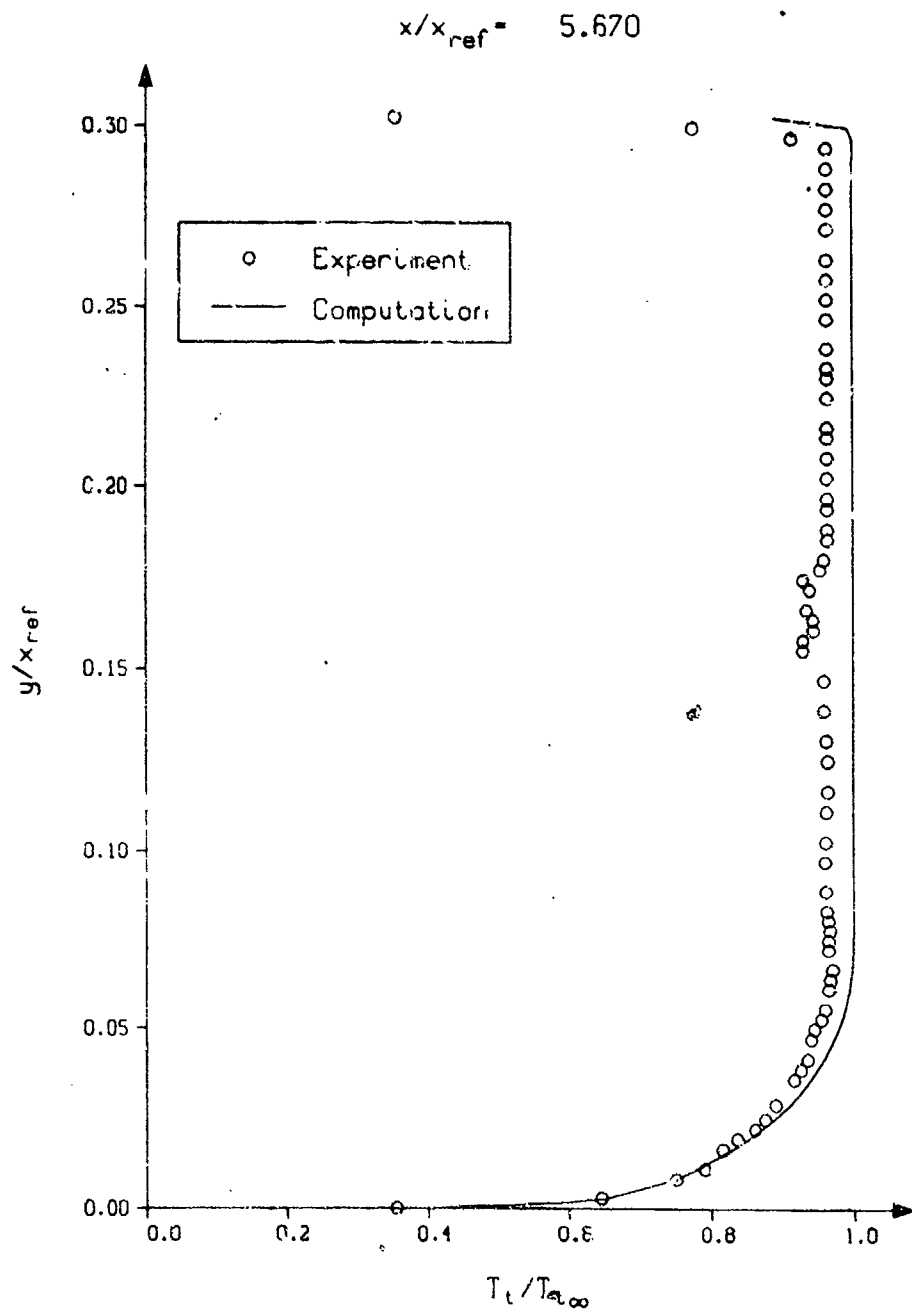


Fig. 5 Total temperature contours

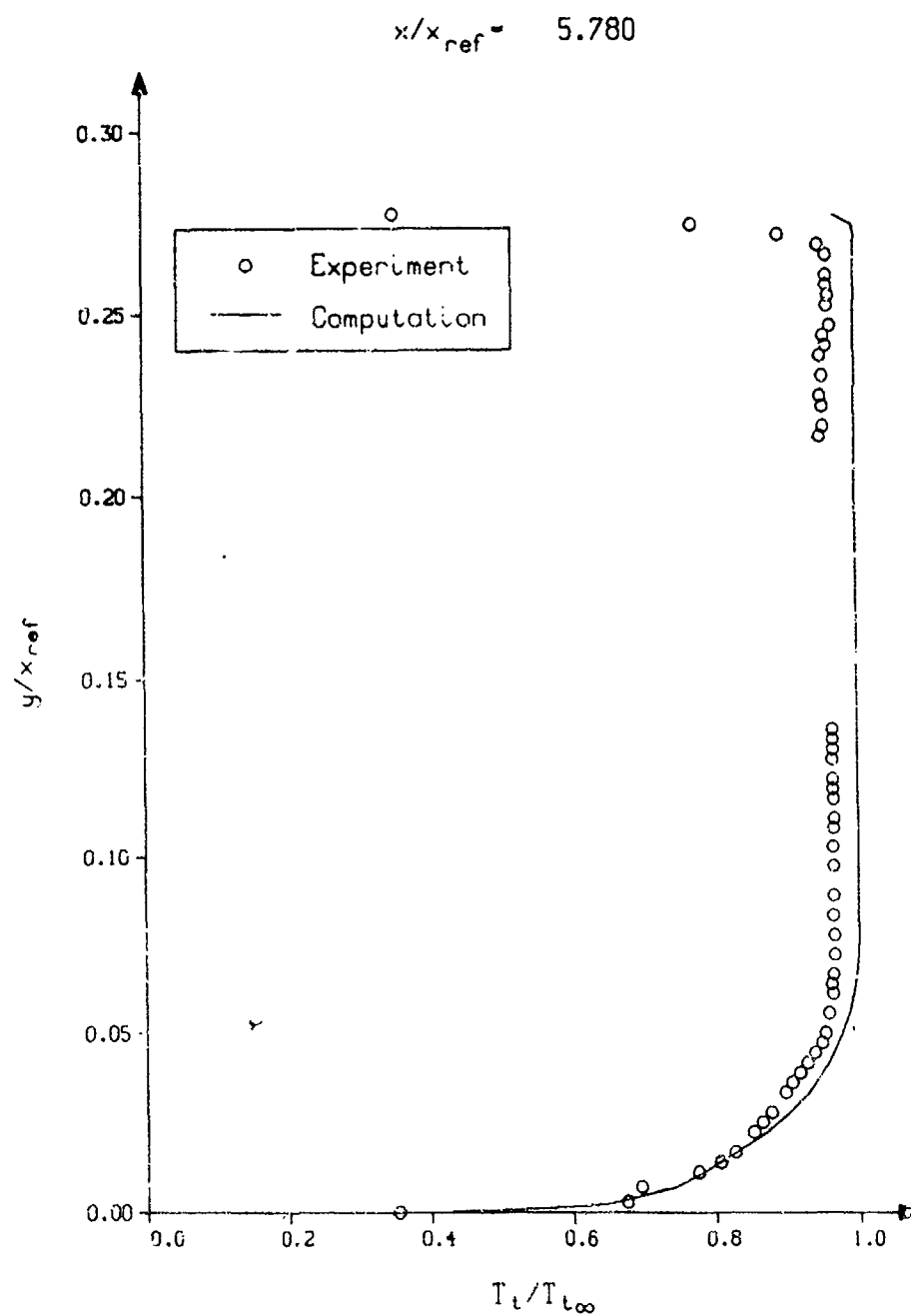


Fig. 5 Total temperature contours (continued)

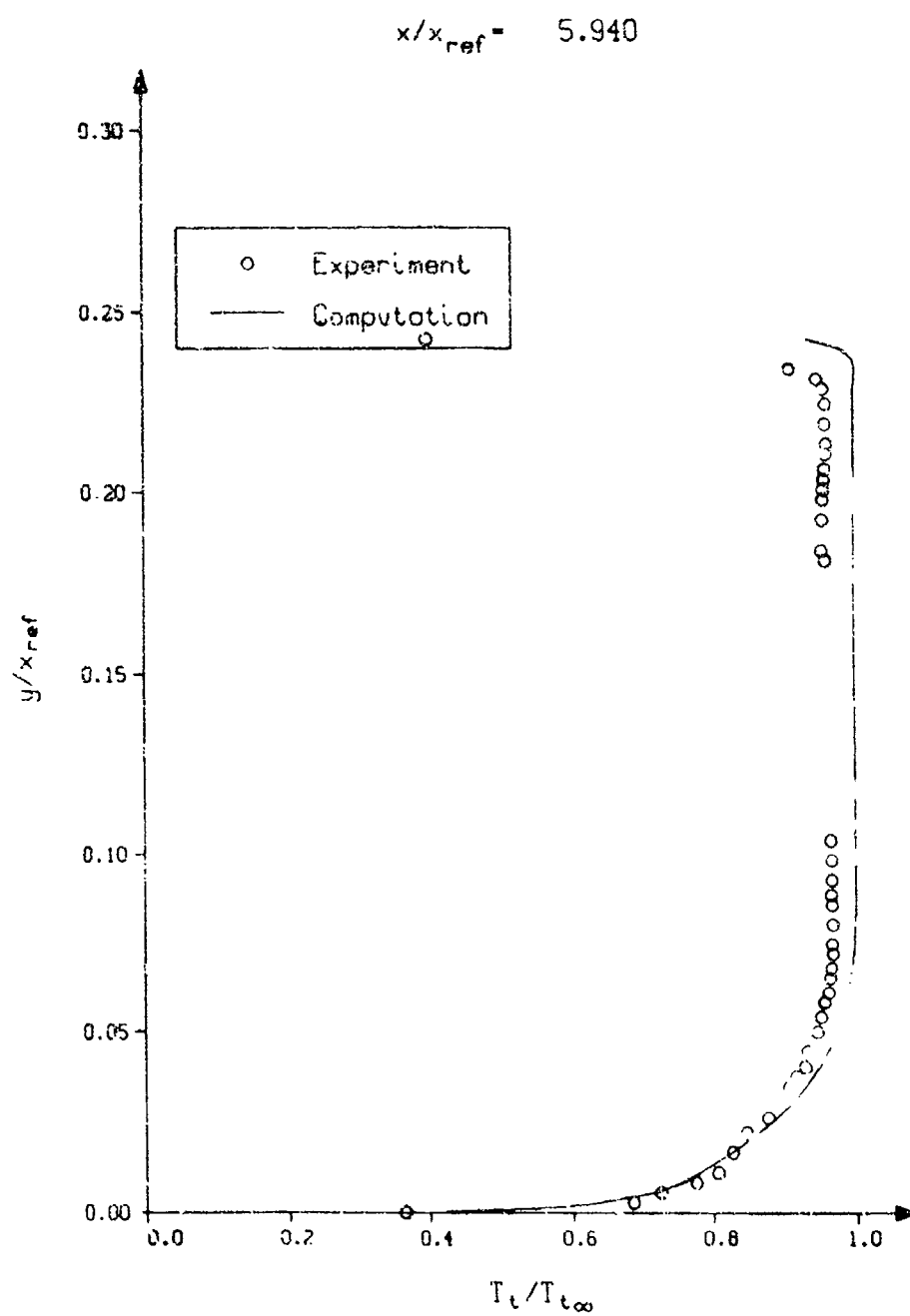


Fig. 5 Total temperature contours (continued)

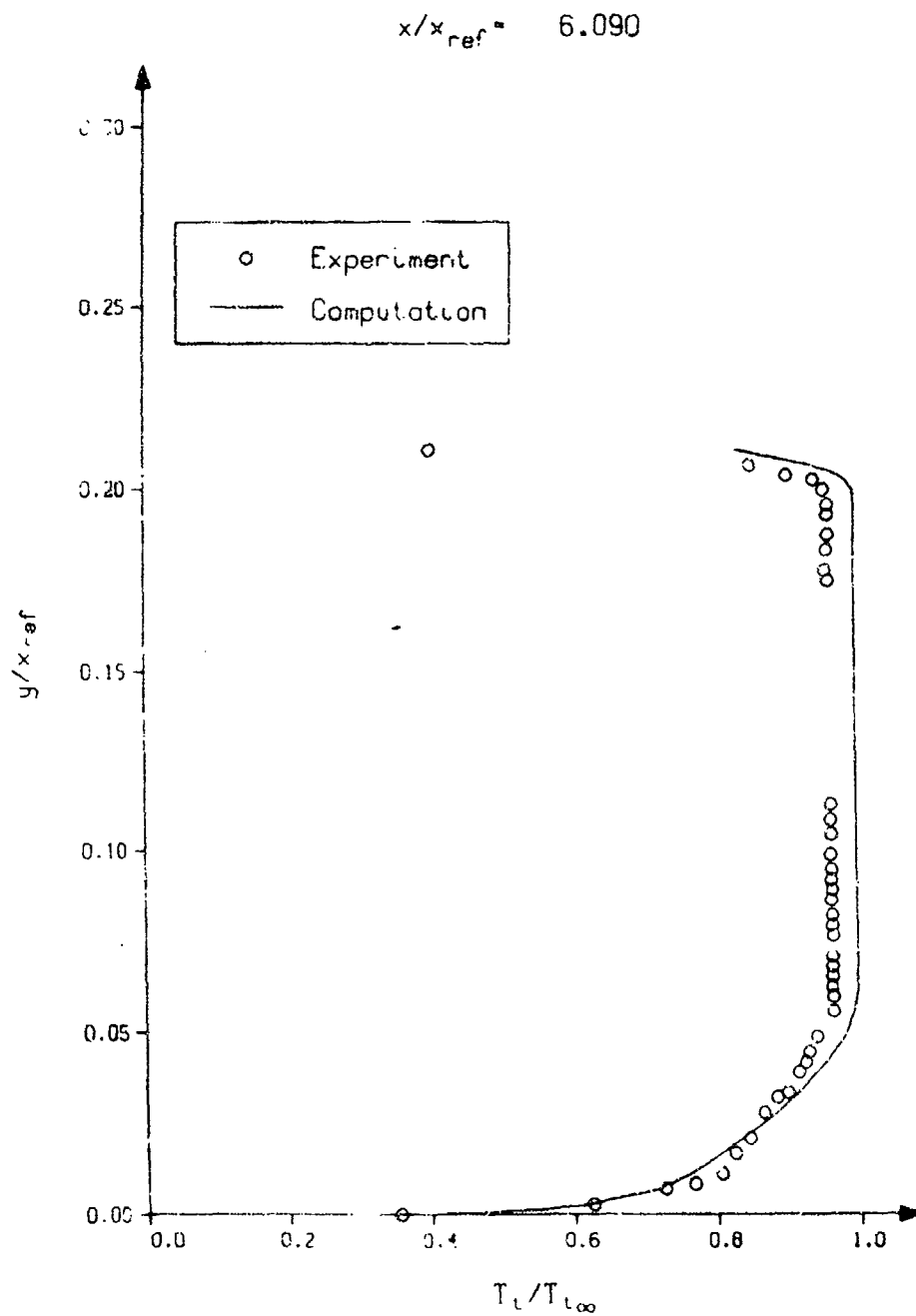


Fig. 5 Total temperature contours (continued)

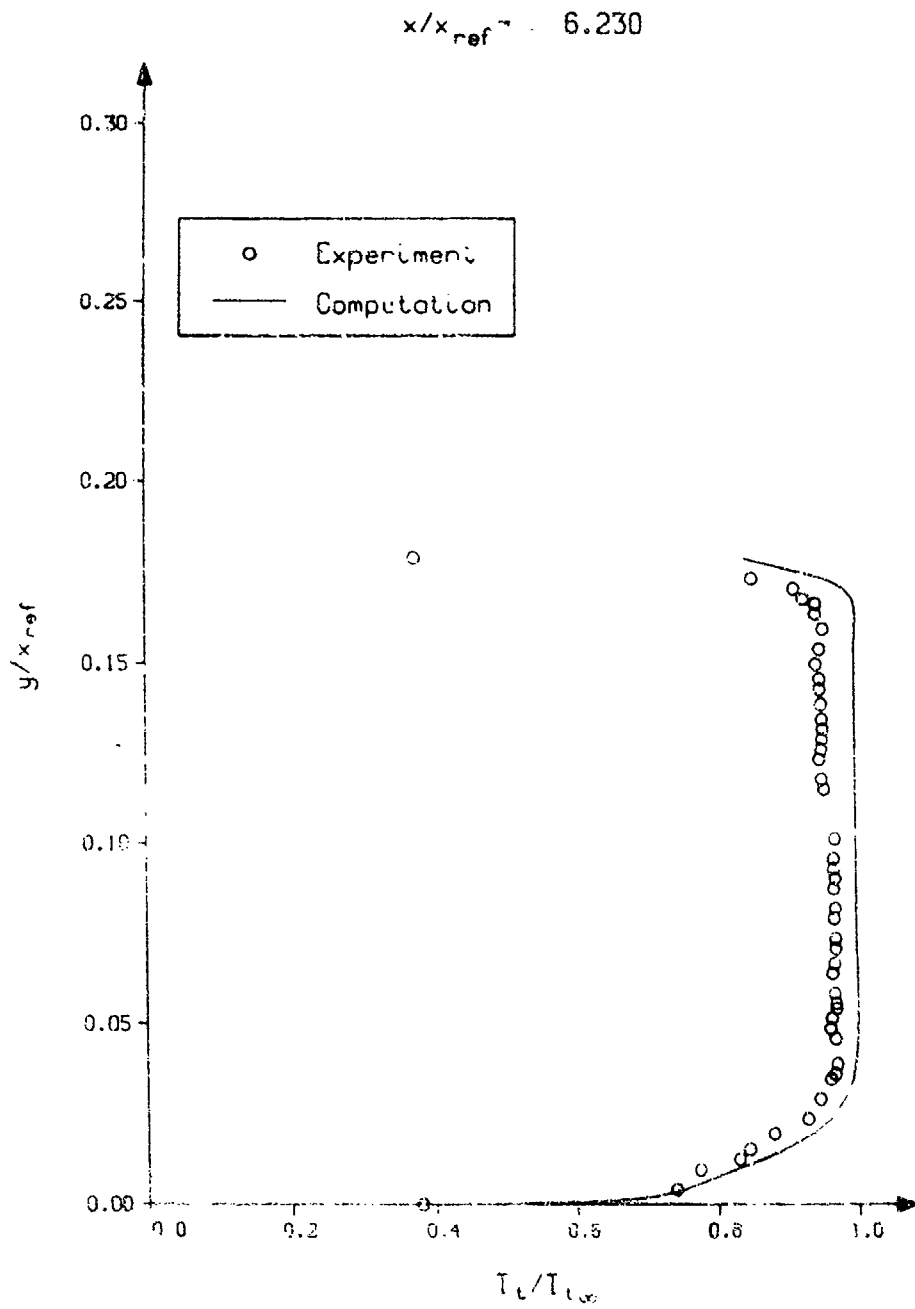


Fig. 5 Total temperature contours (continued)

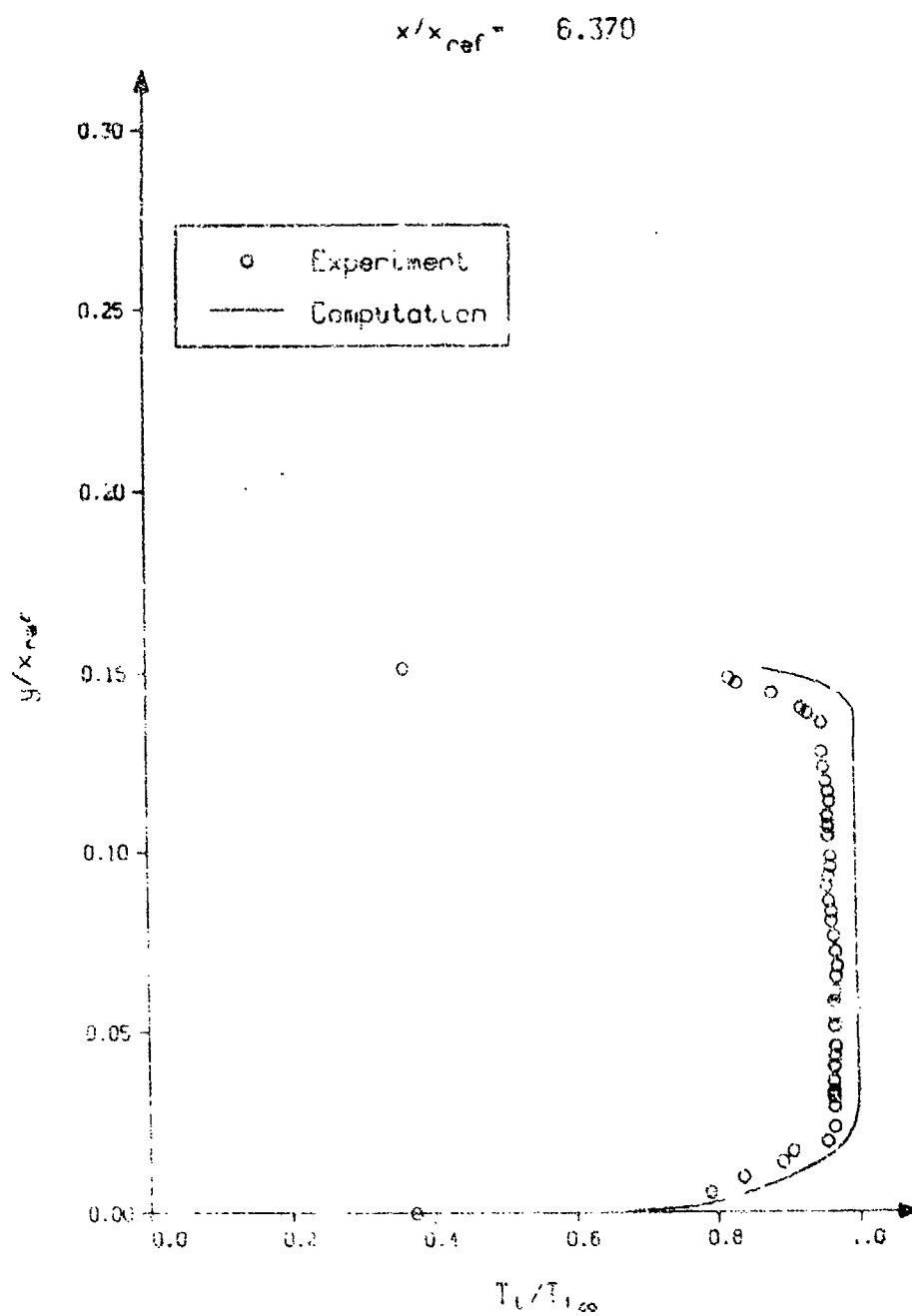


Fig. 5 Total temperature contours (continued)

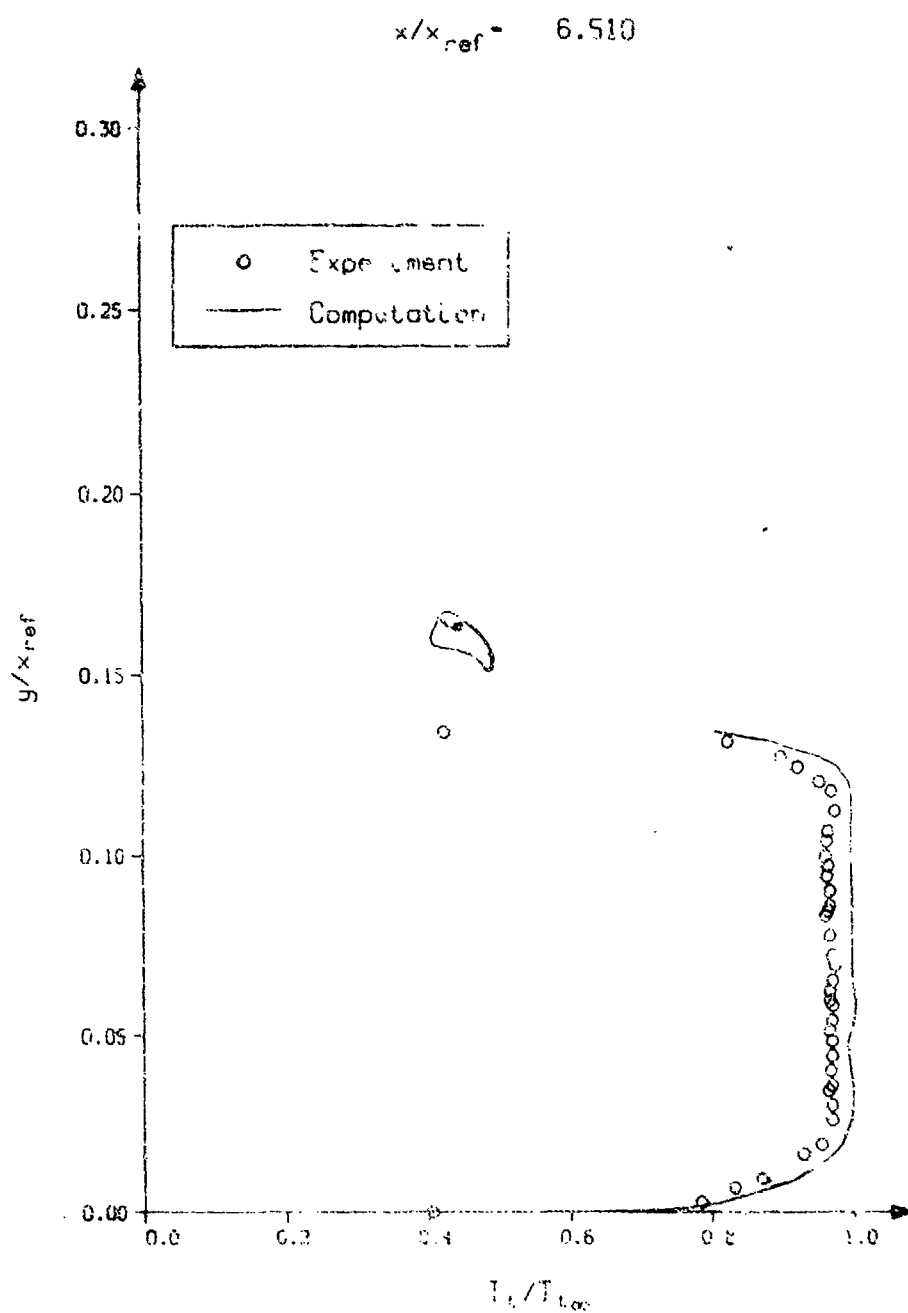


Fig. 5 Total temperature contours (continued)



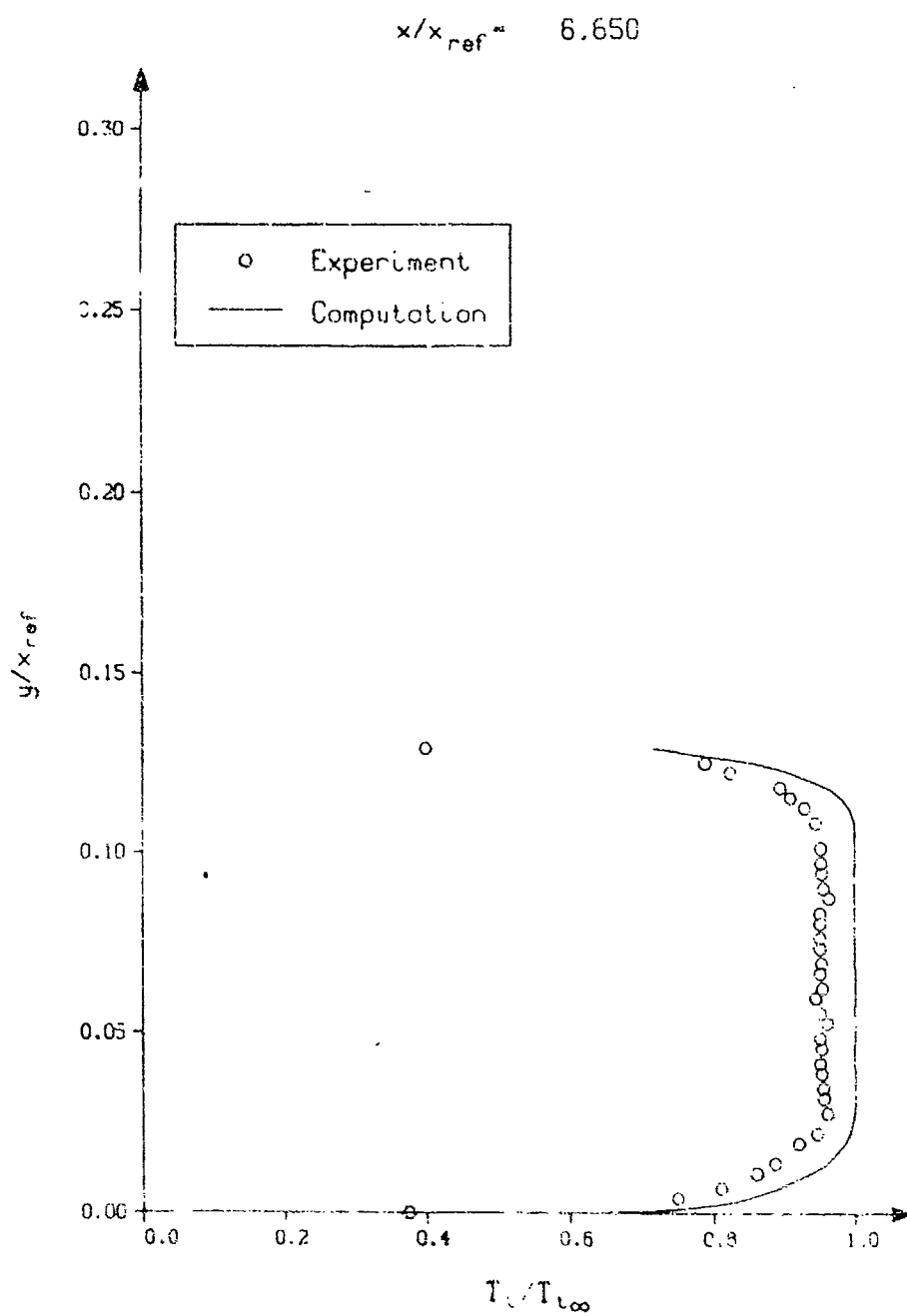


Fig. 5 Total temperature contours (continued)

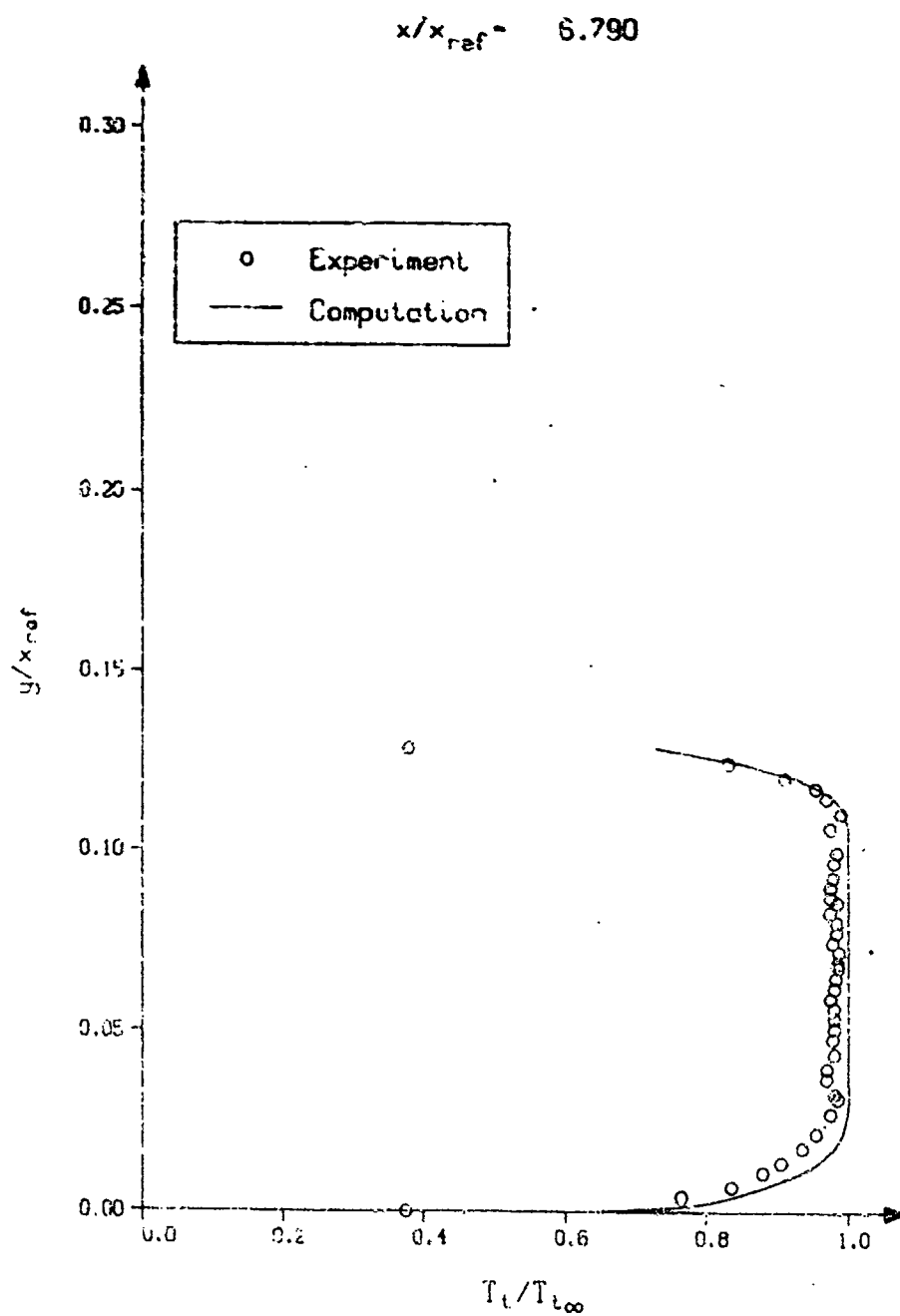


Fig. 5 Total temperature contours (continued)

A colour reproduction of this  
illustration can be found on  
fiche number 5.

MIN= 0.009 . MAX= 7.406 STE= 0.289

Fig. 6 Isolines of Mach number

A colour reproduction of this  
illustration can be found on  
fiche number 5.

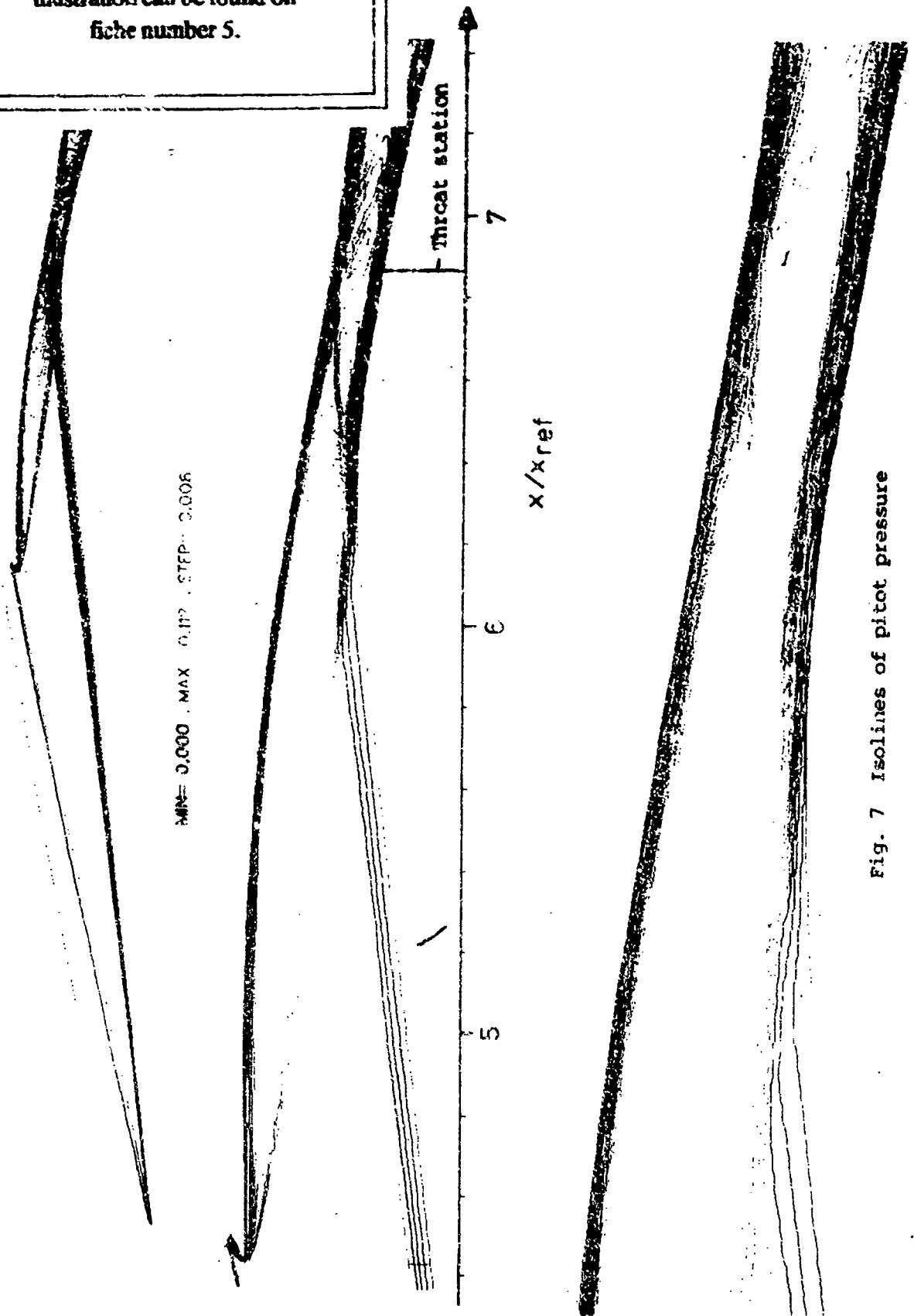


Fig. 7 Isolines of pitot pressure

A colour reproduction of this  
illustration can be found on  
fiche number 5.

MIN= 0.000 . MAX = 0.955 STEP = 0.050

Throat station

Fig. 8 Isolines of pressure coefficient  $C_p$

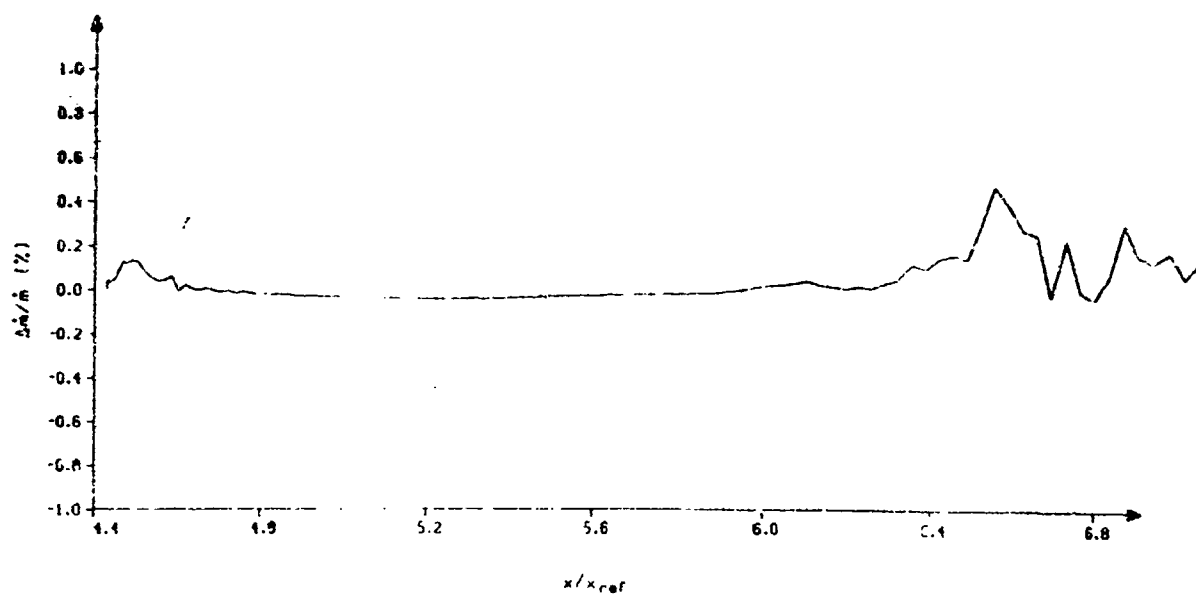


Fig. 9 Mass loss along inlet

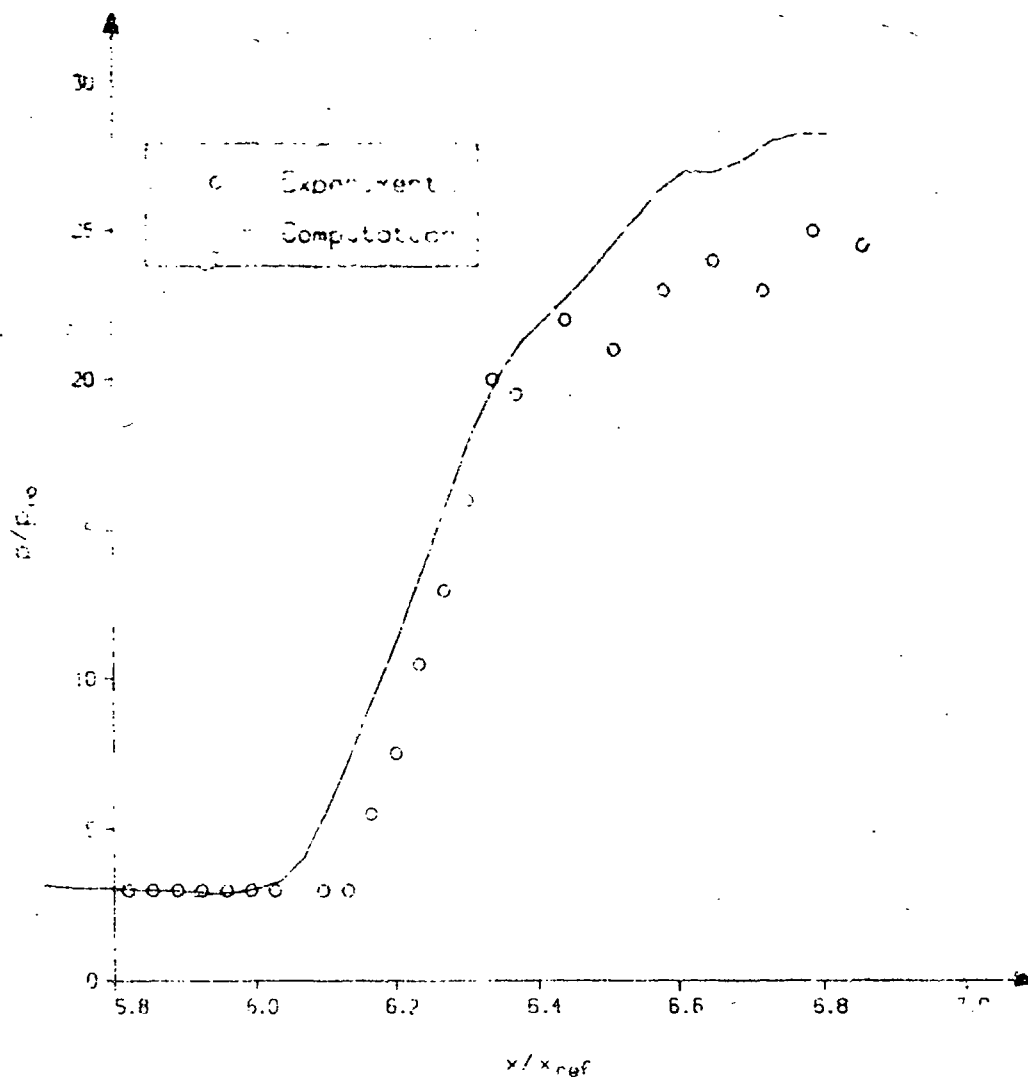


Fig. 10 Surface static pressure on the centerline of the ramp with high numerical viscosity

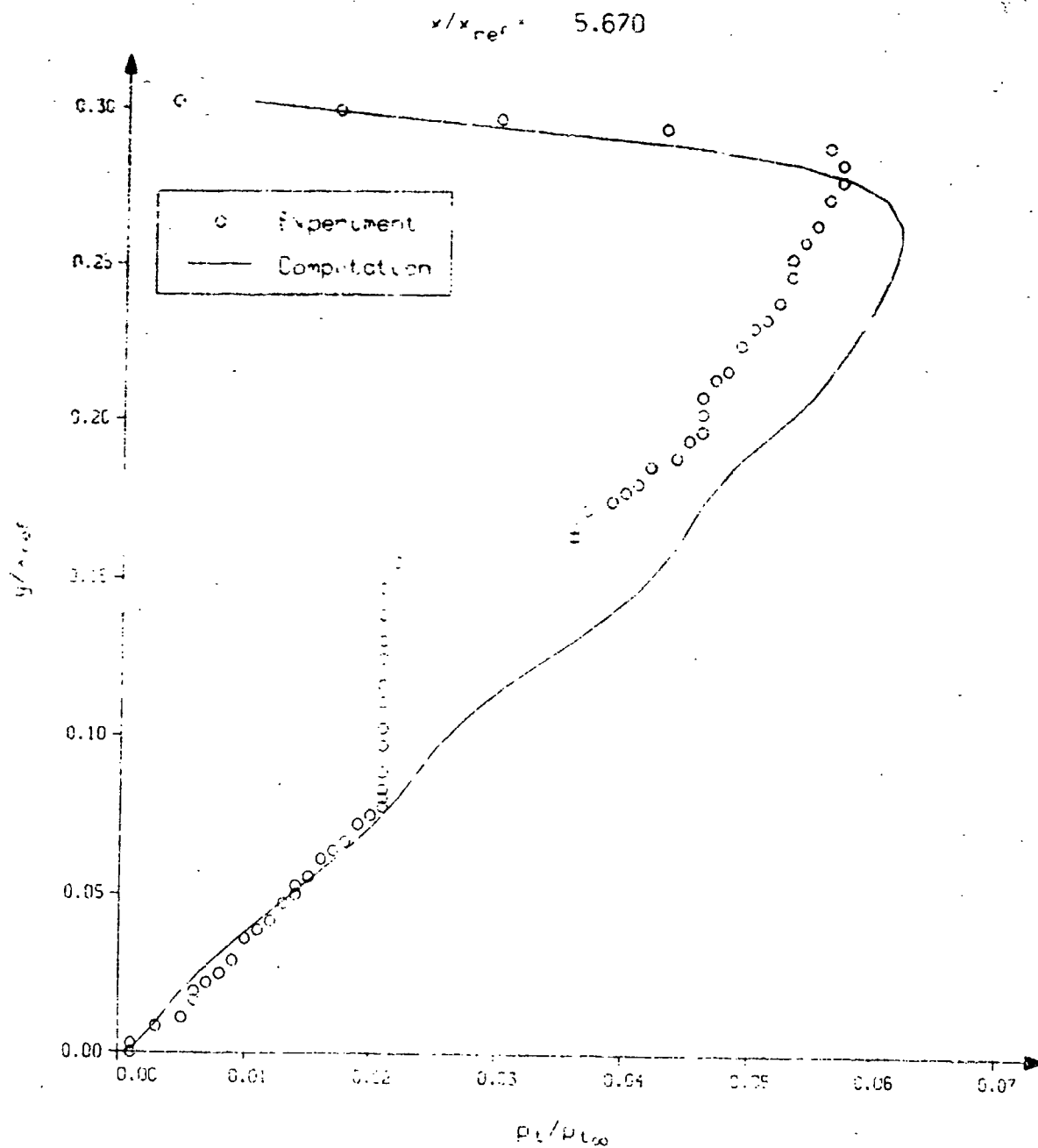


Fig. 11 Pitot pressure contours with high numerical viscosity



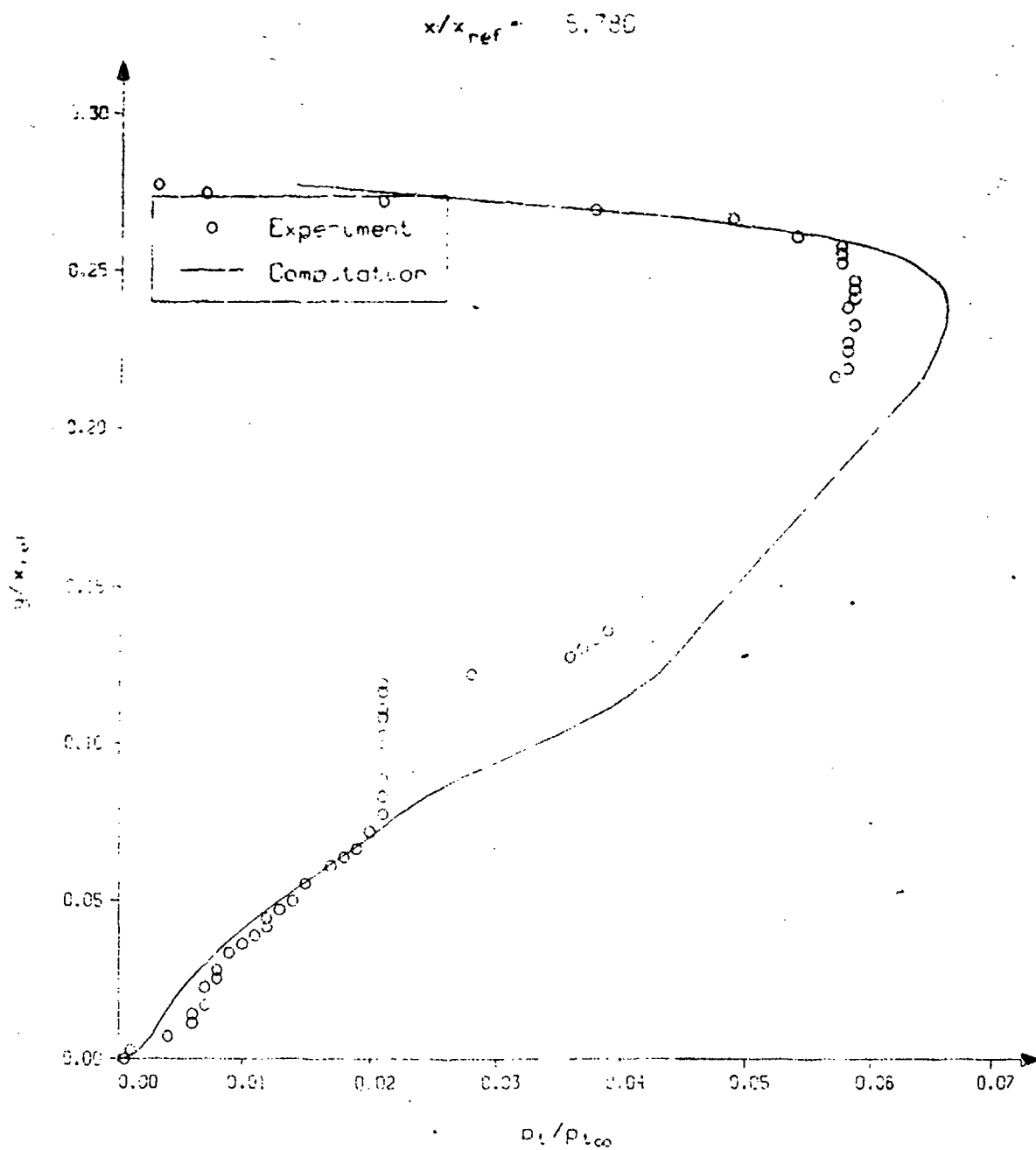


Fig. 11 Pitot pressure contours with high numerical viscosity (continued)

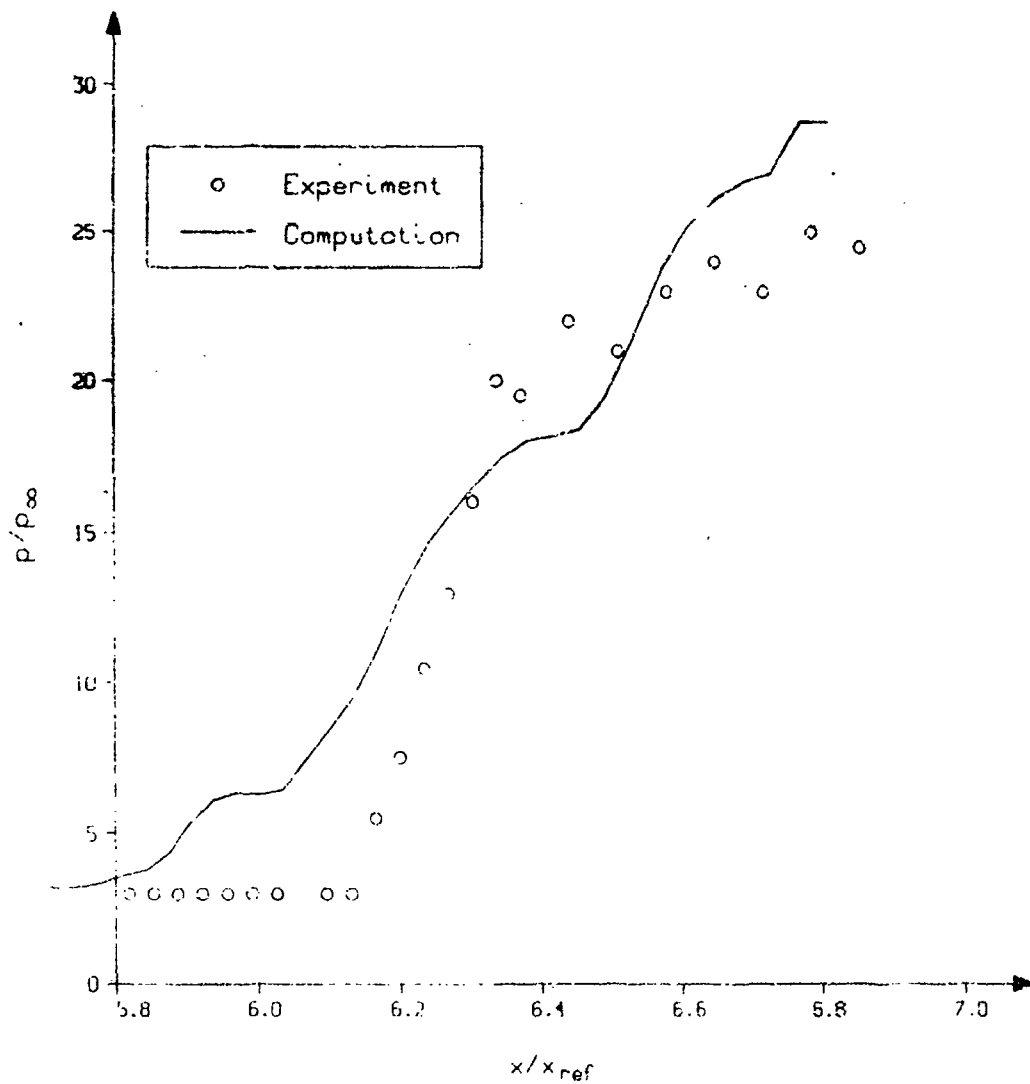


Fig. 12 Surface static pressure on the centerline of the ramp with adiabatic wall condition

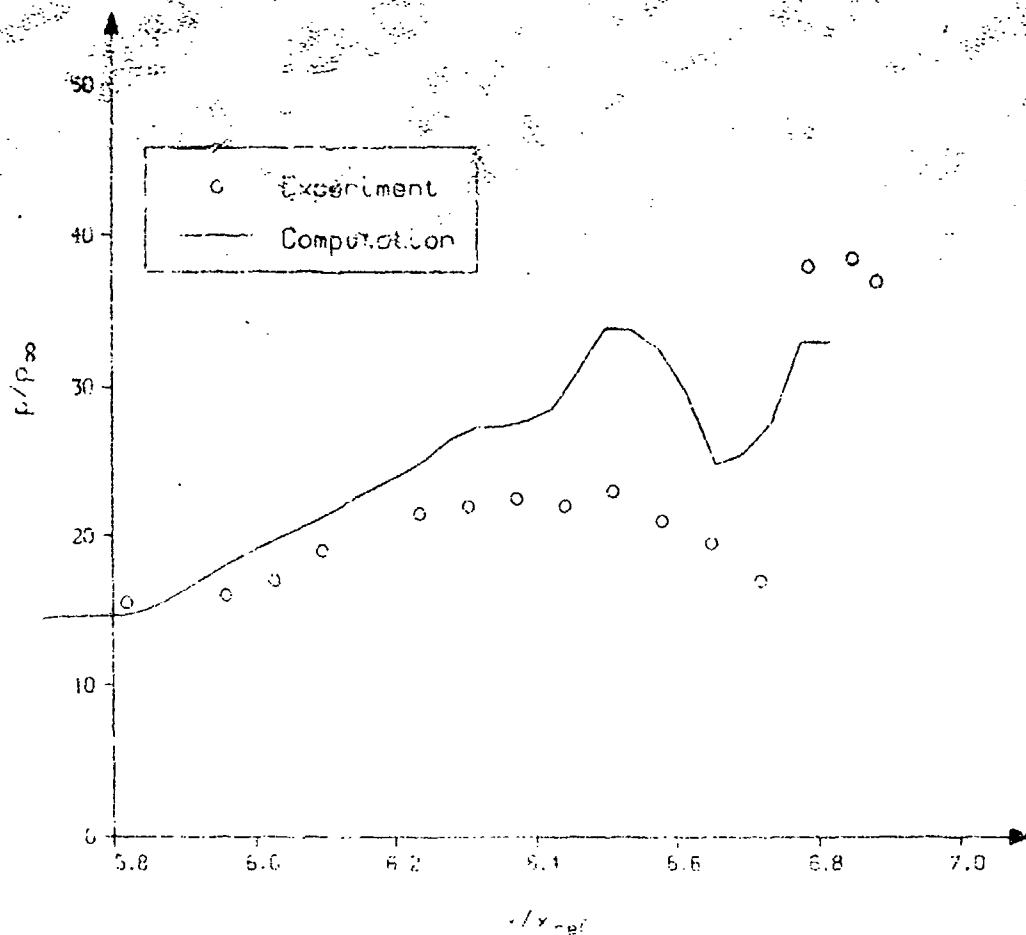


Fig. 1. Surface static pressure on the cowl of the inlet with adiabatic wall condition

A colour reproduction of this  
illustration can be found on  
fiche number 5.

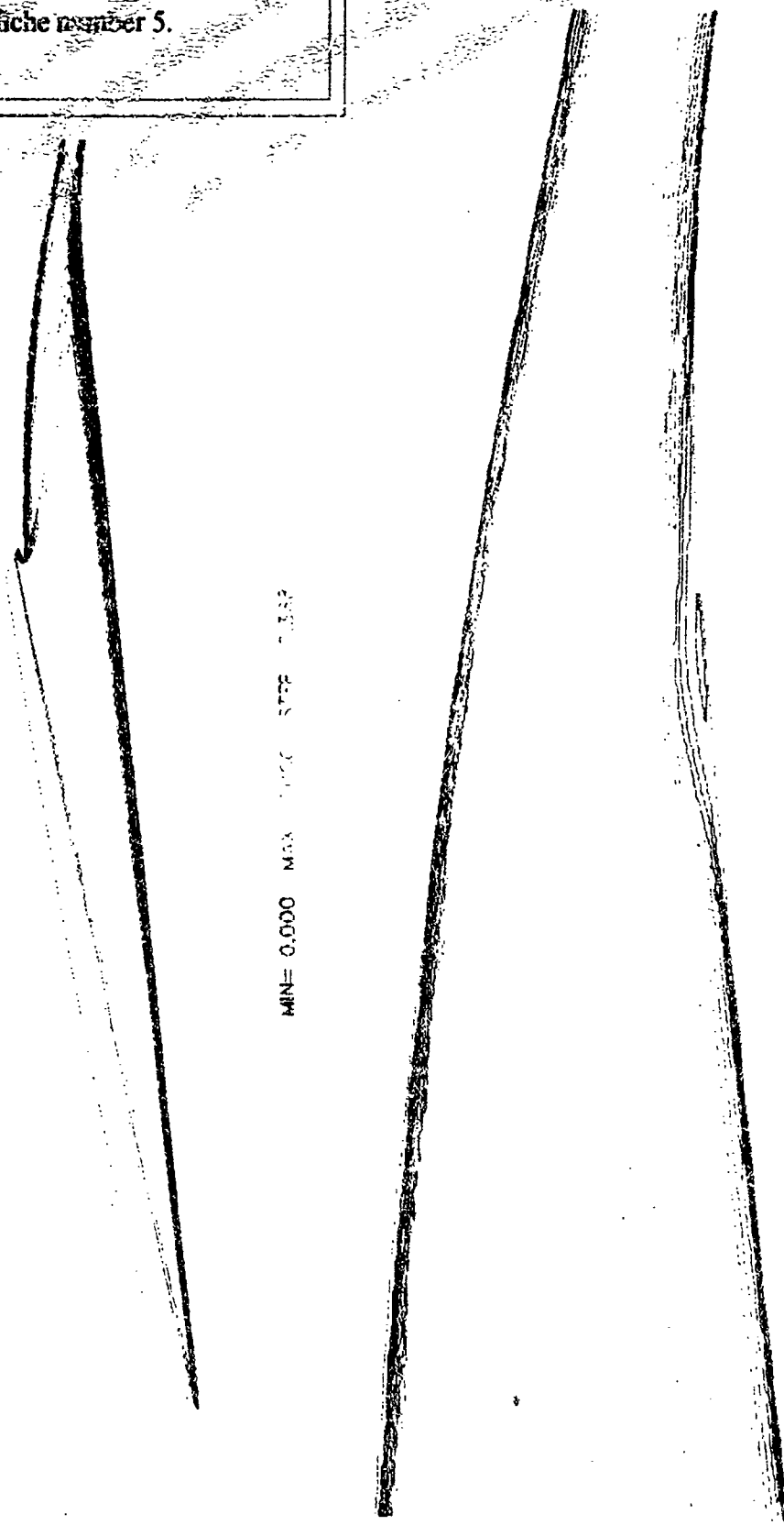


Fig. 14 Isolines of Mach number with adiabatic wall condition

May 15, 1990

Subject: AGARD Working Group 13, PARC Results

To : Tom Benson

The AEDC developed PARC code has been applied to four of the AGARD Working Group 13 test cases. Results were requested in the form of plotted data for preliminary screening and final results on magnetic media. We were unable to provide results in time for the preliminary screening, but are however now providing final results to three of the cases in the form of plotted data and magnetic media. At this time we have not received sufficient information regarding Case 7 to respond, even though a solution has been generated for one of the four geometries provided.

The three cases for final results are being provided are.

1. Case 1 : Transonic shock boundary layer
2. Case 2 : Glancing shock boundary interaction
3. Case 6 : NASA P8 inlet

Brief notes regarding these cases are included with the plotted results. Both Case 1 and Case 2 had deficiencies in the provided geometries and/or flow conditions that affected the final results.

The fourth case for which calculations were performed was Case 8 (Tailormate fuselage/inlet). A single solution has been generated at freestream conditions of Mach 0.9 and 0 degrees angle-of-attack. Inlet mass flow conditions were approximated based on information provided by Wright Research Development Center. At this time we have no information as to what data is to be returned as final results. We will gladly respond, given sufficient information.

James R. Sirbaugh  
Sverdrup Tech., Inc.  
Arnold Air Force Base, Tn.  
37389

(615) 454-3475

## Attachment III

## Re-Submittal:

## AGARD Test Case 6, NASA P8 Inlet

AGARD Test Case 6: NASA High Aspect Ratio Mixed Compression Intake  
(supersonic part only)

## A. CrD Methodology

code definition: 2D single block and multi-block PARC

code reference:

gas model: ideal constant gamma (=1.4)

turbulence model: Baldwin-Lomax

## B. Computer Resources

CPU time(CRAY-XMP): 10000 seconds

no. of iterations: 2000 (multi-block code)

memory requirements/grid size:

4 blocks; total of 146200 grid points

largest block &lt; 50000 points to fit XMP core

memory requirements

## C. Boundary Conditions/Starting Conditions

inflow boundary: fixed supersonic at freestream conditions

 $P_{\infty} = 600$  psia ;  $T_{\infty} = 1460^{\circ}\text{R}$  ;  $M_{\infty} = 7.58$ 

outflow boundary: fixed static pressure and temperature

 $P/P_{\infty} = 0.001452$  ;  $T/T_{\infty} = 0.08006$  (external flow) $P/P_{\infty} = 0.004354$  ;  $T/T_{\infty} = 0.2115$  (inlet flow region)

ramp/inlet surfaces: isothermal no-slip boundaries

 $T/T_{\infty} = 0.3738$ 

initial conditions: outer flow region set to freestream conditions

inlet region set to mach no. behind  
cowl shock

## D. Convergence

solution considered converged when maximum residual reduced  
to less than  $10^{-7}$ 

## E. Solution Quality Redundancy Checks

none performed

## F. Experience in obtaining solution

started with single block grid(200x130)....was found to be  
inadequate to resolve boundary layers, shocks, etc.  
went to multi-block problem

## G. Special Tricks or Techniques

1. used experimentally determined laminar to turbulent transition point on ramp. Boundary layer models switched in code at that point to obtain better boundary layer thickness in inlet

2. used option in code to fix inlet surface temperatures
3. used grid blocking to pack grid points in regions of high gradients
4. fixed freestream mach no. to value expected at inlet entrance region based on tunnel experimental data

special note: cowl shock intersection with centerbody boundary layer caused small separation bubble  
 ....This is reflected in the centerbody static pressure plot at  $x/x_{ref} = 6.0$

AGARD Test Case 6: NASA P8 high aspect ratio mixed compression intake (supersonic part only)

The test was conducted in the NASA-Ames 3.5-foot Hypersonic Wind Tunnel at a nominal test mach number of 7.4 and freestream Reynolds number of  $2.7 \times 10^6$  per foot. The geometry consisted of a scaled hypersonic inlet model, combined with a wedge forebody to simulate the flowfield conditions at the entrance of the internal passage shown in the attached figure. Other conditions were total pressure of 600 psia. and total temperature of 1460°R. The wedge angle was seven degrees and the design inlet pressure compression ratio was eight.

The analysis performed was on the centerplane of the inlet allowing for 2-dimensional computations. The 2-d Blocked PARC code was used with 146000 grid points in 4 blocks.

In addition to the above assumptions, the laminar to turbulent boundary layer transition point on the wedge was also simulated. This transition was indicated experimentally using a flourine-sublimation technique.

Examination of the attached data plots shows differences between experimental results and PARC results. There are two known sources of error in the results.

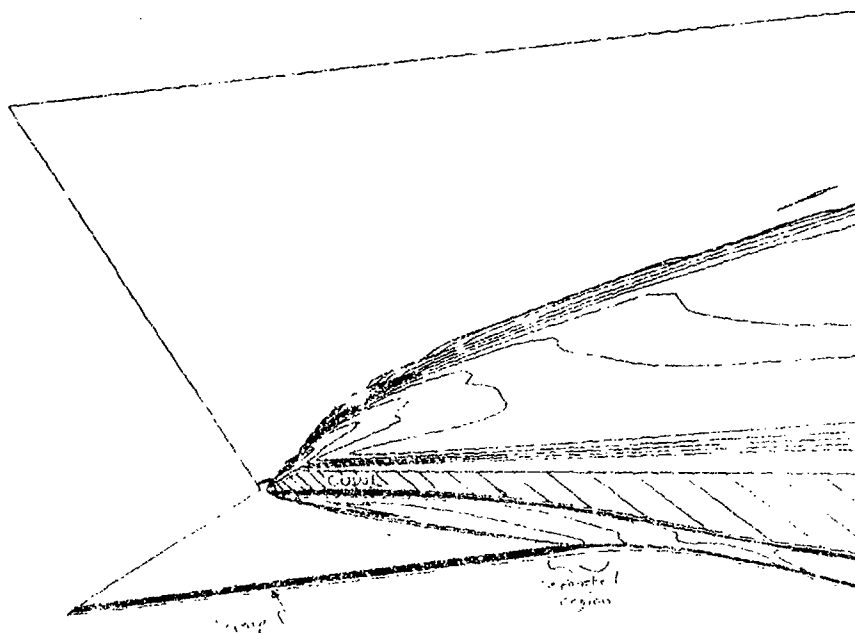
1.) Experimental freestream conditions were not uniform in the test section. The mach number varied from the nominal value of 7.4 at the wedge tip to 7.58 at the inlet entrance station. Flow angularity variations were also observed. The data for these off-nominal freestream conditions were not given. A uniform freestream mach number of 7.58 was used to best simulate conditions in the inlet entrance region.

2.) The geometry definition given to us is inadequate due primarily to an insufficient number of points defining the internal surfaces of the inlet. Supersonic flow in a channel is sensitive to not only surface slopes, but also derivatives of the slopes. Differences in indicated inlet heights, at given inlet x-stations, is a reflection of the non-uniform spacing of the base spline points that were provided.

AGARD HYPERSONIC NOZZLE (COOLED)  
MACH NO. CONTOURS

COLOR LEVEL LOG. R P<sub>0</sub>

2.000×10<sup>0</sup>  
2.500×10<sup>0</sup>  
3.000×10<sup>0</sup>  
3.500×10<sup>0</sup>  
4.000×10<sup>0</sup>  
4.500×10<sup>0</sup>  
5.000×10<sup>0</sup>  
5.500×10<sup>0</sup>  
6.000×10<sup>0</sup>  
6.500×10<sup>0</sup>  
7.000×10<sup>0</sup>  
7.200×10<sup>0</sup>  
7.300×10<sup>0</sup>

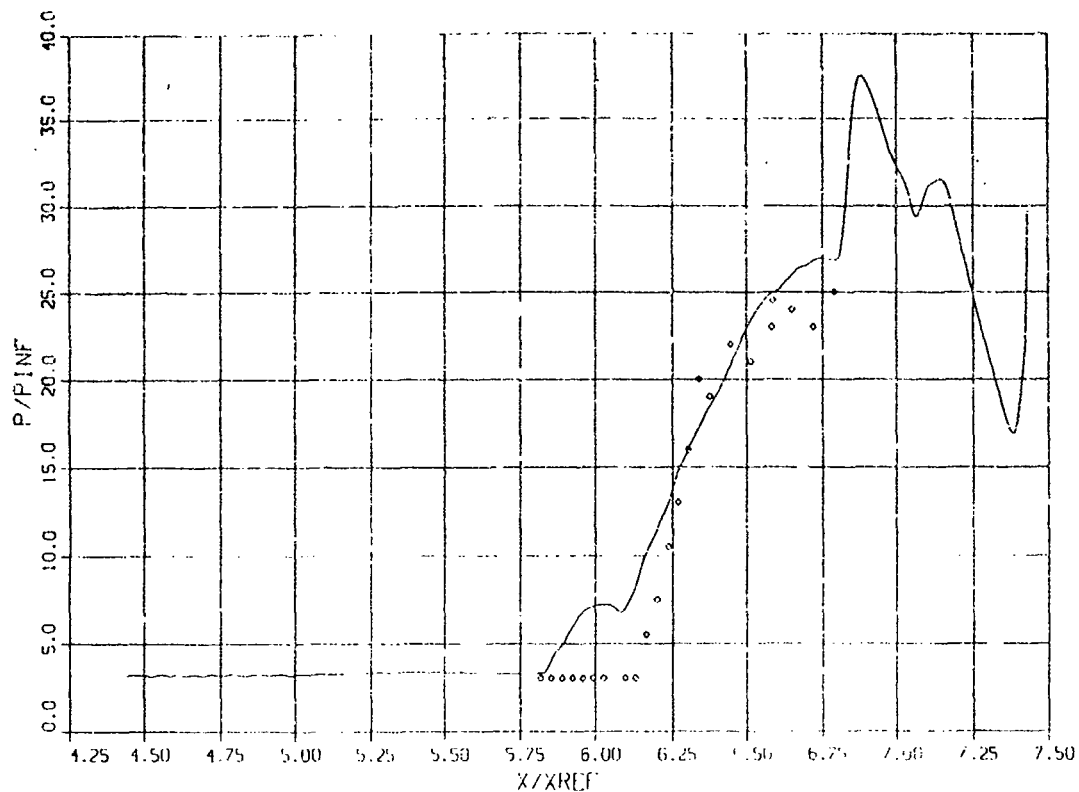




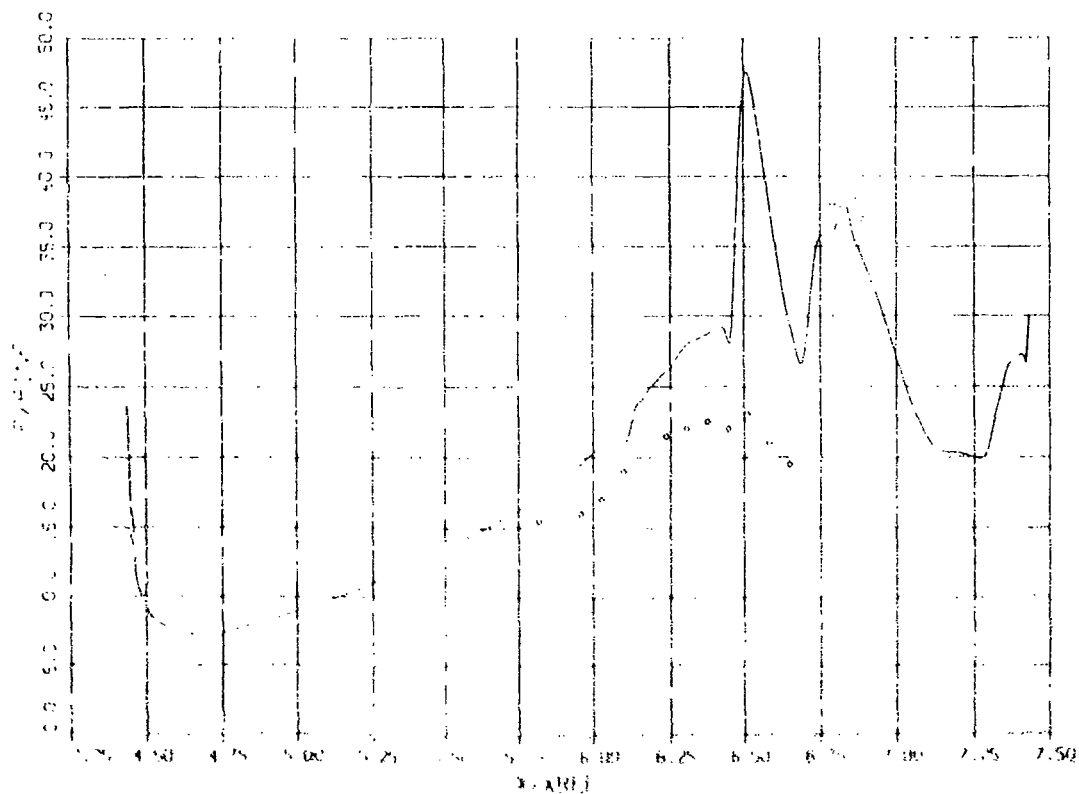
## CENTERBODY STATICS

— AEDC PARC

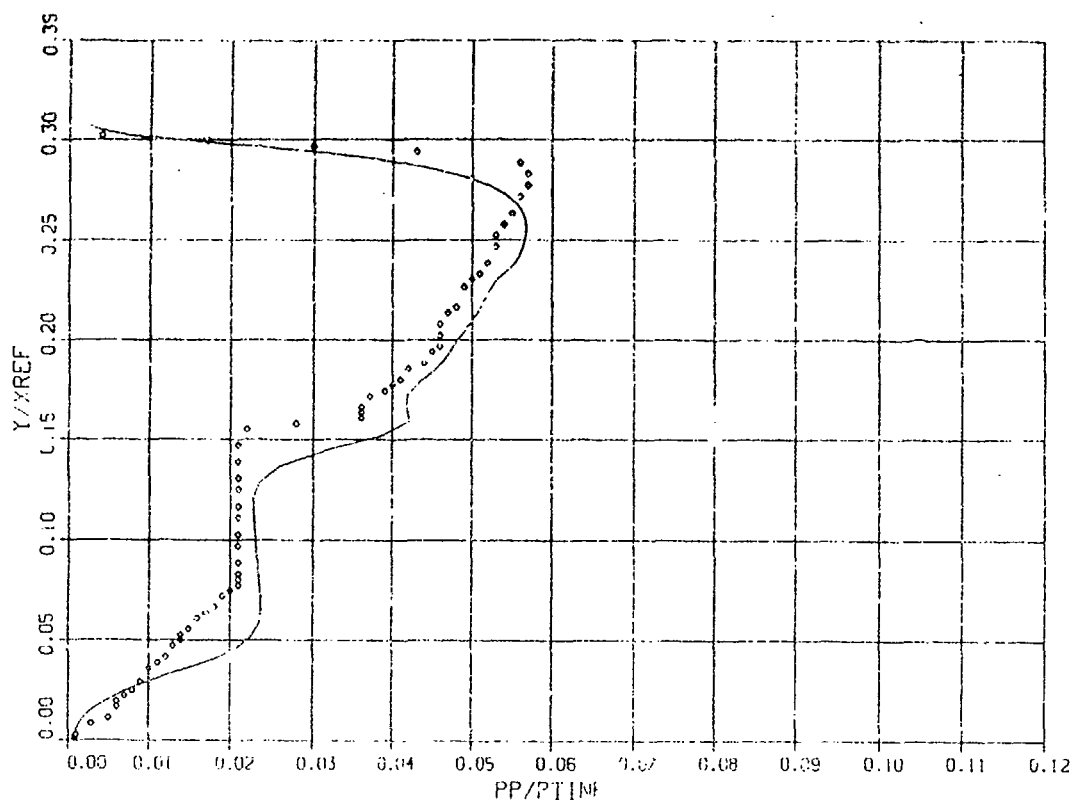
○ EXPERIMENT



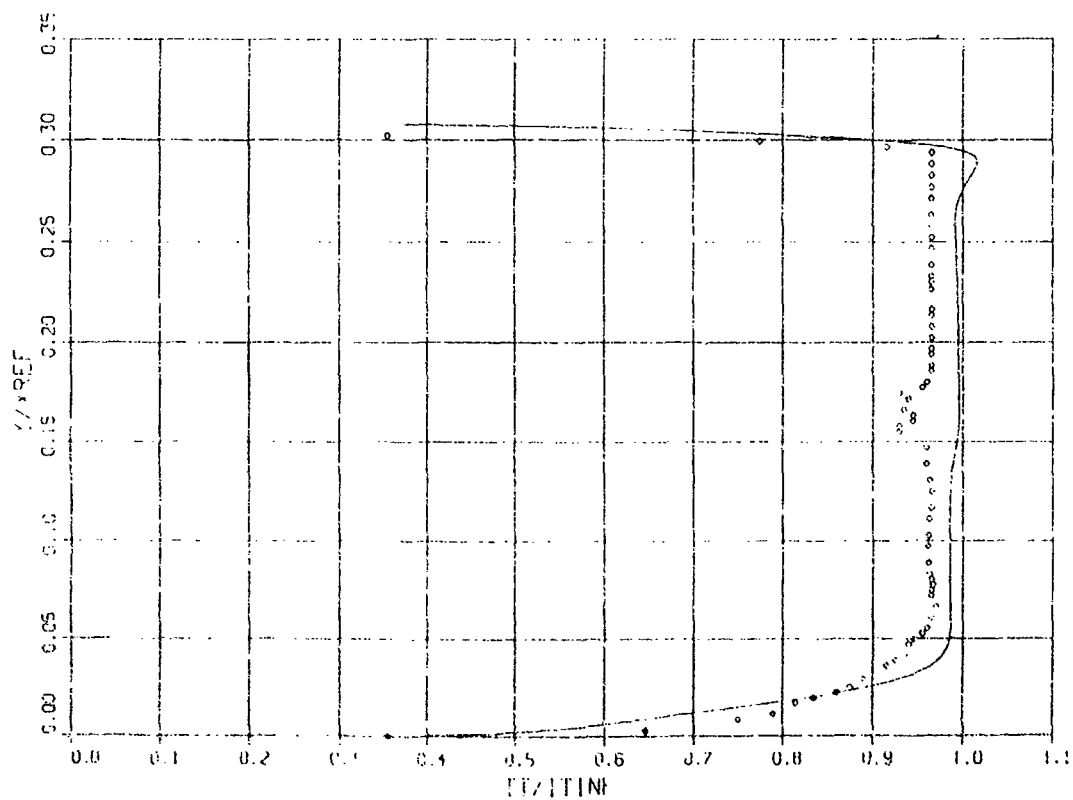
## COWL STATICS



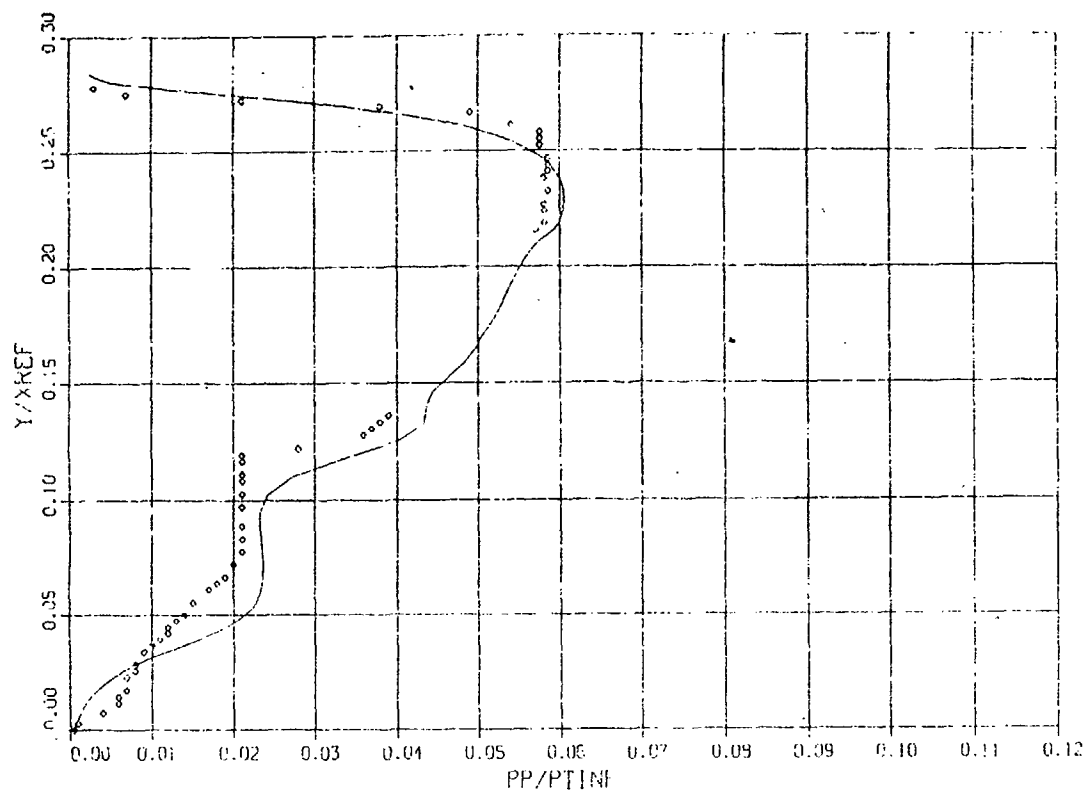
PITOT PRESSURE  
 $X/X_{REF} = 5.67$



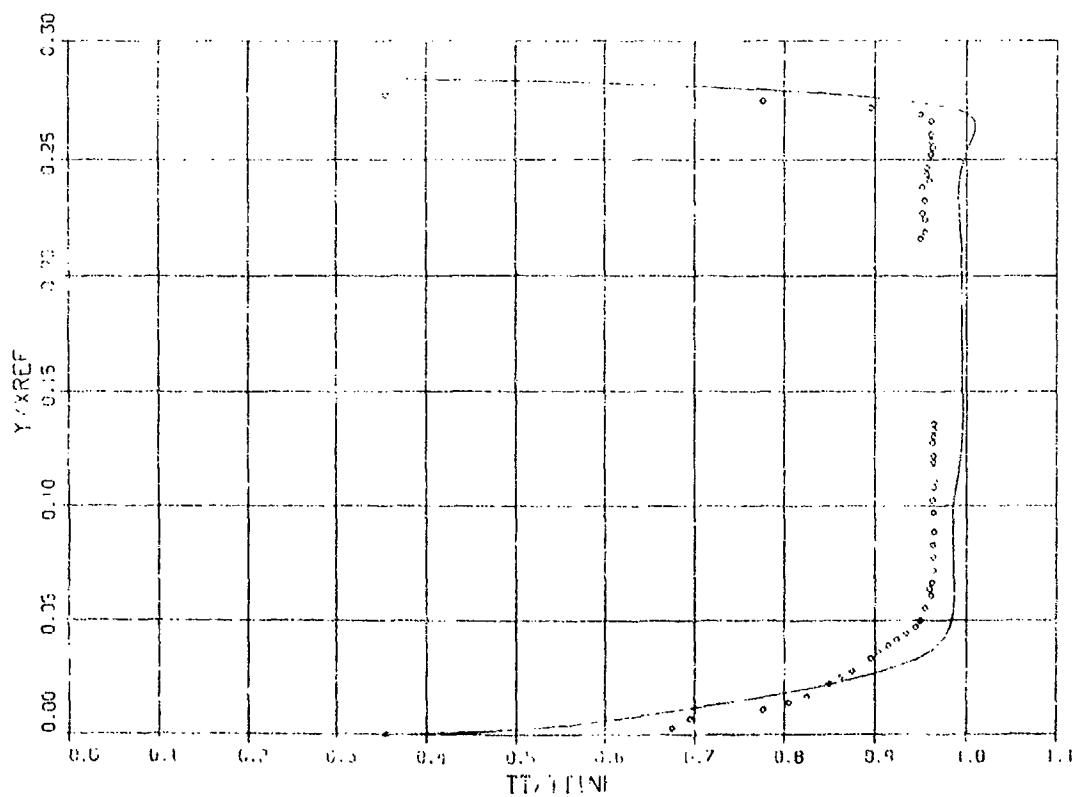
TOTAL TEMPERATURE  
 $X/X_{REF} = 5.67$



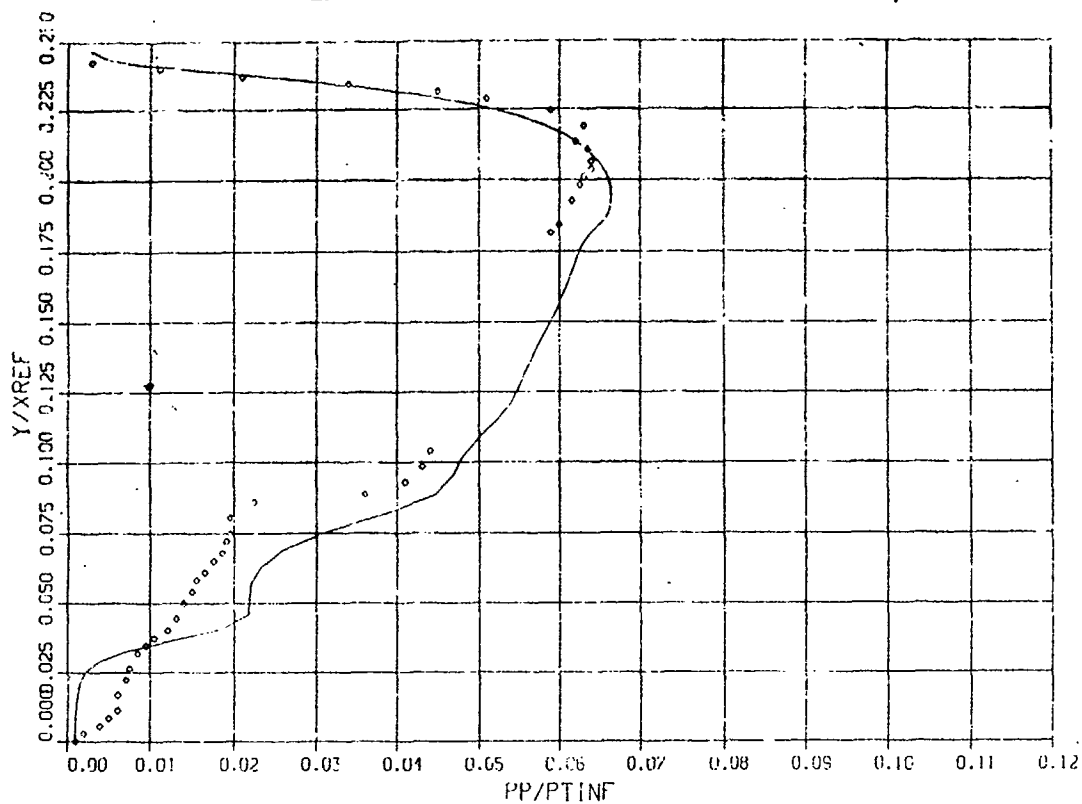
PITOT PRESSURE  
 $X/XREF = 5.78$



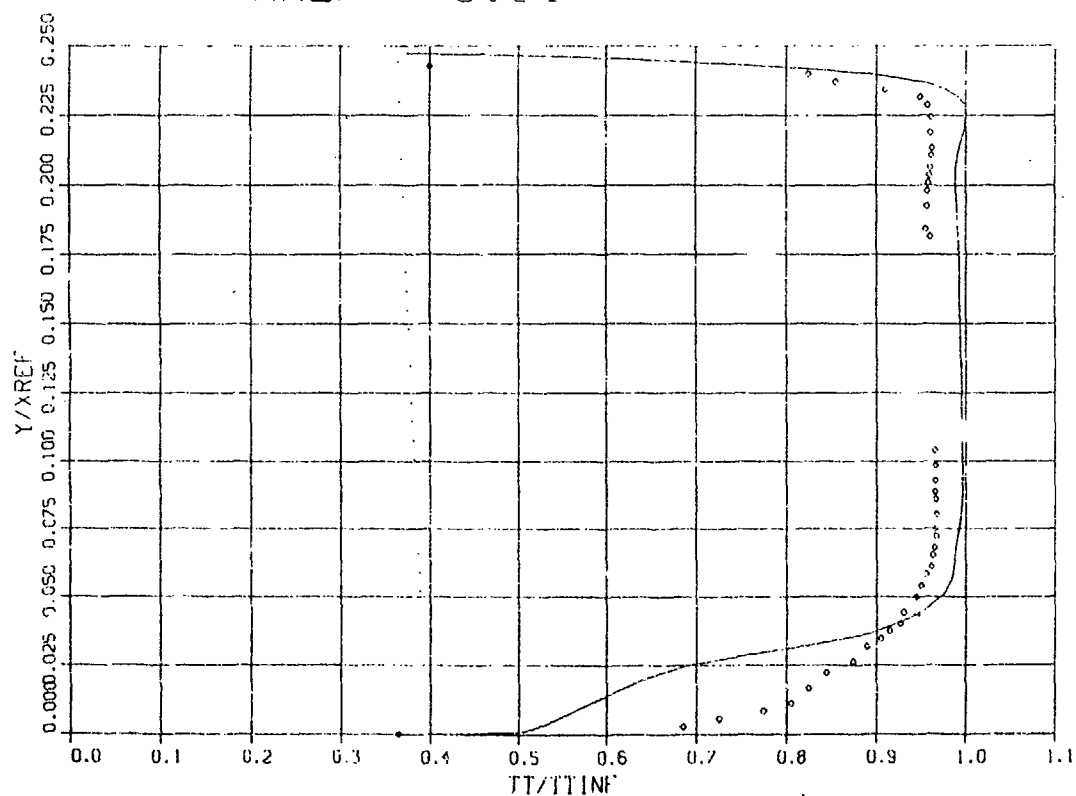
TOTAL TEMPERATURE  
 $X/XREF = 5.78$



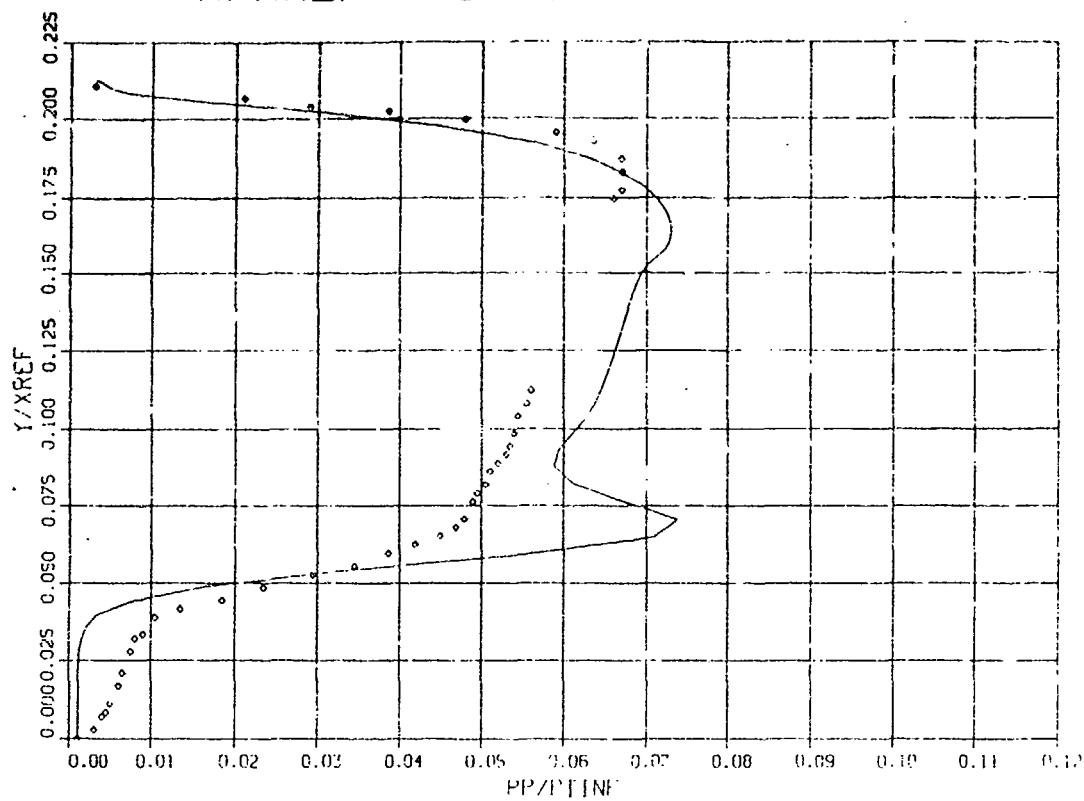
PITOT PRESSURE  
 $X/X_{REF} = 5.94$



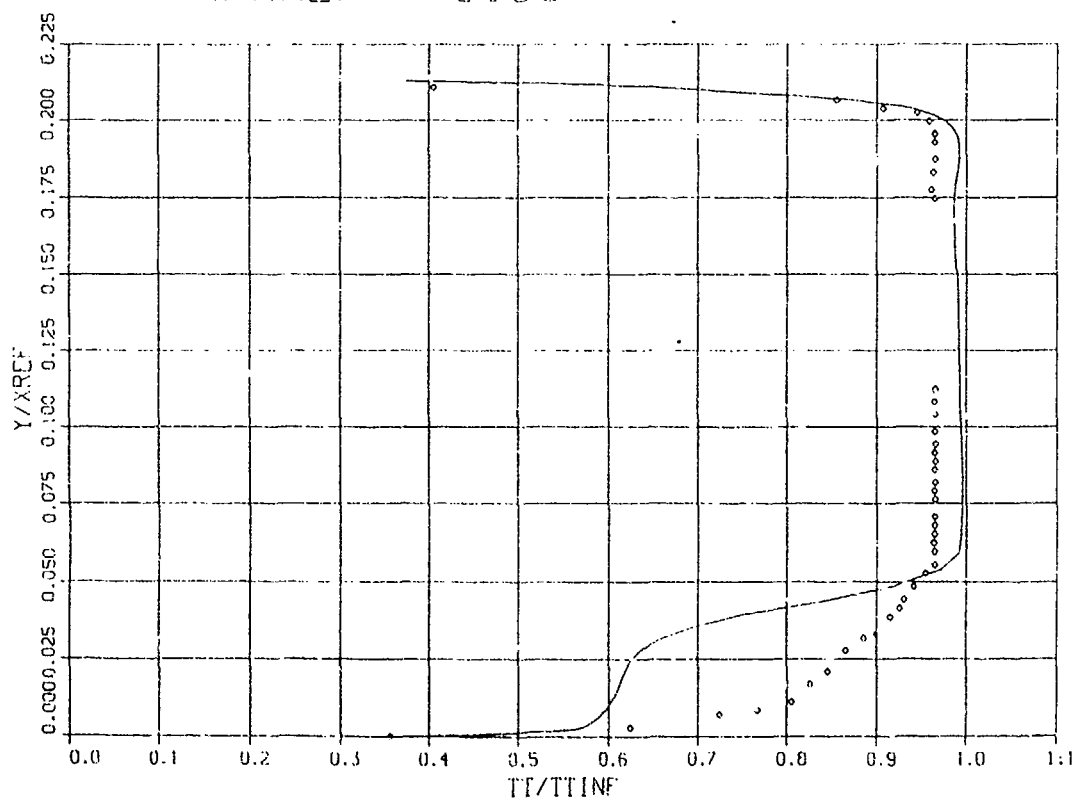
TOTAL TEMPERATURE  
 $X/X_{REF} = 5.94$



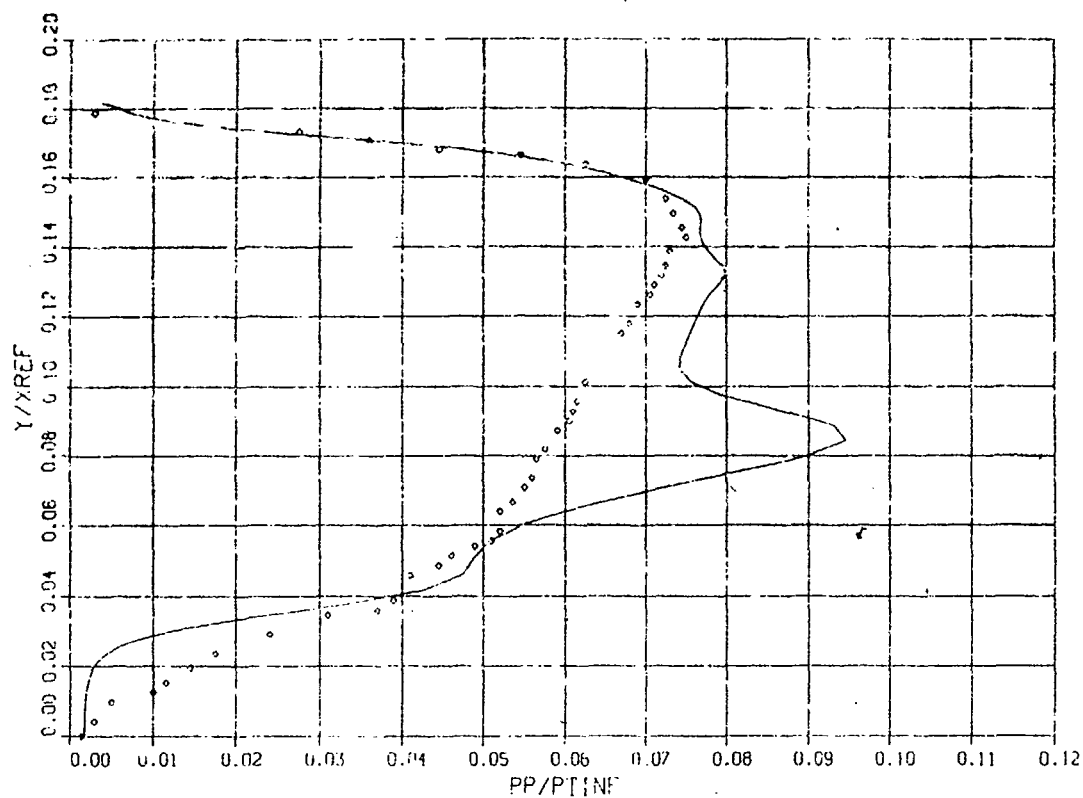
PITOT PRESSURE  
 $X/X_{REF} = 6.09$



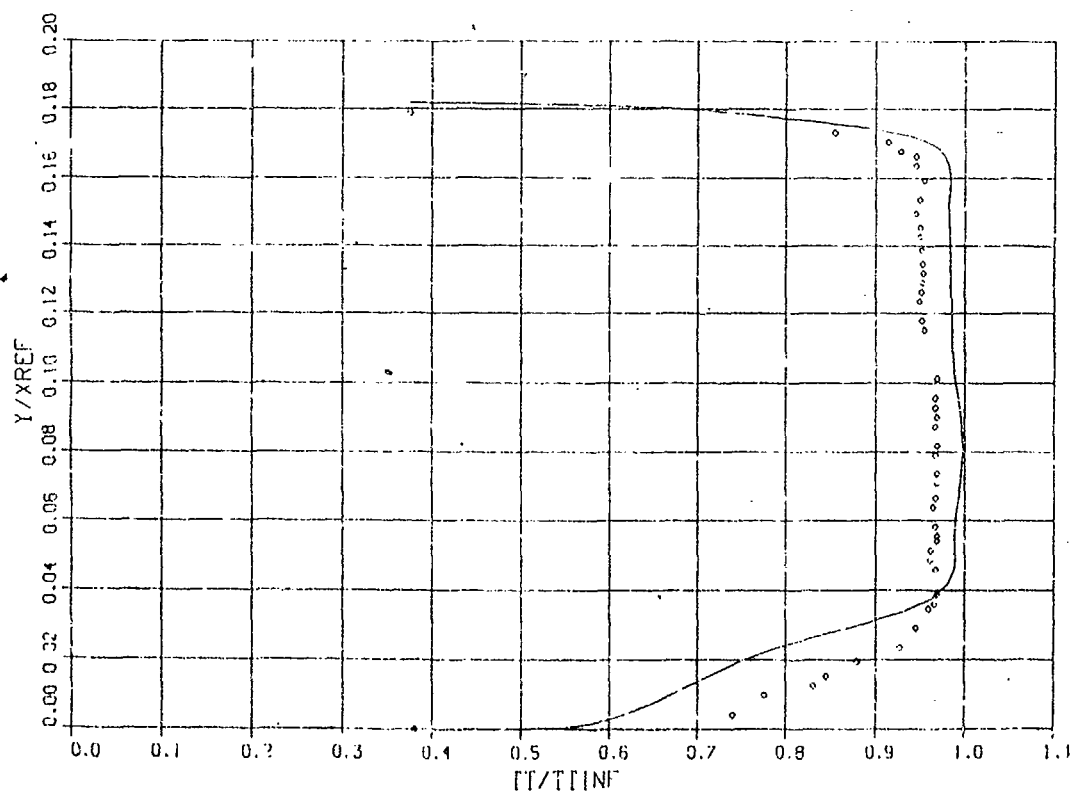
TOTAL TEMPERATURE  
 $X/X_{REF} = 6.09$



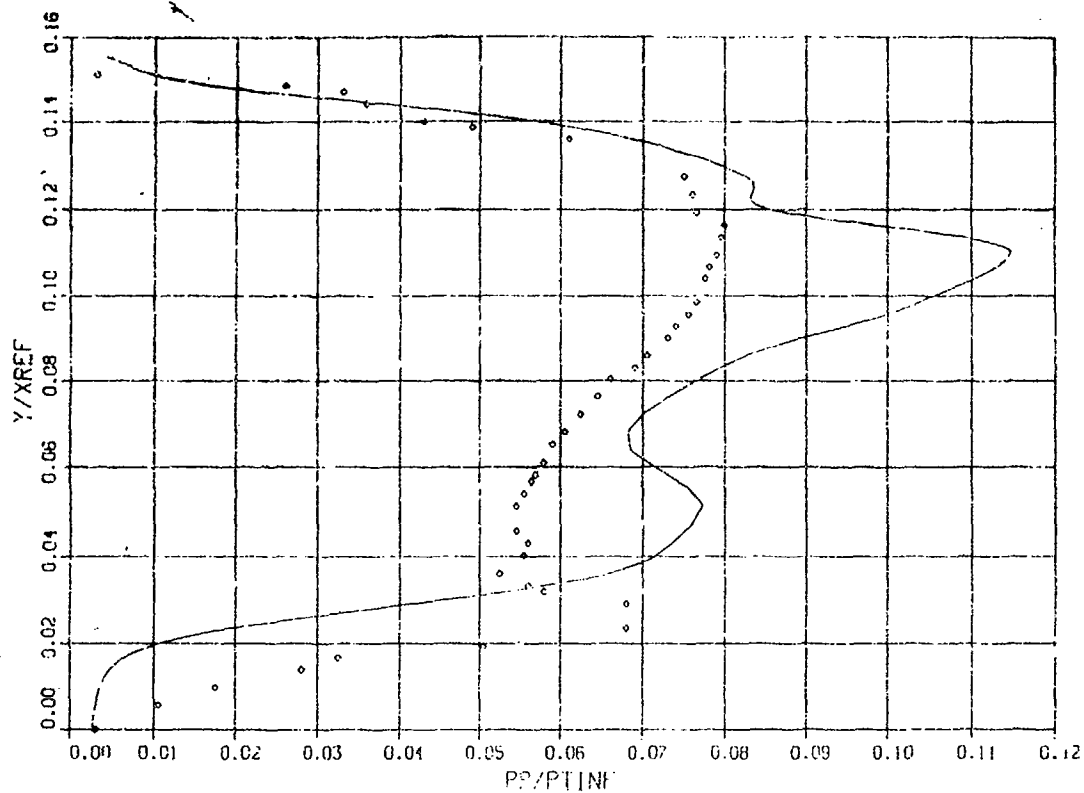
PITOT PRESSURE  
 $X/X_{REF} = 6.23$



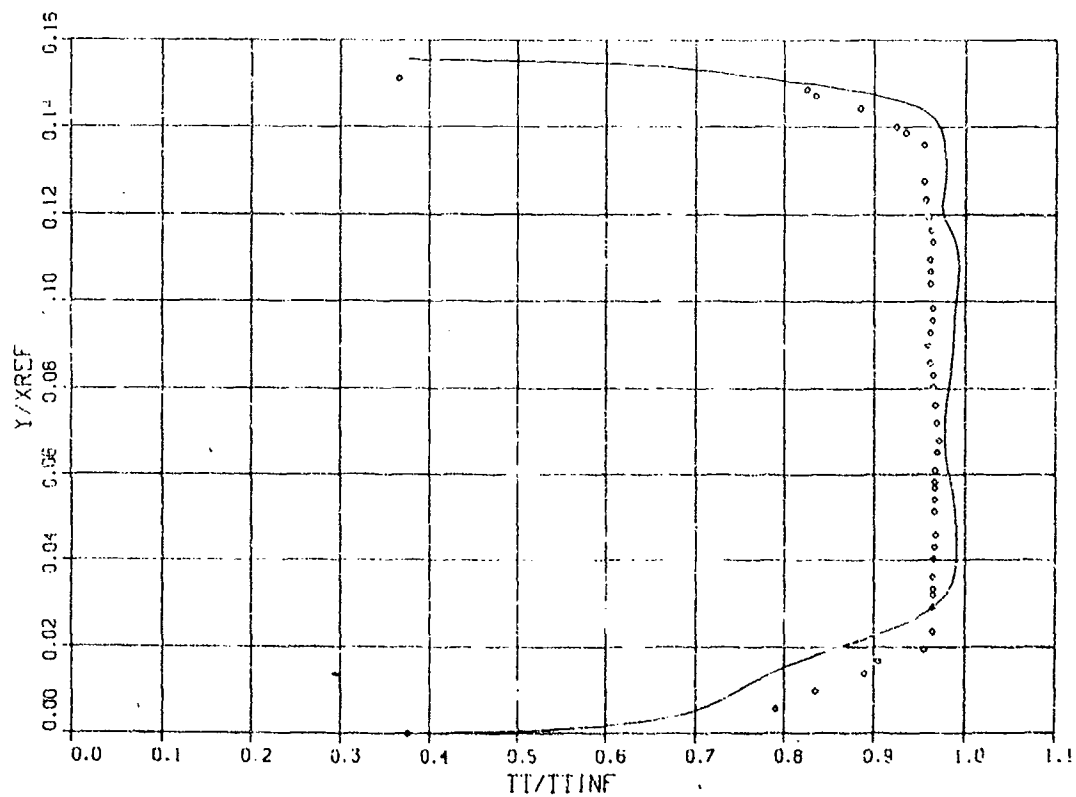
TOTAL TEMPERATURE  
 $X/X_{REF} = 6.23$



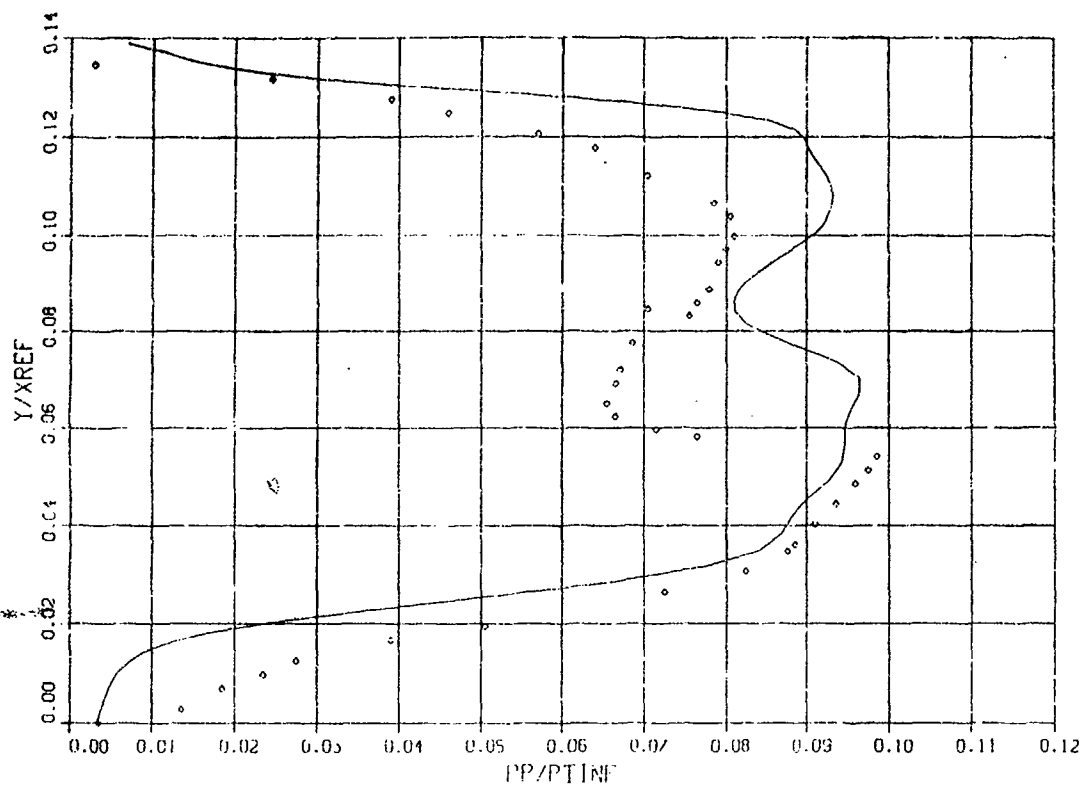
PITOT PRESSURE  
 $X/XREF = 6.37$



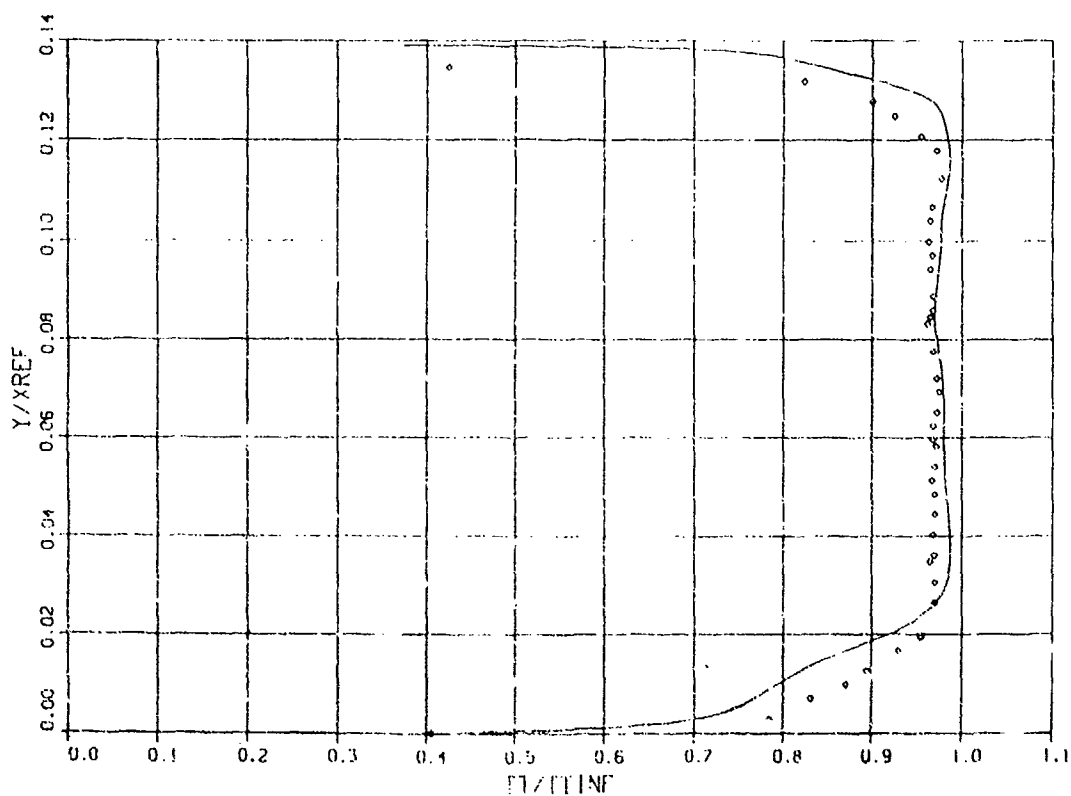
TOTAL TEMPERATURE  
 $X/XREF = 6.37$



PITOT PRESSURE  
 $X/XREF = 6.51$

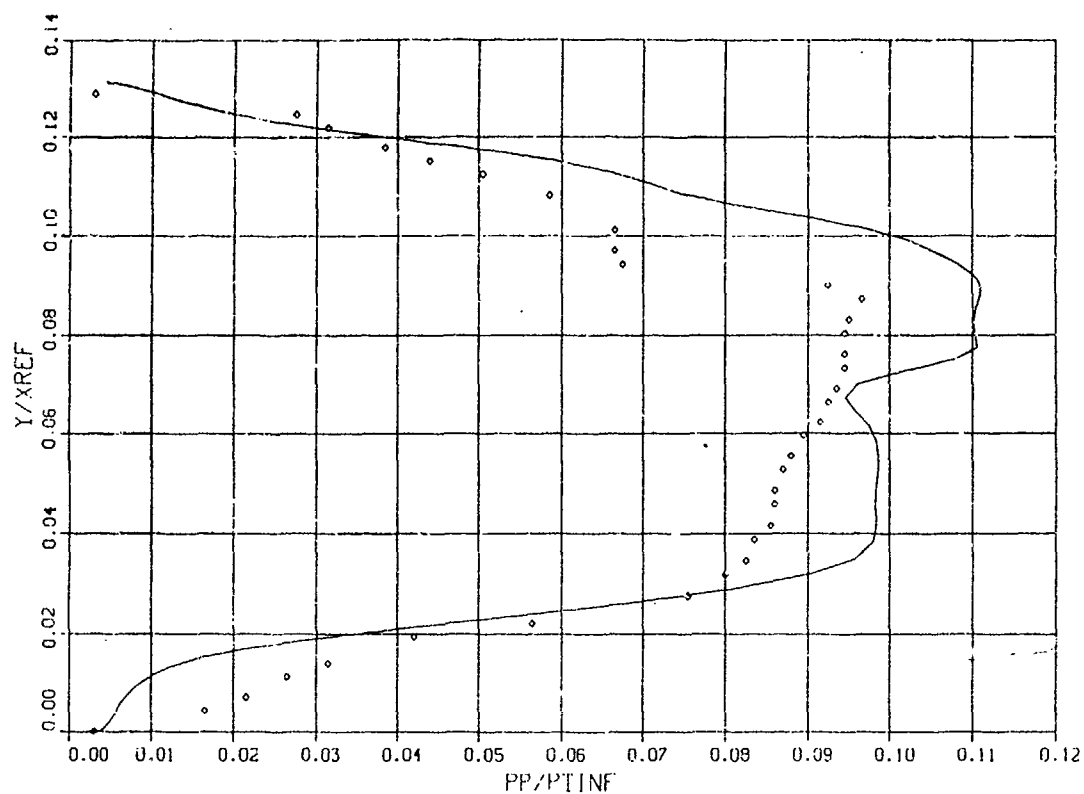


TOTAL TEMPERATURE  
 $X/XREF = 6.51$

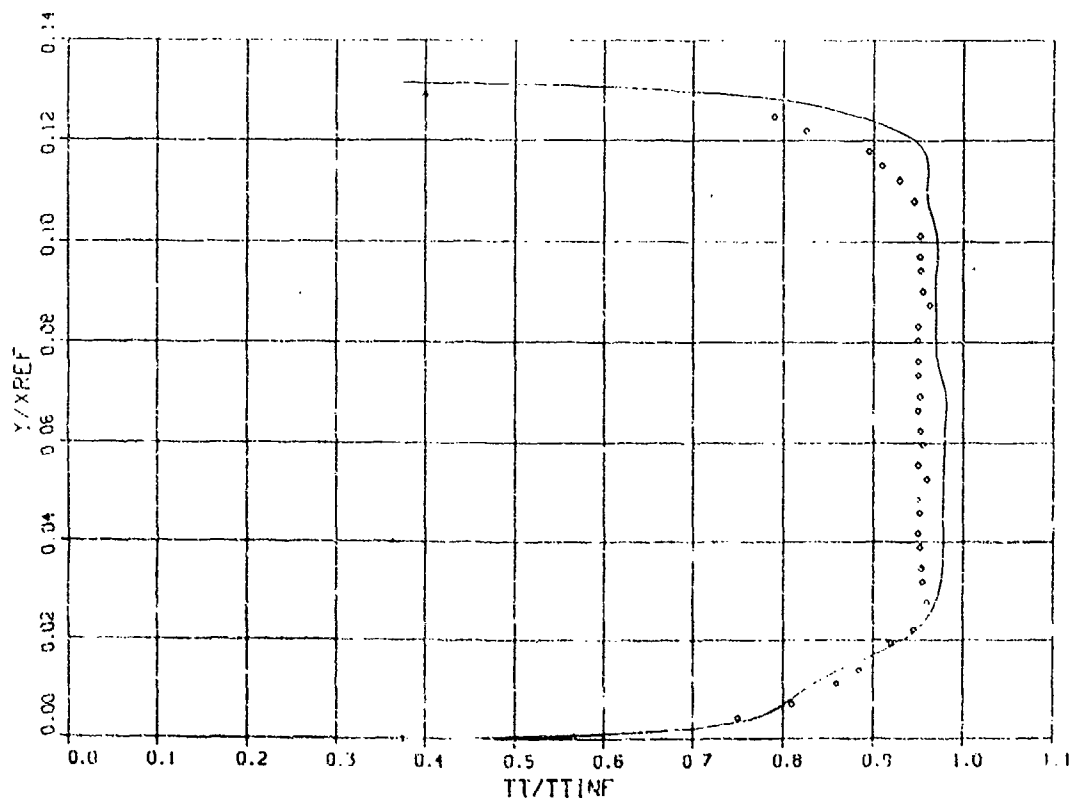




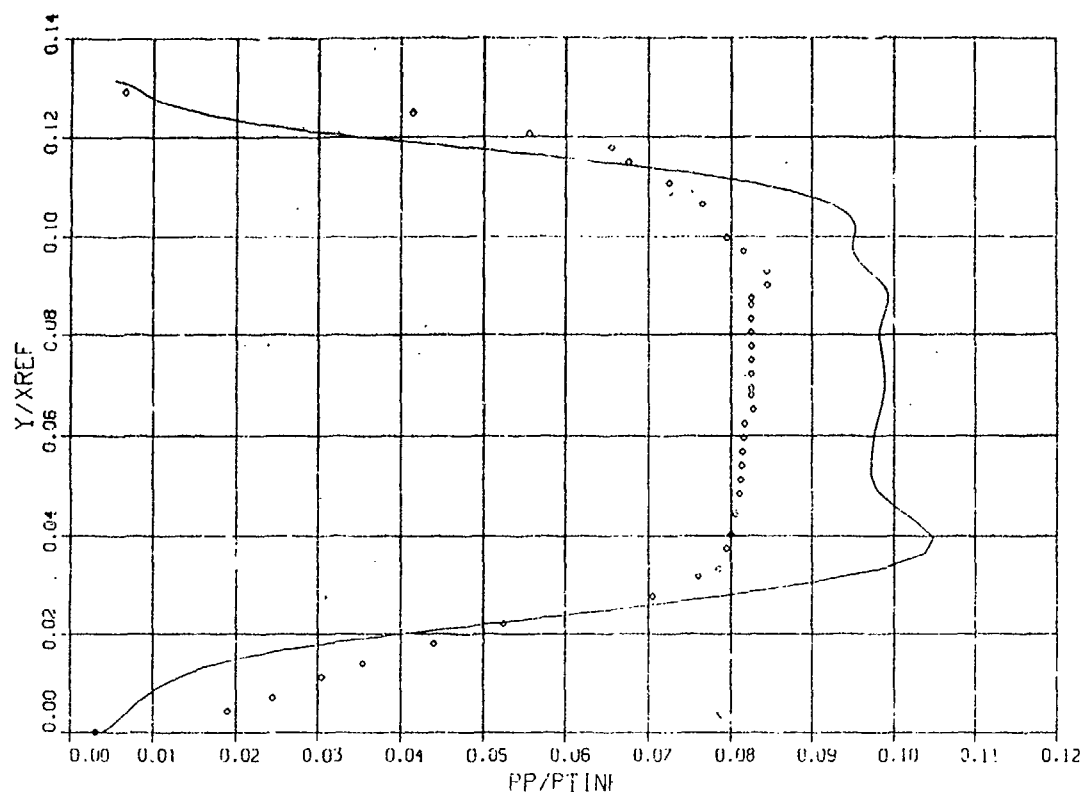
PITOT PRESSURE  
 $X/X_{REF} = 6.65$



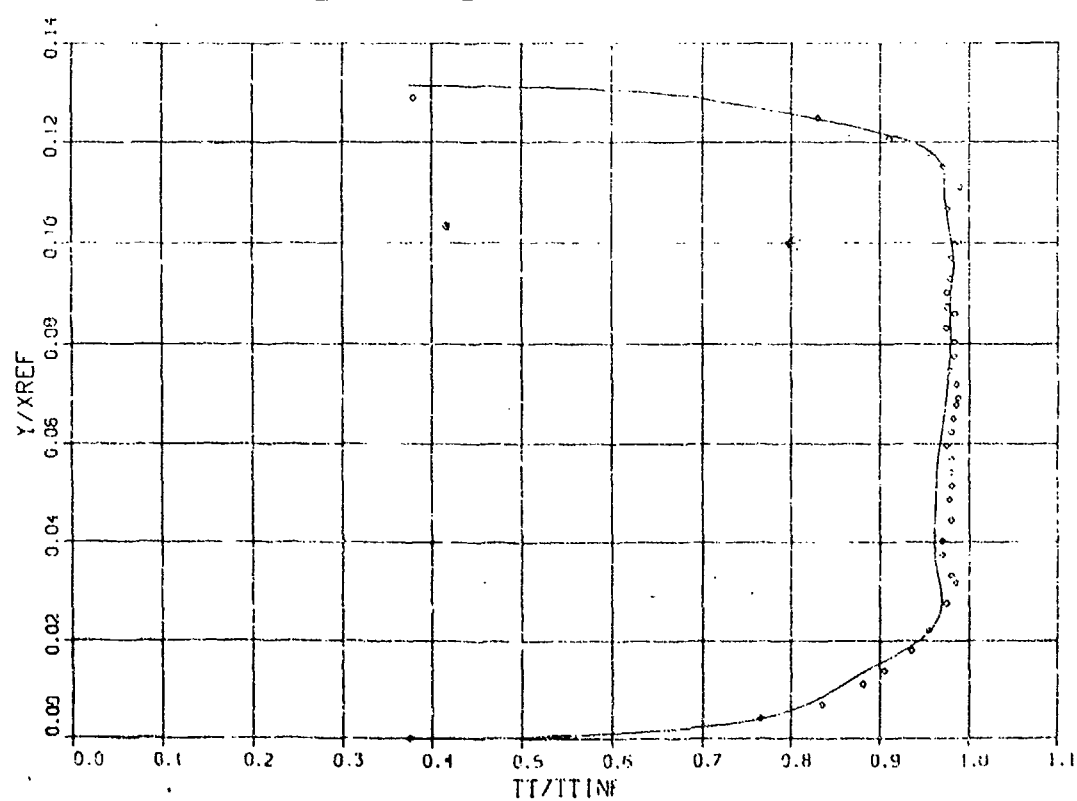
TOTAL TEMPERATURE  
 $X/X_{REF} = 6.65$



PITOT PRESSURE  
 $X/X_{REF} = 6.79$



TOTAL TEMPERATURE  
 $X/X_{REF} = 6.79$



## Test Case 6 - Hypersonic Inlet

William G. Kunik and Thomas J. Benson  
National Aeronautics and Space Administration  
Lewis Research Center  
Cleveland, Ohio 44135

A three-dimensional Parabolized Navier-Stokes code has been used to investigate the flow through the P-8 Mach 7.4 inlet. Parametric studies of grid resolution, and turbulence modeling have been conducted in both two and three dimensions, although the results presented here represent the best of these calculations. The results indicate a significant three dimensional effect exists in this nominally two dimensional inlet. This effect has been caused by the glancing shock/boundary layer interaction present on the inlet sidewall as the internal cowl shock reflects from the ramp and cowl surfaces.

The three-dimensional supersonic viscous marching analysis used in this study is the PEPSIS code. The code solves the PNS equations for supersonic flow by an efficient Briley-McDonald, linearized block implicit scheme. The code solves for the flowfield in a single sweep, can be run with a variety of turbulence models, in either two or three dimensional mode, and can either solve the energy equation or impose constant stagnation enthalpy. The two dimensional result presented in the enclosed figures was run on a CRAY-XMP at the Lewis Research Center on a 130x1200 grid with constant stagnation enthalpy imposed. Each flow computation required about five minutes of CPU time with much more time used to refine grids, post process results, etc. The turbulence model used in this calculation is the standard McDonald-Camarata mixing length model with a compressibility correction based on the work of Bushnell and Beckwith. The calculation was started with uniform free stream conditions as specified in the report. This case was run fully turbulent; no transition model was used here, although one is available in the code.

Once the two-dimensional parametric study was completed, it was decided that the inlet should be examined three-dimensionally to determine the effect of the sideplates on the internal flowfield. Previous calculations of a Mach 5.0 inlet and benchmark studies of Test Case 2 indicate strong three-dimensional effects occur in rectangular inlet with sideplates, although the experiment did not provide sufficient instrumentation for detailed study of three-dimensional effects. The three-dimensional calculation employed a computational mesh of 100X50 mesh points in the cross plane, with a plane of symmetry along the inlet centerline. To simplify the calculations, the sideplate in the calculation begins at the cowl lip and is perpendicular to the ramp surface. In the experiment, the sideplate was cut back; the calculation does not model this cut back. The calculation was marched 1400 stations streamwise and required about two hours CPU time on the CRAY-XMP. The energy equation was solved in this computation; the

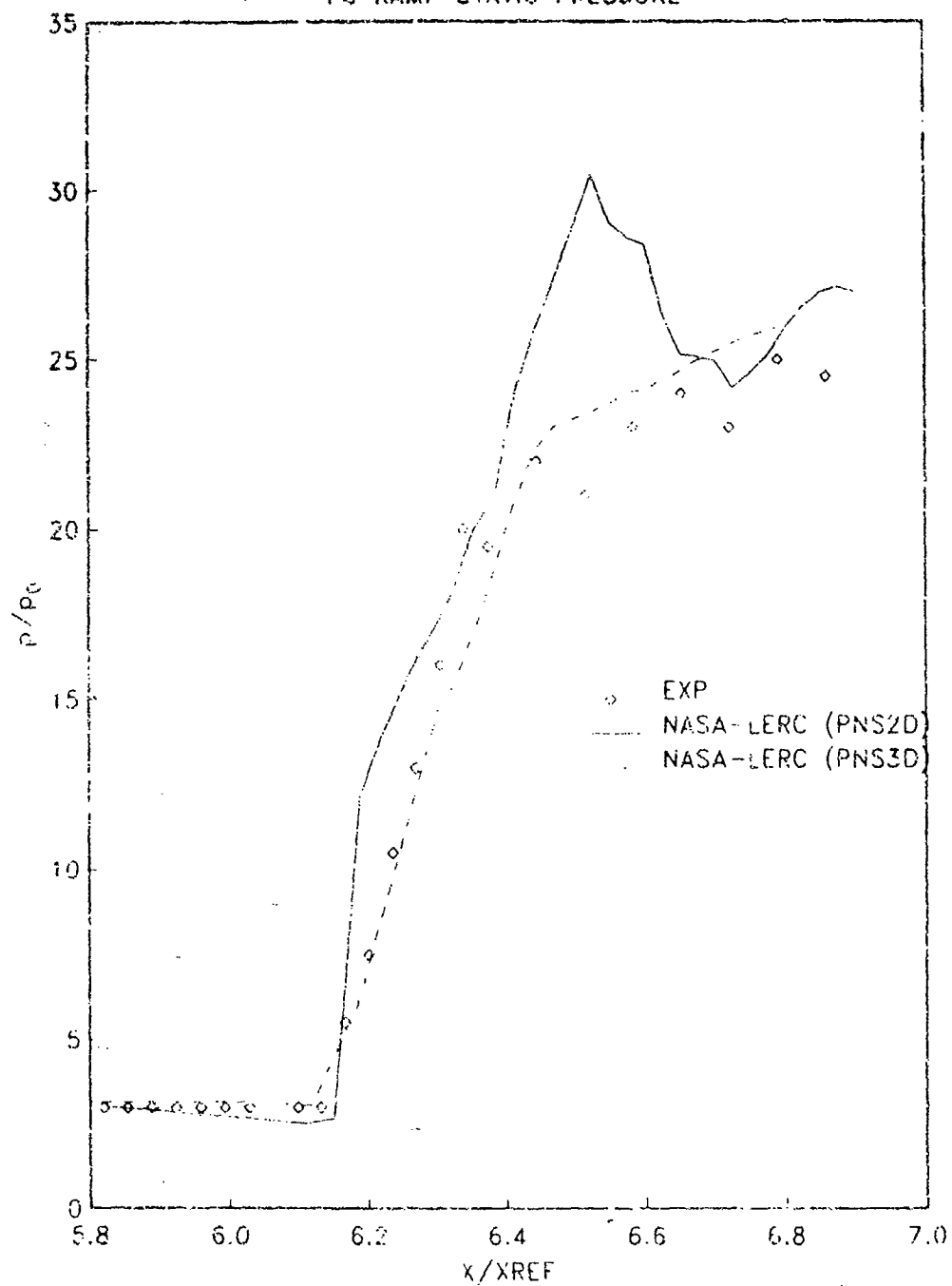
421

temperature results indicate some problems with this piece of the code ! All other conditions were run the same as the two dimensional calculation.

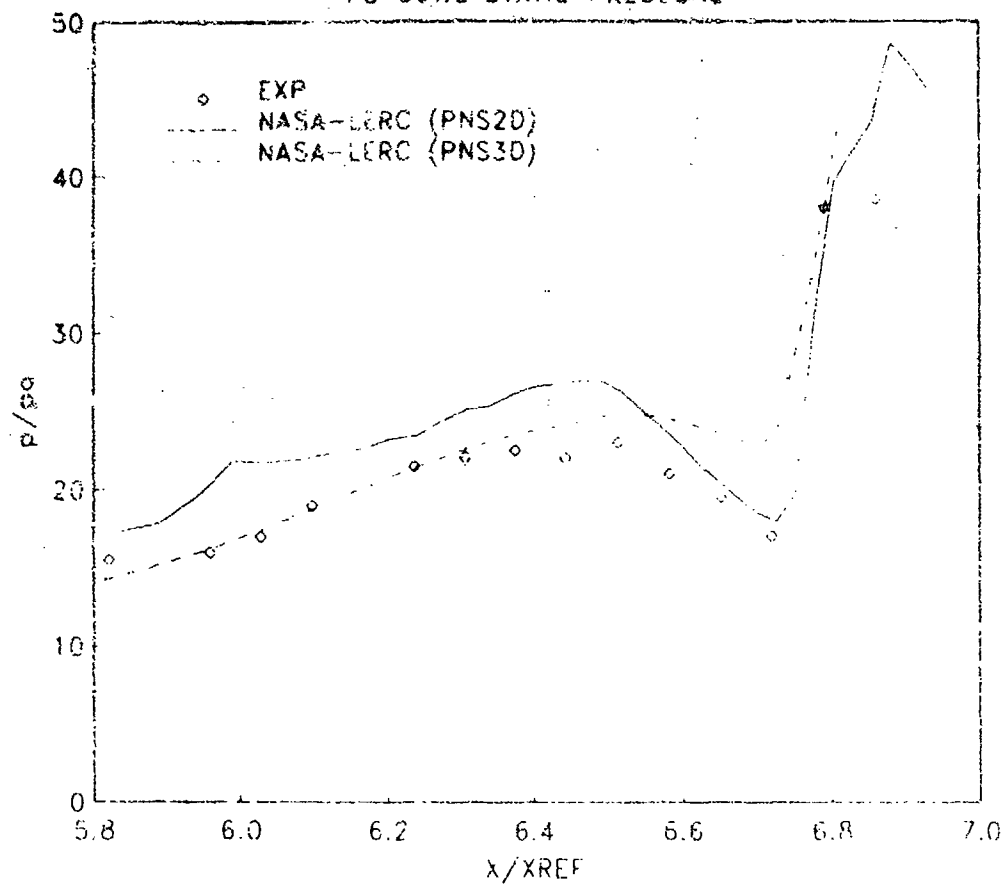
In general, the accompanying figures indicate that the three dimensional calculation compares much better with the experiment than the two dimensional calculation, with the exception of the temperature which is so non-physical that something is wrong in the code. We are submitting for this report some contour plots of the three dimensional calculation which indicate the computed three-dimensional nature of the flow in this inlet. These figures show Mach number contours and secondary velocity vectors at various Y-Z planes in the internal portion of the inlet. The bottom of the figures show the flowfield in a cross-section of the inlet; the ramp surface is on the bottom, the cowl surface is on the top, and the sideplates are on both sides. A side view of the inlet is shown at the top of each figure indicating with a vertical line the relative location of the plane in the inlet. An unreadable scale is shown on the left hand side for the Mach number contours and on the right hand side a reference vector of one-tenth of the free stream velocity is shown. Boundary layers are noted by the concentration of Mach contours near a solid surface and shock waves are shown as a concentration of Mach contours away from a solid surface. Shock waves are also noted in the secondary velocity vectors when the direction of the vectors change abruptly. The figures show that a vortex is formed on the back side of the shock wave as it glances across the sideplate boundary layer; this interaction was verified in Test Case 2. The vortex is pumping the low energy fluid in the cowl boundary layer down along the sideplate to the ramp surface. The Mach number contours show this by the thickening of the sideplate boundary layer on the back side of the shock wave. The vortex formed by the GSBLI has pumps fluid along the ramp surface toward the centerline of the inlet. The boundary layer in the lower corner has thickened much more than in the rest of the cross-section. The effect of the strong vortex is seen in the boundary layer along the ramp surface by its thickening to about the fifty per cent point in the spanwise direction.

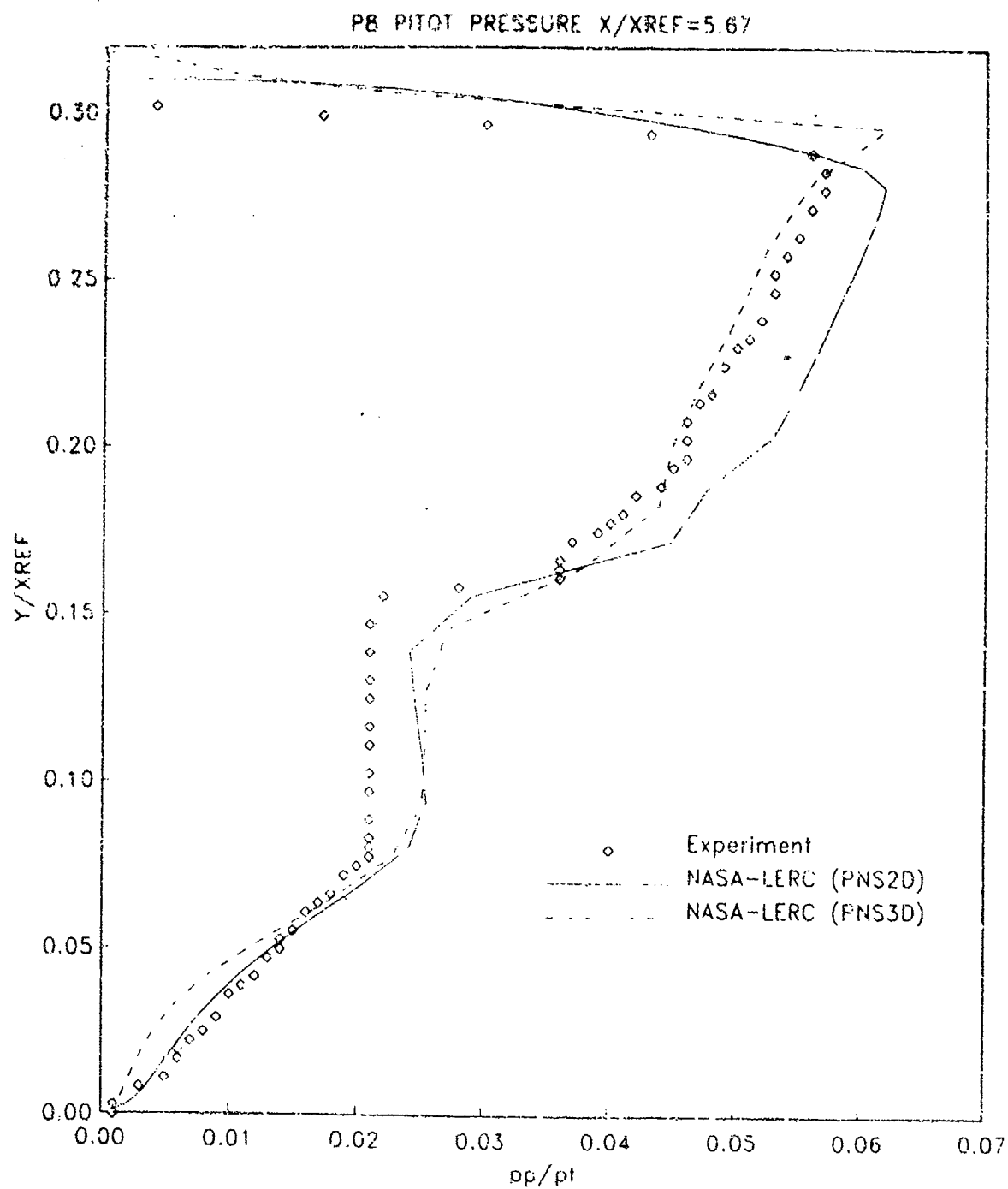
The three-dimensional calculation presented in this report have led to the following conclusions. The glancing shock/boundary layer interaction produces a strong vortex that persists throughout the internal passage of the inlet. This vortex redistributes the boundary layer into the lower corner of the inlet and then proceeds to distort the ramp boundary layer. To achieve a canceled shock wave in the inlet, the boundary layers effect on the shock wave interaction at solid boundaries must be taken into account. Also, the effect of the sideplates on the shock wave should lead the inlet designer to think in terms of three-dimensions instead of two.

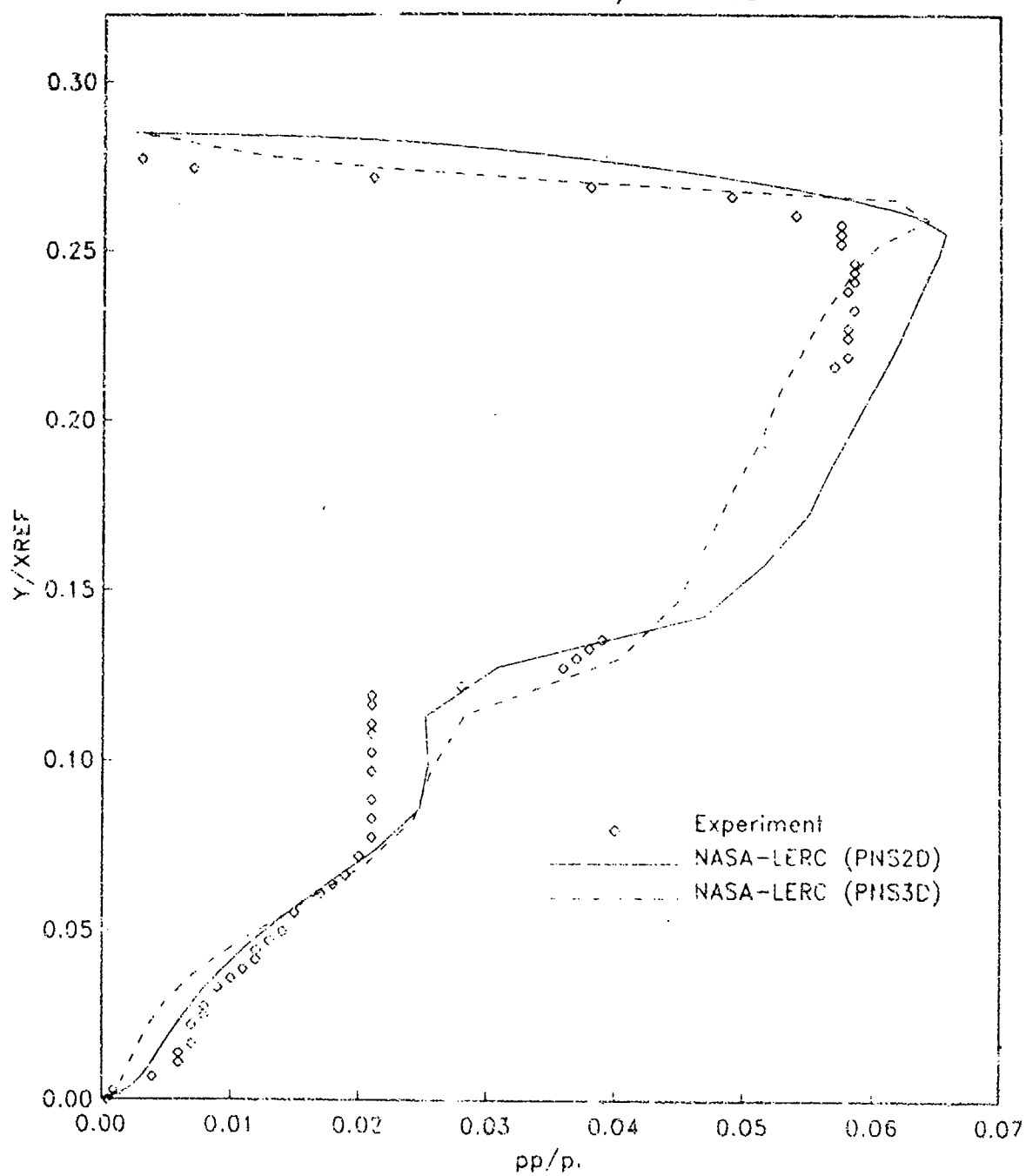
## P8 RAMP STATIC PRESSURE



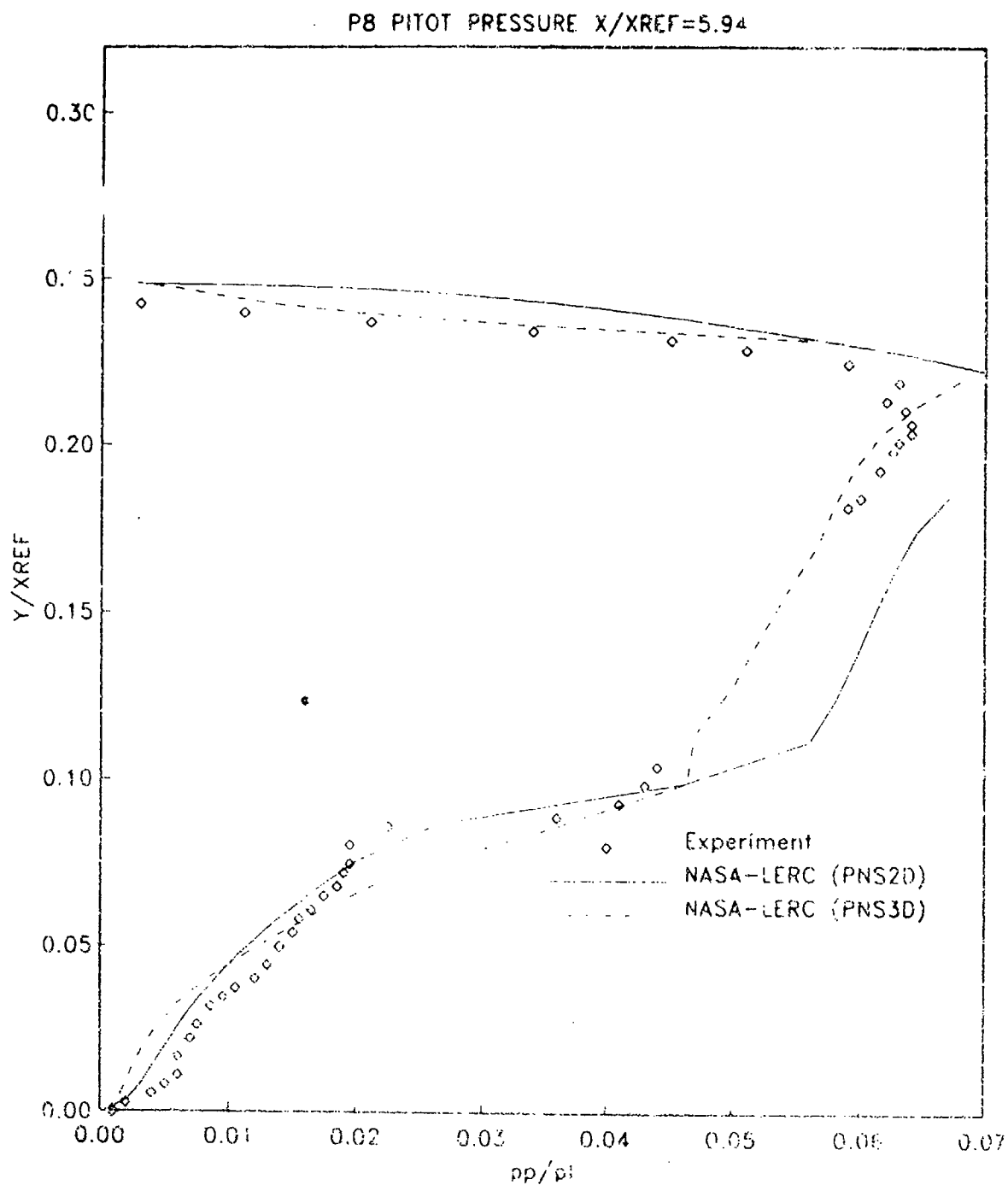
# P8 COWL STATIC PRESSURE

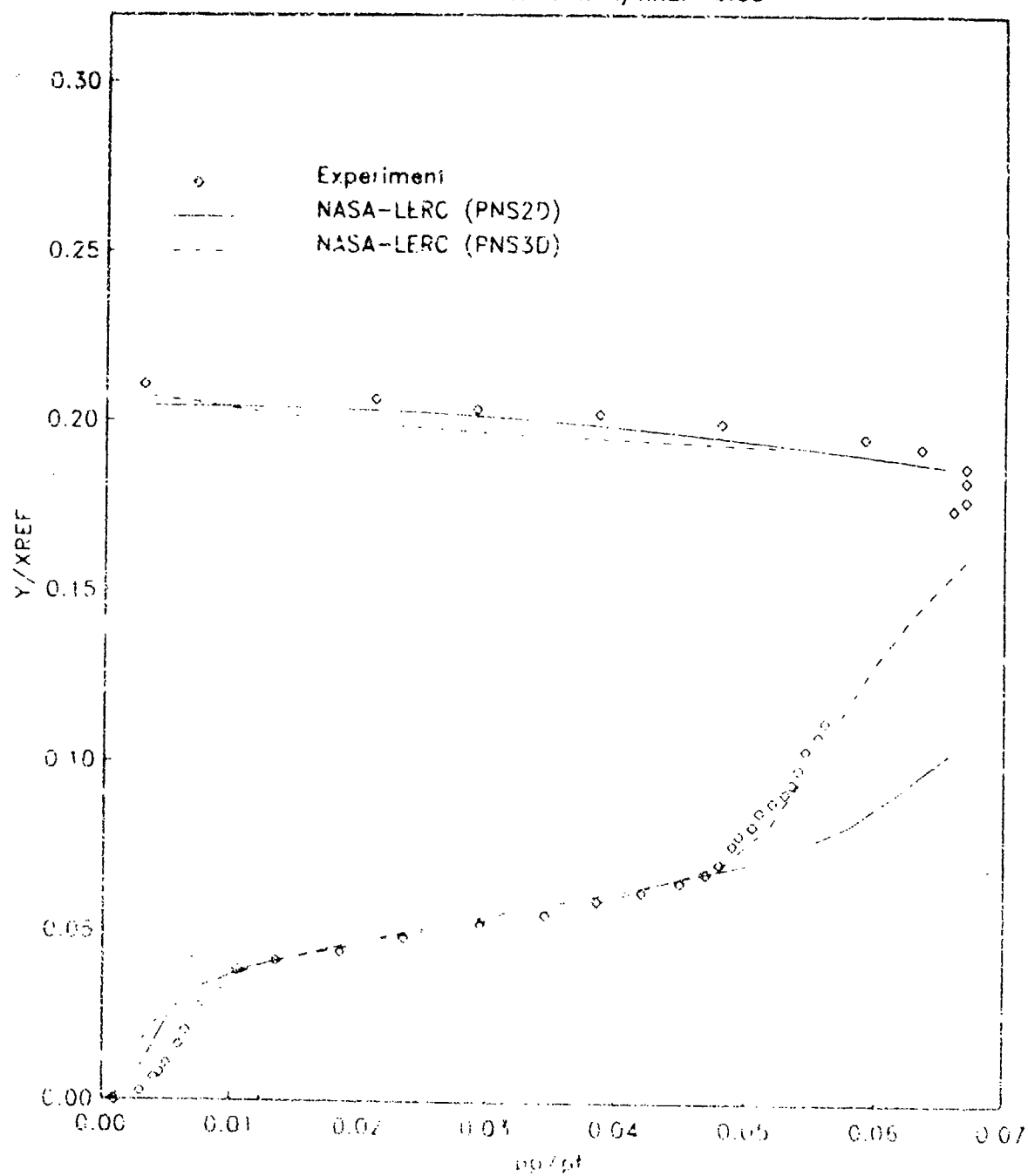


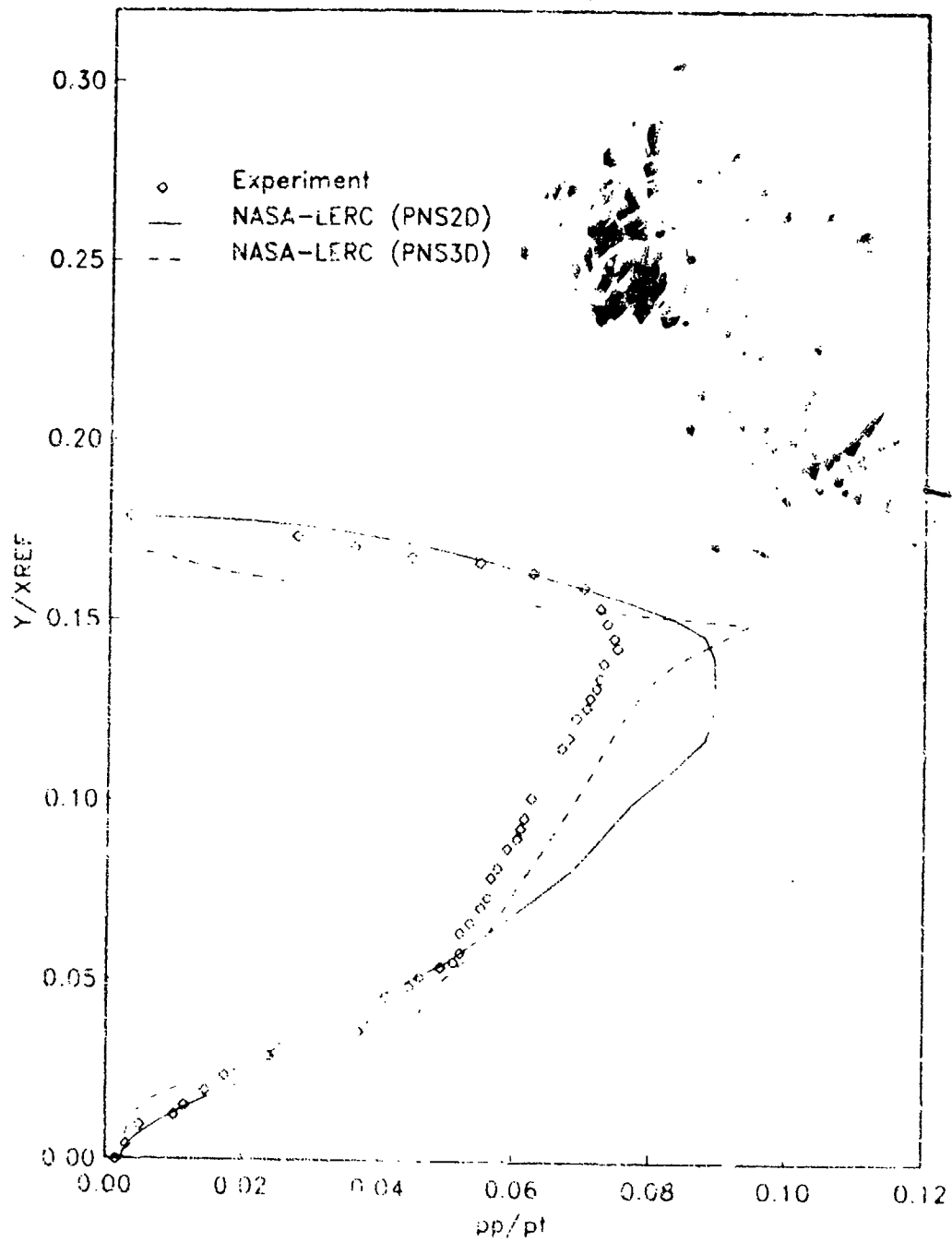


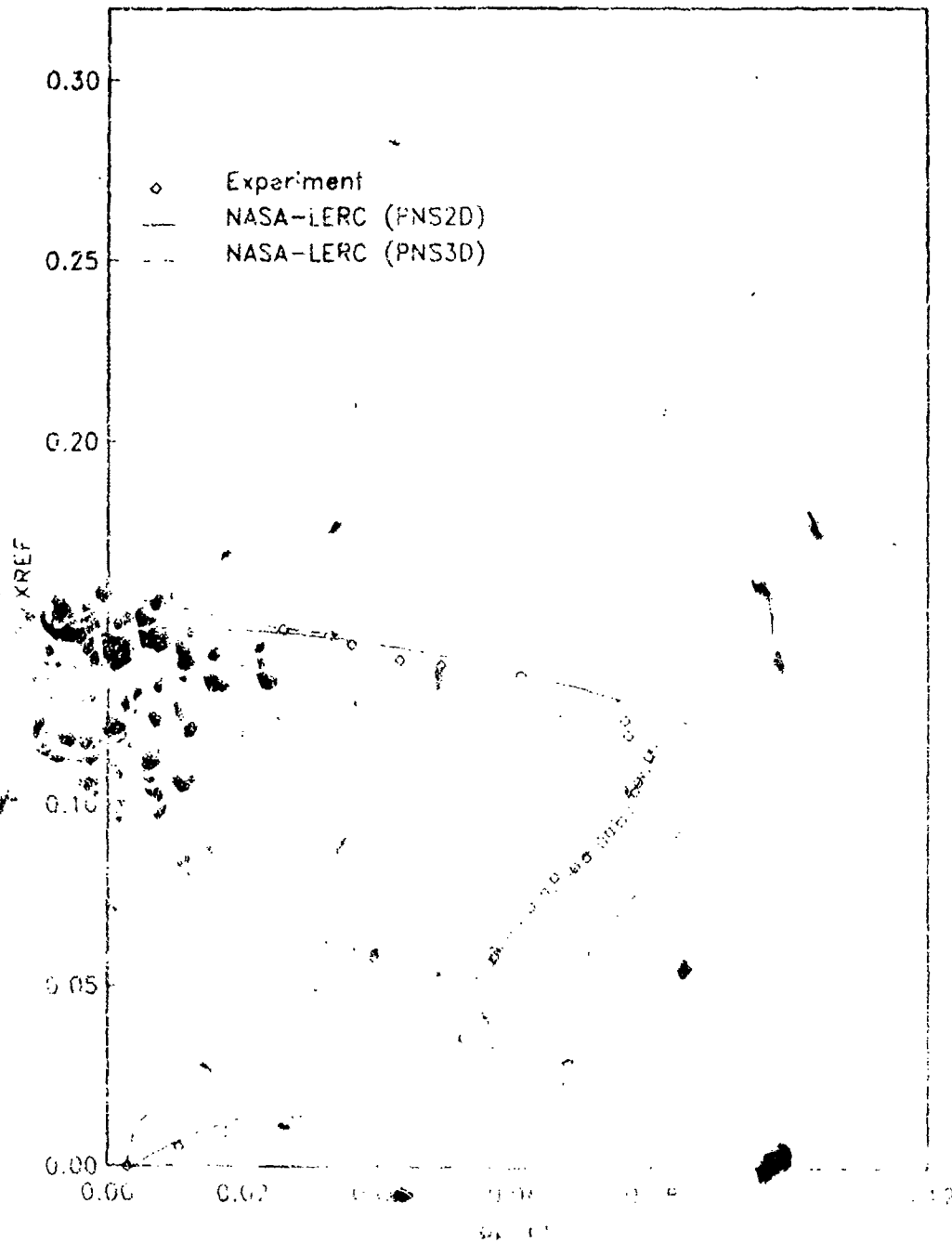
P8 PITOT PRESSURE  $X/X_{REF}=5.78$ 

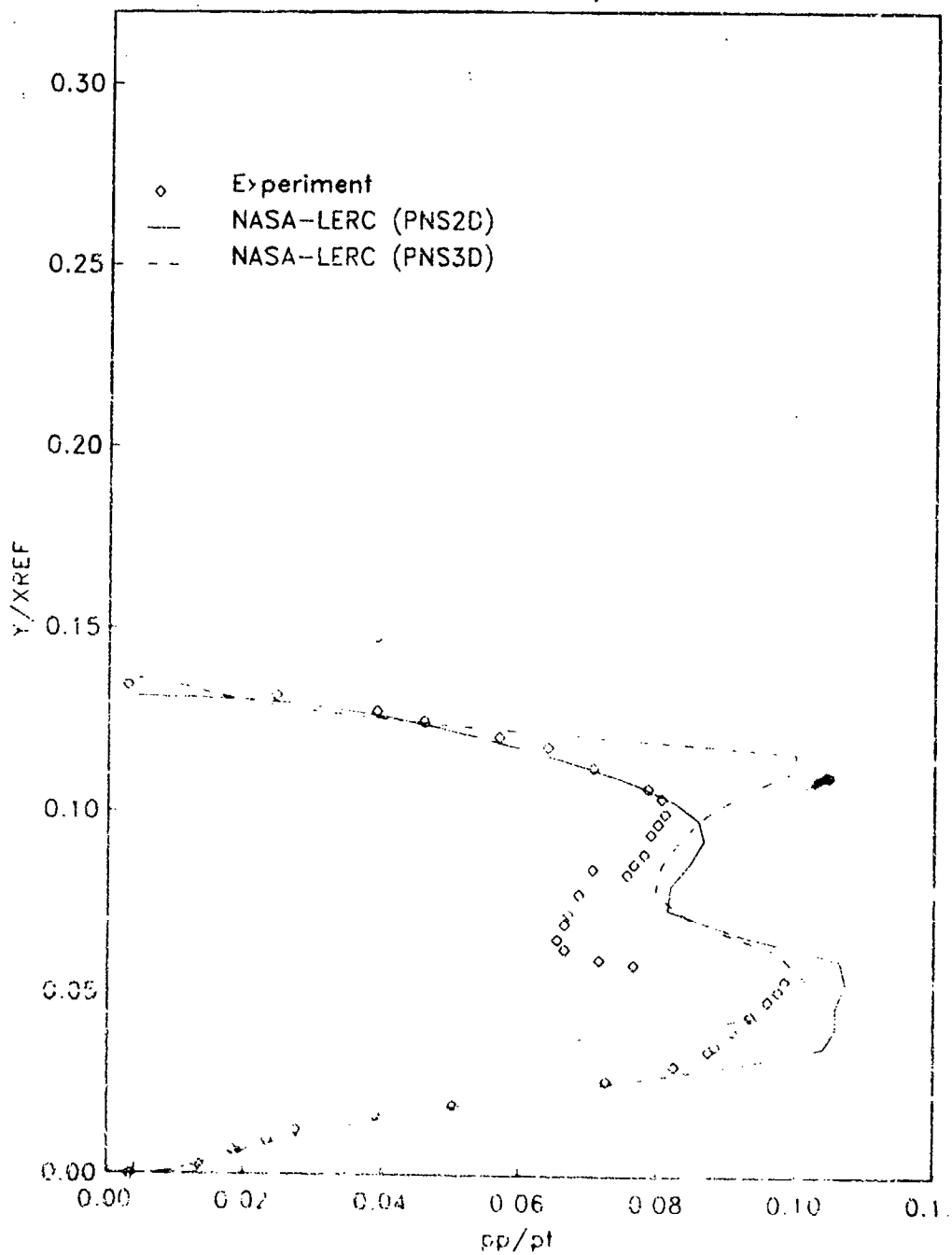


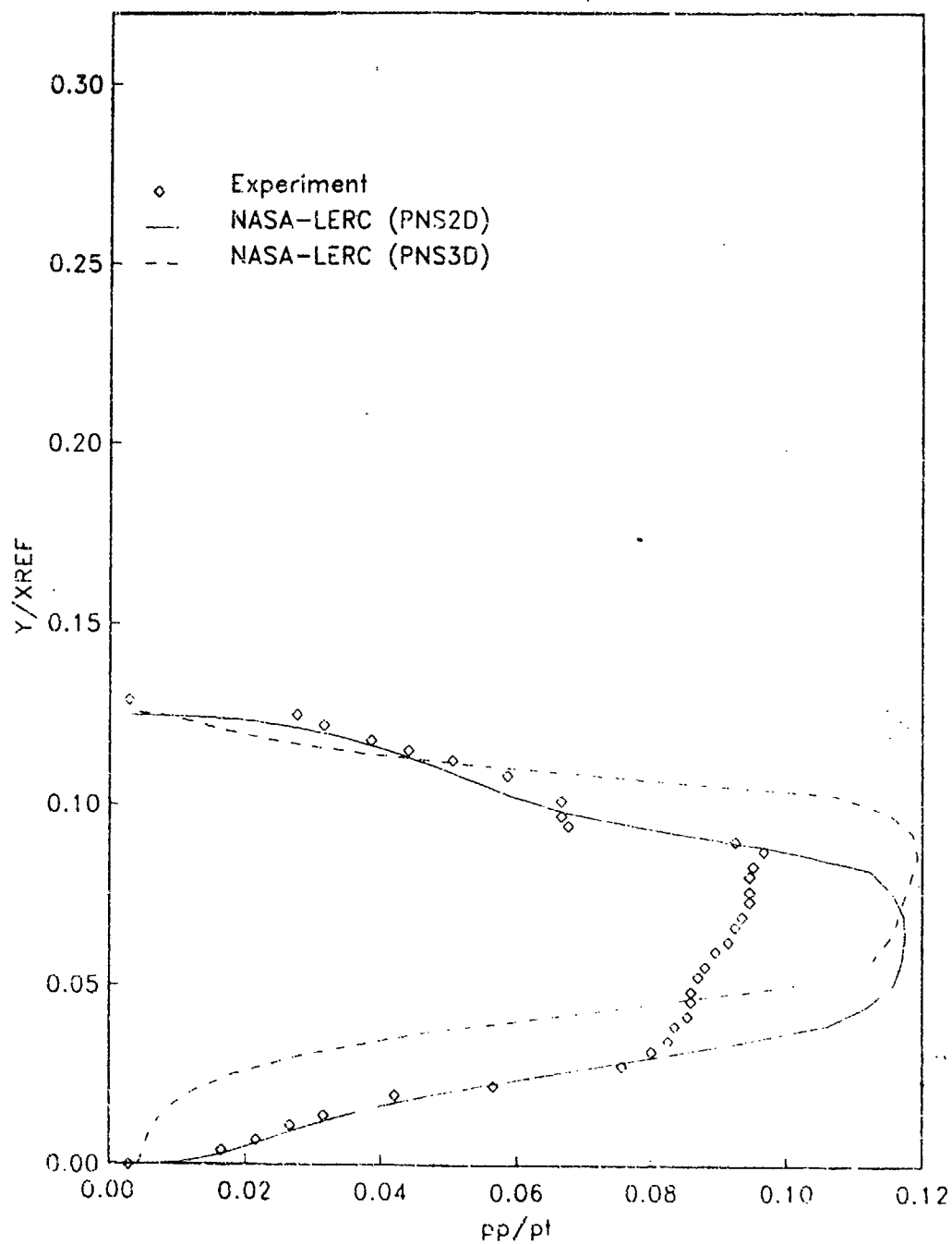


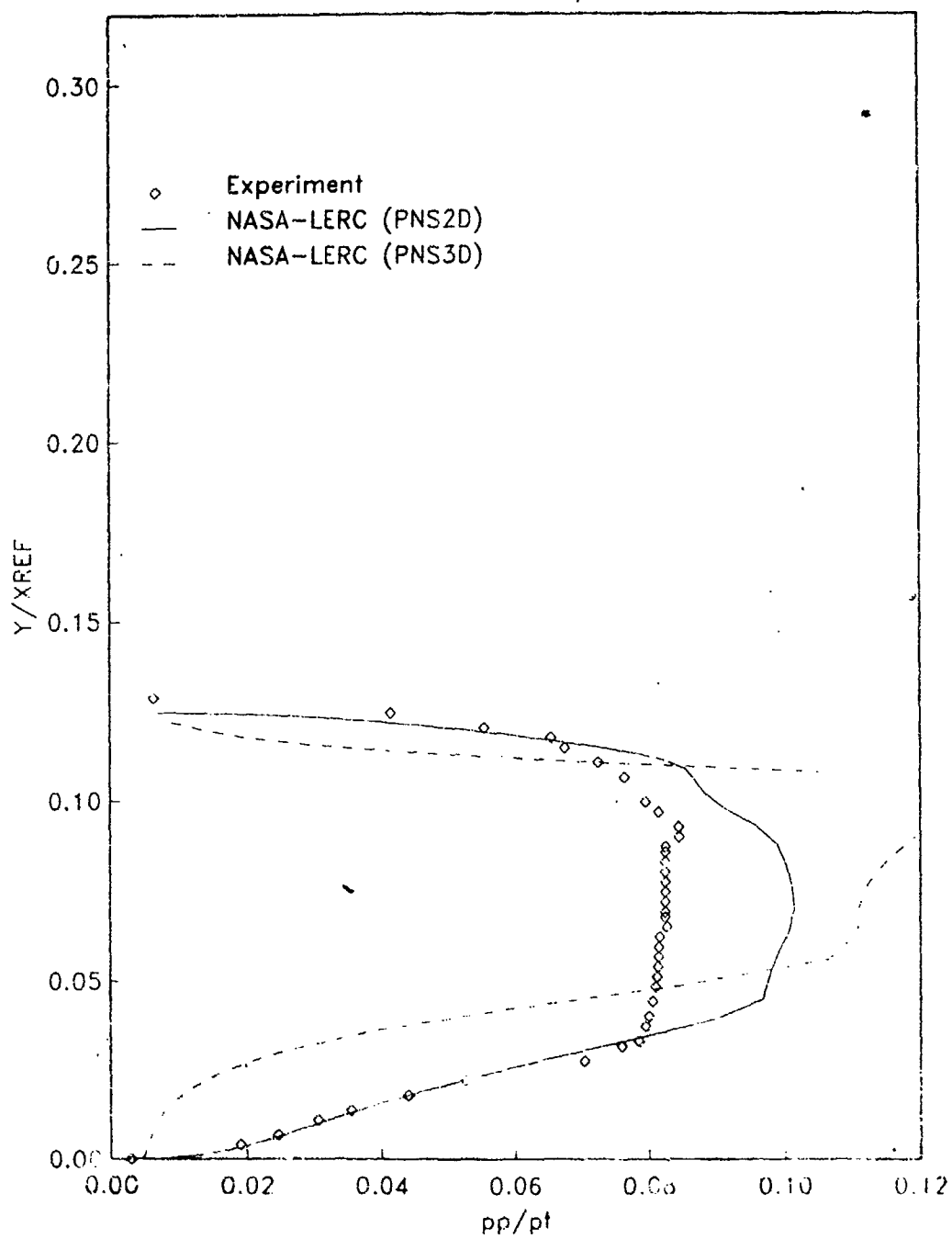
P8 PITOT PRESSURE  $X/X_{REF}=6.09$ 

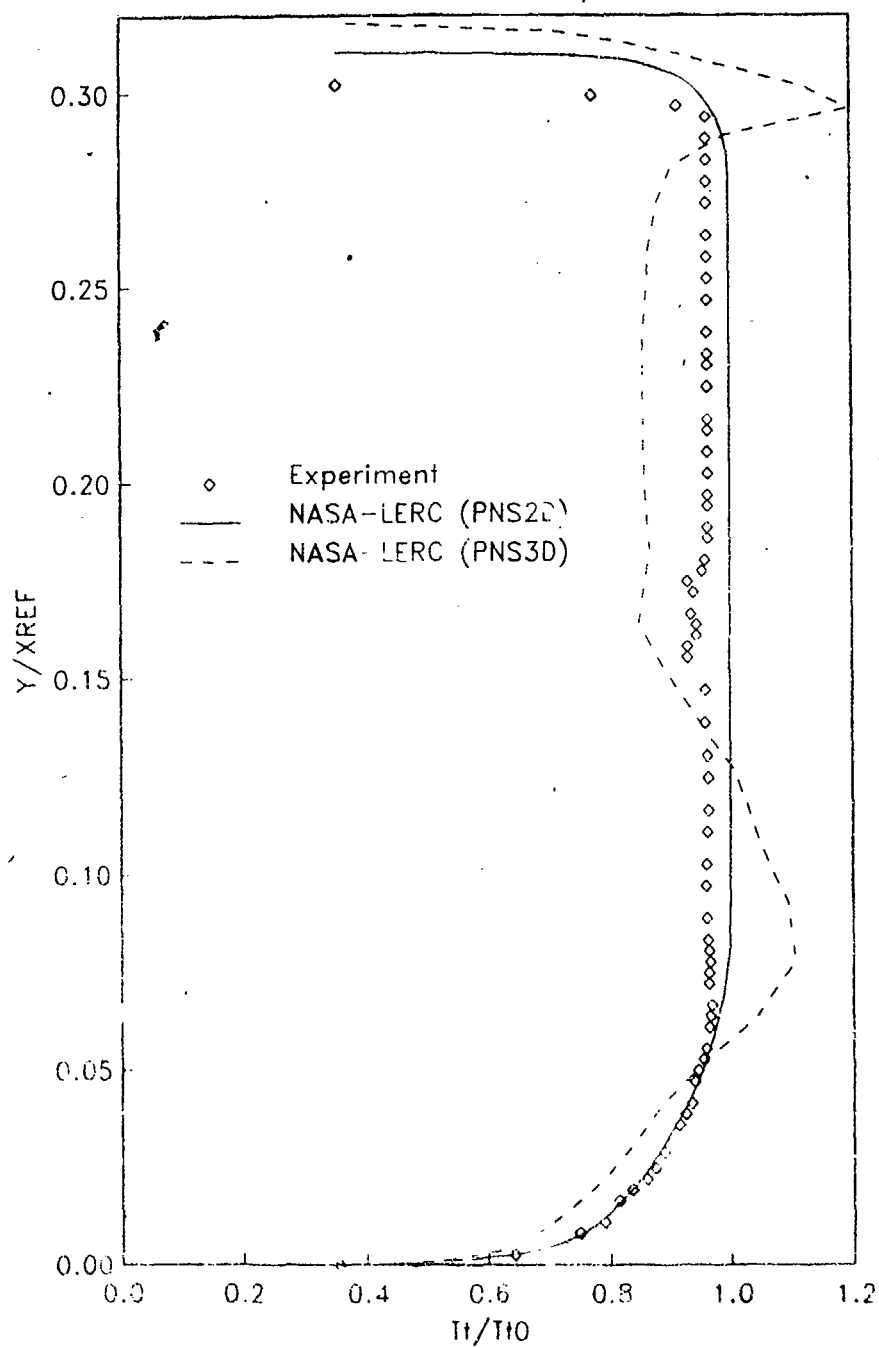
P8 PITOT PRESSURE  $X/X_{REF}=6.23$ 

P8 PITOT PRESSURE  $X/X_{REF}=6.37$ 

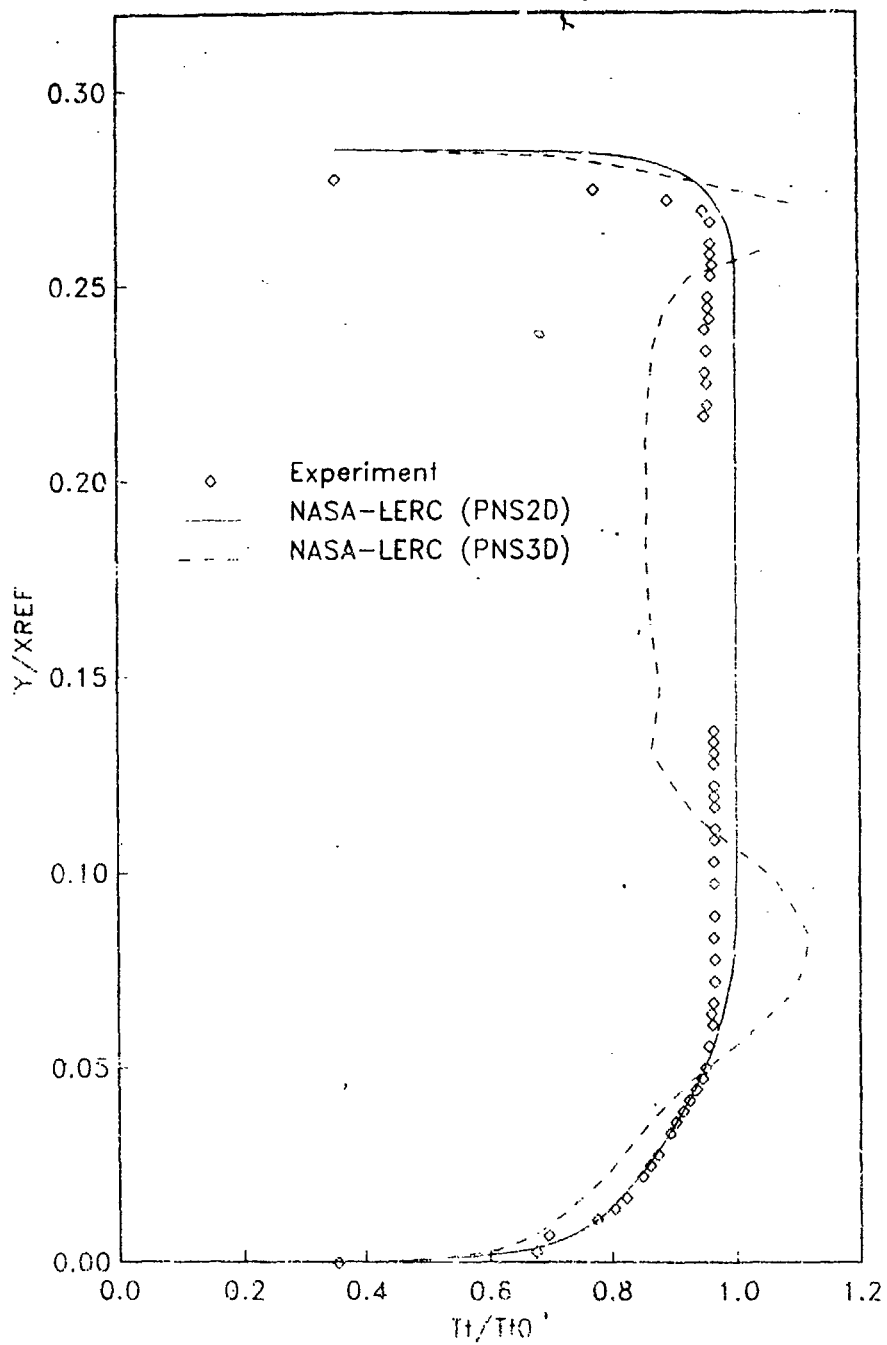
P8 PITOT PRESSURE  $X/X_{REF}=6.51$ 

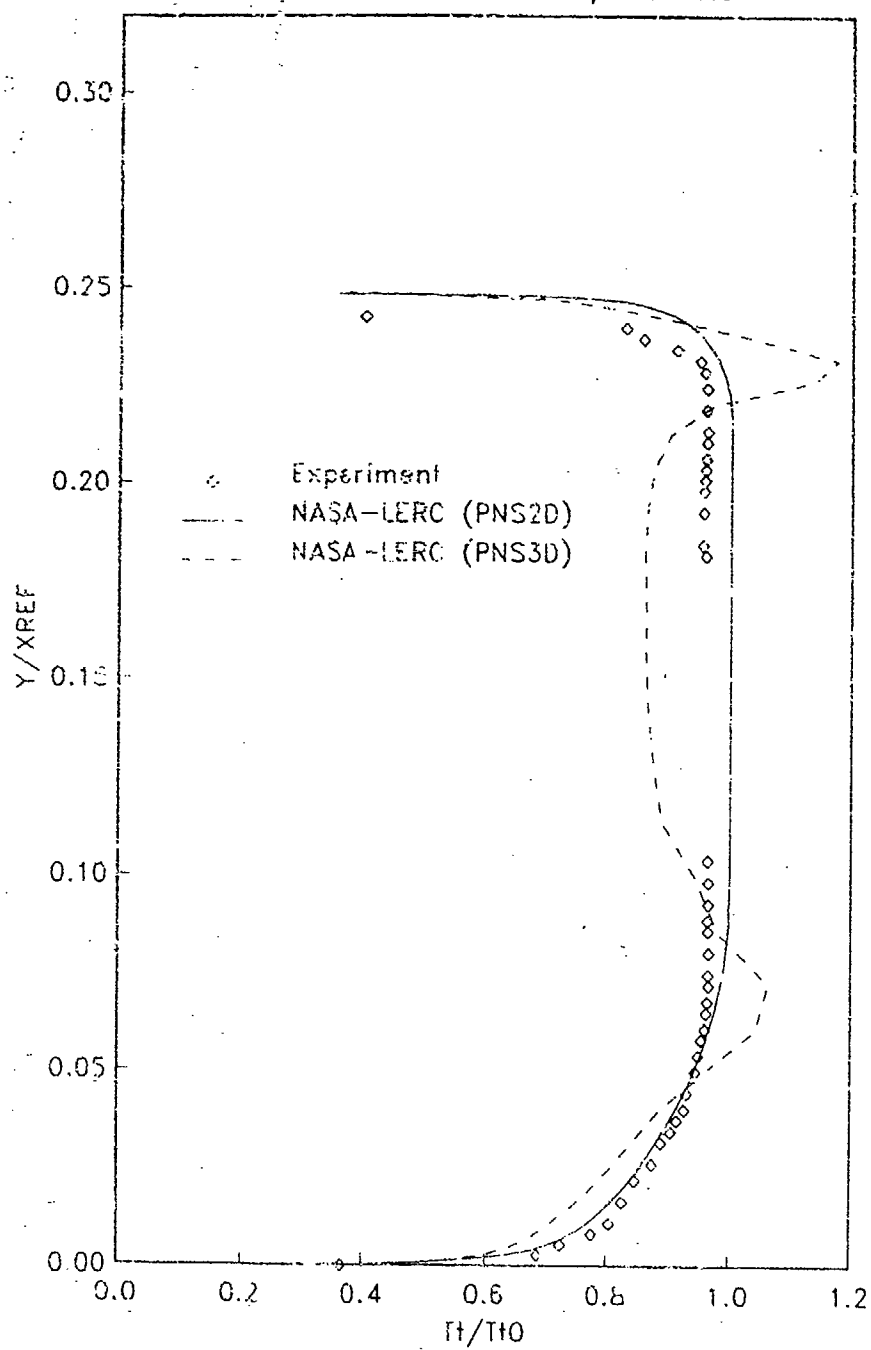
P8 PITOT PRESSURE  $X/X_{REF}=6.65$ 

P8 PITOT PRESSURE  $X/X_{REF}=6.79$ 

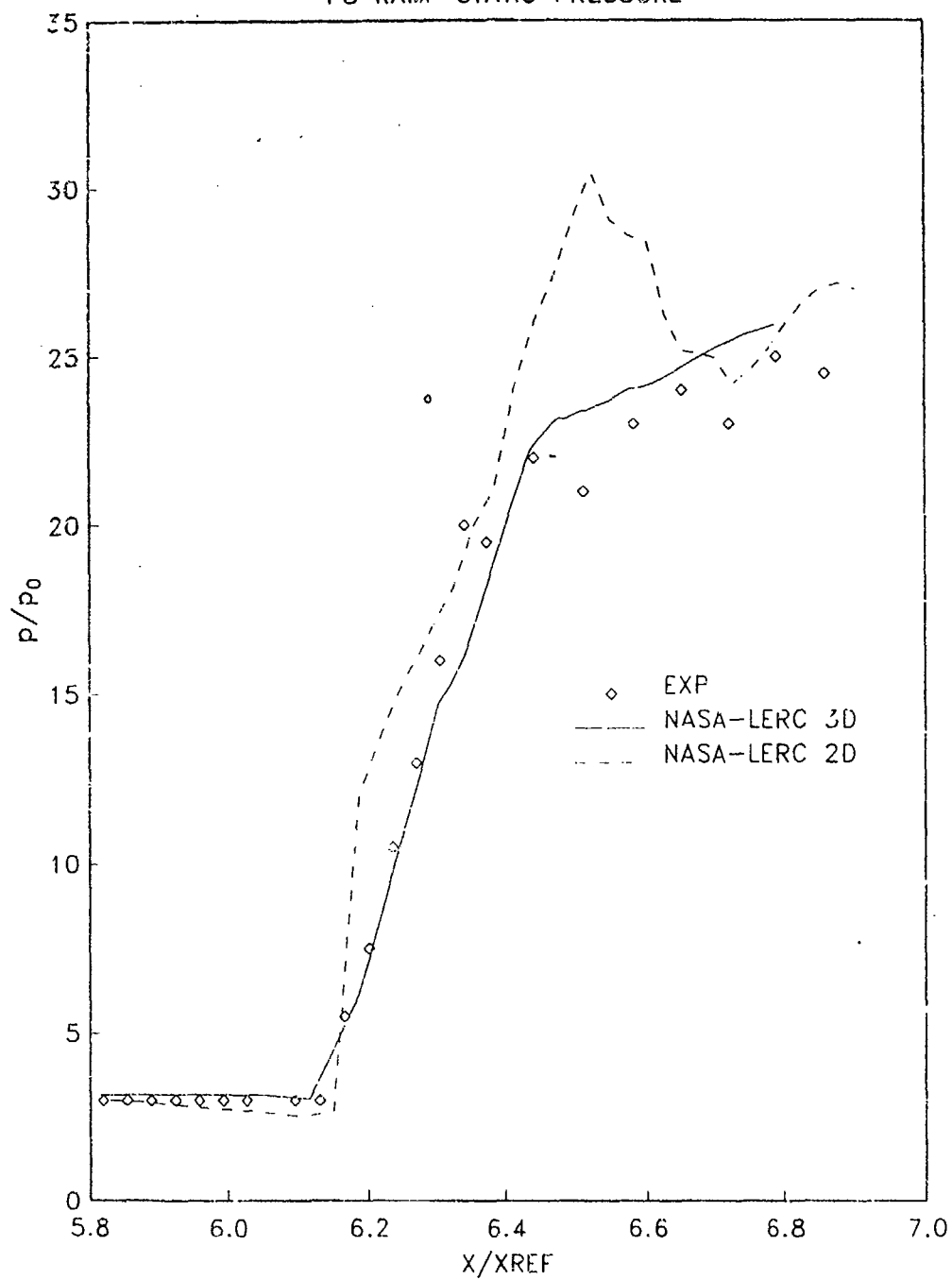
P8 TOTAL TEMPERATURE  $X/X_{REF}=5.67$ 

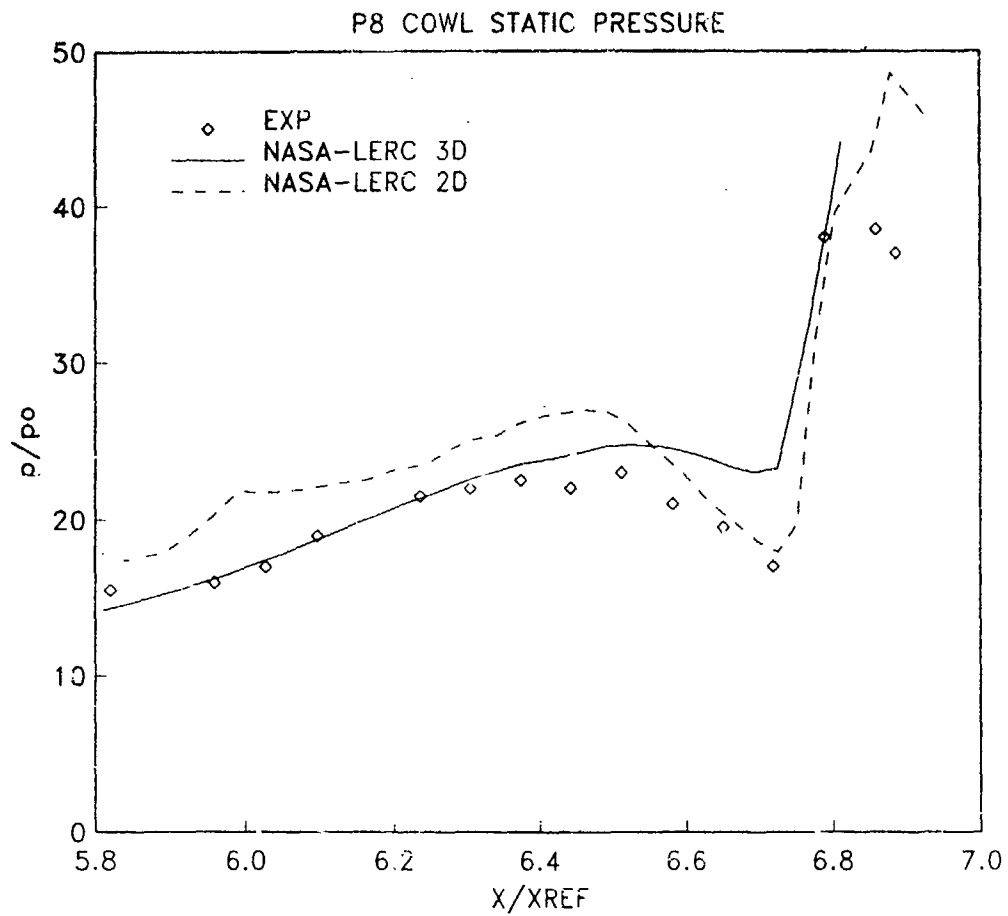


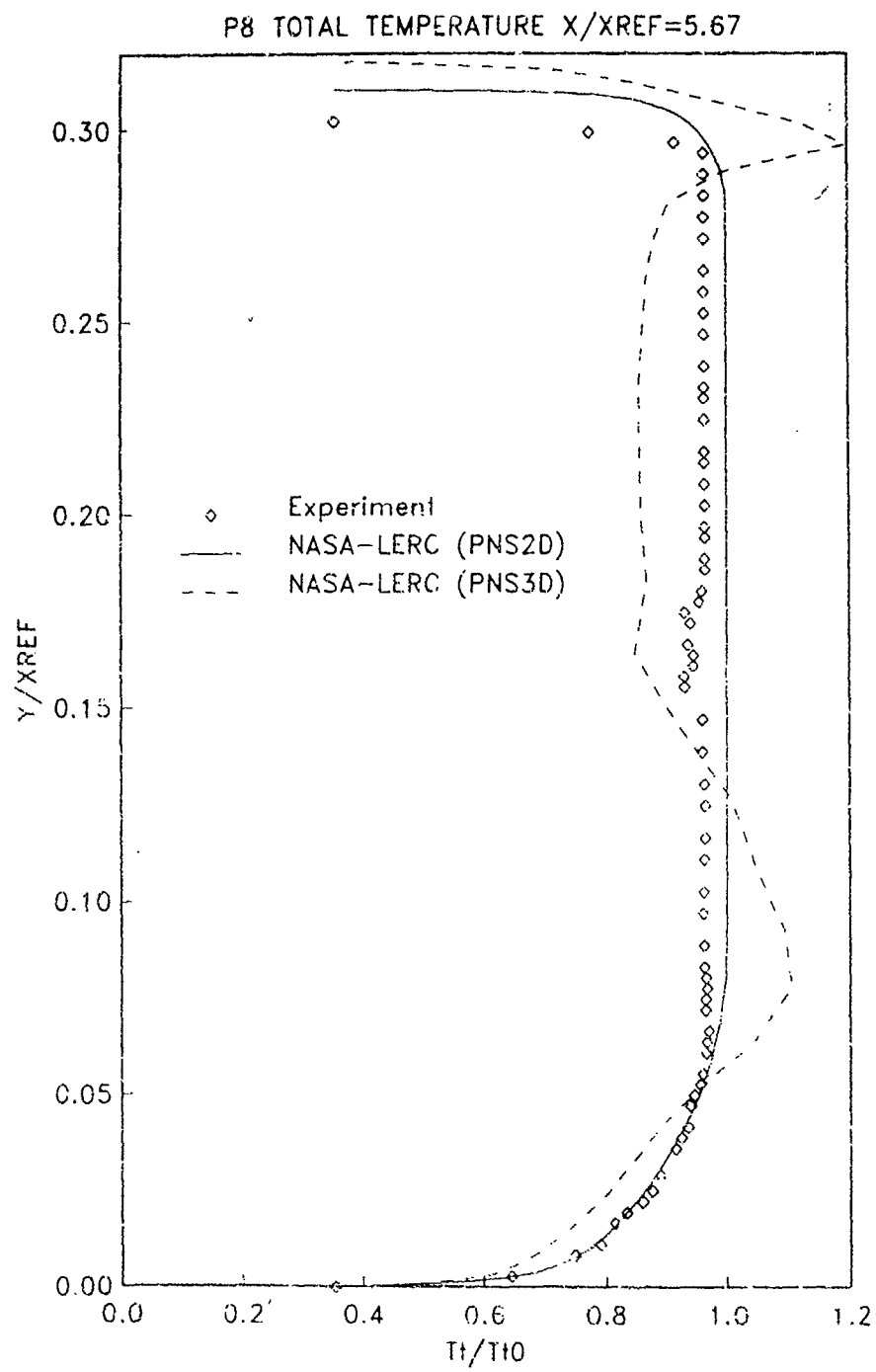
P8 TOTAL TEMPERATURE  $X/Y_{REF}=5.78$ 

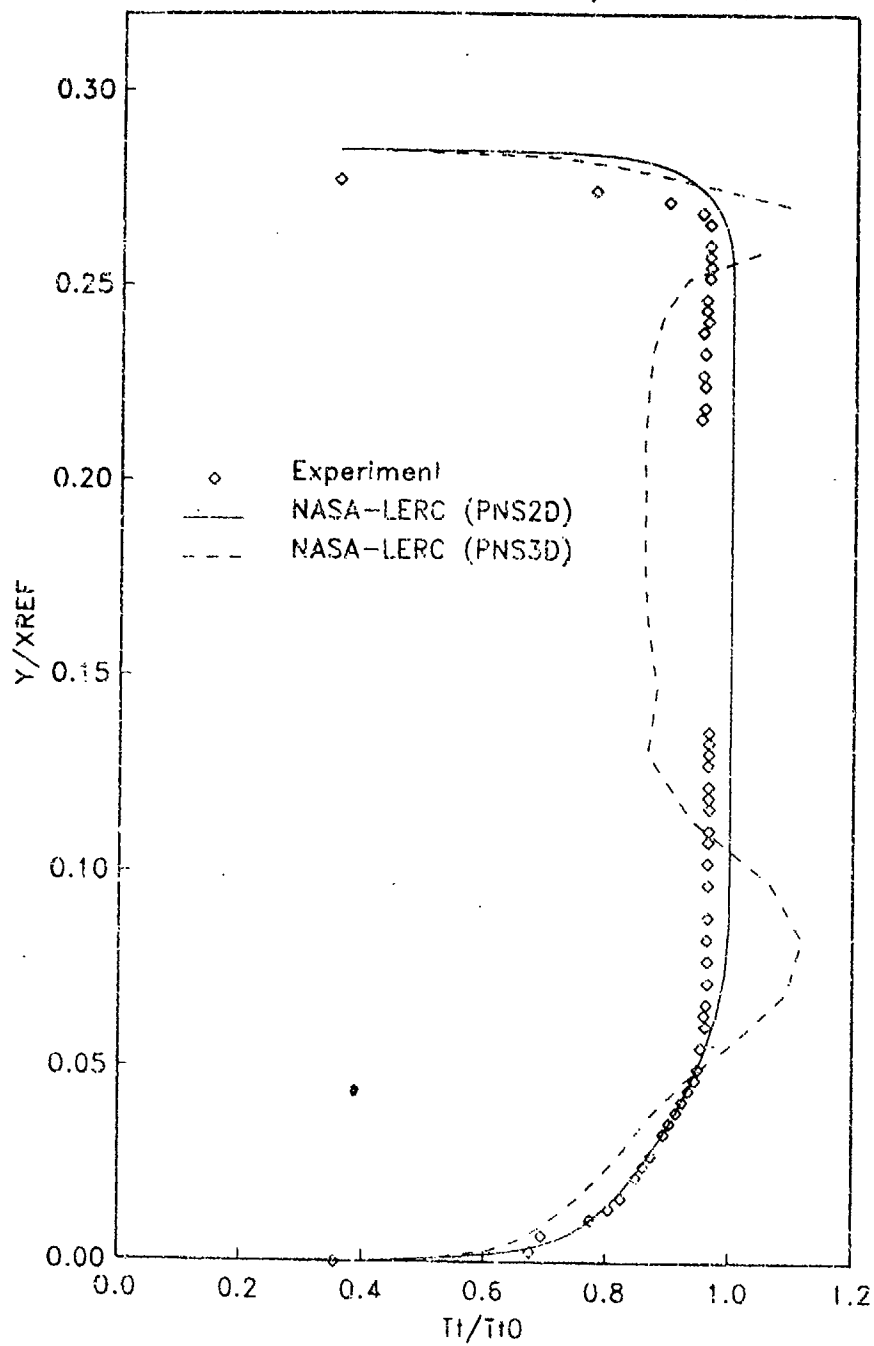
P8 TOTAL TEMPERATURE  $X/X_{REF}=5.94$ 

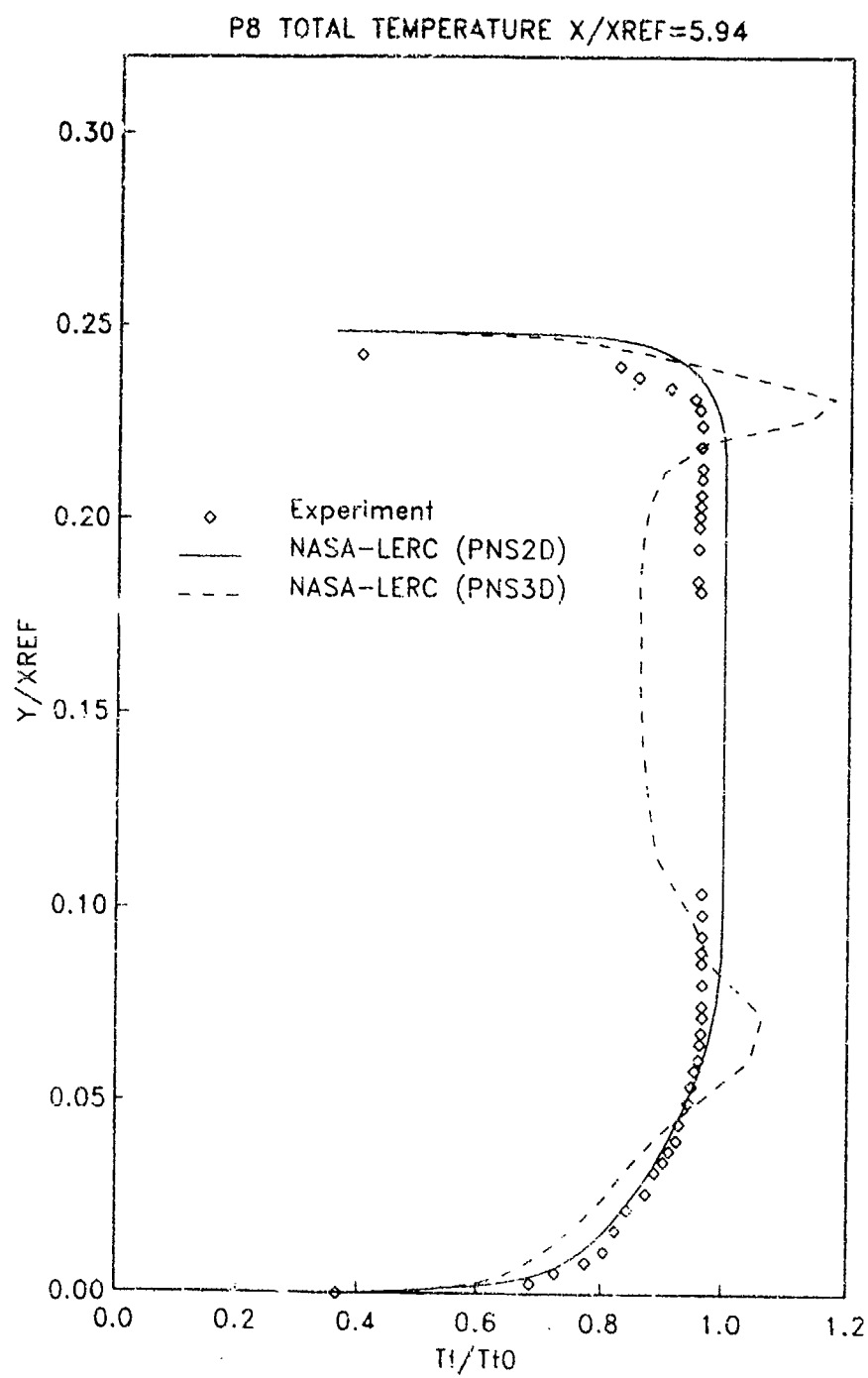
## P8 RAMP STATIC PRESSURE

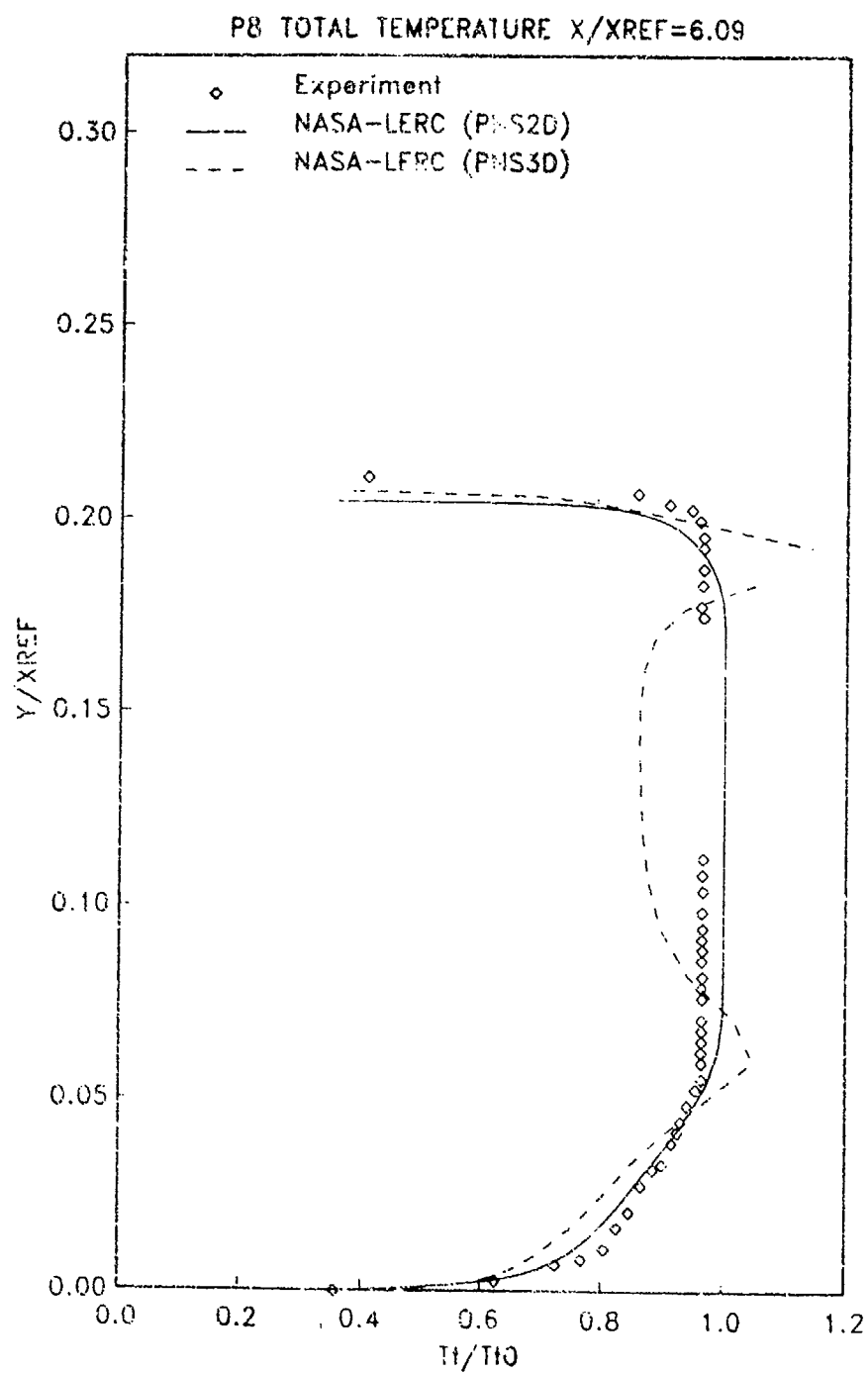




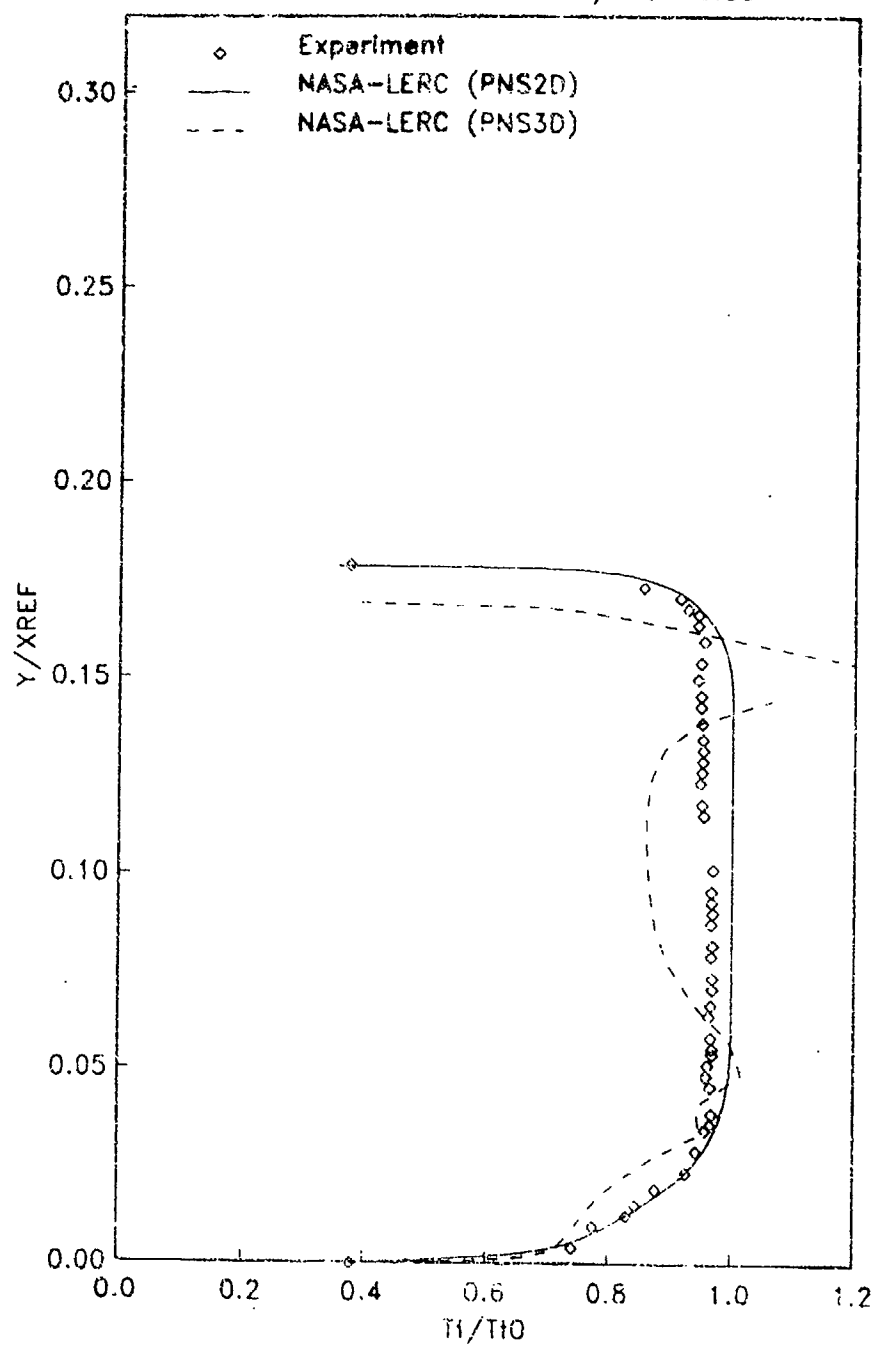


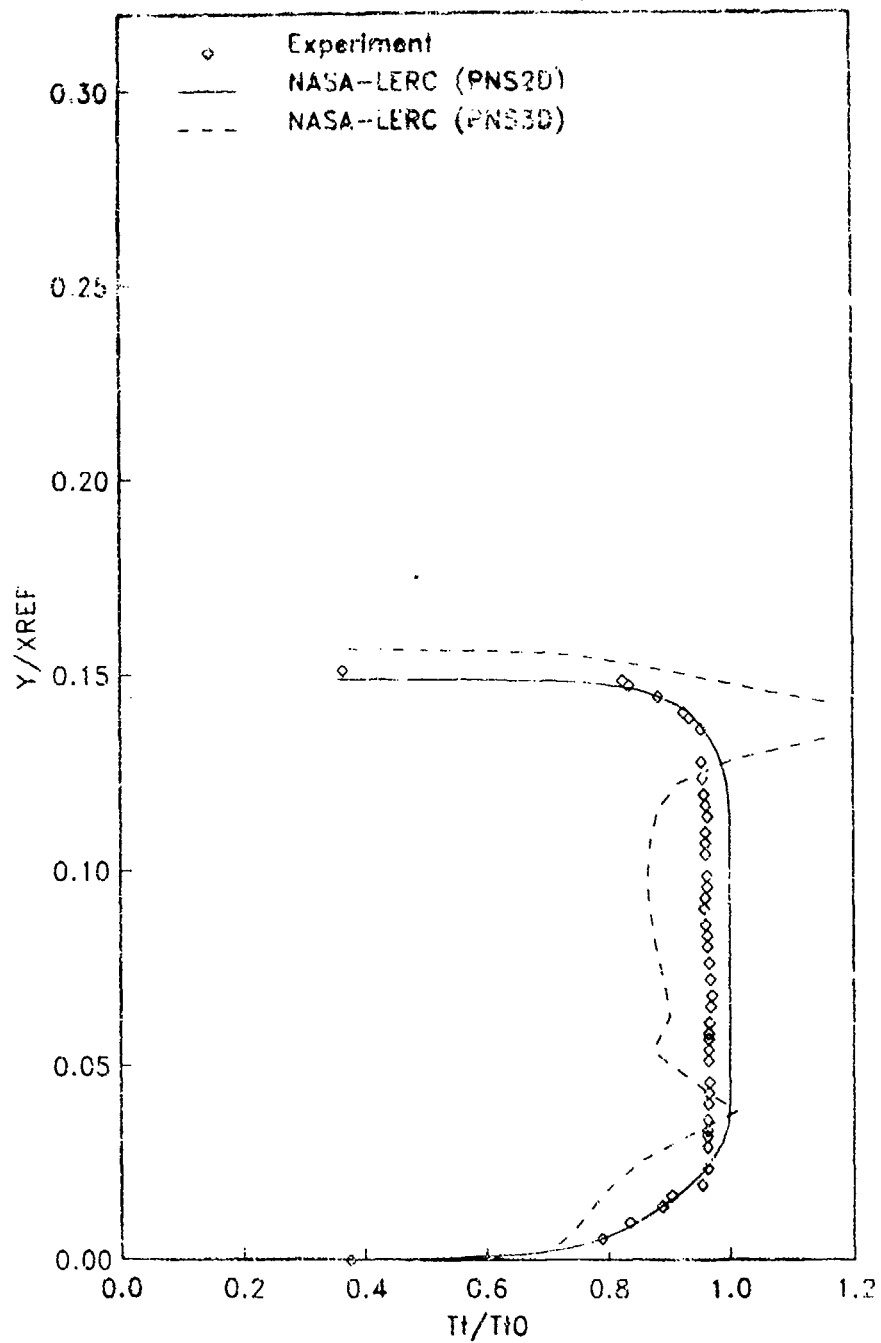
P8 TOTAL TEMPERATURE  $X/X_{REF}=5.78$ 

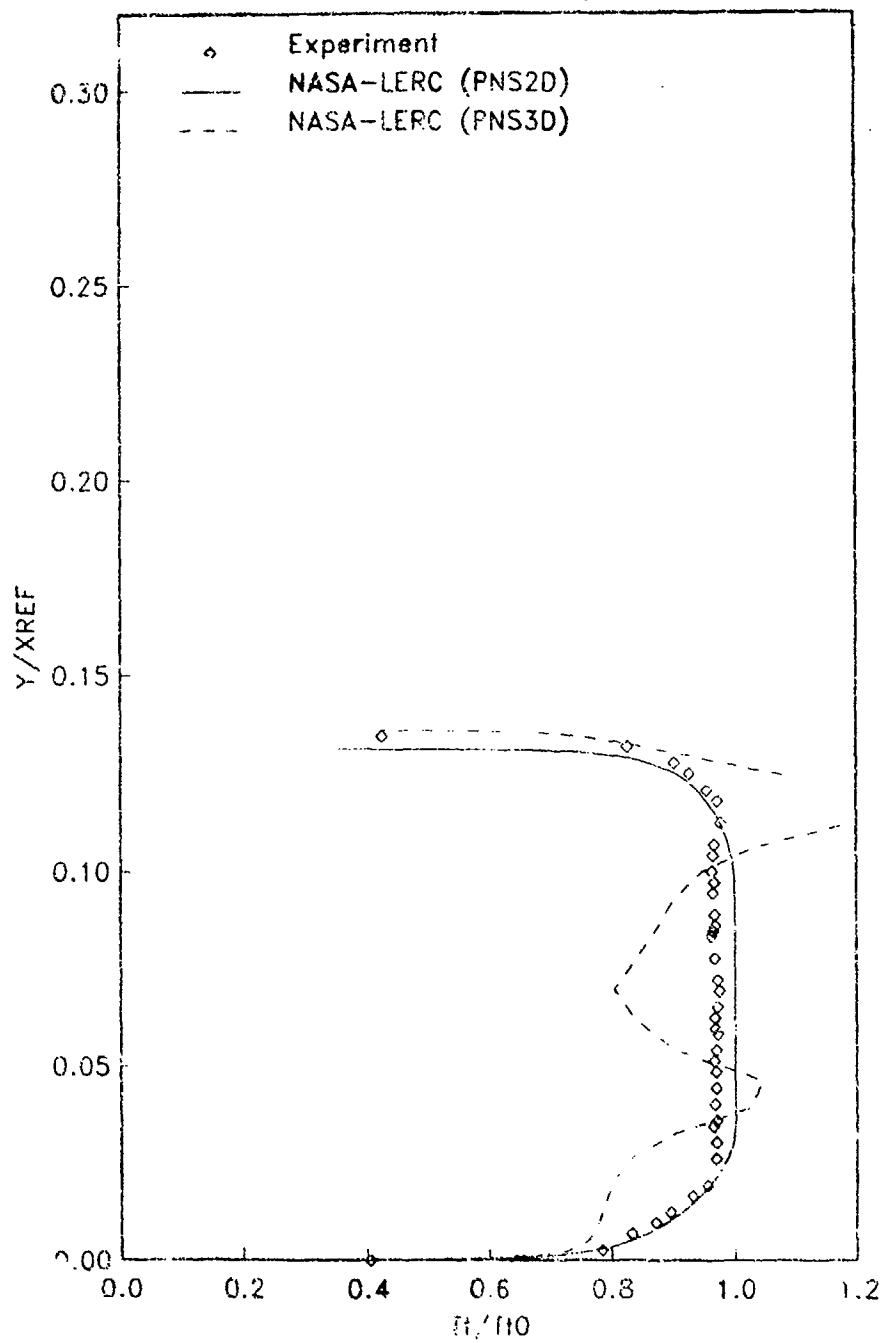


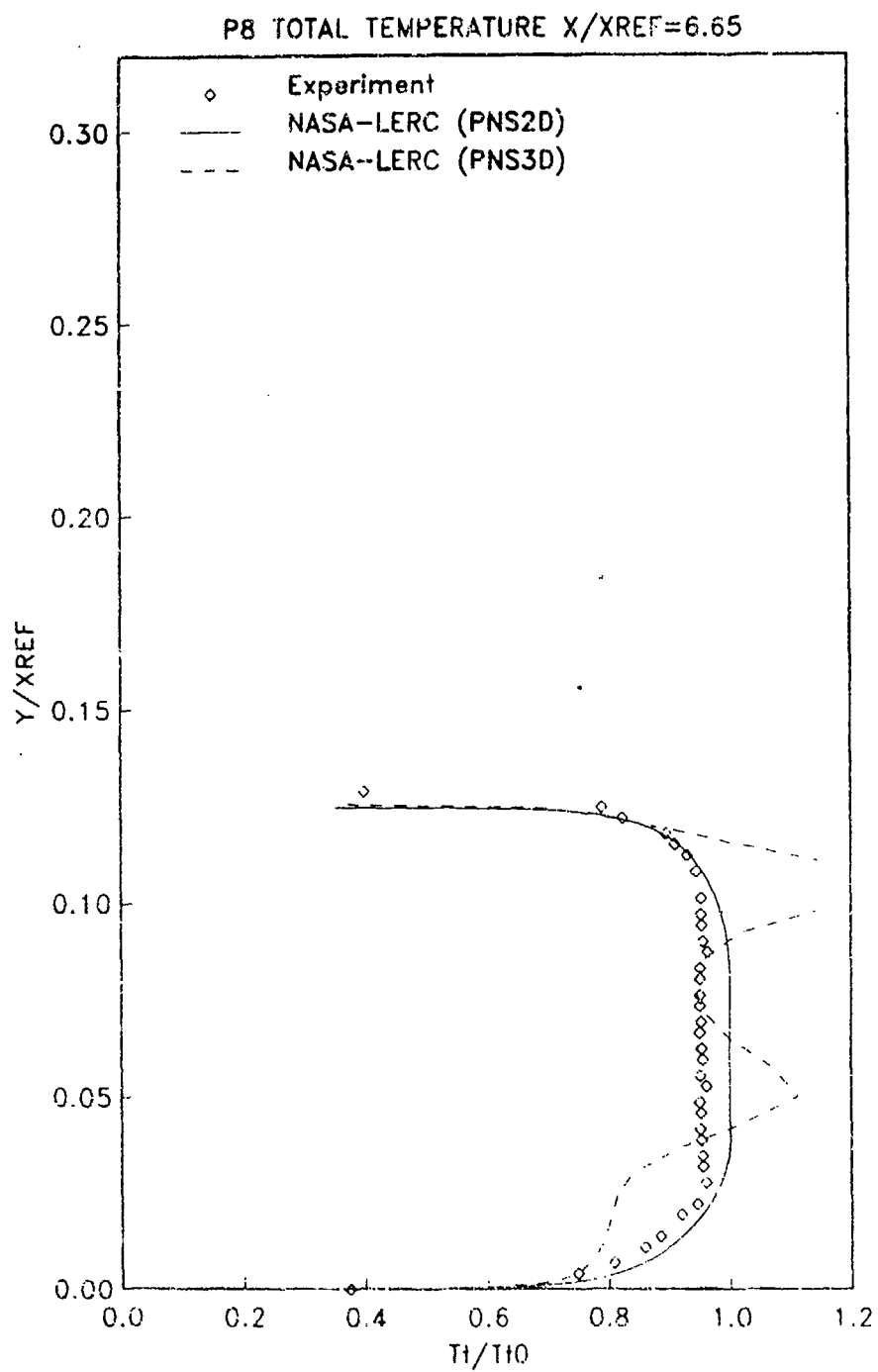


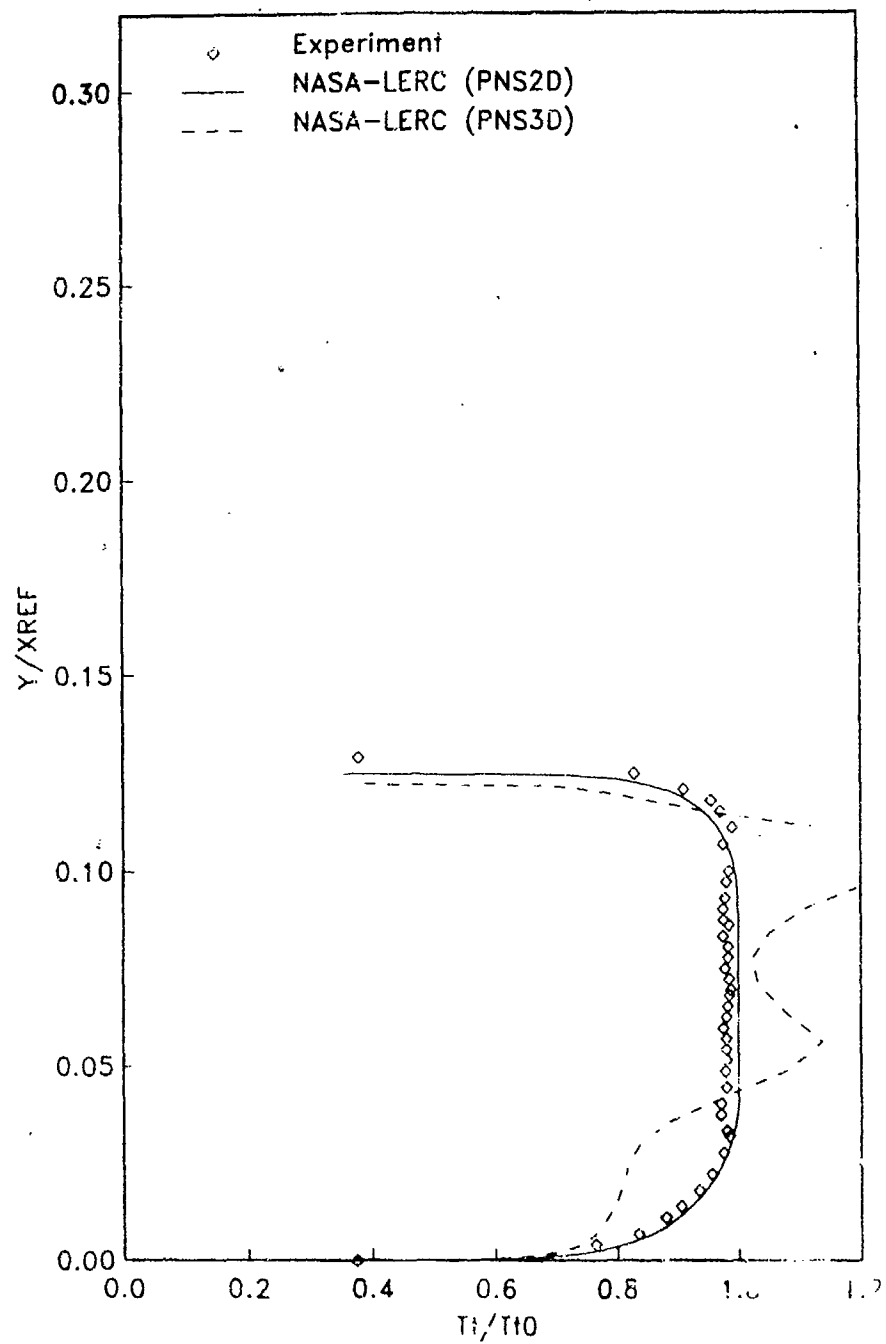


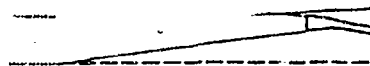
PB TOTAL TEMPERATURE  $X/X_{REF}=6.23$ 

P8 TOTAL TEMPERATURE  $x/x_{REF}=6.37$ 

P8 TOTAL TEMPERATURE  $X/X_{REF}=6.51$ 



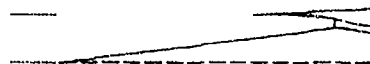
P8 TOTAL TEMPERATURE  $X/X_{REF}=6.79$ 



STATION            1039  
X/H<sub>C</sub> =            0.6710E01



FIGURE 7.- MACH NUMBER CONTOURS AND SECONDARY VELOCITY VECTORS DOWNSTREAM OF COMB LIP.



STATION            1119  
X/H<sub>C</sub> =            0.7232E01

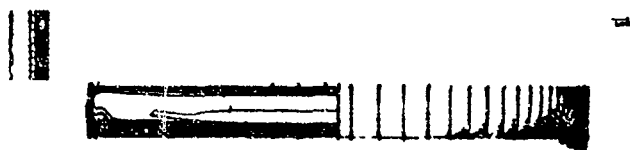
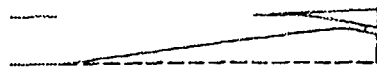


FIGURE 8.- MACH NUMBER CONTOURS AND SECONDARY VELOCITY VECTORS AT CENTERBODY SHOCK REFLECTION.



STATION  
X/HC = .

1299  
0.7913E01



FIGURE 9.- MACH NUMBER CONTOURS AND SECONDARY VELOCITY VECTORS AT COM1 SHOCK REFLECTION.



STATION  
X/HC =

1379  
0.8178E01



FIGURE 10.- MACH NUMBER CONTOURS AND SECONDARY VELOCITY VECTORS AT THE INLET EXIT.

# **AR 270**

## **Microfiche Appendix to Sub-Section 3.3.7**

### **Contributions to Test Case 7**

#### **Axisymmetric mixed compression inlet**

**Sverdrup, Cleveland**

**NASA Lewis**

**Page No's**

**No Submittal**

**A340 to A345**



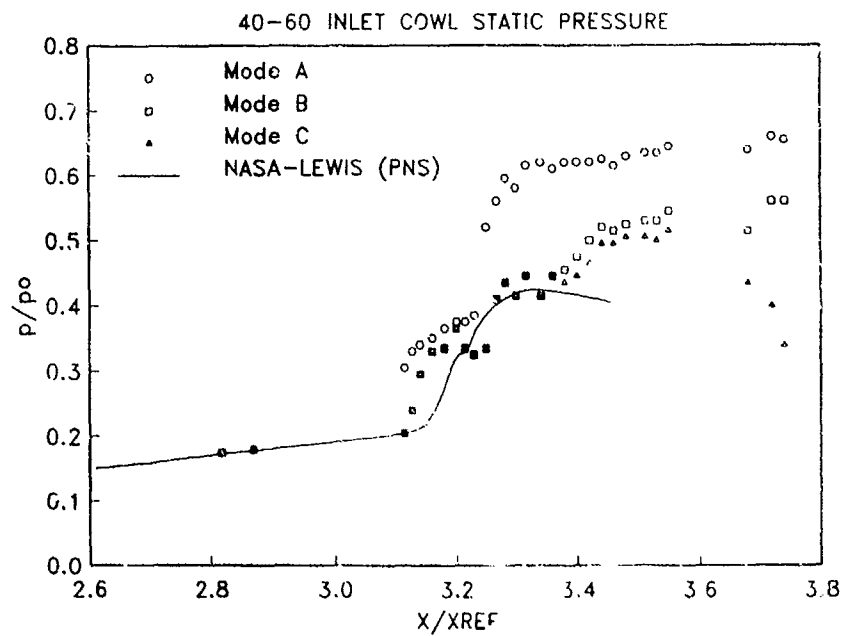
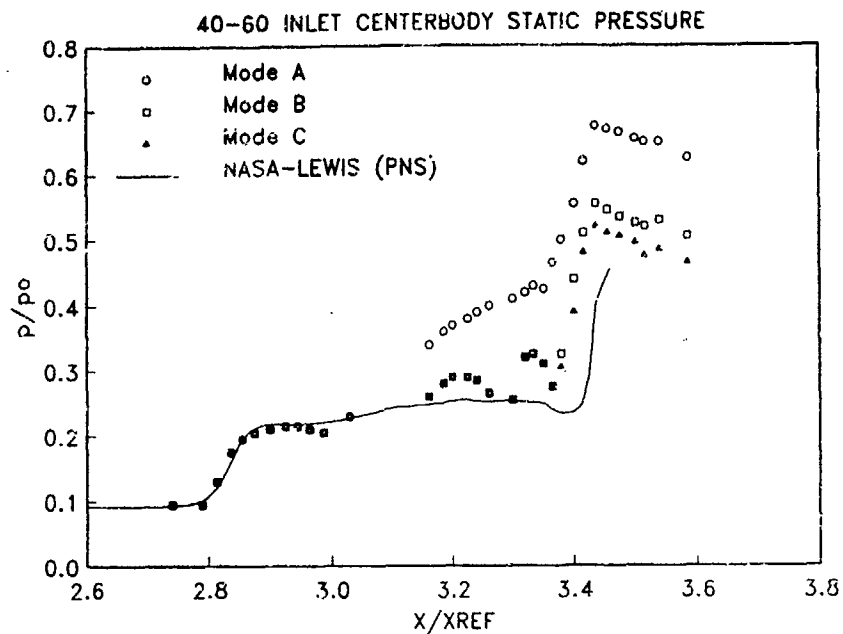
## Test Case 7 - Axisymmetric Inlet

Thomas J. Benson  
National Aeronautics and Space Administration  
Lewis Research Center  
Cleveland, Ohio 44135

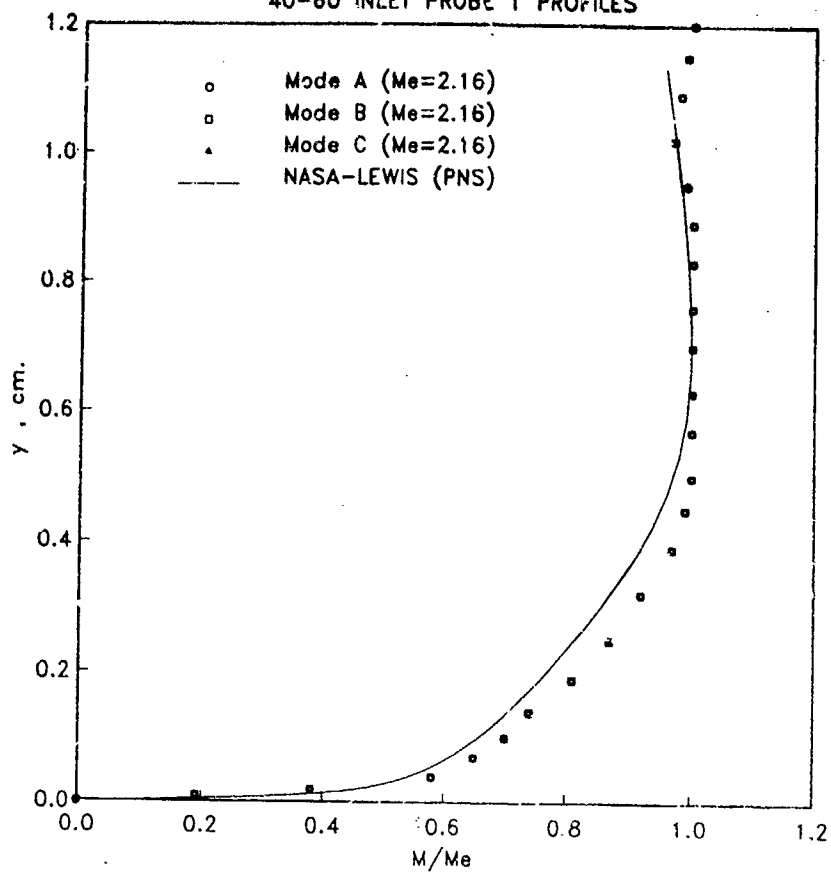
A two dimensional supersonic Parabolized Navier-Stokes code has been used to investigate the flow through the 40-60 inlet. Parametric studies of grid resolution, and turbulence modeling have been conducted, although the results presented here represent the best of these calculations. The inlet contains significant amounts of boundary layer control bleed and this was modelled in the computation.

The supersonic viscous marching analysis used in this study is the PEPISIS code. The code solves the PNS equations by an efficient Briley-McDonald, linearized block implicit scheme. The code solves for the flowfield in a single sweep, can be run with a variety of turbulence models, in either two or three dimensional mode, and can either solve the energy equation or impose constant stagnation enthalpy. The two dimensional result presented in the enclosed figures was run on a CRAY-XMP at the Lewis Research Center on a 90x600 grid with constant stagnation enthalpy imposed. Each flow computation required about five minutes of CPU time with much more time used to refine grids, post process results, etc. Both the standard McDonald-Camarata mixing length turbulence model and a one equation turbulent kinetic energy model have been studied; the results presented here use the one equation k-model. The calculation was started with uniform free stream conditions as specified in the report. The bleed was modelled as a uniformly distributed mass removal at the appropriate location and with the amount specified in the reports. The bleed along the centerbody was only given as the combination of the forward and aft bleed. It was assumed that twice as much mass would be removed at the downstream centerbody bleed than at the forward because of the higher static pressure and higher porosity.

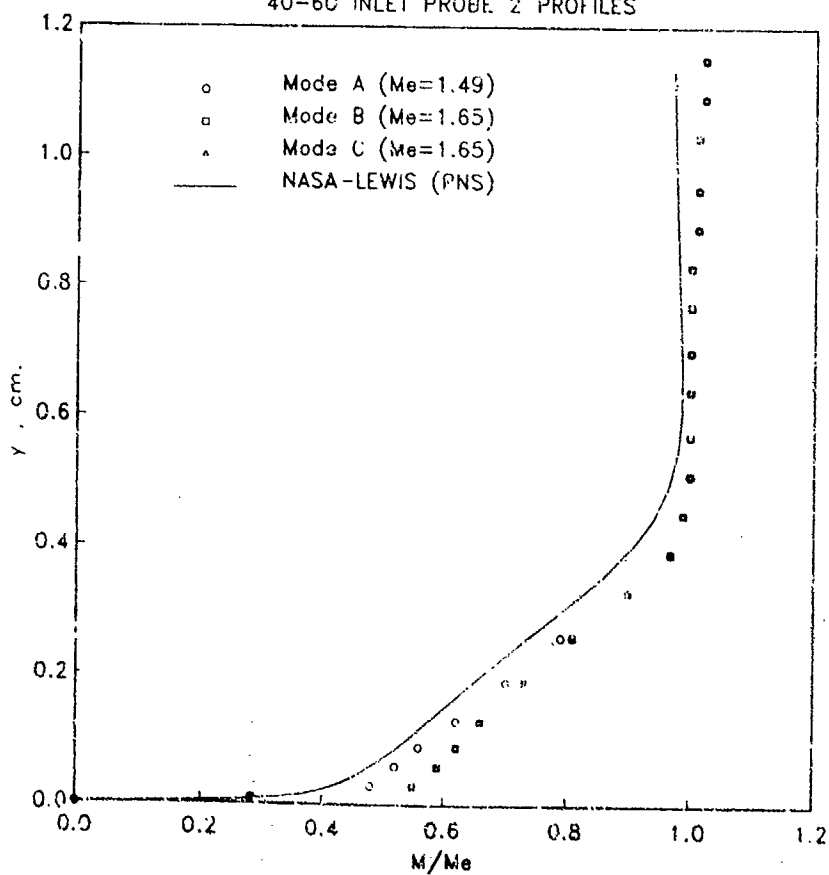
Because this analysis is a single sweep PNS type, it is not possible to vary the downstream mass flow as was done in the experiment. In fact, comparisons with experiment can only be made in the supersonic portion of the inlet at the highest mass flow ratio available. This is the price that is paid for quick PNS calculations. It does appear, however, that this type of analysis is quite accurate and very valuable in the supersonic portion of the inlet. The downstream output of this code can be used to interface with slower running Navier-Stokes type analysis to predict full inlet performance.



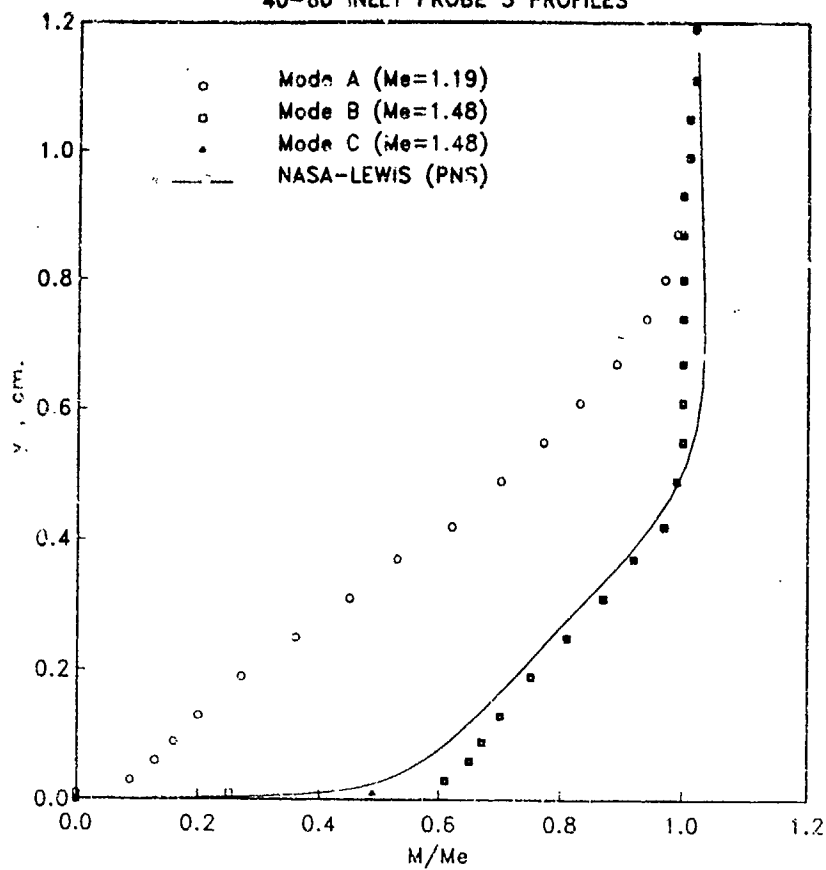
40-60 INLET PROBE 1 PROFILES



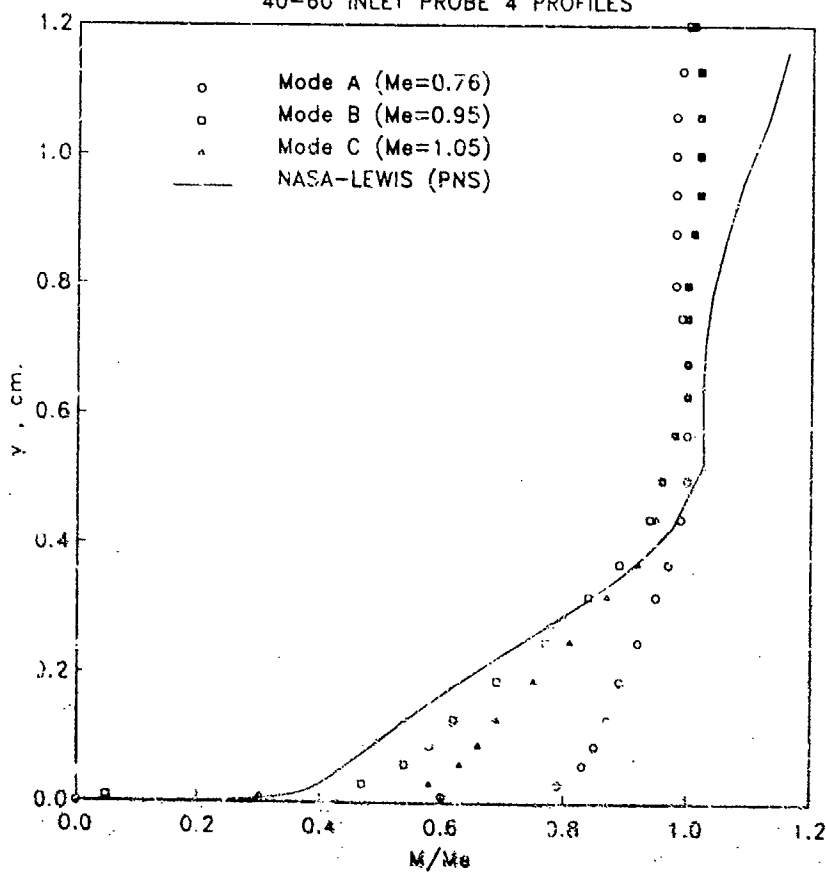
40-60 INLET PROBE 2 PROFILES



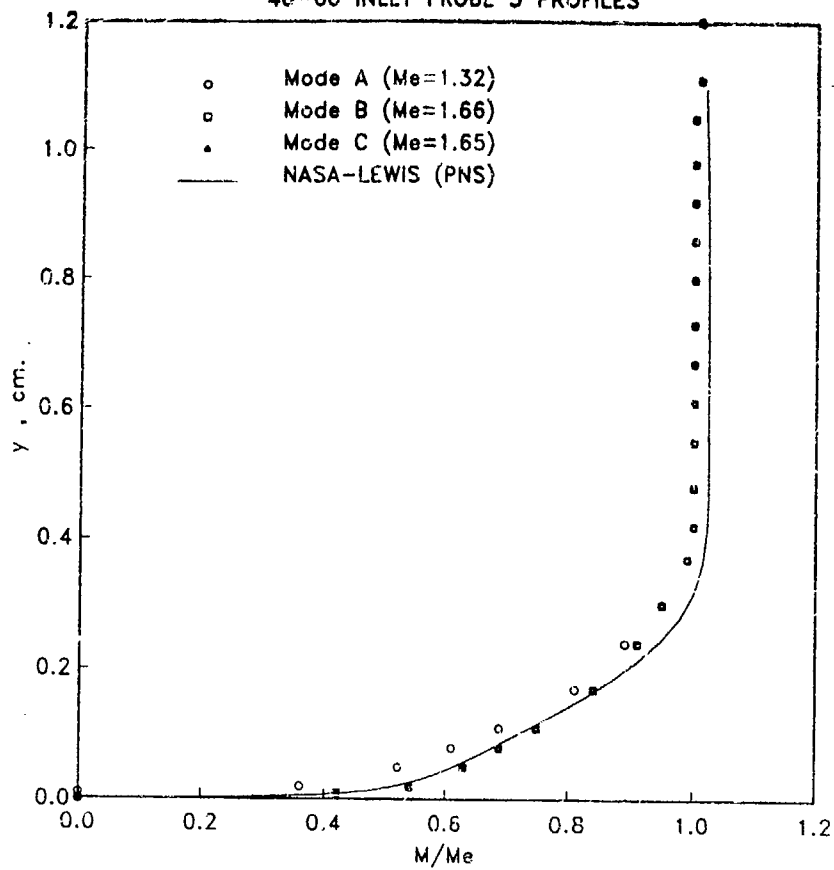
40-60 INLET PROBE 3 PROFILES



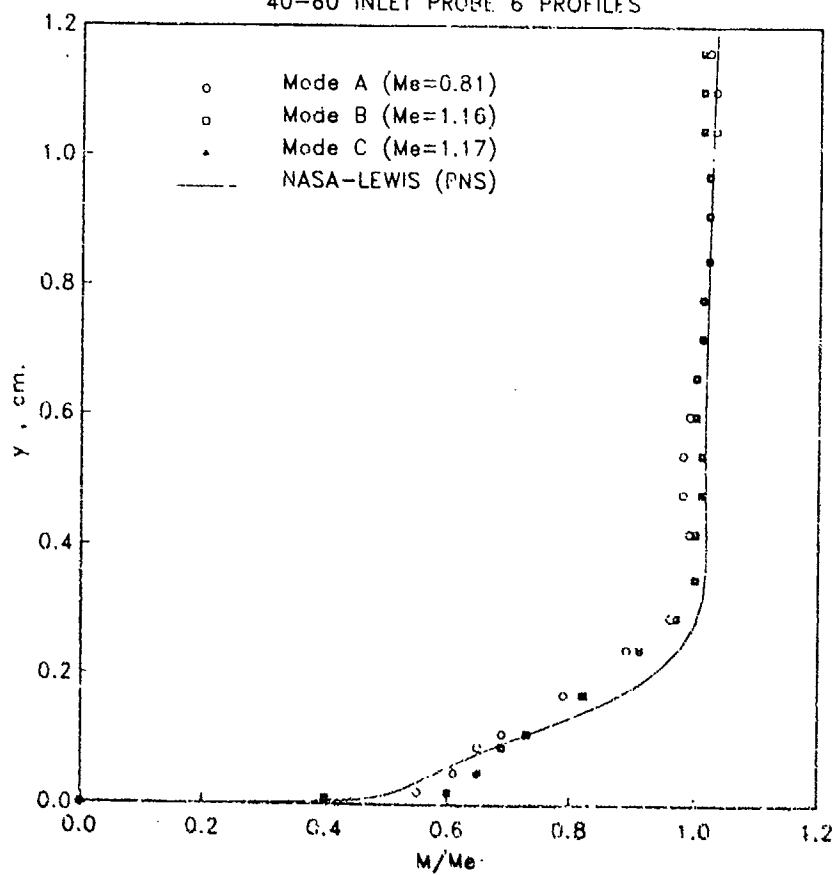
40-60 INLET PROBE 4 PROFILES

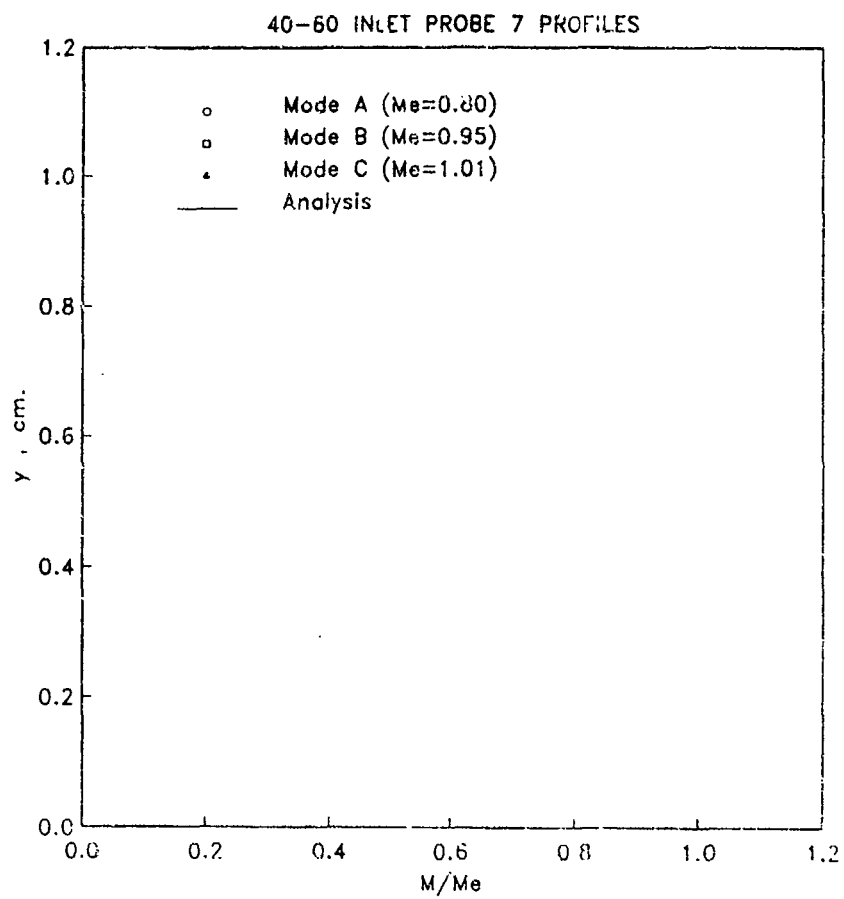


40-60 INLET PROBE 5 PROFILES



40-60 INLET PROBE 6 PROFILES





# **AR 270**

## **Microfiche Appendix to Sub-Section 3.3.8**

### **Contributions to Test Case 8**

#### **Intake/airframe integration**

**Aérospatiale**

**Sverdrup, AEDC**

**Page No's**

**A347 to A367**

**A368 to A373**

**aerospatiale**

division engins tactiques

Les Gâtines  
the 30/08/90**P. GARNERO**

Service Aérodynamique Théorique

Les Gâtines - 91370 Verrières le Buisson

FRANCE

Phone number: 1 69.81.61.33

Télécopy number: 1 69.81.65.92

**Subject:**Flow calculations of test cases defined by AGARD Working Group 13  
"Air Intakes for High Speed Vehicles"

Dear M. BISSINGER,

enclosed find a tape concerning our results for test case 6 (corresponding to the paper I have sent to you) and a new paper concerning our results for test case 3 (it replaces the last paper concerning test case 8).

Could you send our new paper concerning test case 8 to M. BENSON (NASA Lewis) who want it to make comparisons between computation and experiments? .

**Informations concerning the tape:**

Magnetic tape density: 1600 tpi

ASCII

Length of one recording in characters: 80 characters

Number of recordings by physical block: 1

Kind regards,

P. GARNERO



We have joined a tape containing all the results we have presented in the report for WG 13 TEST CASE 6.

Files have been recorded in the following order:

**FLU3M results :**

- Static pressure on the centerbody
  1. with the actual leading edge
  2. with the virtual leading edge
- Static pressure on the cowl
  3. with the actual leading edge
  4. with the virtual leading edge
- 5. Mach numbers in the cowl entrance section
- 6. Pitot pressure in the cowl entrance section

**NS2D results :**

- 7. Static pressure on the centerbody
- 8. Static pressure on the cowl
- 9. Mach numbers in the cowl entrance section
- 10. Pitot pressure  $X/X_{REF} = 5.67$
- 11. Pitot pressure  $X/X_{REF} = 5.78$
- 12. Pitot pressure  $X/X_{REF} = 5.94$
- 13. Pitot pressure  $X/X_{REF} = 6.09$
- 14. Pitot pressure  $X/X_{REF} = 6.23$
- 15. Pitot pressure  $X/X_{REF} = 6.37$
- 16. Pitot pressure  $X/X_{REF} = 6.51$
- 17. Pitot pressure  $X/X_{REF} = 6.65$
- 18. Pitot pressure  $X/X_{REF} = 6.79$

P. GARNERO - J. DE LA VIUDA  
Service Aérodynamique Théorique  
Les Gâtines - 91370 Verrières le Buisson

Les Gâtines  
the 30/08/90

Flow calculations of test cases defined by AGARD Working Group 13  
"Air Intakes for High Speed Vehicles"

TEST CASE 8  
Tailor Mate A-1 intake with fuselage

We have made 3D calculations of the Tailor Mate A-1 intake with fuselage.

1. Code used:

The code used is the 3D multi domain Euler code FLU3M using finite volume method, which has been developed by ONERA with the collaboration of *aérospatiale* (Ref. 1 and 2).

FLU3M numerically simulate flows of gases around and in complex configurations with an emphasis on supersonic and hypersonic flows.

The code organisation is built around 3 key units: a command interpreter which assumes the user interface, a plane monitoring unit which decides of the type of the computation, and a plane processor including the numerical scheme.

Its very modular coding allows the implementation of various numerical variants of Van Leer MUSCL scheme and a large variety of boundary conditions. The scheme used for our calculations was built around Van Leer fluxes and Van Albada limiter.

2. Computer used:

The FLU3M code run on a CONVEX C220 bi-processor with 512 M-octets of central memory.

### 3. Grid:

The treatment of complex geometries has led us to adopt a multiblock grid made of several structured, possibly overlapping or patched domains. This choice considerably simplifies the mesh construction and allows the same generality as unstructured grids. Such multiblock grid strategies are currently being used by *aerospatiale*.

The Tailor Mate A-1 intake/fuselage configuration needed 11 blocks built with the MULCAD procedure developed at *aerospatiale* (Ref. 3).

Two grids have been built on the right side intake configuration:

- a coarse grid made of 117626 nodes
- a fine grid made of 882511 nodes

### 4. Starting conditions:

$$M_0=2.2 \quad \alpha=0^\circ \quad \beta=0^\circ$$

Each block was initialised with the infinite upstream conditions.

We didn't know the geometry of the tested configuration after the compressor face, so we had to impose a average static pressure of 0.783 PT0 corresponding to the experimental data on the compressor face. Likewise, we didn't know the geometry of the tested configuration in the internal bleed, so we had to impose a average static pressure of 0.221 PT0 on the exit of the simplified bleed we had.

#### Remarks:

1. The grid configuration is a right side one (right side of the pilot)
2. The computation was made with the boundaries conditions (0.783 PT0 ) of the left hand inlet test data.

So the calculation corresponds to the left hand inlet configuration.

## 5. Results:

Two computations have been made:

- the first with a coarse grid
- the second with a fine grid

Figure 1 presents the coarse grid for the complete configuration (fuselage + intake)

Figure 2 presents the Mach number contours on the body and in the vertical plane of symmetry (coarse grid).

Figure 3 presents the Mach number distributions on the body and in the vertical plane of symmetry (coarse grid).

Figure 4 presents the fine grid for the complete configuration (fuselage + intake)

Figure 5 presents the Mach number contours on the body and in the vertical plane of symmetry (fine grid)

Figure 6 presents the static pressure ( $P/P_0$ ) contours on the body and in the plane of symmetry of the plane (fine grid).

Figure 7 presents the static pressure ( $P/P_0$ ) distribution on the body and in the plane of symmetry of the plane (fine grid).

Figure 8 presents the Mach number distribution in the intake (fine grid)

Figure 9 presents the static pressure ( $P/P_0$ ) distribution in the intake (fine grid)

Figure 9bis presents the Mach number distribution in the intake (fine grid)

Figure 10 presents the local Mach number ( $M_L$ ) contours for the fine grid at the entrance of the intake (in the crossflow plane going through the leading edge of the first ramp and perpendicular to the longitudinal axe of the configuration: F.S.=86.14).

Figure 11 presents the local angle of attack ( $\alpha_L$ ) contours for the fine grid at the entrance of the intake (in the crossflow plane going through the leading edge of the first ramp and perpendicular to the longitudinal axis of the configuration: F.S.=86.14).

$\alpha$  is the angle between the longitudinal axis and the projection of the speed-air vector on the plane of symmetry of the configuration.

Figure 12 presents the local sideslip angle ( $\beta_L$ ) contours for the fine grid at the entrance of the intake (in the crossflow plane going through the leading edge of the first ramp and perpendicular to the longitudinal axis of the configuration: F.S.=86.14).

$\beta$  is the angle between the velocity and the plane of symmetry of the configuration

Figure 13 presents the FLU3M results at the entrance of the intake for  $M_L$ ,  $PT_L/PT_0$ ,  $\alpha$  and  $\beta$ . These results can be compared with experimental data.

Figure 14 presents the experimental results at the entrance of the intake for  $M_L$ ,  $PT_L/PT_0$ ,  $\alpha$  and  $\beta$ .

The results in the intake, wanted in August 1990 by M. Thomas J. BENSON, concerning Surface Static Pressure, Pitot Pressure and Compressor Face Pitot, will be sent as soon as possible.

## 6. References:

1. *Numerical Simulation of perfect fluid flows around complex 3D configurations by a multidomain solver using the MUSCL approach* Ph. Guillen, M. Borrel, M. Dormieux  
Conference GAMNI/SMIA-IMA sur les Méthodes de Calcul en Mécanique des Fluides Appliquées à l'Aéronautique  
Antibes, Mai 1989
2. *Design of a 3D Multidomain Euler Code*  
Ph. Guillen, M. Dormieux  
Supercomputing in Fluid Flow - Boston October 1989.
3. *Géométrie et Maillage de Configurations Complexes pour les Calculs Aérodynamiques*  
G. Ranoux, J. Lordon, J. Diet  
AGARD - Specialists' Meeting on Applications of Mesh Generation to Complex 3D Configurations - Loen/Norway May 1989.

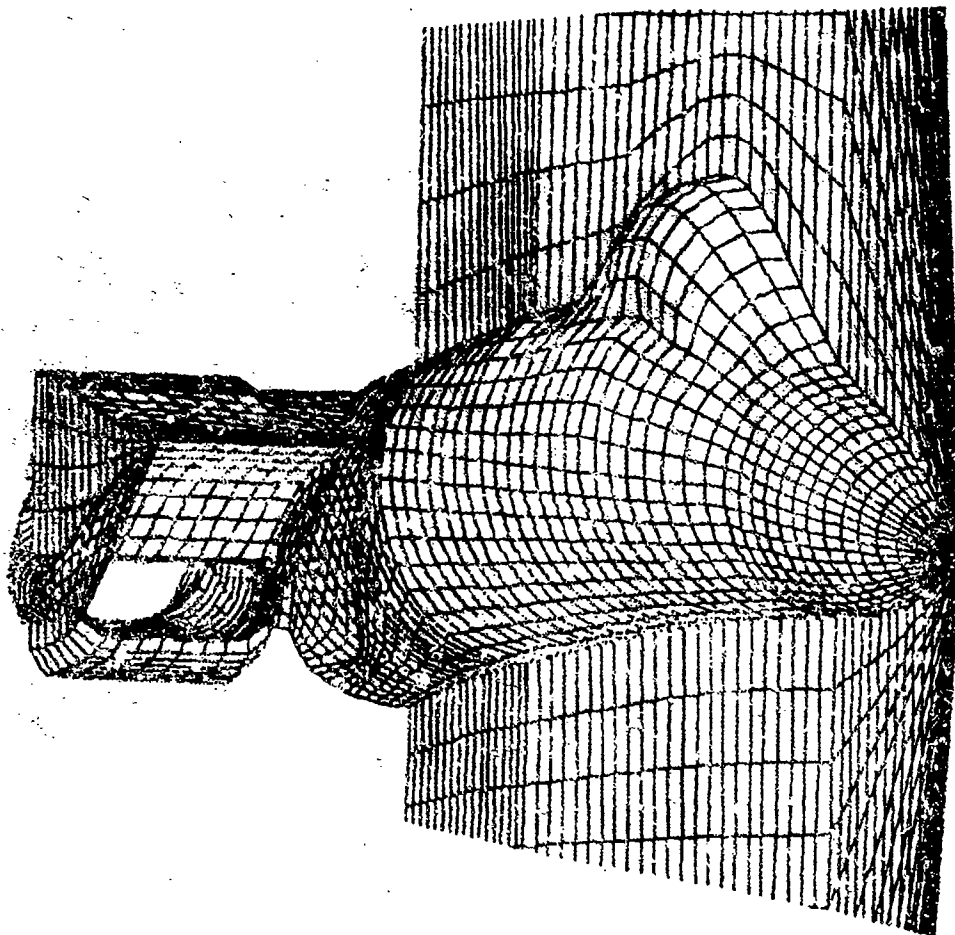


Figure 1: the coarse grid for the complete configuration (fuselage + intake)

A colour reproduction of this  
illustration can be found on  
fiche number 5.

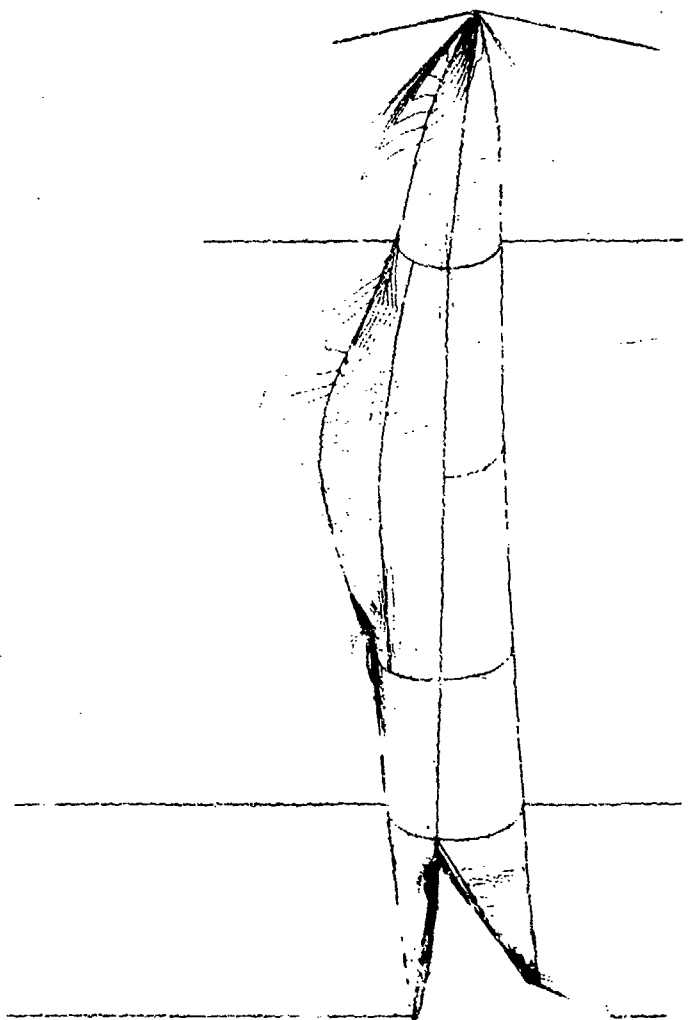


Figure 2: the Mach number contours on the body and  
in the vertical plane of symmetry (coarse grid).

STEP=0.05

2.4  
2.1  
1.8  
1.5  
1.2



A colour reproduction of this  
illustration can be found on  
fiche number 5.



2.7  
2.4  
2.1  
1.8  
1.5  
1.2

Figure 3: the Mach number distributions on the body  
and in the vertical plane of symmetry (coarse grid).

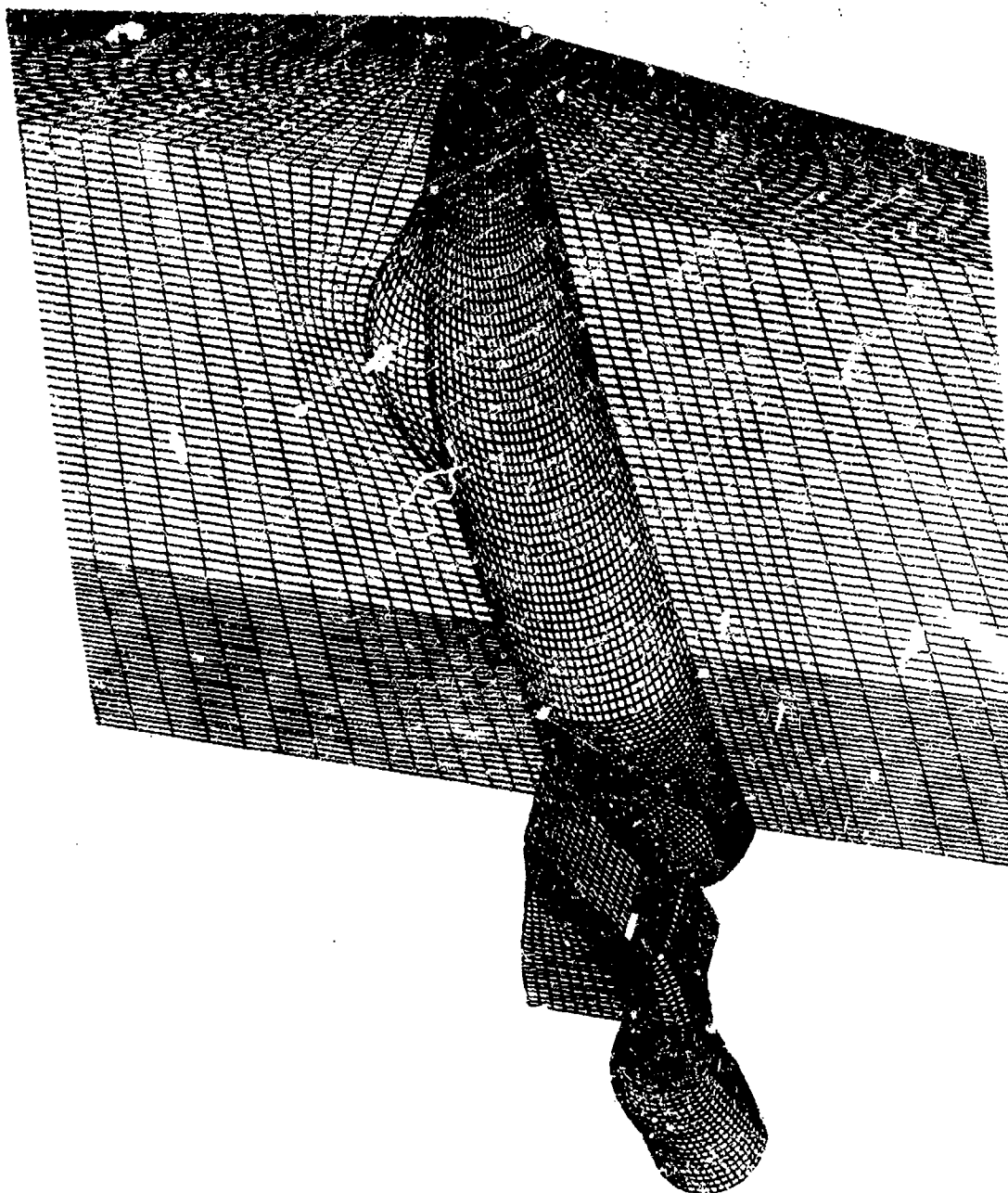


Figure 4: the fine grid for the complete configuration  
(fuselage + intake)

A colour reproduction of this  
illustration can be found on  
fiche number 5.

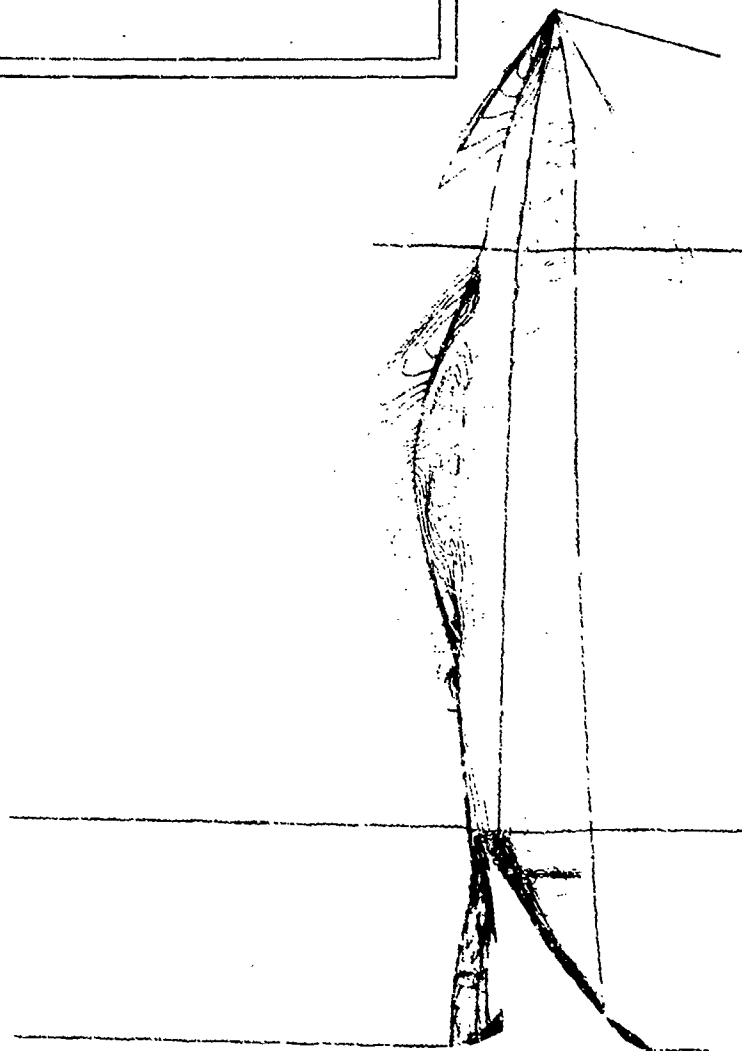
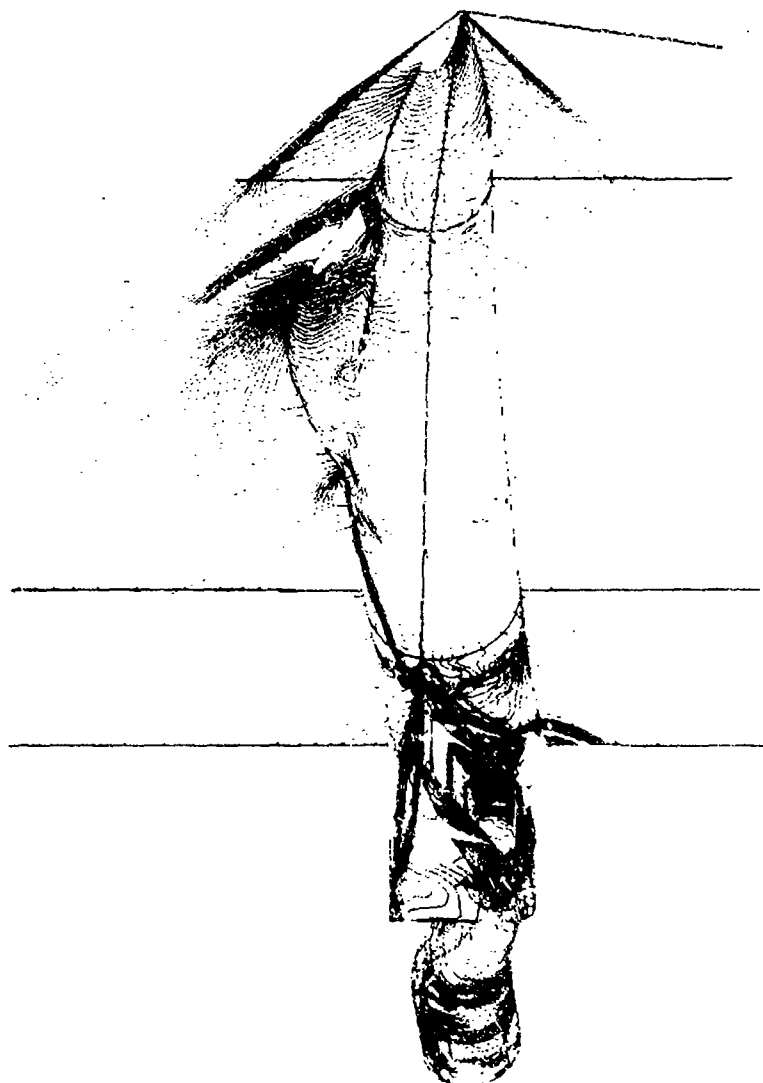


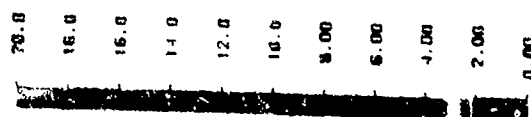
Figure 5 : the Mach number contours on the body and  
in the vertical plane of symmetry  
(fine grid)

2.8  
2.4  
2.0  
1.6  
1.2  
0.8

STEP=0.05



A colour reproduction of this illustration can be found on fiche number 5.



**STEP=0.05**



Figure 7: the static pressure (P/P0) distribution on the body and in the plane of symmetry of the plane (fine grid).

A colour reproduction of this  
illustration can be found on  
fiche number 5.

3.00  
2.75  
2.50  
2.25  
2.00  
1.75  
1.50  
1.25  
0.900  
0.825  
0.750  
0.600



Figure 8: the Mach number distribution in the intake  
(fine grid)

A colour reproduction of this  
illustration can be found on  
fiche number 5.

10.0  
9.0  
8.0  
7.0  
6.0  
5.0  
4.0  
3.0  
2.0  
1.0  
0.00

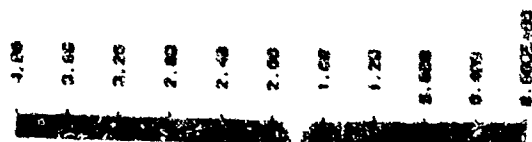


Figure 9: the static pressure ( $P/P_0$ ) distribution in  
the intake (fine grid)

A colour reproduction of this  
illustration can be found on  
fiche number 5.



Figure 9bis: the Mach number distribution in the  
intake (fine grid)



A colour reproduction of this  
illustration can be found on  
fiche number 5.

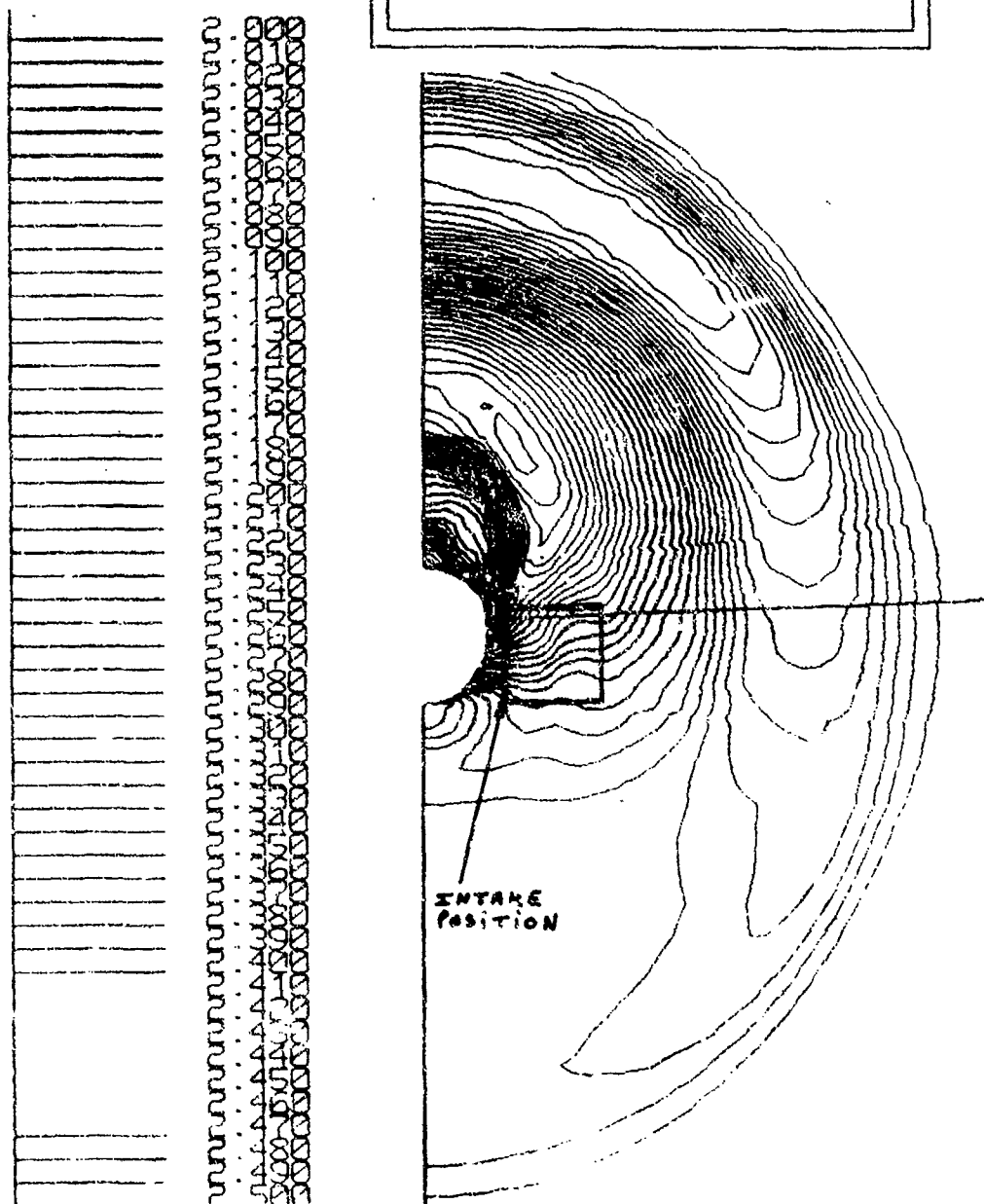


Figure 10 : Local Mach number ( $M_L$ ) contours for the fine grid at the entrance of the intake (in the crossflow plane going through the leading edge of the first ramp and perpendicular to the longitudinal axe of the configuration: F.S.=86.14).



A colour reproduction of this  
illustration can be found on  
fiche number 5.

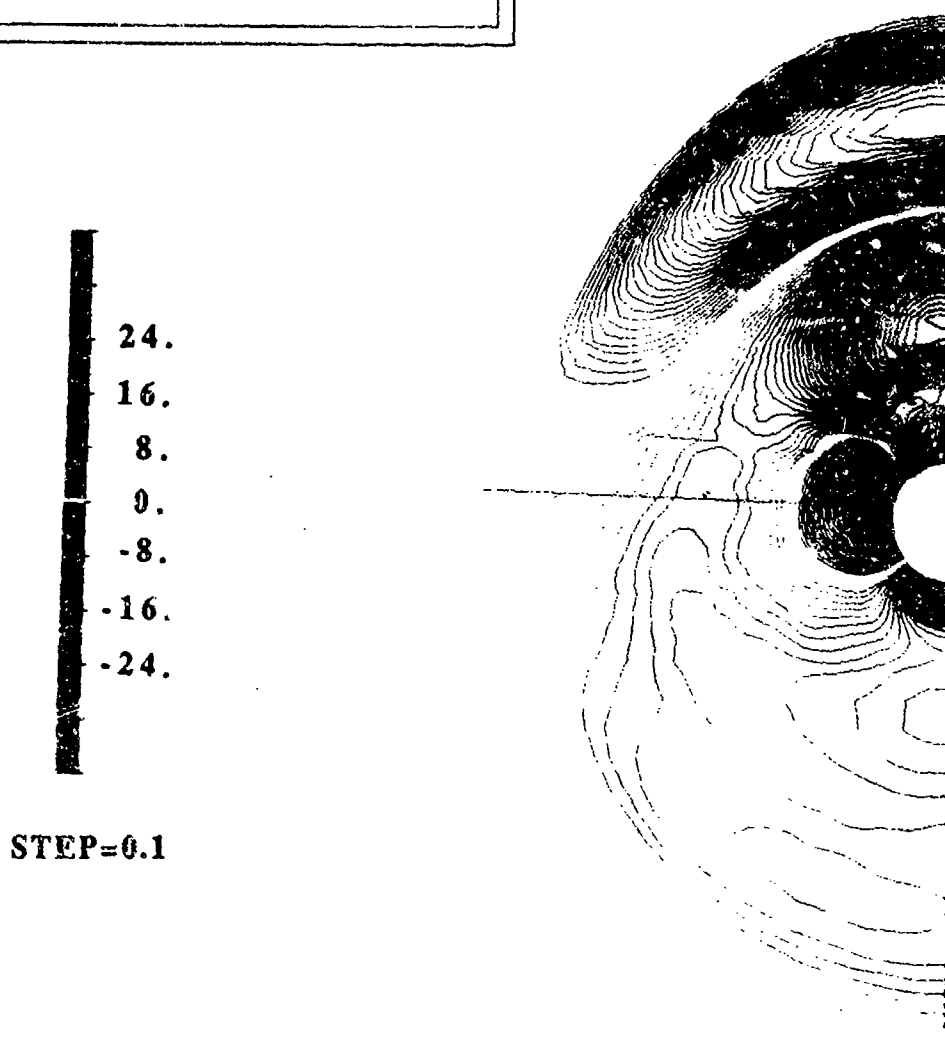


Figure 11: Local angle of attack ( $\alpha_L$ ) contours for the fine grid at the entrance of the intake (in the crossflow plane going through the leading edge of the first ramp and perpendicular to the longitudinal axis of the configuration: F.S.=86.14).

$\alpha$  is the angle between the longitudinal axis and the projection of the speed air vector on the plane of symmetry of the configuration.

A colour reproduction of this  
illustration can be found on  
fiche number 5.

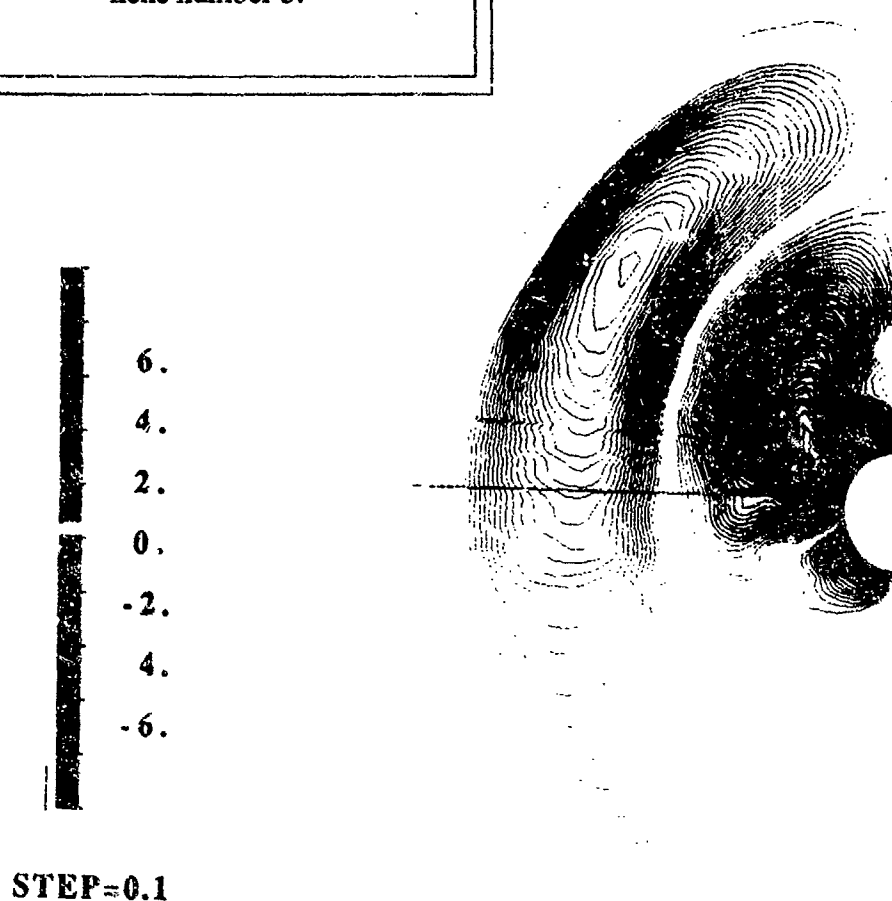


Figure 12: Local sideslip angle ( $\beta_L$ ) contours on the fine grid at the entrance of the intake (in the crossflow plane going through the leading edge of the first rampe and perpendicular to the longitudinal axis of the configuration: F.S.=86.14).

$\beta$  is the angle between the velocity and the plane of symmetry of the configuration

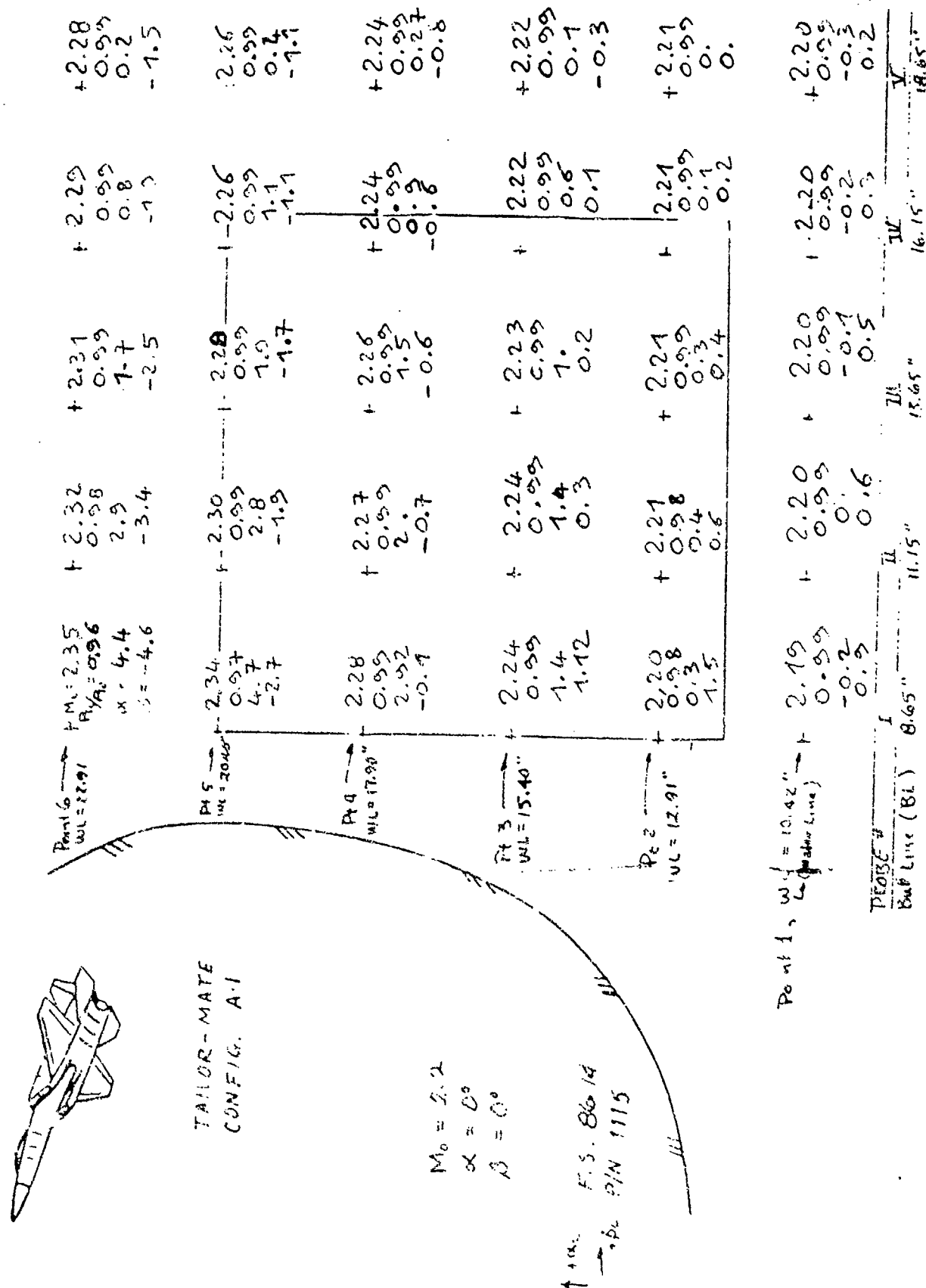


Figure 13: FLU3M results at the entrance of the intake for ML, PTL/PTG,  $\alpha$  and  $\beta$ . These results can be compared with experimental data.

Promer 366  
(Identification)



TAILOR-MATE  
CONFIG. A-1  
Flowfield data

$M_0 = 2.2$   
 $\alpha = 0^\circ$   
 $\beta = 0^\circ$

F.S. 8614  
P/N 1115

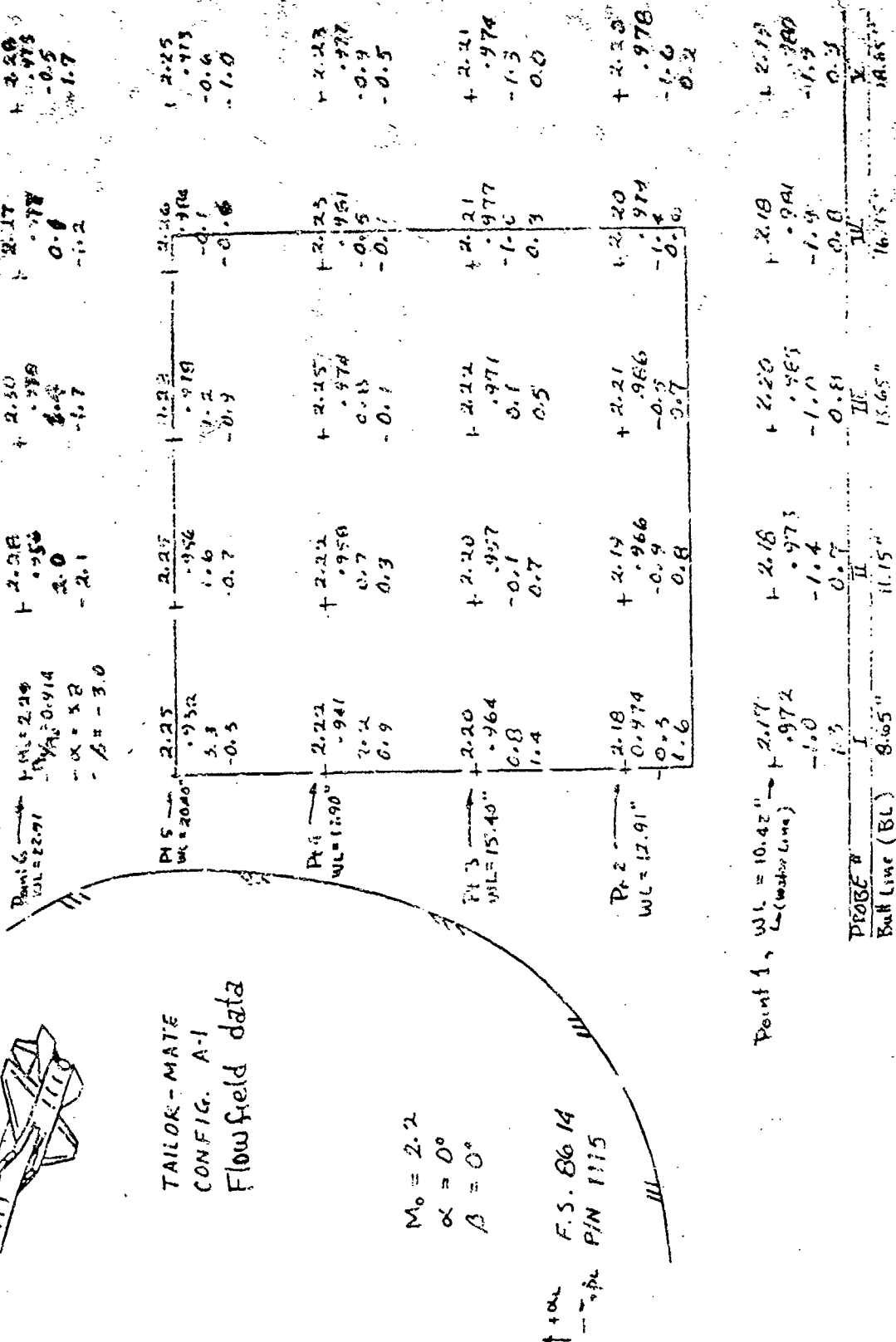


Figure 14: the experimental results at the entrance of the entake for  $M_L$ ,  $PT_L/PT_0$   $\alpha$  and  $\beta$ .

**Soundings**

**Soundings Technology, Inc.**  
 AEDC Group  
 Mail Stop 900  
 Arnold Air Force Station  
 Tennessee 37229-9000  
 615-484-3000

August 7, 1990

Dr. Tom J. Benson  
 Internal Fluid Mechanics Division  
 MSS-7  
 NASA Lewis Research Center  
 Cleveland, OH 44135  
 216-433-5920

Dear Tom:

SUBJECT: AGARD-FDP WORKING GROUP 13, SVT/AEDC CONTRIBUTION TO HIGH SPEED AIR INTAKES STUDY

Relative to our discussions in July, we have finished the AGARD Test Case 8 for the Tailor-Mate configuration at a Mach No. of .9 with zero pitch and yaw conditions (Attachment I). Enclosed please find the flow field data asked for at the fuselage station 86.14. In our analysis of the results from these calculations, we were surprised at the large discrepancies between the mean Mach No. level at the reference station between calculations and experimental data. As noted in the additional comments to follow, we made some exploratory simplified calculations to try and understand these differences. We believe that the calculation trends are correct and consistent with expected behavior for inlets with high spillage. In addition, the experimental data does not appear to capture expected trends of pitch angle and Mach No. just above the upper inlet lip. As a result, we believe that the experimental data should be reviewed for accuracy before it is included in the AGARD summary report.

Within this transmittal, we have also included additional information on each of the calculations submitted to you so that a more complete picture of the calculation approach may be made (Attachment II). The additional information is broken down into seven basic areas: (1) CFD methodology, (2) computer resources, (3) boundary conditions/starting conditions, (4) convergence, (5) solution quality redundancy checks, (6) experience in obtaining solution, and (7) special tricks or techniques. All of our computations utilized the current released version of the 2-D/3-D PARC code which is documented in:

Cooper, G. K. and Sirbaugh, J. R., "The PARC Distinction: A Practical Flow Simulator", AIAA-90-2002 presented at AIAA/SAE/ASME/ASCE 26th Joint Propulsion Conference, July 16-18, 1990, Orlando, Florida.

All calculations utilized the standard PARC Baldwin Lomax Turbulence Model with no specialized tuning to perform the test case calculations. It should be noted that this model has been tuned specifically for wake type flows, enhanced computational robustness and efficiency. Since most of the test cases were wall viscous dominated, our results do not compare with the experimental data as well as calculations made with a more appropriate turbulence model such as the k-epsilon model or the conventional Baldwin/Lomax Turbulence Model.

Dr. Tom J. Benson  
Page 2  
August 7, 1990

In general, no special tricks were used to force the calculations and data to agree. We made a special effort to execute these calculations in a production type mode where standard job set-up, execution, and post-processing activities were followed.

In addition, a review of the previous AGARD submittal to you uncovered a significant error in the presentation of the results for test case 6. We have corrected this error and are resubmitting the test case 6 results in terms of plotted results and a floppy disk containing requested information (Attachment III). If it is not too late, please discard the previous test case 6 results for the hypersonic inlet and replace them with the corresponding results from this package.

I trust that the additional information supplied in this package will be timely enough to include in the AGARD Summary Report. We have a sincere desire to be responsive to this AGARD initiative and will provide additional information if the current transmittals are insufficient in selected areas or miss the intended purposes. Please call if I can be of further help in bringing this important activity to a fruitful conclusion. We would appreciate any pre-release of comparative information and are looking forward to the ultimate conclusion and publication of the AGARD Summary Report.

Sincerely,



Dr. M. O. Varner, Supervisor  
Propulsion Computational Technology Section

## Attachment I

## AGARD Test Case 8:

## Tailor-Mate Test Point 4

## A. CFD Methodology

code definition: 3D multi-blocked PARC

code reference:

gas model: ideal constant gamma(=1.4)

turbulence model: ran inviscid with slip walls

## B. Computer Resources

CPU time(CRAY-XMP): 72000 seconds

no. of iterations: 8400

memory requirements/grid size:

3 blocks; total of 114000 points

## C. Boundary Conditions/Starting Conditions

inflow boundary: free, fixed total pressure and temperature... $P_{\infty} = 7.414$  psia;  $T_{\infty} = 569^{\circ}\text{R}$

outflow boundary: free, fixed static pressure and temperature... $P/P_{\infty} = 0.5914$ ;  $T/T_{\infty} = 0.8606$

internal mass flow boundaries: static pressure manually changed to achieve required mass flow values

wetted surfaces: slip boundaries

initial conditions: uniform freestream conditions, ie.  $M_{\infty} = 0.9$ , and  $\alpha = \beta = 0.0$

## D. Convergence

solution was considered converged when desired mass flow rates through ducts and bleeds were not changing by more than a few percent

## E. Solution Quality Redundancy Checks

none performed

## F. Experience in obtaining Solution

initially the upstream bleeds were not modeled. Later in solution the bleeds were put in with little effect on the overall solution. A considerable amount of difference was seen between the CFD results and the wind tunnel data at the data reference plane. Two possible reasons for the disagreement were investigated.

1. Upstream bleeds were not modeled initially. These bleeds were included later with only small changes in the reference plane data.
2. The influence of the downstream outflow boundary on the reference plane flowfield was shown to be negligible when a simplified axisymmetric model was

run with the outflow plane moved far downstream from the region of interest.

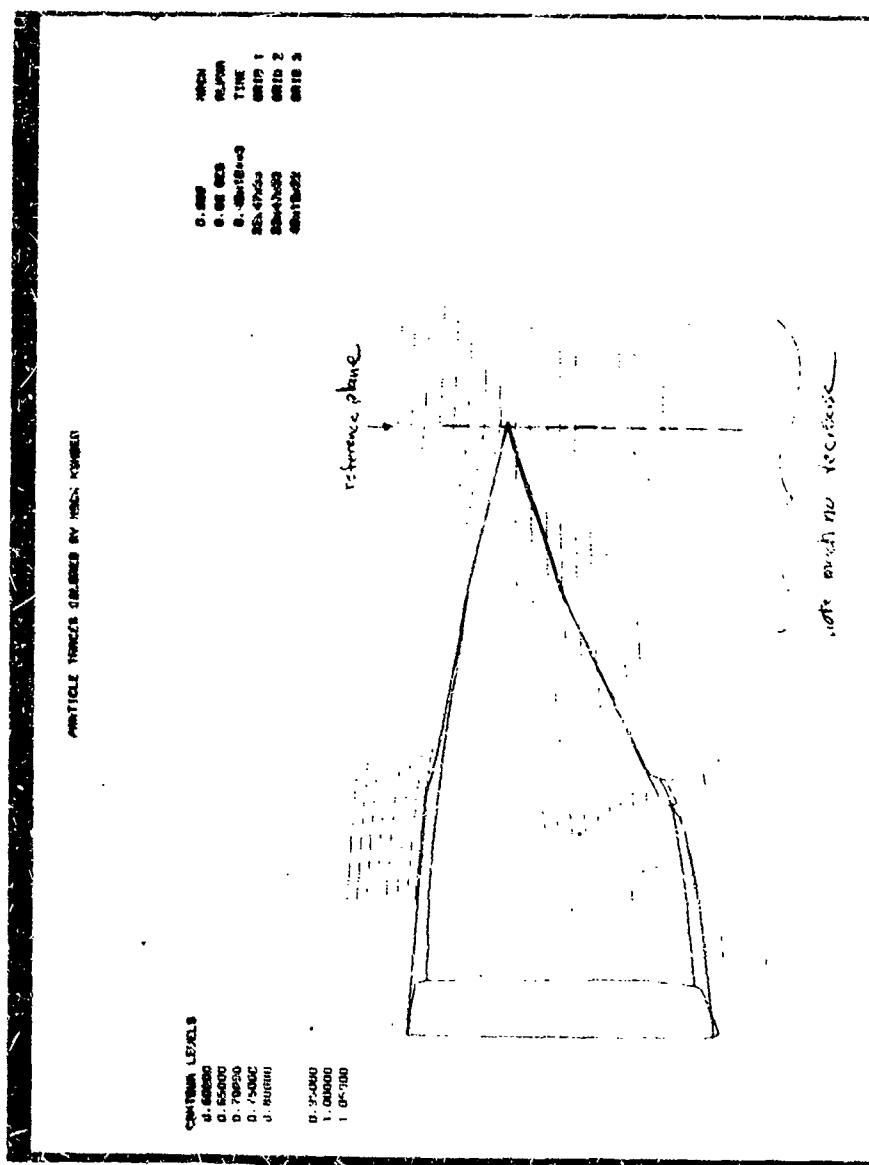
The disagreement in the data near the upper cowl lip is especially puzzling. CFD results show significant upwash angles in the flow. A simple 2D ramp problem was run with the same cowl surface slope (~13.8 deg) as the model and showed upwash angles of several degrees near the ramp leading edge as does the full model calculations. A general decrease in the mach number in front of the inlet is noted which is as great as ten percent. A visual look at the flowfield in this region using PLOT3D streamline capability with mach no. contouring reveals the inlet is definitely spilling mass. The given capture ratio of 0.589 would tend to bear out these results.

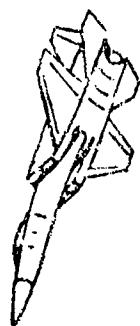
G. Special Tricks or Techniques

none other than those already mentioned



A colour reproduction of this  
illustration can be found on  
fiche number 5.




 $W.L. = 24.92$ 

TAILOR-MATE  
CONFIG. A-1  
Flowfield  
Data

(AEDC PARC)

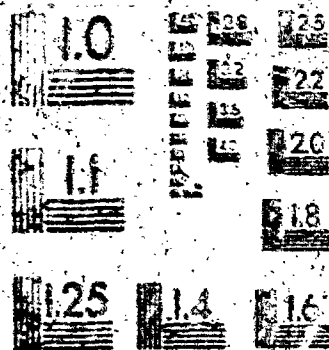
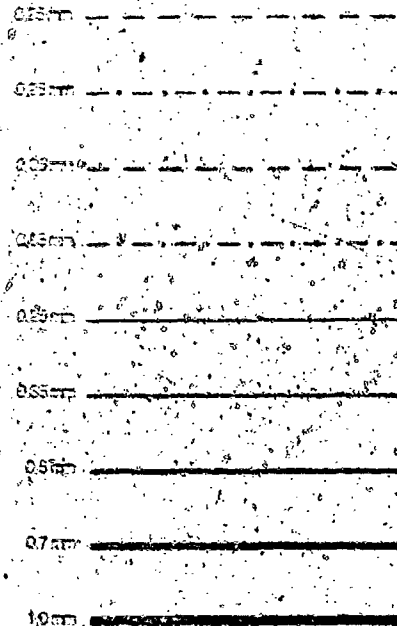
$M_0 = 0.9$   
 $\alpha = 0^\circ$   
 $\beta = 0^\circ$

F.S. 86.14  
P/N 2475

$M_L = 0.76$ $R_L/R_0 = +0.998$ $\alpha_L = 4.8$ $\beta_L = -3.5$	$+0.75$ $+0.999$ $5.0$ $-1.7$	$+0.74$ $+0.998$ $4.5$ $0.1$	$+0.76$ $+1.003$ $3.4$ $1.9$	$+0.79$ $+1.000$ $1.9$ $2.7$
$+0.64$ $+0.995$ $5.4$ $-4.3$	$+0.61$ $+0.999$ $6.8$ $-1.7$	$+0.62$ $+0.994$ $8.5$ $0.5$	$+0.67$ $+0.996$ $5.8$ $3.1$	$+0.80$ $+1.003$ $-0.3$ $3.3$
$+0.77$ $+1.006$ $1.3$ $0.2$	$+0.77$ $+1.003$ $-0.4$ $0.7$	$+0.78$ $+1.003$ $-0.8$ $1.2$	$+0.79$ $+1.002$ $-0.9$ $1.9$	$+0.81$ $+1.002$ $-0.3$ $2.1$
$+0.79$ $+1.010$ $0.9$ $1.0$	$+0.79$ $+1.003$ $-0.2$ $1.1$	$+0.80$ $+1.002$ $-0.5$ $1.4$	$+0.81$ $+1.002$ $-0.5$ $1.7$	$+0.82$ $+1.002$ $-0.3$ $1.7$
$+0.80$ $+1.005$ $-0.1$ $1.7$	$+0.80$ $+1.002$ $-0.3$ $1.3$	$+0.81$ $+1.002$ $-0.5$ $1.3$	$+0.82$ $+1.002$ $-0.5$ $1.4$	$+0.83$ $+1.001$ $-0.4$ $1.6$
$+0.81$ $+1.001$ $-0.9$ $1.5$	$+0.81$ $+1.000$ $-0.7$ $1.4$	$+0.82$ $+1.000$ $-0.7$ $1.4$	$+0.83$ $+1.001$ $-0.6$ $1.4$	$+0.83$ $+1.001$ $-0.5$ $1.4$
10.40	11.15	13.05	16.15	18.65
$B.L. = 8.65$				

Mikrofilmtechnisches Test-Bild  
Micro Copy Resolution Test Chart  
Mire pour contrôle de netteté

Linienmuster

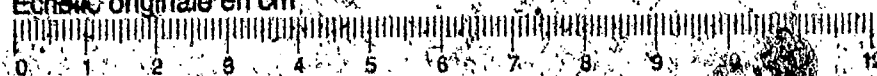


MICROCOPY RESOLUTION TEST CHART  
NATIONAL BUREAU OF STANDARDS  
STANDARD REFERENCE MATERIAL 1010A  
(ANSI and ISO TEST CHART No. 2)

Verkleinerungsfaktoren von:  
Scale of reduction of:  
Facteur de réduction:

- a) dieser Aufnahme  
the present copy 24 x  
de cette photo
- b) allen nachfolgenden Aufnahmen  
all following copies  
de toutes les photos suivantes

Originalmaßstab in cm  
Original scale in cm  
Échelle originale en cm



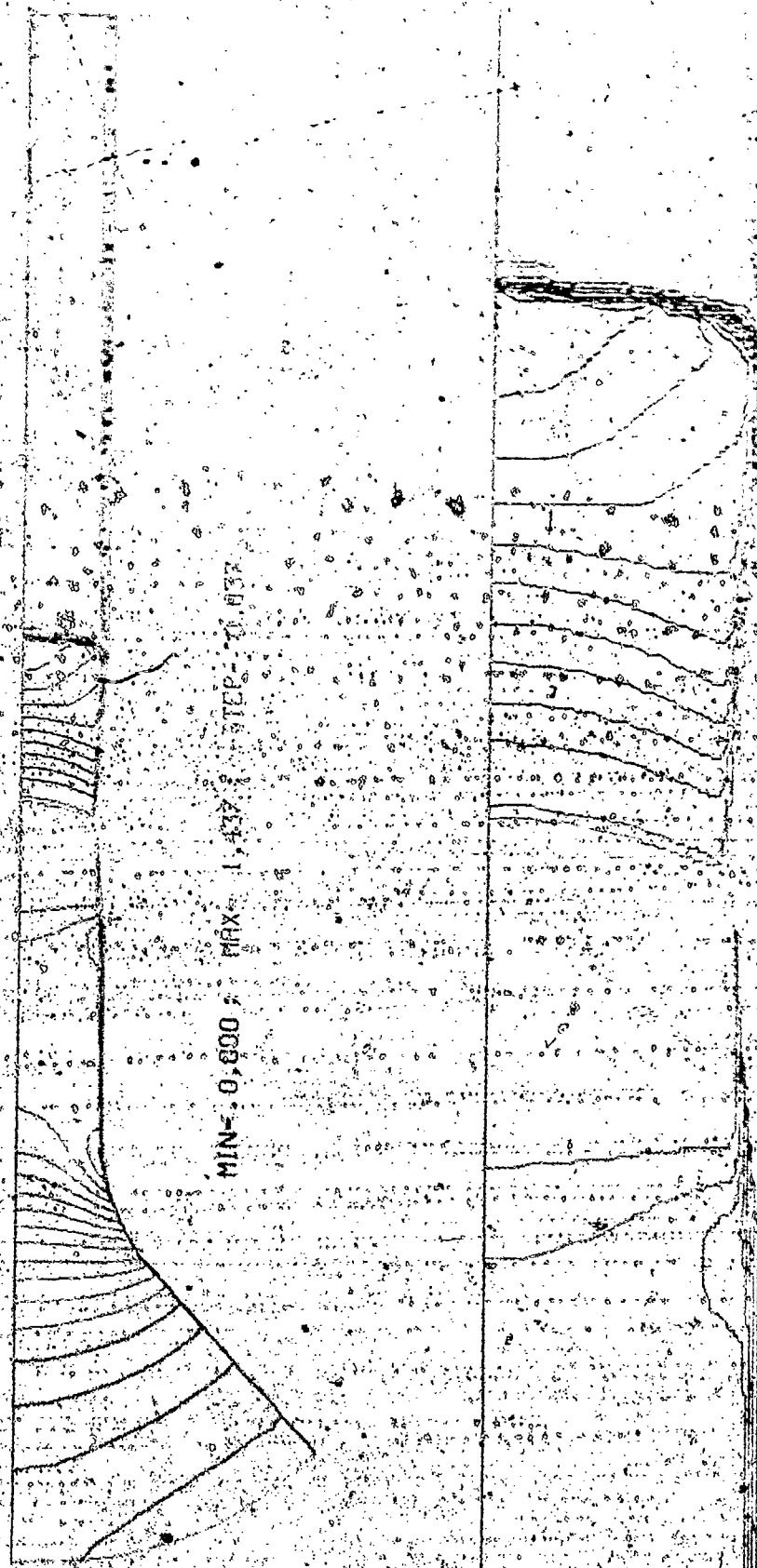


FIG. 8. Elevation of the dam crest, 1.1

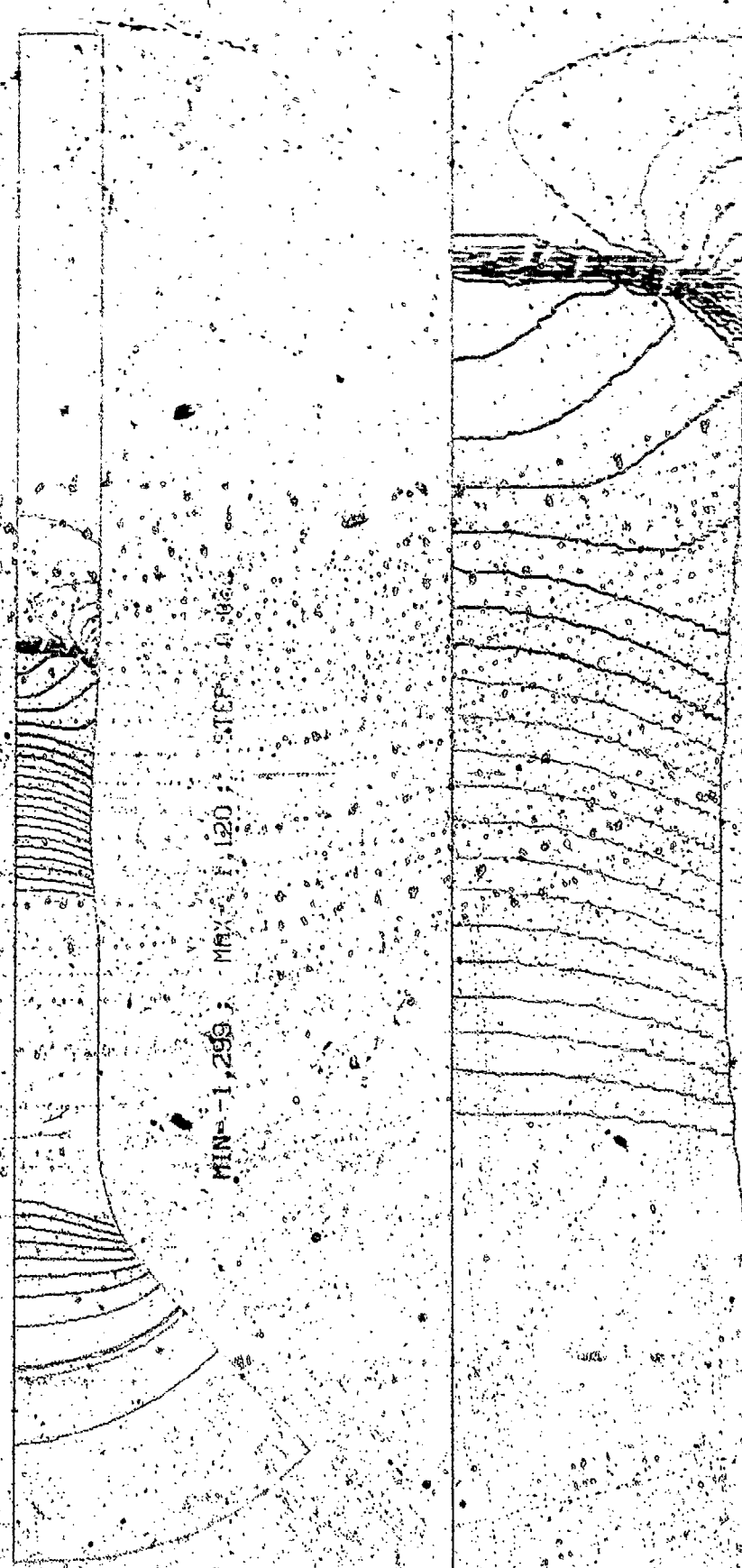


Fig. 9 Isolines of pressure coefficient  $C_p$ , test case 1:1

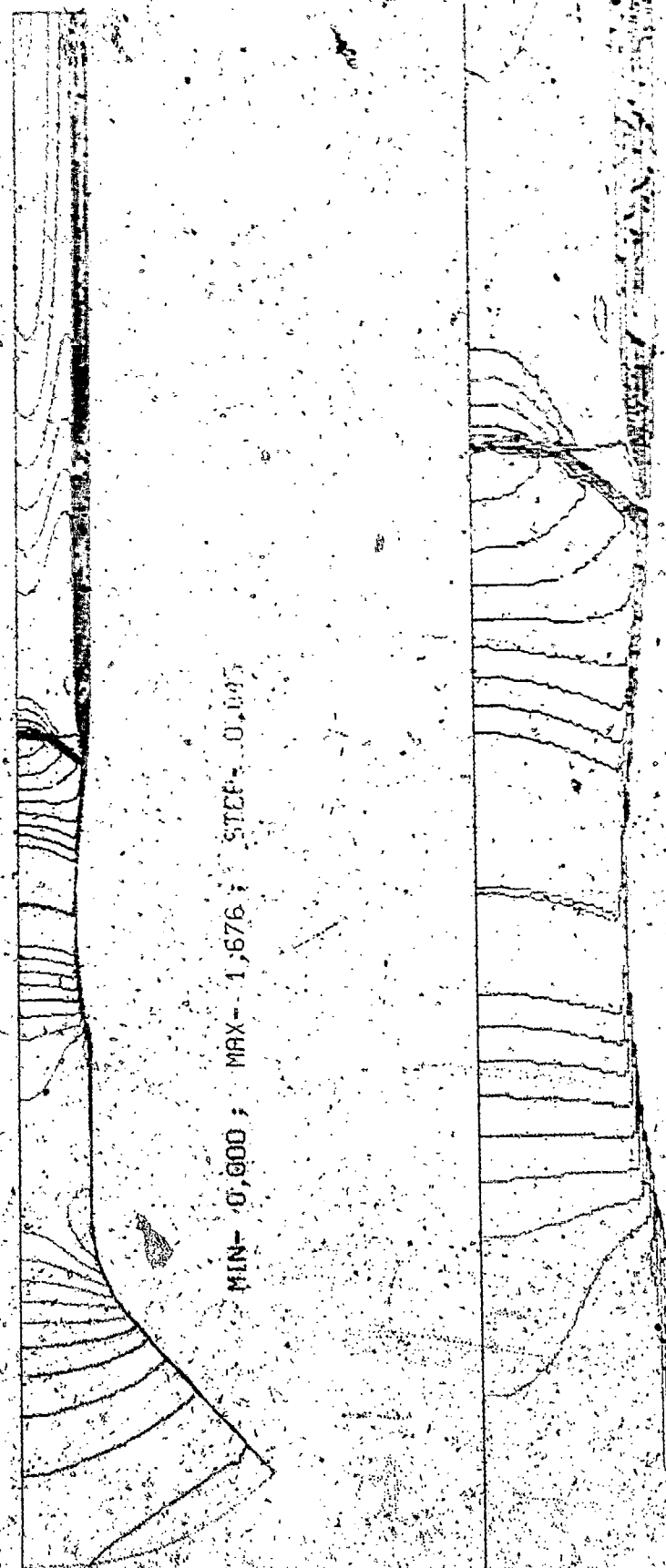


Fig. 14 Isolines of Mach number, test case 1.2

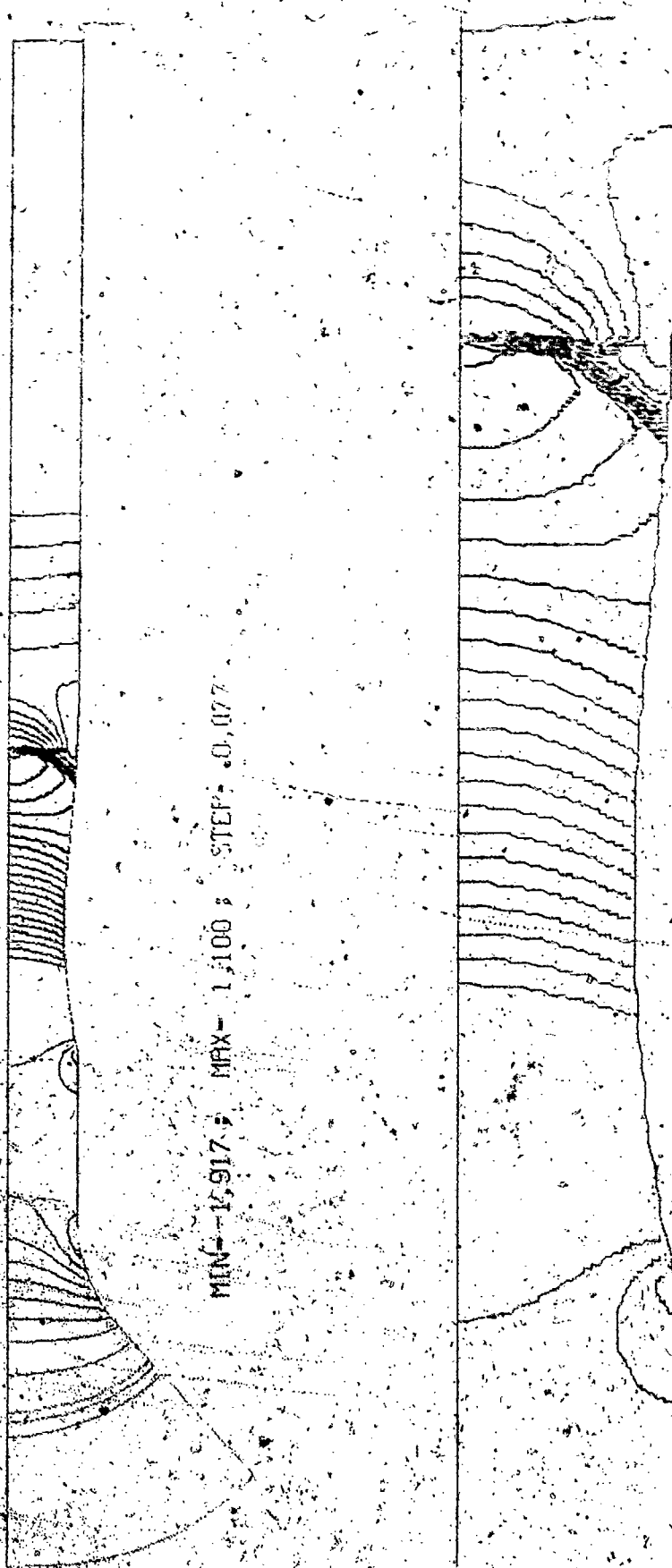


Fig. 15. Isolines of pressure coefficient  $C_p$ , test case 1.52



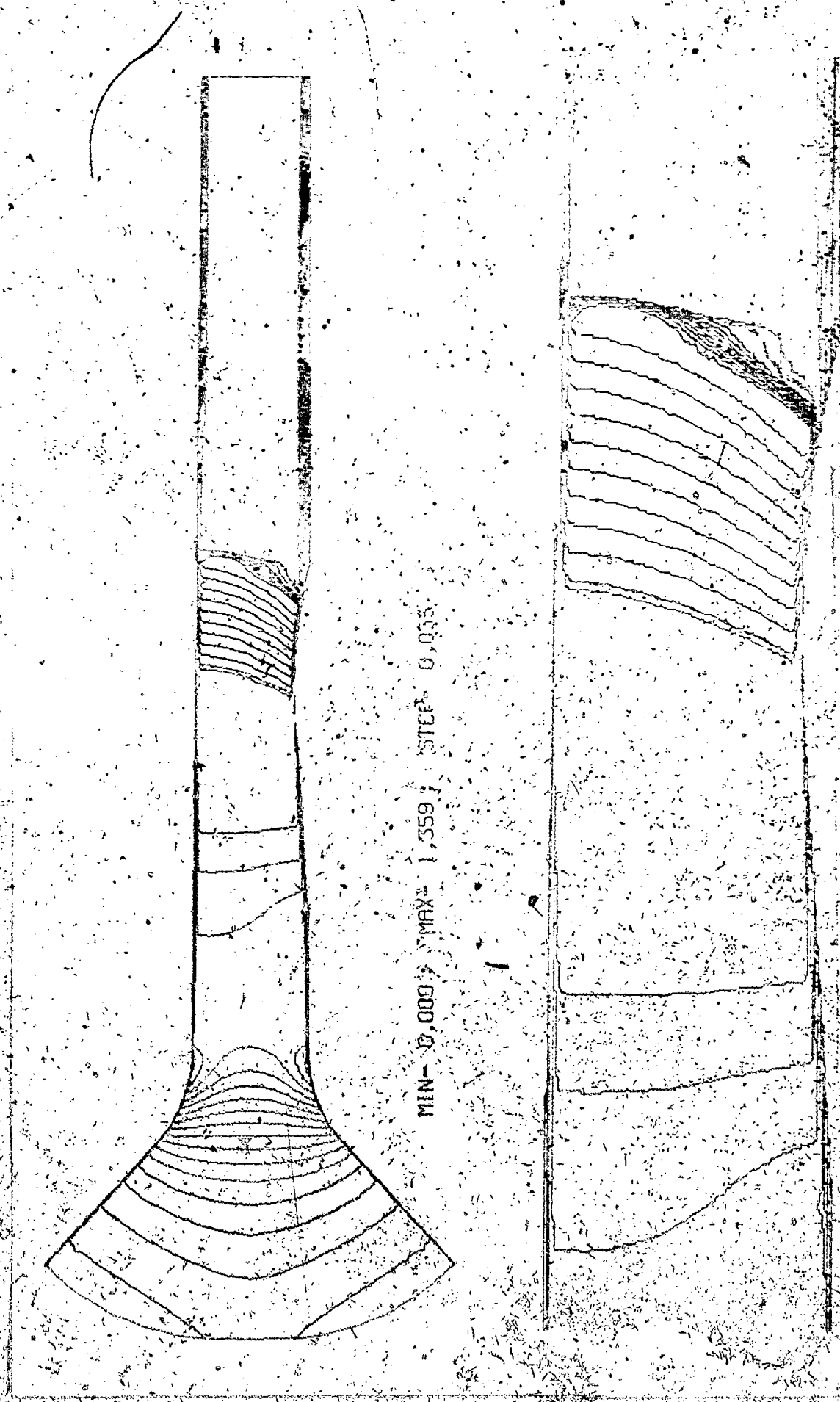


Fig. 20 Isolines of Mach number, test case 1.3



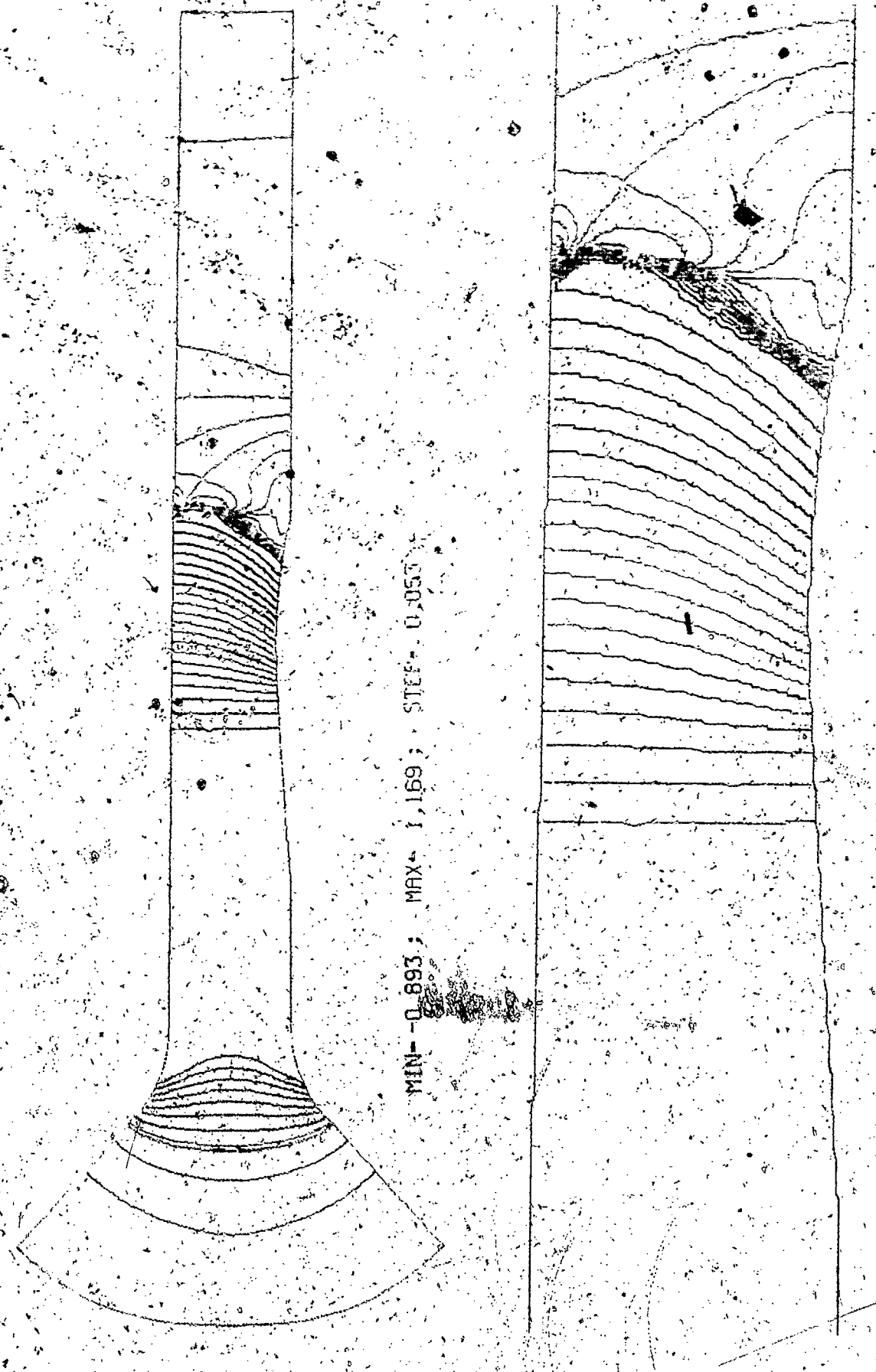
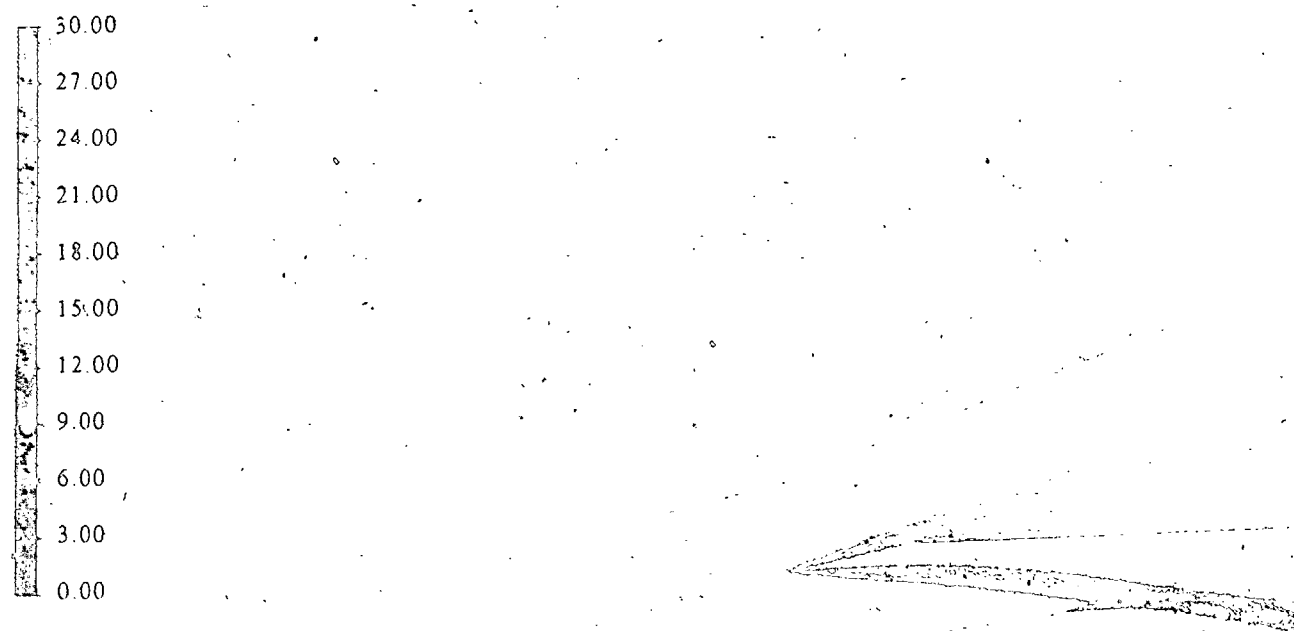
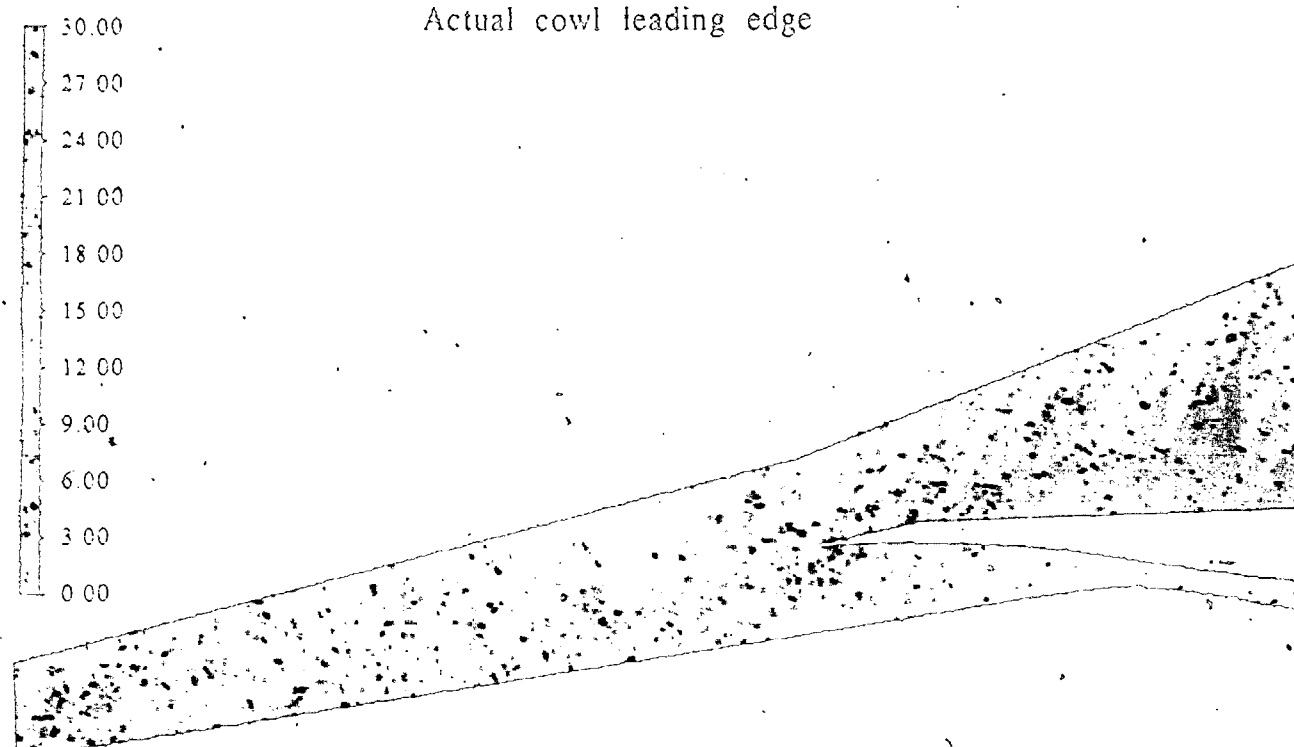


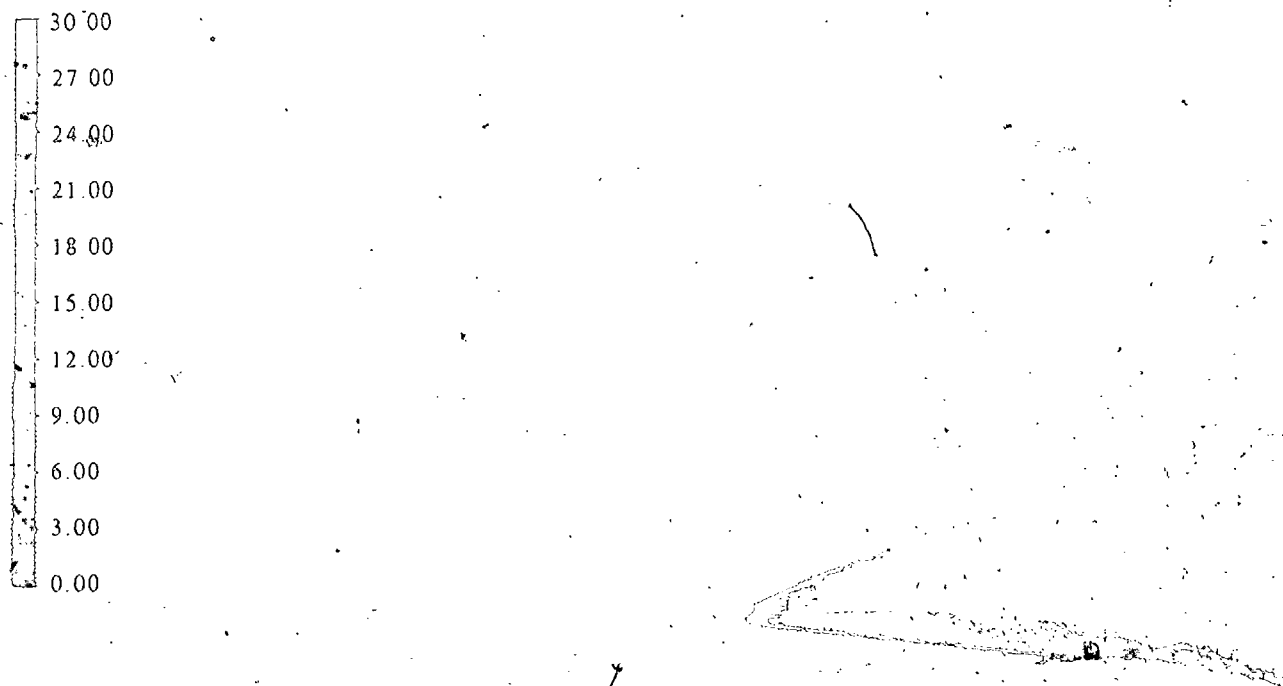
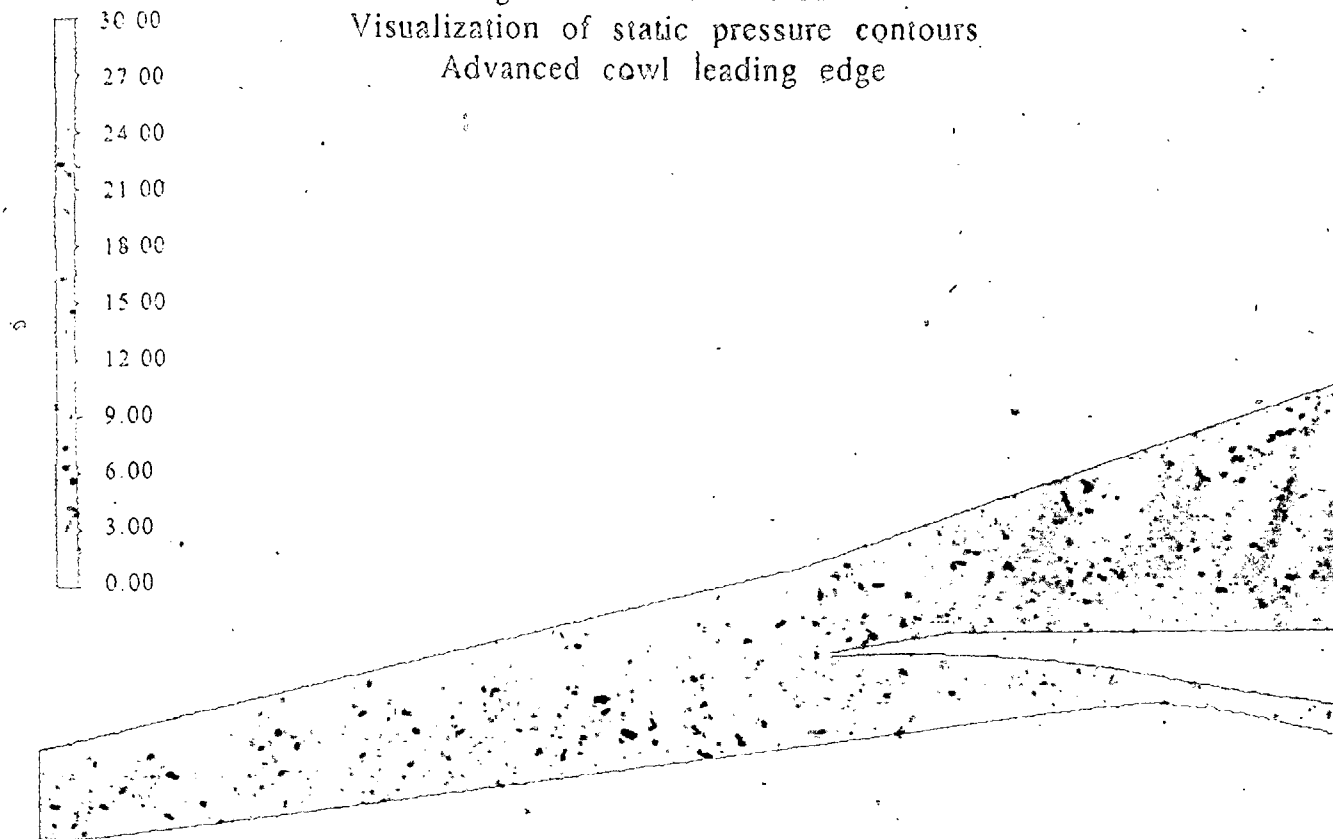
fig. 21 isolines of pressure coefficient  $c_p$ , test case 1.3

Figure 8.: FLU3M results  
Visualization of static pressure contours  
Actual cowl leading edge



Step of 0.8

Figure 9 : FLU3M results  
Visualization of static pressure contours  
Advanced cowl leading edge



Step of 0.9

Figure 10: FLU3M results  
Visualization of Mach number contours  
Actual cowl leading edge

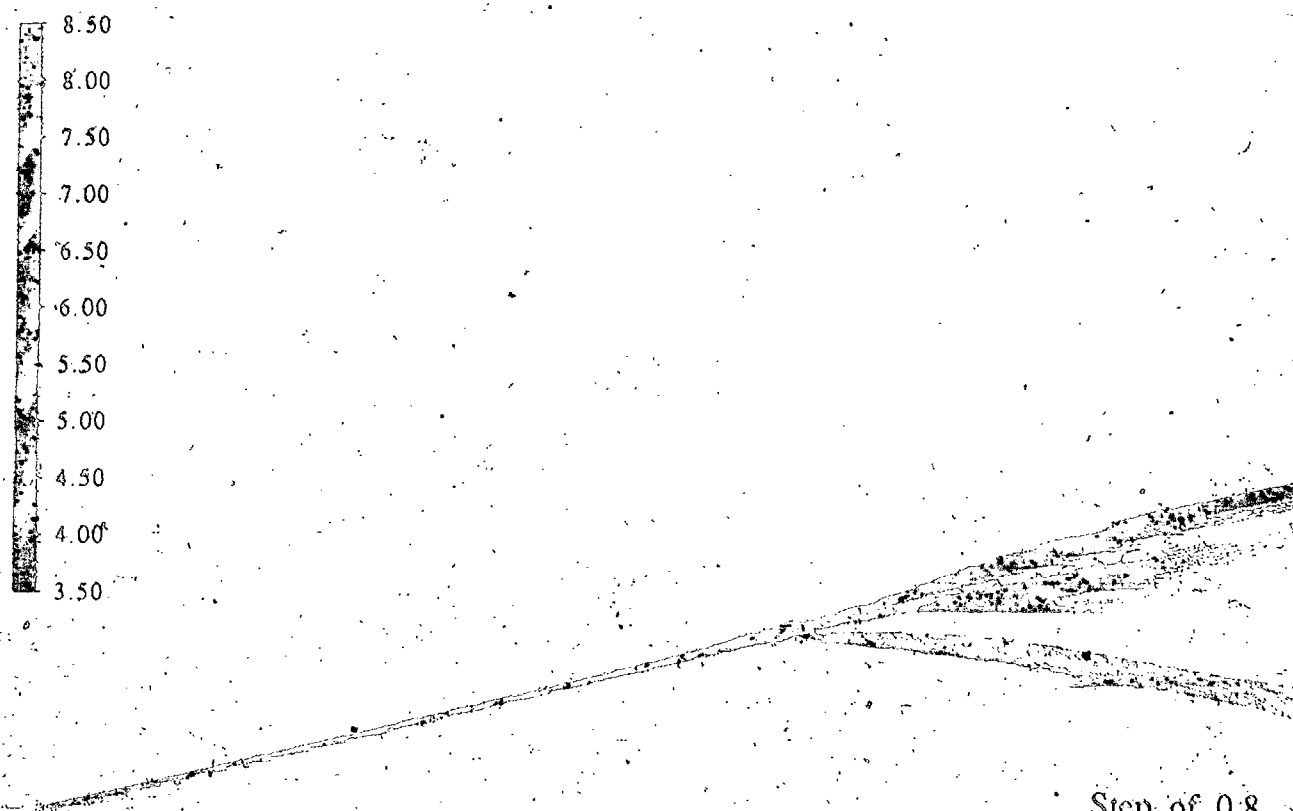
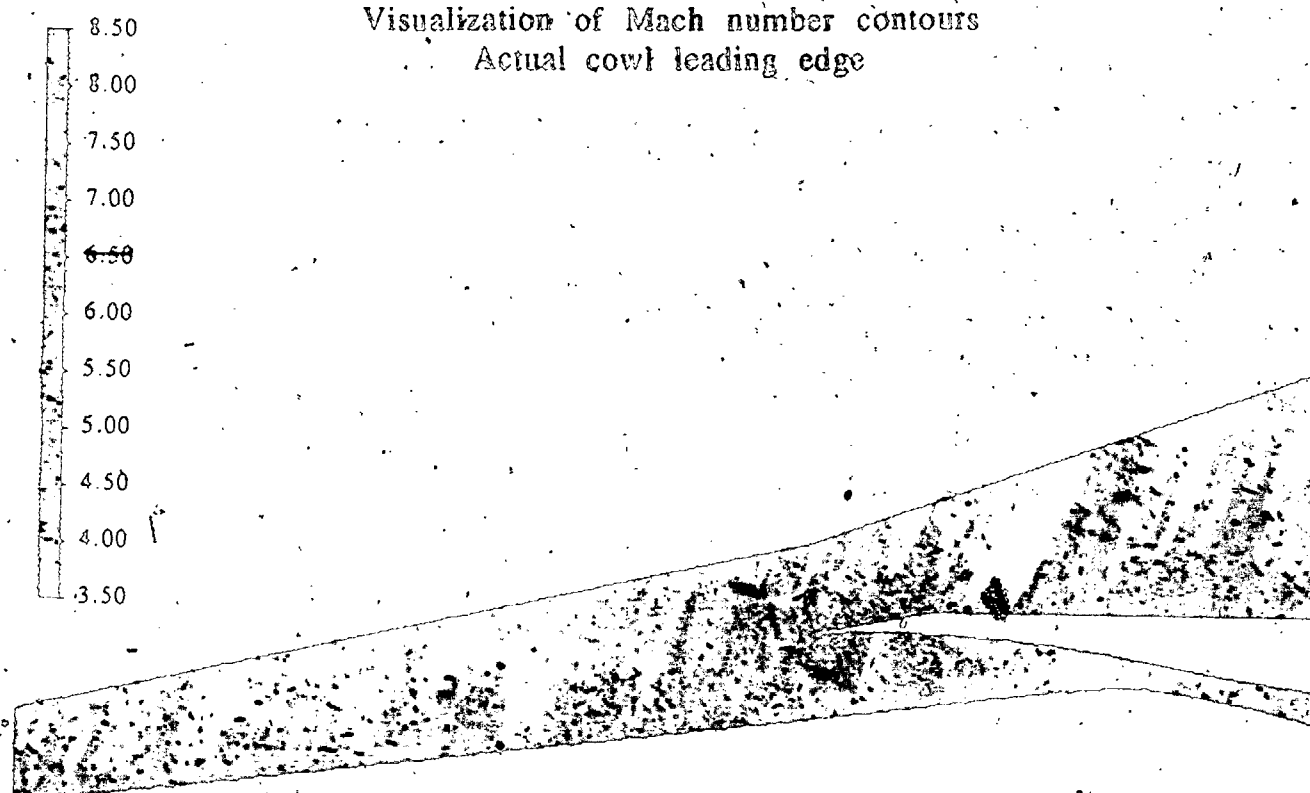
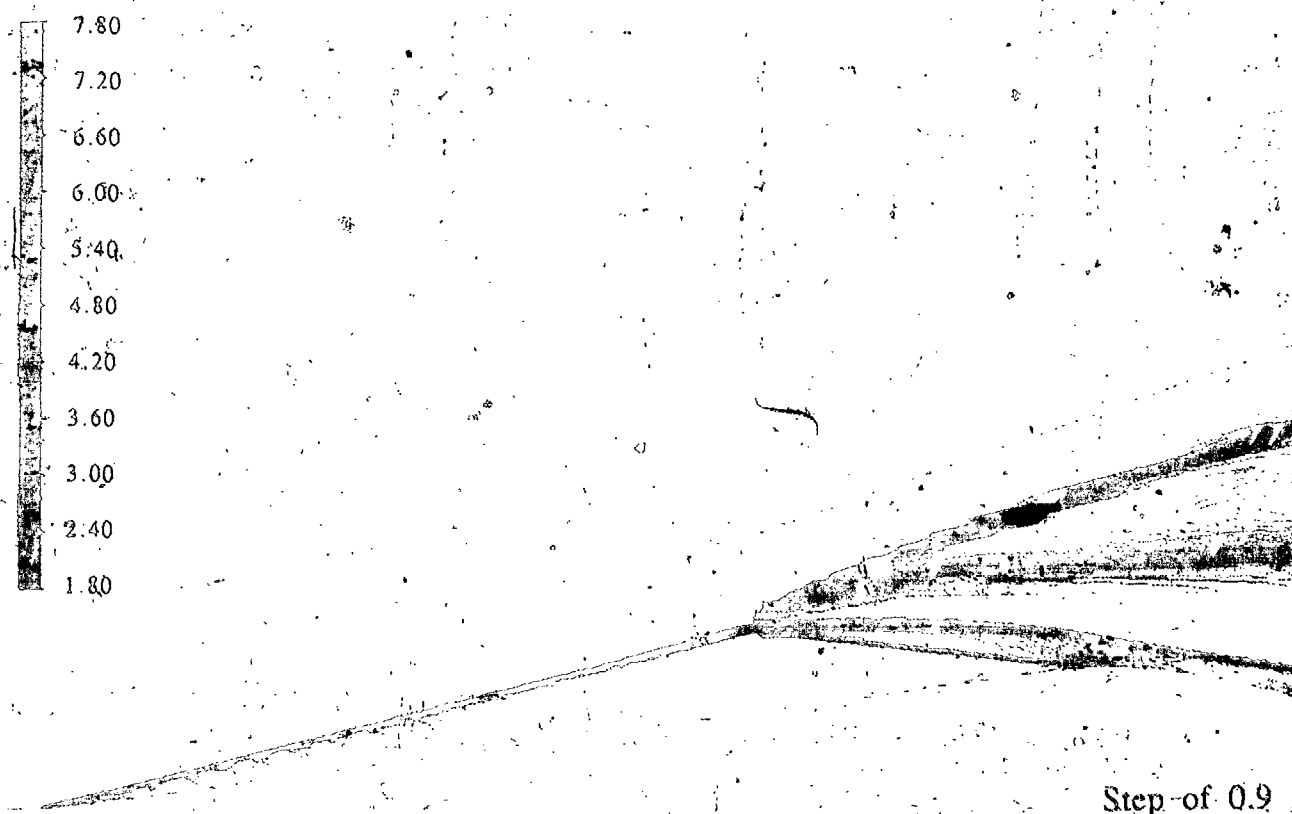
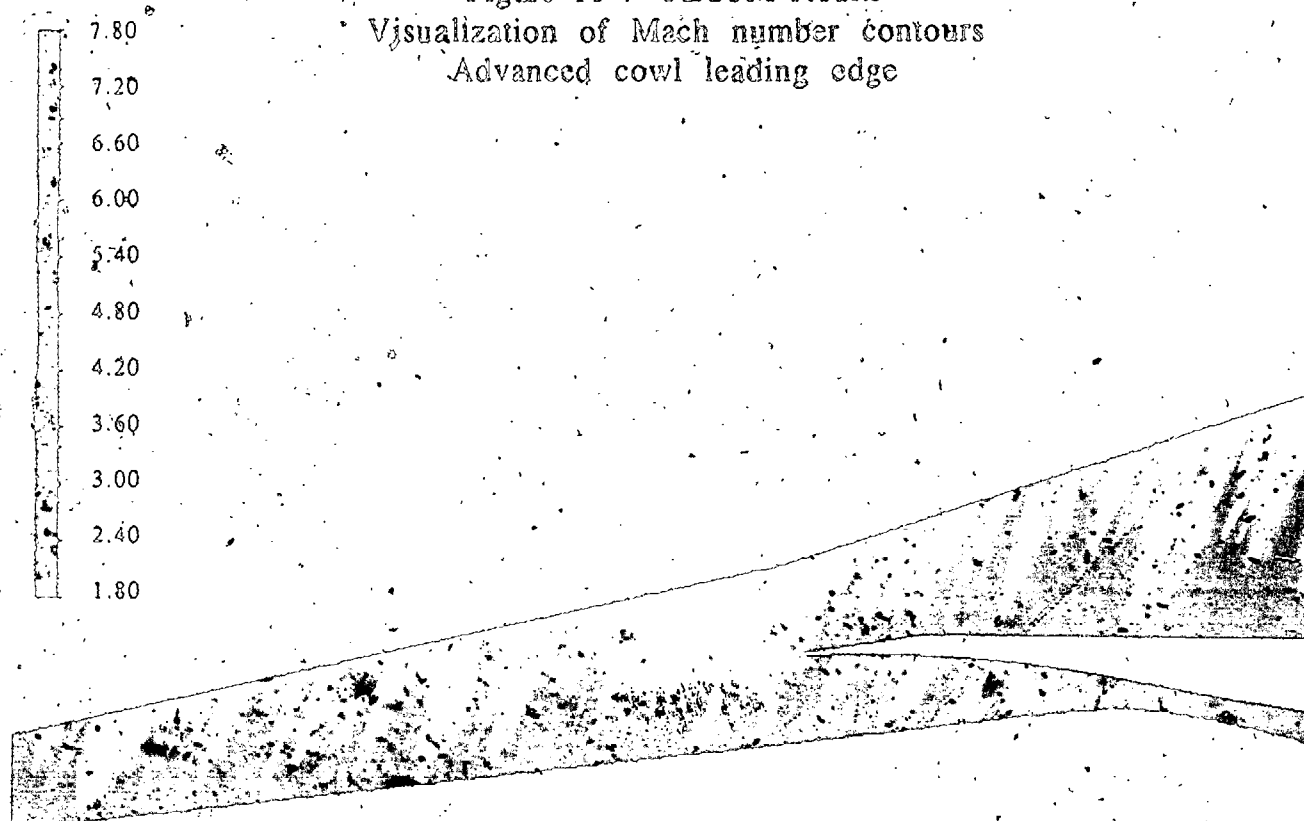


Figure 11 : FLU3M results  
Visualization of Mach number contours  
Advanced cowl leading edge



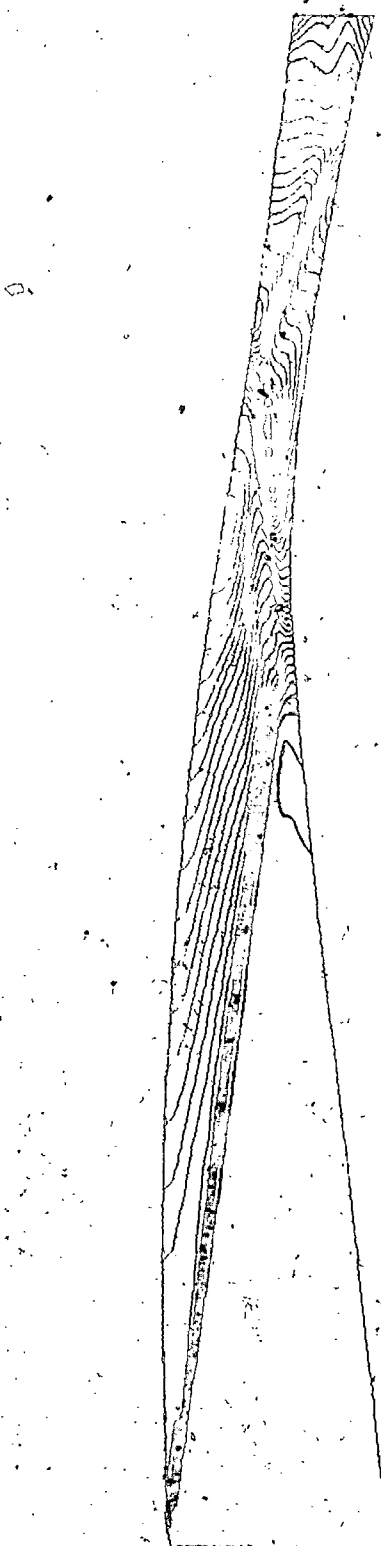


Figure 19 :  
NS2D Results  
Static pressure contours in the inlet

1	0.000
2	0.000
3	0.000
4	0.000
5	0.000
6	0.000
7	0.000
8	0.000
9	0.000
10	0.000
11	0.000
12	0.000
13	0.000
14	0.000
15	0.000
16	0.000
17	0.000
18	0.000
19	0.000
20	0.000
21	0.000
22	0.000
23	0.000
24	0.000
25	0.000
26	0.000
27	0.000
28	0.000
29	0.000
30	0.000
31	0.000
32	0.000
33	0.000
34	0.000
35	0.000
36	0.000
37	0.000
38	0.000
39	0.000

INLET

Mach = 7.40

Incidence = 0

0.000  
 0.500  
 1.000  
 1.500  
 2.000  
 2.500  
 3.000  
 3.500  
 4.000  
 4.500  
 5.000  
 5.500  
 6.000  
 6.500  
 7.000

INLET  
 TIME = 7.43  
 SCALAR = 0

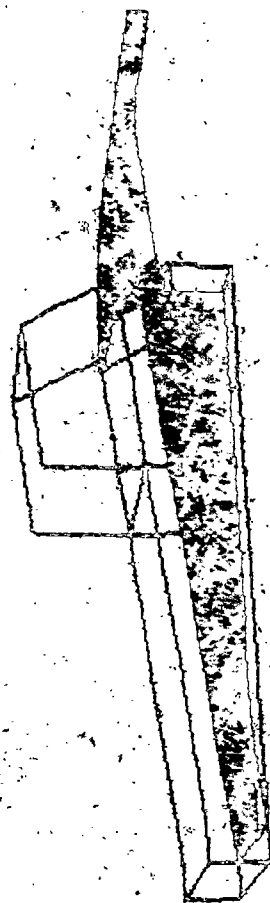


Figure 20 :  
 NS2D Results  
 Mach number contours in the whole domain  
 in the inlet

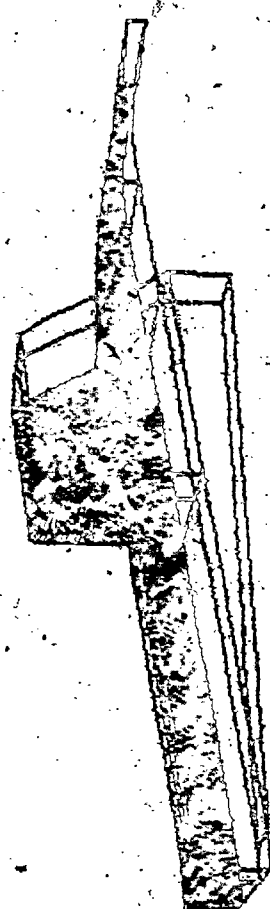


# Grid and Block Structure Utilized in P8 Inlet Analysis with the FALCON Navier-Stokes Solver

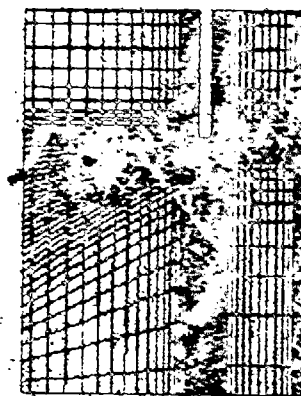
Block Structure of the grid used for the P8 Inlet analysis. The grid represents the right-half of the test configuration. The surface cells are shaded.



Grid lines are shown along the plane of symmetry (centerline). Dimensions along this cut are 251 x 41 for the 3D analysis and 251 x 81 for the 2D case.



The grid at the entrance to the inlet shows the clustering of lines to the surfaces. Dimensions in this plane are 51 x 41 for the 3D analysis with 31 points on the ramp and cowl surfaces.



Cowl

Inlet sidewall

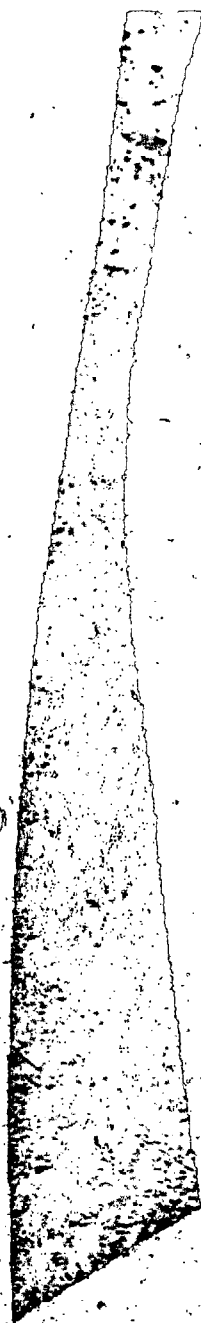


2D P2 INLET ANALYSIS (WARD TEST CASE 68)  
FALCON 2D with Baldwin-Lomax Turbulence

Converged Solution

Contour  
Levels  
0.60000  
0.25000  
0.50000  
0.75000  
1.00000  
1.25000  
1.50000  
1.75000  
2.00000  
2.25000  
2.50000  
2.75000  
3.00000  
3.25000  
3.50000  
3.75000  
4.00000  
4.25000  
4.50000  
4.75000  
5.00000  
5.25000  
5.50000  
5.75000  
6.00000  
6.25000  
6.50000  
6.75000  
7.00000  
7.25000  
7.50000

Contour  
Levels  
 $\times 1.0$

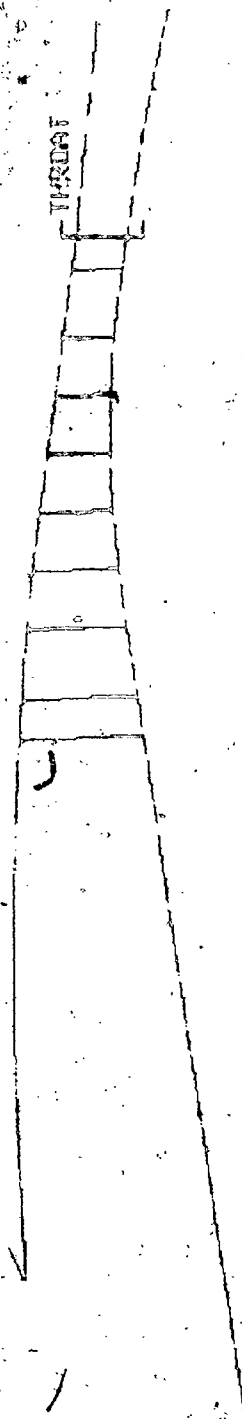


Mach Number Contours

Contour  
Levels  
 $\times 100$



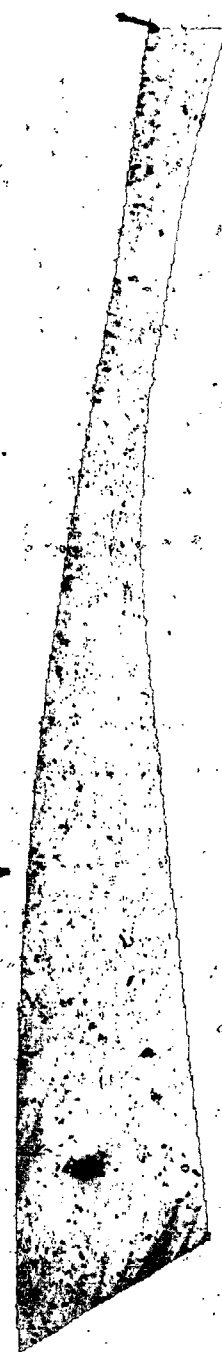
Pitot Pressure Ratio Contours



# 3D P2 INLET ANALYSIS (AGARD TEST CASE 25) FALCON 3D with BALDWIN-LDMAX TURBULENCE

Results after 5250 Iterations

- Contour Levels
- 0.60000
- 0.70000
- 0.80000
- 0.90000
- 1.00000
- 1.25000
- 1.50000
- 1.75000
- 2.00000
- 2.25000
- 2.50000
- 2.75000
- 3.00000
- 3.25000
- 3.50000
- 3.75000
- 4.00000
- 4.25000
- 4.50000
- 4.75000
- 5.00000
- 5.25000
- 5.50000
- 5.75000
- 6.00000
- 6.25000
- 6.50000
- 6.75000
- 7.00000
- 7.25000
- 7.50000



Centerline Mach Number Contours

Contour levels x 1.0



Centerline Pitot Pressure Ratio Contours

Contour levels x 100



Pitot Pressure Ratio Profiles at Station M = 0.5



Contour levels x 100

Symmetry

# 3D Falcon PB Inlet Analysis (AGARD Case J 3)

Pitot Pressure Ratio Contours

5256 Iterations

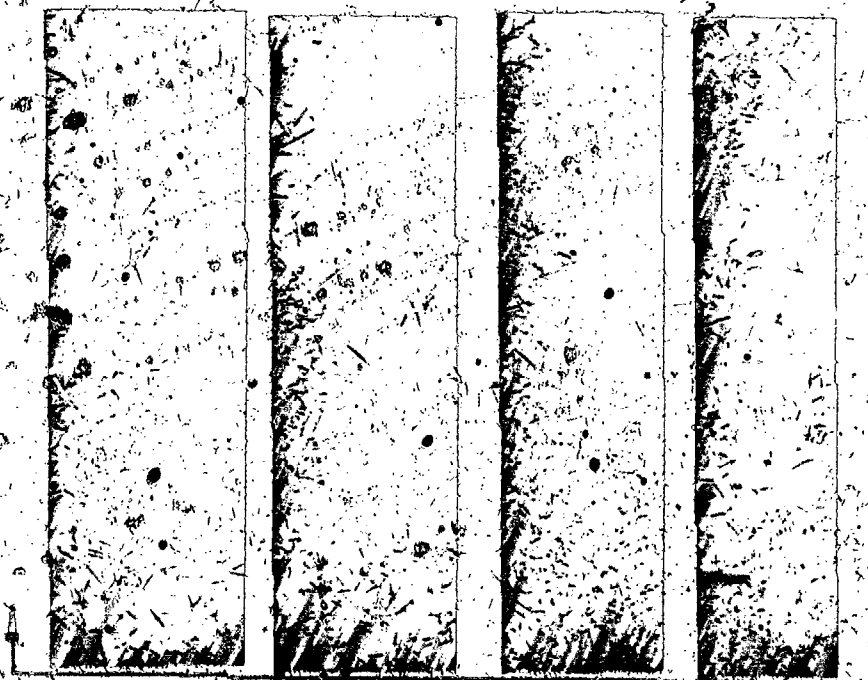
PB Inlet

Geometry

B C D E G I J K M

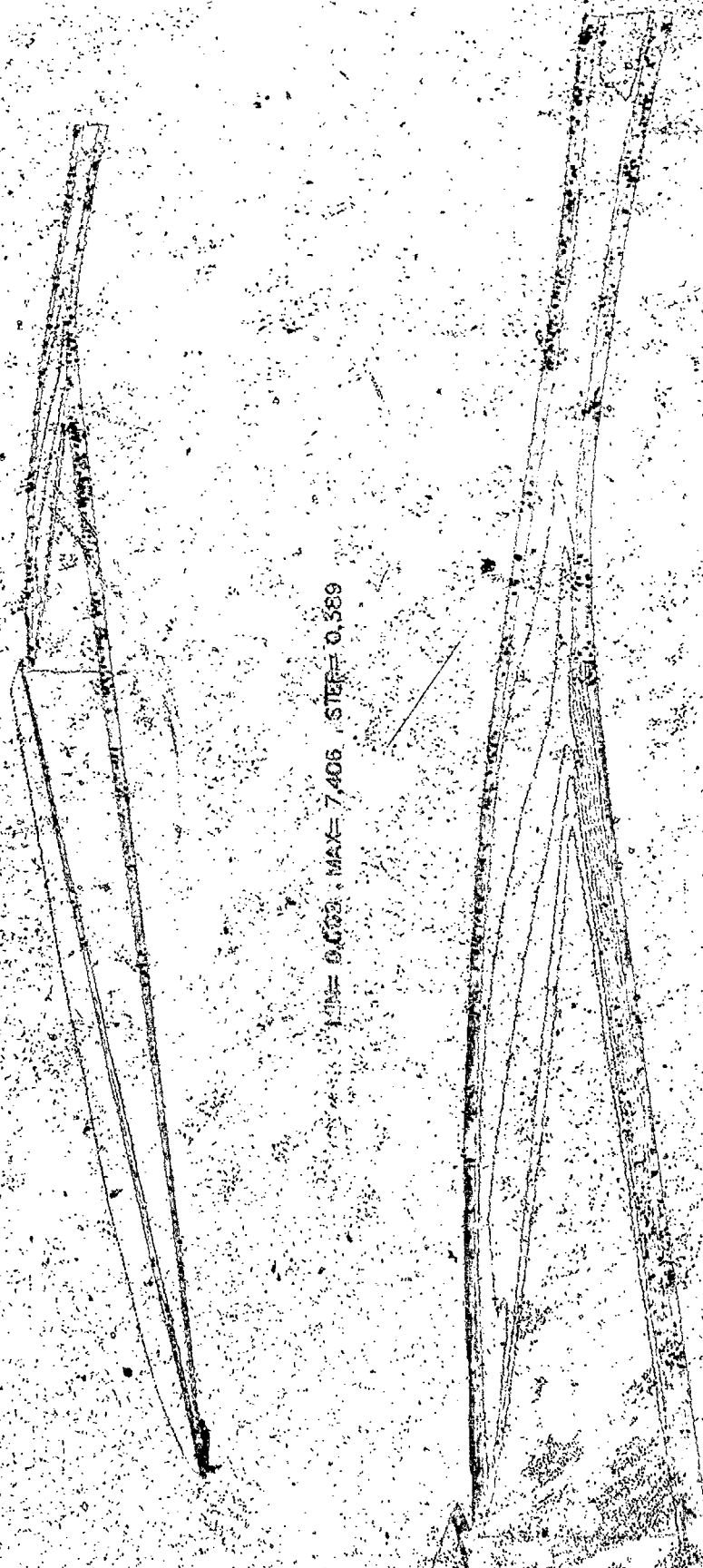
Contour

6.00000  
7.00000  
8.00000  
9.00000  
10.0000  
11.0000  
12.0000  
13.0000  
14.0000  
15.0000  
16.0000  
17.0000  
18.0000  
19.0000  
20.0000  
21.0000  
22.0000  
23.0000  
24.0000  
25.0000  
26.0000  
27.0000  
28.0000  
29.0000  
30.0000  
31.0000  
32.0000  
33.0000  
34.0000  
35.0000  
36.0000  
37.0000  
38.0000  
39.0000  
40.0000  
41.0000  
42.0000  
43.0000  
44.0000  
45.0000  
46.0000  
47.0000  
48.0000  
49.0000  
50.0000  
51.0000  
52.0000  
53.0000  
54.0000  
55.0000  
56.0000  
57.0000  
58.0000  
59.0000  
60.0000  
61.0000  
62.0000  
63.0000  
64.0000  
65.0000  
66.0000  
67.0000  
68.0000  
69.0000  
70.0000  
71.0000  
72.0000  
73.0000  
74.0000  
75.0000



Symmetry Plane

Symmetry Plane

Fig. 6 Isolines of  $\lambda$  with number

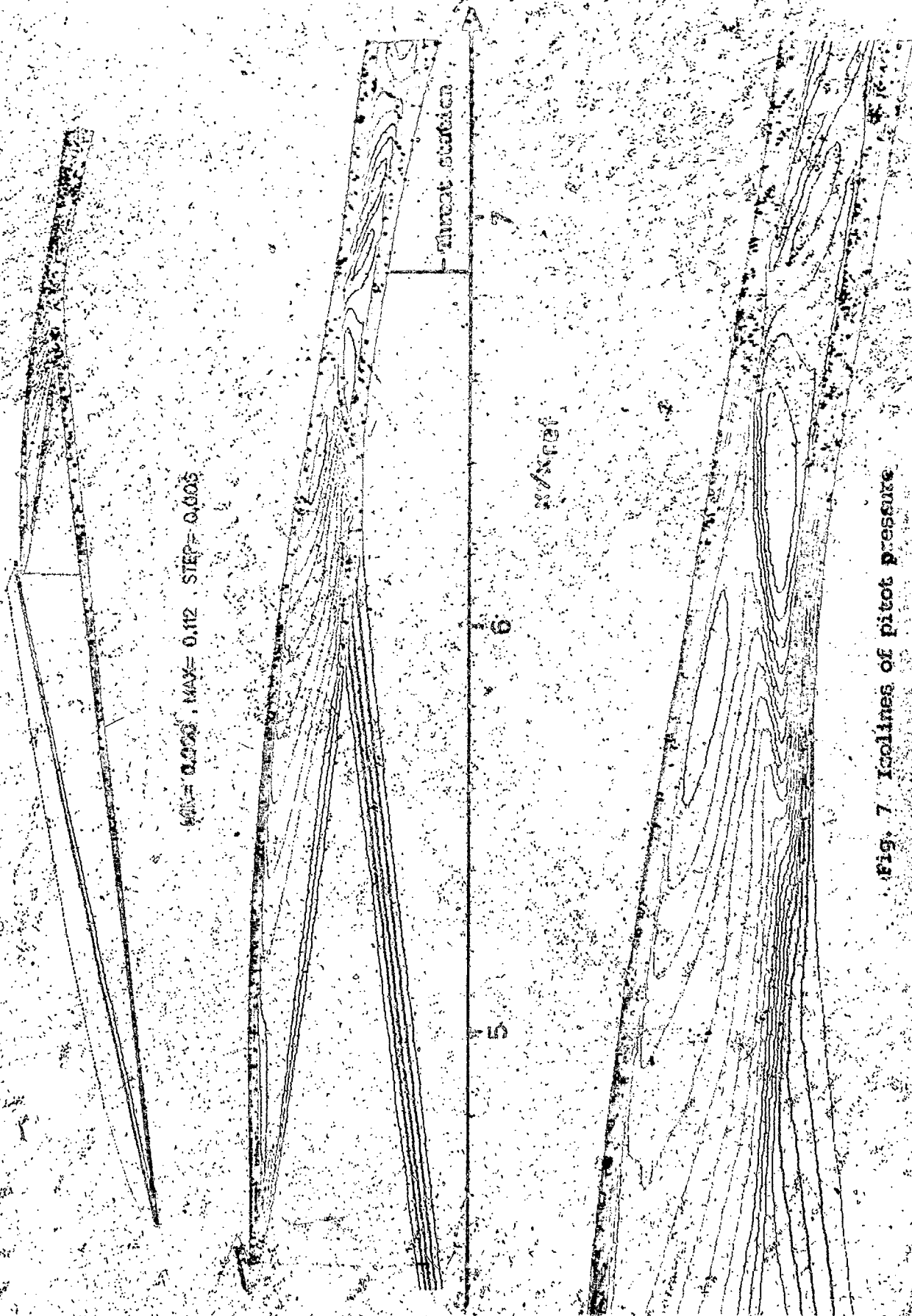


Fig. 7 Isolines of pitot pressure





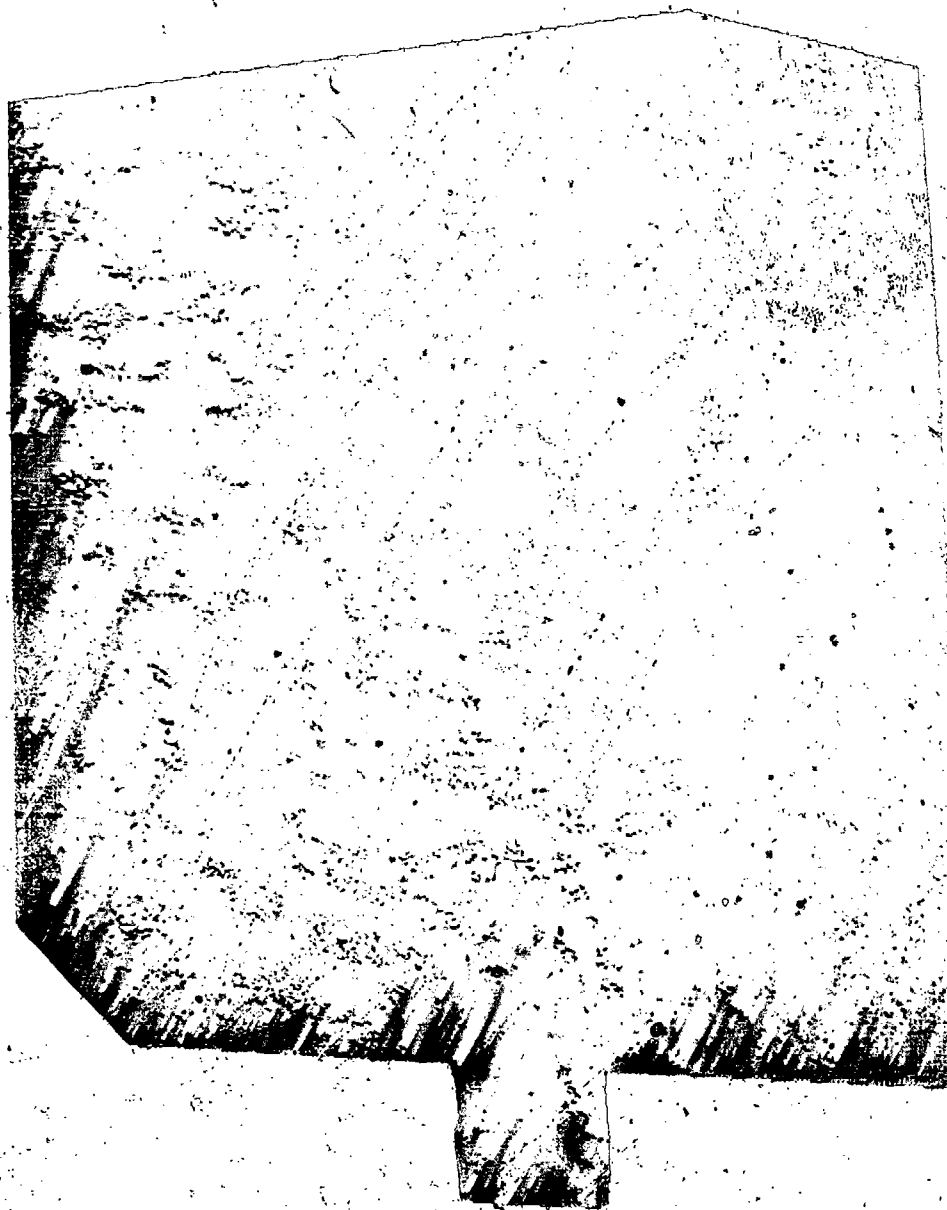
Fig. 8 Isolines of pressure coefficient  $C_p$



Fig. 14 Isolines of Kach number with adiabatic wall condition







2.7  
2.4  
2.1  
1.8  
1.5  
1.2

Figure 3: the Mach number distributions on the body and in the vertical plane of symmetry (coarse grid).





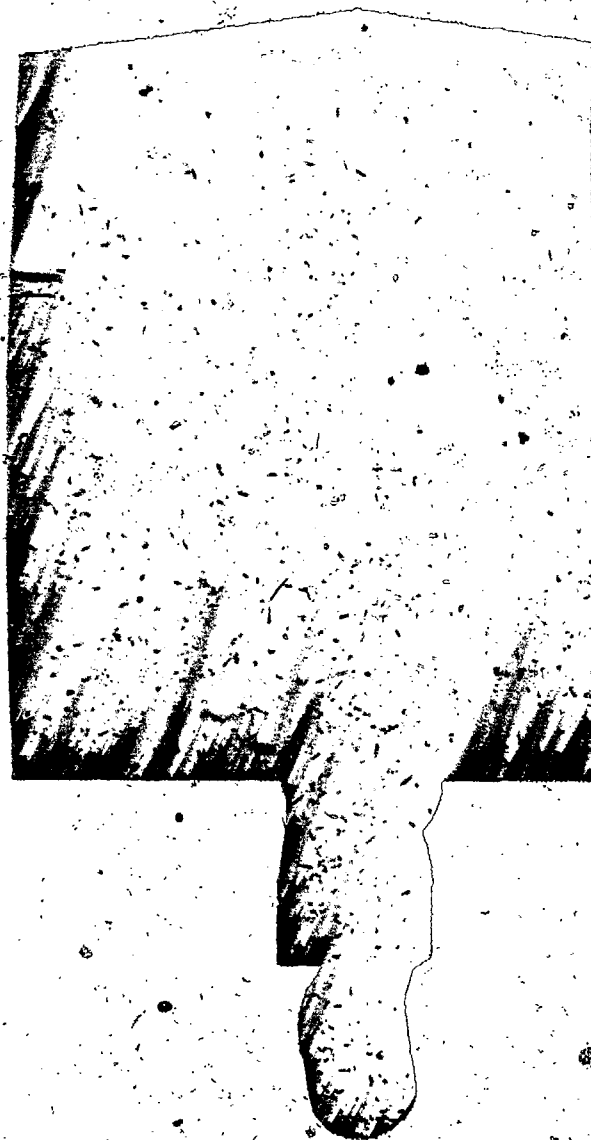


Figure 7: the static pressure ( $P/P_0$ ) distribution on the body and in the plane of symmetry of the plane (fine grid).

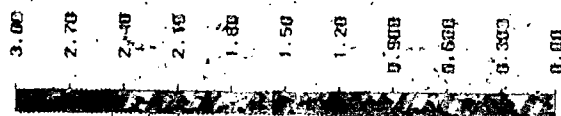


Figure 8: the Mach number distribution in the intake  
(fine grid)

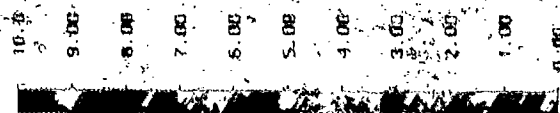


Figure 9: the static pressure (P/P0) distribution in  
the intake (fine grid)





Figure 9b1s: the Mach number distribution in the intake (fine grid)









